

平成 26 (2014) 年度 研究成果
著書・総説・発表論文等

著書・総説・発表論文等リスト

著書・総説・解説

1. 増川一、北島正治、櫻井英博、井上和仁
「糸状性シアノバクテリアの窒素固定酵素ニトロゲナーゼを利用した光生物学的水素生産」
光合成研究と産業応用最前線, **2014**, エヌ・ティー・エス, pp.273-279.
2. 大坂武男、岡島武義、松本太、北村房男
「電気化学 基礎と応用」
2015年、東京化学同人.
3. 上村大輔
「一研究者としてのひとり言」
分子研レターズ、巻頭言 (2014).
4. 上村大輔
「俊英を預かる薬学の魅力と期待」
ファルマシア、巻頭言（オピニオン） (2014).
5. 高村浩由、門田功、上村大輔
「構造解析を指向したポリオール天然物シンビオジノライドの合成研究」
有機合成化学協会誌、72 (1)、2-13 (2014).
6. 上村大輔
「生命のアイデアを、化学する」
神奈川大学Magazine PROUD BLUE、01、10-11 (2015).
7. 上村大輔
Interview, フロントランナーに聞く (座談会)
日本化学会編「生物活性分子のケミカルバイオロジー」化学同人、2-13 (2015).

発表論文

1. Kenji V. P. Nagashima, André Verme'glio, Naoki Fusada, Sakiko Nagashima, Keizo Shimada and Kazuhito Inoue
Exchange and Complementation of Genes Coding for Photosynthetic Reaction Center Core Subunits among Purple Bacteria
J. Mol. Evol. **2014**, *79*, 52–62.
2. Hajime Masukawa, Hidehiro Sakurai, Robert P. Hausinger and Kazuhito Inoue
Sustained photobiological hydrogen production in the presence of N₂ by nitrogenase mutants of the heterocyst-forming cyanobacterium *Anabaena*
International journal of hydrogen energy **2014**, *39*, 19444-19451.
3. Hidehiro Sakurai, Hajime Masukawa, Masaharu Kitashima and Kazuhito Inoue
How Close We Are to Achieving Commercially Viable Large-Scale Photobiological Hydrogen Production by Cyanobacteria: A Review of the Biological Aspects
Life **2015**, *5*, 997-1018.
4. Z.-X Zhang, M. Sadakane, S. Noro, T. Murayama, T. Kamachi, K. Yoshizawa, W. Ueda
Selective Carbon Dioxide Adsorption of ε-Keggin-type Zincomolybdate-based Purely-Inorganic 3D Frameworks
J. Mat. Chem. A **2015**, *3*, 746-755.
5. N. Narischat, T. Takeguchi, T. Tsuchiya, T. Mori, I. Ogino, S. Mukai, W. Ueda
Effect of Activation Degree of Resorcinol-Formaldehyde Carbon Gels on Carbon Monoxide Tolerance of Platinum-Ruthenium Polymer Electrolyte Fuel Cell Anode Catalyst
J. Phys. Chem. C **2014**, *118*, 23003-23010.
6. S. Ishikawa, M. Tashiro, T. Murayama, W. Ueda
Seed-assisted synthesis of crystalline Mo₃VO_x oxides and their crystal formation mechanism
Crystal Growth & Design **2014**, *14*, 4553-4561.
7. C. T. Qiu, C. Chen, S. Ishikawa, T. Murayama, W. Ueda
Crystalline Mo-V-W-mixed Oxide with Orthorhombic and Trigonal Structures as

Highly Efficient Oxidation Catalysts of Acrolein to Acrylic Acid
Top. Catal. **2014**, *57*, 1163-1170.

8. Y. Nakamura, T. Murayama, W. Ueda
Hydrogen-transfer dehydration between alcohols over V_2O_3 and MoO_2 catalysts for the formation of corresponding alkanes and aldehydes
J. Mol. Catal. A: Chem. **2014**, *394*, 137-144.
9. T. Murayama, J.-L. Chen, J. Hirata, K. Matsumoto, W. Ueda
Hydrothermal synthesis of octahedra-based layered niobium oxide and its catalytic activity as a solid acid
Catal. Sci. Technol. **2014**, *4*, 4250-4257.
10. Z.-X. Zhang, M. Sadakane, T. Murayama, W. Ueda
Investigation of the formation process of zeolite-like 3D frameworks constructed with ϵ -Keggin-type polyoxovanadomolybdates with binding bismuth ions and preparation of a nano-crystal
Dalton Trans. **2014**, *43*, 13584-13590.
11. Z.-X. Zhang, M. Sadakane, T. Murayama, N. Sakaguchi, W. Ueda
Preparation, Structural Characterization, and Ion-exchange Properties of two New Zeolite-like 3D Frameworks Constructed by ϵ -Keggin-type Polyoxometalates with Binding Metal Ions, $H_{11.4}[ZnMo_{12}O_{40}Zn_2]^{1.5-}$ and $H_{7.5}[Mn_{0.2}Mo_{12}O_{40}Mn_2]^{2.1-}$
Inorg. Chem. **2014**, *53*, 7309-7318.
12. S. Ishikawa, T. Murayama, W. Ueda
Catalysis field in orthorhombic Mo_3VO_x oxide catalyst for the selective oxidation of ethane, propane and acrolein
Catal. Today **2014**, *238*, 35-40.
13. Y. Nakamura, T. Murayama, W. Ueda
Reduced Vanadium and Molybdenum Oxides Catalyzed the Equivalent Formation of Ethane and Acetaldehyde from Ethanol
ChemCatChem **2014**, *6*, 741-744.
14. Z. X. Zhang, M. Sadakane, T. Murayama, S. Izumi, N. Yasuda, N. Sakaguchi, W. Ueda

- Tetrahedral connection of ϵ -Keggin-type polyoxometalates to form an all-inorganic octahedral molecular sieve with an intrinsic 3D pore system
Inorg. Chem. **2014**, *53*, 903-911.
15. K. Omata, K. Matasumoto, T. Murayama, W. Ueda
Direct Oxidative Transformation of Glycerol into Acrylic Acid over Phosphoric Acid Added W-V-Nb Complex Metal Oxide Catalysts
Chem. Lett. **2014**, *43*, 435-437.
16. S. Ishikawa, X. D. Yi, T. Murayama, and W. Ueda
Heptagonal channel micropore of orthorhombic Mo_3VO_x as catalysis field for the selective oxidation of ethane
Appl. Catal., General A **2014**, *474*, 10-17.
17. J. Ohyama, Y. Okata, N. Watabe, M. Katagiri, A. Nakamura, N. Arikawa, K. Shimizu, K. Takeguchi, W. Ueda, A. Satsuma
Oxygen Reduction Reaction over Silver Particles with Various Morphologies and Surface Chemical States
J. Power Sources **2014**, *245*, 998-1004.
18. T. Sengoku, S. Xu, K. Ogura, Y. Emori, K. Kitada, D. Uemura, H. Arimoto
Total Synthesis of the Antibiotic Kendomycin: A Macrocyclization Using the Tsuji-Trost Etherification
Angew. Chem. Int. Ed. **2014**, *53*, 4213-4216.
19. Y. Kawazoe, Y. Tanaka, S. Omura, D. Uemura
Design, synthesis, and evaluation, derivatives of the fat-accumulation inhibitor ternatin: toward ternatin molecular probes
Tetrahedron Lett. **2014**, *55*, 4445-4447.
20. T. Inuzuka, K. Yamamoto, A. Iwasaki, O. Ohno, K. Suenaga, Y. Kawazoe, D. Uemura
An inhibitor of the adipogenic differentiation of 3T3-L1 cells, yoshinone A, and its analogs, isolated from the marine cyanobacterium *Leptolyngbya* sp.
Tetrahedron Lett. **2014**, *55*, 6711-6714.
21. H. Takamura, H. Wada, M. Ogino, T. Kikuchi, I. Kadota, D. Uemura

- Stereodivergent Synthesis and Relative Stereostructure of the C1-C13 Fragment of Symbiodinolide
J. Org. Chem. **2015**, *80*, 3111-3123.
22. N. Hanif, K. Yamada, M. Kitamura, Y. Kawazoe, N. J. Voogd, D. Uemura
New indole alkaloids from the sponge *Plakortis* sp.
Chem. Nat. Comp, *in press*.
23. Mitsuhiro Kuriyama, Kaichiro Haruta, Takenori Dairaku, Takuya Kawamura, Shoko Kikkawa, Kiyofumi Inamoto, Hirokazu Tsukamoto, Yoshinori Kondo, Hidetaka Torigoe, Itaru Okamoto, Akira Ono, Eugene Hayato Morita, Yoshiyuki Tanaka
Hg²⁺-Trapping Beads: Hg²⁺-Specific Recognition through Thymine–Hg(II)–Thymine Base Pairing
Chem. Pharm. Bull. **2014**, *62*, 709–712.
24. Tatsuya Funai, Junko Nakamura, Yuki Miyazaki, Risa Kiri, Osamu Nakagawa, Shunichi Wada, Akira Ono, Hidehito Urata
Regulated Incorporation of Two Different Metal Ions into Programmed Sites in a Duplex by DNA Polymerase Catalyzed Primer Extension
Angew. Chem. Int. Ed. **2014**, *53*, 6624-6627.
25. Hidenobu Murata, Yusuke Kataoka, Tatsuya Kawamoto, Isao Tanaka, Takashi Taniguchi
Photocatalytic activity of α -PbO₂-type TiO₂
Phys. Status Solidi RRL **2014**, *8*, 822-826.
26. H. Aoto, K. Matsui, Y. Sakai, T. Kuchizi, H. Sekiya, H. Osada, T. Yoshida, S. Matsunaga, K. Nomiya
Zirconium(IV)- and Hafnium(IV)-Containing Polyoxometalates as Oxidation Precatalysts: Homogeneous Catalytic Epoxidation of Cyclooctene with Hydrogen Peroxide
J. Mol. Catal. A: Chem. **2014**, *394*, 224-231.
27. T. Yoshida, Y. Yasuda, E. Nagashima, H. Arai, S. Matsunaga, K. Nomiya
Various Oxygen-Centered Phosphane-gold(I) Cluster Cations Formed by Polyoxometalate (POM)-Mediated Clusterization: Effects of POMs and Phosphanes

Special Issue "Frontiers in Gold Chemistry", *Inorganics*, **2014**, 2, 660-673.

28. A. Takayama, Y. Takagi, K. Yanagita, C. Inoue, R. Yoshikawa, N. C. Kasuga, K. Nomiya
Synthesis, characterization and antimicrobial activities of sodium salt of *L*-histidinatoargentate(I) derived from the pH 11 solution
Polyhedron **2014**, 80, 151-156.
29. T. Tsuruta, T. Yamazaki, K. Watanabe, Y. Chiba, A. Yoshida, S. Naito, J. Nakazawa, S. Hikichi
Mimicking the Active Sites of Non-heme Iron Oxygenases on the Solid Supports of Catalysts: Formation of Immobilized Iron Complexes with Imidazolyl and Carboxylate Ligands
Chem. Lett. **2015**, 44, 144-146.
30. T. Nozawa, A. Yoshida, S. Hikichi, S. Naito
Effects of Re addition upon aqueous phase reforming of ethanol over TiO₂ supported Rh and Ir catalysts
Int. J. Hyd. Energy **2015**, 40, 4129-4140.
31. H. Hori, T. Sakamoto, K. Ohmura, H. Yoshikawa, T. Seita, T. Fujita, Y. Morizawa
Efficient-oxygen induced mineralization of melt-processable fluoropolymers in subcritical and supercritical water
Industrial & Engineering Chemistry Research **2014**, 53, 6934-6940.
32. H. Hori, T. Sakamoto, T. Tanabe, M. Kasuya, A. Chin, Q. Wu, K. Kannan
Iron-induced efficient decomposition of perchlorate using pressurized hot water
Organohalogen Compounds **2014**, 76, 454-458.
33. Nor A. Fadil, Govindachetty Saravanan, Gubbala V. Ramesh, Futoshi Matsumoto, Hideki Yoshikawa, Shigenori Ueda, Toyokazu Tanabe, Toru Hara, Shinsuke Ishihara, Hideyuki Murakami, Katsuhiko Ariga, Hideki Abe
Synthesis and Electrocatalytic Performance of Atomically Ordered Nickel Carbide (Ni₃C) Nanoparticles
Chem. Comm. **2014**, 50, 6451-6453.

34. Takao Gunji, Takashi Tsuda, Arockiam John Jeevagan, Masanari Hashimoto, Toyokazu Tanabe, Shingo Kaneko, Masahiro Miyauchi, Govindachetty Saravanan, Hideki Abe, Futoshi Matsumoto
Visible Light Induced Decomposition of Organic Compounds on WO₃ Loaded PtPb Cocatalysts
Catalysis Communications **2014**, *56*, 96-100.
35. Takao Gunji, Toyokazu Tanabe, Arockiam John Jeevagan, Sho Usui, Takashi Tsuda, Shingo Kaneko, Govindachetty Saravanan, Hideki Abe, Futoshi Matsumoto
Facile Route for the Preparation of Ordered Intermetallic Pt₃Pb-PtPb Core-Shell Nanoparticles and Its Enhanced Activity for Alkaline Methanol and Ethanol Oxidation
J. Power Sources **2014**, *273*, 990-998.
36. Takao Gunji, Keisuke Sakai, Yukiko Suzuki, Shingo Kaneko, Toyokazu Tanabe Futoshi Matsumoto
Enhanced Oxygen Reduction Reaction on PtPb Ordered Intermetallic Nanoparticle/TiO₂/Carbon Black in Acidic Aqueous Solutions
Catalysis Communications **2015**, *61*, 1-5.
37. Masanari Hashimoto, Takao Gunji, Arockiam John Jeevagan, Toyokazu Tanabe, Takashi Tsuda, Shingo Kaneko, Masahiro Miyauchi, Futoshi Matsumoto
Photocatalytic Activity of Pt₃Ti/WO₃ Photocatalyst under Visible-Light Irradiation
ECS Transactions, Electrochemical Society, Inc., **2014**, *61(26)*, 17-22.
38. Takao Gunji, Takashi Tsuda, Arockiam John Jeevagan, Masanari Hashimoto, Shingo Kaneko, Toyokazu Tanabe, Futoshi Matsumoto
Site-Selective Deposition of Ordered Intermetallic PtPb Nanoparticle Co-Catalysts on WO₃ Surfaces to Enhance Photocatalytic Activity
ECS Transactions, Electrochemical Society, Inc., **2014**, *61(22)*, 55-59.
39. Toshiaki Matsubara, Chikako Ueta
Computational Study of the Effects of the Steric Hindrance on the Amide Bond Cleavage
J. Phys. Chem. A **2014**, *118*, 8664-8675.
40. H. Katayama, N. Kubota, H. Hojo, A. Okada, S. Kotaka, N. Tsutsui, T. Ohira

Direct evidence for the function of crustacean insulin-like androgenic gland factor (IAG): Total chemical synthesis of IAG
Bioorg. Med. Chem. **2014**, *22*, 5783-5789.

41. M. Fukushima, S. Kotaka, N. Tsutsui, K. Asahina, S. Izumi, T. Ohira
Isolation of crustacean hyperglycemic hormone-family peptides with vitellogenesis-inhibiting activity from the shiba shrimp *Metapenaeus joyneri*
Fish. Sci. **2015**, *81*, 65-72.

42. Y. Koyama, N. Watanabe, H. K. Ijuin, M. Matsumoto
Synthesis of bicyclic dioxetanes bearing a hydroxyphenanthrene or hydroxy[4]helicene moiety and their base-induced chemiluminescent decomposition
Heterocycles **2015**, *90*, 462-481.

報告書・紀要

1. 松木悠介、星野 貴弘、増田佳奈、松井敬祐、力石紀子、松永諭、野宮健司
2013 年度神奈川大学総合理学研究所共同研究助成論文「チタン(IV)三置換 Dawson 型ポリ酸塩単量体とそれを用いた NH_4^+ イオン内包テトラポッド型四量体の合成」
Science J. of Kanagawa University, **2014**, *25*, 69-72.
2. 引地 史郎, 内藤 周弐, 吉田 暁弘, 中澤 順
錯体化学を基盤とする Bio-inspired 酸化触媒の開発
神奈川大学工学研究所所報 **2014**, 第37号, 66-75.

光合成研究と 産業応用最前線

第2編 産業応用を見据えた実用化研究 ——水素生成，人工光合成，有機系太陽電池

第3章 水素生成

第2節 糸状性シアノバクテリアの窒素固定酵素ニトロゲナーゼを
利用した光生物学的水素生産

神奈川大学 増川 一
神奈川大学 北島 正治
神奈川大学 櫻井 英博
神奈川大学 井上 和仁

「光合成研究と産業応用最前線」(2014年12月15日 株式会社エヌ・ティー・エス 刊)



第2節 糸状性シアノバクテリアの窒素固定酵素ニトロゲナーゼを利用した光生物学的水素生産

神奈川大学 増川 一 神奈川大学 北島 正治
神奈川大学 櫻井 英博 神奈川大学 井上 和仁

1. はじめに

大気中の CO₂ などの温室効果ガスの濃度上昇が気候変動に及ぼす悪影響が、世界的に懸念されている。このような状況を背景に、我が国においては、原子力発電所の深刻な事故もあり、自然エネルギーを利用した再生可能エネルギー資源（燃料）の大規模な創出が強く望まれている。地表に到達する太陽光エネルギーは、人類が消費する化石燃料エネルギーの 6,000 倍以上と膨大であり、量的に再生可能エネルギー源として有望であるが、その平均エネルギー密度は約 1,500 kWh・m⁻²・yr⁻¹ と低く、いかにして経済性を確保しつつこれを利用するかが課題となる。植物や藻類などの光合成生物を利用したバイオ燃料の研究はさまざまに行われているが、エネルギー変換効率、経済性、大規模化、食料生産との競合など克服すべき課題は多い。本稿では、糸状性シアノバクテリアを利用した光生物学的水素生産に関する研究の現状について、筆者らが行っている研究を中心に紹介する。

2. 糸状性シアノバクテリア

シアノバクテリアは植物や藻類と同様に水を光合成の電子供与体として用いる酸素発生型の光合成を行う原核生物（細菌）である。紅色光合成細菌や緑色細菌などのいわゆる光合成細菌は水を光合成の電子供与体に用いることができず、有機酸や硫化水素などを用いて光合成を行う。水を使って光合成を行うシアノバクテリアを利用したバイオ燃料の生産は、資源量が大きいという利点がある。シアノバクテリアは形態学的にも、生態学的にも非常に大きな多様性をもつ細菌群である。この中で一部の糸状性シアノバクテリア (*Anabaena* や *Nostoc* 属など) は、硝酸塩類などの窒素栄養源が欠乏した条件下では、通常酸素発生型光合成を行う栄養細胞の一部が、約 10~20 細胞の間隔で異型細胞（ヘテロシスト）へと分化し、窒素固定酵素ニトロゲナーゼの反応により大気中の N₂ を還元しアンモニア (NH₃) を生産する。

ヘテロシストは、酸素発生の源となる光化学系Ⅱが不活性化され、加えて細胞壁を肥厚させて外部から細胞内への酸素透過を防ぎ、呼吸活性を増加させて酸素を除去しているため、細胞内部の酸素濃度は低い状態に保たれている。このため、酸素により失活しやすいニトロゲナーゼが、ヘテロシスト内では活性を維持することができる。このとき、糸状体全体としては、栄養細胞で酸素発生型光合成による糖質合成が行われ、その糖質がヘテロシストに供給され、ニ

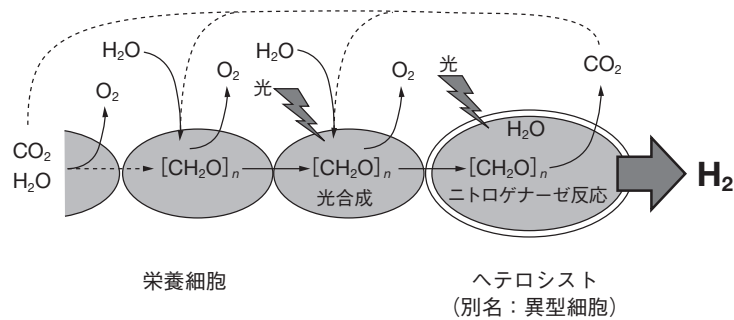
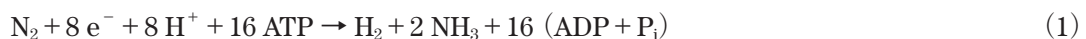


図1 糸状性シアノバクテリアにおけるヘテロシストと栄養細胞の分業

トロゲナーゼ反応を駆動する還元力の源となる。また、ヘテロシストには光化学系 I が存在するので、循環的な電子伝達を利用した光リン酸化反応により、ニトロゲナーゼ反応に必要な ATP を生産できる。また、ATP は活発な呼吸活性によっても供給される。ニトロゲナーゼにより合成された NH_3 はグルタミンに変換されて栄養細胞へと輸送される。このように2種の細胞の分業によって、光合成と窒素固定が空間的に分離されることにより、糸状体全体として酸素発生型光合成とニトロゲナーゼ反応の両立が可能となる (図1)。

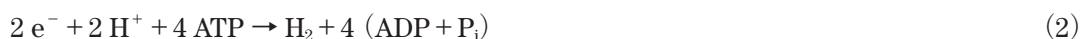
3. ニトロゲナーゼ

ニトロゲナーゼは N_2 を固定する酵素として知られているが、必然的な副産物として H_2 も生産される (式(1))。シアノバクテリアのほか、マメ科植物の根に共生する根粒菌など一部の原核生物がその活性をもつ。酸素発生型光合成生物のうち、ニトロゲナーゼをもつのは一部のシアノバクテリアに限られ、クロレラなどの真核光合成生物はもたない。この酵素は、多くの場合、モリブデン (Mo)、鉄 (Fe)、硫黄 (S) からなる金属クラスターを結合している (Mo 型ニトロゲナーゼ) が、Mo の代わりにバナジウム (V) を結合するもの (V 型ニトロゲナーゼ) や Fe のみ (Fe-only 型ニトロゲナーゼ) をもつものもある。窒素固定の効率が最も高いとき (N_2 濃度が十分高いとき)、Mo 型ニトロゲナーゼの反応は、式(1) のように表され、電子の 1/4 が水素生産に向けられる：



V 型、Fe-only 型ニトロゲナーゼは、Mo 型よりも窒素固定の効率が低いといわれる。換言すれば、多くの割合の電子が水素生産に向けられる。

N_2 が存在しない条件下 (例：Ar 気相) では、すべての電子が水素生産に向かう。



ニトロゲナーゼは、式(2) に示されるように大量の ATP (生体の高エネルギー物質) を消費するので、水素生産の理論的最低エネルギー変換効率は低いが、水素生産が不可逆的に起こることが、その利点である。

水素生産に利用できる酵素として、シアノバクテリアはヒドロゲナーゼをもつ。可逆的ヒド

ロゲナーゼは反応に ATP を消費しないので、水素生産の理論的最高エネルギー変換効率が高いが、反応は可逆的なため、光合成により生成する O_2 の存在下では生産された H_2 の再吸収が起こりやすい。また、ほとんどの窒素固定生物は、ニトロゲナーゼによって発生した H_2 を再吸収する取り込み型ヒドロゲナーゼ (Hup) をもち、Hup 活性の存在は、水素生産を妨げるが、その活性除去は可能である (以下参照)。

筆者らは、このような総合的判断から、ニトロゲナーゼを基礎とする水素生産方式を採用し、その研究開発に取り組んでいる¹⁻⁴⁾。

4. 遺伝子工学による改良

4.1 形質転換法

光合成の研究によく用いられる *Synechocystis* sp. PCC6803 は自然形質転換が可能で、単に DNA と細胞を混合するだけで DNA は細胞内に取り込まれて、相同組み換えでゲノムに取り込ませることが可能であるが、窒素固定活性をもたない。一方、多くのシアノバクテリア (*Nostoc*, *Anabaena* など) は、自然形質転換は起こりにくく、独自の制限酵素系をもつため、形質転換にはその認識部位をあらかじめ DNA メチラーゼ遺伝子を組み込んだ大腸菌内でメチル化する必要がある。筆者らは、Wolk らの開発した triparental mating 法⁵⁾を用いて、*Nostoc* や *Anabaena* の形質転換を行っている。この方法は、形質転換させたいシアノバクテリア株と、その株がもつ制限酵素の認識部位をメチル化するメチラーゼ遺伝子と導入したい遺伝子の両方をもつ大腸菌株、さらに接合性プラスミドをもつ大腸菌の3種の細菌細胞を混合後、形質転換されたシアノバクテリア株を薬剤耐性によりスクリーニングする。*Nostoc* や *Anabaena* では、相同組換えはまず1点で起こるが、このような変異株では復帰突然変異を生じやすい。復帰突然変異を防ぐために、2点での相同組換えによる遺伝子置換株を選抜するが、1点相同組換え株を単離後、もう一度接合による形質転換、薬剤耐性および *sacB* 遺伝子を用いたスクロース耐性によるスクリーニングを行うので、自然形質転換法に比べて時間と労力が必要となる。

4.2 取り込み型ヒドロゲナーゼの遺伝子 *hupL* の破壊

Nostoc/Anabaena sp. PCC7210 株は、窒素固定シアノバクテリアとして初めて全ゲノム塩基配列が明らかにされた株である⁶⁾。この株は、取り込み型 (Hup) および双方向型 (Hox) の2種類のヒドロゲナーゼ遺伝子をもつ²⁷⁾。また、*Nostoc* sp. PCC7422 株は、筆者らが各国の株保存センターから入手した13種のシアノバクテリア株の中から、光合成に基づくニトロゲナーゼ活性が最も高い株として選んだものである⁸⁾。この株は Hox 活性がほとんどなく、Hup 活性のみが高い。筆者らは、この2株を主に用いて遺伝子工学的な改良を行った。*Nostoc* sp. PCC7422 の Hup 活性を遺伝子工学的に不活性化した変異株 Δ Hup 株では、水素生産活性が野生株に比べて3倍程度増加し、光合成による酸素発生を行いながら水素を約 30% (v/v) まで蓄積できた⁸⁾。

4.3 ホモクエン酸合成酵素遺伝子 *nifV* の破壊

Mo 型ニトロゲナーゼは N_2 還元のための触媒活性部位である FeMo-cofactor と呼ばれる金属クラスターを結合するモリブデン・鉄タンパク質（ジニトロゲナーゼ）とこれに電子を供給する鉄タンパク質（ジニトロゲナーゼレダクターゼ）から構成される⁹⁾。モリブデン・鉄タンパク質は *nifD* 遺伝子がコードする α サブユニット 2 個と *nifK* 遺伝子がコードする β サブユニット 2 個からなるヘテロ四量体から構成されるが、結晶構造解析によると FeMo-cofactor はシステイン残基とヒスチジン残基を介して α サブユニットに結合している（図 2）。FeMo-cofactor の Mo 原子に結合するホモクエン酸は、効率的な窒素固定反応を行うためには必須であり、従属栄養細菌 *Klebsiella pneumoniae* では、ホモクエン酸の合成酵素遺伝子 *nifV* を破壊すると、ホモクエン酸の代わりに炭素鎖が 1 つ短いクエン酸が FeMo-cofactor に結合するようになり¹⁰⁾、 N_2 還元はほとんどできなくなるが、水素生産は野生株と同程度の活性をもつ¹¹⁾。Masukawa ら¹²⁾は *Anabaena* PCC7120 の Δ Hup 株を親株としてヘテロシスト内で発現するホモクエン酸合成酵素の遺伝子 *nifVI* の破壊株を作成した。この株は親株である Δ Hup 株に比べて培養液あたり水素生産性が 2 倍程度増加した。

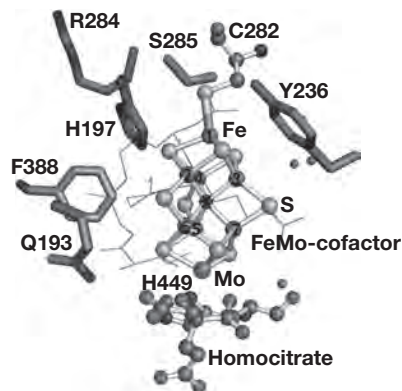


図 2 Mo 型ニトロゲナーゼの FeMo-cofactor 周辺の立体構造

文献 13) 中の fig. 1

Copyright©American Society for Microbiology; *Appl. Environ. Microbiol.*, 76, 6741-6750 (2010)

※口絵参照

4.4 FeMo-cofactor 周辺を取り巻くアミノ酸残基の部位特異的置換株

Masukawa ら¹³⁾は、 N_2 ガス存在下ではニトロゲナーゼ反応（式 1）における電子の大部分（約 3/4）が窒素固定に使われ、水素生産に使われる電子がわずか（約 1/4）であるため、この電子配分比率を遺伝子工学的的手法により変更し、 N_2 存在下でも窒素固定活性が低く、水素生産活性が上昇する変異株を作成した。ニトロゲナーゼは、その活性部位に Mo と Fe からなる金属クラスターをもち、その近傍には高度に保存されたアミノ酸残基が位置している。*Azotobacter* の酵素の立体構造情報をもとに、活性中心近傍アミノ酸残基の中から 6 つの残基を選び（図 2）、別の残基への置換株（一点交差置換株）を合計 49 株作成した。ほとんどの変異株で窒素固定活性が大幅に低下したが、そのうちのいくつかの株は、 N_2 存在下でも水素生産の低下が見られず、親株 Δ Hup 株と比較して、約 3~4 倍高い水素生産活性を示した。 N_2 存在下での約 1 週間にわたる水素蓄積実験では、親株は窒素固定活性が高いため、1~2 日で窒素栄養充足となりニトロゲナーゼ活性、水素生産活性がともに低下し、その結果、蓄積された水素濃度は 1% 以下であった。一方、ニトロゲナーゼのアミノ酸残基置換株の一部（例：Q193S, R284H 株など）は、窒素固定活性が大幅に低下しているのに、 N_2 存在下でも窒素栄養充足になりやすく、活性が数日間持続し、蓄積した水素の濃度は最大で気相の 6% (v/v) に達した。このような改変株を用いることで、 N_2 存在下でも高活性を持続させることができ、水素生産のための Ar のガスコストを削減できる可能性が示された。

5. 水素バリア性プラスチック素材を利用したバイオリクター

Amos¹⁴⁾は藻類の光合成を利用した大規模エネルギー生産において、経済性を確保するためにはバイオリクターのコスト低減が重要な課題だと指摘し、受光面1m²あたり\$10台以内のバイオリクターが必要だと結論している。

筆者らは水素バリア性プラスチック膜を含む3層のプラスチックバックを用いることで、安価なバイオリクターの作成が可能であると提案している¹⁵⁾。水素バリア性プラスチック膜を用いた実験用にガスサンプリングポートの開発を行った(図3)。ガスサンプリングポートは、バック内にブチルゴムセパタムを付けたインナーパッドを入れ、プラスチックフィルムの外からブチルゴムセパタムを付けた押しネジもしくはニードルポートで挟み込み、ナットホイールで押しネジを繰り出すことで、プラスチックフィルムの内側と外側からブチルゴムセパタムで挟み込む構造のものを設計した。水素バリア性プラスチック膜として、Besela フィルムおよび GL フィルム (いずれも凸版印刷株)

を選択し、水素のバリア性について検討した。両者とも PET 樹脂フィルムをベースとしたラミネート膜で、水素ガスバリア層は前者がアクリル酸樹脂系高分子コート、後者が酸化アルミニウムコートとなっている。どちらも水素ガスバリア層の上に、二軸延伸ナイロン層、さらに無延伸ポリプロピレン (CPP) または直鎖状低密度ポリエチレン (LLDPE) 層がラミネートされている。これら4種類のバックをオートクレーブ滅菌処理 (120℃,

20 min), または間歇滅菌処理 (100℃, 20 min, 3 回) したものを、および未加熱処理のものを熱融着によって密閉バックを作り、内部に封入した水素ガスの透過性を測定した(表1)。一例を挙げると、ガスサンプリングポートを付けた GI-E バックに 17.1% (v/v) となるように水素ガスを注入し、ニードルポートから適時サンプリングを行い、内部水素ガス濃度の測定を行ったところ、15日目でも

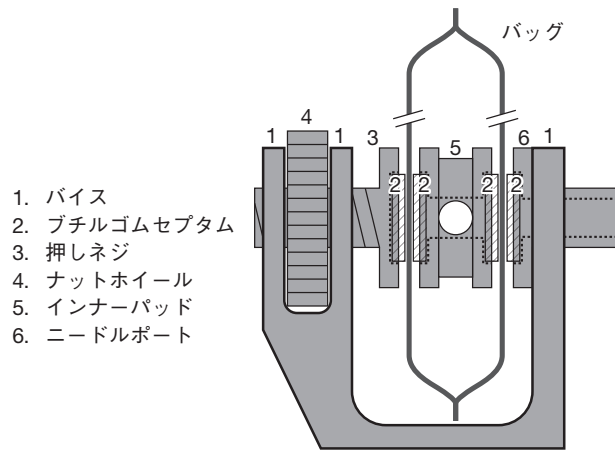


図3 ガスサンプリングデバイス

文献 15) より改変((公社)日本農芸化学会の許可を得て掲載)

表1 Besela フィルムおよび GL フィルムの水素透過性

処理方法	プラスチック素材	Km:H ₂ 透過性 [cm ³ ・m ⁻² ・day ⁻¹ ・atm ⁻¹]
未処理	Be-E	87
	Be-P	44
	GI-E	49
	GI-P	44
100℃×20 min 3 回間歇滅菌	Be-E	22
	Be-P	53
	GI-E	29
	GI-P	48
120℃×20 min オートクレーブ滅菌	Be-E	89
	Be-P	67
	GI-P	41

Be: Besela フィルム, GI: GL フィルム, E: 直鎖状低密度ポリエチレン, P: 無延伸ポリプロピレン

文献 15) より改変((公社)日本農芸化学会の許可を得て掲載)

15%程度の濃度が保たれた。同様の測定を4種類の未加熱および加熱処理済みフィルムで行い、水素透過性を算出した。これらプラスチックバッグの水素透過性は $20\sim 90\text{ cm}^3\cdot\text{m}^{-2}\cdot\text{day}^{-1}\cdot\text{atm}^{-1}$ 程度であり、将来の実用化の材料として候補となりうることが示された。なお、上記の水素バリア性バッグ、ガスサンプリングポートは Wakhy 社が製作したものが、GLサイエンスから市販されている。

また、加熱処理の GI-E を用いて、密閉容器内での水素生産量とプラスチックバッグ内での水素生産量を比較した。窒素栄養充足培地 (BG11) から窒素欠乏培地 (BG11₀) へと移した *Nostoc* sp. PCC7422 ΔHupL 株の細胞培養液を、同じ直径で高さの異なるガラス容器に等量ずつ分注し、一方の容器はブチルゴム栓で密閉、もう一方の容器はガスサンプリングポートを付けたプラスチックバッグに入れ、初期気体体積はほぼ同じにした。プラスチックバッグ内の初期気相を N₂ が 1%、CO₂ が 5%、Ar が 94% になるようにして、12 時間ごとの明暗周期光照射を行いながら生産された H₂ の蓄積量を測定した(図 4)。その結果、3 日目まではどちらの H₂ 蓄積量もほぼ同等であったが、光照射後 9 日目ではプラスチックバッグの H₂ 蓄積量が密閉容器に比べて約 30% 程度多かった。これは、シアノバクテリアの光生物学的水素生産に伴って生じた O₂ の分圧が、気体の膨張が可能なバッグ中では密閉容器中よりも低く保たれ、ニトロゲナーゼの活性低下の程度が軽減されたためだと説明されよう。



図 4 水素バリア性プラスチックバッグを用いたシアノバクテリアの培養
縦 300 mm, 横 100 mm のプラスチックバッグにガスサンプリングポートを 1 個装着し、250 mL のシアノバクテリア培養液を入れた。初期気相 (1% N₂, 5% CO₂, 94% Ar) を 250 mL として植物培養用の蛍光灯下に置くと、H₂ と O₂ がほぼ 2:1 の比で蓄積し、しだいにバッグが膨らんでいく

6. 今後の課題

シアノバクテリアを利用した水素生産の実用化のためには、経済的かつ大規模に行うためのさまざまな課題を克服する必要がある。水素生産の低コスト化につながるシアノバクテリアのさまざまな改良が必要で、上述のように筆者らは、ニトロゲナーゼのアミノ酸残基置換により、コストのかかる Ar ガスを使用せず、N₂ 気相下でも高い水素生産活性を数週間にわたり持続させることに成功したが、今後、エネルギー変換効率や長期の生産安定性をさらに向上させる必要がある。そのための改変として、現在筆者らが取り組んでいる研究例を最後に紹介する。

水素生産に最適なシアノバクテリア株を作出するために、水素生産を行う細胞であるヘテロシストの形成頻度を通常の 5~10% から増加させることが考えられ、これまでにその頻度を 10% 以上に増加させた変異株を多数作成することに成功している。これらの変異株では、特定の条件下で水素生産性がさらに向上する可能性がある。N₂ 気相下での水素生産の変換効率は、優先的に発現する Mo 型ニトロゲナーゼよりも、V 型や Fe-only 型ニトロゲナーゼのほうが高

い可能性が考えられるので、後者のタイプのニトロゲナーゼを発現させたシアノバクテリア株の作成は試みる価値がある。また、屋外での水素生産では強光阻害を受けるので、強光により光合成活性が低下しないように、光化学系や色素系などの改変が考えられる。水素生産の大規模化のために、プラスチックバッグの大型化、多層化も今後必要である。これらの改良を積み重ねることで、水素生産が強光下で数週間持続するようにし、光から水素へのエネルギー変換効率を1%以上に高めることが当面の目標である。

文 献

- 1) H. Masukawa et al. : *Ambio*, **41**, 169–173 (2012).
- 2) H. Sakurai et al. : *J. Photochem. Photobiol., C-Photochem. Rev.*, **17**, 1–25 (2013).
- 3) H. Sakurai et al. : *Mar. Biotechnol.*, **9**, 128–145 (2007).
- 4) 増川一ほか：微細藻類によるエネルギー生産と事業展望，80–87，シーエムシー出版(2012)。
- 5) T. Thiel et al. : *Methods Enzymol.*, **153**, 232–243 (1987).
- 6) T. Kaneko et al. : *DNA Res.*, **8**, 205–213 (2001).
- 7) P. Tamagnini et al. : *Microbiol. Mol. Biol. Rev.*, **66**, 1–20 (2002).
- 8) F. Yoshino et al. : *Mar. Biotechnol.*, **9**, 101–112 (2007).
- 9) L.C. Seefeldt et al. : *Annu. Rev. Biochem.*, **78**, 701–722 (2009).
- 10) S.M. Mayer et al. : *J. Biol. Chem.*, **277**, 35263–35266 (2002).
- 11) P.A. McLean et al. : *Nature*, **292**, 655–656 (1981).
- 12) H. Masukawa et al. : *Appl. Environ. Microbiol.*, **73**, 7562–7570 (2007).
- 13) H. Masukawa et al. : *Appl. Environ. Microbiol.*, **76**, 6741–6750 (2010).
- 14) W.A. Amos : Milestone Completion Report NREL, Golden, CO, 2004, Jan., <http://www.nrel.gov/docs/fy04osti/35593.pdf> (2014年5月3日アクセス)。
- 15) M. Kitashima et al. : *Biosci. Biotech. Biochem.*, **76**, 831–833 (2012).

電気化学 基礎と応用

K.B.Oldham・J.C.Myland・A.M.Bond 著

大坂武男・岡島武義・松本 太・北村房男 訳



東京化学同人

一研究者としてのひとり言

上村 大輔

神奈川大学 理学部 教授

最近10月になると、やたらそわそわする。私達にとってノーベル週間がそれほど遠いものではなくなったのである。ある時期、11年間に6人の日本人がノーベル化学賞を受賞し、加えてノーベル物理学賞の受賞も重なった。いったいどうした事であろうか。優秀な人材が科学の世界に飛び込み、日々努力していた結果であることは当然であるが、他にも幾つかの理由が見えて来る。少し私なりに考えてみたい。

昭和40年ごろ高度成長に日本中が沸き返り、社会全体は世界の中心での活躍に向けて大きく舵取りを進めることになっていった。多くの若者は、世界の動向をより知ろうと、少しでも多くの知識を持った人をもとめていたし、出会いに喚起されて実際に世界に飛び出し、さらに情報量、研究力を深め、世界を思い切り取り込もうとした。日本の頭脳流出と言われたのもこの時代であった。

一方、国内に残った若者も、ただ手をこまねいていたわけではない。黙々と力をつけた者もいた。京都、大阪での講演会や、研究室勉強会に参加し、お互いに力をつけていたのである。社会的な封鎖感、保守的な傾向に対して、許された状況の中で頑張った人たちもいたが、反発して研究室を変え国内の地方へと散っていった人たちも数多かった。じっと待ってはおれなかったし、上述の留学を含めて自発的に行動を起こしたのである。個性と自己主張を大切にしつつ初志貫徹を貫いたといえる。ある人は政治的な活動や、また大学の閉塞感から脱出して、地方で自由を獲得したことになる。地方で若

い人材が目立ち始めた時期でもあった。輝き解き放たれた駿馬を予感した。ただし、国内の研究費は未だ十分ではなく、そもそも制度設計のうえで、どういった研究資金の配分が適切かと試行錯誤がなされている段階であった。アメリカからの研究費援助を受けていた国内研究室もちらほらあった。一方、世界へ飛び出た人たちは、財政的な辛苦から解き放たれ、全力で研究に没頭できた。しかし、研究費申請など、国外でも大変であった事は後から分かってきた。

こういった状況の中で、研究分野を問わず広く研究費を配分するという日本独特の、素晴らしい環境が出来ていった。これが科学研究費の誕生であり、広く薄いが新鮮味のあるボーナス的な意味を持った研究費で、胸躍るものであった。定年までに一度は一般研究Aを獲得できないかと思った時代でもある。大きな有名研究室でなければ採択されない、厳しい研究費と認識されていた。若い研究者には一般研究B、Cに加えて、特定研究、がん特別研究などもあり、各分野も潤ったし、人的交流も深まった。この時代の研究費が血となり肉となって、若い研究者の足腰を丈夫にしたことは、皆さんの認識されている通りである。冒頭で述べた日本人研究者のノーベル賞受賞に繋がったことも事実であろう。科学研究費の枠組み構築に関与された先輩諸氏に心より御礼したいと考える昨今である。

今日を見てみると、応用的な方面や一部若手の補助など限られた研究者に対する特別大型な予算が増えている。これはそれで良いのだが、研究者の層



の厚さについて今少し配慮されるべきであろう。アメリカのオバマ大統領は日本の産業界の強さに感服して国立高等専門学校機構の視察を行うように命じたと聞く。これも我が国の強みが、研究者の層の厚さ、技術力の確かさにあることを知ってのことだろう。層の厚さを支える科学研究費と、選抜的な大型予算は異なるもので、同じ審査システムで科学研究費が配分されてはならないことを強調したい。

誠心誠意、それぞれの分野の世界最先端で研究を推進する限り、無駄な研究などはないのである。個性と自己主張を大切に、宇宙環境での新材料生産研究や新分子科学なども含めて、新しい未開拓分野に挑戦しようではないか。

うえむら・だいすけ

1973年名古屋大学理学部助手、1979年静岡大学教養部助教授、1991年教授、1995年同理学部教授、その間、ハーバード大学客員研究員（1982年6月～9月）、(財)相模中央化学研究所研究顧問（1991年～2000年）。1997年名古屋大学大学院理学研究科教授、2008年慶應義塾大学理工学部教授、2011年神奈川大学理学部化学科教授、現在に至る。1977年日本化学会進歩賞、2006年日本化学会学会賞、2007年中日文化賞、2009年内藤記念科学振興賞、2009年紫綬褒章、2012年ナカニシプライズを受賞。

Exchange and Complementation of Genes Coding for Photosynthetic Reaction Center Core Subunits among Purple Bacteria

Kenji V. P. Nagashima, André Verméglio, Naoki Fusada, Sakiko Nagashima, Keizo Shimada & Kazuhito Inoue

Journal of Molecular Evolution

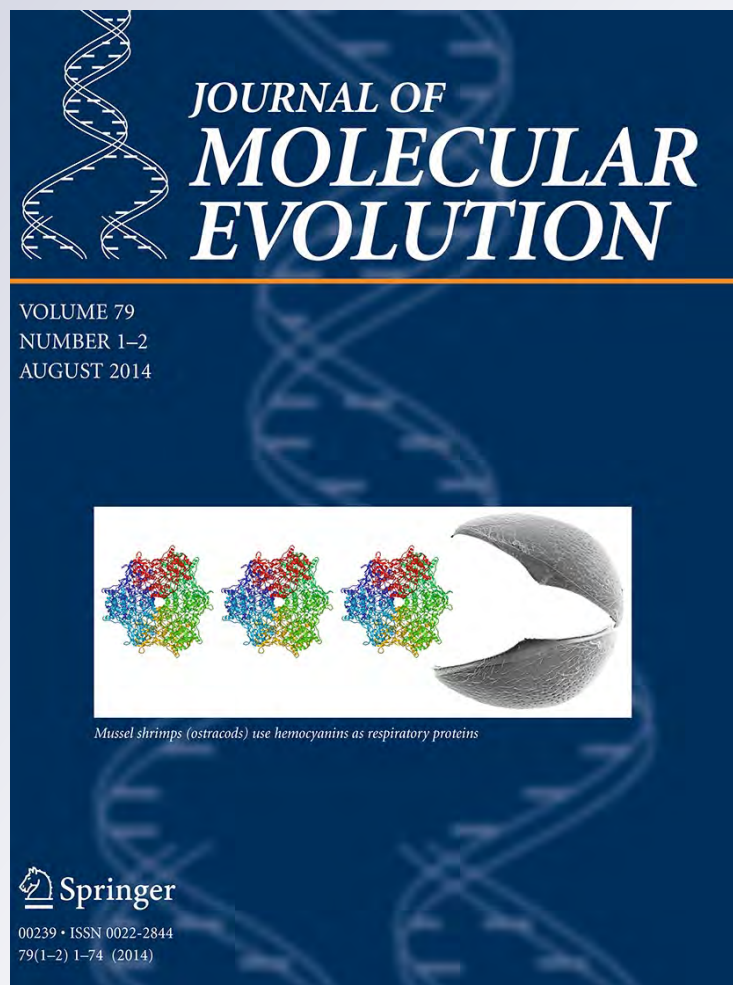
ISSN 0022-2844

Volume 79

Combined 1-2

J Mol Evol (2014) 79:52-62

DOI 10.1007/s00239-014-9634-z



Your article is protected by copyright and all rights are held exclusively by Springer Science +Business Media New York. This e-offprint is for personal use only and shall not be self-archived in electronic repositories. If you wish to self-archive your article, please use the accepted manuscript version for posting on your own website. You may further deposit the accepted manuscript version in any repository, provided it is only made publicly available 12 months after official publication or later and provided acknowledgement is given to the original source of publication and a link is inserted to the published article on Springer's website. The link must be accompanied by the following text: "The final publication is available at link.springer.com".

Exchange and Complementation of Genes Coding for Photosynthetic Reaction Center Core Subunits among Purple Bacteria

Kenji V. P. Nagashima · André Verméglio ·
Naoki Fusada · Sakiko Nagashima ·
Keizo Shimada · Kazuhito Inoue

Received: 17 March 2014 / Accepted: 11 July 2014 / Published online: 31 July 2014
© Springer Science+Business Media New York 2014

Abstract A mutant of the phototrophic species belonging to the β -proteobacteria, *Rubrivivax gelatinosus*, lacking the photosynthetic growth ability was constructed by the removal of genes coding for the L, M, and cytochrome subunits of the photosynthetic reaction center complex. The L, M, and cytochrome genes derived from five other species of proteobacteria, *Acidiphilium rubrum*, *Allochro-matium vinosum*, *Blastochloris viridis*, *Pheospirillum molis-chianum*, and *Roseateles depolymerans*, and the L and M subunits from two other species, *Rhodobacter sphaeroides* and *Rhodopseudomonas palustris*, respectively, have been introduced into this mutant. Introduction of the genes from three of these seven species, *Rte. depolymerans*, *Ach. vinosum*, and *Psp. molis-chianum*, restored the photosynthetic growth ability of the mutant of *Rvi. gelatinosus*,

although the growth rates were 1.5, 9.4, and 10.7 times slower, respectively, than that of the parent strain. Flash-induced kinetic measurements for the intact cells of these three mutants showed that the photo-oxidized cytochrome *c* bound to the introduced reaction center complex could be rereduced by electron donor proteins of *Rvi. gelatinosus* with a $t_{1/2}$ of less than 10 ms. The reaction center core subunits of photosynthetic proteobacteria appear to be exchangeable if the sequence identities of the LM core subunits between donor and acceptor species are high enough, i.e., 70 % or more.

Keywords Photosynthetic reaction center complex · Proteobacteria (Purple bacteria) · *puf* operon · Gene exchange

K. V. P. Nagashima (✉) · N. Fusada · K. Inoue
Research Institute for Photobiological Hydrogen Production,
Kanagawa University, 2946 Tsuchiya,
Hiratsuka 259-1293, Kanagawa, Japan
e-mail: wt503649bw@kanagawa-u.ac.jp

K. V. P. Nagashima
PRESTO/JST, 4-1-8 Honcho, Kawaguchi 332-0012, Saitama,
Japan

A. Verméglio
CEA-Cadarache DSV-SBVM Laboratoire de Bioénergétique
Cellulaire UMR 7265 CNRS-CEA-Aix-Marseille II,
13108 Saint Paul lez Durance Cedex, France

S. Nagashima · K. Inoue
Department of Biological Sciences, Kanagawa University, 2946
Tsuchiya, Hiratsuka 259-1293, Kanagawa, Japan

S. Nagashima · K. Shimada
Department of Biology, Tokyo Metropolitan University,
Hachioji 192-0397, Tokyo, Japan

Introduction

Photosynthesis was developed early in the evolution of bacteria (Woese 1987) and has been improved with the differentiation of organisms and environmental changes in their habitats. In proteobacteria (purple bacteria), bacteriochlorophyll (BChl) *a* or *b* is used as the main photosynthetic pigment, which can absorb both infrared and visible lights. Light energy captured by the BChls bound to two hydrophobic small peptides, α and β , of the light-harvesting complex is funneled to the photochemical reaction center complex (Gabrielsen et al. 2009). The reaction center complex of purple bacteria consists of, at least, three subunits called L, M, and H (Jones 2009). The L and M subunits are both membrane-bound peptides showing approximately 20 % amino acid sequence identities to each other and form a heterodimeric core of the reaction center complex (Michel et al. 1986). The amino

acid sequences of the L and M subunits are related to those of the D1 and D2 subunits, respectively, of the photosystem 2 reaction center of cyanobacteria and plants, signifying a common origin. The L and M core subunits bind four BChls, two bacteriopheophytins, and two quinones, which are arranged with a two-fold symmetry for transferring electrons across the membrane. Two of the four BChls form a dimer, called the special pair, in the vicinity of the periplasmic surface, which releases an electron when excited by light. In many species, a cytochrome subunit, which contains three or four *c*-type hemes, is bound to the LM core at the periplasmic side and works as the electron donor to the photo-oxidized special pair. The electron from the special pair is transferred through a bacteriopheophytin to the primary electron acceptor, a quinone molecule named Q_A . The electron is then transferred to the second quinone molecule, Q_B , loosely bound to the cytoplasmic side of the LM core. After receiving two electrons and two protons, the reduced Q_B diffuses out of the RC and donates its electrons to the cytochrome bc_1 complex (Okamura et al. 2000), although some of these are used for reduction of NAD^+ via a reverse electron flow mediated by the complex I, according to the redox state in the membrane (Verméglio and Joliot 2014). One of the electrons from the quinol to the bc_1 complex is transferred to the water-soluble electron carrier proteins, such as cytochrome c_2 and HiPIP, and then to the oxidized *c*-type hemes in the RC-bound cytochrome subunit (Lavergne et al. 2009). Some species, such as *Rba. sphaeroides* and *Rps. palustris*, do not have the cytochrome subunit. In this case, the electron is directly transferred from the cytochrome c_2 to the photo-oxidized special pair in the RC (Bullough et al. 2009). This completes a light-induced cyclic electron transfer found in all purple photosynthetic bacteria.

The genes coding for the subunits of the RC together with those of the light-harvesting 1 (LH1) complex form an operon called *puf*. The arrangement of genes in this operon is well conserved among the purple photosynthetic bacteria in the order of *pufB*, *-A*, *-L*, and *-M*, coding for the β and α subunits of the LH1 and the L and M subunits of the RC, respectively. In species having the RC-bound cytochrome subunit, the *pufC* gene coding for this subunit is located at the end of this operon as *pufBALMC*. The gene coding for the H subunit of the RC, *puhA*, is not included in the *puf* operon and forms an operon called *puh* together with the genes encoding proteins, possibly functioning in the formation process or stabilization of the RC-LH1 complex (Aklujkar et al. 2005, 2006). In *Rhodobacter capsulatus* and *Rba. sphaeroides*, the genes coding for the enzymes required for synthesis of BChls and carotenoids are flanked by the *puf* and *puh* operons (Coomber et al. 1990; Bauer et al. 1991). Such a gene island is called the photosynthesis gene cluster (PGC). Other species of purple photosynthetic

bacteria also have the PGC, although the arrangement of operons in this gene cluster is not always conserved (Igarashi et al. 2001; Nagashima and Nagashima 2013). In photosynthetic organisms other than purple bacteria and Heliobacteria, the genes for photosynthesis show scattered locations.

The purple photosynthetic bacteria group is not monophyletic. Phylogenetic studies based on comparison of the nucleotide sequences of 16S rRNA have shown that purple bacteria can be divided into five groups (classes): α , β , γ , δ , and ϵ (Woese 1987). Photosynthetic species, including aerobic anoxygenic phototrophic species, which can synthesize BChls but are incapable of photosynthetic growth under anaerobic conditions (Shimada 1995; Yurkov and Csotonyi 2009), are found only in the α , β , and γ groups with mixed distributions in many non-photosynthetic species. Such scattered distribution of photosynthetic species has been interpreted as the result of independent losses of the photosynthetic phenotype in many lineages in the course of adaptation to different environments without any light, from a common ancestor possessing photosynthetic ability (Woese 1987). This interpretation seems to be reasonable in the view of multiple metabolic pathways for energy conversion other than photosynthesis. In addition, horizontal gene transfer may also have contributed to the scattered distribution of photosynthetic species in purple bacteria. When the amino acid sequences of the L and M subunits of the RC are used for phylogenetic tree construction, species belonging to the β and γ groups are positioned among members of the α group while retaining the branching topology in each of the groups. Such positioning, inconsistent with that in the phylogenetic tree based on 16S rRNA sequences, has been interpreted as the result of the horizontal transfer of photosynthesis genes between ancestral species of the β and γ groups and those of the α group (Igarashi et al. 2001; Nagashima et al. 1997a).

Horizontal transfer of photosynthesis genes has not been fully verified by laboratory experiments. The PGC from the *Rhodobacter* species has been cloned in *Escherichia coli* (Marrs 1981), but no photosynthetic phenotypes and no BChl syntheses have been reported so far. Among photosynthetic species, however, it has been shown that a deficiency in the process of BChl synthesis can be restored by introducing genes from distantly related species (Xiong et al. 1998; 2000). The *puf* operon deletion mutant of *Rba. capsulatus* recovered the ability of photosynthetic growth by the expression of the *puf* operon from *Rba. sphaeroides* (Zilsel et al. 1989) but not by the introduction of the *puf* operon from the aerobic anoxygenic phototrophic bacterium *Roseobacter denitrificans*, although a functional reaction center is heterologously assembled (Kortlücke et al. 1997).

In the present study, the genes coding for the subunits of the reaction center complex were exchanged between a β -purple bacterium, *Rvi. gelatinosus*, and seven additional species belonging to various lineages of purple bacteria in order to estimate how much difference in the core of the reaction center complex is acceptable for restoring the photosynthetic phenotype. This should be the first step in providing experimental evidence of the horizontal transfer of photosynthesis genes and will contribute to studies on artificial photosynthesis using biosystems.

Materials and Methods

Cultivation of Bacterial Strains and DNA Purification

Rte. depolymerans 61A (DSM 11813^T), *Rvi. gelatinosus* IL144 (NBRC 100245), and its derivatives were grown in a PYS medium (Nagashima et al. 1997a). *Blc. viridis* (DSM133^T), *Rps. palustris* CGA009 (ATCC BAA-98), and *Rba. sphaeroides* IL106 (NBRC 100037) were photosynthetically grown in a malate-basal medium (0.5 % sodium malate, 0.1 % ammonium sulfate, 0.1 % yeast extract, 0.1 % vitamin solution (Nagashima et al. 1997a), and 20 mM potassium phosphate, pH 6.8). *Ach. vinosum* D (DSM180^T) and *Psp. molischianum* (DSM120^T) were grown under photosynthetic conditions according to Bose (1963) and Nagashima et al. (1993), respectively. *Aph. rubrum* (ATCC 35905^T) was aerobically grown according to Nagashima et al. (1997b). The cells grown to exponential growth phase were sedimented by centrifugation and used for DNA purification as described in a previous paper (Nagashima et al. 1996).

Construction of *Rvi. gelatinosus* Mutant Lacking the Reaction Center L, M, and Cytochrome Subunits

A plasmid pGELPUF (Maki et al. 2003), which is a pUC119-based plasmid containing whole *puf* genes of *Rvi. gelatinosus* IL144, was digested by restriction enzymes *Sph*I and *Stu*I. The linearized plasmid was self-ligated by treatments with a Klenow fragment and a DNA ligase using a Blunting Kit (TAKARA BIO INC., Otsu, Japan). These treatments removed the entire lengths of *pufL* and *pufM* and about 4/5 of the length of the N-terminal of *pufC* from the plasmid, as shown in Fig. 1. This manipulated DNA insert was transferred to a suicide vector, pJPCm (Ohmine et al. 2009), after digestion with *Sac*I and *Bam*HI restriction enzymes, and maintained in cells of *E. coli* strain S17-1 λ pir. Then, a DNA fragment containing *sacRB* genes and a kanamycin-resistant cartridge was inserted at the unique *Sac*I restriction site in this plasmid. The resultant plasmid was named pJP Δ gelpufLMC and

introduced into the cells of *Rvi. gelatinosus* IL144RL2 by trans-conjugation from the *E. coli* S17-1 λ pir host cells. The *pufLMC* genes were removed from the *Rvi. gelatinosus* IL144RL2 genome via a two-step homologous recombination, which had been screened by kanamycin resistance for the first and by sucrose resistance for the second, as previously described (Ohmine et al. 2009). The *Rvi. gelatinosus* mutant lacking *pufLMC* without any insertions of antibiotics-resistant cartridges was named Δ pufLMC after confirmations of the mutation by genomic Southern hybridization, PCR, and DNA sequencing experiments.

Introduction of Exogenous *pufLM(C)* Genes into the Cells of *Rvi. gelatinosus* Δ pufLMC

A 1-kb *Rvi. gelatinosus* DNA region immediately upstream of the start codon of *pufL* was amplified by PCR using the plasmid pGELPUF (Maki et al. 2003) as the template and a set of primers, M13F+7 (5'-GTAAAACGACGGCCAGT GAATTTCG) and GpufL-23R (5'-CATATTGATTCTCCGACCGACGG). The M13F+7 primer has a cohesive sequence (24-bases) to the 5' side of the M13 multi cloning site in the *lacZ* gene of the plasmid. A DNA region containing whole *pufLMC* of each of *Aph. rubrum*, *Ach. vinosum*, *Blc. viridis*, *Psp. molischianum*, and *Rte. depolymerans* or whole *pufLM* of each of *Rba. sphaeroides* and *Rps. palustris* was also amplified by PCR using primer sets as shown in Table 1. Through these PCR experiments, the forward primers have a cohesive sequence (15-bases) to the direct upstream of *Rvi. gelatinosus pufL* in addition to the operative sequence for the PCR, which is identical to the sequence of the 5'-end region of the exogenous *pufL* gene. The reverse primers have a 15-base of the cohesive sequence to the 3' side of the M13 multiple cloning site in the *lacZ* gene, in addition to the operative sequence for PCR. Each of the amplified *pufLM(C)* fragments was mixed with the 1-kb *Rvi. gelatinosus* PCR product described above and with the *Eco*RI-digested pJP5603 suicide plasmid (Penfold and Pemberton 1992) DNA with a molar ratio of 1:1:1. The three DNA fragments were connected at their cohesive ends via homologous recombination using an In-Fusion HD Cloning Kit (TAKARA BIO INC., Otsu, Japan), generating a plasmid construct containing a chimeric *puf* operon consisting of *Rvi. gelatinosus pufBA* and the exogenous *pufLM(C)* (Fig. 1). This construct was cloned in *E. coli* S17-1 λ pir and introduced into the cells of *Rvi. gelatinosus* Δ pufLMC by conjugal transfer. *Rvi. gelatinosus* IL144RL2 mutants, in which the *pufLMC* was replaced by the exogenous *pufLM(C)* via homologous recombination, were screened by kanamycin resistance and named AR-1, AV-1, BV-1, PM-1, RD-1, RP-1, or RS-1, according to the source of the *pufLM(C)* gene, *Aph. rubrum*, *Ach. vinosum*, *Blc. viridis*, *Psp. molischianum*, *Rte.*

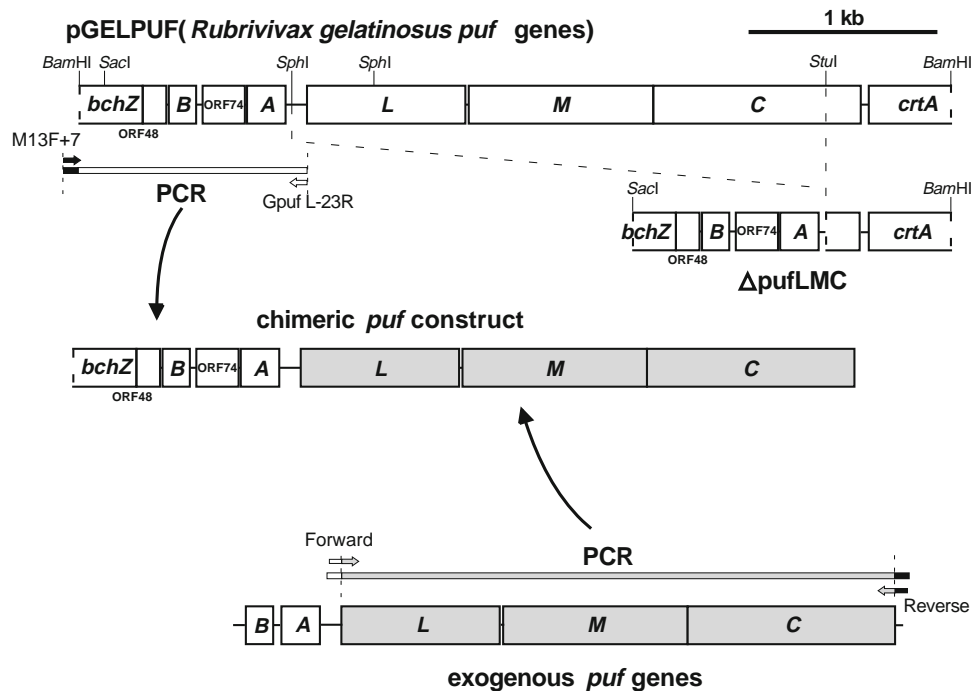


Fig. 1 Schematic representation of gene manipulations performed in this study. A 3-kb DNA region flanked by the *Sph*I and *Stu*I restriction sites, containing *pufL*, *pufM*, and *pufC*, was deleted from the *puf* operon DNA region of *Rvi. gelatinosus* IL144RL2. The mutant named ΔpufLMC, lacking this 3-kb DNA region containing *pufLMC*, was generated via a two-step homologous recombination method using a suicide vector, pJPCm, and had no insertions of antibiotics-resistant

cartridges. The PCR-amplified 1-kb *Rvi. gelatinosus* DNA region immediately upstream of the start codon of *pufL* was ligated with the PCR-amplified DNA region containing whole *pufLMC* or whole *pufLM* of each of seven other purple photosynthetic bacteria. Such a chimeric DNA construct was cloned in a pJP5603 suicide plasmid and inserted into the genomic DNA of the *Rvi. gelatinosus* ΔpufLMC mutant via single homologous recombination

depolymerans, *Rps. palustris*, or *Rba. sphaeroides*, respectively. A DNA fragment containing original *Rvi. gelatinosus* *pufBALMC* was also cloned in the pJP5603 suicide plasmid and introduced into the cells of ΔpufLMC to generate a control mutant, RG-LMC, in the same manner as used to generate the other mutants. Replacements of the genes in these mutants were confirmed by genomic Southern hybridization, PCR, and DNA sequencing experiments.

Growth Tests for *Rvi. gelatinosus* Mutants

Rvi. gelatinosus IL144RL2 and mutants were aerobically grown to mid-exponential growth phases in the dark at 30 °C in a PYS medium and used as precultures. Measurements were started with an addition of 0.3 ml of the preculture to a fresh PYS medium in a screw cap test tube with a diameter of 18 mm and a volume of 30 ml. The tube was filled with the growth medium and placed in a transparent water bath under light supplemented with a 60 W halogen lamp 15–25 cm away from the tubes. The temperature was kept at 30 °C by water circulation. The bacterial growth was monitored as the optical density at the wavelength of 660 nm. The minimum and maximum values among the five

independent measurements were omitted, and the average of the other three values was plotted against the time.

Biochemical and Spectrophotometric Assays

Rvi. gelatinosus mutants grown by aerobic respiration in the dark have been used for assays on the protein content and pigment accumulation. Three to five colonies on a plate culture were picked up (or 40 μl of the liquid culture was taken) and added to a 4 ml PYS growth medium in an open-top glass tube with a diameter of 18 mm and a height of 130 mm. The tube was covered by a loosely fitted aluminum cap and shaken in a reciprocal shaker with 140 cycles/min at 30 °C in the dark. A ten microliter of the liquid culture grown to a rate exponential to stationary growth phase was mixed with the same volume of a buffer containing 40 mM Tris (pH 7.0), 1 % Tween20, 0.2 % Nonidet P-40, and 0.2 mM EDTA to lyse the bacterial cells. A protein content in the lysate was assayed by a method of pyrogallol red-molybdate complex reaction using a Protein Assay Rapid Kit (Wako Pure Chemical Industries, Ltd., Osaka, Japan). Bovine serum albumin (BSA) was used as the protein standard. Pigments were extracted from the cells in the liquid culture by mixed with

Table 1 Primers used to amplify genes coding reaction center subunits, *pufLM* or *pufLMC*

Source of DNA template	Forward primer	Reverse primer
<i>Allochromatium vinosum</i>	5'-CGGAGGAATCAATATGGCCATGCTCAGITTTGAGAG	5'-TACCGAGCTCGAATTTACAGCTGTTGGGAGCCC
<i>Acidiphilium rubrum</i>	5'-CGGAGGAATCAATATGGCAATGCTCAGITTTGAAAG	5'-TACCGAGCTCGAATTTATTTGCCCGTTGCCCCG
<i>Blastochloris viridis</i>	5'-CGGAGGAATCAATATGGCACTGCTCAGITTTGAGAG	5'-TACCGAGCTCGAATTTACTTCGCAGCAGCCITGATCG
<i>Pheospirillum molischianum</i>	5'-CGGAGGAATCAATATGGCCATGCTCAGITTTGAGAAG	5'-TACCGAGCTCGAATTCGGAAGGATTAATTTCTTGCTCGTC
<i>Roseateles depolymerans</i>	5'-CGGAGGAATCAATATGGCCATGCTGAACITTCGAGAGG	5'-TACCGAGCTCGAATTCACGCCATTTGTTTCAGCTGGG
<i>Rhodospseudomonas palustris</i>	5'-CGGAGGAATCAATATGGCAATGCTCAGITTTGAGAAG	5'-TACCGAGCTCGAATTCGATAGACGTGCGGTTGTATTACCC
<i>Rhodobacter sphaeroides</i>	5'-CGGAGGAATCAATATGGCACTGCTCAGITTTGAGGCG	5'-TACCGAGCTCGAATTTCCCGAGACTTTGTTCTCAGACGAGATG

Cohesive sequences to the 5'-end of *pufL* and to the 3'-end of *pufM* or *pufC* are underlined

a 25 volume of acetone/methanol (7:2) solution. The absorption spectrum of the supernatant after a centrifugation at 10,000×g for 1 min was recorded with a UV-2600 spectrophotometer (Shimadzu Co., Kyoto, Japan). The concentration of BChl *a* was determined based on the absorbance at 770 nm, applying the extinction coefficient of 75 mM⁻¹ in a cuvette with a 1-cm optical path-length. Membranes of the *Rvi. gelatinosus* strains were prepared by a passage through a French pressure cell and ultracentrifugation, according to the procedure described previously (Maki et al. 2003) and used for measurements of absorption spectra.

Kinetic Measurements for Intact Cells

Kinetic measurements of flash-induced absorbance changes of the cytochromes were carried out using a double beam spectrophotometer as described previously (Schoepp et al. 1995).

Phylogenetic Tree Construction

Phylogenetic trees were constructed using the programs ClustalX (Thompson et al. 1997) and MEGA 3.1 (Kumar et al. 2004). Amino acid sequences of the L and M subunits were concatenated for each species and used for generating a sequence alignment. Unnatural gaps in the alignment were located by eyes and corrected. Construction of the tree was performed by the neighbor-joining method, applying the *p*-distance as a distance estimator, in which all gaps in the sequence alignment were completely omitted in calculations. The sequences were obtained from the DDBJ/EMBL/GenBank databases.

Results

Rvi. gelatinosus IL144RL2, which is a spontaneous mutant generated from the wild-type strain IL144, shows a greatly depressed production of the light-harvesting 2 (LH2 or B800–860) complex but synthesizes a significant amount of reaction center (RC) and light-harvesting 1 (LH1 or B875) complexes, even under dark-aerobic respiratory conditions (Maki et al. 2003). Therefore, using this strain as a parent for gene manipulation experiments, it can be expected that the mutated RC-LH1 complex is expressed enough to be analyzed even if the mutation caused a functional deficiency of photosynthesis. In the present study, the genes coding the L, M, and cytochrome subunits of the photochemical reaction center complex (*pufLMC*) were deleted from the genomic DNA of this strain, IL144RL2, to generate the mutant strain Δ*pufLMC*, which is, of course, not able to grow under light-anaerobic

(photosynthetic) conditions. The PCR-amplified *pufLMC* genes from the five species of purple photosynthetic bacteria, *Aph. rubrum*, *Ach. vinosum*, *Blc. viridis*, *Psp. molischianum*, and *Rte. depolymerans*, and *pufLM* genes of the two species without the cytochrome subunit, *Rps. palustris* and *Rba. sphaeroides*, have been independently incorporated *in cis* into the genomic DNA of the Δ *pufLMC* mutant cells. The growth rates of these “*puf*-exchanged” mutants grown under the dark respiratory conditions were almost identical (about 2 h of a doubling time) to that of the parent strain, IL144RL2, and the all mutants showed much amount of syntheses of BChl *a* and LH1 complex (Table 2), comparable to those in the parent strain. Possibly, the chimeric *puf* operons are similarly transcribed and translated as that in the parent strain. Three of such *puf*-exchanged mutants, PM-1 (*Psp. molischianum*), RD-1 (*Rte. depolymerans*), and AV-1 (*Ach. vinosum*), were capable of photosynthetic growth under light-anaerobic conditions. Figure 2 shows their photosynthetic growth curves as measured by the optical densities (at 660 nm) of their liquid cultures placed under light provided by halogen lamps (photon flux density $\approx 30 \mu\text{mol m}^{-2} \text{s}^{-1}$). The RD-

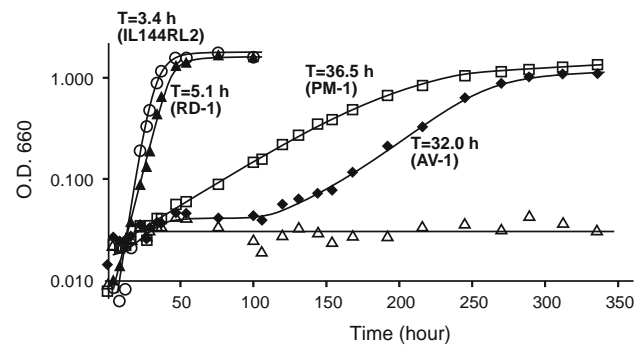


Fig. 2 Growth curves of *Rvi. gelatinosus* mutant cells grown under photosynthetic (light-anaerobic) conditions. The measurements were started by inoculation of 1/100 volume of exponential-phase cells grown aerobically. The absorbance at 660 nm was measured in a screw cap tube with a diameter of 18 mm. Symbols used are open circles for the original *Rvi. gelatinosus* strain IL144RL2, open triangles for Δ *pufLMC*, closed triangles for RD-1 (*Rte. depolymerans*), open squares for PM-1 (*Psp. molischianum*), and closed diamonds for AV-1 (*Ach. vinosum*). The doubling time, T, of each strain or mutant was calculated by exponential fitting to the data points ranging from 0.08 to 0.8 of the optical densities

Table 2 Accumulation of photosynthetic components in cultures of *R. gelatinosus pufLMC*-exchanged mutant strains

Strains	Protein content (mg/ml of growth medium)	Amount of BChl <i>a</i> ($\mu\text{g}/\text{mg}$ of protein)	Extent of LH1 spectral band ($A_{878-920}/A_{660}$) ^a	Photosynthetic growth ability ^b
IL144RL2	1.4 (0.9)	3.3 (6.0)	0.39 (0.81)	+
RD-1	2.0 (0.7)	2.0 (5.7)	0.43 (0.48)	+
PM-1	1.9 (0.9)	2.3 (4.1)	0.48 (0.68)	+
AV-1	1.7 (0.6)	2.7 (10.5)	0.49 (0.55)	+
RG-LMC	1.5 (1.0)	1.7 (3.0)	0.31 (0.36)	+
Δ <i>pufLMC</i>	2.2	2.2	0.49	–
AR-1	1.3	2.3	0.31	–
BV-1	1.4	3.5	0.37	–
RP-1	1.4	1.4	0.31	–
RS-1	1.9	2.2	0.46	–

Liquid cultures grown to the stationary growth phase (optical density at 660 nm = 2.0–3.5) in a PYS medium under the dark respiratory conditions were used for the measurements. Values measured for the photosynthetically grown cultures are shown in parentheses

^a Absorbance at the peak (878 nm) of the spectral band derived from the LH1, subtracted by absorbance around 920 nm as the baseline, was measured for the culture medium and normalized by the cell densities (optical density at 660 nm = 1.0)

^b When placed under the light (20 cm apart from a 60 W tungsten lamp) and anaerobic growth conditions after an inoculation with a 1/100 volume of the respiratory-grown culture, the culture of the strain showing an optical density at 660 nm (in a screw-capped glass tube with a diameter of 18 mm) of less than 0.1 was judged as negative (–) in photosynthetic growth

1 mutant grew faster than the other two mutants and showed a doubling time comparable to that of the original strain, IL144RL2. This shows that the reaction center subunits of *Rte. depolymerans* can fully compensate for the deletion of those in *Rvi. gelatinosus*. This may not be surprising, since the amino acid sequences of the L and M core subunits of *Rvi. gelatinosus* show the highest identities to those of *Rte. depolymerans*, 84.0 and 78.2 %, respectively, among those of the seven species used as donors in this study (Table 3). An interesting point is that *Rte. depolymerans* is a so-called “aerobic photosynthetic bacterium” and cannot grow under light-anaerobic conditions, contrary to what is observed for the RD-1 conjugant. The reaction center subunits of *Psp. molischianum* and *Ach. vinosum* also compensated for the deletion of these subunits of *Rvi. gelatinosus*, although the photosynthetic growth rates were significantly slower than that of the original strain, IL144RL2. These two species are distantly related to *Rvi. gelatinosus*, based on the phylogenetic analysis of 16S rRNA sequences, although their amino acid sequences of the L and M subunits show relatively high identities to those of *Rvi. gelatinosus* (Table 3).

Figure 3 shows the absorption spectra of membranes purified from the *Rvi. gelatinosus pufLMC*-exchanged mutants, RD-1, PM-1, and AV-1, grown under photosynthetic conditions. The spectrum of the membrane of Δ *pufLMC*, the direct parent strain of these mutants, is also shown for comparison. A large absorption band that peaked at 877 nm (at 874 nm only in Δ *pufLMC*) was seen in all of the spectra, attributable to the Q_y band of BChl *a* bound to the LH1 complex. Around the shorter wavelength region of

Table 3 Identities of amino acid sequences between *Rvi. gelatinosus* and other species used in this study

Species	PufL	PufM	PufC	PuhA	Accession numbers of sequence information used
<i>Allochrochromatium vinosum</i>	81.8	72.3	51.1	47.2	AB011811, CP001896
<i>Acidiphilium rubrum</i>	75.6	72.0	44.4	nd	AB005218
<i>Blastochloris viridis</i>	66.2	61.7	45.9	44.6	X03915, X05768, X02659
<i>Pheospirillum molischianum</i>	83.3	67.6	48.2	49.6	D50654, CAHP01000001.1
<i>Roseateles depolymerans</i>	84.0	78.2	58.2	nd	AB028938
<i>Rhodopseudomonas palustris</i>	75.0	73.4	none	50.6	BX571963
<i>Rhodobacter sphaeroides</i>	69.5	65.9	none	41.4	AF195122 (for strain 2.4.1)

Accession number of sequence information used for *Rvi. gelatinosus* IL144 is AP012320
nd sequence is not determined

this large band, a small band peaked at 803 nm, and a faint absorption around 760 nm could be found in the spectra of the *pufLMC*-exchanged mutants. These two bands could be assigned to be contributions from the accessory BChl *a* and bacteriopheophytin *a* bound to the RC complex, respectively. Note, however, that the absorption band that peaked at 803 nm may also include a contribution from the BChl *a* in the very small amount of LH2 complex, as seen in the spectrum of the Δ pufLMC membrane. Even taking into account the presence of this LH2, the ratio between the LH1 and RC complexes is very similar to those among PM-1, AV-1, RD-1, and IL144RL2. Therefore, the significant difference in the photosynthetic growth rates among these strains could not be due to a difference in the LH1/RC ratio. In Fig. 3, the absorption spectra of membranes purified from the dark-aerobically grown cells of the mutants showing no growths under the photosynthetic conditions, RS-1 (*Rba. sphaeroides*), BV-1 (*Blc. viridis*), AR-1 (*Aph. rubrum*), and RP-1 (*Rps. palustris*), are also shown. It is noteworthy that the absorption bands possibly derived from the BChl *a* and Bphe *a* in the RC complex are detected although their signals are weaker than those detected in the spectra of the membranes from the photosynthetically grown mutants. This suggests that the process of expression of exogenous *puf* genes is basically reconstructible in *Rvi. gelatinosus*.

To assess the reason for the difference in the photosynthetic growth rates among PM-1, AV-1, RD-1, and IL144RL2, the photosynthetic electron transfer in *Rvi. gelatinosus* has been analyzed by flash-induced kinetic measurements for redox changes of cytochromes *c* in intact cells (Fig. 4). The measurements were performed by applying a low-intensity continuous light to eliminate participation of low-potential hemes in the RC-bound cytochrome subunit. This keeps the low-potential hemes oxidized and allows recording of the light-induced changes of the high-potential hemes solely related to the cyclic electron transfer. Under these conditions, the kinetic trace obtained for the IL144RL2 original strain showed a flash-

induced rapid photo-oxidation of cytochrome *c* and biphasic reduction with a fast ($t_{1/2} \approx 300 \mu\text{s}$) and a slow ($t_{1/2} \approx 8 \text{ ms}$) phase of approximately equal amplitudes. These changes were nearly identical to those reported for the cells of the *Rvi. gelatinosus* wild-type strain IL144 (Menin et al. 1999; Nagashima et al. 2002). The fast phase was assigned to the fast reduction of the photo-oxidized heme in the RC-bound cytochrome subunit by the high-potential iron sulfur protein (HiPIP) bound to this subunit. Due to the low amount of cytochrome *bc*₁ complex in comparison to the amount of RCs, the complete reduction of the tetraheme cytochrome requires several turnovers of the cytochrome *bc*₁ complex; this is conducted to the slow reduction phase of the flash-oxidized high-potential heme in the RC-bound cytochrome subunit. The kinetic trace measured for the RD-1 intact cells also showed a similar biphasic reduction of photo-oxidized cytochrome *c*, although the contribution of the fast phase (about 75 %) was higher than that estimated (about 50 %) in IL144RL2 cells. This suggests that the ratio of HiPIP to RC is higher in the RD-1 conjugant than that in the IL144RL2 strain. Alternatively, the difference in midpoint potential between the RC-bound high-potential heme and the HiPIP could be higher for the RD-1 conjugant than that for *Rvi. gelatinosus*. For the other two mutants, AV-1 and PM-1, the fast rereduction of the photo-oxidized cytochromes observed in IL144RL2 and RD-1 was not detected. Most of the photo-oxidized cytochromes bound to the RC in these two mutant cells were rereduced with $t_{1/2} \approx 4 \text{ ms}$ in PM-1 and $t_{1/2} \approx 10 \text{ ms}$ in AV-1, which is comparable to the rate of the slow phase in IL144RL2. The main electron donor to the RC-bound cytochromes in these two mutants is suspected to be the HiPIP but not a soluble cytochrome *c*, since no clear spectral shifts were detected during the process of the reaction (data not shown). In any case, the slower rereduction of the RC-bound cytochromes in AV-1 and PM-1 is certainly related to the slower growth of these mutants under photosynthetic conditions. This interpretation is in agreement with results obtained in our previous studies, in

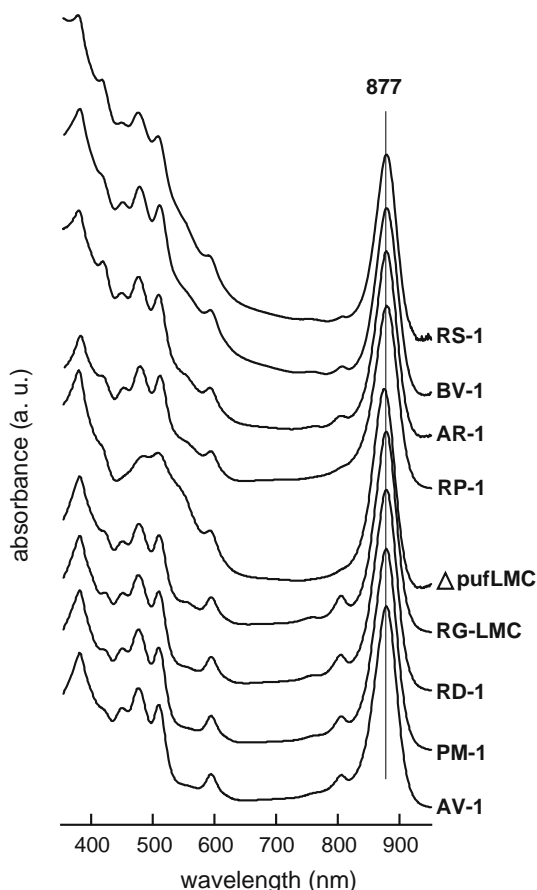


Fig. 3 Absorption spectra of membranes prepared from *Rvi. gelatinosus* mutants in which the reaction center genes (*pufLMC*) have been replaced by those from other species. The membranes of AV-1, PM-1, RD-1, and RG-LMC were prepared from the photosynthetically grown cells. The membranes of RS-1, BV-1, AR-1, RP-1, and Δ pufLMC were prepared from cells grown under dark-aerobic conditions. The membranes were suspended in a buffer containing 50 mM potassium phosphate (pH 7.0) and 50 mM potassium chloride to be a concentration of 100 μ g of protein/ml. The absorption spectra were normalized at 877 nm which is the peak position of LH1 Q_y-band

which the lack of fast (<1 ms) rereduction of the RC due to genetic deletions of HiPIP and/or the RC-bound cytochrome made the cell growth more than twice as slow of that of the wild-type cells under photosynthetic conditions (Nagashima et al. 1996, 2002; Verméglio et al. 2012).

Discussion

In the present study, the exchange of genes coding for the L, M, and cytochrome subunits (*pufL*, *pufM*, and *pufC*) of the photosynthetic reaction center has been tried using the β -purple bacterium *Rvi. gelatinosus* as a host and various species of purple bacteria as donors. Introduction of the *puf* genes from three of the seven species tested, *Rte.*

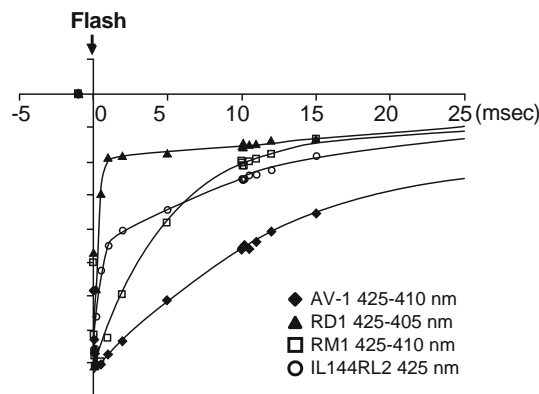
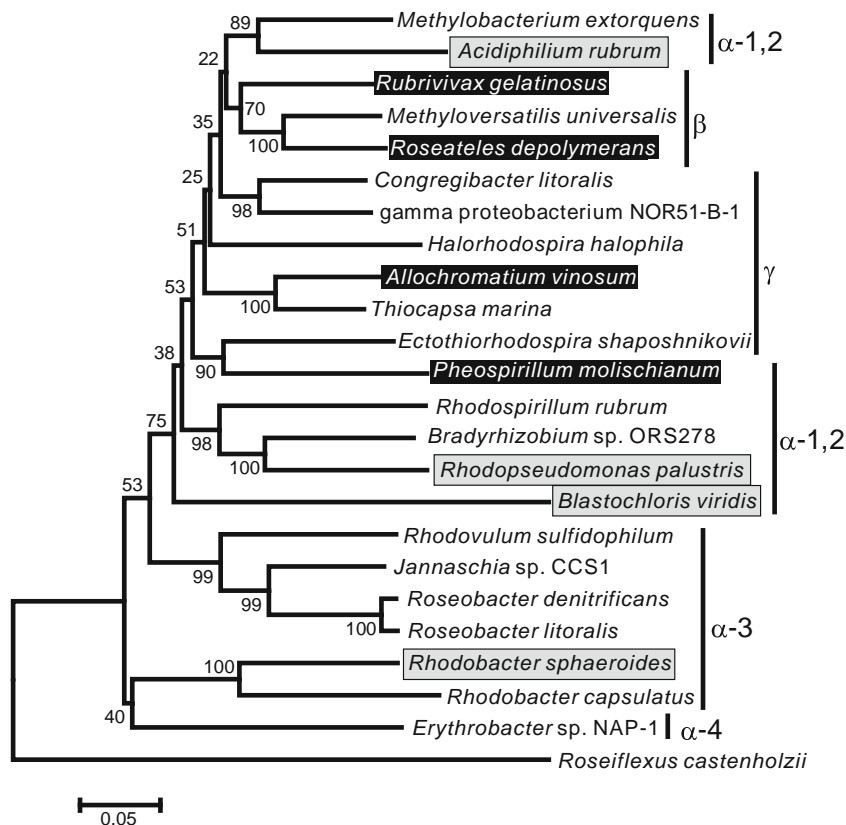


Fig. 4 Flash-induced redox changes of cytochrome *c* in intact cells of *Rvi. gelatinosus* IL144RL2 and mutants grown under light-anaerobic conditions. Cell suspensions were placed under anaerobic conditions. A low-intensity continuous light was used to photo-oxidize the low-potential hemes in the RC-bound cytochrome subunit. Flash excitation reveals solely the photo-oxidation of the high-potential hemes in this subunit

depolymerans, *Psp. molischianum*, and *Ach. vinosum*, into the cells of the deletion mutant of these genes recovered the photosynthetic growth phenotype. The latter two species are α - and γ -purple bacteria, respectively, distantly related to *Rvi. gelatinosus* in the phylogenetic relationship based on 16S rRNA sequences (Woese 1987). However, a phylogenetic tree based on the amino acid sequences of the L and M subunits of the reaction center placed these species closer to *Rvi. gelatinosus*, as shown in Fig. 5. Such an inconsistency, observed among phylogenetic trees, has been explained by the horizontal transfer of photosynthesis genes between the ancestral species of α -1 or α -2 subclasses and the ancestral species of β - and γ -classes (Nagashima et al. 1997a; Igarashi et al. 2001; Nagashima and Nagashima 2013). The results obtained in the present study may reflect such an evolutionary process. Indeed, the amino acid sequences of the L and M subunits used in the mutants recovering photosynthetic growth showed higher identities to those of *Rvi. gelatinosus*, which are over 81 % for the L subunits and over 67 % for the M subunits (Table 2). Possibly, these “carried-in” L and M subunits form a functional reaction center complex with the native H subunit of *Rvi. gelatinosus*. The carried-in cytochrome subunit was also incorporated into these chimeric reaction center complexes and showed a fast oxidation to reduce the special pair of the BChls oxidized by a flash illumination. However, the rate of rereduction of the hemes in the cytochrome subunit was significantly slowed in the two mutants expressing the *pufLMC* of *Psp. molischianum* (PM-1) and *Ach. vinosum* (AV-1). This slow rereduction can cause the significantly slower growth of these two mutants under photosynthetic conditions and may be

Fig. 5 Phylogenetic tree based on amino acid sequences of L and M subunits of RC. Species for which the genes coding for the L, M, and cyt subunits were introduced into the *Rvi. gelatinosus* mutant lacking these subunit genes are in boxes. When such gene exchanges resulted in the PS⁺ phenotype, the names of the donor species are highlighted. Strain names and accession numbers of the sequence data used in the tree construction can be found in (Nagashima and Nagashima 2013)



due to differences in the distribution of charged amino acids on the surface of the cytochrome subunits that provide binding sites to the soluble electron donor proteins (Nagashima et al. 1998). The amino acid sequence identities of the cytochrome subunits between *Rvi. gelatinosus* and these two species are 48 and 51 %, respectively. On the other hand, the mutant expressing the *Rte. depolymerans* *pufLMC* (RD-1) showed a comparable growth rate with the parent *Rvi. gelatinosus* strain and fast rereduction of the hemes in the cytochrome subunit after the photo-oxidation by flash-activation. Likewise, the amino acid sequence identity between the cytochrome subunits of *Rvi. gelatinosus* and *Rte. depolymerans* is not very high, 58 %. However, the local structure for the binding sites to the electron donor proteins may be well conserved between these two species, since they are closely related in β -purple bacteria.

Recovery of the photosynthetic growth ability in the *Rvi. gelatinosus* mutant expressing the reaction center genes from *Rte. depolymerans* is particularly interesting. *Rte. depolymerans* is an aerobic bacterium and does not grow phototrophically under light-anaerobic conditions in spite of the potential production of photosynthetic apparatuses (Suyama et al. 1999). Synthesis of BChl *a* has been reported to be induced by a sudden decrease in the concentration of carbon sources in the growth medium and to

be advantageous in maintaining the viability of the starved cells in the presence of light (Suyama et al. 2002). Through studies on many other species of aerobic photosynthetic bacteria, it has been suggested that their photosynthetic apparatuses help generate membrane potential and give them advantages for surviving in natural environments (Shimada 1995; Yurkov and Csotonyi 2009). However, biochemical or thermodynamical reasons for their inability to grow photosynthetically have not been straightforward. One possible explanation is that the primary quinone, Q_A, with relatively high redox midpoint potential might be over-reduced under anaerobic conditions (Okamura et al. 1985). This explanation is consistent with a study of the expression of *puf* genes of the aerobic photosynthetic species, *Rsb. denitrificans*, of the *puf*-deleted mutant of the genuine phototrophic species, *Rba. capsulatus*, in which the transconjugants did not grow under light-anaerobic conditions, although the reaction center was synthesized and showed a charge separation by flash activation (Kortlücke et al. 1997). However, the present study clearly shows that the reaction center L, M, and cytochrome subunits of the aerobic photosynthetic species *Rte. depolymerans* are perfectly functional in *Rvi. gelatinosus*, showing that the midpoint potentials of quinones, special pair of BChls *a*, and hemes *c* are adjusted to function in the cyclic electron flow of the genuine phototrophic species placed under

light-anaerobic growth conditions. Possibly, the aerobic photosynthetic bacteria's inability to grow photosynthetically is related to an electron transfer step other than at the reaction center level. Measurements of the electron transfer to the cytochrome bc_1 and the concomitant electrogenic phase in the RC-exchanged mutant, RD-1, as well as those in the original *Rte. depolymerans* under various redox conditions will be required to clarify the importance of appropriate equilibrium among the Q_A , Q_B , and quinone pool.

Four of the seven *puf*-exchanged mutants, AR-1, RP-1, BV-1, and RS-1, in which the *pufLMC* or *pufLM* genes of *Aph. rubrum*, *Rps. palustris*, *Blc. viridis*, and *Rba. sphaeroides*, respectively, are introduced into the *Rvi. gelatinosus* Δ *pufLMC* mutant, showed no apparent growth under light-anaerobic photosynthetic conditions for at least 10 days. These mutants showed synthesis of a large amount of LH1 complexes, even under aerobic respiratory growth conditions, as in the parent strains of *Rvi. gelatinosus*. A small absorption band that peaked at 803 nm and approximately 760 nm could also be seen in the spectra of the membranes of these mutants (Fig. 3). However, flash-induced kinetic measurements using intact cells of these four mutants grown under aerobic conditions showed no apparent signals linked to a charge separation between P^+ and Q_A^- (data not shown). This suggests that the reaction center complex, composed of the introduced LM core subunits and the H subunit of *Rvi. gelatinosus*, is not correctly assembled or is unstable in these mutants. Related to this possibility, the Q_A site in the chimeric reaction center may not be occupied by an appropriate quinone molecule. It has been shown that the deletion of the gene coding for the H subunit, *puhA*, results in deficiency in the synthesis of the reaction center complex and abolishment of the photosynthetic growth ability (Wong et al. 1996; Lupu and Ghosh 2004). Sequence identities between the RC subunits of *Rvi. gelatinosus* and the four species might be too low to support the tight interaction between the H subunit of *Rvi. gelatinosus* and the introduced LM core. Concerning the AR-1 and BV-1 mutants, in which the *pufLMC* genes are derived from *Aph. rubrum* and *Blc. viridis*, respectively, differences in pigment preferences might be another reason why the reaction center becomes deficient. They use Zn-BChl *a* and BChl *b*, respectively, different from BChl *a* used in the other species, including *Rvi. gelatinosus*.

The present study shows that reaction center genes are exchangeable without a loss of the photosynthetic phenotype if the sequence identities between the donor and acceptor species are within some threshold, i.e., more than 70 or 80 % identical. The introduced reaction center can be incorporated into the electron transfer pathway in the acceptor species. This means that the process of the evolution of photosynthesis is possible to trace by experiments,

and that we may create new metabolic pathways driven by light energy.

Acknowledgments This work was supported in part by PRESTO of the Japan Science and Technology Agency (to K.V.P.N.) and grant-in aid for Scientific Research on Innovative Areas (No.24107004) and Strategic Research Base Development Program for Private Universities from MEXT, Japan (to K. I.).

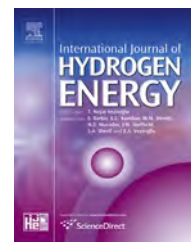
References

- Aklujkar M, Prince RC, Beatty JT (2005) The PuhB protein of *Rhodobacter capsulatus* functions in photosynthetic reaction center assembly with a secondary effect on light-harvesting complex 1. *J Bacteriol* 187:1334–1343. doi:10.1128/JB.187.4.1334-1343.2005
- Aklujkar M, Prince RC, Beatty JT (2006) The photosynthetic deficiency due to *puhC* gene deletion in *Rhodobacter capsulatus* suggests a PuhC protein-dependent process of RC/LH1/PufX complex reorganization. *Arch Biochem Biophys* 454:59–71. doi:10.1016/j.abb.2006.07.009
- Bauer CE, Buggy JJ, Yang ZM, Marrs BL (1991) The superoperon organization of genes for pigment biosynthesis and reaction center proteins is a conserved feature in *Rhodobacter capsulatus*: analysis of overlapping *bcbB* and *puhA* transcripts. *Mol Gen Genet* 228:433–444
- Bose SK (1963) Media for anaerobic growth of photosynthetic bacteria. In: Gest H (ed) Bacterial photosynthesis. The Antioch Press, Yellow Springs, pp 501–510
- Bullough PA, Qian P, Hunter CN (2009) Reaction center-light harvesting core complexes of purple bacteria In: Hunter CN, Daldal F, Thurnauer MC, Beatty JT (eds) The Purple Phototrophic Bacteria. Advances in Photosynthesis and Respiration, vol 28. Springer, Netherlands, pp 155–179
- Coomer SA, Chaudhri M, Connor A, Britton G, Hunter CN (1990) Localized transposon Tn5 mutagenesis of the photosynthetic gene cluster of *Rhodobacter sphaeroides*. *Mol Microbiol* 4:977–989
- Gabrielsen M, Gardiner AT, Cogdell RJ (2009) Peripheral complexes of purple bacteria. In: Hunter C, Daldal F, Thurnauer M, Beatty J (eds) The purple phototrophic bacteria. Advances in Photosynthesis and Respiration, vol 28. Springer, Netherlands, pp 135–153
- Igarashi N, Harada J, Nagashima S, Matsuura K, Shimada K, Nagashima KVP (2001) Horizontal transfer of the photosynthesis gene cluster and operon rearrangement in purple bacteria. *J Mol Evol* 52:333–341. doi:10.1007/s002390010163
- Jones MR (2009) Structural plasticity of reaction centers from purple bacteria. In: Hunter CN, Daldal F, Thurnauer M, Beatty JT (eds) The purple phototrophic bacteria, vol 28., Advances in Photosynthesis and Respiration, Springer, Netherlands, pp 295–321
- Kortlücke C, Breese K, Gad'on N, Labahn A, Drews G (1997) Structure of the *puf* operon of the obligately aerobic, bacteriochlorophyll α -containing bacterium *Roseobacter denitrificans* OCh114 and its expression in a *Rhodobacter capsulatus puf puc* deletion mutant. *J Bacteriol* 179:5247–5258
- Kumar S, Tamura K, Nei M (2004) MEGA3: integrated software for Molecular Evolutionary Genetics Analysis and sequence alignment. *Brief Bioinform* 5:150–163
- Lavergne J, Verméglio A, Joliot P (2009) Functional coupling between reaction centers and cytochrome bc_1 complexes. In: Hunter CN, Daldal F, Thurnauer M, Beatty JT (eds) The purple phototrophic bacteria, vol 28., Advances in Photosynthesis and Respiration, Springer, Netherlands, pp 509–536

- Lupo D, Ghosh R (2004) The reaction center H subunit is not required for high levels of light-harvesting complex 1 in *Rhodospirillum rubrum* mutants. *J Bacteriol* 186:5585–5595. doi:10.1128/JB.186.17.5585-5595.2004
- Maki H, Matsuura K, Shimada K, Nagashima KVP (2003) Chimeric photosynthetic reaction center complex of purple bacteria composed of the core subunits of *Rubrivivax gelatinosus* and the cytochrome subunit of *Blastochloris viridis*. *J Biol Chem* 278:3921–3928. doi:10.1074/jbc.M209069200
- Marrs B (1981) Mobilization of the genes for photosynthesis from *Rhodopseudomonas capsulata* by a promiscuous plasmid. *J Bacteriol* 146:1003–1012
- Menin L, Yoshida M, Jaquinod M, Nagashima KVP, Matsuura K, Parot P, Verméglio A (1999) Dark aerobic growth conditions induce the synthesis of a high midpoint potential cytochrome c_8 in the photosynthetic bacterium *Rubrivivax gelatinosus*. *Biochemistry* 38:15238–15244
- Michel H, Weyer KA, Gruenberg H, Dunger I, Oesterhelt D, Lottspeich F (1986) The 'light' and 'medium' subunits of the photosynthetic reaction centre from *Rhodopseudomonas viridis*: isolation of the genes, nucleotide and amino acid sequence. *EMBO J* 5:1149–1158
- Nagashima S, Nagashima KVP (2013) Comparison of photosynthesis gene clusters retrieved from total genome sequences of purple bacteria. In: Beatty TJ (ed) *Genome Evolution of Photosynthetic Bacteria*, vol 66. Academic Press, Elsevier Inc., pp 151–178
- Nagashima KVP, Itoh S, Shimada K, Matsuura K (1993) Photo-oxidation of reaction center-bound cytochrome c and generation of membrane potential determined by carotenoid band shift in the purple photosynthetic bacterium, *Rhodospirillum molischiannum*. *Biochim Biophys Acta* 1140:297–303
- Nagashima KVP, Shimada K, Matsuura K (1996) Shortcut of the photosynthetic electron transfer in a mutant lacking the reaction center-bound cytochrome subunit by gene disruption in a purple bacterium, *Rubrivivax gelatinosus*. *FEBS Lett* 385:209–213
- Nagashima KVP, Hiraishi A, Shimada K, Matsuura K (1997a) Horizontal transfer of genes coding for the photosynthetic reaction centers of purple bacteria. *J Mol Evol* 45:131–136
- Nagashima KVP, Matsuura K, Wakao N, Hiraishi A, Shimada K (1997b) Nucleotide sequences of genes coding for photosynthetic reaction centers and light-harvesting proteins of *Acidiphilium rubrum* and related aerobic acidophilic bacteria. *Plant Cell Physiol* 38:1249–1258
- Nagashima KVP, Sakuragi Y, Shimada K, Matsuura K (1998) Comparative analysis of the primary structure of the reaction center-bound cytochrome subunit in purple bacteria. *Photosynth Res* 55:349–355. doi:10.1023/a:1005912810674
- Nagashima KVP, Matsuura K, Shimada K, Verméglio A (2002) High-potential iron-sulfur protein (HiPIP) is the major electron donor to the reaction center complex in photosynthetically growing cells of the purple bacterium *Rubrivivax gelatinosus*. *Biochemistry* 41:14028–14032
- Ohmine M, Matsuura K, Shimada K, Alric J, Verméglio A, Nagashima KVP (2009) Cytochrome c_4 can be involved in the photosynthetic electron transfer system in the purple bacterium *Rubrivivax gelatinosus*. *Biochemistry* 48:9132–9139. doi:10.1021/bi901202m
- Okamura K, Takamiya K, Nishimura M (1985) Photosynthetic electron transfer system is inoperative in anaerobic cells of *Erythrobacter* species strain OCh 114. *Arch Microbiol* 142:12–17. doi:10.1007/bf00409229
- Okamura MY, Paddock ML, Graige MS, Feher G (2000) Proton and electron transfer in bacterial reaction centers. *Biochimica et Biophysica Acta* 1458:148–163. doi:10.1016/S0005-2728(00)00065-7
- Penfold RJ, Pemberton JM (1992) An improved suicide vector for construction of chromosomal insertion mutations in bacteria. *Gene* 118:145–146
- Schoepp B, Parot P, Menin L, Gaillard J, Richaud P, Verméglio A (1995) *In vivo* participation of a high potential iron-sulfur protein as electron donor to the photochemical reaction center of *Rubrivivax gelatinosus*. *Biochemistry* 34:11736–11742
- Shimada K (1995) Aerobic anoxygenic phototrophs. In: Blankenship RE, Madigan MT, Bauer CE (eds) *Anoxygenic Photosynthetic Bacteria*, vol 2., *Advances in Photosynthesis and Respiration*, Springer, Netherlands, pp 105–122
- Suyama T, Shigematsu T, Takaichi S, Nodasaka Y, Fujikawa S, Hosoya H, Tokiwa Y, Kanagawa T, Hanada S (1999) *Roseateles depolymerans* gen. nov., sp. nov., a new bacteriochlorophyll a -containing obligate aerobe belonging to the beta-subclass of the *Proteobacteria*. *Int J Syst Bacteriol* 49:449–457
- Suyama T, Shigematsu T, Suzuki T, Tokiwa Y, Kanagawa T, Nagashima KVP, Hanada S (2002) Photosynthetic apparatus in *Roseateles depolymerans* 61A is transcriptionally induced by carbon limitation. *Appl Environ Microbiol* 68:1665–1673
- Thompson JD, Gibson TJ, Plewniak F, Jeanmougin F, Higgins DG (1997) The CLUSTAL_X windows interface: flexible strategies for multiple sequence alignment aided by quality analysis tools. *Nucleic Acids Res* 25:4876–4882. doi:10.1093/nar/25.24.4876
- Verméglio A, Joliot P (2014) Modulation of the redox state of quinones by light in *Rhodobacter sphaeroides* under anaerobic conditions. *Photosynth Res* 120:237–246. doi:10.1007/s11120-013-9961-8
- Verméglio A, Nagashima S, Alric J, Arnoux P, Nagashima KVP (2012) Photo-induced electron transfer in intact cells of *Rubrivivax gelatinosus* mutants deleted in the RC-bound tetraheme cytochrome: insight into evolution of photosynthetic electron transport. *Biochim Biophys Acta* 1817:689–696. doi:10.1016/j.bbabi.2012.01.011
- Woese CR (1987) Bacterial evolution. *Microbiol Rev* 51:221–271
- Wong DK-H, Collins WJ, Harmer A, Lilburn TG, Beatty JT (1996) Directed mutagenesis of the *Rhodobacter capsulatus* *puhA* gene and orf 214: pleiotropic effects on photosynthetic reaction center and light-harvesting 1 complexes. *J Bacteriol* 178:2334–2342
- Xiong J, Inoue K, Bauer CE (1998) Tracking molecular evolution of photosynthesis by characterization of a major photosynthesis gene cluster from *Heliobacillus mobilis*. *Proc Natl Acad Sci USA* 95:14851–14856
- Xiong J, Fischer WM, Inoue K, Nakahara M, Bauer CE (2000) Molecular evidence for the early evolution of photosynthesis. *Science* 289:1724–1730
- Yurkov V, Csotonyi JT (2009) New light on aerobic anoxygenic phototrophs. In: Hunter CN, Daldal F, Thurnauer M, Beatty JT (eds) *The purple phototrophic bacteria*, vol 28., *Advances in Photosynthesis and Respiration*, Springer, Netherlands, pp 31–55
- Zilsel J, Lilburn TG, Beatty JT (1989) Formation of functional interspecies hybrid photosynthetic complexes in *Rhodobacter capsulatus*. *FEBS Lett* 253:247–252

Available online at www.sciencedirect.com

ScienceDirect

journal homepage: www.elsevier.com/locate/ijhe

Sustained photobiological hydrogen production in the presence of N₂ by nitrogenase mutants of the heterocyst-forming cyanobacterium *Anabaena*

Hajime Masukawa^{a,*}, Hidehiro Sakurai^a, Robert P. Hausinger^{b,c}, Kazuhito Inoue^{a,d}

^a Research Institute for Photobiological Hydrogen Production, Kanagawa University, Hiratsuka, Kanagawa 259-1293, Japan

^b Department of Microbiology and Molecular Genetics, Michigan State University, East Lansing, MI 48824, USA

^c Department of Biochemistry and Molecular Biology, Michigan State University, East Lansing, MI 48824, USA

^d Department of Biological Sciences, Kanagawa University, Hiratsuka, Kanagawa 259-1293, Japan

ARTICLE INFO

Article history:

Received 20 June 2014

Received in revised form

11 August 2014

Accepted 18 September 2014

Available online 12 October 2014

Keywords:

Cyanobacteria

Anabaena

Hydrogen production

Biofuel

Nitrogenase

Site-directed mutagenesis

ABSTRACT

Heterocyst-forming cells of the cyanobacterium *Anabaena* sp. strain PCC 7120 ΔHup, lacking an uptake hydrogenase, photobiologically produce H₂ by nitrogenase. Under N₂-rich atmosphere, the nitrogenase activity declines in a rather short time due to the sufficiency of combined nitrogen. From the parental ΔHup strain, site-directed double-cross-over variants, dc-Q193S and dc-R284H, were created with amino acid substitutions presumed to be located in the vicinity of the FeMo-cofactor of nitrogenase. Unlike the case for the ΔHup strain, H₂ production activities of the variants were not decreased by the presence of high concentrations of N₂ and they continuously produced H₂ over 21 days with occasional headspace gas replacement. This property of N₂ insensitivity is a potentially useful strategy for reducing the cost of the culture gas in future practical applications of sustainable biofuel production. This *Anabaena* strain has only the Mo-containing nitrogenase which reduces acetylene to ethylene, but the dc-Q193S variant also produced ethane at low but measurable rates along with greater rates of ethylene production.

Copyright © 2014, Hydrogen Energy Publications, LLC. Published by Elsevier Ltd. All rights reserved.

Introduction

Photobiological production of H₂ by cyanobacteria is an attractive source of renewable energy because these microorganisms have simple needs: readily available sunlight for energy and water as the electron donor [1–5]. H₂ is an efficient

substrate for fuel cells that cleanly generate electrical and thermal power with water as the final product, in contrast to the situation for fossil fuels that also form green-house gases and pollute the environment.

H₂-producing enzymes in cyanobacteria include hydrogenases and nitrogenases [3,5]. We have chosen to focus on nitrogenase as the enzyme for H₂ production because it

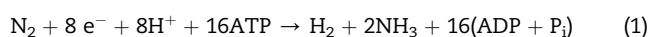
* Corresponding author. Tel.: +81 463 59 4111; fax: +81 463 58 9684.

E-mail addresses: jimimasu@gmail.com, wtk-0488gg@kanagawa-u.ac.jp (H. Masukawa).
<http://dx.doi.org/10.1016/j.ijhydene.2014.09.090>

0360-3199/Copyright © 2014, Hydrogen Energy Publications, LLC. Published by Elsevier Ltd. All rights reserved.

catalyzes essentially unidirectional H₂ production and thus does not consume H₂ as a substrate. When the hydrogenase activity is eliminated by genetic engineering, the cyanobacterial mutants accumulate a high concentration of H₂ (about 7–30%) even in the presence of O₂ [6,7]. By contrast, wild-type nitrogen-fixing cyanobacteria accumulate significantly less of this product because their hydrogenase(s) catalyze the uptake of H₂ [8].

H₂ is produced as an inevitable by-product of nitrogen fixation. The optimized reaction for nitrogen fixation can be expressed as:



In the absence of N₂ (e.g., under argon; Ar), all electrons are directed to H₂ production:



For the filamentous N₂-fixing cyanobacterium used here, *Anabaena* (also called *Nostoc*) sp. strain PCC 7120, nitrogen deficiency leads to the development of specialized cells called heterocysts that protect nitrogenase against inactivation by O₂ [9], however, elevated O₂ partial pressures remain harmful to nitrogenase activity to some extent [6,10–12]. The enzyme activity is induced during the late stages of heterocyst differentiation and then declines in a rather short time (usually less than several hours) under ambient air or N₂, because its product ammonia meets the nitrogen nutritional requirements of the cells and consequently suppresses *de novo* nitrogenase synthesis [9]. While the mechanism of ammonia inhibition of nitrogenase in cyanobacteria had been considered to be different from that in other bacteria [13], an ammonia “switch-off” of the enzyme (within a few tens of minutes) in the presence of O₂ was reported for other heterocyst-forming strains [9,14]. However, the mechanism and the presence/absence of ammonia “switch-off” in cyanobacteria is still under debate [9]. For sustained, high-level production of H₂ by nitrogenase, Ar purging is frequently

used to both decrease N₂ concentration (thus minimizing repression of nitrogenase activity due to the increased cellular N/C ratio) and alleviate the rise in O₂ partial pressure produced by photosynthesis (thus minimizing nitrogenase inactivation) [11,15].

In a previous study, over 40 single-crossover (sc) mutants were created in *Anabaena* sp. strain PCC 7120 ΔHup [7] in which the uptake hydrogenase (Hup) activity had been inactivated by genetic engineering [16]. Each of these isolates contained a 9.4-kb DNA fragment inserted into the *nif* gene cluster along with distinct site-directed mutations in *nifD* (Fig. 1, top) resulting in separate amino acid substitutions presumed to be located in the vicinity of the catalytic FeMo-cofactor of nitrogenase. Some of the sc-mutants photo-biologically produced H₂ under N₂ at rates comparable to those under Ar over the course of several days. These properties of the sc-mutants suggested that such a mutational strategy could decrease the cost of gases for use in photobiological H₂ production in the future. Thus, we have chosen two potentially useful sc-site-directed mutants and constructed the corresponding double-crossover (dc) strains which lack the inserted DNA fragment (Fig. 1, bottom) so that revertants can not be generated. Using the dc-mutants, we studied the effects of gas composition on the sustainability of photobiological H₂ production activity more closely, and found that they allow more efficient expression of nitrogenase activity than the sc-mutants under high N₂ atmosphere.

Materials and methods

Bacterial strains and growth conditions

Cyanobacterial strains were grown at 28 °C in an 8-fold dilution of Allen and Arnon (AA/8) liquid medium [17] with or without added nitrate. The cultures were placed on a rotary shaker in air or bubbled with air under continuous illumination (using cool white fluorescent lamps at 30 or 50 μmol photons m⁻² s⁻¹ of photosynthetically active radiation, PAR), unless otherwise indicated.

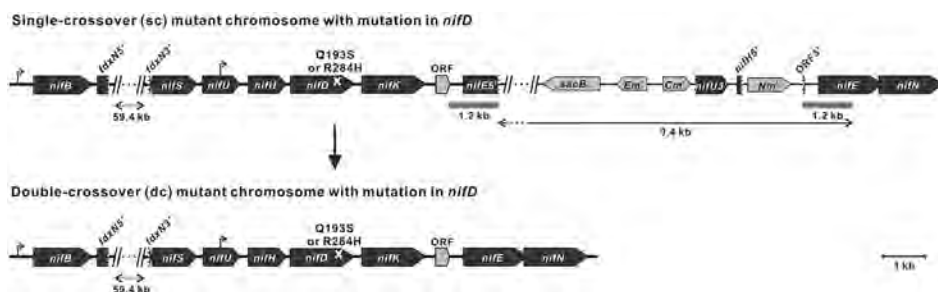


Fig. 1 – Organization of the *Anabaena* sp. PCC 7120 *nif* gene cluster for sc- and dc-mutants with site-directed substitutions in *nifD*. The sc-mutant chromosome contains 8.2-kb of inserted sequence (line with arrows) and a 1.2-kb duplicated region (horizontal gray bars) between *nifK* and *nifE*. These components were completely segregated in the dc-mutant chromosome, thus eliminating the genes conferring sucrose sensitivity and antibiotic resistance. The dots indicate gaps in the DNA for the two panels, with the lengths of the omitted sequences provided. The wild-type *nif* gene cluster has two excision elements: a 59.4-kb element in *fdxN* and an 11.3-kb element in *nifD* [34]; however, the latter element is absent in the parental ΔHup strain [7]. Bent arrows show the putative transcription start sites (upstream of *nifB* and within *nifU*) and their orientations of transcription [32].

The chlorophyll *a* (Chl *a*) concentration of the cultures was determined by the method of Porra [18].

Construction of *Anabaena double-crossover recombinants*

The sc-variants sc-AnNif-Q193S- Δ Hup and sc-AnNif-R284H- Δ Hup (hereafter referred to as sc-Q193S and sc-R284S, respectively) containing site-directed mutations in *nifD* to provide the indicated variant proteins [7] were chosen for further analysis because they exhibited high levels of nitrogenase-based H₂ production that was not strongly inhibited by the presence of N₂. To remove the 9.4-kb DNA insertion from the sc-variant chromosomes, they were grown in AA/8 liquid medium without nitrate for one week, and portions of the cultures were spread over AA agar solid medium containing nitrate and 5% sucrose for isolation of the dc-recombinants [19]. Among the sucrose resistant recombinants (due to loss of *sacB*), neomycin- and erythromycin-sensitive isolates (missing *Nm^r* and *Em^r*, respectively) were selected to identify fully segregated cells (Fig. 1). The *nifUHDK*-ORF region of the dc-variant genomes was confirmed by PCR with the primer pairs *nifSUH-F/nifSUH-R* and *ORFnifE-F/ORFnifE-R* [7] (data not shown). These two dc-variants were designated dc-Q193S and dc-R284H, respectively. In some experiments, the sc-AnNif Δ Hup strain (previously denoted AnNif Δ Hup) containing the wild-type version of *nifD* [7] was used for comparison.

H₂ accumulation and determination of H₂ production and acetylene reduction activities

For assays of cumulative H₂ production, cells were grown in AA/8-plus-nitrate medium while bubbling with air under illumination, washed, and suspended in BG11₀ medium (without added nitrate) [20] that was supplemented with 5 mM *N*-tris(hydroxymethyl)methyl-2-aminoethanesulfonic acid (TES)-KOH buffer (pH 8.2). Portions of the cultures (8 ml, containing 30 or 60 μ g of Chl *a*) were transferred into 25-ml serum

bottles that were sealed with butyl rubber stoppers. The bottles were flushed with Ar or N₂, and CO₂ was added to a final concentration of 5%. Where indicated, N₂ also was added to the Ar-based gas to provide final concentrations of 1.2–24%. The flasks were illuminated with PAR of 90–100 μ mol photons m⁻² s⁻¹ from cool white fluorescent lamps on a rotary shaker (80–90 rpm) at 28 °C. Triplicate samples were prepared for each assay of different gas composition. The concentration of H₂ accumulated in the headspace was measured by gas chromatography (GC) using a GC-2010 Plus (Shimadzu Co., Ltd., Kyoto, Japan) equipped with a thermal conductivity detector and a Rt-Msieve 5A PLOT capillary column (I.D. 0.53 mm \times 50 m, Restek Co., Ltd., USA), and the headspace gas was renewed to the initial gas composition every 3–4 days as indicated in Figs. 2 and 3.

Photobiological activities of proton reduction to H₂ and acetylene reduction to ethylene and ethane were measured essentially as described previously [7]. Portions (2 ml) of the culture samples grown in air were collected after combined-nitrogen step-down at the day indicated in Tables and Figures, transferred to sealed vials (9 ml) and incubated with PAR of 60–65 μ mol photons m⁻² s⁻¹ for 1–1.5 h. The headspace gases in the vials were replaced with Ar or N₂ for assay of H₂ production or with 12% acetylene (C₂H₂) in Ar for assay of the C₂H₂ reduction. After 2–3 h of incubation under illumination, the concentrations of H₂, C₂H₄ and C₂H₆ in the headspace were measured by GC as described previously [7].

Results and discussion

Effect of varying N₂ concentrations on long-term H₂ production by the parental Δ Hup cells

Prior studies with *Anabaena* sp. strain PCC 7120 Δ Hup cells incubated in closed flasks containing 5% CO₂ in Ar without gas replacement resulted in continuous production of H₂ for

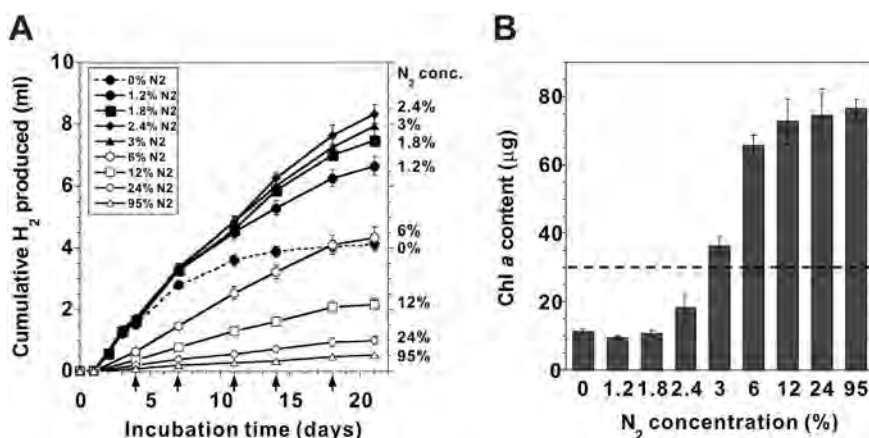


Fig. 2 – Cumulative H₂ production (A) and Chl *a* contents (B) of the parental Δ Hup culture in the presence of varied N₂ concentration in Ar and 5% CO₂. The cultures were incubated under continuous illumination (90–100 μ mol photons m⁻² s⁻¹ of PAR) at 28 °C for 21 days and the headspace gas was renewed with the respective initial gases every 3–4 days at the times indicated by the vertical arrows. The initial Chl *a* content of the cultures at the start of incubation was 30 μ g per vial, indicated by the horizontal dashed line in Fig. 2B, and the contents shown were assessed after 21 days. Values are average \pm the standard deviation of triplicate samples.

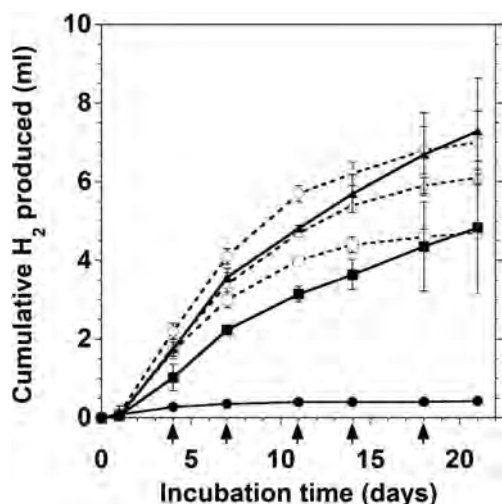


Fig. 3 – Effects of N₂ on sustained H₂ production by the two dc-variants and the parental ΔHup culture. Cultures of two site-directed dc-variants, dc-Q193S (squares) and dc-R284H (triangles), and the parental ΔHup strain (circles) were incubated under 5% CO₂ in Ar (dashed line, open symbols) or under 5% CO₂ in N₂ (solid lines, closed symbols) for 21 days with periodic gas replacement at the times indicated by the vertical arrows. Values are averages of two or three independent experiments, each performed with triplicate samples. The initial Chl *a* contents of the cultures were 60 μg per vial. H₂ production activities of the two dc-variants under 5% CO₂ in N₂ were sustained at least for a total period of about one month.

several days, with the H₂ concentration leveling off after 5–7 days [7]. Such limited timing of hydrogen production represents a major shortcoming associated with this culture method for photobiological production of H₂. Some investigators [21,22] working with different cyanobacterial strains showed that H₂ production could be sustained for longer times by periodic gas replacement (Ar) to relieve increased pressure of O₂ accumulated in the closed flasks, resulting in increased cumulative amounts of H₂ produced. A similar effect of gas renewal was shown in the same ΔHup strain immobilized in Ca²⁺-alginate thin films [23]. These findings raised the question of whether renewal of the headspace gas in suspension cultures of the *Anabaena* ΔHup strain may similarly lead to sustained H₂ production activity.

Effects of varied concentrations of N₂ on the production of H₂ over 20 days by the parental ΔHup with periodic replacement of the headspace gas every 3–4 days are shown in Fig. 2A. The sample lacking added N₂ in the gas phase evolved H₂ for a shorter time of about 10 days, whereas the cultures provided with 1.2–6% N₂ continuously produced H₂ throughout the 21 days of the experiment. More precisely, the samples containing 1.8%–3% N₂ produced the largest amounts of H₂, whereas cultures containing 6% or more N₂ exhibited smaller levels of H₂ production activity (Fig. 2A). The latter effects likely relate to the formation of N₂-derived nitrogenous products leading to decreased nitrogenase activity [9,14]. It is also probable that at high N₂ concentrations more energy is consumed for nitrogen fixation and

subsequent cell growth, thus decreasing the H₂ production [24]. Interestingly, the K_m values for N₂ of isolated nitrogenase of *Azotobacter vinelandii* [25,26], *Clostridium pasteurianum* and *Klebsiella pneumoniae* [27] have been reported to be 0.122 or 0.136, 0.069, and 0.099 atm, respectively. Assuming that the *Anabaena* wild-type dinitrogenase, which shares more than 70% identity in amino acid sequences with those from the other bacteria, has a similar K_m value (between 0.069 and 0.136 atm), the enzyme activity with the parental ΔHup cells at 1, 3, 6 and 79% (air) N₂ is calculated to be about 13, 30, 47, and 92% (K_m = 0.069 atm) or 7, 18, 27 and 85% (K_m = 0.136 atm) of the maximal velocity (V_{max}), respectively. From these calculations, it seems that when N₂ concentration exceeds 6%, the N₂ fixation activity operates at around 27–47% or higher of the maximum in the wild-type cells, which leads to a drastic decline of H₂ production activity due to the sufficiency of combined nitrogen produced by the culture's nitrogenase activity. Our results in Fig. 2A and Fig. 3 also indicate that the enzymatic provision of small amounts of combined nitrogen is required for sustaining nitrogenase activity at high levels for several weeks in this strain.

The status of the cultures on day 21 was assessed by quantification of Chl *a* content (Fig. 2B). When the N₂ concentrations were less than 3%, the Chl *a* contents were found to have decreased from the initial level. The colors of these cultures were consistent with some portions of the chlorophyll being degraded (data not shown), presumably due to the nutrients being recruited to the developing heterocysts as observed in phycobiliprotein degradation following nitrogen starvation [28]. In contrast, for cultures provided with more than 3% N₂ the Chl *a* contents increased over the initial level due to cell growth. Considering that the cultures containing higher contents of chlorophyll absorbed more light than those with less chlorophyll during incubation in the bottles under our experimental conditions, the former cultures tend to yield apparently higher H₂ productivity per bottle than the latter ones. Accordingly, the optimum N₂ concentration for efficient H₂ production by the cultures may be lower than 2.4–3.0%.

In an earlier study involving N₂-starved cultures of heterocystous *Anabaena cylindrica* grown with continuous gassing by CO₂ in Ar [10], periodic additions of NH₄Cl (10⁻⁴ M) were shown to sustain the H₂ production activity for 7–19 days. This strain exhibited similar effects of N₂ supply (0.2–0.8% v/v N₂ and 0.5% CO₂ in Ar) on the sustainability of H₂ production, but with the peak rate of H₂ production decreasing to half within about 10 days [29,30]. The decline in H₂ production for that case may arise, at least in part, from H₂ uptake by hydrogenase(s), which is not the case for the ΔHup-derived mutants described here. These earlier reports highlight the importance of supplying small amounts of combined nitrogen to heterocystous cyanobacterial cultures for sustained H₂ production by nitrogenase-based H₂ production. In agreement with those results, sustained H₂ production by the *Anabaena* ΔHup cells can be attained by optimizing the N₂ concentration in the headspace gases (Fig. 2A). Using the same *Anabaena* ΔHup mutant, Marques et al. (2011) [31] reported the results of experiments extending over 20 days that the H₂ production activity of the culture was kept at lower levels by daily addition of 1% N₂ and 1% CO₂ in Ar (thus resulting in daily increasing concentrations of N₂ and CO₂) than by daily

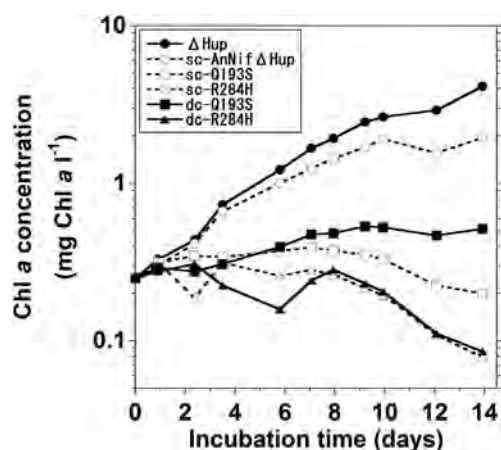


Fig. 4 – Diazotrophic growth curves after combined-nitrogen step-down. Cultures were inoculated from nitrate-grown cultures into AA/8 medium lacking combined nitrogen and incubated on a rotary shaker under a light intensity of 20–30 $\mu\text{mol photons m}^{-2} \text{s}^{-1}$ of PAR. The Chl *a* content was monitored as the cultures grew. The parental ΔHup strain (closed circle) along with the dc-Q193S (closed square) and ds-R284H (closed triangle) variants are shown by solid lines while the sc-AnNif ΔHup strain (open circle) containing the wild-type version of *nifD* and the sc-Q193S (open square) and sc-R284H (open triangle) variants are shown by dashed lines. A replicate experiment provided analogous results.

addition of only 1% CO_2 in Ar. Their results seem to indicate that the increased N_2 concentrations decrease the H_2 production activity of the ΔHup culture to lower levels, which is partly in harmony with our results in Fig. 2A, although the regime of experiments somewhat differ between the two groups. We found that the presence of low concentrations (1.2–3%) of N_2 help sustain the H_2 production activity at higher levels than that of the culture under gas devoid of N_2 (Fig. 2A).

Long-term H_2 production by the dc-Q193S and dc-R284H nitrogenase variants in an N_2 -rich atmosphere

The *Anabaena* ΔHup cells exhibited the desired property of continuous H_2 production for prolonged time periods; however, this required careful control of the N_2 concentration at low levels by diluting with Ar. We reasoned that some nitrogenase mutants of this strain would fix less nitrogen and may exhibit long-term H_2 production activities even in the presence of high concentrations of N_2 . Previous studies had characterized over 40 sc-nitrogenase mutants of this strain and identified two that produced H_2 under N_2 at rates comparable to those under Ar over 7 days without periodic gas renewal [7]. In order to assess the effects of N_2 on the sustainability of H_2 production, the corresponding dc-variants, dc-Q193S and dc-R284H, were constructed and characterized for H_2 production under incubation with N_2 -rich or Ar-rich gas (Fig. 3). Although the magnitudes of the activity fluctuated among different batches of the culture of the same strains, we have consistently observed that the desirable properties of the sc-variants were essentially maintained in the dc-

counterparts; i.e., in contrast with the ΔHup cultures, the dc-mutants produced H_2 when incubated with 5% CO_2 in N_2 at rates roughly comparable to those with 5% CO_2 in Ar over long time periods when the headspace gases were renewed every 3–4 days. Close examination revealed subtle differences between the respective sc- and dc-counterparts: The H_2 production activity of the dc-R284H culture under N_2 -rich gas was about the same level with that under Ar-rich gas through 10 days, and gradually exceeded the latter thereafter.

The former activity also exceeded the activity of the parental ΔHup culture under Ar-rich gas after 10 days. The dc-Q193S culture exhibited steady, long-term H_2 productivity under N_2 while it initially exhibited a greater rate of H_2 production under Ar, but the rate was slowed within about 10 days. Compared to the parental ΔHup culture, it showed recognizably lower long-term H_2 productivity under Ar that could be attributed to the disturbed active site environment of the catalytic Fe–Mo cofactor of dinitrogenase caused by the amino acid substitution. In contrast, both sc-variant cultures were unable to sustain H_2 production for longer than 7 days and the accumulated levels of H_2 under N_2 -rich gas for 7 days were recognizably less than what was observed for the corresponding dc-counterparts (Table S1 in the supplementary data). Furthermore, the sc-variants were incapable of diazotrophic growth on agar plates [7] or in liquid medium (Fig. 4), whereas the dc-Q193S variant, but not the dc-R284H variant, could grow at very low rates in either medium as measured on the basis of Chl *a* content (Fig. 4). These results indicate that the nitrogen fixation activity of the dc-Q193S culture was slightly more active under N_2 -rich gas than the corresponding sc-culture, allowing the culture to obtain the combined nitrogen which was required for maintenance of its activities.

Differences in H_2 production activity between the sc- and dc-Q193S cultures can be ascribed to their altered capacities for synthesis of active nitrogenase. Of likely relevance, transcription of *nifB-fdxN-nifSUHDK* in *Anabaena variabilis* ATCC 29413 requires two promoters that are located upstream of *nifB* and within *nifU*; these transcripts are cleaved in the *nifU-nifH* intergenic region by posttranscriptional processing producing the *nifB-fdxN-nifSU* and *nifHDK* transcripts [32]. Also, Northern blot analysis of the unicellular cyanobacterium *Synechococcus* sp. strain RF-1 showed *nifEN*, located downstream of the *nifHDK*-ORF, is expressed as a separate transcript [33]. Finally, a stem-loop structure(s) is predicted to exist in the ORF-*nifE* intergenic region of *Anabaena* PCC 7120 [34] implying that the *nifEN* transcript also may be a cleavage product of the larger transcripts. On the basis of these lines of evidence, we speculate that the differences in H_2 production activities between sc- and dc-Q193S can be explained by differences in transcription of the various *nif* genes due to variation in the length of the *nifHDK*-ORF-*nifEN* region: this portion of the sc-variant is 9.4 kb longer than that of the dc-mutant (Fig. 1). The relatively unstable transcripts of *nifE* and *nifN* are degraded more rapidly than the other *nif* genes [33], yet the corresponding products are required for the biosynthesis of FeMo-cofactor [35], so the shorter transcript of the dc-variants could more efficiently synthesize active nitrogenase proteins than the sc-counterparts. These speculations remain to be investigated. The results obtained for the two dc-mutants in Fig. 3 indicate that a small amount of combined nitrogen is

Table 1 – H₂ production rates of the two dc-variants and the parental ΔHup strain assayed under Ar or N₂.

Strain	H ₂ production activities ($\mu\text{mol mg of Chl } \alpha^{-1} \text{ h}^{-1}$) \pm SD			
	Under Ar		Under N ₂	
	2 days	3 days	2 days	3 days
ΔHup	25 \pm 8	8.6 \pm 2.6	6.8 \pm 2.3	2.3 \pm 0.8
dc-Q193S	35 \pm 5	36 \pm 7	29 \pm 5	30 \pm 5
dc-R284H	29 \pm 12	23 \pm 8	29 \pm 10	23 \pm 9

Cultures were grown in air on a rotary shaker for 2 or 3 days after nitrogen deprivation and aliquots of the cultures were transferred to the closed flasks for assays under Ar or N₂ for 2–3 h in the light. Values are averages of three to five independent experiments, each performed with duplicate samples.

required for sustaining the nitrogenase-based H₂ production activity at higher levels presumably by maintaining cell metabolism as with the parental ΔHup strain, although the details of how the fixed nitrogen helps sustain the activity remains to be elucidated. The N₂ concentrations required for optimum H₂ production, although not yet investigated in detail, appear to be lower with the dc-Q193S than with the dc-R284H.

Prior studies of vanadium (V) nitrogenase-expressing and H₂-uptake-deficient *A. variabilis* PK84 in a photobioreactor demonstrated continuous H₂ production when placed under 2% CO₂ in air for 2.5 months in the laboratory [36] and 40 days outdoors [37]. It should be noted that these long-term H₂ production studies were achieved by chemostat-type operation by diluting the growing cell cultures with fresh medium. The H₂ production activity of that culture under N₂ was about half of that under Ar due to its inhibition by N₂ [36]. In contrast, our site-directed variants have a potential cost advantage in sustaining H₂ production at high rates by periodic gas renewal using the less expensive N₂ gas without changing the culture medium.

Short-term assays of H₂ production and acetylene reduction by the dc-Q193S and dc-R284H variants

The *in vivo* H₂ production activities of the parental strain and the cultures containing the two dc-variant nitrogenases were

measured by short term incubation with aliquots of 2- and 3-day cultures after combined-nitrogen step-down with growth in air (Table 1). For both samples of the ΔHup strain the H₂-evolving activity when assayed under N₂ was about 27% of that assayed under Ar. On the other hand, the activities of the dc-R284H and dc-Q193S cultures assayed under N₂ were about 100% and 83% of those obtained when assayed under Ar, respectively. These values are similar to those reported previously for the sc-variants [7]. From these results together with Fig. 4 we conclude that the N₂-fixing activities of variant nitrogenases in dc-R284H or dc-Q193S were extremely low or absent, and these substituted enzymes directed nearly all the electrons to H₂ production even in the presence of N₂. This finding suggests that the N₂-fixing activity, especially in the dc-R284H culture, may be too low to support diazotrophic growth of the mutant cells under the conditions tested.

The two variants and the ΔHup strain were further characterized by examining the products (C₂H₄, C₂H₆, and H₂) obtained after incubation in an acetylene gas mixture (12% C₂H₂ in Ar) after growing under air for two or three days after nitrogen step-down (Table 2). The acetylene reduction assay has been widely used as a convenient surrogate for assessing the nitrogenase activity of the cultures. Although it is generally accepted that the conventional molybdenum (Mo)-containing nitrogenase reduces acetylene only to ethylene, while V-containing and Fe-only nitrogenases reduce acetylene to both ethylene and ethane [38,39], we had previously reported the production of ethane by several of the sc-mutants [7]. The parental cyanobacterial strain *Anabaena* sp. strain PCC 7120 only encodes the Mo-nitrogenase according to whole genome analysis [34]. Notably, the dc-Q193S culture produced ethane at low but measurable rates along with greater rates of ethylene production, while neither the ΔHup nor dc-R284H cultures produced measurable ethane. The percentages of electron allocation to each gas product were similar for the 2-day and 3-day cultures grown under air within the respective strains. The parental ΔHup strain with the normal protein environment surrounding the FeMo-cofactor reduced C₂H₂ at much greater rates in air-grown cultures subjected to 2 days of nitrogen step-down, but lower rates were observed in cultures after 3 days. By contrast, the dc mutants with alterations of the protein environment near the FeMo-cofactor exhibited similar C₂H₂ reduction rates for both periods of nitrogen

Table 2 – Composition of gas products when assayed in the presence of 12% C₂H₂ in Ar and the calculated total electron utilization for the two dc-variants and the parental ΔHup strain.

Strain	Reduction activities in the presence of acetylene ($\mu\text{mol mg of Chl } \alpha^{-1} \text{ h}^{-1}$) \pm SD						Calculated total electron utilization	
	Products							
	C ₂ H ₄		C ₂ H ₆		H ₂			
	2 days	3 days	2 days	3 days	2 days	3 days	2 days	3 days
ΔHup	24 \pm 9 (96%)	8.1 \pm 2.5 (93%)	ND	ND	1.0 \pm 0.5 (3.9%)	0.61 \pm 0.06 (6.9%)	50	17
dc-Q193S	8.8 \pm 0.6 (56%)	10 \pm 2 (57%)	0.078 \pm 0.008 (0.49%)	0.091 \pm 0.016 (0.52%)	6.8 \pm 1.2 (43%)	7.2 \pm 1.0 (42%)	32	35
dc-R284H	17 \pm 5 (81%)	13 \pm 5 (80%)	ND	ND	4.0 \pm 0.6 (19%)	3.1 \pm 0.8 (20%)	42	32

Conditions of culture growth and activity measurements were as described in Table 1, except that gas phase was C₂H₂ (12%) in Ar for the acetylene reduction assay. Values are averages of three to five independent experiments, each performed with duplicate samples. For calculation of the electron utilization associated with each product, C₂H₄, C₂H₆, and H₂ require 2, 4, and 2 electrons, respectively, and the total utilization of electrons was calculated by summing all of these values. The percentages of the total electrons allocated to each product in the presence of 12% C₂H₂ in Ar are given in parentheses.

deprivation. All strains produced H₂ at much lower rates when assayed in the presence of C₂H₂ compared to those when assayed with N₂ (Table 1). However, it should be noted that the proportions of electrons allocated to H₂ in the presence of C₂H₂ by the dc-Q193S and dc-R284H cultures were greater than that of the ΔHup strain. This result illustrates that the total nitrogenase activities of the variants are underestimated by the conventional acetylene reduction assay. A comparison of the total electron utilization by nitrogenase for the 2 day and 3 day samples assayed in the presence of C₂H₂ revealed that the activity of the ΔHup strain declined rapidly, whereas electron utilization by the two dc-variants was much more stable, as seen also in H₂ production activities under Ar and N₂. This observation is explained by sufficiency and insufficiency of fixed-nitrogen in the air-grown cultures of the ΔHup strain and the two variant cultures, respectively.

Conclusions

We have shown that two site-directed mutants of a heterocyst-forming cyanobacterium with amino acid substitutions presumed to be located in the vicinity of the catalytic FeMo-cofactor of nitrogenase rapidly produced H₂ under N₂-rich gas at higher sustained rates than under Ar-rich gas over 3 weeks, in contrast to the parental ΔHup strain which requires low N₂ concentration for prolonged H₂ production. Both of the sc- and dc-variants have desirable properties in which their H₂ production activities under N₂ are comparable to those under Ar. It is noteworthy that diazotrophic growth capability was seen in the dc-Q193S variant, although at very low levels, but not in the sc-variant. In contrast, the dc-R284H variant did not show any diazotrophic growth. The extremely low diazotrophic growth capability could allow the dc-Q193S variant to supply itself with a small amount of combined nitrogen which is required for maintenance of its cell metabolism, leading to long-term, higher H₂ production. This property of N₂ insensitivity of the variants is a potentially useful strategy for reducing the cost of the culture gas in future practical applications of sustainable biofuel production.

Acknowledgments

This work was supported by the JST PRESTO and the Great Lakes Bioenergy Research Center (DOE BER Office of Science DE-FC02-07ER64494) and in part by grant-in aid for Scientific Research on Innovative Areas (No. 24107004) and Strategic Research Base Development Program for Private Universities from Ministry of Education, Culture, Sports, Science, and Technology, Japan (to KI). We thank Miho Hosoya for assistance with the experiments.

Appendix A. Supplementary data

Supplementary data related to this article can be found at <http://dx.doi.org/10.1016/j.ijhydene.2014.09.090>.

REFERENCES

- [1] Prince RC, Ksheshgi HS. The photobiological production of hydrogen: potential efficiency and effectiveness as a renewable fuel. *Crit Rev Microbiol* 2005;31:19–31.
- [2] Sakurai H, Masukawa H. Promoting R & D in photobiological hydrogen production utilizing mariculture-raised cyanobacteria. *Mar Biotechnol* (NY) 2007;9:128–45.
- [3] Sakurai H, Masukawa H, Kitashima M, Inoue K. Photobiological hydrogen production: bioenergetics and challenges for its practical application. *J Photochem Photobiol C* 2013;17:1–25.
- [4] Bothe H, Schmitz O, Yates MG, Newton WE. Nitrogen fixation and hydrogen metabolism in cyanobacteria. *Microbiol Mol Biol Rev* 2010;74:529–51.
- [5] Tamagnini P, Leitão E, Oliveira P, Ferreira D, Pinto F, Harris DJ, et al. Cyanobacterial hydrogenases: diversity, regulation and applications. *FEMS Microbiol Rev* 2007;31:692–720.
- [6] Yoshino F, Ikeda H, Masukawa H, Sakurai H. High photobiological hydrogen production activity of a *Nostoc* sp. PCC 7422 uptake hydrogenase-deficient mutant with high nitrogenase activity. *Mar Biotechnol* (NY) 2007;9:101–12.
- [7] Masukawa H, Inoue K, Sakurai H, Wolk CP, Hausinger RP. Site-directed mutagenesis of the *Anabaena* sp. strain PCC 7120 nitrogenase active site to increase photobiological hydrogen production. *Appl Environ Microbiol* 2010;76:6741–50.
- [8] Houchins JP. The physiology and biochemistry of hydrogen metabolism in cyanobacteria. *Biochim Biophys Acta* 1984;768:227–55.
- [9] Wolk CP, Ernest A, Elhai J. Heterocyst metabolism and development. In: Bryant DA, editor. *The molecular biology of Cyanobacteria*. Dordrecht, The Netherlands: Springer (Kluwer Academic Publishers); 1994. p. 769–823.
- [10] Weissman JC, Benemann JR. Hydrogen production by nitrogen-starved cultures of *Anabaena cylindrica*. *Appl Environ Microbiol* 1977;33:123–31.
- [11] Yeager CM, Milliken CE, Bagwell CE, Staples L, Berseth PA, Sessions HT. Evaluation of experimental conditions that influence hydrogen production among heterocystous cyanobacteria. *Int J Hydrogen Energy* 2011;36:7487–99.
- [12] Lambert GR, Daday A, Smith GD. Effects of ammonium ions, oxygen, carbon monoxide, and acetylene on anaerobic and aerobic hydrogen formation by *Anabaena cylindrica* B629. *Appl Environ Microbiol* 1979;38:521–9.
- [13] Durner J, Böhm I, Hiltz H, Böger P. Posttranslational modification of nitrogenase – differences between the purple bacterium *Rhodospirillum rubrum* and the cyanobacterium *Anabaena variabilis*. *Eur J Biochem* 1994;220:125–30.
- [14] Reich S, Böger P. Regulation of nitrogenase activity in *Anabaena variabilis* by modification of the Fe protein. *FEMS Microbiol Lett* 1989;58:81–6.
- [15] Asada Y, Tomizuka N, Kuwamura S. Prolonged hydrogen evolution by a cyanobacterium (blue-green alga), *Anabaena* sp. *J Ferment Technol* 1985;63:85–90.
- [16] Masukawa H, Mochimaru M, Sakurai H. Disruption of the uptake hydrogenase gene, but not of the bidirectional hydrogenase gene, leads to enhanced photobiological hydrogen production by the nitrogen-fixing cyanobacterium *Anabaena* sp. PCC 7120. *Appl Microbiol Biotechnol* 2002;58:618–24.
- [17] Allen MB, Arnon DI. Studies on nitrogen-fixing blue-green algae. 1. Growth and nitrogen fixation by *Anabaena cylindrica* Lemm. *Plant Physiol* 1955;30:366–72.

- [18] Porra RJ. Recent advances and re-assessments in chlorophyll extraction and assay procedures for terrestrial, aquatic, and marine organisms, including recalcitrant algae. In: Scheer H, editor. *Chlorophylls*. Boca Raton, FL: CRC Press; 1991. p. 31–57.
- [19] Cai YP, Wolk CP. Use of a conditionally lethal gene in *Anabaena* sp. strain PCC 7120 to select for double recombinants and to entrap insertion sequences. *J Bacteriol* 1990;172:3138–45.
- [20] Rippka R. Isolation and purification of cyanobacteria. *Methods Enzymol* 1988;167:3–27.
- [21] Kumazawa S, Mitsui A. Efficient hydrogen photoproduction by synchronously grown cells of a marine cyanobacterium, *Synechococcus* sp. Miami BG 043511, under high cell density conditions. *Biotechnol Bioeng* 1994;44:854–8.
- [22] Kumazawa S, Asakawa H. Simultaneous production of H₂ and O₂ in closed vessels by marine cyanobacterium *Anabaena* sp. TU37-1 under high-cell-density conditions. *Biotechnol Bioeng* 1995;46:396–8.
- [23] Leino H, Kosourov SN, Saari L, Sivonen K, Tsygankov AA, Aro EM, et al. Extended H₂ photoproduction by N₂-fixing cyanobacteria immobilized in thin alginate films. *Int J Hydrogen Energy* 2012;37:151–61.
- [24] Thorneley RNF, Lowe DJ. Kinetics and mechanism of the nitrogenase enzyme system. In: Spiro TG, editor. *Molybdenum enzymes*. New York: Wiley; 1985. p. 221–84.
- [25] Hwang JC, Burris RH. Nitrogenase-catalyzed reactions. *Biochim Biophys Acta* 1972;283:339–50.
- [26] Riveraortiz JM, Burris RH. Interactions among substrates and inhibitors of nitrogenase. *J Bacteriol* 1975;123:537–45.
- [27] Jensen BB, Burris RH. Effect of high pN₂ and high pD₂ on NH₃ production, H₂ evolution, and HD formation by nitrogenases. *Biochemistry* 1985;24:1141–7.
- [28] Wood NB, Haselkorn R. Control of phycobiliprotein proteolysis and heterocyst differentiation in *Anabaena*. *J Bacteriol* 1980;141:1375–85.
- [29] Miyamoto K, Hallenbeck PC, Benemann JR. Solar-energy conversion by nitrogen-limited cultures of *Anabaena cylindrica*. *J Ferment Technol* 1979;57:287–93.
- [30] Miyamoto K, Hallenbeck PC, Benemann JR. Effects of nitrogen supply on hydrogen production by cultures of *Anabaena cylindrica*. *Biotechnol Bioeng* 1979;21:1855–60.
- [31] Marques AE, Barbosa AT, Jotta J, Coelho MC, Tamagnini P, Gouveia L. Biohydrogen production by *Anabaena* sp. PCC 7120 wild-type and mutants under different conditions: light, nickel, propane, carbon dioxide and nitrogen. *Biomass Bioenergy* 2011;35:4426–34.
- [32] Ungerer JL, Pratte BS, Thiel T. RNA processing of nitrogenase transcripts in the cyanobacterium *Anabaena variabilis*. *J Bacteriol* 2010;192:3311–20.
- [33] Huang TC, Lin RF, Chu MK, Chen HM. Organization and expression of nitrogen-fixation genes in the aerobic nitrogen-fixing unicellular cyanobacterium *Synechococcus* sp. strain RF-1. *Microbiology* 1999;145(Pt 3):743–53.
- [34] Kaneko T, Nakamura Y, Wolk CP, Kuritz T, Sasamoto S, Watanabe A, et al. Complete genomic sequence of the filamentous nitrogen-fixing cyanobacterium *Anabaena* sp. strain PCC 7120. *DNA Res* 2001;8:205–13. 27–53.
- [35] Hu Y, Ribbe MW. Biosynthesis of nitrogenase FeMoco. *Coord Chem Rev* 2011;255:1218–24.
- [36] Borodin VB, Tsygankov AA, Rao KK, Hall DO. Hydrogen production by *Anabaena variabilis* PK84 under simulated outdoor conditions. *Biotechnol Bioeng* 2000;69:478–85.
- [37] Tsygankov AA, Fedorov AS, Kosourov SN, Rao KK. Hydrogen production by cyanobacteria in an automated outdoor photobioreactor under aerobic conditions. *Biotechnol Bioeng* 2002;80:777–83.
- [38] Dilworth MJ, Eady RR, Robson RL, Miller RW. Ethane formation from acetylene as a potential test for vanadium nitrogenase in vivo. *Nature* 1987;327:167–8.
- [39] Pau RN, Mitchenall LA, Robson RL. Genetic evidence for an *Azotobacter vinelandii* nitrogenase lacking molybdenum and vanadium. *J Bacteriol* 1989;171:124–9.

Review

How Close We Are to Achieving Commercially Viable Large-Scale Photobiological Hydrogen Production by Cyanobacteria: A Review of the Biological Aspects

Hidehiro Sakurai ^{1,*}, Hajime Masukawa ^{1,2}, Masaharu Kitashima ³ and Kazuhito Inoue ^{1,3}

¹ Research Institute for Photobiological Hydrogen Production, Kanagawa University, Tsuchiya, Hiratsuka, Kanagawa 259-1293, Japan

² The OCU Advanced Research Institute for Natural Science and Technology (OCARINA), Osaka City University, 3-3-138 Sugimoto, Sumiyoshi-ku, Osaka 558-8585, Japan; E-Mail: masukawa@ocarina.osaka-cu.ac.jp

³ Department of Biological Sciences, Kanagawa University, Tsuchiya, Hiratsuka, Kanagawa 259-1293, Japan; E-Mails: pt125536zy@kanagawa-u.ac.jp (M.K.); inouek01@kanagawa-u.ac.jp (K.I.)

* Author to whom correspondence should be addressed; E-Mail: sakurai@waseda.jp; Tel.: +81-463-59-4111; Fax: +81-463-58-9694.

Academic Editors: John C. Meeks and Robert Haselkorn

Received: 5 January 2015 / Accepted: 9 March 2015 / Published: 18 March 2015

Abstract: Photobiological production of H₂ by cyanobacteria is considered to be an ideal source of renewable energy because the inputs, water and sunlight, are abundant. The products of photobiological systems are H₂ and O₂; the H₂ can be used as the energy source of fuel cells, *etc.*, which generate electricity at high efficiencies and minimal pollution, as the waste product is H₂O. Overall, production of commercially viable algal fuels in any form, including biomass and biodiesel, is challenging, and the very few systems that are operational have yet to be evaluated. In this paper we will: briefly review some of the necessary conditions for economical production, summarize the reports of photobiological H₂ production by cyanobacteria, present our schemes for future production, and discuss the necessity for further progress in the research needed to achieve commercially viable large-scale H₂ production.

Keywords: cyanobacteria; hydrogen; photosynthesis; nitrogenase; heterocyst; renewable energy; mariculture

1. Introduction

1.1. Global Climate Change

The concentration of atmospheric CO₂ has been increasing since the era of the industrial revolution when it was estimated to be 270–280 ppm initially, rising to current levels of about 400 ppm. According to the fifth assessment report of the UN IPCC (United Nations Intergovernmental Panel on Climate Change) [1,2], the greatest contribution to the global increase in greenhouse gases comes from CO₂ emitted by burning fossil fuels (65%) and land use changes (deforestation) (11%), followed by methane (16%), N₂O (6%) and fluorocarbons, *etc.* (2%). Currently, the amounts of greenhouse gases emitted have continued to rise due to the increases in human activities and population growth. If we are able to stabilize the atmospheric greenhouse gases at 530–580 ppm-CO₂ equivalent (approximately twice that of the pre-industrial level), one of the ICPP scenarios predicts that we will need to reduce global greenhouse gas emissions by 19%–47% in 2050 and 59%–81% in 2100 (relative to 2010 emissions) (Figure 1). Some scenarios predict that we will need to go beyond reduction strategies and achieve “negative emissions” by CO₂ sequestration, *etc.* Economically advanced countries will likely be required to reduce emissions the most, perhaps by as much as 80% compared to present levels. Even if we succeed in stabilizing greenhouse gases at the level of 530–580 ppm CO₂ equivalent, the global average temperature will rise around 2.0–2.2 °C relative to the 1850–1900 temperatures. Stabilizing emissions at a less-stringent level of 720–1000 ppm-CO₂ equivalent, would still require substantial emissions reduction from current, largely unregulated levels, and result in the average temperature rising around 3.1–3.7 °C relative to the 1850–1900 temperatures. From all of these considerations, it is evident that we urgently need viable renewable energy technologies as part of a global strategy to drastically reduce CO₂ emissions from burning fossil fuels and thus avert potentially catastrophic climate change.

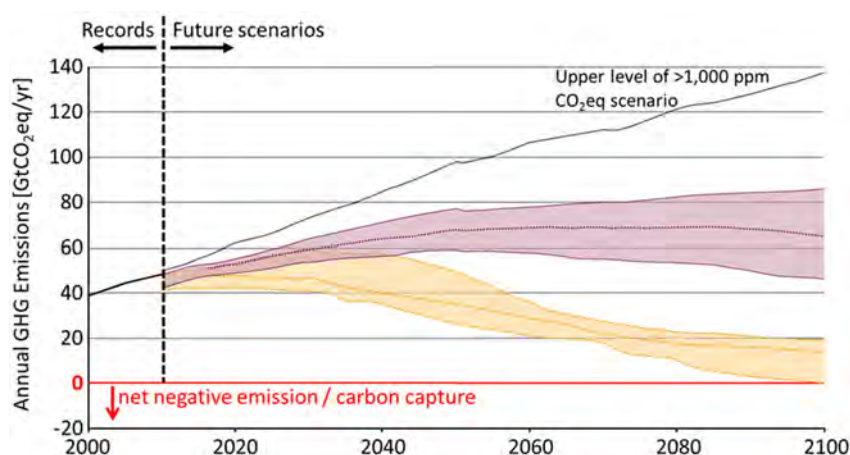


Figure 1. Some scenarios for annual greenhouse gas (GHG) emission, UN IPCC. Due to uncertainty regarding future emissions and prediction of the outcome, probable ranges are shown for each stabilization targets. ■ Stabilization at 530–580 and ■ 720–1000 ppm CO₂-eq respectively in 2100. The upper level of the probable range of >1000 ppm CO₂-eq line in IPCC scenario is also shown. (Adapted from Figure SPM4, IPCC, 2014: Summary for Policy Makers, the Climate Change 2014 [1]).

1.2. Prospects for Large-Scale Algal Biofuel Production

We are currently consuming energy at an unsustainably high rate, with much of the consumption (about 82%) coming from fossil fuels (Table 1) (International Energy Agency (IEA), IEA 2014) [3]. Land-based production of biofuels has been proposed to meet at least some of our energy needs. One method for assessing the energy potential of land-based production systems is to consider total primary energy consumption in the context of the nutritional energy consumption largely derived from current land-based crop systems. In terms of total primary energy consumption, on a world-wide average, people consume about 25 times their nutritional energy (20 times, compared with the fossil fuel-derived energy) (Table 1): people in US 136, Germany 76, Japan 70, China 43 times, respectively (IEA Energy Indicators 2012 in (IEA Energy Outlook 2014)) [4]. From this comparison, it is evident that we cannot expect much more additional energy from land-based agricultural crops, such as sugar cane and corn. Accordingly, there are growing interests in the development and production of biofuels, such as biomass, biodiesel, and H₂, using a variety of microalgae grown on lands that are not suitable for agricultural production [5–9]. However, commercially viable large-scale fuel production from microalgae has yet to be realized.

Table 1. Solar energy and human energy consumption.

	Energy Intensity and Quantity	Ratios			Refs./ Remarks
Solar energy received on Earth surface					
Intensity	165 W·m ⁻² (1450 kWh·m ⁻² ·yr ⁻¹)				[10]
Total energy	2,660,000 × 10 ¹⁸ J·yr ⁻¹	4750	5800	440,000	[10]
Photosynthetically active radiation	1,200,000 × 10 ¹⁸ J·yr ⁻¹				45% of the total
Human social energy consumption					
Total primary energy supply	560 × 10 ¹⁸ J·yr ⁻¹	1	1.22	25	[3]
Fossil fuel consumption	460 × 10 ¹⁸ J·yr ⁻¹	0.82	1	21	[3]
Human digestive energy intake	22 × 10 ¹⁸ J·yr ⁻¹	0.039	0.048	1	Population: 7.2 × 10 ⁹ 2000 kcal·capita ⁻¹ ·day ⁻¹

1.3. Examples of Policies to Promote the Development of Renewable Energy Technologies

1.3.1. Feed-In Tariff Scheme in Germany

Feed-in electricity tariffs were introduced in Germany in 2004 to encourage the use of new energy technologies, such as wind, hydro- and geo-thermal power, biomass, and solar photovoltaics. Feed-in tariffs are a policy employed by governments to encourage investment in renewable energy technologies by providing them a fee (or “tariff”) above the retail rate of electricity. Feed-in tariffs provide long-term investment security to renewable energy producers and are typically based on the costs of specific technology. Wind power, for instance, costs less to produce than solar PV or tidal powers, so the tariff awarded is correspondingly lower. In a Wikipedia entry [11], the German feed-in tariff system is described as one of the most efficient and effective support schemes in the world for promoting

renewable electricity. As of August 2014, a revised Renewable Energy Sources Act (EEG 2014, also called EEG 2.0) was implemented in Germany, with some modifications to the feed-in tariffs. The aim is to meet Germany's renewable energy goals of 40% to 45% of electricity consumption in 2025 and 55% to 60% in 2035 [12].

For an international comparison of the price of energy and feed-in tariff, the following currency exchange rates (approximate average currency exchange rates in 2014) were assumed in this paper: 1 Euro = 132 US¢, and 100 Japanese Yen = 94 US¢. The German feed-in tariffs in August of 2014 are: 4.62 US¢/kWh for hydropower facilities up to 50 MW, 16.5 ¢/kWh for those up to 500 kWh, 16.4 ¢/kWh for solar installations on buildings up to 10 kW and 25.6 ¢/kWh for offshore wind [12]. The tariffs for photovoltaics in 2014 decreased by about 80% compared with those in 2004, the starting year of the German program, demonstrating the effectiveness of the policy strategy.

1.3.2. Feed-In Tariff Scheme in Japan [13]

The government of Japan introduced feed-in tariffs in 2012. In April 2014, the purchase prices (excluding the tax, with the purchase period of 10 or 20 years at fixed prices) were: 34.8 ¢/kWh for photovoltaics up to 10 kWh, 30.1 ¢/kWh for those 10 kW or more, 20.7 ¢/kWh for land-based wind power, 33.8 ¢/kWh for offshore wind power, and 13.2 ¢/kWh for medium hydropower. Because the prices offered by the government were so favorable to investors, in southern Japan, Kyushu Electric Power Co. had to suspend receipt of applications from large-sized renewable-energy producers (photovoltaics) wishing to access the company's grid while it reviews how much more clean energy it's capable of handling on sunny days.

1.3.3. Estimated Cost of Electricity in the USA

According to the 2012 estimates by the US Energy Information Administration (eia), the levelized cost of electricity in ¢/kWh for plants entering service in 2019 are: conventional coal 9.56 (no subsidy), geothermal 4.79 (4.45, with subsidy), solar photovoltaic 13.0 (11.86 with subsidy), *etc.* [14]. These estimates illustrate that for the US, coal continues to be a relatively cheap source of electricity even though burning coal emits a large amount of CO₂ into the atmosphere. In order to decrease CO₂ emissions from coal, the integrated coal-gasification combined cycle (IGCC) (estimated to be 11.59 ¢/kWh) and IGCC with carbon control and sequestration (CCS) systems have been proposed (estimated to be 14.74 ¢/kWh). The CO₂ captured in these systems is transported to a storage site, normally an underground geological formation. The effectiveness of CCS, and its long-term effects on the environment need to be carefully assessed.

1.3.4. Possible Merit of H₂ as Motor Fuels

The next-generation of fuel-efficient cars is entering the consumer market. Toyota recently announced the commercialization of hydrogen fuel-cell vehicles called "Mirai" in December 2014 [15]. According to Toyota, using measurements based on the Japanese JC08 test cycle, a cruising range of approximately 700 km can be achieved when fueled with H₂ at 70 MPa. In comparison, the cruising ranges of electric cars might be around 100–200 km per full battery charge. In the same month, several Japanese

gas companies announced opening commercial hydrogen refueling stations with the introductory prices of H₂ (subsidized by the government) ranging from 9.4 to 10.3 US\$ (1000–1100 Japanese Yen) per kg, or 23.8–26.1 ¢/kWh [16]. Because the energy efficiency of fuel cell cars is better than internal combustion engine cars, it is estimated that H₂ fuel will be competitive with gasoline 1.22–1.60 US\$/L (retail price of about 13.9–18.3 ¢/kWh including tax, calculated on an energy density of 8.76 kWh/L).

2. Outline of the Biological Processes of Photobiological H₂ Production by Heterocyst-Forming Cyanobacteria

Photobiological production of biomass by photosynthetic organisms (trees, grasses, algae, *etc.*) is considered one of the better candidates for large-scale, renewable energy because the amount of solar energy is almost infinite (Table 1). Photobiological H₂ production by cyanobacteria is one of the options, and this review briefly discusses nitrogenase (N₂ase)-based photobiological H₂ production by cyanobacteria because it is the focus of our current studies. In doing so, we do not intend to supplant other systems, such as hydrogenase (H₂ase)-based photobiological H₂ production by various algae including cyanobacteria, as well as biofuel production (e.g., biomass, biodiesel) by various photosynthetic microorganisms.

Some strains of cyanobacteria possessing N₂ase are good candidates for optimization of photobiological H₂ production [17–21]. N₂ase catalyzes the following reaction under optimal conditions for N₂ fixation:



whereas, in the absence of N₂ (e.g., under Ar), all e⁻s are allocated to H₂ production:



The above reactions catalyzed by N₂ase are essentially irreversible. N₂ase is extremely O₂ sensitive and quickly inactivated by O₂. In order to reconcile the activities of the O₂-sensitive N₂ase with O₂-evolving photosynthesis, cyanobacteria have evolved various means to address to the physiological challenges [22]. There are three basic groups. In Group 1, the two processes are separated spatially as found in heterocystous filamentous types (e.g., *Anabaena*, *Nostoc*, *Calothrix*). In Group 2, the processes are separated temporally by circadian rhythm as found in non-heterocystous unicellular and filamentous types (e.g., *Cyanothece*, *Lyngbya*). In Group 3, other non-heterocystous filamentous types (e.g., *Trichodesmium*) seem to sporadically perform the two processes: some of the cells have ordinary O₂-evolving photosynthesis activity, while the others temporally cease photosynthesis and fix N₂ [23].

In this review, we will discuss mainly Group 1 cyanobacteria, as these strains are the focus of our research and because they are the most extensively studied among the three groups with respect to physiology, molecular biology, *etc.* [24–26]. The cells are organized as filaments, with the majority of the cells (called vegetative cells) synthesizing organic compounds by ordinary photosynthesis. Under combined-nitrogen deficiency a few of the cells develop into heterocysts, cells specialized for nitrogen fixation. Heterocysts lacking photosystem II activity, have increased respiration and are surrounded by a thick cell envelope that impedes the entry of O₂, thus providing a micro-oxic environment to protect the N₂ase from inactivation by O₂. They receive saccharides from neighboring vegetative cells and the saccharides are then used as the electron donors for the N₂ase reaction (Figure 2). Within heterocysts,

photosystem I reduces low-potential ferredoxin and/or flavodoxin and contributes to the generation of ATP through photophosphorylation. The fixed nitrogen is converted to glutamine, which is transported to vegetative cells. In this manner, heterocystous cyanobacteria are able to simultaneously perform O₂-evolving photosynthesis and the O₂-labile N₂ase reaction.

Many of these types of cyanobacterial strains have the uptake hydrogenase (Hup) and some (but not all) of them also have the bidirectional hydrogenase (Hox) [27–29]. The former H₂ase reabsorbs H₂ produced by N₂ase and thus the presence of Hup activity can limit the net production of H₂ by the N₂ase. There has been a report of an environmental isolate of the non-heterocystous *Oscillatoria* sp. strain Miami BG7 that lacks Hup activity and is able to accumulate H₂ in the presence of photosynthetically evolved O₂ [30]. When Hup activity was eliminated by molecular genetic techniques [28,31–36] or chemical mutagenesis [37], the resulting cyanobacterial mutants showed enhanced H₂ production activity. Since in contrast to H₂ase activity, N₂ase catalyzes an essentially unidirectional H₂ production and thus does not consume H₂, cyanobacterial mutants lacking Hup activity are able to accumulate H₂ to about 7%–30% (v/v) in the presence of O₂ evolved [35,38].

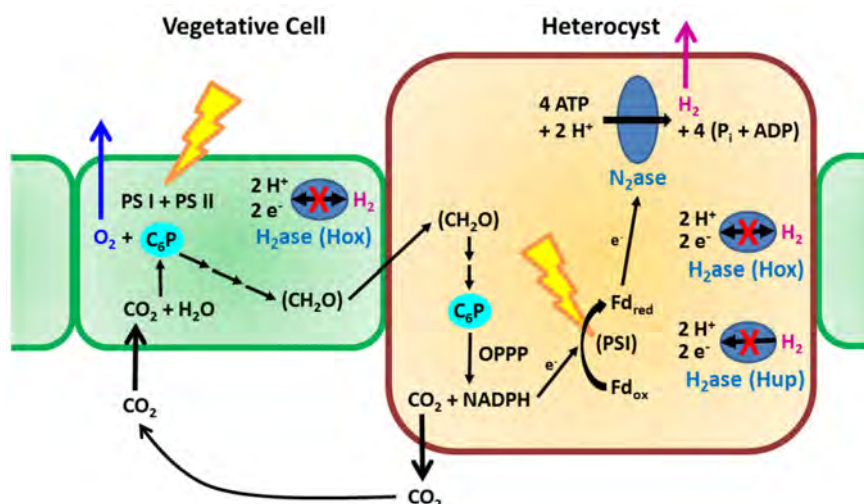


Figure 2. Outline of H₂-related metabolic routes in heterocyst-forming cyanobacteria. Vegetative cells synthesize saccharides (CH₂O) by ordinary photosynthesis with accompanying evolution of O₂ and uptake of CO₂. Heterocysts receive the saccharides, and use them (accompanied by CO₂ evolution) as the sources of e⁻ for N₂ase reaction. For efficient net production of H₂, H₂ase(s) (uptake H₂ase Hup and bidirectional H₂ase Hox) have been inactivated. C₆P: hexose phosphate, Fd_{ox} and Fd_{red}: ferredoxin oxidized and reduced respectively, OPPP: oxidative pentose phosphate pathway, PSI and PSII: photosystem I and II, respectively (adapted from [21] with modification).

In the unicellular diazotrophic cyanobacterium *Cyanothece* sp. strain PCC 7822, the N₂ase and H₂ production activities are inactivated following disruption of the *hupL* gene (encoding a large subunit of Hup) via molecular genetic techniques, indicating that Hup protects N₂ase from oxygen toxicity by removing O₂ in this strain [39].

Although Hup may play such a role, the degree of its N₂ase protection may differ among strains, and we can selectively use the strains (either heterocystous or unicellular) in which the negative effects of elimination of Hup on net H₂ production are low.

3. Some Lessons from Studies of the Economics of Large-Scale Algal Fuel Production

3.1. Benemann's Critical View of Algal Biofuel Production

Benemann has been studying photobiological biofuel production by various algae, since the first discovery of N₂ase-based photobiological H₂ production by cyanobacteria [40]. He critically examined the viability of microalgae for the production of gaseous fuels, specifically H₂ and CH₄, and assessed various proposed schemes on the basis of their technological and economic feasibility. In 2004, he summarized his opinion [41] as: "Processes for the production of gaseous fuels, H₂ and CH₄, using microalgae culture have been studied from a scientific perspective for several decades, and the practical cultures have been studied relatively recently. The lack of practical results in H₂ and CH₄ production cannot be ascribed to limited R&D funding. The only present practical application is the harvesting of algal biomass from wastewater treatment ponds by chemical flocculation, followed by the anaerobic digestion of the algal biomass. Overall, costs of such a process were estimated at about \$10 per GJ of H₂ (3.6 ¢/kWh)." Benemann's conceptual steps for a techno-economic analysis consisted of: (1) Production in open ponds (costing \$7 m⁻², 0.5 km² in area in some of his analyses), at a solar efficiency of 10%, of a nitrogen-limited biomass (that accumulates large amounts of storage carbohydrates); (2) Concentration of the biomass from the ponds in a settling pond; (3) Anaerobic dark fermentation to yield 4 H₂/glucose stored in the algal cells, plus two acetate moles; and (4) Reaction in a photobioreactor in which the algal cells would be converted from the two acetate moles to eight moles of H₂. The cost of the process was estimated at about \$10 per·GJ⁻¹ of H₂, (3.6 ¢/kWh) with the photobioreactor comprising about half of the total cost. In our opinion, a photosynthesis efficiency of 10%, required for economical production, is very difficult to attain even if an algal H₂ase serving as a highly efficient H₂ catalyst is used.

3.2. Life-Cycle Analysis (LCA) of the Energy Requirements for Algal Fuel Production

Clarens *et al.* [42] made LCA analyses of biofuel production by microalgae based on published records (first-generation algae production), and found that algae production systems release more CO₂ to the atmosphere than is taken up during growth of the biomass. Their schemes are: (1) Growth of algae in open ponds using a raceway configuration, with slow-moving paddle wheels to aerate and circulate the algae growth medium; (2) fertilizers are added as water is pumped in to or out of (for harvesting) the ponds; and (3) CO₂ is bubbled into the ponds. The result of the analyses for a production site in California, for example, indicated that for producing 1.00 unit of energy, about 1.18 unit of energy is consumed; nutrients: 0.49 unit (about 0.2 unit for urea), CO₂-derived: 0.35 unit, direct: 0.04 unit, and others (water, *etc.*): 0.29 unit. They pointed out that in addition to anticipated improvements in algal productivity (next-generation production), the uses of flue gas (from coal fired plants) and municipal wastewater (to reduce nutrient energy costs) could lead to a net-positive bioenergy production by microalgae in these systems.

3.3. Life-Cycle Analysis (LCA) of the Costs for Large-Scale Microalgal Production

A comparative LCA study of the potential environmental impact and economic viability of producing biodiesel from microalgae grown in large virtual ponds (4 km²) of coastal Australian land were made [43]. In terms of GHG (greenhouse gas) emissions, algae GHG (−27.6 to 18.2 (CO₂-unit)) compare very favorably with canola (35.9) and ultra-low sulfur (ULS) diesel from oil (81.2). Costs are not so favorable, with algae ranging from 2.2 to 4.8 (cost-unit), compared with canola (4.2) and ULS diesel (3.8). The large footprint of algae cultivation is driven predominantly by upstream factors, such as the demands for CO₂ and fertilizer. To reduce these factors, flue gas and, to a greater extent, municipal waste-water could be used to offset the economic and environmental burdens associated with algae, highlighting the need for a high production rate to make algal biodiesel economically attractive.

4. Our Scheme for Large-Scale Photobiological H₂ Production by Mariculture-Raised Cyanobacteria

We briefly discuss several issues for achieving commercially viable large-scale photobiological H₂ production by cyanobacteria. Photobiological H₂ production is considered to be one of the better candidates for renewable energy production because H₂ pollutes environment minimally both in production as well as in utilization stages, and is relatively easily storable and transportable.

We will first describe an outline of our conceptual scheme [44] for large-scale photobiological H₂ production by mariculture-raised cyanobacteria. We will then discuss some of the key issues in greater detail. Our scheme is: (1) Production of H₂ in large plastic bioreactors consisting of several layers of plastic film; (2) repeated harvesting of crude H₂; (3) initial separation of H₂ from O₂ possibly by gas-selective permeability membranes on factory ships followed by further purification of H₂ by pressure-swing adsorption (PSA); and (4) compression or transformation to a form suitable for transportation by ship and storage (Figures 3 and 4).

Table 2. Expected sales of photobiologically produced H₂.

Energy Conversion Efficiency (%)	Produced H ₂ (kWh·m ⁻² ·yr ⁻¹)	Energy Recovery (Ratio)	Purified H ₂ (kWh·m ⁻² ·yr ⁻¹)	H ₂ Total Sale (cents m ⁻² ·yr ⁻¹)			
				Selling Price (cents·kWh ⁻¹)			
				10	20	30	40
1	15	0.3	4.5	45	90	135	180
1	15	0.5	7.5	75	150	225	300
1	15	0.7	10.5	105	210	315	420
2	30	0.3	9	90	180	270	360
2	30	0.5	15	150	300	450	600
2	30	0.7	21	210	420	630	840
3	45	0.3	9	135	270	405	540
3	45	0.5	15	225	450	675	900
3	45	0.7	21	315	630	945	1260

The ΔH of 1 kg crude oil (Oeq) is 41.9 MJ or 11.6 kWh (HHV, higher heating value: the product water is condensed liquid). The ΔH of 1 m³ (STP) H₂ is 12.8 MJ, 3.56 kWh, or 0.30 kg·Oeq (Oil equivalent) and that of 1kg of H₂ is 142 MJ, 39.4 kWh or 3.39 kg Oeq (HHV).

Assuming the total solar radiation of about $1500 \text{ kWh}\cdot\text{m}^{-2}\cdot\text{yr}^{-1}$ [10] and an energy conversion efficiency of 1%–3% (of total radiation), which will be discussed later, the energy produced as crude H_2 is $15\text{--}45 \text{ kWh}\cdot\text{m}^{-2}\cdot\text{yr}^{-1}$ (Table 2). Assuming an energy recovery ratio (energy in purified H_2 /energy in crude H_2) of 0.3–0.7, we calculated a total price for H_2 of $10\text{--}40 \text{ ¢/kWh}$ (*cf.* Section 1.3 for the price ranges of renewable fuels). Table 2 gives sales projections for photobiologically produced H_2 and the energy conversion efficiency targets that will promote the adoption of photobiological renewable production.

4.1. Flexible Plastic Bioreactors Floating on the Surface of Sea Could Reduce Costs

Bioreactors for commercially viable algal biomass or liquid fuel production should be large (a total of a few km^2 as a production unit) and inexpensive. Currently, open ponds with raceway configurations are the leading candidates for the first step of biomass production of algae. For H_2 production, closed bioreactors are required in at least some part of the process. A variety of closed hard panel or tubular photobioreactors are described for laboratory or pilot-scale studies (e.g., [45,46]), but they are likely much more expensive than open ponds.

We have proposed flexible H_2 -barrier plastic bags floating on the calm sea or ocean surface (e.g., the calm belt about 30° north or south, such as the “mysterious Bermuda triangle” region) [17,44]. The culture medium is based on freshwater, and the bioreactors would spread over the sea surface because of the difference in density between the culture medium and the surrounding seawater. Salt lakes can also be used as the fields for cultivation. The size of the bags is flexible; for large-scale H_2 production for example, 20 bags of $25 \text{ m} \times 200 \text{ m}$ in surface area, could cover the surface of 1 km^2 . As proof of this concept, Kitashima *et al.* [47] demonstrated that transparent flexible H_2 -barrier plastic bags are usable for studies of photobiological H_2 production by cyanobacteria in the laboratory. The H_2 permeability (P_m) value of the transparent plastic bags ranged from 44 to $87 \text{ cm}^3\cdot\text{m}^{-2}\cdot\text{atm}^{-1}\cdot\text{day}^{-1}$. H_2 -barrier bags for laboratory use (Wakhy bags, www.ab.auone-net.jp/~wakhylab) are now commercially available (GL Sciences, Tokyo. info@gls.co.jp).

The cost of the bioreactor was estimated as follows [44]. The bioreactor is composed of three layers of plastic bags (Figure 3), for a total of six layers (sunny side and shady side) of transparent plastic film. The innermost bag holds the cyanobacteria culture, the middle bag has very low permeability to H_2 , and the outermost bag serves to mechanically protect the inner bags. The thickness of each film is 0.08 mm , and 480 cm^3 of plastic per m^2 of the bioreactor’s sunny side surface is required. Assuming an average plastic price of $\$2\text{--}\4 per kg (or liter), the material cost is $96\text{--}192$ cents per m^2 of bioreactor. The used plastic bags can be recycled many times to regenerate plastic films at about half the price of the new materials. The above assumptions result in the cost of the bioreactor being about $24\text{--}48$ cents per m^2 of bioreactor surface per year, assuming a renewal cycle of every two years. The plastic films of 480 cm^3 are assumed to be produced by consuming 360 mL of crude oil for processing that is equivalent to $3.92 \text{ kWh}\cdot\text{per}\cdot\text{m}^2$ per year. The plastic bags can be recycled at an energy cost of 20% of the feedstocks (0.78 kWh). The amount of energy in feedstocks derived from fossil fuels can be further decreased because currently H_2 generated from fossil fuels is used as a part of the feedstocks for plastic film production, and photobiologically-produced H_2 can replace some part of it.

4.2. Cost-Effective Strategy for Achieving Adequate Cell Growth with Repeated Harvesting of H_2 without Changing the Culture Medium

Under our proposed strategy, H_2 ase-less mutant cyanobacterial cells grow in large ordinary plastic bags containing CO_2 (with its occasional replenishment) floating on the sea without mechanical agitation of the medium (Step 1, in Figure 3). The need for additional combined nitrogen for growth would be minimal and thus the cost of fertilizer would be much less as compared to systems using non-nitrogen-fixing microalgae. Cyanobacterial stock cultures are transferred to photobioreactors for H_2 production (Step 2). The innermost bag (Figure 3) is filled with gas containing CO_2 in Ar. In the H_2 production stage, no mechanical agitation or bubbling are applied, as CO_2 is recycled within the bag (absorbed during photosynthetic carbon assimilation in vegetative cells and released from heterocysts when saccharides are degraded as electron donors to N_2 ase (Figure 2)). The cyanobacterial cell waste can be recycled as fish feed [48].

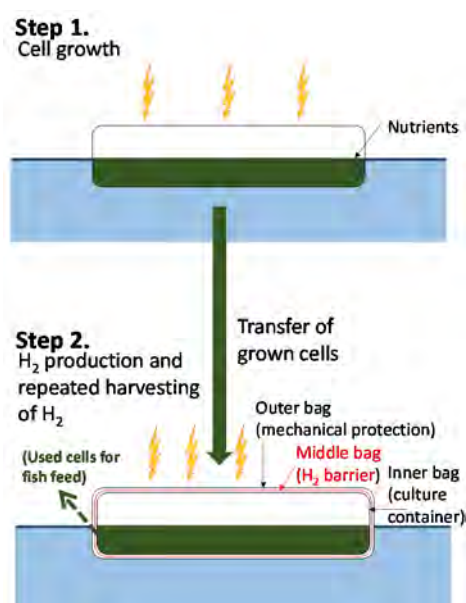


Figure 3. Outline of H_2 production by mariculture-raised cyanobacteria. **Step 1:** Cell growth in a transparent plastic bag floating on the sea surface. The bioreactor is filled with air containing CO_2 ; **Step 2:** H_2 production in a photobioreactor composed of three bags (at least one layer is a H_2 gas barrier membrane) floating on the sea surface. The spent cells can be used as fish feed [48].

The proposed strategy can be modified in response to changes in production costs. For example, when the cost of Ar is high, N_2 ase mutants can be used [49]. Some of the mutants have high H_2 production activity under N_2 -rich gas as compared to the parent strain activity under Ar gas, and also have extremely low N_2 -fixing activity. Examples of such mutants have been characterized; with the amino acid substitutions presumed to be located in the vicinity of the FeMo-cofactor of N_2 ase (e.g., Q193S and R284H) [49]. The N_2 ase activity of such mutants is not inhibited by the presence of high concentrations of N_2 and thus the use of costly Ar could be avoided. However, these strains require combined nitrogen in the growth stage, and the advantages and disadvantages of using this type of mutant needs to be carefully assessed.

4.3. Initial Separation of crude H₂ Followed by Further Purification by Pressure-Swing Adsorption (PSA) on Factory Ships

The H₂ produced within the bag is allowed to accumulate for several weeks to a few months before “harvesting” the gas mixture (Figure 4). After removal of O₂ from the harvested gas mixture, H₂ is purified on factory ships by PSA (pressure-swing adsorption) for transportation to ports [44]. The separated Ar and CO₂ are recycled back to the bioreactors, along with replenishment of H₂O (substrate necessary for H₂ production) to resume the next round of H₂ production. The amount of H₂O needed is relatively small, (0.8 kg H₂O is required for 1 m³·H₂, or 18 g for 22.4 L·H₂). Some of the downstream technologies outlined in Figure 4 are still in the developmental stage, notably the initial separation of H₂ from O₂ in the gas mixtures. One of the candidate technologies involves the use of gas-selective membranes that allow the penetration of H₂ at much higher rates than that of O₂. For example, there is a report of a carbon molecular sieve membrane that allows permeation of H₂ about 10–15 times faster than O₂ (the gas permeability constant of 372–473 and 25–50 in gas permeability units for H₂ and O₂, respectively) [50]. We expect that there will be a concomitant development of these technologies if photobiological H₂ production on the sea surface is adopted as one of the best options for large-scale renewable energy production (an example of “necessity is the mother of invention”).

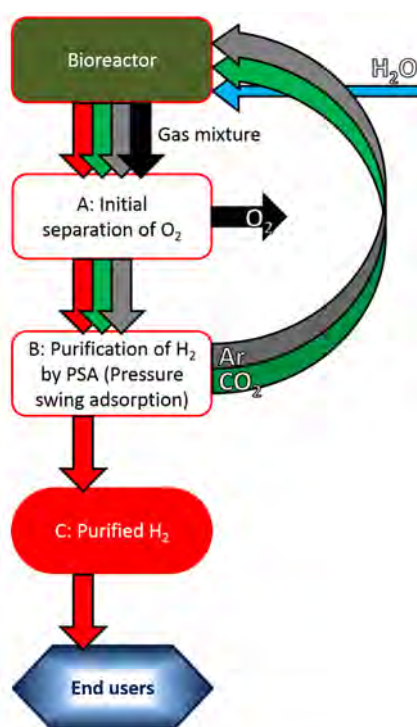


Figure 4. Outline of photobiological H₂ production by mariculture-raised cyanobacteria and delivery of purified H₂ to end-users (possible scheme). The fully grown cells (Step 1, Figure 3) are transferred to the photobioreactor (Step 2, Figure 3), which is filled with Ar and CO₂ (+ trace amount of N₂, not shown) and allowed accumulation of the produced gases (H₂ and O₂). (A) Initial separation of O₂ from the gas mixture; (B) Further purification of H₂ by PSA (pressure-swing adsorption), and the removed CO₂ and Ar are recycled to the bioreactor. H₂O consumed for H₂ production is replenished; (C) Purified H₂ is processed for transportation to end-users (for details, see text).

The purified H₂ may be condensed (high pressure or liquefied) or chemically transformed (e.g., to NH₃ which can subsequently be used as a fuel rather than fertilizer, or reversible hydrogenation of toluene (C₇H₈) to methyl cyclohexane (C₇H₁₄)) for transportation to end-users (Figure 4).

4.4. The Advantages of Sustained High H₂ Production without Changing the Culture Medium

We would like to emphasize that one of the economic advantages of photobiological H₂ production by cyanobacteria is that the culture medium can be used continuously. During the growth stage, cyanobacteria do not produce H₂ and the input costs of labor, energy, nutrients, *etc.* are minimal. A major advantage that the N₂ase-based photobiological H₂ production by cyanobacteria systems have over the other types of algal biofuel production systems is that once established, cultures can produce H₂ for a long time (several weeks) without changing the culture medium and with multiple rounds of gas harvesting [49,51,52] (Table 3), thus off-setting the initial costs of the cell growth phase. Several groups have reported the duration of active H₂ production to be several weeks, and we expect that this could be further extended by carefully managing the culture conditions (Table 3). Attaining sustained high H₂ production without changing the culture medium will mitigate costs of nutrients, a criticism raised by Clarens *et al.* [42] (see Section 3.2).

Table 3. Some records of duration (>2 day) of H₂ production activity without changing the culture medium.

Strains	Light Intensity	Efficiency (%)	Light Energy	Duration of expt.	Gas	Remarks	Refs.
<i>Anabaena cylindrica</i> 629	4.0×10^5 erg·cm ⁻² ·s ⁻¹	0.4% av.	total rad.	8 d	Ar/CO ₂ (99.7/0.3), gassing	250 mL culture: about 0.6 L gas/h Cell density of 200– 260 Klett units Periodic addition of 10 ⁻⁴ M·NH ₄ Cl	[53]
<i>Anabaena cylindrica</i> 629	32 W·m ⁻²	0.85% max.	PAR	6 d	Ar/CO ₂ (99.5/0.5), gassing	0.875 L culture: 0.3–0.9 L gas/h	[54]
<i>Anabaena cylindrica</i> 629	6 W·m ⁻²	0.35% av.	PAR	28 d	Ar/CO ₂ (99.5/0.5), gassing	0.875 L culture: 0.3–0.9 L gas/h	[54]
<i>Mastigocladus laminosus</i> NZ-86-m	3.0×10^4 erg·cm ⁻² ·s ⁻¹	2.7% max.	PAR	2–3 d	Ar/N ₂ /CO ₂ (98.5/1/0.5), gassing	1.2 L culture	[55]
<i>Nostoc</i> sp. PCC 7422 ΔHup deficient of Hup	70 μmol photons m ⁻² ·s ⁻¹	3.7% av.	PAR	6 d	Ar/CO ₂ (9.5/5), (no gassing)	6 mL batch culture	[35]
<i>Anabaena variabilis</i> ATCC 29413	32 W·m ⁻²	0.96% av. 1.32% max.	PAR	8 d	Stage 1: Ar, gassing, Stage 2: air/CO ₂ (95/5), gassing	H ₂ producing activity in stage 2	[56]
<i>Nostoc/Anabaena</i> sp. PCC 7120ΔHup, site-directed N ₂ ase variants, Q193S and R284H	90–100 μmol photons·m ⁻² ·s ⁻¹	not given	PAR	21 d	N ₂ /CO ₂ (95/5), (no gassing with periodic gas replacement of every 3 or 4 days)	Sustained, high- level production of H ₂ through 21 days	[49]

5. Improvements Needed in the Energy Conversion Efficiency under Outdoor Conditions

If photobiological H₂ production is to be developed as a source of large-scale renewable energy, improvements are needed in both the light energy conversion efficiency and in the rates of H₂ production. The maximum theoretical energy conversion for N₂ase-based photoautotrophic H₂ production by cyanobacteria has yet to be precisely calculated. This is because N₂ase requires a considerable amount of ATP and the energy conversion efficiency of photophosphorylation has yet to be conclusively determined. There is a lack of information on the structure and function of the membrane ATP synthase (H⁺-ATPase) that consumes the proton-motive force generated across membranes as the source of energy as predicted by the chemi-osmotic mechanism proposed by P. Mitchell [57,58]. Most likely, the H⁺/ATP ranges between 8/3 and 14/3 (for discussion, see [21,59,60]). By assuming an H⁺/ATP ratio of between 3 and 4, Sakurai and Masukawa [17] calculated the maximum energy conversion efficiency of between 16.3% and 13.9% for 550 nm light and between 7.3% and 6.3% for the total solar radiation, assuming cyanobacteria can use 45% (400–700 nm light, PAR: photosynthetically active radiation) of total radiation.

Of special significance is a report of a record high H₂ production activity on a chlorophyll basis by cyanobacteria. The N₂ase activity of the unicellular cyanobacterium *Cyanothece* sp. ATCC 51142 is regulated by circadian rhythms: photosynthesis in the light, and N₂ase reaction in the dark. When the cells were grown in the presence of glycerol for 12 h under the light to accumulate photosynthetic products (the first stage), they showed high photobiological H₂ activity on a chlorophyll (Chl) basis of 465 μmol mg Chl⁻¹·h⁻¹ when the illumination was continued for another 12 h (the second stage) [61]. This type of strain may be potentially useful if low cost organics are available, such as wastewater rich in useable organic compounds (e.g., from the food industry). However, as many of the heterocystous strains very poorly use organic compounds, this is currently not very promising for the improvement of H₂ production by heterocystous strains.

5.1. Comparing Measured Values for Light Energy Conversion Efficiency of Photobiological H₂ Production by Cyanobacteria to Our Tentative Target Values of 1.2%

Although values of 2.6%–3.7% of PAR in laboratory experiments were reported by several groups [35,55,62], the values drop to 0.2% or less in outdoor experiments lasting for more than two days [51,52,63,64] (daily maximum of 0.6%, Miyamoto [51]) (Table 4). For our proposed scheme, we believe that 1.2% (of total radiation) or 2.7% of PAR for outdoor conditions are reasonable targets for improved efficiency.

Table 4. Some records of light energy conversion efficiency and duration of the activity.

Strains	Light Intensity	Efficiency (%)	Light Energy	Duration of expt.	Gas	Remarks	Refs.
<i>Mastigocladus laminosus</i> NZ-86-m	4.4×10^5 $\text{erg} \cdot \text{cm}^{-2} \cdot \text{s}^{-1}$	0.17% av.	total rad.	17–24 d	Ar/N ₂ /CO ₂ (98.7/1.0/0.3), gassing	1 L culture: 6.5 L·gas/h	[52]
<i>Anabaena cylindrica</i> 629	about 50–330 $\text{cal} \cdot \text{cm}^{-2} \cdot \text{d}^{-1}$	0.2% av. 0.6% max.	total rad.	36 d	Ar/N ₂ /CO ₂ (balance/ 0.2–0.4/0.5), gassing	0.8 L culture: 5.0 L·gas/h	[51]
<i>Anabaena variabilis</i> PK84	400 $\text{W} \cdot \text{m}^{-2}$ (sunny day) 100 $\text{W} \cdot \text{m}^{-2}$ (cloudy day)	0.14% (sunny day) 0.33% (cloudy day)		18 d	air/CO ₂ (98/2), gassing	chemostat-type bioreactor, possibly V-type N ₂ ase expressing conditions	[65]
<i>Anabaena variabilis</i> PK84 deficient of the activities of both Hup and Hox	max. 850 $\text{W} \cdot \text{m}^{-2}$	0.029%–0.094%	total rad.	40 d	air/CO ₂ (98/2), gassing	chemostat-type bioreactor, possibly V-type N ₂ ase expressing conditions, June–July, London	[64]
<i>Anabaena</i> sp. PCC 7120 AMC 414 deficient of Hup	max. 600 $\text{W} \cdot \text{m}^{-2}$	0.042% max.	total rad.	9 d	air/CO ₂ (98/2), gassing	chemostat-type bioreactor, August, London	[63]

5.2. Some Potential Strategies to Achieve Higher Light Conversion Efficiencies

Many aspects of the H₂ production and the related technologies are under development currently, making it challenging to estimate production costs. Nevertheless, such estimates are informative for both policy-makers and investors in R&D efforts. Sakurai *et al.* [44] presented a preliminary estimate of 26.4 ¢/kWh (assuming the price of plastics at \$2 per kg) as a means to identify the needed R&D efforts to achieve efficient photobiological H₂ production by cyanobacteria. The conditions were: (1) mariculture-raised cyanobacteria produce H₂ at an energy conversion efficiency of 1.2% (18 kWh·m⁻²·yr⁻¹) in plastic bioreactors floating on the sea surface (solar radiation 1500 kWh·m⁻²·yr⁻¹); (2) the crude H₂ is purified on factory ships and transported to final destination ports in storage tanks by container ships; and (3) the energy recovery (from production to the final commodity of H₂) is 0.5. Although the tentatively estimated price above is more expensive than the currently leveled price of electricity, it is reasonably close to the prices in several countries with feed-in tariff schemes (see Section 1.3). The price of H₂ can be further decreased with improvements in both light conversion efficiency and energy recovery, and by decreasing the processing costs with advancements in relevant technologies. Because photobiologically produced H₂ contributes to the reduction of the greenhouse gas CO₂ emissions, and because H₂ fuel cells are expected to be more energy efficient than internal combustion engines, the R&D of photobiological renewable energy sources should be pursued in more earnest.

Amos [66] estimated the cost of H₂ produced by *Chlamydomonas* to be 22.8 ¢/kWh when H₂ is compressed and stored in high-pressure tanks for storage and transportation, and 7.2 ¢/kWh when direct connections to H₂ pipelines are available. In certain locations, such as salt lakes, a pipeline could be used to transport gas products with reduction of the total cost of H₂ photobiologically produced by cyanobacteria.

5.2.1. Selection of Strains with High N₂ase Activity Outdoors Followed by Further Improvements via Genetic Engineering

Yoshino *et al.* [35] compared the photobiologically driven N₂ase activity under laboratory conditions among 13 heterocystous strains maintained in academic centers, and selected *Nostoc* sp. PCC 7422. The uptake hydrogenase knocked out mutant (Δ Hup) produced H₂ at an energy conversion efficiency of 3.7% vs. PAR under laboratory conditions. Selection of strains with high N₂ase activity under outdoor conditions with high light intensities followed by further targeted improvements via genetic engineering seems to be one of the most promising strategies for achieving higher light conversion efficiencies.

5.2.2. Truncated Antenna Complexes

Light-saturation of photobiological activity is one of the main reasons light conversion efficiencies are decreased under outdoor conditions as compared with the laboratory conditions for cyanobacteria. Many cyanobacterial strains have large antenna complexes containing pigments such as phycocyanin, which enable them to survive even under conditions of low light intensity such as in a dense culture or in sediment. In order for photobiological H₂ production schemes of the culture as a whole to operate at optimum efficiency, large antenna size is a problem because cells near the surface absorb the most part of incident light and are unable to use it efficiently because of light saturation, while other cells beneath them receive only the residual low light. It is hypothesized that truncation of antenna size would help to alleviate excess absorption of sunlight and the ensuing wasteful dissipation of excitation energy, and to improve solar-to-product energy conversion efficiency and photosynthetic productivity in high-density mass cultivations. As proof of this concept, there are reports of truncated antenna cyanobacterial mutants showing higher rates of photosynthetic activity in culture over the wild-type strains [67].

5.2.3. Increase in Heterocyst Frequency

Under conditions of nitrogen deprivation, heterocystous cyanobacterial cells differentiate heterocysts at intervals of 10–20 vegetative cells, depending upon the strains. While heterocyst frequency may be optimized to support growth of the strains while fixing N₂ under their ordinary natural habitats, the frequency can also be modified to increase H₂ production because the cells do not grow in the H₂ production stage and thus the supply of organic compounds for growth can be dispensed. Many genes involved in heterocyst differentiation have been reported and the mutants of several of these genes (via disruption, overexpression, and duplication of genes and point mutation) result in higher frequencies of heterocysts [25,26,68]. However, many of the mutants form multiple contiguous heterocysts and their N₂ase activities measured by acetylene reduction do not exceed the wild-type activities. PatN is required for normal heterocyst patterning and has a role in the biased initiation of heterocyst differentiation. In *Nostoc/Anabaena* sp. PCC 7120, disruption of *patN* led to formation of multiple singular heterocysts.

Although the *patN* mutant exhibited lower N₂ase activity and diazotrophic growth rate compared with the wild-type [69], it will be interesting to see the effects of modification of heterocyst frequency on photobiological H₂ production by other strains or under different experimental conditions.

5.2.4. Improvement of the Enzymatic Activity of N₂ase

Other H₂-producing enzymes, FeFe and NiFe H₂ases, have high H₂ production activity with a turnover rate of 6000–9000 and about 100 s⁻¹, respectively, although the latter enzyme also has greater H₂ uptake activity with a turnover rate of 450–600 s⁻¹ [70]. In contrast, although N₂ase has an advantage in catalyzing unidirectional production of H₂, it has a very low turnover rate of about 6.4 s⁻¹ [71,72]. The rate-limiting step in N₂ase catalysis is the dissociation of the dinitrogenase reductase Fe protein (Complex 2) from the dinitrogenase MoFe protein (Complex 1). The dissociation occurs after ATP-coupled electron transfer between the two proteins. In the N₂ase reaction, H₂ is evolved initially when N₂ binds to the enzyme. The slow protein dissociation is considered to contribute to maximizing N₂ reduction by suppressing H₂ evolution, futile to nitrogen fixation, at the midpoint of the whole reaction. It will be interesting to engineer N₂ase, either MoFe-protein or Fe-protein, or both, by site-directed mutagenesis, to increase the turnover rate of H₂ production by the enzyme.

When maintaining the N₂ase-based reactions at high levels, cyanobacteria require high levels of amino acids to support the synthesis of the inefficient enzyme, and the increase in the specific catalytic activity will decrease the burden of protein synthesis.

5.2.5. Metabolic Engineering

As in other organisms, studies of genomes, transcriptomes, proteomes, and metabolomes are ongoing in cyanobacteria. The information from these studies will undoubtedly contribute to improving the overall activity of photobiological H₂ production by cyanobacteria, as targeted improvements will be made [73]. For example, it will be interesting to pursue repression of the expression of glutamine synthetase in heterocysts. In normal cells, the enzyme is required for the massive export of fixed nitrogen from heterocyst to vegetative cells, and the gene expression level is greatly increased during the course of heterocyst differentiation [74]. In H₂ producing cyanobacteria, however, massive glutamine transport is not necessary because the cells almost cease growing, and the investment of amino acids for the synthesis of proteins such as glutamine synthetase seems to be a waste of amino acid reserves.

6. Conclusions

Future Prospects for Large-Scale Photobiological H₂ Production

In order for photobiologically produced H₂ to make meaningful contributions to the mitigation of global warming caused by greenhouse gases, notably CO₂, economical production of H₂ is essential. Although many of the technologies required for the practical application of large-scale photobiological H₂ production are in the development stages and the cost estimates of the produced H₂ are preliminary due to various unpredictable factors, Sakurai *et al.* [44] presented a very preliminary estimate of 26.4 cents·kWh⁻¹ of H₂ produced on the sea surface using many presumptive assumptions, for example assuming the solar energy conversion efficiency of 1.2%. Currently, the maximum energy conversion

efficiency of cyanobacterial H₂ production under outdoor conditions is about 0.2%. There is an urgent need to demonstrate higher efficiencies to policy makers and developers in order to convince them of the potential benefits of photobiological H₂ production by cyanobacteria. Increasing the solar energy conversion efficiency with improvements in technologies for purifying and transporting H₂ will decrease the total cost. Public acceptance of renewable fuels very much depends upon the affordability of the price and will go a long way towards convincing consumers and government leaders to adopt technologies that will ultimately mitigate global climate change. Future cost estimates will be more accurate as the technologies in cyanobacterial H₂ production and its related processes advance. We also expect that more refined cost estimates will allow for additional targeted improvements in the technologies, ultimately resulting in an overall cost reduction.

If we are able to produce H₂ at 1.2% of total radiation (18 kWh·m⁻²·yr⁻¹) on the sea surface and purified H₂ is delivered to the end users with a final energy yield of 0.5, the net energy obtained is calculated to be 9 kWh·m⁻²·yr⁻¹ or 32.4 × 10⁶ J·m⁻²·yr⁻¹ [44]. The current world fuel energy consumption is estimated to be 460 × 10¹⁸ J·yr⁻¹ (Table 1, [3]). It follows that by using a surface of the sea equivalent to 1% of the global surface (1.36 × 10⁶ km², about 2.3 times the area of the island of Tasmania, or 3.1 times the area of the island of Great Britain), we will be able to replace 19% of the current world fossil fuel consumption.

In order to make a meaningful contribution to the mitigation of the hazards to the human population that are predicted to occur with global climate change, the promotion of R&D efforts for economical large-scale photobiological biofuel production and the advancements of biological and other needed technologies should be encouraged.

Acknowledgments

We thank Susan Carlson for critically reading the manuscript. This work was supported in part by grant-in aid for Scientific Research on Innovative Areas (No. 24107004) and Strategic Research Base Development Program for Private Universities from MEXT, Japan (to KI).

Conflicts of Interest

One of the authors (H.S.) is a stakeholder of Wakhy Laboratories.

References

1. Intergovernmental Panel on Climate Change (IPCC). Summary for policymakers. Available online: https://ipcc-wg2.gov/AR5/images/uploads/WG2AR5_SPM_FINAL.pdf (accessed on 15 February 2015).
2. United Nations Intergovernmental Panel on Climate Change (UNIPCC). Fifth Assessment Report. Available online: <http://www.ipcc.ch/report/ar5/> (accessed on 15 February 2015).
3. International Energy Agency (IEA). Key World Energy Statistics. Available online: <http://www.iea.org/publications/freepublications/publication/KeyWorld2014.pdf> (accessed on 15 February 2015).
4. International Energy Agency (IEA). World Energy Outlook 2014. Available online:

- http://www.iea.org/publications/freepublications/publication/WEO_2014_ES_English_WEB.pdf (accessed on 15 February 2015).
5. Angermayr, S.A.; Hellingwerf, K.J.; Lindblad, P.; de Mattos, M.J.T. Energy biotechnology with cyanobacteria. *Curr. Opin. Biotech.* **2009**, *20*, 257–263.
 6. Ghirardi, M.L.; Dubini, A.; Yu, J.; Maness, P.C. Photobiological hydrogen-producing systems. *Chem. Soc. Rev.* **2009**, *38*, 52–61.
 7. Huesemann, M.H.; Hausmann, T.S.; Carter, B.M.; Gerschler, J.J.; Benemann, J.R. Hydrogen generation through indirect biophotolysis in batch cultures of the nonheterocystous nitrogen-fixing cyanobacterium *Plectonema boryanum*. *Appl. Biochem. Biotechnol.* **2010**, *162*, 208–220.
 8. Hallenbeck, P. Hydrogen Production by Cyanobacteria. In *Microbial Technologies in Advanced Biofuels Production*; Hallenbeck, P.C., Ed.; Springer: New York, NY, USA, 2012; pp. 15–28.
 9. Hallenbeck, P.C.; Abo-Hashesh, M.; Ghosh, D. Strategies for improving biological hydrogen production. *Bioresour. Technol.* **2012**, *110*, 1–9.
 10. Stephens, G.L.; Li, J.; Wild, M.; Clayson, C.A.; Loeb, N.; Kato, S.; L'Ecuyer, T.; Stackhouse, P.W.; Lebsack, M.; Andrews, T. An update on Earth's energy balance in light of the latest global observations. *Nat. Geosci.* **2012**, *5*, 691–669.
 11. Wikipedia. Feed-in tariffs in Germany. Available online: http://en.wikipedia.org/wiki/Feed-in_tariffs_in_Germany (accessed on 15 February 2015).
 12. Lang, M.; Lang, A. German Feed-in Tariffs 2014 (from 08). Available online: http://www.germanenergyblog.de/?page_id=16379 (accessed on 15 February 2015).
 13. The Ministry of Economy, Trade and Industry (METI), Japan. Settlement of FY2014 Purchase Prices and FY2014 Surcharge Rates under the Feed-in Tariff Scheme for Renewable Energy. Available online: http://www.meti.go.jp/english/press/2014/0325_03.html (accessed on 15 February 2015).
 14. US Energy Information Administration (EIA). Levelized Cost of New Generation Resources in the Annual Energy Outlook 2013. Available online: http://www.eia.gov/forecasts/aeo/er/pdf/electricity_generation.pdf (accessed on 15 February 2015).
 15. Toyota Motor Corporation. Powering the future—hydrogen fuel cell vehicles could change mobility forever. Available online: http://www.toyota-global.com/innovation/environmental_technology/fuelcell_vehicle/ (accessed on 15 February 2015).
 16. Response JP. Tokyo Gas sets price of hydrogen for FCVs at 1100 yen per kilo. Available online: <http://en.responsejp.com/article/2015/01/08/241157.html/> (accessed on 15 February 2015).
 17. Sakurai, H.; Masukawa, H. Promoting R&D in photobiological hydrogen production utilizing mariculture-raised cyanobacteria. *Mar. Biotechnol.* **2007**, *9*, 128–145.
 18. Tamagnini, P.; Leitão, E.; Oliveira, P.; Ferreira, D.; Pinto, F.; Harris, D.J.; Heidorn, T.; Lindblad, P. Cyanobacterial hydrogenases: Diversity, regulation and applications. *FEMS Microbiol. Rev.* **2007**, *31*, 692–720.
 19. Tsygankov, A.A. Nitrogen-fixing cyanobacteria: A review. *Appl. Biochem. Microbiol.* **2007**, *43*, 250–259.
 20. Bothe, H.; Schmitz, O.; Yates, M.G.; Newton, W.E. Nitrogen fixation and hydrogen metabolism in cyanobacteria. *Microbiol. Mol. Biol. Rev.* **2010**, *74*, 529–551.
 21. Sakurai, H.; Masukawa, H.; Kitashima, M.; Inoue, K. Photobiological hydrogen production:

- Bioenergetics and challenges for its practical application. *J. Photochem. Photobiol. C* **2013**, *17*, 1–25.
22. Berman-Frank, I.; Lundgren, P.; Falkowski, P. Nitrogen fixation and photosynthetic oxygen evolution in cyanobacteria. *Res. Microbiol.* **2003**, *154*, 157–164.
 23. Finzi-Hart, J.A.; Pett-Ridge, J.; Weber, P.K.; Popa, R.; Fallon, S.J.; Gunderson, T.; Hutcheon, I.D.; Nealson, K.H.; Capone, D.G. Fixation and fate of C and N in the cyanobacterium *Trichodesmium* using nanometer-scale secondary ion mass spectrometry. *Proc. Natl. Acad. Sci. USA* **2009**, *106*, 6345–6350.
 24. Wolk, C.P.; Ernest, A.; Elhai, J. Heterocyst Metabolism and Development. In *The Molecular Biology of Cyanobacteria*; Bryant, D.A., Ed.; Kluwer Academic Publishers: Dordrecht, The Netherlands, 1994; pp. 769–823.
 25. Kumar, K.; Mella-Herrera, R.A.; Golden, J.W. Cyanobacterial heterocysts. *Csh. Perspect. Biol.* **2010**, *2*, a000315.
 26. Herrero, A.; Picossi, S.; Flores, E. Gene expression during heterocyst differentiation. *Adv. Bot Res.* **2013**, *65*, 281–329.
 27. Tamagnini, P.; Axelsson, R.; Lindberg, P.; Oxelfelt, F.; Wunschiers, R.; Lindblad, P. Hydrogenases and hydrogen metabolism of cyanobacteria. *Microbiol. Mol. Biol. Rev.* **2002**, *66*, 1–20.
 28. Schütz, K.; Happe, T.; Troshina, O.; Lindblad, P.; Leitão, E.; Oliveira, P.; Tamagnini, P. Cyanobacterial H₂ production—a comparative analysis. *Planta* **2004**, *218*, 350–359.
 29. Masukawa, H.; Zhang, X.H.; Yamazaki, E.; Iwata, S.; Nakamura, K.; Mochimaru, M.; Inoue, K.; Sakurai, H. Survey of the distribution of different types of nitrogenases and hydrogenases in heterocyst-forming cyanobacteria. *Mar. Biotechnol.* **2009**, *11*, 397–409.
 30. Kumazawa, S.; Mitsui, A. Comparative amperometric study of uptake hydrogenase and hydrogen photoproduction activities between heterocystous cyanobacterium *Anabaena cylindrica* B629 and nonheterocystous cyanobacterium *Oscillatoria* sp. strain Miami BG7. *Appl. Environ. Microbiol.* **1985**, *50*, 287–291.
 31. Happe, T.; Schütz, K.; Böhme, H. Transcriptional and mutational analysis of the uptake hydrogenase of the filamentous cyanobacterium *Anabaena variabilis* ATCC 29413. *J. Bacteriol.* **2000**, *182*, 1624–1631.
 32. Lindberg, P.; Schütz, K.; Happe, T.; Lindblad, P. A hydrogen-producing, hydrogenase-free mutant strain of *Nostoc punctiforme* ATCC 29133. *Int. J. Hydrog. Energ.* **2002**, *27*, 1291–1296.
 33. Masukawa, H.; Mochimaru, M.; Sakurai, H. Disruption of the uptake hydrogenase gene, but not of the bidirectional hydrogenase gene, leads to enhanced photobiological hydrogen production by the nitrogen-fixing cyanobacterium *Anabaena* sp. PCC 7120. *Appl. Microbiol. Biot.* **2002**, *58*, 618–624.
 34. Carrasco, C.D.; Holliday, S.D.; Hansel, A.; Lindblad, P.; Golden, J.W. Heterocyst-specific excision of the *Anabaena* sp strain PCC 7120 *hupL* element requires *xisC*. *J. Bacteriol.* **2005**, *187*, 6031–6038.
 35. Yoshino, F.; Ikeda, H.; Masukawa, H.; Sakurai, H. High photobiological hydrogen production activity of a *Nostoc* sp. PCC 7422 uptake hydrogenase-deficient mutant with high nitrogenase activity. *Mar. Biotechnol.* **2007**, *9*, 101–112.
 36. Khetkorn, W.; Lindblad, P.; Incharoensakdi, A. Inactivation of uptake hydrogenase leads to enhanced and sustained hydrogen production with high nitrogenase activity under high light

- exposure in the cyanobacterium *Anabaena siamensis* TISTR 8012. *J. Biol. Eng.* **2012**, *6*, 19.
37. Mikheeva, L.E.; Schmitz, O.; Shestakov, S.V.; Bothe, H. Mutants of the cyanobacterium *Anabaena variabilis* altered in hydrogenase activities. *Z. Naturforsch C* **1995**, *50*, 505–510.
 38. Masukawa, H.; Inoue, K.; Sakurai, H.; Wolk, C.P.; Hausinger, R.P. Site-directed mutagenesis of the *Anabaena* sp. strain PCC 7120 nitrogenase active site to increase photobiological hydrogen production. *Appl. Environ. Microbiol.* **2010**, *76*, 6741–6750.
 39. Zhang, X.H.; Sherman, D.M.; Sherman, L.A. The uptake hydrogenase in the unicellular diazotrophic cyanobacterium *Cyanothece* sp. strain PCC 7822 protects nitrogenase from oxygen toxicity. *J. Bacteriol.* **2014**, *196*, 840–849.
 40. Benemann, J.R.; Weare, N.M. Hydrogen evolution by nitrogen-fixing *Anabaena cylindrica* cultures. *Science* **1974**, *184*, 174–175.
 41. Benemann, J.R. Hydrogen and methane production by microalgae. In *Handbook of Microalgal Culture: Biotechnology and Applied Phycology*; Richmond, A., Ed.; Blackwell Publishing Ltd.: Oxford, UK, 2004; pp. 403–429.
 42. Clarens, A.F.; Resurreccion, E.P.; White, M.A.; Colosi, L.M. Environmental life cycle comparison of algae to other bioenergy feedstocks. *Environ. Sci Technol.* **2010**, *44*, 1813–1819.
 43. Campbell, P.K.; Beer, T.; Batten, D. Life cycle assessment of biodiesel production from microalgae in ponds. *Bioresour Technol* **2011**, *102*, 50–56.
 44. Sakurai, H.; Masukawa, H.; Kitashima, M.; Inoue, K. A feasibility study of large-scale photobiological hydrogen production utilizing mariculture-raised cyanobacteria. *Adv. Exp. Med. Biol.* **2010**, *675*, 291–303.
 45. Tredici, M.R. Mass production of microalgae: photobioreactors. In *Handbook of Microalgal Culture: Biotechnology and Applied Phycology*; Richmond, A., Ed.; Blackwell Publishing Ltd.: Oxford, UK, 2004; pp. 178–214.
 46. Fernández-Sevilla, J.M.; Acién-Fernández, F.G.; Molina-Grima, E. Photobioreactors Design for Hydrogen Production. In *Microbial BioEnergy: Hydrogen Production*; Zannoni, D., Philippis, R.D., Eds.; Springer: Dordrecht, The Netherlands, 2014; pp. 291–320.
 47. Kitashima, M.; Masukawa, H.; Sakurai, H.; Inoue, K. Flexible plastic bioreactors for photobiological hydrogen production by hydrogenase-deficient cyanobacteria. *Biosci. Biotech. Bioch.* **2012**, *76*, 831–833.
 48. Mitsui, A.; Murray, R.; Entermann, B.; Miyazawa, K.; Polk, E. Utilization of marine blue-green algae and microalgae in warm water mariculture. In *Biosaline Research—A Look to the Future Environmental Science Research*; San Pietro, A., Ed.; Plenum Press: New York, NY, USA, 1981; pp. 215–225.
 49. Masukawa, H.; Sakurai, H.; Hausinger, R.P.; Inoue, K. Sustained photobiological hydrogen production in the presence of N₂ by nitrogenase mutants of the heterocyst-forming cyanobacterium *Anabaena*. *Int. J. Hydrog. Energ* **2014**, *39*, 19444–19451.
 50. Geiszler, V.C.; Koros, W.J. Effects of Polyimide Pyrolysis Conditions on Carbon Molecular Sieve Membrane Properties. *Ind. Eng. Chem. Res.* **1996**, *35*, 2999–3003.
 51. Miyamoto, K.; Hallenbeck, P.C.; Benemann, J.R. Solar-energy conversion by nitrogen-limited cultures of *Anabaena cylindrica*. *J. Ferment Technol.* **1979**, *57*, 287–293.
 52. Miyamoto, K.; Hallenbeck, P.C.; Benemann, J.R. Hydrogen production by the thermophilic alga

- Mastigocladus laminosus*: effects of nitrogen, temperature, and inhibition of photosynthesis. *Appl. Environ. Microbiol.* **1979**, *38*, 440–446.
53. Weissman, J.C.; Benemann, J.R. Hydrogen production by nitrogen-starved cultures of *Anabaena cylindrica*. *Appl. Environ. Microbiol.* **1977**, *33*, 123–131.
54. Jeffries, T.W.; Timourian, H.; Ward, R.L. Hydrogen production by *Anabaena cylindrica*: Effects of varying ammonium and ferric ions, pH, and light. *Appl. Environ. Microbiol.* **1978**, *35*, 704–710.
55. Miyamoto, K.; Hallenbeck, P.C.; Benemann, J.R. Nitrogen fixation by thermophilic blue-green algae (cyanobacteria): Temperature characteristics and potential use in biophotolysis. *Appl. Environ. Microbiol.* **1979**, *37*, 454–458.
56. Berberoğlu, H.; Jay, J.; Pilon, L. Effect of nutrient media on photobiological hydrogen production by *Anabaena variabilis* ATCC 29413. *Int. J. Hydrog. Energ.* **2008**, *33*, 1172–1184.
57. Mitchell, P. Chemiosmotic coupling in oxidative and photosynthetic phosphorylation. *Biol. Rev. Camb. Philos. Soc.* **1966**, *41*, 445–502.
58. Mitchell, P. Possible molecular mechanisms of the protonmotive function of cytochrome systems. *J. Theor. Biol.* **1976**, *62*, 327–367.
59. Junge, W. Structure and function of photosystem I. In *Primary Processes of Photosynthesis—Part 2: Principles and Apparatus*; Renger, G., Ed.; RSC Publishing: Cambridge, UK, 2007; Volume 2, pp. 447–487.
60. Petersen, J.; Förster, K.; Turina, P.; Gräber, P. Comparison of the H⁺/ATP ratios of the H⁺-ATP synthases from yeast and from chloroplast. *Proc. Natl. Acad. Sci. USA* **2012**, *109*, 11150–11155.
61. Bandyopadhyay, A.; Stöckel, J.; Min, H.T.; Sherman, L.A.; Pakrasi, H.B. High rates of photobiological H₂ production by a cyanobacterium under aerobic conditions. *Nat. Commun.* **2010**, *1*, doi:10.1038/ncomms1139.
62. Kumazawa, S.; Mitsui, A. Efficient hydrogen photoproduction by synchronously grown cells of a marine cyanobacterium, *Synechococcus* sp. Miami BG 043511, under high cell-density conditions. *Biotech. Bioeng.* **1994**, *44*, 854–858.
63. Lindblad, P.; Christensson, K.; Lindberg, P.; Fedorov, A.; Pinto, F.; Tsygankov, A. Photoproduction of H₂ by wildtype *Anabaena* PCC 7120 and a hydrogen uptake deficient mutant: from laboratory experiments to outdoor culture. *Int. J. Hydrog. Energ.* **2002**, *27*, 1271–1281.
64. Tsygankov, A.A.; Fedorov, A.S.; Kosourov, S.N.; Rao, K.K. Hydrogen production by cyanobacteria in an automated outdoor photobioreactor under aerobic conditions. *Biotech. Bioeng.* **2002**, *80*, 777–783.
65. Fedorov, A.S.; Tsygankov, A.A.; Rao, K.K.; Hall, D.O. Production of hydrogen by an *Anabaena variabilis* mutant in a photobioreactor under aerobic outdoor conditions. In *Biohydrogen II*; Miyake, J., Matsunaga, T., San Pietro, A., Eds.; Elsevier Science Ltd.: Oxford, UK, 2001; pp. 223–228.
66. Amos, W.A. *Updated Cost Analysis of Photobiological Hydrogen Production from Chlamydomonas reinhardtii Green Algae*; NREL/MP-560-35593; NREL: Golden, CO, USA, 2004.
67. Nakajima, Y.; Ueda, R. Improvement of photosynthesis in dense microalgal suspension by reduction of light harvesting pigments. *J. Appl. Phycol.* **1997**, *9*, 503–510.
68. Meeks, J.C.; Elhai, J. Regulation of cellular differentiation in filamentous cyanobacteria in free-living and plant-associated symbiotic growth states. *Microbiol. Mol. Biol. Rev.* **2002**, *66*, 94–121.

69. Risser, D.D.; Wong, F.C.Y.; Meeks, J.C. Biased inheritance of the protein patn frees vegetative cells to initiate patterned heterocyst differentiation. *Proc. Natl. Acad. Sci. USA* **2012**, *109*, 15342–15347.
70. Hallenbeck, P.C.; Benemann, J.R. Biological hydrogen production; fundamentals and limiting processes. *Int. J. Hydrog. Energ.* **2002**, *27*, 1185–1193.
71. Thorneley, R.N.F.; Lowe, D.J. Kinetics and Mechanism of the Nitrogenase Enzyme System. In *Molybdenum Enzymes*; Spiro, T.G., Ed.; John Wiley: New York, NY, USA, 1985; pp. 221–284.
72. Burgess, B.K.; Lowe, D.J. Mechanism of molybdenum nitrogenase. *Chem. Rev.* **1996**, *96*, 2983–3011.
73. Lindblad, P.; Lindberg, P.; Oliveira, P.; Stensjö, K.; Heidorn, T. Design, engineering, and construction of photosynthetic microbial cell factories for renewable solar fuel production. *Ambio* **2012**, *41*, 163–168.
74. Ehira, S.; Ohmori, M.; Sato, N. Genome-wide expression analysis of the responses to nitrogen deprivation in the heterocyst-forming cyanobacterium *Anabaena* sp strain PCC 7120. *DNA Res.* **2003**, *10*, 97–113.

© 2015 by the authors; licensee MDPI, Basel, Switzerland. This article is an open access article distributed under the terms and conditions of the Creative Commons Attribution license (<http://creativecommons.org/licenses/by/4.0/>).

CrossMark
click for updatesCite this: *J. Mater. Chem. A*, 2015, 3,
746

Selective carbon dioxide adsorption of ϵ -Keggin-type zirconomolybdate-based purely inorganic 3D frameworks†

Zhenxin Zhang,^a Masahiro Sadakane,^{*bc} Shin-ichiro Noro,^{cde} Toru Murayama,^a Takashi Kamachi,^f Kazunari Yoshizawa^f and Wataru Ueda^{*a}

Polyoxometalate-based 3D frameworks, $\text{Na}_{1.5}\text{H}_{11.4}[\text{ZnMo}_{12}\text{O}_{40}(\text{Zn}_2)] \cdot 5.5\text{H}_2\text{O}$ and $(\text{NH}_4)_{1.5}\text{H}_{8.5}[\text{ZnMo}_{12}\text{O}_{40}(\text{Zn}_2)] \cdot 6\text{H}_2\text{O}$, are synthesized in moderate yields. Rotation of the reactor under hydrothermal conditions is essential to improve the yield. The materials show zeolite-like selective molecule adsorption properties. Depending on the micropore aperture size of the materials, small molecules can be adsorbed in the materials, while large molecules cannot. The enthalpy of adsorption and DFT calculation indicate that the materials strongly interact with CO_2 , but weakly interact with CH_4 , due to electrostatic interactions between the materials and molecules. CO_2/CH_4 co-adsorption experiments show that the materials can selectively adsorb CO_2 , and CO_2 adsorption selectivity of the material with sodium cations is higher than that of the material with ammonium cations. The material with sodium ions can be utilized for gas chromatographic separation of CH_4 and CO_2 .

Received 14th October 2014
Accepted 10th November 2014

DOI: 10.1039/c4ta05496b

www.rsc.org/MaterialsA

CO_2 separation is an important topic from the viewpoints of industrial processes and environmental protection, and many techniques for CO_2 separation have been developed over the past few decades.^{1–5} Generally, there are two kinds of materials for CO_2 separation based on different separation mechanisms. One type of materials for CO_2 separation is based on chemisorption. Such materials include calcium oxide and amine solutions. However, these materials have significant disadvantages such as toxicity, corrosiveness, and high energy for regeneration. The second type of materials is based on physisorption. Such materials include zeolites and metal-organic frameworks (MOFs), and they are considered to have higher application potential because the corresponding processes are environmentally friendly and economically feasible techniques.

Polyoxometalates (POMs) are metal oxide clusters of early transition metals, such as tungsten, molybdenum, vanadium and niobium, which display characteristic redox and acidic

properties, and they therefore have many applications including catalysis, adsorption, separation, electrochemistry, and medicine.^{6–9} In materials chemistry, POMs act as building blocks, and inorganic metal oxides can be synthesized on the basis of connection of POMs with other metal ions.^{10–14} POMs also interact with organic ligands or organic metal complexes to form hybrid materials, including POMOFs^{15–20} and POM-macrocation materials.^{21–29} POM-macrocation materials show interesting adsorption properties.

A novel catalog of POM-based materials has recently been prepared and structurally characterized and is best described to be fully inorganic microporous POM-based metal oxides.^{30,31} Frameworks of the materials are comprised of ϵ -Keggin POM with metal ion linkers (Fig. 1). The materials show zeolite-like properties such as ion exchange, molecule adsorption, and acid catalysis.

An important property of the POM-based microporous material is its high chemical composition diversity, which allows different kinds of elements to be incorporated in the material. The composition of POM units, linker ions, and counterions can be easily changed without altering the basic structure of the material. Several iso-structural materials have been successfully synthesized.³²

Herein, we describe the synthesis of ϵ -Keggin POM-based 3D frameworks composed of $[\text{ZnMo}_{12}\text{O}_{40}]$ and Zn ion linkers with sodium ions or ammonium cations, $\text{Na}_{1.5}\text{H}_{11.4}[\text{ZnMo}_{12}\text{O}_{40}(\text{Zn}_2)] \cdot 5.5\text{H}_2\text{O}$ or $(\text{NH}_4)_{1.5}\text{H}_{8.5}[\text{ZnMo}_{12}\text{O}_{40}(\text{Zn}_2)] \cdot 6\text{H}_2\text{O}$, denoted as Na-Mo-Zn oxide or NH_4 -Mo-Zn oxide, respectively. We demonstrate the adsorption properties of the materials. Small

^aCatalysis Research Center, Hokkaido University, N-21, W-10, Kita-ku, Sapporo 001-0021, Japan. E-mail: ueda@cat.hokudai.ac.jp; Fax: +81-11-706-9163; Tel: +81-11-706-9164

^bDepartment of Applied Chemistry, Graduate School of Engineering, Hiroshima University, 1-4-1 Kagamiyama, Higashi Hiroshima 739-8527, Japan

^cJST, PRESTO, 4-1-8 Honcho, Kawaguchi, Saitama 332-0012, Japan

^dResearch Institute for Electronic Science, Hokkaido University, Sapporo 001-0020, Japan

^eCreative Research Institute (CRIS), Hokkaido University, Sapporo 001-0021, Japan

^fInstitute for Materials Chemistry and Engineering and International Research Center for Molecular Systems, Kyushu University, Fukuoka 819-0395, Japan

† Electronic supplementary information (ESI) available. See DOI: 10.1039/c4ta05496b

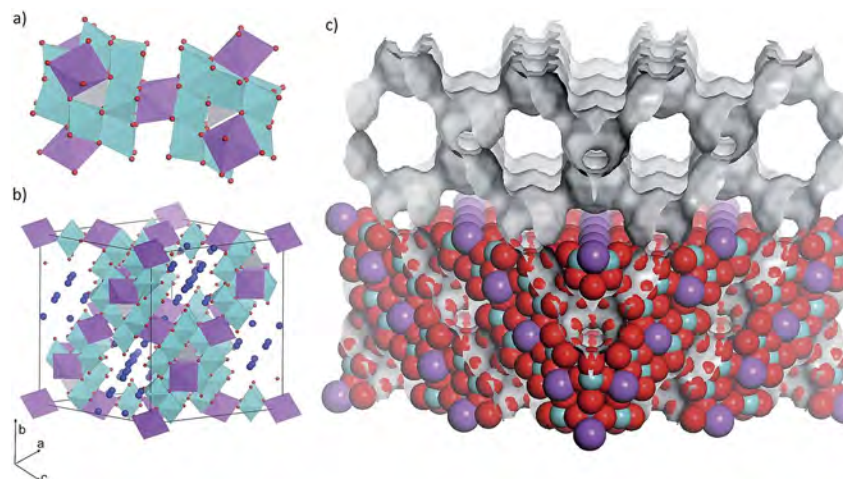


Fig. 1 Polyhedral representations of (a) ϵ -Keggin POM unit and its connection; (b) unit cell of an ϵ -Keggin POM-based framework – gray tetrahedron: central Zn–O tetrahedron, blue octahedron: surrounding Mo–O octahedron, purple octahedron: linker Zn–O octahedron, and deep blue ball: cations and water; and (c) CPK (Corey, Pauling, and Koltun) representation of the material with a Connolly surface (gray curved surface) that shows the micropore system of the material.

molecules such as CO_2 , CH_4 , and C_2H_6 are adsorbed in the materials, while a large molecule such as C_3H_8 is not adsorbed. CO_2/CH_4 co-sorption experiments showed that the materials selectively adsorb CO_2 from a CO_2/CH_4 mixture. CO_2 adsorption in the materials can be tuned by altering counteranions, and CO_2 separation efficiency can be remarkably enhanced by incorporating sodium ions in the material. The Na–Mo–Zn oxide material can be used as a material for gas chromatographic separation of CO_2 and CH_4 .

Experimental

Material synthesis

Synthesis of Na–Mo–Zn oxide. $\text{Na}_2\text{MoO}_4 \cdot 2\text{H}_2\text{O}$ (2.823 g, 11.7 mmol based on Mo) was dissolved in 40 mL of water. Then metal molybdenum (0.2 g, 2.08 mmol) and ZnCl_2 (0.453 g, 3.33 mmol) were added in sequence. The pH value of the precursor solution was adjusted to 4.8 by addition of H_2SO_4 (1 M). The mixture solution was well sealed in an autoclave with a Teflon liner, and the autoclave was fixed in an oven with a mechanical rotation system. Hydrothermal synthesis was performed at 448 K with rotation (1 rpm) for 24 h (see the experimental apparatus in ESI Fig. S1†). After hydrothermal reaction and cooling of the autoclave, the crude solid was transferred to a 100 mL beaker and 60 mL of water was added. For purification and solid recovery, the mixture was centrifuged (1700 rpm, 2 min), and the suspension (containing the product) solution was separated from the precipitate formed at the bottom after centrifugation. Then after addition of 60 mL of water to the precipitate, the solution was centrifuged and the new upper suspension solution was separated. Addition of water, centrifugation, and separation were carried out two more times. The collected suspension (containing the product) was centrifuged (3500 rpm, 120 min), and the solid at the bottom of the centrifugation tube was collected. The collected solid was washed with water by dispersing in 10 mL of water and subsequent centrifugation

(3500 rpm, 120 min). After the washing process was carried out two more times, the obtained solid was dried at 333 K overnight. Then 1.18–1.34 g of Na–Mo–Zn oxide (yield: 57–63% based on Mo) was obtained.

Synthesis of NH_4 –Mo–Zn oxide. $(\text{NH}_4)_6\text{Mo}_7\text{O}_{24} \cdot 4\text{H}_2\text{O}$ (2.060 g, 11.7 mmol based on Mo) was dissolved in 40 mL of water. Then metal molybdenum (0.2 g, 2.08 mmol) and ZnCl_2 (0.453 g, 3.33 mmol) were added in sequence. The pH value of the precursor solution was adjusted to 4.8 by addition of H_2SO_4 (1 M). The mixture solution was well sealed in an autoclave with a Teflon liner, and the autoclave was fixed in an oven with a mechanical rotation system. Hydrothermal synthesis was performed at 448 K with rotation (1 rpm) for 24 h. After the hydrothermal reaction, the purification process was the same as that for Na–Mo–Zn oxide. Then 1.29–1.46 g of NH_4 –Mo–Zn oxide (yield: 62–71% based on Mo) was obtained.

Synthesis of NH_4 –Na–Mo–Zn oxide by ion-exchange of Na–Mo–Zn oxide with NH_4^+ . 0.3 g of Na–Mo–Zn oxide was dispersed into 15 mL of water. Then NH_4Cl (0.065 g, 1.21 mmol) was added. The solution was heated at 353 K for 6 h with stirring. The resulting material was separated by filtration, washed with water 3 times and dried at 333 K overnight.

Elemental analysis: Na–Mo–Zn oxide: calcd for $\text{Na}_{1.5}\text{Zn}_3\text{Mo}_{12}\text{O}_{45.5}\text{H}_{22.4}$: Zn, 9.20; Mo, 53.99; Na, 1.62; H, 1.05, found: Zn, 9.70; Mo, 53.45; Na, 1.39; H, 0.97.

NH_4 –Mo–Zn oxide: calcd for $\text{N}_{1.5}\text{Zn}_3\text{Mo}_{12}\text{O}_{46}\text{H}_{26.5}$: Zn, 9.21; Mo, 54.03; N, 0.99; H, 1.24, found: Zn, 9.25; Mo, 53.95; N, 1.02; H, 1.22.

NH_4 –Na–Mo–Zn oxide: calcd for $\text{N}_{1.4}\text{Na}_{0.1}\text{Zn}_3\text{Mo}_{12}\text{O}_{45.5}\text{H}_{28}$: Zn, 9.23; Mo, 54.17; Na, 0.11, N, 0.92; H, 1.32, found: Zn, 9.61; Mo, 54.24; Na, 0.07; N, 1.20; H, 1.39.

Characterization

Powder X-ray diffraction (XRD) patterns were obtained on RINT2200 (Rigaku) with $\text{Cu K}\alpha$ radiation (tube voltage: 40 kV, tube current: 20 mA). Scanning electron microscopy (SEM)

images were obtained with HD-2000 (HITACHI). Transmission electron microscopy (TEM) images were taken with a 200 kV TEM (JEOL JEM-2100F). Temperature-programmed desorption mass spectrometry (TPD-MS) measurements were carried out from 313 K to 893 K at a heating rate of 10 K min⁻¹ under helium (flow rate: 50 mL min⁻¹). Samples were set up between two layers of quartz wool. A TPD apparatus (BEL Japan, Inc.) equipped with a quadrupole mass spectrometer (M-100QA; Anelva) was used to detect NH₃ (*m/z* = 16) and H₂O (*m/z* = 18). For TPD-MS measurements of the materials after heat treatment, the samples were heated at 473 K under a high vacuum for 2.5 h in a TPD instrument before measurements. After the temperature was decreased to 373 K, TPD measurement was started. Fourier transform infrared (FT-IR) analysis was carried out on a PARAGON 1000, Perkin Elmer. X-ray photoelectron spectroscopy (XPS) was performed on a JPS-9010MC (JEOL). The spectrometer energies were calibrated using the C 1s peak at 284.8 eV. Thermal analysis (TG-DTA) was performed on a Thermo Plus, TG8120 (Rigaku), under N₂ (200 mL min⁻¹). Elemental compositions were determined by an inductive coupling plasma (ICP-AES) method (ICPE-9000, Shimadzu). CHN elemental composition was determined at Instrumental Analysis Division, Equipment Management Center, Creative Research Institution, Hokkaido University.

Sorption experiments

Na–Mo–Zn oxide and NH₄–Mo–Zn oxide were calcined at 473 K for 2.5 h under a vacuum (denoted as Cal–Na–Mo–Zn oxide and Cal–NH₄–Mo–Zn oxide) before all adsorption experiments.

N₂ sorption isotherms were obtained using a BELSORP MAX (BEL Japan Inc.) sorption analyzer at 77 K. Pore size distribution was calculated by the SF method. Molecule (CO₂, CH₄, C₂H₆, and C₃H₈) adsorption was performed on the materials by a BELSORP MAX (BEL Japan Inc.) sorption analyzer. The adsorption temperature was kept at 278, 288, and 298 K using a water bath. Surface areas of the materials were calculated from the CO₂ adsorption isotherm by the BET method, and the cross-sectional area of CO₂ was 0.201 nm².³³

CO₂/CH₄ co-sorption measurements were carried out using a multicomponent gas adsorption apparatus, BELSORP VC (BEL Japan Inc.). In this apparatus, the total adsorbed amount was calculated by a constant volume method, and the composition ratio of CO₂ and CH₄ gases in equilibrium was determined using an Agilent 490 Micro gas chromatographic (GC) system equipped with a thermal conductive detector. From these data, we calculated adsorbed amounts and equilibrium partial pressures for each gas. The initial dosing total pressures were set to 14.5 and 278.7 kPa for Cal–Na–Mo–Zn oxide and 14.5 and 279.9 kPa for Cal–NH₄–Mo–Zn oxide. The initial gas proportion was CO₂ : CH₄ = 40 : 60 (mol). After reaching the equilibrium, a small portion of the gas phase was used for GC analysis, leading to a slight decrease in system total pressure. Then co-sorption measurements were continued by using the residual gas. This process was repeated 5 times for each initial dosing pressure.

The selectivity of CO₂ over CH₄ was calculated by the following equation.

$$S_{\text{CO}_2} = (x_{\text{CO}_2}/y_{\text{CO}_2})/(x_{\text{CH}_4}/y_{\text{CH}_4})$$

y_{CO_2} : mole fraction of component CO₂ in the gas phase;

y_{CH_4} : mole fraction of component CH₄ in the gas phase;

x_{CO_2} : mole fraction of component CO₂ in the adsorbed phase;

x_{CH_4} : mole fraction of component CH₄ in the adsorbed phase.

Calculation of enthalpy of adsorption. Pure gas adsorption of CO₂ and CH₄ was carried out at different temperatures of 278, 288, and 298 K on the materials (Fig. S2–S5†). The isotherms of CO₂ and CH₄ were fitted with several adsorption models (Table S1†), and it was found that the dual-site Langmuir–Freundlich model was the best model, for which the equation is as follows:

$$q = \frac{q_1 b_1 p^{n_1}}{1 + b_1 p^{n_1}} + \frac{q_2 b_2 p^{n_2}}{1 + b_2 p^{n_2}},$$

where q is the adsorbed amount, p is pressure, and q_1 , q_2 , b_1 , b_2 , n_1 , and n_2 are fitting parameters, which are listed in Tables S2–S5.†

The resulting R^2 values of the fitting processes were quite close to 1, indicating that simulated isotherms by using the dual-site Langmuir–Freundlich model fitted the experimental isotherms well.

The enthalpy of adsorption was calculated by the Clausius–Clapeyron equation using the dual-site Langmuir–Freundlich fitting results.

$$\frac{d \ln p}{dT} = \frac{\Delta H}{RT^2},$$

where p is pressure, T is temperature, and ΔH is enthalpy of adsorption.

GC separation of CO₂ and CH₄. GC separation of a gas mixture of CO₂ and CH₄ using a column packed with Na–Mo–Zn oxide was performed with a Shimadzu GC-8A system equipped with a thermal conductivity detector. Na–Mo–Zn oxide was well grounded and screened with a mesh (aperture: 150 μm), and about 20 mL of Na–Mo–Zn oxide was densely packed into a column (length: 1 m, inner diameter: 3 mm). The fresh column of Na–Mo–Zn oxide was treated at 473 K by introducing a carrier gas of He for 2.5 h to remove the original water in the material and open the micropores of the material. The gas mixture (0.1 mL, mole ratio of CO₂ : CH₄ = 1 : 1) was injected, and separation was carried out at 363 K.

Structural determination, computer-based simulation, and DFT calculations

Structural determination of NH₄–Mo–Zn oxide was performed by *ab initio* structural determination with powder diffraction,³⁴ the detailed process of which is shown in the ESI.† Material modeling, X-cell program,³⁵ Pawley refinement, and Rietveld refinement³⁶ were performed with the Materials Studio package (Accelrys Software Inc.). The programs of DICVOL06 (ref. 37) and EdPCR were carried out with the Fullprof package. A charge-flipping algorithm³⁸ was performed with the superflip program in Jana2006, and electron density maps were generated with Chimera 1.8.1.

Monte Carlo simulation was performed to predict the adsorbed structure of the guest molecules in the primitive cell of Ca–Na–Mo–Zn oxide with the adsorption locator program in the Materials Studio package. First, the structure of the material, CO₂, and CH₄ were optimized by using the DMol³ program.^{39,40} We employed the Perdew–Burke–Ernzerhof (PBE) generalized gradient functional and DND basis set. Calculated Mulliken atomic charge was applied for Monte Carlo simulation. Partial atomic charges of CO₂ were C = +0.70e and O = –0.35e,⁴¹ and CH₄ was recognized as an electrostatic neutral molecule.⁴² The guest molecules were introduced into the framework of the material one by one.

Results and discussion

Material synthesis and characterization

The synthesis process for Mo–Zn oxides was carried out mainly according to our previous paper.³² However, the previous process produced Na–Mo–Zn oxide with a low yield (14% based on Mo) with some impurities such as MoO₂, ZnMoO₄ and Mo (Fig. S6†), which might have been caused by an insoluble starting material such as metal Mo and the poorly mixed precursor solution. It was known that mixing of solid precursors during reactions change selectivity of products.^{43,44} Here, we applied the dynamic method for material synthesis, in which the reactors were rotated under hydrothermal conditions (Fig. S1†). In the case of synthesis of Mo–Zn oxides, we found that applying rotation affected the purity and yield of the material. XRD patterns of the crude solids of Na–Mo–Zn oxide and NH₄–Mo–Zn oxide with and without rotation (Fig. S6†) indicated that rotation synthesis suppressed the side-reactions and increased the isolated yields of the materials (about 57–63% based on Mo for Na–Mo–Zn oxide and about 62–71% based on Mo for NH₄–Mo–Zn oxide). We carried out the synthesis many times and found that the reproducibilities of the synthesis of both materials are very good.

Furthermore, it was found that the rotation speed affected the yields of the materials. Low rotation (1 rpm) speed resulted in high isolated yields of both Mo–Zn oxides, and increasing the rotation speed would decrease the yields of products (Fig. S7†). The main impurity in crude solids of the materials from the synthesis with different rotation speeds was metal Mo (Fig. S6†). The amount of metal Mo increased in the crude solid with increase in rotation speed (Fig. S6B†), which illustrated that high rotation speeds hindered Mo consumption. This might ascribe to our rotation apparatus (Fig. S1†), in which a centripetal force would be applied to the solid in the solution to cause non-uniform mixing of the Mo metal in the solution.

By using different Mo sources with different cations (Na₂MoO₄·2H₂O and (NH₄)₆Mo₇O₂₄·4H₂O), materials of Mo–Zn oxide with different counteranions, Na–Mo–Zn oxide and NH₄–Mo–Zn oxide, were prepared. Elemental analysis indicated that the Na : Mo : Zn ratio of Na–Mo–Zn oxide obtained by the dynamic method that we used was the same as that of Na–Mo–Zn oxide obtained by our last non-dynamic method.³² The NH₄ : Mo : Zn ratio of NH₄–Mo–Zn oxide was 1.5 : 12 : 3. XRD patterns and FT-IR spectra (peaks below 1000

cm⁻¹ ascribed to the POM moiety) of both materials were similar to those of Mo–V–Bi oxide and Na–Mo–Zn oxide obtained by our last non-dynamic method (Fig. 2),^{30,32} indicating that the structures of materials synthesized by the dynamic method were similar to the structure of the reported Na–Mo–Zn oxide obtained by our last non-dynamic method. SEM images of the resulting materials showed octahedral morphologies typical of ϵ -Keggin-type heteropolyoxometalate-based framework compounds with sizes of the crystallite being 100–300 nm (Fig. 3a and b).

The structure of NH₄–Mo–Zn oxide was obtained by powder diffraction Rietveld analysis (Fig. S8) (detailed process shown in the ESI) combined with elemental analysis, FT-IR, and XPS analysis (Fig. S9†). The detailed chemical formulae of Na–Mo–Zn oxide and NH₄–Mo–Zn oxide were estimated to be Na_{1.5}H_{11.4}[Zn^{II}Mo^{VI}_{1.1}Mo^V_{10.9}O₄₀{Zn^{II}₂}]·5.5H₂O and (NH₄)_{1.5}H_{8.5}[Zn^{II}Mo^{VI}₄Mo^V₈O₄₀{Zn^{II}₂}]·6H₂O, respectively. The frameworks of

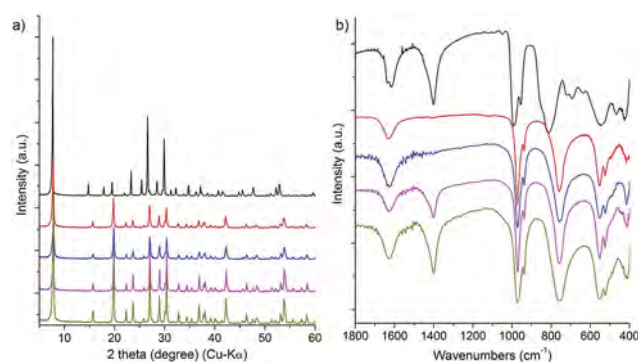


Fig. 2 (a) Powder XRD patterns of POM-based materials – lattice parameter of Na–Mo–Zn oxide: 19.4675 Å and lattice parameter of NH₄–Mo–Zn oxide: 19.4533 Å; and (b) FT-IR spectra of POM-based materials – black: Mo–V–Bi oxide, red: Na–Mo–Zn oxide using a non-dynamic method,³² blue: Na–Mo–Zn oxide using a dynamic method, purple: NH₄–Mo–Zn oxide, and yellow: NH₄–Na–Mo–Zn oxide.

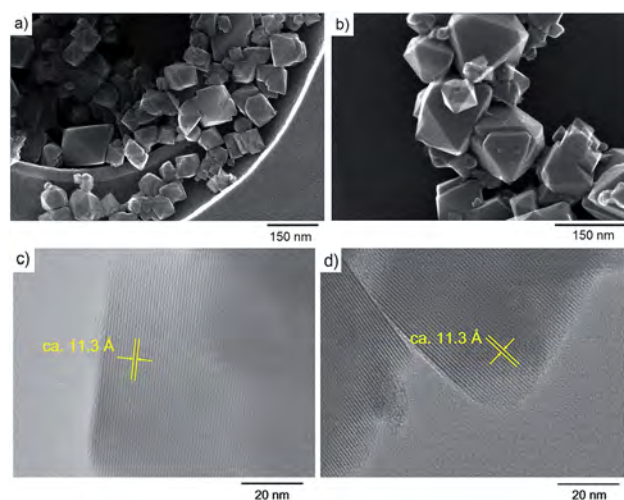


Fig. 3 SEM images of (a) Na–Mo–Zn oxide and (b) NH₄–Mo–Zn oxide and TEM images of (c) Na–Mo–Zn oxide and (d) NH₄–Mo–Zn oxide.

both materials were formed by assembly of ϵ -Keggin-type zirconomolybdate, $[\text{ZnMo}_{12}\text{O}_{40}]$, where one Zn–O tetrahedron was surrounded by 12 Mo–O octahedra. TEM showed that the distance of the (1 1 1) plane was close to each other, indicating that the basic structures of the materials were the same (Fig. 3c and d), and in good agreement with the results of structural analysis.

The difference between the two oxides was the counteranions, because cation species of the starting materials were different. The void space surrounded by the frameworks of Na–Mo–Zn oxide and NH_4 –Mo–Zn oxide was occupied by guest species, including water and sodium ions for Na–Mo–Zn oxide and water and ammonium cations for NH_4 –Mo–Zn oxide, in the as-synthesized materials. FT-IR spectra of the materials showed peak maxima of 1620 cm^{-1} and 1400 cm^{-1} , corresponding to water and ammonium cations in the materials (Fig. 2b). The amounts of sodium and ammonium in the materials of Na–Mo–Zn oxide and NH_4 –Mo–Zn oxide were the same (1.5 per POM unit).

Micropores were constructed by cages and channels, and the cages were connected with the channels in a tetrahedral fashion to build a 3D pore system (Fig. 1c). The numbers of cages and channels per POM were 1 and 2, respectively.

Heat treatment could remove the existing water from Na–Mo–Zn oxide and water and NH_4^+ from NH_4 –Mo–Zn oxide. TPD-MS was applied to investigate desorption of guest molecules from the as-synthesized materials (Fig. S10a and b†). The mass numbers m/z of 16 and 18 corresponded to ammonia and water, respectively. In the case of NH_4 –Mo–Zn oxide, the TPD-MS profile ($m/z = 16$) revealed only one peak with a peak maximum at 600 K, indicating desorption of ammonia at 600 K. Na–Mo–Zn oxide did not contain any ammonia in the structure. After removal of ammonia from NH_4 –Mo–Zn oxide, protons remained in the structure to make charge balance. There were two water desorption peaks, whose peak maxima were at about 400 K and 600 K, in both materials. For Na–Mo–Zn oxide, Na^+ could not be removed by heating and remained in the structure after heating. TG-DTA profiles indicated the weight loss of the materials during heating. The total weight loss of Na–Mo–Zn oxide was 7.5% and that of NH_4 –Mo–Zn oxide was 10.7% (Fig. S10c and d†).

Thermal stability and hydrothermal stability

Thermal stability of the materials was tested. The materials were calcined under N_2 flow (50 mL min^{-1}) for 2 h at 473 K, 523 K, 573 K, and 623 K (NH_4 –Mo–Zn oxide only). The resulting materials were characterized by powder XRD. Na–Mo–Zn oxide was stable at 473 K, and it started to decompose at 523 K as the diffraction peak of (111) decreased dramatically (Fig. S11A†). Compared with Na–Mo–Zn oxide, NH_4 –Mo–Zn oxide was thermally more stable, whose structure did not change at 523 K. Further heating would collapse the structure (Fig. S11B†).

Hydrothermal stability of the materials was also tested. The material (0.15 g) was dispersed in water (20 mL) followed by introducing the mixture into a 50 mL autoclave, and then the autoclave was heated for 24 h at 373 K, 413 K, 448 K, and 503 K in an oven. XRD showed that the peak intensities of both

materials almost did not decrease after hydrothermal treatments, indicating that the crystallinity of the materials did not drastically decrease (Fig. S11C and D†). However, the recovery rate of Na–Mo–Zn oxide decreased with increase in the treatment temperature, demonstrating that the material slowly dissolved in water during the hydrothermal treatment (Fig. S11E†). In the case of NH_4 –Mo–Zn oxide, the recovery rate of the material was higher than that of Na–Mo–Zn oxide. The material was stable under the hydrothermal conditions below 448 K (Fig. S11E†).

Both Mo–Zn oxides were thermally stable at 473 K (Fig. S11†). It was found that calcination at 473 K for 2.5 hours under a high vacuum could remove water and NH_3 without collapse of the structure. The remaining guest molecules, water in the calcined material of Na–Mo–Zn oxide (Cal–Na–Mo–Zn oxide) and NH_4^+ and water in calcined NH_4 –Mo–Zn oxide (Cal– NH_4 –Mo–Zn oxide), were estimated by TPD measurement (Fig. S12†). In the case of Na–Mo–Zn oxide, 63% of the water was removed by heating. Heating of NH_4 –Mo–Zn oxide removed 41% of the water and 65% of NH_3 . The chemical formulae of Cal– NH_4 –Mo–Zn oxide and Cal– NH_4 –Mo–Zn oxide were estimated to be $\text{Na}_{1.5}\text{H}_{11.4}[\text{Zn}^{\text{II}}\text{Mo}^{\text{VI}}_{1.1}\text{Mo}^{\text{V}}_{10.9}\text{O}_{40}\{\text{Zn}^{\text{II}}\}_2] \cdot 2\text{H}_2\text{O}$ and $(\text{NH}_4)_{0.5}\text{H}_{9.6}[\text{Zn}^{\text{II}}\text{Mo}^{\text{VI}}_4\text{Mo}^{\text{V}}_8\text{O}_{40}\{\text{Zn}^{\text{II}}\}_2] \cdot 3.5\text{H}_2\text{O}$, respectively. The amounts of guest species in the two calcined Mo–Zn oxides were similar, 3.5–4 per POM unit (Table S6†).

Adsorption properties

N_2 sorption measurements of both calcined oxides showed a sudden N_2 uptake at very low relative pressure ($p/p_0 = 0.001$), indicating that the materials were microporous materials (Fig. S13a and Table S7†). Pore size distribution calculated by the SF method further demonstrated that both Mo–Zn oxides were microporous materials (Fig. S13b†). The adsorption properties of Cal–Na–Mo–Zn oxide and Cal– NH_4 –Mo–Zn oxide were further studied by small molecule adsorption. The materials selectively adsorbed different kinds of small molecules based on the size of the molecules. Fig. 4 shows the adsorption isotherms of CH_4 , CO_2 , C_2H_6 , and C_3H_8 on the materials at 298 K. The results indicated that the materials adsorbed small molecules including CH_4 , CO_2 and C_2H_6 with kinetic diameters of 0.38, 0.33, and 0.40 nm, respectively, whereas a larger molecule of C_3H_8 with a kinetic diameter of 0.42 nm was not adsorbed by either of the materials.

Surface areas of the materials were calculated by the BET method from CO_2 adsorption isotherms to be $88\text{ m}^2\text{ g}^{-1}$ and $68\text{ m}^2\text{ g}^{-1}$ for Cal–Na–Mo–Zn oxide and Cal– NH_4 –Mo–Zn oxide, respectively. Pore volumes for Cal–Na–Mo–Zn oxide and Cal– NH_4 –Mo–Zn oxide were estimated by the DA method⁴⁵ from CO_2 adsorption isotherms to be $0.039\text{ cm}^3\text{ g}^{-1}$ and $0.033\text{ cm}^3\text{ g}^{-1}$, respectively. For Cal–Na–Mo–Zn oxide, about 1.84 of CO_2 , 0.86 of CH_4 , and 1.04 of C_2H_6 per POM unit were adsorbed. For Cal– NH_4 –Mo–Zn oxide, about 1.44 of CO_2 , 0.89 of CH_4 , and 0.99 of C_2H_6 per POM unit were adsorbed (Table 1).

Moreover, Mo–Zn oxide with NH_4^+ was obtained by an ion-exchange process (NH_4 –Na–Mo–Zn oxide). Here we used a high dosage of NH_4Cl expecting to replace all Na^+ in Na–Mo–Zn

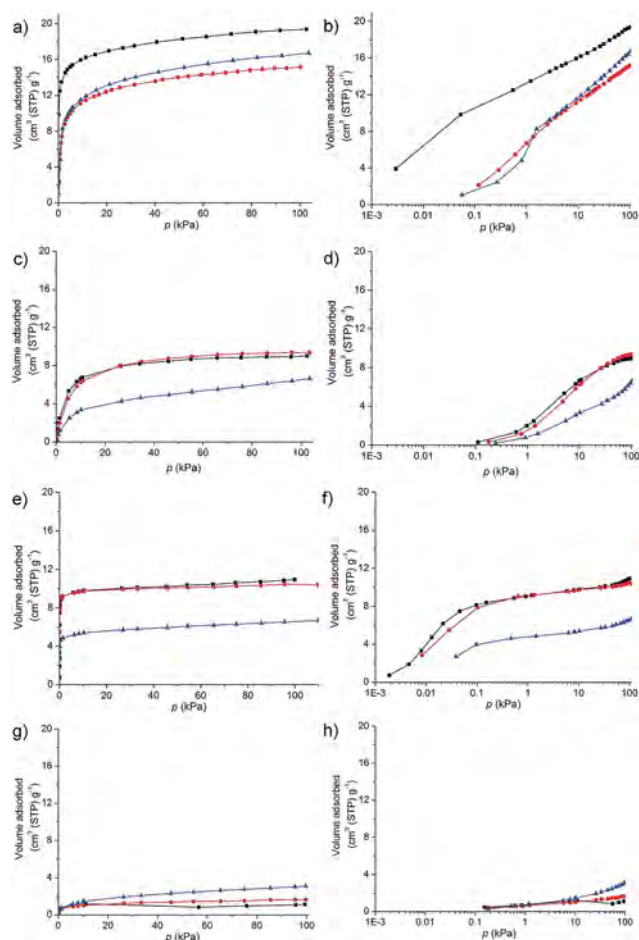


Fig. 4 Adsorption isotherms of (a and b) CO_2 , (c and d) CH_4 , (e and f) C_2H_6 , and (g and h) C_3H_8 at 298 K – black: Cal-Na-Mo-Zn oxide, red: Cal-NH₄-Mo-Zn oxide, and blue: Cal-NH₄-Na-Mo-Zn oxide.

oxide. XRD pattern and FT-IR spectra confirmed that the basic structure of NH₄-Na-Mo-Zn oxide was the same as those of the other two Mo-Zn oxides (Fig. 2). The appearance of an IR band at 1400 cm⁻¹ indicated that NH₄⁺ was successfully introduced into Na-Mo-Zn oxide. Elemental analysis demonstrated that there was still Na⁺ in the material and the chemical formula of as-synthesized NH₄-Na-Mo-Zn oxide was $(\text{NH}_4)_{1.4}\text{Na}_{0.1}\text{H}_{11.4}[\text{ZnMo}_{12}\text{O}_{40}\{\text{Zn}_2\}]\cdot 5.5\text{H}_2\text{O}$. After calcination at 473 K (denoted as Cal-NH₄-Na-Mo-Zn oxide), TPD-MS (Fig. S12d and e†) indicated that the chemical formula of the calcined material

was $(\text{NH}_4)_{1.4}\text{Na}_{0.1}\text{H}_{11.4}[\text{ZnMo}_{12}\text{O}_{40}\{\text{Zn}_2\}]\cdot 3\text{H}_2\text{O}$ and most of the NH₄⁺ remained.

Molecule adsorption was also carried out on Cal-NH₄-Na-Mo-Zn oxide, showing that the material could also adsorb small molecules (Fig. 4). Compared to other two Mo-Zn oxides, the adsorption capacity of Cal-NH₄-Na-Mo-Zn oxide was lower, which might have resulted from remaining NH₄⁺ and water in the Cal-NH₄-Na-Mo-Zn oxide (Table S6†). Therefore, we would like to use Cal-NH₄-Mo-Zn oxide and Cal-Na-Mo-Zn oxide for further experiments.

CO₂ and CH₄ adsorption. CO₂ uptake in both materials sharply increased in the low pressure range (<1 kPa), indicating that both Mo-Zn oxides had strong interactions with CO₂, and both materials showed high CO₂ adsorption capacity (19 cm³(STP) g⁻¹ for Na-Mo-Zn oxide and 15 cm³(STP) g⁻¹ for Cal-NH₄-Mo-Zn oxide at 100 kPa) (Fig. 4a and b). In the case of CH₄ adsorption, the molecule uptake in the low pressure range increased gradually, indicating that the materials showed weaker interaction with CH₄ than that with CO₂ (Fig. 4c and d). Both calcined Mo-Zn oxides adsorbed CO₂ at a low pressure (<1 kPa), whereas they could not adsorb CH₄ at such a low pressure.

The enthalpy of adsorption was calculated using the Clausius-Clapeyron equation, which is shown in Fig. 5. The enthalpies of CO₂ and CH₄ adsorption for Na-Mo-Zn oxide were calculated to be 46–65 kJ mol⁻¹ and 18–30 kJ mol⁻¹, respectively. The enthalpies of CO₂ and CH₄ adsorption for NH₄-Mo-Zn oxide were calculated to be 35–45 kJ mol⁻¹ and 25–30 kJ mol⁻¹, respectively. The enthalpy of CO₂ adsorption in both materials was higher than that of CH₄ adsorption, indicating that the materials strongly interacted with CO₂ but weakly interacted with CH₄.

CO₂ adsorption isotherms of Cal-Na-Mo-Zn oxide and Cal-NH₄-Mo-Zn oxide were different. Cal-Na-Mo-Zn oxide showed much higher adsorption capacity than that of Cal-NH₄-Mo-Zn oxide not only at a high pressure but also at a low pressure (<1 kPa), at which adsorption in micropores occurred (Fig. 4a and b). The enthalpy of CO₂ adsorption (Fig. 5) for Cal-Na-Mo-Zn oxide (46–65 kJ mol⁻¹) appeared to be higher than that of CO₂ for Cal-NH₄-Mo-Zn oxide (35–45 kJ mol⁻¹), indicating that Na⁺ in Cal-Na-Mo-Zn oxide showed stronger interaction with CO₂ than did protons or ammonium cations in Cal-NH₄-Mo-Zn oxide.

On the other hand, adsorption isotherms of CH₄ in Cal-Na-Mo-Zn oxide and Cal-NH₄-Mo-Zn oxide were almost the same. For both calcined Mo-Zn oxides, about 10 cm³ g⁻¹ of gas molecules was adsorbed at 298 K and at 100 kPa. Enthalpies of

Table 1 Numbers of small molecules per POM unit adsorbed in the materials at 100 kPa^a

	POM unit	CO ₂	CH ₄	C ₂ H ₆	C ₃ H ₈
Cal-Na-Mo-Zn oxide	ZnMo ₁₂ O ₄₀	1.84	0.86	1.04	0.11
Cal-NH ₄ -Mo-Zn oxide	ZnMo ₁₂ O ₄₀	1.44	0.89	0.99	0.16
Cal-NH ₄ -Na-Mo-Zn oxide	ZnMo ₁₂ O ₄₀	1.58	0.63	0.63	0.30

^a The values were calculated by the equation: number of molecule adsorbed = $\frac{\text{adsorbed amount (cm}^3 \text{ g}^{-1}) \times \text{molecule weight of the material (g mol}^{-1})}{22400 (\text{cm}^3 \text{ mol}^{-1})}$.

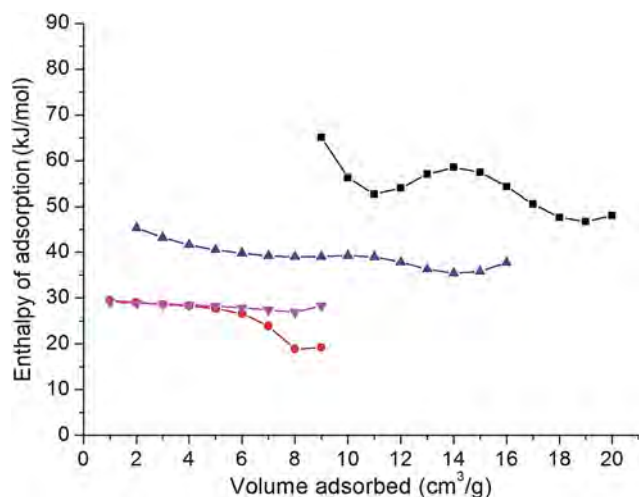


Fig. 5 Enthalpy of CO₂ and CH₄ adsorption for Cal-Na-Mo-Zn oxide and Cal-NH₄-Mo-Zn oxide – black: Cal-Na-Mo-Zn oxide adsorbed CO₂, red: Cal-Na-Mo-Zn oxide adsorbed CH₄, blue: Cal-NH₄-Mo-Zn oxide adsorbed CO₂, and purple: Cal-NH₄-Mo-Zn oxide adsorbed CH₄.

CH₄ adsorption for Cal-Na-Mo-Zn oxide (18–30 kJ mol⁻¹) and Cal-NH₄-Mo-Zn oxide (25–30 kJ mol⁻¹) were almost the same. Therefore, Na⁺ did not affect the adsorption of CH₄ in the materials.

It was reported that the electronic properties of CO₂ and CH₄ caused the different adsorption behaviors. CO₂ has a large quadrupole moment (13.4×10^{-40} cm²), whereas CH₄ is non-polar.⁴⁶ The large amount of CO₂ adsorption and the strong interaction of CO₂ with frameworks were attributed to large quadrupole moment of CO₂ molecules,⁴⁷ which resulted in a relatively strong attraction to the electrostatic field of frameworks.⁴⁸ Cation species would have influence on the adsorption of CO₂. The effect of a cation is complicated. In some reports, it was claimed that the enhancement of CO₂ adsorption after introducing alkaline metal ions is due to increase in the basicity of the material.⁴⁸ In other reports, this was ascribed to alkaline metal ions with high positive atomic partial charge, which strongly interacted with CO₂.⁴⁹

In the present study, partial atomic charges of Na-Mo-Zn oxide and NH₄-Mo-Zn oxide were analyzed by DFT calculations, and the results are shown in Tables S8 and S9.† Frameworks of the materials were covered with oxygen atoms that were all negatively charged. Counteranions such as protons and Na⁺ in the material were positively charged. This framework would display an electrostatic field, and therefore CO₂ would have stronger electrostatic interactions than CH₄ with the framework. Furthermore, the atomic charge of Na⁺ was much higher than that of protons in the material, indicating stronger interactions between Na⁺ and CO₂.

Monte Carlo simulation. A primitive cell of Cal-Na-Mo-Zn oxide contained 2 POM units of [ZnMo₁₂O₄₀] with 2 cages, 23 protons and 3 Na⁺. Assuming that Na⁺ were located in two cages of the material, one cage contains two Na⁺ (cage A) and

another cage contains the other Na⁺ (cage B) (Fig. 6a). Monte Carlo simulation was performed on Cal-Na-Mo-Zn oxide to estimate affinity of CO₂ with Na⁺. CO₂ was loaded one by one during the simulation. It was found that the first CO₂ was located in cage A and the second CO₂ was located in cage B (Fig. 6b and c). In cage A, these two Na ions were bridged by CO₂ in a μ - η^1 - η^1 fashion, as shown in Fig. 6b and c. The distance between the Na⁺ and the carbon atoms of CO₂ was calculated to be 2.35 Å, indicating that CO₂ strongly interacted with Na⁺ in cage A. Adsorption energies estimated by Monte Carlo simulation for CO₂ in cage A (Fig. 6b) and CO₂ in cage B (Fig. 6c) were 53 and 41 kJ mol⁻¹, respectively. The results of calculation were consistent with the observed trend of adsorption enthalpy of CO₂ in the material. In the case of CH₄, it was first filled in cage B, because cage B had more space and CH₄ had weak electrostatic interactions with Na⁺ (Fig. 6d and e). The adsorption energy from Monte Carlo simulation for CH₄ in both sites was 24 kJ mol⁻¹, also indicating that CH₄ would weakly interact with Na⁺.

Co-adsorption and separation experiments. CO₂ exists widely in landfill gas. CO₂ selective adsorption from a CO₂/CH₄ mixture is of great importance for improvement of gas quality. Co-adsorption experiments were carried out on Cal-Na-Mo-Zn

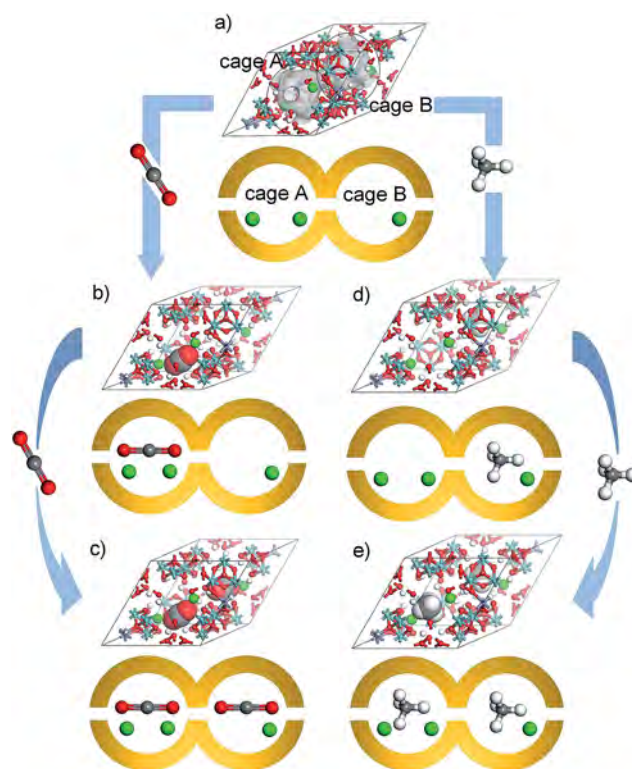


Fig. 6 Representations of adsorbed structures of Cal-Na-Mo-Zn oxide from Monte Carlo simulation – upper: ball-and-stick representations and lower: schematic representations. (a) Primitive cell with cage A and cage B, (b) Cal-Na-Mo-Zn oxide adsorbed first CO₂, (c) Cal-Na-Mo-Zn oxide adsorbed second CO₂, (d) Cal-Na-Mo-Zn oxide adsorbed first CH₄, and (e) Cal-Na-Mo-Zn oxide adsorbed second CH₄ – blue sphere: Mo, purple sphere: Zn, red sphere: O, white sphere: H, gray sphere: C, and green sphere: Na.

oxide and Cal-NH₄-Mo-Zn oxide under both high pressures (125.2 and 127.5 kPa of equilibrium total pressures) and low pressures (1.5 and 1.6 kPa of equilibrium total pressures) at 298 K. The initial ratio of CO₂ and CH₄ was 40 : 60, a typical composition of biogas.⁵⁰ According to the individual adsorption isotherms, in the low pressure range, the materials might show high separation efficiency of CO₂.

Equilibrium total pressure, total adsorbed amount, CO₂ and CH₄ partial pressures, and CO₂ and CH₄ adsorbed amounts are shown in Fig. 7. Under high pressure conditions, both materials adsorbed more CO₂ than CH₄. When the materials continued to be left under mixed gas pressure, they further adsorbed CO₂, while CH₄ desorbed from the materials (Fig. 7a and b), indicating that adsorbed CH₄ was partly replaced by CO₂. Moreover, Cal-Na-Mo-Zn oxide (15 cm³ g⁻¹ at the fifth co-sorption equilibrium) tended to adsorb more CO₂ than did Cal-NH₄-Mo-Zn oxide (11 cm³ g⁻¹ at the fifth co-sorption equilibrium). Under low pressure conditions, the two materials adsorbed similar amounts of CO₂ and CH₄. With prolongation of the adsorption process, Cal-Na-Mo-Zn oxide

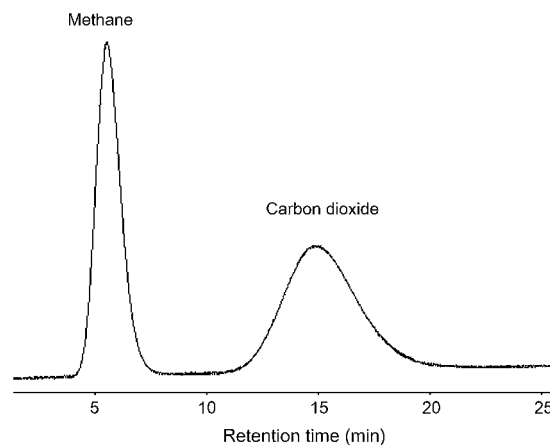


Fig. 8 Gas chromatograms of a gas mixture of CO₂ and CH₄ separated on a column of Cal-Na-Mo-Zn oxide.

further adsorbed CO₂ and concurrently desorbed CH₄, while Cal-NH₄-Mo-Zn oxide adsorbed both CH₄ and CO₂ (Fig. 7c and d).

CO₂ selectivity of the final equilibrium (5th equilibrium data in Fig. 7) for the material was calculated and is summarized in Table 2. Cal-Na-Mo-Zn oxide showed higher selectivity to CO₂ adsorption than that of Cal-NH₄-Mo-Zn oxide under both high and low pressure conditions. Co-sorption experiments demonstrated that Cal-Na-Mo-Zn oxide had better performance of CO₂ separation than that of Cal-NH₄-Mo-Zn oxide.

Table S10† summarizes the performance of different adsorbents, such as zeolites, MOF materials, and other porous materials, for CO₂ selective adsorption from a CO₂/CH₄ mixture. CO₂ selectivity of Cal-Na-Mo-Zn oxide was higher than that of the reported materials in Table S10,† which indicated that Cal-Na-Mo-Zn oxide was a good candidate for CO₂ selective adsorption and separation.

Furthermore, Cal-Na-Mo-Zn oxide was successfully applied to GC separation of CO₂ from a CO₂/CH₄ mixture. The gas mixture (CO₂ : CH₄ = 1 : 1) was injected into a gas chromatograph equipped with a column filled with Na-Mo-Zn oxide. As shown in Fig. 8, CH₄ and CO₂ were separated within a few minutes at 363 K. The peak of CO₂ appeared slower and was broader than that of CH₄, indicating that the material had stronger interactions with CO₂ than with CH₄.

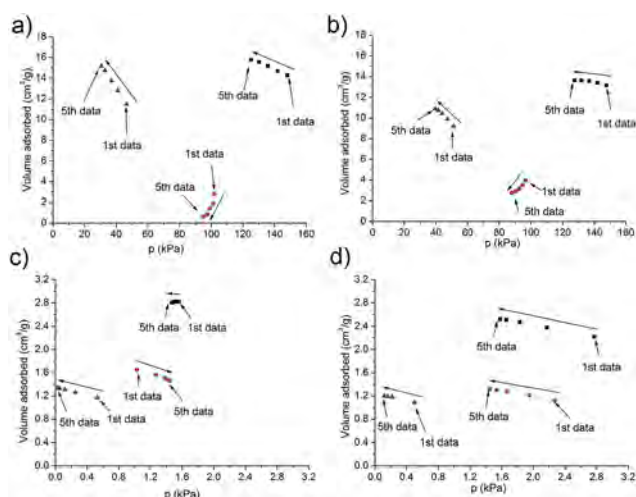


Fig. 7 CO₂/CH₄ co-sorption results of (a) Cal-Na-Mo-Zn oxide at high pressure, (b) Cal-NH₄-Mo-Zn oxide at high pressure, (c) Cal-Na-Mo-Zn oxide at low pressure, and (d) Cal-NH₄-Mo-Zn oxide at low pressure – black square: system total pressure (x-axis) and adsorbed amount (y-axis), red cycle: CH₄ partial pressure (x-axis) and adsorbed amount (y-axis), and blue triangle: CO₂ partial pressure (x-axis) and adsorbed amount (y-axis).

Table 2 CO₂/CH₄ co-sorption in the materials^a

Entry	Material	p_c^b (kPa)	Ratio in gas phase (%)		Ratio in adsorbed phase (%)		CO ₂ selectivity
			CO ₂	CH ₄	CO ₂	CH ₄	
1	Cal-Na-Mo-Zn oxide	1.5	1.70	98.3	47.4	52.6	52
2	Cal-Na-Mo-Zn oxide	125.2	24.4	75.6	96.0	4.0	75
3	Cal-NH ₄ -Mo-Zn oxide	1.6	7.80	92.2	47.7	52.3	11
4	Cal-NH ₄ -Mo-Zn oxide	127.5	31.0	69.0	79.8	20.2	9

^a These are 5th equilibrium data. ^b p_c denotes the equilibrium total pressure.

Conclusion

The materials of Cal–Na–Mo–Zn oxide and Cal–NH₄–Mo–Zn oxide adsorbed small molecules including CO₂, C₂H₆, and CH₄. Both oxides selectively adsorbed CO₂ from the CO₂/CH₄ mixture, because the materials showed higher adsorption capacity of CO₂ than that of CH₄. Cal–Na–Mo–Zn oxide showed stronger interactions with CO₂ than Cal–NH₄–Mo–Zn oxide did, while both oxides showed similar interactions with CH₄. Co-sorption experiments showed that selectivity of CO₂ on Na–Mo–Zn oxide was higher than that on Cal–NH₄–Mo–Zn oxide. Cal–Na–Mo–Zn oxide was applied to GC separation, and CO₂ could be efficiently separated from the CO₂/CH₄ mixture by using the material.

Acknowledgements

This work was financially supported by a Grant-in-Aid for Scientific Research (A) (grant no. 2324-6135) from the Ministry of Education, Culture, Sports, Science, and Technology, Japan. M.S. thanks PRESTO, JST and Nippon Sheet Glass Foundation for Materials Science and Engineering (NSG Foundation) for financial support. S.N. thanks a Grant-in-Aid for Science Research from the Ministry of Education, Culture, Sports, Science and Technology, Japan (grant no. 24550068). K.Y. thanks Grants-in-Aid (grant nos 22245028 and 24109014) for Scientific Research from JSPS and MEXT and the MEXT Projects of “Integrated Research on Chemical Synthesis” and “Elements Strategy Initiative for Catalysts and Batteries”.

Notes and references

- G. Férey, C. Serre, T. Devic, G. Maurin, H. Jobic, P. L. Llewellyn, G. De Weireld, A. Vimont, M. Daturi and J.-S. Chang, *Chem. Soc. Rev.*, 2011, **40**, 550–562.
- K. Sumida, D. L. Rogow, J. a. Mason, T. M. McDonald, E. D. Bloch, Z. R. Herm, T.-H. Bae and J. R. Long, *Chem. Rev.*, 2012, **112**, 724–781.
- N. Du, H. B. Park, M. M. Dal-Cin and M. D. Guiver, *Energy Environ. Sci.*, 2012, **5**, 7306–7322.
- N. A. Khan, Z. Hasan and S. H. Jung, *J. Hazard. Mater.*, 2013, **244–245**, 444–456.
- A. M. Kierzkowska, R. Pacciani and C. R. Müller, *ChemSusChem*, 2013, **6**, 1130–1148.
- Y. Kamiya, M. Sadakane, W. Ueda and J. Reedijk, *Heteropoly Compounds in Comprehensive Inorganic Chemistry II*, ed. K. Poeppelmeier, Elsevier, Oxford, 2013, vol. 7.
- Special thematic issue on polyoxometalates. C. L. Hill, *Chem. Rev.*, 1998, **98**, 1–390.
- Special thematic issue on polyoxometalates. L. Cronin and A. Müller, *Chem. Soc. Rev.*, 2012, **41**, 7325–7648.
- D.-L. Long, R. Tsunashima and L. Cronin, *Angew. Chem., Int. Ed.*, 2010, **49**, 1736–1758.
- M. Sadakane, K. Kodato, T. Kuranishi, Y. Nodasaka, K. Sugawara, N. Sakaguchi, T. Nagai, Y. Matsui and W. Ueda, *Angew. Chem., Int. Ed.*, 2008, **47**, 2493–2496.
- M. Sadakane, K. Yamagata, K. Kodato, K. Endo, K. Toriumi, Y. Ozawa, T. Ozeki, T. Nagai, Y. Matsui, N. Sakaguchi, W. D. Pyrz, D. J. Buttrey, D. A. Blom, T. Vogt and W. Ueda, *Angew. Chem., Int. Ed.*, 2009, **48**, 3782–3786.
- M. Sadakane, N. Watanabe, T. Katou, Y. Nodasaka and W. Ueda, *Angew. Chem., Int. Ed.*, 2007, **46**, 1493–1496.
- S. G. Mitchell, C. Streb, H. N. Miras, T. Boyd, D.-L. Long and L. Cronin, *Nat. Chem.*, 2010, **2**, 308–312.
- D. Liu, Y. Lu, H.-Q. Tan, W.-L. Chen, Z.-M. Zhang, Y.-G. Li and E.-B. Wang, *Chem. Commun.*, 2013, 3673–3675.
- A. Dolbecq, C. Mellot-Draznieks, P. Mialane, J. Marrot, G. Férey and F. Sécheresse, *Eur. J. Inorg. Chem.*, 2005, 3009–3018.
- G. Férey, C. Mellot-Draznieks, C. Serre, F. Millange, J. Dutour, S. Surblé and I. Margiolaki, *Science*, 2005, **309**, 2040–2042.
- L. M. Rodriguez-Albelo, A. Rabdel Ruiz-Salvador, A. Sampieri, D. W. Lewis, A. Gomez, B. Nohra, P. Mialane, J. Marrot, F. Secheresse, C. Mellot-Draznieks, R. N. Biboum, B. Keita, L. Nadjjo and A. Dolbecq, *J. Am. Chem. Soc.*, 2009, **131**, 16078–16087.
- J. Song, Z. Luo, D. K. Britt, H. Furukawa, O. M. Yaghi, K. I. Hardcastle and C. L. Hill, *J. Am. Chem. Soc.*, 2011, **133**, 16839–16846.
- C.-Y. Sun, S.-X. Liu, D.-D. Liang, K.-Z. Shao, Y.-H. Ren and Z.-M. Su, *J. Am. Chem. Soc.*, 2009, **131**, 1883–1888.
- B. Nohra, H. El Moll, L. M. Rodriguez Albelo, P. Mialane, J. Marrot, C. Mellot-Draznieks, M. O’Keeffe, R. N. Biboum, J. Lemaire, B. Keita, L. Nadjjo and A. Dolbecq, *J. Am. Chem. Soc.*, 2011, **133**, 13363–13374.
- H. Tagami, S. Uchida and N. Mizuno, *Angew. Chem., Int. Ed.*, 2009, **48**, 6160–6164.
- S. Uchida, R. Eguchi and N. Mizuno, *Angew. Chem., Int. Ed.*, 2010, **49**, 9930–9934.
- S. Uchida, M. Hashimoto and N. Mizuno, *Angew. Chem., Int. Ed.*, 2002, **6**, 2814–2817.
- R. Eguchi, S. Uchida and N. Mizuno, *Angew. Chem., Int. Ed.*, 2012, **51**, 1635–1639.
- N. Mizuno and S. Uchida, *Chem. Lett.*, 2006, **35**, 688–693.
- S. Uchida, S. Hikichi, T. Akatsuka, T. Tanaka, R. Kawamoto, A. Lesbani, Y. Nakagawa, K. Uehara and N. Mizuno, *Chem. Mater.*, 2007, **19**, 4694–4701.
- R. Eguchi, S. Uchida and N. Mizuno, *J. Phys. Chem. C*, 2012, **116**, 16105–16110.
- Y. Ogasawara, S. Uchida and N. Mizuno, *J. Phys. Chem. C*, 2007, **6**, 8218–8227.
- S. Uchida and N. Mizuno, *J. Am. Chem. Soc.*, 2004, **6**, 1602–1603.
- Z. Zhang, M. Sadakane, T. Murayama, S. Izumi, N. Yasuda, N. Sakaguchi and W. Ueda, *Inorg. Chem.*, 2014, **53**, 903–911.
- Z. Zhang, M. Sadakane, T. Murayama and W. Ueda, *Dalton Trans.*, 2014, 13584–13590.
- Z. Zhang, M. Sadakane, T. Murayama, N. Sakaguchi and W. Ueda, *Inorg. Chem.*, 2014, **53**, 7309–7318.
- A. L. McClellan and H. F. Harnsberger, *J. Colloid Interface Sci.*, 1967, **23**, 577–599.

- 34 *Structure Determination from Powder Diffraction Data*, ed. W. I. F. David, K. Shankland, L. B. McCusker and C. Baerlocher, Oxford University Press, 2006, vol. 47.
- 35 M. A. Neumann, *J. Appl. Crystallogr.*, 2003, **36**, 356–365.
- 36 R. A. Young, *The Rietveld Method*, Oxford University Press, Oxford, 1995.
- 37 A. Boulfif and D. Louer, *J. Appl. Crystallogr.*, 2004, **37**, 724–731.
- 38 L. Palatinus and G. Chapuis, *J. Appl. Crystallogr.*, 2007, **40**, 786–790.
- 39 B. Delley, *J. Chem. Phys.*, 2000, **113**, 7759–7764.
- 40 B. Delley, *J. Chem. Phys.*, 1990, **92**, 508–517.
- 41 E. D. Akten, R. Siriwardane and D. S. Sholl, *Energy Fuels*, 2003, **17**, 977–983.
- 42 T. R. Zeitler, M. D. Allendorf and A. Greathouse, *J. Phys. Chem. C*, 2012, **116**, 3492–3502.
- 43 X. Li, Z. Wang, J. Zheng, S. Shao, Y. Wang and Y. Yan, *Chin. J. Catal.*, 2011, **32**, 217–223.
- 44 S. Aguado, J. Gascón, J. C. Jansen and F. Kapteijn, *Microporous Mesoporous Mater.*, 2009, **120**, 170–176.
- 45 M. M. Dubinin, *Prog. Surf. Membr. Sci.*, 1975, **9**, 1–70.
- 46 D. M. D'Alessandro, B. Smit and J. R. Long, *Angew. Chem., Int. Ed.*, 2010, **49**, 6058–6082.
- 47 J. Zhang, N. Burke, S. Zhang, K. Liu and M. Pervukhina, *Chem. Eng. Sci.*, 2014, **113**, 54–61.
- 48 X. Xu, X. Zhao, L. Sun and X. Liu, *J. Nat. Gas Chem.*, 2008, **17**, 391–396.
- 49 A. Zúkal, J. Mayerová and J. Čejka, *Phys. Chem. Chem. Phys.*, 2010, **12**, 5240–5247.
- 50 X. Zhu, K. Li, J.-L. Liu, X.-S. Li and A.-M. Zhu, *Int. J. Hydrogen Energy*, 2014, **39**, 13902–13908.

Effect of Activation Degree of Resorcinol–Formaldehyde Carbon Gels on Carbon monoxide Tolerance of Platinum–Ruthenium Polymer Electrolyte Fuel Cell Anode Catalyst

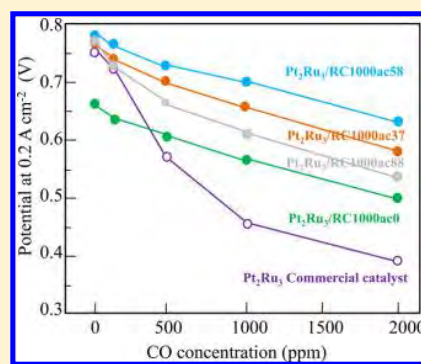
Napan Narischat,[†] Tatsuya Takeguchi,^{*,†,‡} Takanori Tsuchiya,[§] Takeshi Mori,[§] Isao Ogino,[§] Shin R. Mukai,[§] and Wataru Ueda[†]

[†]Catalysis Research Center, Hokkaido University, 5 Chome Kita 8 Jonishi Kita, Sapporo, Hokkaido 060-0808, Japan

[‡]Department of Chemistry and Bioengineering, Iwate University, 4-3-5 Ueda, Morioka, Iwate 020-8551, Japan

[§]Graduate School of Engineering, Hokkaido University, 5 Chome Kita 8 Jonishi Kita, Sapporo, Hokkaido 060-0808, Japan

ABSTRACT: Resorcinol–formaldehyde carbon gels (RFCs) show several advantageous properties as a catalyst support over other carbons, as their pore volume and pore size can be readily tailored, for example, via CO₂ activation. In this study, RFCs were synthesized with various activation degrees (burn-off) as 0, 37, 58, and 88% and used as the support for a PtRu anode electrode; a commercial Pt₂Ru₃/C anode catalyst was used as a reference. The catalysts were characterized by powder X-ray diffraction (PXRD), BET surface area, transmission electron microscopy (TEM), and scanning transmission electron microscopy (STEM). The performance and CO tolerance of the obtained catalysts were tested through single cell performance analysis with CO contaminations ranging from 100 to 2000 ppm. The prepared Pt₂Ru₃/RFC catalysts showed superior CO tolerance. Especially Pt₂Ru₃/RFC prepared using an RFC with a burn-off of 58% (RC1000Ac58) showed the highest performance and best CO tolerance. The activation degree could affect the volumes and sizes of mesopores and micropores, resulting in differences in size and dispersion of PtRu particles, and accessibility to the particles both of which govern the performance and CO tolerance of the catalysts. Pt₂Ru₃/RC1000Ac58 showed the highest cell voltage of 0.787 V and highest CO tolerance at 2000 ppm of CO (0.655 V, only 16.8% overvoltage). Supporting PtRu particles by using a carbon support with an optimum activation degree could be a practical method to improve the performance and CO tolerance of a PtRu electrocatalyst.



1. INTRODUCTION

Polymer electrolyte fuel cells (PEFCs) are considered to become promising energy storage devices because of their low operating temperature, high power density, and lightweight. Key technologies for automotive, stationary, and portable applications have been developed in academic, institutional, and industrial sectors.¹ In Japan, residential PEFC systems have been developed rapidly during the last 10 years. Osaka Gas has commercialized a residential gas engine cogeneration system, also known as CHP (combined heat and power) in March, 2003. And recently, a 0.7–1.0 kW class PEFC cogeneration system has become available in the Japanese residential market.² A joint-project led by Panasonic and Tokyo gas also has reported a significant development in residential PEFC.³ Many other countries around the world also have been developing this battery system.^{4–6}

In order to utilize a PEFC for residential applications, the fuel source is the most important factor. Natural gas appears to be the best fuel, as it is a hydrogen-rich gas. The primary route for the reforming of natural gas fuel for PEFC applications is steam reforming. However, fuel obtained through this route contain CO, which is an undesired byproduct because it strongly adsorbs onto the Pt surface that is used in a PEFC, and

seriously hinders the hydrogen oxidation reaction (HOR) which occurs at the anode Pt catalyst layer.^{7,8} Electrode catalysts insensitive to CO poisoning are thus desired. For more than 30 years since its discovery, the only catalyst that can endure CO for practical uses has been a carbon-supported Pt–Ru bimetallic catalyst. The function of Ru is to generate oxygen containing species, or to weaken Pt–CO bonding by reducing the *d*-electron deficiency of Pt atoms.⁹ Because of the limited availability of Ru, other metals that can substitute Ru have been sought after for more than a decade.^{10–12} Although there has been significant effort to develop multimetallic Pt-based anode electrocatalysts with higher CO tolerance, the common use of PtRu bimetallic catalysts for anodes only permits less than 100 ppm of CO at the anode inlet.¹³

The previous study on the CO tolerance of PtRu anode catalysts clarified the effect of Pt/Ru ratio, alloying degree and particle size. It was found that, in order to obtain a high CO tolerant PtRu catalyst, its alloying degree should be high, its particle size should be about 3–5 nm, and its Pt/Ru ratio

Received: March 12, 2014

Revised: August 15, 2014

Published: August 27, 2014

should be 2:3. And also, it was shown that the size and alloying degree can be controlled by adjusting the condition of the preparation and heat treatment processes.^{14–16} Moreover, the structure of the catalyst support could influence the physical and electrical properties of the catalyst significantly considering concept of strong metal support interactions (SMSI).^{17,18} To investigate the effects of support, we chose resorcinol–formaldehyde (RF) resin derived carbon gels because we can tailor its surface area porosity by adjusting synthesis conditions.

Pekala et al. reported the successful synthesis of carbon aerogels by carbonization of resorcinol–formaldehyde resins and suggested that carbon aerogels are suitable for a number of electrochemical applications due to their monolithic structure, high surface area, controllable pore size, and low electrical resistance. The structure and properties of carbon aerogel electrodes depend upon synthesis conditions, pyrolysis temperature, activation procedure, and the presence of selected dopants.^{19,20}

Tamon et al. demonstrated the controlling of the mesoporous structure of aerogels by adjusting the molar ratio of resorcinol to Na₂CO₃ used as the catalyst (R/C) and the ratio of resorcinol to distilled water used as the diluent (R/W) in the polycondensation process.²¹ Mesopore volume can be controlled by adjusting the carbonization temperature. K. Kraiwattanawong et al. found that the solvent exchange prior to drying of hydrogels can reduce the pore shrinkage caused by capillary forces and enhance mesoporosity of carbon xerogels.²²

Marie et al. have investigated many carbon aerogels for cathode electrodes and demonstrated that the texture of the carbon support of the cathode has a significant impact on the performance of the resulting MEA, especially the gas diffusion rate can be improved by more than a factor of 2.²³ Job et al. reported that carbon xerogels which are very simple to prepare, could replace carbon aerogels previously used in the same system without decreasing the performances.²⁴

Recently, some researchers reported the effects of the structure of the carbon support on the performance of the PtRu anode catalyst. It was found that surface area, pore volume and accessibility to PtRu particles highly affects the efficiency of electrocatalyst.^{25–27} However, how the structure of the carbon support affects the formation of PtRu particles and how it affects the CO tolerant of the resulting catalyst is not yet understood.

The aim of this present study is to clarify how the activation degree of the catalyst support affects the performance and CO tolerance of a carbon-gel base PtRu anode catalyst. Single cell analysis was conducted using fuels containing 0–2000 ppm of CO, and the results were compared with a well-known high CO tolerant commercial catalyst.

2. EXPERIMENTAL SECTION

2.1. Resorcinol-Formaldehyde Carbon Gel Preparation. Resorcinol–formaldehyde (RF) solutions were prepared from resorcinol (R), formaldehyde (F), sodium carbonate (C), and distilled water (W). The molar ratios of resorcinol to catalyst (R/C), and resorcinol to formaldehyde (R/F), and the mass to volume ratio of resorcinol to water (R/W) were fixed to 1000 mol/mol, 0.5 mol/mol, and 0.5 g/mL, respectively. The prepared RF solutions were first kept at room temperature until they transformed to gels. Then, the obtained RF hydrogels were aged at 60 °C for 3 days. Solvent was then exchanged by immersing the RF hydrogels in *t*-butanol kept at 60 °C for 3 days, the solvent was replaced every day. Then, the RF

hydrogels were dried at 120 °C for 3 days before being carbonized. Carbonization was conducted in a 100 cm³-STP min⁻¹ (ccm) flow of nitrogen gas. Samples were heated up to 250 °C at a 250 °C/h heating rate, and were kept at this temperature for 2 h. Heating was then continued at a rate of 250 °C/h until the temperature reached 1000 °C, and the temperature was kept constant for 4 h. Activation was carried out in a 20 ccm CO₂ and 100 ccm N₂ flow at 1000 °C. Activation degree (or burn-off ratio) was calculated as followed: Activation degree = weight loss after activation × 100/weight before activation.

RF Carbons were named by their R/C ratio and activation degree, for example, RC1000ac0 denotes that the carbon was prepared at an R/C ratio of 1000 without activation and RC1000ac58 indicates that the carbon was prepared under the same R/C ratio but was activation to a burn-off of 58%.

2.2. Preparation of Pt₂Ru₃ Anode Catalysts. The Pt₂Ru₃ anode catalyst were prepared through a three-step process. In the first step, the preparation of Pt/RC1000ac58, 189.6 mg of Pt(NH₃)₂(NO₃)₂ solution (4.554 wt % Pt, Tanaka Kikinzoku Kogyo) and 283.7 mg of RC1000ac58 283.7 mg in were mixed with 300 mL distilled water in a three-neck flask at room temperature (20 °C) for 1 h, Pt was then reduced by adding 30 mL of ethanol to the mixture and heating the mixture up to 95 °C followed by holding the mixture at this temperature overnight. After that, the catalysts were filtered out and washed with distilled water. Then the catalysts were dried in air at 80 °C for 10 h. In the second step, for example for the preparation of Pt₂Ru₃/RC1000ac58, 303.8 mg of RuCl₃·*n*H₂O (99.9%, Wako) was dissolved in 100 mL distilled water and the obtained solution was mixed with Pt/RC1000ac58 at room temperature for 1 h. Then Ru was reduced by adding 20 mL of methanol to the mixture and heating the mixture up to 70 °C, followed by holding the mixture at this temperature overnight. After that, the obtained catalysts were filtered and washed with distilled water. Then the catalysts were dried in N₂ at 80 °C for 10 h. In the final step, the heat treatment process, the catalysts were reduced in H₂/Ar (5% H₂) at room temperature for 1 h followed by rapid heating in He up to 880 °C within 12 min. The oven was turned off when the temperature reached 880 °C to cool the catalysts immediately. Then, the catalysts were reduced again in H₂/Ar (5% H₂) at 150 °C for 2 h. Pt₂Ru₃/RC1000ac0, Pt₂Ru₃/RC1000ac37 and Pt₂Ru₃/RC1000ac88 were also prepared by the same method. A commercial catalyst Pt₂Ru₃/TKK TEC61E54 (Pt 29.6%, Ru 23.0%, Tanaka Kikinzoku Kogyo) was used as received for comparison.

2.3. Physical Characterization. In order to estimate the PtRu metal crystallite size, XRD patterns of the catalysts were measured using a powder X-ray diffractometer (RIGAKU, RINT 2000). The tube current used for Cu K α radiation was 40 mA and the tube voltage was 40 kV. The angular region of the 2 θ scan was set between 10° and 85°, and the scan rate was 1° min⁻¹. The peak profile of the (2 2 0) reflection of Pt fcc structure was fitted with a Gaussian function. The crystallite sizes were evaluated from the position and width of the optimum Gaussian functions. Catalyst morphology was also investigated by using a Hitachi HD-2000 a scanning transmission electron microscope (STEM) instrument with an electron energy of 200 kV and a beam current of 30 μ A. Transmission electron microscopy (TEM) images were obtained with a JEM-2000FX (JEOL) equipped with LaB₆ filament using an accelerating voltage of 200 kV.

2.4. MEA Preparation and Single Cell Performance Testing. For preparation of the membrane electrode assembly (MEA), carbon paper (P50T) was used as the backing layers of the anode and cathode. Anode catalyst inks were prepared by dispersing PtRu/RC1000 catalysts in 4 drops of distilled water and ethanol with Nafion solution (5 wt % dispersion, Aldrich). Cathode catalyst ink was prepared by dispersing commercial catalyst TEC61E54, 54 wt % PtRu in distilled water and ethanol with Nafion. In both electrodes, the catalysts were painted onto each electrode at a metal loading of 0.5 mg cm^{-2} , followed by a coating of Nafion at density of 0.5 mg cm^{-2} . Finally, the anode and cathode ($22 \times 22 \text{ mm}^2$) were placed onto the two sides of a Nafion NRE-212 membrane (Aldrich) and hot-pressed at $135 \text{ }^\circ\text{C}$ and 10 MPa for 20 min to form the MEA.

The MEA was assembled into a single cell with flow field plates made of graphite and copper end plates attached to a heater (FC05-01SP, ElectroChem, Inc.). The single cell was connected to fuel cell test equipment (Chino Corp.). Pure H_2 (or H_2/CO mixture) and O_2 were supplied at flow rates of 80 mL/min to the anode and cathode, respectively, at ambient pressure. During the measurement, the anode and cathode humidifiers were set at 70 and $68 \text{ }^\circ\text{C}$, respectively, and a single cell was operated at $70 \text{ }^\circ\text{C}$.

2.5. CO Tolerance Experiment. The CO tolerance experiments were performed basically under the same conditions as single cell performance tests. But the current density was fixed at (0.2 A cm^{-2}). Experiments were conducted by first providing pure H_2 for 1 h and then 100 ppm of CO was introduced in the H_2 flow for 2 h. Next, the CO concentration was increased to 500 , 1000 , and 2000 ppm at an interval of 2 h.

3. RESULTS AND DISCUSSION

3.1. Structural Characterization- BET. Table 1 shows the surface area of RF carbon RC1000 with various activation

Table 1. Relation between Activation Degree and Surface Area

RF gel RC 1000	surface area of support (m^2g^{-1})	AVG pore diameter (nm)
Ac 0	633	0.52
Ac 37	1671	0.57
Ac 58	2775	0.79
Ac 88	3429	1.22
Commercial Catalyst	823	

degrees from ac0 to ac88. As the activation degree was increased, the surface area and average pore diameter increased. Carbon RC1000Ac0 has a surface area of $633 \text{ m}^2\text{g}^{-1}$, which is smaller than that of the carbon support of the commercial catalyst ($823 \text{ m}^2\text{g}^{-1}$). With an increase in activation degree from 37 to 88, surface areas increased from 1671 to $3429 \text{ m}^2\text{g}^{-1}$.

3.2. Structural Characterization by XRD. Figure 1 shows the XRD patterns of $\text{Pt}_2\text{Ru}_3/\text{RC1000}$ with various activation degrees from ac0 to ac88 and the Pt_2Ru_3 commercial catalyst. All XRD data were summarized in Table 2. The peaks positioned at 2θ degrees of 39.2 , 42.9 and 67.5° (corresponding d -spacings are 2.30 , 2.11 , and 1.39 \AA , respectively), can be respectively assigned to the (111), (200), (220), and (311) planes of the face-centered cubic (fcc) crystal structure. The

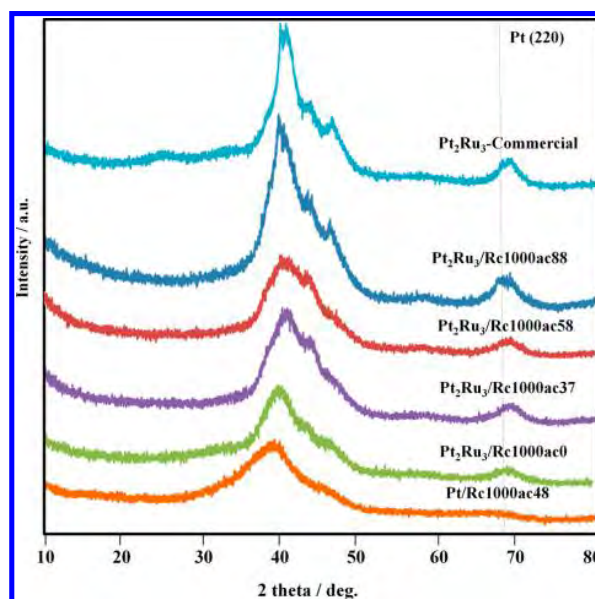


Figure 1. XRD patterns of Pt_2Ru_3 -commercial catalyst and prepared catalysts.

Table 2. XRD Peak Positions for (220) Plane of Pt Metal in the Supported Pt_2Ru_3 and Calculated Metal Crystal Sizes

catalyst	Pt (220) peak position (2θ) (deg)	crystallite size (nm)
Ac 0	68.75	2.48
Ac 37	69.15	2.86
Ac 58	69.47	2.81
Ac 88	69.14	2.94
commercial catalyst	68.83	3.48

crystallite sizes were estimated from the (220) plane using the Scherer's equation because there are no interferences from the carbon background. Pure $50 \text{ wt } \%$ Pt/RC1000ac48 was analyzed as a reference.

All diffractograms show the three peaks. These d -spacings are close to those characteristic of (111), (200), and (220) planes of the face-centered cubic (fcc) crystal structure Pt metal but shifted slightly. Thus, the results indicate all of the samples have a similar degree of alloying of Pt with Ru.

It was found that Pt_2Ru_3 commercial catalyst has the largest PtRu particles (3.48 nm), followed by $\text{Pt}_2\text{Ru}_3/\text{RC1000ac88}$ and $\text{Pt}_2\text{Ru}_3/\text{RC1000ac37}$ (2.94 and 2.86 nm , respectively). The crystallite size of $\text{Pt}_2\text{Ru}_3/\text{RC1000ac58}$ was calculated to be 2.81 nm , and that of $\text{Pt}_2\text{Ru}_3/\text{RC1000ac0}$ was the smallest and was 2.48 nm . In the case of peak position, Pure $50 \text{ wt } \%$ Pt/RC1000ac48 peak of (220) plane at 67.5° .

A larger surface area was expected to result in a smaller PtRu crystallite size but from BET and XRD data, this was not the case. For example, the crystallite size of $\text{Pt}_2\text{Ru}_3/\text{RC1000ac88}$ which has the largest surface area but the crystallite size was 2.86 nm , larger than or almost equal to that of $\text{Pt}_2\text{Ru}_3/\text{RC1000ac58}$ (2.81 nm), which has a much smaller surface area. As another example, the crystallite size of $\text{Pt}_2\text{Ru}_3/\text{RC1000ac0}$ is smaller than that of the commercial catalyst even though it has the smallest surface area. Therefore, the surface area of the support may not be the major factor which governs the crystallite size.

3.3. Structural Characterizations-STEM. In order to understand how PtRu particles are formed on the surface of the catalyst support, STEM technique was used. Figure 2A–F

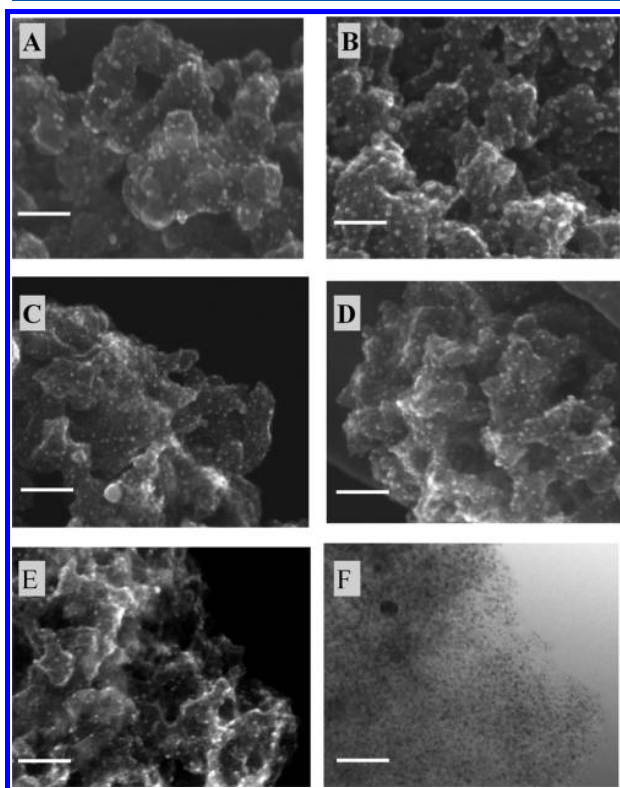


Figure 2. STEM image: (A) commercial $\text{Pt}_2\text{Ru}_3/\text{C}$, (B) $\text{Pt}_2\text{Ru}_3/\text{RC1000ac0}$, (C) $\text{Pt}_2\text{Ru}_3/\text{RC1000ac37}$, (D) $\text{Pt}_2\text{Ru}_3/\text{RC1000ac58}$, (E) $\text{Pt}_2\text{Ru}_3/\text{RC1000ac88}$, and (F) transmission mode of $\text{Pt}_2\text{Ru}_3/\text{RC1000ac88}$. Scale bars = 50 nm.

shows STEM pictures of the Pt_2Ru_3 commercial catalyst, $\text{Pt}_2\text{Ru}_3/\text{RC1000ac0}$, $\text{Pt}_2\text{Ru}_3/\text{RC1000ac37}$, $\text{Pt}_2\text{Ru}_3/\text{RC1000ac58}$, and $\text{Pt}_2\text{Ru}_3/\text{RC1000ac88}$, respectively. Since only the micropore structure is changed by activation except for $\text{Pt}_2\text{Ru}_3/\text{RC1000ac88}$ (Figure 2E,F, 88% activation degree), macro and mesopore structures are essentially identical. The comparison of the Pt_2Ru_3 commercial catalyst and all prepared catalysts clearly shows that the dispersion of metal particles on the surface of prepared catalysts are much better than the commercial one. It should be noted that all catalysts were prepared based on the same metal content of about 53%.

Figure 2B–E shows that the carbon structures of the prepared catalysts were quite the same because all catalysts were prepared from the same RC1000 carbon through the same preparation process. It was observed that the PtRu particle size of $\text{Pt}_2\text{Ru}_3/\text{RC1000ac0}$ was much larger than other catalysts (different from PXRD results).

Unfortunately, in Figure 2F (bright field mode), the existence of agglomerated particles can be confirmed. Many pictures of $\text{Pt}_2\text{Ru}_3/\text{RC1000ac88}$ showed agglomerated particles located inside the carbon but not on its surface. It is possible that sintering occurred as the micropores within the carbon are interconnected. Activation degree increases surface area via introduction of additional micropores but it was confirmed by STEM that the basic structure of RF carbons was not changed significantly.

3.4. Structural Characterizations by TEM. Figure 3 shows the TEM pictures of the prepared catalysts and the commercial catalyst. Particle size distribution obtained from TEM pictures are also shown. The distributions focus on the range of 1–6 nm, as particles must have sizes in the range about 3–5 nm to show high catalytic activities.¹⁶ About 200 particles per catalyst were measured to obtain these distributions. In Figure 3A, TEM picture of the commercial catalyst; large metal particles with sizes around 9 nm can be found. The sizes of the metal particles were not uniform, ranging from 2 to 12 nm. Figure 3B, the TEM picture of $\text{Pt}_2\text{Ru}_3/\text{RC1000ac0}$, a catalyst with a lower surface area than commercial catalyst, shows that the PtRu particles are not uniform but the sized are a little bit smaller, in the range of 1–10 nm. Figure 3C reveals that the sizes of metal particles in $\text{Pt}_2\text{Ru}_3/\text{RC1000ac37}$ are much smaller (1–5 nm) and are quite uniform, Figure 3D, shows that $\text{Pt}_2\text{Ru}_3/\text{RC1000ac58}$ has the most uniform sized particles in the range of 1–4 nm. As shown in Figure 3E, although $\text{Pt}_2\text{Ru}_3/\text{RC1000ac88}$ has the largest surface area, the size of its PtRu particles is not as uniform as those of $\text{Pt}_2\text{Ru}_3/\text{RC1000ac58}$. It was found that the size of the metal particles size between 1 and 8 nm and a large particle (30 nm) was also found. This is consistent with Figure 2F.

These results clearly show that all the prepared catalysts have a narrower PtRu particle size distribution than the commercial catalyst, even RC1000ac0, which surface area is less than that of the commercial catalyst. This strongly suggests that the structure of the carbon support plays a major role in Pt–Ru particle formation, not only its surface area. TEM pictures also show the effect of activation degree. The Pt–Ru particle size distribution basically becomes narrower with the increase in activation degree (from Ac0 to Ac58), but when the degree becomes too large (Ac88), large particles appear, probably due to the sintering through the developed micropore network of the highly activated carbon support.

3.5. Performance and CO Tolerance Examination via Single Cell Analysis. Figure 4 shows the current density–voltage curves and power density curves of electrodes constructed using the catalysts. The metal content in all of the anode electrodes were 0.5 g cm^{-2} . Figure 4 (a), the power density curve of $\text{Pt}_2\text{Ru}_3/\text{RC1000 ac37}$ shows a maximum power density of 0.73 W cm^{-2} , which value is higher than those of $\text{Pt}_2\text{Ru}_3/\text{RC1000ac58}$ and Pt_2Ru_3 commercial catalyst, which are quite similar and at 0.66 and 0.67 W cm^{-2} , respectively. However, the current density of the commercial catalyst at 0.6 V potential is 0.9 A cm^{-2} , lower than those of $\text{Pt}_2\text{Ru}_3/\text{RC1000 ac58}$ and $\text{Pt}_2\text{Ru}_3/\text{RC1000 ac37}$ which are 1.0 and 1.1 A cm^{-2} , respectively. If we consider the three potential loss region, all catalysts except $\text{Pt}_2\text{Ru}_3/\text{RC1000 ac0}$ show high activation polarization (reaction rate loss are low) in the first region. In the second region, the region of ohmic polarization (resistance loss), catalyst synthesis using a higher activation degree carbon, such as $\text{Pt}_2\text{Ru}_3/\text{RC1000 ac58}$ and $\text{Pt}_2\text{Ru}_3/\text{RC1000 ac88}$ lose more potential due to their larger surface areas. In the final region, the region of concentration polarization (gas transport loss), not only are catalysts synthesized using higher activation degree carbons, such as $\text{Pt}_2\text{Ru}_3/\text{RC1000ac88}$, but also those synthesized using lower activation degree carbon such as $\text{Pt}_2\text{Ru}_3/\text{RC1000 ac0}$ show a sharp drop of potential, indicating that optimizing the activation degree of the carbon support may also lead to gas transportation enhancement. However, Figure 4(a) showed that $\text{Pt}_2\text{Ru}_3/\text{RC1000 ac37}$ exhibits a better performance than that exhibited by the Pt_2Ru_3 commercial

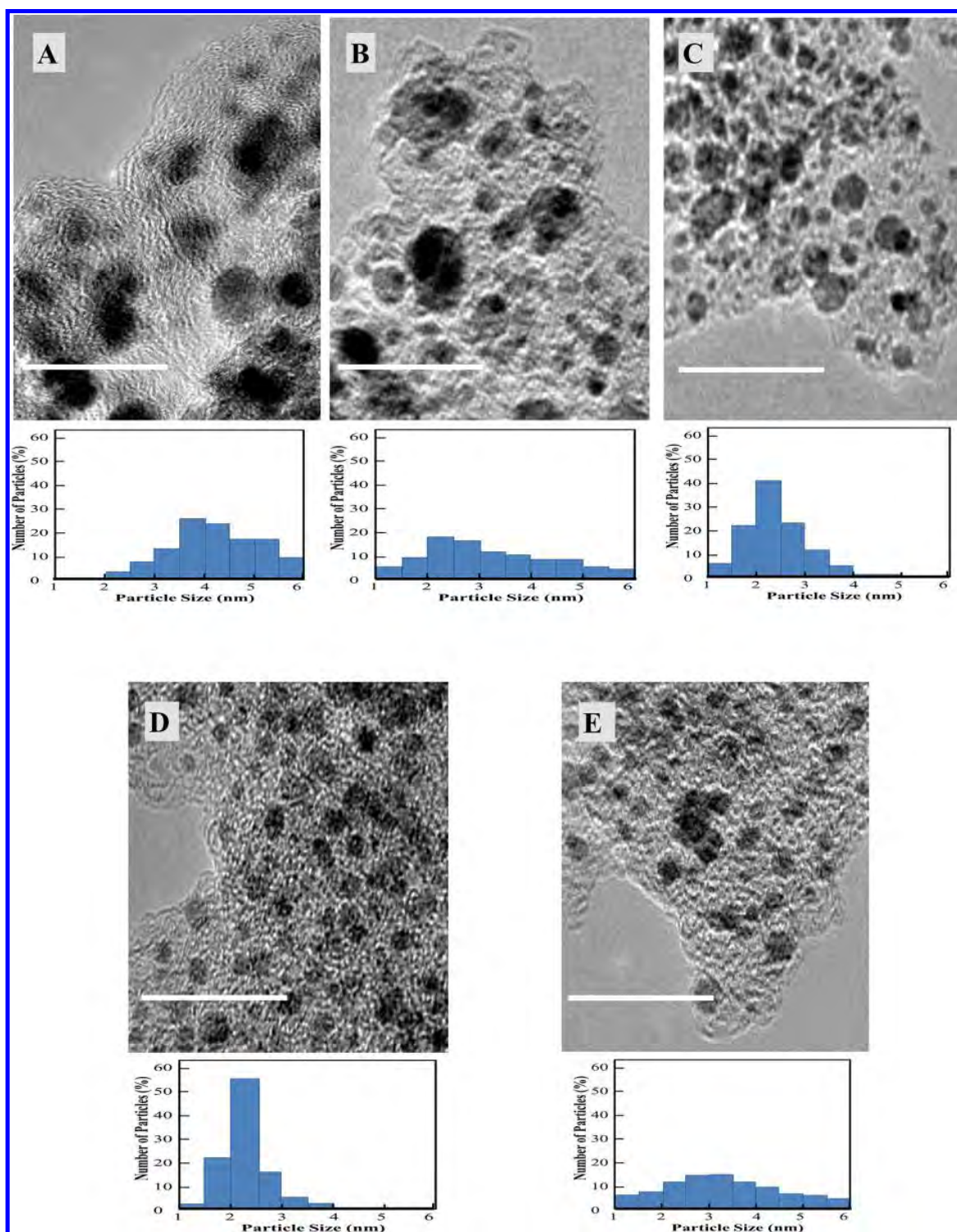


Figure 3. TEM micrograph: (A) Pt₂Ru₃/C commercial catalyst, (B) Pt₂Ru₃/RC1000ac0, (C) Pt₂Ru₃/RC1000ac37, (D) Pt₂Ru₃/RC1000ac58, and (E) Pt₂Ru₃/RC1000ac88. Scale bars = 20 nm.

PtRu/C catalyst in a unit cell test. Figure 4(b), an enlarged portion of Figure 4(a) reveal that the order of the catalyst are Pt₂Ru₃/RC1000 ac58 > Pt₂Ru₃/RC1000 ac37 > Pt₂Ru₃/RC1000 ac88 > Pt₂Ru₃ commercial catalyst > Pt₂Ru₃/RC1000 ac0. Better catalytic activity indicates the possibly of

the enhancement of CO oxidation reaction, resulting in the enhancement of CO removal process.

Therefore, we checked the CO tolerance of the catalysts Figure 5(a) shows the relation between cell efficiency and CO contamination. At the beginning, pure H₂ was fed to the anode side, and it was found that Pt₂Ru₃/RC1000 ac58 showed the

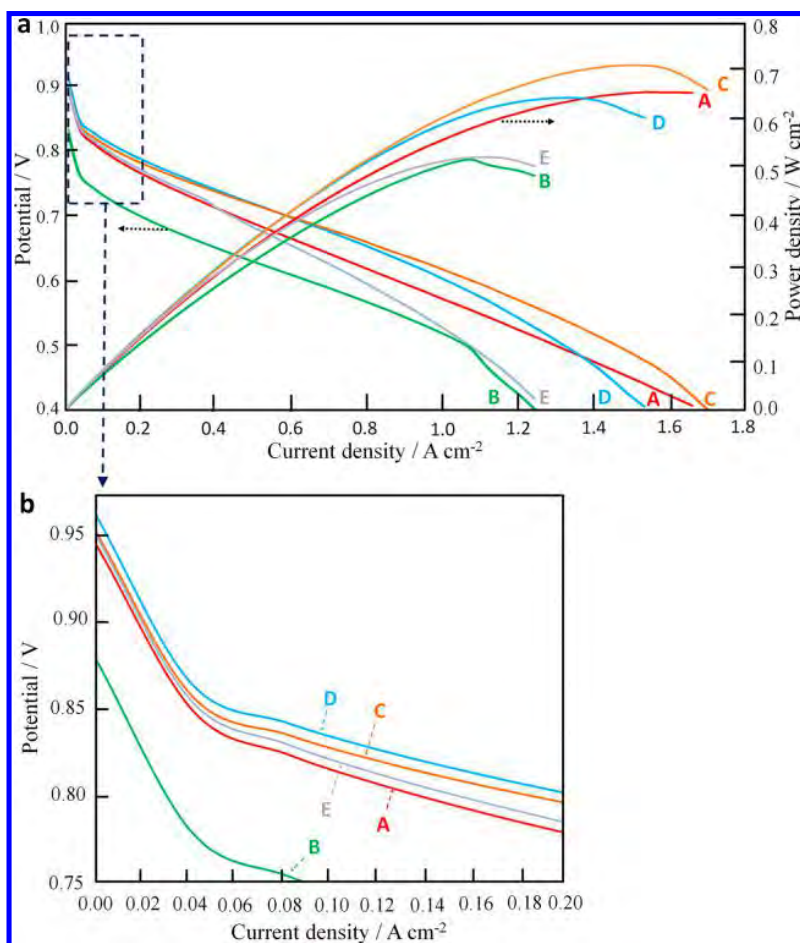


Figure 4. Comparison of unit cell performance. Current–voltage curves of electrodes and power density curves of electrodes with prepared and commercial catalysts as respective anode electrocatalyst. (a) Full range, (b) zoom at activity loss range: (A) Pt₂Ru₃/C commercial catalyst, (B) Pt₂Ru₃/RC1000ac0, (C) Pt₂Ru₃/RC1000ac37, (D) Pt₂Ru₃/RC1000ac58, and (E) Pt₂Ru₃/RC1000ac88.

highest cell voltage of 0.787 V after the current density was fixed to 0.2 A cm⁻² for 1 h, followed by 0.767 V of Pt₂Ru₃/RC1000 ac37. Pt₂Ru₃/RC1000 ac88 and the Pt₂Ru₃ commercial catalyst showed cell voltages of 0.755 and 0.748 V, respectively. Pt₂Ru₃/RC1000 ac0 showed a cell voltage of 0.745 V for a few seconds but the voltage suddenly dropped to 0.667 V. Then, 100 ppm of CO was mixed with the H₂ and fed to the anode side of the cells. Pt₂Ru₃/RC1000 ac58 still showed the highest performance, although the cell voltage slightly decreased to 0.758 V after the current density was fixed at 0.2 A cm⁻². The cell voltage of Pt₂Ru₃/RC1000 ac37 decreased to 0.736 V, and that of Pt₂Ru₃/RC1000 ac88 to 0.722 V. The Pt₂Ru₃ commercial catalyst showed a cell voltage of 0.719 V. That of Pt₂Ru₃/RC1000 ac0 was 0.635 V, indicating that this catalyst still shows the lowest efficiency.

The critical level of CO contamination is 500 ppm, which is thought to be the actual possible CO concentration in H₂ from refineries and also from CO shift converters in residential gas systems. All of the reported catalysts including the Pt₂Ru₃ commercial catalyst, which is well-known as the best CO tolerant catalyst, cannot tolerate this level. After 2 h at a fixed current density of 0.2 A cm⁻², the cell voltage of the Pt₂Ru₃ commercial catalyst dropped to 0.567 V, which indicates a 24.2% efficiency decrease. Surprisingly, all prepared catalysts, including Pt₂Ru₃/RC1000ac0 showed higher performances at

this CO level. Pt₂Ru₃/RC1000ac58 still showed the highest cell voltage of at 0.72 V, which dropped by only 8.5% from when compared with the voltage of starting period. Cell voltage of Pt₂Ru₃/RC1000 ac37, ac88 and ac0 were 0.704, 0.669, and 0.593 V, respectively.

CO tolerance analysis at 2000 ppm confirmed that all of the prepared catalysts show a better CO tolerance than the commercial catalyst. The catalyst showing the highest performance and the order among the catalysts did not change. Pt₂Ru₃/RC1000ac58 showed a cell voltage of 0.655 V (0.132 V or only 16.8% overvoltage). The cell voltages of Pt₂Ru₃/RC1000ac37, Pt₂Ru₃/RC1000ac88 and Pt₂Ru₃/RC1000ac0 were 0.556, 0.583, and 0.514 V, respectively. However, the Pt₂Ru₃ commercial catalyst generated only 0.394 V, 0.354 V or 47.3% overvoltage.

The commercial catalyst is well-known for its high CO tolerance, but this investigation reveals that Pt₂Ru₃/RC1000 ac37, 58, and 88 anode catalysts show higher performance than the Pt₂Ru₃ commercial catalyst in the CO concentration range from 500 to 2000 ppm. Even PtRu/RC1000 ac0, the catalyst showing the lowest performance, showed a higher efficiency than the commercial catalyst. Especially the over potential of Pt₂Ru₃/RC1000ac58 at 2000 ppm of CO contamination was 0.132 V (16.8%) which is much lower than that of the commercial catalyst (0.354 V 47.3%). The activation degree of

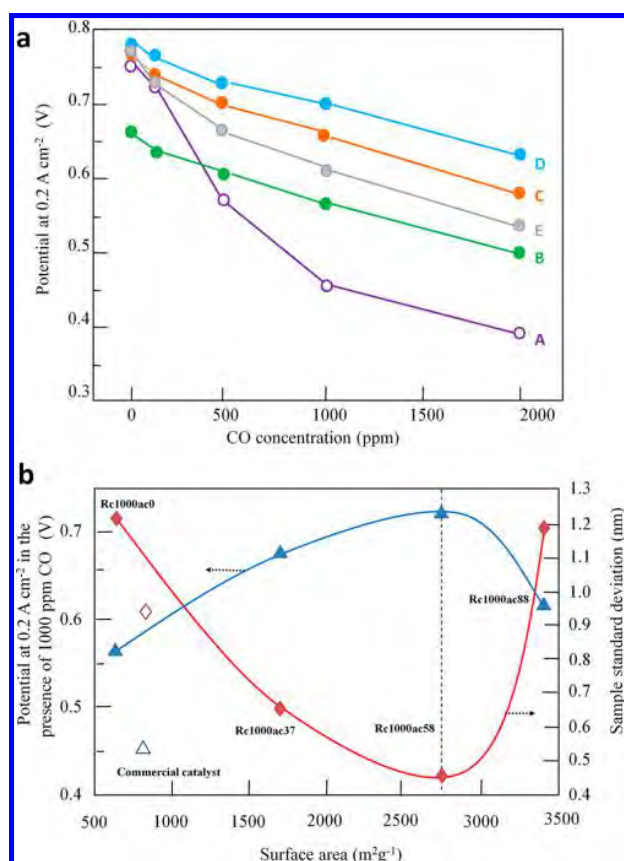


Figure 5. (a) Effect of CO concentration on potential at 0.2 A cm⁻². Cell temp.: 70 °C; Electrolyte: Nafion NRE 212; Cathode: Pt/C (0.5 mg cm⁻²); O₂ humidified at 68 °C; Flow rate: 80 mL min⁻¹; Anode: Pt₂Ru₃/C (0.5 mg-PtRu cm⁻²); H₂ containing 0, 100, 500, and 2000 ppm of CO humidified at 70 °C; Flow rate: 80 mL min⁻¹: (A) Pt₂Ru₃/C commercial catalyst, (B) Pt₂Ru₃/RC1000ac0, (C) Pt₂Ru₃/RC1000ac37, (D) Pt₂Ru₃/RC1000ac58, and (E) Pt₂Ru₃/RC1000ac88. (b) Comparison of surface area (m² g⁻¹) and potential at 0.2 A cm⁻² in the presence of CO 1000 ppm (V) contamination by single cell performance. The second axis present sample standard deviation (SSD) of PtRu particle dispersion which observed by TEM.

the support highly affects the CO tolerance of the resulting catalyst. Figure 5 (b) shows the relation between the potential at 0.2 A cm⁻² in the presence of 1000 ppm of CO and the surface area of the catalyst support, it can be seen that an optimum surface area which the highest potential exists. Moreover, the standard deviation of PtRu particle size observed by TEM confirmed the higher uniformity of particle size. Adjusting the activation degree of the catalyst support is thought to have led to the optimization of micropore structure, resulting in the uniform dispersion of catalyst particles.

4. CONCLUSIONS

Resorcinol–formaldehyde carbon gels with various volumes of micropores were prepared by changing the degree of CO₂ activation from 0 to 88%. Pt and Ru nanoparticles were dispersed on these carbons by a rapid quenching method. The crystallite sizes of the PtRu particles within the prepared catalysts were smaller than those in a typical commercial catalyst. STEM pictures show that increasing the degree of activation, leads to a better distribution of PtRu particles on the surface of carbon. TEM pictures also showed the same trend

that a higher degree of activation, leads to smaller PtRu particles, but when the degree becomes too large (Pt₂Ru₃/RC1000ac88), large particle tend to be formed inside the carbon. Micropores play an important role to stabilized PtRu particles on the support surface but too high volume of micropore increase the electrical resistance of the cell. Finally, single cell experiments were performed. With pure H₂, the cell voltage of all anode catalysts at a constant current of 0.2 A cm⁻² was in the range of 0.759–0.795 V, except that of Pt₂Ru₃/RC1000ac0 (0.66 V). After CO was introduced to H₂ from 100 to 2000 ppm, the decrease in the cell voltage of the prepared showed was much smaller than that commercial catalyst showed. When the contamination level reached 500 ppm even Pt₂Ru₃/RC1000ac0 generated a higher potential than the commercial catalyst. Pt₂Ru₃/RC1000ac58, which is thought to be prepared with the carbon support having the optimum degree of activation, showed the best performance due to its proper carbon micropore structure which allows the uniform dispersion of PtRu particles. From this study, it was shown that adjusting the degree of activation of the carbon support leads to the efficient loading of PtRu particles, both in terms of particle size and distribution resulting in a higher performance and higher CO tolerance.

AUTHOR INFORMATION

Corresponding Author

*Phone: +81-19-621-6335; fax: +81-19-621-6335; e-mail: takeguch@iwate-u.ac.jp.

Notes

The authors declare no competing financial interest.

ACKNOWLEDGMENTS

This work was partly supported by the New Energy and Industrial Technology Development Organization (NEDO) Japan.

REFERENCES

- Rabis, A.; Rodriguez, P.; Schmidt, T. Electrocatalysis for Polymer Electrolyte Fuel Cells: Recent Achievements and Future Challenges. *ACS Catal.* **2012**, *2*, 864–890.
- Rena, H.; Gaoa, W.; Ruanb, Y. Optimal Sizing for Residential CHP System. *Appl. Therm. Eng.* **2008**, *28*, 514–523.
- IPHE: International Partnership for Hydrogen and Fuel Cells in the Economy; Statement from Panasonic on Residential fuel cell m-CHP; [http://www.iphe.net/docs/Meetings/Germany_11-11/presentations/\(4\)%20Kani%20Panasonic-Presentation-02112011-IPHE.pdf](http://www.iphe.net/docs/Meetings/Germany_11-11/presentations/(4)%20Kani%20Panasonic-Presentation-02112011-IPHE.pdf).
- Aliabadi, A.; Thomson, M.; Wallace, J. Efficiency Analysis of Natural Gas Residential Micro-cogeneration Systems. *Energy Fuels.* **2010**, *24*, 1704–1710.
- Bendaikhaa, W.; Larbib, S.; Mahma, B. Hydrogen Energy System Analysis for Residential Applications in the Southern Region of Algeria. *Int. J. Hydrogen Energy* **2011**, *36*, 8159–8166.
- Schmersahl, R.; Mumme, J.; Scholz, V. Farm-Based Biogas Production, Processing, and Use in Polymer Electrolyte Membrane (PEM) Fuel Cells. *Ind. Eng. Chem. Res.* **2007**, *46*, 8946–8950.
- Igarashi, H.; Fujino, T.; Watanabe, M. Hydrogen Electro-oxidation on Platinum Catalysts in the Presence of Trace Carbon Monoxide. *J. Electroanal. Chem.* **1995**, *391*, 119–123.
- Wakisaka, M.; Mitsui, S.; Hirose, Y.; Kawashima, K.; Uchida, H.; Watanabe, M. Electronic Structures of Pt–Co and Pt–Ru Alloys for CO-Tolerant Anode Catalysts in Polymer Electrolyte Fuel Cells Studied by EC–XPS. *J. Phys. Chem. B* **2006**, *110*, 23489–23496.

- (9) Dhar, H.; Christner, L.; Kush, A. Nature of CO Adsorption during H₂ Oxidation in Relation to Modeling for CO Poisoning of a Fuel Cell Anode. *J. Electrochem. Soc.* **1987**, *134*, 3021–3026.
- (10) Scott, F.; Mukerjee, S.; Ramaker, D. Contrast in Metal–Ligand Effects on Pt_nM Electro catalysts with M Equal Ru vs Mo and Sn As Exhibited by in Situ XANES and EXAFS Measurements in Methanol. *J. Phys. Chem. C* **2010**, *114*, 442–453.
- (11) Leng, Y.; Wang, X.; Hsing, I. Assessment of CO-Tolerance for Different Pt-Alloy Anode Catalysts in a Polymer Electrolyte Fuel Cell Using AC Impedance Spectroscopy. *J. Electroanal. Chem.* **2002**, *528*, 145–152.
- (12) Xu, L.; Wu, Z.; Zhang, Y.; Chen, B.; Jiang, Z.; Ma, Y.; Huang, W. Hydroxyls-Involved Interfacial CO Oxidation Catalyzed by FeOx(111) Monolayer Islands Supported on Pt(111) and the Unique Role of Oxygen Vacancy. *J. Phys. Chem. C* **2011**, *115*, 14290–14299.
- (13) Yano, H.; Ono, C.; Shiroishi, H.; Saito, M.; Uchimoto, Y.; Okada, T. High CO Tolerance of *N,N*-Ethylenebis-(salicylideneaminato)oxovanadium(IV) as a Cocatalyst to Pt for the Anode of Reformate Fuel Cells. *Chem. Mater.* **2006**, *18*, 4505–4512.
- (14) Takeguchi, T.; Yamanaka, T.; Asakura, K.; Muhamad, E. N.; Uosaki, K.; Ueda, W. Evidence of Nonelectrochemical Shift Reaction on a CO-Tolerant High-Entropy State Pt–Ru Anode Catalyst for Reliable and Efficient Residential Fuel Cell Systems. *J. Am. Chem. Soc.* **2012**, *134*, 14508–14512.
- (15) Yamanaka, T.; Takeguchi, T.; Wang, G.; Muhamad, E. N.; Ueda, W. Particle Size Dependence of CO Tolerance of Anode PtRu Catalysts for Polymer Electrolyte Fuel Cells. *J. Power Sources* **2010**, *195*, 6398–6404.
- (16) Wang, G.; Takeguchi, T.; Muhamad, E. N.; Yamanaka, T.; Ueda, W. Investigation of Grain Boundary Formation in PtRu/C Catalyst Obtained in a Polyol Process with Post-Treatment. *Int. J. Hydrogen Energy* **2011**, *36*, 3322–3332.
- (17) Matsui, T.; Okanishi, T.; Fujiwara, K.; Tsutsui, K.; Kikuchi, R.; Takeguchi, T.; Eguchi, K. Effect of Reduction–Oxidation Treatment on the Catalytic Activity over Tin Oxide Supported Platinum Catalysts. *Sci. Technol. Adv. Mater.* **2006**, *7*, 524–530.
- (18) Wang, Q.; Wang, G.; Sasaki, K.; Takeguchi, T.; Yamanaka, T.; Sadakane, M.; Ueda, W. Structure and Electrochemical Activity of WO_x-Supported PtRu Catalyst Using Three-Dimensionally Ordered Macroporous WO₃ as the Template. *J. Power Sources* **2013**, *241*, 728–735.
- (19) Pekala, R. Organic Aerogels from the Polycondensation of Resorcinol with Formaldehyde. *J. Mater. Sci.* **1989**, *24*, 3221–3227.
- (20) Pekala, R.; Farmer, J.; Alviso, C.; Tran, T.; Mayer, S.; Miller, J.; Dunn, B. Carbon Aerogels for Electrochemical Applications. *J. Non-Cryst. Solids* **1998**, *225*, 74–80.
- (21) Tamon, H.; Ishizaka, H.; Araki, T.; Okazaki, M. Control of Mesoporous Structure of Organic and Carbon Aerogels. *Carbon* **1998**, *36*, 1257–1262.
- (22) Kraiwattanawong, K.; Tamon, H.; Praserttham, P. Influence of Solvent Species Used in Solvent Exchange for Preparation of Mesoporous Carbon Xerogels from Resorcinol and Formaldehyde via Subcritical Drying. *Microporous Mesoporous Mater.* **2011**, *138*, 8–16.
- (23) Marie, J.; Berthon-Fabry, S.; Achard, P.; Chatenet, M.; Pradourat, A.; Chainet, E. Highly Dispersed Platinum on Carbon Aerogels as Supported Catalysts for PEM Fuel Cell-Electrodes: Comparison of Two Different Synthesis Paths. *J. Non-Cryst. Solids* **2004**, *350*, 88–96.
- (24) Job, N.; Marie, J.; Lambert, S.; Berthon-Fabry, S.; Achard, P. Carbon Xerogels as Catalyst Supports for PEM Fuel Cell Cathode. *Energy Convers. Manage.* **2008**, *49*, 2461–2470.
- (25) Chai, G.; Yoon, S.; Yu, J.; Choi, J.; Sung, Y. Ordered Porous Carbons with Tunable Pore Sizes as Catalyst Supports in Direct Methanol Fuel Cell. *J. Phys. Chem. B* **2004**, *108*, 7074–7079.
- (26) Lin, M.; Huang, C.; Lo, M.; Mou, C. Well-Ordered Mesoporous Carbon Thin Film with Perpendicular Channels: Application to Direct Methanol Fuel Cell. *J. Phys. Chem. C* **2008**, *112*, 867–873.
- (27) Wang, Z.; Zhao, C.; Shi, P.; Yang, Y.; Yu, Z.; Wang, W.; Yin, G. Effect of a Carbon Support Containing Large Mesopores on the Performance of a Pt–Ru–Ni/C Catalyst for Direct Methanol Fuel Cells. *J. Phys. Chem. C* **2010**, *114*, 672–677.

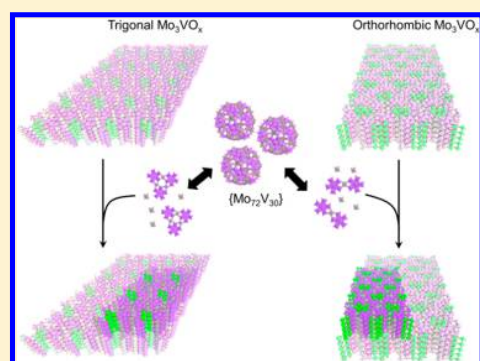
Seed-Assisted Synthesis of Crystalline Mo_3VO_x Oxides and Their Crystal Formation Mechanism

Satoshi Ishikawa,* Masaya Tashiro, Toru Murayama, and Wataru Ueda*

Catalysis Research Center, Hokkaido University, N-21, W-10, Sapporo, 001-0021, Japan

Supporting Information

ABSTRACT: The effects of the addition of crystalline Mo_3VO_x oxides (MoVO) seeds on an assembly of pentagonal $[\text{Mo}_6\text{O}_{21}]^{6-}$ building units with Mo and V octahedra for forming MoVO were investigated. In the absence of the seeds, the crystal phase of formed MoVO depended on the pH of the preparative solution, while the crystal phase of the formed MoVO was decided by the phase of the MoVO seeds used irrespective of the pH. Interestingly, MoVO were formed even in the pH condition where no crystals were formed in the absence of the seeds. It was shown by X-ray diffraction, scanning transmission electron microscopy–energy-dispersive X-ray spectroscopy, and scanning electron microscopy that MoVO crystals were grown from the cross-section of the rod-shaped crystals of the MoVO seeds.



1. INTRODUCTION

Orthorhombic Mo_3VO_x oxide (Orth-MoVO) and trigonal Mo_3VO_x oxide (Tri-MoVO) are well-known as effective catalysts for the selective oxidation of ethane,^{1–4} propane,^{5–7} and acrolein.^{4,8,9} These oxides have specific structures in their a – a or a – b plane. These planes are constructed with pentagonal $[\text{Mo}_6\text{O}_{21}]^{6-}$ units (shown by purple color in Figure 1a,b) and $\{\text{Mo}_6\}$ ($M = \text{Mo}, \text{V}$) octahedra to form micropore channels, hexagonal channel and heptagonal channel. We have reported that the heptagonal channel provides an effective catalysis field for the selective oxidation of ethane.^{3,4}

Orth-MoVO and Tri-MoVO are formed by the hydrothermal method. The formations of these phases are dependent on the pH condition of the preparative solution. When the pH value of precursor solution is over 3.6, no solids are formed. When the pH of precursor solution is in the range of 3.4–2.7 (no pH control: pH = 3.2), Orth-MoVO is formed. Tri-MoVO is formed by decreasing the pH of precursor solution to 2.2. The pH value is lower than 1.7, and $\text{Mo}_{0.87}\text{V}_{0.13}\text{O}_{2.94}$ (JCPDF: 00-048-0766) is formed.¹⁰ We have proposed the formation schemes of Orth-MoVO and Tri-MoVO under hydrothermal conditions.^{10,11} The proposed structure formation schemes are shown in Figure 1. Ball-type polyoxometalate, $[\text{Mo}_{72}\text{V}_{30}\text{O}_{282}(\text{H}_2\text{O})_{56}(\text{SO}_4)_{12}]^{36-}$ ($\{\text{Mo}_{72}\text{V}_{30}\}$), in which 12 pentagonal $[\text{Mo}_6\text{O}_{21}]^{6-}$ polyoxomolybdate units connected with 30 $[\text{V}=\text{O}]^{2+}$ units, is first generated in preparative solution.^{12,13} Since the pentagonal $[\text{Mo}_6\text{O}_{21}]^{6-}$ unit in ball-shaped polyoxomolybdates is kinetically stable, $\{\text{Mo}_{72}\text{V}_{30}\}$ can steadily provide the pentagonal $[\text{Mo}_6\text{O}_{21}]^{6-}$ unit.^{10,11,14} The pentagonal $[\text{Mo}_6\text{O}_{21}]^{6-}$ unit and other Mo and V octahedral form building units and Orth-MoVO or Tri-MoVO are formed by an assembly of the building units.

For forming Orth-MoVO, two pentagonal units connected with a V octahedral are the building unit. In the case of Tri-MoVO, a more condensed pentagonal polyoxometalate unit comprised of three pentagonal units and three V octahedra is the building unit. Voids produced by an arrangement of the building units are filled with clusters comprised of the octahedra, resulting in the formation of the hexagonal and the heptagonal channels. The clusters are a pentamer in Orth-MoVO and a trimer in Tri-MoVO.¹⁵

Seed-assisted syntheses of high dimensional structure such as zeolites, metal–organic frameworks (MOFs) and polyoxometalate based frameworks (POFs) are widely applied.^{16–28} In zeolite, Okubo et al. have recently reported a working hypothesis for the seed-assisted synthesis on zeolite.^{19,20} They suggested that composited building units which are contained both in the seed zeolite and the obtained zeolite from a reactant gel without seeds are the key factor in the seed-assisted synthesis. The composited building units in the gel are stacked on the surface of the seed crystals, and zeolites having the same crystal phase with the seed are formed. This zeolites synthesis method has attracted much attention because of the structure directing ability derived from a change of the condensation condition of the composited building units.²⁰ As described above, Orth-MoVO and Tri-MoVO have been proposed to be formed by the building block assembly of the pentagonal $[\text{Mo}_6\text{O}_{21}]^{6-}$ units with Mo and V octahedra. The assembly of the building units may be controllable by using Orth-MoVO or Tri-MoVO as a seed because Orth-MoVO, Tri-MoVO, and $\{\text{Mo}_{72}\text{V}_{30}\}$ contain the same structural parts. Control of the

Received: May 6, 2014

Revised: June 20, 2014

Published: August 4, 2014

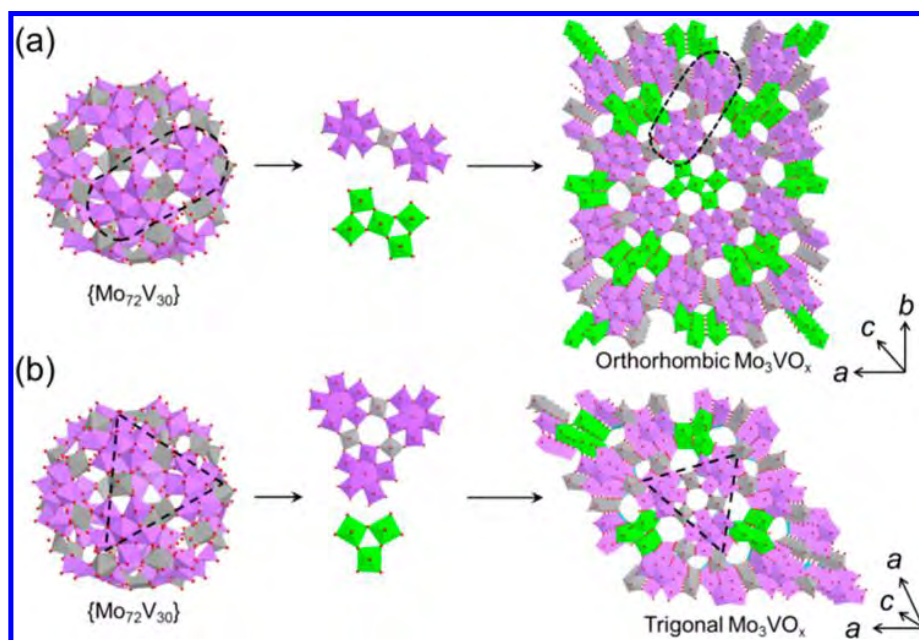


Figure 1. Proposed schemes of structure formation of (a) orthorhombic Mo_3VO_x oxide and (b) trigonal Mo_3VO_x oxide. Purple, Mo; gray, V; green, mixture of Mo and V.

building units assembly have a lot of possibilities for the material synthesis and may enable us to synthesize new materials or provide new insights for synthesizing MoVO. This paper investigated the roles of MoVO seeds on the building block assembly for forming MoVO and showed benefits in the seed-assisted synthesis of MoVO.

2. EXPERIMENTAL SECTION

Synthesis of Orthorhombic Mo_3VO_x Oxide. Orth-MoVO was synthesized by a hydrothermal method. A total of 8.83 g of $(\text{NH}_4)_6\text{Mo}_7\text{O}_{24}\cdot 4\text{H}_2\text{O}$ (Mo: 50 mmol, Wako) was dissolved in 120 mL of distilled water. Separately, an aqueous solution of VOSO_4 was prepared by dissolving 3.29 g of hydrated VOSO_4 (V: 12.5 mmol, Mitsui Chemicals) in 120 mL of distilled water. The two solutions were mixed at ambient temperature and stirred for 10 min. Then, the obtained mixed solution was introduced into an autoclave with a 300 mL Teflon inner vessel and 4000 cm^2 of a Teflon thin sheet to occupy about half of the Teflon inner vessel space. This sheet is necessary to obtain a well-crystallized sample. After the introduction, N_2 was fed into the solution in the tube in order to remove residual oxygen. At this stage, the pH of the solution was 3.2. Then the hydrothermal reaction was started at 175 $^\circ\text{C}$ for x h ($x = 20, 48$) under static conditions in an electric oven. Gray solids formed on the Teflon sheet were separated by filtration, washed with distilled water, and dried in air at 80 $^\circ\text{C}$ overnight. If needed, purification with oxalic acid was conducted on the obtained solids in order to remove an impurity formed with Orth-MoVO. To 25 mL aqueous solution (0.4 mol L^{-1} , 60 $^\circ\text{C}$) of oxalic acid (Wako), 1 g of the dried material was added and stirred for 30 min and then washed with 500 mL of distilled water after filtration. The samples purified with oxalic acid were described as “oxa” in the bottom of the sample name. The obtained solid was denoted as Orth- x -(oxa), where x represents the synthesis time.

Synthesis of Trigonal Mo_3VO_x Oxide. Almost the same synthetic procedure as that for the Orth-MoVO was applied to the synthesis of Tri-MoVO except for the pH condition. The pH value of the mixed solution was adjusted to 2.2 by adding H_2SO_4 (2 mol L^{-1}). If needed, purification with oxalic acid was conducted on the obtained solids. The obtained solid was denoted as Tri-20-(oxa).

Synthesis of Amorphous Mo_3VO_x Oxide. As described in our previous paper,¹ Mo_3VO_x material was well-crystallized in the c -

direction but disorder in the other direction was obtained when the concentration of the mixed aqueous solution was twice as high. The other preparative conditions were the same as those for the orthorhombic Mo_3VO_x . Hydrothermal reaction was performed for 48 h at 175 $^\circ\text{C}$. Here in this paper this material is abbreviated as Amor.

Synthesis of Tetragonal Mo_3VO_x Oxide. Tetragonal Mo_3VO_x (Tet-MoVO) was synthesized by phase transformation from Orth-48-oxa by heat treatment as follows. The dried Orth-48-oxa was heated in air at a heating ramp of 10 $^\circ\text{C min}^{-1}$ to 400 $^\circ\text{C}$, kept at this temperature for 2 h, and then cooled to ambient temperature. This heat-treated sample was again heated in a nitrogen stream (50 mL min^{-1}) at a heating ramp of 10 $^\circ\text{C min}^{-1}$ to 575 $^\circ\text{C}$ and kept at this temperature for 2 h. Obtained solid was abbreviated as Tet.

Seed-Assisted Synthesis of Mo_3VO_x Oxides. In the seed-assisted synthesis, Orth-48-oxa, Tri-20-oxa, Amor, and Tet were used as seeds. y g of the seed ($y = 0.05, 0.10, 0.30, 0.60, \text{ and } 1.00$) after being ground for 5 min by an agate mortar was added into the precursor solution prepared in the same manner as synthesizing Orth-MoVO. pH of the precursor solution was controlled to z ($z = 1.0\text{--}4.0$) by using H_2SO_4 (2 mol L^{-1}) or 10% NH_3 solution before introducing into the Teflon inner vessel. After N_2 bubbling for 10 min, a hydrothermal reaction was conducted for x h ($x = 2\text{--}96$). Obtained materials were filtrated, washed with distilled water, and then dried in air at 80 $^\circ\text{C}$ overnight. In this case, no purification was conducted. Obtained materials were abbreviated as (Orth, Tri, Amor, Tet) (s)- x - y - z (x , synthesis time; y , the amount of the seed; z , pH of the precursor solution).

Characterization of Synthesized Materials. The synthesized materials were characterized by the following techniques. Powder X-ray diffraction (XRD) patterns were recorded with a diffractometer (RINT Ultima+, Rigaku) using $\text{Cu-K}\alpha$ radiation (tube voltage: 40 kV, tube current: 20 mA). For XRD measurements, prepared samples were ground for 5 min and were put on a horizontal sample holder. Diffractions were recorded in the range of 4–60 $^\circ$ with 1 $^\circ/\text{min}$ scan speed. Scanning electron microscopy (SEM) images were taken using an electron microscope (JSM-6360LA, JEOL). Scanning transmission electron microscopy–energy-dispersive X-ray spectroscopy (STEM-EDX) analysis was conducted by using HD-2000 (Hitachi). For STEM analysis, samples were dispersed with ethanol and treated by ultrasonic equipment. Supernatant liquid was dropped on the Cu-grid and dried overnight. The obtained grid was set to the machine and an

analysis was taken. Transmission electron microscopy (TEM) analysis was conducted by JEM-2100F (JEOL). For TEM analysis, samples were dispersed with ethanol and treated by ultrasonic equipment. Supernatant liquid was dropped on the Cu-grid and dried overnight for the analysis. Elemental compositions in the bulk were determined by inductively coupled plasma atomic emission spectroscopy (ICP-AES) (ICPE-9000, Shimadzu). N_2 adsorption isotherms at liquid N_2 temperature were obtained using an autoadsorption system (BELSORP MAX, Nippon BELL). External surface area was determined using a t -plot. Prior to N_2 adsorption, the catalysts heat-treated under air atmosphere at 400 °C for 2 h were evacuated under a vacuum at 300 °C for 2 h.

Catalytic Test. The selective oxidation of ethane in gas phase was carried out at atmospheric pressure in a conventional vertical flow system with a fixed bed Pyrex tubular reactor. As-synthesized catalysts were ground with an agate mortar for 5 min, followed by heat-treatment under N_2 atmosphere at 400 °C for 2 h for Orth-MoVO and under air atmosphere at 400 °C for 2 h for Tri-MoVO. Then, the 0.50 g of the treated catalysts was diluted with 2.10 g of silica and put into the tubular reactor for ethane oxidation. The reactor was heated gradually from room temperature at a rate of 10 °C min^{-1} to 350 °C under nitrogen flow (40 mL min^{-1} from the top of the reactor). The temperature was measured with a thermocouple inserted into the middle of the catalyst zone. When the temperature reached 350 °C, a reactant gas with the composition of $C_2H_6/O_2/N_2 = 10/10/80$ (mol %) was fed in with a total flow rate of 50 mL min^{-1} , and the catalysts were kept at this temperature for 2 h under the reactant gas flow in order to attain stable catalytic activity. Then, the temperature was decreased to 330 °C, 310 °C, 290 °C, 270 °C, and 250 °C with their catalytic activities being analyzed. Reactants and products were analyzed with three online gas chromatographs (molecular sieve 13X for O_2 , N_2 , and CO with a TCD detector, Gaskuropack for CO_2 , C_2H_4 , and C_2H_6 with a TCD detector, and Porapak Q for acetic acid with a FID detector). Blank runs showed that under the experimental conditions used in this study, homogeneous gas-phase reactions were negligible. Carbon balance was always ca. 98–100%, so that the product selectivity was calculated on the basis of the product sum.

3. RESULTS AND DISCUSSION

Crystal Structure and Yield of the Products Formed under Hydrothermal Condition. Table 1 shows the crystal phase and the yield of the products formed under the hydrothermal condition in various pH of the precursor solution. Synthesis time was set to be 20 h, and the amount of the added seeds was fixed at 0.30 g. pH of the precursor solution was changed in the range of 1.0–4.0 by using 10% NH_3 solution or 2 M H_2SO_4 (no pH control: pH = 3.2). The seeds used in this study were Orth-48-oxa, Tri-20-oxa, Amor, and Tet. These seeds were rod-shaped crystals. The structural arrangements in a – a or a – b plane attributed to the cross-section of the rods were different for each crystal phase. Crystal yield was calculated based on MoO_3 and V_2O_5 as described in the footnote in Table 1. Yields of the products formed in the presence of the seeds were calculated after subtracting the amount of the added seeds (0.30 g) from the total products amount. In all cases, yield without purification is shown. The yield and crystal phase of the products formed in the absence of the seeds are shown in Entry 1–4.

As we have previously reported, pseudo-hexagonal $Mo_{0.87}V_{0.13}O_{2.94}$ (JCPDF: 00-048-0766) was formed at pH = 1.0 (Table 1, Entry 1). Tri-MoVO was formed when the pH of the precursor solution was 2.2. Orth-MoVO was formed at pH = 3.2 (Table 1, Entry 2, 3). The yield of Tri-20 was 50.9% and was higher than that of Orth-20. We have reported that a higher pH was not suitable for the formation of MoVO under our reaction conditions. For this reason, no products were formed

Table 1. Crystal Phase and Yield of the Products Formed by Changing pH Value with or without the Seeds^a

entry	seed (phase) ^b /g	pH	crystal phase of the formed solids ^b	yield ^c /%
1	0	1.0	Hexa	79.6
2	0	2.2	Tri + Amor	50.9
3	0	3.2	Orth + Amor	9.7
4	0	4.0		0.0
5	0.3 (Orth)	1.0	Hexa	78.7
6	0.3 (Orth)	2.2	Tri + Orth	45.7
7	0.3 (Orth)	3.2	Orth	29.8
8	0.3 (Orth)	4.0	Orth	10.5
9	0.3 (Tri)	1.0	Hexa	67.8
10	0.3 (Tri)	2.2	Tri	53.3
11	0.3 (Tri)	3.2	Tri	29.5
12	0.3 (Tri)	4.0	Tri	12.0
13	0.3 (Amor)	4.0	Amor	5.8
14	0.3 (Tet)	4.0		0.0

^aSynthesis time was fixed at 20 h. ^bOrthorhombic, trigonal, tetragonal, amorphous, and pseudo-hexagonal were abbreviated as Orth, Tri, Tet, Amor, and Hexa, respectively. ^cYield was calculated as (total products amount (g) – amount of the added seed (g))/(50 × M_{MoO_3} + 12.5 × 0.5 × $M_{V_2O_5}$), where M_{MoO_3} corresponds to the molecular weight of MoO_3 (144 g mol^{-1}) and $M_{V_2O_5}$ corresponds to the molecular weight of V_2O_5 (182 g $mmol^{-1}$).

at pH = 4.0 (Table 1, Entry 4). An existing ball-type polyoxometalate $\{Mo_{72}V_{30}\}$ in the precursor solution was revealed by UV–vis and Raman analysis in the range of pH = 1.5–4.7.¹⁰ In the presence of $\{Mo_{72}V_{30}\}$, MoVO were formed by tuning the pH value of the precursor solution (Orth-MoVO: pH = 2.7–3.4, Tri-MoVO: pH = 1.7–2.2). When the pH of the precursor solution is over 4.0, $\{Mo_{72}V_{30}\}$ in the precursor solution might be hydrolyzed in the hydrothermal condition.¹⁰ Therefore, no nuclei are formed in the precursor solution, resulting in no product formation. Below pH 1.5, the Raman bands attributed to $[Mo_{36}O_{112}]^{8-}$ ($\{Mo_{36}\}$) were observed in the precursor solution, which was reported as a nucleus for forming the pseudo-hexagonal $Mo_{0.87}V_{0.13}O_{2.94}$.^{10,11} Figure 2 shows the XRD patterns of the products formed in the absence or presence of the seeds.

The XRD peaks around 10° are ascribed to the structure of a – a or a – b plane, and the peaks at 22° and 45° represents the layered structure in the c axis.¹ In addition to the peaks at 22° and 45°, Orth-20 showed peaks at 6.6°, 7.8°, 9.0° and Tri-20 showed peaks at 4.7° and 8.3°, deriving from the crystalline structure of Orth-MoVO and Tri-MoVO, respectively (Figure 2a,d). In both cases, the broad peak were observed concomitantly under 10°, suggesting that Orth-20 and Tri-20 contained Amor as an impurity.¹ When Orth-48-oxa was added to the precursor solution as a seed, Orth-MoVO was formed in pH = 2.2–4.0 (Table 1, Entry 6–8). The yield of the products formed at different pHs was 45.7% at pH = 2.2, 29.8% at pH = 3.2, and 10.5% at pH = 4.0. Nevertheless, Orth-MoVO was formed in a wide pH range under hydrothermal conditions by using the Orth-48-oxa seed. In the presence of the Orth-48-oxa seed, other than the very small amounts of Tri-MoVO, Orth-MoVO was formed at pH = 2.2, where no Orth-MoVO was formed in the absence of the seeds (Table 1, Entry 2, 6). The Orth-48-oxa seed was found to have a structure-directing ability. Surprisingly, in the presence of the Orth-48-oxa seed, more than three times the amount of Orth-MoVO for the

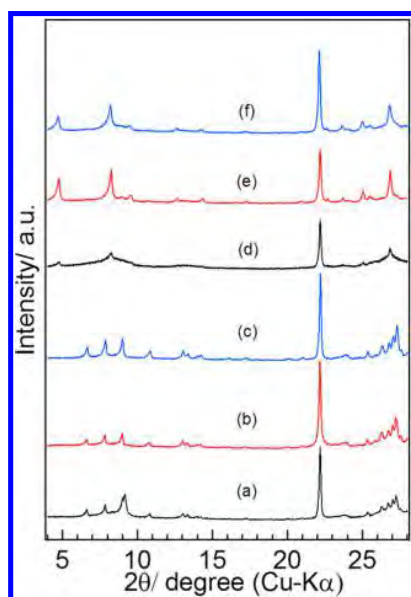


Figure 2. XRD patterns of (a) Orth-20, (b) Orth-20-oxa, (c) Orth (s)-20-0.30-4.0, (d) Tri-20, (e) Tri-20-oxa, and (f) Tri (s)-20-0.30-4.0.

amount of added seed was formed at pH = 4.0 where no products could be recovered in the absence of the seeds (Table 1, Entry 4, 8). This experimental result clearly shows that the Orth-48-oxa seed facilitates crystal formation in a wide pH range, even where $\{\text{Mo}_{72}\text{V}_{30}\}$ can be hydrolyzed in hydrothermal conditions. In the same manner, Tri-MoVO was formed at pH = 2.2–4.0 by adding Tri-20-oxa as the seed (Table 1, Entry 10–12). Yields of the products were 53.3% at pH = 2.2, 29.5% at pH = 3.2, and 12.0% at pH = 4.0. Nevertheless, products other than the Tri-20-oxa seed could be recovered by the hydrothermal reaction. In this case also, the Tri-20-oxa seed was found to have a structure-directing ability since only Tri-MoVO was formed at pH = 3.2 where only Orth-MoVO was formed in the absence of the seeds. At pH = 4.0 where no products were formed in the absence of the seeds, more than four times the amount of Tri-MoVO for the amount of added seed was formed. Obviously, the Tri-20-oxa seed facilitated the crystal formation in a wide pH range as well as that of Orth-48-oxa seed. In both cases of Orth (s)-20-0.30-4.0 and Tri (s)-20-0.30-4.0, almost no broad peaks at 10° were observed, indicating that these contained almost no Amor like Orth-20-oxa and Tri-20-oxa (Figure 2c,f). The high pH value prevented the self-condensation of the building units as shown in Entry 4. Therefore, almost no Amor formation occurred in the hydrothermal condition. At pH = 1.0, pseudohexagonal $\text{Mo}_{0.87}\text{V}_{0.13}\text{O}_{2.94}$ was formed irrespective of the addition of the seeds (Table 1, Entry 5, 9). In this condition, $\{\text{Mo}_{36}\}$ was detected instead of $\{\text{Mo}_{72}\text{V}_{30}\}$ in the precursor solution irrespective of the addition of the seeds. This experimental fact implies that no MoVO can be formed when no $\{\text{Mo}_{72}\text{V}_{30}\}$ is in the precursor solution even in the presence of the seeds. In the case that Amor was used as a seed, Amor was formed at pH = 4.0 with 5.8% yield (Table 1, Entry 13). It was found that the Amor seed could facilitate the crystal formation as well as Orth-48-oxa and Tri-20-oxa. On the other hand, different from the other seeds, lesser amounts of the products than that of the added seed were recovered when Tet was used as a seed (Table 1, Entry 14). Obviously, no products

were formed hydrothermally when Tet was used. Tet-MoVO is formed by the phase transformation from Orth-48-oxa by the heat treatment. The metal–oxygen bonds in the Tet-MoVO are normally shorter than those in the other crystal phase used as seeds in this study.^{11,29,30} Therefore, no structural units related to Tet-MoVO could be provided in the hydrothermal condition, resulting in no products formation. These experimental facts imply that the structure in the *a*–*a* or *a*–*b* plane of the seeds, attributed to the cross-section of the rods, affects crystal formation in the seed-assisted synthesis. In the presence of the seeds, the situation of recovering the products after the hydrothermal reaction differed from that in the absence of the seeds. In the absence of the seeds, products were recovered from the Teflon sheet which was added in the Teflon inner tube. On the other hand, in the presence of the seeds, almost all the products were recovered from the bottom of the Teflon inner tube. This situation suggests that the seeds that have sunk to the bottom of the Teflon inner tube under the static synthesis condition facilitate crystal formation.

Yield change of the products formed at pH 4.0 (10% NH_3 solution was used for pH control) in the absence or presence of the seeds as a function of the synthesis time is shown in Figure 3. The amount of the seeds was fixed at 0.30 g. The synthesis

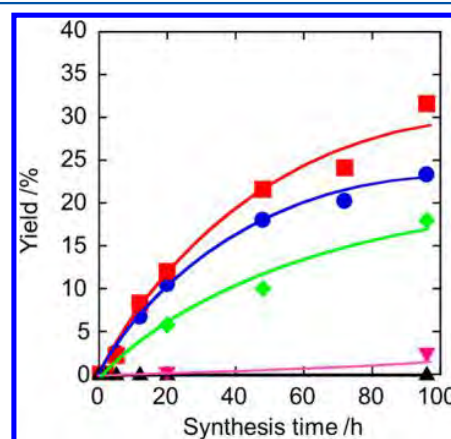


Figure 3. Yield of the formed products as a function of the synthesis time. Synthesis condition: pH of the precursor solution; 4.0, amounts of the seeds; 0.30 g, synthesis time; 2–96 h. The added seeds were Orth-48-oxa (circle), Tri-20-oxa (square), Amor (logenze), Tet (inverted triangle), and no seed (triangle). Yield was calculated as (total products amount (g) – amount of the added seeds (g))/($50 \times M_{\text{MoO}_3} + 12.5 \times 0.5 \times M_{\text{V}_2\text{O}_5}$), where M_{MoO_3} corresponds to the molecular weight of MoO_3 (144 g mol⁻¹) and $M_{\text{V}_2\text{O}_5}$ corresponds to the molecular weight of V_2O_5 (182 g mmol⁻¹).

time was changed in the range of 2–96 h. No products were formed by the hydrothermal reaction in whole synthesis time in the absence of the seeds (black triangle).

As described above, almost no products were formed when Tet was added as a seed. After 96 h, however, a material of which showed a sharp peak at 9.6° in XRD pattern was obtained with 2.5% yield (data not shown). To the best of our knowledge, the obtained material was new and unidentified at this stage. An investigation of this structure is now in progress. When Orth-48-oxa, Tri-20-oxa, and Amor were used as seeds, the materials having the same crystal phase with the seeds were formed hydrothermally at each synthesis time. Their yields were increased with an increase of the synthesis time. The rate

of the increase of the yield, however, depended on their crystal structure and was in the order of Tri-MoVO > Orth-MoVO > Amor-MoVO. The external surface area of Tri-MoVO is $12.4 \text{ m}^2 \text{ g}^{-1}$ and is about twice as large as that of Orth-MoVO and Amor-MoVO ($7.3 \text{ m}^2 \text{ g}^{-1}$ in Orth-MoVO, $5.7 \text{ m}^2 \text{ g}^{-1}$ in Amor-MoVO).¹ As discussed later, Tri-MoVO is considered to provide the specific surface which can contribute to the crystal evolution, leading to a higher yield than that of Orth-MoVO and Amor-MoVO. The yield of Orth-MoVO, however, was much higher than that of Amor-MoVO at each synthesis time, even though they had similar external surface area. Since the morphology of these seeds were rod-shaped and were almost the same, the structure in the a - a or a - b plane attributed to the cross-section of the rod-shaped crystals may affect the crystal formation rate as well as the external surface area.

The yield of the products obtained by changing the seed amounts of Orth-48-oxa or Tri-20-oxa is shown in Figure 4.

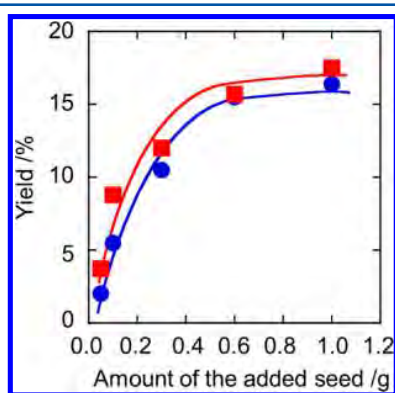


Figure 4. Yield of the formed products as a function of the amounts of the seeds. Synthesis condition: pH of the precursor solution; 4.0, amounts of the seeds; 0.05–1.00 g, synthesis time; 20 h. The added seeds were Orth-48-oxa (circle) and Tri-20-oxa (square). Yield was calculated as $(\text{total products amount (g)} - \text{amount of the added seeds (g)}) / (50 \times M_{\text{MoO}_3} + 12.5 \times 0.5 \times M_{\text{V}_2\text{O}_5})$, where M_{MoO_3} corresponds to the molecular weight of MoO_3 (144 g mol^{-1}) and $M_{\text{V}_2\text{O}_5}$ corresponds to the molecular weight of V_2O_5 (182 g mmol^{-1}).

The pH of the precursor solution was fixed at 4.0 by using 10% NH_3 solution in order to avoid the self-formation of MoVO irrespective of the addition of the seeds. The synthesis time was fixed at 20 h, and the amounts of the seed were changed in the range of 0.05–1.00 g. In both cases, the crystal phase of the formed products was the same with the added seeds. The yields of the products were increased with an increase of the amounts of the added seeds. In all cases, the yield of Tri-MoVO was higher than that of Orth-MoVO, probably due to the external surface area of the seeds. The products yield became constant when over 0.60 g of Orth-48-oxa or Tri-20-oxa seed was added. With the addition of over 0.60 g of the seed, the added seed formed two layers in the bottom of the Teflon tube. Only the surface of the upper layer was considered to contribute to the crystal formation, which limited the increase of the products yield.

Crystal Growth in Seed-Assisted Synthesis. We investigated how the rod-shaped crystals were formed in the seed-assisted synthesis of Orth-MoVO and Tri-MoVO. The experimental conditions and yield of the products are listed in Table 2. In our seed-assisted synthesis, seeds were added as a solid. However, under the hydrothermal conditions, a part of

Table 2. Crystal Yield of the Products Synthesized by the Seed-Assisted Synthesis in Various Conditions^a

entry	seed ^b	seed condition ^c		yield ^d /%
1	Orth	ground	solid	10.5
2	Tri	ground	solid	12.0
3	Tri	ground	dissolved in distilled water	0.0
4	Orth ^e	ground	solid	0.0
5	Tri ^e	ground	solid	0.0
6	Orth	unground	Solid	4.4
7	Tri	unground	Solid	4.0
8	MoVWO	ground	Solid	12.8

^aSynthesis condition: the amount of the seeds; 0.30 g, pH of the precursor solution; 4.0, synthesis time; 20 h. ^bAdded seed. Orth and Tri represent Orth-48-oxa and Tri-20-oxa, respectively. ^cSeed condition before the seed-assisted synthesis. ^dYield was calculated as $(\text{total products amount (g)} - \text{amount of the added seeds (g)}) / (50 \times M_{\text{MoO}_3} + 12.5 \times 0.5 \times M_{\text{V}_2\text{O}_5})$, where M_{MoO_3} corresponds to the molecular weight of MoO_3 (144 g mol^{-1}) and $M_{\text{V}_2\text{O}_5}$ corresponds to the molecular weight of V_2O_5 (182 g mmol^{-1}). ^e0.30 g of the seeds were added into the precursor solution prepared by $(\text{NH}_4)_6\text{Mo}_7\text{O}_{24} \cdot 4\text{H}_2\text{O}$ (Mo: 50 mmol) and NH_4VO_4 (V: 12.5 mmol) dissolved in 240 mL at pH = 4.0. Synthesis time was fixed at 20 h.

the solid seeds can be dissolved likewise for the case of zeolites.^{19,20} It is difficult to evaluate and observe the amounts of the dissolved seeds. This situation made it difficult to evaluate the roles of the dissolved and undissolved seeds for the crystal growth.

Therefore, dissolved seeds are used for the seed-assisted synthesis in order to evaluate the roles of the dissolved seeds for the crystal growth. Figure S1, Supporting Information shows the solid amounts recovered after the hydrothermal treatment at 175 °C. In this experiment, 0.30 g of Orth-48-oxa or Tri-20-oxa seeds was added into 240 mL of distilled water, and the amounts of the seeds recovered from the solution were measured. Orth-48-oxa was not completely dissolved under this condition. When Tri-20-oxa was treated in this condition, however, the amount of Tri-20-oxa decreased with the reaction time and was completely dissolved at 20 h. The solution prepared by dissolving 0.30 g of Tri-20-oxa in distilled water was used as the solution for synthesizing Tri-MoVO instead of distilled water. To 240 mL of the prepared solution, 8.83 g of $(\text{NH}_4)_6\text{Mo}_7\text{O}_{24} \cdot 4\text{H}_2\text{O}$ and 3.29 g of hydrated VOSO_4 were added and the mixture was stirred for 10 min before the pH was adjusted to be 4.0 by adding 10% NH_3 solution. After the N_2 bubbling for 10 min, a hydrothermal reaction was conducted for 20 h at 175 °C. After the hydrothermal reaction, no products were formed (Table 2, Entry 3). This experimental fact showed that the seeds dissolved under hydrothermal condition can contribute to no crystal formation. Therefore, solid seeds are essential for the seed-assisted synthesis. In our seed-assisted synthesis, crystals grew because the crystal growth rate was superior to the dissolving rate of the solid seeds.

Then, we investigated the role of $\{\text{Mo}_7\text{V}_3\}$ in the seed-assisted synthesis since the existing of $\{\text{Mo}_7\text{V}_3\}$ in the precursor solution was revealed at pH = 4.0.¹⁰ For this purpose, the precursor solution prepared by $(\text{NH}_4)_6\text{Mo}_7\text{O}_{24} \cdot 4\text{H}_2\text{O}$ (Mo: 50 mmol) and NH_4VO_3 (V: 12.5 mmol) was used for synthesizing Orth-MoVO and Tri-MoVO. A total of 8.83 g of $(\text{NH}_4)_6\text{Mo}_7\text{O}_{24} \cdot 4\text{H}_2\text{O}$ and 1.46 g of NH_4VO_3 were mixed with 240 mL of distilled water. A total of 0.30 g of Orth-MoVO or Tri-MoVO was added before the pH was adjusted to 4.0 using

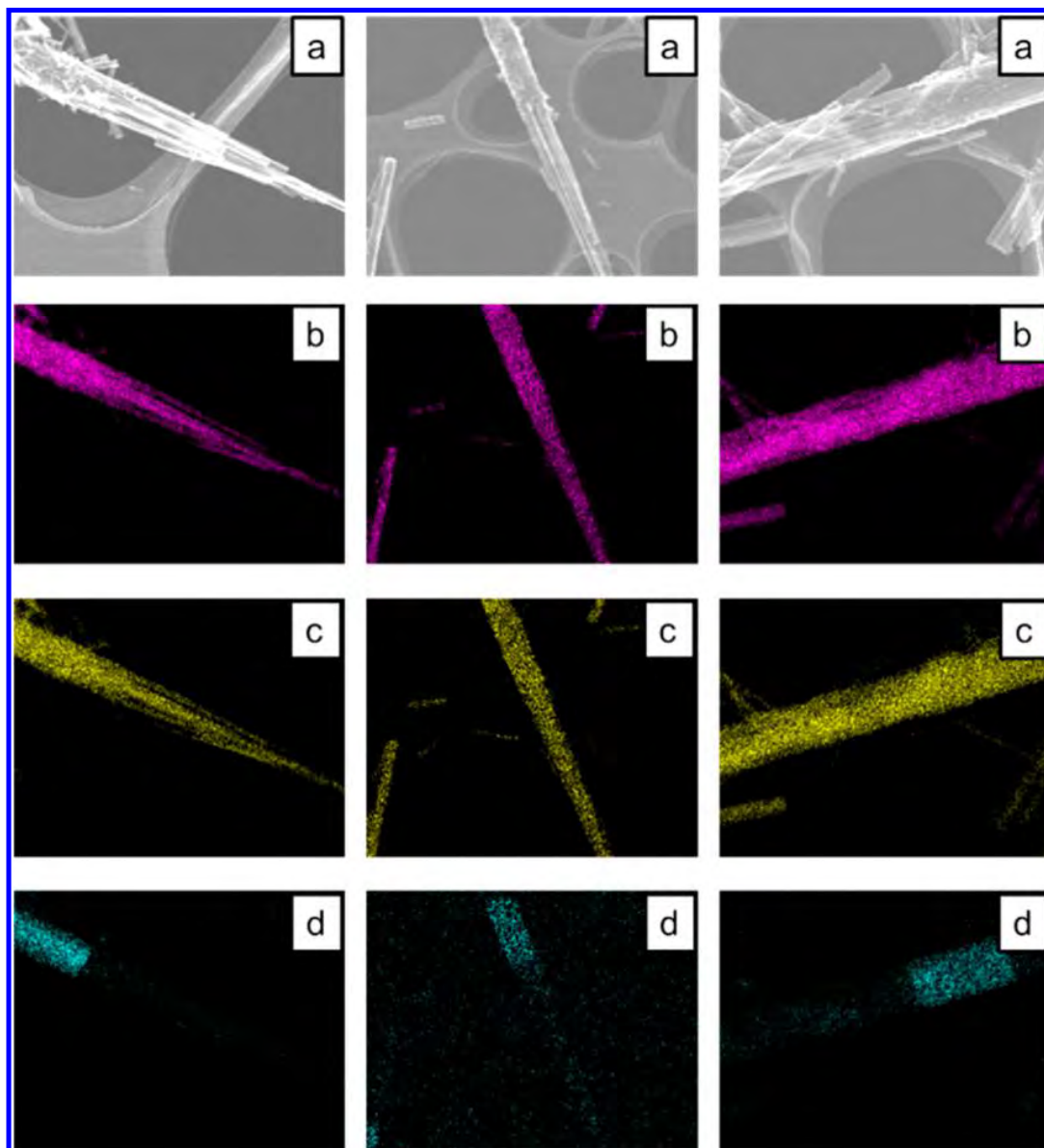


Figure 5. STEM images (a) and the mapping images of Mo (b), V (c), and W (d) of the product obtained by the seed-assisted synthesis by using MoVVO as a seed. Synthesis condition: the amount of the seed, 0.30 g; pH of the precursor solution, 4.0; synthesis time, 20 h.

2 M H_2SO_4 (no pH control: pH = 5.4). In the preparative solution, no $\{\text{Mo}_{72}\text{V}_{30}\}$ was detected by liquid Raman analysis. After the N_2 bubbling for 10 min, a hydrothermal reaction was conducted for 20 h at 175 °C. As a consequence, no products were obtained in both cases (Table 2, Entry 4, 5). This experimental fact suggests that $\{\text{Mo}_{72}\text{V}_{30}\}$ is needed for the crystal formation in the seed-assisted synthesis of Orth-MoVO and Tri-MoVO. As described in Figure 3, no products were formed by the hydrothermal synthesis at pH = 4.0 when no seeds were used, although $\{\text{Mo}_{72}\text{V}_{30}\}$ was in the precursor solution. However, in the presence of the seeds, $\{\text{Mo}_{72}\text{V}_{30}\}$ is found to work for the crystal formation, suggesting that $\{\text{Mo}_{72}\text{V}_{30}\}$ contributes not to crystal nucleation but to crystal growth in the seed-assisted synthesis. The above results show that the solid seeds work as the crystal nucleus and $\{\text{Mo}_{72}\text{V}_{30}\}$ is responsible for the crystal growth in the seed-assisted synthesis. As discussed above, crystal structure in the a - a or a -

b plane attributed to the cross-section of the rods was implied to play crucial roles in the crystal formation. In order to investigate the roles of the cross-section of the rod-shaped crystals, the seeds having almost no cross-section were applied to the seed-assisted synthesis. For this purpose, Orth-48-oxa or Tri-20-oxa without grind treatment was used as the seeds since rod-shaped crystals of Orth-MoVO and Tri-MoVO had lesser cross-section compared with that of the ground seeds.³ The synthesis procedure was the same as that shown in the experimental section except for the grind treatment for the seeds. In both cases, the synthesis condition was as follows: pH of the precursor solution, 4.0; amount of the seeds, 0.30 g; synthesis time, 20 h. Orth-MoVO or Tri-MoVO was formed irrespective of the grind treatment of the seeds. The yield of the products, however, was decreased to 4.4% in Orth-MoVO and 4.0% in Tri-MoVO, although 10.5% and 12.0% yield was achieved in Orth-MoVO and Tri-MoVO when the ground

seeds were used (Table 2, Entry 1, 2, 6, 7). It is reported that the rod-shaped crystals of Orth-MoVO were solely cut for the *c*-direction by the grind treatment.^{1,3} Irrespective of the grind, the external surface area was almost unchanged since the exposed section surface area was only ca. 10% against the external surface area. The cross-section of the rod-shaped crystals exposed by the grind treatment provided more than twice the yield even the exposed surface area was ca. 10%. Obviously, the cross-section of the rod-shaped crystals prefers to facilitate the crystal growth rather than the side surface of the rods.

For further confirmation, STEM-EDX analysis was conducted in order to investigate the details about the crystal growth in seed-assisted synthesis. Mo–V–W–O oxide (MoVWO) which has the same crystal structure with Tri-MoVO was synthesized by $(\text{CH}_3\text{CH}_2\text{NH}_3)_2\text{Mo}_3\text{O}_{10}$ and VOSO_4 (for detailed preparation conditions, see Supporting Information). In this experiment, only the seed contains W in the structure, and the formed products are expected to have no W, since no W species are being in the precursor solution. The synthesis condition in the presence of MoVWO seed was as follows: pH of the precursor solution, 4.0; amount of the seed, 0.30 g; synthesis time, 20 h. The obtained product showed the same XRD pattern with Tri-MoVO, and the product yield was 12.8%, which was almost the same yield as that obtained by using Tri-20-oxa as a seed (Table 2, Entry 8).

The STEM images and the mapping images of Mo, V, W of the product are shown in Figure 5. In STEM images, rod-shaped crystals were observed. The W mapping images clearly show that there are two different contrasts in the rods (Figure 5d). The thin contrast shows the distribution of Cu which was used as a grid. It was inevitable because the energy level of Cu and W in EDX analysis was close. The bright blue contrast distributed through only the center part of the rods showing the distribution of W. On the other hand, Mo and V were uniformly distributed through the rods (Figure 5b,c). The rods which contain Mo, V, and W are the seed and the rods only containing Mo and V are the formed crystals under hydrothermal conditions. Tri-MoVO was revealed to evolve from the cross-section of the seed rod-shaped crystals. The TEM images and select area electron diffraction (SAED) of Orth (s)-20–0.30–4.0 and Tri (s)-20–0.30–4.0 are shown in Figure S2, Supporting Information. The small rod-shaped crystal evolved from the rod-shaped crystals of the seeds shows a clear diffraction pattern. The rod-shaped crystals evolved from the seeds have a crystalline structure, which is in agreement with the clear XRD patterns of the products as shown in Figure 2.

The length of the rod-shaped crystals obtained at the different synthesis time was measured. In this experiment, seed-assisted syntheses using Orth-48-oxa or Tri-20-oxa were conducted at 175 °C for *x* h (*x* = 2, 5, 12, 20). The pH of the precursor solution was fixed at 4.0, and the amount of the added seeds was set to be 0.30 g. The yield of the formed products has already been described in Figure 2. The histograms of the length of the rod-shaped crystals obtained by measuring 30–40 crystallites are shown in Figure 6. At 2 h, where almost no products were formed, the average lengths of the rod-shaped crystals were 1.0 μm in Orth-MoVO and 0.8 μm in Tri-MoVO. At 5 h, the histogram of the length shifted to the longer direction, and the average lengths of the rod-shaped crystals increased to be 2.3 μm in Orth-MoVO and 1.5 μm in Tri-MoVO. The histogram of the length subsequently shifted

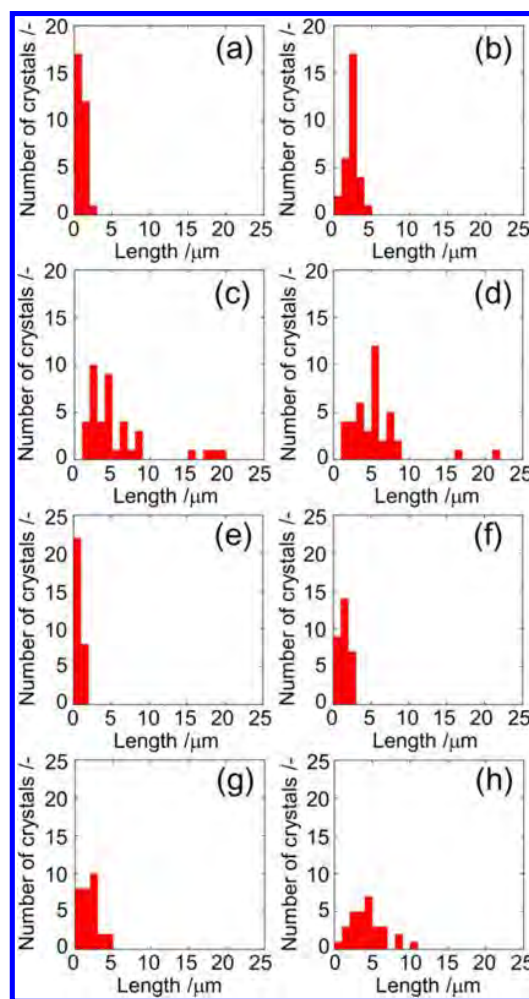


Figure 6. Histogram of the length of the rod-shaped crystals of (a–d) Orth-MoVO and (e–h) Tri-MoVO obtained by seed-assisted synthesis. The length of 30–40 rods in SEM images were measured. Synthesis condition: the amount of the seeds, 0.30 g; pH of the precursor solution, 4.0; synthesis time (a, e) 2 h, (b, f) 5 h, (c, g) 12 h, (d, h) 20 h.

to a longer direction by increasing the synthesis time. Their average lengths increased to 5.4 μm in Orth-MoVO and 1.9 μm in Tri-MoVO at 12 h and 5.5 μm in Orth-MoVO and 4.3 μm in Tri-MoVO at 20 h. Over 20 h, the lengths of the rod-shaped crystals was too long to measure by SEM in both cases. Obviously, the length of the rod-shaped crystals increased with the synthesis time. The rod-shaped crystals were found to grow along with *c*-axis for the seed-assisted synthesis.

On the basis of the above results, we propose a crystal growth scheme of the seed-assisted synthesis and is described in Figure 7. The $\{\text{Mo}_7\text{V}_{30}\}$ being in the precursor solution provides the building units to the *a*–*a* or *a*–*b*-plane of the crystalline Mo_3VO_x oxides. The building units are stacked on the planes and crystals grew along with *c*-axis. As a consequence, rod-shaped crystals were formed.

Physicochemical Properties and Their Catalytic Activity for the Selective Oxidation of Ethane. The external surface area, the micropore volume, the average diameter of the rod-shaped crystals, and the bulk composition of the products formed in the absence or presence of the seeds

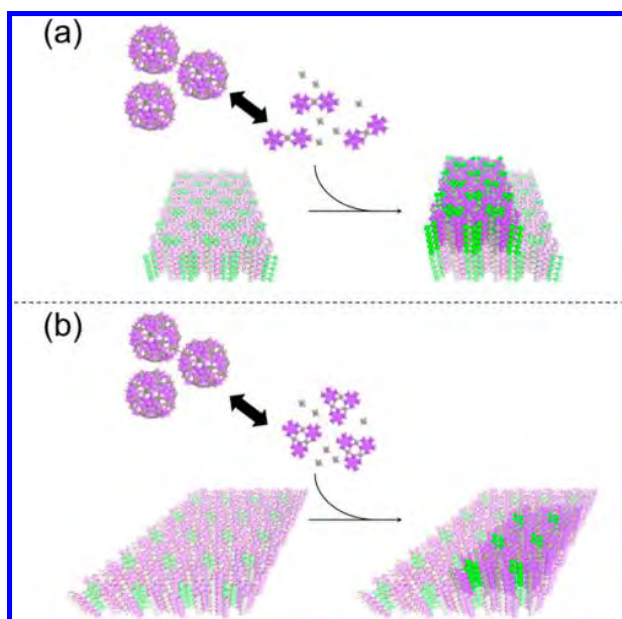


Figure 7. Crystal formation schemes of seed-assisted synthesis of (a) Orth-MoVO and (b) Tri-MoVO. Purple, Mo; gray, V; green, mixture of Mo and V.

are listed in Table 3. The external surface areas of Orth-48-oxa and Tri-20-oxa were 7.3 and 12.4 m² g⁻¹, respectively. On the

Table 3. Physicochemical Properties of the Products Formed in the Absence or Presence of the Seeds

catalyst ^a	external surface area ^b / m ² g ⁻¹	micropore volume ^b / 10 ⁻³ cm ³ g ⁻¹	average rod diameter ^c / μm	bulk V/Mo ^d
Orth	7.3	8.2	0.42	0.40
Orth (s)	12.4	7.2	0.17	0.37
Tri	12.4	4.0	0.22	0.33
Tri (s)	21.4	5.1	0.14	0.36

^aOrth, Tri, Orth (s), and Tri (s) represent Orth-48-oxa, Tri-20-oxa, Orth (s)-20–0.30–4.0, and Tri (s)-20–0.30–4.0, respectively. ^bExternal surface area and micropore volume were measured by N₂ adsorption at -196 °C for the catalysts after the heat treatment under air at 400 °C for 2 h and were determined by t-plot method. ^cAverage of 100 crystallites in SEM images. ^dDetermined by ICP.

other hand, the external surface areas of Orth (s)-20–0.30–4.0 and Tri (s)-20–0.30–4.0 were 12.4 and 21.4 m² g⁻¹, respectively, and were about 1.7 times higher than that of Orth-48-oxa and Tri-20-oxa. As shown in Table 3, the average diameters of the rod-shaped crystals obtained with 100 of crystallites were 0.17 and 0.14 μm in Orth (s)-20–0.30–4.0 and Tri (s)-20–0.30–4.0, respectively. These were smaller than that of Orth-48-oxa and Tri-20-oxa (Orth-48-oxa, 0.42 μm; Tri-20-oxa, 0.22 μm). The small crystal size of the products obtained by seed-assisted synthesis caused the increase of the external surface area. There are two possibilities in regard to the crystallite size decrease when the seeds were used: (1) due to the high pH of the precursor solution, (2) due to the addition of the seed. However, the possibility (1) could be easily excluded since the products formed at pH = 3.2 in Orth-MoVO and pH = 2.2 in Tri-MoVO with the same synthesis time and amount of the seed showed a similar diameter with that formed at pH = 4.0. Thus, the addition of the seeds should be related

to the crystal size decrease, although the details are still unknown. The micropore volumes were almost the same irrespective of the addition of the seeds and were c.a. 7.2–8.2 cm³ g⁻¹ in Orth-MoVO and 4.2–5.1 cm³ g⁻¹ in Tri-MoVO. The micropore volumes of Orth-MoVO were smaller than that of our previous papers.^{1,31} Orth-MoVO was treated under air atmosphere before the adsorption, which related to the small micropore volumes because the micropore volume of Orth-MoVO strongly depended on their reduction state.³² Nevertheless, the products obtained by the seed-assisted synthesis were found to have microporosity. The elemental compositions were almost the same irrespective of the addition of the seeds, and the ratios of V/Mo were 0.37–0.40 in Orth-MoVO and 0.33–0.36 in Tri-MoVO, respectively. The catalytic performance over the catalysts formed in the absence or presence of the seeds at each reaction temperature is illustrated in Figure 8.

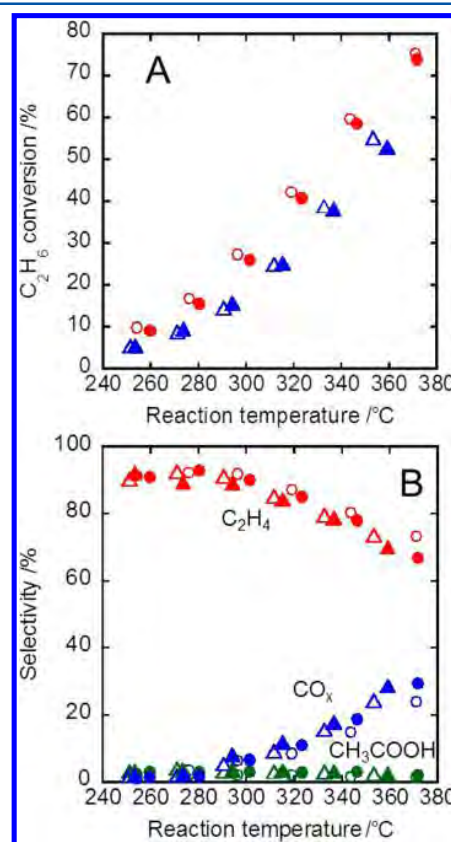


Figure 8. Conversion (A) and selectivity (B) changes as a function of reaction temperature in the oxidative dehydrogenation of ethane over Orth (s)-20–0.30–4.0 (closed circles), Orth-48-oxa (open circles), Tri (s)-20–0.30–4.0 (closed triangles), and Tri-20-oxa (open triangles). Reaction condition: catalyst amount, 0.5 g; gas feed, C₂H₆/O₂/N₂ = 5/5/40 mL min⁻¹.

After the catalytic reaction, crystal structure of the catalysts was unchanged except for the small changes of the lattice parameter and the peaks intensities. The conversion of ethane increased with the reaction temperature (Figure 8A). The conversion of ethane of Orth-48-oxa and Orth (s)-20–0.30–4.0 was almost the same at each reaction temperature. As well, Tri-20-oxa and Tri (s)-20–0.30–4.0 showed almost the same conversion of ethane at each reaction temperature. The products detected were ethene, acetic acid, and CO_x. The selectivity to ethene was

over 90% at the low ethane conversion range under the low reaction temperature and then decreased gradually upon increasing the reaction temperature. The CO_x selectivity was increased subsequently with the reaction temperature. Acetic acid selectivity was almost unchanged at each reaction temperature and was in the range of 1–3%. The products selectivity was almost the same at each reaction temperature over these catalysts. We have reported that ethane is converted in the heptagonal channel in the structure.^{3,4} As pointed out by the N₂ adsorption analysis, the obtained catalysts had microporosity irrespective of the addition of the seeds, which led to a similar catalytic performance for the selective oxidation of ethane.

4. CONCLUSIONS

Seed-assisted syntheses of crystalline Mo₃VO_x oxides (MoVO) were conducted for the first time. MoVO having the same crystal phase with the seeds were formed under hydrothermal conditions in a wide pH range of the precursor solution. The rod-shaped crystals of MoVO were formed from the cross-section of the rod-shaped crystals of the seeds and grew along the *c* axis. We concluded that the building units provided from ball-type polyoxomolybdate, [Mo₇₂V₃₀O₂₈₂(H₂O)₅₆(SO₄)₁₂]³⁶⁻ ({Mo₇₂V₃₀}), staked on the *a*–*a* or *a*–*b* plane of MoVO seeds, leading to the formation of MoVO. The present work successfully demonstrates the seed-assisted synthesis method on MoVO and will pave a new way for synthesizing materials based on building-block assembly.

■ ASSOCIATED CONTENT

Supporting Information

Synthesis procedure of MoVWO, recovered solid seed amounts of Orth-48-oxa and Tri-20-oxa from 0.30 g as a function of the hydrothermal treatment time at 175 °C in 240 mL of distilled water at pH = 4.0, TEM images, and SAED images of Orth (s)-20–0.30–4.0 and Tri(s)-20–0.30–4.0. This material is available free of charge via the Internet at <http://pubs.acs.org>.

■ AUTHOR INFORMATION

Corresponding Authors

*(W.U.) E-mail: ueda@cat.hokudai.ac.jp.

*(S.I.) Research Fellow of Japan Society for the Promotion of Science.

Notes

The authors declare no competing financial interest.

■ ACKNOWLEDGMENTS

This work was supported by JSPS KAKENHI Grant Number 2324-6135.

■ REFERENCES

- (1) Konya, T.; Katou, T.; Murayama, T.; Ishikawa, S.; Sadakane, M.; Buttrey, D. J.; Ueda, W. *Catal. Sci. Technol.* **2013**, *3*, 380–387.
- (2) Ishikawa, S.; Murayama, T.; Ohmura, S.; Sadakane, M.; Ueda, W. *Chem. Mater.* **2013**, *25*, 2211–2219.
- (3) Ishikawa, S.; Yi, X.; Murayama, T.; Ueda, W. *Appl. Catal. A: Gen.* **2014**, *474*, 10–17.
- (4) Ishikawa, S.; Yi, X.; Murayama, T.; Ueda, W. *Catal. Today*, in press.
- (5) Ueda, W.; Vitry, D.; Kato, T.; Watanabe, N.; Endo, Y. *Res. Chem. Intermed.* **2006**, *32* (No. 3–4), 217–233.
- (6) Katou, T.; Vitry, D.; Ueda, W. *Catal. Today* **2004**, *91–92*, 237–240.

- (7) Watanabe, N.; Ueda, W. *Ind. Eng. Chem. Res.* **2006**, *45*, 607–614.
- (8) Sadakane, M.; Watanabe, N.; Katou, T.; Nodasaka, Y.; Ueda, W. *Angew. Chem., Int. Ed.* **2007**, *46*, 1493–1496.
- (9) Chen, C.; Nakatani, K.; Murayama, T.; Ueda, W. *ChemCatChem* **2013**, *5*, 2869–2873.
- (10) Sadakane, M.; Endo, K.; Kodato, K.; Ishikawa, S.; Murayama, T.; Ueda, W. *Eur. J. Inorg. Chem.* **2013**, *10–11*, 1731–1736.
- (11) Sadakane, M.; Yamagata, K.; Kodato, K.; Endo, K.; Toriumi, K.; Ozawa, Y.; Ozeki, T.; Nagai, T.; Matsui, Y.; Sakaguchi, N.; Pyrz, W. D.; Buttrey, D. J.; Blom, D. A.; Vogt, T.; Ueda, W. *Angew. Chem., Int. Ed.* **2009**, *48*, 3782–3786.
- (12) Bogdan, B.; Paul, K.; Craig, L. H. *Chem. Commun.* **2005**, *25*, 3138–3140.
- (13) Achim, M.; Pierre, G. *Chem. Soc. Rev.* **2012**, *41*, 7431–7463.
- (14) Canioni, R.; Roch, C. M.; Laronze, N. L.; Haouas, M.; Taulèlle, F.; Marrot, J.; Paul, S.; Lamonier, C.; Paul, J. F.; Lorient, S.; Millet, J. M. M.; Cadot, E. *Chem. Commun.* **2011**, *47*, 6413–6415.
- (15) Ueda, W. *Jpn. Petrol. Inst.* **2013**, *56*, 122–132.
- (16) Cundy, C. S.; Cox, P. A. *Chem. Rev.* **2003**, *103*, 663–701.
- (17) Xie, B.; Song, J.; Ren, L.; Li, Y.; Xiao, F. S. *Chem. Mater.* **2008**, *20*, 4533–4553.
- (18) Kamimura, Y.; Iyoki, K.; Elangovan, S. P.; Itabashi, K.; Shimojima, A.; Okubo, T. *Microporous Mesoporous Mater.* **2012**, *163*, 282–290.
- (19) Itabashi, K.; Kamimura, Y.; Iyoki, K.; Shimojima, A.; Okubo, T. *J. Am. Chem. Soc.* **2012**, *134*, 11542–11549.
- (20) Iyoki, K.; Itabashi, K.; Okubo, T. *Microporous Mesoporous Mater.* **2014**, *189*, 22–30.
- (21) Kamimura, Y.; Tanahashi, S.; Itabashi, K.; Sugawara, A.; Wakihara, T.; Shimojima, A. *J. Phys. Chem. C* **2011**, *115*, 744–750.
- (22) Iyoki, K.; Itabashi, K.; Chaikittisilp, W.; Elangovan, S. P.; Wakihara, T.; Kohara, S.; Okubo, T. *Chem. Mater.* **2014**, *26*, 1957–1966.
- (23) Liu, S.; Zhang, Y.; Meng, Y.; Gao, F.; Jiao, S.; Ke, Y. *Cryst. Growth Des.* **2013**, *13*, 2697–2702.
- (24) Cubillas, P.; Anderson, M. W.; Attfield, M. P. *Cryst. Growth Des.* **2013**, *13*, 4526–4532.
- (25) Falcaro, P.; Buso, D.; Hill, A. J.; Doherty, C. M. *Adv. Mater.* **2012**, *24*, 3153–3168.
- (26) Ranjan, R.; Tsapatsis, M. *Chem. Mater.* **2009**, *21*, 4920–4924.
- (27) Zhang, X.; Liu, Y.; Li, S.; Kong, L.; Liu, H.; Li, Y.; Han, W.; Yeung, K. L.; Zhu, W.; Yang, W.; Qiu, J. *Chem. Mater.* **2014**, *26*, 1975–1981.
- (28) Zhang, Z.; Sadakane, M.; Murayama, T.; Izumi, S.; Yasuda, N.; Sakaguchi, N.; Ueda, W. *Inorg. Chem.* **2014**, *53*, 903–911.
- (29) Dieterle, M.; Mestl, G.; Jäger, J.; Uchida, Y.; Hibstl, H.; Schlögl, R. *J. Mol. Catal. A: Chem.* **2001**, *174*, 169–185.
- (30) Yamazoe, N.; Kihlberg, L. *Acta Crystallogr.* **1975**, *B31*, 1666–1672.
- (31) Sadakane, M.; Kodato, K.; Kuranishi, T.; Nodasaka, Y.; Sugawara, K.; Sakaguchi, N.; Nagai, T.; Matsui, Y.; Ueda, W. *Angew. Chem., Int. Ed.* **2008**, *47*, 2493–2496.
- (32) Sadakane, M.; Ohmura, S.; Kodato, K.; Fujisawa, T.; Kato, K.; Shimidzu, K.; Murayama, T.; Ueda, W. *Chem. Commun.* **2011**, *47*, 10812–10814.

Crystalline Mo-V-W-mixed Oxide with Orthorhombic and Trigonal Structures as Highly Efficient Oxidation Catalysts of Acrolein to Acrylic Acid

Chuntian Qiu · Chen Chen · Satoshi Ishikawa · Toru Murayama · Wataru Ueda

Published online: 5 August 2014
© Springer Science+Business Media New York 2014

Abstract We succeeded in introducing W in Mo_3VO_x with keeping the orthorhombic, trigonal, and amorphous structures. Synthesized crystalline $\text{Mo(W)}_3\text{VO}_x$ with orthorhombic and trigonal structures, both of which possess heptagonal channels, showed catalytic activity for gas-phase selective acrolein oxidation to acrylic acid superior to amorphous $\text{Mo(W)}_3\text{VO}_x$ and to tetragonal Mo_3VO_x . The results strongly suggest that the crystalline $\text{Mo(W)}_3\text{VO}_x$ with orthorhombic and trigonal structures are real active phase of industrial acrolein oxidation catalysts based on Mo, W, and V oxides. Furthermore, we found that the resulting W-containing catalyst showed less-dependency of water partial pressure in the reactant feed on the acrolein conversion.

Keywords $\text{Mo(W)}_3\text{VO}_x$ · Acrolein · Oxidation · Acrylic acid · Crystal structure · Amorphous · Industrial catalysts

1 Introduction

Catalytic oxidation is a key technology for converting petroleum-based feedstocks to useful chemicals. The obtained oxygen-containing products such as alcohols, aldehydes, ketones, or acid are widely used as raw materials for manufacturing plastics, synthetic fiber, polyesters, etc. [1–3]. As for solid-state oxidation catalysts, transition metal oxides are most used as a key component of various heterogeneous oxidation catalysts because of their diversity in composition and valence state. Among various metal

oxide and complex metal oxides, Mo-V-based complex metal oxides have long attracted much attention, back to the sixties in the last century.

Mo-V-based complex metal oxide is very well known as the selective oxidation catalyst of acrolein to acrylic acid. Acrylic acid is one of the most important chemicals largely employed by the chemical industry for the production of super absorber, polymer, adhesive, paint, plastic, rubber synthesis, detergent, etc. Currently all acrylic acid is manufactured via two steps propylene based oxidation processes, where initial stage is the formation of acrolein followed by oxidation of acrolein to acrylic acid in which Mo-V-based complex metal oxide is used. During the long period of optimization of industrial catalysts, a large number of metal promoters (Me) such as W, Cu, Mn, Fe, Sb, Cr, and Sr were introduced to modify the catalytic performance of these complex oxides [4]. A brief characteristic of the industrial catalysts is in Table 1. In the selective catalysts, Mo is always richer than V in content and these components are usually in lower oxidation states. Since the catalysts contain various elements for achieving necessary catalyst performance, materials are basically X-ray amorphous but show a diffraction of 0.4 nm d-spacing. Though these conventional investigations apparently facilitated an increase in the efficiency of the catalysts, little has been provided in terms of the understanding of the real active material and structural phase and underlying mechanisms so far due to the complexity of the industrial catalysts.

Nevertheless, there are some useful and important researches. The most important is a report by Andrushkevich [5]. She nicely listed up important characteristics of Mo-V-based oxide catalyst on the basis of the reported results and information on mixed Mo-V oxides, which are shown in Table 1. One can easily see common features

C. Qiu · C. Chen · S. Ishikawa · T. Murayama · W. Ueda (✉)
Catalysis Research Center, Hokkaido University, N-21, W-10,
Sapporo 001-0021, Japan
e-mail: ueda@cat.hokudai.ac.jp

Table 1 Typical features of Mo–V–O catalysts for gas-phase acrolein oxidation

Features	Industrial catalysts	Mixed Mo–V oxide
Composition	Mo/V = 2~8	Mo ₃ VO _{11-x}
Additives	Cu, W, Fe, Sb etc.	none
XRD	X-ray amorphous (with peak of <i>d</i> = 0.4 nm)	Phase mixture (with peak of <i>d</i> = 0.4 nm)
Valence state	Highly reduced	Mo ⁶⁺ , V ⁴⁺
IR band (cm ⁻¹)	not available	870 (st), 917 (sh), 824 (sh)

between industrial catalysts and mixed Mo–V oxides in the table. Her most important conclusion amongst the features is the elemental composition of Mo₃VO₁₁ as the catalytically active material. However, detailed information like crystal structure about this material has been lacking.

After the report by Andrushkevich, there are an appreciable number of reports on the topics of mixed Mo–V oxide catalysts. However, there seem no results confirming active material phase for the selective acrolein oxidation. For example, Mestl et al. suggested (MoVW)₅O₁₄ with a tetragonal structure as the active and selective phase [6], while it was concluded by Vogel et al. that only X-ray amorphous Mo/V mixed oxides contained selective oxidation centers in contrast to the crystalline samples [7]. Obviously, mixed Mo–V oxide catalysts with tetragonal structure or with amorphous structure could be a candidate real active material. The situation, however, is still complicated owing to the diversity of components and the lack of full structural information of the catalysts. One of the possible ways to reach the real state is to make a catalytically highly active material with simpler components and well characterized.

Meanwhile, Mitsubishi Chemicals developed a complex Mo–V–O based catalyst, which has an orthorhombic structural phase, so-called M1, for propane oxidation to acrylic acid and the ammoxidation of propane to acrylonitrile [8–11]. The catalysts commonly contain various levels of Nb and Te or Sb which are considered able to affect catalyst activity either through promotion of product selectivity as with Te or structurally as with Nb. This development not only contributes to realize catalytic propane ammoxidation processes but also helps to understand the active phase of acrolein oxidation. More recently, we reported four different pure crystalline Mo₃VO_x materials assuming trigonal, orthorhombic, tetragonal, and amorphous systems (denoted as Tri-MoVO, Orth-MoVO, Tetra-MoVO, and Amor-MoVO, respectively) without containing a third metal elements [12] and eventually we found that Tri-MoVO and Orth-MoVO are extremely active and

selective for ethane oxidation and for acrolein oxidation to acrylic acid, of which acrolein oxidation performance is superior to the industrial catalyst as far as compared under laboratory scale experiments [13].

HAADF-STEM images of these four materials and crystal structure models of Tri-MoVO and Orth-MoVO have been reported as shown in Fig. 1 [14, 15]. The materials have a rod-like morphology along its *c*-axis direction. All of the complex Mo–V–O based catalysts are layered with a lattice constant of 0.4 nm, in which each layer is comprised of MO₆ octahedra and pentagonal bipyramidal M(M₅O₂₇) units [16–19]. The units are arranged forming heptagonal and hexagonal channels in the *a*-*b* plane in Tri-MoVO, Orth-MoVO, and Amor-MoVO but without these channels in Tetra-MoVO. All the above structural characterizations were fully confirmed by HAADF-STEM images shown in Fig. 1. Owing to the simplicity of the components and the uniformity of the structures of these materials, study of the structure–activity relationship between the properties of the catalysts and their performance is possible.

In the present work, four different pure crystalline Mo₃VO_x phases materials and W-containing analogues were synthesized and tested as catalysts in the selective oxidation of acrolein to acrylic acid. By these experiments, real active structural phase for acrolein oxidation will be identified, it will be elucidated that active surface is *a*-*b* plane because the heptagonal channel sites are available, and finally role of W in term of water addition effect will be evidenced.

2 Experimental

2.1 Synthesis of Four Distinct Crystalline Mo₃VO_x

The catalysts were synthesized as previously reported [12, 13]. Briefly for Orth-MoVO, a solution of VOSO₄·*n*H₂O (*n* = 5.4, 3.28 g, Mitsuwa Chemicals) in deionized water (120 mL) was added to a solution of (NH₄)₆Mo₇O₂₄ (8.82 g) (Mo: 50 mmol, Wako) in deionized water (120 mL) with stirring. The mixture was stirred for 10 min and then transferred into an autoclave with a Teflon inner tube and a Teflon thin sheet. The reaction mixture was purged with N₂ for 10 min and then hydrothermally treated at 175 °C for 48 h. The procedure for Tri-MoVO was the same as that above except that the pH value of the mixture was adjusted to 2.2 with H₂SO₄. Duration of hydrothermal reaction was 20 h. As-synthesized Orth-MoVO and Tri-MoVO was purified by the treatment in a solution of oxalic acid at 60 °C for 30 min to remove amorphous impurities. Synthesis of Tetra-MoVO was done through heat treatment of Orth-MoVO (400 °C in air for 2 h and 575 °C under an

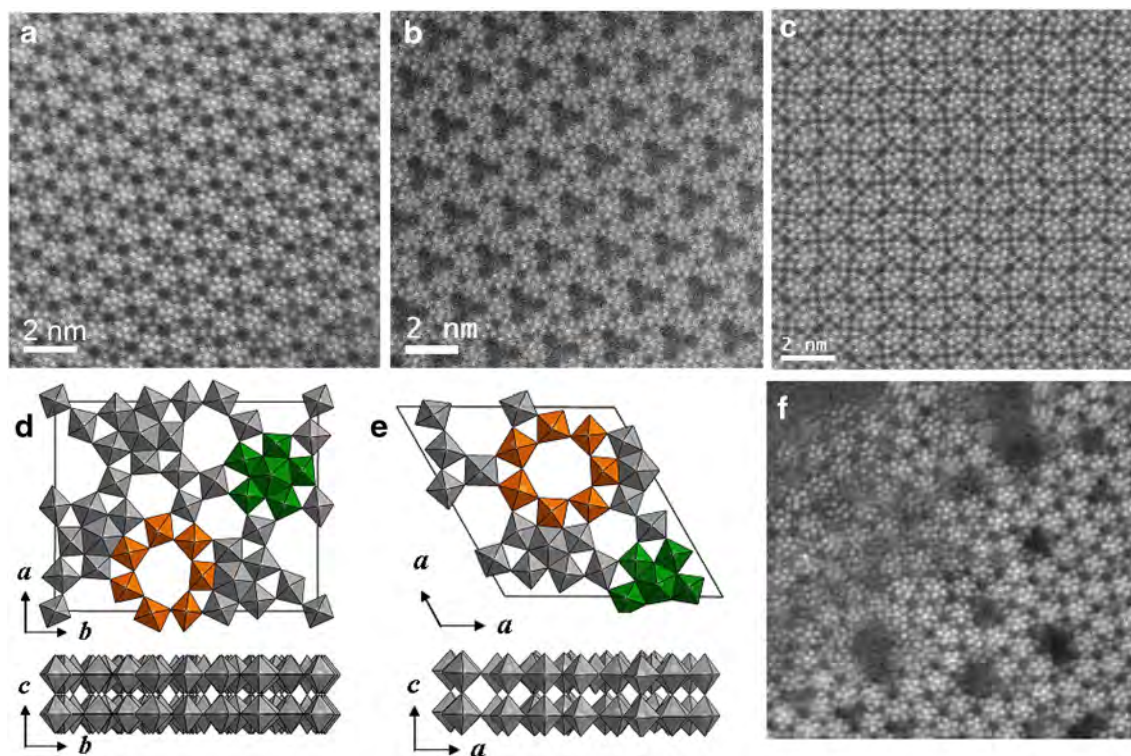


Fig. 1 HAADF-STEM images of **a** orthorhombic, **b** trigonal, **c** tetragonal, and **f** amorphous Mo_3VO_x and structural models for **d** orthorhombic, **e** trigonal phases

atmosphere of N_2 for 2 h). Amor-MoVO was obtained by the same procedure of Orth-MoVO synthesis except the twofold precursor concentration, without use of the Teflon sheet, and no N_2 bubbling.

2.2 Synthesis of W-Containing Mo_3VO_x

Orthorhombic $\text{Mo}_3\text{VW}_{0.25}\text{O}_x$ (denoted as Orth-MoVWO) was synthesized with $(\text{NH}_4)_6\text{Mo}_7\text{O}_{24}\cdot 4\text{H}_2\text{O}$, $(\text{NH}_4)_6[\text{H}_2\text{W}_{12}\text{O}_{40}]\cdot 6\text{H}_2\text{O}$, and $\text{VOSO}_4\cdot 5.4\text{H}_2\text{O}$ under hydrothermal conditions. Firstly, solution A was obtained with 8.38 g of $(\text{NH}_4)_6\text{Mo}_7\text{O}_{24}\cdot 4\text{H}_2\text{O}$ and 0.64 g of $(\text{NH}_4)_6[\text{H}_2\text{W}_{12}\text{O}_{40}]\cdot 6\text{H}_2\text{O}$ being dissolved in 120 mL of deionized water, and solution B was obtained with 3.28 g of $\text{VOSO}_4\cdot 5.4\text{H}_2\text{O}$ being dissolved in another 120 mL of deionized water. Secondly, solution B was poured into solution A under stirring conditions. The other synthetic procedures are the same as described above. Hydrothermal reaction was conducted at 448 K for 48 h. As-synthesized material was treated with oxalic acid solution (10 mmol L^{-1}) at 60°C for two times. The treatment was kept for 30 min every time.

Amorphous $\text{Mo}_3\text{VW}_{0.25}\text{O}_x$ (denoted as Amor-MoVWO) was also synthesized with the same precursor with twice high concentration and by the same procedure but without Teflon sheet.

For synthesizing trigonal $\text{Mo}_3\text{VW}_{0.25}\text{O}_x$ (denoted as Tri-MoVWO), ethylammonium trimolybdate [EATM, $(\text{CH}_3\text{CH}_2\text{NH}_3)_2\text{Mo}_3\text{O}_{10}$] was used as a Mo source instead of $(\text{NH}_4)_6\text{Mo}_7\text{O}_{24}\cdot 4\text{H}_2\text{O}$ used to synthesizing Tri-MoVO. EATM was first prepared as follows. 21.594 g of MoO_3 (Kanto; 0.150 mol) was dissolved in 28.0 mL of 70 % ethylamine solution (ethylamine: 0.300 mol, Wako) diluted with 28.0 mL of distilled water. The reason for the addition of distilled water is to reduce the viscosity of the mixed solutions. After being completely dissolved, the solution was evaporated under vacuum condition at 70°C and then solid powder was obtained. The powder was dried in air at 80°C overnight.

8.995 g of EATM (Mo: 50 mmol) was dissolved in 120 mL of distilled water. Separately, an aqueous solution of VOSO_4 was prepared by dissolving 3.29 g of hydrated VOSO_4 in 120 mL of distilled water. The two solutions were mixed at ambient temperature and stirred for 10 min before the addition of 2.40 g of $(\text{NH}_4)_6[\text{H}_2\text{W}_{12}\text{O}_{40}]\cdot n\text{H}_2\text{O}$ (W: 9.1 mmol). Then, the obtained mixed solution was introduced into an autoclave with a 300 mL-Teflon inner vessel and $4,000 \text{ cm}^2$ of Teflon thin sheet to occupy about half of Teflon inner vessel space. After being introduced, N_2 was fed into the solution in the tube in order to remove residual oxygen. At this stage, the pH of the solution was 2.4. Then the hydrothermal reaction was started at 175°C

for 48 h under static conditions in an electric oven. Gray solids formed on the Teflon sheet were separated by filtration, washed with distilled water, and dried in air at 80 °C overnight. Purification with oxalic acid was conducted to the obtained solids in order to remove amorphous type materials contained as an impurity. To 25 mL aqueous solution (0.4 mol L⁻¹, 60 °C) of oxalic acid (Wako), 1 g of the dried material was added and stirred for 30 min, then washed with 500 mL of distilled water after filtration.

2.3 Characterization

X-ray diffraction patterns were measured by using an X-ray diffractometer (RINT-Ultima III, Rigaku) with Cu K α to study their crystalline structure. Scanning electron microscopy (SEM) images were taken using an electron microscope (JSM-6360LA, JEOL). Scanning transmission electron microscope (STEM) image and metal element mapping of Mo, W, and V were obtained on an HD-2000 (HITACHI). The chemical compositions of the catalysts determined by ICP-AES method with a VISTA-PRO apparatus (Varian). N₂ adsorption–desorption isotherms measurements were carried out on an auto-adsorption system (BELSORP MAX, Nippon BELL) using *t*-plot method to obtain the external surface area and micropore volume. Before measurements, the samples were treated at 400 °C for 2 h under air and outgassed at 300 °C under vacuum for 2 h.

2.4 Gas-Phase Catalytic Oxidation

Catalytic oxidation of acrolein to acrylic acid was carried out using a fixed bed stainless tubular reactor at an atmospheric pressure. The amount of catalyst was 0.25 g (with 2.5 g of carborundum) or 0.125 g (with 2.5 g of carborundum). The catalysts were firstly heated from room temperature to 400 °C under N₂ of 50 mL min⁻¹ and were kept for 2 h at this temperature. Then the temperature was decreased to a desired reaction temperature. The reaction was conducted under two different water pressure. With higher water pressure, the feed composition was acrolein/O₂/H₂O/N₂ + He = 2.3/7.4/25.2/65.1 (mol%), and total flow rate was 107.6 mL min⁻¹. With lower water pressure, the fed amount of H₂O was reduced to 12.6 mol%, and the total flow rate was kept constant with the increase of N₂ as balance gas. The quantitative analysis was carried out using three on-line gas chromatographs with columns of Molecular Sieve 13X, Gaskuropack 54, and Porapak Q. Blank runs showed that no reaction took place without catalysts under the experimental conditions. Carbon balance was always ca. 96–100 %.

3 Results and Discussion

3.1 Acrolein Oxidation Over Four Different Pure Crystalline Mo₃VO_x Catalysts and W-Containing Analogues

Gas-phase selective oxidation of acrolein to acrylic acid was conducted over crystalline Mo₃VO_x catalysts with four different crystal structure phases and W-containing Mo₃VO_x catalysts. The results are summarized in Table 2 with structural parameters and catalytic performance changes as the function of reaction temperature are illustrated in Fig. 2. As we have already reported [13, 20], there is a large difference in the performance of these four Mo₃VO_x catalysts with the different crystal phases. Tri-MoVO was the most active catalyst, giving appreciable conversion of acrolein even at 175 °C and achieving almost 100 % conversion at 215 °C with high acrylic acid selectivity more than 97 %. This catalytic performance is surprisingly high and totally not comparable to other reported data [4, 6, 7]. This catalyst is followed by Orth-MoVO in terms of the conversion as shown in Fig. 2. By taking it into account that the external surface area of Tri-MoVO is about three times higher than that of Orth-MoVO (Table 2), the activity of Orth-MoVO giving 68 % at 215 °C is reasonable and thus it should be concluded that both Tri-MoVO and Orth-MoVO assume a similar intrinsic catalytic property for the acrolein selective oxidation. Amor-MoVO, on the other hand, was less active and gave only 25 % conversion at 223 °C which is a little higher than those applied to Tri-MoVO and Orth-MoVO. To reach 95 % conversion with the Amor-MoVO catalyst, the reaction temperature needed to be elevated to nearly 300 °C, as can be seen in Fig. 2. The temperature necessary for 95 % conversion is approximately 90 °C higher than that for Tri-MoVO catalyst. Tetra-MoVO which has often been examined as an active phase for the reaction [21] was found almost inactive under the temperature condition below 250 °C.

In order to understand the observed clear relationship between crystal structure and catalytic activity, various determining factors of acrolein oxidation activity should be considered. The four catalysts having different crystal structures were carefully prepared phase-purely, so that any effects by impurity materials can be ruled out. One may notice that the Mo/V values of Orth-MoVO and Tri-MoVO are slightly higher than those of Amor-MoVO and Tetra-MoVO as listed in Table 2. At present, we consider that this is a structure requisite and such difference may not cause big difference in the activity. External surface area should be a direct effect on the conversion as already stated above in the activity comparison between Orth-MoVO and Tri-MoVO catalysts. In the case of a comparison between

Table 2 Structural information of Mo₃VO_x catalysts and W-containing analogues, and their catalytic performance in acrolein oxidation

Catalyst	Elemental composition (%) ^a			Lattice parameter (nm)			External surface area (m ² /g) ^b	Reac. temp. (°C)	Acrolein conv. (%) ^c	Selectivity (%)		
	Mo	V	W	<i>a</i>	<i>b</i>	<i>c</i>				AA ^d	AcOH ^e	CO _x
Orth-MoVO	75.6	24.4	0	2.108	2.657	0.3997	6.2	215	68.2	98.1	0.1	1.8
Orth-MoVWO	69.8	25.5	4.7	2.102	2.648	0.3994	28.9	215	91.1	97.1	0.3	2.6
Tri-MoVO	75.8	24.2	0	2.127		0.4011	16.3	215	99.3	97.3	0.3	2.4
Tri-MoVWO	74.1	20.7	5.2	2.129		0.3996	18.0	215	53.9	97.5	0.2	2.3
Amor-MoVO	72.2	27.8	0	–	–	0.3996	3.0	223	25.2	98.4	0.0	1.6
Amor-MoVWO	71.9	22.3	5.8	–	–	0.3994	3.4	223	16.0	98.8	0.0	1.2

^a Determined by ICP-AES^b Measured by N₂adsorption and determined by *t*-plot^c Reaction conditions: 107.6 mL min⁻¹ of reactant gas with the composition of acrolein/O₂/H₂O/N₂ + He = 2.3/7.4/25.2/65.1(mol%) was fed in 0.25 g of catalysts diluted with carborundum(2.5 g)^d Acrylic acid^e Acetic acid

Orth-MoVO and Amor-MoVO catalysts, however, twice amount of Amor-MoVO to compensate the external surface area of Orth-MoVO could not cover the reaction temperature difference of about 30 °C between Orth-MoVO and Amor-MoVO (Fig. 2). There are no ways to compensate in

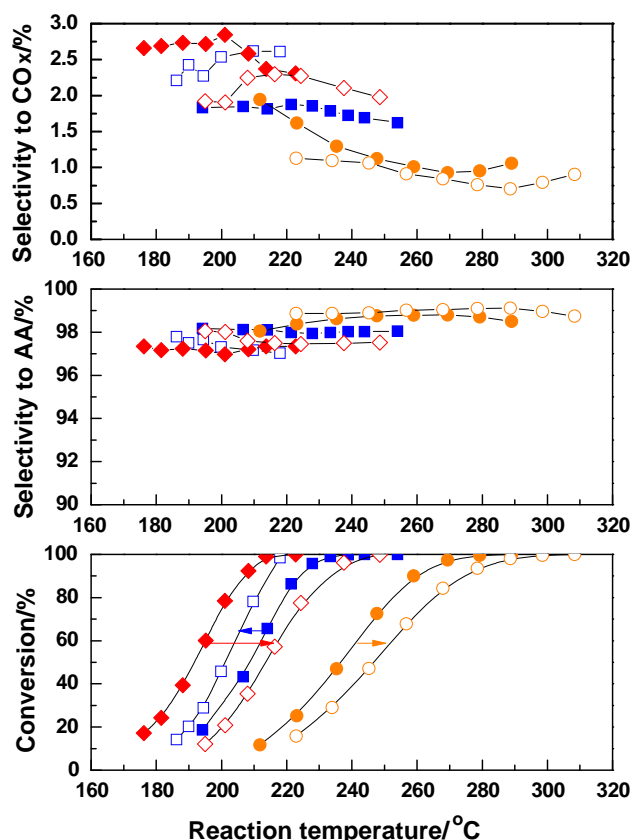


Fig. 2 Acrolein oxidation over Orth-MoVO (filled square), Orth-MoVWO (square), Tri-MoVO (filled diamond), Tri-MoVWO (diamond), Amor-MoVO (filled circle), and Amor-MoVWO (circle) catalysts under H₂O: 25.2 mol%

the case of Tetra-MoVO. These may allow us to consider the activity-determining factor on the basis of crystal structure straightforwardly. Tri-MoVO, Orth-MoVO, and Amor-MoVO all possess heptagonal channels and hexagonal channels in their structures, whereas Tetra-MoVO does not. This simple fact can suggest that the catalytically active sites could exist around the heptagonal channels and the hexagonal channels. Then next it has to be explained why Amor-MoVO was inferior to Tri-MoVO and Orth-MoVO. From structural point of view, Amor-MoVO has the disordered arrangement of the pentagonal units in *a*-*b* plane, so that the number of the heptagonal channels and the hexagonal channels should be decreased. This causes lower number of the active sites associated with the heptagonal channels and the hexagonal channels than those of Tri-MoVO and Orth-MoVO. This could be the reason why Amor-MoVO had the lower catalytic activity than the other two catalysts.

The above discussion may suggest that the acrolein oxidation mainly takes place on the surface of the *a*-*b* plane of the catalysts where the heptagonal channels and the hexagonal channels locate and not on the side surface of the rod-shaped catalysts. In order to clarify which contributes more to the oxidation activity, the side surface or the section surface of the rod-shaped crystals, unground Orth-MoVO catalyst was tested for the selective oxidation of acrolein. The acrylic acid selectivity (96 %) of the unground catalyst was almost the same with the ground catalyst but the acrolein conversion (9.8 %) was far less compared with the ground catalyst (37.8 %) in spite of similar external surface areas (ground; 6.2 m² g⁻¹, unground; 4.0 m² g⁻¹). This fact clearly indicates that the section surface exposed by the grind treatment is far more active for the selective oxidation of acrolein than the side surface of the rod-shaped crystals. As a consequence,

acrolein oxidation to acrylic acid can proceed over the external surface of the rod-shaped crystals but dominantly on the section surface of the rod-shaped crystals.

3.2 Acrolein Oxidation Over W-Containing Mo_3VO_x Catalysts

We succeeded in introducing W in Mo_3VO_x with keeping the orthorhombic, trigonal, and amorphous structures by the preparative procedure shown in the experimental section. The W contents in Orth-MoVWO, Tri-MoVWO, and Amor-MoVWO are determined by ICP-AES method to be 4.7, 5.2, and 5.8 % respectively, as shown in Table 2, manifesting that W was successfully introduced into the synthesized materials. The crystalline structure of the catalysts was studied by XRD characterization. Diffraction peaks at 22.2° and 45.4° was observed for all the catalysts, which indicates that the present catalysts are a kind of layered-type material with a layer lattice distance of about 0.4 nm (Table 2). These two peaks were ascribed to (001) and (002) plane reflections. Besides these two peaks, diffraction peaks corresponding to the orthorhombic crystal system emerged in the pattern of Orth-MoVWO at 6.6° , 7.9° , 9.0° , and 27.3° ($\text{Cu K}\alpha$), which were ascribed to the plane of (020), (120), (210), and (630), respectively. These diffraction peaks at the low angle region less than 10° indicates that Orth-MoVWO was well crystallized along *a*- and *b*-axis as well as *c*-axis. Similarly, diffraction peaks corresponding to the trigonal crystal system emerged in the pattern of Tri-MoVWO at 4.6° , 8.2° , and 9.5° ($\text{Cu K}\alpha$), which were ascribed to the plane of (100), (110), and (200), respectively. These are the most distinct difference compared with the amorphous samples. Amor-MoVWO showed only a broad peak below 10° with sharp peaks ascribed to (001) and (002) plane reflections. These data satisfactory support the introduction of W in the lattice of orthorhombic and amorphous structures. Further details on the state of W in Orth-MoVWO and Amor-MoVWO will be reported elsewhere.

The morphology analyses of the present catalysts were conducted through SEM characterization. Orth-MoVWO presented as rod-shaped crystals, which is similar to that of Orth-MoVO. The average diameter of Orth-MoVO was about 300 nm, while that of Orth-MoVWO was apparently smaller to be less than 200 nm. Since the surface area of Orth-MoVWO was quit high, the actual diameter of Orth-MoVWO rods should be much smaller, which is likely caused by the rod-segregation of the rod-shaped crystals due to lattice contraction generated by the incorporation of W. Accompanying the decrease of the rod diameter and the length, the external surface area of Orth-MoVWO reached $28.9 \text{ m}^2 \text{ g}^{-1}$, which is 4.8 times as high as that of Orth-MoVO ($6.2 \text{ m}^2 \text{ g}^{-1}$, Table 2). The rod shape was also

observed by STEM characterization in Tri-MoVWO and Amor-MoVWO. However, the introduction of W in Tri-MoVO and Amor-MoVO had no clear effect on the external surface area and the rod size did not change obviously by the introduction of W.

Table 2 lists the acrolein conversion and product selectivities over three W-containing catalysts, Orth-MoVWO, Tri-MoVWO, and Amor-MoVWO. It can be clearly seen that the catalytic activity of Orth-MoVWO is higher than that of Orth-MoVO and higher than those of Tri-MoVWO and Amor-MoVWO. Total conversion of acrolein could be realized at much lower temperature when Orth-MoVWO is used, which is comparable to Tri-MoVO (Table 2). For example, 91 % conversion of acrolein could be obtained at the temperature of 215°C over Orth-MoVWO catalyst, while 68 % conversion was only obtained at the same temperature of 215°C over Orth-MoVO catalyst. On the contrary, the addition of W introduction into the trigonal and amorphous type catalysts caused a negative effect on the conversion as can be seen in Fig. 2. Nevertheless, nearly 100 % conversion of acrolein

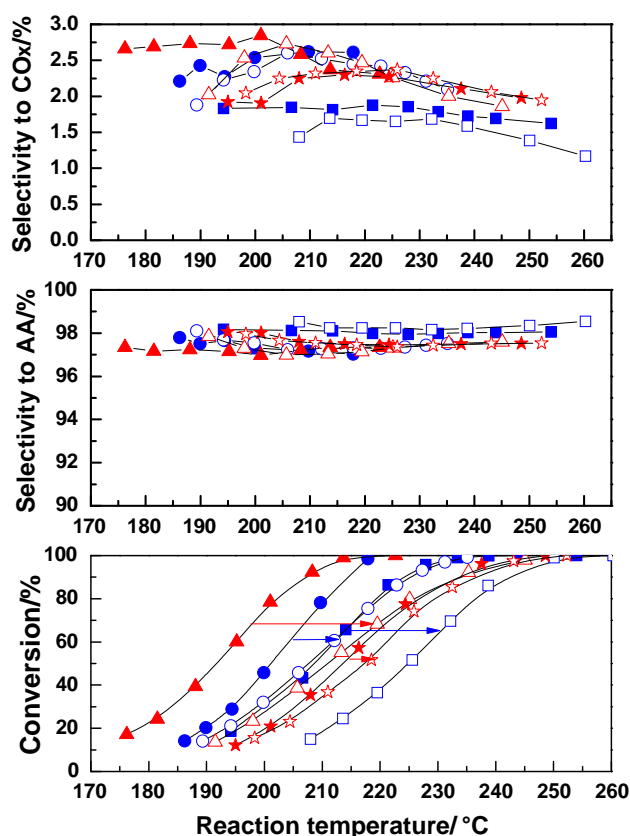


Fig. 3 Water-addition effect on acrolein oxidation over Orth-MoVO (H_2O : filled square: 25.2 mol%, square: 12.6 mol%), Orth-MoVWO (H_2O : filled circle: 25.2 mol%, circle: 12.6 mol%), Tri-MoVO (H_2O : filled triangle: 25.2 mol%, triangle: 12.6 mol%), and Tri-MoVWO (H_2O : filled star: 25.2 mol%, star: 12.6 mol%) catalysts (0.25 g)

could be obtained at the temperature of 280 °C over Amor-MoVWO with a bit higher selectivity to acrylic acid than that over Orth-MoVWO and Tri-MoVWO catalysts.

The extremely high catalytic activity was achieved over Orth-MoVWO catalyst compared to those over Tri-MoVWO and Amor-MoVWO catalysts. This is obviously due to the largely increased surface area by the introduction of W, but at the same time this fact suggests that the introduction of W the introduction may affect the orthorhombic structure material specifically. In fact, the introduction of W showed the clear negative promotion effect on the catalytic activity for the trigonal and amorphous system. We consider at the present stage that only when W is incorporated into the orthorhombic crystalline structure with bringing about the increase of active surface area and structural strain, excellent catalytic activity can be realized at lower temperature. On the contrary, the negative effect of W addition observed in the Tri-MoVO is presumably due to structural stabilization by W in the structure with decreasing structural strain and thus active surface area.

3.3 Effect of Water on the Acrolein Oxidation Over W-Containing Mo₃VO_x Catalysts

In order to understand the addition effect of W from other aspect, we tested water addition effect on the acrolein oxidation. Although the promotion mechanism of added water in reactant feed is still not clear, it is well accepted

that water is able to act as an important promoter for the conversion of acrolein. For example, with Mo/V/W-mixed oxides as catalyst, the conversion of acrolein decreased with the reduction of fed amount of water at lower temperature.

Figure 3 illustrates the acrolein conversion and product selectivities as the function of the reaction temperature over four catalysts, Orth-MoVWO, Orth-MoVO, Tri-MoVWO, Tri-MoVO, under two different water feed concentrations. Table 3 also summarizes water feed effect on the conversion and the selectivity over Orth-MoVWO, Orth-MoVO, Tri-MoVWO, Tri-MoVO, Amor-MoVWO, and Amor-MoVO catalysts in different catalyst weights. As expected, the acrolein conversion over Orth-MoVO and Tri-MoVO catalysts appreciably decreased when the water concentration decreased to half. Higher reaction temperature is required when the water concentration is lower (see arrows in Fig. 3). On the other hand, the conversion of acrolein over the W-containing catalysts, Orth-MoVWO and Tri-MoVWO, showed only small decreases even when the fed amount of water decreased by half. These results clearly demonstrate that the role of W in the oxidation of acrolein over Mo–V–O catalysts is to moderate the effect of water.

It should be noted in Table 3 that different from the other two catalysts, no clear effect of W on the water addition effect was observed when the catalysts are amorphous. We speculate that the W effect can appear only when W is incorporated into the framework of the

Table 3 Water-addition effect on acrolein oxidation over Orth-MoVO, Orth-MoVWO, Tri-MoVO, Tri-MoVWO, Amor-MoVO, Amor-MoVWO catalysts

Catalyst	Catalyst weight (g)	Water content (mol%) ^a	Reac. temp. (°C)	Acrolein conv. (%)	Selectivity (%)		
					AA ^b	AcOH ^c	CO _x
Orth-MoVO	0.25	25.2 ^a	215	68.2	98.1	0.1	1.8
Orth-MoVO	0.25	12.6 ^b	215	27.0	98.2	0.1	1.7
Orth-MoVWO	0.15	25.2	215	73.6	97.5	0.2	2.3
Orth-MoVWO	0.15	12.6	215	58.9	97.6	0.2	2.2
Tri-MoVO	0.10	25.2	215	50.7	98.1	0.1	1.8
Tri-MoVO	0.10	12.6	215	29.2	97.9	0.1	2.0
Tri-MoVWO	0.25	25.2	215	53.9	97.5	0.2	2.3
Tri-MoVWO	0.25	12.6	215	44.9	97.5	0.2	2.3
Amor-MoVO	0.25	25.2	245	67.4	98.7	0.1	1.2
Amor-MoVO	0.25	12.6	245	58.8	98.8	0.1	1.1
Amor-MoVWO	0.25	25.2	245	47.2	98.9	0.1	1.0
Amor-MoVWO	0.25	12.6	245	45.2	99.0	0.1	0.9

^a Reaction conditions(H₂O: 25.2 mol%): 107.6 mL min⁻¹ of reactant gas with the composition of acrolein/O₂/H₂O/N₂ + He = 2.3/7.4/25.2/65.1(mol%) was fed in 0.25 g of catalysts diluted with carborundum(2.5 g); reaction conditions(H₂O: 12.6 mol%): 107.6 mL min⁻¹ of reactant gas with the composition of acrolein/O₂/H₂O/N₂ + He = 2.3/7.4/12.6/77.7(mol%)

^b Acrylic acid

^c Acetic acid

orthorhombic or the trigonal crystalline structure. Obviously further experiments are necessary, which are on going.

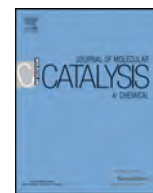
4 Conclusions

The present work on acrolein oxidation catalysts based on $\text{Mo(W)}_3\text{VO}_x$ was conducted in three different approaches; first, structure–activity relationship by using different crystal phase materials as catalysts, second, effect of W addition effects in Mo_3VO_x on the conversion and third, effect of water addition depending on the presence of W in the catalyst structures. By combining all collected data in these three approaches, it was concluded that the network of the pentagonal units forming the heptagonal and hexagonal channels is indispensable for creating active sites on the surface the Mo_3VO_x catalyst and that the *a-b* plane with the heptagonal and hexagonal channels on the surface is responsible for acrolein oxidation activity. This active surface formation is assisted by the W-addition in the case of orthorhombic Mo_3VO_x catalyst. It was clearly demonstrated that the active surface containing W can work even under low partial pressure of water in the reactant feed.

Many years have passed since the discovery of active Mo and V-based oxide catalyst for acrolein selective oxidation to acrylic acid. Now, the present work proposes that crystalline $\text{Mo(W)}_3\text{VO}_x$ with orthorhombic or trigonal structure is the real active phase for the reaction.

References

1. Punniyamurthy T, Velusamy S, Iqbal J (2005) Chem Rev 105:2329–2364
2. Centi G, Cavani F, Trifiro F, (2001) Selective oxidation by heterogeneous catalysis. In: Twigg M. T, Spencer M. S. Kluwer Academic/Plenum Publishers, New York, 2001
3. Hodnett BK (2000) Heterogeneous Catalytic Oxidation. Wiley, New York
4. Nojiri N, Sakai Y, Watanabe Y (1995) Catal Rev Sci Eng 31:145–178
5. Andrushkevich TV (1993) Catal Rev Sci Eng 35:213–259
6. Dieterle A, Mestl G, Jager J, Uchida Y, Hibst H, Schlogl R (2001) J Mol Catal A 174:169–185
7. Vogel H, Bohling R, Hibst H (1999) Catal Lett 62:71–78
8. Ushikubo T, Oshima K, Kayou A, Umezawa T, Kiyono K, Sawaki I (1993) Mitsubishi Chem. Corp Patent EP 529853
9. Ushikubo T, Oshima K, Kayou A, Vaarkamp M, Hatano M (1997) J Catal 169:394–396
10. Tsuji H, Koyasu Y (2002) J Am Chem Soc 124:5608–5609
11. Ueda W (2013) J Jpn Petrol Inst 56:122–132
12. Konya T, Katou T, Murayama T, Ishikawa S, Sadakane M, Buttrey D, Ueda W (2013) Catal Sci Technol 3:380–387
13. Chen C, Nakatani K, Murayama T, Ueda W (2013) ChemCat-Chem 5:2869–2873
14. Pyrz WD, Blom DA, Sadakane M, Kodato K, Ueda W, Vogt T, Buttrey DJ (2010) Proc Natl Acad Sci USA 107:6152–6157
15. Pyrz WD, Blom DA, Sadakane M, Kodato K, Ueda W, Vogt T, Buttrey DJ (2010) Chem Mater 22:2033–2040
16. Sadakane M, Watanabe N, Katou T, Nodasaka Y, Ueda W (2007) Angew Chem Int Ed 46:1493–1496
17. Sadakane M, Kodato K, Kuranishi T, Nodasaka Y, Sugawara K, Sakaguchi N, Nagai T, Matsui Y, Ueda W (2008) Angew Chem Int Ed 47:2493–2496
18. Sadakane M, Yamagata K, Kodato K, Endo K, Toriumi K, Ozawa Y, Ozeki T, Nagai T, Matsui Y, Sakaguchi N, Pyrz WD, Buttrey DJ, Blom DA, Vogt T, Ueda W (2009) Angew Chem Int Ed 48:3782–3786
19. Sadakane M, Endo K, Kodato K, Ishikawa S, Murayama T, Ueda W (2013) Eur J Inorg Chem 10–11:1731–1736
20. Ishikawa S, Yi X, Murayama T, Ueda W (2014) Appl Catal A-Gen 474:10–17
21. Mestl G (2006) Top Catal 38:69–82



Hydrogen-transfer dehydration between alcohols over V_2O_3 and MoO_2 catalysts for the formation of corresponding alkanes and aldehydes



Yoichi Nakamura, Toru Murayama, Wataru Ueda*

Catalysis Research Center, Hokkaido University, N-21, W-10, Sapporo 001-0021, Japan

ARTICLE INFO

Article history:

Received 14 April 2014
Received in revised form 5 July 2014
Accepted 5 July 2014
Available online 14 July 2014

Keywords:

Alcohols
Alkanes
 V_2O_3
 MoO_2
Hydrogen-transfer dehydration

ABSTRACT

Conversion of alcohols in a gas phase under N_2 flow at 573 K was carried out using V_2O_3 and MoO_2 oxides with low valence oxidation states. It was found in the reaction of ethanol that equimolar amounts of ethane and acetaldehyde were catalytically formed as the main products over the oxides. Bi-products were small amounts of ethene and C4 compounds. Reactions of other alcohols (methanol, 1-propanol and 2-propanol) over the V_2O_3 and MoO_2 catalysts also led to the equimolar formation of corresponding alkanes and aldehydes or ketone. It was confirmed by XRD and XPS that the low valence states of V_2O_3 and MoO_2 were unchanged during the reactions and the oxides stably worked as the catalyst. Based on catalytic reaction results obtained under various reaction conditions (reaction temperature, contact time, introduction of H_2 and C_2H_4 into reaction stream) and on experiments of kinetic isotope effects on the ethanol reaction, a reaction scheme is proposed, in which hydrogen transfer reaction between two alcohol molecules adsorbed on metal- O^{2-} -metal sites on the surface of V_2O_3 and MoO_2 catalysts takes place via 6-membered transition state, followed by dehydration.

© 2014 Elsevier B.V. All rights reserved.

1. Introduction

Vanadium oxides and molybdenum oxides are one of the most frequently used catalytic materials in industrial chemical processes, such as partial oxidations of hydrocarbons and alcohols, dehydration of alcohols, de- NO_x reaction and so forth. In most of the cases of these catalytic reactions, the oxidation states of V and Mo under working conditions are either the highest or slightly reduced, but much reduced states like V^{3+} and Mo^{4+} are quite rare in any metal oxide forms under catalytically working states. Recently, we found that ethanol conversion can catalytically proceed over highly reduced vanadium oxides and molybdenum oxides, particularly over V_2O_3 and MoO_2 oxides and that the reaction selectively produces ethane and acetaldehyde in equimolar amounts [1]. This reaction itself and catalytic function of low valence V and Mo in metal oxides seem quite unique in catalysis and interesting in terms of reaction mechanism.

Formation of alkanes from aliphatic alcohols has been little studied in contrast to extensive studies of catalytic dehydration and dehydrogenation of alcohols. A few research results, however,

have been reported for the formation so far. They showed that the formation of alkanes from corresponding alcohols mostly occurs via either direct hydrogenation of the alcohols or alkenes formed by dehydration of the alcohols with hydrogen that was formed by dehydrogenation of the alcohols [2–4]. Cd–Cr–O [2] and 12-molybdophosphate [3] catalysts were reported to form ethane from ethanol via hydrogenation of ethylene, on the basis of that the selectivity to ethane increased with decrease of the selectivity to ethylene. Lobo et al. also showed that propane could be formed via hydrogenation of 1-propanol over Pt supported catalysts (Pt/TiO₂, CeO₂, Al₂O₃) [4].

There seems other possible formation mechanisms of alkanes from alcohols. For example, Mohamed et al. reported that ethane and methane were formed as major products from ethanol over Fe ion-exchanged mordenite. They explained that the preferential formation of alkanes was due to the O-abstracting affinity of Fe^{3+} [5]. Ochoa et al. also reported that ethane, acetaldehyde and water were observed at low temperature on TPD profiles in the ethanol reaction over ferrite catalyst [6]. They proposed that ethane was formed via disproportionation of ethanol or coupling of methyl species formed by dissociation of acetaldehyde. Jin et al. found that butane was formed from 1-, 2-butanols over Fe_2O_3 , Fe_2O_3 -ZrO₂ and Fe_2O_3 -ZnO. On the basis of hydrogen effect over Fe_2O_3 -ZrO₂, they concluded that formation of butane from butanol was via

* Corresponding author. Tel.: +81 0454815661.

E-mail addresses: ueda@cat.hokudai.ac.jp, uedaw@kanagawa-u.ac.jp (W. Ueda).

nucleophilic substitution (S_N2) of hydroxyl group of alcohols by a hydride ion [7].

In the case of aromatic alcohol reaction like benzyl alcohol, there are several research reports on equimolar formation of toluene and benzyl aldehyde. Jayamani et al. and Ganesan et al. reported that toluene and benzaldehyde were produced in an equal amount from benzyl alcohol over alumina catalyst [8–10] and Ganesan et al. proposed that the disproportionation of di-benzyl ether is a pathway to form the toluene and benzaldehyde in a 1:1 ratio in addition to a direct disproportionation of benzyl alcohol. Moreover, they also proposed that the reaction mechanism is a hydride transfer reaction from one surface benzyloxy species to a neighboring one. Mathew et al. reported that the conversion of benzyl alcohol to toluene and benzaldehyde occurred over molybdenum supported $Al(OH)_3$ [11,12]. $AB'B'O_3$ ($A = Ba, B = Pb, Ce, Ti$ and $B' = Bi, Cu, Sb$)-type perovskite oxides [13] and Au–Pd nanoparticle [14,15] are also found active for the reaction. In the case of the former, hydrogenation of benzyl alcohol to form toluene was proposed, while in the latter Hutching's group proposed a disproportionation of benzyl alcohol as a main pathway to form toluene and benzaldehyde since Au–Pd led to the equimolar formation of toluene and benzaldehyde in benzyl alcohol reaction under He.

Among the catalytic systems mentioned above, 12-molybdophosphate [3], Pt-supported catalysts [4] are the unique cases that simultaneously produced equivalent amounts of alkanes and aldehydes from aliphatic alcohols, although some other products were formed along with them and the proposed reaction mechanisms are still controversial. In addition, it seems have been considered that higher oxidation states of metal elements in the case of oxide catalysts favor the alkane formation. Meanwhile, our results reported recently using vanadium oxides and molybdenum oxides as catalysts for ethanol conversion evidently showed that equivalent amounts of alkanes and aldehydes were formed from corresponding alcohols as main products without H_2 formation and clarified that lower oxidation states of metal elements in these oxide catalysts are active for the equimolar formation [1]. Apparently vanadium oxides and molybdenum oxides in low valence states are now one of the representative catalysts for equimolar formation of alkanes and aldehydes from corresponding alcohols. In order to further confirm the simultaneous formation of equivalent amounts of alkanes and aldehydes and to elucidate a plausible reaction mechanism for the reaction, we conducted the reaction under different conditions and kinetic analysis. Here in this report, an intermolecular hydrogen-transfer dehydration of aliphatic alcohols will be described based on observed results.

2. Experimental

2.1. Catalyst preparation

V_2O_5 was prepared by the calcination of NH_4VO_3 (99% Wako Pure Chemical Industries) at 773 K for 2 h in air. V_2O_3 was then prepared by the reduction of the prepared V_2O_5 (0.3 g) in a tubular furnace under a H_2 stream (30 ml/min) at 773 K for 2 h. The reduced samples were then exposed to air when they cooled at room temperature before use for catalysis. MoO_3 was prepared by the calcination of $(NH_4)_6Mo_7O_{24}$ (99% Wako Pure Chemical Industries) at 773 K for 2 h in air. MoO_2 was obtained by the reduction of the obtained MoO_3 (0.3 g) in a tubular furnace under a H_2 stream (30 ml/min) at 773 K for 2 h. Subsequently, the reduced molybdenum oxide samples were exposed to air once after they cooled at room temperature. Then the samples were treated again in a tubular furnace under a 5% H_2 /Ar (30 ml/min) stream at 773 K for 2 h. Finally the reduced sample was cooled to room temperature,

followed by an exposure in air. Thus obtained MoO_2 was provided for catalysis.

2.2. Catalytic test

Catalytic reactions were carried out in a continuous flow fixed bed reactor (Pyrex). A similar volume mixture of the catalyst (0.03–1.5 g) and SiO_2 sands (1.3–2.6 g) as a diluent, which showed no catalytic activity in the alcohol reaction, was placed in the reactor and heated to a desired reaction temperature (533–633 K) under a N_2 flow (21.4 ml/min). Then, the catalytic reaction was started by the introduction of ethanol (99.5%, Wako Pure Chemical Industries) with N_2 carrier into the reactor. The total flow rate of the reactant gas was kept constant (21.4 ml/min) for all the reactions. Ethanol concentration was changed from 1.8–7.5 mol%. The concentrations of methanol (99.8%, Wako Pure Chemical Industries), 1-propanol (99.5%, Wako Pure Chemical Industries) and 2-propanol (99.7%, Wako Pure Chemical Industries) were 2.7, 1.7, and 4.3 mol%, respectively. For study on kinetic isotopic effect, two types of isotope-labeled ethanol, CH_3CH_2OD (99%, Wako Pure Chemical Industries) and CD_3CD_2OD (99%, Wako Pure Chemical Industries), were used as reactant.

The reaction products were analyzed by gas chromatography. Two gas chromatographs, Shimadzu GC-8A equipped with a thermal conductivity detector and a packed column Porapack-QS and GL Science GC-380 equipped with a thermal conductivity detector and a flame-ionization detector and two packed columns, Unicarbon and molecular sieve 5A, were used. N_2 gas was used as internal standard for quantitative GC analysis. Alcohol conversion, the product selectivity, and carbon balance were defined as the following Eqs. (1)–(3), respectively.

$$\text{Conversion}(\%) = \frac{X}{X_0} \times 100 \quad (1)$$

$$\text{Selectivity}(\%) = \frac{A}{\bar{X}} \times 100 \quad (2)$$

$$\text{Carbon balance} = \text{Selectivity}_{\text{total}} \quad (3)$$

where X_0 , X , and A refer to the amount of alcohol feed, the amount of reacted, and amounts of products, respectively.

2.3. Catalyst characterization

Powder X-ray diffraction (XRD) measurements were performed with a RINT Ultima+ diffractometer (Rigaku) with $Cu-K\alpha$ radiation ($\lambda = 0.1540$ nm) and X-ray power of 40 kV/20 mA. Specific surface areas were measured by the BET method from N_2 adsorption at 77 K using a BELSORP MAX (BEL Japan Inc.). XPS measurements were performed using a JPS-9010 MC (JEOL). An $Mg-K\alpha$ radiation source (1253.3 eV) operated at a power of 100 W (10 kV, 10 mA) was employed. Vacuum in the analysis chamber was $<5 \times 10^{-6}$ during all measurements. Pass energy of 30 eV was used to acquire all survey scans. The binding energy (BE) was corrected for surface charging by taking the C1s peak of carbon as a reference at 284.7 eV. Data were analyzed using the SpecSurf including Shirley background subtraction and fitting procedure. Quantification of the components for the surface oxidation state of vanadium and molybdenum was made using the SpecSurf. The binding energies of 517.2, 516.0 and 515.2 eV were attributed to V^{5+} , V^{4+} and V^{3+} , respectively in the V_2O_3 [16,17], and Mo^{6+} , Mo^{5+} and Mo^{4+} oxidation states ($Mo3d_{3/2}$ and $Mo3d_{5/2}$) were identified at 235.8, 234.7 and 232.7 eV, and 232.2, 231.9 and 229.1 eV, respectively [18,19].

Table 1Ethanol reaction in the presence of H₂ and C₂H₄ over V₂O₃ and MoO₂ catalysts.

Catalysts	S _{BET} (m ² /g _{cat}) ^a	Condition	Conversion (%)	Selectivity (%)			
				C ₂ H ₄	C ₂ H ₆	CH ₃ CHO	Others ^f
V ₂ O ₃	17	N ₂ ^b	13.4	2.0	42.7	43.6	11.7
		With H ₂ ^c	16.5	1.1	45.7	42.4	10.8
		With C ₂ H ₄ ^d	16.8	1.3 ^e	45.8	41.5	11.4
MoO ₂	6	N ₂ ^b	41.0	1.2	47.4	47.6	3.8
		With H ₂ ^c	38.0	1.1	44.4	45.9	8.6
		With C ₂ H ₄ ^d	36.8	4.3 ^e	43.4	45.5	6.8

Reaction condition: reaction temperature 573 K, catalyst 0.15 g, 5 h time on stream.

^a Specific surface area of the catalysts measured by N₂ adsorption -196 °C.^b N₂ 21 ml/min, ethanol 0.39 ml/min.^c N₂ 20 ml/min, C₂H₅OH 0.39 ml/min, H₂ 1.0 ml/min.^d N₂ 20 ml/min, C₂H₅OH 0.39 ml/min, C₂H₄ 1.0 ml/min.^e Obtained by subtraction of the concentration of ethylene introduced into the feed from the concentration of ethylene in the products.^f Others are attributed to C₄ compounds mainly.

3. Results and discussion

3.1. Catalytic activity of V₂O₃ and MoO₂ in ethanol reaction

Over the V₂O₃ catalyst and the MoO₂ catalyst, we observed the formation of ethane and acetaldehyde as the main products in the conversion of ethanol. Main by-product detected was ethylene and trace amounts of C₄ compounds such as ethyl acetate, *n*-butanol, crotonaldehyde and 2-butanone were also detected. We also observed heavy products in the outlet of the reactor, so that the carbon balances were around 90% in the ethanol reaction. The product selectivity of these products including C₄ compounds was calculated on the basis of the carbon balances and is listed as others in Tables 1 and 3. No formations of diethyl ether and H₂ were observed. Ethylene can be simply formed by dehydration and the C₄ by-products can be formed *via* condensation reaction of ethanol.

Fig. 1 shows the conversion of ethanol and the selectivity to products as a function of time on stream on the V₂O₃ and MoO₂ catalysts. The conversion of ethanol on the V₂O₃ catalyst, as can be seen in Fig. 1(a), was 24% at the beginning of the time on stream and decreased sharply to 15% with the increase of the time on stream. The reason for the sharp decrease is unclear, but possibly due to a change of oxidation state of V on the surface during the reaction as observed in our previous paper [1]. Nevertheless, the conversion then kept unchanged after 2 h time on stream. On the other hand, the ethane selectivity of 38% and the acetaldehyde selectivity of 43% were observed at the beginning of the reaction and the ethane selectivity gradually increased, giving 43% selectivity to ethane with 44% selectivity to acetaldehyde at 5 h time on stream (Table 1).

Compared to the above V₂O₃ catalyst, the MoO₂ catalyst showed more stable and better performance for the conversion of ethanol to ethane and acetaldehyde, as can be seen in Fig. 1(b) and Table 1. The conversion was about three times higher than that of the V₂O₃ catalyst and only slightly decreased from 47% to 41% at 2 h time on stream and then was stabilized. Obviously, intrinsic activity the MoO₂ catalyst for the ethanol reaction seems higher than that of the V₂O₃ catalyst, since the surface area of the V₂O₃ (17 m²/g shown in Table 1) is higher than that of MoO₂ (5 m²/g). In addition, the MoO₂ catalyst clearly revealed the high selectivity performance for the equimolar product formation in which 47% ethane selectivity and 48% acetaldehyde selectivity were achieved from the beginning of the ethanol reaction and continued to 9 h time on stream without appreciable changes in the selectivities.

For both the V₂O₃ and MoO₂ catalysts, the equimolar formation of ethane and acetaldehyde from ethanol is now apparent and active sites on the catalysts are stable during the ethanol reaction. Interesting thing is that very small amount of ethylene and no

formation of diethyl ether were observed for both the V₂O₃ and MoO₂ catalysts. This fact indicates that no acid sites, which can promote dehydration of ethanol to ethylene and diethyl ether, exist on the surface of the low valence V₂O₃ and MoO₂. This result suggests at the same time that the reaction is not a simple acid-catalyzed reaction.

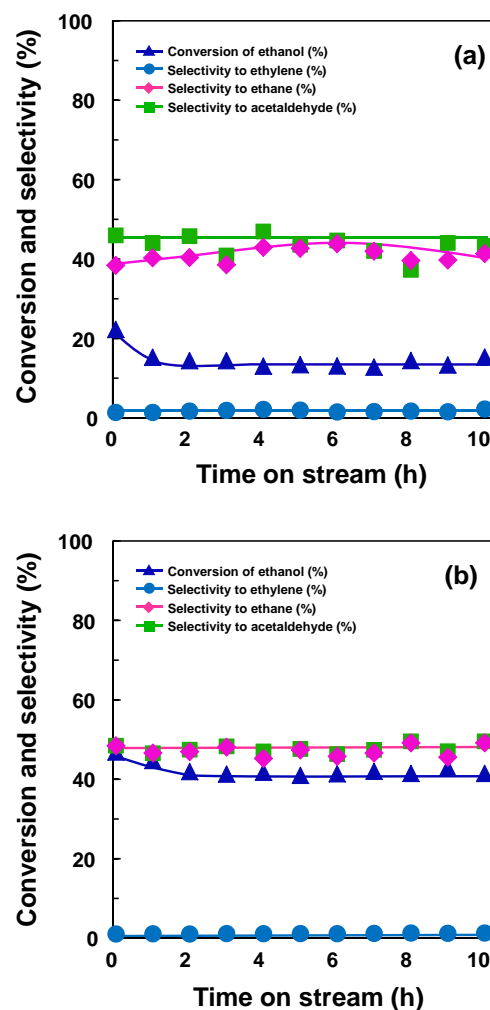


Fig. 1. Ethanol conversion to ethane and acetaldehyde as the function of time on stream over V₂O₃ (a) and MoO₂ (b) catalysts at 573 K. Reaction condition: cat. 0.15 g, flow rate N₂ 21 ml/min, ethanol 0.39 ml/min.

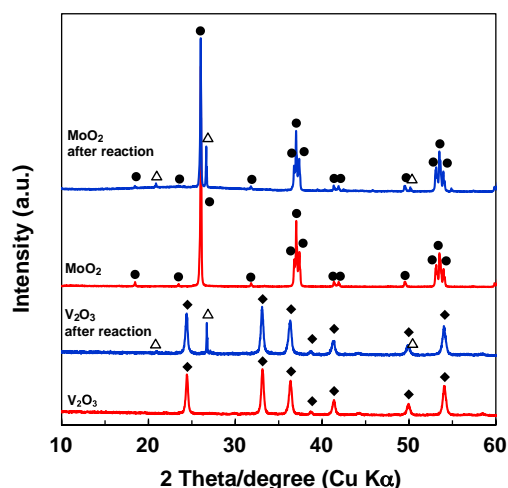


Fig. 2. XRD patterns of the V_2O_3 , MoO_2 before and after ethanol reaction. Reaction condition: cat. 0.15 g, reaction temperature 573 K, 9 h time on stream, flow rate N_2 21 ml/min, ethanol 0.39 ml/min. (◆) V_2O_3 , (●) MoO_2 , (△) SiO_2 (diluent).

3.2. Oxidation state of the catalysts after the reaction

XRD measurements were carried out for the V_2O_3 and MoO_2 catalysts before and after the ethanol reaction. Results are shown in Fig. 2. A typical XRD pattern of V_2O_3 was observed without any other crystal phases both before and after the ethanol reaction. MoO_2 phase was also confirmed by XRD and the XRD after the ethanol reaction showed no additional peaks of any impurities such as H_xMoO_3 [20] and other molybdenum oxides. These results evidently reveal that the reduced state of V and Mo in each oxide can be maintained under the reaction conditions and no decomposition of the oxide catalysts takes place during the reaction. To obtain further insight into the stability of the oxidation state of the catalysts, surface oxidation states of V and Mo before and after the ethanol reaction were examined by XPS. Since the measurements were unable to be conducted on the samples without exposure to air, note that obtained XPS results are not for actual surface under the reaction. Nevertheless, the results summarized in Table S1 showed that the surfaces kept highly reduced states and consisted of V^{3+} and Mo^{4+} species mainly and these reduced states were almost the same before and after the reaction. This result is apparently consistent with the XRD result. As a consequence, it is reasonable to conclude that the crystal phases and the surface oxidation states of the V_2O_3 and MoO_2 catalysts are stable under the ethanol reaction.

3.3. Addition of H_2 and C_2H_4 into the reaction stream

Hydrogenation of ethanol or of ethylene formed by dehydration of ethanol with formed hydrogen molecules during the reaction was thought to be a likely pathway for the formation of ethane [2,3,13]. Direct hydrogenation of ethylene with ethanol as a source of hydrogen molecules is also a possible pathway to form ethane. To investigate whether reactions on these pathways actually occur or not, the ethanol reaction was carried out in the presence of H_2 and/or C_2H_4 into the reaction stream. H_2 (1.0 ml/min) or C_2H_4 (1.0 ml/min) was added into the reaction stream and the total flow rate was maintained at 21.4 ml/min. Ethanol conversion and products distribution in the presence of H_2 or C_2H_4 in the reaction stream over the V_2O_3 catalyst and the MoO_2 catalyst are listed in Table 1. For both the V_2O_3 and MoO_2 catalysts, the conversion of ethanol and the selectivities to all kind of the products did not change in the presence of H_2 in the reaction stream. Therefore, it can be concluded that hydrogen molecule is not involved in the

formation of ethane from ethanol. Similarly, the addition of C_2H_4 had also no effect on the conversion of ethanol and the selectivities to the products. These results suggest that the pathway of the hydrogenation of ethylene is not responsible for the formation of the equivalent amount of ethane and acetaldehyde from ethanol over V_2O_3 and MoO_2 .

Coupling reaction of methylene group formed by decomposition of diethyl ether [2] or dissociation of acetaldehyde [6] are also a possible reaction mechanism as proposed for the formation of ethane from ethanol. However, we could observe no formation of formaldehyde and no diethyl ether conversion over the both catalysts under the same reaction conditions for ethanol conversion, so that these two reaction pathways can be excluded.

3.4. Effect of reaction condition

Effects of the reaction temperature on the selectivities to ethane and acetaldehyde were examined over V_2O_3 and MoO_2 in the temperature range from 533 K to 653 K. Results are shown in Fig. 3. V_2O_3 showed the selectivities to ethane and acetaldehyde of 43.4% and 45.3%, respectively, at low reaction temperature (573 K). The selectivity to these products did not change even when the

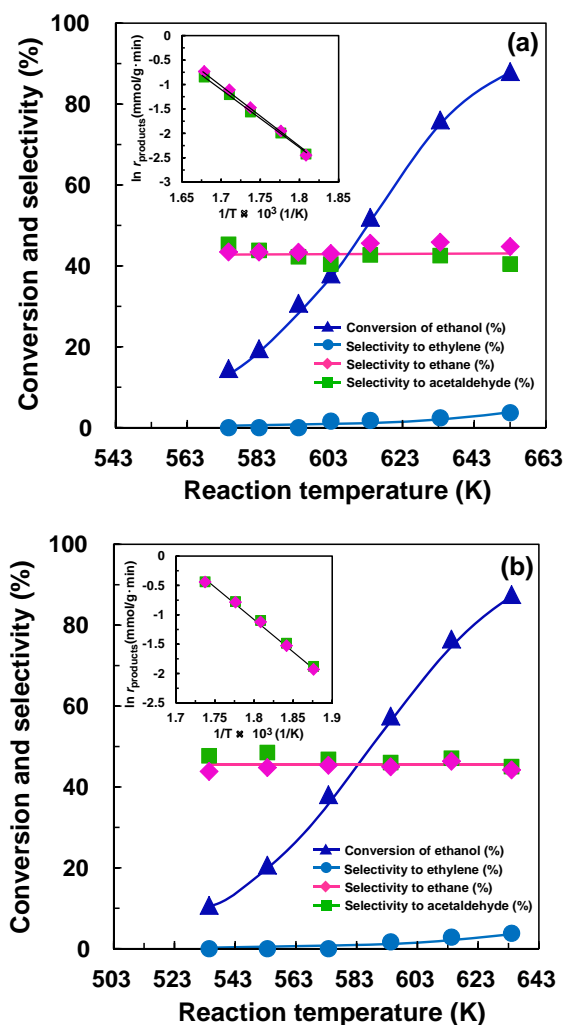


Fig. 3. Ethanol reaction over V_2O_3 (a) and MoO_2 (b) catalysts at different reaction temperature from 533 K to 653 K. Reaction condition: cat. 0.15 g, flow rate N_2 21 ml/min, ethanol 0.39 ml/min. The inset shows Arrhenius plots using the rate of formation of ethane and acetaldehyde.

Table 2Kinetic parameters of ethanol reaction over V_2O_3 and MoO_2 catalysts.

Catalysts	Reaction order	E_{app} (kJ/mol) for the formation of	
		C_2H_6	CH_3CHO
V_2O_3	0.35	106	100
MoO_2	0.40	90	87

reaction temperature was increased until 653 K, although the some amounts of ethylene with the selectivity 1.3% was appreciably produced at 603 K and increased to 3.7% at 653 K. MoO_2 also showed no temperature effect on the selectivities to ethane and acetaldehyde. The selectivities to ethane and acetaldehyde in all reaction temperatures were within the range of 44–46% and 45–48%, respectively. The insets of Fig. 3 show Arrhenius plots for the formation of ethane and acetaldehyde over V_2O_3 and MoO_2 . Apparent activation energies ($E_{a,app}$) of ethane and acetaldehyde formation were calculated to be 106 kJ/mol and 100 kJ/mol, respectively, for V_2O_3 and 96 kJ/mol and 90 kJ/mol for MoO_2 as listed in Table 2. The $E_{a,app}$ values for ethane and acetaldehyde formation were similar both over V_2O_3 and MoO_2 , but the values over V_2O_3 were slightly higher than those of MoO_2 . In the oxidative dehydrogenation of ethanol to acetaldehyde $VO_x/TiO_2/SiO_2$ catalyst [21] and MO_x/Al_2O_3 ($M=V, Mo, W$) catalysts [22] have been reported to give apparent activation energies of 46 kJ/mol and 17–23 kJ/mol, respectively. These values are obviously much lower than those observed in the ethanol reaction over V_2O_3 and MoO_2 which is a non-oxidative reaction. This comparison may suggest that the equimolar formation of ethane and acetaldehyde from ethanol takes place without accompanying a reduction–oxidation process of the V_2O_3 and MoO_2 catalysts.

Effects of contact time on the selectivities ethane and acetaldehyde were shown in Fig. 4. Ethane and acetaldehyde were formed with an equal amount over V_2O_3 under the W/F conditions of lower than 0.023 g ml/min. However, the selectivity to acetaldehyde constantly decreased with increase of the contact time and reached to 34.9% under the W/F of 0.07 g ml/min, while the selectivity to ethane kept unchanged in all contact time range tested. MoO_2 also revealed a similar selectivity change, that is, the selectivity to acetaldehyde slightly decreased from 50.9% at 0.03 g ml/min to 39.4% at 0.07 g ml/min and on the other hand the selectivity to ethane did not change in this contact time range. The observed decrease of the selectivity to acetaldehyde seems due to a consecutive condensation reaction of formed acetaldehyde when concentration of acetaldehyde increased under longer contact times. By summarizing all the data collected under the different reaction conditions, it is evident that the product selectivities are practically independent of the reaction temperature and the conversion of ethanol. This clearly indicates that ethane and acetaldehyde are not formed by consecutive reactions but in a single step from common intermediate.

3.5. Reaction of various alcohols over V_2O_3 and MoO_2 catalysts

In order to further study the equimolar formation of alkanes and aldehydes, catalytic reactions using methanol, 1-propanol, 2-propanol were carried out over V_2O_3 and MoO_2 oxide catalysts. Results are summarized in Table 3. Like as ethanol, almost the same selectivities to alkanes and corresponding aldehydes or ketones were observed in all kind of tested alcohols over both V_2O_3 and MoO_2 oxide catalysts, except for the 2-propanol reaction in which much amounts of propylene were simultaneously formed by the dehydration of 2-propanol and also the selectivity to acetone in the reaction over MoO_2 was slightly higher than that of propane probably due to a occurrence of simple dehydrogenation of 2-propanol

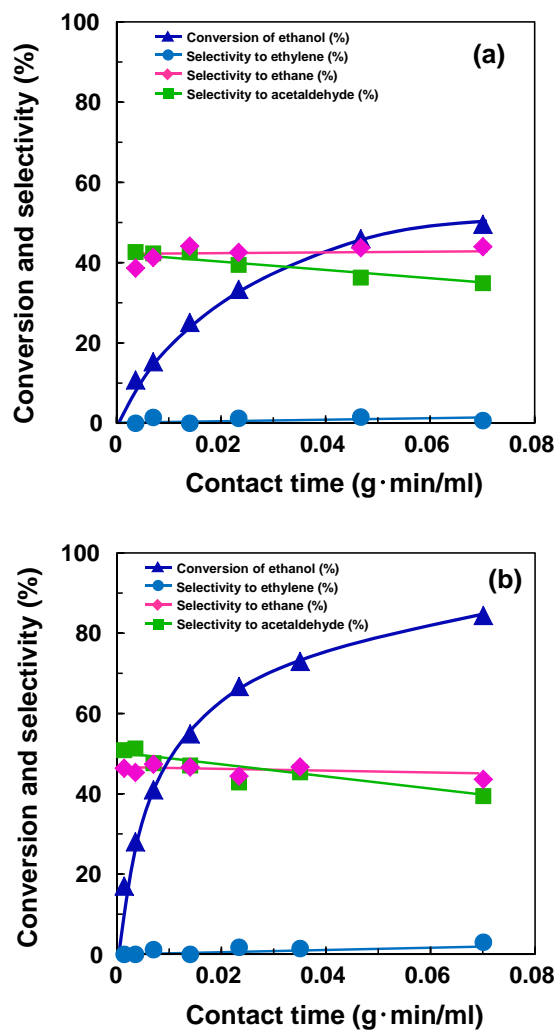


Fig. 4. Ethanol reaction at different contact time over V_2O_3 (a) and MoO_2 (b) catalysts at 573 K. Reaction condition: cat. 0.03–1.50 g, flow rate N_2 21 ml/min, ethanol 0.39 ml/min.

to acetone. It is now evident from the data that the equimolar formation of alkanes and aldehydes or ketones occurs regardless of alcohols. Moreover, it is noteworthy that methane was obtained from methanol with reasonably high selectivity. This result strongly confirms that the equimolar formation of alkanes and aldehydes from alcohols is not *via* the formation of olefin.

Formation rates of the products of each alcohol were calculated by using the data summarized in Table 3 and the values are listed in Table 4. The order of the product formation rates of the different alcohols over V_2O_3 was as follows: 2-propanol \gg ethanol $>$ 1-propanol $>$ methanol. In the case of MoO_2 , the order was as follows: 2-propanol \gg methanol $>$ ethanol $>$ 1-propanol. There are difference in the order between the catalysts but the order among normal alcohols seem to have less meanings, since the rates of these alcohols are more or less similar. More prominent is that much higher production rates were obtained in the reaction of 2-propanol for both the V_2O_3 and the MoO_2 catalysts than those of the other alcohols. This interesting result of the high reaction rate of 2-propanol could be related to reactivity of α -hydrogen of 2-propanol, namely easy elimination of α -hydrogen in 2-propanol compared with the other alcohols. Then a hydrogen transfer reaction at α -position of alcohols is suggested involved in the rate-determining step for the equimolar formation of alkanes and aldehydes from alcohols.

Table 3
Reaction of various alcohols over V₂O₃ and MoO₂ catalysts^a.

Catalysts	Reactants	Conv. (%) ^b	Selectivity to products (%) ^c										
			MA	EE	EA	PE	PA	FA	ACA	ACT	PPA	Others ^d	
V ₂ O ₃	CH ₃ OH	10.8	40.7	–	–	–	–	–	47.1	–	–	–	12.2
	C ₂ H ₅ OH	14.6	–	2.0	42.7	–	–	–	–	43.6	–	–	11.7
	C ₃ H ₇ OH	11.4	–	–	–	<1	47.6	–	–	–	–	47.2	4.8
	CH ₃ CH(OH)CH ₃	72.1	–	–	–	17.9	39.1	–	–	–	42.5	–	0.5
MoO ₂	CH ₃ OH	19.8	47.8	–	–	–	–	–	43.1	–	–	–	9.1
	C ₂ H ₅ OH	41.0	–	1.2	47.4	–	–	–	–	47.6	–	–	3.8
	C ₃ H ₇ OH	29.5	–	–	–	4.3	44.9	–	–	–	–	44.8	6.0
	CH ₃ CH(OH)CH ₃	100.0	–	–	–	41.4	26.2	–	–	–	32.0	–	0.4

^a Reaction condition: cat. 0.15 g, reaction temperature 573 K, time on stream 5 h, flow rate: N₂ 21 ml/min, CH₃OH 0.59 ml/min, C₂H₅OH 0.39 ml/min, C₃H₇OH 0.36 ml/min, CH₃CH(OH)CH₃ 0.93 ml/min.

^b Conversion of the reactants.

^c Selectivity to product, MA: methane, EE: ethylene, EA: ethane, PE: propylene, PA: propane, FA: formaldehyde, ACA: acetaldehyde, ACT: acetone, PPA: propionaldehyde.

^d Others are attributed to condensation products.

3.6. Kinetic investigation for the formation of ethane and acetaldehyde

Study on H–D kinetic isotope effects (KIE) was conducted to reveal the reaction mechanism. KIE was measured using CH₃CH₂OD and CD₃CD₂OD with respect to CH₃CH₂OH. The results are shown in Table 5. The KIE values in the conversion of C₂H₅OD (KIE; $\nu_{\text{C}_2\text{H}_5\text{OH}}/\nu_{\text{C}_2\text{H}_5\text{OD}}$) were 1.09 for V₂O₃ and 1.12 for MoO₂ catalysts. On the other hand, slightly high KIE value for MoO₂ (KIE; $\nu_{\text{C}_2\text{H}_5\text{OH}}/\nu_{\text{C}_2\text{H}_5\text{OD}}$ is 1.32) was observed when C₂D₅OD was used as the reactant. Very differently, V₂O₃ showed an inverse isotope effect (KIE; $\nu_{\text{C}_2\text{H}_5\text{OH}}/\nu_{\text{C}_2\text{H}_5\text{OD}}$ is 0.84). This will be discussed in the following section.

We estimated KIE value as primary isotope effect for $\nu_{\text{-CH}}/\nu_{\text{-CD}}$ at 573 K for C–H cleavage (α -H elimination) to be 2.8, which is obviously higher than that of the experimental values (entry 1, 2 in Table 5) of 0.80 and 1.32 for V₂O₃ and MoO₂, respectively. The experimental KIE values ($\nu_{\text{C}_2\text{H}_5\text{OH}}/\nu_{\text{C}_2\text{H}_5\text{OD}} = 4.9$, entry 3 in Table 5) in the case of oxidative cleavage of C–H bond of alcohols have been reported very close to the estimated KIE value as primary isotope effect (KIE = 5.0), indicating that C–H bond in methylene group is completely dissociated [23]. Ru/carbon catalyst (entry 4) showed KIE values for both O–H and C–H which are lower than those of estimated value, suggesting that α -hydrogen elimination is not a rate-determining step [24]. Hydroxyapatite [25], Al-complex [26] and Zr-complex [27], which have been reported as catalysts for hydrogen transfer reaction, showed also small KIE values as primary isotope effect for the cleavage of C–H bond. All of these reports (entry 5–7) indicate that C–H and O–H bonds are not completely dissociated in the transition states and hydride

Table 4
Rate of product formation in the various alcohol reactions on V₂O₃ and MoO₂ catalysts^a.

Catalysts	Reactant	Rate of product formation ($\mu\text{mol/g min}$)		
		Alkene	Alkane	Aldehyde
V ₂ O ₃	CH ₃ OH	–	7.6	8.4
	C ₂ H ₅ OH	0.6	6.9	7.4
	C ₃ H ₇ OH	0.2	5.3	5.2
	CH ₃ CH(OH)CH ₃	33.2	74.6	80.4 ^b
MoO ₂	CH ₃ OH	–	12.9	11.6
	C ₂ H ₅ OH	0.6	23.8	24.1
	C ₃ H ₇ OH	1.5	14.7	14.5
	CH ₃ CH(OH)CH ₃	106.9	62.3	70.4 ^b

^a Reaction condition: cat. 0.15 g, reaction temperature 573 K, 5 h time on stream, flow rate N₂ 21 ml/min, CH₃OH 0.59 ml/min, C₂H₅OH 0.39 ml/min, C₃H₇OH 0.36 ml/min, CH₃CH(OH)CH₃ 0.93 ml/min.

^b Acetone.

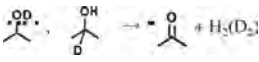
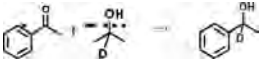
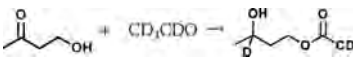
transfer favorably occurred via a concerted mechanism [25–27]. The experimental KIE values ($\nu_{\text{-CH/CD}}$) for the V₂O₃ and MoO₂ are similar to that of these reports, so that a hydrogen transfer-type reaction could occur as a rate-determining step for the equivalent formation of ethane and acetaldehyde from ethanol over V₂O₃ and MoO₂.

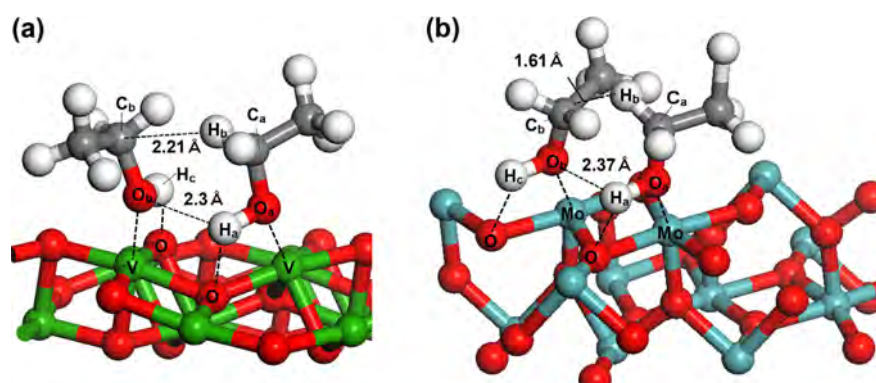
3.7. Co-formation of ethane and acetaldehyde from ethanol over V₂O₃ and MoO₂

For better discussion, we made adsorbed state models of ethanol on (0 1 2) plane of V₂O₃ and (–1 1 1) plane of MoO₂. The models are illustrated in Fig. 5. A chosen hexagonal crystal structure of the V₂O₃ catalyst grows in the direction to (0 1 2) plane [28], and the preferential orientation is reported along (1 1 1) directions for normal MoO₂ [29]. Almost the same distance of H_a–O_b was able to set for both V₂O₃ (2.30 Å) and MoO₂ (2.37 Å) catalyst surface. However, a much longer distance of H_b–C_b was necessary for V₂O₃ catalyst (2.21 Å) while a short distance (1.61 Å) was realized on MoO₂ catalyst (1.61 Å). The model can help to reasonably explain the observed various kinetic results by assuming that simultaneous formation of ethane and acetaldehyde proceeds via the hydrogen transfer dehydration through a 6-membered cyclic intermediate, which is a concerted process where two ethanol molecules are adsorbed at V–O and Mo–O sites on the surface of the catalysts.

First, the apparent activation energy for the formation of ethane and acetaldehyde over V₂O₃ (106 kJ/mol and 100 kJ/mol, respectively, in Table 2) was higher than that of MoO₂ (90 kJ/mol and 86 kJ/mol, respectively, in Table 2). The higher activation energy seems caused by the longer distance between H_b and C_b over V₂O₃ than MoO₂, i.e., the interaction of H_b in methylene group and adjacent C_b in methylene group is more difficult over V₂O₃ compared with MoO₂. The KIE values when C₂H₅OD was reacted were almost the same for V₂O₃ ($\nu_{\text{C}_2\text{H}_5\text{OH}}/\nu_{\text{C}_2\text{H}_5\text{OD}} = 1.09$ in Table 4) and MoO₂ ($\nu_{\text{C}_2\text{H}_5\text{OH}}/\nu_{\text{C}_2\text{H}_5\text{OD}} = 1.12$ in Table 4), and the KIE values when C₂D₅OD was used were, on the other hand, very different between V₂O₃ ($\nu_{\text{C}_2\text{H}_5\text{OH}}/\nu_{\text{C}_2\text{H}_5\text{OD}} = 0.84$ in Table 4) and MoO₂ ($\nu_{\text{C}_2\text{H}_5\text{OH}}/\nu_{\text{C}_2\text{H}_5\text{OD}} = 1.32$ in Table 4). The observed KIE values when C₂H₅OD was reacted clearly indicate that the OH interaction of alcohol with oxide surface is not a rate-limiting step. Although the observed KIE over MoO₂ was rather small, the KIE values for $\nu_{\text{C}_2\text{H}_5\text{OH}}/\nu_{\text{C}_2\text{H}_5\text{OD}}$ more than unity is not discrepant with the assumption that α -hydrogen is eliminated by a concerted mechanism and hydrogen transfer as the rate-determining step takes place via formation of the 6-membered cyclic (nonlinear) intermediate, followed by dehydration to form the products. In fact, KIE values in hydrogen transfer reaction are more than 6 when the reaction takes place in

Table 5
KIE in alcohol reactions over several catalytic systems.

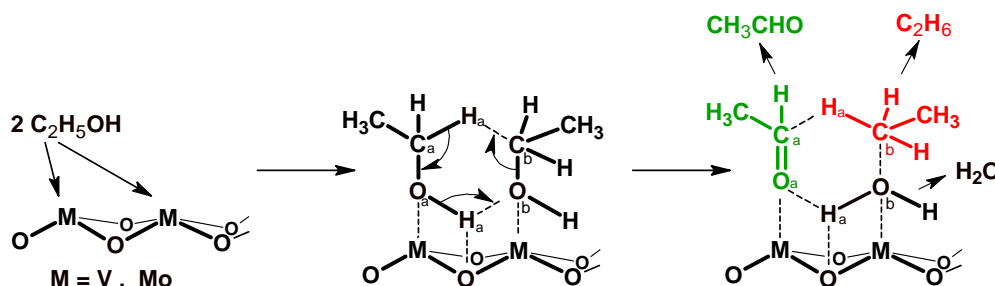
Entry	Catalysts	Reactions	Temp. (K)	KIE values		Ref.
				$\nu_{\text{-OH/-OD}}$ ($^{\circ}$) ^a	$\nu_{\text{-CH/-CD}}$ ($^{\circ}$) ^a	
1	V ₂ O ₃	C ₂ H ₅ OD, C ₂ D ₅ OD → ethane, acetaldehyde, H ₂ O	573	1.09 (3.1)	0.84 (2.8)	This work
2	MoO ₂	C ₂ H ₅ OD, C ₂ D ₅ OD → ethane, acetaldehyde, H ₂ O	573	1.12 (3.1)	1.32 (2.8)	This work
3	VO _x /Al ₂ O ₃	C ₂ H ₅ OD, C ₂ D ₅ OD $\xrightarrow{\text{O}_2}$ acetaldehyde, H ₂ O	473	1.02 (3.9)	4.90 (5.0)	[23]
4	Ru/carbon		373	1.57 (5.6)	1.69 (4.6)	[24]
5	Hydroxyapatite		573		1.80 (2.8)	[25]
6	Al-complex ^b		310		2.33 (6.5)	[26]
7	Zr-complex ^c		353		1.80 (4.1)	[27]

^a Estimated values for KIE as primary isotope effect are shown in parenthesis.^b BINOLate/Al⁺PrOH system, BINOL (2,2'-dihydroxy-1,1'-binaphthyl).^c Zirconocene complex, Cp₂ZrH₂.**Fig. 5.** Model of adsorbed ethanol on (012) planes of V₂O₃ (a) and (−111) plane of MoO₂ (b) surface. Green, blue, red, grey and white balls correspond to V, Mo, O, C and H, respectively. (For interpretation of the references to color in this figure legend, the reader is referred to the web version of this article.)

linear transition structure [30], and nonlinear transition structure shows decreased KIE values as low as 2^{1/2} [31]. On the other hand, an inverse kinetic isotope effect was observed on V₂O₃. It appears that the inverse kinetic isotope effect should be related to conformation of the 6-membered cyclic intermediate over the oxide surface. The intermediate with C₂H₅OD cannot stably form due to the long distance of H_b–C_b over V₂O₃. However, when C₂D₅OD is reacted, an adsorbed state of C₂D₅OD may alter the conformation of the 6-membered cyclic intermediate to facilitate easier hydrogen transfer.

Based on these results, we proposed a plausible reaction scheme for the co-formation of ethane and acetaldehyde from ethanol

on V₂O₃ and MoO₂ as shown in Scheme 1. In the first step, the 6-membered cyclic intermediate is formed by a interaction between two adjacently adsorbed ethanol over coordinatively unsaturated V–O and Mo–O sites than can be created when the metal elements are in a low valence state. The H atoms of the hydroxyl groups of alcohol may be stabilized by hydrogen bonding with lattice oxygen atoms of V₂O₃ and MoO₂ catalysts. H_a adsorbed on lattice oxygen simultaneously interacts with the O_bH of adjacent adsorbed alcohol and H_b in methylene group also interact with C_b in adjacent methylene group. Then 6-membered cyclic intermediate as a transition state is formed [32,33]. Subsequently, H_a in hydroxyl group adsorbed on lattice oxygen completely

**Scheme 1.** A reaction mechanism for the equivalent formation of ethane and acetaldehyde from ethanol over V₂O₃ and MoO₂ catalysts.

transfers as proton to the hydroxyl group adsorbed at adjacent site ($-O_bH$), forming water. Concertedly H_b in the methylene group also transfers as hydride ion to the C_b in methylene group of another ethanol adsorbed on the adjacent site accompanied by the cleavage of C_b-O_b bond. Thus, ethane and acetaldehyde are simultaneously formed.

4. Conclusion

Equimolar amounts of ethane and acetaldehyde were formed from ethanol over V_2O_3 and MoO_2 catalysts. The selectivity to ethane and acetaldehyde were almost independent of the reaction temperature in the range of 533–653 K and contact time in the range 0.0014–0.07 g/ml/min, confirming the equimolar formation scheme. Both over the V_2O_3 and MoO_2 catalysts, the reactions of methanol, 1-propanol and 2-propanol also produced the equivalent amount of corresponding alkanes and aldehydes. The reaction over the V_2O_3 and MoO_2 catalysts is generally applicable for aliphatic alcohols. The formation of methane strongly supports that olefin is not an intermediate in the co-formation of alkanes from aliphatic alcohols. Kinetic isotope effects for C_2H_5OD and C_2D_5OD respect to C_2H_5OH were rather small for both the V_2O_3 and MoO_2 catalysts. It is concluded that plausible reaction mechanism for the co-formation of ethane and acetaldehyde from ethanol is a hydrogen transfer reaction between two ethanol molecules adsorbed on metal- O^{2-} -metal sites of V_2O_3 and MoO_2 catalysts surface *via* formation of six-membered transition states. This reaction itself and catalytic function of low valence V and Mo in metal oxide form seem quite unique in catalysis field and interesting for further application.

Appendix A. Supplementary data

Supplementary data associated with this article can be found, in the online version, at <http://dx.doi.org/10.1016/j.molcata.2014.07.009>.

References

- [1] Y. Nakamura, T. Murayama, W. Ueda, *ChemCatChem* 6 (2014) 741–744.
- [2] B.M. Abu-Zied, A.M. El-Awad, *J. Mol. Catal. A: Chem.* 176 (2001) 227–246.
- [3] J.B. Mcmonagle, J.B. Moffat, *J. Catal.* 91 (1985) 132–141.
- [4] R. Lobo, C.L. Marshall, P.J. Dierich, F.H. Ribeiro, C. Akatay, E.A. Stach, A. Mane, Y. Lei, J. Elam, J.T. Miller, *ACS Catal.* 2 (2012) 2316–2326.
- [5] M.M. Mohamed, *J. Mol. Catal. A: Chem.* 200 (2003) 301–3137.
- [6] J.V. Ochoa, C. Trevisanut, J.M.M. Millet, G. Busca, F. Cavani, *J. Phys. Chem. C* 117 (2013) 23908–23918.
- [7] T. Jin, H. Hattori, K. Tanabe, *Chem. Lett.* 1 (1981) 533–1534.
- [8] K. Ganesan, C.P. Pillai, *J. Catal.* 119 (1989) 8–13.
- [9] M. Jayamani, N. Murugasen, C.N. Pillai, *J. Catal.* 85 (1984) 527–529.
- [10] M. Jayamani, C.N. Pillai, *J. Catal.* 82 (1983) 485–488.
- [11] S. Mathew, J.B. Nagy, N. Nagaraju, *Catal. Commun.* 7 (2006) 177–183.
- [12] S. Mathew, C.S. Kumara, N. Nagaraju, *J. Mol. Catal. A: Chem.* 255 (2006) 243–248.
- [13] R. Sumathi, K. Johnson, B. Viswanathan, T.K. Varadarajan, *Appl. Catal., A: Gen.* 172 (1998) 15–22.
- [14] M. Sanker, E. Nowicka, G.J. Hutchings, *Faraday Discuss.* 145 (2010) 341–356.
- [15] M. Sanker, E. Nowicka, R. Tiruvalam, Q. He, S.H. Taylor, C.J. Kiely, D. Behell, D.W. Knight, G.J. Hutchings, *Chem. Eur. J.* 17 (2011) 6524–6532.
- [16] B.P. Barbero, L.E. Cadus, L. Hilarire, *Appl. Catal., A: Gen.* 246 (2003) 237–242.
- [17] J. Mendiadua, R. Casanova, Y. Barbaux, *J. Electron Spectrosc. Relat. Phenom.* 71 (1995) 249–261.
- [18] P.A. Spevack, N.S. McIntyre, *J. Phys. Chem.* 96 (1992) 9029–9035.
- [19] H.A. Kandari, F.A. Kharafi, A. Katrib, *Appl. Catal., A: Gen.* 361 (2009) 81–85.
- [20] T. Ohno, Z. Sakai, H. Sakagami, N. Takahashi, T. Matsuda, *Appl. Catal., A: Gen.* 389 (2010) 52–59.
- [21] Y.C. Lin, C.H. Chang, C.C. Chen, J.M. Jehng, S.G. Shyu, *Catal. Commun.* 9 (2008) 675–679.
- [22] H. Nair, C.D. Baerthsch, *J. Catal.* 258 (2008) 1–4.
- [23] B. Kilos, A.T. Bell, E. Iglesia, *J. Phys. Chem. C* 113 (2009) 2830–2836.
- [24] M. Yamashita, T. Kawamura, M. Suzuki, Y. Saito, *Bull. Chem. Soc. Jpn.* 64 (1991) 272–278.
- [25] C.L. Kibby, W.K. Hall, *J. Catal.* 31 (1973) 65–73.
- [26] (a) R. Cohen, C.R. Graves, S.T. Nguyen, J.M.L. Martin, M.A. Ratner, *J. Am. Chem. Soc.* 126 (2004) 14796–14803;
(b) P. Nandi, Y.I. Matvieiev, V.I. Boyko, K.A. Durkin, V.I. Kalchenko, A. Katz, *J. Catal.* 284 (2011) 42–49.
- [27] Y. Umekawa, S. Sakaguchi, Y. Nishiyama, Y. Ishi, *J. Org. Chem.* 62 (1997) 3409–3412.
- [28] Y. Bai, P. Jin, S. Ji, H. Luo, Y. Gao, *Ceram. Int.* 39 (2013) 7803–7808.
- [29] T. Leisegang, A.A. Levin, J. Walter, D.C. Meyer, *Cryst. Res. Technol.* 40 (2005) 95–105.
- [30] F.H. Westheimer, *Chem. Rev.* 61 (1961) 265–273.
- [31] H. Kwart, *Acc. Chem. Res.* 15 (1982) 401–408.
- [32] Y. Zhu, G. Chuah, S. Jaenicke, *J. Catal.* 227 (2004) 1–10.
- [33] J.M. Hidalgo, C.J. Sanchidrin, J.R. Ruiz, *Appl. Catal., A: Gen.* 470 (2014) 311–317.



CrossMark
click for updates

Cite this: *Catal. Sci. Technol.*, 2014, 4, 4250

Hydrothermal synthesis of octahedra-based layered niobium oxide and its catalytic activity as a solid acid†

Toru Murayama,* Junli Chen, Jun Hirata, Keeko Matsumoto and Wataru Ueda*

Layered-structure-type niobium oxides were synthesized by the hydrothermal method by using ammonium niobium oxalate as a precursor. The X-ray diffraction pattern (Cu-K α) of the synthesized niobium oxide showed characteristic peaks at $2\theta = 22.7^\circ$ and 46.2° , indicating the linear corner-sharing of NbO₆ octahedra in the *c*-direction. From Raman measurements, the layered-structure-type niobium oxide was composed of NbO₆ octahedra and {Nb₆O₂₁} pentagonal units. The presence of micropores was confirmed by N₂ adsorption at low pressure (1.0×10^{-6}), indicating that the arrangement of the *a*-*b* plane was an interconnection of the crystal structure motifs of {Nb₆O₂₁} units and micropore channels but without long-range order (deformed orthorhombic). Ammonium cations and water were desorbed from the deformed orthorhombic niobium oxide by calcination at 400 °C, and Brønsted acid sites were formed. The deformed orthorhombic niobium oxide showed high catalytic activity as a solid acid compared to the catalytic activities of other crystalline niobium oxides. The order of catalytic activity for the alkylation of benzyl alcohol and anisole was deformed orthorhombic Nb₂O₅ > TT-Nb₂O₅, amorphous Nb₂O₅ \gg T-Nb₂O₅, pyrochlore Nb₂O₅.

Received 2nd June 2014,
Accepted 18th July 2014

DOI: 10.1039/c4cy00713a

www.rsc.org/catalysis

Introduction

Niobium oxide is widely used in catalysis and in electrochromic and photoelectrochemical devices.^{1,2} Niobium oxide (or hydrated niobium oxide) has been used especially as a water-tolerant solid acid catalyst for many reactions such as alkylation, esterification, hydrolysis, dehydration and hydration.^{3,4} Hydrated niobium oxide (Nb₂O₅·*n*H₂O, niobic acid) has high acid strength ($H_0 \leq -5.6$) and possesses Lewis and Brønsted acidity. Therefore, much effort has been focused on the preparation of new morphologies of nanocrystalline niobium oxide (or hydrated niobium oxide) in order to obtain niobium oxide with a large surface area, such as nanoparticles,^{5,6} rods,^{7,8} wires,⁹ and nanoplates.^{10–12} Niobium oxide forms different polyhedral structures and transforms its phase depending on the heat treatment performed. Amorphous niobium oxide, Nb₂O₅·*n*H₂O, possesses distorted NbO₆ octahedra, NbO₇ pentagonal bipyramids and NbO₈ hexagonal bipyramids as structural units.^{13,14} With heat treatment of Nb₂O₅·*n*H₂O, pseudohexagonal niobium oxide (TT-Nb₂O₅) is formed at 300–500 °C, orthorhombic

niobium oxide (T-Nb₂O₅) at 700–800 °C and monoclinic niobium oxide (H-Nb₂O₅) at temperatures higher than 1000 °C. With an increase in the heat treatment temperature and the degree of crystallinity, its catalytic activity as a solid acid (Brønsted acidity) and surface area decreased.¹⁵ Therefore, the protons did not form on the ordered crystalline structure but formed on the distorted polyhedra in amorphous Nb₂O₅·*n*H₂O, having been regarded as active Brønsted acid sites.

For improving the Brønsted acidity and catalytic properties of niobium oxide, modification of niobium oxide or supported niobium oxide with sulfates and phosphates has been tried.^{16–18} Complex metal oxides such as layered HNbMO_x (M = Ti, Mo, W) have been reported to be a strong solid catalyst, and M(OH)Nb was regarded as a strong Brønsted acid site.^{19,20} Some researchers reported that the acid centers were due to isomorphous substitutions of Nb⁵⁺ by the higher-valence M⁶⁺ cation (M = Mo, W) in the mixed oxide.^{21,22}

We have long studied the relationship between the crystalline structure of complex metal oxides and their catalytic activity.^{23–25} Studies on the crystalline metal oxides of Mo₃VO_x have demonstrated that their oxidation activities depend on the crystalline arrangement of pentagonal {Mo₆O₂₁} units and MO₆ octahedra in the *a*-*b* plane. These materials contain heptagonal channels in their structure. For the synthesis of these catalysts, the formation of a pentagonal

Catalysis Research Center, Hokkaido University, N-21, W-10, Sapporo 001-0021, Japan. E-mail: murayama@cat.hokudai.ac.jp, ueda@cat.hokudai.ac.jp;
Fax: +81 11 706 9163; Tel: +81 11 706 9164

† Electronic supplementary information (ESI) available. See DOI: 10.1039/c4cy00713a

{Mo₆O₂₁} unit in the precursor solution was important, and the pentagonal unit assembled further into a metal oxide complex under hydrothermal conditions.^{26,27} A metal oxide complex that possesses a similar layered structure in the *c*-direction by corner-sharing of MO₆ (M = Mo, W, V, Ta, Nb) octahedra has been synthesized by a hydrothermal method.^{28–30} These catalysts were found to function as solid acids, the property of which was understood from a structural point of view.

We report herein the synthesis of niobium oxide by a hydrothermal process from niobic acid and niobium oxalate as the precursors. The Nb atom has a pentagonal bipyramidal environment in the crystal structure of NH₄[NbO(C₂O₄)₂(H₂O)₂]*n*H₂O,³¹ and under hydrothermal conditions, pentagonal {Nb₆O₂₁} units may be formed by the hydrolysis of [NbO(C₂O₄)₂(H₂O)₂][−] (ref. 32) and then self-assemble into niobium oxide. The structure and catalytic activity of the obtained niobium oxides were investigated. Various crystalline niobium oxides, including pseudohexagonal (TT phase), orthorhombic (T phase), pyrochlore, and amorphous, were also prepared, enabling us to discuss the relationships between the crystalline structure and their catalytic activity and acidity.

Experimental

Preparation of niobium oxides

Layered-structure-type niobium oxides were synthesized by a hydrothermal method from ammonium niobium oxalate (NH₄[NbO(C₂O₄)₂(H₂O)₂]*n*H₂O), denoted as NbO-ANO. Typically, ammonium niobium oxalate (supplied by CBMM) containing 6 mmol of Nb was dissolved in 40 mL of deionized water and then sealed in a 60 mL Teflon-lined stainless-steel autoclave. Hydrothermal reaction was carried out at 175 °C for 3 days. The obtained solid was filtered, washed thoroughly with deionized water, and dried at 80 °C overnight. The same type of niobium oxide was obtained from ammonium niobium oxalate (Aldrich), and similar characterization results were obtained (Table S1†). Pseudohexagonal niobium oxide and pyrochlore niobium oxide were also synthesized by a hydrothermal method using a niobic acid (Nb₂O₅·*n*H₂O, Soekawa Chemical) precursor, denoted as NbO-NA(d) and NbO-NA(c), respectively. 4 mmol based on Nb of niobic acid was dispersed in 40 mL of deionized water for NbO-NA(c) and 0.25 mmol for NbO-NA(d). The hydrothermal conditions and the following process were the same as those of NbO-ANO. The yields of niobium oxides calculated as Nb₂O₅ were more than 90% for all of the catalysts. The samples were calcined at 400 °C for 4 h under air before being used as catalysts. The rate of temperature increase was 10 °C min^{−1} from room temperature. For comparison, amorphous niobium oxide was prepared by calcination of niobic acid at 400 °C for 4 h under air (denoted as NbO-cal).

The as-synthesized material (NbO-ANO, 0.3 g) was dispersed in 15 mL of KNO₃ solution (0.1 mol L^{−1}) for ion-exchange treatment. The dispersed sample was stirred at 80 °C for 8 h. The resulting solid was collected by filtration. Then the

sample was washed with water (3 × 100 mL) and dried at 80 °C overnight. The obtained sample was denoted as NbO-ANO (K⁺). A NbO-ANO (K⁺) sample treated with NH₄NO₃ solution was denoted as NbO-ANO (NH₄⁺). NbO-ANO (NH₄⁺) was prepared by ion-exchange treatment of NbO-ANO (K⁺) in 15 mL of NH₄NO₃ solution (0.1 mol L^{−1}) at 80 °C for 8 h.

Alkylation reaction

A 50 mL round-bottom three-neck flask equipped with a reflux condenser was used as a stirred bed reactor to test the catalytic activities. Typically, a mixture of benzyl alcohol (1 mmol), anisole (50 mmol), and an internal standard, decane (0.5 mmol), was added to the reactor and the reaction temperature was adjusted to 100 °C. Then 0.1 g of a catalyst and a Teflon-coated magnetic stir bar were loaded into the reactor. Aliquots (each 0.1 mL) were collected at intervals. The concentrations of the reactant and the product were measured by gas chromatography using a flame ionization detector (GL Science GC390B) with a ZB-1 column.

Characterization

The catalysts were characterized by the following techniques. Powder XRD patterns were recorded with a diffractometer (RINT Ultima+, Rigaku) using Cu-Kα radiation (tube voltage: 40 kV, tube current: 20 mA). Diffractions were recorded in the range of 4–60° at 5° min^{−1}. Morphology was investigated by using a scanning transmission electron microscope (HD-2000, Hitachi) at 200 kV and 30 μA and a transmission electron microscope (JEM-2100F, JEOL) at 200 kV. The samples were dispersed in ethanol by ultrasonic treatment for several minutes, and drops of the suspension were placed on a copper grid for STEM and TEM observations. Raman spectra were obtained using a spectrometer (inVia Reflex, Renishaw, 2 cm^{−1} spectral resolution) at a wavelength of 532 nm and a collection time of 10 s. N₂ adsorption isotherms at liquid N₂ temperature were measured by using an autoadsorption system (BELSORP-max, BEL Japan) for the samples. The samples before the reactions were heat-treated in air at 400 °C for 2 h (300 °C for the NbO-NA(c) sample). Prior to N₂ adsorption, the catalysts were evacuated under vacuum at 300 °C for 2 h. External surface area was calculated by a multipoint Brunauer–Emmett–Teller (BET) method and the *t* method. Temperature-programmed desorption (TPD) of ammonia, NH₃-TPD, was employed to measure oxide surface acidity. The experiment was carried out using an autochemisorption system (BEL Japan). The experimental procedure was as follows. The catalyst (*ca.* 50 mg) was set between two layers of quartz wool and preheated under helium (50 mL min^{−1}) at 400 °C for 1 h (300 °C for the NbO-NA(c) sample). Then ammonia was introduced at 150 °C for 30 min. The desorption profile from 150 to 700 °C was recorded with a mass spectrometer under helium flow (50 mL min^{−1}). Temperature-programmed decomposition mass spectrometry (TPD-MS) measurements were performed from 40 to 700 °C at a heating rate of 10 °C min^{−1} in helium flow (50 mL min^{−1}).

The decomposed gas molecules were monitored by a mass spectrometer (ANELVA, Quadrupole Mass Spectrometer, M-100QA, BEL Japan), collecting several mass fragments: CO₂ (44), O₂ (32), CO and N₂ (28), H₂O (18, 17, 16) and NH₃ (17, 16, 15). XPS (JPC-9010MC, JEOL) with non-monochromatic Mg-K α radiation was used for measuring binding energy values of Nb. Binding energy was based on Au 4f_{7/2} (84.0 eV) deposited by an auto fine coater (JFC-1600, JEOL). Measurements of thermogravimetric-differential thermal analysis (TG-DTA) were performed on a Rigaku TG-8120 thermogravimetric analyzer. Dry air provided by a pressure tank with a flow rate of 30 mL min⁻¹ was used as the carrier gas. The catalyst sample and a standard were loaded onto two alumina pans and heated at 10 °C min⁻¹ to the desired temperature.

Results and discussion

Several niobium precursors were used for the hydrothermal synthesis of niobium oxides, and the characterization results of the obtained niobium oxides are summarized in Table 1. Fig. 1 shows XRD patterns of the obtained niobium oxide samples. When 0.15 mol L⁻¹ ammonium niobium oxalate (NH₄[NbO(C₂O₄)₂(H₂O)₂] \cdot *n*H₂O) dissolved in 40 mL of water was used as a precursor solution (NbO-ANO), the XRD pattern of NbO-ANO calcined at 400 °C showed only a tense and sharp peak at $2\theta = 22.7^\circ$ and a relatively weak peak at $2\theta = 46.2^\circ$. The peaks at $2\theta = 22.7^\circ$ and 46.2° can be attributed to (001) and (002) planes, respectively. The XRD pattern of NbO-ANO was very similar to that of amorphous Mo₃VO_x (Fig. S1†), which possesses a layered structure in the *c*-direction with an interval layer distance of 4.01 Å. The arrangement of the *a*-*b* plane of amorphous Mo₃VO_x is a network of pentagonal units.²³ The results of XRD suggested that the arrangement of niobium oxide in the *a*-*b* plane is also a deformed orthorhombic structure as shown Fig. 2b. In the case of the NbO-ANO sample, the interval layer distance of Nb-O-Nb was 3.92 Å, calculated from the diffraction peak. This distance is smaller than that of Mo-O-Mo due to Nb

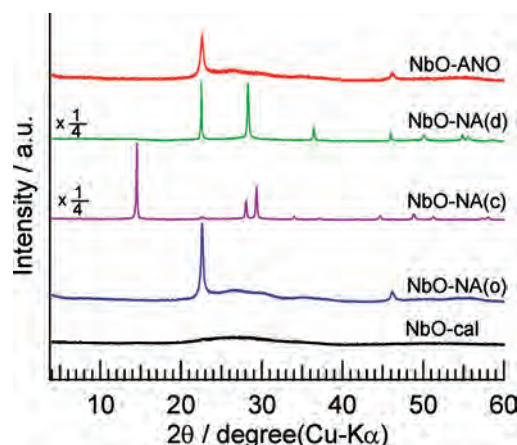


Fig. 1 XRD patterns of various niobium oxides after heat treatment.

octahedra which tend to be more symmetric than Mo. High-resolution transmission electron microscopy (HRTEM) images and selected area electron diffraction of NbO-ANO were collected to confirm its crystal structure (Fig. 2a). The layer distance in the *c*-direction was estimated to be 3.91 Å from the HRTEM image, which is in good agreement with the results obtained from the XRD pattern of that catalyst. Leite *et al.* reported the synthesis of pseudohexagonal niobium oxide nanorods by hydrothermal treatment (140 °C) of a niobium peroxy complex precursor formed by ammonium niobium oxalate (NH₄[NbO(C₂O₄)₂(H₂O)₂] \cdot *n*H₂O) and hydrogen peroxide.⁷ It is thought that these different phases of layered-type and pseudohexagonal niobium oxides were formed due to different niobium precursors and hydrothermal conditions.

Niobic acid, which is often used as a solid acid, was also subjected to hydrothermal synthesis. Crystalline niobium oxides possessing a pseudohexagonal phase (NbO-NA(d)) and a pyrochlore phase (NbO-NA(c)) were synthesized by adjusting the amount of niobic acid in the precursor solution, and their diffraction patterns are shown in Fig. 1. Fig. S2† shows the effects of the amount of niobic acid on the XRD patterns of

Table 1 Results of the characterization of various niobium oxides obtained by a hydrothermal method

Catalyst	Synthesis method	Calcination temp./°C	Crystallinity	<i>d</i> (001)	Morphology (particle size/nm)	BET surface area/m ² g ⁻¹	<i>t</i> -plot/m ² g ⁻¹	Mesopore volume ^a /cm ³ g ⁻¹
NbO-ANO	Hydrothermal	400	Deformed orthorhombic	3.922	Rod (10 × 50–100)	193	202	0.563
NbO-NA(d)	Hydrothermal	400	Pseudohexagonal (TT-Nb ₂ O ₅)	3.938	Rod (200 × 2000)	47	48	0.228
NbO-NA(c)	Hydrothermal	300	Pyrochlore	—	Sphere (50–250)	38	38	0.035
NbO-NA(o)	Hydrothermal	400	Deformed orthorhombic	3.928	Rod (10 × 30–50)	100	107	0.131
NbO-cal	Calcination	400	Amorphous	—	Sphere (50–250)	27	27	0.002
NbO-ANO	Hydrothermal	500	Deformed orthorhombic	3.921	n.d.	113	115	0.071
NbO-ANO	Hydrothermal	550	Orthorhombic (T-Nb ₂ O ₅)	3.935	n.d.	66	67	0.010
NbO-ANO	Hydrothermal	700	Orthorhombic (T-Nb ₂ O ₅)	3.933	n.d.	21	21	0.003

^a Calculated by the BJH method.

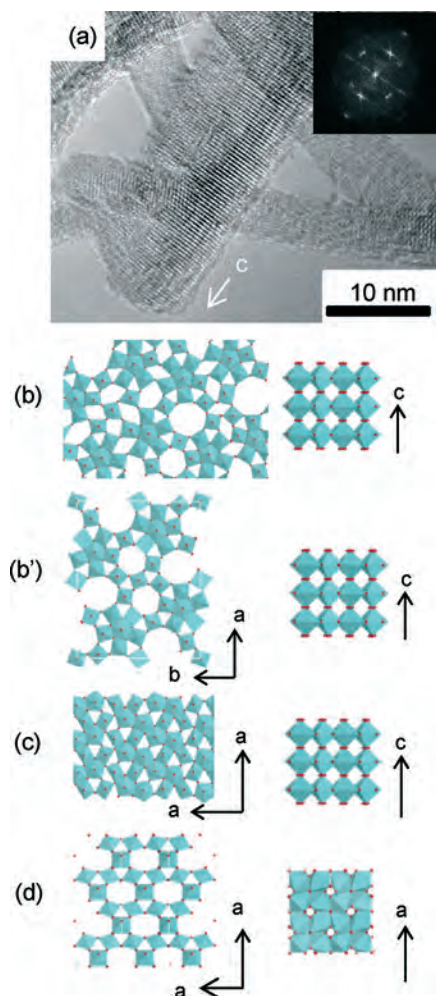


Fig. 2 (a) HRTEM image and electron diffraction pattern of NbO-ANO, (b) proposed structure model of NbO-ANO (deformed orthorhombic), and (b') crystalline models of orthorhombic, (c) pseudo-hexagonal (TT-Nb₂O₅) and orthorhombic (T-Nb₂O₅) niobium oxides, and (d) pyrochlore niobium oxide. (Blue octahedron: Nb–O octahedron, red dot: oxygen)

niobium oxides obtained before calcination. The sample obtained from 0.25 mmol of Nb₂O₅ in 40 mL of deionized water (NbO-NA(d)) gave diffraction peaks at $2\theta = 22.5, 28.3, 36.5, 46.0, 50.1, 54.9^\circ$. This pattern was in agreement with the pseudo-hexagonal structure called TT-Nb₂O₅ phase (JCPDS card no. 28-0317, lattice constants: $c = 3.94 \text{ \AA}$ and $a = 3.64 \text{ \AA}$). The structure of TT-Nb₂O₅ is shown in Fig. 2c. The a - b plane comprises edge-shared NbO₆ and NbO₇ units. These are linked by corner-sharing polyhedra along the c -axis to form the three-dimensional structure.^{33–35} The XRD patterns of niobium oxide obtained from 4 mmol of Nb₂O₅ in 40 mL of deionized water (NbO-NA(c)) gave diffraction peaks at $2\theta = 14.5, 28.0, 29.2, 33.9, 37.0, 41.8, 44.5, 48.7, 51.1, 57.1, 57.9^\circ$ ($Fd\bar{3}m$ (227), JCPDS 61-0608), which are ascribed to a pyrochlore-type crystalline structure (Fig. 2d). The pyrochlore structure comprises corner-shared NbO₆. There are a few reports on pyrochlore H₄Nb₂O₇. Wu *et al.* reported photocatalytic activity over pyrochlore H₄Nb₂O₇ obtained by a hydrothermal method,² and Nalbandyan *et al.* described a method

for synthesis by a solid-state reaction in the JCPDS database (JCPDS 61-0608). In the case of ammonium niobium oxalate, regardless of the concentration in the range of 0.0125 to 0.25 mol L⁻¹, the XRD patterns of the niobium oxide samples gave the same peaks at $2\theta = 22.7^\circ$ and 46.2° (Fig. S3†).

Niobium oxide was also synthesized under hydrothermal conditions from a mixture of niobic acid and oxalic acid. Oxalic acid was added to a niobic acid (2 mmol)-dispersed solution. By the addition of more than 0.125 mol L⁻¹ oxalic acid, niobic acid was completely dissolved. Fig. S4† shows the effects of the ratio of oxalic acid and niobium acid on the XRD pattern of niobium oxide. In the case of niobic acid only, the diffraction pattern was a mixture of layered, pseudo-hexagonal and pyrochlore structures, and the peaks based on the pyrochlore structure decreased upon calcination at 400 °C, while the peaks based on the pseudo-hexagonal phase remained, as will be described later. The peaks based on the pyrochlore and pseudo-hexagonal structures decreased with the addition of oxalic acid, and the peaks of the pyrochlore and pseudo-hexagonal structures were not observed with the addition of 0.25 mol L⁻¹ oxalic acid. This sample was denoted as NbO-NA(o). The XRD pattern of the NbO-NA(o) sample showed peaks at $2\theta = 22.7^\circ$ and 46.2° as in the case of NbO-ANO. For niobium oxide synthesis by a hydrothermal process, it is considered that niobium oxide is formed through a dissolution–crystallization mechanism and rearrangement of the niobium polyhedra occurs. In the presence of oxalic acid, Nb forms pentagonal bipyramidal units with an oxalate ligand in the precursor solution, and the pentagonal {Nb₆O₂₁} units would be formed under hydrothermal conditions. The pentagonal units play an important role in the formation of a new crystalline structure under hydrothermal conditions.

Fig. S5† shows STEM images of the obtained niobium oxides synthesized under hydrothermal conditions, and their morphologies are summarized in Table 1. NbO-ANO consists of one-dimensional nanorods with diameters of *ca.* 10 nm and lengths of 50–100 nm. The nanorods suggest growth along the [001] direction. NbO-NA(o) also consisted of nanorods with diameters of *ca.* 10 nm and lengths of 30–50 nm. NbO-NA(d) was relatively large rods with diameters of *ca.* 200 nm and lengths of 2 μm. NbO-NA(c) and NbO-cal consist of spherical particles with diameters of 50–250 nm.

The samples were heat-treated at different temperatures under air in order to examine their thermal stability. Fig. 3 shows the effect of calcination temperature on the XRD patterns of NbO-ANO and NbO-NA(c). The XRD patterns of the as-synthesized NbO-ANO showed tense and sharp peaks at $2\theta = 22.7^\circ$ and 46.2° as described above. The structure of layered niobium oxide was maintained after 500 °C treatment. When NbO-ANO was calcined at 550 and 700 °C, the peaks at 22.7° shifted to lower angles and diffraction peaks based on orthorhombic niobium oxide (T-Nb₂O₅, *Pbam* (55), JCPDS 30-0837) appeared. The orthorhombic (T-Nb₂O₅) and pseudo-hexagonal (TT-Nb₂O₅) phases are difficult to distinguish in terms of structure. The T phase is thought to be simply a more ordered structure of the TT phase (Fig. 2c).^{33–35}

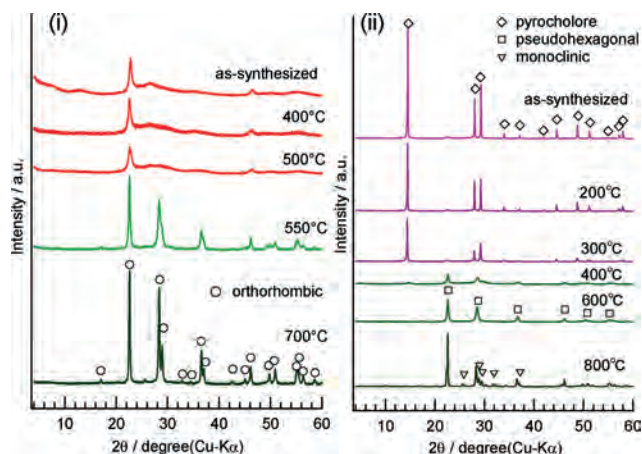


Fig. 3 Effects of calcination temperature on the XRD patterns of (i) NbO-ANO and (ii) NbO-NA(c).

The pyrochlore sample was not stable for heat treatment. The positions of the diffraction peaks of samples heat-treated at 200 and 300 °C for 4 h did not shift, but intensities of the peaks decreased with increasing calcination temperature. The diffraction pattern of pyrochlore niobium oxide calcined at a temperature higher than 400 °C was in the hexagonal phase, revealing a phase transition, and the monoclinic phase was observed in the sample calcined at 800 °C. In order to evaluate the characteristics of the pyrochlore structure, NbO-(c) was treated at 300 °C.

Raman spectroscopy was performed to confirm the niobium oxide structure of the NbO-ANO catalyst. The Raman band in 500–800 cm^{-1} is assigned to the symmetric stretching modes of slightly distorted NbO_6 octahedra, and the associated bending modes of Nb–O–Nb linkages appear in the low wavenumber region at around 200 cm^{-1} .^{13,14} In the case of pseudohexagonal (TT phase) Nb_2O_5 , the Raman band of the symmetric stretching modes of NbO_6 octahedra is observed at around 700 cm^{-1} . The weak broad Raman band at around 900 cm^{-1} is assigned to the symmetric stretching mode of Nb=O surface sites. Fig. 4 shows Raman spectra of obtained niobium oxides after calcination. The Raman band of pyrochlore NbO-NA(c), the corner-shared structure of NbO_6 octahedra, showed a characteristic band based on the symmetric stretching modes (690 cm^{-1}) and the bending modes of the Nb–O–Nb linkage (260, 365, 475 cm^{-1}). The Raman band at 170 cm^{-1} was assigned to the translational modes of Nb, and the Raman bands at 860 and 940 cm^{-1} were assigned to the symmetric stretching mode of terminal Nb–O for pyrochlore NbO-(c).³⁶ The Raman band at 710 cm^{-1} of pseudohexagonal NbO-NA(d), which possesses NbO_6 octahedra and NbO_7 in its structure, is assigned to the symmetric stretching mode of the polyhedra. The Raman bands at 230 and 970 cm^{-1} were assigned to the bending modes of Nb–O–Nb and the symmetric stretching mode of Nb=O, respectively. The Raman band of NbO-ANO was almost the same as that of NbO-NA(d), indicating that NbO-ANO also consists of NbO_6 and NbO_7 . For NbO-cal and NbO-NA(o) samples, the band of

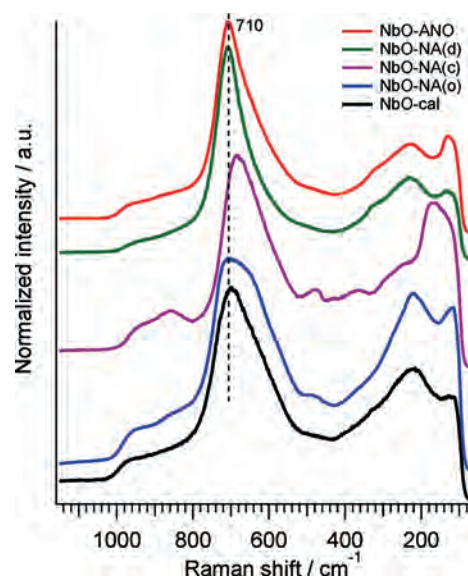


Fig. 4 Raman spectra of various niobium oxides synthesized by a hydrothermal method with niobic acid.

the symmetric stretching mode of the polyhedra shifted to 690 cm^{-1} . For the NbO-NA(o) sample, the band of the symmetric stretching mode of the polyhedra broadened compared to that of the NbO-NA(d) sample, indicating that these samples contain distorted NbO_6 octahedra, NbO_7 pentagonal bipyramids and NbO_8 hexagonal bipyramids.¹³

The XRD pattern and the Raman spectra of NbO-ANO indicated that NbO-ANO is a layered-structure composed of NbO_6 octahedra and NbO_7 pentagonal bipyramids interconnected in the a – b plane. This structure can be regarded as a niobium bronze structure based on pentagonal $\{\text{Nb}_6\text{O}_{21}\}$ building units. Lundberg *et al.* reported orthorhombic $\text{Cs}_x(\text{Nb},\text{W})_5\text{O}_{14}$ (ref. 32) that possesses a tungsten or niobium bronze structure based on the pentagonal unit. This $\text{Cs}_x(\text{Nb},\text{W})_5\text{O}_{14}$ was synthesized by solid-state reaction at high temperature, so that a small surface area (3 $\text{m}^2 \text{g}^{-1}$) is inevitable and it is difficult to remove the cesium cations in the heptagonal channel.²⁹ We have reported on molybdenum bronze based on the pentagonal $\{\text{Mo}_6\text{O}_{21}\}$ unit of orthorhombic Mo_3VO_x obtained by a hydrothermal method. Ammonium cations derived from the precursor are located in the heptagonal channel and they can be removed as ammonia by calcination. After calcination, the heptagonal channel acts as a micropore.²³ Therefore, the presence of micropores confirms the formation of a bronze structure as an orthorhombic phase (Fig. 2b'). In order to investigate microporosity, N_2 adsorption of NbO-ANO, NbO-NA(d), NbO-NA(c), NbO-NA(o) and NbO-cal was examined (Fig. S6[†]), and the calculated data are summarized in Table 1. Orthorhombic Mo_3VO_x showed N_2 adsorption at a relative pressure P/P_0 lower than 1.0×10^{-5} , revealing microporosity. The NbO-ANO sample also showed N_2 adsorption at low pressure (1.0×10^{-6}), suggesting the formation of micropore-like heptagonal channels. In addition, the difference in surface areas between the BET method and

the *t* method indicates the existence of micropores. After adsorption at 1.0×10^{-6} , the amount of adsorbed nitrogen gradually increased with nitrogen pressure for NbO-ANO, suggesting that the micropores formed within NbO-ANO are partially non-uniform. NbO-NA(o) and NbO-NA(d) also adsorbed N_2 at a relatively low pressure, but the adsorption volume increased gradually, implying that the size of micropores was not ordered. NbO-NA(c) and NbO-cal did not show N_2 adsorption at low pressure.

Results of XRD, Raman and adsorption analyses suggested that the *a*-*b* plane of NbO-ANO is a deformed orthorhombic structure as illustrated in Fig. 2b. The deformed orthorhombic structure in the *a*-*b* plane perpendicular to the *c*-axis is an interconnection of crystal structure motifs such as pentagonal $\{Nb_6O_{21}\}$ units and micropore channels but without any long-range order. In order to confirm its structure, TPD-MS, TG and XPS were carried out (Fig. S7, S8†). From these analyses, the formula of as-synthesized NbO-ANO can be expressed as $H_{19.9}(NH_4)_{4.1}Nb_{40}O_{112} \cdot 3.6H_2O$, calculated on the basis of a lattice unit of the orthorhombic phase. Elemental composition is expressed as $A^I_4M^{V/VI}_{40}O_{112} \cdot nH_2O$ (A: cation, M: metal) for the orthorhombic structure. The ratio of ammonia cation to metal was matched from a structural point of view. This result indicated that NH_3 is located in the heptagonal channel.

NH_4^+ formed by NbO_6 octahedra (NH_4-ONb) in the heptagonal channel can be released by calcination, and Brønsted acid sites ($HO-Nb$) will be produced. Thus, the solid acid catalytic activity was examined by the relationship between structure and catalytic activity. Results of the Friedel-Crafts alkylation reactions of anisole with benzyl alcohol over various niobium oxides are presented in Table 2 and Fig. S9†. Several catalysts showed 100% conversion under condition I, therefore catalytic tests were also conducted under condition II in order to compare the catalytic activities. Acid amounts of niobium oxides were measured by NH_3 -TPD (Fig. S10† and Table 2). The products were benzyl anisole and dibenzyl ether. Carbon balance was always more than 97% in all experiments. The NbO-ANO (deformed orthorhombic) catalyst had

the highest activity, with 100% conversion of benzyl alcohol in 94% yield (benzyl anisole) under condition I. Catalyst reuse experiment was done under condition II for three runs (Fig. S11†). The collected catalyst was repeatedly rinsed with acetone and dried in an oven at 80 °C. No significant decrease in benzyl alcohol conversion and benzyl anisole yield was observed after three reuses of the catalyst. The conversion of benzyl alcohol decreased with increasing heat treatment temperature, and the NbO-ANO sample calcined at 550 °C showed 31% conversion in 29% yield, while NbO-ANO calcined at 700 °C (orthorhombic, $T-Nb_2O_5$) showed no catalytic activity. NbO-NA(d) (pseudo-hexagonal) samples (83% conversion, 78% yield) and NbO-cal (amorphous) samples (12% conversion, 9% yield) showed less activity.

NbO-NA(c) (pyrochlore) showed no catalytic activity as a solid acid, even though it adsorbed many NH_3 molecules as revealed by NH_3 -TPD. The amount of adsorbed NH_3 was 1.36 mmol g^{-1} when NH_3 was adsorbed at 150 °C, and this value corresponded to $(NH_4)_{0.36}Nb_2O_5 \cdot nH_2O$. The adsorbed NH_3 would be located inside the hexagonal channel like other pyrochlore $A_2Nb_2O_7$ types,³⁷⁻³⁹ and this site potentially acts as a solid acid site, but the hexagonal channel is too small for an organic substrate to access.

The NbO-NA(o) samples showed less activity than that of NbO-ANO under condition II (Table 2). Fig. 5 shows the results of characterization and alkylation reaction for niobium oxide obtained from a mixture of niobic acid and oxalic acid. By the addition of oxalic acid to niobic acid, the BET surface area and acid amount increased, and with an increase in the concentration of oxalic acid, the BET surface area and acid amount gradually decreased. On the other hand, the yield of benzyl anisole increased with increasing oxalic acid concentration in the precursor solution. Although NbO-NA(o) showed an XRD pattern similar to that of NbO-ANO, the catalytic activities were different under condition II. From the Raman spectra of NbO-NA(o), the band of the symmetric stretching mode of niobium polyhedra was broad (Fig. 4) and N_2 adsorption at low pressure indicated that micropores based on the heptagonal channel were not formed in an

Table 2 Alkylation over various niobium oxides

Catalyst	Calcination temp./°C	Acid amounts ^a		Conv. (benzyl alcohol)/% (yield (benzyl anisole)/%)		F. r. ^b /mmol h ⁻¹ m ⁻²
		mmol g ⁻¹	μmol m ⁻²	Condition I ^c	Condition II ^d	
NbO-ANO	400	0.152	0.788	100 (93.9)	51.7 (36.4)	0.094
NbO-NA(d)	400	0.025	0.532	82.8 (77.6)	5.4 (2.7)	0.029
NbO-NA(c)	300	1.362	—	0.0 (0.0)	0.0 (0.0)	0.000
NbO-NA(o)	400	0.078	0.729	100 (91.6)	20.7 (11.6)	0.054
NbO-cal	400	0.008	0.296	12.4 (8.6)	2.1 (1.3)	0.024
NbO-ANO	500	0.028	0.248	100 (96.3)	43.6 (26.2)	0.116
NbO-ANO	550	0.003	0.045	31.2 (29.1)	14.9 (9.7)	0.073
NbO-ANO	700	0.000	0.000	4.5 (0.8)	0.0 (0.0)	0.000
NbO-ANO(K ⁺)	400	0.038	0.208	5.6 (0.7)	0.0 (0.0)	0.000
NbO-ANO(NH ₄ ⁺)	400	0.168	0.840	100 (93.2)	43.6 (28.2)	0.071

^a Acid amounts were calculated by NH_3 -TPD and BET surface area. ^b Formation rate of benzyl anisole per BET surface area for condition II.

^c Reaction condition I: benzyl alcohol (1.0 mmol), anisole (50 mmol), catalyst (0.1 g), 100 °C, 30 min. ^d Reaction condition II: benzyl alcohol (10 mmol), anisole (100 mmol), catalyst (0.1 g), 100 °C, 120 min.

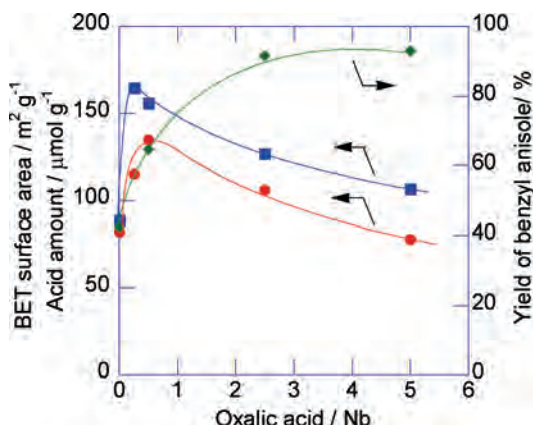


Fig. 5 Effects of the ratio of oxalic acid and niobium oxide in the precursor solution on BET surface area (■), acid amount calculated by NH_3 -TPD (●) and alkylation results (◆) of the obtained sample. (Reaction condition was condition I in Table 2.)

orderly manner. In the case of orthorhombic Mo_3VO_x , the cation in the precursor solution acts as a stabilizer and a structure-directing agent under hydrothermal conditions.⁴⁰ For niobium oxide, it is considered that the ammonium cation has an important role in the formation of a uniform crystalline structure and micropores based on the heptagonal channel. These results also suggested that a stronger Brønsted acid site was formed around the open mouth of the heptagonal channel after desorption of ammonia.

A comparison of the formation rates of benzyl anisole per surface area showed that the order of catalytic activity was NbO-ANO (deformed orthorhombic) > NbO-NA(o) > NbO-NA(d) (TT-Nb₂O₅), NbO-cal (amorphous) ≫ NbO-ANO(T-Nb₂O₅), NbO-NA(c) (pyrochlore). It is difficult to relate the acid amount to alkylation activity because the acid amount calculated by NH_3 -TPD includes both Lewis acid and Brønsted acid sites. It is known that the activity for the alkylation of anisole and benzyl alcohol over niobic acid can be promoted on Brønsted acid sites.^{16–22} To demonstrate the effect of Brønsted acid sites, ion exchange treatments were conducted. After K^+ -exchange treatment (NbO-ANO(K^+)), 85% of NH_4^+ in niobium oxide was ion-exchanged by K^+ as confirmed by TPD measurements (Fig. S12[†]). IR spectra also confirmed that NH_4^+ existed in the NbO-ANO precursor and NH_4^+ was removed by ion exchange treatment. In addition, after the NH_4^+ -exchange treatment of NbO-ANO(K^+), the amount of NH_4^+ in NbO-ANO(NH_4^+) was 81% of NbO-ANO. NbO-ANO(K^+) showed no activity for the alkylation reaction of benzyl alcohol. On the other hand, NbO-ANO(NH_4^+) showed activity similar to that of NbO-ANO (Table 2). These results suggested that NbO-ANO possesses ion-exchange capacity. The ion exchange treatment by K^+ deactivated the Brønsted acid sites but these sites were recovered with further ion exchange by NH_4^+ and calcination.

NbO-ANO ($\text{H}_{19.9}(\text{NH}_4)_{4.1}\text{Nb}_{40}\text{O}_{112}\cdot 3.8\text{H}_2\text{O}$) desorbed NH_3 and water during calcination at 400 °C without changing its structure. A Brønsted acid site would be formed around the open mouth of the heptagonal channel after desorption of

ammonia. This acid site of NbO-ANO can explain the solid acid activity for crystalline niobium oxide. A more crystalline niobium oxide must be prepared for its exact structure analysis. However, layered-structure niobium oxide formed by NbO₆ octahedra and NbO₇ pentagonal bipyramids, possessing a crystalline structure such as an orthorhombic structure, would form exceptional acid sites.

Conclusions

Crystalline niobium oxides (deformed orthorhombic, pseudo-hexagonal (TT-Nb₂O₅), orthorhombic (T-Nb₂O₅) and pyrochlore niobium oxides) were synthesized by a hydrothermal process. The NbO-ANO sample obtained from ammonium niobium oxalate showed a layered-type structure, in which NbO₆ octahedra were corner-sharing in the *c*-direction. Raman spectra indicated that the layered niobium consisted of NbO₆ octahedra and NbO₇ in its structure. Adsorption results showed the presence of micropore channels, indicating the formation of a high-dimensional structure in the *a*-*b* plane. From these results, we concluded that the structure of NbO-ANO was in a deformed orthorhombic phase. As-synthesized NbO-ANO was expressed as $\text{H}_{19.9}(\text{NH}_4)_{4.1}\text{Nb}_{40}\text{O}_{112}\cdot 3.8\text{H}_2\text{O}$, and NH_3 and water were desorbed by calcination at 400 °C, forming a Brønsted acid site without changing its structure. This material showed high catalytic activity as a solid acid. The layered-structure niobium oxide composed of NbO₆ octahedra and pentagonal {Nb₆O₂₁} units forms exceptional Brønsted acid sites around the open mouth of the heptagonal channel.

Acknowledgements

This work was supported by JSPS KAKENHI Grant-in-Aid for Young Scientists 24760635.

Notes and references

- 1 A. Llordés, G. Garcia, J. Gazquez and D. J. Milliron, *Nature*, 2013, **500**, 323–326.
- 2 J. Wu, J. Li, X. Lü, L. Zhang, J. Yao, F. Zhang, F. Huang and F. Xu, *J. Mater. Chem.*, 2010, **20**, 1942–1946.
- 3 K. Tanabe and S. Okazaki, *Appl. Catal., A*, 1995, **133**, 191–218.
- 4 K. Nakajima, Y. Baba, R. Noma, M. Kitano, J. N. Kondo, S. Hayashi and M. Hara, *J. Am. Chem. Soc.*, 2011, **133**, 4224–4227.
- 5 C. Feldmann and H.-O. Jungk, *Angew. Chem., Int. Ed.*, 2001, **40**, 359–362.
- 6 N. Uekawa, T. Kudo, F. Mori, Y. J. Wu and K. Takegawa, *J. Colloid Interface Sci.*, 2003, **264**, 378–384.
- 7 E. R. Leite, C. Vila, J. Bettini and E. Longo, *J. Phys. Chem. B*, 2006, **110**, 18088–18090.
- 8 Y. Zhou, Z. Qiu, M. Lü, A. Zhang and Q. Ma, *J. Lumin.*, 2008, **128**, 1369–1372.
- 9 M. Mozetič, U. Cvelbar, M. K. Sunkara and S. Vaddiraju, *Adv. Mater.*, 2005, **17**, 2138–2142.

- 10 W. Hu, Z. Liu, G. Nie, Y. Mi, Y. Zhao and K. Yao, *Mater. Chem. Phys.*, 2009, **113**, 511–514.
- 11 N. Pinna, M. Antonietti and M. Niederberger, *Colloids Surf., A*, 2004, **250**, 211–213.
- 12 W. Fan, Q. Zhang, W. Deng and Y. Wang, *Chem. Mater.*, 2013, **25**, 3277–3287.
- 13 J. M. Jehng and I. E. Wachs, *Chem. Mater.*, 1991, 100–107.
- 14 R. Brayner and F. Bozon-Verduraz, *Phys. Chem. Chem. Phys.*, 2003, **5**, 1457–1466.
- 15 V. Lebarbier, M. Houalla and T. Onfroy, *Catal. Today*, 2012, **192**, 123–129.
- 16 Y. Rao, M. Trudeau and D. Antonelli, *J. Am. Chem. Soc.*, 2006, **128**, 13996–13997.
- 17 M. Delacruz, J. Dasilva and E. Lachter, *Catal. Today*, 2006, **118**, 379–384.
- 18 R. M. West, D. J. Braden and J. A. Dumesic, *J. Catal.*, 2009, **262**, 134–143.
- 19 A. Takagaki, M. Sugisawa, D. Lu, J. N. Kondo, M. Hara, K. Domen and S. Hayashi, *J. Am. Chem. Soc.*, 2003, **125**, 5479–5485.
- 20 C. Tagusagawa, A. Takagaki, S. Hayashi and K. Domen, *J. Am. Chem. Soc.*, 2008, **130**, 7230–7231.
- 21 K. Yamashita, M. Hirano, K. Okumura and M. Niwa, *Catal. Today*, 2006, **118**, 385–391.
- 22 T. Shishido, T. Kitano, K. Teramura and T. Tanaka, *Catal. Lett.*, 2009, **129**, 383–386.
- 23 T. Konya, T. Katou, T. Murayama, S. Ishikawa, M. Sadakane, D. Buttrey and W. Ueda, *Catal. Sci. Technol.*, 2013, **3**, 380–387.
- 24 S. Ishikawa, X. Yi, T. Murayama and W. Ueda, *Catal. Today*, 2014, 8–13.
- 25 S. Ishikawa, X. Yi, T. Murayama and W. Ueda, *Appl. Catal., A*, 2014, **474**, 10–17.
- 26 M. Sadakane, N. Watanabe, T. Katou, Y. Nodasaka and W. Ueda, *Angew. Chem., Int. Ed.*, 2007, **46**, 1493–1496.
- 27 M. Sadakane, K. Kodato, T. Kuranishi, Y. Nodasaka, K. Sugawara, N. Sakaguchi, T. Nagai, Y. Matsui and W. Ueda, *Angew. Chem., Int. Ed.*, 2008, **47**, 2493–2496.
- 28 T. Murayama, N. Kuramata, S. Takatama, K. Nakatani, S. Izumi, X. Yi and W. Ueda, *Catal. Today*, 2012, **185**, 224–229.
- 29 K. Omata, S. Izumi, T. Murayama and W. Ueda, *Catal. Today*, 2013, **201**, 7–11.
- 30 K. Omata, K. Matsumoto, T. Murayama and W. Ueda, *Chem. Lett.*, 2014, **43**, 435–437.
- 31 N. Galešić, N. Brničević, B. Matković, M. Herceg, B. Zelenko, M. Šljukić, B. Prelesnik and R. Herak, *J. Less-Common Met.*, 1977, **51**, 259–270.
- 32 M. Lundberg and M. Sundberg, *Ultramicroscopy*, 1993, **52**, 429–435.
- 33 K. Kato and S. Tamura, *Acta Crystallogr., Sect. B: Struct. Crystallogr. Cryst. Chem.*, 1975, **31**, 673–677.
- 34 H. Schäfer, R. Gruehn and F. Schulte, *Angew. Chem., Int. Ed. Engl.*, 1966, **5**, 40–52.
- 35 Y. Kobayashi, H. Hata, M. Salama and T. E. Mallouk, *Nano Lett.*, 2007, **7**, 2142–2145.
- 36 M. Maćzka, A. V. Knyazev, A. Majchrowski, J. Hanuza and S. Kojima, *J. Phys.: Condens. Matter*, 2012, **24**, 195902.
- 37 Z. Zou, J. Ye and H. Arakawa, *Chem. Mater.*, 2001, **13**, 1765–1769.
- 38 Z. Zou, J. Ye and H. Arakawa, *J. Phys. Chem. C*, 2002, **106**, 517–520.
- 39 L. Zhang, H. Fu, C. Zhang and Y. Zhu, *J. Phys. Chem. C*, 2008, **112**, 3126–3133.
- 40 S. Ishikawa, T. Murayama, S. Ohmura, M. Sadakane and W. Ueda, *Chem. Mater.*, 2013, **25**, 2211–2219.

Cite this: *Dalton Trans.*, 2014, **43**,
13584

Investigation of the formation process of zeolite-like 3D frameworks constructed with ϵ -Keggin-type polyoxovanadomolybdates with binding bismuth ions and preparation of a nano-crystal[†]

Zhenxin Zhang,^a Masahiro Sadakane,^{*b,c} Toru Murayama^a and Wataru Ueda^{*a}

Reaction conditions for the synthesis of an ϵ -Keggin-type polyoxometalate-based 3D framework, $(\text{NH}_4)_{2.8}\text{H}_{0.9}[\epsilon\text{-VMo}_{9.4}\text{V}_{2.6}\text{O}_{40}\text{Bi}_2]\cdot 7.2\text{H}_2\text{O}$ (denoted as Mo–V–Bi oxide), are studied. It is found that the reaction time, temperature, pH of the solution, and starting compounds affect the production of Mo–V–Bi oxide. The crystal size of Mo–V–Bi oxide is controllable by changing bismuth compounds. Nanometer-sized Mo–V–Bi oxide is produced using a water-soluble bismuth compound, $\text{Bi}(\text{NO}_3)_3\cdot 5\text{H}_2\text{O}$, whereas micrometer to submicrometer-sized Mo–V–Bi oxide is produced using $\text{Bi}(\text{OH})_3$, which is less soluble in water. The particle size of the material affects the properties of the material, such as surface area and catalysis. The investigation of the formation process of the material is carried out with Raman spectroscopy, which indicates that mixing $(\text{NH}_4)_6\text{Mo}_7\text{O}_{24}\cdot 4\text{H}_2\text{O}$, $\text{VOSO}_4\cdot 5\text{H}_2\text{O}$, and bismuth ions in water produces the ϵ -Keggin polyoxovanadomolybdate together with a ball-shaped polyoxovanadomolybdate, $[\text{Mo}_{72}\text{V}_{30}\text{O}_{282}(\text{H}_2\text{O})_{56}(\text{SO}_4)_{12}]^{36-}$ (denoted as $\{\text{Mo}_{72}\text{V}_{30}\}$). By heating the reaction mixture, the ϵ -Keggin polyoxovanadomolybdate assembles with bismuth ions to form Mo–V–Bi oxide, whereas $\{\text{Mo}_{72}\text{V}_{30}\}$ assembles with other vanadium and molybdenum ions to form orthorhombic Mo–V oxide.

Received 26th April 2014,
Accepted 16th July 2014
DOI: 10.1039/c4dt01227e

www.rsc.org/dalton

Introduction

Polyoxometalates (POMs) are anionic metal oxygen clusters of W, Mo, V, and Nb. POMs have attracted much attention because they have been applied to various fields.^{1–5} In materials science, POMs are known to be well-defined building blocks for well-ordered crystalline materials, because they can interact with not only various organic compounds but also inorganic ions, resulting in the synthesis of POM-based materials, including polyoxometalate organic framework (POMOF) materials,^{6–9} POM-macrocation materials,^{10–15} and microporous Mo-based complex oxides.^{16–21}

Recently, we have reported the first ϵ -Keggin POM-based microporous metal oxide, $(\text{NH}_4)_{2.8}\text{H}_{0.9}[\epsilon\text{-VMo}_{9.4}\text{V}_{2.6}\text{O}_{40}\text{Bi}_2]\cdot 7.2\text{H}_2\text{O}$, formed by connecting ϵ -Keggin polyoxovano-

molybdate ($[\text{VMo}_{9.4}\text{V}_{2.6}\text{O}_{40}]^{9.7-}$) units with Bi^{3+} in a tetrahedral fashion (Fig. 1a and b).²² Micropores of the material, which are derived from cages and channels surrounded by the framework, can be opened by heat treatment. The material shows interesting zeolite-like properties such as ion-exchange, molecule adsorption, and acid catalysis.

However, the formation process of Mo–V–Bi oxide has not been elucidated. Moreover, the yield of well-crystallized Mo–V–Bi oxide is low (3% based on Mo after purification), which should be improved for further investigations of this material. Furthermore, from the viewpoint of applications, the size of

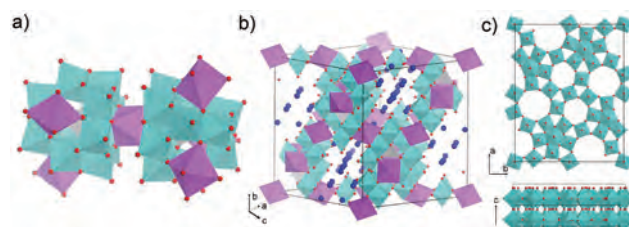


Fig. 1 Polyhedral representations of (a) ϵ -Keggin units and their connection, (b) unit cell of Mo–V–Bi oxide, and (c) orthorhombic Mo–V oxide, Mo–O and V–O octahedra (blue octahedra), V–O tetrahedra (gray tetrahedra), Bi–O octahedra (purple octahedra), cation or water (deep blue spheres), and O (red spheres).

^aCatalysis Research Center, Hokkaido University, N-21, W-10, Kita-ku, Sapporo 001-0021, Japan. E-mail: ueda@cat.hokudai.ac.jp; Fax: +81-11-706-9163; Tel: +81-11-706-9164

^bDepartment of Applied Chemistry, Graduate School of Engineering, Hiroshima University, 1-4-1 Kagamiyama, Higashi Hiroshima 739-8527, Japan. E-mail: sadakane09@hiroshima-u.ac.jp; Fax: +81-82-424-5494; Tel: +81-82-424-4456

^cJST, PRESTO, 4-1-8 Honcho, Kawaguchi, Saitama 332-0012, Japan

[†]Electronic supplementary information (ESI) available. See DOI: 10.1039/c4dt01227e

the material is also important, and many examples of nanometer-sized materials showing properties superior to those of larger materials have been presented.^{23–26}

In this paper, we describe in detail the conditions for synthesis of Mo–V–Bi oxide. Crystal size of the resulting Mo–V–Bi oxide was found to be highly dependent on the starting materials and could be controlled by altering the solubility of the starting materials. Nanometer-sized Mo–V–Bi oxide crystals, denoted as nano-Mo–V–Bi oxide, could be synthesized by applying all soluble starting materials. Formation of the ϵ -Keggin POM as building blocks is proposed on the basis of Raman spectra of the precursor solution during the synthesis.

Results and discussion

Preparation of Mo–V–Bi oxide

In our previous paper,²² well-crystallized Mo–V–Bi oxide was synthesized by a hydrothermal reaction of $(\text{NH}_4)_6\text{Mo}_7\text{O}_{24}\cdot 4\text{H}_2\text{O}$ (denoted as AHM), $\text{VOSO}_4\cdot 5\text{H}_2\text{O}$, and $\text{Bi}(\text{OH})_3$ at 448 K for 48 hours (Table 1, entry 3). After the hydrothermal synthesis, the powder XRD pattern of the resulting material showed that the crude material in the autoclave was a mixture of Mo–V–Bi oxide and orthorhombic Mo–V oxide (Fig. 2a). Orthorhombic Mo–V oxide was synthesized by a hydrothermal reaction of AHM and VOSO_4 , and it was constructed by connecting pentagonal polyoxomolybdate units with metal–oxygen octahedra in the a – b plane that grows in the c -axis (Fig. 1c). Purification processes were essential to obtain pure Mo–V–Bi oxide. Mo–V–Bi oxide tended to form on the bottom of the Teflon liner, and a material formed on the Teflon sheet inserted in the Teflon

liner was orthorhombic Mo–V oxide (Fig. 2b) (see the Experimental section for details).¹⁷ Most of the material of orthorhombic Mo–V oxide could be removed by removal of the Teflon sheet, and the rest of the material of orthorhombic Mo–V oxide on the bottom was removed by filtration with cotton and centrifugation. Mo–V–Bi oxide could be separated from orthorhombic Mo–V oxide because of the shape difference of these oxides. Orthorhombic Mo–V oxide, which has a rod-like shape,¹⁷ attached to the cotton, whereas Mo–V–Bi oxide, which has an octahedral shape, easily passed through the cotton (Fig. 3a), and thus Mo–V–Bi oxide could be separated from orthorhombic Mo–V oxide. Centrifugation was also an effective method for separating Mo–V–Bi oxide. After centrifugation, Mo–V–Bi oxide tended to settle on the bottom of the centrifugation tube, and orthorhombic Mo–V oxide was still dispersed in the solution. After the purification process, we could obtain pure well-crystallized Mo–V–Bi oxide (Fig. 2c).

The effects of synthesis conditions including reaction time, reaction temperature, pH value of the precursor, and starting materials were investigated. The results are summarized in Table 1, and the powder XRD patterns of the resulting solids are shown in ESI† Fig. S1. Reaction time of over 4 hours was necessary to obtain Mo–V–Bi oxide (Table 1, entries 1–4, Fig. S1a–d†) at 448 K. After 4 hours, no orthorhombic Mo–V oxide had formed, but Mo–V–Bi oxide and $\text{Bi}(\text{OH})_3$ were detected, indicating that Mo–V–Bi oxide formed faster than orthorhombic Mo–V oxide. Low temperature (293 K) was not suitable for formation of Mo–V–Bi oxide (Table 1, entry 5, Fig. S1e†), and Mo–V–Bi oxide formed at high temperatures (373–448 K, Table 1, entries 6–7, Fig. S1f–g†). A hydrothermal reaction at 373 K produced only Mo–V–Bi oxide, and no other

Table 1 Synthesis of Mo–V–Bi oxide under different conditions^a

Entry	Mo	V	Bi	pH	Time (h)	Temp. (K)	Mo–V–Bi oxide ^b	Orthorhombic Mo–V Oxide ^c	Other phases ^{c,d}
1	AHM ^e	VOSO_4	$\text{Bi}(\text{OH})_3$	3.45	1	448	N	N	Amorphous phase
2	AHM	VOSO_4	$\text{Bi}(\text{OH})_3$	3.45	4	448	Y	N	$\text{Bi}(\text{OH})_3$
3	AHM	VOSO_4	$\text{Bi}(\text{OH})_3$	3.45	48	448	Y	Y	N
4	AHM	VOSO_4	$\text{Bi}(\text{OH})_3$	3.45	120	448	Y	Y	Hexagonal Mo–V oxide
5	AHM	VOSO_4	$\text{Bi}(\text{OH})_3$	3.45	48	293	N	N	Unknown phase
6	AHM	VOSO_4	$\text{Bi}(\text{OH})_3$	3.45	48	373	Y	N	N
7	AHM	VOSO_4	$\text{Bi}(\text{OH})_3$	3.45	48	423	Y	Y	N
8	AHM	VOSO_4	$\text{Bi}(\text{OH})_3$	1.03	48	448	N	N	Hexagonal Mo–V oxide
9	AHM	VOSO_4	$\text{Bi}(\text{OH})_3$	2.07	48	448	Y	N	Unknown phase, VO
10	AHM	VOSO_4	$\text{Bi}(\text{OH})_3$	4.92	48	448	Y	N	Hexagonal Mo–V oxide
11	AHM	VOSO_4	$\text{Bi}(\text{OH})_3$	6.39	48	448	N	N	$\text{Bi}_{24}(\text{VO}_4)(\text{BiO}_4)\text{O}_{32}$, BiVO_4
12	Na_2MoO_4	VOSO_4	$\text{Bi}(\text{OH})_3$	3.38	48	448	N	N	$\text{Na}_{0.32}\text{Bi}_{0.56}(\text{MoO}_4)$, $\text{VO}_{0.9}$
13	K_2MoO_4	VOSO_4	$\text{Bi}(\text{OH})_3$	3.41	48	448	N	N	Unknown phase
14	AHM	NH_4VO_3	$\text{Bi}(\text{OH})_3$	3.55	48	448	N	N	$\text{Na}_{0.32}\text{Bi}_{0.56}(\text{MoO}_4)$
15	AHM	NaVO_3	$\text{Bi}(\text{OH})_3$	3.35	48	448	N	N	$\text{Na}_{0.32}\text{Bi}_{0.56}(\text{MoO}_4)$
16	AHM	VOSO_4	Bi_2O_3	3.42	48	448	Y	Y	N
17	AHM	VOSO_4	BiOCl	3.42	48	448	Y	Y	N
18	AHM	VOSO_4	$\text{Bi}_2(\text{SO}_4)_3$	3.38	48	448	Y	Y	N
19	AHM	VOSO_4	$\text{Bi}(\text{NO}_3)_3$	3.32	48	448	Y	N	Hexagonal Mo–V oxide

^a Mo source (50 mmol based on Mo), V source (12.5 mmol), Bi source (1.67 mmol), 240 mL of water, with the value of pH adjusted by H_2SO_4 (1 M) or NH_3 solution (28%). ^b Presence of Mo–V–Bi oxide was examined by powder XRD after purification. Y: Mo–V–Bi oxide was formed, N: Mo–V–Bi oxide was not formed. Corresponding powder XRD patterns are presented in ESI Fig. S1. ^c Presence of orthorhombic Mo–V oxide and other phases were examined by powder XRD using all solids formed in the autoclave, Y: orthorhombic Mo–V oxide was formed, N: orthorhombic Mo–V oxide was not formed. ^d N: other phase was not formed. ^e AHM: $(\text{NH}_4)_6\text{Mo}_7\text{O}_{24}\cdot 4\text{H}_2\text{O}$.

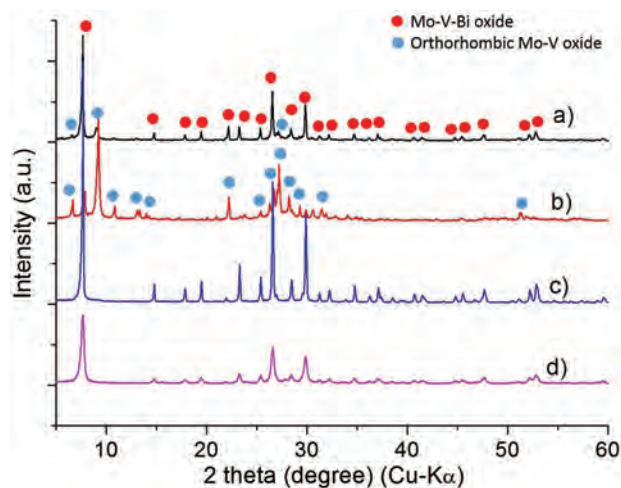


Fig. 2 Powder XRD patterns of (a) the crude solid of Mo–V–Bi oxide, (b) the solid of orthorhombic Mo–V oxide collected on the Teflon sheet, (c) the solid of Mo–V–Bi oxide after purification, and (d) nano-Mo–V–Bi oxide.

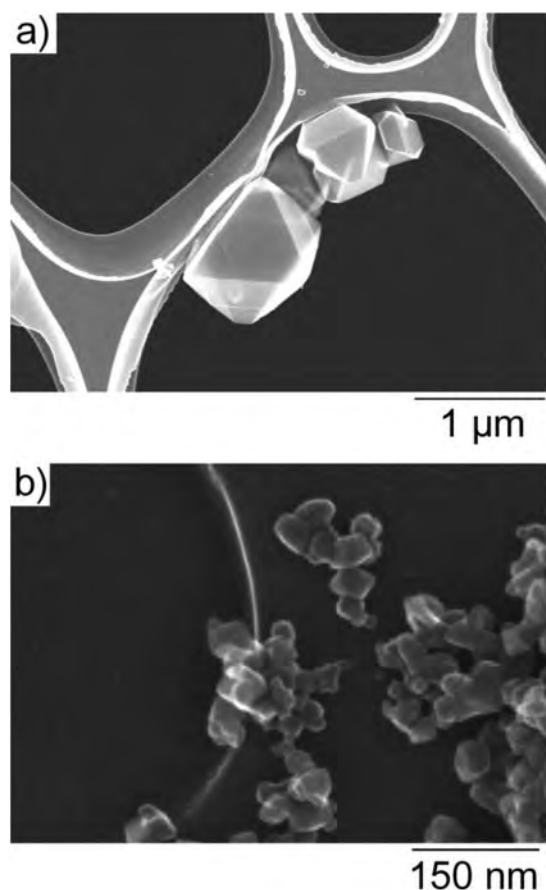


Fig. 3 SEM images of (a) Mo–V–Bi oxide and (b) nano-Mo–V–Bi oxide.

phase was observed. The suitable pH range for production of Mo–V–Bi oxide was from 2 to 5, and Mo–V–Bi oxide did not form at pH higher than 5 or lower than 2 (Table 1, entries 8–11, Fig. S1h–k†). We have reported that orthorhombic Mo–V

oxide is produced in solutions with pH values between *ca.* 2.7 to 3.4 and that trigonal Mo–V oxide and hexagonal Mo–V oxide are produced in a solution with a pH value of 2.¹⁶ These results indicate that Mo–V–Bi oxide can be produced under wider conditions than can orthorhombic Mo–V oxide. It was found that synthesis at 373 K (Table 1, entry 6) could produce mostly pure Mo–V–Bi oxide, but XRD peaks of the Mo–V–Bi oxide (Fig. S1c and f†) were broader than that of well-crystallized Mo–V–Bi oxide (Table 1, entry 3), indicating small crystallite size of the materials. Therefore, well-crystallized material large enough for single crystal structure analysis was obtained at 448 K for 48 h and purification was necessary (Table 1, entry 3).²²

K_2MoO_4 and $Na_2MoO_4 \cdot 2H_2O$ were not suitable to yield Mo–V–Bi oxide (Table 1, entries 12–13, Fig. S1l–m†) despite pH values being between 2 and 5, indicating that Na^+ and K^+ hinder the formation of Mo–V–Bi oxide.

$VOSO_4 \cdot 5H_2O$ was necessary for the production of Mo–V–Bi oxide, and other vanadium compounds could not produce the material (Table 1, entries 14–15, Fig. S1n–o†). Vanadium and molybdenum in Mo–V–Bi oxide were partially reduced, and $VOSO_4 \cdot 5H_2O$ also acted as a reducing reagent. Therefore, NH_4VO_3 and $NaVO_3$ are not suitable vanadium sources.

Several bismuth sources could produce Mo–V–Bi oxide with orthorhombic or hexagonal Mo–V oxide (Table 1, entries 16–19, Fig. S1p–s†). A reaction with $Bi(NO_3)_3 \cdot 5H_2O$ produced Mo–V–Bi oxide as well as hexagonal Mo–V oxide¹⁶ without formation of orthorhombic Mo–V oxide. Interestingly, XRD peaks of Mo–V–Bi oxide produced by synthesis using $Bi(NO_3)_3$ were broader than those of Mo–V–Bi oxide produced using other Bi sources (Fig. S1s†), indicating that smaller crystals of Mo–V–Bi oxide are produced by using $Bi(NO_3)_3$. Crystallite sizes calculated by the Scherrer equation were >100, 63, 76, 81, and 40 nm for materials prepared from $Bi(OH)_3$, Bi_2O_3 , $BiOCl$, $Bi_2(SO_4)_3$, and $Bi(NO_3)_3$, respectively. High solubility of $Bi(NO_3)_3$ (Table S1†) might be a reason for the small crystallite sizes of Mo–V–Bi oxide form.

Synthesis and characterization of nanometer-sized Mo–V–Bi oxide

We found that the use of the dynamic hydrothermal method (the autoclave being rotated during hydrothermal synthesis) and increasing the amount of $Bi(NO_3)_3$ (Mo–V–Bi = 4 : 1 : 0.67) can decrease the amount of impurities. Addition of glycerol increased the solubility of $Bi(NO_3)_3$ (Table S1†), which further suppressed side-reactions and resulted in the production of mostly Mo–V–Bi oxide (Fig. 2d) (the synthesis procedure is presented in the Experimental section). Broad powder diffraction peaks indicated smaller crystals of Mo–V–Bi oxide (denoted as nano-Mo–V–Bi oxide), and crystallite size estimated using the Scherrer equation was *ca.* 24 nm. Nano-Mo–V–Bi oxide was obtained in a high yield (22% based on Mo) compared with the yield of the material obtained using $Bi(OH)_3$ (3% based on Mo).

Powder XRD patterns (Fig. 2c and d) and FT-IR spectra (Fig. S2†) of well-crystallized Mo–V–Bi oxide and nano-Mo–V–Bi oxide confirmed that the basic structures of both oxides are the same. SEM images of nano-Mo–V–Bi oxide and Mo–V–Bi

oxide (Fig. 3) showed that the size of nano-Mo-V-Bi oxide (20–50 nm in one diameter) is much smaller than that of Mo-V-Bi oxide (1 μm in one diameter). Clear lattice images of Mo-V-Bi oxide and nano-Mo-V-Bi oxide could be observed by high-resolution TEM (HR-TEM). An HR-TEM image of nano-Mo-V-Bi oxide showed that the layer distance of the (111) plane was 11.4 \AA (Fig. 4), which is in accordance with the results of powder XRD,²² demonstrating that nano-Mo-V-Bi oxide is a well-ordered nanometer-sized single crystal (Fig. 4b). Elemental analysis showed that the Mo:V:Bi ratio in nano-Mo-V-Bi oxide was 9.4:3.6:2, which is the same as the Mo:V:Bi ratio of well-crystallized Mo-V-Bi oxide.

Nitrogen sorption isotherms of Mo-V-Bi oxide and nano-Mo-V-Bi oxide are shown in Fig. 5a, illustrating that both materials are microporous materials. The amounts of nitrogen gas uptake at very low relative pressure (less than 0.01) of Mo-V-Bi oxide and nano-Mo-V-Bi oxide were similar, indicating that both oxides have similar volumes of micropores. The micropore size distribution showed that the micropore size of both oxides was the same, 5.5 \AA (Fig. 5b). However, the nitrogen gas uptake of nano-Mo-V-Bi oxide continued to increase with increase in relative pressure, indicating that nano-Mo-V-Bi has a larger external surface area. BET surface areas of Mo-V-Bi oxide and nano-Mo-V-Bi oxide were calculated to be 60 $\text{m}^2 \text{g}^{-1}$

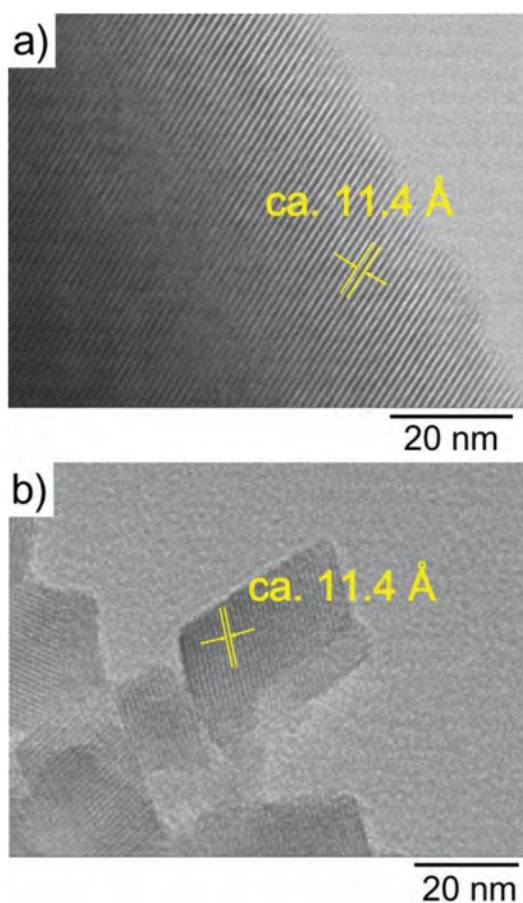


Fig. 4 TEM images of (a) Mo-V-Bi oxide and (b) nano-Mo-V-Bi oxide.

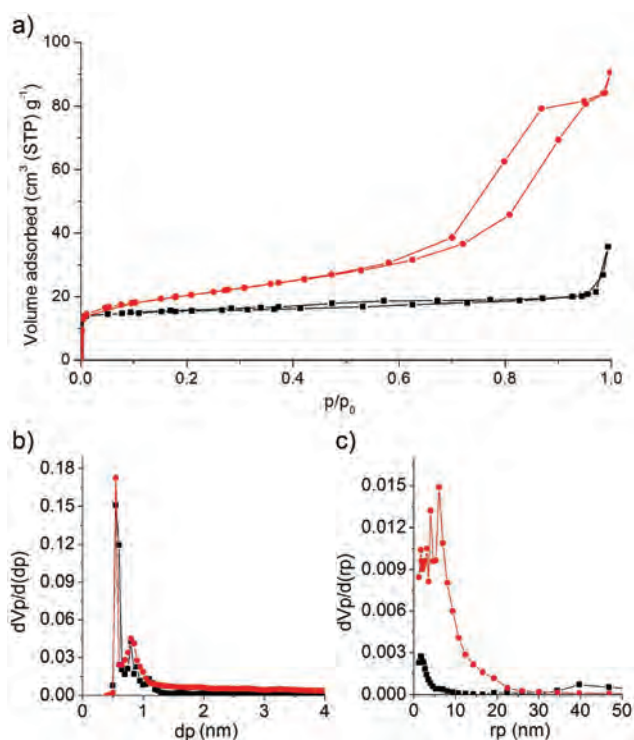


Fig. 5 (a) Nitrogen adsorption-desorption isotherms, (b) pore size distribution calculated by the SF method, and (c) pore size distribution calculated by the BJH method of Mo-V-Bi oxide (black squares) and nano-Mo-V-Bi oxide (red circles).

and 75 $\text{m}^2 \text{g}^{-1}$, respectively. An obvious hysteresis in the N_2 sorption isotherm of nano-Mo-V-Bi oxide was observed in the pressure range from 0.6 to 1.0, which is ascribed to mesopores of the material formed by particle aggregation.^{27,28} Mesopore size distribution of nano-Mo-V-Bi oxide was wide, indicating that mesopores were not uniform (Fig. 5c).

Heat-treatment removed ammonia and water in both Mo-V-Bi oxides. TPD profiles showed ammonia desorbed from the material during heating (Fig. 6), and protons would leave the materials to make charge balance and acted as acid sites. The amount of ammonium cation in both oxides estimated by TPD was similar. For both oxides, their basic struc-

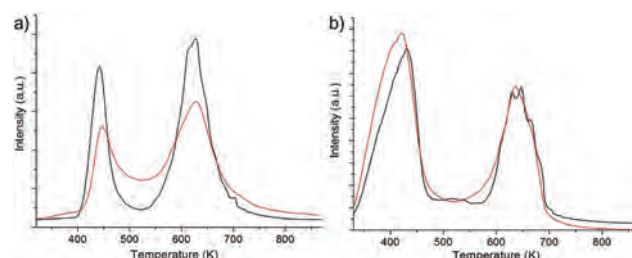


Fig. 6 TPD profiles of Mo-V-Bi oxide (black) and nano-Mo-V-Bi oxide (red), (a) $m/z = 16$ (NH_3 desorption), peak area (Mo-V-Bi oxide): peak area (nano-Mo-V-Bi oxide) = 1.03 : 1, and (b) $m/z = 18$ (water desorption), peak area (Mo-V-Bi oxide): peak area (nano-Mo-V-Bi oxide) = 0.88 : 1.

tures, chemical composition, and the amount of acid sites was almost the same, but the particle size was different. Catalytic activities of as-synthesized nano-Mo-V-Bi oxide, calcined nano-Mo-V-Bi oxide, and calcined Mo-V-Bi oxide for dehydration of benzyl alcohol were examined (Fig. S3†). The as-synthesized nano-Mo-V-Bi oxide did not show catalytic activity, but the calcined one showed enhanced catalytic activity due to the presence of acid sites generated by calcination. Catalytic activity of nano-Mo-V-Bi oxide was enhanced compared to Mo-V-Bi oxide, because the dehydration reaction occurs on the surface of the crystals (Fig. S3†). Smaller particles had more acid sites on the external surface.

Formation mechanism

It was found that Mo-V-Bi oxide can be obtained simply by heating the AHM, $\text{VOSO}_4 \cdot 5\text{H}_2\text{O}$, and $\text{Bi}(\text{NO}_3)_3$ in H_2O -glycerol solution at 373 K for 150 min in a flask under atmospheric conditions (synthesis conditions are shown in the caption of Fig. 7) (Fig. S4†). The solution was monitored by Raman spectroscopy during the synthesis. When AHM and $\text{VOSO}_4 \cdot 5\text{H}_2\text{O}$

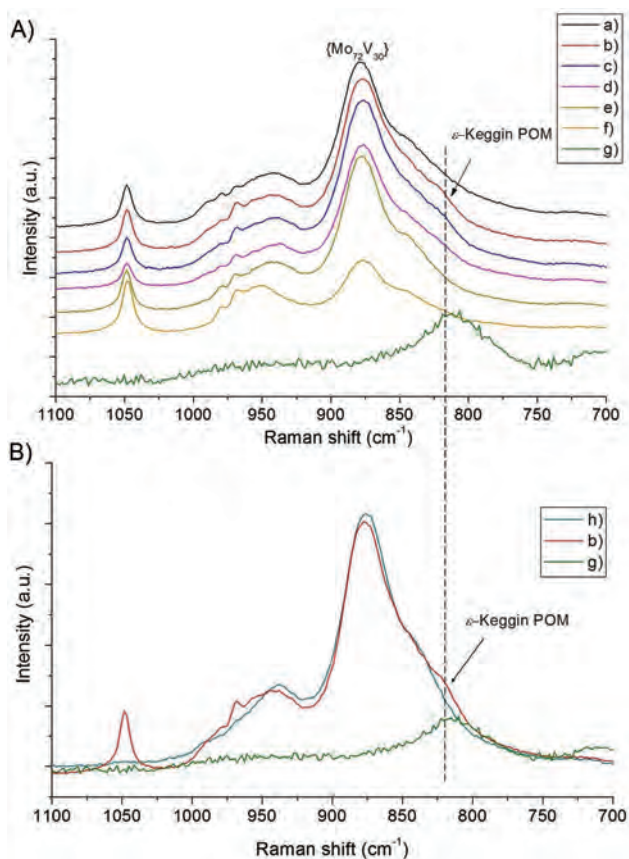


Fig. 7 (A) Raman spectra of the solution: AHM (8.33 mmol based on Mo), $\text{VOSO}_4 \cdot 5\text{H}_2\text{O}$ (2.08 mmol), and $\text{Bi}(\text{NO}_3)_3 \cdot 5\text{H}_2\text{O}$ (1.40 mmol) in 1.7 mL of solution (glycerol-water = 1 : 1), 40 mL of water, pH of 3.4, 373 K for (a) 0 min, (b) 7 min, (c) 15 min, (d) 20 min, (e) 60 min (f) 150 min, (g) Raman spectrum of solid Mo-V-Bi oxide, and (B) Raman spectra of the solution: (h) AHM (8.33 mmol based on Mo), $\text{VOSO}_4 \cdot 5\text{H}_2\text{O}$ (2.08 mmol), 40 mL of water. The band at 1050 cm^{-1} was ascribed to nitrate.

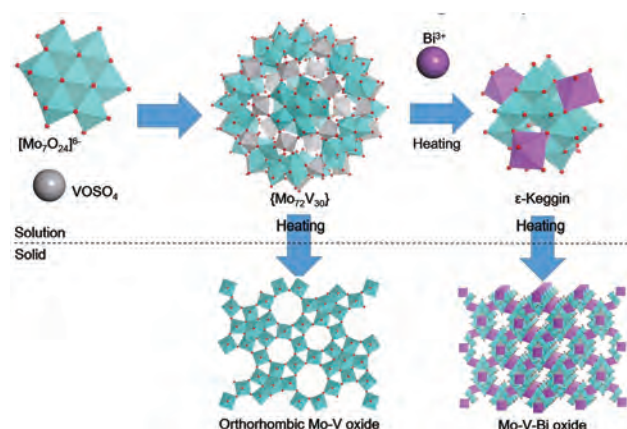


Fig. 8 Formation pathway of Mo-V-Bi oxide and orthorhombic Mo-V oxide: Mo-O octahedra (blue octahedra), V-O tetrahedra or octahedra (gray tetrahedra or octahedra), Bi-O octahedra (purple octahedra), and O (red spheres).

were mixed in H_2O -glycerol solution, a Raman spectrum with a band top of 880 cm^{-1} , typical for the ball-type molybdovanadate of $\{\text{Mo}_{72}\text{V}_{30}\}$, was observed (Fig. 7 and S4†).^{16,29,30} We have reported that mixing AHM and $\text{VOSO}_4 \cdot 5\text{H}_2\text{O}$ in an aqueous solution spontaneously produces $\{\text{Mo}_{72}\text{V}_{30}\}$, which then produces orthorhombic Mo-V oxide under hydrothermal conditions.²¹ When $\text{Bi}(\text{NO}_3)_3$ was added to the solution of AHM and $\text{VOSO}_4 \cdot 5\text{H}_2\text{O}$ and then the solution was heated for 7–15 min, a new band ascribed to $[\epsilon\text{-VMo}_{9.4}\text{V}_{2.6}\text{O}_{40}\{\text{Bi}\}_x]^{n-}$ at 820 cm^{-1} appeared (Fig. 7), and peak intensity was decreased by increasing the reaction time. Furthermore, Raman analysis indicated that heating a solution of AHM and $\text{VOSO}_4 \cdot 5\text{H}_2\text{O}$ without Bi^{III} ions does not produce the Raman band at 820 cm^{-1} (Fig. S5†).

The formation process of Mo-V-Bi oxide is proposed (Fig. 8). After mixing AHM with $\text{VOSO}_4 \cdot 5\text{H}_2\text{O}$ in an aqueous solution, $\{\text{Mo}_{72}\text{V}_{30}\}$ forms immediately.^{16,20} In the presence of $\text{Bi}(\text{NO}_3)_3$, the ϵ -Keggin POM, $[\epsilon\text{-VMo}_{9.4}\text{V}_{2.6}\text{O}_{40}\{\text{Bi}\}_x]^{n-}$, also forms. By heating this solution, the ϵ -Keggin POMs assemble in a tetrahedral fashion to form Mo-V-Bi oxide.

Conclusions

In summary, the formation of Mo-V-Bi oxide was investigated, and appropriate conditions for synthesis of Mo-V-Bi oxide were confirmed. It was found that the solubility of the starting materials affects the crystal size of the resulting material. Soluble starting materials produce nanometer-sized Mo-V-Bi oxide (nano-Mo-V-Bi oxide). Crystal size of Mo-V-Bi oxide affects the properties of Mo-V-Bi oxide including adsorption properties and catalytic activity, which are enhanced by decreasing the crystal size. The formation mechanism was studied by Raman spectroscopy, which indicated the presence of ϵ -Keggin POM and $\{\text{Mo}_{72}\text{V}_{30}\}$ in solution, forming Mo-V-Bi oxide and orthorhombic Mo-V oxide, respectively.

Experimental

Synthetic procedures

Synthesis of well-crystallized Mo–V–Bi oxide. $(\text{NH}_4)_6\text{Mo}_7\text{O}_{24}\cdot 4\text{H}_2\text{O}$ (8.828 g, 50 mmol based on Mo) was dissolved in 110 mL of water. $\text{VOSO}_4\cdot 5\text{H}_2\text{O}$ (3.219 g, 12.5 mmol) was dissolved in 110 mL of water. After the solids had been completely dissolved, the solution of $\text{VOSO}_4\cdot 5\text{H}_2\text{O}$ was rapidly poured into a solution of AHM. After stirring at room temperature for 3 min, $\text{Bi}(\text{OH})_3$ (0.438 g, 1.67 mmol) was added. Then the mixture was stirred for 7 min followed by N_2 bubbling for 10 min. The mixture was introduced into a 300 mL Teflon liner of a stainless-steel autoclave with the help of 20 mL of water. A Teflon sheet (4 m \times 0.1 m \times 0.1 mm) was inserted into the liner. The autoclave was placed in an oven and heated at 448 K for 48 h. After the autoclave had been cooled down to room temperature, Mo–V–Bi oxide formed at the bottom of the liner. For purification, the Teflon sheet, on which most of the impurity of Mo–V oxide had formed, was carefully removed. Then the solid at the bottom was filtered by two cotton sheets. The filtrate that contained Mo–V–Bi oxide was transferred into centrifugation tubes with the help of 200 mL of water and separated by centrifugation (2000 rpm, 3 min). The solid at the bottom of the centrifugation tube was collected and then the solid was dispersed in water (200 mL) and separated by centrifugation (2000 rpm, 3 min). This washing process was repeated 6 times, and the obtained solid was dried at 353 K overnight. Then 0.45 g of Mo–V–Bi oxide (yield: 3.3% based on Mo) was obtained.

Synthesis of nano-Mo–V–Bi oxide with high yield. $\text{Bi}(\text{NO}_3)_3\cdot 5\text{H}_2\text{O}$ (0.68 g, 1.40 mmol) was dissolved in a solution (1.7 mL) of glycerol and water with a volume ratio of 1:1. $(\text{NH}_4)_6\text{Mo}_7\text{O}_{24}\cdot 4\text{H}_2\text{O}$ (1.471 g, 8.33 mmol based on Mo) was dissolved in 20 mL of water. $\text{VOSO}_4\cdot 5\text{H}_2\text{O}$ (0.5365 g, 2.08 mmol) was dissolved in 20 mL of water. After the solids had been completely dissolved, the solution of $\text{VOSO}_4\cdot 5\text{H}_2\text{O}$ was rapidly poured into the solution of $(\text{NH}_4)_6\text{Mo}_7\text{O}_{24}\cdot 4\text{H}_2\text{O}$. After stirring at room temperature for 3 min, $\text{Bi}(\text{NO}_3)_3$ solution was added. Then the mixture was stirred for 7 min. The pH of the precursor was adjusted to 3.7 with 28% of ammonia aqueous solution. After the mixture had been purged by N_2 for 10 min, the mixture was introduced into a 50 mL Teflon liner of a stainless-steel autoclave. The autoclave was placed in an oven with rotation equipment and heated at 448 K for 48 h with rotation (~ 1 rpm). After the autoclave had been cooled down to room temperature, the black solid was collected by filtration, washed with 20 mL of water 3 times, and dried at 353 K overnight. Then 0.506 g of Mo–V–Bi oxide (yield: 22% based on Mo) was obtained. Elemental analysis: Calcd for $(\text{NH}_4)_{2.8}\text{H}_{0.9}[\varepsilon\text{-VMo}_{9.4}\text{V}_{2.6}\text{O}_{40}\text{Bi}_2]\cdot 7.2\text{H}_2\text{O}$: Bi, 17.98; Mo, 38.80; V, 7.89; N, 1.68; H, 1.14, found: Bi, 18.14; Mo, 39.51; V, 7.37.

Characterization

Nitrogen sorption isotherms were obtained by a BELSORP MAX (BEL Japan Inc.) sorption analyzer at 77 K. Surface area was calculated by the BET method. The materials were cal-

culated under nitrogen gas for 2 h and then evacuated at 573 K for 2.5 h before measurement. Pore size distribution was calculated by the SF method (for micropore) and the BJH method (for mesopore). Temperature-programmed desorption mass spectrometry (TPD-MS) measurements were carried out from 313 K to 893 K at a heating rate of 10 K min^{-1} under helium (flow rate: 50 mL min^{-1}). Samples were set up between two layers of quartz wool. A TPD apparatus (BEL Japan Inc.) equipped with a quadrupole mass spectrometer (M-100QA; Anelva) was used to detect NH_4 ($m/z = 16$) and H_2O ($m/z = 18$). Powder X-ray diffraction (XRD) patterns were obtained on RINT2200 (Rigaku) with Cu $\text{K}\alpha$ radiation (tube voltage: 40 kV, tube current: 20 mA). Scanning electron microscopy (SEM) images were obtained with HD-2000 (HITACHI). Transmission electron microscopy (TEM) images were taken with a 200 kV TEM (JEOL JEM-2100F). Fourier transform infrared (FT-IR) analysis was carried out on PARAGON 1000, Perkin Elmer. Raman spectra were recorded with a Renishaw inVia Raman microscope. Elemental compositions were determined by an inductive coupling plasma (ICP-AES) method (ICPE-9000, Shimadzu). Crystallite size was calculated from the most intensive powder diffraction peak (peak at 7.6 degree) with the MID Jade 7 software package by using the Scherrer equation.

Acknowledgements

This work was financially supported by a Grant-in-Aid for Scientific Research (A) (grant no. 2324-6135) from the Ministry of Education, Culture, Sports, Science, and Technology, Japan. M. S. thanks PRESTO, JST and Nippon Sheet Glass Foundation for Materials Science and Engineering (NSG Foundation) for financial support.

Notes and references

- 1 Special thematic issue on polyoxometalates. *Chem. Soc. Rev.*, 2012, **41**, 7325–7648.
- 2 M. T. Pope, *Heteropoly and Isopoly Oxometalates*, Springer-Verlag, Berlin, 1983.
- 3 Y. Kamiya, M. Sadakane, W. Ueda, J. Reedijk and K. Poeppelmeier, Heteropoly Compounds, in *Comprehensive Inorganic Chemistry II*, Elsevier, Oxford, 2013, vol. 7.
- 4 Special thematic issue on polyoxometalates. *Chem. Rev.*, 1998, **98**, 1–390.
- 5 D.-L. Long, R. Tsunashima and L. Cronin, *Angew. Chem., Int. Ed.*, 2010, **49**, 1736–1758.
- 6 S. Mandic, M. R. Healey, J. M. Gotthardt, K. G. Alley, R. W. Gable, C. Ritchie and C. Boskovic, *Eur. J. Inorg. Chem.*, 2013, 1631–1634.
- 7 B. Nohra, H. El Moll, L. M. Rodriguez Albelo, P. Mialane, J. Marrot, C. Mellot-Draznieks, M. O’Keeffe, R. N. Biboum, J. Lemaire, B. Keita, L. Nadjjo and A. Dolbecq, *J. Am. Chem. Soc.*, 2011, **133**, 13363–13374.

- 8 L. M. Rodriguez-Albelo, A. Rabdel Ruiz-Salvador, A. Sampieri, D. W. Lewis, A. Gomez, B. Nohra, P. Mialane, J. Marrot, F. Secheresse, C. Mellot-Draznieks, R. N. Biboum, B. Keita, L. Nadjo and A. Dolbecq, *J. Am. Chem. Soc.*, 2009, **131**, 16078–16087.
- 9 A. Dolbecq, P. Mialane, F. Secheresse, B. Keita and L. Nadjo, *Chem. Commun.*, 2012, **48**, 8299–8316.
- 10 R. Eguchi, S. Uchida and N. Mizuno, *J. Phys. Chem. C*, 2012, **116**, 16105–16110.
- 11 R. Eguchi, S. Uchida and N. Mizuno, *Angew. Chem., Int. Ed.*, 2012, **51**, 1635–1639.
- 12 S. Uchida and N. Mizuno, *Coord. Chem. Rev.*, 2007, **251**, 2537–2546.
- 13 S. Uchida, A. Lesbani, Y. Ogasawara and N. Mizuno, *Inorg. Chem.*, 2012, **51**, 775–777.
- 14 S. Uchida, R. Eguchi, S. Nakamura, Y. Ogasawara, N. Kurosawa and N. Mizuno, *Chem. Mater.*, 2012, **24**, 325–330.
- 15 S. Uchida, S. Hikichi, T. Akatsuka, T. Tanaka, R. Kawamoto, A. Lesbani, Y. Nakagawa, K. Uehara and N. Mizuno, *Chem. Mater.*, 2007, **19**, 4694–4701.
- 16 M. Sadakane, K. Endo, K. Kodato, S. Ishikawa, T. Murayama and W. Ueda, *Eur. J. Inorg. Chem.*, 2013, 1731–1736.
- 17 M. Sadakane, K. Kodato, T. Kuranishi, Y. Nodasaka, K. Sugawara, N. Sakaguchi, T. Nagai, Y. Matsui and W. Ueda, *Angew. Chem., Int. Ed.*, 2008, **47**, 2493–2496.
- 18 M. Sadakane, S. Ohmura, K. Kodato, T. Fujisawa, K. Kato, K. Shimidzu, T. Murayama and W. Ueda, *Chem. Commun.*, 2011, **47**, 10812–10814.
- 19 M. Sadakane and W. Ueda, Ordered Porous Crystalline Transition Metal Oxides, in *Porous Materials*, ed. D. W. Bruce, D. O'Hare and R. I. Walton, Wiley, 2011, vol. 11, pp. 147–216.
- 20 M. Sadakane, N. Watanabe, T. Katou, Y. Nodasaka and W. Ueda, *Angew. Chem., Int. Ed.*, 2007, **46**, 1493–1496.
- 21 M. Sadakane, K. Yamagata, K. Kodato, K. Endo, K. Toriumi, Y. Ozawa, T. Ozeki, T. Nagai, Y. Matsui, N. Sakaguchi, W. D. Pyrz, D. J. Buttrey, D. A. Blom, T. Vogt and W. Ueda, *Angew. Chem., Int. Ed.*, 2009, **48**, 3782–3786.
- 22 Z. Zhang, M. Sadakane, T. Murayama, S. Izumi, N. Yasuda, N. Sakaguchi and W. Ueda, *Inorg. Chem.*, 2014, **53**, 903–911.
- 23 L. H. Wee, M. R. Lohe, N. Janssens, S. Kaskel and J. a. Martens, *J. Mater. Chem.*, 2012, **22**, 13742–13746.
- 24 H. Guo, Y. Zhu, S. Wang, S. Su, L. Zhou and H. Zhang, *Chem. Mater.*, 2012, **24**, 444–450.
- 25 M. Ma, D. Zacher, X. Zhang, R. a. Fischer and N. Metzler-Nolte, *Cryst. Growth Des.*, 2011, **11**, 185–189.
- 26 S. Ishikawa, X. Yi, T. Murayama and W. Ueda, *Appl. Catal., A*, 2013, **474**, 10–17.
- 27 M. Choi, K. Na, J. Kim, Y. Sakamoto, O. Terasaki and R. Ryoo, *Nature*, 2009, **461**, 246–249.
- 28 B. Tokay, O. Karvan and A. Erdem-Şenatalar, *Microporous Mesoporous Mater.*, 2010, **131**, 230–237.
- 29 A. Müller, A. M. Todea, J. van Slageren, M. Dressel, H. Bögge, M. Schmidtman, M. Luban, L. Engelhardt and M. Rusu, *Angew. Chem., Int. Ed.*, 2005, **44**, 3857–3861.
- 30 B. Delley, *J. Chem. Phys.*, 1990, **92**, 508–517.

Preparation, Structural Characterization, and Ion-Exchange Properties of Two New Zeolite-like 3D Frameworks Constructed by ϵ -Keggin-Type Polyoxometalates with Binding Metal Ions, $\text{H}_{11.4}[\text{ZnMo}_{12}\text{O}_{40}\text{Zn}_2]^{1.5-}$ and $\text{H}_{7.5}[\text{Mn}_{0.2}\text{Mo}_{12}\text{O}_{40}\text{Mn}_2]^{2.1-}$

Zhenxin Zhang,[†] Masahiro Sadakane,^{*,‡,§} Toru Murayama,[†] Norihito Sakaguchi,^{||} and Wataru Ueda^{*,†}

[†]Catalysis Research Center, Hokkaido University, N-21, W-10 Kita-ku, Sapporo 001-0021, Japan

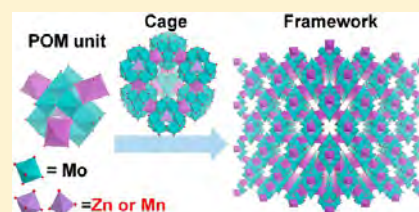
[‡]Department of Applied Chemistry, Graduate School of Engineering, Hiroshima University, 1-4-1 Kagamiyama, Higashi, Hiroshima 739-8527, Japan

[§]PRESTO, JST, 4-1-8 Honcho, Kawaguchi, Saitama 332-0012, Japan

^{||}High Voltage Electron Microscope Laboratory, Center for Advanced Research of Energy Conversion Materials, Hokkaido University, N-13, W-8, Sapporo 060-8626, Japan

Supporting Information

ABSTRACT: Two new ϵ -Keggin-type polyoxometalate-based 3D frameworks, $\text{Na}_{1.5}\text{H}_{11.4}[\epsilon\text{-Zn}^{\text{II}}\text{Mo}^{\text{V}}_{10.9}\text{Mo}^{\text{VI}}_{1.1}\text{O}_{40}\{\text{Zn}^{\text{II}}\}_2]$ and $(\text{NH}_4)_{2.1}\text{H}_{7.5}[\epsilon\text{-Mn}^{\text{II}}_{0.2}\text{Mo}^{\text{V}}_6\text{Mo}^{\text{VI}}_6\text{O}_{40}\{\text{Mn}^{\text{II}}\}_2]$, are prepared, and their structures are determined by powder X-ray diffraction, Fourier transform infrared, Raman spectroscopy, and elemental analysis. ϵ -Keggin-type polyoxomolybdate units, $[\epsilon\text{-ZnMo}_{12}\text{O}_{40}]$ and $[\epsilon\text{-Mn}_{0.2}\text{Mo}_{12}\text{O}_{40}]$, are linked with Zn^{2+} and Mn^{2+} , respectively, in a tetrahedral fashion to form 3D frameworks. They show zeolite-like ion-exchange properties and redox properties. The ϵ -Keggin-based 3D framework shows high chemical composition diversity and can incorporate different elements in the framework.



INTRODUCTION

Polyoxometalates (POMs) are anionic metal oxide clusters comprised of mainly early transition metals such as tungsten, molybdenum, niobium, and vanadium.^{1–3} POMs have attracted much attention because they are applicable to functional materials, such as catalysts and electrode, optical, and magnetic materials. Furthermore, their molecular properties, such as multielectron-transfer, strong acidic, and magnetic properties, are tunable by changing their structures and incorporating metal components in the structures.

POMs are also known to be well-defined building units for the construction of nanostructured materials and well-ordered crystalline materials, such as polyoxometalate–organic frameworks (POMOFs),^{4–10} macrocations–POM materials,^{11–18} and complex metal oxides.^{19–21} These materials have been prepared by the assembly of POMs with other structural building blocks. The resulting materials exhibit interesting properties and have various applications, such as adsorption,^{11,12,22,23} separation,^{11,12} catalysis,^{16,20,24–27} ion exchange,²⁸ and electrocatalysis.⁶ The most popular POM building unit is the α isomer of a Keggin-type POM.

In the case of POMOF materials, the ϵ isomer of a Keggin-type POM composed of one central XO_4 tetrahedron and 12 metal–oxygen octahedra with T_d symmetry is of great interest. Four hexagonal faces of the ϵ -Keggin POM are bound to metal ions (Figure 1), and linking of these four metal ions by a bidentate organic ligand results in the formation of a 3D-

ordered framework of POM and an organic moiety.^{4,6,7} Recently, we have reported the first all-inorganic 3D framework composed of ϵ -Keggin POM, $[\epsilon\text{-VMo}_{9.4}\text{V}_{2.6}\text{O}_{40}]$, with a bismuth linker (denoted as Mo–V–Bi oxide). A total of 10 $[\epsilon\text{-VMo}_{9.4}\text{V}_{2.6}\text{O}_{40}]$ units surround a cage that is connected by channels, forming a zigzag 3D pore system.²⁹ Compared with POMOFs, the Mo–V–Bi oxide is thermally more stable so that water and ammonium cations presented in the pores can be removed by thermal treatment, and the opened pores are analyzable by the N_2 adsorption–desorption technique. Furthermore, ammonium cations are exchangeable with other cations.

One of the important properties of POMs is diversity of the elements in the structures, and it is desirable for many kinds of elements to be able to be incorporated into the structures of ϵ -Keggin POM-based 3D frameworks and their properties, such as stability, ion-exchange property, acidity, and redox, magnetic, and pore properties, to be easily tuned.

Here, we describe the synthesis and structural characterization of two new members of all-inorganic ϵ -Keggin POM-based 3D frameworks, ϵ -Keggin polyoxomolybdates with metal ions (Zn^{II} and Mn^{II}), $\text{Na}_{1.5}\text{H}_{11.4}[\epsilon\text{-Zn}^{\text{II}}\text{Mo}^{\text{V}}_{10.9}\text{Mo}^{\text{VI}}_{1.1}\text{O}_{40}\{\text{Zn}^{\text{II}}\}_2]$ and $(\text{NH}_4)_{2.1}\text{H}_{7.5}[\epsilon\text{-Mn}^{\text{II}}_{0.2}\text{Mo}^{\text{V}}_6\text{Mo}^{\text{VI}}_6\text{O}_{40}\{\text{Mn}^{\text{II}}\}_2]$, denoted as Mo–Zn oxide and

Received: March 19, 2014

Published: July 9, 2014

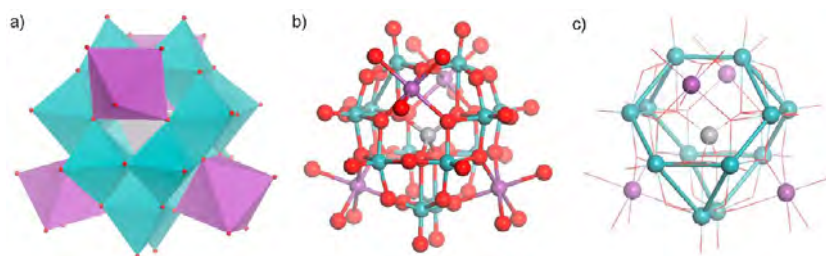


Figure 1. (a) Polyhedral representation, (b) ball–stick representation, and (c) metal skeleton representation of ϵ -Keggin-type POM with four capping metal ions. Central metal site: gray. Surrounding metal site: blue. Linking metal: purple. Oxygen: red.

Mo–Mn oxide, respectively. Structures of the materials are determined by powder X-ray diffraction (XRD), Fourier transform infrared (FT-IR), and elemental analysis. The thermal stability of the materials is investigated, and it is found that the existing guest molecules can be mostly removed by heat treatment. The materials are found to have selective ion-exchange properties that are similar to those of zeolites.

EXPERIMENTAL SECTION

Materials. All chemicals were of reagent grade and were used as supplied, and house-made distilled water was used throughout. Mo–V–Bi oxide was prepared according to our paper.²⁹

Synthesis of Mo–Zn Oxide. $\text{Na}_2\text{MoO}_4 \cdot 2\text{H}_2\text{O}$ (2.823 g, 11.7 mmol based on Mo) was dissolved in 40 mL of distilled water. Metal Mo (0.2 g, 2.1 mmol) and ZnCl_2 (0.453 g, 3.3 mmol) were added to the mixture sequentially, followed by adjustment of the pH to 4.8 with 1 M H_2SO_4 . The mixture was introduced into a 50 mL Teflon liner of a stainless-steel autoclave. The autoclave was placed in an oven heated at 448 K for 24 h. After the autoclave had been cooled to room temperature, the mixture was placed in a 100 mL beaker. For solid recovery, 60 mL of water was added to the beaker, and the beaker was kept at room temperature for 5 min. Then the upper 50% part of the suspension was collected by filtration. The recovery process was repeated three times. The resulting solid was washed with 10 mL of water three times and dried at 353 K overnight. Then 0.28 g of Mo–Zn oxide (yield: 14% based on Mo) was obtained. Elem anal. Calcd for $\text{Na}_{1.5}\text{Zn}_3\text{Mo}_{12}\text{O}_{45}\text{H}_{21.4}$: Zn, 9.24; Mo, 54.22; Na, 1.62; H, 1.02. Found: Zn, 9.63; Mo, 54.14; Na, 1.54; H, 1.18.

Synthesis of Mo–Mn Oxide. $(\text{NH}_4)_6\text{Mo}_7\text{O}_{24} \cdot 4\text{H}_2\text{O}$ (2.060 g, 11.7 mmol based on Mo) was dissolved in 40 mL of distilled water. Metal Mo (0.2 g, 2.1 mmol) and MnO (0.235 g, 3.3 mmol) were added to the mixture sequentially (pH of 5.1). The mixture was introduced into a 50 mL Teflon liner of a stainless-steel autoclave. The autoclave was placed in an oven heated at 448 K for 24 h. After the autoclave had been cooled to room temperature, the mixture was placed in a 100 mL beaker. For solid recovery, 60 mL of water was added to the beaker, and the beaker was kept at room temperature for 5 min. Then the upper 50% part of the suspension was collected by filtration. The recovery process was repeated three times. The resulting solid was washed with 10 mL of water three times and dried at 353 K overnight. Then 0.32 g of Mo–Mn oxide (yield: 16% based on Mo) was obtained. Elem anal. Calcd for $\text{N}_{2.1}\text{Mn}_{2.2}\text{Mo}_{12}\text{O}_{44}\text{H}_{23.9}$: Mn, 5.95; Mo, 56.72; N, 1.45; H, 1.19. Found: Mn, 5.91; Mo, 56.45; N, 1.62; H, 1.23.

Ion Exchange. As-synthesized material (Mo–Zn oxide or Mo–Mn oxide, 0.3 g) was dispersed in 15 mL of water containing 0.61 mmol each of LiCl , NaCl , NH_4Cl , KCl , RbCl , CsCl , BeSO_4 , MgCl_2 , CaCl_2 , SrCl_2 , and BaCl_2 . The mixture was stirred at 353 K for 6 h. The resulting solid (M–Mo–Zn oxide or M–Mo–Mn oxide, where M = Li, Na, NH_4 , K, Rb, Cs, Be, Mg, Ca, Sr, and Ba) was collected by filtration, washed with water (3×10 mL), and dried at 353 K overnight. To synthesize a proton-exchanged sample, 0.5 mL of concentrated HCl was dissolved in 14.5 mL of water. Then 0.3 g of as-synthesized material (Mo–Zn oxide or Mo–Mn oxide) was added.

The mixture was stirred at 353 K for 6 h. The resulting solid was recovered by filtration, washed with water (3×10 mL), and dried at 353 K overnight.

Elemental Analysis. H–Mo–Zn oxide. Calcd for $\text{Na}_{0.6}\text{Zn}_3\text{Mo}_{12}\text{O}_{45}\text{H}_{22.3}$: Zn, 9.32; Mo, 54.73; Na, 0.66; H, 1.07. Found: Zn, 9.18; Mo, 54.98; Na, 0.67; H, 1.38.

Li–Mo–Zn oxide. Calcd for $\text{Li}_{0.7}\text{Na}_{0.8}\text{Zn}_3\text{Mo}_{12}\text{O}_{45}\text{H}_{21.4}$: Li, 0.23; Zn, 9.29; Mo, 54.51; Na, 0.87; H, 1.15. Found: Li, 0.07; Zn, 9.19; Mo, 54.88; Na, 0.72; H, 1.19.

NH_4 –Mo–Zn oxide. Calcd for $\text{Na}_{0.1}\text{N}_{1.4}\text{Zn}_3\text{Mo}_{12}\text{O}_{45}\text{H}_{27}$: Na, 0.11; Zn, 9.27; Mo, 54.40; N, 0.93; H, 1.29. Found: Na, 0.08; Zn, 9.32; Mo, 54.37; N, 1.19; H, 1.45.

K–Mo–Zn oxide. Calcd for $\text{K}_{1.4}\text{Na}_{0.1}\text{Zn}_3\text{Mo}_{12}\text{O}_{45}\text{H}_{21.4}$: K, 2.55; Zn, 9.14; Mo, 53.65; Na, 0.11; H, 1.01. Found: K, 2.31; Zn, 9.26; Mo, 53.43; Na, 0.07; H, 1.16.

Rb–Mo–Zn oxide. Calcd for $\text{Rb}_{1.3}\text{Na}_{0.2}\text{Zn}_3\text{Mo}_{12}\text{O}_{45}\text{H}_{21.4}$: Rb, 5.04; Zn, 8.90; Mo, 52.22; Na, 0.21; H, 0.98. Found: Rb, 5.02; Zn, 8.93; Mo, 52.02; Na, 0.07; H, 1.10.

Cs–Mo–Zn oxide. Calcd for $\text{Cs}_{1.5}\text{Zn}_3\text{Mo}_{12}\text{O}_{45}\text{H}_{21.4}$: Cs, 8.71; Zn, 8.57; Mo, 50.31; Na, 0; H, 0.94. Found: Cs, 8.73; Zn, 8.67; Mo, 50.47; Na, 0; H, 1.01.

H–Mo–Mn oxide. Calcd for $\text{N}_{1.7}\text{Mn}_{2.2}\text{Mo}_{12}\text{O}_{43}\text{H}_{20.7}$: Mn, 6.03; Mo, 57.43; N, 1.19; H, 1.04. Found: Mn, 5.78; Mo, 57.75; N, 0.95; H, 1.47.

Li–Mo–Mn oxide. Calcd for $\text{Li}_{0.1}\text{N}_{2.0}\text{Mn}_{2.2}\text{Mo}_{12}\text{O}_{43}\text{H}_{21.5}$: Li, 0.03; Mn, 6.01; Mo, 57.26; N, 1.39; H, 1.08. Found: Li, 0.04; Mn, 6.12; Mo, 57.15; N, 1.28; H, 1.47.

Na–Mo–Mn oxide. Calcd for $\text{Na}_{0.4}\text{N}_{1.7}\text{Mn}_{2.2}\text{Mo}_{12}\text{O}_{43}\text{H}_{20.3}$: Na, 0.46; Mn, 6.00; Mo, 57.18; N, 1.18; H, 1.02. Found: Na, 0.52; Mn, 5.89; Mo, 56.99; N, 1.20; H, 1.38.

K–Mo–Mn oxide. Calcd for $\text{K}_{1.4}\text{N}_{0.7}\text{Mn}_{2.2}\text{Mo}_{12}\text{O}_{43}\text{H}_{16.3}$: K, 2.68; Mn, 5.92; Mo, 56.41; N, 0.48; H, 0.80. Found: K, 2.63; Mn, 6.37; Mo, 56.53; N, 0.38; H, 1.16.

Rb–Mo–Mn oxide. Calcd for $\text{Rb}_{1.3}\text{N}_{0.6}\text{Mn}_{2.2}\text{Mo}_{12}\text{O}_{43}\text{H}_{15.9}$: Rb, 6.07; Mn, 5.72; Mo, 54.49; N, 0.40; H, 0.76. Found: Rb, 6.03; Mn, 5.81; Mo, 54.55; N, 0.12; H, 1.07.

Cs–Mo–Mn oxide. Calcd for $\text{Cs}_{1.4}\text{N}_{0.7}\text{Mn}_{2.2}\text{Mo}_{12}\text{O}_{44}\text{H}_{18.3}$: Cs, 8.49; Mn, 5.52; Mo, 52.56; N, 0.45; H, 0.84. Found: Cs, 8.65; Mn, 5.44; Mo, 52.65; N, 0.17; H, 1.08.

Be–Mo–Zn oxide. Calcd for $\text{Be}_{0.3}\text{Na}_{0.9}\text{Zn}_3\text{Mo}_{12}\text{O}_{44}\text{H}_{19.4}$: Be, 0.13; Zn, 9.37; Mo, 54.97; Na, 0.99; H, 0.93. Found: Be, 0.12; Zn, 9.72; Mo, 54.72; Na, 1.04; H, 1.13.

Mg–Mo–Zn oxide. Calcd for $\text{Mg}_{0.6}\text{Na}_{0.3}\text{Zn}_3\text{Mo}_{12}\text{O}_{46}\text{H}_{23.4}$: Mg, 0.69; Zn, 9.22; Mo, 54.09; Na, 0.32; H, 1.11. Found: Mg, 0.62; Zn, 9.68; Mo, 53.77; Na, 0.44; H, 1.16.

Ca–Mo–Zn oxide. Calcd for $\text{Ca}_7\text{Zn}_3\text{Mo}_{12}\text{O}_{47}\text{H}_{24.9}$: Ca, 1.85; Zn, 9.06; Mo, 53.19; Na, 0; H, 1.16. Found: Ca, 1.75; Zn, 8.95; Mo, 52.79; Na, 0.03; H, 1.22.

Sr–Mo–Zn oxide. Calcd for $\text{Sr}_{0.8}\text{Na}_{0.1}\text{Zn}_3\text{Mo}_{12}\text{O}_{45}\text{H}_{21.2}$: Sr, 3.24; Zn, 9.08; Mo, 53.27; Na, 0.11; H, 0.98. Found: Sr, 3.29; Zn, 9.28; Mo, 52.94; Na, 0.13; H, 1.13.

Ba–Mo–Zn oxide. Calcd for $\text{Ba}_{1.4}\text{Zn}_3\text{Mo}_{12}\text{O}_{45}\text{H}_{20.1}$: Ba, 8.43; Zn, 8.60; Mo, 50.50; Na, 0; H, 0.89. Found: Ba, 8.30; Zn, 8.16; Mo, 50.34; Na, 0.02; H, 1.08.

Be–Mo–Mn oxide. Calcd for $\text{Be}_{0.2}\text{N}_{1.7}\text{Mn}_{2.2}\text{Mo}_{12}\text{O}_{45}\text{H}_{24.3}$: Be, 0.09; Mn, 5.92; Mo, 56.37; N, 1.17; H, 1.20. Found: Be, 0.07; Mn, 5.95; Mo, 56.01; N, 1.20; H, 1.36.

Mg–Mo–Mn oxide. Calcd for $\text{Mg}_{0.6}\text{N}_{1.2}\text{Mn}_{2.2}\text{Mo}_{12}\text{O}_{43}\text{H}_{18}$: Mg, 0.73; Mn, 6.01; Mo, 57.29; N, 0.84; H, 0.90. Found: Mg, 0.75; Mn, 6.10; Mo, 57.42; N, 0.86; H, 1.12.

Ca–Mo–Mn oxide. Calcd for $\text{Ca}_{0.9}\text{N}_1\text{Mn}_{2.2}\text{Mo}_{12}\text{O}_{45}\text{H}_{20.8}$: Ca, 1.75; Mn, 5.86; Mo, 55.80; N, 0.68; H, 1.02. Found: Ca, 1.78; Mn, 5.95; Mo, 55.60; N, 0.69; H, 1.28.

Sr–Mo–Mn oxide. Calcd for $\text{Sr}_{0.8}\text{N}_1\text{Mn}_{2.2}\text{Mo}_{12}\text{O}_{45}\text{H}_{21}$: Sr, 3.34; Mn, 5.76; Mo, 54.89; N, 0.67; H, 1.01. Found: Sr, 3.43; Mn, 5.55; Mo, 54.74; N, 0.67; H, 1.22.

Ba–Mo–Mn oxide. Calcd for $\text{Ba}_{1.6}\text{Mn}_{2.2}\text{Mo}_{12}\text{O}_{44}\text{H}_{14.4}$: Ba, 9.94; Mn, 5.47; Mo, 52.09; N, 0; H, 0.66. Found: Ba, 10.13; Mn, 5.24; Mo, 51.96; N, 0; H, 0.88.

Characterization. N_2 sorption isotherms were obtained by a BELSORP-max (BEL Japan Inc., Osaka, Japan) sorption analyzer at 77 K. The surface area was calculated by the Brunauer–Emmett–Teller (BET) method using an adsorption branch. Mo–V–Bi oxide was evacuated at 573 K for 2.5 h and the samples of Mo–Zn oxide and Mo–Mn oxide were evacuated at 473 K for 2.5 h before measurement. Powder XRD patterns were obtained on RINT2200 (Rigaku) with Cu $K\alpha$ radiation (tube voltage, 40 kV, tube current, 20 mA). Scanning electron microscopy (SEM) images were obtained with a HD-2000 microscope (Hitachi). Transmission electron microscopy (TEM) images were taken with a 200 kV transmission electron microscope (JEOL JEM-2010F). FT-IR analysis was carried out on a PARAGON 1000 analyzer (PerkinElmer). Raman spectra were recorded with a Renishaw inVia Raman microscope. Thermogravimetric–differential thermal analysis (TG-DTA) measurements were carried out up to 773 K at a heating rate of 10 K min^{-1} under nitrogen (flow rate, 10 mL min^{-1}) and air (flow rate, 30 mL min^{-1}) flow with Thermo plus TG-8120 (Rigaku). Temperature-programmed desorption mass spectrometry (TPD-MS) measurements were carried out from 313 to 893 K at a heating rate of 10 K min^{-1} under helium (flow rate, 50 mL min^{-1}). Samples were set up between two layers of quartz wool. A TPD apparatus (BEL Japan, Inc.) equipped with a quadrupole mass spectrometer (M-100QA; Anelva) was used to detect NH_3 (m/z 16), H_2O (m/z 18), O_2 (m/z 32), and N_2 (m/z 28). For TPD-MS measurements of the materials after heat treatment, the samples were heated at 473 K under high vacuum for 2.5 h in a TPD instrument before measurements. X-ray photoelectron spectroscopy (XPS) was performed on a JPS-9010MC spectrometer (JEOL). The spectrometry energies were calibrated using the C 1s peak at 284.8 eV. Diffuse-reflectance (DR) UV–vis spectra were obtained using a JASCO V-570 spectrophotometer equipped with an ISN-470 reflectance spectroscopy accessory. Elemental compositions were determined by an inductive coupling plasma atomic emission spectroscopy (ICP-AES) method (ICPE-9000, Shimadzu). The CHN elemental composition was determined at Instrumental Analysis Division, Equipment Management Center, Creative Research Institution, Hokkaido University.

Structure Determination and Computer-Based Simulation.

The structures of Mo–Zn and Mo–Mn oxides were determined by powder XRD. Powder XRD patterns were recorded on a RINT2200 diffractometer (Rigaku) with Cu $K\alpha$ radiation (tube voltage, 40 kV; tube current, 40 mA; scan speed, 1 deg min^{-1} ; step, 0.01 deg). First, the powder XRD pattern was indexed by programs, including *DICVOL06*³⁰ and *X-cell*,³¹ which gave the same results. After Pawley refinement was performed, the most reasonable space group was obtained. Then the Le Bail method³² was applied for intensity extraction with the *EdPCR* program. The initial structure was solved by a charge-flipping algorithm.³³ The positions and types of heavy-metal atoms (Mo, Zn, and Mn) were obtained by analyzing the generated electron density maps. Most of the O atoms and cations were assigned according to the residual peaks, which were indicated by the charge-flipping algorithm, with consideration of the crystal structure of Mo–V–Bi oxide. The initial structures from the charge-flipping algorithm are shown in Supporting Information (SI) Tables S1 and S2.

The initial structures of Mo–Zn and Mo–Mn oxides were refined by powder XRD Rietveld refinement.³⁴ The lattice and pattern parameters of the material were first refined by Pawley refinement. Then isotropical temperature factors (see the SI for detailed information) were given for every atom in the initial structure. Rietveld analysis was started with the initial model of the material and lattice and pattern parameters from Pawley refinement. Every atom position was refined. The occupancy of atoms in the framework was fixed without further refinement, and occupancies of atoms in micropores were refined with consideration of the elemental analysis results. Finally, the pattern parameters were refined again for obtaining the lowest R_{wp} value. Crystallographic and Rietveld analysis parameters are shown in SI Tables S3–S6.

Material modeling, the *X-cell* program, and Pawley and Rietveld refinement were performed with the *Materials Studio v6.1.0* package (Accelrys Software Inc.). *DICVOL06* and *EdPCR* were carried out with the *Fullprof* package. The charge-flipping algorithm was performed with *Superflip* in *Jana2006*, and electron density maps were generated with *Chimera 1.8.1*.

The Connolly surfaces and free space of POM-based materials were simulated by the *Atom Volume & Surfaces* program in *Materials Studio*. The diameters of the cage and channel were estimated from the Connolly surfaces of the cage and the channel with a Connolly radius of 1 Å,³⁵ and the shortest values are presented.

RESULTS AND DISCUSSION

Preparation of Mo–Zn and Mo–Mn Oxides. Two novel POM-based crystalline metal oxides, Mo–Zn and Mo–Mn oxides, are synthesized under hydrothermal conditions. The hydrothermal reaction of $\text{Na}_2\text{MoO}_4 \cdot 2\text{H}_2\text{O}$, Mo metal, and ZnCl_2 at 448 K for 24 h produces Mo–Zn oxide, and the powder XRD profile of the solid is presented in Figure 2b. A profile similar to that of Mo–V–Bi oxide is observed. XRD peaks corresponding to ZnMoO_4 , MoO_2 , and unreacted Mo metal are also obtained in the crude solid.

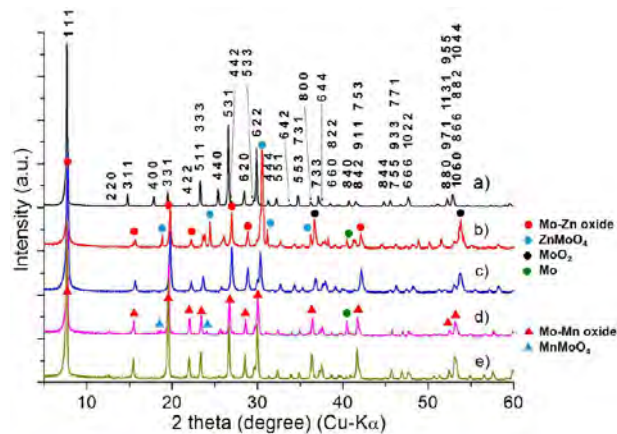


Figure 2. XRD patterns of (a) Mo–V–Bi oxide, (b) a crude solid of Mo–Zn oxide, (c) Mo–Zn oxide after purification, (d) a crude solid of Mo–Mn oxide, and (e) Mo–Mn oxide after purification. PDF number: ZnMoO_4 , 00-025-1024; MnMoO_4 , 01-082-2166; MoO_2 , 00-050-0739; Mo, 00-004-0809.

The desired solid is isolatable by settlement of the obtained crude solid in water and decantation of the upper solution, because the desired Mo–Zn oxide is smaller than ZnMoO_4 , MoO_2 , and Mo metal (Figure 3 and SI Figure S1). The XRD profile of isolated Mo–Zn oxide is similar to that of Mo–V–Bi oxide (Figure 2c).

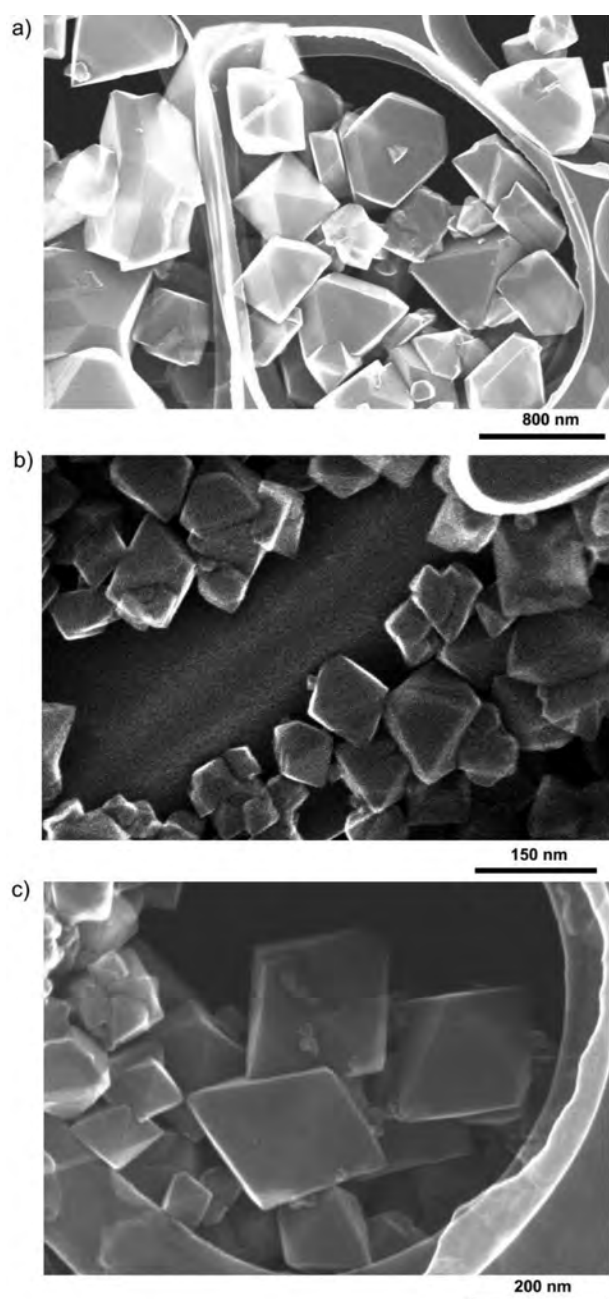


Figure 3. SEM images of (a) Mo–V–Bi, (b) Mo–Zn, and (c) Mo–Mn oxides.

Crystalline Mo–Mn oxide is prepared by the same method as that used for Mo–Zn oxide except for replacement of ZnCl_2 by MnO . A powder XRD profile similar to that of Mo–V–Bi oxide is observed in the profile of the resulting solid (Figure 2d). XRD peaks corresponding to MnMoO_4 and unreacted Mo metal are also detected.

The desired product is separated by settlement of the obtained crude solid in water and decantation of the upper solution, because the desired Mo–Mn oxide is smaller than MnMoO_4 and Mo metal (Figure 3 and Supporting Information Figure S1). The XRD profile of the isolated Mo–Mn oxide is also similar to that of Mo–V–Bi oxide (Figure 2e).

Structural Characterizations of Mo–Zn and Mo–Mn Oxides. The powder XRD profiles of Mo–Zn and Mo–Mn oxides are similar to that of Mo–V–Bi oxide with a slight shift of 2θ and different intensity ratios (Figure 2 and SI Figure S2a), and XRD pattern indexing and Pawley refinement show that these three materials are cubic systems with the same space group of $Fd\bar{3}m$ and similar lattice parameters (Table 1). Mo–

Table 1. Refined Parameters and Agreement Factors of Rietveld Analysis for Mo–Zn and Mo–Mn Oxides

	Mo–Zn oxide	Mo–Mn oxide
empirical formula	$\text{O}_{45.6}\text{Na}_{1.56}\text{Zn}_3\text{Mo}_{12}$	$\text{O}_{47.9}\text{Mn}_{2.24}\text{Mo}_{12}$
cryst syst	cubic	cubic
space group	$Fd\bar{3}m$	$Fd\bar{3}m$
$a = b = c$ (Å)	19.4675	19.6578
$\alpha = \beta = \gamma$ (deg)	90	90
V (Å ³)	7377.86	7596.34
agreement factors		
R_{wp} (%)	7.10	6.19
$R_{\text{wp}}(\text{w/o bck})$ (%)	12.09	11.92
R_{p} (%)	5.35	4.66
pattern parameter	pseudo-Voigt	pseudo-Voigt
peak-shape function		
fwhm	$U = 1.24597, V = -0.65679, W = 0.13636$	$U = 0.64154, V = -0.26116, W = 0.05624$
profile parameter	$N_{\text{A}} = 1.02040, N_{\text{B}} = -0.005$	$N_{\text{A}} = 1.03398, N_{\text{B}} = -0.008$
line shift	10	52
instrument geometry	Bragg–Brentano	Bragg–Brentano
zero point	–1.01992	–0.31358
shift#1	0.93425	0.18755
shift#2	0.09903	0.08589
correction method	Berar–Baldinozzi	Berar–Baldinozzi
parameter	$P1 = 0.19643, P2 = -0.10651, P3 = -0.48315, P4 = 0.20029$	$P1 = 1.67562, P2 = 0.35040, P3 = -3.51892, P4 = -0.73820$
background coefficients	polynomial = 100	polynomial = 100
preferred orientation	$R0 = 1.53623$	$R0 = 1.45685$
March–Dollase		

Zn and Mo–Mn oxides have octahedral morphologies that are similar to that of Mo–V–Bi oxide (Figure 3). Therefore, we consider the structures of Mo–Zn and Mo–Mn oxides to be similar to that of Mo–V–Bi oxide. The structure of Mo–V–Bi oxide has been determined by single-crystal X-ray analysis,²⁹ which showed that the material is comprised of ϵ -Keggin POM units, $\epsilon\text{-VMo}_{9.4}\text{V}_{3.6}\text{O}_{40}$, with a Bi^{III} linker (Figure 1). A V–O tetrahedron is surrounded by 12 M–O ($M = \text{Mo}$ and V) octahedra to form the ϵ -Keggin-type POM, which is linked by Bi^{III} to form a diamond-like framework. There are three metal sites in the framework of the materials: a central metal site, surrounding 12 metal sites, and linking metal sites in an asymmetric unit.

SEM images (Figure 3) of Mo–Zn and Mo–Mn oxides show that both of these materials are too small to perform single-crystal analysis (100–200 nm in one diameter). Therefore, structure analysis based on powder XRD is carried out.

For Mo–Zn oxide, the results obtained by using the charge-flipping algorithm reveal the three most intensive peaks of the electron density map with intensity order of surrounding metal sites > central metal site ~ linking metal site (Figure 4a–c and

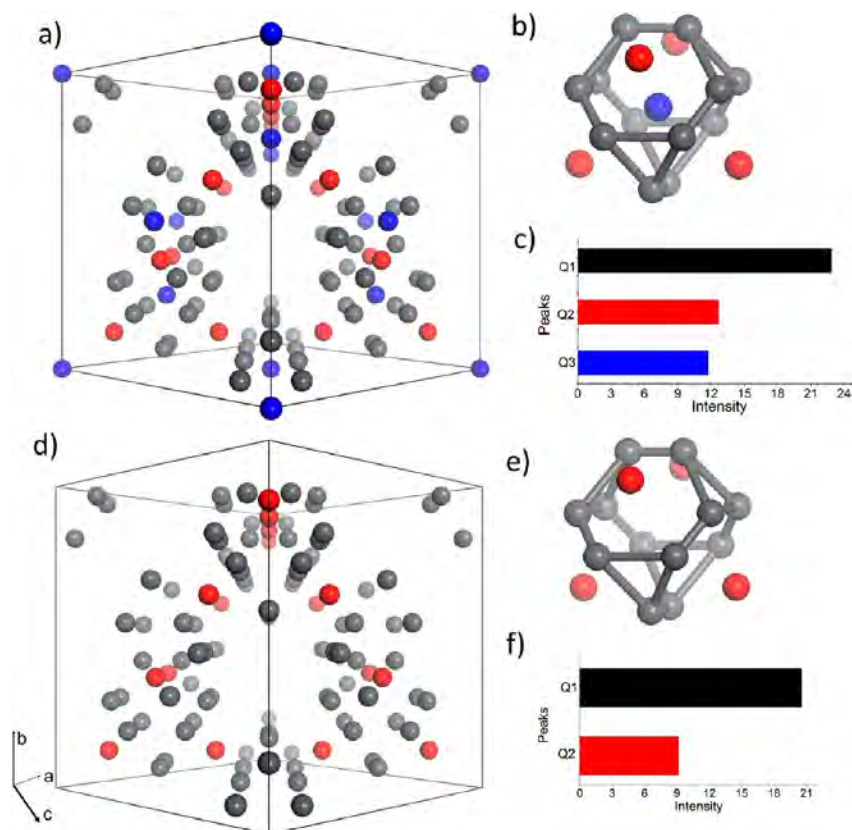


Figure 4. Schematic representations of the charge-flipping algorithm results: (a) electron density map from the charge-flipping method showing positions of the intensive peaks [surrounding metal sites (Q1; gray), linking metal sites (Q2; red), and central metal sites (Q3; blue)] in a unit cell; (b) ϵ -Keggin unit with four linking metal sites; (c) intensity difference of the peaks of Mo–Zn oxide; (d) electron density map from the charge-flipping method showing positions of the intensive peaks [surrounding metal sites (Q1; gray) and linking metal sites (Q2; red)] in a unit cell; (e) ϵ -Keggin unit with four linking metal sites; (f) intensity difference of the peaks of Mo–Mn oxide.

SI Table S1). Elemental analysis of Mo–Zn oxide reveals that the ratio of Mo:Zn is 12:3. These results indicate that Zn is present in the central and linking metal sites and that Mo is present in the surrounding metal sites. In the case of Mo–Mn oxide, the two most intensive peaks of the electron density map correspond to the surrounding metal sites and linking metal sites, where the intensity of the surrounding metal sites is much higher than that of the linking metal site (Figure 4d–f). A weak peak is found at the central metal site, indicating that the position is occupied partly or by light atoms (SI Table S2). Elemental analysis of Mo–Mn oxide reveals that the ratio of Mo:Mn is 12:2.2. These results indicate that Mo is present in the surrounding metal sites, Mn is present in the linking metal site, and the central metal site is occupied by Mn with 0.2 occupancy. Other sites are assigned as O atoms of the Keggin unit, counteranions, and O atoms of water.

The initial structures of Mo–Zn and Mo–Mn oxides are refined with Rietveld refinement. Figure 5 shows the simulated powder XRD patterns of Mo–Zn and Mo–Mn oxides. The R_{wp} values of Mo–Zn and Mo–Mn oxides are 7.10% and 6.19%, respectively. The results of Rietveld and elemental analyses demonstrate that the POM building blocks of Mo–Zn and Mo–Mn oxides are ϵ -Keggin POMs ϵ -ZnMo₁₂O₄₀ and ϵ -Mn_{0.2}Mo₁₂O₄₀, respectively (Figure 6a). A total of 12 MoO₆ octahedra surrounded an MO₄ (M = Zn or Mn) tetrahedron to form the ϵ -Keggin cores, which are connected by metal ions (Zn or Mn) in a tetrahedral fashion to form a 3D framework

(Figure 6b). In the case of other ϵ -Keggin POMs, there are four capping metal ions for one ϵ -Keggin POM.^{36–39} In the case of Mo–V–Bi, Mo–Zn, and Mo–Mn oxides, capping metal ions connect the POM units.

FT-IR and Raman spectra (SI Figure S3) of Mo–Zn and Mo–Mn oxides are similar to those of other ϵ -Keggin polyoxomolybdates, [ϵ -H₂Mo₁₂O₄₀Ni₄(H₂O)]³⁶ and [ϵ -H₂Mo₁₂O₄₀Co₄(H₂O)]⁴⁰ [ϵ -H₂Mo₁₂O₄₀Ni₄(H₂O)] and [ϵ -H₂Mo₁₂O₄₀Co₄(H₂O)] are composed of ϵ -Keggin polyoxomolybdate [ϵ -H₂Mo^{VI}_xMo^V_{12-x}O₄₀] and four Ni²⁺ or Co²⁺ on the hexagonal surfaces of the ϵ -Keggin polyoxomolybdate. These results confirm that the surrounding metal sites in the ϵ -Keggin cores are mostly occupied by Mo in Mo–Zn and Mo–Mn oxides.

High-resolution transmission electron microscopy (HRTEM) images are obtained to further confirm the structures. Figure 7 shows a comparison of the generated polyhedral image using the crystal structure of Mo–V–Bi oxide with HRTEM images of the materials along the (101) direction. HRTEM reveals characteristic face-centered-cubic lattice images for Mo–Zn and Mo–Mn oxides. The ordering of the rhombic black and white spots in the HRTEM images is exactly the same as the ordering of ϵ -Keggin POM building blocks and pores. The lattice parameters of the unit cells and distances of the (111) plane are also obtained from the HRTEM images, and they are in good agreement with the

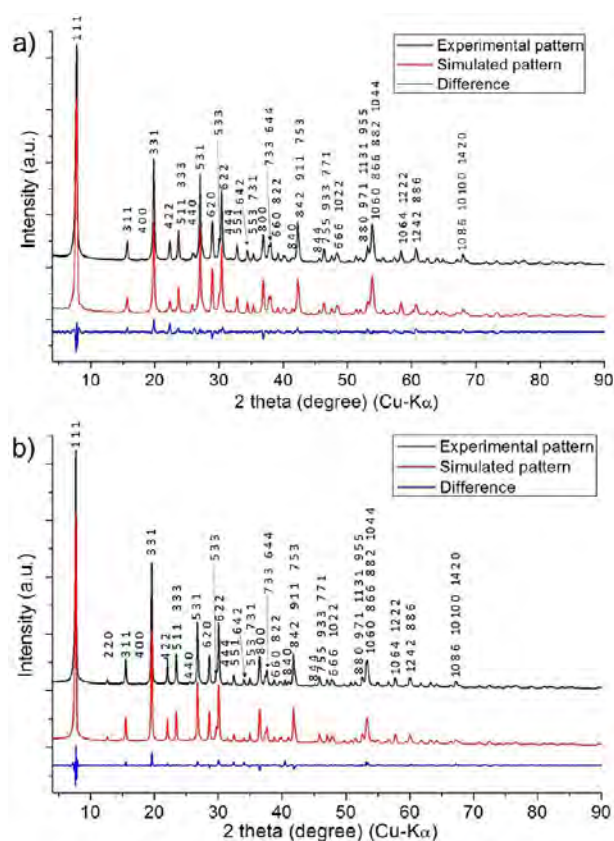


Figure 5. Comparison of the experimental XRD patterns with simulated XRD patterns using the Rietveld method: (a) Mo–Zn oxide, $R_{wp} = 7.10\%$; (b) Mo–Mn oxide, $R_{wp} = 6.19\%$.

results obtained from crystal structures of the materials (Figure 7d).

The oxidation states of the metal elements in Mo–Zn and Mo–Mn oxides are studied by XPS, and the results are presented in SI Figure S4. For linker metals, the bond valence sum (BVS) values of Zn and Mn are 2.13 and 1.93, respectively. For center metals, the BVS values of Zn and Mn are 2.14 and 2.24, respectively, confirming that the oxidation states of both Zn^{II} and Mn^{II} are 2+. The surrounding 12 Mo atoms are mostly reduced, as in the case of other ϵ -Keggin polyoxomolybdates.^{7,36,38} In the case of Mo–Zn oxide, the ratio of $Mo^{VI}:Mo^V$ is 0.1:1.0. The ratio of $Mo^{VI}:Mo^V$ in Mo–Mn oxide is 1.0:1.0. The detailed chemical formulas of these two POM units are estimated to be $[e-Zn^{II}Mo^{V}_{10.9}Mo^{VI}_{1.1}O_{40}\{Zn^{II}\}_2]^{12.9-}$ and $[e-Mn^{II}_{0.2}Mo^V_6Mo^{VI}_6O_{40}\{Mn^{II}\}_2]^{9.6-}$.

The presence of water in Mo–Zn oxide and the presence of water and NH_4^+ in Mo–Mn oxide are confirmed by FT-IR analysis. The FT-IR spectrum (SI Figure S2b) of Mo–Mn oxide shows peak maxima at 1628 and 1401 cm^{-1} , corresponding to water and NH_4^+ , respectively. For Mo–Zn oxide, a peak at 1630 cm^{-1} corresponding to water is observed. The cationic species of Mo–Zn oxide is Na^+ , which results from the starting agent of $Na_2MoO_4 \cdot 2H_2O$. The amounts of cationic species (NH_4^+ and Na^+) and water are estimated by elemental analysis. The detailed formulas of Mo–Zn and Mo–Mn oxides are $Na_{1.5}H_{11.4}[e-Zn^{II}Mo^{V}_{10.9}Mo^{VI}_{1.1}O_{40}\{Zn^{II}\}_2] \cdot 5H_2O$ and $(NH_4)_{2.1}H_{7.5}[e-Mn^{II}_{0.2}Mo^V_6Mo^{VI}_6O_{40}\{Mn^{II}\}_2] \cdot 4H_2O$, respectively.

Cages and channels exist in the materials. One cage is surrounded by 10 ϵ -Keggin POM units with metal-ion linkers (Bi^{III} , Zn^{II} , or Mn^{II}).²⁹ The cages are connected with channels in a tetrahedral fashion to form a periodical 3D pore system as FAU-type zeolites (Faujasite) do. The sizes of the cages are estimated from the Connolly surfaces (see details in the Experimental Section) to be 7.7, 7.6, and 7.6 Å and the sizes of the channels are estimated to be 3.4, 2.9, and 2.9 Å for Mo–V–Bi, Mo–Zn, and Mo–Mn oxides, respectively (Figure 6c). The pore systems of these materials are unique. In one direction, the tunnel of the pore is not straight but in a zigzag fashion (Figure 6d). The existing NH_4^+ (or Na^+) and water occupy the cages and channels in the as-synthesized materials.

TPD-MS analysis under helium flow shows that the water and NH_4^+ in the materials desorb with heat treatment (SI Figure S5). m/z 16, 18, 28, and 32 are attributed to the signals of NH_3 , water, N_2 , and O_2 , respectively. TPD-MS (m/z 16) shows that Mo–V–Bi oxide has two NH_4^+ desorption processes when the temperature is increased to 873 K. One NH_4^+ has a weak interaction with the framework and desorbs at 433 K, and the other has a strong interaction with the framework and desorbs at 633 K.²⁹ Mo–Mn oxide only shows a peak at 593 K in the TPD profile (m/z 16), indicating only one kind of NH_4^+ in the framework. Mo–Zn oxide does not have any NH_4^+ in the structure, and therefore no signal of m/z 16 is found in the TPD profile. For water desorption, TPD profiles of these three materials show two water desorption processes. TG-DTA of Mo–Zn and Mo–Mn oxides under nitrogen flow (SI Figure S5d,e) shows weight losses of 8.2% and 7.2% until ca. 620 K for Mo–Zn and Mo–Mn oxides, respectively. The theoretical weight loss related to removal of the included water calculated from the chemical formula is 4.2% for Mo–Zn oxide, and that related to removal of the included water and ammonium cation is 5.4% for Mo–Mn oxide, which are remarkably smaller than the observed weight losses of the oxides. It is known that heating of POMs generates water from protons and O atoms of POM.^{41,42} The calculated weight losses of removal of the included water, ammonium cation, and water generated from protons and O atoms of polyoxomolybdate are 8.7% and 8.7% for Mo–Zn and Mo–Mn oxides, respectively, which are close to the observed values. Therefore, we conclude that heating Mo–Zn and Mo–Mn oxides generates water from protons and O atoms of polyoxomolybdates.

Thermal Stability. Mo–V–Bi oxide is stable, and the structure of the framework is maintained under the condition of heat treatment at 623 K under a nitrogen gas atmosphere. The stabilities of these two materials are tested by calcination at different temperatures under nitrogen gas. The materials are stable up to 523 K. The powder XRD patterns (SI Figure S6) of the samples calcined at 573 K show that the peak intensities decreased remarkably and FT-IR spectra of the materials also change (SI Figure S7), indicating that both Mo–Zn and Mo–Mn oxides start to collapse at 573 K and are less stable than Mo–V–Bi oxide.

The guest molecules, ammonia and water, in the as-synthesized POM-based materials can be removed by sufficient heat treatment without structural decomposition. Mo–V–Bi oxide is calcined at 623 K for 2 h under a nitrogen atmosphere followed by treatment at 573 K for 2.5 h under high vacuum. Mo–Zn and Mo–Mn oxides are treated at 473 K for 2.5 h under high vacuum. Most of the guest molecules occupying the cages and channels are removed by heat treatment (SI Figure S8) without collapse of the structures (SI Figure S6). TPD-MS

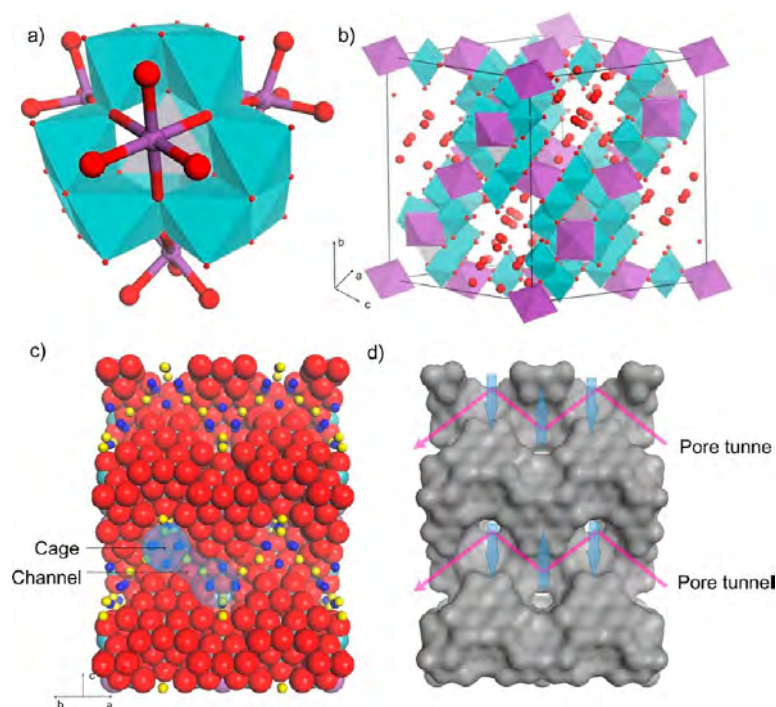


Figure 6. Polyhedral representations of (a) ϵ -Keggin POM with capping metal ions. (b) Unit cell. Surrounding MoO_6 octahedra: blue. Central MO_4 tetrahedra: gray. Metal-ion linkers (Bi, Zn, and Mn): purple. Oxygen: red. (c) CPK (Corey, Pauling, and Koltun) representations of the (110) plane. Framework oxygen: red. Species in the channel: yellow. Species in the cages: deep blue. (d) Connolly surface of the materials in the (110) plane. The pink arrow shows the pore tunnel along the (110) plane, and the blue arrow shows the pore tunnel perpendicular to the (110) plane.

(m/z 16 and 18) profiles of the samples treated at 473 K for 2.5 h under high vacuum show that small amounts of strongly bound water and ammonia remained.

N_2 adsorption–desorption measurement of calcined Mo–V–Bi oxide at 623 K shows a characteristic type I isotherm (Figure 8), indicating that the material is a microporous material. Mo–Zn and Mo–Mn oxides are heated at 473 K for 2.5 h under high vacuum, which are expected to remove most of NH_3 and water, before sorption measurement (SI Figure S8). The results show that the micropores of Mo–Zn and Mo–Mn oxides are also opened, although the adsorbed volume of N_2 on the materials is lower than that on Mo–V–Bi oxide. Surface areas are calculated as 60, 37, and 27 $\text{m}^2 \text{g}^{-1}$ for Mo–V–Bi, Mo–Zn, and Mo–Mn oxides, respectively, using the BET method. The largest BET surface area mainly results from the highly opened micropores of Mo–V–Bi oxide. The less opened micropores of Mo–Zn and Mo–Mn oxides might be caused by the remaining NH_4^+ and Na^+ , which would block pores and decrease the pore volume of the materials.²⁹

Ion-Exchange Property. POM-based materials that show ion-exchange property are interesting.^{43,44} Mo–V–Bi oxide shows an ion-exchange property similar to that of zeolite.²⁹ There are two kinds of NH_4^+ in Mo–V–Bi oxide, a strongly bound one and a weakly bound one. Small cations, including H^+ , Li^+ , and Na^+ , selectively replace the weakly bound NH_4^+ , and large cations, including K^+ , Rb^+ , and Cs^+ , selectively replace the strongly bound one. We confirm that K^+ is present in the channel and that strongly bound NH_4^+ exists in the channel. Mo–Zn and Mo–Mn oxides show ion-exchange properties. The counterions, NH_4^+ in Mo–Mn oxide and Na^+ in Mo–Zn oxide, are exchangeable with other cations. Various counterions, including H^+ , Li^+ , Na^+ , K^+ , Rb^+ , and Cs^+ ,

were tested for ion exchange with Mo–Zn and Mo–Mn oxides. After the ion-exchange process, the ion-exchanged samples are characterized by powder XRD (SI Figure S9), which shows that all of the characteristic peaks of Mo–Zn and Mo–Mn oxides are retained in the corresponding ion-exchanged materials and demonstrate that the basic structures of the materials are unchanged. For K^+ , Rb^+ , and Cs^+ -exchanged samples, powder XRD patterns reveal that the relative peak intensity of ion-exchanged samples changes compared with that of the as-synthesized sample. Moreover, diffraction peaks shift, especially after ion exchange with Rb^+ and Cs^+ , which implies a slight alteration of the lattice parameters (SI Figure S9). In FT-IR spectra of the materials, the vibration peaks of the POM moiety are unchanged, indicating the high stability of the materials during the ion-exchange process. A decrease of the NH_4^+ peaks in FT-IR spectra of Mo–Mn oxide also indicates that NH_4^+ is replaced by other counterions (SI Figure S10).

Elemental analysis confirms that the cations are exchanged with NH_4^+ or Na^+ and introduced into the materials. The chemical formulas of the ion-exchanged samples are summarized in Table 2. The results show that the ion-exchange properties of the materials depend on the size of the ions. Large cations, including K^+ , Rb^+ , and Cs^+ , show a high ion-exchange capacity for both Mo–Zn and Mo–Mn oxides. Small ions, H^+ , Li^+ , and Na^+ , are not as efficient as the large ions to replace NH_4^+ or Na^+ in as-synthesized materials of Mo–Zn and Mo–Mn oxides. Elemental analysis further shows that the amounts of Mo, Zn, and Mn remain constant after the ion-exchange process, indicating that Mo, Zn, and Mn are in the frameworks of the materials.

Furthermore, the ion-exchange properties of Mo–Zn and Mo–Mn oxides with alkaline-earth metal ions are also

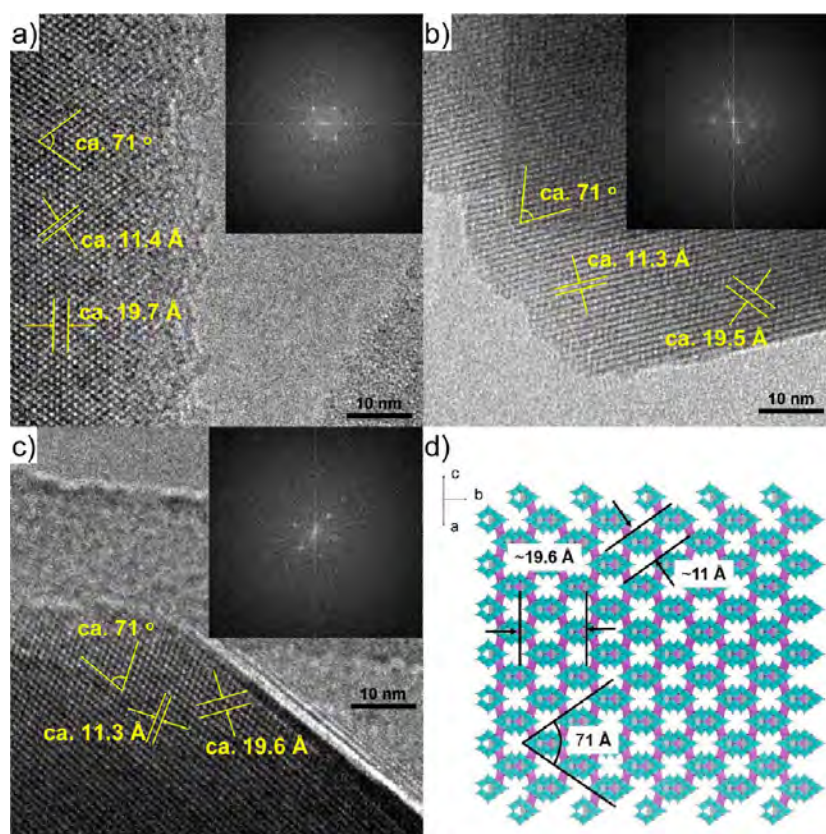


Figure 7. HRTEM images of (a) Mo–V–Bi, (b) Mo–Zn, and (c) Mo–Mn oxides with comparison of (d) the polyhedral representation. Inset: power spectra.

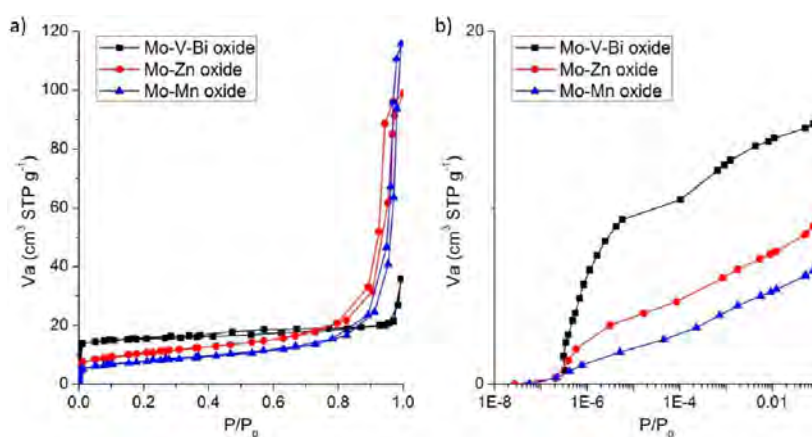


Figure 8. (a) N_2 adsorption–desorption isotherms of Mo–V–Bi, Mo–Zn, and Mo–Mn oxides and (b) the low pressure range.

investigated. After ion exchange, the basic structures of the materials do not change, as indicated by powder XRD patterns (SI Figure S11) and FT-IR spectra (SI Figure S12). Elemental analysis shows that the alkaline-earth metal ions are successfully replaced by the original cations in the materials. Chemical formulas calculated from elemental analysis show that heavy alkaline-earth metal ions, such as Ba^{2+} and Sr^{2+} , can exchange not only with cation species (Na^+ or NH_4^+) but also with protons in the materials (Table 3).

Redox Behavior. A comparison of TG-DTA of Mo–Zn and Mo–Mn oxides under nitrogen and air flow (SI Figure S5)

shows that weight losses in air flow are less than those in nitrogen flow. These results indicate that Mo–Zn and Mo–Mn oxides are oxidized by air. After heating of these oxides in air at 398 K for 2 h, all characteristic peaks of the XRD patterns (SI Figure S13) are retained with a peak shift to higher angles. These results indicate that the structures of these oxides are stable under the heating conditions and the lattice parameters become smaller. Oxidation of Mo^V to Mo^{VI} is confirmed by XPS (Table 4 and SI Figure S14 and Table S7).

Furthermore, reduction of the materials is conducted under hydrogen flow at 423 K. After reduction, the basic structures of

Table 2. Chemical Formulas of Mo–Zn and Mo–Mn Oxides with Alkaline-Metal Ions

	formula
as-synthesized Mo–Zn oxide	$\text{Na}_{1.5}\text{H}_{11.4}[\epsilon\text{-ZnMo}_{12}\text{O}_{40}\{\text{Zn}\}_2]\cdot 5\text{H}_2\text{O}$
H–Mo–Zn oxide	$\text{Na}_{0.6}\text{H}_{12.3}[\epsilon\text{-ZnMo}_{12}\text{O}_{40}\{\text{Zn}\}_2]\cdot 5\text{H}_2\text{O}$
Li–Mo–Zn oxide	$\text{Li}_{0.7}\text{Na}_{0.8}\text{H}_{11.4}[\epsilon\text{-ZnMo}_{12}\text{O}_{40}\{\text{Zn}\}_2]\cdot 5\text{H}_2\text{O}$
NH_4 –Mo–Zn oxide	$(\text{NH}_4)_{1.4}\text{Na}_{0.1}\text{H}_{11.4}[\epsilon\text{-ZnMo}_{12}\text{O}_{40}\{\text{Zn}\}_2]\cdot 5\text{H}_2\text{O}$
K–Mo–Zn oxide	$\text{K}_{1.4}\text{Na}_{0.1}\text{H}_{11.4}[\epsilon\text{-ZnMo}_{12}\text{O}_{40}\{\text{Zn}\}_2]\cdot 5\text{H}_2\text{O}$
Rb–Mo–Zn oxide	$\text{Rb}_{1.3}\text{Na}_{0.2}\text{H}_{11.4}[\epsilon\text{-ZnMo}_{12}\text{O}_{40}\{\text{Zn}\}_2]\cdot 5\text{H}_2\text{O}$
Cs–Mo–Zn oxide	$\text{Cs}_{1.3}\text{H}_{11.4}[\epsilon\text{-ZnMo}_{12}\text{O}_{40}\{\text{Zn}\}_2]\cdot 5\text{H}_2\text{O}$
as-synthesized Mo–Mn oxide	$(\text{NH}_4)_{2.1}\text{H}_{7.5}[\epsilon\text{-Mn}_{0.2}\text{Mo}_{12}\text{O}_{40}\{\text{Mn}\}_2]\cdot 4\text{H}_2\text{O}$
H–Mo–Mn oxide	$(\text{NH}_4)_{1.7}\text{H}_{7.9}[\epsilon\text{-Mn}_{0.2}\text{Mo}_{12}\text{O}_{40}\{\text{Mn}\}_2]\cdot 3\text{H}_2\text{O}$
Li–Mo–Mn oxide	$\text{Li}_{0.1}(\text{NH}_4)_{2.0}\text{H}_{7.5}[\epsilon\text{-Mn}_{0.2}\text{Mo}_{12}\text{O}_{40}\{\text{Mn}\}_2]\cdot 3\text{H}_2\text{O}$
Na–Mo–Mn oxide	$\text{Na}_{0.4}(\text{NH}_4)_{1.7}\text{H}_{7.5}[\epsilon\text{-Mn}_{0.2}\text{Mo}_{12}\text{O}_{40}\{\text{Mn}\}_2]\cdot 3\text{H}_2\text{O}$
K–Mo–Mn oxide	$\text{K}_{1.4}(\text{NH}_4)_{0.7}\text{H}_{7.5}[\epsilon\text{-Mn}_{0.2}\text{Mo}_{12}\text{O}_{40}\{\text{Mn}\}_2]\cdot 3\text{H}_2\text{O}$
Rb–Mo–Mn oxide	$\text{Rb}_{1.5}(\text{NH}_4)_{0.6}\text{H}_{7.5}[\epsilon\text{-Mn}_{0.2}\text{Mo}_{12}\text{O}_{40}\{\text{Mn}\}_2]\cdot 3\text{H}_2\text{O}$
Cs–Mo–Mn oxide	$\text{Cs}_{1.4}(\text{NH}_4)_{0.7}\text{H}_{7.5}[\epsilon\text{-Mn}_{0.2}\text{Mo}_{12}\text{O}_{40}\{\text{Mn}\}_2]\cdot 4\text{H}_2\text{O}$

Table 3. Chemical Formulas of Mo–Zn and Mo–Mn Oxides with Alkaline-Earth Metal Ions

	formula
as-synthesized Mo–Zn oxide	$\text{Na}_{1.5}\text{H}_{11.4}[\epsilon\text{-ZnMo}_{12}\text{O}_{40}\{\text{Zn}\}_2]\cdot 5\text{H}_2\text{O}$
Be–Mo–Zn oxide	$\text{Be}_{0.3}\text{Na}_{0.9}\text{H}_{11.4}[\epsilon\text{-ZnMo}_{12}\text{O}_{40}\{\text{Zn}\}_2]\cdot 4\text{H}_2\text{O}$
Mg–Mo–Zn oxide	$\text{Mg}_{0.6}\text{Na}_{0.3}\text{H}_{11.4}[\epsilon\text{-ZnMo}_{12}\text{O}_{40}\{\text{Zn}\}_2]\cdot 6\text{H}_2\text{O}$
Ca–Mo–Zn oxide	$\text{CaH}_{10.9}[\epsilon\text{-ZnMo}_{12}\text{O}_{40}\{\text{Zn}\}_2]\cdot 7\text{H}_2\text{O}$
Sr–Mo–Zn oxide	$\text{Sr}_{0.8}\text{Na}_{0.1}\text{H}_{11.2}[\epsilon\text{-ZnMo}_{12}\text{O}_{40}\{\text{Zn}\}_2]\cdot 5\text{H}_2\text{O}$
Ba–Mo–Zn oxide	$\text{Ba}_{1.4}\text{H}_{10.1}[\epsilon\text{-ZnMo}_{12}\text{O}_{40}\{\text{Zn}\}_2]\cdot 5\text{H}_2\text{O}$
as-synthesized Mo–Mn oxide	$(\text{NH}_4)_{2.1}\text{H}_{7.5}[\epsilon\text{-Mn}_{0.2}\text{Mo}_{12}\text{O}_{40}\{\text{Mn}\}_2]\cdot 4\text{H}_2\text{O}$
Be–Mo–Mn oxide	$\text{Be}_{0.2}(\text{NH}_4)_{1.7}\text{H}_{7.5}[\epsilon\text{-Mn}_{0.2}\text{Mo}_{12}\text{O}_{40}\{\text{Mn}\}_2]\cdot 5\text{H}_2\text{O}$
Mg–Mo–Mn oxide	$\text{Mg}_{0.6}(\text{NH}_4)_{1.2}\text{H}_{7.2}[\epsilon\text{-Mn}_{0.2}\text{Mo}_{12}\text{O}_{40}\{\text{Mn}\}_2]\cdot 3\text{H}_2\text{O}$
Ca–Mo–Mn oxide	$\text{Ca}_{0.9}(\text{NH}_4)_1\text{H}_{6.8}[\epsilon\text{-Mn}_{0.2}\text{Mo}_{12}\text{O}_{40}\{\text{Mn}\}_2]\cdot 5\text{H}_2\text{O}$
Sr–Mo–Mn oxide	$\text{Sr}_{0.8}(\text{NH}_4)_1\text{H}_7[\epsilon\text{-Mn}_{0.2}\text{Mo}_{12}\text{O}_{40}\{\text{Mn}\}_2]\cdot 5\text{H}_2\text{O}$
Ba–Mo–Mn oxide	$\text{Ba}_{1.6}\text{H}_{6.4}[\epsilon\text{-Mn}_{0.2}\text{Mo}_{12}\text{O}_{40}\{\text{Mn}\}_2]\cdot 4\text{H}_2\text{O}$

Table 4. Ratio of Mo Ions with Different Oxidation States in Mo–Zn and Mo–Mn Oxides after Redox Treatment and Their Corresponding Chemical Formulas

	ratio of Mo ions	chemical formula
Mo–Zn oxide	$\text{Mo}^{\text{VI}}:\text{Mo}^{\text{V}} = 0.10$	$\text{Na}_{1.5}\text{H}_{11.4}[\epsilon\text{-Zn}^{\text{II}}\text{Mo}^{\text{VI}}_{10.9}\text{Mo}^{\text{V}}_{1.1}\text{O}_{40}\{\text{Zn}^{\text{II}}\}_2]$
Mo–Zn oxide heated at 398 K in air	$\text{Mo}^{\text{VI}}:\text{Mo}^{\text{V}} = 0.85$	$\text{Na}_{1.5}\text{H}_7[\epsilon\text{-Zn}^{\text{II}}\text{Mo}^{\text{V}}_{6.5}\text{Mo}^{\text{VI}}_{5.5}\text{O}_{40}\{\text{Zn}^{\text{II}}\}_2]$
Mo–Zn oxide heated at 423 K under hydrogen flow	$\text{Mo}^{\text{V}}:\text{Mo}^{\text{IV}} = 0.25$	$\text{Na}_{1.5}\text{H}_{22.1}[\epsilon\text{-Zn}^{\text{II}}\text{Mo}^{\text{V}}_{2.4}\text{Mo}^{\text{IV}}_{9.6}\text{O}_{40}\{\text{Zn}^{\text{II}}\}_2]$
Mo–Mn oxide	$\text{Mo}^{\text{VI}}:\text{Mo}^{\text{V}} = 1.00$	$(\text{NH}_4)_{2.1}\text{H}_{7.5}[\epsilon\text{-Mn}^{\text{II}}_{0.2}\text{Mo}^{\text{VI}}_6\text{O}_{40}\{\text{Mn}^{\text{II}}\}_2]$
Mo–Mn oxide heated at 398 K in air	$\text{Mo}^{\text{VI}}:\text{Mo}^{\text{V}} = 6.10$	$(\text{NH}_4)_{2.1}\text{H}_{3.2}[\epsilon\text{-Mn}^{\text{II}}_{0.2}\text{Mo}^{\text{V}}_{1.7}\text{Mo}^{\text{VI}}_{10.3}\text{O}_{40}\{\text{Mn}^{\text{II}}\}_2]$
Mo–Mn oxide heated at 423 K under hydrogen flow	$\text{Mo}^{\text{VI}}:\text{Mo}^{\text{V}} = 1.00$	$(\text{NH}_4)_{2.1}\text{H}_{7.5}[\epsilon\text{-Mn}^{\text{II}}_{0.2}\text{Mo}^{\text{VI}}_6\text{O}_{40}\{\text{Mn}^{\text{II}}\}_2]$

the materials do not change (SI Figure S13). XPS results (Table 4 and SI Figure S14 and and Table S7) demonstrate

that the Mo ion in Mo–Zn oxide can be reduced to Mo^{V} and Mo^{IV} , while the Mo ion is not reduced in Mo–Mn oxide under the current conditions. Furthermore, redox treatments of the materials affect the DR UV–vis spectra of the materials (SI Figure S15).

These results indicate that these oxides can accept and release electrons without collapse of the structures. Further investigations to understand and control the redox behavior of these materials are now in progress in our group.

CONCLUSION

Two new ϵ -Keggin polyoxomolybdate-based 3D framework materials, cubic Mo–Zn and Mo–Mn oxides, have been successfully synthesized and characterized. In both oxides, ϵ -Keggin polyoxomolybdates with 12 Mo atoms, $[\epsilon\text{-ZnMo}_{12}\text{O}_{40}]$ or $[\epsilon\text{-Mn}_{0.2}\text{Mo}_{12}\text{O}_{40}]$, are linked by Zn^{II} or Mn^{II} ions to form 3D diamond-like frameworks. The guest molecules in as-synthesized materials can be mostly removed by heat treatment (473 K), although they are thermally less stable than the previously reported Mo–V–Bi oxide. These oxides show ion-exchange properties similar to those of zeolite materials. Furthermore, these oxides can accept and release electrons without collapse of the structures. Our results, indicating that a variety of transition metals can be incorporated into the ϵ -Keggin polyoxomolybdate-based materials, open a door for the development of ϵ -Keggin polyoxomolybdate-based 3D framework materials as functional materials, such as ion-exchange, catalyst, adsorption, and magnetic materials.

ASSOCIATED CONTENT

Supporting Information

Detailed experimental procedures, including figures and tables. This material is available free of charge via the Internet at <http://pubs.acs.org>.

AUTHOR INFORMATION

Corresponding Authors

*E-mail: sadakane09@hiroshima-u.ac.jp. Phone: +81-82-424-4456. Fax: +81-82-424-5494.

*E-mail: ueda@cat.hokudai.ac.jp. Phone: +81-11-706-9164. Fax: +81-11-706-9163.

Author Contributions

All authors have given approval to the final version of the manuscript.

Notes

The authors declare no competing financial interest.

ACKNOWLEDGMENTS

This work was financially supported by a Grant-in-Aid for Scientific Research (A) (Grant 2324-6135) from the Ministry of Education, Culture, Sports, Science, and Technology, Japan. M.S. thanks PRESTO, JST, for financial support.

REFERENCES

- (1) Special thematic issue on polyoxometalates: Hill, C. L. *Chem. Rev.* **1998**, *98*, 1–390.
- (2) Special thematic issue on polyoxometalates: Cronin, L.; Müller, A. *Chem. Soc. Rev.* **2012**, *41*, 7325–7648.
- (3) Pope, M. T. *Heteropoly and Isopoly Oxometalates*; Springer-Verlag: Berlin, 1983.
- (4) Dolbecq, A.; Mialane, P.; Secheresse, F.; Keita, B.; Nadjo, L. *Chem. Commun.* **2012**, *48*, 8299–8316.

- (5) Mandic, S.; Healey, M. R.; Gotthardt, J. M.; Alley, K. G.; Gable, R. W.; Ritchie, C.; Boskovic, C. *Eur. J. Inorg. Chem.* **2013**, 1631–1634.
- (6) Nohra, B.; El Moll, H.; Rodriguez Albelo, L. M.; Mialane, P.; Marrot, J.; Mellot-Draznieks, C.; O'Keefe, M.; Biboum, R. N.; Lemaire, J.; Keita, B.; Nadjo, L.; Dolbecq, A. *J. Am. Chem. Soc.* **2011**, *133*, 13363–13374.
- (7) Rodriguez-Albelo, L. M.; Rabdel Ruiz-Salvador, A.; Sampieri, A.; Lewis, D. W.; Gomez, A.; Nohra, B.; Mialane, P.; Marrot, J.; Secheresse, F.; Mellot-Draznieks, C.; Biboum, R. N.; Keita, B.; Nadjo, L.; Dolbecq, A. *J. Am. Chem. Soc.* **2009**, *131*, 16078–16087.
- (8) Song, J.; Luo, Z.; Britt, D. K.; Furukawa, H.; Yaghi, O. M.; Hardcastle, K. I.; Hill, C. L. *J. Am. Chem. Soc.* **2011**, *133*, 16839–16846.
- (9) Sun, C.-Y.; Liu, S.-X.; Liang, D.-D.; Shao, K.-Z.; Ren, Y.-H.; Su, Z.-M. *J. Am. Chem. Soc.* **2009**, *131*, 1883–1888.
- (10) Kamiya, Y.; Sadakane, M.; Ueda, W. Heteropoly Compounds. In *Comprehensive Inorganic Chemistry II*; Reedijk, J., Poeppelmeier, K., Eds.; Elsevier: Oxford, U.K., 2013; Vol. 7, pp 185–204.
- (11) Eguchi, R.; Uchida, S.; Mizuno, N. *J. Phys. Chem. C* **2012**, *116*, 16105–16110.
- (12) Eguchi, R.; Uchida, S.; Mizuno, N. *Angew. Chem., Int. Ed.* **2012**, *51*, 1635–1639.
- (13) Jiang, C.; Lesbani, A.; Kawamoto, R.; Uchida, S.; Mizuno, N. *J. Am. Chem. Soc.* **2006**, *128*, 14240–14241.
- (14) Kawamoto, R.; Uchida, S.; Mizuno, N. *J. Am. Chem. Soc.* **2005**, *127*, 10560–10567.
- (15) Uchida, S.; Eguchi, R.; Nakamura, S.; Ogasawara, Y.; Kurosawa, N.; Mizuno, N. *Chem. Mater.* **2012**, *24*, 325–330.
- (16) Uchida, S.; Lesbani, A.; Ogasawara, Y.; Mizuno, N. *Inorg. Chem.* **2012**, *51*, 775–777.
- (17) Uchida, S.; Mizuno, N. *Coord. Chem. Rev.* **2007**, *251*, 2537–2546.
- (18) Uchida, S.; Hikichi, S.; Akatsuka, T.; Tanaka, T.; Kawamoto, R.; Lesbani, A.; Nakagawa, Y.; Uehara, K.; Mizuno, N. *Chem. Mater.* **2007**, *19*, 4694–4701.
- (19) Sadakane, M.; Endo, K.; Kodato, K.; Ishikawa, S.; Murayama, T.; Ueda, W. *Eur. J. Inorg. Chem.* **2013**, 1731–1736.
- (20) Sadakane, M.; Watanabe, N.; Katou, T.; Nodasaka, Y.; Ueda, W. *Angew. Chem., Int. Ed.* **2007**, *46*, 1493–1496.
- (21) Sadakane, M.; Yamagata, K.; Kodato, K.; Endo, K.; Toriumi, K.; Ozawa, Y.; Ozeki, T.; Nagai, T.; Matsui, Y.; Sakaguchi, N.; Pyrz, W. D.; Buttrey, D. J.; Blom, D. A.; Vogt, T.; Ueda, W. *Angew. Chem., Int. Ed.* **2009**, *48*, 3782–3786.
- (22) Sadakane, M.; Ohmura, S.; Kodato, K.; Fujisawa, T.; Kato, K.; Shimidzu, K.; Murayama, T.; Ueda, W. *Chem. Commun.* **2011**, *47*, 10812–10814.
- (23) Sadakane, M.; Kodato, K.; Kuranishi, T.; Nodasaka, Y.; Sugawara, K.; Sakaguchi, N.; Nagai, T.; Matsui, Y.; Ueda, W. *Angew. Chem., Int. Ed.* **2008**, *47*, 2493–2496.
- (24) Wang, F.; Ueda, W. *Top. Catal.* **2008**, *50*, 90–97.
- (25) Wang, F.; Ueda, W. *Catal. Today* **2009**, *144*, 358–361.
- (26) Konya, T.; Katou, T.; Murayama, T.; Ishikawa, S.; Sadakane, M.; Buttrey, D.; Ueda, W. *Catal. Sci. Technol.* **2013**, *3*, 380–387.
- (27) Watanabe, N.; Ueda, W. *Ind. Eng. Chem. Res.* **2006**, *45*, 607–614.
- (28) Mitchell, S. G.; Streb, C.; Miras, H. N.; Boyd, T.; Long, D.-L.; Cronin, L. *Nat. Chem.* **2010**, *2*, 308–312.
- (29) Zhang, Z.; Sadakane, M.; Murayama, T.; Izumi, S.; Yasuda, N.; Sakaguchi, N.; Ueda, W. *Inorg. Chem.* **2014**, *53*, 903–911.
- (30) Boulitif, A.; Louer, D. *J. Appl. Crystallogr.* **2004**, *37*, 724–731.
- (31) Neumann, M. A. *J. Appl. Crystallogr.* **2003**, *36*, 356–365.
- (32) Le Bail, A. *Powder Diffr.* **2008**, *23*, S5–S12.
- (33) Palatinus, L.; Chapuis, G. *J. Appl. Crystallogr.* **2007**, *40*, 786–790.
- (34) Young, R. A. *The Rietveld Method*; Young, R. A., Ed.; Oxford University Press: Oxford, U.K., 1995.
- (35) Kim, D.-S.; Ryu, J.; Park, R. *J. Comput. Sci. Technol.* **2006**, *21*, 255–260.
- (36) Müller, A.; Beugholt, C.; Kogerler, P.; Bogge, H.; Bud'ko, S.; Luban, M. *Inorg. Chem.* **2000**, *39*, 5176–5177.
- (37) Sloboda-Rozner, D.; Neimann, K.; Neumann, R. *J. Mol. Catal. A: Chem.* **2007**, *262*, 109–113.
- (38) Mialane, P.; Dolbecq, A.; Lisnard, L.; Mallard, A.; Marrot, J.; Secheresse, F. *Angew. Chem., Int. Ed.* **2002**, *41*, 2398–2401.
- (39) Tucher, J.; Nye, L. C.; Ivanovic-Burmazovic, I.; Notarnicola, A.; Streb, C. *Chem.—Eur. J.* **2012**, *18*, 10949–10953.
- (40) Ellern, A.; Kögerler, P. *Acta Crystallogr., Sect. C* **2012**, *68*, i17–i19.
- (41) Tong, X.; Zhu, W.; Wu, Q.; Qian, X.; Liu, Z.; Yan, W.; Gong, J. *J. Alloys Compd.* **2011**, *509*, 7768–7772.
- (42) Wu, Q.; Wang, S.; Li, D.; Xie, X. *Inorg. Chem. Commun.* **2002**, *5*, 308–311.
- (43) Rehder, D.; Haupt, E. T. K.; Bögge, H.; Müller, A. *Chem.—Asian J.* **2006**, *1*, 76–81.
- (44) Rehder, D.; Haupt, E. T. K.; Müller, A. *Magn. Reson. Chem.* **2008**, *46*, S24–S29.



Catalysis field in orthorhombic Mo_3VO_x oxide catalyst for the selective oxidation of ethane, propane and acrolein



Satoshi Ishikawa^a, Xiaodong Yi^b, Toru Murayama^a, Wataru Ueda^{a,*}

^a Catalysis Research Center, Hokkaido University, N-21, W-10, Sapporo 001-0021, Japan

^b State Key Laboratory for Physical Chemistry of Solid Surfaces, Department of Chemistry, Xiamen University, Xiamen 361005, Fujian, China

ARTICLE INFO

Article history:

Received 27 November 2013

Received in revised form

26 December 2013

Accepted 28 December 2013

Available online 11 February 2014

Keywords:

Orthorhombic Mo_3VO_x oxide catalysts

Micropore

Selective oxidation

Catalysis field

ABSTRACT

Orthorhombic Mo_3VO_x oxide catalysts in various crystal sizes with different external surface areas and the same micropore volumes were synthesized hydrothermally by adding sodium dodecyl sulphonate (SDS, $\text{C}_{12}\text{H}_{25}\text{SO}_3\text{Na}$) to preparation solution and by changing synthesis temperature. The synthesized catalysts were then tested for the selective oxidations of ethane, propane, and acrolein, in order to clarify catalysis field for the reactions. It was found that ethane converted to ethene in the heptagonal channel in the structure of the catalyst and propane was also oxidized to CO_x in the heptagonal channel. Acrolein, on the other hand, was converted to acrylic acid at the mouth of the heptagonal channel. It is concluded that the heptagonal channel is all responsible for the catalysis for ethane, propane, and acrolein. However, the catalysis field is different in a reflection of the molecular size of the reactants.

© 2014 Elsevier B.V. All rights reserved.

1. Introduction

Orthorhombic Mo_3VO_x is well known as an effective catalyst for the selective oxidation of light alkanes [1–5], alcohols [6,7], and acrolein [8]. Fig. 1 shows the structural model and SEM images of orthorhombic Mo_3VO_x before and after grinding. The structure is a layer-type with a slab comprising hexagonal and heptagonal channels of corner-sharing octahedra and pentagonal $\{(\text{Mo})\text{Mo}_5\}$ units [9]. In a reflection of the complex arrangement in the a – b plane and the simple stacking in the c axis, crystals were rod-shaped. The rod-shaped crystals are easily broken by grinding to shorter rod crystals with keeping the diameter of the rod due to the crystal habit. In this structure, the heptagonal channel works as a micropore adsorbing small molecules like CO_2 , CH_4 , and C_2H_6 [10,11] because the heptagonal channel is enough large in diameter to accept these small molecules. Therefore, the heptagonal channel seems play a crucial role for the selective oxidation of ethane, propane, and acrolein.

Recently, we have reported that ethane is converted in the heptagonal channel micropore of orthorhombic Mo_3VO_x , which leads the extremely high catalytic activity for the selective oxidation of ethane [12]. In the case of the selective oxidation of propane, we have reported that catalytic activities of Mo–V–Te–O and Mo–V–Sb–O oxide catalysts, which assume the same structure with orthorhombic Mo_3VO_x , were increased drastically when grind

treatment was conducted before the selective oxidation of propane [13]. We concluded that the section surface of the rod-shaped crystals of the catalysts attributed to the a – b plane in the orthorhombic structure is active for the reaction. Shiju et al. have reported that Mo–V–Te–Nb–O coated with alumina showed almost no catalytic activity for the ammoxidation of propane, while the catalytic activity was increased drastically when the catalyst was ground [14]. The result shows that the a – b plane exposed by the grind treatment is active for the ammoxidation of propane. We have reported the relationships of the catalytic activity for the selective oxidation of alkane to the crystal phase of crystalline Mo–V–O oxide catalysts. We found that the catalysts which have heptagonal channel in the structure showed the catalytic activity, on the other hand, no catalytic activity was observed in the catalysts without heptagonal channel in the structure [2,5].

In the case of the selective oxidation of acrolein, there are many reports which deal with Mo–V–O oxide catalysts [15–17]. The active catalytic material for the selective oxidation of acrolein was composed by $\text{Mo}_3\text{VO}_{11+y}$ ($y=0$ – 0.2). However, there are few researches showing what kind of structural phase is active and how catalysis can take place. Recently, we have reported that crystalline Mo_3VO_x catalysts having heptagonal channel in the structure showed extremely high catalytic activity for the selective oxidation of acrolein, while the catalysts with no heptagonal channel showed no catalytic activity [8]. It is now no doubt that the heptagonal channel of Mo_3VO_x is responsible for activating acrolein. However, there are still no reports which investigate actual catalysis field for the reactions.

* Corresponding author. Tel.: +81 11 762 9164; fax: +81 11 762 9163.
E-mail address: ueda@cat.hokudai.ac.jp (W. Ueda).



Fig. 1. Structural model (Mo, cyan; V, gray; O, red) (left) and SEM images (middle; unground, right; ground) of the orthorhombic Mo_3VO_x oxide catalyst. (For interpretation of the references to color in this figure legend, the reader is referred to the web version of this article.)

More recently, we have reported that the crystal sizes of the orthorhombic Mo_3VO_x oxide catalysts can be controlled by adding sodium dodecyl sulphonate (SDS, $\text{C}_{12}\text{H}_{25}\text{SO}_3\text{Na}$) and by changing the synthesis temperature under hydrothermal preparative conditions [12]. This method can afford no change of catalytically affective properties such as crystal structure, micropore volume, and chemical compositions except the external surface area with these catalysts. Catalysis fields of orthorhombic Mo_3VO_x can be clarified by evaluating the dependency of the catalytic activity upon the external surface area. Here, we studied the selective oxidation of ethane, propane, and acrolein over the catalysts in order to reveal contributions of the external surface and micropore channel for the reactions.

2. Experiments

2.1. Catalyst preparation

Catalysts were prepared according to our previous paper [12]. An aqueous solution of Mo prepared by 8.83 g of $(\text{NH}_4)_6\text{Mo}_7\text{O}_{24}\cdot 4\text{H}_2\text{O}$ (Mo: 50 mmol, Wako) dissolved in 120 mL of distilled water was mixed with an aqueous solution of VOSO_4 prepared by dissolving 3.29 g of hydrated VOSO_4 (V: 12.5 mmol, Mitsuwa Chemicals) in 120 mL of distilled water. The two solutions were mixed and stirred for 10 min. Then, an appropriate amount of sodium dodecyl sulphonate (SDS, $\text{C}_{12}\text{H}_{25}\text{SO}_3\text{Na}$, Wako) was added and stirred for another 10 min. The amount of SDS added was $x = 0, 0.15, 0.30,$ and 0.60 , where x corresponds to the molar ratio of $\text{SDS}/(\text{Mo} + \text{V})$. Then, the obtained mixed solution was introduced into an autoclave with a 300 mL-Teflon inner vessel and 4000 cm^3 of Teflon thin sheet. After the introduction, N_2 bubbling was conducted in order to remove residual oxygen. The hydrothermal reaction was started at 175°C for 48 h. Gray solids formed on the Teflon sheet was separated by filtration, washed with 1000 mL of distilled water, and dried at 80°C over night. Obtained solid contained amorphous type of materials as an impurity phase, so that the dried samples were treated with oxalic acid for purification. To 25 mL aqueous solution (0.4 mol L^{-1} , 60°C) of oxalic acid (Wako), 1 g of the dried material was added and stirred for 30 min, then washed with 500 mL of distil water. When SDS was added, materials were washed with 500 mL of distil water, followed by washing with 300 mL of ethanol to remove SDS and drying at 80°C over night. FT-IR and CHN elemental analysis confirmed that SDS was completely removed by ethanol washing. Hydrothermal synthesis was also conducted at 230°C for 20 h using 250 mL-Teflon inner vessel. In this case, the amount of $(\text{NH}_4)_6\text{Mo}_7\text{O}_{24}\cdot 4\text{H}_2\text{O}$, hydrated VOSO_4 , and SDS were set to be half with the same concentration. The other procedure was the same as described above. The general abbreviation for the synthesized samples is MoVO-SDS_{x-y} , where x corresponds to the molar ratio of $\text{SDS}/(\text{Mo} + \text{V})$ and y corresponds to the synthetic temperature.

2.2. Characterization of synthesized materials

Catalysts were characterized by the following techniques. Powder XRD patterns were measured with a diffractometer (RINT Ultima+, Rigaku) using $\text{Cu-K}\alpha$ radiation (tube voltage: 40 kV, tube current: 20 mA). Diffractions were recorded in the range of $4\text{--}60^\circ$ with 5° min^{-1} . FT-IR spectra were obtained using a spectrometer (Paragon 1000, Perkin Elmer) at room temperature in the range of $500\text{--}2000 \text{ cm}^{-1}$. SEM images were taken using an electron microscope (JSM-7400F, JEOL). XPS (JPC-9010MC, JEOL) with a non-monochromatic $\text{Mg-K}\alpha$ radiation was used for measuring binding energy values of Mo and V. Binding energy was referred by $\text{Au } 4f_{7/2}$ (84.0 eV) which was deposited by an auto fine coater (JFC-1600, JEOL). Elemental compositions in the bulk were determined by ICP-AES (ICPE-9000, Shimadzu). N_2 adsorption isotherms at liq. N_2 temperature were measured by using an auto-adsorption system (BELSORP MAX, Nippon BELL) for the samples both before and after the catalytic tests. The samples before the reactions were heat treated in air at 400°C for 2 h. Prior to N_2 adsorption, the catalysts were evacuated under vacuum at 300°C for 2 h. External surface area was determined using a t -plot.

2.3. Catalytic test

Selective oxidation of ethane was performed according to our previous report [12]. Selective oxidation of propane in gas phase was carried out at atmospheric pressure in a conventional vertical flow system with a fixed bed Pyrex tubular reactor. As-synthesized catalysts were ground with an agate mortar for 5 min, followed by heat-treatment under N_2 atmosphere at 400°C for 2 h with a fixed bed Pyrex tubular furnace. Then, 0.500 g of the treated catalysts were diluted with 2.300 g of silica and put into the tubular reactor for propane oxidation. The reactor was heated gradually from room temperature at a rate of $10^\circ\text{C min}^{-1}$ to 360°C under mixed gas flow of nitrogen and helium flow (14.8 mL min^{-1}) from the top of the reactor. The temperature was measured with a thermocouple inserted in the middle of the catalyst zone. When the temperature reached 360°C , a reactant gas with the composition of $\text{C}_3\text{H}_8/\text{O}_2/\text{H}_2\text{O}/(\text{N}_2 + \text{He}) = 7.5/10.0/45.5/37.0$ (mol%) was fed in with total flow rate of 40 mL min^{-1} and started the reaction. Water was supplied by helium bubbling with 8.1 mL min^{-1} of flow rate to hot water at 90°C . Reaction temperature was then decreased to 330, 300, 270, and 250°C . Reactants and products were analyzed with three online gas chromatographs (Molecular sieve 5A for O_2, N_2 and CO with a TCD detector, Gaskuropack54 for $\text{CO}_2, \text{C}_3\text{H}_8$ and C_3H_6 with a TCD detector, and Porapak Q for acetone, acetic acid and acrylic acid with a FID detector). Blank runs showed that under the experimental conditions used in this study, homogeneous gas-phase reactions were negligible. Carbon balance was always ca. 95–100%.

Table 1
External surface area of MoVO-SDS_{x-y} catalysts.

	External surface area/m ² g ⁻¹			
	As synthesis	After catalysis		
		Ethane	Propane	Acrolein
MoVO-SDS0-175	7.3	7.2	6.4	6.7
MoVO-SDS0-175-non	–	6.8	8.3	4.0
MoVO-SDS0.15-175	5.9	7.2	–	–
MoVO-SDS0.30-175	5.7	7.3	–	–
MoVO-SDS0.60-175	15.4	14.0	15.1	19.2
MoVO-SDS0-230	2.9	5.3	4.8	4.5
MoVO-SDS0.15-230	0.8	1.2	0.6	1.6
MoVO-SDS0.30-230	2.4	3.9	–	–
MoVO-SDS0.60-230	2.8	5.5	–	–

Selective oxidation of acrolein was also carried out at atmospheric pressure in the same conventional vertical flow system with a stainless tubular reactor. As-synthesized catalysts were ground with an agate mortar for 5 min, followed by heat-treatment under N₂ atmosphere at 400 °C for 2 h with a fixed bed Pyrex tubular furnace. Then, 0.125 g of the treated catalysts were diluted with 1.200 g of silica and put into the tubular reactor for acrolein oxidation. The reactor was heated at a rate of 10 °C min⁻¹ to the desired reaction temperature under mixed gas flow of nitrogen and helium (70 mL min⁻¹). When the temperature reached the desired reaction temperature, 107.5 mL min⁻¹ of reactant gas with the composition of 2.3/7.4/25.2/65.1 (mol%) was fed in and started the reaction. Acrolein was supplied by nitrogen bubbling with 20.6 mL min⁻¹ of flow rate to acrolein solution at 0 °C. Water was supplied by helium bubbling with 30.5 mL min⁻¹ of flow rate to hot water at 80 °C. Reaction temperature was then decreased. Reactants and products were analyzed with three on-line gas chromatographs (Molecular Sieve 13X for O₂, N₂, and CO with a TCD detector, Gaskuropack54 for CO₂ with a TCD detector, and Porapak Q for C₂H₃COH, CH₃COOH, C₂H₃COOH with a FID detector). Blank runs showed that no reaction took place without catalysts under the experimental conditions used in this study. Carbon balance was always ca. 96–100%.

3. Results and discussion

The catalysts synthesized with SDS were characterized by XRD, XPS, ICP, SEM, and N₂ adsorption. Irrespective of the addition of SDS and of the synthesis temperature, properties strongly relating to catalysis, such as crystal structure, elemental compositions (bulk and surface), and micropore volume, were almost the same in the synthesized catalysts. Size of the rod-shaped crystals was only changed by the addition of SDS and by changing the synthesis temperature, which thus caused change of external surface area. The external surface area of the catalysts before and after the selective oxidation of ethane, propane, and acrolein are listed in Table 1. As can be seen in Table 1, the external surface area was widely changed by altering the preparative conditions. After the selective oxidations, the external surface areas of each catalyst were slightly changed. Practically no XRD peaks and pattern changes were observed after the catalytic tests of the selective oxidation of ethane, propane, and acrolein, revealing that the catalysts could be kept stable structurally under the catalytic reaction conditions. Physicochemical properties of the catalysts after the selective oxidation of ethane are summarized in Fig. 2. The side surface area and the section surface area were calculated by using the average diameter and the average length of the rod-shaped crystals, which were obtained by measuring 100 of rod-shaped crystals by using SEM photos. The average diameter and the average length of the rod-shaped crystals after the selective oxidation

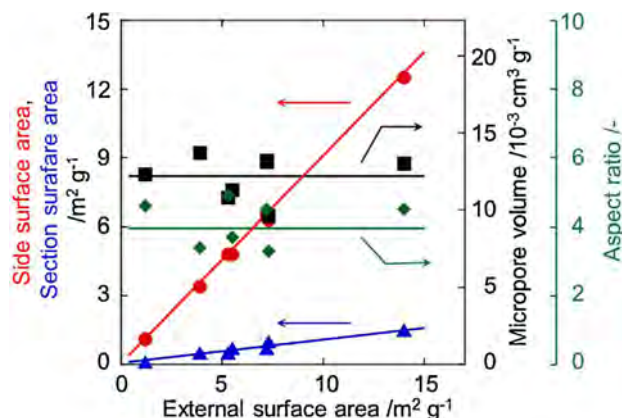


Fig. 2. Side surface area (circle), section surface area (triangle), micropore volume (square), and aspect ratio (lozenge) of the rod-shaped crystals of the catalysts after the selective oxidation of ethane. Side surface area and section surface area were calculated based on the measured external surface area by using the values of the average diameter and the average length of the rod-shaped crystals obtained by measuring 100 of the crystals in SEM images. Micropore volume was determined by the *t*-plot method. Aspect ratio is the ratio of the average length to the average diameter of the rod-shaped crystals.

of ethane were in the range of 0.22–1.04 μm in the diameter and 0.7–4.8 μm in the length, respectively. Aspect ratio is the ratio of the average length to the average diameter of the crystals. The side surface area and the section surface area of the rod-shaped crystals were linearly increased with the external surface area, since the aspect ratio of the rod-shaped crystals was almost the same with the same rod-shaped crystals of the catalysts. On the other hand, the micropore volume measured by N₂ adsorption at liquid N₂ temperature was found almost constant. Micropore volume measured by ethane adsorption was also almost the same and was in the range of 16.1–18.8 × 10⁻³ cm³ g⁻¹ after the ethane selective oxidation. The molar ratio of V/Mo measured by ICP was in the range of V/Mo = 0.36–0.39 in the catalysts. No change of the elemental composition was observed after the selective oxidation of ethane.

We now compare the catalytic performance of these catalysts for the oxidation of ethane, propane, and acrolein in Fig. 3. As described in the experimental section, MoVO-SDS_{x-y} represents the catalysts synthesized with *x* mol% of SDS adding (*x* = SDS/(Mo + V)) at *y* °C. The catalysts shown in Fig. 3 were MoVO-SDS0-175, MoVO-SDS0.60-175, MoVO-SDS0-230, and MoVO-SDS0.15-230, of which the external surface area were 7.2, 15.4, 2.8, and 0.8 m² g⁻¹ before the reactions, respectively. These external surface areas were slightly changed after the reaction as mentioned before (Table 1), but a large difference in the external surface area among the catalysts was still remained. Therefore we can evaluate the effects of the external surface area on the reaction. The conversion of ethane and the selectivity to ethene and CO_x are shown in Fig. 3(A) and (A'). With increasing the reaction temperature from 250 °C to 380 °C, the conversion of ethane increased. The selectivity to ethene decreased with the reaction temperature. At the same time, the selectivity to CO_x increased. Strikingly all the catalysts showed almost the same conversion of ethane and the same selectivity to ethene and CO_x at whole the reaction temperature range. Fig. 4(A) shows the relationship between the external surface area and the conversion of ethane at 300 °C. Irrespective of the increase of the external surface area of the catalysts, the ethane conversion was ca. 30% for all the catalysts. This figure clearly shows no dependency of the catalytic activity on the external surface area of the catalyst. The result suggests that the external surface area provides no practical impacts to the catalytic activity. Therefore, catalysis field in the catalyst for the ethane oxidation is considered to be the micropore channel. However, since

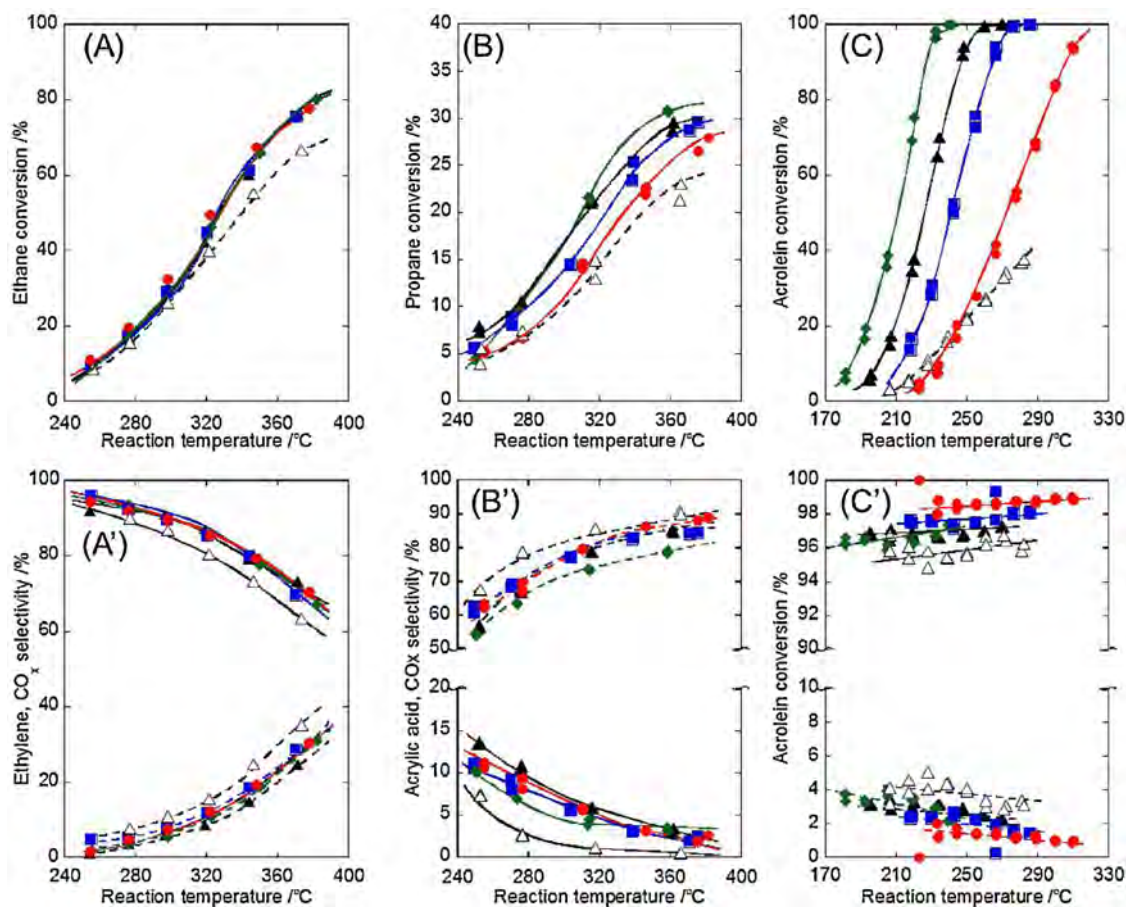


Fig. 3. Conversion (top) and selectivity (bottom) changes as a function of reaction temperature in the selective oxidation of ethane (A), (A'), propane (B), (B'), and acrolein (C), (C'). MoVO-SDSO-175 (closed triangle), MoVO-SDSO.60-175 (closed lozenge), MoVO-SDSO-230 (closed square), MoVO-SDSO.15-230 (closed circle), MoVO-SDSO-175-non (open triangle). Selective oxidation of ethane, selectivity to ethene (solid line) and CO_x (dot line) are plotted. Selective oxidation of propane, selectivity to acrylic acid (solid line) and CO_x (dot line) are plotted. Selective oxidation of acrolein, selectivity to acrylic acid (solid line) and CO_x (dot line) are plotted.

the section surface area of the catalysts was quite small compared with the side surface area as shown in Fig. 2, the effects of section surface for the selective oxidation of ethane are difficult to be evaluated. In order to investigate the contributions of section surface

area of the rod-shaped crystals for the reaction, a catalyst (MoVO-SDSO-175-non) without grinding before catalysis was tested for the reaction. The external surface area of MoVO-SDSO-175-non was $6.8 \text{ m}^2 \text{ g}^{-1}$, almost the same with that of MoVO-SDSO-175 as

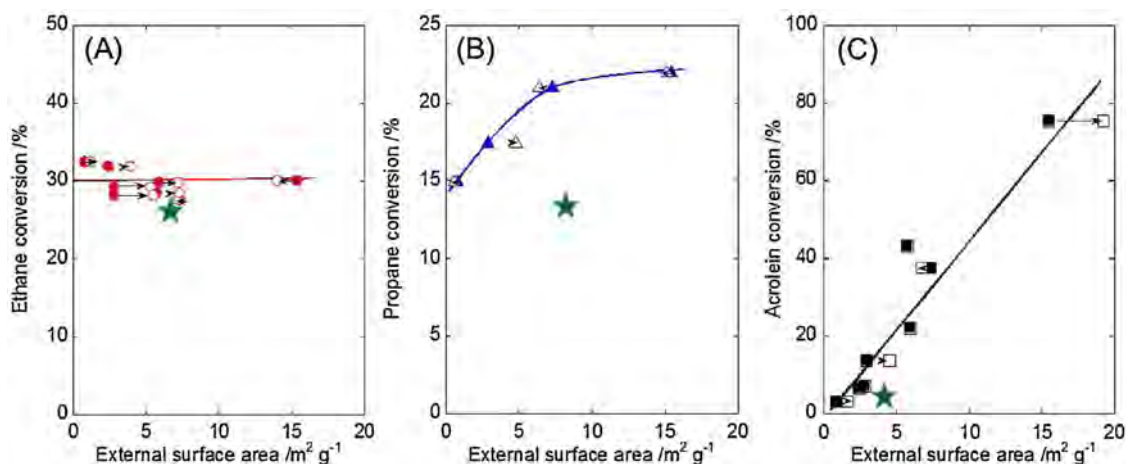


Fig. 4. Conversion changes as a function of external surface area in the selective oxidation of ethane (A), propane (B), and acrolein (C). Substrates conversion of MoVO-SDSO-175-non is represented by a closed star in either figure. External surface area changes by the reactions are represents by closed symbols (before reaction) and open symbols (after reaction).

shown in Table 1. No change in the micropore volume measured by ethane adsorption was observed between MoVO-SDSO-175-non and MoVO-SDSO-175 (MoVO-SDSO-175-non, $22.3 \text{ cm}^3 \text{ g}^{-1}$; MoVO-SDSO-175, $17.7 \text{ cm}^3 \text{ g}^{-1}$). Fig. 3(A), (A') shows the conversion of ethane and the selectivity to ethene and CO_x when MoVO-SDSO-175-non was used. MoVO-SDSO-175-non (open triangle) showed the same ethane conversion with the ground catalyst (closed triangle) until 320°C . The selectivity to ethene was slightly low and the selectivity to CO_x was slightly high compared with the ground catalyst at all the reaction temperature. This result implies that the contribution of the section surface exposed by the grind treatment for the ethane oxidation was negligible. The slight change of the selectivity to ethene and CO_x was due to the deep oxidation of ethane in the micropore channel, because the long diffusion distance of the heptagonal channel derived from the long length of the rod-shaped crystals. MoVO-SDSO-175-non is considered to provide an active sites in the heptagonal channel more chances for attacking ethane, which leads the over oxidation. As a consequence, it can be concluded that the micropore provides catalysis field for the selective oxidation of ethane.

The orthorhombic Mo_3VO_x oxide catalyst has two micropores, hexagonal channel and heptagonal channel in the a - b plane. The size of the hexagonal channel in the a - b plane is calculated to be 0.25 nm and the size of the heptagonal channel is calculated to be 0.40 nm by using the structural model. The size of ethane is 0.40 nm , so that the hexagonal channel is too small to accept ethane. On the other hand, the heptagonal channel can adsorb ethane, which was revealed by the ethane adsorption analysis and the Monte Carlo simulation [12]. Therefore, the hexagonal channel can contribute no catalytic activity for the selective oxidation of ethane, supporting that the heptagonal channel responsible for the catalysis for the reaction.

The propane conversion and the selectivity to acrylic acid and CO_x are shown in Fig. 3(B) and (B'). Propane conversion was increased with the reaction temperature. The selectivity to acrylic acid was decreased with the reaction temperature and become almost 0 at 370°C . Instead, the CO_x selectivity increased with the reaction temperature. The selectivity to acrylic acid and CO_x was almost the same for all the catalysts. Different from the selective oxidation of ethane, the catalysts with low external surface area showed lower propane conversion than that of the catalysts with high external surface area at all the reaction temperature. Fig. 4(B) shows the relationship between the external surface area of the catalysts and the propane conversion at 315°C . The conversion of propane was increased from ca. 15% to ca. 22% with increasing the external surface area, indicating an effect of the external surface area on the conversion of propane. On the other hand, the conversion of propane over MoVO-SDSO.60-175 and MoVO-SDSO-175 was almost the same, although the external surface area of MoVO-SDSO.60-175 was almost twice as high as that of MoVO-SDSO-175. In order to understand the details of the catalysis field for the oxidation of propane, propane oxidation by using MoVO-SDSO-175-non was conducted. Fig. 3(B), (B') shows the conversion of propane and the selectivity to acrylic acid and CO_x when MoVO-SDSO-175-non was used. The conversion of propane gradually increased with the reaction temperature. The selectivity to acrylic acid was decreased with the increase of CO_x selectivity, along with the increase of the reaction temperature. The propane conversion of MoVO-SDSO-175-non was about the half compared with that of MoVO-SDSO-175 in all the reaction temperature. This result is also illustrated in Fig. 4(B). It is interesting to note that the catalysts, MoVO-SDSO-175-non and MoVO-SDSO.15-230, both of which have a very small section surface area but have largely different external surface area, showed almost the same propane conversion as can be seen in Fig. 4(B) (star mark). This fact clearly indicates that the catalytic activity is independent of

the apparent external surface area and rather suggests that the propane oxidation takes place in the heptagonal channel like as ethane.

The acrolein conversion and the selectivity to acrylic acid and CO_x are shown in Fig. 3(C) and (C'). The acrolein conversion was increased with the increase of the reaction temperature. The selectivity to acrylic acid was in the range of 96–98% and was unchanged by the increase of the reaction temperature. CO_x selectivity was also unchanged irrespective of the reaction temperature. The catalysts with high external surface area showed higher acrolein conversion than that of the catalysts with low external surface area in all the reaction temperature. Fig. 4(C) shows the relationship between the conversion of acrolein at 220°C and the external surface area of the catalyst. With increasing the external surface area, the acrolein conversion increased proportionally. The acrolein conversion over the catalysts clearly depended on the external surface area, implying that acrolein is converted on the external surface of the catalyst. Then, in order to clarify the contribution of the side surface and of the section surface of the rod-shaped crystals, a catalyst without the grind treatment was tested for the selective oxidation of acrolein. Fig. 3(C) shows the acrolein conversion and the selectivity to acrylic acid and CO_x when MoVO-SDSO-175-non was used. The acrolein conversion increased linearly with the increase of the reaction temperature. The selectivity of the unground catalyst was almost the same with the ground catalyst in all the reaction temperature. However, the acrolein conversion was far less compared with the ground catalyst, in spite of almost the same external surface area. This fact clearly indicates that the section surface exposed by the grind treatment is far more active for the selective oxidation of acrolein than the side surface of the rod-shaped crystals. As a consequence, acrolein is oxidized to acrylic acid mainly on the section surface of the rod-shaped crystals.

Ethane with 0.40 nm in diameter evidently enters the heptagonal channel. This situation satisfactory explains the independence of the conversion of ethane upon the external surface area shown in Fig. 4(A). Therefore we can convincingly conclude that the conversion of ethane to ethene can proceed smoothly in the heptagonal channel. The relationship for propane oxidation in Fig. 4(B) can be similarly explained, since the molecular size of propane is similar to that of the diameter of the heptagonal channel (0.40 nm in diameter). However, due to more bulky size of propane than that of ethane for entering into the heptagonal channel, propane should have much difficulty to go through the heptagonal channel. This kind of diffusion effect may become more prominent when the diffusion length is long in the case of the long rod-shaped catalysts with low external surface area. This might be the reason for the observation that the propane conversion over catalysts with low external surface area became clearly lowered while the conversion became independent of the external surface area when the catalyst is short rod-shaped (Fig. 4(B)). Obviously we need further experiments for confirming the above discussion.

In the case of the acrolein selective oxidation, it is pronounced that the section surface of the rod-shaped crystals was exclusively active. Since only the catalysts possessing the heptagonal channel are active for the acrolein oxidation [8], the heptagonal structural part is responsible for the reaction. Therefore we suggest that the mouth of heptagonal channel on the surface can trap the aldehyde group of acrolein effectively and convert to the acid by active oxygen species around the heptagonal channel, which leads to the extremely high catalytic activity for the reaction. The heptagonal channel existing in the section surface has strained bond derived from the low symmetric shape. This situation may produce an active oxygen species and is expected to contribute the catalytic reaction.

4. Conclusion

Selective oxidations of ethane, propane, and acrolein were conducted by using the orthorhombic Mo_3VO_x oxide catalysts with different external surface area. The molecular size of ethane is small enough to enter the heptagonal channel, so that ethane can enter the heptagonal channel and convert to ethene. Propane is considered to convert in the heptagonal channel. However, because of the bulky molecular size of propane for entering into the heptagonal channel, the heptagonal channel with short length may prefer to provide the catalysis field to propane. Acrolein is effectively converted to acrylic acid on the section surface of the catalyst. Strained bonds derived from the low symmetric shape of the heptagonal channel in the section surface of the rod-shaped crystals are considered to produce an active oxygen species and to activate acrolein effectively, resulting in the extremely high catalytic activity for the reaction. Although the heptagonal channel is obviously responsible for the catalysis of ethane, propane, and acrolein, the catalysis field of the channel is found to be different in a reflection of the molecular size and the functional group of the reactants. The presented work successfully demonstrates the catalysis field for the selective oxidation of ethane, propane, and acrolein and will provide a way to design a new evolutionary oxidation catalyst.

References

- [1] W. Ueda, *Jpn. Petrol. Inst.* 56 (2013) 122–132.
- [2] T. Konya, T. Katou, T. Murayama, S. Ishikawa, M. Sadakane, D. Buttrey, W. Ueda, *Catal. Sci. Technol.* 3 (2013) 380–387.
- [3] S. Ishikawa, T. Murayama, S. Ohmura, M. Sadakane, W. Ueda, *Chem. Mater.* 25 (2013) 2211–2219.
- [4] W. Ueda, D. Vitry, T. Katou, *Catal. Today* 96 (2004) 235–240.
- [5] W. Ueda, D. Vitry, T. Katou, *Catal. Today* 99 (2005) 43–49.
- [6] F. Wang, W. Ueda, *Appl. Catal. A: Gen.* 346 (2008) 155–163.
- [7] F. Wang, W. Ueda, *Catal. Today* 144 (2009) 358–361.
- [8] C. Chen, N. Kosuke, T. Murayama, W. Ueda, *ChemCatChem* 5 (2013) 2869–2873.
- [9] M. Sadakane, K. Endo, K. Kodato, S. Ishikawa, T. Murayama, W. Ueda, *Eur. J. Inorg. Chem.* 10–11 (2013) 1731–1736.
- [10] M. Sadakane, K. Kodato, T. Kuranishi, Y. Nodasaka, K. Sugawara, N. Sakaguchi, T. Nagai, Y. Matsui, W. Ueda, *Angew. Chem. Int. Ed.* 47 (2008) 2493–2496.
- [11] M. Sadakane, S. Ohmura, K. Kodato, T. Fujisawa, K. Kato, K. Shimidzu, T. Murayama, W. Ueda, *Chem. Commun.* 47 (2011) 10814–10821.
- [12] S. Ishikawa, X. Yi, T. Murayama, W. Ueda, *Appl. Catal. A: Gen.* (2013) (in press).
- [13] W. Ueda, K. Oshihara, *Appl. Catal. A: Gen.* 200 (2000) 135–143.
- [14] N.R. Shiju, X. Liang, A.W. Weimer, C. Liang, S. Dai, V.V. Gulians, *J. Am. Chem. Soc.* 130 (2008) 5850–5851.
- [15] J. Tichy, *Appl. Catal. A: Gen.* 157 (1997) 363–385.
- [16] T. Jekewitz, N. Bickhan, S. Endres, A. Drochner, H. Vogel, *Catal. Commun.* 20 (2012) 25–28.
- [17] L. Giebler, P. Kampe, A. Wirth, A.H. Adams, J. Kunert, H. Fuess, H. Vogel, *J. Mol. Catal. A: Chem.* 259 (2006) 309–318.

DOI: 10.1002/cctc.201300991

Reduced Vanadium and Molybdenum Oxides Catalyze the Equivalent Formation of Ethane and Acetaldehyde from Ethanol

Yoichi Nakamura, Toru Murayama, and Wataru Ueda^{*[a]}

Catalytic tests for ethanol conversion were performed on vanadium and molybdenum oxides with different oxidation states. We found for the first time that equivalent amounts of ethane and acetaldehyde were formed catalytically over V_2O_3 and MoO_2 . No influence of the reaction temperature was observed on the selectivity to ethane and acetaldehyde in the range of 533–653 K over V_2O_3 and MoO_2 . The reactions of methanol, 1-propanol, and 2-propanol also produced the corresponding alkanes and aldehydes in a 1:1 ratio. A reaction scheme for the formation of ethane and acetaldehyde from ethanol is proposed in which a hydrogen transfer reaction occurs between two ethanol molecules adsorbed on the adjacent metal cation–oxygen anion pair sites to form ethane, acetaldehyde, and water in one step.

Vanadium and molybdenum oxide catalysts have attracted much attention because of their unique catalytic properties and commercial application in various chemical processes. These catalysts are known to be active as oxidation and acid catalysts in reactions such as the partial oxidation of alkanes^[1] and dehydration of alcohols.^[2] In reports on the reaction of alcohols over vanadium and molybdenum oxide catalysts, the catalytic reaction was performed in the presence of oxygen and aldehydes, and carboxylic acid and CO_2 were produced. However, we found that ethane was formed from ethanol conversion over vanadium and molybdenum oxides under N_2 . The formation of alkanes from the corresponding alcohols is not normally a feature of the dehydration and dehydrogenation of alcohols. There is no report that describes the formation of alkanes from alcohols over reduced vanadium or molybdenum oxides. However, several reports describe the formation of alkanes from the corresponding alcohols, which are summarized in Table 1.

McMonagle and Moffat proposed that the formation of ethane from ethanol over 12 molybdophosphates proceeds through the secondary hydrogenation of ethylene formed by the dehydration of ethanol because the selectivity to ethane increased in the presence of H_2 and the selectivity to acetaldehyde was always higher than that of ethane. In this study, Mo^{6+} in the catalyst was reduced to Mo^{5+} during the reaction.

The selectivities to ethane and acetaldehyde decreased and the selectivity to ethylene increased over the reduced catalyst because of the loss of active sites for the dehydrogenation of ethanol.^[3] Other reports also show the relationship between the selectivities to alkanes and aldehydes and the catalytic oxidation states. Abu-Zied and El-Awad showed that the formation of ethane from ethanol over Cd–Cr–O catalysts proceeded through the hydrogenation of ethylene produced by the dehydration of ethanol. As the selectivity to ethane increased with an increase in the selectivity to acetaldehyde and Cr is known to form hydride species, Cr–H was proposed as the active species in the hydrogenation of alcohols over Cr. In this reaction, Cr was reduced from Cr^{6+} to Cr^{3+} during the catalysis because of the absence of oxygen in the reaction stream. The reduced Cr is highly active for the dehydration reaction.^[4] Mohamed showed that ethane and methane were formed as major products over Fe-ion-exchanged mordenite. In this report, the formation of ethane as a dominant product was explained mainly by the high O-abstracting affinity of the Fe^{3+} ions.^[5] Sumathi et al. showed that the reducibility of the B site of ABO_3 -type perovskite oxides ($A = Ba, B = Pb, Ce, Ti, B' = Bi, Cu, Sb$) played an important role in the catalytic activity and selectivity in the selective oxidation of benzyl alcohol. They showed that the mechanism for the formation of toluene proceeded through the hydrogenation of benzyl alcohol. The possibility that the adsorbed hydrogen species formed from the dehydrogenation of benzyl alcohol take up lattice oxide ions increases as the reducibility of the B sites decreased.^[6]

On the other hand, some reports showed that almost the same yield of alkanes and aldehydes were formed from corresponding alcohols. Ohtani et al. showed that the simultaneous formation of ethane and acetaldehyde occurred by the hydrogenation of hemiacetal via the acetalization of ethanol and acetaldehyde using acidified ethanol over TiO_2 – PtO_2 in a postirradiation dark reaction. The yield of ethane increased with decreasing yields of acetal and H_2 .^[7] Lobo et al. reported the formation of propane and propionaldehyde in the same quantity with H_2 as the main product in the reaction of 1-propanol over Pt-supported catalysts (Pt/Al_2O_3 , Pt/Ce_2O_3 , Pt/TiO_2).^[8] They proposed the mechanism for the formation of propane from 1-propanol to be through the hydrogenation of 1-propanol. They indicated that the hydrogenation of propylene and the shift of OH to other propanol molecules were unlikely because propylene and diols were not observed. Jin et al. showed that butane was formed from 1- and 2-butanol over Fe_2O_3 , Fe_2O_3 – ZrO_2 , and Fe_2O_3 – ZnO . They indicated that the formation of

[a] Y. Nakamura, Prof. Dr. T. Murayama, Prof. Dr. W. Ueda
Catalysis Research Center
Hokkaido University
N-21, W-10, Sapporo (Japan)
Fax: (+81) 117069163
E-mail: ueda@cat.hokudai.ac.jp

Table 1. Formation of alkanes from the corresponding alcohols over various solid catalysts.

Catalyst	Reactant	T [K]	Carrier	Conversion [%]	Selectivity [%]			Other products	Ref.
					Alkane	Alkene	Aldehyde		
(NH ₄) ₃ PMo ₁₂ O ₄₀	C ₂ H ₅ OH	498	He	38.3	32.9	15.3	51.8	–	[3]
Cd-Cr-O	C ₂ H ₅ OH	673	N ₂	58.0	5.5	5.0	73.0	–	[4]
Fe-ion-exchanged mordenite	C ₂ H ₅ OH	673	N ₂	68.0	68.0	–	7.0	CH ₄ , (C ₂ H ₅) ₂ O	[5]
TiO ₂ -PtO	C ₂ H ₅ OH	RT	–	–	2.6	–	3.7	hemiacetal	[7]
Pt-Al	C ₃ H ₇ OH	523	N ₂	–	13.0	–	12.0	H ₂	[8]
Pt-Ti	C ₃ H ₇ OH	523	N ₂	–	12.0	–	10.0	H ₂	[8]
Pt-Ce	C ₃ H ₇ OH	523	N ₂	–	10.0	–	15.0	H ₂	[8]
Fe ₂ O ₃	2-butanol	523	He	8.8	16.8	7.7	76.5	–	[9]
Fe ₂ O ₃ -ZnO	2-butanol	523	He	24.9	2.4	3.2	94.4	–	[9]
Fe ₂ O ₃ -ZrO ₂	2-butanol	523	He	8.5	13.8	11.9	85.3	–	[9]
Au-Pd/TiO ₂	benzyl alcohol	353	He	27.0	45.4	–	54.6	–	[10]
BaPb _{0.6} Bi _{0.4} O ₃	benzyl alcohol	637	N ₂	28.8	23.4	–	76.6	–	[6]
V ₂ O ₃	C ₂ H ₅ OH	573	N ₂	16.5	39.9	<1	41.7	–	this work
MoO ₂	C ₂ H ₅ OH	573	N ₂	42.9	45.6	1.3	47.1	–	this work

butane from butanol proceeded through the nucleophilic substitution (S_N2) of the alcoholic hydroxyl ion by a hydride ion.

In the nucleophilic mechanism, the source of hydride ions may be a hydrogen molecule that is adsorbed heterolytically, which is produced by the dehydrogenation of butanol.^[9] Mee-nakshisundaram et al. showed that nearly equal amounts of toluene and benzaldehyde were formed from benzyl alcohol on Au-Pd nanoparticles under He. They proposed a mechanism for the formation of toluene and benzaldehyde through the disproportionation of benzaldehyde over Pd.^[10]

Rintramee et al. observed the formation of ethane in ethanol temperature-programmed desorption (TPD) profiles of a Pt catalyst at high temperatures and proposed the hydrogenation of ethylene to form ethane from ethanol.^[11] Ochoa et al. observed ethane, acetaldehyde, and water at low temperatures in ethanol TPD profiles over ferrite catalysts, however, they suggested that the reaction mechanism for the formation of ethane is ethanol disproportionation and coupling of the methyl species formed by the dissociation of acetaldehyde.^[12]

Several reaction schemes for the formation of alkanes from the corresponding alcohols have been proposed, however, the reaction mechanism and the relationship between the catalytic states and catalytic activity for the formation of alkanes are still not clear.

In the present study, we found that the reduced states of vanadium and molybdenum oxides were active for the formation of ethane and acetaldehyde in an equivalent amount from ethanol. The objective of the present study is to understand the catalytic properties of vanadium and molybdenum oxides in relation

to their oxidation states for the formation of alkane from the corresponding alcohol. A reaction mechanism that leads to alkanes and aldehydes is proposed, in which a hydrogen transfer reaction occurs between two ethanol molecules adsorbed on adjacent metal cation–oxygen anion pair sites.

The product distribution for the conversion of ethanol on vanadium and molybdenum oxide catalysts with different oxidation states is given in Table 2. Over V₂O₅, ethane was not formed, but a high selectivity to acetaldehyde of 64.7% was observed with the complete transformation of ethanol at 0.1 h time on stream. However, the formation of ethane in 37% selectivity and decreases in the conversion and selectivity to acetaldehyde were also observed at 2 h time on stream. With a further increase of the time on stream, the selectivity to ethane reached 45.7% at 9 h time on stream, and almost the same selectivities to ethane and acetaldehyde with 42.5% selectivity were observed at this time on stream. Other minor products are attributed to C₄ compounds. The formation of C₄

Table 2. Catalytic activity of V₂O_x and MoO_x for the formation of products in ethanol conversion.^[a]

Catalyst	Time on stream [h]	Conversion [%]	Selectivity [%]				
			C ₂ H ₆	C ₂ H ₄	CH ₃ CHO	C ₂ H ₅ O	C ₂ H ₅
V ₂ O ₅	0.1	100.0	<1	10.5	64.7	0	24.8
	2	74.5	37.0	1.1	43.7	0	18.2
	9	73.7	45.7	0.9	42.5	0	10.9
VO ₂	0.1	35.5	7.7	1.2	82.8	0	8.3
	2	31.5	37.7	0.6	53.2	0	8.5
	9	28.0	42.7	0.9	44.4	0	10.0
V ₂ O ₃	0.1	22.8	41.8	<1	46.1	0	12.1
	2	15.3	41.4	<1	43.3	0	15.3
	9	16.5	39.9	<1	41.7	0	18.3
MoO ₃	0.1	98.4	<1	28.2	65.5	6.0	0.3
	2	59.6	19.1	28.1	36.4	4.4	12.0
	9	47.7	24.8	35.9	28.2	5.9	5.2
MoO ₂	0.1	46.9	48.4	1.1	48.5	<1	2.0
	2	42.0	47.0	1.1	47.5	<1	4.4
	9	42.9	45.6	1.3	47.1	<1	6.0

[a] Reaction conditions: 573 K, catalyst 0.15 g, SiO₂ 2.5 g, N₂ flow rate 21 mLmin⁻¹, ethanol flow rate 0.24 mLmin⁻¹.

compounds, such as ethyl acetate, *n*-butanol, crotonaldehyde, and 2-butanone, as condensation products of acetaldehyde was observed. A decrease of the selectivity to acetaldehyde with increased time on stream over V_2O_5 was caused by the reduction of vanadium oxide. In the initial time on stream, the preferential formation of acetaldehyde occurred from the dehydrogenation of ethanol with the concomitant removal of lattice oxygen atoms of V_2O_5 because the catalytic reaction was performed under N_2 , which suggests that V_2O_5 was reduced during the catalytic reaction. This result indicates that the state of V_2O_5 after ethanol conversion at 9 h time on stream was different from that in the initial reaction period at 0.1 h time on stream.

The decreased conversion was caused mainly by the reduction of V_2O_5 as we observed an increased surface area of the catalyst after the reaction. This result indicates that reduced vanadium oxide was active for the formation of ethane from ethanol. VO_2 showed the formation of a small amount of ethane with 7.7% selectivity at 0.1 h time on stream, which suggests that the degree of reduction was not enough to form the equivalent amount of ethane and acetaldehyde in the initial reaction period. The selectivity to ethane was still lower than that of acetaldehyde until 2 h time on stream, then almost the same selectivity to ethane (42.7%) and acetaldehyde (44.4%) was observed at 9 h time on stream.

These results show that V_2O_5 and VO_2 were reduced during the reaction to the same surface state of V_2O_3 , which is active to form ethane and acetaldehyde in equal amounts. A similar tendency of the change in the selectivities to ethane and acetaldehyde was observed over molybdenum oxides.

MoO_3 showed a very high selectivity to acetaldehyde with no formation of ethane at a time on stream of 0.1 h. Moreover, ethylene with 28.2% selectivity and diethyl ether with 6.0% selectivity were formed by the dehydration of ethanol over the acid sites of MoO_3 .^[13] However, the selectivity to ethane increased and the selectivity to acetaldehyde decreased with increased time on stream. At a time on stream of 9 h, almost the same selectivities to ethane (24.8%) and acetaldehyde (28.2%) were observed. This result indicates that MoO_3 was also reduced during the catalytic reaction. In addition, the selectivity to ethylene increased to 35.9% at 9 h time on stream. Ohno et al. reported that a H_xMoO_3 phase is formed by the partial reduction of MoO_3 with H_2 , which is active for the dehydration of 2-propanol.^[14] Therefore, in this case, a H_xMoO_3 phase seems to be formed on MoO_x during ethanol conversion, which may act as protonic acid sites to promote the dehydration of ethanol.

However, MoO_2 showed the same selectivity to ethane (48.4%) and acetaldehyde (48.5%) from the beginning of the reaction.

From these results, we can conclude that V^3 and Mo^{4+} species are active for the equivalent formation of ethane and acetaldehyde from ethanol.

The effects of the reaction temperature on the selectivities to ethane and acetaldehyde were examined over V_2O_3 and MoO_2 in the temperature range from 533–653 K (Figure 1). The reaction temperature had no effect on the selectivities to

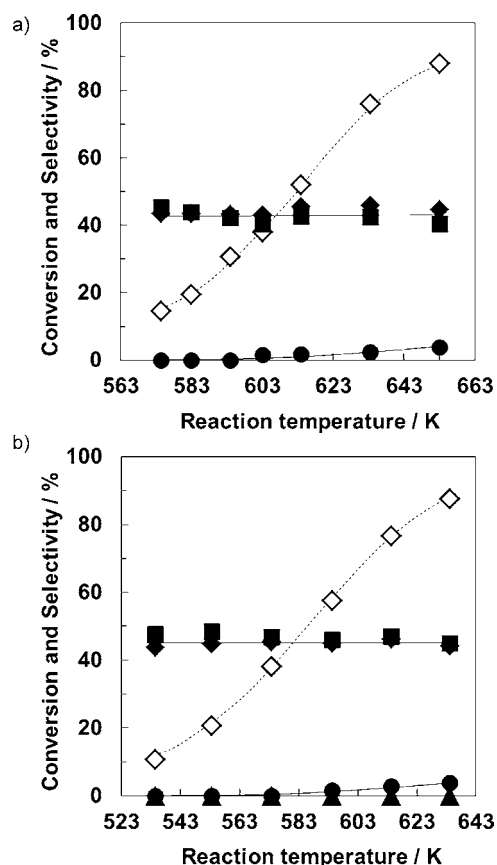


Figure 1. Reaction of ethanol from 533–653 K over a) V_2O_3 and b) MoO_2 . Conditions: catalyst 0.15 g, SiO_2 2.5 g, time on stream 3 h, N_2 flow rate 21 mL min^{-1} , ethanol flow rate 0.24 mL min^{-1} . Conversion of ethanol (\diamond) and selectivity to ethane (\blacktriangle), ethylene (\bullet), and acetaldehyde (\blacksquare).

ethane and acetaldehyde over V_2O_3 (Figure 1(a)) and MoO_2 (Figure 1(b)). For both V_2O_3 and MoO_2 , the selectivities to ethane and acetaldehyde were almost the same and were unchanged throughout the reaction temperature range or the conversion range. If ethane and acetaldehyde were formed in successive steps, the selectivities to ethane and acetaldehyde would vary with the reaction temperature or conversion unless the activation energies for the formation of ethane and acetaldehyde were the same for these steps. The results suggest that ethane and acetaldehyde are formed in a single step from a common intermediate.

To study the reaction scheme for alcohol conversion on reduced vanadium and molybdenum oxides, a catalytic reaction was performed by using methanol, 1-propanol, and 2-propanol over reduced vanadium oxide (Table 3). The formation of methane and formaldehyde with 42.9 and 43.2% selectivity, respectively, was observed if methanol was used as the substrate. In the case of 1-propanol, we observed the formation of propane and propionaldehyde with 43.1 and 36.0% selectivity, respectively. The formation of propane with 22.6% selectivity and acetone with 19.4% selectivity was observed if 2-propanol was used, and a higher selectivity to propylene of 55.9% was obtained. Almost the same selectivities to alkanes and their corresponding aldehydes were observed in all kinds of alcohols. This result indicates that the equivalent formation of alkanes

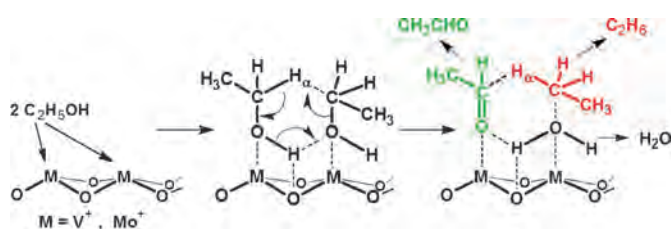
Table 3. Reaction of various alcohols on reduced vanadium oxide as catalyst.^[a]

Reactant	Conversion ^[b] [%]	Selectivity to products ^[c] [%]									
		MA	EE	EA	PE	PA	FA	ACA	ACT	PPA	Other
CH ₃ OH	40.4	42.9	0	0	0	0	43.2	0	0	0	13.9
C ₂ H ₅ OH	73.7	0	0.9	45.7	0	0	0	42.5	0	0	10.9
n-C ₃ H ₇ OH	47.8	0	0	0	0	43.1	0	0	0	36.0	20.9
CH ₃ CH(OH)CH ₂	100.0	0	0	0	55.9	22.6	0	0	19.4	0	2.2

[a] Reaction conditions: V₂O₅ 0.15 g, SiO₂ 2.5 g, 573 K, 4 h, flow rates: N₂ 21 mL min⁻¹, ethanol 0.24 mL min⁻¹, methanol 0.74 mL min⁻¹, 1-propanol 0.41 mL min⁻¹, 2-propanol 0.80 mL min⁻¹. [b] Conversion of reactants. [c] MA: methane, EE: ethylene, EA: ethane, PE: propylene, PA: propane, FA: formaldehyde, ACA: acetaldehyde, ACT: acetone, PPA: propionaldehyde.

and aldehydes occurs with corresponding alcohols, regardless of the alcohol. Moreover, the result of the formation of methane from methanol suggests that the reaction mechanism for the equivalent formation of alkanes and aldehydes is not the hydrogenation of an olefin.

Based on these results, we propose a plausible reaction scheme for the co-formation of ethane and acetaldehyde from ethanol on V₂O₃ and MoO₂ (Scheme 1). The simultaneous formation of ethane and acetaldehyde proceeds through a hydrogen transfer reaction between two ethanol molecules adsorbed on adjacent metal cation–oxygen anion pairs on reduced vanadium and molybdenum oxides.

**Scheme 1.** Reaction scheme for the co-formation of ethane and acetaldehyde from ethanol over reduced vanadium and molybdenum oxides.

Cation sites of certain catalysts, such as ZrO₂, are known to act as Lewis acid sites, which are active for the hydrogen transfer reaction between alcohols and aldehydes through a six-membered transition state.^[15] Therefore, in the present case, two ethanol molecules are adsorbed on a pair of cation–oxygen anion sites on reduced vanadium and molybdenum oxides. The H atoms on the hydroxyl groups may be stabilized by H bonding with lattice O atoms. As a result, the six-membered transition state is formed. The methylene H_α transfers to the positively charged C atom of methylene group of another ethanol adsorbed on the adjacent site as a hydride ion. At the same time, the H atom of the hydroxyl group transfers to the hydroxyl group of the ethanol adsorbed at the adjacent site accompanied by the cleavage of the C–O bond of the ethanol molecule. As a result, ethane and acetaldehyde are formed simultaneously.

Experimental Section

V₂O₅ was prepared by the calcination of NH₄VO₃ (99% Wako Purer Chemical Industries) at 773 K for 2 h in air. VO₂ was purchased from Wako Purer Chemical Industries. V₂O₃ was prepared by the reduction of V₂O₅ under a H₂ stream (30 mL min⁻¹) at 773 K for 2 h. MoO₃ was prepared by the calcination of (NH₄)₆Mo₇O₂₄ (99% Wako Purer Chemical Industries) at 773 K in air. MoO₂ was prepared by the reduction of MoO₃ under a H₂ stream (30 mL min⁻¹) at 773 K for 2 h and then treated again under a H₂/Ar stream (5% H₂, 30 mL min⁻¹) at 773 K for 2 h.

Catalytic reactions were performed in a continuous-flow fixed reactor. A mixture of catalyst (0.15 g) and SiO₂ (2.5 g) as diluent was placed in the reactor and heated to 573 K. Then, the catalytic reaction was started by the introduction of EtOH (1.8%) with N₂ carrier gas into the reactor. N₂ gas was used both as the carrier gas and internal standard.

Catalytic activity tests with other alcohols as reactants were conducted by the same procedure with different flow rates of the reactants.

The products were analyzed by GC. Two gas chromatographs were used: Shimadzu GC-8A and GC-380. The GC-8A chromatograph was equipped with a thermal conductivity detector and the column was packed with Porapack-QS. The GC-380 chromatograph was equipped with a thermal conductivity detector and flame-ionization detector and two columns packed with Unicarbon and molecular sieves (5A).

Keywords: alcohols · aldehydes · alkanes · molybdenum · vanadium

- [1] S. Song, S. Jiang, R. Rao, H. Yang, A. Zhang, *Appl. Catal. A* **2011**, *401*, 215–219.
- [2] A. Benadda, A. Katrib, A. Barama, *Appl. Catal. A* **2003**, *251*, 93–105.
- [3] J. B. McMonagle, J. B. Moffat, *J. Catal.* **1985**, *91*, 132–141.
- [4] B. M. Abu-Zied, A. M. El-Awad, *J. Mol. Catal. A* **2001**, *176*, 227–246.
- [5] M. M. Mohamed, *J. Mol. Catal. A* **2003**, *200*, 301–3137.
- [6] R. Sumathi, K. Johnson, B. Viswanathan, T. K. Varadarajan, *Appl. Catal. A* **1998**, *172*, 15–22.
- [7] B. Ohtani, M. KAKimoto, S. Nishimoto, T. Kagiya, *J. Photochem. Photobiol. A* **1993**, *70*, 265–272.
- [8] R. Lobo, C. L. Marshall, P. J. Dierich, F. H. Ribeiro, C. Akatay, E. A. Stach, A. Mane, Y. Lei, J. Elam, J. T. Miller, *ACS Catal.* **2012**, *2*, 2316–2326.
- [9] T. Jin, H. Hattori, K. Tanabe, *Chem. Lett.* **1981**, *1*, 533–1534.
- [10] S. Meenakshisundaram, E. Nowicka, G. J. Hutchings, *Faraday Discuss.* **2010**, *145*, 341–356.
- [11] K. Rintramee, K. Föttinger, G. Rupprechter, J. Wittayakun, *Appl. Catal. B* **2012**, *115*, 225–235.
- [12] J. V. Ochoa, C. Trevisanut, J. M. M. Millet, G. Busca, F. Cavani, *J. Phys. Chem. C* **2013**, *117*, 23908–23918.
- [13] F. Bertinchamps, E. M. Gaigneaux, *Catal. Today* **2004**, *91*, 105–110.
- [14] T. Ohno, Z. Sakai, H. Sakagami, N. Takahashi, T. Matsuda, *Appl. Catal. A* **2010**, *389*, 52–59.
- [15] Y. Zhu, G. Chuah, S. Jaenicke, *J. Catal.* **2004**, *227*, 1–10.

Received: November 20, 2013

Published online on February 12, 2014

Tetrahedral Connection of ϵ -Keggin-type Polyoxometalates To Form an All-Inorganic Octahedral Molecular Sieve with an Intrinsic 3D Pore System

Zhenxin Zhang,[†] Masahiro Sadakane,^{*,‡,§} Toru Murayama,[†] Shoko Izumi,[†] Nobuhiro Yasuda,^{||} Norihito Sakaguchi,[⊥] and Wataru Ueda^{*,†}

[†]Catalysis Research Center, Hokkaido University, N-21, W-10, Kita-ku, Sapporo 001-0021, Japan

[‡]Department of Applied Chemistry, Graduate School of Engineering, Hiroshima University, 1-4-1 Kagamiyama, Higashi Hiroshima 739-8527, Japan

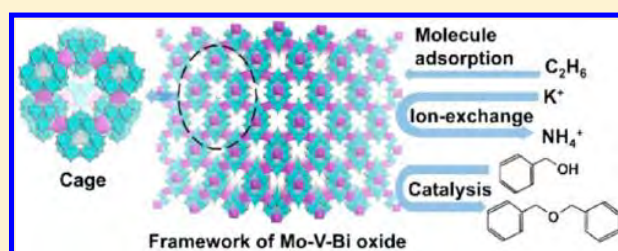
[§]JST, PRESTO, 4-1-8 Honcho, Kawaguchi, Saitama 332-0012, Japan

^{||}Japan Synchrotron Radiation Research Institute/SPring-8, 1-1-1 Kouto, Sayocho, Sayogun, Hyogo 679-5198, Japan

[⊥]High Voltage Electron Microscope Laboratory, Center for Advanced Research of Energy Conversion Materials, Hokkaido University, Sapporo 060-8626, Japan

S Supporting Information

ABSTRACT: A new type of polyoxometalate-based porous material was successfully synthesized. The new material is the first fully inorganic Keggin-type polyoxometalate-based microporous material with intrinsically ordered open micropores and is the third member of the small family of octahedral molecular sieves (OMSs). Twelve MoO_6 or VO_6 octahedra surround a central VO_4 tetrahedron to form ϵ -Keggin polyoxometalate building blocks ($\epsilon\text{-VMo}_{9,4}\text{V}_{2,6}\text{O}_{40}$) that are linked by Bi^{III} ions to form crystalline Mo–V–Bi oxide with a diamondoid topology. The presence of a tetrahedral shape of the ϵ -Keggin polyoxometalate building block results in arrangement of microporosity in a tetrahedral fashion which is new in OMSs. Owing to its microporosity, this Mo–V–Bi oxide shows zeolitic-like properties such as ion-exchange and molecule adsorption.



INTRODUCTION

Polyoxometalates (POMs) are anionic metal oxide clusters of early transition metals such as molybdenum, vanadium, and tungsten. These materials have been widely applied to various fields such as catalysis, photocatalysis, materials science, magnetism, biology, and medicine.^{1–6}

Crystalline solids based on POMs with porosity are of great interest, because properties of POMs such as redox and acidic properties can be combined with pore-based properties such as size selective sorption of molecules and ions. A classical example of porous POM materials was microporous and/or mesoporous cesium or ammonium salts of α -Keggin-type POMs.^{4,7–10} The porosity of the materials was derived from aggregation of nanometer-size crystallites of POMs, and the pores were present between the crystallites. Control of the pores was an important factor for enhancing catalytic activity of these materials.

Recently, new approaches to form porous POMs have attracted much attention. Mizuno's group successfully developed a method to use large cation molecules (macro-cations) to synthesize porous POMs. The large cation molecules, which were composed of three chromium cations and six organic carboxylate such as $[\text{Cr}_3\text{O}\{\text{RCO}_2\}_6\text{L}_3]^+$ ($\text{L} =$

ligand), and POMs formed crystalline materials with intrinsic micropores in their crystal structure.^{11–16} Pore properties were tunable by selection of organic moiety, metals, and/or POMs, and selective adsorption and catalytic reaction in the pores have been achieved.

Another new approach is assembly of POMs to form microporous complex metal oxides.^{17–19} We have succeeded in synthesizing orthorhombic and trigonal Mo–V oxides by assembly of pentagonal $[(\text{Mo})\text{Mo}_5\text{O}_{21}]^{6-}$ polyoxomolybdate units of giant POMs, $\{\text{Mo}_{132}\}^{20}$ or $\{\text{Mo}_{72}\text{V}_{30}\}^{21}$ with other MoO_6 and VO_6 octahedra. The microporosity of the materials resulted from 7-member-ring channels of octahedra. Thus formed Mo–V oxides were redox active and showed outstanding catalytic activity for selective oxidations of light alkanes,^{22–24} acrolein,²⁵ and alcohols.^{26,27} Furthermore, the microporous properties were reversibly tunable by redox treatment.²⁸ Recently, the orthorhombic Mo–V oxide was applied as high capacity electrode materials for rechargeable lithium batteries.²⁹

Received: September 8, 2013

Published: December 30, 2013

There have been a few reports on inorganic POM-based frameworks.^{30–32} Linking of POM units with metal ions formed the frameworks with internal spaces. However, some organic molecules and/or ions occupied the spaces and were difficult to remove, and the pore of these materials could not be opened.

Another example of POM-based frameworks was achieved by using POMs as building blocks for construction of metal organic frameworks (so-called POMOFs).^{4,33–36} In POMOF materials, the ϵ -isomer of Keggin-type POMs is an ideal building block because ϵ -Keggin POMs have a truncated tetrahedral shape (T_d) with four hexagonal faces that can coordinate to metal ions (capping metal ions), such as Ni, Cu, Co, Bi, and La, by three oxygen atoms on one of the hexagonal faces (Figure 1).^{36–40} The capping metal ions can be

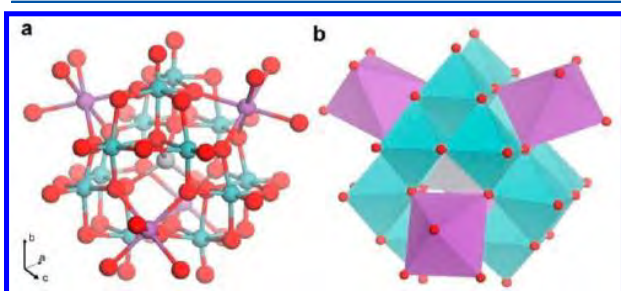


Figure 1. Representations of ϵ -VMo_{9.4}V_{2.6}O₄₀ Keggin core with capping Bi^{III} ions: (a) ball-and-stick representation and (b) polyhedron representation. Central V: gray. Bi: purple. Mo or V: blue. O: red.

coordinated by multidentate organic ligands that bridge the ϵ -Keggin POMs to form POMOFs.³⁴ However, the organic linkers result in materials with low oxidative and thermal stabilities, and the materials therefore cannot survive under harsh conditions.³⁴ Thus, no porosity was found in POMOFs due to molecules occupying the pores that cannot be removed without framework collapse.³⁴ A more inventive way would be to use metal ions to bridge ϵ -Keggin POMs without any organic linkers. So far, no example has been reported following this strategy.

Here, we report the first all-inorganic microporous material based on ϵ -Keggin-type POM (ϵ -VMo_{9.4}V_{2.6}O₄₀, designated as Mo–V–Bi oxide), in which intrinsic micropores can be opened. These POM units are connected by Bi^{III} ions to form a three-dimensional (3D) network. Mo–V–Bi oxide has a 3D pore system like FAU zeolite (Faujasite)⁴¹ and shows zeolitic-like properties such as selective molecule adsorption, ion-exchange, and catalysis.

Moreover, Mo–V–Bi oxide contained mostly octahedral coordinating metals and can be called “octahedral molecular sieves (OMSs)”. Two kinds of OMSs have been reported, the family of microporous Todorokite-type Mn and Fe oxides^{42,43} and Mo–V mixed oxides,^{19,28} and both of these have one-dimensional channels as with MTW-type (ZSM-12) zeolite.⁴⁴ Mo–V–Bi oxide is the third member of OMSs, and the 3D pore system is new in OMS materials.

EXPERIMENTAL SECTION

Material Preparation. (NH₄)₆Mo₇O₂₄·4H₂O (8.828 g, 50 mmol based on Mo) was dissolved in 110 mL of water. VOSO₄·5H₂O (3.219 g, 12.5 mmol) was dissolved in 110 mL of water. After the solids had been dissolved, the solution of VOSO₄·5H₂O was poured into the solution of (NH₄)₆Mo₇O₂₄·4H₂O. After the mixture was stirred at room temperature for 3 min, Bi(OH)₃ (0.438 g, 1.67 mmol) was

added. Then, the mixture was stirred for 7 min followed by N₂ bubbling for 10 min. The mixture was introduced into a 300-mL Teflon liner of a stainless-steel autoclave with the help of 20 mL of water. A Teflon sheet (4 m × 0.1 m × 0.1 mm) was inserted into the liner. The autoclave was placed in an oven heated at 448 K for 48 h. After the autoclave had been cooled down, the black solid on the bottom of the liner was transferred into centrifuge tubes with the help of water (200 mL) and separated by centrifugation (2000 rpm, 3 min). The collected solids were dispersed in water (200 mL) and separated by centrifugation (2000 rpm, 3 min). This washing process was repeated 6 times. The obtained solid was dried at 353 K overnight, and 0.45 g of Mo–V–Bi oxide (yield: 3.3% based on Mo) was obtained. FT-IR (KBr pellets, ν/cm^{-1}): 1620, 1402, 991, 955, 856, 813, 718, 698, 642, and 546 cm^{-1} . Anal. Calcd for Bi₂Mo_{9.4}V_{3.6}N_{2.8}O_{47.2}H_{26.5}: Bi, 17.98; Mo, 38.80; V, 7.89; N, 1.68; H, 1.15. Found: Bi, 18.45; Mo, 38.41; V, 7.51; N, 1.66; H, 0.97.

Ion-Exchange. As-synthesized Mo–V–Bi oxide (0.3 g) was dispersed in 15 mL of water that contained KCl (0.0455 g), LiCl (0.0259 g), NaCl (0.0367 g), RbCl (0.074 g), or CsCl (0.103 g). The mixture was stirred at 353 K for 6 h. The resulting solids were collected by filtration, washed with water (3 × 10 mL), and dried at 353 K overnight. For ion-exchange with protons, 0.5 mL of HCl (36%) was dissolved in 14.5 mL of water, and 0.3 g of Mo–V–Bi oxide was added to the solution. The mixture was stirred for 6 h at 353 K. The solid was recovered by filtration, washed with water (3 × 10 mL), and dried at 353 K overnight. The ion-exchanged materials were designated as M–Mo–V–Bi oxide (M = H, Li, Na, K, Rb, or Cs).

Elemental Analysis. H–Mo–V–Bi oxide ((NH₄)_{2.1}H_{0.7}H_{0.9}[ϵ -VMo_{9.4}V_{2.6}O₄₀Bi₂]:7.2H₂O), Calcd for Bi₂Mo_{9.4}V_{3.6}N_{2.1}O_{47.2}H_{24.4}: Bi, 18.08; Mo, 39.00; V, 7.93; N, 1.27; H, 1.06. Found: Bi, 18.13; Mo, 39.11; V, 7.54; N, 1.29; H, 0.98.

Li–Mo–V–Bi oxide ((NH₄)_{2.6}Li_{0.2}H_{0.9}[ϵ -VMo_{9.4}V_{2.6}O₄₀Bi₂]:7.2H₂O), Calcd for Li_{0.2}Bi₂Mo_{9.4}V_{3.6}N_{2.6}O_{47.2}H_{25.7}: Bi, 18.00; Mo, 38.84; V, 7.90; Li, 0.06; N, 1.57; H, 1.11. Found: Bi, 18.55; Mo, 38.41; V, 7.68; Li, 0.05; N, 1.48; H, 0.94.

Na–Mo–V–Bi oxide ((NH₄)_{2.2}Na_{0.6}H_{0.9}[ϵ -VMo_{9.4}V_{2.6}O₄₀Bi₂]:7.2H₂O), Calcd for Na_{0.6}Bi₂Mo_{9.4}V_{3.6}N_{2.0}O_{47.2}H_{24.1}: Bi, 17.96; Mo, 38.75; V, 7.88; Na, 0.59; N, 1.32; H, 1.04. Found: Bi, 18.51; Mo, 38.69; V, 7.44; Na, 0.58; N, 1.05; H, 0.86.

K–Mo–V–Bi oxide ((NH₄)_{0.9}K_{1.9}H_{0.9}[ϵ -VMo_{9.4}V_{2.6}O₄₀Bi₂]:6.1H₂O), Calcd for K_{1.9}Bi₂Mo_{9.4}V_{3.6}N_{0.9}O_{46.1}H_{16.5}: Bi, 17.83; Mo, 38.47; V, 7.82; K, 3.17; N, 0.54; H, 0.70. Found: Bi, 18.03; Mo, 38.27; V, 7.42; K, 3.15; N, 0.42; H, 0.67.

Rb–Mo–V–Bi oxide ((NH₄)_{0.7}Rb_{2.1}H_{0.9}[ϵ -VMo_{9.4}V_{2.6}O₄₀Bi₂]:7.2H₂O), Calcd for Rb_{2.1}Bi₂Mo_{9.4}V_{3.6}N_{0.7}O_{47.2}H_{18.1}: Bi, 16.95; Mo, 36.58; V, 7.44; Rb, 7.28; N, 0.40; H, 0.73. Found: Bi, 16.58; Mo, 37.21; V, 7.52; Rb, 7.12; N, 0.20; H, 0.53.

Cs–Mo–V–Bi oxide ((NH₄)_{0.8}Cs_{2.0}H_{0.9}[ϵ -VMo_{9.4}V_{2.6}O₄₀Bi₂]:7.2H₂O), Calcd for Cs₂Bi₂Mo_{9.4}V_{3.6}N_{0.8}O_{47.2}H_{18.5}: Bi, 16.36; Mo, 35.31; V, 7.18; Cs, 10.41; N, 0.44; H, 0.73. Found: Bi, 16.81; Mo, 34.97; V, 6.89; Cs, 10.49; N, 0.21; H, 0.57.

Calcination. The synthesized Mo–V–Bi oxide (1 g) was placed in a glass tube in a furnace, heated at 2 K/min to 623 K under N₂ (50 mL/min), and then maintained for 2 h at 623 K.

Crystal Growth. Low concentration of the precursor, long synthesis time, and seed were applied to obtain a large single crystal for X-ray single crystal analysis. An aqueous solution (110 mL) of (NH₄)₆Mo₇O₂₄·4H₂O (7.062 g, 40 mmol based on Mo) was mixed with 110 mL of an aqueous solution of VOSO₄·5H₂O (2.575 g, 10 mmol). After the mixture was stirred at room temperature for 3 min, Bi(OH)₃ (0.438 g, 1.67 mmol) was added, and synthesized Mo–V–Bi oxide (100 mg) was added as a seed. Then, the mixture was stirred for 7 min followed by N₂ bubbling for 10 min. The mixture was introduced into a 300-mL Teflon liner of a stainless-steel autoclave with the help of 20 mL of water, and a Teflon sheet (4 m × 0.1 m × 0.1 mm) was inserted into the liner. The autoclave had been heated at 448 K for 96 h. After the autoclave was cooled down to room temperature, the black solid on the bottom of the liner was transferred into centrifuge tubes with the help of 200 mL of water and separated by centrifugation (2000 rpm, 3 min). The collected solids were

dispersed in water (200 mL) and separated by centrifugation (2000 rpm, 3 min.). This washing process was repeated six times, and the obtained solid was dried at 353 K overnight. The obtained solid was used as a seed again. After repeating this crystal growth procedure four times, the crystal of Mo–V–Bi oxide was large enough for single crystal analysis.

To obtain a large crystal of K–Mo–V–Bi oxide for single crystal analysis, the large crystal of as-synthesized Mo–V–Bi oxide (50 mg) was dispersed in 2.5 mL of water followed by addition of KCl (7.6 mg). The mixture was heated at 353 K for 6 h. The solid was recovered by centrifugation, washed with water three times, and dried at 353 K overnight.

Characterization. Redox titration: The concentration of KMnO_4 solution was determined by using $\text{H}_2\text{C}_2\text{O}_4 \cdot 2\text{H}_2\text{O}$ as a standard compound. $\text{H}_2\text{C}_2\text{O}_4 \cdot 2\text{H}_2\text{O}$ (0.1157 g) was dissolved in 30 mL of water, followed by acidification with 15 mL of 16% H_2SO_4 . Titration was performed at 343–358 K. The concentration of KMnO_4 was 0.04848 mol/L. Then, Mo–V–Bi oxide (0.2867 g) was dissolved in 40 mL of 50% of H_2SO_4 that was degassed by N_2 bubbling in a 100-mL beaker. A Horiba D-52 pH meter with a metal (ORP) electrode was used to detect the potential of the Mo–V–Bi oxide solution. The solution of Mo–V–Bi oxide was titrated with the standard solution of KMnO_4 at room temperature. Measured potential was plotted against amount of KMnO_4 solution. Molecule (CO_2 , CH_4 , C_2H_6 , and C_3H_8) adsorption was performed on Mo–V–Bi oxide by a BELSORP MAX (BEL Japan Inc.) sorption analyzer at 298 K. The samples were evacuated at 573 K for 2 h before the measurement. Nitrogen isotherms were obtained by a BELSORP MAX (BEL Japan Inc.) sorption analyzer at 77 K. Surface area was calculated by the BET method using an adsorption branch, and pore distribution was estimated by the SF method using an adsorption branch. The samples were evacuated at 573 K for 2 h before the measurement. Powder X-ray diffraction (XRD) patterns were obtained on RINT2200 (Rigaku) with $\text{Cu K}\alpha$ radiation (tube voltage 40 kV, tube current 20 mA). Scanning electron microscopy (SEM) images were obtained with an HD-2000 (HITACHI). Transmission electron microscopy (TEM) images were taken with a 200 kV TEM (JEOL JEM-2010F). Carbon was deposited on the sample prior to TEM observation to reduce charging-up of the sample. Fourier transform infrared spectroscopy (FT-IR) was carried out on a PARAGON 1000 (Perkin-Elmer). Thermal analysis (TG-DTA) was performed on Thermo Plus, TG8120 (Rigaku). Temperature-programmed desorption mass spectrometry (TPD-MS) measurements were carried out from 313 to 893 K at a heating rate of 10 K min^{-1} under helium (flow rate: 50 mL min^{-1}). The Mo–V–Bi oxide sample was set between two layers of quartz wool. A TPD apparatus (BELJAPAN, Inc.) equipped with a quadrupole mass spectrometer (M-100QA; Anelva) was used to detect NH_3 ($m/z = 16$), H_2O ($m/z = 18$), O_2 ($m/z = 32$), and N_2 ($m/z = 28$). X-ray photoelectron spectroscopy (XPS) was performed on a JPS-9010MC (JEOL). The spectrometer energies were calibrated using the C 1s peak at 284.8 eV. Elemental compositions were determined by an inductive coupling plasma (ICP-AES) method (ICPE-9000, Shimadzu). CHN elemental composition was determined at Instrumental Analysis Division, Equipment Management Center, Creative Research Institution, Hokkaido University.

Computer-Based Simulation. All computer-based simulation was performed using Materials Studio v 6.1.0 (Accelrys Software Inc.). Rietveld analysis⁴⁵ of a powder XRD pattern was performed using “Reflex” tool in Materials studio. The lattice parameter and pattern parameters were refined by Pawley refinement based on the structural data obtained by single crystal structure analysis. All peak indexes were listed in Supporting Information (Table S1). Connolly surfaces, solvent surfaces, free space of Mo–V–Bi oxide, and volume of an C_2H_6 molecule were simulated by “Atom Volume & Surfaces” program in Materials Studio. The diameters of the cage and the channel were estimated from the Connolly surfaces of the cage and the channel with Connolly radius of 1 Å, and the shortest values were presented.⁴⁶ The theoretical accessible space of Mo–V–Bi oxide (without ammonium cations and water) was obtained by solvent surface calculation with solvent radius of 1.4 Å.⁴⁶ The volume of an

C_2H_6 molecule was obtained by Connolly surface calculation with Connolly radius of 1 Å.

Single Crystal Analysis. Since the crystals that had been grown were still too small for the diffractometer in the laboratory system, data collection was performed on a high-precision diffractometer installed in the SPring-8 BL40XU beamline.^{47,48} The synchrotron radiation emitted from helical undulator was monochromated by using a Si(111) channel cut monochromator and focused with a Fresnel zone plate. A Rigaku Saturn724 CCD detector was used. The measurement was performed at 100 (2) K. An empirical absorption correction based on Fourier series approximation was applied. The data were corrected for Lorentz and polarization effects. The structure was solved by direct methods and refined by full-matrix least-squares (SHELX-97),⁴⁹ where the unweighted and weighted agreement factors of $R = \sum ||F_o| - |F_c|| / \sum |F_o|$ ($I > 2.00\sigma(I)$) and $wR = [\sum w(F_o^2 - F_c^2)^2 / \sum w(F_o^2)^2]^{1/2}$, respectively, were used. Position of K in the structure of K–Mo–V–Bi oxide was determined from differential Fourier map. Nitrogen atoms of ammonium cations were modeled as oxygen atoms because nitrogen atoms could not be distinguished from oxygen atoms. Oxygen atoms of water in Mo–V–Bi oxide were refined isotropically, and other atoms were refined anisotropically. Total amounts of water and ammonium cations estimated by elemental analysis were slightly larger than those obtained by single crystal structure analysis. This is because of the difference in the crystal sample and bulk sample. The sample for elemental analysis may contain surface waters. Crystallographic data of Mo–V–Bi oxide and K–Mo–V–Bi oxide were listed in Table 1.

Table 1. Crystallographic Data of Mo–V–Bi Oxide and K–Mo–V–Bi Oxide

	Mo–V–Bi oxide	K–Mo–V–Bi oxide
formula	$\text{H}_{14.10}\text{Bi}_2\text{Mo}_9\text{O}_{47.05}\text{V}_{3.6}$	$\text{H}_{10.07}\text{Bi}_2\text{K}_{1.7}\text{Mo}_9\text{O}_{45.03}\text{V}_{3.6}$
M_r	2270.19	2300.21
cryst syst	cubic	cubic
space group	$Fd\bar{3}m$	$Fd\bar{3}m$
a (Å)	19.662(3)	19.6850(6)
V (Å ³)	7600.9(18)	7627.9(4)
T (K)	100(2)	100(2)
Z	8	8
ρ_{calcd} (g cm ⁻³)	3.968	4.006
F_{000}	8273	8369
λ (Å)	0.830 77	0.831 12
μ (mm ⁻¹)	14.593	14.838
measured reflns	3748	10 887
unique reflns	372	430
$R1(I > 2\sigma(I))$	0.0580	0.0344
$wR2(\text{all data})$	0.1552	0.0646
GOF	1.091	0.904

Anisotropic displacement ellipsoids were presented in the Supporting Information Figure S1. Metal–oxygen bond lengths, atom coordinates, and atom occupancies are summarized in Table 2 and Supporting Information Tables S2 and S3, respectively. CIF data are available in

Table 2. Metal–Oxygen Bond Lengths from Single Crystal Analysis of As-Synthesized Mo–V–Bi Oxide^a

	bond length of Mo–V–Bi oxide (Å)	bond length of K–Mo–V–Bi oxide (Å)
V1–O4	1.76(2)	1.719(9)
Bi2–O3	2.355(12)	2.335(6)
M3–O1	1.640(12)	1.674(6)
M3–O2	1.894(5)	1.906(3)
M3–O3	1.964(8)	1.980(4)
M3–O4	2.428(12)	2.454(6)

^aM includes V and Mo.

copy (HRTEM) image of Mo–V–Bi oxide along the 101 direction. The HRTEM revealed a characteristic face-centered cubic lattice image for Mo–V–Bi oxide. Ordering of the rhombic black and white spots in the HRTEM image was exactly the same as the ordering of ϵ -VMo_{9.4}V_{2.6}O₄₀ building blocks and pores. The unit cell lengths and distances of the (111) plane were obtained from the HRTEM image: 19.7 Å and 11.4 Å, respectively.

The oxidation states of the metal elements were studied by X-ray photoelectron spectroscopy (XPS) (Figure 5), which indicated that reduced states of molybdenum (Mo^V) and vanadium (V^{IV}) existed, and the oxidation state of bismuth was 3+. Furthermore, XPS showed that 25% of the molybdenum and 50% of the vanadium were Mo^V and V^{IV}, respectively. The total reduced metal content (molybdenum and vanadium) was

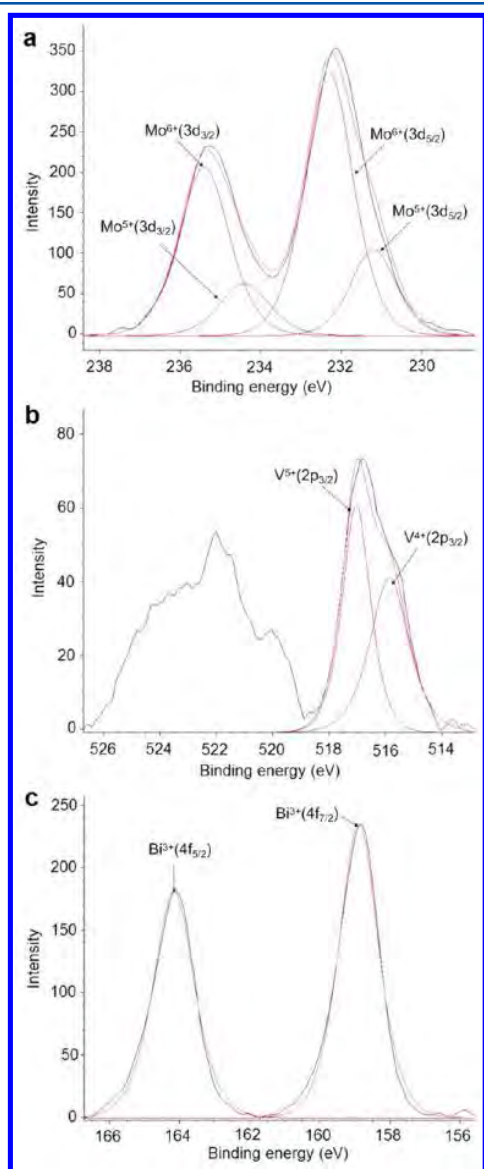


Figure 5. XPS and curve fitting results of Mo–V–Bi oxide of (a) molybdenum, Mo⁶⁺/Mo⁵⁺ = 3, (b) vanadium, V⁵⁺/V⁴⁺ = 1, and (c) bismuth. Blue: experimental data. Purple: sum of every simulated peak. Red: simulated peak.

32%. Manganometric redox titration also confirmed that ca. 28% of the total metal (molybdenum and vanadium) was reduced (Figure 6). Partial reduction was in good agreement with other reported ϵ -Keggin POM molecules. In the case of $[\epsilon\text{-Mo}^{\text{VI}}\text{Mo}^{\text{V}}_{12}\text{O}_{40}(\text{C}_5\text{Me}_5\text{Rh}^{\text{III}})_8]^{2+}$,^{5,2} $[\epsilon\text{-P}^{\text{V}}\text{Mo}^{\text{V}}_8\text{Mo}^{\text{VI}}_4\text{O}_{36}(\text{OH})_4\{\text{La}^{\text{III}}(\text{H}_2\text{O})_4\}_4]^{5+}$,^{3,8} and $[\epsilon\text{-H}_2\text{Mo}^{\text{V}}_{12}\text{O}_{30}(\text{OH})_{10}\{\text{Ni}^{\text{II}}(\text{H}_2\text{O})_3\}_4]^{3+}$, all or part of the surrounding 12 metal ions are reduced. Thus, the detailed formula of the ϵ -Keggin POM framework was $[\epsilon\text{-V}^{\text{V}}_{1.0}\text{Mo}^{\text{V}}_{2.3}\text{Mo}^{\text{VI}}_{7.1}\text{V}^{\text{IV}}_{1.8}\text{V}^{\text{V}}_{0.8}\text{O}_{40}\text{Bi}^{\text{III}}_2]^{3.7-}$.

There were cages and channels in Mo–V–Bi oxide. A cage was composed of 10 ϵ -VMo_{9.4}V_{2.6}O₄₀ building blocks that were connected by Bi^{III} ions (Figure 7a,b). The internal diameter of the cage was ca. 7.7 Å. One cage was tetrahedrally connected with four other adjacent cages by four channels (Figure 7c,d). The diameter of the channel was ca. 3.4 Å. The cages and channels constructed a periodical 3D pore system for Mo–V–Bi oxide in a tetrahedral fashion. In one direction, the tunnel of the micropore was not straight but in a zigzag-like fashion (Figure 7e and Supporting Information Figure S3), which is new in OMSs.

Single crystal structure analysis of Mo–V–Bi oxide revealed that there were two types of sites for water or NH₄⁺ (10 sites per one ϵ -VMo_{9.4}V_{2.6}O₄₀ unit). One was in the cage, and the other was in the channel. Nitrogen (represented NH₄⁺) could not be distinguished from oxygen (represented H₂O) by single crystal analysis (Figure 7e). An FT-IR spectrum (Supporting Information Figure S4a) of Mo–V–Bi oxide showed the presence of water (1620 cm⁻¹) and NH₄⁺ (1402 cm⁻¹) together with bands at 991, 955, 856, 813, 718, 698, 642, and 546 cm⁻¹, which were attributed to the framework. The amount of NH₄⁺ was estimated by elemental analysis to be ca. 2.8 for one ϵ -Keggin POM. Therefore, the detailed formula can be expressed as (NH₄)_{2.8}H_{0.9}[$\epsilon\text{-V}^{\text{V}}_{1.0}\text{Mo}^{\text{V}}_{2.3}\text{Mo}^{\text{VI}}_{7.1}\text{V}^{\text{IV}}_{1.8}\text{V}^{\text{V}}_{0.8}\text{O}_{40}\text{Bi}^{\text{III}}_2$] $\cdot 7.2\text{H}_2\text{O}$.

The NH₄⁺ and H₂O in Mo–V–Bi oxide were removable by heat-treatment. TG-DTA of Mo–V–Bi oxide indicated that there were two weight losses: one was between ca. 310 and 490 K, and the other was between ca. 580 and 710 K (Supporting Information Figure S5). Temperature programmed desorption (TPD) analysis revealed that the first weight loss corresponded to desorption of water and NH₃ and that the second weight loss corresponded to desorption of water, NH₃, and N₂ (Supporting Information Figure S5). N₂ was produced by decomposition of NH₄⁺. Total weight loss from room temperature to 773 K was ca. 7.8%, which was in accord with the total amount of NH₄⁺ and water estimated by elemental analysis. TPD results showed that there were two kinds of NH₄⁺ in the material. One NH₄⁺, which had a strong interaction with the framework, desorbed at 633 K (peak top) and is denoted as NH₄⁺(S). The other, which had a relatively weak interaction with the framework, desorbed at 443 K (peak top) and is denoted as NH₄⁺(W). These results indicated that NH₄⁺ and water co-occupied two different positions in the as-synthesized material: one was in the cage, and the other was in the channel. Total NH₄⁺ amount estimated by TPD was slightly less than NH₄⁺ amount estimated by elemental analysis, because some NH₄⁺ were released as N₂ (Table 3, entry 1).

Microporosity. The NH₄⁺ and water were removed by calcination (2 K/min, 623 K for 2 h, N₂ flow rate of 50 mL/min) without structural collapse (Supporting Information Figure S6a,b). However, further heating (calcination at 673 K) caused the framework of Mo–V–Bi oxide to collapse

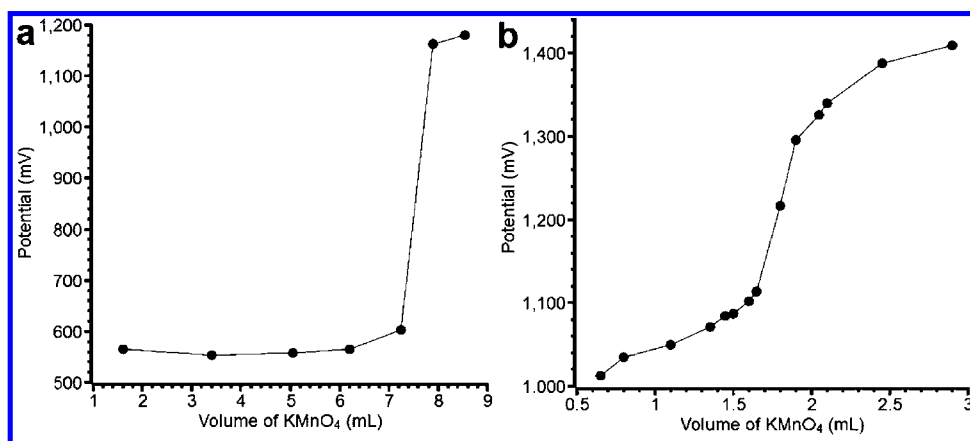


Figure 6. Manganometric redox titration curves of (a) $\text{H}_2\text{C}_2\text{O}_4 \cdot 2\text{H}_2\text{O}$ and (b) Mo-V-Bi oxide.

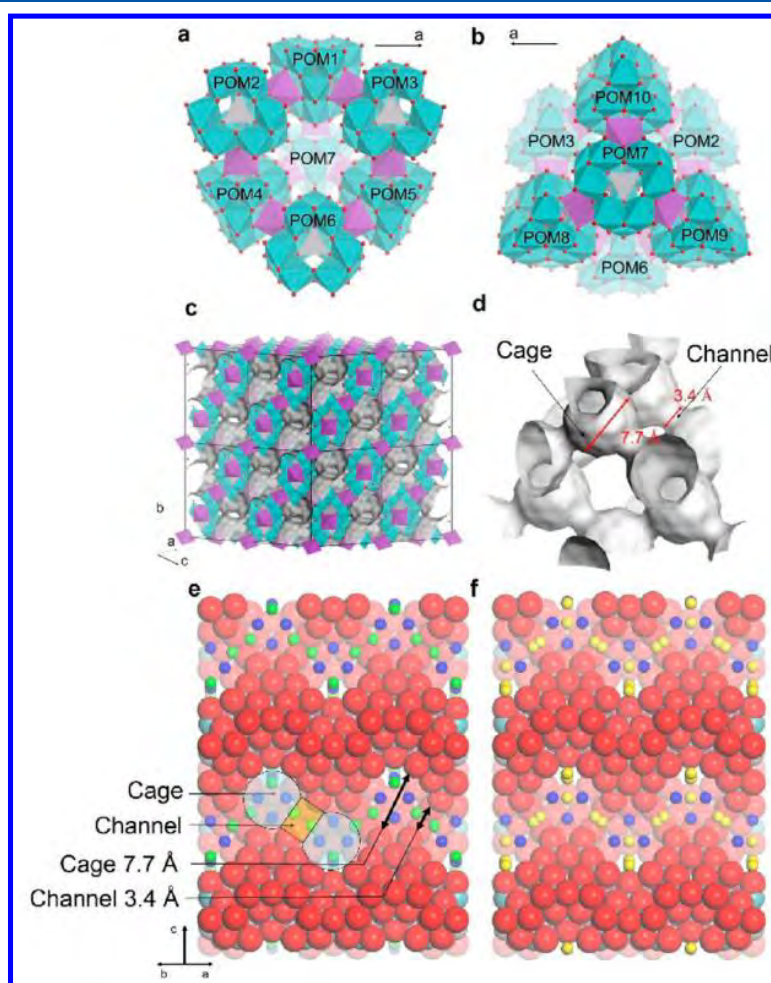


Figure 7. Polyhedral representations of (a) a front image of the cage, (b) the back image of the cage, (c) filling representation of the pore system with framework, with gray curved surface described the morepores, (d) filling representation of the pore system without framework and linkage of a cage by channels, gray curved surface described the morepores (central V, gray; Bi, purple; Mo or V, blue; O, red), (e) CPK (Corey, Pauling, and Koltun) representations of the (110) plane of Mo-V-Bi oxide (N or O in cage, blue; N or O in channel, green), and (f) K-Mo-V-Bi oxide. K: yellow. N or O in cage: blue.

(Supporting Information Figure S6c). The nitrogen adsorption-desorption isotherm of calcined Mo-V-Bi oxide was best described as a type I isotherm, indicating that Mo-V-Bi oxide was a microporous material (Figure 8a,b, black). The

BET surface area and pore volume of this material were calculated to be $60 \text{ m}^2/\text{g}$ and $0.0202 \text{ cm}^3/\text{g}$, respectively, which are similar to those of other reported POM-based porous materials (Supporting Information Table S4). The pore size

Table 3. Changes in Formulas by Ion-Exchange

entry	cation	formula ^a	amount of NH ₄ ⁺ per one ε-VMo _{9.4} V _{2.6} O ₄₀ ^b	
			NH ₄ ⁺ (W)	NH ₄ ⁺ (S)
1	before ion-exchange	(NH ₄) _{2.8} H _{0.9} [ε-VMo _{9.4} V _{2.6} O ₄₀ Bi ₂]	0.7	1.4
2	H ⁺	(NH ₄) _{2.1} H _{0.7} H _{0.9} [ε-VMo _{9.4} V _{2.6} O ₄₀ Bi ₂]	0	1.6
3	Li ⁺	(NH ₄) _{2.6} Li _{0.2} H _{0.9} [ε-VMo _{9.4} V _{2.6} O ₄₀ Bi ₂]	0.3	1.4
4	Na ⁺	(NH ₄) _{2.2} Na _{0.6} H _{0.9} [ε-VMo _{9.4} V _{2.6} O ₄₀ Bi ₂]	0.2	1.4
5	K ⁺	(NH ₄) _{0.9} K _{1.9} H _{0.9} [ε-VMo _{9.4} V _{2.6} O ₄₀ Bi ₂]	0.6	0
6	Rb ⁺	(NH ₄) _{0.7} Rb _{2.1} H _{0.9} [ε-VMo _{9.4} V _{2.6} O ₄₀ Bi ₂]	0.2	0
7	Cs ⁺	(NH ₄) _{0.8} Cs _{2.0} H _{0.9} [ε-VMo _{9.4} V _{2.6} O ₄₀ Bi ₂]	0.3	0

^aEstimated by elemental analysis. ^bEstimated by TPD.

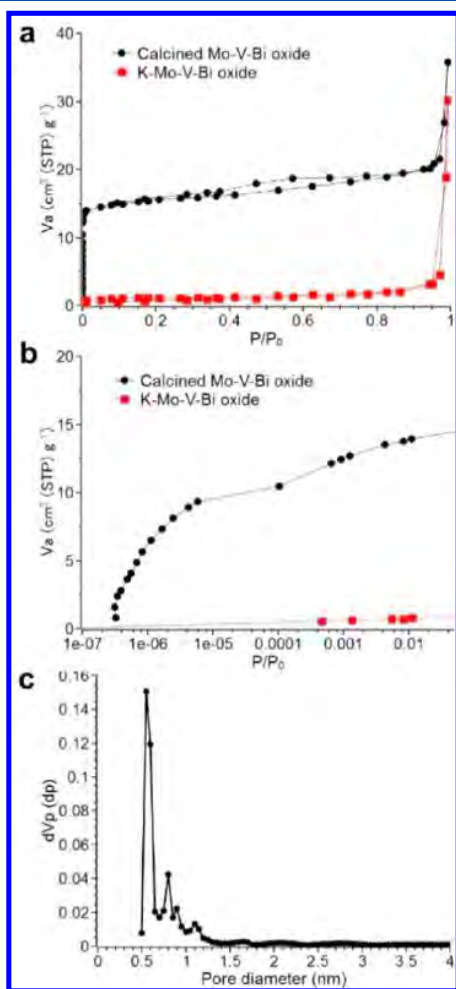


Figure 8. Nitrogen adsorption–desorption isotherms: (a) P/P_0 0–1, (b) low P/P_0 range. Black: calcined Mo–V–Bi oxide. Red: K–Mo–V–Bi oxide. (c) Pore size distribution of calcined Mo–V–Bi oxide using the SF method.

distribution curve (obtained by the SF method) showed that the average diameter of the micropores was 5.5 Å, attributed to the cages and channels in the framework (Figure 8c). The

powder XRD pattern of the material after adsorption measurement showed that the structure of the material did not change, indicating that the framework was stable under the measurement conditions.

Mo–V–Bi oxide selectively adsorbed different molecules depending on the size of the molecule (Figure 9). The size of

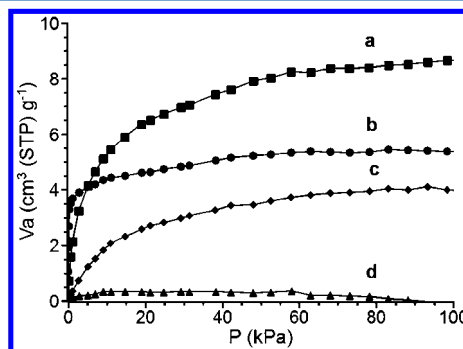


Figure 9. Molecule adsorption isotherms of Mo–V–Bi oxide (a) CO₂, (b) C₂H₆, (c) CH₄, and (d) C₃H₈.

the channel (3.4 Å) of Mo–V–Bi oxide was similar to that of C (3.4 Å) and O (3.04 Å) atoms. Therefore, the straight molecules (CO₂, CH₄, and C₂H₆), in which skeleton atoms (C and O) were in a straight line, were able to pass the channel and adsorbed in the material. C₃H₈ whose carbon skeleton was bent and larger than the channel was not adsorbed. Interestingly, Mo–V–Bi oxide adsorbed C₂H₆ at low pressure from 0.002 to 0.06 kPa (type I isotherm, Figure 9b). The theoretical accessible space of a cage (49.84 Å³) was similar to the volume of a C₂H₆ (47.28 Å³) molecule, so that C₂H₆ could fit in the cage, which may be the reason for the type I adsorption of C₂H₆.

Ion-Exchange. The ammonium cation in the micropores was exchangeable with other cations in aqueous solution, such as H⁺, Li⁺, Na⁺, K⁺, Rb⁺, and Cs⁺ (corresponding materials designated as M–Mo–V–Bi oxide, M = H, Li, Na, K, Rb, and Cs). The powder XRD patterns showed that the basic structure of ion-exchanged Mo–V–Bi oxide did not change (Supporting Information Figure S6d–g,i,j). Table 3 summarizes the formulas and amounts of NH₄⁺(S) and NH₄⁺(W) after ion-exchange estimated by elemental analysis and TPD, respectively. Moreover, TPD profiles ($m/z = 16$ for NH₃) of exchanged Mo–V–Bi oxide indicated that smaller cations such as H⁺, Li⁺, and Na⁺ selectively replaced the weakly bound ammonium cation NH₄⁺(W), whereas larger K⁺, Rb⁺, and Cs⁺ cations selectively replaced the strongly bound ammonium cation NH₄⁺(S) (Supporting Information Figure S7d–j).

In K–Mo–V–Bi oxide, in which only NH₄⁺(S) was exchanged, ca. 1.9 NH₄⁺ per one ε-VMo_{9.4}V_{2.6}O₄₀ building block were exchanged with K⁺. In the case of H–Mo–V–Bi oxide, in which only NH₄⁺(W) was exchanged, ca. 0.7 NH₄⁺ per one ε-VMo_{9.4}V_{2.6}O₄₀ building block were exchanged with H⁺. From this result, we estimated the ratio of NH₄⁺(W) and NH₄⁺(S) to be ca. 0.7–0.9:1.9–2.1. Single crystal analysis of K–Mo–V–Bi oxide revealed that 89% of K⁺ selectively occupied the channel and that the remaining 11% of K⁺, NH₄⁺, and H₂O occupied the cage in K–Mo–V–Bi oxide (Figure 7f). Therefore, we speculate that K⁺ replaced NH₄⁺ in the channel and that the NH₄⁺(S) was located in the channel and NH₄⁺(W) was located in the cage. The K⁺ blocked the

micropores of Mo–V–Bi oxide and could not be removed by calcination. The material lost microporosity with decrease in BET surface area (4.4 m²/g) after ion-exchange with K⁺ (Figure 8a, red).

Activity as an Acid Catalyst. Removal of NH₃ from NH₄⁺(W) and NH₄⁺(S) produced weak and strong H⁺ acid sites on the Mo–V–Bi oxide, respectively. Table 4 shows

Table 4. Benzyl Alcohol Dehydration To Form Dibenzyl Ether Catalyzed by Mo–V–Bi Oxide^a

entry	catalyst	conv (%)	yield (%)	sel (%)
1	as-synthesized Mo–V–Bi oxide	3	3	100
2	calcined Mo–V–Bi oxide at 623 K	95	94	99
3	calcined Mo–V–Bi oxide at 473 K	92	91	99
4	H–Mo–V–Bi oxide	99	95	95 ^b
5	recovered catalyst in entry 2	100	97	97
6	calcined Mo–V–Bi oxide at 673 K	98	91	93 ^c
7	no catalyst	5	0	0

^aReaction conditions: 20 mg of Mo–V–Bi oxide, 10 mmol of benzyl alcohol, 403 K, 3 h. After the reaction, 4 mmol of tridecane was added as an internal standard. ^bApproximately 3% of benzaldehyde was formed. ^cApproximately, 4% of benzaldehyde was formed.

results of catalytic performance of Mo–V–Bi oxide for benzyl alcohol etherification. Mo–V–Bi oxide without calcination was not active (entry 1). Calcined Mo–V–Bi oxide showed catalytic activity (entry 2). Mo–V–Bi oxide calcined at temperatures over 473 K (entries 2 and 3), and proton-exchanged H–Mo–V–Bi oxide (entry 4) showed catalytic activity. These results indicated that a weak acid had sufficient catalytic activity for this reaction. Filtration experiments (Figure 10) showed that calcined Mo–V–Bi oxide was a heterogeneous

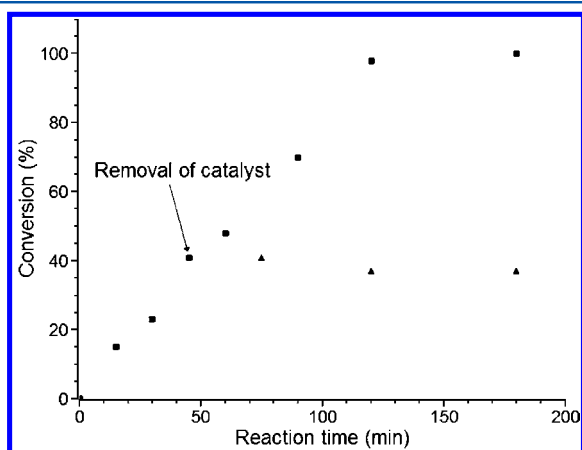


Figure 10. Filtration experiment on calcined (at 623 K) Mo–V–Bi oxide. Squares presented the reaction with catalyst. Triangles presented the reaction after removal of catalyst.

catalyst. The material could be reused without loss of activity (entry 5). The XRD pattern and IR of the recovered catalyst (Supporting Information Figure S8) confirmed high stability of Mo–V–Bi oxide during catalytic reaction. Benzyl alcohol was larger than the pore size; thus, the reaction occurred on the surface of Mo–V–Bi oxide. Therefore, Mo–V–Bi oxide calcined at 673 K, which did not contain micropores (Supporting Information Figure S9), was also active (entry 6). However, Mo–V–Bi oxide showed higher conversion of

benzyl alcohol, and the yield of dibenzyl ether compared to other reported heterogeneous catalysts (Supporting Information Table S5), which indicates that Mo–V–Bi oxide has high potential as an acid catalyst.

CONCLUSION

The first all-inorganic Keggin-type polyoxometalate-based microporous material with intrinsically ordered open micropores, Mo–V–Bi oxide, was successfully synthesized and characterized. Structural characterization showed that the material constructed by assembly of ϵ -Keggin POMs with Bi^{III} ions in a tetrahedral fashion. Heat treatment can remove the existing NH₄⁺ and H₂O from the material to open the 3D micropores. The 3D micropore system of Mo–V–Bi oxide resulted from cages and channels in the material. Mo–V–Bi oxide exhibited zeolite-like properties such as molecule adsorption, ion-exchange, and acid catalysis. POMs have a diversity of elements, and they can incorporate other metals in the structure. We believe our results will open a door for production of new porous materials based on ϵ -Keggin-type POM building blocks with tunable properties.

ASSOCIATED CONTENT

Supporting Information

Detailed experimental procedures, including figures and tables. Crystallographic data in CIF format. This material is available free of charge via the Internet at <http://pubs.acs.org>.

AUTHOR INFORMATION

Corresponding Authors

*E-mail: sadakane09@hiroshima-u.ac.jp. Phone: +81-82-424-4456. Fax: +81-82-424-5494.

*E-mail: ueda@cat.hokudai.ac.jp. Phone: +81-11-706-9164. Fax: +81-11-706-9163.

Author Contributions

All authors have given approval to the final version of the manuscript.

Funding

Notes

The authors declare no competing financial interest.

ACKNOWLEDGMENTS

This work was financially supported by a Grant-in-Aid for Scientific Research (A) (Grant 2324-6135) from the Ministry of Education, Culture, Sports, Science, and Technology, Japan. The synchrotron radiation experiments were performed at the BL40XU of SPring-8 with the approval of the Japan Synchrotron Radiation Research Institute (JASRI) (Proposal 2011B1181, 2012A1161, and 2012B1110). M.S. thanks PRESTO, JST, for financial support.

REFERENCES

- (1) Special thematic issue on polyoxometalates. *Chem. Rev.* **1998**, *98*, 1–390.
- (2) Special thematic issue on polyoxometalates. *Chem. Soc. Rev.* **2012**, *41*, 7325–7648.
- (3) Long, D.-L.; Tsunashima, R.; Cronin, L. *Angew. Chem., Int. Ed.* **2010**, *49*, 1736–1758.
- (4) Kamiya, Y.; Sadakane, M.; Ueda, W. Heteropoly Compounds. In *Comprehensive Inorganic Chemistry II*; Reedijk, J., Poeppelmeier, K., Ed.; Oxford: Elsevier, 2013; Vol. 7, pp 185–204.

- (5) Song, J.; Luo, Z.; Britt, D. K.; Furukawa, H.; Yaghi, O. M.; Hardcastle, K. I.; Hill, C. L. *J. Am. Chem. Soc.* **2011**, *133*, 16839–16846.
- (6) Sun, C.-Y.; Liu, S.-X.; Liang, D.-D.; Shao, K.-Z.; Ren, Y.-H.; Su, Z.-M. *J. Am. Chem. Soc.* **2009**, *131*, 1883–1888.
- (7) Mizuno, N.; Misono, M. *Chem. Rev.* **1998**, *98*, 199–218.
- (8) Taylor, D. B.; McMonagle, J. B.; Moffat, J. B. *J. Colloid Interface Sci.* **1985**, *108*, 278–284.
- (9) Okamoto, K.; Uchida, S.; Ito, T.; Mizuno, N. *J. Am. Chem. Soc.* **2007**, *129*, 7378–7384.
- (10) Inumaru, K. *Catal. Surv. Asia* **2006**, *10*, 151–160.
- (11) Uchida, S.; Mizuno, N. *Coord. Chem. Rev.* **2007**, *251*, 2537–2546.
- (12) Eguchi, R.; Uchida, S.; Mizuno, N. *J. Phys. Chem. C* **2012**, *116*, 16105–16110.
- (13) Eguchi, R.; Uchida, S.; Mizuno, N. *Angew. Chem., Int. Ed.* **2012**, *51*, 1635–1639.
- (14) Jiang, C.; Lesbani, A.; Kawamoto, R.; Uchida, S.; Mizuno, N. *J. Am. Chem. Soc.* **2006**, *128*, 14240–14241.
- (15) Kawamoto, R.; Uchida, S.; Mizuno, N. *J. Am. Chem. Soc.* **2005**, *127*, 10560–10567.
- (16) Uchida, S.; Hikichi, S.; Akatsuka, T.; Tanaka, T.; Kawamoto, R.; Lesbani, A.; Nakagawa, Y.; Uehara, K.; Mizuno, N. *Chem. Mater.* **2007**, *19*, 4694–4701.
- (17) Sadakane, M.; Yamagata, K.; Kodato, K.; Endo, K.; Toriumi, K.; Ozawa, Y.; Ozeki, T.; Nagai, T.; Matsui, Y.; Sakaguchi, N.; Pyrz, W. D.; Buttrey, D. J.; Blom, D. A.; Vogt, T.; Ueda, W. *Angew. Chem., Int. Ed.* **2009**, *48*, 3782–3786.
- (18) Sadakane, M.; Endo, K.; Kodato, K.; Ishikawa, S.; Murayama, T.; Ueda, W. *Eur. J. Inorg. Chem.* **2013**, 1731–1736.
- (19) Sadakane, M.; Kodato, K.; Kuranishi, T.; Nodasaka, Y.; Sugawara, K.; Sakaguchi, N.; Nagai, T.; Matsui, Y.; Ueda, W. *Angew. Chem., Int. Ed.* **2008**, *47*, 2493–2496.
- (20) Müller, A.; Krickemeyer, E.; Bögge, H.; Schmidtman, M.; Peters, F. *Angew. Chem., Int. Ed.* **1998**, *37*, 3359–3363.
- (21) Müller, A.; Todea, A. M.; van Slageren, J.; Dressel, M.; Bögge, H.; Schmidtman, M.; Luban, M.; Engelhardt, L.; Rusu, M. *Angew. Chem., Int. Ed.* **2005**, *44*, 3857–3861.
- (22) Konya, T.; Katou, T.; Murayama, T.; Ishikawa, S.; Sadakane, M.; Buttrey, D.; Ueda, W. *Catal. Sci. Technol.* **2013**, *3*, 380–387.
- (23) Kubo, J.; Watanabe, N.; Ueda, W. *Chem. Eng. Sci.* **2008**, *63*, 1648–1653.
- (24) Watanabe, N.; Ueda, W. *Ind. Eng. Chem. Res.* **2006**, *45*, 607–614.
- (25) Sadakane, M.; Watanabe, N.; Katou, T.; Nodasaka, Y.; Ueda, W. *Angew. Chem., Int. Ed.* **2007**, *46*, 1493–1496.
- (26) Wang, F.; Ueda, W. *Catal. Today* **2009**, *144*, 358–361.
- (27) Wang, F.; Ueda, W. *Top. Catal.* **2008**, *50*, 90–97.
- (28) Sadakane, M.; Ohmura, S.; Kodato, K.; Fujisawa, T.; Kato, K.; Shimidzu, K.; Murayama, T.; Ueda, W. *Chem. Commun.* **2011**, *47*, 10812–10814.
- (29) Kaveevitichai, W.; Jacobson, A. *J. Chem. Mater.* **2013**, *25*, 2708–2715.
- (30) Liu, D.; Lu, Y.; Tan, H.-Q.; Chen, W.-L.; Zhang, Z.-M.; Li, Y.-G.; Wang, E.-B. *Chem. Commun.* **2013**, *49*, 3673–3675.
- (31) Mitchell, S. G.; Streb, C.; Miras, H. N.; Boyd, T.; Long, D.-L.; Cronin, L. *Nat. Chem.* **2010**, *2*, 308–312.
- (32) Mitchell, S. G.; Boyd, T.; Miras, H. N.; Long, D.-L.; Cronin, L. *Inorg. Chem.* **2011**, *50*, 136–143.
- (33) Mandic, S.; Healey, M. R.; Gotthardt, J. M.; Alley, K. G.; Gable, R. W.; Ritchie, C.; Boskovic, C. *Eur. J. Inorg. Chem.* **2013**, *2013*, 1631–1634.
- (34) Nohra, B.; El Moll, H.; Rodriguez Albelo, L. M.; Mialane, P.; Marrot, J.; Mellot-Draznieks, C.; O’Keeffe, M.; Biboum, R. N.; Lemaire, J.; Keita, B.; Nadjo, L.; Dolbecq, A. *J. Am. Chem. Soc.* **2011**, *133*, 13363–13374.
- (35) Rodriguez-Albelo, L. M.; Rabdel Ruiz-Salvador, A.; Sampieri, A.; Lewis, D. W.; Gomez, A.; Nohra, B.; Mialane, P.; Marrot, J.; Secheresse, F.; Mellot-Draznieks, C.; Biboum, R. N.; Keita, B.; Nadjo, L.; Dolbecq, A. *J. Am. Chem. Soc.* **2009**, *131*, 16078–16087.
- (36) Dolbecq, A.; Mialane, P.; Secheresse, F.; Keita, B.; Nadjo, L. *Chem. Commun.* **2012**, *48*, 8299–8316.
- (37) Müller, A.; Beugholt, C.; Kogerler, P.; Bogge, H.; Bud’ko, S.; Luban, M. *Inorg. Chem.* **2000**, *39*, 5176–5177.
- (38) Mialane, P.; Dolbecq, A.; Lisnard, L.; Mallard, A.; Marrot, J.; Secheresse, F. *Angew. Chem., Int. Ed.* **2002**, *41*, 2398–2401.
- (39) Sloboda-Rozner, D.; Neimann, K.; Neumann, R. *J. Mol. Catal. A: Chem.* **2007**, *262*, 109–113.
- (40) Tucher, J.; Nye, L. C.; Ivanovic-Burmazovic, I.; Notarnicola, A.; Streb, C. *Chem.—Eur. J.* **2012**, *18*, 10949–10953.
- (41) Baur, W. H. *Am. Mineral.* **1964**, *49*, 697–704.
- (42) Suib, S. L. *Acc. Chem. Res.* **2008**, *41*, 479–487.
- (43) Suib, S. L. *J. Mater. Chem.* **2008**, *18*, 1623–1631.
- (44) Fyfe, C. A.; Gies, H.; Kokotailo, G. T.; Marler, B.; Cox, D. E. *J. Phys. Chem.* **1990**, *94*, 3718–3721.
- (45) Young, R. A. *The Rietveld Method*; Young, R. A., Ed.; Oxford University Press: Oxford, 1995.
- (46) Ryu, J.; Park, R.; Kim, D.-S. *J. Comput. Sci. Technol.* **2006**, *21*, 225–260.
- (47) Yasuda, N.; Fukuyama, Y.; Toriumi, K.; Kimura, S.; Takata, M. Submicrometer Single Crystal Diffractometry for Highly Accurate Structure Determination. In *AIP Conference Proceedings*; Garrett, R., Gentle, I., Nugent, K., Wilkins, S., Eds.; 2010; Vol. 1234, pp 147–150.
- (48) Yasuda, N.; Murayama, H.; Fukuyama, Y.; Kim, J.; Kimura, S.; Toriumi, K.; Tanaka, Y.; Moritomo, Y.; Kuroiwa, Y.; Kato, K.; Tanaka, H.; Takata, M. *J. Synchrotron Radiat.* **2009**, *16*, 352–357.
- (49) Sheldrick, G. M. *SHELX-97, Program for Crystal Structure Analysis*; Universität Göttingen: Göttingen, Germany, 1997.
- (50) Zhang, Q.-Z.; Lu, C.-Z.; Yang, W.-B.; Wu, C.-D.; Yu, Y.-Q.; Yan, Y.; Liu, J.-H.; He, X. *J. Cluster Sci.* **2003**, *14*, 381–390.
- (51) Zang, X.; Tan, H.; Wu, Q.; Li, Y.; Li, Y.; Wang, E. *Inorg. Chem. Commun.* **2010**, *13*, 471–474.
- (52) Chae, K.; Day, V. W.; Eberspacher, T. A. *Inorg. Chem.* **1992**, *8*, 3187–3189.

Direct Oxidative Transformation of Glycerol into Acrylic Acid over Phosphoric Acid-added W–V–Nb Complex Metal Oxide Catalysts

Kaori Omata, Keeko Matsumoto, Toru Murayama, and Wataru Ueda*

Catalysis Research Center, Hokkaido University, N-21, W-10, Sapporo, Hokkaido 001-0021

(E-mail: ueda@cat.hokudai.ac.jp)

The addition of phosphoric acid to W–Nb–O catalyst active for glycerol transformation to acrolein and to W–V–Nb–O catalyst active for direct transformation of glycerol to acrylic acid appreciably improved their catalytic performance. The phosphoric acid-added W–Nb–O catalyst gave acrolein yield of 81.8%, and the phosphoric acid-added W–V–Nb–O catalyst gave acrylic acid yield of 59.2% in the direct glycerol transformation. The improvement of the catalytic performance seems due to the increases of the acid amount and the Brønsted acidity.

Glycerol is a main by-product in biodiesel production by transesterification of plant oils or animal fat with methanol and has been produced heavily at a relatively low price.¹ Because of this situation, transformation of glycerol into other desirable chemicals by various catalytic reactions has been attempted by many researchers.² Dehydration of glycerol to acrolein is one of the most valuable reactions, since acrolein is an important intermediate for chemical and agricultural industries. Various solid acid catalysts have been reported for the dehydration of glycerol.³ We have reported that layer-structured W–Nb–O catalysts synthesized via hydrothermal method gave acrolein in high yield (75%) in gas-phase glycerol dehydration.⁴ Direct oxidative transformation of glycerol to acrylic acid is also a very important reaction.⁵ Achievement of this reaction is, however, challenging because not only improvement of selectivity for both dehydration of glycerol and selective oxidation of acrolein but also tuning of optimum catalytic functions for each reaction are required to achieve higher acrylic acid yield. Nevertheless, we have recently found that modification of the W–Nb–O catalyst with vanadium turned out to be an efficient catalyst for the direct transformation of glycerol to acrylic acid⁶ but the yield of acrylic acid was as low as 45%.

Very recently we found that the addition of phosphoric acid to the W–Nb–O catalyst and the W–V–Nb–O catalysts had pronounced effects on the transformation of glycerol to acrolein and the direct transformation to acrylic acid, respectively. The achieved single pass yield of acrylic acid was about 60% and is currently the highest amongst the reported results. This paper reports the effects of phosphoric acid addition to the W–Nb–O catalyst and the W–V–Nb–O catalysts on the selectivity in the glycerol transformation.

The complex metal oxide catalysts of W, V, and Nb (W–V–Nb–O) were prepared by hydrothermal synthesis. $(\text{NH}_4)_6\text{[H}_2\text{W}_{12}\text{O}_{40}] \cdot n\text{H}_2\text{O}$ (W: 2.7 mmol), $\text{VOSO}_4 \cdot n\text{H}_2\text{O}$ (V: 0.6 mmol), and $\text{Nb}_2\text{O}_5 \cdot n\text{H}_2\text{O}$ (Nb: 2.0 mmol) were added to 45 mL of ion-exchanged water under stirring. This mixed suspension was put in a stainless steel autoclave with a Teflon liner and heated at 448 K for 72 h. The formed solid was filtered, washed with ion-exchanged water, dried at 353 K, and then calcined at 673 K for 4 h in air. W–Nb–O (W/Nb = 1.35) was similarly prepared.

Phosphoric acid-added catalysts were prepared by impregnation of uncalcined W–Nb–O or W–V–Nb–O with an aqueous solution of phosphoric acid, followed by calcination at 673 K in air. Phosphoric acid-added W–Nb–O and W–V–Nb–O were denoted as $\text{H}_3\text{PO}_4/\text{WNb}$ and $\text{H}_3\text{PO}_4/\text{WVNb}$, respectively. The content of P was set to be 2.5 wt% of the supports after optimization of P content. XRD analysis confirmed that the layered structure of the W–Nb–O and W–V–Nb–O catalysts was maintained after the phosphoric acid treatment (Figure S1).⁷

Surface area of the catalysts was estimated by BET method where nitrogen physisorption amount was measured at 77 K with a BELSORP max (BEL Japan Inc.). Prior to the measurement, the samples were evacuated at 473 K for 2 h. Powder X-ray diffraction (XRD) pattern of the catalysts was recorded on a RINT2200 (Rigaku) with $\text{Cu K}\alpha$ radiation (tube voltage: 40 kV, tube current: 20 mA). The acid amount of catalysts was measured with NH_3 -TPD with a TPD apparatus (BEL Japan Inc.). Prior to the measurement, the samples were pretreated under He flow at 673 K for 2 h. NH_3 was adsorbed on the catalysts at 473 K. Acidity of catalysts was measured by FT-IR spectroscopy (PARAGON 1000, Perkin-Elmer) of adsorbed pyridine with an evacuable furnace cell with CaF_2 windows, containing a self-supporting disk of sample. Pyridine was adsorbed at 373 K, and after evacuation at 523 K for 1 h the adsorption spectrum was recorded. The spectrum of adsorbed pyridine on sample in the presence of water vapor (4.6 Torr) was also recorded.

Transformation of glycerol was carried out in a vertical fixed-bed reactor. The molar percent composition of reaction gas was glycerol/ O_2 / N_2 / H_2O = 5/14/56/25 (mol %). Reaction products and unconverted glycerol in both gas and liquid phases were collected hourly and analyzed with GC. Oxidation of acrolein was carried out in the same reactor as the transformation of glycerol.

The catalytic performance of the W–Nb–O and $\text{H}_3\text{PO}_4/\text{WNb}$ catalysts in the glycerol transformation was first examined, and the results are shown in Table 1. Both the glycerol conversion and the acrolein yield were clearly increased by the phosphoric acid addition, and the $\text{H}_3\text{PO}_4/\text{WNb}$ catalyst gave the acrolein in yield of 81.8% at $W/F = 2.5 \times 10^{-3} \text{ g}_{\text{cat}} \text{ min mL}^{-1}$. The improvement can be explained by changes in the surface acidity because of the following results. As shown in Table 2, the number of acid sites per gram largely increased by the addition of phosphoric acid. At the same time, the addition increased the ratio of Brønsted to Lewis acidity. Moreover, it was observed in the FT-IR study that water substantially decreased the intensity of the IR-band ascribed to the adsorption of pyridine on Lewis acid sites and on the other hand increased the intensity of IR-band ascribed to that on Brønsted acid sites. This result indicates that Lewis acid sites are hydrated and change into Brønsted acid sites in the presence of

Table 1. Effect of phosphoric acid addition on catalytic performance of W–Nb–O and W–V–Nb–O

Catalyst	(W/F) / $\text{g}_{\text{cat}} \text{min mL}^{-1}$	GLR ^a conv. ^b /%	O ₂ conv. /%	Yield ^c /%								
				ACRL	AA	ACAL	PRAL	HACT	ACA	CO _x	others	
W–Nb–O	6.3×10^{-4}	64.3	1.4	32.4	0.1	0.5	0.3	2.5	0.1	0.8	27.6	
	2.5×10^{-3}	98.9	6.5	74.5	0.1	2.9	1.0	0.4	0.7	3.8	15.5	
H ₃ PO ₄ /WVNB	6.3×10^{-4}	72.3	2.6	43.2	0.1	0.4	0.2	2.6	0.1	0.6	25.1	
	2.5×10^{-3}	100	5.6	81.8	0.3	2.1	0.6	0.5	0.3	2.7	11.7	
W–V–Nb–O	6.7×10^{-3}	100	48.6	3.5	46.2	1.4	<0.1	<0.1	12.7	33.8	2.4	
	1.0×10^{-2}	100	45.3	0.5	59.2	0.3	<0.1	<0.1	8.2	22.3	9.5	

^aGLR: glycerol. ^bReaction conditions: set temperature of the furnace, 558 K; composition of reactant gas, glycerol/O₂/N₂/H₂O = 5/14/56/25 (mol %). ^cACRL: acrolein, AA: acrylic acid, ACAL: acetaldehyde, PRAL: propanal, HACT: hydroxyacetone, ACA: acetic acid.

Table 2. Surface area and acid properties of the W–Nb–O and H₃PO₄/WVNB catalysts

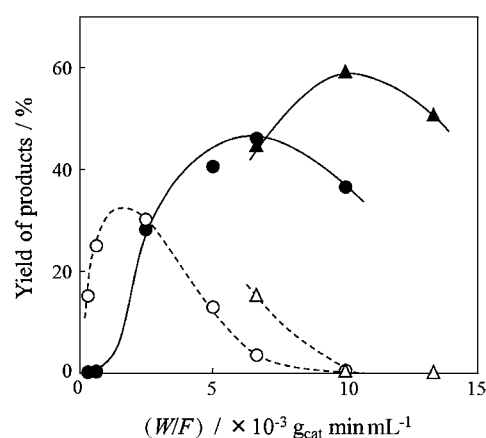
Catalyst	Surface area / $\text{m}^2 \text{g}^{-1}$	Acid amount / $\mu\text{mol g}^{-1}$	B/L ^a	
			—	+H ₂ O ^b
W–Nb–O	118	136	0.4	3.6
H ₃ PO ₄ /WVNB	91	244	1.5	23.4
W–V–Nb–O	120	129	0.4	3.2
H ₃ PO ₄ /WVNB	97	250	1.7	25.6

^aRatio of the integral absorbance (peak area) of the peak at 1540 cm⁻¹ (Brønsted) to 1450 cm⁻¹ (Lewis). ^bB/L in the presence of water (4.6 Torr).

water. This change more clearly occurs over H₃PO₄/WVNB, and in fact Lewis acidity was hardly observed on H₃PO₄/WVNB in the presence of water vapor. The same effect of the phosphoric acid addition was observed in the case of W–V–Nb–O as shown in Table 2. As a consequence, such high Brønsted acidity of H₃PO₄/WVNB and H₃PO₄/WVNB should be beneficial for the catalytic reaction, since it is considered that Brønsted acid sites are responsible for the glycerol transformation to acrolein. The observed clear effect of water on the surface acid properties in the case of H₃PO₄/WVNB is interesting, but the actual function of surface H₃PO₄ is under investigation.

Next, the catalytic performance of the W–V–Nb–O and H₃PO₄/WVNB catalysts in the direct glycerol transformation to acrylic acid was examined, and the results are also shown in Table 1. Like acrolein formation, addition effect of H₃PO₄ is also prominent. The attained maximum yield of acrylic acid was 59.2% at $W/F = 1.0 \times 10^{-2} \text{ g}_{\text{cat}} \text{min mL}^{-1}$. The performance of this catalyst was the highest of the catalysts reported for the direct transformation of glycerol to acrylic acid.⁵ Of additional importance is that the yield of acrylic acid was kept almost constant during 5 h of the reaction; that is, no deactivation occurs within this reaction period, while appreciable deactivation occurs in the transformation of glycerol to acrolein.

Figure 1 illustrates the yield of acrolein and acrylic acid in the glycerol transformation at various contact times over the W–V–Nb–O and H₃PO₄/WVNB catalysts. Acrylic acid yield increased with decreasing acrolein yield over both W–V–Nb–O and H₃PO₄/WVNB, indicating that acrolein formed on acid sites was consecutively oxidized to acrylic acid on V sites. Over the

**Figure 1.** Effect of contact time on the yields of acrolein and acrylic acid in the glycerol transformation over W–V–Nb–O (acrolein, ○; acrylic acid, ●) and H₃PO₄/WVNB (acrolein, △; acrylic acid, ▲). Reaction conditions: set temperature of the furnace, 558 K; composition of reactant gas, glycerol/O₂/N₂/H₂O = 5/14/56/25 (mol %).

W–V–Nb–O catalyst, acrylic acid yield reached the maximum value (46.2%) when acrolein was mostly consumed at $W/F = 6.7 \times 10^{-3} \text{ g}_{\text{cat}} \text{min mL}^{-1}$. At a contact time above $W/F = 6.7 \times 10^{-3} \text{ g}_{\text{cat}} \text{min mL}^{-1}$, the acrylic acid yield decreased because the sequential oxidation to CO_x started. Over H₃PO₄/WVNB, on the other hand, 15.3% yield of acrolein was still sustained at $W/F = 6.7 \times 10^{-3} \text{ g}_{\text{cat}} \text{min mL}^{-1}$, and a further increase of the contact time increased the acrylic acid yield. Then the yield of acrylic acid reached 59.2% at $W/F = 1.0 \times 10^{-2} \text{ g}_{\text{cat}} \text{min mL}^{-1}$.

The results shown in Figure 1 evidently indicate the sequential reactions from glycerol to acrylic acid via acrolein and ultimately to CO_x. In order to elucidate the role of phosphoric acid in this course of the transformation, we separately conducted acrolein oxidation over W–V–Nb–O and H₃PO₄/WVNB. Figure 2 shows the conversion of acrolein and the yield of acrylic acid and CO_x in the oxidation of acrolein. The difference of acrolein conversion was little observed between W–V–Nb–O and H₃PO₄/WVNB, while the maximum acrylic acid yield was improved from 64.4% (581 K) over W–V–Nb–O to 71.7% (577 K) over H₃PO₄/WVNB. This indicates that

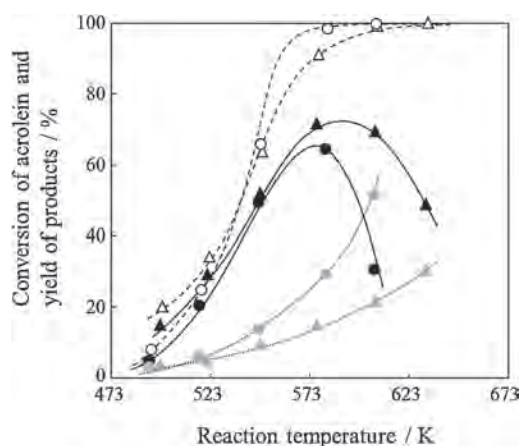


Figure 2. Conversion of acrolein, yield of acrylic acid and CO_x in the acrolein oxidation over W-V-Nb-O (acrolein, \circ ; acrylic acid, \bullet ; CO_x , \bullet) and $\text{H}_3\text{PO}_4/\text{WVNB}$ (acrolein, \triangle ; acrylic acid, \blacktriangle ; CO_x , \blacktriangle). Reaction conditions: catalyst weight, 0.2 g; flow rate, 77 mL min^{-1} ; composition of reactant gas, acrolein/ $\text{O}_2/\text{N}_2/\text{H}_2\text{O} = 1/15/58/26$ (mol %).

phosphoric acid enhances not only the selectivity to acrolein in the glycerol transformation but also the selectivity to acrylic acid in the acrolein oxidation. It should be noted in Figure 2 that over W-V-Nb-O acrylic acid yield decreased drastically at a reaction temperature above 581 K but that this decrease was retarded appreciably over $\text{H}_3\text{PO}_4/\text{WVNB}$. It is clear that the phosphoric acid can suppress the sequential overoxidation of acrylic acid to CO_x which would inevitably occur on V site of the catalysts.

In summary, the addition of phosphoric acid increased the acid amount and the Brønsted acidity of the W-Nb-O catalyst. In addition to the improvement of the acidity, phosphoric acid interacts with V sites for suppressing the sequential oxidation of acrylic acid to CO_x . As a result, acrylic acid yield in the glycerol transformation increased significantly. The $\text{H}_3\text{PO}_4/\text{WVNB}$ catalyst gave acrylic acid in yield of 59.2% directly from glycerol ($W/F = 1.0 \times 10^{-2} \text{ g}_{\text{cat}} \text{ min mL}^{-1}$, reaction temperature 594 K).

References and Notes

- B. Katryniok, S. Paul, V. Bellière-Baca, P. Reye, F. Dumeignil, *Green Chem.* **2010**, *12*, 2079.
- a) S. Gil, M. Marchena, L. Sánchez-Silva, A. Romero, P. Sánchez, J. L. Valverde, *Chem. Eng. J.* **2011**, *178*, 423. b) A. C.-C. Chang, W.-H. Lin, K.-H. Lin, C.-H. Hsiao, H.-H. Chen, H.-F. Chang, *Int. J. Hydrogen Energy* **2012**, *37*, 13110. c) Y. Kusunoki, T. Miyazawa, K. Kunimori, K. Tomishige, *Catal. Commun.* **2005**, *6*, 645. d) M. S. Khayoon, B. H. Hameed, *Appl. Catal., A* **2012**, *433–434*, 152. e) M. Kapoor, M. N. Gupta, *Process Biochem.* **2012**, *47*, 503. f) H. J. Lee, D. Seung, K. S. Jung, H. Kim, I. N. Filimonov, *Appl. Catal., A* **2010**, *390*, 235. g) A. Martin, M. Richter, *Eur. J. Lipid Sci. Technol.* **2011**, *113*, 100. h) T. Tago, T. Masuda, WO 2011108509, **2011**.
- a) Y. T. Kim, K.-D. Jung, E. D. Park, *Appl. Catal., A* **2011**, *393*, 275. b) C.-J. Jia, Y. Liu, W. Schmidt, A.-H. Lu, F. Schüth, *J. Catal.* **2010**, *269*, 71. c) E. Tsukuda, S. Sato, R. Takahashi, T. Sodesawa, *Catal. Commun.* **2007**, *8*, 1349. d) A. Alhanash, E. F. Kozhevnikova, I. V. Kozhevnikov, *Appl. Catal., A* **2010**, *378*, 11. e) M. Massa, A. Andersson, E. Finocchio, G. Busca, F. Lenrick, L. R. Wallenberg, *J. Catal.* **2013**, *297*, 93. f) A. Ulgen, W. F. Hoelderich, *Appl. Catal., A* **2011**, *400*, 34. g) F. Cavani, S. Guidetti, L. Marinelli, M. Piccinini, E. Ghedini, M. Signoretto, *Appl. Catal., B* **2010**, *100*, 197.
- K. Omata, S. Izumi, T. Murayama, W. Ueda, *Catal. Today* **2013**, *201*, 7.
- a) J. Deleplanque, J.-L. Dubois, J.-F. Devaux, W. Ueda, *Catal. Today* **2010**, *157*, 351. b) M. D. Soriano, P. Concepción, J. M. L. Nieto, F. Cavani, S. Guidetti, C. Trevisanut, *Green Chem.* **2011**, *13*, 2954. c) A. Chierigato, F. Basile, P. Concepción, S. Guidetti, G. Liosi, M. D. Soriano, C. Trevisanut, F. Cavani, J. M. L. Nieto, *Catal. Today* **2012**, *197*, 58.
- K. Omata, K. Matsumoto, T. Murayama, W. Ueda, 7th International Symposium on Acid-Base Catalysis, **2013**, PA-067.
- Supporting Information is available electronically on the CSJ-Journal Web site, <http://www.csj.jp/journals/chem-lett/index.html>.



Heptagonal channel micropore of orthorhombic Mo_3VO_x as catalysis field for the selective oxidation of ethane



Satoshi Ishikawa^{a,*}, Xiaodong Yi^b, Toru Murayama^a, Wataru Ueda^{a,*}

^a Catalysis Research Center, Hokkaido University, N-21, W-10, Sapporo 001-0021, Japan

^b State Key Laboratory for Physical Chemistry of Solid Surfaces, Department of Chemistry, Xiamen University, Xiamen 361005, Fujian, China

ARTICLE INFO

Article history:

Received 10 April 2013

Received in revised form 7 June 2013

Accepted 22 July 2013

Available online 16 August 2013

Keywords:

Orthorhombic Mo_3VO_x oxide catalysts

Crystal engineering

Micropore

Selective oxidation of ethane

ABSTRACT

A number of orthorhombic Mo_3VO_x oxide catalysts with different external surface areas measured by N_2 adsorption and with the same micropore volumes measured by ethane adsorption were synthesized hydrothermally by adding sodium dodecyl sulphonate (SDS, $\text{C}_{12}\text{H}_{25}\text{SO}_3\text{Na}$) and by changing synthesis temperature. The synthesized catalysts were then tested for the selective oxidations of ethane accessible to the micropore and of 2-propanol inaccessible to the micropore in order to investigate the role of the micropore in the gas-phase oxidation of ethane. It was found that the conversion of ethane was almost similar for all the catalysts irrespective of their largely different external surface areas. On the other hand, the oxidation of 2-propanol to acetone clearly depended on the external surface area of the catalysts. Since other catalytically affective properties such as crystal structure, elemental compositions, and oxidation states of Mo and V were comparable for all the catalysts, it was concluded that the heptagonal channel micropore of the orthorhombic Mo_3VO_x oxide catalyst was responsible for the catalytic activity for the ethane selective oxidation and that the catalytic oxidation of ethane could take place inside the micropore.

© 2013 Elsevier B.V. All rights reserved.

1. Introduction

Crystalline Mo-V-M-O ($\text{M} = \text{Nb}, \text{Te}, \text{Sb}, \text{etc.}$) complex oxides have been received much attention because of their characteristic crystal structures and high catalytic activity for the selective oxidation of light alkanes [1–13]. The structure is orthorhombic and a layer-type with a slab comprising hexagonal and heptagonal channels of corner-sharing octahedra and pentagonal $\{(\text{Mo})\text{Mo}_5\}$ units (Fig. 1). We have reported that Mo and V are essential elements to form the orthorhombic structure [4–8,11]. The additional element M (=Te and Sb) locates in the hexagonal and heptagonal channels [5–8]. We have recently reported that the heptagonal channel of the orthorhombic Mo_3VO_x catalysts works as a micropore adsorbing small molecules like CO_2 , CH_4 , and C_2H_6 [14,15] because the heptagonal channel is enough large in diameter to accept these small molecules and is empty. In addition, the orthorhombic Mo_3VO_x catalysts showed extremely high catalytic activity for the selective oxidation of ethane, compared to other orthorhombic Mo-V-M-O catalysts where the heptagonal channel micropore was partly occupied by the additional element M (=Te and Sb) [16]. The big difference of the orthorhombic Mo_3VO_x and the other Mo-V-M-O complex oxide catalysts is whether the heptagonal channels are

empty or partly occupied. We, therefore, speculate that ethane oxidation can take place not only in the mouth of the heptagonal channel but also in the whole part of the channel.

To verify our speculation, we tried to synthesize the orthorhombic Mo_3VO_x catalysts with the same microporous property and different external surface area. We employed crystal engineering methods for this purpose. Crystal engineering is a new area of research encompassing various domains of chemistry, physics, biology, materials science, engineering, and pharmaceuticals [17,18]. In the area of solid-state chemistry, crystal engineering is well recognized and widely used for the design of crystalline solids with controllable structure and tunable physicochemical properties [19]. The area of solid-state catalysts, for example zeolite [20,21] and nano crystals [19], crystal engineering is also important because crystal size and shape generically affect catalytic activity. There are various methods of controlling crystal size and shape of catalysts. Since the orthorhombic Mo_3VO_x material has been synthesized by hydrothermal reaction, bottom-up approaches through controlled nucleation and crystal growth process can be used to synthesize crystals with different sizes.

In crystallization, crystal size is determined by the ratio between rate of nucleation and rate of growth. Both rates increase with supersaturation, but the nucleation rate rises more sharply than the growth rate [22]. As a consequence, smaller crystals are observed at high supersaturation. Liu et al. have reported that sodium dodecyl sulphonate (SDS, $\text{C}_{12}\text{H}_{25}\text{SO}_3\text{Na}$), an anionic surfactant, increases

* Corresponding authors. Tel.: +81 11 762 9164; fax: +81 11 762 9163.
E-mail address: ueda@cat.hokudai.ac.jp (W. Ueda).

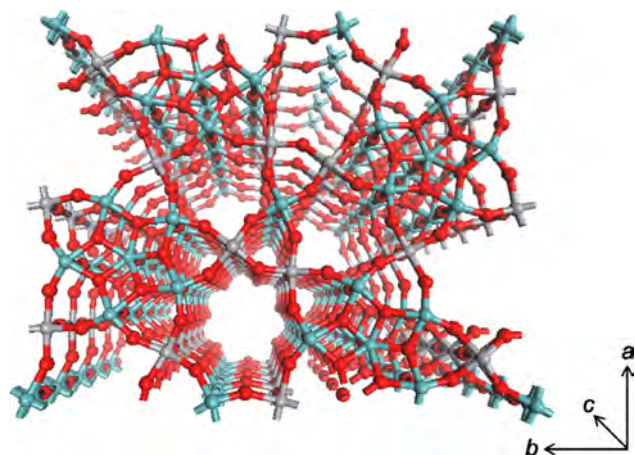


Fig. 1. Structure of the orthorhombic Mo_3VO_x oxide catalyst (Mo, cyan; V, gray; O, red). (For interpretation of the references to color in this figure legend, the reader is referred to the web version of the article.)

the supersaturation and decreases the interface energy of the nucleus, which induces easier formation of crystal nuclei [23–26]. Besides, the synthesis parameters like as concentration of the precursor solution, synthesis temperature, and synthesis time are known to affect the size of the produced crystals [27,28].

In this paper, the orthorhombic Mo_3VO_x oxide catalysts in various crystal sizes with different external surface areas and the same micropore volumes were synthesized hydrothermally by adding sodium dodecyl sulphonate (SDS, $\text{C}_{12}\text{H}_{25}\text{SO}_3\text{Na}$) to preparation solution and by changing synthesis temperature. Then, the size-controlled catalysts were tested for the selective oxidations of ethane and 2-propanol in order to clarify the role of the micropore for oxidation catalysis.

2. Experiments

2.1. Catalyst preparation

The orthorhombic Mo_3VO_x oxides catalysts were synthesized by hydrothermal method. 8.83 g of $(\text{NH}_4)_6\text{Mo}_7\text{O}_{24}\cdot 4\text{H}_2\text{O}$ (Mo: 50 mmol, Wako) was dissolved in 120 mL of distilled water. Separately, an aqueous solution of VOSO_4 was prepared by dissolving 3.29 g of hydrated VOSO_4 (V: 12.5 mmol, Mitsuwa Chemicals) in 120 mL of distilled water. The two solutions were mixed at ambient temperature and stirred for 10 min. Then, an appropriate amount of sodium dodecyl sulphonate (SDS, $\text{C}_{12}\text{H}_{25}\text{SO}_3\text{Na}$, Wako) was added and stirred for another 10 min. The amount of SDS added was $x = 0, 0.15, 0.30,$ and 0.60 , where x corresponds to the molar ratio of $\text{SDS}/(\text{Mo} + \text{V})$. At this stage, the pH value of the solution was 3.1. Then, the obtained mixed solution was introduced into an autoclave with a 300 mL-Teflon inner vessel and 4000 cm^2 of Teflon thin sheet to occupy about half of Teflon inner vessel space. This sheet is indispensable to get well-crystallized samples. After the introduction, N_2 was fed into the solution in the vessel in order to remove residual oxygen. The hydrothermal reaction was started at 175°C for 48 h under static conditions in an electric oven. Gray solids formed on the Teflon sheet was separated by filtration, washed with 1000 mL of distilled water, and dried at 80°C over night. Obtained solid contained amorphous type of materials as an impurity phase, so that the dried samples were treated with oxalic acid for purification. To 25 mL aqueous solution (0.4 mol L^{-1} , 60°C) of oxalic acid (Wako), 1 g of the dried material was added and stirred for 30 min, then washed with 500 mL of distilled water after filtration. When SDS was added, materials were washed with 500 mL of distilled water, followed

by washing with 300 mL of ethanol to remove SDS and drying at 80°C over night. FT-IR (Fig. S1) and CHN elemental analysis confirmed that SDS was completely removed by ethanol washing.

Hydrothermal synthesis was also conducted at 230°C using 250 mL-Teflon inner vessel. In this case, the amount of $(\text{NH}_4)_6\text{Mo}_7\text{O}_{24}\cdot 4\text{H}_2\text{O}$, hydrated VOSO_4 , and SDS were set to be half with the same concentration. Hydrothermal reaction at this temperature was carried out for 20 h without the Teflon sheet. Under this condition the sheet was unnecessary because highly crystallized materials were formed. The other procedure was the same as described above. The general abbreviation for the synthesized samples is MoVO-SDSx-y , where x corresponds to the molar ratio of $\text{SDS}/(\text{Mo} + \text{V})$ and y corresponds to the synthetic temperature.

2.2. Characterization of synthesized materials

The catalysts used for the ethane oxidation were characterized by the following techniques. Powder XRD patterns were recorded with a diffractometer (RINT Ultima+, Rigaku) using $\text{Cu-K}\alpha$ radiation (tube voltage: 40 kV, tube current: 20 mA). For XRD measurements, as-synthesized samples were briefly ground and the used samples were mixed with Si. The samples were put on a horizontal sample holder made of glass. Diffractions were recorded in the range of $4\text{--}60^\circ$ with $1^\circ/\text{min}$. FT-IR spectra were obtained using a spectrometer (Paragon 1000, Perkin Elmer) at room temperature in the range of $500\text{--}2000 \text{ cm}^{-1}$. SEM images were taken using an electron microscope (JSM-7400F, JEOL). Elemental compositions in the bulk were determined by ICP-AES (ICPE-9000, Shimadzu). XPS (JPC-9010MC, JEOL) with a non-monochromatic $\text{Mg-K}\alpha$ radiation was used for measuring binding energy values of Mo and V. Au was deposited for reference ($\text{Au } 4f_{7/2}$ (84.0 eV)) by using an auto fine coater (JFC-1600, JEOL). N_2 adsorption isotherms at liq. N_2 temperature were obtained using an auto-adsorption system (BELSORP MAX, Nippon BELL). External surface area was determined using a t -plot. Prior to N_2 adsorption, the catalysts were evacuated under vacuum at 300°C for 2 h. Ethane adsorption isotherms at 25°C were also obtained using the same apparatus. TPD of ammonia was carried out on a BELSORP apparatus. 50 mg of as-synthesized samples were set between two layers of quartz wool. Desorption profile was recorded with a mass spectrometer from 40°C to 600°C under He flow.

2.3. Catalytic test

The selective oxidation of ethane in gas phase was carried out at atmospheric pressure in a conventional vertical flow system with a fixed bed Pyrex tubular reactor. As-synthesized catalysts were ground with an agate mortar for 5 min, followed by heat-treatment under N_2 atmosphere at 400°C for 2 h with a fixed bed Pyrex tubular furnace. Then, the treated catalysts were diluted with silica and put into the tubular reactor for ethane oxidation. The reactor was heated gradually from room temperature at a rate of $10^\circ\text{C min}^{-1}$ to 350°C under nitrogen flow (40 mL min^{-1} from the top of the reactor). The temperature was measured with a thermocouple inserted in the middle of the catalyst zone. When the temperature reached 350°C , a reactant gas with the composition of $\text{C}_2\text{H}_6/\text{O}_2/\text{N}_2 = 10/10/80$ (mol%) was fed in with total flow rate of 50 mL min^{-1} and the catalysts were kept at this temperature for 2 h under the reactant gas flow in order to attain stable catalytic activity. Then, the temperature was decreased to 300°C and the catalytic test started at this temperature. Reaction conditions were as follows: catalyst weight; 0.1–0.7 g, reactant gas composition; $\text{C}_2\text{H}_6/\text{O}_2/\text{N}_2 = 10/10/80$ (mol%), total flow rate; 20–50 mL min^{-1} , reaction temperature; 300°C . Reactants and products were analyzed with three online gas chromatographs (molecular sieve $13\times$

Table 1
Structural characteristics of MoVO-SDSx-y catalysts.

Catalyst	Mo/V/SDS ^a	Rod-shaped crystal		Aspect ratio ^c	Lattice parameter (nm)			Int ₍₁₂₀₎ /Int ₍₀₀₁₎
		Average diameter ^b (μm)	Average length ^b (μm)		a	b	c	
MoVO-SDS0-175	50/12.5/0	0.40 (0.42)	1.8	4.5	2.109	2.658	0.3997	0.27
MoVO-SDS0.15-175	50/12.5/9.4	0.44 (0.53)	2.0	4.5	2.111	2.663	0.3996	0.26
MoVO-SDS0.30-175	50/12.5/18.8	0.45 (0.45)	1.5	3.3	2.110	2.660	0.3996	0.30
MoVO-SDS0.60-175	50/12.5/37.5	0.21 (0.22)	0.7	3.5	2.109	2.654	0.3996	0.17
MoVO-SDS0-230	25/6.3/0	0.76 (0.84)	3.7	4.9	2.105	2.653	0.4000	0.31
MoVO-SDS0.15-230	25/6.3/4.7	1.04 (1.10)	4.8	4.6	2.109	2.661	0.3998	0.37
MoVO-SDS0.30-230	25/6.3/9.4	0.99 (0.97)	3.4	3.4	2.104	2.653	0.3998	0.33
MoVO-SDS0.60-230	25/6.3/18.8	0.95 (0.97)	3.5	3.7	2.104	2.653	0.3998	0.32

^a Preparative composition (mmol).

^b Average of 100 crystallites in SEM images. Average diameter of as-synthesized crystals is shown in parentheses.

^c Aspect ratio = length/diameter.

for O₂, N₂ and CO with a TCD detector, Gaskuropack for CO₂, C₂H₄ and C₂H₆ with a TCD detector, and Porapak Q for acetic acid with a FID detector). Blank runs showed that under the experimental conditions used in this study, homogeneous gas-phase reactions were negligible. Carbon balance was always ca. 98–100%, so that the product selectivity was calculated on the basis of the product sum. After the catalytic oxidation, the catalysts were cooled down to room temperature under N₂ flow and subjected to the various characterizations as described above.

The oxidation of 2-propanol to acetone was also carried out at atmospheric pressure in the same conventional vertical flow system with a fixed bed Pyrex tubular reactor. Typical reaction conditions for the selective oxidation of 2-propanol were as follows: catalyst weight; 0.2 g, reactant gas composition; (CH₃)₂CHOH/O₂/N₂ = 4/6/90 (mol%), total flow rate; 50 mL min⁻¹, reaction temperature; 150 °C. Blank runs showed that no reaction took place without catalysts under the experimental conditions used in this study.

3. Results and discussion

3.1. Structural characteristics of MoVO-SDSx-y catalysts

Fig. 2 shows SEM images of the as-synthesized catalysts. In all cases the crystals were rod-shaped regardless of the SDS addition and the synthetic temperature, while the diameter of the rod-shaped crystals was found appreciably different depending on the synthetic conditions. In the case of the y = 175 condition, only faint SDS addition effects on crystal size were observed in x = 0.15, 0.30, probably because the amount of SDS was not enough to change the crystal size. Nevertheless, further addition of SDS to x = 0.60 caused clear decrease in the diameter of the rods. As expected, SDS tended to form smaller size of rods in diameter in the case of MoVO-SDSx-175 synthesis, implying that SDS facilitates the nucleation more than the crystal growth at 175 °C. In the case of y = 230 on the other hand, the average diameters of the rods of x = 0, 0.15, 0.30, and 0.60 were determined to be 0.76, 1.04, 0.99, and 0.95 μm, respectively, which were apparently larger compared to 0.40 μm of MoVO-SDS0-175. SDS seems not accelerate the nucleation in the case of y = 230 and even facilitate the uniform crystal growth. State of SDS and its behavior seem different depending on the hydrothermal temperature [29]. This observation was clearly supported by XRD analysis of the as-synthesized samples as shown in Fig. S2(A). All of the MoVO-SDSx-y samples showed characteristic XRD peaks (Cu-Kα) at 2θ = 6.6°, 7.8°, 9.0°, 22.2°, and 45.3°, which were derived from the orthorhombic structure. No XRD peaks other than those of the orthorhombic structure were observed in the as-synthesized MoVO-SDSx-y. Furthermore, most of the as-synthesized samples gave intense peaks at 2θ = 6.6°, 7.8°, and 9.0° ascribable to (002), (120), and (210) planes compared to those at 2θ = 22.2° and 45.3°

ascribable to (001) and (002) planes. The prominent example was MoVO-SDS0.60-230 with very high peak intensities ratios of (120) and (001), Int₍₁₂₀₎/Int₍₀₀₁₎, whereas the poor example in term of Int₍₁₂₀₎/Int₍₀₀₁₎ was MoVO-SDS0.60-175. This result indicates that crystallization to a–b direction was prominently enhanced by temperature with an additional effect of SDS, since the higher Int₍₁₂₀₎/Int₍₀₀₁₎ is, the higher the crystallization to a–b direction is.

Fig. S2 also shows XRD patterns of the catalysts used for the ethane oxidation and Table 1 summarizes the lattice parameters and the peak intensities ratios Int₍₁₂₀₎/Int₍₀₀₁₎ of the catalysts after the catalytic test. Again, all of the MoVO-SDSx-y samples showed the characteristic XRD peaks derived from the orthorhombic structure with no other XRD peaks even after the use for the oxidation, revealing high structural stability of the catalysts under the catalytic reaction conditions. However, slight changes were observed in the lattice parameters compared to those of the as-synthesized samples (MoVO-SDS0-175: a = 2.105 nm, b = 2.647, c = 0.3996). This is due to the change in oxidation state of the catalysts, as we have reported that the lattice parameters of the orthorhombic Mo₃VO_x depend on its oxidation state [15]. In other words, the lattice parameter reflects the oxidation state of the catalysts. On the basis of this relationship, one can confirm that all the catalysts after the use assumed almost the same oxidation state, as listed in Table 1 which shows very faint differences in the lattice parameters among the used catalysts.

Large changes in the peak intensities ratios of Int₍₁₂₀₎/Int₍₀₀₁₎ were observed as can be seen in Fig. S2(B). This is simply because of the grinding effect before use as catalysts. Important is that the peak intensities ratios (Table 1) are not largely different among the used catalysts except MoVO-SDS0.60-175 of which crystal size is too small compared to the others. All of the rod-shaped crystals are easily broken by grinding to shorter rod crystals because of the crystal habit [16]. In fact, it was observed in the SEM images shown in Fig. 2 that the diameter of the rod-shaped crystals was kept in the used catalysts but the length was diminished largely. The histograms of the diameter and length of the ground catalysts after the catalytic test are shown in Fig. 3 and the average diameter of the rods, average length of the crystalline, and aspect ratio are summarized in Table 1. Although there observed distributions of the diameter and the length to some extents in all the samples, it is notable that the lengths increased as the diameters increased in average. This result is concomitant with the observed similar XRD peak intensities ratio shown in Table 1. Thus, the aspect ratios of the ground catalysts after the catalytic test were found almost comparable. The catalysts synthesized here are still mixtures of the similarly shaped crystalline with different sizes but it appears that the crystalline size was effectively controlled by using SDS and by changing the temperature under the hydrothermal condition.

Chemical compositions for the ground catalysts after the catalytic test are listed in Table 2. The bulk compositions of the

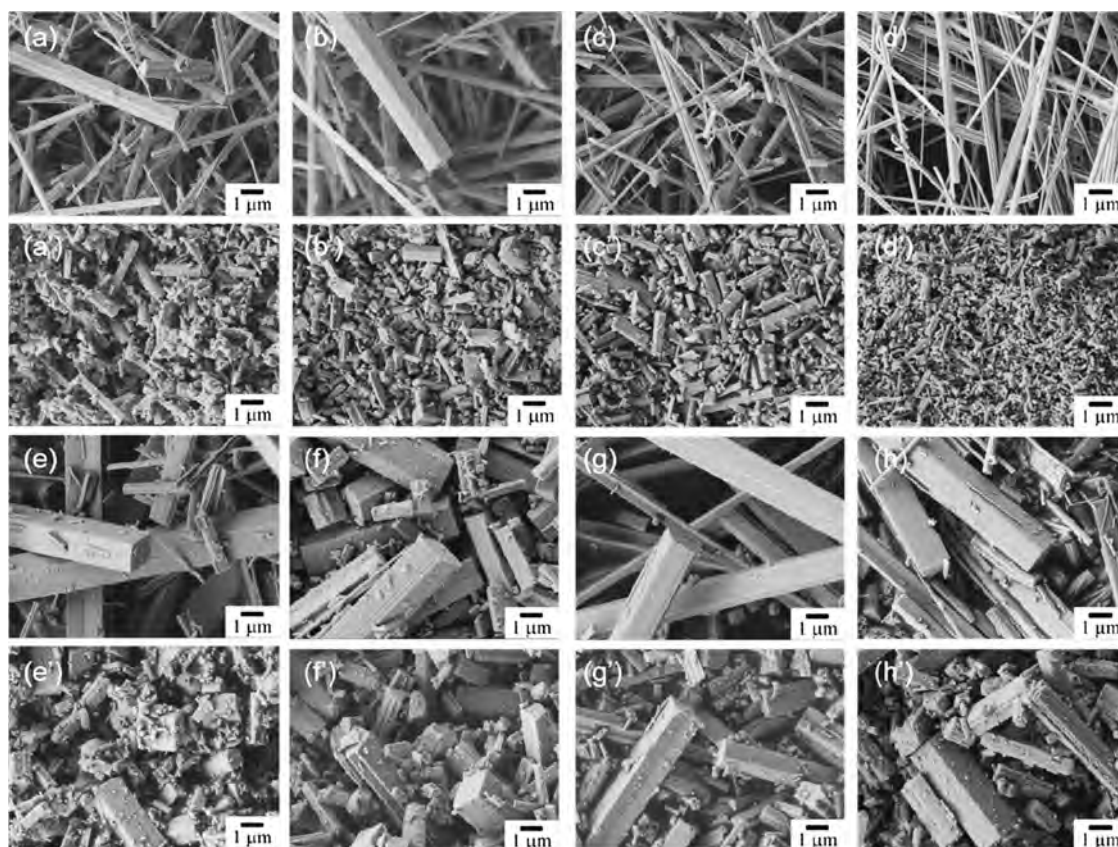


Fig. 2. SEM images of as-synthesized catalysts and used catalysts. (a), (a') MoVO-SDS0-175; (b), (b') MoVO-SDS0.15-175; (c), (c') MoVO-SDS0.30-175; (d), (d') MoVO-SDS0.60-175; (e), (e') MoVO-SDS0-230; (f), (f') MoVO-SDS0.15-230; (g), (g') MoVO-SDS0.30-230; and (h), (h') MoVO-SDS0.60-230. Apostrophe represents used catalysts.

catalysts were found to be almost the same and the ratios of V/Mo were in the range of 0.36–0.39. The ratios indicate that the unit cells of synthesized orthorhombic structure are comprised by *ca.* 29 of Mo, *ca.* 11 of V, and 112 of O, respectively, and the values were consistent with the previously reported data [11,16]. It was also confirmed by XPS that the surface compositions as well as binding energies (Table 2) of Mo and V were almost the same for all the catalysts, indicating that the catalysts are in the same oxidation state, in accordance with the results of XRD analysis as described above.

3.2. Surface area and microporous property of MoVO-SDS x - y catalysts

N_2 adsorption isotherms are illustrated in Fig. S3. All of the ground catalysts after the catalytic test adsorbed N_2 appreciably at a relative pressure of P/P_0 lower than 1.0×10^{-5} , which reveals

microporosity, and N_2 adsorption on the external surface continued at higher region of the relative pressure of P/P_0 . From these data we calculated external surface area by t -plot method in order to obtain conformity between the crystalline size and the external surface area. The results are listed in Table 3. When compared both of them, one can easily see that the external surface area decreased in order of the crystalline size increase. This reasonable conformity may allow us to eliminate a considerable contribution of possible voids that might exist in the crystal to the external surface area. The side area and the section area are also listed, which were calculated based on the measured external surface area by using the values of the average diameter and the average length of the rod-shaped crystals (Table 1). The side area and the section area decreased with the increase of the average diameters of the rod-shaped crystals.

Different from the substantial changes in the external surface area along with the crystalline size, the catalysts showed unambiguous constancy in microporous property as follows. We have already reported that the orthorhombic Mo_3VO_x possessed the empty heptagonal channel with 0.39 nm in diameter, which can act as a micropore and was proposed as catalytic active sites for ethane selective oxidation [14–16]. Here again, ethane adsorption experiments at room temperature were carried out for the used catalysts with various crystalline sizes. Fig. 4 and Table 3 show the ethane adsorption isotherms and the micropore volume estimated by DA method using the ethane adsorption isotherms. The micropore volume was in the range of 16.1 – $18.8 \times 10^{-3} \text{ cm}^3 \text{ g}^{-1}$ and apparently unaffected by the crystalline size. The theoretical micropore volume of the orthorhombic Mo_3VO_x crystal was calculated to be $22.4 \times 10^{-3} \text{ cm}^3 \text{ g}^{-1}$ [14]. The calculated value was obviously higher than those of the observed. The fact suggests

Table 2
Elemental composition and binding energy of Mo and V of MoVO-SDS x - y catalysts.

Catalyst	Composition		Binding energy (eV)	
	Bulk V/Mo	Mo–V–O atomic ratio	Mo3d _{5/2}	V2p _{3/2}
MoVO-SDS0-175	0.38	Mo _{29.0} V _{11.0} O ₁₁₂	232.0	516.0
MoVO-SDS0.15-175	0.38	Mo _{29.0} V _{11.0} O ₁₁₂	232.0	515.8
MoVO-SDS0.30-175	0.39	Mo _{28.8} V _{11.2} O ₁₁₂	231.8	515.7
MoVO-SDS0.60-175	0.36	Mo _{29.4} V _{10.6} O ₁₁₂	231.9	515.9
MoVO-SDS0-230	0.39	Mo _{28.8} V _{11.2} O ₁₁₂	231.9	515.9
MoVO-SDS0.15-230	0.39	Mo _{28.8} V _{11.2} O ₁₁₂	231.8	515.6
MoVO-SDS0.30-230	0.39	Mo _{28.8} V _{11.2} O ₁₁₂	231.9	515.9
MoVO-SDS0.60-230	0.37	Mo _{29.2} V _{10.8} O ₁₁₂	232.0	515.8

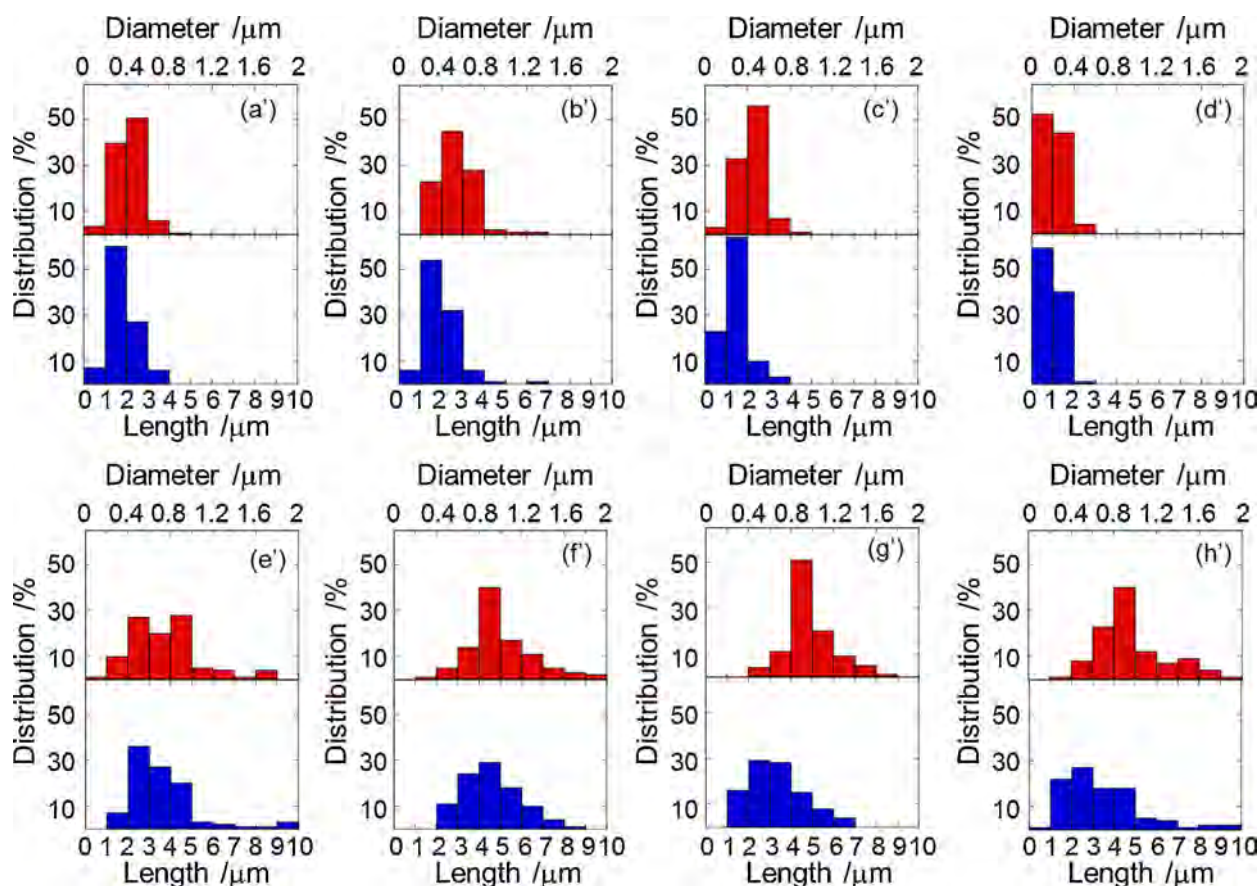


Fig. 3. Diameter (red bar) and length (blue bar) of used catalysts. (a') MoVO-SDS0-175, (b') MoVO-SDS0.15-175, (c') MoVO-SDS0.30-175, (d') MoVO-SDS0.60-175, (e') MoVO-SDS0-230, (f') MoVO-SDS0.15-230, (g') MoVO-SDS0.30-230, and (h') MoVO-SDS0.60-230. (For interpretation of the references to color in this figure legend, the reader is referred to the web version of the article.)

that the heptagonal channels in the some parts of the crystalline cannot be utilized for the ethane adsorption probably due to structure faults during the crystal formation. Nevertheless, the ethane adsorption results evidently confirm the existence of the heptagonal channel micropore where ethane molecules can freely access.

The existing of the heptagonal channel micropore in all of the catalysts was also elucidated by ammonia TPD analysis. If ammonia is assumed to exist only on the external surface, in MoVO-SDS0.15-230 with $1.2 \text{ m}^2 \text{ g}^{-1}$ external surface area for example, the amount of ammonia was calculated to be $25.4 \mu\text{mol g}^{-1}$. On the other hand, if ammonia is assumed to be confined as ammonium cation in the heptagonal channel only (note that the hexagonal channel is too

small to confine the ammonia), the amount of ammonia in the orthorhombic Mo_3VO_x was calculated to be $745 \mu\text{mol g}^{-1}$ which should be independent of the external surface area [30]. In the ammonia TPD results, the amounts of ammonia desorbed from the as-synthesized catalysts were in the range of $520\text{--}786 \mu\text{mol g}^{-1}$ (Table 3), which are closer to the calculated value when ammonia was assumed to be confined in the heptagonal channel rather than those on the external surface only. The results strongly support that the heptagonal channel in the whole crystalline particles provides place where ammonia cations can locate to neutralize the charge of the Mo-V-O structure matrix and migrate to outside particles under TPD conditions leaving empty heptagonal channels.

Table 3
Surface properties and micropore volume of MoVO-SDSx-y catalysts.

Catalyst	Surface area ($\text{m}^2 \text{ g}^{-1}$)			Micropore volume ^a ($10^{-3} \text{ cm}^3 \text{ g}^{-1}$)	Amount of ammonia desorption ^b ($\mu\text{mol g}^{-1}$)
	External surface area	Side area	Section area		
MoVO-SDS0-175	7.2	6.5	0.7	17.7	771
MoVO-SDS0.15-175	7.2	6.5	0.7	16.6	671
MoVO-SDS0.30-175	7.3	6.3	1.0	18.8	621
MoVO-SDS0.60-175	14.0	12.1	1.9	17.3	520
MoVO-SDS0-230	5.3	4.8	0.5	16.7	786
MoVO-SDS0.15-230	1.2	1.1	0.1	16.6	762
MoVO-SDS0.30-230	3.9	3.4	0.5	18.5	721
MoVO-SDS0.60-230	5.5	4.8	0.7	16.1	591

^a Measured by ethane adsorption at room temperature and determined by the DA method.

^b Desorbed amount ammonia from as-synthesized catalysts analyzed by TPD.

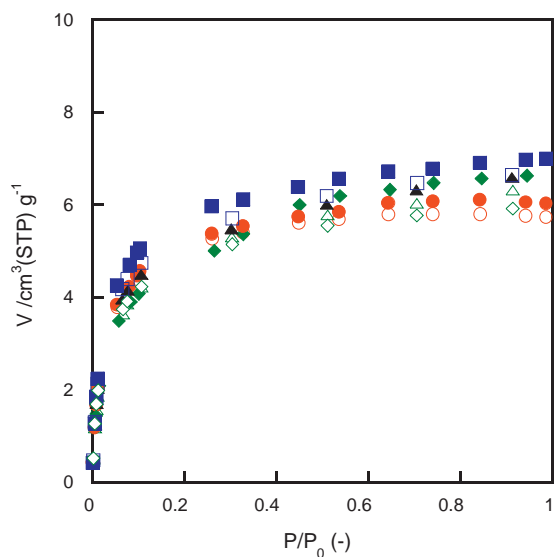


Fig. 4. Ethane adsorption isotherms at room temperature for used catalysts. MoVO-SDS0-175 (closed triangle), MoVO-SDS0.15-175 (closed circle), MoVO-SDS0.30-175 (closed square), MoVO-SDS0.60-175 (closed lozenge), MoVO-SDS0-230 (open triangle), MoVO-SDS0.15-230 (open circle), MoVO-SDS0.30-230 (open square), MoVO-SDS0.60-230 (open lozenge).

3.3. Selective oxidation of ethane and 2-propanol

As demonstrated above we successfully prepared a number of the orthorhombic Mo_3VO_x catalysts with different crystalline sizes, so that by using these catalysts we are now allowed to evaluate the contributions of external surface as well as micropore to oxidation catalysis. Here, the selective oxidative dehydrogenation of ethane that accessible to the micropore and that of 2-propanol that inaccessible to the micropore were conducted over the synthesized catalysts. The catalytic results are shown in Fig. 5 and summarized in Table 4. All of the catalysts showed *ca.* 30% of conversion for

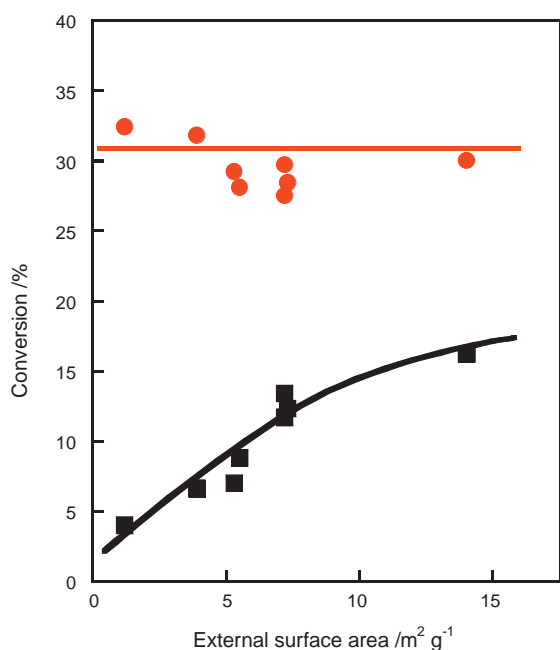


Fig. 5. Conversion changes as a function of external surface area in the selective oxidation of ethane (circle) and 2-propanol (square) over MoVO-SDSx-y catalysts.

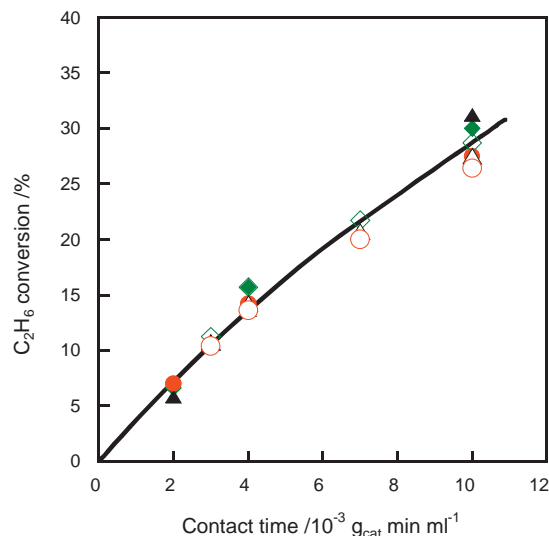


Fig. 6. Change of ethane conversion over MoVO-SDS0-175 (triangle), MoVO-SDS0.60-175 (lozenge), and MoVO-SDS0.15-230 (circle) catalysts as a function of contact time. Contact time was controlled by changing the reaction gas feed (open symbol) or by changing the catalyst amount (closed symbol).

ethane and *ca.* 90% of selectivity to ethene at 300 °C at the contact time of 0.010 $\text{g}_{\text{cat}} \text{min mL}^{-1}$. It is rather surprising to see from Fig. 5 that the catalysts revealed almost the same catalytic activity for the selective oxidation of ethane in spite of that the external surface of the catalysts are largely different each other. This fact strongly implies that the external surface area had almost no contribution to the catalytic activity for ethane oxidation and even suggests that ethane molecules are activated in the micropore under the catalytic oxidation conditions. This suggestion seems reasonable by taking into account the fact that ethane can freely enter the heptagonal channel micropore.

To obtain more supports to the suggestion, we conducted three more catalytic tests; (1) under different contact time by changing either catalyst amount or reactant flow rate, (2) over the catalyst without grinding, and (3) over the catalyst with more uniform crystalline size distribution. The results for the first are illustrated in Fig. 6. The tested catalysts were MoVO-SDS0-175, MoVO-SDS0.60-175, and MoVO-SDS0.15-230, of which crystal sizes were 0.40 μm , 1.04 μm , and 0.22 μm , respectively. Here again, these three catalysts showed almost the same catalytic activity for the ethane oxidation even under the different contact times and also no effect of the way of changing the contact time on the conversion of ethane was observed. The latter result reveals no diffusion effects on the selective oxidation of ethane over the catalysts.

For the second, the following experiment was conducted. The treatment of grinding before the catalytic tests is important for the orthorhombic Mo_3VO_x , because the section part possessing the heptagonal channel micropore as catalytic active sites for selective oxidations of light alkanes can be easily exposed by grinding because of the rod-shaped crystals [16]. In fact, the grind treatment has been reported to give a significant increase in the catalytic activity for the selective oxidation of propane [2]. However, in the case of the selective oxidation of ethane, no change by grinding should be observed if our speculation in the above-mentioned is correct. Thus, MoVO-SDS0-175 catalysts with or without the grind treatment were tested. The catalyst without grinding is abbreviated as MoVO-SDS0-175-non. Fig. S5 showed SEM images of MoVO-SDS0-175 and MoVO-SDS0-175-non. The length of the rod-shaped crystal of MoVO-SDS0-175-non was absolutely longer than that of MoVO-SDS0-175. We hardly measured the aspect ratio of the

Table 4
Selective oxidation of ethane over MoVO-SDS_x-y catalysts.^a

Catalyst	Reaction temperature (°C)	Conversion (%)		Selectivity (%)		
		C ₂ H ₆	O ₂	C ₂ H ₄	CO _x	CH ₃ COOH
MoVO-SDS0-175	302	27.5	24.5	92.4	5.3	2.7
MoVO-SDS0-175-non	298	26.2	21.3	86.9	11.0	1.3
MoVO-SDS0.15-175	299	29.0	20.6	89.4	7.1	2.9
MoVO-SDS0.30-175	300	28.4	20.1	89.4	7.0	2.7
MoVO-SDS0.60-175	298	30.0	20.9	89.6	5.6	2.3
MoVO-SDS0-230	297	29.2	20.4	89.5	8.0	2.1
MoVO-SDS0-230-oxa	301	31.5	22.8	90.3	6.9	2.5
MoVO-SDS0.15-230	298	32.1	23.0	90.4	7.4	2.1
MoVO-SDS0.30-230	301	31.8	23.6	88.9	8.0	2.1
MoVO-SDS0.60-230	300	28.1	17.4	89.6	8.2	2.2

^a Reaction condition for ethane oxidation: catalyst weight, 0.5 g; reaction temperature, 300 °C; reaction gas feed, C₂H₆/O₂/N₂ = 5/5/40 mL min⁻¹.

rod-shaped crystals of MoVO-SDS0-175-non because the length was too long (roughly 100 μm). Therefore, the exposed section area of MoVO-SDS0-175-non should be much smaller than that of MoVO-SDS0-175. However, surprisingly both MoVO-SDS0-175 and MoVO-SDS0-175-non showed almost the same ethane conversion as can be seen in Table 4. This astonishing result may imply either that the micropore in the whole particle involves in the reaction or that the side surface only contributes to the oxidation activity, because both the factors, the micropore volume and the external side surface area are the same for the two catalysts. The latter possibility is, however, easily excluded by the experimental facts that the catalysts having different side areas showed almost the same catalytic activity as already shown in Tables 3 and 4. At the same time, it can be confirmed that the contribution of the section

surface to the oxidation activity is negligible, since the section surface area is expected extremely low for the unground sample.

For the third, the following experiment was conducted. Prior to the reaction tests, the grinding treatment was made for all of the catalysts. In this process, crystalline fragments might form and possibly possess a significant catalytic activity in the ethane oxidation. To exclude this possibility, the ground MoVO-SDS0-230 sample, which had clearly some small crystalline fragments as can be seen in the SEM images (Fig. 2(e')), was treated with oxalic acid to remove the fragments and then tested for the ethane selective oxidation. The oxalic acid treatment was carried out for the sample which was ground for 5 min by an agate mortar. To 25 mL aqueous solution (0.4 mol L⁻¹, 60 °C) of oxalic acid, 1 g of the sample was added and stirred for 30 min at this solution temperature,

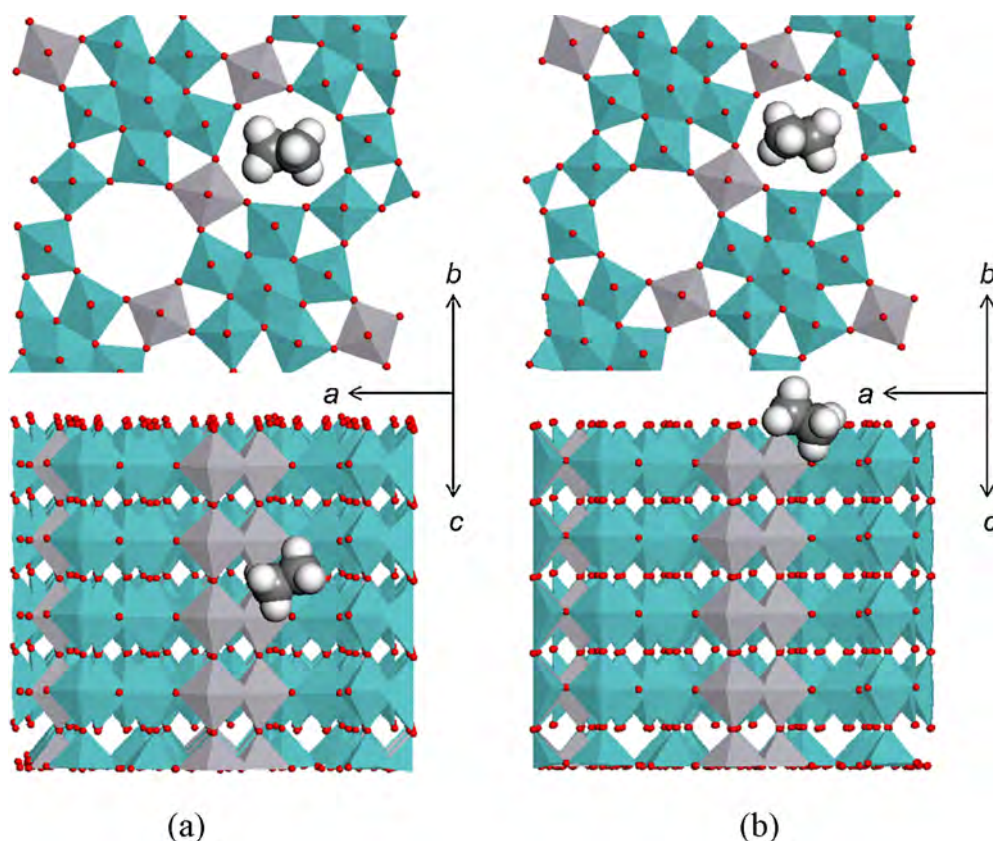


Fig. 7. Top (top) and side (bottom) perspective views showing the ethane/orthorhombic Mo₃VO_x catalysts analyzed by Monte Carlo method. (a) ethane is located in the heptagonal channel ($\Delta E = 12.1$ kcal mol⁻¹) and (b) ethane is located on the surface of the heptagonal channel ($\Delta E = 9.7$ kcal mol⁻¹).

then washed with 500 mL of distilled water, followed by the heat-treatment under N_2 flow at $400^\circ C$ for 2 h. The obtained sample is abbreviated as MoVO-SDSO-230-oxa. Although little fragments were still observed in MoVO-SDSO-230-oxa in SEM image (Fig. S4), the oxalic acid treatment substantially removed the fragments. MoVO-SDSO-230 and MoVO-SDSO-230-oxa were compared for the ethane selective oxidation to investigate the effects of the fragments to the reaction. Even after the oxalic acid treatment, no catalytic activity changes were found (Table 4). The results directly support that the oxidation activity of the catalysts was not affected by the crystalline size and oxidation activity per weight is independent of the crystalline size.

In order to further demonstrate the role of the micropore we tested the catalysts for the oxidation of 2-propanol. 2-Propanol is much larger molecule (0.47 nm in diameter of the smallest by D-Mol calculation) than ethane (0.40 nm in diameter), so that catalytic function of only external surface will be evaluated. The results are also illustrated in Fig. 5. As expected, the conversions of 2-propanol to acetone increased monotonously with the increase of the external surface area of the catalysts. The conversion became nearly zero when MoVO-SDSO.15-230 with the lowest external surface area was used. The molecular size of 2-propanol is too large to enter the heptagonal channel. Therefore, the strong dependency on the external surface area was observed in the oxidation of 2-propanol. However, at present it is hard to speculate where 2-propanol oxidation can take place, either or both of the heptagonal channel sites on the section surface and the side surface.

3.4. Monte Carlo simulation

Monte Carlo simulation for orthorhombic Mo_3VO_x was carried out to calculate the adsorption energies of ethane in the heptagonal channel micropore. Two representative configurations of ethane adsorption with low ethane adsorption energies are shown in Fig. 7 (view of the crystal side of the orthorhombic Mo_3VO_x). In each configuration ethane molecule locates in or near the heptagonal channel. The highest ethane adsorption energy ($12.1 \text{ kcal mol}^{-1}$) was obtained when ethane molecule is confined inside the heptagonal channel in horizontal arrangement. Compared to this configuration, lower ethane adsorption energies ($9.7 \text{ kcal mol}^{-1}$) were calculated when ethane adsorbed on the surface of the heptagonal channel. This simulation result is also a strong support of our assumption that ethane favorably goes into the micropore to be reacted.

4. Conclusion

Based on all the above results we conclude that ethane molecule enter the heptagonal channel micropore and go through without diffusion barrier under the condition of the ethane selective oxidation. During ethane going through the heptagonal channel micropore, ethane oxidation takes place. Ethane could be activated and converted to ethene by oxidative dehydrogenation with

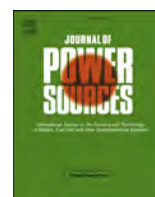
lattice oxygen of the heptagonal channel. This is the reason why the present orthorhombic Mo_3VO_x catalyst with empty micropore is superior to the same type of the catalyst with occupied micropore. There are tremendous numbers of scientific researches on clarifying the role of pores in zeolite catalysts. However, effects of micropore on gas-phase oxidation of organic compounds over complex metal oxide catalysts have been merely studied since micropore is simply thought responsible for deep oxidation to form CO_2 . The presented work here successfully demonstrates the role of micropore in the selective oxidation of ethane for the first time and will pave a way for developing evolutional oxidation catalysts based on complex metal oxides with high-dimensional crystal structures.

Appendix A. Supplementary data

Supplementary data associated with this article can be found, in the online version, at <http://dx.doi.org/10.1016/j.apcata.2013.07.050>.

References

- [1] T. Ushikubo, K. Oshima, A. Kayou, M. Vaarkamp, M. Hatano, *J. Catal.* 169 (1997) 394–396.
- [2] W. Ueda, K. Oshihara, *Appl. Catal. A: Gen.* 200 (2000) 135–143.
- [3] K. Oshihara, Y. Nakamura, M. Sakuma, W. Ueda, *Catal. Today* 71 (2001) 153–159.
- [4] T. Katou, D. Vitry, W. Ueda, *Chem. Lett.* 32 (2003) 1028–1029.
- [5] D. Vitry, J.L. Dubois, W. Ueda, *J. Mol. Catal. A: Chem.* 220 (2004) 67–76.
- [6] N. Watanabe, W. Ueda, *Ind. Eng. Chem. Res.* 45 (2006) 607–614.
- [7] W. Ueda, D. Vitry, T. Katou, *Catal. Today* 96 (2004) 235–240.
- [8] W. Ueda, D. Vitry, T. Katou, *Catal. Today* 99 (2005) 43–49.
- [9] H. Murayama, D. Vitry, W. Ueda, G. Fuchs, M. Anne, J.L. Dubois, *Appl. Catal. A: Gen.* 318 (2007) 137–142.
- [10] W.D. Pyrz, D.A. Blom, T. Vogt, D.J. Buttrey, *Angew. Chem. Int. Ed.* 47 (2008) 2788–2791.
- [11] W.D. Pyrz, D.A. Blom, M. Sadakane, K. Kodato, W. Ueda, T. Vogt, D.J. Buttrey, *Chem. Mater.* 22 (2010) 2033–2040.
- [12] P. Botella, J.M. López Nieto, B. Solsona, A. Mifsud, F. Marquez, *J. Catal.* 209 (2002) 445–455.
- [13] P. Botella, E.G. González, A. Dejoz, J.M. López Nieto, M.I. Vázquez, J.G. Calbet, *J. Catal.* 225 (2004) 428–438.
- [14] M. Sadakane, K. Kodato, T. Kuranishi, Y. Nodasaka, K. Sugawara, N. Sakaguchi, T. Nagai, Y. Matsui, W. Ueda, *Angew. Chem. Int. Ed.* 47 (2008) 2493–2496.
- [15] M. Sadakane, S. Ohmura, K. Kodato, T. Fujisawa, K. Kato, K. Shimidzu, T. Murayama, W. Ueda, *Chem. Commun.* 47 (2011) 10812–10814.
- [16] T. Konya, T. Katou, T. Murayama, S. Ishikawa, M. Sadakane, D. Buttrey, W. Ueda, *Catal. Sci. Technol.* 3 (2013) 380–387.
- [17] K. Biradha, C.Y. Su, J.J. Vittal, *Cryst. Growth Des.* 11 (2011) 875–886.
- [18] G.R. Desiraju, *J. Mol. Struct.* 656 (2003) 5–15.
- [19] T.D. Nguyen, T.O. Do, *Nanocrystal, InTech, Croatia*, 2011, pp. 55–84.
- [20] S. Sang, Z. Liu, P. Tian, Z. Liu, L. Qu, Y. Zhang, *Mater. Lett.* 60 (2006) 1131–1133.
- [21] B.O. Hincapie, L.J. Garces, Q. Zhang, A. Sacco, S.L. Suib, *Micropor. Mesopor. Mater.* 67 (2004) 19–26.
- [22] F.D. Renzo, *Catal. Today* 41 (1998) 37–40.
- [23] C. Liu, X. Ji, G. Cheng, *Appl. Surf. Sci.* 253 (2007) 6840–6843.
- [24] C. Liu, D. Ma, X. Ji, S. Zhao, S. Li, *Appl. Surf. Sci.* 257 (2011) 4529–4531.
- [25] C. Liu, S. Zhao, X. Ji, B. Wang, D. Ma, *Mater. Chem. Phys.* 133 (2012) 579–583.
- [26] C. Liu, D. Ma, X. Ji, B. Wang, S. Zhao, *J. Am. Ceram. Soc.* 94 (2011) 2266–2268.
- [27] V.P. Valtchev, L. Tosheva, K.N. Bozhilov, *Langmuir* 21 (2005) 10724–10729.
- [28] S. Lee, D. Song, D. Kim, L. Lee, S. Kim, I.Y. Park, Y.D. Choi, *Mater. Lett.* 58 (2004) 342–346.
- [29] N. Pal, A. Bhaumik, *Adv. Colloid Interface Sci.* 189–190 (2013) 21–41.
- [30] T. Katou, Hokkaido University, 2005 (PhD thesis).



Oxygen reduction reaction over silver particles with various morphologies and surface chemical states

Junya Ohyama^{a,b,*}, Yui Okata^a, Noriyuki Watabe^a, Makoto Katagiri^a, Ayaka Nakamura^c, Hidekazu Arikawa^c, Ken-ichi Shimizu^{b,c}, Tatsuya Takeguchi^c, Wataru Ueda^c, Atsushi Satsuma^{a,b,*}

^a Graduate School of Engineering, Nagoya University, Nagoya 464-8603, Japan

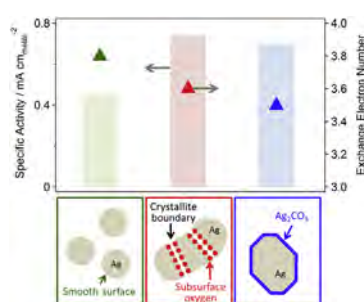
^b Elements Strategy Initiative for Catalysts and Batteries (ESICB), Kyoto University, Katsura, Kyoto 615-8520, Japan

^c Catalysis Research Center, Hokkaido University, Sapporo 001-0021, Japan

HIGHLIGHTS

- Morphology and surface chemical state of Ag powders affected the ORR activity.
- Defective and oxidized surface enhanced Ag active surface area during the ORR.
- Ag particles with defective and angular surfaces exhibited higher specific activity.

GRAPHICAL ABSTRACT



ARTICLE INFO

Article history:

Received 11 April 2013

Received in revised form

4 July 2013

Accepted 6 July 2013

Available online 13 July 2013

Keywords:

Silver

Oxygen reduction reaction

Morphology

Surface chemical state

Raman spectroscopy

ABSTRACT

The oxygen reduction reaction (ORR) in an alkaline solution was carried out using Ag powders having various particle morphologies and surface chemical states (Size: ca. 40–110 nm in crystalline size. Shape: spherical, worm like, and angular. Surface: smooth with easily reduced AgO_x , defective with AgO_x , and Ag_2CO_3 surface layer). The various Ag powders were well characterized by X-ray diffraction, X-ray photoelectron spectroscopy, N_2 adsorption, scanning electron microscopy, Raman spectroscopy, cyclic voltammetry, and stripping voltammetry of underpotential-deposited lead. Defective and oxidized surfaces enhanced the Ag active surface area during the ORR. The ORR activity was affected by the morphology and surface chemical state: Ag particles with defective and angular surfaces showed smaller electron exchange number between three and four but showed higher specific activity compared to Ag particles with smooth surfaces.

© 2013 Elsevier B.V. All rights reserved.

1. Introduction

Alkaline anion exchange membrane fuel cells (AAEMFCs) have attracted considerable attention owing to their potential for the application of non-Pt metals as electrode catalysts due to the less corrosive environment for the catalysts than proton exchange membrane fuel cells (PEMFCs) [1–7]. To achieve high oxygen reduction reaction (ORR) activity, comparable to Pt catalysts, various metals such as Ag [8–16], Au [3,13,17], Pd [12,18,19], Ni [20], and manganese oxides

* Corresponding authors. Graduate School of Engineering, Nagoya University, Nagoya 464-8603, Japan. Tel.: +81 52 789 3191; fax: +81 52 789 3193.

E-mail addresses: ohyama@apchem.nagoya-u.ac.jp (J. Ohyama), satsuma@apchem.nagoya-u.ac.jp (A. Satsuma).

[16,21–24] have been studied. One effective strategy to enhance catalytic activity for the ORR is controlling the size of metal particles. For example, Chen et al. clearly presented the size-dependent ORR activity of Pd supported on carbon (Pd/C) by evaluation of the ORR activity normalized to the Pd active surface area and mass [12]. In their study, the highest ORR activity was observed on Pd particles (ca. 5 nm in diameter) supported on carbon when the size of Pd nanoparticles decreased from 16.7 to 3 nm. For Au catalysts, it has been reported that Au nanoclusters with a diameter less than 2 nm represented high ORR activity deviating from bulk Au behavior [17]. Li et al. represented that large Ag particles (174 nm in diameter) showed a four-electron reduction of oxygen, and fine Ag nanoparticles (4.1 nm in diameter) showed a large two-electron pathway contribution, which indicates that larger Ag particles reduce oxygen more efficiently [11]. On the other hand, a 2.3 electron ORR pathway on 20 wt% Ag/C with 47.7 nm of Ag particles and a 3.6 electron ORR pathway on 20 wt% Ag/C with 15 nm of Ag particles have been also reported [9,25]. Thus, it is evident that the effect of size on the ORR activity is still not well understood. This would be due to other factors related to the ORR, such as loading amount, morphology, and surface chemical state [8,10,16,21,26,27].

Among the non-Pt metals described above, Ag is regarded as the most promising metal to replace Pt owing to its abundance, relatively low cost, and high activity [3,6,8,10,28]. Interestingly, considering Ag catalysts for the ORR in a previous study, it was proposed that the redox property of the Ag catalyst is a controlling factor of the ORR catalytic activity [10,29]. It is assumed that the structure and surface chemical state of Ag affect the redox property and the ORR activity [29,30]. For other metal catalysts, the surface chemical state as well as the structure has an effect on the ORR activity [16,19,21,31–34]. However, few studies have investigated the effect of the surface chemical state of Ag on the ORR activity [30,35,36].

We investigated the effect of Ag morphology and surface chemical state on the ORR activity in alkaline solutions using various Ag particles well characterized by X-ray diffraction (XRD), N₂ adsorption, scanning electron microscopy (SEM), X-ray photoelectron spectroscopy (XPS), Raman spectroscopy, cyclic voltammetry (CV), and stripping voltammetry of underpotential-deposited lead (Pb_{upd}).

2. Experimental

2.1. Catalysts

Ag metal powders used in this study were purchased from Aldrich (Ag-A), Kojundo Chemical Lab. Co., Ltd. (Ag-K), and Kishida Chemical Co., Ltd. (Ag-KC). As a reference, a Ag/C catalyst with 60 wt% loading on a carbon black (CB) was purchased from E-Tek Co. (Ag/C-E). For electrochemical measurements, the Ag powders were physically mixed with Vulcan XC-72R CB (Cabot Corp.) to prepare Ag catalysts (Ag loadings: 60 wt% for Ag-A and Ag-K, 90 wt% for Ag-KC).

2.2. Characterization

XRD patterns of samples were recorded on a Rigaku MiniFlex II/AP diffractometer with Cu K α radiation. The crystallite size of the Ag powder was evaluated from the half-width of the Ag(111) line using the Scherrer equation after correcting for instrumental peak broadening using the half-width of Si(111) of silicon powder purchased from Kishida Chemical Co., Ltd. The Scherrer constant was assumed to be 0.9. The morphology of Ag particles was observed using a JEOL JSM-7500FA scanning electron microscope. XPS were acquired on a JPS-9000MC system (JEOL Ltd.) using Al K α radiation. Brunauer–Emmett–Teller (BET) specific surface area of Ag powders was measured by N₂ adsorption at 77 K on a BELSORP 28SA

(Bel Japan, Inc.) instrument. Prior to measurements, each sample was outgassed at room temperature for 2 h.

Raman spectra were measured on a JASCO RMP-330 spectrophotometer equipped with a 532 nm green semiconductor laser as an excitation source. The samples were filled in an in situ diffuse reflectance cell having a quartz window (15 mm) and an internal heating system connected to a gas flow system [37]. A 20 \times objective optical lens was used to focus the depolarized laser beam on the sample surface and to collect the backscattered light. The backscattered light was dispersed by a single-stage spectrometer with 1800-groove mm⁻¹ grating and acquired by an air-cooled 1024 \times 256 pixel charge-coupled device. The Raman scattering was collected in the spectral region of 89.28–1324.29 cm⁻¹ with a resolution of 1 cm⁻¹. The exposure time was 120 s for Ag-A, 5 s for Ag-K, and 60 s for Ag-KC, and five scans were accumulated for each spectrum. As references, the spectra of Ag₂O and Ag₂CO₃ were purchased from Kishida Chemical Co., Ltd. and Mitsuwa Chemical Co., Ltd., respectively. The sample was filled in the cell and measured at room temperature. The in situ Raman spectra were collected under 20 mL min⁻¹ H₂ flow at a given temperature.

2.3. Cyclic voltammetry, Pb_{upd} stripping voltammetry, and the ORR measurement

Cyclic voltammograms (CVs), Pb_{upd} stripping voltammograms, and linear sweep voltammograms for the ORR were obtained using the rotating disk electrode (RDE) setup with a potentiostat (HZ-5000 (HAG-3001), Hokuto Denko Corp.).

Catalyst ink was prepared by ultrasonic mixing of a suspension of 10–20 mg of catalysts in a mixed solution of 1 mL of 1-hexanol and 21.7 μ L of an ionomer solution (AS-4 solution (5 wt% in 1-propanol, Tokuyama Corp.)). The catalyst ink was dropped on the glassy carbon substrate of the RDE (HR2-D1-GC-5, 5 mm in diameter, 0.196 cm², Hokuto Denko Corp.) in 2.5–5 μ L. After the ink was dried on the substrate, 7 μ L of a diluted ionomer solution (0.05 wt% in 1-propanol) was dropped on the disk.

The ORR was carried out in an O₂-purged 0.1 M NaOH aqueous solution using a three-electrode cell with a Pt wire counter electrode and a Hg/HgO/0.1 M NaOH (Hg/HgO/OH⁻) reference electrode. After the NaOH solution was saturated with O₂ gas by purging for at least 0.5 h, the ORR was recorded by sweeping the potential from 0.2 to -0.8 V vs Hg/HgO/OH⁻ at 20 mV s⁻¹ at 293 K. CV and Pb_{upd} stripping voltammetry were performed in a N₂-purged 0.1 M NaOH solution and the solution containing 125 μ M Pb(NO₃)₂, respectively, (10 mV s⁻¹, 293 K). The Pb_{upd} strip voltammogram was obtained after Pb deposition at -0.7 V vs Hg/HgO/OH⁻ for 300 s.

3. Results and discussion

3.1. Physical characterization

Table 1 lists the crystallite size evaluated by XRD (Fig. S1) and the BET surface area (S_{BET}) of Ag-A, Ag-K, and Ag-KC. The order of crystallite size was Ag-A (38 nm) < Ag-K (62 nm) < Ag-KC (113 nm). Ag powders with smaller crystallite size exhibited larger BET surface area values. Fig. 1 shows typical SEM images of Ag powders used in this study. Ag-A exhibited spherical and relatively mono-dispersed particles ca. 50 nm in diameter (Fig. 1(a)). Ag-K was composed of variously sized (ca. 10 nm–1 μ m) particles having a worm-like shape (Fig. 1(b)). Ag-KC particles had angular shape and various sizes (ca. 50 nm to 2 μ m) (Fig. 1(c)). The particle size of Ag-A observed by SEM (ca. 50 nm) was comparable to the crystallite size evaluated by XRD (38 nm); however, those of Ag-K and Ag-KC were different from the corresponding crystallite sizes. It is likely that the

Table 1
Results of physical and electrochemical characterization of Ag powders used in this study.

Ag powder	Crystallite size (nm) ^a	S _{ABET} (m ² g ⁻¹) ^b	Particle morphology and surface chemical state ^c	ESA (m ² g ⁻¹) ^d	ESA/S _{ABET} (%) ^e
Ag-A	38	4.7	Spherical particle with easily reduced AgO _x species on smooth surface	4.2	90
Ag-K	62	2.5	Worm-like particle with subsurface oxygen at surface defect	3.5	142
Ag-KC	113	0.5	Angular particle with surface Ag ₂ CO ₃ layer and defect	0.6	122

^a Evaluated from XRD line width of Ag(111) using Scherrer equation.

^b BET surface area.

^c Analyzed by CV, SEM observation, and Raman spectroscopy.

^d Electrochemically active surface area determined by Pb_{upd} stripping voltammetry.

^e The ratio of ESA to S_{ABET}.

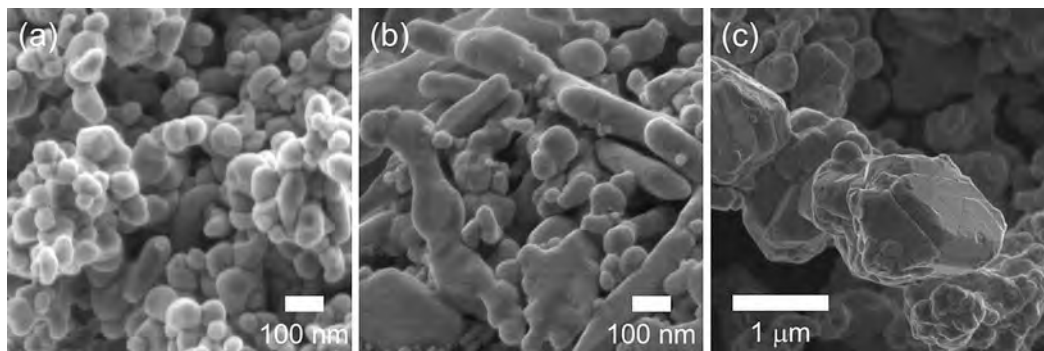


Fig. 1. Typical SEM images of (a) Ag-A, (b) Ag-K, and (c) Ag-KC.

Ag-K and Ag-KC particles were composed of 62 and 113 nm Ag crystallites, respectively, as evaluated by XRD.

Fig. 2 shows Ag 3d XPS of the Ag powders. The Ag 3d_{5/2} XPS peak binding energy of Ag-A was 368.2 eV, which is consistent with the previously reported peak energy of Ag metal [38,39]. On the other hand, the Ag 3d_{5/2} peak energies of Ag-K and Ag-KC were lower than Ag-A (367.6 and 368.0 eV, respectively). It has been reported that Ag oxides (and Ag₂CO₃) present peaks at lower binding energy [38,39]. Thus, the XPS analysis indicated that Ag-K and Ag-KC were in a more oxidized state than Ag-A.

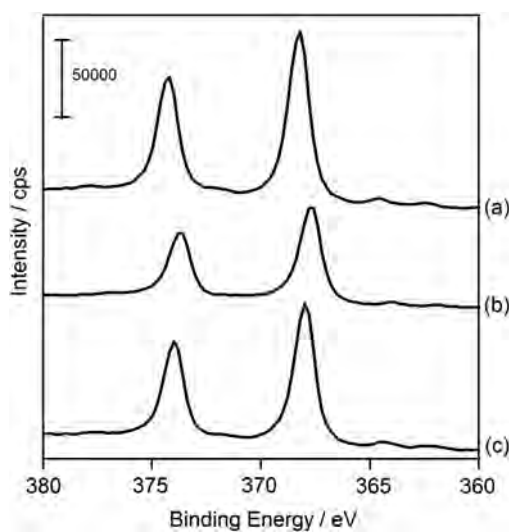


Fig. 2. Ag 3d XPS of (a) Ag-A, (b) Ag-K, and (c) Ag-KC.

Fig. 3 shows the Raman spectra of Ag powders used in this study. Ag₂O and Ag₂CO₃ are used as references. The Raman spectrum of Ag-K exhibited an intense band around 661 cm⁻¹ and small bands around 485, 758, and 960 cm⁻¹ (Fig. 3(b)). We assigned the band at 661 cm⁻¹ to subsurface oxygen species in the vicinity of defects and the other small bands around 485, 758, and 960 cm⁻¹ to dissolved atomic oxygen in the silver lattice, Ag^{III}=O species, and adsorbed

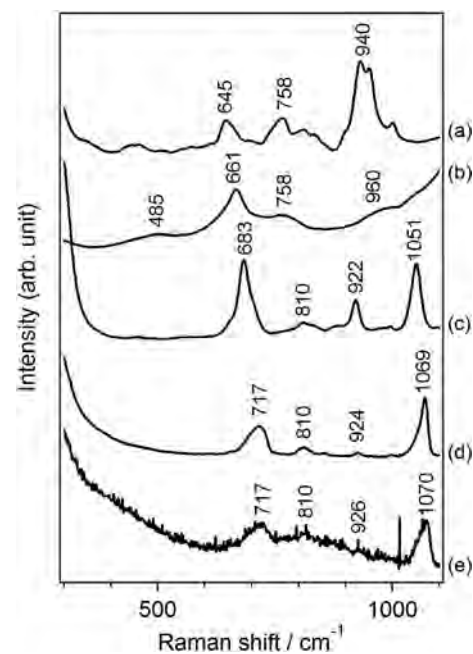


Fig. 3. Raman spectra of (a) Ag-A, (b) Ag-K, and (c) Ag-KC, together with (d) Ag₂CO₃ and (e) Ag₂O as references.

O_2^- species, respectively, although the bands appeared at a different Raman shift from those of previous reports [40–44]. This difference is possibly due to the difference in morphology (size and shape) between Ag-K and previously reported Ag metal. The Raman spectrum of Ag-A powder exhibited a relatively intense band around 940 cm^{-1} , which is attributable to adsorbed O_2^- and small bands around 645 and 758 cm^{-1} , which are attributable to subsurface oxygen species and $Ag^{III}=O$ species, respectively (Fig. 3(a)). The Raman bands of Ag-A were much weaker than those of Ag-K (Fig. S2). In particular, the band around 661 cm^{-1} of Ag-K was (ca. 25 times larger than that around 645 cm^{-1} of Ag-A). It has been reported that an intense band derived from subsurface oxygen species in the vicinity of defects was observed on a Ag catalyst having a highly defected structure and not on that with smooth structures. Thus, the much higher intensity of the band around 661 cm^{-1} of Ag-K than that of Ag-A indicates a highly defected structure and a large amount of subsurface oxygen species for Ag-K compared to Ag-A, although accurate results are not possible owing to the limitations of surface-enhanced Raman spectroscopy [40]. Transmission electron microscopy analysis also showed the defective worm-like structure of Ag-K and the spherical smooth surface of Ag-A (Fig. S3). Compared to Ag-A, the AgO_x species on Ag-K were stable to heat under H_2 flow (Fig. 4). In other words, oxygen species in the boundary of the Ag particle or a defected structure are more stable than those in a Ag particle with a smooth surface [40]. For Ag-KC, the Raman spectrum contained bands at approximately the same Raman shifts as those of Ag_2CO_3 (Fig. 3(c) and (d)); comparable bands were also observed on the spectrum of as purchased Ag_2O (Fig. 3(e)). The Raman spectrum of treated Ag_2O is shown in Fig. S4. Ag-KC might have a Ag_2O layer adsorbing CO_2 ,

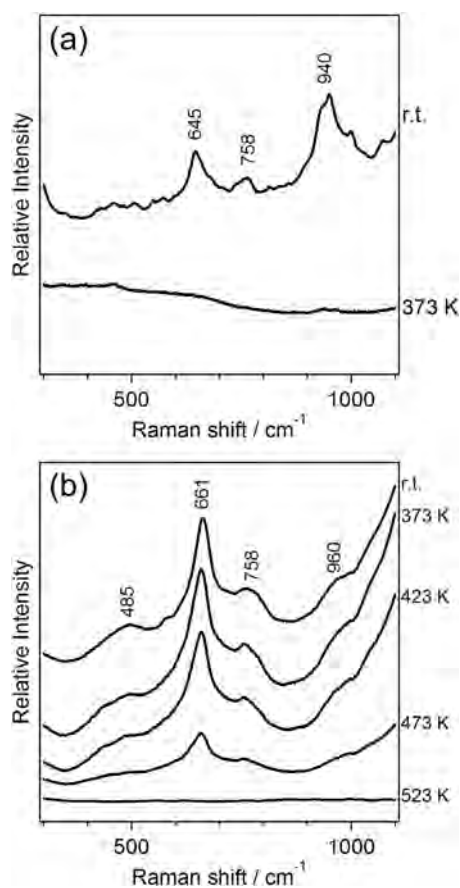


Fig. 4. In situ Raman spectra obtained on (a) Ag-A and (b) Ag-K under H_2 flow at various temperatures.

although the resulting Ag_2CO_3 layer was not detected by XRD (Fig. S1). Table 1 summarizes the results of physical characterization of the Ag powders.

3.2. Electrochemical characterization

Fig. 5 shows the CVs of Ag catalysts in a N_2 saturated 0.1 M NaOH aqueous solution. All Ag catalysts exhibited three anodic peaks and a cathodic peak. The feature of CVs, particularly of the anodic curve, was different from each other. The anodic curve had three peaks derived from silver dissolution and the formation of a surface monolayer of Ag_2O films at ca. 0.23 V (denoted as A_1), the formation of $AgOH$ at ca. 0.30 V (A_2), and the formation of Ag_2O at ca. 0.38 V (A_3) (Table S1). The Ag-A anodic curve was well consistent with that of previously reported Ag spherical nanoparticles [10,30] which agree with the result of physical characterization by SEM and Raman spectroscopy. Ag-K presented smaller peak current ratios of A_1/A_3 and A_2/A_3 than Ag-A (Table S1), and the anodic curve was similar to that of polycrystalline Ag reported elsewhere. Thus, in the case of Ag-K, the CV analysis results supported the physical characterization that Ag-K had defected structures and angular shapes. The CV of Ag-KC was similar to that of Ag-K. It is suggested that Ag-KC with angular shapes and Ag_2CO_3 on the surface has defective structures. On the basis of these results, it is reasonable to conclude that the surfaces of Ag-K and Ag-KC are more defective than Ag-A.

Fig. 6 shows Pb_{upd} stripping voltammograms for the series of Ag catalysts [45]. The Pb_{upd} stripping and deposition reaction on Ag in alkaline solutions can be represented as follows.



It should be noted that the CVs of Ag catalysts (Fig. 5) do not exhibit redox peaks in the potential range of Pb_{upd} stripping voltammograms (Fig. 6). Thus, the anodic and cathodic peaks shown in Fig. 6 are derived from the stripping and deposition of Pb, respectively. The Pb_{upd} stripping curves (anodic curves) of the Ag catalysts show two representative peaks at ca. -0.50 (denoted as S_1) and -0.55 V (S_2) vs $Hg/HgO/OH^-$. The feature of the voltammogram was similar to that of Ag nanoparticles in 0.1 M KOH aqueous solutions, as reported previously [35]. The three catalysts exhibited different ratios of S_1 to S_2 peak current of the anodic curves. More specifically, Ag-A exhibited the highest peak current ratio, and Ag-K showed the lowest. It is possible that S_1 and S_2 are derived from smooth and defective surfaces, respectively.

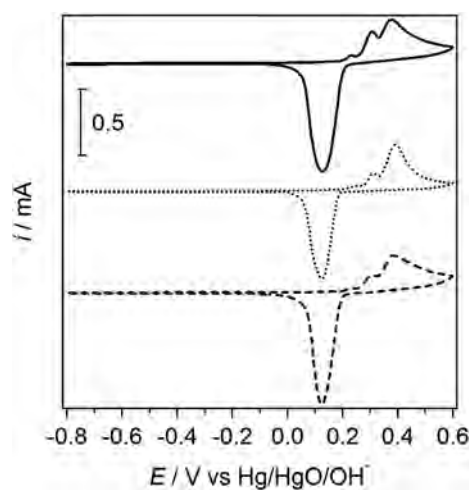


Fig. 5. Cyclic voltammograms of Ag-A (solid), Ag-K (dotted), and Ag-KC (dashed) in N_2 saturated 0.1 M NaOH aqueous solution. Scan rate: 10 mV s^{-1} . The amount of Ag metal on a disk electrode of Ag-A: $30\text{ }\mu\text{g}$; Ag-K: $15\text{ }\mu\text{g}$; Ag-KC: $90\text{ }\mu\text{g}$.

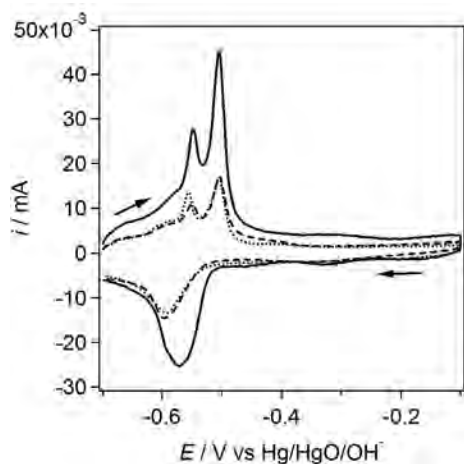


Fig. 6. Strip voltammograms of Pb_{upd} on Ag-A (solid), Ag-K (dotted), and Ag-KC (dashed) in N_2 saturated 0.1 M NaOH + 125 μM $\text{Pb}(\text{NO}_3)_2$ solution. Scan rate: 10 mV s^{-1} . The amount of Ag metal on a disk electrode of Ag-A: 30 μg ; Ag-K: 15 μg ; Ag-KC: 90 μg .

The electrochemically accessible surface area (ESA) of Ag catalysts was determined from underpotential-deposited lead (Pb_{upd}) because Ag is inactive for the deposition and stripping of CO and H_{upd} which is a standard technique for surface area determination of a Pt catalyst. The ESAs of the Ag catalysts were evaluated from the anodic peak area, i.e., the stripping charge of Pb_{upd} using 260 $\mu\text{C cm}^{-2}$ of charge density (Fig. S5) [8,35,46,47]. The calculated ESAs are listed in Table 1. The ESA of Ag-A was slightly smaller than the corresponding S_{BET} . However, it is interesting to note that for Ag-K and Ag-KC, the ESAs were larger than the S_{BET} . In fact, the ratio of ESA to S_{BET} ($\text{ESA}/S_{\text{BET}}$) decreased in the order of Ag-K > Ag-KC > Ag-A, and $\text{ESA}/S_{\text{BET}}$ of Ag-K and Ag-KC was more than 100%. The physical characterization described above indicates that Ag-K and Ag-KC have surface oxygen species in the defected structure and the Ag_2CO_3 surface layer, respectively. However, Ag-A has a smooth surface and easily reduced AgO_x species (Table 1). These oxidized Ag species would be reduced in the ORR measurement according to the Pourbaix diagrams [48]. Thus, Ag species with an oxidized surface and/or defect increases the ESA during the electrochemical measurement. It is suggested that such Ag surfaces induce a roughened surface and/or decomposition into small Ag particles. These results indicate that the ESA is accurate for the Ag

surface area during the ORR; however, BET is not. Therefore, we used the ESA in the following evaluation of the ORR activity.

3.3. ORR measurement

The ORR measurements were performed using the Ag powders in an oxygen saturated 0.1 M NaOH aqueous solution. Fig. 7(a) shows the oxygen reduction polarization curves obtained on Ag-A, Ag-K, and Ag-KC physically mixed with CB. The Ag loading of Ag-A and Ag-K was 60 wt%. However, the Ag loading of Ag-KC was 90 wt% because its low Ag surface area increases catalyst thickness on a disk electrode, which prevents proper evaluation of catalytic activity for the ORR [46]. The amounts of Ag catalysts on a RDE were optimized according to a recent report by Markovic et al. (Fig. S6) [46].

We calculated the mass activity (j_{M}) of the Ag catalysts by normalization of the current at $-0.2 \text{ V vs Hg/HgO/OH}^-$ ($i_{-0.2 \text{ V}}$) with Ag weight on a disk electrode. As a reference, the ORR was also conducted using commercial Ag/C with 60 wt% Ag loading (E-Tek), which is denoted as Ag/C-E (Fig. S7: the ORR curve. Fig. S8: Pb_{upd} strip voltammogram; 1.5 $\text{m}^2 \text{g}^{-1}$ of ESA. Fig. S1: XRD; 79 nm of crystallite size. Fig. S9: SEM image.), and j_{M} was calculated [3]. The j_{M} value decreased in the order of Ag-K (19.7 $\text{mA mg}_{\text{Ag}}^{-1}$) > Ag-A (12.3 $\text{mA mg}_{\text{Ag}}^{-1}$) > Ag/C-E (7.7 $\text{mA mg}_{\text{Ag}}^{-1}$) > Ag-KC (3.3 $\text{mA mg}_{\text{Ag}}^{-1}$), which was consistent with crystallite size. It is noteworthy that Ag-A and Ag-K physically mixed with CB showed higher j_{M} than commercially available Ag/C-E catalysts (1.6 and 2.6 times, respectively).

The catalytic activity per Ag surface area was evaluated from the potential at $-25 \mu\text{A cm}_{\text{Ag}}^{-2}$ of ESA-normalized current density, as shown in Fig. 7(b) [7]. Here we did not use S_{BET} to calculate the specific activity because, as described above, the metal surface area would change under the ORR measurement. As a result, the potential decreased in the order of Ag-K \approx Ag-KC > Ag-A. The result indicates that the catalytic activity per Ag surface area decreased in the order of Ag-K \approx Ag-KC > Ag-A. For further inspection of the catalytic activity, mass-transfer independent kinetics for the ORR on the three well-characterized Ag catalysts were calculated using the Koutecky–Levich (K–L) equation:

$$\frac{1}{j} = \frac{1}{j_{\text{k}}} + \frac{1}{j_{\text{d}}} = \frac{1}{nFkC_0} + \frac{1}{0.62nFD^{2/3}v^{-1/6}C_0\omega^{1/2}}$$

where j_{k} and j_{d} are the kinetic and diffusion limited current densities, n is the exchange electron number, k is the kinetic constant, F is the Faraday constant, D is the O_2 diffusion coefficient in 0.1 M

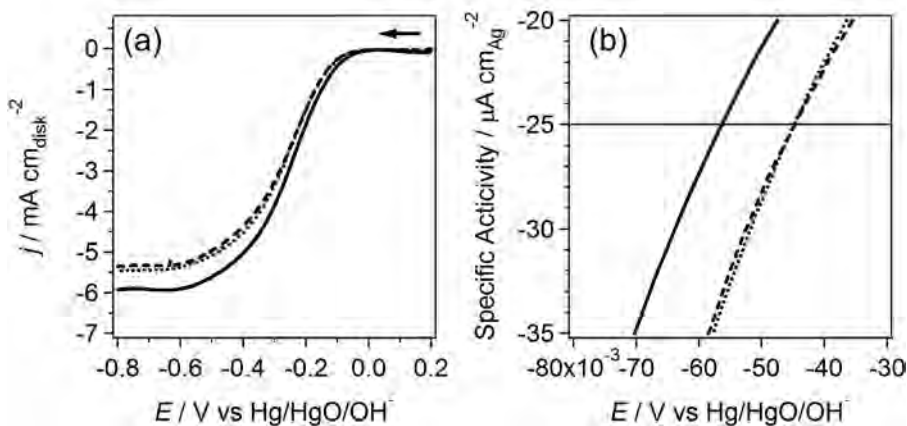


Fig. 7. (a) Oxygen reduction polarization curves obtained on Ag-A (solid), Ag-K (dotted), and Ag-KC (dashed) in O_2 saturated 0.1 M NaOH aqueous solution. Rotation rate: 2500 rpm. Scan rate: 20 mV s^{-1} . The amount of Ag metal on a disk electrode of Ag-A: 30 μg ; Ag-K: 15 μg ; Ag-KC: 90 μg . The current density (j) was calculated using the geometric surface area of a rotating disk electrode. (b) ESA-normalized current density (j_{s}) of Ag-A (solid), Ag-K (dotted), and Ag-KC (dashed). The potentials at $-25 \mu\text{A cm}_{\text{Ag}}^{-2}$ is a benchmark for comparison [7].

Table 2
Specific activity ($j_{k:ESA}$) and exchange electron number (n) for the ORR.

Catalyst	$j_{k:ESA}$ (mA cm _{Ag} ⁻²) ^a	n ^b
Ag-A	0.45	3.8
Ag-K	0.74	3.6
Ag-KC	0.70	3.5

^a Calculated from the intercept of the line fitted to the Koutecky–Levich (K–L) plot for $j_{-0.2}$ V (Fig. S10). $j_{k:ESA} = j_k \times A / (ESA \times wt_{Ag})$, where wt_{Ag} is the Ag weight on a disk electrode, and A is the area of disk electrode (0.196 cm²).

^b Calculated from the slope of the K–L plot for $j_{-0.5}$ V (Fig. S10).

NaOH (1.93×10^{-5} cm² s⁻¹), ν is the kinematic viscosity (1.09×10^{-2} cm² s⁻¹), c_{O_2} is the O₂ concentration in electrolyte (1.26×10^{-6} mol cm⁻³), and ω is the rotation rate in the radian [49]. The j_k value was calculated from the intercept of the line fitted to the K–L plot for j at -0.2 V vs Hg/HgO/OH⁻ (Fig. S10). The specific activity ($j_{k:ESA}$) was obtained using the ESA ($j_{k:ESA} = i_k/ESA = j_k/A/ESA$, where A is the area of the disk electrode), as shown in Table 2. The $j_{k:ESA}$ value decreased in the order of Ag-K > Ag-KC > Ag-A, which is consistent with the order of the potential at -25 μV cm_{Ag}⁻² (Fig. 7(b)). It should be noted that the $j_{k:ESA}$ value does not depend on Ag particle size. The Ag size investigated in this study (>10 nm) has an insignificant effect on the specific activity, although much smaller Ag particles (<3 nm) might show unique size-dependent activity due to the large fraction of coordinatively unsaturated Ag atoms and quantum size effect. From the K–L plot for j at -0.5 V vs Hg/HgO/OH⁻ ($j_{-0.5}$ V), the electron exchange numbers (n) for Ag-A, Ag-K, and Ag-KC were determined to be 3.8, 3.6, and 3.5, respectively (Table 2). The reason for the difference in the $j_{k:ESA}$ and n values between the Ag catalysts is discussed below.

The exchange electron numbers for all Ag catalysts were close to but slightly less than four. The n values were comparable to those previously reported by Buttry et al., who showed slightly less than a four-electron pathway using Ag nanoparticles and polycrystalline Ag [8]. In the present study, the n value decreased in the order of Ag-A > Ag-K > Ag-KC. In other words, the fraction of the two-electron pathway on Ag-K and Ag-KC is larger compared to that on Ag-A. The physical and electrochemical characterization indicates that Ag-K with subsurface oxygen species and Ag-KC with Ag₂CO₃ have defective surfaces. Therefore, the defective and oxidized surfaces of Ag-A and Ag-KC cause the two-electron pathway. It has been reported that strongly adsorbed OH_{ad} on a defective surface decreases the neighboring Ag sites to adsorb O₂ with both O, which results in an increase in the fraction of the two-electron pathway [8].

As described above, the $j_{k:ESA}$ value decreased in the order of Ag-K > Ag-KC > Ag-A (Table 2). This was due to higher affinity with O₂ for Ag-K and Ag-KC than for Ag-A. Previously, Bliznac et al. showed that the activation energy for the ORR is surface structure sensitive [36]. Buttry et al. showed a higher rate constant on polycrystalline Ag with a defective surface than Ag nanoparticles with a smooth surface [8]. On the basis of these results, we propose that the defective and oxidized surface of Ag-K and Ag-KC can more strongly adsorb O₂ and can conduct the first charge-transfer with lower activation energy than Ag-A with a smooth surface.

4. Conclusions

The effect of the Ag particle morphology and surface chemical state on the ORR was investigated using various well-characterized Ag powders.

Ag catalysts having AgO_x on a defective surface and Ag₂CO₃ surface layer demonstrated more than 100% of ESA/SA_{BET}, which was higher than that having easily reduced AgO_x on a smooth

surface. It is assumed that the defective surface and the oxidized species induce a roughened surface and/or decompose into small Ag particles during the ORR, thereby causing an increase of ESA.

All Ag powders physically mixed with CB exhibited close to a four-electron pathway for the ORR. However, the Ag particles with defective and angular surfaces showed smaller n values than those with smooth surfaces. It is strongly suggested that the defective and oxidized (AgO_x or Ag₂CO₃) surface decreases the number of Ag neighboring sites required for a four-electron pathway. On the other hand, due to high affinity for O₂, Ag particles with defective and oxidized surfaces represented higher specific activity than those with smooth surfaces.

Acknowledgment

This study was supported by Grant-in-Aid from the Ministry of Education, Culture, Sports, Science and Technology, Japan (MEXT) program “Elements Strategy Initiative to Form Core Research Center” (since 2012) and by a project of the New Energy and Industrial Technology Development Organization (NEDO) Japan, “Rare Metal Substitute Materials Development”. The authors thank Tokuyama Corp. for supplying ionomer solution (AS-4 solution).

Appendix A. Supplementary data

Supplementary data related to this article can be found at <http://dx.doi.org/10.1016/j.jpowsour.2013.07.034>.

References

- [1] S.F. Lu, J. Pan, A.B. Huang, L. Zhuang, J.T. Lu, Proc. Natl. Acad. Sci. U. S. A. 105 (2008) 20611.
- [2] J.R. Varcoe, R.C.T. Slade, Fuel Cells 5 (2005) 187.
- [3] J.R. Varcoe, R.C.T. Slade, G.L. Wright, Y.L. Chen, J. Phys. Chem. B 110 (2006) 21041.
- [4] H. Bunazawa, Y. Yamazaki, J. Power Sources 182 (2008) 48.
- [5] J.S. Spendelov, A. Wieckowski, Phys. Chem. Chem. Phys. 9 (2007) 2654.
- [6] J.-S. Park, S.-H. Park, S.-D. Yim, Y.-G. Yoon, W.-Y. Lee, C.-S. Kim, J. Power Sources 178 (2008) 620.
- [7] J. Suntivich, H.A. Gasteiger, N. Yabuuchi, H. Nakanishi, J.B. Goodenough, Y. Shao-Horn, Nat. Chem. 3 (2011) 546.
- [8] P. Singh, D.A. Buttry, J. Phys. Chem. C 116 (2012) 10656.
- [9] L. Demarconnay, C. Coutanceau, J.M. Léger, Electrochim. Acta 49 (2004) 4513.
- [10] J. Guo, A. Hsu, D. Chu, R. Chen, J. Phys. Chem. C 114 (2010) 4324.
- [11] J.-J. Han, N. Li, T.-Y. Zhang, J. Power Sources 193 (2009) 885.
- [12] L. Jiang, A. Hsu, D. Chu, R. Chen, J. Electrochem. Soc. 156 (2009) B643.
- [13] L. Kuai, B.Y. Geng, S.Z. Wang, Y.Y. Zhao, Y.C. Luo, H. Jiang, Chem. Eur. J. 17 (2011) 3482.
- [14] Y. Lu, W. Chen, J. Power Sources 197 (2012) 107.
- [15] C. Tan, F. Wang, J. Liu, Y. Zhao, J. Wang, L. Zhang, K.C. Park, M. Endo, Mater. Lett. 63 (2009) 969.
- [16] Q.E. Tang, L.H. Jiang, J. Qi, Q. Jiang, S.L. Wang, G.Q. Sun, Appl. Catal. B Environ. 104 (2011) 337.
- [17] W. Chen, S.W. Chen, Angew. Chem. Int. Ed. 48 (2009) 4386.
- [18] L. Jiang, A. Hsu, D. Chu, R. Chen, Electrochim. Acta 55 (2010) 4506.
- [19] M. Shao, T. Yu, J.H. Odell, M. Jin, Y. Xia, Chem. Commun. 47 (2011) 6566.
- [20] S.N.S. Goubert-Renaudin, A. Wieckowski, J. Electroanal. Chem. 652 (2011) 44.
- [21] L. Mao, D. Zhang, T. Sotomura, K. Nakatsu, N. Koshiba, T. Ohsaka, Electrochim. Acta 48 (2003) 1015.
- [22] W. Sun, A. Hsu, R.R. Chen, J. Power Sources 196 (2011) 627.
- [23] T. Takakuwa, T. Kenko, M. Saito, H. Daimon, A. Tasaka, M. Inaba, H. Shiroishi, T. Hatai, J. Kuwano, ECS Trans. 41 (2011) 2185.
- [24] N. Ohno, Y. Akeboshi, M. Saito, J. Kuwano, H. Shiroishi, T. Okumura, Y. Uchimoto, Top. Catal. 52 (2009) 903.
- [25] F.H.B. Lima, C.D. Sanches, E.A. Ticianelli, J. Electrochem. Soc. 152 (2005) A1466.
- [26] S. Guo, S. Zhang, L. Wu, S. Sun, Angew. Chem. Int. Ed. 51 (2012) 11770.
- [27] H. Wu, W. Chen, J. Am. Chem. Soc. 133 (2011) 15236.
- [28] P. Singh, K.L. Parent, D.A. Buttry, J. Am. Chem. Soc. 134 (2012) 5610.
- [29] L. Nagle, A. Ahern, D. Burke, J. Solid State Electrochem. 6 (2002) 320.
- [30] V. Bansal, V. Li, A.P. O'Mullane, S.K. Bhargava, CrystEngComm 12 (2010) 4280.
- [31] J. Guo, H. Li, H. He, D. Chu, R. Chen, J. Phys. Chem. C 115 (2011) 8494.
- [32] J. Kim, S.W. Lee, C. Carlton, Y. Shao-Horn, J. Phys. Chem. Lett. 2 (2011) 1332.
- [33] K. Matsuzawa, T. Fukushima, M. Inaba, Electrochim. Acta 55 (2010) 169.
- [34] A. Toge, T. Yokono, M. Saito, H. Daimon, A. Tasaka, M. Inaba, ECS Trans. 41 (2011) 2283.

- [35] G.K.H. Wiberg, K.J.J. Mayrhofer, M. Arenz, *Fuel Cells* 10 (2010) 575.
- [36] B.B. Blizanac, P.N. Ross, N.M. Markovic, *J. Phys. Chem. B* 110 (2006) 4735.
- [37] A. Satsuma, J. Shibata, A. Wada, Y. Shinozaki, T. Hattori, M.O. Masakazu Anpo, Y. Hiromi, *Studies in Surface Science and Catalysis*, vol. 145, Elsevier, 2003, p. 235.
- [38] N. Ikeo, Y. Iijima, N. Nimura, M. Sigematsu, T. Tazawa, S. Matsumoto, K. Kojima, Y. Nagasawa, *Handbook of X-ray Photoelectron Spectroscopy*, JEOL, 1991.
- [39] C.D. Wagner, W.M. Riggs, L.E. Davis, J.F. Moulder, *Handbook of X-ray Photoelectron Spectroscopy*, Perkin-Elmer Corp., 1979.
- [40] G.J. Millar, J.B. Metson, G.A. Bowmaker, R.P. Cooney, *J. Chem. Soc. Faraday Trans.* 91 (1995).
- [41] X. Bao, M. Muhler, B. Pettinger, R. Schlögl, G. Ertl, *Catal. Lett.* 22 (1993) 215.
- [42] G.I.N. Waterhouse, G.A. Bowmaker, J.B. Metson, *Appl. Surf. Sci.* 214 (2003) 36.
- [43] B. Pettinger, X. Bao, I.C. Wilcock, M. Muhler, G. Ertl, *Phys. Rev. Lett.* 72 (1994) 1561.
- [44] G.I.N. Waterhouse, G.A. Bowmaker, J.B. Metson, *Phys. Chem. Chem. Phys.* 3 (2001) 3838.
- [45] E. Herrero, L.J. Buller, H.D. Abruna, *Chem. Rev.* 101 (2001) 1897.
- [46] K.J.J. Mayrhofer, D. Strmcnik, B.B. Blizanac, V. Stamenkovic, M. Arenz, N.M. Markovic, *Electrochim. Acta* 53 (2008) 3181.
- [47] E. Kirowa-Eisner, Y. Bonfil, D. Tzur, E. Gileadi, *J. Electroanal. Chem.* 552 (2003) 171.
- [48] M. Pourvaix, *Atlas of Electrochemical Equilibria in Aqueous Solutions*, Pergamon Press, Oxford, 1966.
- [49] A.J. Bard, L.R. Faulkner, *Electrochemical Methods: Fundamentals and Applications*, Wiley, New York, 2001.

Total Synthesis of the Antibiotic Kendomycin: A Macrocyclization Using the Tsuji–Trost Etherification**

Tetsuya Sengoku, Shu Xu, Kenji Ogura, Yoshinori Emori, Kenji Kitada, Daisuke Uemura, and Hirokazu Arimoto*

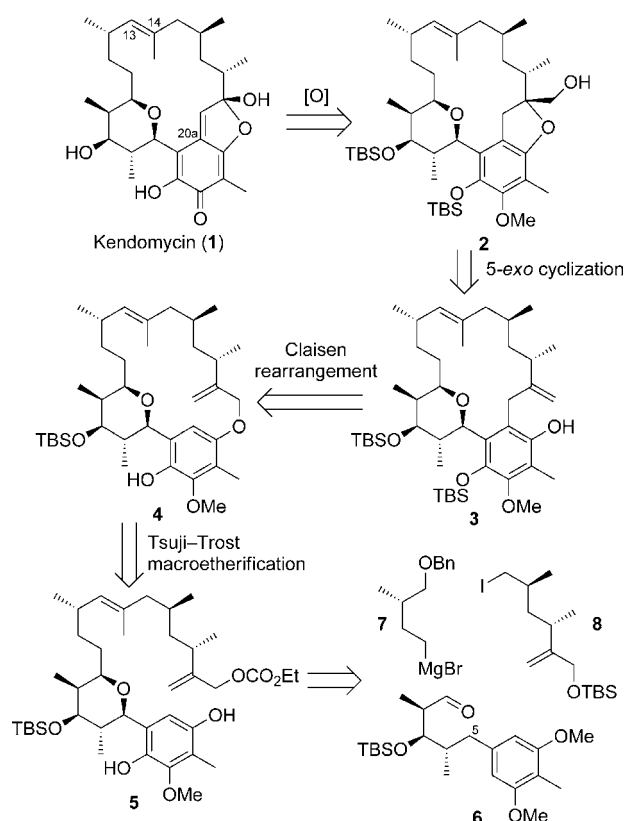
Abstract: A highly stereocontrolled, convergent total synthesis of kendomycin [(–)-TAN2162], an ansa-macrocyclic antibiotic, is reported. The key of the strategy is an unprecedented Tsuji–Trost macrocyclic etherification, followed by a transannular Claisen rearrangement to construct the 18-membered carbocyclic framework. The oxa-six- and five-membered rings were also stereoselectively constructed respectively by a cascade oxidative cyclization at an unfunctionalized benzylic position and using a one-pot epoxidation/5-*exo-tet* epoxide opening.

Kendomycin [(–)-TAN2162; **1**; for structure see Scheme 1] is an ansa-macrocyclic polyketide comprising a quinone methide chromophore, and was originally isolated as an antagonist for the endothelin receptor,^[1] and as an antiosteoporotic agent.^[2] Zeeck and Bode reported that **1** exhibited not only cytotoxic effects against a number of human tumor cell lines but also a strong antibacterial activity against both Gram-positive and Gram-negative bacteria, notably methicillin-resistant *Staphylococcus aureus* (MRSA) and vancomycin intermediate *S. aureus* (VISA) Mu50 strain.^[3] The architectural structure and multiple biological activities of **1** have attracted significant interest in the past decade from biological,^[4] biosynthetic,^[5] and chemically synthetic^[6] perspectives.

The macrocyclic carbon framework of **1** represents a major challenge for an efficient chemical synthesis. Among all the achieved total syntheses and formal total syntheses, several macrocyclization strategies, including C-glycosylation,^[7a] ring-closing metathesis (RCM),^[7b,c,e,f,8] the Barbier reaction,^[7d] photo-Fries rearrangement,^[7e,f] Dötz benzannulation,^[7g] and Prins reaction^[7h] have been reported,

albeit in modest yields. We have attempted an RCM strategy for the macrocyclization at the C13–C14 double bond of **1**.^[8] Unfortunately, the unnatural *Z* diastereomer was the predominant product. However, in our studies the Claisen rearrangement was found to work as a powerful tool for the introduction of a carbon substituent at the highly hindered C20a position.^[8a] We finally found that the macrocyclic etherification/Claisen rearrangement combination could be used for the construction of kendomycin's carbon framework.

The retrosynthetic analysis of **1** is outlined in Scheme 1. It could be derived from **2** through aromatic oxidation and oxidative removal of the terminal hydroxymethyl group. The five-membered ring of **2** could possibly be constructed selectively by a 5-*exo* cyclization of the phenol and the neighboring olefin of **3**. The macro-carbocycle of **3** was envisioned to be derived from the transannular Claisen rearrangement of the allyl aryl ether **4**, which comes from hydroquinone **5** using a selective macrocyclization at the less hindered hydroxy group by means of Tsuji–Trost etherifica-



Scheme 1. Retrosynthetic analysis. TBS = *tert*-butyldimethylsilyl.

[*] Dr. T. Sengoku,^[S1] Dr. S. Xu,^[S1] K. Ogura, Y. Emori, K. Kitada, Prof. Dr. H. Arimoto
Graduate School of Life Sciences, Tohoku University
2-1-1 Katahira, Sendai 980-8577 (Japan)
E-mail: arimoto@biochem.tohoku.ac.jp
Homepage: <http://www.agri.tohoku.ac.jp/bunseki/index-j.html>

Prof. Dr. D. Uemura
Department of Chemistry, Faculty of Science, Kanagawa University
Hiratsuka 259-1293 (Japan)

[[†]] Current address: Department of Materials Science, Faculty of Engineering, Shizuoka University, Shizuoka 432-8561 (Japan)

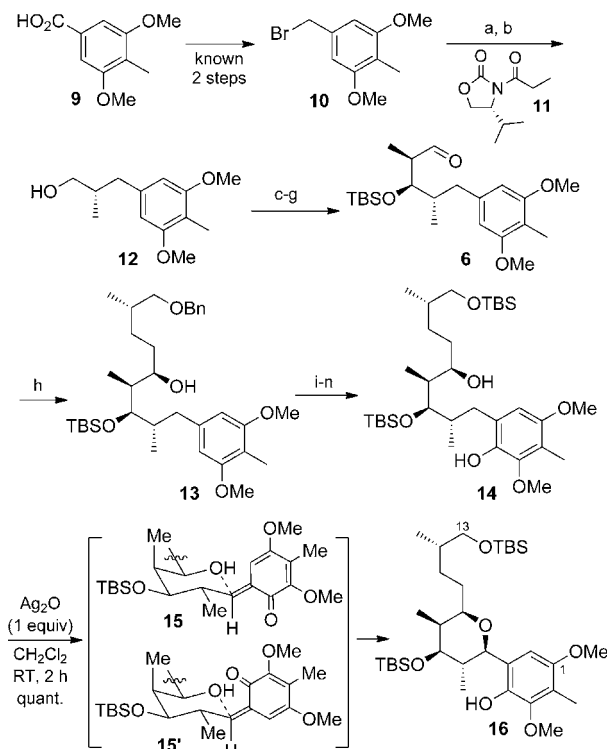
[*] These authors contributed equally to this work.

[**] We are grateful for the financial support of Grants-in-Aid for Scientific Research (Nos.18032010 and 21310136) from the JSPS. T.S. acknowledges the JSPS for the Research Fellowships for Young Scientists.

Supporting information for this article is available on the WWW under <http://dx.doi.org/10.1002/anie.201400305>.

tion. The macrocyclization precursor **5** would be prepared convergently from the aldehyde **6**, alkylmagnesium **7**, and iodide **8**. The tetrahydropyran ring could be cyclized diastereoselectively at the unfunctionalized C5-position by a Ag_2O -triggered cascade reaction, as we have previously reported.^[8a]

We have previously reported on the preparation of the C1–C13 segment of **1**,^[8a] and herein, we present a modified scalable synthetic route (Scheme 2). The modified route

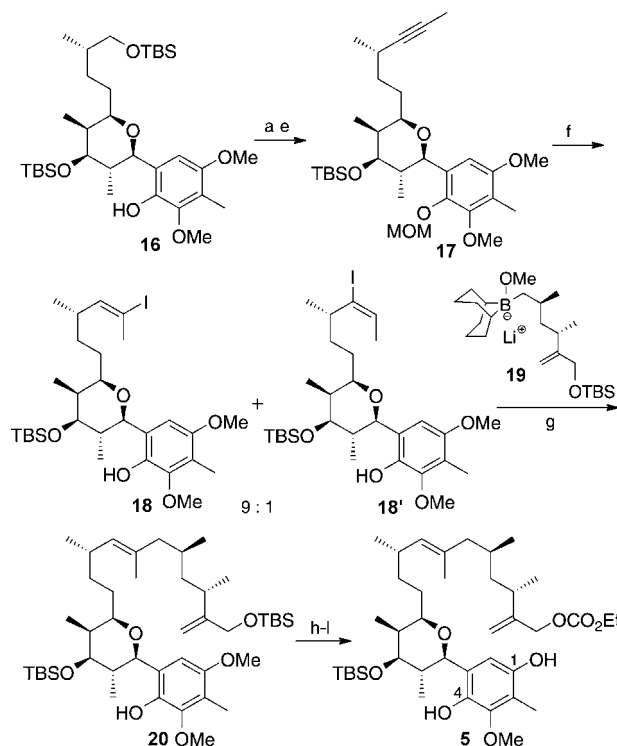


Scheme 2. Synthesis of C1–C13 segment **16**: a) **11**, NaHMDS, THF, -60°C ; b) LiAlH_4 , THF, -78°C to 0°C , 82% (2 steps); c) $(\text{COCl})_2$, DMSO, Et_3N , CH_2Cl_2 , -78°C to 0°C ; d) (R,R) -[(*E*)-2-butenyl]diisopropyl tartrate boronate, 4 Å M.S., PhMe, -78°C , 77% (2 steps); e) TBSOTf, 2,6-lutidine, CH_2Cl_2 , 0°C , quant.; f) OsO_4 (cat.), NMO, acetone/ H_2O (4:1), RT; g) NaIO_4 , $\text{EtOH}/\text{H}_2\text{O}$ (1:1), RT, 93% (2 steps); h) **7**, -78°C , THF, quant. (d.r. 15:1); i) H_2 , $\text{Pd}(\text{OH})_2/\text{C}$, EtOAc , RT; j) TBSOTf, DMAP, Et_3N , CH_2Cl_2 , RT, 85% (2 steps); k) $\text{HBr}_3\cdot\text{Py}$, K_2CO_3 , Py, 0°C to RT; l) ethyl vinyl ether, PPTS, RT, quant. (2 steps); m) $n\text{BuLi}$, $\text{B}(\text{OMe})_3$, THF, -78°C to RT, then 30% H_2O aq., Na_2CO_3 , RT, 90%; n) PPTS, $n\text{PrOH}$, RT, 99%. DMAP = 4-(*N,N*-dimethylamino)pyridine, DMSO = dimethylsulfoxide, HMDS = hexamethyldisilazide, M.S. = molecular sieves, NMO = *N*-methylmorpholine *N*-oxide, PPTS = pyridinium *p*-toluenesulfonate, Py = pyridine, Tf = trifluoromethanesulfonyl, THF = tetrahydrofuran.

commenced with the commercially available benzoic acid **9**, which was easily converted into the aryl bromide **10** with a two-step procedure.^[9] Evans asymmetric alkylation^[10] and reduction furnished the *S*-alcohol **12** with more than 99% *ee*, which was determined using the modified Mosher's method.^[11] Swern oxidation and Roush crotylation^[12] afforded a single diastereomer containing the three desired contiguous stereogenic centers, which was further transformed to aldehyde **6**. Nucleophilic addition of the Grignard

compound **7**^[13] to **6** gave a 15:1 diastereomer mixture of the secondary alcohol **13**, favoring the expected Felkin–Anh-type product. This selectivity is higher than our previous result (5.5:1) which was obtained using a similar alkyl lithium nucleophile.^[8a] After introduction of a phenolic hydroxy group to the aromatic ring, **14** was stereoselectively cyclized at the unfunctionalized benzylic position under phenol oxidation conditions (Ag_2O ^[14]) and quantitatively afforded the tetrahydropyran **16** as a single diastereomer. The excellent selectivity was thought to be due to the chair-form oxamichael-addition transition-state **15** or **15'** with the bulky quinone methide in an equatorial position. This result also proposed another possibility for the unclear biosynthetic mechanism of kendomycin's pyran ring formation.^[5] With this modified route, **16** was obtained on a 3 gram scale.

The conversion of phenol **16** into **5** is shown in Scheme 3. After a manipulation of the protecting groups, Swern oxidation and Corey–Fuchs protocol furnished the alkyne **17**. Hydrozirconation with the Schwartz reagent^[15] and subsequent iodination proceeded with high regioselectivity (9:1) along with removal of a MOM ether. The regioisomers **18** and **18'** were not easily separable from each other, and



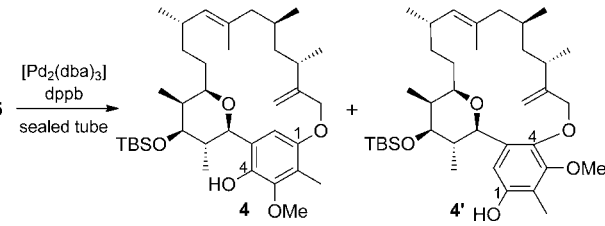
Scheme 3. Synthesis of the macrocyclization precursor **5**: a) MOMCl, NaH, THF, RT; b) PPTS, THF/ MeOH (1:1), RT, 92% (2 steps); c) $(\text{COCl})_2$ -DMSO, Et_3N , CH_2Cl_2 , -78°C ; d) CBr_4 , PPh₃, Et_3N , CH_2Cl_2 , -78°C , 72% (2 steps); e) $n\text{BuLi}$, MeI, THF, -78°C to RT, 98%; f) $[\text{HZrCp}_2\text{Cl}]$, PhH, RT, then I_2 ; g) **8** (2 equiv), $t\text{BuLi}$, Et_2O , -78°C , then MeO-9-BBN, THF, -78°C to RT, then **18** + **18'**, $[\text{Pd}(\text{dppf})_2\text{Cl}_2]\cdot\text{CH}_2\text{Cl}_2$ (20 mol%), 3 M K_3PO_4 aq., DMF, RT, 87% (2 steps); h) MOMCl, NaH, THF, RT, 95%; i) PPTS, THF/ MeOH (1:1), RT, 73%; j) ClCO_2Et , Py, RT, 94%; k) $(\text{NH}_4)_2\text{Ce}(\text{NO}_3)_6$, $\text{MeCN}/\text{H}_2\text{O}$ (2:1), RT; l) $\text{Na}_2\text{S}_2\text{O}_4$, $\text{MeCN}/\text{H}_2\text{O}$ (1:1), 0°C , quant. (2 steps). BBN = borabicyclo[3.3.1]nonane, Cp = cyclopentadienyl, DMF = *N,N*-dimethylformamide, dppf = 1,1'-bis(diphenylphosphino)ferrocene, MOM = methoxymethyl.

were thus used as a mixture for the Suzuki–Miyaura cross-coupling reaction^[16] with boronate **19**. The boronate was prepared by lithiation and transmetalation of **8**.^[17] The desired coupling product **20** was isolated in 87% yield (two steps). Protection of **20** with MOMCl, selective removal of the terminal TBS group, carbonate formation, and exposure of the two hydroxy groups of the *p*-hydroquinone yielded the Tsuji–Trost cyclization precursor **5**.

The examination of the key palladium-catalyzed Tsuji–Trost cyclization is shown in Table 1. Although the Tsuji–Trost reaction is a well-established synthetic protocol,^[18] to the best of our knowledge, the macroetherification with this reaction has not been reported in total synthesis studies of natural products. More challenging is that our substrate, **5**, is actually a hydroquinone which contains two hydroxy nucleophiles, and is sensitive to oxidation, which may render the reaction more complicated. However, to avoid the tedious and poorly selective protecting strategy for the hindered C4–OH group, we decided to perform the cyclization with both free hydroxy groups. Eventually, it was found that the desired macrocyclic ether **4** was obtained with [Pd₂(dba)₃] and dppb at room temperature in THF,^[19] though the regioisomer **4'** was the major product (entry 1). Solvent effects were later found to have great influence on the regioselectivity, with CH₂Cl₂ giving the best result (**4/4'** = 10:1, entries 5 and 6). Notably, when the concentration of **5** was higher than 10 mM, intermolecular coupling became significant. Other palladium catalysts such as [Pd(PPh₃)₄] or Pd(OAc)₂ gave either no reaction or decomposed byproducts.^[20] Although the solvent has been shown to play a key role in the ion-pairing in the Tsuji–Trost reaction,^[21] the specific reason for the selectivity in this study is still not clear.

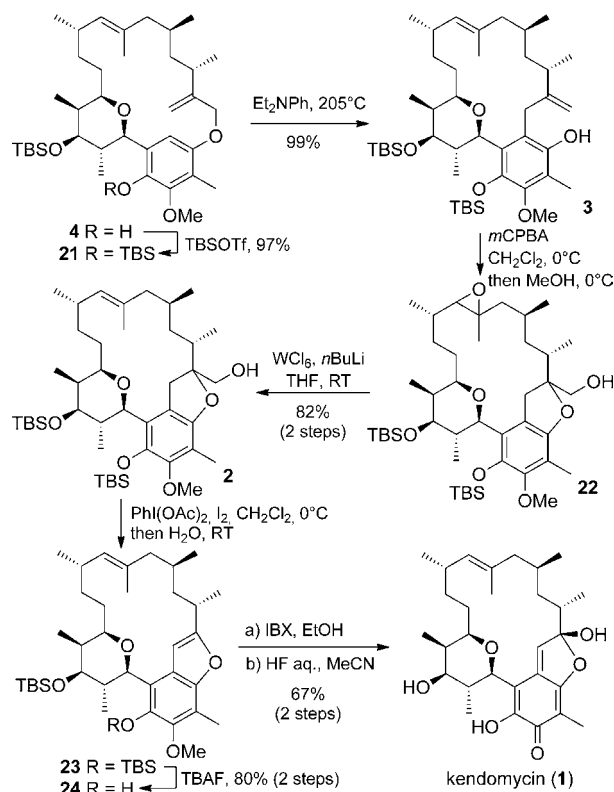
After obtaining the 18-membered macrocyclic ether, we next attempted a ring contraction through a Claisen rearrangement^[22] (Scheme 4). We have reported this transforma-

Table 1: Regioselective macrocyclization using Tsuji–Trost etherification.^[a]



Entry	[Pd ₂ (dba) ₃] (equiv)	dppb (equiv)	Solvent	T [°C]	4/4' ^[b]	Yield 4 [%] ^[c]
1	0.15	0.4	THF	RT	1:3 ^[d]	–
2	0.5	2	toluene	RT	1:1	–
3	1.1	20	DMF	60	3:5	–
4	0.2	1.6	(ClCH ₂) ₂	70	– ^[e]	–
5	0.4	10	CH ₂ Cl ₂	50	10:1	80
6	0.14	0.86	CH ₂ Cl ₂	70	10:1	71

[a] The reaction was performed with 1–5 mM of **5** in the dark in a sealed tube. [b] Determined by ¹H NMR analysis of the crude reaction mixture. [c] Yield of the isolated product. [d] Approximately 20% of the starting material remained. [e] Only starting material recovered. dba = dibenzylideneacetone, dppb = 1,4-bis(diphenylphosphino)butane.



Scheme 4. Complete total synthesis of **1**. *m*CPBA = *m*-chloroperoxybenzoic acid, TBAF = tetra-*n*-butylammonium fluoride.

tion with an acyclic substrate in refluxing Me₂NPh.^[8a] This time, after TBS protection of the phenol **4** and heating at 205 °C in Et₂NPh (a more stable solvent), **21** was smoothly converted into the desired carbocyclic **3** in 99% yield.^[23] Next, several strategies (iodoetherification, oxymercuration, etc.) were attempted to cyclize the five-membered ring of kendomycin. Eventually, epoxidation and subsequent intramolecular epoxide opening proved to be most efficient. Thus, after alkene epoxidation with *m*CPBA in CH₂Cl₂, the 5-*exo*-tet cyclization proceeded smoothly by just adding a protic solvent, MeOH, and furnished predominately one diastereomer of **22**. Since the upper trisubstituted alkene was also epoxidized during the process, a subsequent deoxygenation^[7b,c,24] afforded the compound **2** in 82% yield (two steps) as a single diastereomer. Next a hypervalent-iodine-promoted β-fragmentation of the alkoxyl radical removed the terminal hydroxymethyl group, and presumably provided an unstable intermediate *tert*-iodide, which was gradually eliminated to give the benzofuran **23**. This elimination process was accelerated by the addition of a small amount of water. The compound **23** has the same skeleton as intermediates obtained by the groups of Lee^[7a] and Mulzer.^[7e,f] Finally, the selective removal of the phenolic TBS group, oxidation, and acidic rearrangement of the resulting *o*-quinone, with the simultaneous TBS removal, accomplished the total synthesis of kendomycin.

In summary, we have achieved the total synthesis of the antibiotic kendomycin (**1**) by using a highly stereocontrolled convergent strategy. The key step of this synthetic route is the

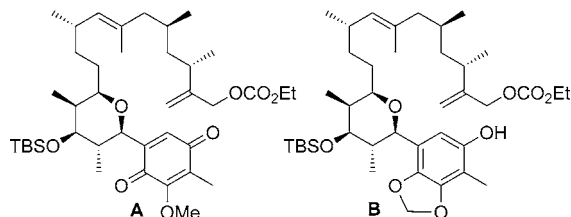
palladium-catalyzed regioselective Tsuji–Trost macroetherification/transannular Claisen rearrangement sequence to construct the macrocyclic framework. Other synthetic features include the tetrahydropyran installation by stereoselective nucleophilic addition to an aldehyde and a Ag₂O-triggered stereoselective cyclization and the establishment of a five-membered ring by one-pot epoxidation/5-*exo*-tet cyclization process.

Received: January 11, 2014
Published online: March 13, 2014

Keywords: antibiotics · macrocycles · natural products · palladium · total synthesis

- [1] a) Y. Funahashi, T. Ishimaru, N. Kawamura, JP Patent 08231551, **1996**; b) Y. Funahashi, N. Kawamura, T. Ishimaru, JP Patent 08231552, **1996**.
- [2] M. H. Su, M. I. Hosken, B. J. Hotovec, T. L. Johnston, US Patent 5728727, **1998**.
- [3] H. B. Bode, A. Zeeck, *J. Chem. Soc. Perkin Trans. 1* **2000**, 323–328.
- [4] a) Y. A. Elnakady, M. Rohde, F. Sasse, C. Backes, A. Keller, H.-P. Lenhof, K. J. Weissman, R. Müller, *ChemBioChem* **2007**, *8*, 1261–1272; b) C. O. Janssen et al., *Bioorg. Med. Chem. Lett.* **2008**, *18*, 5771–5773 (see the Supporting Information for all authors).
- [5] a) H. B. Bode, A. Zeeck, *J. Chem. Soc. Perkin Trans. 1* **2000**, 2665–2670; b) S. C. Wenzel, H. B. Bode, I. Kochems, R. Müller, *ChemBioChem* **2008**, *9*, 2711–2721.
- [6] For reviews, see: a) H. J. Martin, T. Magauer, J. Mulzer, *Angew. Chem.* **2010**, *122*, 5746–5758; *Angew. Chem. Int. Ed.* **2010**, *49*, 5614–5626; b) D. Bicchieri, Y. Borguet, L. Delaude, A. Demonceau, I. Dragutan, V. Dragutan, M. Hans, C. Jossifov, F. Nicks, Q. Willem, *Curr. Org. Synth.* **2012**, *9*, 397–405; c) M. Shan, L. Wang, Q. Zhang, G. A. O'Dooherty, *Chemtracts* **2009**, *22*, 1–17.
- [7] For total syntheses, see: a) Y. Yu, H. Men, C. Lee, *J. Am. Chem. Soc.* **2004**, *126*, 14720–14721; b) A. B. Smith III, E. F. Mesaros, E. A. Meyer, *J. Am. Chem. Soc.* **2005**, *127*, 6948–6949; c) A. B. Smith III, E. F. Mesaros, E. A. Meyer, *J. Am. Chem. Soc.* **2006**, *128*, 5292–5299; d) J. T. Lowe, J. S. Panek, *Org. Lett.* **2008**, *10*, 3813–3816; e) T. Magauer, H. J. Martin, J. Mulzer, *Angew. Chem.* **2009**, *121*, 6148–6152; *Angew. Chem. Int. Ed.* **2009**, *48*, 6032–6036; f) T. Magauer, H. J. Martin, J. Mulzer, *Chem. Eur. J.* **2010**, *16*, 507–519; g) K. Tanaka, M. Watanabe, K. Ishibashi, H. Matsuyama, Y. Saikawa, M. Nakata, *Org. Lett.* **2010**, *12*, 1700–1703; For formal total syntheses, see: h) K. B. Bahnck, S. D. Rychnovsky, *J. Am. Chem. Soc.* **2008**, *130*, 13177–13181; i) K. B. Bahnck, S. D. Rychnovsky, *Chem. Commun.* **2006**, 2388–2390.
- [8] a) T. Sengoku, H. Arimoto, D. Uemura, *Chem. Commun.* **2004**, 1220–1221; b) T. Sengoku, D. Uemura, H. Arimoto, *Chem. Lett.* **2007**, *36*, 726–727.
- [9] S. R. Kasibhatla, K. D. Hong, M. F. Boehm, M. A. Biamonte, L. Zhang, US Patent 20050113340A1, **2005**.

- [10] D. A. Evans, M. D. Ennis, D. J. Mathre, *J. Am. Chem. Soc.* **1982**, *104*, 1737–1739.
- [11] J. M. Seco, E. Quinoa, R. Riguera, *Chem. Rev.* **2004**, *104*, 17–118.
- [12] W. R. Roush, A. D. Palkowitz, K. Ando, *J. Am. Chem. Soc.* **1990**, *112*, 6348–6359.
- [13] The bromide precursor of the alkylmagnesium **7** was prepared one step from the corresponding alcohol. For a three-step synthesis of the alcohol from commercially available starting materials, see: a) T. J. Donohoe, T. J. C. O'Riordan, M. Peifer, C. R. Jones, T. J. Miles, *Org. Lett.* **2012**, *14*, 5460–5463; b) A. W. van Zijl, F. López, A. J. Minnaard, B. L. Feringa, *J. Org. Chem.* **2007**, *72*, 2558–2563.
- [14] S. R. Angle, K. D. Turnbull, *J. Am. Chem. Soc.* **1989**, *111*, 1136–1138.
- [15] D. W. Hart, T. F. Blackburn, J. Schwartz, *J. Am. Chem. Soc.* **1975**, *97*, 679–680.
- [16] a) N. Miyaura, A. Suzuki, *Chem. Rev.* **1995**, *95*, 2457–2483; b) J. A. Marshall, B. A. Johns, *J. Org. Chem.* **1998**, *63*, 7885–7892.
- [17] For the synthesis of **8**, see the Supporting Information.
- [18] B. M. Trost, M. L. Crawley, *Chem. Rev.* **2003**, *103*, 2921–2943.
- [19] a) C. Damez, J.-R. Labrosse, P. Lhoste, D. Sinou, *Synthesis* **2001**, 1456–1458; b) G. Wang, D. Niu, T.-L. Qiu, L. T. Phan, Z. Chen, A. Polemeropoulos, Y. S. Or, *Org. Lett.* **2004**, *6*, 4455–4458; c) C. Goux, P. Lhoste, D. Sinou, *Synlett* **1992**, 725–727.
- [20] Among the byproducts, the quinone **A** and methylenedioxy arene **B** were structurally determined. **A** was speculated to derive from oxidation of the hydroquinone **5** by high-valence palladium intermediates. **B** might be generated from **A** by a light-triggered transformation. For similar examples, see: C. Thommen, C. K. Jana, M. Neuburger, K. Gademann, *Org. Lett.* **2013**, *15*, 1390–1393, and references therein.



- [21] L. A. Evans, N. Fey, J. N. Harvey, D. Hose, G. C. Lloyd-Jones, P. Murray, A. G. Orpen, R. Osborne, G. J. J. Owen-Smith, M. Purdie, *J. Am. Chem. Soc.* **2008**, *130*, 14471–14473.
- [22] E. A. Iardi, C. E. Stivala, A. Zakarian, *Chem. Soc. Rev.* **2009**, *38*, 3133–3148.
- [23] In a recent total synthesis of kendomycin (Ref. [7g]), Nakata's group applied a set of reaction conditions, similar to our previously reported method, on a substrate which was more acidic than **21**. In their case, Ac₂O had to be used for the in situ trap of the Claisen product to avoid further decomposition. In our substrate case, no decomposition was observed.
- [24] K. B. Sharpless, M. A. Umbreit, M. T. Nieh, T. C. Flood, *J. Am. Chem. Soc.* **1972**, *94*, 6538–6540.



Design, synthesis, and evaluation, derivatives of the fat-accumulation inhibitor ternatin: toward ternatin molecular probes



Yoshinori Kawazoe^{a,*}, Yoko Tanaka^b, Sachikazu Omura^a, Daisuke Uemura^{a,b,*}

^a Research Institute of Natural Drug-Leads, Kanagawa University, 2946 Tsuchiya, Hiratsuka, Kanagawa 259-1293, Japan

^b Department of Chemistry, Faculty of Science, Kanagawa University, 2946 Tsuchiya, Hiratsuka, Kanagawa 259-1293, Japan

ARTICLE INFO

Article history:

Received 9 April 2014

Revised 4 June 2014

Accepted 9 June 2014

Available online 14 June 2014

Keywords:

Ternatin

Cyclic peptide

Fat accumulation

Molecular probe

3T3-L1 cell

ABSTRACT

Ternatin, a cyclic heptapeptide derived from mushroom, strongly inhibits fat accumulation in 3T3-L1 adipocytes. However, its mechanism of action remains unclear. In this Letter, we designed, synthesized, and evaluated its derivatives for use as molecular probes to isolate its target protein. Finally, we successfully established a pair of ternatin molecular probes.

© 2014 Elsevier Ltd. All rights reserved.

Obesity is one of the most common problems societies face worldwide and is a strong risk factor for several lifestyle-related diseases, such as hypertension, hyperlipidemia, and diabetes. Although a few medicines for treating obesity have been approved and brought to the market, no fundamental treatment for obesity has yet been established.¹

Ternatin (**1**, see Fig. 1), an unusual amino acid-containing cyclic heptapeptide, was isolated from the mushroom *Coriolus versicolor* as a strong fat-accumulation inhibitor.² The natural product blocks lipid accumulation in 3T3-L1 adipocytes with an EC₅₀ value of 0.14 μg/mL. In addition, compound **1** decreased the blood sugar level in KK-A(y) mice, which is an animal model of type 2 diabetes.³ These results suggest that ternatin may be a potent drug for treating obesity or diabetes. However, a developmental study has not yet been initiated because the mechanism of action of ternatin remains unclear. Thus, it is important to determine how this compound works within cells. To this end, researchers usually try to identify a binding protein or the intracellular localization of the bioactive molecule by using its derivatives as molecular probes. In this letter, we describe the design and synthesis of ternatin derivatives for use as molecular probes. Furthermore, we evaluated

their activities. As a result, we successfully created chemical probes for ternatin.

If we wish to use bioactive molecules as molecular probes, they should contain a free reactive group such as an amino or a carboxyl group to introduce functional molecules, including fluorescent reagents or biotin. We decided to conjugate ternatin analogues to functional molecules via *N*-hydroxysuccinimide. Thus, ternatin molecular probes must contain a free amino group. To introduce a free amino group to ternatin, we checked previous structure–activity relationship studies. Ternatin was expected to have a rigid structure due to three intramolecular hydrogen bonds: between the carbonyl group of *D*-*allo*-Ile¹ and the hydroxyl group of

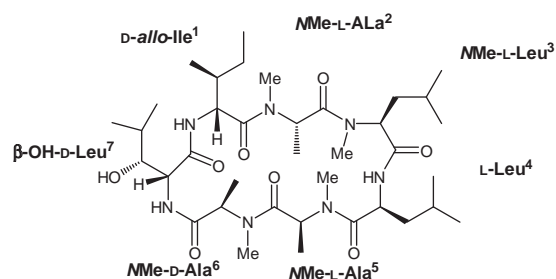


Figure 1. Chemical structure of ternatin (**1**).

* Corresponding authors. Tel.: +81 463 59 4111x2525; fax: +81 463 58 9684 (Y.K.); tel.: +81 463 59 4111x2719; fax: +81 463 58 9684 (D.U.).

E-mail addresses: ss199164bn@kanagawa-u.ac.jp (Y. Kawazoe), uemurad@kanagawa-u.ac.jp (D. Uemura).

β -OH-D-Leu⁷, between the carbonyl group of β -OH-D-Leu⁷ and the amino group of L-Leu⁴, and between the carbonyl group of L-Leu⁴ and the amino group of β -OH-D-Leu⁷. Analogues that could not form these hydrogen bonds such as [NMe-L-Leu⁴]ternatin showed much lower activity than that of ternatin.⁴ In addition, the hydroxyl group in β -OH-D-Leu⁷ was shown to be important for activity.⁵ On the other hand, NMe-D-Ala⁶ could be replaced by other amino acids.⁶ These results suggest that position 6 is suitable for the introduction of an amino group-containing linker. Based on this idea, we designed two kinds of ternatin derivatives. The first type incorporates an amino acid, lysine, at position 6 because it contains a free amino group in its side chain. However, we were afraid that a methylation reaction of the amino group might simultaneously methylate the side-chain amino group. To account for this possibility, we used another approach that involved the reduction of azido derivatives to give free amino group-containing analogues.

Stereoisomers in which D-*allo*-Ile¹, NMe-L-Ala⁵, and NMe-D-Ala⁶ were replaced by D-Ile¹, NMe-D-Ala⁵, and NMe-L-Ala⁶, respectively,

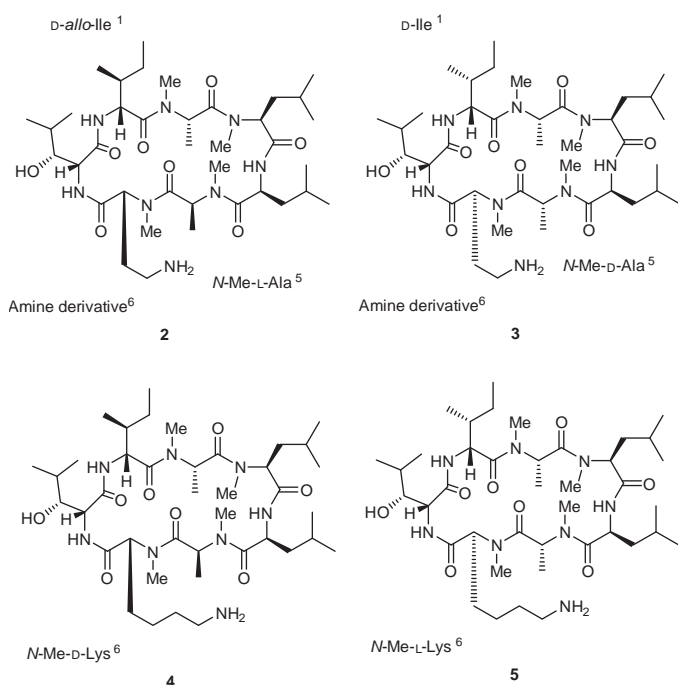


Figure 2. Design of molecular probes for ternatin.

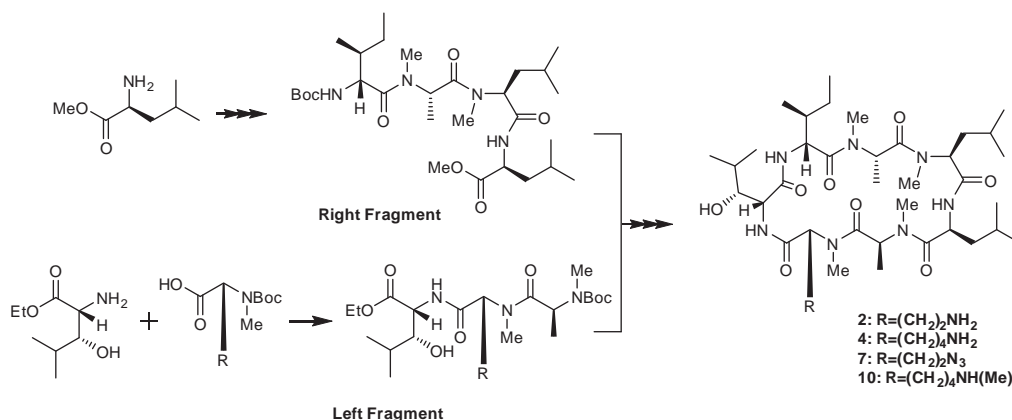
did not inhibit fat accumulation at all.⁷ Thus, the stereoisomer of the molecular probe can be used as a negative control. Finally, we designed four ternatin derivatives: an amine (**2**) and one with NMe-D-Lys⁶ (**4**) as positive controls and a stereoisomeric amine (**3**) and a stereoisomeric one with NMe-L-Lys⁶ (**5**) as negative controls (Fig. 2).

The synthesis of ternatin has been established,⁸ and we followed this previous study to synthesize our molecular probes. Detailed procedure is given in [Supplementary material](#). Briefly, building blocks are condensed to afford a right fragment and a left fragment, which are then coupled, cyclized, and deprotected to give molecular probes (Scheme 1 only shows positive controls. For the negative controls, we used stereoisomers). All of the peptide synthesis was performed in a liquid phase.

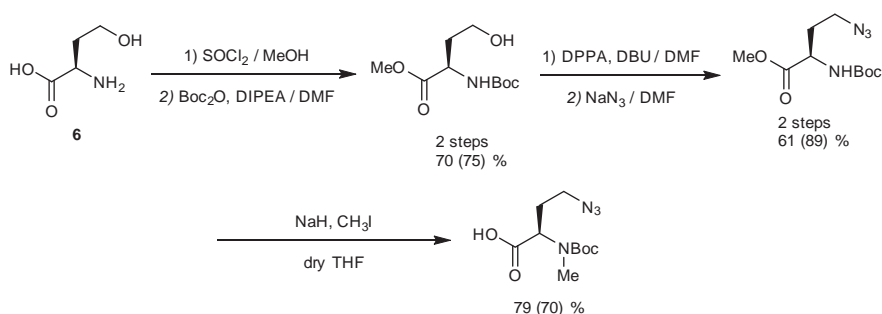
For the amine derivatives (**2** and **3**), we used D- or L-homoserine (Hse: **6** for D-isomer) as a starting material. The hydroxyl group in the side chain of Hse was replaced by an azido group by NaN₃ (Scheme 2). The resulting azido derivatives were used for peptide synthesis. Resulting azido-containing ternatin derivatives (**7** and **8**) were subjected to Staudinger reduction to give free amino group-containing molecules⁹ **2** and **3**, which were obtained in respective yields of 2.3% and 2.3%, in a total of 14 steps.

For the lysine derivatives, we used Boc-D-Lys(Cbz)-OH (**9**) or Boc-L-Lys(Cbz)-OH as a starting material. We expected that the terminal Boc-protected amino groups were preferentially methylated because of higher acidity. However, Cbz-protected side-chain amino groups were also simultaneously converted to give Boc-NMe-D-Lys(NMe)(Cbz)-OH or Boc-NMe-L-Lys(NMe)(Cbz)-OH, respectively (Scheme 3 shows D-isomer, positive control.), in all of the conditions we tested. At this moment, we decided to change synthetic target molecules **4** and **5** to N-methylated-Lys side chain-containing derivatives, **10** and **11**. Although the side chain was converted to a secondary amino group, it could be coupled with NHS-functional molecules. After cyclization, catalytic hydrogenation with Pd/C was performed to remove a Cbz group, however, the reaction would not take place. Next, we applied catalytic transfer hydrogenation with HCO₂NH₄. The reaction proceeded, albeit slowly and in low yield (13% and 13% for the positive and negative controls, respectively). We prepared the lysine-derived ternatin molecular probes **10** and **11** in respective yields of 0.74% and 0.79%, respectively, in a total of 10 steps.

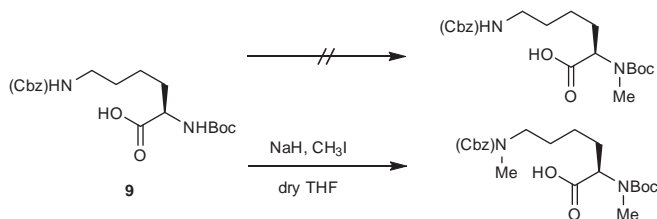
Finally, we evaluated the fat-accumulation inhibitory effects of our molecular probes. 3T3-L1 cells were induced to undergo adipose differentiation by insulin in the presence of various concentrations of compounds **1**, **2**, **3**, **10**, and **11**. After one week of induction of adipogenesis,¹⁰ cellular triglyceride levels were measured using a LabAssay™ Triglyceride kit (WAKO) according to



Scheme 1. Plan for the synthesis of molecular probes for ternatin.



Scheme 2. Conversion of HSE to azido derivative. The D-isomer for compound **2** is shown. A yield for L-isomer is indicated in parentheses.



Scheme 3. Methylation of Lys derivative.

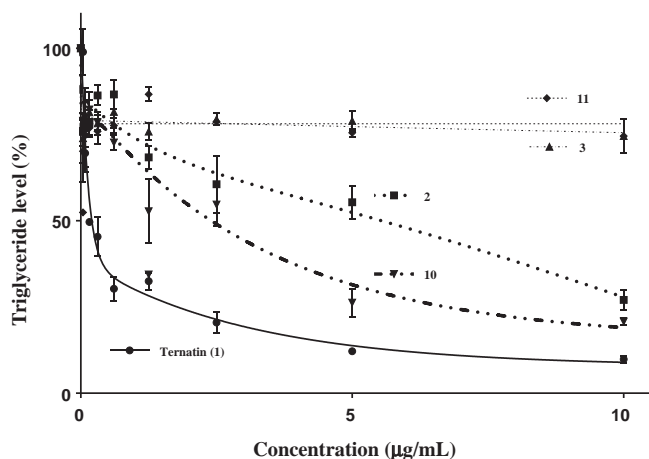


Figure 3. Evaluation of the activity of molecular probes. The cells were induced to differentiate with each probe, **6**, **7**, **8**, **9**, or **1** (ternatin) for one week, then cellular triglyceride levels were measured. Data are expressed as mean values and \pm SEM of three independent experiments.

the manufacture's instructions. Consistent with a previous study, ternatin (**1**) strongly inhibited fat accumulation with an EC_{50} value of $0.16 \mu\text{g/mL}$, which was nearly the same as the value of natural product ($0.14 \mu\text{g/mL}$).² Positive controls **2** and **10** had a moderate effect ($EC_{50} = 5.57$ and $2.40 \mu\text{g/mL}$, respectively). As expected, the negative controls showed no activity ($EC_{50} > 10 \mu\text{g/mL}$) (Fig. 3).

Positive control **10** showed slightly better activity than positive control **2**. This might be explained by the results of our previous structure–activity relationship study, which suggested that a longer side chain at position 6 was associated with better activity. For example, the activity of [NMe-D-Aoc⁶]ternatin was 1.7 times greater than that of original ternatin. If we compare positive controls **2** and **10**, compound **10** has a side chain at position 6 that is two carbon atoms longer than that on **2**. Furthermore, when we consider the terminal methyl group on amine, it seems that 3 carbon atoms are elongated in compound **10**. The side chain length

is almost same as that in the highly active derivative, [NMe-D-Aoc⁶]ternatin. In addition, compound **2** should be much more reactive than compound **10** because of the free amino group in the side chain at position 6. The reactivity of molecules usually affects their kinetics, including binding to serum proteins, cell permeability, and intracellular distribution. Among these, penetration of the cell membrane is highly associated with free polar functional groups. Thus, the combination of length and polarity of the side chain at position 6 may have resulted in the difference in activity between compounds **2** and **10**.

Although both positive controls **2** and **10** were each 15–30-fold less active than the original natural product **1**, there was a big difference in activity between the positive controls and negative controls (Fig. 3). This difference encouraged us to use them as molecular probes for ternatin. We have since been able to introduce a fluorescein isothiocyanate molecule to the probes. Furthermore, we conjugated the probes to resin. Experiments to demonstrate the intracellular localization of ternatin and to identify a ternatin-binding protein are now in progress.

Acknowledgments

This study was supported in part by Grant-in-Aid for Scientific Research from Japan Society for the Promotion of Science (25242069 to D.U. and 24510316 to Y.K.). We are indebted to the Uehara Memorial Foundation to the financial support.

Supplementary data

Supplementary data associated with this article can be found, in the online version, at <http://dx.doi.org/10.1016/j.tetlet.2014.06.036>.

References and notes

- Campfield, L. A.; Smith, F. J.; Burn, P. *Science* **1998**, *280*, 1383.
- Shimokawa, K.; Mashima, A.; Asai, A.; Yamada, K.; Kita, M.; Uemura, D. *Tetrahedron Lett.* **2006**, *47*, 4445–4446.
- Kobayashi, K.; Kawashima, H.; Takemori, K.; Ito, H.; Murai, A.; Masuda, S.; Yamada, K.; Uemura, D.; Horio, F. *Biochem. Biophys. Res. Commun.* **2012**, *427*, 299–304.
- Shimokawa, K.; Miwa, R.; Yamada, K.; Uemura, D. *Org. Biomol. Chem.* **2009**, *7*, 777–784.
- Shimokawa, K.; Iwase, Y.; Yamada, K.; Uemura, D. *Org. Biomol. Chem.* **2008**, *6*, 58–60.
- Shimokawa, K.; Iwase, Y.; Miwa, R.; Yamada, K.; Uemura, D. *J. Med. Chem.* **2008**, *51*, 5912–5914.
- Shimokawa, K.; Mashima, I.; Asai, A.; Ohno, T.; Yamada, K.; Kita, M.; Uemura, D. *Chem. Asian J.* **2008**, *3*, 438–446.
- Shimokawa, K.; Yamada, K.; Kita, M.; Uemura, D. *Bioorg. Med. Chem. Lett.* **2007**, *17*, 4447–4449.
- Weiqing, X.; Derong, D.; Weiwei, Z.; Guangyu, L.; Dawei, M. *Angew. Chem., Int. Ed.* **2008**, *47*, 2844–2848.
- Kawazoe, Y.; Tanaka, S.; Uesugi, M. *Chem. Biol.* **2004**, *11*, 907–913.



An inhibitor of the adipogenic differentiation of 3T3-L1 cells, yoshinone A, and its analogs, isolated from the marine cyanobacterium *Leptolyngbya* sp.



Toshiyasu Inuzuka^{a,*}, Keita Yamamoto^b, Arihiro Iwasaki^c, Osamu Ohno^c, Kiyotake Suenaga^{c,*}, Yoshinori Kawazoe^{d,*}, Daisuke Uemura^{b,d}

^a Life Science Research Center, Gifu University, Yanagido, Gifu 501-1193, Japan

^b Faculty of Science, Kanagawa University, Hiratsuka, Kanagawa 259-1293, Japan

^c Department of Chemistry, Keio University, Yokohama, Kanagawa 223-8522, Japan

^d Research Institute of Natural-Drug Leads, Kanagawa University, Hiratsuka, Kanagawa 259-1293, Japan

ARTICLE INFO

Article history:

Received 25 July 2014

Revised 1 October 2014

Accepted 7 October 2014

Available online 12 October 2014

Keywords:

Yoshinone

γ -Pyrone

Adipogenesis

Obesity

3T3-L1 cells

ABSTRACT

Three novel compounds, yoshinones A, B1, and B2, were isolated from the marine cyanobacterium *Leptolyngbya* sp., and their structures were elucidated by NMR spectral analysis. Yoshinone A, but not yoshinone B1 or B2, inhibited the differentiation of 3T3-L1 cells into adipocytes. In addition, yoshinone A did not exhibit cytotoxicity, suggesting that yoshinone A may be useful in studies on the treatment of obesity.

© 2014 Elsevier Ltd. All rights reserved.

Obesity is a growing health problem in modern society because it is a risk factor for many lifestyle-related diseases including diabetes and cardiovascular disorders.^{1–3} Studies on anti-obesity contribute to the prevention and treatment of various diseases. It is important that we understand the functions and mechanisms of adipocytes to in turn better understand obesity. Therefore, useful tools such as organic compounds that regulate adipocytes are needed. Our studies in this field identified (–)-ternatin, an inhibitor of fat accumulation in 3T3-L1 adipocytes,⁴ and its derivatives have been studied to elucidate its mechanism of action.^{5–8}

Against backgrounds, we sought to identify the novel compounds that could affect the adipogenic differentiation of 3T3-L1 cells from cyanobacteria. Cyanobacteria are widely distributed prokaryotes that produce a variety of secondary metabolites, and marine cyanobacteria are known to be rich sources of biologically or physiologically active compounds.⁹ As a result, we found three novel compounds, yoshinones¹⁰ A (**1**), B1 (**2**), and B2 (**3**) (Fig. 1).

These three yoshinones were composed of γ -pyrone and a linear side chain. Tests on the abilities of these three yoshinones to inhibit differentiation in 3T3-L1 cells revealed that conjugation between γ -pyrone and olefin in the side chain reduced their activities. Details of the isolation, structural analyses, and biological effects of yoshinones are described below.

The cyanobacterium *Leptolyngbya* sp., (600 g) collected at Ishigaki island, Okinawa, Japan, was crushed in aqueous methanol by a blender, and the residue was removed from the aqueous methanol extract by filtration. The aqueous methanol extract was partitioned between water and ethyl acetate, and the ethyl acetate layer was partitioned between hexane and 80% aqueous methanol. The aqueous methanol layer was separated by reverse-phase chromatography with aqueous methanol (20–100%) and reverse-phase HPLC (Develosil ODS HG-5) with an acetonitrile/water eluent. As a result of continuous HPLC purifications, three compounds, yoshinones A (**1**) (1.0 mg), B1 (**2**) (0.1 mg), and B2 (**3**) (0.1 mg), were isolated.

Based on the HRESIMS analysis, the molecular formula of yoshinone A (**1**)¹¹ was found to be C₂₁H₃₂O₅ (*m/z* 387.2163 for [M+Na]⁺, calcd 387.2147). The ¹H NMR spectrum showed the presence of 1 doublet methyl (δ_{H} 1.13), 4 olefin methyls (δ_{H} 1.48, 1.48, 2.01, and 2.13), 2 methoxy groups (δ_{H} 3.03 and 3.23), and 2 olefin

* Corresponding authors. Tel.: +81 58 230 6152; fax: +81 58 293 2035 (T.I.); tel./fax: +81 45 566 1819 (K.S.); tel.: +81 463 59 4111x2525; fax: +81 463 58 9684 (Y.K.).

E-mail addresses: inuzuka@gifu-u.ac.jp (T. Inuzuka), suenaga@chem.keio.ac.jp (K. Suenaga), ss199164bn@kanagawa-u.ac.jp (Y. Kawazoe).

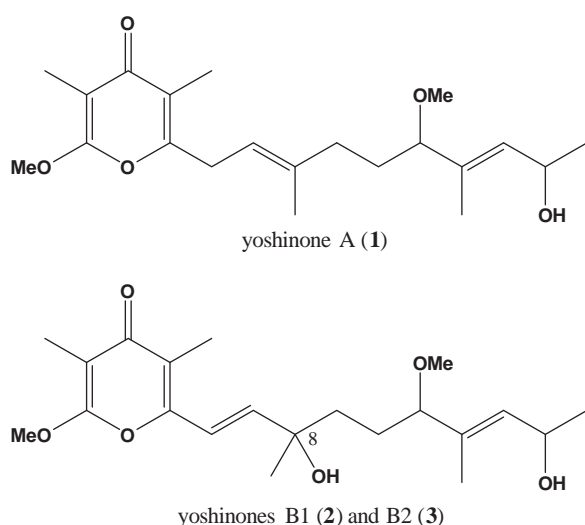


Figure 1. Structures of yoshinones A (**1**), B1 (**2**), and B2 (**3**). Yoshinones B1 and B2 are diastereomers.

protons (δ_{H} 5.16 and 5.36). A 2D-HMQC spectral analysis revealed that other proton signals in the ^1H NMR spectrum could be considered to be 1 methylene proton (δ_{H} 2.86), 4 methylene protons (δ_{H} 1.58, 1.79, 2.03, and 2.10), and 2 oxymethine protons (δ_{H} 3.29 and 4.38). The ^{13}C NMR spectrum revealed that yoshinone A (**1**) contained 5 methyl carbons (δ_{C} 7.1, 10.0, 10.5, 15.9, and 23.8), 3 methylene carbons (δ_{C} 32.1, 32.3, and 35.9), 2 methoxy carbons (δ_{C} 51.8 and 52.8), 2 methine carbons (δ_{C} 64.0 and 86.4), 6 olefin carbons (δ_{C} 118.0, 134.0, 135.0, 138.2, 156.7, and 161.7), and 1 ketone carbon (δ_{C} 179.9). However, signals of 2 carbons in yoshinone A (**1**) were not observed in the ^{13}C NMR spectrum.

COSY correlations revealed three partial structures, C6–C7, C9–C11, and C13–C15 (Fig. 2). Three HMBC correlations, H19–C7, H19–C8, and H19–C9, connected C7 and C9, and three other correlations, H21–C11, H21–C12, and H13–C21, connected C11 and C13. HMBC correlation H20–C11 indicated that a methoxy group was present at C11. On the other hand, HMBC correlations from H17 (H17–C1, H17–C2, and H17–C3) and H18 (H18–C3, H18–C4, and H18–C5) revealed the C1–C5 carbon-chain sequence, including 2 carbons, C2 (δ_{C} 100.1) and C4 (δ_{C} 119.9), which were not observed in ^{13}C NMR spectrum. The H16–C1 correlation showed the presence of a methoxy group at C1 and the correlations of H6–C4 and H6–C5 were shown to connect C5 and C6. Based on the chemical shifts of C1 (δ_{C} 161.7) and C5 (δ_{C} 156.7) and the molecular formula, the C1–C5 portion was considered to be γ -pyrone, and a hydroxyl group was present at oxymethine C14. The geometries of 2 olefins in side chain were determined to be all *E* by NOE correlations, H7–H9 and H11–H13. Based on these results, yoshinone

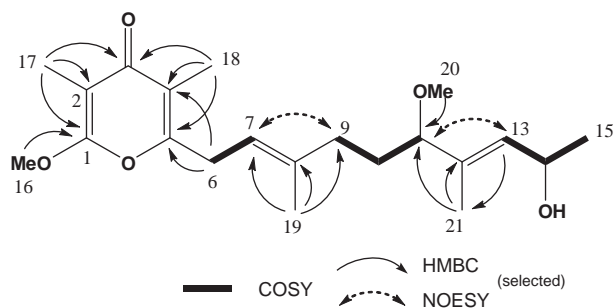


Figure 2. 2D-NMR correlations of yoshinone A (**1**).

A (**1**) was determined to have a planar structure as shown in Figure 2.

Both yoshinones B1 (**2**)¹² and B2 (**3**)¹³ were estimated to have the same chemical formula $\text{C}_{21}\text{H}_{32}\text{O}_6$ based on HRESIMS data (**2**: m/z 403.2085 for $[\text{M}+\text{Na}]^+$, calcd 403.2096. **3**: m/z 403.2067 for $[\text{M}+\text{Na}]^+$, calcd 403.2096). The ^1H NMR spectra of yoshinones B1 (**2**) and B2 (**3**) resembled each other. One singlet methyl proton (**2**: δ_{H} 1.21. **3**: δ_{H} 1.17), 1 doublet methyl proton (**2**: δ_{H} 1.09. **3**: δ_{H} 1.10), 3 olefin methyl protons (**2**: δ_{H} 1.44, 2.10 and 2.14. **3**: δ_{H} 1.47, 2.11, and 2.14), 2 methoxy protons (**2**: δ_{H} 2.99 and 3.16. **3**: δ_{H} 3.00 and 3.14), 4 methylene or methane protons (**2**: δ_{H} 1.53, 1.58, 1.70 and 1.80. **3**: δ_{H} 1.52, 1.63, 1.71, and 1.76), 2 oxymethine protons (**2**: δ_{H} 3.27 and 4.32. **3**: δ_{H} 3.29 and 4.34), and 3 olefin protons (**2**: δ_{H} 5.35, 6.24, and 6.66. **3**: δ_{H} 5.38, 6.25, and 6.62) were observed. The ^1H NMR signals of yoshinones B1 (**2**) and B2 (**3**) appeared to be similar to those of yoshinone A (**1**) (Table 1), and therefore yoshinones B1 (**2**) and B2 (**3**) were predicted to be analogs of yoshinone A (**1**). The presence of α -methoxy- β , β' -dimethyl- γ -pyrone in yoshinones B1 (**2**) and B2 (**3**) was estimated based on comparisons of the ^1H NMR chemical shifts with respect to the protons at H16, H17, and H18 with yoshinone A (**1**). This estimation was supported by a comparison of the NMR data with those of actinopyrones¹⁴ and kalkipyrones.¹⁵ In the linear side chain, the C9–C15 portion of yoshinones B1 (**2**) and B2 (**3**) was also the same as that of yoshinone A (**1**) based on the ^1H NMR spectrum and COSY correlations (Fig. 3). With regard to the C6–C8 moiety, since the proton chemical shifts of olefin protons were 6.24 and 6.66 ppm for yoshinone B1 (**2**) and 6.25 and 6.62 ppm for yoshinone B2 (**3**) these olefins were deduced to be conjugated with γ -pyrone. Based on the coupling constant between H6 and H7 (15.8 Hz for yoshinone B1 (**2**) and H6 of yoshinone B2 (**3**) or 15.2 Hz for H7 of yoshinone B2 (**3**)), the geometry of C6–C7 olefins was estimated to be *E*. Additionally, based on the chemical formula, hydroxyl groups presented at C8, and yoshinones B1 (**2**) and B2 (**3**) were estimated to have same planar structures as shown in Figure 3. They were diastereomers, but it was not clear that which positions were different from each other.

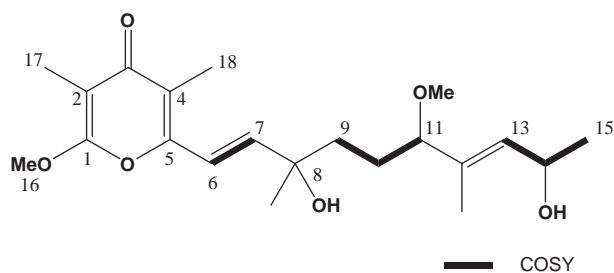
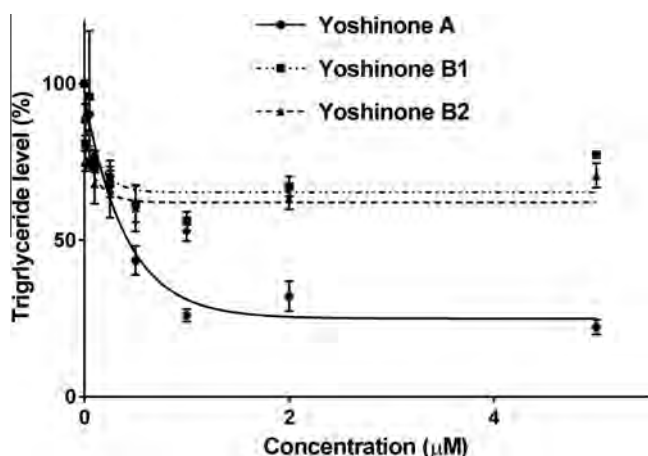
The effects of these three yoshinones on the adipogenic differentiation of 3T3-L1 cells were then observed. The cells were induced to undergo differentiation by insulin¹⁶ in the absence or presence of various concentrations of the yoshinones.

After 7 days of induction, the cellular triglyceride level was measured as an indicator of differentiation (Fig. 4). The concentration of yoshinone A (**1**) required to achieve a 50% inhibition of differentiation (EC_{50}) was 420 nM. On the other hand, the inhibition rates with yoshinones B1 (**2**) or B2 (**3**) were less than 50% even at a concentration of 5 μM . The structures of yoshinones A (**1**) and B (**2** and **3**) differ with respect to the number of hydroxyl groups and the position of one olefin in the side chain. In particular, yoshinones B1 (**2**) and B2 (**3**) have an olefin conjugated with γ -pyrone, while olefins in the side chain of yoshinone A (**1**) are not conjugated. To clarify which is more important for the inhibitory activity, we conducted a structure–activity relationship study with kalkipyrones and aureothin (Fig. S11A). These γ -pyrone-containing compounds have different side chains. Conjugation of the pyrone ring and one olefin in side chain is seen only in yoshinones B1 and B2. The result showed that kalkipyrones inhibited differentiation with an EC_{50} value of 67.5 nM and that of aureothin was 54.2 nM (Fig. S11B), suggesting that a γ -pyrone and an olefin should not be conjugated with each other for the inhibition of adipogenic differentiation. Yoshinone A (**1**) did not have cytotoxic effects on 3T3-L1 or HeLa cells at a concentration of 50 μM .

In conclusion, we isolated three novel compounds, yoshinones A (**1**), B1 (**2**), and B2 (**3**), from the cyanobacterium *Leptolyngbya* sp., and determined their structures by NMR spectral analyses. Yoshinone A (**1**) was not cytotoxic and inhibited the adipose

Table 1
NMR data of yoshinones A (1), B1 (2), and B2 (3)^a

Position	Yoshinone A			Yoshinone B1		Yoshinone B2	
	δ_C^b	δ_H^c multiplicity (J in Hz)		δ_H^d multiplicity (J in Hz)		δ_H^d multiplicity (J in Hz)	
1	161.7						
2	100.1						
3	179.9						
4	119.9						
5	156.7						
6	32.3	2.86	d (7.0)	6.24	d (15.8)	6.25	d (15.8)
7	118.0	5.16	t (7.0)	6.66	d (15.8)	6.62	d (15.2)
8	138.2						
9	35.9	2.10	m	1.70	m	1.71	m
		2.03	m	1.58		1.52	
10	32.1	1.79	m	1.80	m	1.76	m
		1.58	m	1.53	m	1.63	m
11	86.4	3.29	dd (7.5, 5.5)	3.27	dd (8.6, 4.5)	3.29	dd (8.3, 4.8)
12	135.0						
13	134.0	5.36	d (8.5)	5.35	d (8.9)	5.38	d (8.2)
14	64.0	4.38	dq (8.5, 6.5)	4.32	m	4.34	m
15	23.8	1.13	d (6.5)	1.09	d (6.2)	1.10	d (6.2)
16	51.8	3.23	s	3.16	s	3.14	s
17	7.1	2.13	s	2.14	s	2.14	s
18	10.0	2.01	s	2.10	s	2.11	s
19	15.9	1.48	s	1.21	s	1.17	s
20	52.8	3.03	s	2.99	s	3.00	s
21	10.5	1.48	s	1.44	s	1.47	s

^a Solvent: C₆D₆.^b Recorded at 125 MHz.^c Recorded at 500 MHz.^d Recorded at 600 MHz.**Figure 3.** COSY correlations of yoshinones B1 (2) and B2 (3).**Figure 4.** Dose-effect curve for yoshinones on the differentiation of 3T3-L1 cells. After 7 days of induction of adipogenesis by insulin with various concentrations of yoshinones, cellular triglyceride levels were measured. Each value is the mean \pm SEM determined by three independent experiments.

differentiation of 3T3-L1 cells. According to our results, while kalkipyron and aureothin are stronger at inhibiting differentiation than yoshinones, they also are highly cytotoxic (IC_{50} =120 nM and

110 nM for kalkipyron and aureothin, respectively against HeLa cells). Therefore, yoshinone A may be a novel lead compound for the treatment of obesity. We tried to determine the configuration of side-chain regions of yoshinones by a modified Mosher's method, but failed because of the limited availability of samples. We are currently preparing all possible stereoisomers to determine the stereochemistry and to perform studies on the structure-activity relationships of yoshinones.

Acknowledgments

The authors are grateful to Dr. Hiroki Shimogawa for recording the NMR spectra of yoshinones B1 and B2. This study was supported in part by Grant-in-Aid for Scientific Research from JSPS (25810096 to T.I., 24310160 to K.S., 24510316 to Y.K., and 25242069 to D.U.) We are indebted to the Uehara Memorial Foundation (D.U.) to financial support.

Supplementary data

Supplementary data associated with this article can be found, in the online version, at <http://dx.doi.org/10.1016/j.tetlet.2014.10.032>.

References and notes

- Kahn, S. E.; Hull, R. L.; Utzschneider, K. M. *Nature* **2006**, *444*, 840–846.
- Mann, C. C. *Science* **2005**, *307*, 1716–1717.
- Eckel, R. H.; Grundy, S. M.; Zimmet, P. Z. *Lancet* **2005**, *365*, 1415–1428.
- Shimokawa, K.; Masihima, I.; Asai, A.; Yamada, K.; Kita, M.; Uemura, D. *Tetrahedron Lett.* **2006**, *47*, 4445–4446.
- Kobayashi, M.; Kawashima, H.; Takemori, K.; Ito, H.; Murai, A.; Masuda, S.; Yamada, K.; Uemura, D.; Horio, H. *Biochem. Biophys. Res. Commun.* **2012**, *427*, 299–304.
- Ito, M.; Ito, J.; Kitazawa, H.; Shimamura, K.; Fukami, T.; Tokita, S.; Shimokawa, K.; Yamada, K.; Kanatani, A.; Uemura, D. *Peptides* **2009**, *30*, 1074–1081.
- Shimokawa, K.; Ohno, O.; Yamada, K.; Oba, Y.; Uemura, D. *Chem. Lett.* **2009**, *38*, 150–151.
- Kawazoe, Y.; Tanaka, Y.; Omura, S.; Uemura, D. *Tetrahedron Lett.* **2014**, *55*, 4445–4447.

9. Nagarajan, M.; Maruthanayagam, V.; Sundararaman, M. *J. Appl. Toxicol.* **2012**, *32*, 153–185.
10. To clarify that the compounds are similar to actinopyrones and kalkipyronone, hereafter we will refer to the compounds reported in this Letter as 'yoshiopyrones'.
11. Yoshinone A (**1**): $[\alpha]_D^{27} -5.3$ (c 0.2, CH₃OH); IR (film) 2926, 1668, 1585, 1465 cm⁻¹; ¹H NMR and ¹³C NMR: (Table 1); HRESIMS *m/z* found 387.2163 for [M+Na]⁺, calcd for 387.2147.
12. Yoshinone B1 (**2**): ¹H NMR and ¹³C NMR: (Table 1); HRESIMS *m/z* found 403.2085 for [M+Na]⁺, calcd for 403.2096.
13. Yoshinone B2 (**3**): ¹H NMR and ¹³C NMR: (Table 1); HRESIMS *m/z* found 403.2067 for [M+Na]⁺, calcd for 403.2096.
14. Yano, K.; Yokoi, K.; Sato, J.; Oono, J.; Kouda, T.; Ogawa, Y.; Nakashima, T. *J. Antibiot.* **1986**, *39*, 38–43.
15. Graber, M. A.; Gerwick, W. H. *J. Nat. Prod.* **1998**, *61*, 677–680.
16. Kawazoe, Y.; Naka, T.; Fujimoto, M.; Kohzaki, H.; Morita, Y.; Narazaki, M.; Okumura, K.; Saitoh, H.; Nakagawa, R.; Uchiyama, Y.; Akira, S.; Kishimoto, T. *J. Exp. Med.* **2001**, *193*, 263–269.

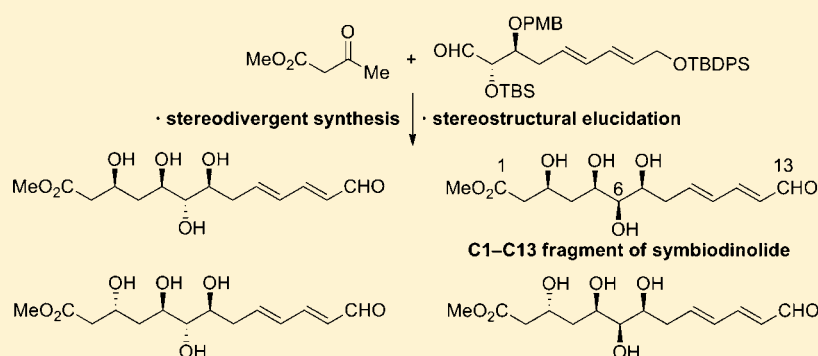
Stereodivergent Synthesis and Relative Stereostructure of the C1–C13 Fragment of Symbiodinolide

Hiro Yoshi Takamura,^{*,†} Hiroko Wada,[†] Mao Ogino,[†] Takahiro Kikuchi,[†] Isao Kadota,[†] and Daisuke Uemura[‡]

[†]Department of Chemistry, Graduate School of Natural Science and Technology, Okayama University, 3-1-1 Tsushimanaka, Kita-ku, Okayama 700-8530, Japan

[‡]Department of Chemistry, Faculty of Science, Kanagawa University, 2946 Tsuchiya, Hiratsuka 259-1293, Japan

Supporting Information



ABSTRACT: Four possible diastereomers of the C1–C13 fragment of symbiodinolide, which were proposed by the stereostructural analysis of the degraded product, were synthesized in a stereodivergent and stereoselective manner. The key transformations were aldol reaction of methyl acetoacetate with the aldehyde, diastereoselective reduction of the resulting β -hydroxy ketone, and the stereoinversion at the C6 position. Comparison of the ^1H NMR data between the four synthetic products and the degraded product revealed the relative stereostructure of the C1–C13 fragment of symbiodinolide.

INTRODUCTION

Integrated use of a spectroscopic method and chemical synthesis is well recognized as a reliable approach to the structural elucidation of natural products.¹ In particular, if the target molecule has a huge molecular size or a number of functional groups, the chemical synthesis is often required for the unambiguous configurational assignment.²

Symbiodinolide (**1**, Figure 1), a 62-membered polyol macrolide marine natural product, was isolated from the 80% aqueous ethanol extract of the cultured dinoflagellate *Symbiodinium* sp. by one of the authors (D.U.).³ This natural product exhibits voltage-dependent N-type Ca^{2+} channel-opening activity at 7 nM and COX-1 inhibition effect at 2 μM (65% inhibition). The planar structure of symbiodinolide (**1**) was assigned by the detailed 2D NMR spectroscopic techniques. However, the stereostructure of **1** has not been elucidated yet because of its complicated molecular structure characterized by 61 stereocenters and molecular weight of 2860. Therefore, we are now examining the degradation of natural symbiodinolide (**1**)^{3,4} and chemical synthesis of each fragment including the stereoisomers⁵ toward the complete stereochemical establishment of **1**. Previously, as a degradation of symbiodinolide (**1**), we carried out the methanolysis and subsequent oxidative cleavage with Grubbs II catalyst/ NaClO

to yield the C1–C13 fragment **2** (Scheme 1).^{4a,c} Herein, as a part of our efforts toward the complete configurational determination of symbiodinolide (**1**), we describe the stereostructural analysis of the degraded product **2**, and stereodivergent and stereoselective synthesis of all four possible diastereomers of the C1–C13 fragment **2**,⁶ which has established the relative stereostructure of this fragment.

RESULTS AND DISCUSSION

Stereochemical Analysis of the Degraded Product **2**.

Prior to starting the synthesis of the C1–C13 fragment, we first analyzed the stereostructure of the degraded product **2** to reduce the number of the possible diastereomers of this fragment. As shown in Figure 2a, the chemical shifts of the H-5 and H-7 in the ^1H NMR spectrum were the same value (3.97 ppm in D_2O); in addition, the two coupling constants were also the same ($^3J_{5,6}$ and $^3J_{6,7} = 4.5$ Hz). Comparison of these results with universal NMR databases for 1,2,3-triols reported by Kishi and co-workers⁷ indicates that the relative stereochemical relationships at the C5 and C7 positions to the C6 position are the same, that is, *syn/syn* or *anti/anti*. Thus, the possible

Received: January 5, 2015

Published: February 27, 2015

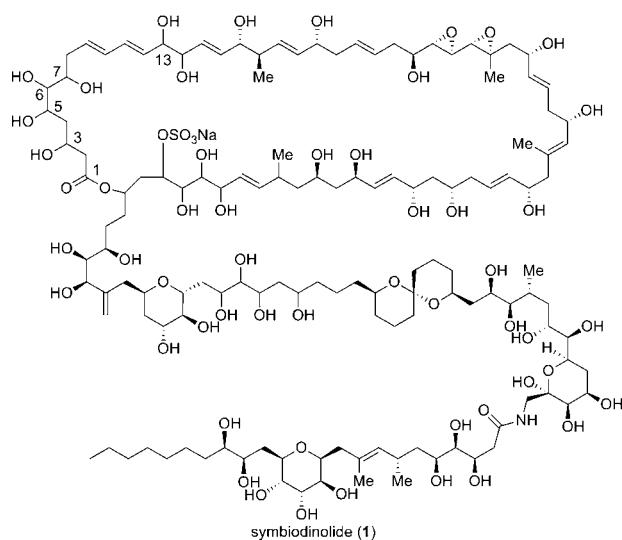
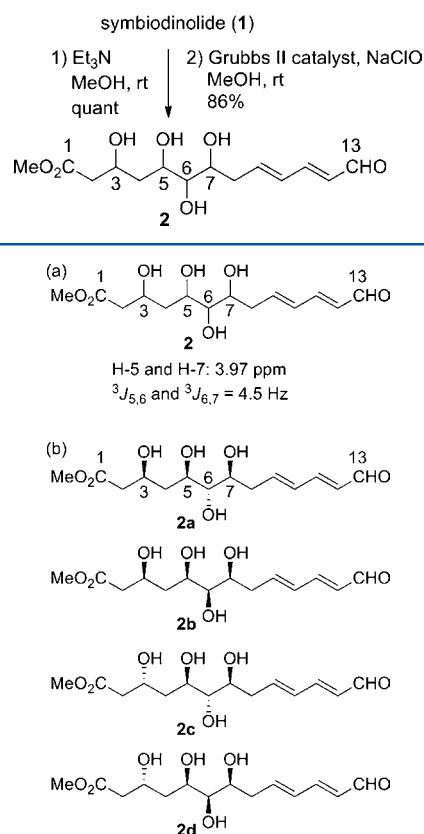


Figure 1. Structure of symbiodinolide (1).

Scheme 1. Degradation of Symbiodinolide (1)

Figure 2. (a) ¹H NMR analysis of the degraded product 2. (b) Four possible diastereomers of the C1–C13 fragment.

diastereomers of the C1–C13 fragment were narrowed down from the eight potential diastereomers and found to be four, which are described as 2a–2d in Figure 2b. We next examined the synthesis of all four of these possible diastereomers 2a–2d in the unified strategy.⁸

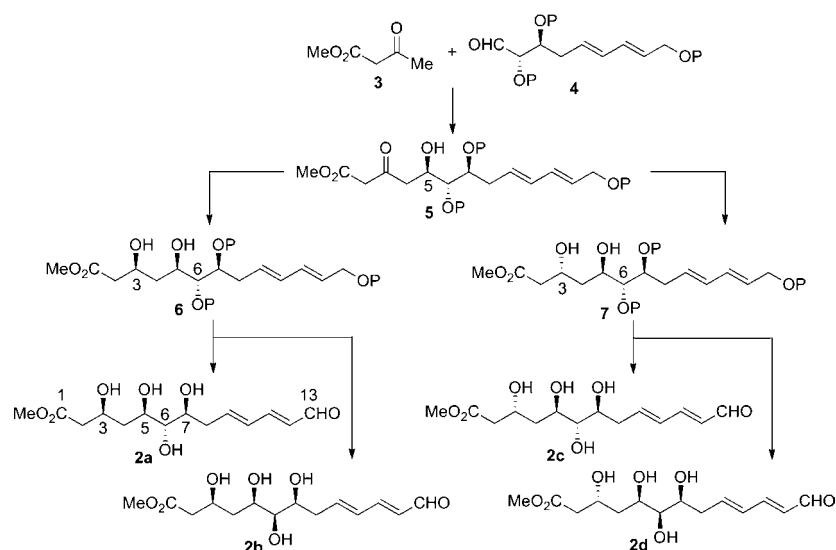
Stereodivergent Synthetic Plan of 2a–2b. The unified and stereodivergent synthetic plan of 2a–2d is depicted in

Scheme 2. Aldol reaction of methyl acetoacetate (3) with aldehyde 4 would provide the coupling product 5 with the desired oxymethine stereochemistry at the C5 position. The substrate-controlled diastereoselective reduction of β-hydroxy ketone 5 by utilizing the resulting C5 stereochemistry with the appropriate reducing reagent could afford *syn*-diol 6 and *anti*-diol 7, respectively. The *syn*-diol 6 could be transformed to the tetraol 2a through the deprotection and oxidation of the allylic alcohol. The tetraol 2b would be also synthesized via the stereoinversion at the C6 position from 6. In the similar way, the tetraols 2c and 2d could be stereoselectively supplied, respectively, by using the *anti*-diol 7 as the common synthetic intermediate.

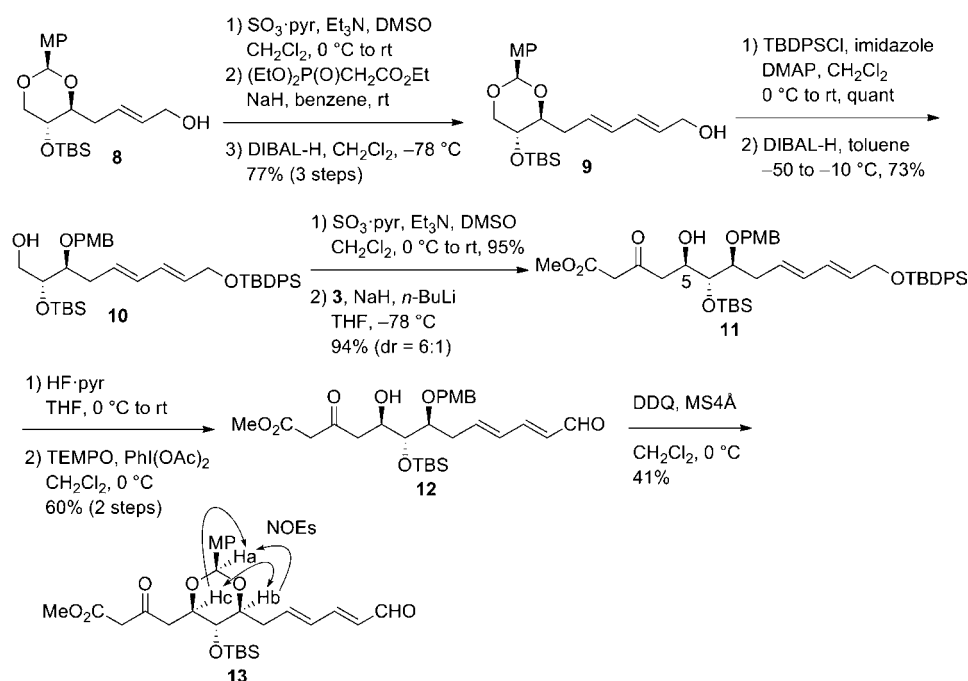
Stereoselective Synthesis of 2a. We investigated the stereoselective synthesis of the first target molecule 2a. Parikh–Doering oxidation⁹ of the known alcohol 8, which was prepared from 2-deoxy-D-ribose in four steps,¹⁰ followed by two-carbon elongation with (EtO)₂P(O)CH₂CO₂Et and DIBAL-H reduction, provided allylic alcohol 9 in 77% yield in three steps (Scheme 3). The alcohol 9 was protected as the TBDPS ether, and the regioselective reductive cleavage of the *p*-methoxybenzylidene acetal moiety with DIBAL-H afforded primary alcohol 10. The alcohol 10 was oxidized to the corresponding aldehyde with SO₃pyr/Et₃N/DMSO.⁹ Stereoselective aldol addition of methyl acetoacetate (3) to the resulting α,β-bisalkoxy aldehyde by using NaH and *n*-BuLi as bases produced β-hydroxy ketone 11 possessing the desired C5 configuration in 94% yield as the inseparable 6:1 diastereomeric mixture.^{11,12} We next tried the derivatization of 11 for the stereochemical confirmation at the C5 position. Thus, removal of the TBDPS protective group with HF·pyr and subsequent oxidation of the allylic alcohol with TEMPO/PhI(OAc)₂¹³ gave unsaturated aldehyde 12. Treatment of the alcohol 12 with DDQ provided *p*-methoxybenzylidene acetal 13.¹⁴ The observed NOEs of Ha/Hb, Ha/Hc, and Hb/Hc in 13, as shown by arrows, indicated that they were in *syn* relationships. Thereby, the absolute stereochemistry at the C5 position of 11 was unambiguously confirmed. Next, we introduced the C3 oxymethine stereochemistry. Thus, diastereoselective reduction of 11 was carried out with Et₃BOMe/NaBH₄¹⁵ to afford *syn*-diol 14 in 98% yield as a single product (Scheme 4). For the stereochemical confirmation at the C3 position, the diol 14 was protected with *p*-MeOC₆H₄CH(OMe)₂/CSA to give *p*-methoxybenzylidene acetal 15. The NOE correlations of Ha/Hb, Ha/Hc, and Hb/Hc in 15 suggested that all of them were oriented in axial positions, respectively. Thus, the absolute configuration at the C3 position of 14 was elucidated.

Next, we examined the transformation of the diol 14 to the tetraol 2a. Protection of 14 with Me₂C(OMe)₂/*p*-TsOH·H₂O gave acetonide 16 (Scheme 5). The TBDPS moiety of 16 was selectively removed with TBAF/AcOH¹⁶ to provide allylic alcohol 17 in 68% yield. TEMPO oxidation¹³ of 17 and removal of the PMB group with DDQ afforded unsaturated aldehyde 18 in 94% yield in two steps. The acetonide moiety of 18 was removed with TiCl₄¹⁷ in CH₂Cl₂ at –30 °C to afford triol 19 in 98% yield. Finally, treatment of the TBS ether 19 with HF·pyr at 0 °C to room temperature produced the tetraol 2a. Although we could obtain the first target molecule 2a, the conversion of 19 to 2a was quite slow and the starting material 19 was recovered in 52% yield. When the reaction time was prolonged, we observed the formation of several byproducts; furthermore, this transformation was irreproducible. Since this deprotection would be problematic in the subsequent synthesis

Scheme 2. Stereodivergent Synthetic Plan of 2a–2d



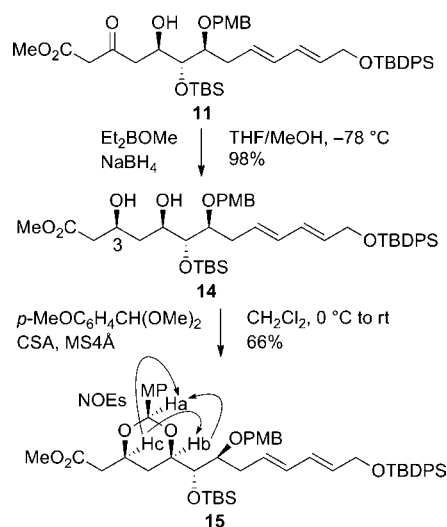
Scheme 3. Synthesis of 11 and Its Stereochemical Confirmation at the C5 Position



of **2b**–**2d**, a change from the TBS protective group to a less-hindered and more easily removed group in the final step was needed.

Removal of the TBS moiety of **17** was carried out with TBAF/AcOH in MeCN at 60 °C to give diol **20** in 86% yield (Scheme 6).¹⁸ Treatment of **20** with TESOTf/2,6-lutidine, followed by selective removal of the primary TES moiety, provided secondary TES ether **21**. TEMPO oxidation¹³ of the allylic alcohol **21** and subsequent removal of the PMB group afforded unsaturated aldehyde **22** in 76% yield in two steps. Finally, when **22** was treated with TiCl₄¹⁷ at –30 °C to room temperature, the acetonide deprotection and subsequent removal of the TES moiety proceeded in one-pot to produce the tetraol **2a** in 74% yield.

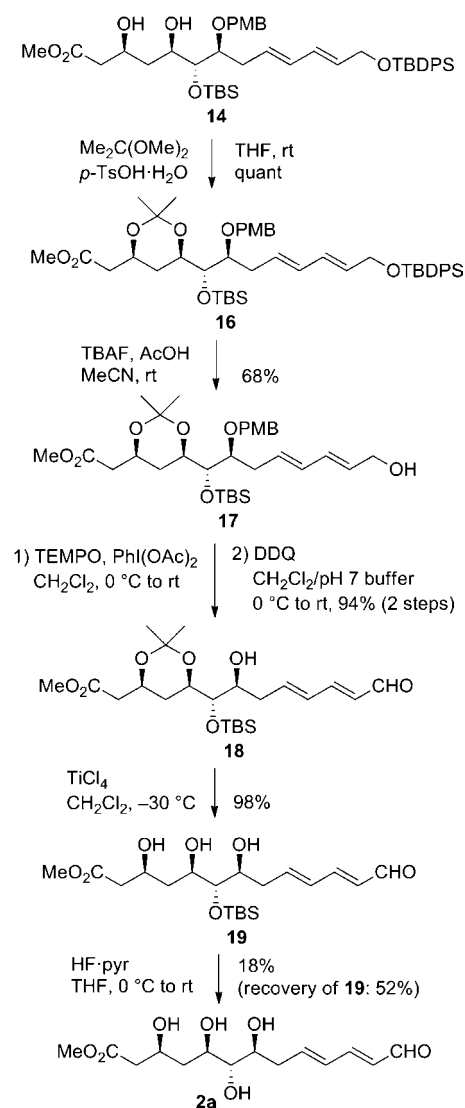
Stereoselective Synthesis of 2b. We next examined the stereoselective synthesis of the second target molecule **2b**, which is the C6-epimer of **2a**. We envisioned the stereo-inversion at the C6 position by the oxidation–reduction process. Thus, selective protection of the primary hydroxy group of the diol **20** with TESCl/imidazole yielded the secondary alcohol, which was subjected to the TPAP oxidation¹⁹ to afford ketone **23** (Scheme 7). Diastereoselective reduction of **23** with NaBH₄ proceeded successfully to provide the desired alcohol **24** in 98% yield as the sole diastereomer. This stereochemical outcome is in line with a Felkin–Anh model, which is doubly effected by the C5 and C7 stereogenic centers. The ¹H NMR spectrum of **24** was clearly different from that of the secondary alcohol obtained in the first step

Scheme 4. Synthesis of **14** and Its Stereochemical Confirmation at the C3 Position

from **20**, which resulted in the configurational confirmation at the C6 stereogenic center of **24**. TES protection of the resulting secondary hydroxy moiety of **24**, followed by selective removal of the primary TES group, yielded alcohol **25**. Oxidation of **25** with TEMPO/PhI(OAc)₂¹³ and subsequent removal of the PMB group gave unsaturated aldehyde **26** in 82% yield in two steps. Stepwise deprotection of **26**, that is, removal of the acetonide moiety by TiCl₄¹⁷ and the TES group by HF-pyr, furnished the second target molecule **2b**.

Stereoselective Synthesis of 2c and 2d. Having completed the stereoselective and stereodivergent synthesis of the first and second target molecules **2a** and **2b** bearing the *syn* relationships at the C3 and C5 positions, we next commenced the synthesis of the third and fourth target molecules **2c** and **2d** with the C3/C5 *anti* correlations. The stereoselective synthesis of **2c** is illustrated in Scheme 8. Treatment of the β-hydroxy ketone **11** with NaBH(OAc)₃²⁰ furnished the desired *anti*-diol **27** in 95% yield as a single diastereomer, as judged by its ¹H NMR spectrum, which was clearly different from that of the *syn*-diol **14**. Further transformation of **27** toward **2c** was similar to that used in the synthesis of **2a**. Protection of the resulting diol moiety of **27** and desilylation afforded diol **28**. The diol **28** was transformed to unsaturated aldehyde **29** by the following four-step sequence: (1) bis-silylation, (2) selective desilylation of the primary TES moiety, (3) TEMPO oxidation¹³ of the allylic alcohol, and (4) removal of the PMB group. Simultaneous removal of the acetonide and TES moieties was performed with TiCl₄¹⁷ to provide the third target molecule **2c** in 44% yield.

The stereocontrolled synthesis of **2d**, whose synthetic route was analogous to that of **2b**, is shown in Scheme 9. The alcohol **28**, which was the key synthetic intermediate toward **2c**, was converted to ketone **30** through the selective silylation of the primary alcohol and TPAP oxidation¹⁹ of the secondary alcohol. The ketone **30** was reduced with NaBH₄ to give alcohol **31** as the sole diastereomer. The resulting stereochemistry at the C6 position of **31** was confirmed by comparing the ¹H NMR spectra between **31** and the secondary alcohol synthesized in the first transformation from **28**. Acetonide **32**, which was synthesized from the alcohol **31** in 54% overall yield

Scheme 5. Synthesis of **2a**

in four steps, was deprotected with TiCl₄¹⁷ to provide the fourth target molecule **2d** in 47% yield.

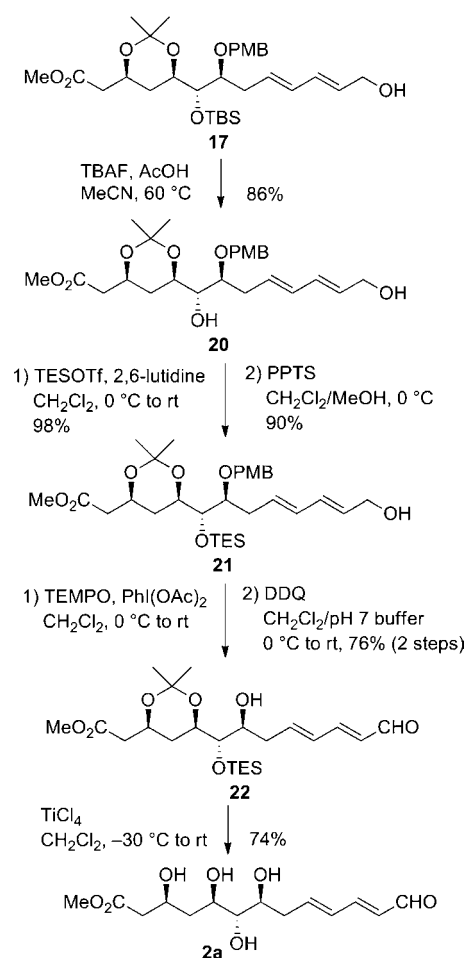
Relative Stereostructure of the C1–C13 Fragment.

With all four possible diastereomers **2a–2d** in hand, we next compared these ¹H NMR data with those of the degraded product **2**. As described in Table 1, the ¹H NMR chemical shifts of the synthetic **2b** were found to be in full agreement with those of the degraded product **2**.²¹ On the other hand, the ¹H NMR chemical shifts of the synthetic **2a**, **2c**, and **2d** were clearly different from those of the degraded product **2**, respectively. Especially, the chemical shifts of two geminal protons at the C4 position of **2a**, **2c**, and **2d** were different to each other, respectively, whereas the chemical shifts of these protons of **2** and **2b** were found to be the same. Therefore, the relative stereostructure of the C1–C13 fragment of symbiodinolide (**1**) was elucidated to be that described in **2b**.

CONCLUSION

First, we have analyzed the ¹H NMR chemical shifts and coupling constants of the degraded product **2** obtained from natural symbiodinolide (**1**) and proposed its four possible

Scheme 6. Improved Synthesis of 2a

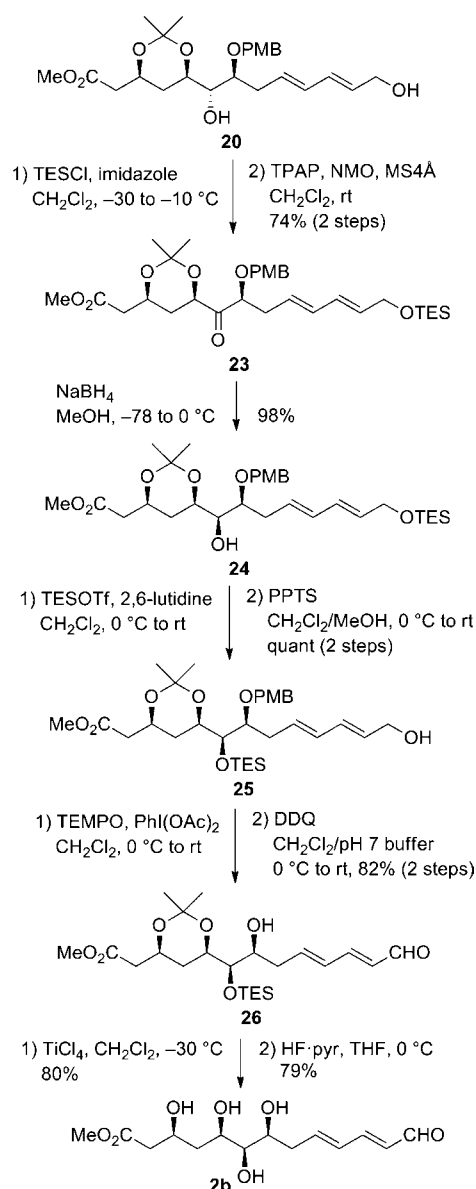


diastereomers **2a–2d** by comparing with the universal NMR databases reported by Kishi's research group. Next, we have examined the stereodivergent synthesis of **2a–2d** in the unified manner. Thus, the β -hydroxy ketone **11**, which would be the key common synthetic intermediate of **2a–2d**, was synthesized by aldol reaction between methyl acetoacetate (**3**) and the aldehyde derived from **10**. Diastereoselective reduction of **11** provided the *syn*-diol **14** (by Et₂BOMe/NaBH₄) and the *anti*-diol **27** (by NaBH(OAc)₃), respectively. Deprotection and oxidation of the allylic alcohol moiety of **14** produced the first target molecule **2a**. The second target molecule **2b** was synthesized via the stereoinversion at the C6 position by diastereoselective reduction of the ketone **23**. In the similar synthetic route, the third and fourth target molecules **2c** and **2d** were yielded from the *anti*-diol **27**, respectively and stereoselectively. Comparison of the ¹H NMR data of the synthetic **2a–2d** with those of the degraded product **2** determined the relative stereochemistry of the C1–C13 fragment of symbiodinolide (**1**) to be depicted in **2b**.

EXPERIMENTAL SECTION

Allylic Alcohol 9. To a solution of allylic alcohol **8** (5.04 g, 12.8 mmol) in CH₂Cl₂ (51 mL) and DMSO (13 mL) were added Et₃N (7.8 mL, 56.3 mmol) and SO₃·pyr (4.07 g, 25.6 mmol) at 0 °C. The mixture was stirred at room temperature for 2 h. The mixture was diluted with EtOAc, washed with saturated aqueous NH₄Cl, H₂O, and brine, and then dried over Na₂SO₄. Concentration and column

Scheme 7. Synthesis of 2b

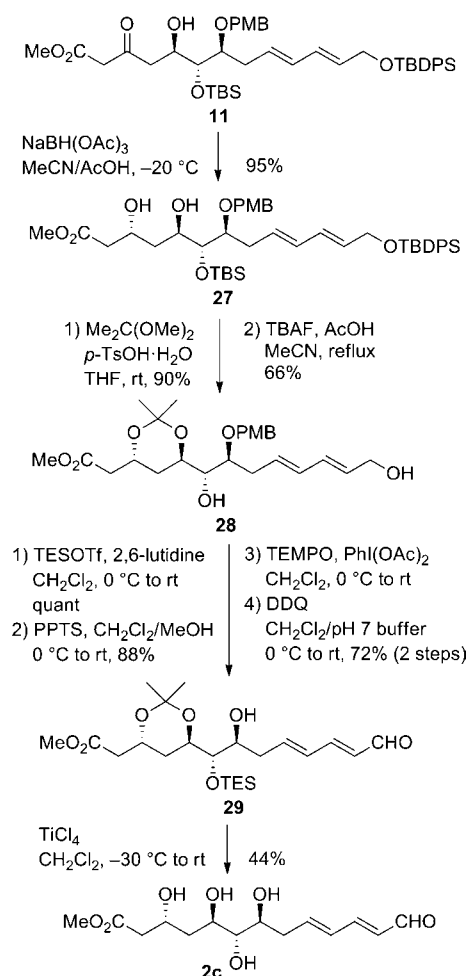


chromatography (hexane/EtOAc = 10:1) gave the corresponding α,β -unsaturated aldehyde (4.53 g), which was used for the next reaction without further purification.

To a suspension of NaH (60% dispersion in oil, 1.11 g, 27.8 mmol), washed with hexane in advance) in benzene (15 mL) was added (EtO)₂P(O)CH₂CO₂Et (6.0 mL, 30.2 mmol) at 0 °C. After the mixture was stirred at room temperature for 15 min, the aldehyde obtained above (4.53 g) in benzene (10 mL + 6.0 mL + 4.0 mL) was added at room temperature. After the mixture was stirred at room temperature for 2 h, the reaction was quenched with H₂O at 0 °C. The mixture was diluted with EtOAc, washed with H₂O and brine, and then dried over Na₂SO₄. Concentration and column chromatography (hexane/EtOAc = 20:1) gave the corresponding α,β -unsaturated ester (4.85 g), which was used for the next reaction without further purification.

To a solution of the ester obtained above (4.85 g) in CH₂Cl₂ (50 mL) was added DIBAL-H (1.04 M solution in hexane, 20 mL, 20.8 mmol) at -78 °C. After the mixture was stirred at -78 °C for 30 min, the reaction was quenched with MeOH. The mixture was filtered through a Celite pad and washed with EtOAc. Concentration and

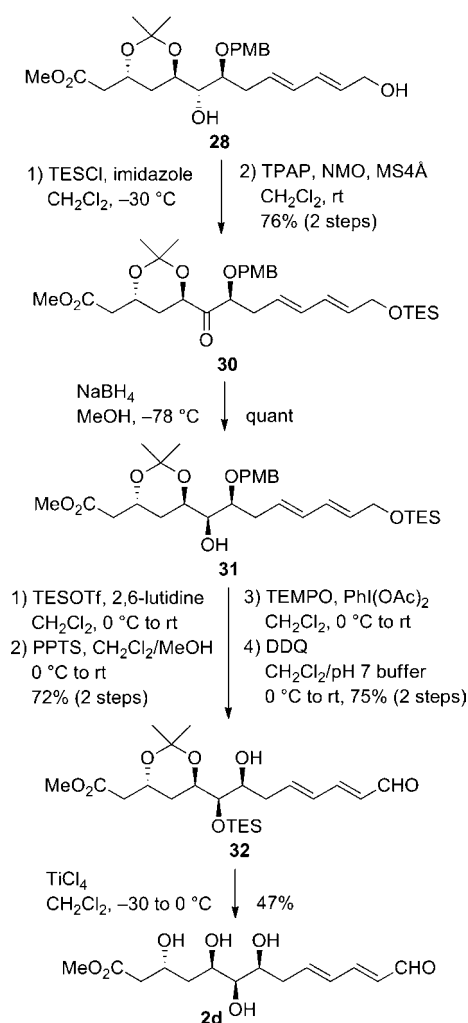
Scheme 8. Synthesis of 2c



column chromatography (hexane/EtOAc = 4:1) gave allylic alcohol **9** (4.11 g, 77% in three steps) as a colorless oil: R_f = 0.19 (hexane/EtOAc = 4:1); $[\alpha]_D^{25}$ -60.6 (c 0.92, CHCl₃); IR (neat) 3427, 2929, 2856, 1615 cm⁻¹; ¹H NMR (400 MHz, CDCl₃) δ 7.39 (d, J = 8.5 Hz, 2 H), 6.88 (d, J = 8.5 Hz, 2 H), 6.28–6.11 (m, 2 H), 5.85 (dt, J = 15.0, 6.6 Hz, 1 H), 5.75 (dt, J = 15.0, 6.6 Hz, 1 H), 5.43 (s, 1 H), 4.19–4.16 (m, 3 H), 3.80 (s, 3 H), 3.60–3.57 (m, 3 H), 2.64 (dd, J = 14.4, 6.6 Hz, 1 H), 2.36 (dd, J = 14.4, 6.6 Hz, 1 H), 1.30–1.25 (m, 1 H), 0.91 (s, 9 H), 0.11 (s, 3 H), 0.09 (s, 3 H); ¹³C NMR (100 MHz, CDCl₃) δ 159.8, 131.7, 130.5, 130.4, 130.0, 127.6, 127.3, 113.5, 100.7, 81.9, 71.7, 66.2, 63.5, 55.3, 34.8, 25.8, 18.0, -4.0, -4.6; HRMS (ESI-TOF) calcd for C₂₃H₃₆O₅SiNa [M + Na]⁺ 443.2230, found 443.2236.

Alcohol 10. To a solution of alcohol **9** (234 mg, 0.558 mmol) in CH₂Cl₂ (5.0 mL) were added DMAP (107 mg, 0.873 mmol), imidazole (59.6 mg, 0.873 mmol), and TBDPSCl (0.17 mL, 0.670 mmol) at 0 °C. After the mixture was stirred at room temperature for 20 min, the reaction was quenched with saturated aqueous NH₄Cl. The mixture was diluted with EtOAc, washed with H₂O and brine, and then dried over Na₂SO₄. Concentration and column chromatography (hexane/EtOAc = 50:1, 10:1) gave the corresponding TBDPS ether (400 mg, quant) as a colorless oil: R_f = 0.76 (hexane/EtOAc = 2:1); $[\alpha]_D^{24}$ -33.7 (c 0.95, CHCl₃); IR (neat) 2930, 2844, 1615 cm⁻¹; ¹H NMR (400 MHz, CDCl₃) δ 7.72–7.69 (m, 4 H), 7.45–7.37 (m, 8 H), 6.91 (dd, J = 8.6, 1.8 Hz, 2 H), 6.32–6.14 (m, 2 H), 5.87 (dt, J = 14.9, 7.8 Hz, 1 H), 5.71 (dt, J = 14.9, 4.9 Hz, 1 H), 5.47 (s, 1 H), 4.26 (d, J = 4.9 Hz, 2 H), 4.19 (dt, J = 8.6, 2.0 Hz, 1 H), 3.82 (s, 3 H), 3.64–3.56 (m, 3 H), 2.67 (dd, J = 14.9, 6.9 Hz, 1 H), 2.42–2.39 (m, 1 H), 1.10 (s, 9 H), 0.94 (s, 9 H), 0.14 (s, 3 H), 0.12 (s, 3 H); ¹³C NMR (100

Scheme 9. Synthesis of 2d

Table 1. ¹H NMR Chemical Shifts of the Degraded Product **2** and the Synthetic Products **2a–2d^a**

position	2 ^b	2a ^c	2b ^c	2c ^c	2d ^c
1-CO ₂ Me	3.67	3.67	3.67	3.67	3.67
2	2.56	2.56	2.56	2.49	2.48
	2.44	2.44	2.44	2.49	2.48
3	4.21	4.31	4.22	4.31	4.27
4	1.75	1.85	1.75	1.78	1.70
	1.75	1.70	1.75	1.60	1.59
5	3.88	3.84	3.89	3.91	3.93
6	3.33	3.39	3.32	3.39	3.23
7	3.81	3.72	3.80	3.73	3.82
8	2.52	2.61	2.52	2.62	2.52
	2.48	2.40	2.47	2.42	2.48
9	6.47	6.48	6.47	6.50	6.49
10	6.47	6.48	6.47	6.50	6.49
11	7.29	7.29	7.29	7.30	7.29
12	6.09	6.08	6.09	6.08	6.09
13-CHO	9.49	9.49	9.49	9.49	9.49

^aChemical shifts are reported in ppm with reference to the solvent signal (CD₃OD, 3.30 ppm). ^bRecorded at 800 MHz. ^cRecorded at 600 MHz.

MHz, CDCl₃) δ 159.8, 135.5, 135.5, 135.4, 133.7, 132.1, 130.4, 129.9, 129.5, 129.3, 127.6, 127.3, 113.5, 100.7, 82.0, 71.7, 66.2, 64.2, 55.3, 34.9, 26.9, 25.8, 19.3, 18.0, -4.0, -4.6; HRMS (ESI–TOF) calcd for C₃₉H₅₄O₅Si₂Na [M + Na]⁺ 681.3408, found 681.3398.

To a solution of the corresponding *p*-methoxybenzylidene acetal (610 mg, 0.926 mmol) in toluene (19 mL) was added DIBAL-H (1.04 M solution in hexane, 5.4 mL, 5.55 mmol) at -50 °C. After the mixture was gradually warmed up to -10 °C for 2 h, the reaction was quenched with MeOH. The mixture was filtered through a Celite pad and washed with EtOAc. Concentration and column chromatography (hexane/EtOAc = 10:1, 7:1, 4:1) gave alcohol **10** (447 mg, 73%) as a colorless oil and the acetal (70.0 mg, 12% recovery). Alcohol **10**: R_f = 0.73 (hexane/EtOAc = 2:1); $[\alpha]_D^{25}$ -14.1 (c 1.00, CHCl₃); IR (neat) 3476, 2930, 2864 cm⁻¹; ¹H NMR (400 MHz, CDCl₃) δ 7.71–7.68 (m, 4 H), 7.45–7.26 (m, 8 H), 6.89 (d, *J* = 8.6 Hz, 2 H), 6.27 (dd, *J* = 15.0, 10.6 Hz, 1 H), 6.14 (dd, *J* = 15.0, 10.6 Hz, 1 H), 5.73–5.68 (m, 2 H), 4.55 (s, 2 H), 4.26 (d, *J* = 4.2 Hz, 2 H), 3.79 (s, 3 H), 3.79–3.55 (m, 4 H), 2.52–2.46 (m, 1 H), 2.39–2.33 (m, 1 H), 2.21 (brs, 1 H), 1.08 (s, 9 H), 0.93 (s, 9 H), 0.12 (s, 3 H), 0.11 (s, 3 H); ¹³C NMR (100 MHz, CDCl₃) δ 159.2, 135.4, 133.7, 132.3, 130.4, 130.3, 129.9, 129.7, 129.5, 127.6, 113.8, 80.4, 74.0, 72.5, 64.2, 55.3, 34.5, 26.9, 25.9, 19.3, 18.1, -4.3, -4.5; HRMS (ESI–TOF) calcd for C₃₉H₅₆O₅Si₂Na [M + Na]⁺ 683.3564, found 683.3555.

β -Hydroxy Ketone 11. To a solution of alcohol **10** (79.3 mg, 0.148 mmol) in CH₂Cl₂ (1.0 mL) and DMSO (0.3 mL) were added Et₃N (0.10 mL, 0.740 mmol) and SO₃·pyr (94.2 mg, 0.592 mmol) at 0 °C. The mixture was stirred at room temperature for 2 h. The mixture was diluted with EtOAc, washed with H₂O and brine, and then dried over Na₂SO₄. Concentration and column chromatography (hexane/EtOAc = 20:1) gave the corresponding aldehyde (75.4 mg, 95%) as a colorless oil: R_f = 0.70 (hexane/EtOAc = 2:1) $[\alpha]_D^{21}$ -14.1 (c 1.06, CHCl₃); IR (neat) 2931, 2858, 1739 cm⁻¹; ¹H NMR (400 MHz, CDCl₃) δ 9.60 (s, 1 H), 7.73–7.68 (m, 4 H), 7.44–7.36 (m, 6 H), 7.25 (d, *J* = 8.3 Hz, 2 H), 6.87 (d, *J* = 8.3 Hz, 2 H), 6.27–6.10 (m, 2 H), 5.70 (dt, *J* = 14.4, 4.6 Hz, 1 H), 5.55 (dt, *J* = 14.4, 6.8 Hz, 1 H), 4.58–4.49 (m, 2 H), 4.25 (d, *J* = 4.6 Hz, 2 H), 4.14–4.12 (m, 1 H), 3.80 (s, 3 H), 3.73–3.69 (m, 1 H), 2.43 (t, *J* = 6.8 Hz, 2 H), 1.08 (s, 9 H), 1.00 (s, 9 H), 0.10 (s, 3 H), 0.09 (s, 3 H); ¹³C NMR (100 MHz, CDCl₃) δ 203.2, 159.1, 135.4, 133.6, 133.2, 131.0, 130.0, 129.5, 129.4, 128.6, 127.6, 113.7, 80.8, 79.0, 71.9, 64.2, 55.3, 33.9, 26.9, 25.8, 19.3, 18.3, -4.6, -4.7; HRMS (ESI–TOF) calcd for C₃₉H₅₄O₅Si₂Na [M + Na]⁺ 681.3408, found 681.3410.

To a suspension of NaH (60% dispersion in oil, 19.7 mg, 0.493 μ mol, washed with hexane in advance) in THF (1.0 mL) was added methyl acetoacetate (**3**) (29.5 μ L, 0.247 mmol) at 0 °C. After the mixture was stirred at 0 °C for 20 min, *n*-BuLi (1.57 M solution in hexane, 0.19 mL, 0.301 mmol) was added at 0 °C. After the mixture was stirred at 0 °C for 10 min, the corresponding aldehyde (90.3 mg, 0.137 mmol) in THF (0.3 mL + 0.2 mL) was added at -78 °C. After the mixture was stirred at -78 °C for 15 min, the reaction was quenched with saturated aqueous NH₄Cl. The mixture was diluted with EtOAc, washed with H₂O and brine, and then dried over Na₂SO₄. Concentration and column chromatography (hexane/EtOAc = 6:1) gave β -hydroxy ketone **11** (100 mg, 94%, dr = 6:1) as a colorless oil: R_f = 0.21 (hexane/EtOAc = 4:1); $[\alpha]_D^{25}$ +2.2 (c 1.00, CHCl₃); IR (neat) 3517, 2930, 2856, 1748, 1715 cm⁻¹; ¹H NMR (400 MHz, C₆D₆) δ 7.80–7.78 (m, 4 H), 7.23–7.22 (m, 8 H), 6.83 (d, *J* = 8.5 Hz, 2 H), 6.42 (dd, *J* = 15.0, 10.6 Hz, 1 H), 6.22 (dd, *J* = 15.0, 10.6 Hz, 1 H), 5.84 (dt, *J* = 15.0, 7.4 Hz, 1 H), 5.69 (dt, *J* = 15.0, 5.1 Hz, 1 H), 4.41 (d, *J* = 4.6 Hz, 2 H), 4.32–4.28 (m, 1 H), 4.24 (d, *J* = 4.6 Hz, 2 H), 3.87 (t, *J* = 4.6 Hz, 1 H), 3.62–3.58 (m, 1 H), 3.32 (s, 3 H), 3.26 (s, 3 H), 3.03 (s, 2 H), 2.80–2.78 (m, 1 H), 2.74 (d, *J* = 2.8 Hz, 1 H), 2.69–2.61 (m, 1 H), 2.50–2.45 (m, 2 H), 1.19 (s, 9 H), 1.01 (s, 9 H), 0.19 (s, 3 H), 0.18 (s, 3 H); ¹³C NMR (100 MHz, C₆D₆) δ 203.3, 159.8, 135.9, 134.2, 132.6, 130.9, 130.8, 130.5, 129.9, 114.1, 79.9, 77.1, 72.1, 69.0, 64.7, 54.9, 51.8, 49.8, 45.6, 34.0, 27.2, 26.5, 19.6, 18.7, -3.9, -4.0; HRMS (ESI–TOF) calcd for C₄₄H₆₂O₅Si₂Na [M + Na]⁺ 797.3881, found 797.3875.

Unsaturated Aldehyde 12. To a solution of TBDPS ether **11** (27.9 mg, 36.0 μ mol) in THF (3.6 mL) was added HF·pyr (100 μ L) at

0 °C. The mixture was stirred at 0 °C for 1 h. After the mixture was stirred at room temperature for 6 h, HF·pyr (100 μ L) was added at 0 °C. The mixture was stirred at 0 °C for 1 h. After the mixture was stirred at room temperature for 2 h, the reaction was quenched with saturated aqueous NaHCO₃. The mixture was diluted with EtOAc, washed with saturated aqueous NaHCO₃, H₂O, and brine, and then dried over Na₂SO₄. Concentration and column chromatography (hexane/EtOAc = 10:1, 2:1) gave the corresponding alcohol (15.4 mg), which was used for the next reaction without further purification.

To a solution of the alcohol obtained above (15.4 mg) in CH₂Cl₂ (3.0 mL) were added PhI(OAc)₂ (25.0 mg, 77.8 μ mol) and TEMPO (0.48 mg, 3.10 μ mol) at 0 °C. After the mixture was stirred at 0 °C for 6 h, the reaction was quenched with saturated aqueous Na₂S₂O₃. The mixture was diluted with EtOAc, washed with H₂O and brine, and then dried over Na₂SO₄. Concentration and column chromatography (hexane/EtOAc = 4:1) gave unsaturated aldehyde **12** (11.6 mg, 60% in two steps) as a colorless oil: R_f = 0.43 (hexane/EtOAc = 1:1); $[\alpha]_D^{25}$ -1.8 (c 0.10, CHCl₃); IR (neat) 3483, 2927, 2855, 1747, 1682, 1638 cm⁻¹; ¹H NMR (400 MHz, CDCl₃) δ 9.54 (d, *J* = 7.8 Hz, 1 H), 7.21 (d, *J* = 8.3 Hz, 2 H), 7.03 (dd, *J* = 15.2, 10.2 Hz, 1 H), 6.86 (d, *J* = 8.3 Hz, 2 H), 6.38–6.32 (m, 1 H), 6.28–6.20 (m, 1 H), 6.12–6.04 (m, 1 H), 4.52 (d, *J* = 11.5 Hz, 1 H), 4.42 (d, *J* = 11.5 Hz, 1 H), 4.17–4.11 (m, 1 H), 3.80 (s, 3 H), 3.74 (s, 3 H), 3.44 (s, 2 H), 2.91–2.85 (m, 1 H), 2.74–2.67 (m, 1 H), 2.50 (t, *J* = 6.2 Hz, 2 H), 0.91 (s, 9 H), 0.10 (s, 6 H); ¹³C NMR (100 MHz, CDCl₃) δ 203.5, 193.6, 167.1, 159.3, 152.1, 143.3, 130.5, 130.3, 129.6, 113.8, 78.9, 76.0, 71.9, 68.6, 55.3, 52.4, 49.7, 45.8, 34.0, 26.1, 18.3, -4.0, -4.4; HRMS (ESI–TOF) calcd for C₂₈H₄₂O₅SiNa [M + Na]⁺ 557.2546, found 557.2552.

***p*-Methoxybenzylidene Acetal 13.** To a suspension of alcohol **12** (5.9 mg, 11.0 μ mol) and MS4 Å (10.0 mg) in CH₂Cl₂ (0.5 mL) was added DDQ (3.7 mg, 16.5 μ mol) at 0 °C. After the mixture was stirred at 0 °C for 1 h, the mixture was filtered through a Celite pad and washed with EtOAc. The mixture was washed with saturated aqueous NaHCO₃ and brine, and then dried over Na₂SO₄. Concentration and column chromatography (hexane/EtOAc = 5:1) gave *p*-methoxybenzylidene acetal **13** (2.4 mg, 41%) as a colorless oil: R_f = 0.47 (hexane/EtOAc = 2:1); $[\alpha]_D^{25}$ -27.6 (c 0.09, CHCl₃); IR (neat) 2925, 2854, 1732, 1682, 1642 cm⁻¹; ¹H NMR (400 MHz, C₆D₆) δ 9.38 (d, *J* = 7.8 Hz, 1 H), 7.41 (d, *J* = 8.8 Hz, 2 H), 6.78 (d, *J* = 8.8 Hz, 2 H), 6.44–6.37 (m, 1 H), 6.05–6.01 (m, 2 H), 5.92 (dd, *J* = 15.4, 7.8 Hz, 1 H), 5.28 (s, 1 H), 3.86–3.80 (m, 1 H), 3.50–3.45 (m, 2 H), 3.34–3.20 (m, 4 H), 3.31 (s, 3 H), 3.18 (s, 3 H), 2.61–2.58 (m, 1 H), 2.29–2.22 (m, 1 H), 1.00 (s, 9 H), 0.09 (s, 3 H), 0.02 (s, 3 H); ¹³C NMR (100 MHz, C₆D₆) δ 192.2, 164.4, 160.8, 159.9, 150.3, 140.1, 131.4, 130.3, 130.0, 114.0, 109.0, 100.9, 81.0, 79.1, 71.6, 54.9, 52.1, 35.8, 31.7, 26.1, 26.0, 18.4, -3.2, -3.4; HRMS (ESI–TOF) calcd for C₂₈H₄₀O₅SiNa [M + Na]⁺ 555.2390, found 555.2383.

Diol 14. To a solution of β -hydroxy ketone **11** (311 mg, 0.401 mmol) in THF (8.6 mL) and MeOH (2.1 mL) was added Et₃BOME (0.48 mL, 0.481 mmol) at -78 °C. After the mixture was stirred at -78 °C for 15 min, NaBH₄ (18.2 mg, 0.481 mmol) was added. After the mixture was stirred at -78 °C for 1 h, the reaction was quenched with AcOH. The mixture was diluted with EtOAc, washed with saturated aqueous NaHCO₃ and brine, and then dried over Na₂SO₄. Addition of MeOH (10 mL) to the mixture and concentration (five times repetition), and column chromatography (hexane/EtOAc = 5:1) gave diol **14** (304 mg, 98%) as a colorless oil: R_f = 0.45 (hexane/EtOAc = 2:1); $[\alpha]_D^{25}$ -2.5 (c 1.00, CHCl₃); IR (neat) 3464, 2930, 2857, 1739, 1613 cm⁻¹; ¹H NMR (400 MHz, C₆D₆) δ 7.80–7.79 (m, 4 H), 7.25–7.22 (m, 8 H), 6.81 (d, *J* = 8.5 Hz, 2 H), 6.43 (dd, *J* = 15.1, 10.5 Hz, 1 H), 6.28 (dd, *J* = 15.1, 10.5 Hz, 1 H), 5.94 (dt, *J* = 15.1, 7.1 Hz, 1 H), 5.74 (dt, *J* = 15.1, 5.1 Hz, 1 H), 4.45 (d, *J* = 4.2 Hz, 2 H), 4.24 (d, *J* = 4.2 Hz, 2 H), 4.07–3.98 (m, 1 H), 3.88–3.75 (m, 2 H), 3.65–3.54 (m, 1 H), 3.31 (s, 3 H), 3.25 (s, 3 H), 2.63–2.60 (m, 2 H), 2.44 (t, *J* = 5.1 Hz, 1 H), 2.25 (dd, *J* = 16.3, 8.5 Hz, 1 H), 2.12 (dd, *J* = 16.3, 3.6 Hz, 1 H), 1.78–1.59 (m, 2 H), 1.20 (s, 9 H), 1.03 (s, 9 H), 0.26 (s, 3 H), 0.20 (s, 3 H); ¹³C NMR (100 MHz, C₆D₆) δ 172.6, 159.7, 135.9, 134.2, 132.9, 132.4, 131.4, 131.1, 130.7, 130.5, 130.2, 129.9, 114.0, 79.9, 77.7, 73.6, 72.1, 69.6, 64.7, 54.8, 51.2, 41.8, 38.6,

33.9, 27.2, 26.6, 19.6, 18.8, -3.7, -3.9; HRMS (ESI-TOF) calcd for $C_{44}H_{64}O_8Si_2Na$ [$M + Na$] $^+$ 799.4037, found 799.4037.

***p*-Methoxybenzylidene Acetal 15.** To a suspension of diol 14 (5.3 mg, 6.82 μ mol) and MS4 Å (5.0 mg) in CH_2Cl_2 (0.5 mL) were added *p*-MeOC₆H₄CH(OMe)₂ (1.7 μ L, 10.2 μ mol) and CSA (1.0 mg, 4.30 μ mol) at 0 °C. The mixture was stirred at room temperature for 4 h. To the mixture were added *p*-MeOC₆H₄CH(OMe)₂ (1.7 μ L, 10.2 μ mol) and CSA (1.0 mg, 4.30 μ mol) at 0 °C. After the mixture was stirred at room temperature for a further 12 h, the reaction was quenched with Et₃N. The mixture was filtered through a Celite pad and washed with EtOAc. Concentration and column chromatography (hexane/EtOAc = 10:1) gave *p*-methoxybenzylidene acetal 15 (4.0 mg, 66%) as a colorless oil: R_f = 0.44 (hexane/EtOAc = 4:1); $[\alpha]_D^{25}$ -16.3 (*c* 0.09, CHCl₃); IR (neat) 2928, 2855, 1741, 1614 cm^{-1} ; ¹H NMR (400 MHz, C₂D₂N) δ 7.85–7.83 (m, 5 H), 7.65 (d, *J* = 8.5 Hz, 2 H), 7.47–7.44 (m, 6 H), 7.04–7.01 (m, 5 H), 6.55 (dd, *J* = 15.1, 10.4 Hz, 1 H), 6.38 (dd, *J* = 15.1, 10.4 Hz, 1 H), 6.00 (dt, *J* = 15.1, 7.3 Hz, 1 H), 5.86 (dt, *J* = 15.1, 4.8 Hz, 1 H), 5.73 (s, 1 H), 4.62 (s, 2 H), 4.54–4.47 (m, 1 H), 4.36 (d, *J* = 4.8 Hz, 2 H), 4.29–4.24 (m, 1 H), 4.17 (t, *J* = 4.8 Hz, 1 H), 3.88–3.84 (m, 1 H), 3.68 (s, 3 H), 3.64 (s, 3 H), 3.63 (s, 3 H), 2.89 (dd, *J* = 15.1, 7.3 Hz, 1 H), 2.76–2.64 (m, 2 H), 1.93–1.80 (m, 2 H), 1.25–1.23 (m, 1 H), 1.13 (s, 9 H), 1.01 (s, 9 H), 0.24 (s, 6 H); ¹³C NMR (100 MHz, C₂D₂N) δ 171.1, 160.3, 159.7, 135.9, 135.0, 134.2, 132.4, 131.9, 131.5, 131.2, 130.8, 130.7, 130.2, 128.3, 128.2, 123.0, 114.2, 113.9, 101.2, 79.1, 77.5, 76.5, 73.8, 71.7, 64.8, 55.3, 51.6, 41.5, 33.5, 32.5, 27.1, 26.5, 19.6, 18.8, -3.7, -3.9; HRMS (ESI-TOF) calcd for $C_{32}H_{70}O_9Si_2Na$ [$M + Na$] $^+$ 917.4456, found 917.4457.

Acetonide 16. To a solution of diol 14 (202 mg, 0.260 mmol) in THF (2.6 mL) were added Me₂C(OMe)₂ (0.32 mL, 2.26 mmol) and *p*-TsOH·H₂O (4.9 mg, 26.0 μ mol) at room temperature. After the mixture was stirred at room temperature for 30 min, the reaction was quenched with saturated aqueous NaHCO₃. The mixture was diluted with EtOAc, washed with H₂O and brine, and then dried over Na₂SO₄. Concentration and column chromatography (hexane/EtOAc = 7:1) gave acetonide 16 (212 mg, quant) as a colorless oil: R_f = 0.62 (hexane/EtOAc = 2:1); $[\alpha]_D^{25}$ -8.2 (*c* 1.25, CHCl₃); IR (neat) 2929, 2858, 1741 cm^{-1} ; ¹H NMR (400 MHz, CDCl₃) δ 7.69 (dd, *J* = 7.6, 1.4 Hz, 4 H), 7.44–7.36 (m, 6 H), 7.25 (d, *J* = 8.6 Hz, 2 H), 6.86 (d, *J* = 8.6 Hz, 2 H), 6.25 (dd, *J* = 15.1, 10.5 Hz, 1 H), 6.11 (dd, *J* = 15.1, 10.5 Hz, 1 H), 5.76–5.65 (m, 2 H), 4.47 (s, 2 H), 4.25–4.24 (m, 3 H), 3.97 (ddd, *J* = 7.3, 4.9, 2.4 Hz, 1 H), 3.79 (s, 3 H), 3.70–3.68 (m, 1 H), 3.68 (s, 3 H), 3.52–3.48 (m, 1 H), 2.54 (dd, *J* = 15.1, 7.3 Hz, 1 H), 2.42–2.33 (m, 3 H), 1.48–1.35 (m, 2 H), 1.41 (s, 3 H), 1.37 (s, 3 H), 1.08 (s, 9 H), 0.90 (s, 9 H), 0.10 (s, 3 H), 0.08 (s, 3 H); ¹³C NMR (100 MHz, CDCl₃) δ 171.2, 159.1, 135.5, 133.7, 131.7, 130.7, 130.1, 130.0, 129.6, 129.5, 129.3, 127.6, 113.6, 98.7, 78.8, 76.4, 71.6, 69.3, 66.0, 64.3, 55.3, 51.6, 41.6, 33.5, 31.7, 29.9, 26.9, 26.2, 19.8, 19.3, 18.5, -4.0, -4.3; HRMS (ESI-TOF) calcd for $C_{47}H_{68}O_8Si_2Na$ [$M + Na$] $^+$ 839.4351, found 839.4358.

Allylic Alcohol 17. To a solution of TBDPS ether 16 (174 mg, 0.213 mmol) in MeCN (2.2 mL) was added a mixed solution of TBAF (1.0 M solution in THF, 0.26 mL, 0.260 mmol) and AcOH (15 μ L, 0.256 mmol) at room temperature. After the mixture was stirred at room temperature for 5 h, the reaction was quenched with saturated aqueous NH₄Cl. The mixture was diluted with EtOAc, washed with H₂O and brine, and then dried over Na₂SO₄. Concentration and column chromatography (hexane/EtOAc = 10:1, 2:1) gave allylic alcohol 17 (84.8 mg, 68%) as a colorless oil: R_f = 0.33 (hexane/EtOAc = 2:1); $[\alpha]_D^{25}$ -5.5 (*c* 0.98, CHCl₃); IR (neat) 3459, 2952, 2858, 1740, 1612 cm^{-1} ; ¹H NMR (400 MHz, CDCl₃) δ 7.23 (d, *J* = 8.8 Hz, 2 H), 6.86 (d, *J* = 8.8 Hz, 2 H), 6.20 (dd, *J* = 15.3, 10.6 Hz, 1 H), 6.08 (dd, *J* = 15.3, 10.6 Hz, 1 H), 5.76–5.70 (m, 2 H), 4.45 (s, 2 H), 4.24–4.16 (m, 4 H), 3.94 (ddd, *J* = 12.6, 4.9, 2.4 Hz, 1 H), 3.80 (s, 3 H), 3.68 (s, 3 H), 3.48 (dt, *J* = 7.1, 4.4 Hz, 2 H), 2.53 (dd, *J* = 15.3, 7.1 Hz, 1 H), 2.38–2.33 (m, 3 H), 1.47 (dt, *J* = 12.6, 2.4 Hz, 1 H), 1.40 (s, 3 H), 1.36 (s, 3 H), 1.28–1.24 (m, 1 H), 0.89 (s, 9 H), 0.09 (s, 3 H), 0.07 (s, 3 H); ¹³C NMR (100 MHz, CDCl₃) δ 171.2, 159.0, 131.9, 131.7, 131.3, 130.6, 129.8, 129.6, 113.6, 98.7, 78.7, 76.3, 71.6, 69.3, 65.9, 63.5, 55.3, 51.6, 41.6, 33.4, 31.7, 29.9, 26.2, 19.8, 18.5, -4.0, -4.3; HRMS

(ESI-TOF) calcd for $C_{31}H_{50}O_8SiNa$ [$M + Na$] $^+$ 601.3173, found 601.3169.

Alcohol 18. To a solution of alcohol 17 (102 mg, 0.176 mmol) in CH_2Cl_2 (2.0 mL) were added PhI(OAc)₂ (146 mg, 0.440 mmol) and TEMPO (5.5 mg, 35.2 μ mol) at 0 °C. After the mixture was stirred at room temperature for 1 h, the reaction was quenched with saturated aqueous Na₂S₂O₃. The mixture was diluted with EtOAc, washed with H₂O and brine, and then dried over Na₂SO₄. Concentration and column chromatography (hexane/EtOAc = 6:1) gave the corresponding unsaturated aldehyde (102 mg), which was used for the next reaction without further purification.

To a solution of the PMB ether obtained above (102 mg) in CH_2Cl_2 (4.0 mL) and phosphate pH standard solution (0.2 mL) was added DDQ (47.9 mg, 0.211 mmol) at 0 °C. After the mixture was stirred at room temperature for 1 h, the reaction was quenched with saturated aqueous NaHCO₃. The mixture was diluted with EtOAc, washed with H₂O and brine, and then dried over Na₂SO₄. Concentration and column chromatography (hexane/EtOAc = 3:1) gave alcohol 18 (76.0 mg, 94% in two steps) as a colorless oil: R_f = 0.52 (hexane/EtOAc = 1:1); $[\alpha]_D^{25}$ -14.4 (*c* 0.97, CHCl₃); IR (neat) 3490, 2953, 2858, 1739, 1681, 1639 cm^{-1} ; ¹H NMR (400 MHz, CDCl₃) δ 9.54 (d, *J* = 7.8 Hz, 1 H), 7.09 (dd, *J* = 15.3, 9.9 Hz, 1 H), 6.43–6.31 (m, 2 H), 6.10 (dd, *J* = 15.3, 7.8 Hz, 1 H), 4.34–4.27 (m, 1 H), 4.03 (ddd, *J* = 8.0, 5.4, 2.4 Hz, 1 H), 3.81–3.76 (m, 1 H), 3.68 (s, 3 H), 3.53 (t, *J* = 5.4 Hz, 1 H), 2.56 (dd, *J* = 15.3, 7.0 Hz, 1 H), 2.55–2.49 (m, 1 H), 2.42–2.31 (m, 3 H), 1.70 (dt, *J* = 12.7, 2.4 Hz, 1 H), 1.45 (s, 3 H), 1.36 (s, 3 H), 0.90 (s, 9 H), 0.12 (s, 3 H), 0.10 (s, 3 H); ¹³C NMR (100 MHz, CDCl₃) δ 193.6, 171.1, 151.9, 143.0, 130.8, 130.6, 98.8, 77.2, 72.7, 69.7, 65.9, 51.7, 41.5, 36.5, 32.7, 29.9, 26.0, 19.8, 18.3, -3.8, -4.2; HRMS (ESI-TOF) calcd for $C_{23}H_{40}O_7SiNa$ [$M + Na$] $^+$ 479.2441, found 479.2440.

Triol 19. To a solution of acetonide 18 (4.8 mg, 10.5 μ mol) in CH_2Cl_2 (0.8 mL) was added TiCl₄ (1.7 μ L, 15.7 μ mol) at -30 °C. After the mixture was stirred at -30 °C for 5 min, the reaction was quenched with saturated aqueous NaHCO₃. The mixture was diluted with EtOAc and washed with H₂O and brine. The aqueous phase was washed with EtOAc three times. The combined organic layer was dried over Na₂SO₄. Concentration and column chromatography (hexane/EtOAc = 4:1, 1:1) gave triol 19 (4.3 mg, 98%) as a colorless oil: R_f = 0.09 (hexane/EtOAc = 1:1); $[\alpha]_D^{27}$ -5.1 (*c* 0.73, CHCl₃); IR (neat) 3449, 2928, 2856, 1737, 1681, 1639 cm^{-1} ; ¹H NMR (400 MHz, CDCl₃) δ 9.54 (d, *J* = 8.0 Hz, 1 H), 7.09 (dd, *J* = 15.3, 9.8 Hz, 1 H), 6.41–6.33 (m, 2 H), 6.10 (dd, *J* = 15.3, 8.0 Hz, 1 H), 4.33–4.27 (m, 1 H), 3.97 (ddd, *J* = 10.4, 5.6, 2.0 Hz, 1 H), 3.89–3.85 (m, 1 H), 3.73 (s, 3 H), 3.55 (t, *J* = 5.2 Hz, 1 H), 2.63–2.57 (m, 1 H), 2.53–2.51 (m, 2 H), 2.43–2.35 (m, 2 H), 1.86 (dt, *J* = 14.4, 2.4 Hz, 1 H), 1.67–1.55 (m, 3 H), 0.91 (s, 9 H), 0.13 (s, 3 H), 0.12 (s, 3 H); ¹³C NMR (100 MHz, CDCl₃) δ 193.7, 172.8, 152.0, 143.2, 130.8, 130.5, 77.9, 73.7, 72.6, 69.2, 51.9, 41.4, 38.4, 36.7, 26.1, 18.3, -4.0; HRMS (ESI-TOF) calcd for $C_{20}H_{36}O_7SiNa$ [$M + Na$] $^+$ 439.2128, found 439.2126.

Tetraol 2a from 19. To a solution of TBS ether 19 (12.4 mg, 29.8 μ mol) in THF (1.5 mL) was added HF-pyr (60 μ L) at 0 °C. The mixture was stirred at 0 °C for 2 h. After the mixture was stirred at room temperature for 2 h, HF-pyr (70 μ L) was added at 0 °C. The mixture was stirred at 0 °C for 30 min. After the mixture was stirred at room temperature for 6 h, the reaction was quenched with saturated aqueous NaHCO₃. The mixture was diluted with EtOAc and washed with saturated aqueous NaHCO₃, H₂O, and brine. The aqueous phase was washed with EtOAc three times. The combined organic layer was dried over Na₂SO₄. Concentration and column chromatography (CH₂Cl₂/MeOH = 20:1) gave tetraol 2a (1.6 mg, 18%) as a colorless oil and TBS ether 19 (6.4 mg, 52% recovery). Tetraol 2a: R_f = 0.33 (CH₂Cl₂/MeOH = 10:1); $[\alpha]_D^{22}$ +13.2 (*c* 0.12, CHCl₃); IR (neat) 3417, 2925, 1731, 1679, 1636 cm^{-1} ; ¹H NMR (600 MHz, CD₃OD) δ 9.49 (d, *J* = 7.8 Hz, 1 H), 7.33–7.27 (m, 1 H), 6.50–6.46 (m, 2 H), 6.08 (dd, *J* = 15.0, 7.8 Hz, 1 H), 4.33–4.27 (m, 1 H), 3.85–3.81 (m, 1 H), 3.73–3.69 (m, 1 H), 3.67 (s, 3 H), 3.39 (t, *J* = 6.3 Hz, 1 H), 2.66–2.54 (m, 2 H), 2.46–2.37 (m, 2 H), 1.85 (ddd, *J* = 14.4, 5.4, 2.4 Hz, 1 H), 1.73–1.67 (m, 1 H); ¹³C NMR (100 MHz, CD₃OD) δ 196.0, 173.8, 155.0, 145.7, 131.9, 131.0, 77.8, 73.0, 72.6, 68.3, 52.0, 43.0, 39.9,

37.9; HRMS (ESI–TOF) calcd for $C_{14}H_{22}O_7Na$ $[M + Na]^+$ 325.1263, found 325.1271.

Diol 20. To a solution of TBS ether **17** (160 mg, 0.277 mmol) in MeCN (2.8 mL) was added a mixed solution of TBAF (1.0 M solution in THF, 2.8 mL, 2.80 mmol) and AcOH (0.16 mL, 2.77 mmol) at room temperature. After the mixture was stirred at 60 °C for 6 days, the reaction was quenched with saturated aqueous NH_4Cl . The mixture was diluted with EtOAc and washed with H_2O and brine. The aqueous phase was washed with EtOAc three times. The combined organic layer was dried over Na_2SO_4 . Concentration and column chromatography (hexane/EtOAc = 2:1, EtOAc) gave diol **20** (111 mg, 86%) as a colorless oil: R_f = 0.09 (hexane/EtOAc = 1:1); $[\alpha]_D^{25} +10.5$ (c 0.71, $CHCl_3$); IR (neat) 3420, 2928, 2858, 1738, 1613 cm^{-1} ; 1H NMR (400 MHz, C_6D_6) δ 7.17 (d, J = 8.6 Hz, 2 H), 6.80 (d, J = 8.6 Hz, 2 H), 6.26–6.16 (m, 2 H), 5.91–5.86 (m, 1 H), 5.62 (dt, J = 14.0, 5.6 Hz, 1 H), 4.51–4.47 (m, 1 H), 4.43 (d, J = 11.2 Hz, 1 H), 4.33–4.29 (m, 1 H), 4.22 (d, J = 11.2 Hz, 1 H), 4.11–4.06 (m, 1 H), 3.92–3.84 (m, 3 H), 3.60–3.56 (m, 1 H), 3.33 (s, 3 H), 3.31 (s, 3 H), 2.62–2.48 (m, 3 H), 2.18 (dd, J = 15.6, 5.2 Hz, 1 H), 1.46–1.40 (m, 2 H), 1.39 (s, 3 H), 1.29 (s, 3 H), 0.92 (t, J = 7.2 Hz, 1 H); ^{13}C NMR (100 MHz, C_6D_6) δ 170.9, 159.9, 132.7, 131.2, 130.9, 130.7, 130.0, 114.2, 99.0, 77.6, 73.8, 71.2, 69.7, 66.3, 63.3, 54.9, 51.2, 41.6, 32.9, 31.4, 30.3, 19.9; HRMS (ESI–TOF) calcd for $C_{25}H_{36}O_8Na$ $[M + Na]^+$ 487.2308, found 487.2306.

Allylic Alcohol 21. To a solution of diol **20** (94.4 mg, 0.163 mmol) in CH_2Cl_2 (1.6 mL) were added 2,6-lutidine (67 μL , 0.456 mmol) and TESOTf (88 μL , 0.391 mmol) at 0 °C. After the mixture was stirred at room temperature for 40 min, the reaction was quenched with saturated aqueous NH_4Cl . The mixture was diluted with EtOAc, washed with H_2O and brine, and then dried over Na_2SO_4 . Concentration and column chromatography (hexane/EtOAc = 20:1, 10:1) gave the corresponding bis-TES ether (111 mg, 98%) as a colorless oil: R_f = 0.71 (hexane/EtOAc = 2:1); $[\alpha]_D^{25} +4.2$ (c 0.49, $CHCl_3$); IR (neat) 2953, 2871, 1742, 1612 cm^{-1} ; 1H NMR (400 MHz, C_6D_6) δ 7.24 (d, J = 8.6 Hz, 2 H), 6.84 (d, J = 8.6 Hz, 2 H), 6.41 (dd, J = 15.0, 10.6 Hz, 1 H), 6.30 (dd, J = 15.0, 10.6 Hz, 1 H), 5.95–5.87 (m, 1 H), 5.73 (dt, J = 15.0, 5.3 Hz, 1 H), 4.48 (d, J = 11.2 Hz, 1 H), 4.35 (d, J = 11.2 Hz, 1 H), 4.35–4.27 (m, 1 H), 4.15 (d, J = 5.3 Hz, 2 H), 4.12–4.07 (m, 1 H), 3.95 (t, J = 5.0 Hz, 1 H), 3.61 (q, J = 5.4 Hz, 1 H), 3.35 (s, 3 H), 3.33 (s, 3 H), 2.60–2.53 (m, 3 H), 2.22 (dd, J = 15.4, 5.4 Hz, 1 H), 1.50–1.44 (m, 2 H), 1.46 (s, 3 H), 1.33 (s, 3 H), 1.09 (t, J = 8.2 Hz, 9 H), 1.02 (t, J = 7.4 Hz, 9 H), 0.80 (q, J = 8.2 Hz, 6 H), 0.62 (q, J = 7.4 Hz, 6 H); ^{13}C NMR (100 MHz, C_6D_6) δ 170.8, 159.8, 132.5, 131.3, 131.1, 131.0, 130.4, 130.0, 114.1, 99.0, 78.8, 76.9, 71.9, 69.8, 66.4, 63.5, 54.9, 51.1, 41.8, 33.7, 31.8, 30.2, 19.9, 7.5, 7.2, 5.9, 5.2; HRMS (ESI–TOF) calcd for $C_{37}H_{64}O_8Si_2Na$ $[M + Na]^+$ 715.4037, found 715.4031.

To a solution of the corresponding TES ether (99.7 mg, 0.144 mmol) in CH_2Cl_2 (7.0 mL) and MeOH (0.7 mL) was added PPTS (11.0 mg, 43.0 μmol) at 0 °C. After the mixture was stirred at room temperature for 1 h, the reaction was quenched with Et_3N . The mixture was diluted with EtOAc, washed with H_2O and brine, and then dried over Na_2SO_4 . Concentration and column chromatography (hexane/EtOAc = 10:1, 2:1) gave allylic alcohol **21** (75.1 mg, 90%) as a colorless oil: R_f = 0.53 (hexane/EtOAc = 1:1); $[\alpha]_D^{25} +2.5$ (c 1.53, $CHCl_3$); IR (neat) 3460, 2952, 2875, 1739, 1612 cm^{-1} ; 1H NMR (400 MHz, C_6D_6) δ 7.23 (d, J = 8.0 Hz, 2 H), 6.83 (d, J = 8.0 Hz, 2 H), 6.26–6.16 (m, 2 H), 5.90–5.83 (m, 1 H), 5.64–5.57 (m, 1 H), 4.48 (d, J = 11.5 Hz, 1 H), 4.36 (d, J = 11.5 Hz, 1 H), 4.32–4.31 (m, 1 H), 4.11–4.07 (m, 1 H), 3.96–3.93 (m, 1 H), 3.90 (brs, 2 H), 3.62–3.58 (m, 1 H), 3.34 (s, 3 H), 3.33 (s, 3 H), 2.59–2.54 (m, 3 H), 2.24 (dd, J = 15.5, 5.1 Hz, 1 H), 1.49–1.46 (m, 2 H), 1.46 (s, 3 H), 1.33 (s, 3 H), 1.08 (t, J = 7.9 Hz, 9 H), 0.79 (q, J = 7.9 Hz, 6 H); ^{13}C NMR (100 MHz, C_6D_6) δ 170.9, 159.8, 132.4, 131.3, 131.2, 131.1, 131.0, 130.0, 114.1, 99.0, 78.7, 76.8, 71.8, 69.8, 66.4, 63.2, 54.9, 51.2, 41.8, 33.7, 31.7, 30.2, 19.9, 7.5, 5.9; HRMS (ESI–TOF) calcd for $C_{31}H_{50}O_8SiNa$ $[M + Na]^+$ 601.3173, found 601.3171.

Alcohol 22. To a solution of alcohol **21** (45.6 mg, 78.8 μmol) in CH_2Cl_2 (1.6 mL) were added PhI(OAc) $_2$ (65.0 mg, 0.197 mmol) and TEMPO (2.5 mg, 15.8 μmol) at 0 °C. After the mixture was stirred at

room temperature for 5 h, the reaction was quenched with saturated aqueous $Na_2S_2O_3$. The mixture was diluted with EtOAc, washed with H_2O and brine, and then dried over Na_2SO_4 . Concentration and column chromatography (hexane/EtOAc = 5:1) gave the corresponding unsaturated aldehyde (44.5 mg), which was used for the next reaction without further purification.

To a solution of the PMB ether obtained above (44.5 mg) in CH_2Cl_2 (1.7 mL) and phosphate pH standard solution (0.1 mL) was added DDQ (26.0 mg, 0.116 mmol) at 0 °C. After the mixture was stirred at room temperature for 3 h, the reaction was quenched with saturated aqueous $NaHCO_3$. The mixture was diluted with EtOAc, washed with H_2O and brine, and then dried over Na_2SO_4 . Concentration and column chromatography (hexane/EtOAc = 2:1) gave alcohol **22** (27.5 mg, 76% in two steps) as a colorless oil: R_f = 0.23 (hexane/EtOAc = 2:1); $[\alpha]_D^{23} -15.2$ (c 1.00, $CHCl_3$); IR (neat) 3479, 2953, 2876, 1739, 1682, 1639 cm^{-1} ; 1H NMR (400 MHz, $CDCl_3$) δ 9.54 (d, J = 7.8 Hz, 1 H), 7.09 (dd, J = 15.4, 10.0 Hz, 1 H), 6.44–6.30 (m, 2 H), 6.10 (dd, J = 15.4, 7.8 Hz, 1 H), 4.35–4.28 (m, 1 H), 4.05–4.01 (m, 1 H), 3.78–3.75 (m, 1 H), 3.68 (s, 3 H), 3.54 (d, J = 5.5 Hz, 1 H), 2.60–2.51 (m, 2 H), 2.43–2.32 (m, 2 H), 1.72–1.64 (m, 2 H), 1.46 (s, 3 H), 1.36 (s, 3 H), 0.97 (t, J = 8.0 Hz, 9 H), 0.65 (q, J = 8.0 Hz, 6 H); ^{13}C NMR (100 MHz, $CDCl_3$) δ 193.6, 171.1, 151.9, 143.0, 130.8, 130.6, 98.8, 72.8, 70.0, 65.9, 51.7, 41.5, 36.6, 32.5, 29.9, 19.8, 7.0, 5.3; HRMS (ESI–TOF) calcd for $C_{23}H_{40}O_7SiNa$ $[M + Na]^+$ 479.2441, found 479.2446.

Tetraol 2a from 22. To a solution of acetone **22** (4.1 mg, 8.99 μmol) in CH_2Cl_2 (0.5 mL) was added $TiCl_4$ (2.0 μL , 18.2 μmol) at –30 °C. The mixture was gradually warmed up to room temperature for 1 h. After the mixture was stirred at room temperature for 27 h, the reaction was quenched with saturated aqueous $NaHCO_3$. The mixture was diluted with EtOAc and washed with H_2O and brine. The aqueous phase was washed with EtOAc four times. The combined organic layer was dried over Na_2SO_4 . Concentration and column chromatography ($CH_2Cl_2/MeOH$ = 10:1) gave tetraol **2a** (2.0 mg, 74%).

Ketone 23. To a solution of diol **20** (59.5 mg, 0.128 mmol) in CH_2Cl_2 (1.2 mL) were added imidazole (12.2 mg, 0.179 mmol) and TESCl (26 μL , 0.154 mmol) at –30 °C. After the mixture was gradually warmed up to –10 °C for 30 min, the reaction was quenched with saturated aqueous NH_4Cl . The mixture was diluted with EtOAc, washed with H_2O and brine, and then dried over Na_2SO_4 . Concentration and column chromatography (hexane/EtOAc = 5:1) gave the corresponding mono-TES ether (60.8 mg), which was used for the next reaction without further purification.

To a suspension of the alcohol obtained above (60.8 mg) and MS4 Å (50.0 mg) in CH_2Cl_2 (1.3 mL) were added NMO (64.0 mg, 0.546 mmol) and TPAP (1.8 mg, 5.30 μmol) at room temperature. After the mixture was stirred at room temperature for 8 h, the mixture was filtered through a Celite pad and washed with EtOAc. Concentration and column chromatography (hexane/EtOAc = 4:1) gave ketone **23** (54.8 mg, 74% in two steps) as a colorless oil: R_f = 0.56 (hexane/EtOAc = 2:1); $[\alpha]_D^{22} +15.6$ (c 0.50, $CHCl_3$); IR (neat) 2953, 2871, 1738, 1613 cm^{-1} ; 1H NMR (400 MHz, C_6D_6) δ 7.31 (d, J = 8.5 Hz, 2 H), 6.80 (d, J = 8.5 Hz, 2 H), 6.31 (dd, J = 14.0, 10.6 Hz, 1 H), 6.17 (dd, J = 15.0, 10.6 Hz, 1 H), 5.86 (dt, J = 15.0, 7.6 Hz, 1 H), 5.72 (dt, J = 14.0, 5.0 Hz, 1 H), 4.59–4.51 (m, 2 H), 4.37–4.16 (m, 3 H), 4.10 (d, J = 4.7 Hz, 2 H), 3.30 (s, 3 H), 3.29 (s, 3 H), 2.66–2.55 (m, 2 H), 2.43 (dd, J = 15.8, 7.6 Hz, 1 H), 2.09 (dd, J = 15.8, 5.0 Hz, 1 H), 1.65 (dt, J = 12.9, 2.7 Hz, 1 H), 1.42–1.35 (m, 1 H), 1.40 (s, 3 H), 1.20 (s, 3 H), 1.00 (t, J = 7.9 Hz, 9 H), 0.60 (q, J = 7.9 Hz, 6 H); ^{13}C NMR (100 MHz, C_6D_6) δ 206.8, 170.5, 159.8, 132.9, 132.1, 130.6, 130.0, 129.7, 129.1, 114.1, 99.4, 80.4, 73.4, 72.3, 66.1, 63.4, 54.8, 51.2, 41.2, 35.7, 32.2, 30.1, 19.3, 7.2, 5.1; HRMS (ESI–TOF) calcd for $C_{31}H_{48}O_8SiNa$ $[M + Na]^+$ 599.3016, found 599.3012.

Alcohol 24. To a solution of ketone **23** (8.5 mg, 14.7 μmol) in MeOH (0.5 mL) was added $NaBH_4$ (1.0 mg, 26.4 μmol) at –78 °C. After the mixture was gradually warmed up to 0 °C for 20 min, the reaction was quenched with saturated aqueous NH_4Cl . The mixture was diluted with EtOAc, washed with H_2O and brine, and then dried over Na_2SO_4 . Concentration and column chromatography (hexane/EtOAc = 3:1) gave alcohol **24** (8.3 mg, 98%) as a colorless oil: R_f =

0.30 (hexane/EtOAc = 2:1); $[\alpha]_D^{25} +20.8$ (c 0.44, CHCl₃); IR (neat) 3518, 2953, 2885, 1740, 1612 cm⁻¹; ¹H NMR (400 MHz, C₆D₆) δ 7.20 (d, *J* = 8.5 Hz, 2 H), 6.80 (d, *J* = 8.5 Hz, 2 H), 6.40 (dd, *J* = 15.1, 10.5 Hz, 1 H), 6.25 (dd, *J* = 15.1, 10.5 Hz, 1 H), 5.80–5.69 (m, 2 H), 4.49 (d, *J* = 11.2 Hz, 1 H), 4.28–4.24 (m, 2 H), 4.15 (d, *J* = 4.9 Hz, 2 H), 4.00–3.97 (m, 1 H), 3.52 (t, *J* = 4.7 Hz, 2 H), 3.33 (s, 3 H), 3.32 (s, 3 H), 2.68–2.63 (m, 2 H), 2.50–2.44 (m, 2 H), 2.12 (dd, *J* = 15.6, 4.9 Hz, 1 H), 1.41 (s, 3 H), 1.41–1.34 (m, 1 H), 1.30 (s, 3 H), 1.02 (t, *J* = 7.9 Hz, 9 H), 0.62 (q, *J* = 7.9 Hz, 6 H); ¹³C NMR (100 MHz, C₆D₆) δ 170.8, 159.8, 132.8, 131.6, 131.1, 130.2, 130.2, 129.9, 114.1, 99.1, 78.4, 74.7, 71.7, 70.0, 66.2, 63.4, 54.9, 51.1, 41.4, 34.2, 32.4, 30.3, 19.8, 7.2, 5.1; HRMS (ESI–TOF) calcd for C₃₁H₅₀O₈SiNa [M + Na]⁺ 601.3173, found 601.3183.

Allylic Alcohol 25. To a solution of alcohol 24 (8.3 mg, 14.4 μ mol) in CH₂Cl₂ (0.5 mL) were added 2,6-lutidine (17 μ L, 0.113 mmol) and TESOTf (24 μ L, 0.107 mmol) at 0 °C. After the mixture was stirred at room temperature for 4 h, the reaction was quenched with saturated aqueous NH₄Cl. The mixture was diluted with EtOAc, washed with H₂O and brine, and then dried over Na₂SO₄. Concentration and column chromatography (hexane/EtOAc = 10:1) gave the corresponding bis-TES ether (10.1 mg), which was used for the next reaction without further purification.

To a solution of the TES ether obtained above (10.1 mg) in CH₂Cl₂ (0.5 mL) and MeOH (0.1 mL) was added PPTS (1.8 mg, 7.30 μ mol) at 0 °C. After the mixture was stirred at 0 °C for 2 h, the reaction was quenched with Et₃N. Concentration and column chromatography (hexane/EtOAc = 3:1) gave allylic alcohol 25 (8.5 mg, quant in two steps) as a colorless oil: *R*_f = 0.22 (hexane/EtOAc = 2:1); $[\alpha]_D^{21} +11.2$ (c 1.15, CHCl₃); IR (neat) 3463, 2952, 2871, 1739, 1612 cm⁻¹; ¹H NMR (400 MHz, C₆D₆) δ 7.22 (d, *J* = 8.6 Hz, 2 H), 6.80 (d, *J* = 8.6 Hz, 2 H), 6.25–6.21 (m, 2 H), 5.81–5.74 (m, 1 H), 5.64–5.57 (m, 1 H), 4.53 (d, *J* = 11.5 Hz, 1 H), 4.35 (d, *J* = 11.5 Hz, 1 H), 4.33–4.30 (m, 1 H), 4.16–4.10 (m, 1 H), 3.89 (d, *J* = 2.9 Hz, 2 H), 3.73 (dd, *J* = 7.1, 3.2 Hz, 1 H), 3.54–3.49 (m, 1 H), 3.32 (s, 3 H), 3.31 (s, 3 H), 2.75–2.68 (m, 1 H), 2.57–2.48 (m, 2 H), 2.16 (dd, *J* = 15.6, 4.9 Hz, 1 H), 1.48 (s, 3 H), 1.48–1.42 (m, 2 H), 1.41 (s, 3 H), 1.10 (t, *J* = 7.8 Hz, 9 H), 0.76 (q, *J* = 7.8 Hz, 6 H); ¹³C NMR (100 MHz, C₆D₆) δ 170.9, 159.8, 132.4, 131.5, 131.2, 130.9, 129.8, 129.6, 114.1, 99.1, 79.6, 76.4, 71.4, 66.1, 63.2, 54.9, 51.2, 41.6, 33.5, 32.9, 30.4, 19.8, 7.6, 5.9; HRMS (ESI–TOF) calcd for C₃₁H₅₀O₈SiNa [M + Na]⁺ 601.3173, found 601.3170.

Alcohol 26. To a solution of alcohol 25 (8.5 mg, 14.6 μ mol) in CH₂Cl₂ (0.5 mL) were added PhI(OAc)₂ (12.1 mg, 36.5 μ mol) and TEMPO (1.0 mg, 6.40 μ mol) at 0 °C. After the mixture was stirred at room temperature for 3 h, the reaction was quenched with saturated aqueous Na₂S₂O₃. The mixture was diluted with EtOAc, washed with H₂O and brine, and then dried over Na₂SO₄. Concentration and column chromatography (hexane/EtOAc = 5:1) gave the corresponding unsaturated aldehyde (7.6 mg), which was used for the next reaction without further purification.

To a solution of the PMB ether obtained above (7.6 mg) in CH₂Cl₂ (0.4 mL) and phosphate pH standard solution (40 μ L) was added DDQ (3.6 mg, 16.0 μ mol) at 0 °C. After the mixture was stirred at room temperature for 2 h, the reaction was quenched with saturated aqueous NaHCO₃. The mixture was diluted with EtOAc, washed with saturated aqueous NaHCO₃, H₂O, and brine, and then dried over Na₂SO₄. Concentration and column chromatography (hexane/EtOAc = 2:1) gave alcohol 26 (5.5 mg, 82% in two steps) as a colorless oil: *R*_f = 0.16 (hexane/EtOAc = 2:1); $[\alpha]_D^{21} -35.7$ (c 0.47, CHCl₃); IR (neat) 3490, 2954, 2871, 1739, 1682, 1641 cm⁻¹; ¹H NMR (400 MHz, CDCl₃) δ 9.55 (d, *J* = 8.1 Hz, 1 H), 7.08 (dd, *J* = 15.2, 10.4 Hz, 1 H), 6.42–6.26 (m, 2 H), 6.09 (dd, *J* = 15.2, 7.8 Hz, 1 H), 4.32–4.26 (m, 1 H), 3.98–3.94 (m, 1 H), 3.71–3.69 (m, 1 H), 3.69 (s, 3 H), 3.45 (d, *J* = 6.6 Hz, 1 H), 2.57–2.30 (m, 4 H), 1.65–1.60 (m, 1 H), 1.45 (s, 3 H), 1.38 (s, 3 H), 1.26–1.17 (m, 1 H), 0.97 (t, *J* = 7.9 Hz, 9 H), 0.69–0.61 (m, 6 H); ¹³C NMR (100 MHz, CDCl₃) δ 193.6, 171.0, 151.9, 142.6, 130.7, 130.6, 98.9, 77.1, 71.0, 69.3, 65.5, 51.7, 41.4, 39.2, 31.9, 29.9, 19.6, 7.1, 5.3; HRMS (ESI–TOF) calcd for C₂₃H₄₀O₇SiNa [M + Na]⁺ 479.2441, found 479.2442.

Tetraol 2b. To a solution of acetone 26 (4.1 mg, 8.98 μ mol) in CH₂Cl₂ (0.4 mL) was added TiCl₄ (1.2 μ L, 10.8 μ mol) at –30 °C. After the mixture was stirred at –30 °C for 5 min, the reaction was quenched with saturated aqueous NaHCO₃. The mixture was diluted with EtOAc and washed with saturated aqueous NaHCO₃, H₂O, and brine. The aqueous phase was washed with EtOAc three times. The combined organic layer was dried over Na₂SO₄. Concentration and column chromatography (hexane/EtOAc = 1:1) gave the corresponding triol (3.0 mg, 80%) as a colorless oil: *R*_f = 0.09 (hexane/EtOAc = 1:1); $[\alpha]_D^{24} -14.1$ (c 0.42, CHCl₃); IR (neat) 3451, 2954, 2871, 1737, 1681, 1639 cm⁻¹; ¹H NMR (400 MHz, CDCl₃) δ 9.54 (d, *J* = 7.8 Hz, 1 H), 7.09 (dd, *J* = 15.2, 10.1 Hz, 1 H), 6.44–6.29 (m, 2 H), 6.09 (dd, *J* = 15.2, 7.8 Hz, 1 H), 4.27–4.21 (m, 1 H), 3.96–3.92 (m, 1 H), 3.87 (brs, 1 H), 3.72 (s, 3 H), 3.59–3.57 (m, 1 H), 2.52 (d, *J* = 5.9 Hz, 2 H), 2.43 (t, *J* = 6.3 Hz, 2 H), 1.71 (d, *J* = 5.9 Hz, 2 H), 0.99 (t, *J* = 7.9 Hz, 9 H), 0.67 (q, *J* = 7.9 Hz, 6 H); ¹³C NMR (100 MHz, CDCl₃) δ 193.7, 172.9, 152.0, 142.8, 130.7, 130.6, 75.9, 73.3, 69.7, 69.1, 51.9, 41.4, 39.0, 37.7, 7.0, 5.3; HRMS (ESI–TOF) calcd for C₂₀H₃₆O₇SiNa [M + Na]⁺ 439.2128, found 439.2131.

To a solution of the corresponding TES ether (9.6 mg, 23.0 μ mol) in THF (1.0 mL) was added HF·pyr (50 μ L) at 0 °C. After the mixture was stirred at 0 °C for 3 h, the reaction was quenched with saturated aqueous NaHCO₃. The mixture was diluted with EtOAc and washed with saturated aqueous NaHCO₃, H₂O, and brine. The aqueous phase was washed with EtOAc three times. The combined organic layer was dried over Na₂SO₄. Concentration and column chromatography (CH₂Cl₂/MeOH = 30:1) gave tetraol 2b (5.5 mg, 79%) as a colorless oil: *R*_f = 0.35 (CH₂Cl₂/MeOH = 10:1); $[\alpha]_D^{21} -6.1$ (c 0.10, CHCl₃); IR (neat) 3367, 2924, 2858, 1727, 1675, 1635 cm⁻¹; ¹H NMR (600 MHz, CD₃OD) δ 9.49 (d, *J* = 7.8 Hz, 1 H), 7.29 (dd, *J* = 15.6, 9.9 Hz, 1 H), 6.51–6.41 (m, 2 H), 6.09 (dd, *J* = 15.6, 7.8 Hz, 1 H), 4.25–4.20 (m, 1 H), 3.90–3.86 (m, 1 H), 3.83–3.79 (m, 1 H), 3.67 (s, 3 H), 3.33–3.31 (m, 1 H), 2.56 (dd, *J* = 15.0, 4.2 Hz, 1 H), 2.53–2.43 (m, 2 H), 2.44 (dd, *J* = 15.0, 8.7 Hz, 1 H), 1.76–1.72 (m, 2 H); ¹³C NMR (100 MHz, CD₃OD) δ 196.0, 173.7, 154.8, 145.0, 131.9, 131.2, 76.1, 72.9, 71.7, 67.7, 52.0, 43.1, 41.1, 38.7; HRMS (ESI–TOF) calcd for C₁₄H₂₂O₇Na [M + Na]⁺ 325.1263, found 325.1266.

Diol 27. To a solution of β -hydroxy ketone 11 (595 mg, 0.767 mmol) in MeCN (9.0 mL) and AcOH (9.0 mL) was added NaBH(OAc)₃ (244 mg, 1.15 mmol) at –20 °C. After the mixture was stirred at –20 °C for 2 h, NaBH(OAc)₃ (81.3 mg, 0.383 mmol) was added. After the mixture was stirred at –20 °C for a further 1 h, the reaction was quenched with saturated aqueous NaHCO₃. The mixture was diluted with EtOAc, washed with H₂O and brine, and then dried over Na₂SO₄. Concentration and column chromatography (hexane/EtOAc = 5:1) gave diol 27 (565 mg, 95%) as a colorless oil: *R*_f = 0.45 (hexane/EtOAc = 2:1); $[\alpha]_D^{24} -9.1$ (c 1.00, CHCl₃); IR (neat) 3476, 2930, 2857, 1739, 1613 cm⁻¹; ¹H NMR (400 MHz, C₆D₆) δ 7.73–7.71 (m, 4 H), 7.25–7.09 (m, 8 H), 6.77 (d, *J* = 8.8 Hz, 2 H), 6.35 (dd, *J* = 15.1, 10.5 Hz, 1 H), 6.18 (dd, *J* = 15.1, 10.5 Hz, 1 H), 5.84 (dt, *J* = 15.1, 7.6 Hz, 1 H), 5.61 (dt, *J* = 15.1, 4.9 Hz, 1 H), 4.40 (d, *J* = 1.9 Hz, 2 H), 4.37–4.30 (m, 1 H), 4.16 (d, *J* = 4.6 Hz, 2 H), 4.07 (brs, 1 H), 3.84–3.81 (m, 1 H), 3.70–3.67 (m, 1 H), 3.25 (s, 3 H), 3.21 (s, 3 H), 2.52 (t, *J* = 6.4 Hz, 2 H), 2.34–2.29 (m, 2 H), 2.20–2.15 (m, 1 H), 1.71–1.66 (m, 2 H), 1.12 (s, 9 H), 0.94 (s, 9 H), 0.16 (s, 3 H), 0.12 (s, 3 H); ¹³C NMR (100 MHz, C₆D₆) δ 173.1, 159.7, 135.9, 134.2, 132.4, 131.4, 131.1, 130.7, 130.5, 129.9, 114.0, 80.3, 77.7, 72.2, 70.0, 66.3, 64.7, 54.8, 51.3, 41.4, 38.4, 34.2, 27.2, 26.5, 19.6, 18.8, –3.6, –4.1; HRMS (ESI–TOF) calcd for C₄₄H₆₄O₈Si₂Na [M + Na]⁺ 799.4037, found 799.4036.

Diol 28. To a solution of diol 27 (871 mg, 1.12 mmol) in THF (11 mL) were added Me₂C(OMe)₂ (1.4 mL, 11.2 mmol) and *p*-TsOH·H₂O (21.0 mg, 0.112 mmol) at room temperature. After the mixture was stirred at room temperature for 2 h, the reaction was quenched with saturated aqueous NaHCO₃. The mixture was diluted with EtOAc, washed with H₂O and brine, and then dried over Na₂SO₄. Concentration and column chromatography (hexane/EtOAc = 7:1) gave the corresponding acetone (822 mg, 90%) as a colorless oil: *R*_f = 0.62 (hexane/EtOAc = 2:1); $[\alpha]_D^{24} -0.4$ (c 0.99, CHCl₃); IR (neat)

2929, 2856, 1742 cm^{-1} ; ^1H NMR (400 MHz, CDCl_3) δ 7.69 (dd, $J = 7.8, 1.5$ Hz, 4 H), 7.44–7.36 (m, 6 H), 7.25 (d, $J = 8.5$ Hz, 2 H), 6.86 (d, $J = 8.5$ Hz, 2 H), 6.26 (dd, $J = 15.0, 10.5$ Hz, 1 H), 6.11 (dd, $J = 15.0, 10.5$ Hz, 1 H), 5.73–5.65 (m, 2 H), 4.47 (s, 2 H), 4.25–4.16 (m, 3 H), 3.99–3.94 (m, 1 H), 3.81–3.78 (m, 1 H), 3.79 (s, 3 H), 3.69 (s, 3 H), 3.42–3.38 (m, 1 H), 2.52 (dd, $J = 15.6, 8.3$ Hz, 1 H), 2.44–2.33 (m, 3 H), 2.08–2.01 (m, 1 H), 1.59 (brs, 1 H), 1.34 (s, 3 H), 1.31 (s, 3 H), 1.08 (s, 9 H), 0.90 (s, 9 H), 0.10 (s, 3 H), 0.08 (s, 3 H); ^{13}C NMR (100 MHz, CDCl_3) δ 173.1, 159.1, 135.5, 133.7, 131.9, 130.5, 130.2, 130.0, 129.5, 129.3, 127.6, 113.7, 100.6, 79.3, 75.9, 71.8, 66.8, 64.3, 63.8, 55.3, 51.6, 40.7, 33.8, 32.8, 26.9, 26.2, 24.6, 24.5, 19.3, 18.4, –4.0, –4.3; HRMS (ESI–TOF) calcd for $\text{C}_{47}\text{H}_{68}\text{O}_8\text{Si}_2\text{Na}$ [$M + \text{Na}$] $^+$ 839.4351, found 839.4348.

To a solution of the corresponding bis-silyl ether (409 mg, 0.501 mmol) in MeCN (5.0 mL) was added a mixed solution of TBAF (1.0 M solution in THF, 2.0 mL, 2.00 mmol) and AcOH (0.10 mL, 2.00 mmol) at room temperature. After the mixture was stirred at reflux for 3 days, the reaction was quenched with saturated aqueous NH_4Cl . The mixture was diluted with EtOAc and washed with H_2O and brine. The aqueous phase was washed with EtOAc twice. The combined organic layer was dried over Na_2SO_4 . Concentration and column chromatography (hexane/EtOAc = 4:1, 1:1) gave diol **28** (154 mg, 66%) as a colorless oil: $R_f = 0.19$ (hexane/EtOAc = 1:1); $[\alpha]_D^{20} +43.1$ (c 0.68, CHCl_3); IR (neat) 3459, 2925, 1739, 1612 cm^{-1} ; ^1H NMR (400 MHz, C_6D_6) δ 7.19–7.16 (m, 2 H), 6.79 (d, $J = 8.6$ Hz, 2 H), 6.25–6.15 (m, 2 H), 5.92–5.85 (m, 1 H), 5.63–5.57 (m, 1 H), 4.43 (d, $J = 11.5$ Hz, 1 H), 4.37–4.30 (m, 1 H), 4.23 (d, $J = 11.5$ Hz, 1 H), 4.18–4.13 (m, 1 H), 3.96 (d, $J = 5.7$ Hz, 1 H), 3.89 (d, $J = 5.4$ Hz, 2 H), 3.54–3.50 (m, 1 H), 3.33 (s, 3 H), 3.33 (s, 3 H), 2.61–2.55 (m, 2 H), 2.48 (dd, $J = 15.6, 8.8$ Hz, 1 H), 2.23–2.18 (m, 2 H), 2.08–2.01 (m, 1 H), 1.37 (s, 3 H), 1.28 (s, 3 H); ^{13}C NMR (100 MHz, C_6D_6) δ 170.8, 159.8, 132.8, 131.2, 131.2, 130.9, 130.6, 129.8, 114.2, 100.8, 77.8, 73.8, 71.3, 67.1, 64.2, 63.3, 54.9, 51.1, 40.9, 32.9, 32.5, 25.1, 25.0; HRMS (ESI–TOF) calcd for $\text{C}_{25}\text{H}_{36}\text{O}_8\text{Na}$ [$M + \text{Na}$] $^+$ 487.2308, found 487.2302.

Alcohol 29. To a solution of diol **28** (22.4 mg, 48.2 μmol) in CH_2Cl_2 (1.0 mL) were added 2,6-lutidine (40 μL , 0.270 mmol) and TESOTf (52 μL , 0.232 mmol) at 0 $^\circ\text{C}$. After the mixture was stirred at room temperature for 2 h, the reaction was quenched with saturated aqueous NH_4Cl . The mixture was diluted with EtOAc, washed with H_2O and brine, and then dried over Na_2SO_4 . Concentration and column chromatography (hexane/EtOAc = 10:1, 4:1) gave the corresponding bis-TES ether (34.1 mg, quant) as a colorless oil: $R_f = 0.50$ (hexane/EtOAc = 4:1); $[\alpha]_D^{25} +16.4$ (c 0.23, CHCl_3); IR (neat) 2953, 2871, 1743, 1612 cm^{-1} ; ^1H NMR (400 MHz, C_6D_6) δ 7.23 (d, $J = 8.8$ Hz, 2 H), 6.82 (d, $J = 8.8$ Hz, 2 H), 6.46–6.35 (m, 1 H), 6.34–6.24 (m, 1 H), 5.95–5.86 (m, 1 H), 5.73 (dt, $J = 15.1, 5.4$ Hz, 1 H), 4.47 (d, $J = 11.2$ Hz, 1 H), 4.46–4.38 (m, 1 H), 4.34 (d, $J = 11.2$ Hz, 1 H), 4.22–4.13 (m, 3 H), 4.05 (dd, $J = 5.9, 4.1$ Hz, 1 H), 3.50 (q, $J = 5.3$ Hz, 1 H), 3.34 (s, 3 H), 3.33 (s, 3 H), 2.62–2.45 (m, 3 H), 2.25 (dd, $J = 15.5, 5.1$ Hz, 1 H), 2.21–2.12 (m, 1 H), 1.44 (s, 3 H), 1.43–1.34 (m, 1 H), 1.32 (s, 3 H), 1.10 (t, $J = 7.9$ Hz, 9 H), 1.02 (t, $J = 7.9$ Hz, 9 H), 0.84–0.76 (q, $J = 7.9$ Hz, 6 H), 0.62 (q, $J = 7.9$ Hz, 6 H); ^{13}C NMR (100 MHz, C_6D_6) δ 170.8, 159.8, 132.6, 131.3, 130.7, 130.4, 129.9, 114.1, 100.9, 79.2, 76.4, 71.9, 67.3, 64.2, 63.5, 54.9, 51.1, 41.0, 33.9, 32.9, 24.9, 24.8, 7.5, 7.2, 5.9, 5.2; HRMS (ESI–TOF) calcd for $\text{C}_{37}\text{H}_{64}\text{O}_8\text{Si}_2\text{Na}$ [$M + \text{Na}$] $^+$ 715.4037, found 715.4037.

To a solution of the corresponding TES ether (15.0 mg, 21.6 μmol) in CH_2Cl_2 (0.7 mL) and MeOH (70 μL) was added PPTS (1.6 mg, 6.32 μmol) at 0 $^\circ\text{C}$. The mixture was stirred at 0 $^\circ\text{C}$ for 2 h. After the mixture was stirred at room temperature for 30 min, the reaction was quenched with Et_3N . The mixture was diluted with EtOAc, washed with H_2O and brine, and then dried over Na_2SO_4 . Concentration and column chromatography (hexane/EtOAc = 7:1, 2:1) gave the corresponding allylic alcohol (10.7 mg, 88%) as a colorless oil: $R_f = 0.66$ (hexane/EtOAc = 1:1); $[\alpha]_D^{23} +12.8$ (c 0.74, CHCl_3); IR (neat) 3462, 2952, 2875, 1742, 1612 cm^{-1} ; ^1H NMR (400 MHz, C_6D_6) δ 7.23 (d, $J = 8.6$ Hz, 2 H), 6.81 (d, $J = 8.6$ Hz, 2 H), 6.24–6.15 (m, 2 H), 5.88–5.81 (m, 1 H), 5.63–5.57 (m, 1 H), 4.47 (d, $J = 11.5$ Hz, 1 H), 4.44–4.39 (m, 1 H), 4.35 (d, $J = 11.5$ Hz, 1 H), 4.20–4.15 (m, 1 H), 4.04 (t, $J = 4.9$ Hz, 1 H), 3.89 (d, $J = 5.4$ Hz, 2 H), 3.51–3.47 (m,

1 H), 3.33 (s, 3 H), 3.33 (s, 3 H), 2.59–2.49 (m, 4 H), 2.25 (dd, $J = 15.5, 4.9$ Hz, 1 H), 2.19–2.12 (m, 1 H), 1.44 (s, 3 H), 1.40–1.30 (m, 1 H), 1.32 (s, 3 H), 1.10 (t, $J = 8.0$ Hz, 9 H), 0.79 (q, $J = 8.0$ Hz, 6 H); ^{13}C NMR (100 MHz, C_6D_6) δ 170.8, 159.8, 132.5, 131.2, 131.1, 131.0, 129.9, 114.1, 100.9, 79.1, 76.3, 71.9, 67.3, 64.2, 63.2, 54.9, 51.1, 41.0, 33.8, 32.8, 24.9, 24.8, 7.5, 5.9; HRMS (ESI–TOF) calcd for $\text{C}_{31}\text{H}_{50}\text{O}_8\text{SiNa}$ [$M + \text{Na}$] $^+$ 601.3173, found 601.3168.

To a solution of the corresponding allylic alcohol (52.8 mg, 91.3 μmol) in CH_2Cl_2 (1.8 mL) were added $\text{PhI}(\text{OAc})_2$ (76.0 mg, 0.228 mmol) and TEMPO (2.9 mg, 18.3 μmol) at 0 $^\circ\text{C}$. After the mixture was stirred at room temperature for 4 h, the reaction was quenched with saturated aqueous $\text{Na}_2\text{S}_2\text{O}_3$. The mixture was diluted with EtOAc, washed with H_2O and brine, and then dried over Na_2SO_4 . Concentration and column chromatography (hexane/EtOAc = 5:1) gave the corresponding unsaturated aldehyde (48.8 mg), which was used for the next reaction without further purification.

To a solution of the PMB ether obtained above (48.8 mg) in CH_2Cl_2 (1.7 mL) and phosphate pH standard solution (0.1 mL) was added DDQ (26.0 mg, 0.115 mmol) at 0 $^\circ\text{C}$. After the mixture was stirred at room temperature for 2 h, the reaction was quenched with saturated aqueous NaHCO_3 . The mixture was diluted with EtOAc, washed with H_2O and brine, and then dried over Na_2SO_4 . Concentration and column chromatography (hexane/EtOAc = 2:1) gave alcohol **29** (29.9 mg, 72% in two steps) as a colorless oil: $R_f = 0.61$ (hexane/EtOAc = 1:1); $[\alpha]_D^{25} +5.8$ (c 0.88, CHCl_3); IR (neat) 3472, 2953, 2876, 1741, 1682, 1639 cm^{-1} ; ^1H NMR (400 MHz, CDCl_3) δ 9.54 (d, $J = 7.8$ Hz, 1 H), 7.09 (dd, $J = 15.2, 10.2$ Hz, 1 H), 6.44–6.29 (m, 2 H), 6.10 (dd, $J = 15.2, 7.8$ Hz, 1 H), 4.26–4.19 (m, 1 H), 4.00–3.95 (m, 1 H), 3.68 (s, 3 H), 3.67–3.63 (m, 2 H), 2.59–2.51 (m, 2 H), 2.46 (dd, $J = 15.6, 5.2$ Hz, 1 H), 2.39–2.31 (m, 2 H), 2.07–2.00 (m, 1 H), 1.63–1.56 (m, 1 H), 1.35 (s, 3 H), 1.34 (s, 3 H), 0.97 (t, $J = 7.8$ Hz, 9 H), 0.65 (q, $J = 7.8$ Hz, 6 H); ^{13}C NMR (100 MHz, CDCl_3) δ 193.6, 171.2, 151.8, 142.9, 131.0, 130.7, 100.8, 72.8, 67.3, 63.7, 51.7, 40.7, 36.8, 33.5, 24.6, 24.5, 7.0, 5.4; HRMS (ESI–TOF) calcd for $\text{C}_{23}\text{H}_{40}\text{O}_7\text{SiNa}$ [$M + \text{Na}$] $^+$ 479.2441, found 479.2446.

Tetraol 2c. To a solution of acetone-diol **29** (20.7 mg, 45.4 μmol) in CH_2Cl_2 (2.3 mL) was added TiCl_4 (10 μL , 90.8 μmol) at –30 $^\circ\text{C}$. The mixture was gradually warmed up to room temperature for 2 h. After the mixture was stirred at room temperature for 3 h, the reaction was quenched with saturated aqueous NaHCO_3 . The mixture was diluted with EtOAc and washed with H_2O and brine. The aqueous phase was washed with EtOAc four times. The combined organic layer was dried over Na_2SO_4 . Concentration and column chromatography ($\text{CH}_2\text{Cl}_2/\text{MeOH} = 10:1$) gave tetraol **2c** (6.1 mg, 44%) as a colorless oil: $R_f = 0.35$ ($\text{CH}_2\text{Cl}_2/\text{MeOH} = 10:1$); $[\alpha]_D^{24} -8.9$ (c 0.10, CHCl_3); IR (neat) 3388, 2925, 2853, 1730, 1674, 1636 cm^{-1} ; ^1H NMR (600 MHz, CD_3OD) δ 9.49 (d, $J = 7.8$ Hz, 1 H), 7.33–7.28 (m, 1 H), 6.50–6.47 (m, 2 H), 6.08 (dd, $J = 15.0, 7.8$ Hz, 1 H), 4.32–4.27 (m, 1 H), 3.93–3.89 (m, 1 H), 3.75–3.71 (m, 1 H), 3.67 (s, 3 H), 3.39 (t, $J = 6.6$ Hz, 1 H), 2.65–2.61 (m, 1 H), 2.54–2.47 (m, 2 H), 2.43–2.37 (m, 1 H), 1.78 (ddd, $J = 14.4, 9.6, 2.4$ Hz, 1 H), 1.60 (ddd, $J = 14.4, 9.6, 2.4$ Hz, 1 H); ^{13}C NMR (100 MHz, CD_3OD) δ 196.0, 173.8, 155.5, 145.8, 131.8, 131.0, 78.1, 73.1, 70.6, 66.4, 52.0, 43.9, 40.3, 37.8; HRMS (ESI–TOF) calcd for $\text{C}_{14}\text{H}_{22}\text{O}_7\text{Na}$ [$M + \text{Na}$] $^+$ 325.1263, found 325.1271.

Ketone 30. To a solution of diol **28** (10.8 mg, 23.4 μmol) in CH_2Cl_2 (0.3 mL) were added imidazole (2.2 mg, 32.8 μmol) and TESCl (4.7 μL , 28.1 μmol) at –30 $^\circ\text{C}$. After the mixture was stirred at –30 $^\circ\text{C}$ for 30 min, the reaction was quenched with saturated aqueous NH_4Cl . The mixture was diluted with EtOAc, washed with H_2O and brine, and then dried over Na_2SO_4 . Concentration and column chromatography (hexane/EtOAc = 4:1) gave the corresponding mono-TES ether (12.9 mg), which was used for the next reaction without further purification.

To a suspension of the alcohol obtained above (12.9 mg) and MS4 A (15.0 mg) in CH_2Cl_2 (0.3 mL) were added NMO (13.4 mg, 0.115 mmol) and TPAP (1.0 mg, 2.85 μmol) at room temperature. After the mixture was stirred at room temperature for 8 h, the mixture was filtered through a Celite pad and washed with EtOAc. Concentration and column chromatography (hexane/EtOAc = 4:1) gave ketone **30**

(10.3 mg, 76% in two steps) as a colorless oil: $R_f = 0.56$ (hexane/EtOAc = 2:1); $[\alpha]_D^{25} +28.7$ (c 0.53, CHCl_3); IR (neat) 2953, 2871, 1739, 1613 cm^{-1} ; ^1H NMR (400 MHz, C_6D_6) δ 7.28 (d, $J = 8.5$ Hz, 2 H), 6.80 (d, $J = 8.5$ Hz, 2 H), 6.34 (dd, $J = 13.7, 10.2$ Hz, 1 H), 6.15 (dt, $J = 15.1, 10.2$ Hz, 1 H), 5.83–5.76 (m, 1 H), 5.72–5.64 (m, 1 H), 4.56 (dd, $J = 10.8, 3.3$ Hz, 1 H), 4.47 (t, $J = 5.9$ Hz, 1 H), 4.34–4.27 (m, 3 H), 4.10 (t, $J = 4.6$ Hz, 2 H), 3.31 (s, 6 H), 2.64–2.58 (m, 2 H), 2.38 (dd, $J = 16.0, 8.4$ Hz, 1 H), 2.13–2.04 (m, 2 H), 1.60–1.53 (m, 1 H), 1.36 (s, 3 H), 1.25 (s, 3 H), 1.00 (t, $J = 8.0$ Hz, 9 H), 0.60 (q, $J = 8.0$ Hz, 6 H); ^{13}C NMR (100 MHz, C_6D_6) δ 207.5, 170.4, 159.9, 133.0, 132.1, 130.6, 129.9, 128.8, 114.1, 101.3, 81.2, 72.2, 70.5, 63.8, 63.4, 54.9, 51.2, 40.4, 35.8, 33.1, 25.1, 24.5, 7.2, 5.1; HRMS (ESI–TOF) calcd for $\text{C}_{31}\text{H}_{48}\text{O}_8\text{SiNa}$ $[\text{M} + \text{Na}]^+$ 599.3016, found 599.3013.

Alcohol 31. To a solution of ketone **30** (5.2 mg, 9.02 μmol) in MeOH (0.4 mL) was added NaBH_4 (1.0 mg, 26.4 μmol) at -78°C . After the mixture was stirred at -78°C for 20 min, the reaction was quenched with saturated aqueous NH_4Cl . The mixture was diluted with EtOAc, washed with H_2O and brine, and then dried over Na_2SO_4 . Concentration and column chromatography (hexane/EtOAc = 3:1) gave alcohol **31** (5.4 mg, quant) as a colorless oil: $R_f = 0.33$ (hexane/EtOAc = 2:1); $[\alpha]_D^{25} +32.0$ (c 1.11, CHCl_3); IR (neat) 3518, 2953, 2871, 1739, 1613 cm^{-1} ; ^1H NMR (400 MHz, C_6D_6) δ 7.19 (d, $J = 7.6$ Hz, 2 H), 6.79 (d, $J = 7.6$ Hz, 2 H), 6.39 (dd, $J = 15.0, 10.5$ Hz, 1 H), 6.24 (dd, $J = 15.0, 10.5$ Hz, 1 H), 5.78–5.67 (m, 2 H), 4.47 (d, $J = 11.2$ Hz, 1 H), 4.34–4.25 (m, 1 H), 4.26 (d, $J = 11.2$ Hz, 1 H), 4.14 (d, $J = 4.9$ Hz, 2 H), 4.04–3.98 (m, 1 H), 3.54–3.48 (m, 2 H), 3.32 (s, 3 H), 3.32 (s, 3 H), 2.69–2.62 (m, 1 H), 2.53–2.38 (m, 2 H), 2.12 (dd, $J = 11.2, 4.4$ Hz, 1 H), 1.80–1.73 (m, 1 H), 1.38 (s, 3 H), 1.27 (s, 3 H), 1.22–1.15 (m, 1 H), 1.01 (t, $J = 7.8$ Hz, 9 H), 0.61 (q, $J = 7.8$ Hz, 6 H); ^{13}C NMR (100 MHz, C_6D_6) δ 170.7, 159.8, 132.9, 131.6, 130.1, 130.1, 129.9, 129.8, 114.1, 100.9, 78.3, 74.4, 71.7, 67.7, 63.9, 63.4, 54.9, 51.1, 40.7, 34.1, 33.8, 24.9, 7.2, 5.1; HRMS (ESI–TOF) calcd for $\text{C}_{31}\text{H}_{50}\text{O}_8\text{SiNa}$ $[\text{M} + \text{Na}]^+$ 601.3173, found 601.3165.

Alcohol 32. To a solution of alcohol **31** (23.2 mg, 40.0 μmol) in CH_2Cl_2 (0.4 mL) were added 2,6-lutidine (17 μL , 0.113 mmol) and TESOTf (24 μL , 0.107 mmol) at 0°C . After the mixture was stirred at room temperature for 30 min, the reaction was quenched with saturated aqueous NH_4Cl . The mixture was diluted with EtOAc, washed with H_2O and brine, and then dried over Na_2SO_4 . Concentration and column chromatography (hexane/EtOAc = 10:1) gave the corresponding bis-TES ether (28.1 mg), which was used for the next reaction without further purification.

To a solution of the TES ether obtained above (28.1 mg) in CH_2Cl_2 (1.4 mL) and MeOH (0.2 mL) was added PPTS (3.1 mg, 12.5 μmol) at 0°C . The mixture was stirred at 0°C for 2 h. After the mixture was stirred at room temperature for 20 min, the reaction was quenched with Et_3N . The mixture was diluted with EtOAc, washed with H_2O and brine, and then dried over Na_2SO_4 . Concentration and column chromatography (hexane/EtOAc = 7:1, 1:1) gave the corresponding allylic alcohol (16.9 mg, 72% in two steps) as a colorless oil: $R_f = 0.44$ (hexane/EtOAc = 1:1); $[\alpha]_D^{25} +27.5$ (c 0.65, CHCl_3); IR (neat) 3465, 2952, 2885, 1739, 1612 cm^{-1} ; ^1H NMR (400 MHz, C_6D_6) δ 7.24 (d, $J = 8.8$ Hz, 2 H), 6.80 (d, $J = 8.8$ Hz, 2 H), 6.27–6.11 (m, 2 H), 5.83–5.74 (m, 1 H), 5.65–5.54 (m, 1 H), 4.53 (d, $J = 11.5$ Hz, 1 H), 4.42 (d, $J = 11.5$ Hz, 1 H), 4.40–4.32 (m, 1 H), 4.17–4.08 (m, 1 H), 3.88 (d, $J = 4.9$ Hz, 2 H), 3.78 (dd, $J = 10.8, 3.7$ Hz, 1 H), 3.57–3.48 (m, 1 H), 3.33 (s, 6 H), 2.74–2.65 (m, 1 H), 2.59–2.44 (m, 3 H), 2.20 (dd, $J = 15.8, 5.0$ Hz, 1 H), 1.92–1.83 (m, 1 H), 1.44 (s, 3 H), 1.42 (s, 3 H), 1.09 (t, $J = 7.9$ Hz, 9 H), 0.80–0.69 (m, 6 H); ^{13}C NMR (100 MHz, C_6D_6) δ 170.8, 159.8, 132.3, 131.5, 131.4, 131.2, 131.0, 129.7, 114.1, 100.9, 80.1, 75.6, 71.7, 68.3, 63.9, 63.2, 54.9, 51.1, 40.9, 34.6, 33.8, 25.2, 24.6, 7.5, 5.9; HRMS (ESI–TOF) calcd for $\text{C}_{31}\text{H}_{50}\text{O}_8\text{SiNa}$ $[\text{M} + \text{Na}]^+$ 601.3173, found 601.3170.

To a solution of the corresponding allylic alcohol (16.9 mg, 29.2 μmol) in CH_2Cl_2 (0.7 mL) were added $\text{PhI}(\text{OAc})_2$ (24.2 mg, 73.0 μmol) and TEMPO (1.0 mg, 6.40 μmol) at 0°C . After the mixture was stirred at room temperature for 3 h, the reaction was quenched with saturated aqueous $\text{Na}_2\text{S}_2\text{O}_3$. The mixture was diluted with EtOAc, washed with H_2O and brine, and then dried over Na_2SO_4 . Concentration and column chromatography (hexane/EtOAc = 5:1)

gave the corresponding unsaturated aldehyde (13.5 mg), which was used for the next reaction without further purification.

To a solution of the PMB ether obtained above (13.5 mg) in CH_2Cl_2 (0.5 mL) and phosphate pH standard solution (25 μL) was added DDQ (6.3 mg, 28.0 μmol) at 0°C . The mixture was stirred at 0°C for 1 h. After the mixture was stirred at room temperature for 4 h, the reaction was quenched with saturated aqueous NaHCO_3 . The mixture was diluted with EtOAc, washed with H_2O and brine, and then dried over Na_2SO_4 . Concentration and column chromatography (hexane/EtOAc = 4:1, 2:1) gave alcohol **32** (10.0 mg, 75% in two steps) as a colorless oil: $R_f = 0.23$ (hexane/EtOAc = 2:1); $[\alpha]_D^{24} -5.8$ (c 1.16, CHCl_3); IR (neat) 3490, 2952, 2871, 1739, 1681, 1640 cm^{-1} ; ^1H NMR (400 MHz, CDCl_3) δ 9.54 (d, $J = 7.8$ Hz, 1 H), 7.08 (dd, $J = 15.0, 10.0$ Hz, 1 H), 6.42–6.26 (m, 2 H), 6.09 (dd, $J = 15.0, 7.8$ Hz, 1 H), 4.27–4.19 (m, 1 H), 3.93–3.87 (m, 1 H), 3.68 (s, 3 H), 3.68–3.65 (m, 1 H), 3.47 (dd, $J = 17.1, 7.6$ Hz, 1 H), 2.59–2.30 (m, 5 H), 1.76–1.69 (m, 1 H), 1.65–1.57 (m, 1 H), 1.35 (s, 3 H), 1.33 (s, 3 H), 0.97 (t, $J = 7.8$ Hz, 9 H), 0.69–0.61 (m, 6 H); ^{13}C NMR (100 MHz, CDCl_3) δ 193.6, 171.2, 151.8, 142.5, 130.7, 130.7, 100.9, 69.3, 67.9, 63.3, 51.7, 40.5, 39.4, 34.0, 24.8, 24.3, 7.1, 5.4; HRMS (ESI–TOF) calcd for $\text{C}_{23}\text{H}_{40}\text{O}_7\text{SiNa}$ $[\text{M} + \text{Na}]^+$ 479.2441, found 479.2438.

Tetraol 2d. To a solution of acetonide **32** (18.2 mg, 39.9 μmol) in CH_2Cl_2 (2.0 mL) was added TiCl_4 (8.8 μL , 80.3 μmol) at -30°C . After the mixture was gradually warmed up to 0°C for 30 min, the reaction was quenched with saturated aqueous NaHCO_3 . The mixture was diluted with EtOAc and washed with H_2O and brine. The aqueous phase was washed with EtOAc four times. The combined organic layer was dried over Na_2SO_4 . Concentration and column chromatography ($\text{CH}_2\text{Cl}_2/\text{MeOH} = 10:1$) gave tetraol **2d** (5.7 mg, 47%) as a colorless oil: $R_f = 0.25$ ($\text{CH}_2\text{Cl}_2/\text{MeOH} = 10:1$); $[\alpha]_D^{26} -19.1$ (c 0.03, CHCl_3); IR (neat) 3390, 2921, 2852, 1730, 1677, 1637 cm^{-1} ; ^1H NMR (600 MHz, CD_3OD) δ 9.49 (d, $J = 7.8$ Hz, 1 H), 7.29 (dd, $J = 15.6, 10.4$ Hz, 1 H), 6.51–6.41 (m, 2 H), 6.09 (dd, $J = 15.6, 7.8$ Hz, 1 H), 4.29–4.24 (m, 1 H), 3.95–3.91 (m, 1 H), 3.82–3.79 (m, 1 H), 3.67 (s, 3 H), 3.23 (t, $J = 3.9$ Hz, 1 H), 2.56–2.43 (m, 4 H), 1.70 (ddd, $J = 14.4, 10.2, 3.0$ Hz, 1 H), 1.59 (ddd, $J = 14.4, 10.2, 3.0$ Hz, 1 H); ^{13}C NMR (100 MHz, CD_3OD) δ 196.0, 173.7, 154.8, 145.0, 131.9, 131.2, 77.1, 72.8, 70.1, 66.4, 52.0, 43.8, 41.9, 38.7; HRMS (ESI–TOF) calcd for $\text{C}_{14}\text{H}_{22}\text{O}_7\text{Na}$ $[\text{M} + \text{Na}]^+$ 325.1263, found 325.1270.

■ ASSOCIATED CONTENT

📄 Supporting Information

Copies of ^1H and ^{13}C NMR spectra for new compounds. This material is available free of charge via the Internet at <http://pubs.acs.org>.

■ AUTHOR INFORMATION

✉ Corresponding Author

*E-mail: takamura@cc.okayama-u.ac.jp (H.T.).

Notes

The authors declare no competing financial interest.

■ ACKNOWLEDGMENTS

We are grateful to Dr. Chunguang Han and Dr. Yoshi Yamano (Nagoya University) for valuable discussions. We also gratefully thank Division of Instrumental Analysis, Okayama University, for the NMR measurements. We appreciate The Naito Foundation, The Research Foundation for Pharmaceutical Sciences, The Sumitomo Foundation, and The Uehara Memorial Foundation for their financial support. This research was supported by a Grant-in Aid for Scientific Research (No. 24710250) from the Japan Society for the Promotion of Science (JSPS).

■ REFERENCES

- (1) Molinski, T. F.; Morinaka, B. I. *Tetrahedron* **2012**, *68*, 9307.

- (2) For selected reviews on the structural elucidation of natural products by the chemical synthesis, see: (a) Nicolaou, K. C.; Snyder, S. A. *Angew. Chem., Int. Ed.* **2005**, *44*, 1012. (b) Maier, M. E. *Nat. Prod. Rep.* **2009**, *26*, 1105. (c) Suyama, T. L.; Gerwick, W. H.; McPhail, K. L. *Bioorg. Med. Chem.* **2011**, *19*, 6675.
- (3) Kita, M.; Ohishi, N.; Konishi, K.; Kondo, M.; Koyama, T.; Kitamura, M.; Yamada, K.; Uemura, D. *Tetrahedron* **2007**, *63*, 6241.
- (4) (a) Han, C.; Uemura, D. *Tetrahedron Lett.* **2008**, *49*, 6988. (b) Han, C.; Yamano, Y.; Kita, M.; Takamura, H.; Uemura, D. *Tetrahedron Lett.* **2009**, *50*, 5280. (c) Han, C.; Yamano, Y.; Kakiuchi, F.; Nakamura, K.; Uemura, D. *Tetrahedron* **2011**, *67*, 9622.
- (5) (a) Takamura, H.; Ando, J.; Abe, T.; Murata, T.; Kadota, I.; Uemura, D. *Tetrahedron Lett.* **2008**, *49*, 4626. (b) Murata, T.; Sano, M.; Takamura, H.; Kadota, I.; Uemura, D. *J. Org. Chem.* **2009**, *74*, 4797. (c) Takamura, H.; Murata, T.; Asai, T.; Kadota, I.; Uemura, D. *J. Org. Chem.* **2009**, *74*, 6658. (d) Takamura, H.; Kadonaga, Y.; Yamano, Y.; Han, C.; Aoyama, Y.; Kadota, I.; Uemura, D. *Tetrahedron Lett.* **2009**, *50*, 863. (e) Takamura, H.; Kadonaga, Y.; Yamano, Y.; Han, C.; Kadota, I.; Uemura, D. *Tetrahedron* **2009**, *65*, 7449. (f) Takamura, H.; Kadonaga, Y.; Kadota, I.; Uemura, D. *Tetrahedron Lett.* **2010**, *51*, 2603. (g) Takamura, H.; Kadonaga, Y.; Kadota, I.; Uemura, D. *Tetrahedron* **2010**, *66*, 7569. (h) Takamura, H.; Tsuda, K.; Kawakubo, Y.; Kadota, I.; Uemura, D. *Tetrahedron Lett.* **2012**, *53*, 4317. (i) Takamura, H.; Fujiwara, T.; Kadota, I.; Uemura, D. *Beilstein J. Org. Chem.* **2013**, *9*, 1931.
- (6) For selected recent examples of the stereodivergent and stereoselective synthesis of natural products toward the structural elucidation, see: (a) Kotaki, T.; Shinada, T.; Kaihara, K.; Ohfuné, Y.; Numata, H. *Org. Lett.* **2009**, *11*, 5234. (b) Sui, B.; Yeh, E. A.-H.; Curran, D. P. *J. Org. Chem.* **2010**, *75*, 2942. (c) Tamura, S.; Ohno, T.; Hattori, Y.; Murakami, N. *Tetrahedron Lett.* **2010**, *51*, 1523. (d) Urabe, D.; Todoroki, H.; Masuda, K.; Inoue, M. *Tetrahedron* **2012**, *68*, 3210. (e) Takamura, H.; Wada, H.; Lu, N.; Ohno, O.; Suenaga, K.; Kadota, I. *J. Org. Chem.* **2013**, *78*, 2443.
- (7) Higashibayashi, S.; Czechtizky, W.; Kobayashi, Y.; Kishi, Y. *J. Am. Chem. Soc.* **2003**, *125*, 14379.
- (8) In ref 4c, we reported that the relative stereostructural relationships of the C5/C6 and C6/C7 could be proposed as *syn* and *syn*, respectively. After the detailed consideration of the ¹H NMR data analysis, we concluded that we could not exclude the possibility of the combination of *anti* (C5/C6) and *anti* (C6/C7) relationships. Therefore, we decided to synthesize **2a–2d** for the unambiguous configurational determination.
- (9) Parikh, J. R.; Doering, W. v. E. *J. Am. Chem. Soc.* **1967**, *89*, 5505.
- (10) Inoue, M.; Wang, J.; Wang, G.-X.; Ogasawara, Y.; Hiramata, M. *Tetrahedron* **2003**, *59*, 5645.
- (11) Evans, D. A.; Cee, V. J.; Siska, S. J. *J. Am. Chem. Soc.* **2006**, *128*, 9433.
- (12) Our detailed examination of separating **11** and its C5-epimer was unfruitful. The minor diastereomers, which were derived from the C5-epimer of **11**, could be separated by silica gel column chromatography at the final stage of **2a–2d**, respectively.
- (13) De Mico, A.; Margarita, R.; Parlanti, L.; Vescovi, A.; Piancatelli, G. *J. Org. Chem.* **1997**, *62*, 6974.
- (14) The transformation of **11** to the corresponding *p*-methoxybenzylidene acetal with DDQ was unsuccessful presumably due to the incompatibility of the 1,3-diene moiety.
- (15) Chen, K.-M.; Hardtmann, G. E.; Prasad, K.; Repič, O.; Shapiro, M. J. *Tetrahedron Lett.* **1987**, *28*, 155.
- (16) Higashibayashi, S.; Shinko, K.; Ishizu, T.; Hashimoto, K.; Shirahama, H.; Nakata, M. *Synlett* **2000**, 1306.
- (17) Ghosh, S.; Rao, C. N. *Tetrahedron Lett.* **2010**, *51*, 2052.
- (18) When the TBS ether **19** was subjected to the same reaction conditions, the formation of several products was observed.
- (19) For a review on TPAP oxidation, see: Ley, S. V.; Norman, J.; Griffith, W. P.; Marsden, S. P. *Synthesis* **1994**, 639.
- (20) Saksena, A. K.; Mangiaracina, P. *Tetrahedron Lett.* **1983**, *24*, 273.
- (21) For a comparison of the ¹H NMR spectra of the degraded product **2** and the synthetic products **2a–2d**, see the Supporting Information.

Hg²⁺-Trapping Beads: Hg²⁺-Specific Recognition through Thymine–Hg(II)–Thymine Base Pairing

Mituhiko Kuriyama,^{a,#} Kaichiro Haruta,^{a,#} Takenori Dairaku,^a
Takuya Kawamura,^a Shoko Kikkawa,^a Kiyofumi Inamoto,^a Hirokazu Tsukamoto,^a
Yoshinori Kondo,^a Hidetaka Torigoe,^b Itaru Okamoto,^c Akira Ono,^c Eugene Hayato Morita,^{*,d} and
Yoshiyuki Tanaka^{*,a}

^a Graduate School of Pharmaceutical Sciences, Tohoku University; 6–3 Aza Aoba, Aramaki, Aoba-ku, Sendai, Miyagi 980–8578, Japan; ^b Department of Applied Chemistry, Faculty of Science, Tokyo University of Science; 1–3 Kagurazaka, Shinjuku-ku, Tokyo 162–8601, Japan; ^c Department of Material & Life Chemistry, Faculty of Engineering, Kanagawa University; 3–27–1 Rokkakubashi, Kanagawa-ku, Yokohama, Kanagawa 221–8686, Japan; and ^d Department of Bioresources, Faculty of Agriculture, Ehime University; 3–5–7 Tarumi, Matsuyama, Ehime 790–8566, Japan.

Received November 25, 2013; accepted April 8, 2014

Mercury pollution poses a severe threat to human health. To remove Hg²⁺ from contaminated water, we synthesized Hg²⁺-trapping beads that include oligo-thymidine functionalities that can form thymine–Hg(II)–thymine base pairs on the solid support. The beads can selectively trap Hg²⁺ even in the presence of other metal cations. More interestingly, Hg²⁺-trapping efficiency was higher in the presence of the co-existing cations. Thus, the developed Hg²⁺-trapping beads can capture Hg²⁺ without affecting the mineral balance of water so much. The Hg²⁺-trapping beads presented here show promise for removing Hg²⁺ from environmental water.

Key words mercury removal; thymine; thymine–Hg(II)–thymine base pair; DNA–metal interaction; oligo-nucleotide

Mercury is a reputable highly toxic element.^{1–3} Notably, World Health Organization (WHO), Environmental Protection Agency (EPA), and U.S. Food and Drug Administration (FDA) reported that certain kinds of fishes accumulate high level of mercury which is harmful enough to fetuses, babies and children.^{3,4} Such an accumulation of mercury in fishes occurred through a food chain.^{2,5} Based on these facts, the provisional tolerable weekly intake (PTWI) for methylmercury and the reference dose (RfD) for mercuric chloride have been set at 1.6 μg/kg/week and 0.3 μg/kg/d, respectively.³ In any case, mercury originates from natural sources (such as volcanoes) and human activities (such as industrial wastes). To reduce mercury contamination in the environment, it is necessary to reduce and remove mercury from environments (oceans, rivers, and lakes).

For this purpose, various techniques have been reported. These include bioremediation,^{5,6} precipitation,⁷ non-specific adsorption (using activated carbon,^{8,9} aerogels,¹⁰ and chitosan^{8,11} as sorbents), and metal chelations (using imidazoles,¹² thiols,¹³ and DNA/nucleobases^{14–19}). However, these techniques generally trap several kinds of metals, resulting in the loss of mineral balance in the treated water. It is thus indispensable to develop methods for the selective removal of mercury.

For this purpose, thymine–Hg(II)–thymine (T–Hg(II)–T) base pairing system which was used in a DNA-based Hg²⁺-specific sensor by the Ono and Togashi²⁰ gave us a hint, since thymine is a highly Hg(II)-specific ligand. The key structural element of the T–Hg(II)–T base pair was originally proposed by Katz,²¹ based on pre-existing studies on Hg²⁺–DNA inter-

actions.^{22–25} New insights were recently reported by Ono and colleagues.^{20,26,27} Although extensive structural and theoretical studies on the structure of this base pair in a DNA oligomer have been performed,^{28–41} the experimental structure of the T–Hg(II)–T base pair from NMR and Raman spectroscopy was recently reported^{27,42} (see the chemical structure of the T–Hg(II)–T base pair for that shown within Fig. 1b). Thermal denaturation experiments⁴³ showed that the T–Hg(II)–T base pair is as stable as the Watson–Crick A–T base pairs. More importantly, it was demonstrated that a T–T mismatch can specifically bind to Hg²⁺ without binding to other divalent metal cations.²⁶ Thus, such Hg²⁺-specificity of thymine base is suitable to develop an Hg²⁺-specific trapping system. We thus prepared Hg²⁺-trapping beads based on this concept (Fig. 1), and examined their trapping efficiency.

The Hg²⁺-trapping beads consist of oligo-thymidine (T20) attached onto the polystyrene (PS) beads (solid support), as shown in Fig. 1a. Following capture of the Hg²⁺ ions by T20, the Hg²⁺-trapped PS beads can be easily separated from the solution by filtration (Fig. 1b). To give mobility to T20, polyethylene glycol 400 (PEG 400) was used as a linker to attach T20 onto the PS beads, since PEG 400 is long enough to give attached molecules their mobility on the polymer surface.⁴⁴ The detailed preparation is given in Chart S1 and Supplemental Methods in Supplemental Information.

Inductively coupled plasma atomic emission spectroscopy (ICP-AES) was used to assess the performance of the prepared Hg²⁺-trapping beads. This technique is suitable for the quantification of low levels of Hg²⁺ as well as the simultaneous determination of co-existing metal cations in solution.

Prior to conducting the Hg²⁺-trapping experiments, we confirmed the linearity between the Hg²⁺-concentration and the ICP-AES peak intensities, measured at the 253 nm

The authors declare no conflict of interest.

#These authors contributed equally to this work.

* To whom correspondence should be addressed. e-mail: morita.hayato.mu@ehime-u.ac.jp;
tanaka@mail.pharm.tohoku.ac.jp

© 2014 The Pharmaceutical Society of Japan

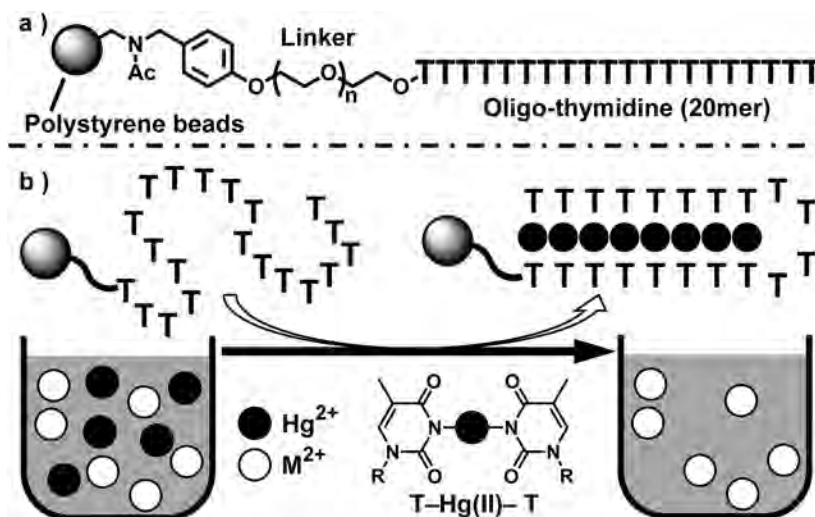


Fig. 1. Hg^{2+} -Trapping Concept

a) Structure of the Hg^{2+} -trapping beads. b) Procedure of Hg^{2+} removal from Hg^{2+} -contaminated water by the Hg^{2+} -trapping beads.

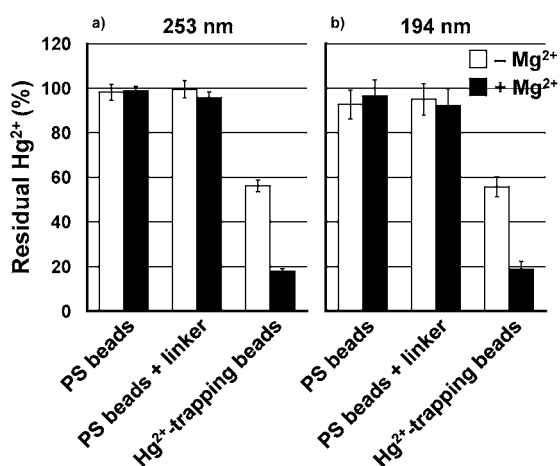


Fig. 2. Mercury Removal Ratios by the PS Beads, PS Beads+Linker, and Hg^{2+} -Trapping Beads

The experiments were performed in $50\ \mu\text{M}$ HgCl_2 , and either in the absence of Mg^{2+} ($-\text{Mg}^{2+}$) or the presence of $5.0\ \text{mM}$ MgCl_2 ($+\text{Mg}^{2+}$). Residual ratios determined at a) 253 nm and b) 194 nm mercury emission. No obvious spectroscopic interferences between mercury and magnesium was observed, since emission intensities for “PS beads” and “PS beads + linker” were not change significantly irrespective of whether Mg^{2+} is present or absent.

and 194 nm mercury emissions (Hg^{2+} concentration range: $0.5\text{--}10\ \mu\text{M}$ = $0.1\text{--}2.0\ \text{ppm}$) (Fig. S1).

Based on the obtained linear range and signal to noise ratio, the Hg^{2+} -trapping experiments were conducted at $50\ \mu\text{M}$ ($10\ \text{ppm}$) Hg^{2+} , and the supernatant solutions after Hg^{2+} removal were diluted 10 times (maximum $5.0\ \mu\text{M}$ Hg^{2+}) for Hg^{2+} quantitation. The residual Hg^{2+} ratios (%), monitored at the 253 and 194 nm emissions, as calculated by Eq. 1 in Supplemental Methods in Supplemental Information, are presented in Fig. 2. A *ca.* 50% reduction in the residual Hg^{2+} -concentration was observed for the Hg^{2+} -trapping beads (white bars in Fig. 2). It should be also mentioned that capture of Hg^{2+} was negligible in the absence of the oligo-thymidine moieties (PS beads and PS beads+linker samples in Fig. 2 and Table S1). Thus, the Hg^{2+} -trapping capabilities of the beads are exclusively reliant on the presence of oligo-thymidine moieties.

The Hg^{2+} -selective trapping was initially examined in the

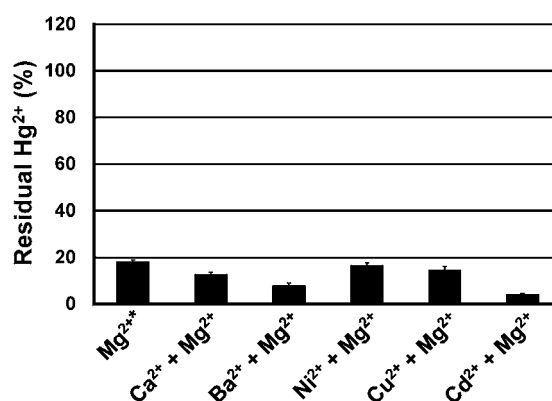


Fig. 3. Mercury Removal Ratios by Hg^{2+} -Trapping Beads in the Presence of Mg^{2+} Only (Mg^{2+*}), and Mg^{2+} and Co-existing Metal Cations

The experiments were performed in $50\ \mu\text{M}$ HgCl_2 , $5.0\ \text{mM}$ MgCl_2 , and 0 or $0.5\ \text{mM}$ of the respective co-existing metal cations. Residual ratios were determined from the 253 nm mercury emission.

presence of Mg^{2+} to simulate the natural conditions of seawater that contains minerals such as Na^+ , Mg^{2+} , and Ca^{2+} . Because the actual concentration of Na^+ ($481\ \text{mM}$) and possibly Mg^{2+} ($54\ \text{mM}$) in seawater exceeds the upper limit of the ICP-AES measurements, the present experiments were conducted under a $5.0\ \text{mM}$ Mg^{2+} solution. Unexpectedly, in the presence of Mg^{2+} , the residual Hg^{2+} concentration decreased from *ca.* 50 to *ca.* 20% (Fig. 2, Table S1). The same trend was observed for both 253 nm and 194 nm mercury emissions (Fig. 2, Tables S1 and S2). Therefore, for the subsequent studies, only the results from the 253 nm emission spectra are presented as the 253 nm emission generated stronger signals.

As seawater includes several kinds of divalent metal cations, we investigated the performance of the beads to selectively trap Hg^{2+} over other divalent metal cations (Ca^{2+} , Ba^{2+} , Ni^{2+} , Cu^{2+} , Cd^{2+}) in the presence of Mg^{2+} (Fig. 3, Fig. S2). The Hg^{2+} -trapping efficiency of the beads, examined in the presence of co-existing metal cations (Ca^{2+} , Ba^{2+} , Ni^{2+} , Cu^{2+} , Cd^{2+}), was similar or greater than that obtained in the presence of Mg^{2+} only (absence of the co-existing cations) (Fig. 3, Table S1). For the Hg^{2+} -trapping efficiencies in the absence of

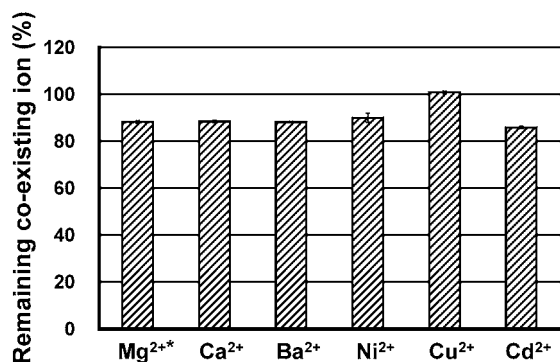


Fig. 4. Residual Ratios of the Co-existing Metal Cations after Hg²⁺-Trapping

The emission wavelengths of the corresponding co-existing metal cations are listed in Table S3. All the experiments were performed in 50 μM HgCl₂, 5.0 mM MgCl₂, and 0.5 mM of the respective co-existing metal cation except for sample Mg²⁺* whereby the experiment was conducted in the absence of the co-existing cations.

Mg²⁺, see Fig. S2.

The non-specific binding of the co-existing metal cations by the Hg²⁺-trapping beads was then examined (Fig. 4, Figs. S3, S4, Tables S3, S4). The residual ratios (%) of the co-existing cations after Hg²⁺-trapping are shown in Fig. 4 and Table S3. As observed, the remaining percentages of all the co-existing metal cations in the corresponding supernatant solutions, after Hg²⁺-trapping, were very high.

The DNA-based Hg²⁺-trapping beads effectively removed mercury in both the presence of Mg²⁺ only, and several co-existing metal cations that included Mg²⁺ (Fig. 3). In contrast to this effective Hg²⁺-trapping, non-specific trapping of co-existing cations did not occur so much (Fig. 4). The results are consistent with our previous study that showed the specific binding of Hg²⁺ by thymine bases.²⁶⁾ Thus the herein developed Hg²⁺-trapping beads are suitable for use in natural conditions that involve a variety of mineral ingredients.

The enhanced performance of the Hg²⁺-trapping beads in the presence of co-existing metal cations is explained as follows. The formation of T–Hg(II)–T base pairs implies the formation of a DNA duplex. For the latter to form, electrostatic repulsion between the negatively-charged phosphates in the respective DNA strands needs to be suppressed. The Mg²⁺ and other co-existing cations thus suppress the electrostatic repulsion between the phosphate groups by neutralizing the negative charges (Fig. S5). Hence, in the absence of a charge compensation effect of the co-existing cations, formation of T–Hg(II)–T base pair and the resulting DNA duplex formation cannot occur efficiently. In addition, the competition between Mg²⁺ and Hg²⁺ during their phosphate-binding steps may assist preferential Hg²⁺-binding to thymine bases. This phenomenon was evident in the presence of Mg²⁺, as indicated by the considerable increase in the Hg²⁺-trapping efficiency (Figs. S2, S5c, d). A slight increase in the trapping efficiency was observed in the presence of the co-existing cations under Mg²⁺-depleted conditions (Figs. S2, S5e). These findings and some foregoing studies^{45,46)} support our hypothesis that co-existing cations stabilize the formation of a DNA duplex following formation of T–Hg(II)–T base pair. The measured residual ratio of the co-existing metal cations after Hg²⁺-trapping (Fig. S3) further supported our hypothesis that co-existing cations served as counter ions for DNA, as explained: in the ab-

sence of Mg²⁺, the other co-existing cations were captured by the Hg²⁺-trapping beads, possibly as counter ions for the phosphate groups (Fig. S5e), hence other co-existing cations rarely remained in solution in the absence of Mg²⁺ (Fig. S3). The present experimental data indicate that the Hg²⁺-trapping beads show potential for their usage under natural environmental conditions, particularly in seawater with a high salt concentration.

The present findings were compared to those obtained by other reported methods (bioremediation,^{5,6)} precipitation,⁷⁾ non-specific adsorbents,^{8–10)} and some metal chelators^{12,13)}. In these studies, the Hg²⁺-specificity was not indicated nor was it expected on the basis of metal-specificities of the ligands.^{5–10,12,13)} Only Hg²⁺-trapping beads, containing thymine moieties,^{14–19)} showed good Hg²⁺-selectivity and these data are consistent with our previous results.²⁶⁾ As an exception, chitosan-based Hg²⁺-trapping beads showed Hg²⁺ selectivity,¹¹⁾ however, the origin of the Hg²⁺-specificity is unclear on the basis of an intrinsic metal-specificity of chitosan.

In conclusion, the prepared Hg²⁺-trapping beads can exclusively capture Hg²⁺ even in the presence of co-existing cations. More interestingly, the Hg²⁺-trapping efficiency of the beads improved in the presence of co-existing cations. The Hg²⁺-trapping beads are suitable for the elimination of Hg²⁺ from environmental water, especially seawater. As a practical usage of the Hg²⁺-trapping beads, the Hg²⁺-decontamination from industrial wastes would be possible.

Acknowledgments The authors would like to thank Dr. Hiroshi Naka at Nagoya University for his discussion. This work was supported by two Grants-in-Aid for Scientific Research (B) and (C) (Grant Nos. 24310163 and 18550146 to Y.T.) from the Ministry of Education, Culture, Sports, Science and Technology of Japan. Y.T. is also supported by a Human Frontier Science Program for Young Investigators from Human Frontier Science Program Organization (HFSP) (France) and the Intelligent Cosmos Academic Foundation. M.K. is the recipient of a Japan Society for the Promotion of Science (JSPS) Research Fellowship for Young Scientists. ICP-AES measurements were performed at the Integrated Center for Sciences (INCS_Johoku station) at Ehime University.

References

- Clarkson T. W., Magos L., *Crit. Rev. Toxicol.*, **36**, 609–662 (2006), and references cited therein.
- Clarkson T. W., Magos L., Myers G. J., *N. Engl. J. Med.*, **349**, 1731–1737 (2003).
- World Health Organization, “Guidance for Identifying Populations at Risk from Mercury Exposure.”: <http://www.who.int/foodsafety/publications/chem/mercury/en/index.html>, cited 11th November, 2013.
- Environmental Protection Agency and US Food and Drug Administration, “What You Need to Know about Mercury in Fish and Shellfish.”: http://water.epa.gov/scitech/swguidance/fishshellfish/outreach/advice_index.cfm, cited 11th November, 2013.
- Morel F. M. M., Kraepiel A. M. L., Amyot M., *Annu. Rev. Ecol. Syst.*, **29**, 543–566 (1998).
- Rugh C. L., Bizily S. P., Meagher R. B., “Phytoremediation of Toxic Metals,” ed. by Raskin I., Ensley B. D., Wiley-Interscience, New York, 2000, pp. 151–169 and references cited therein.
- Porter S. K., Scheckel K. G., Impellitteri C. A., Ryan J. A., *Crit. Rev. Environ. Sci. Technol.*, **34**, 495–604 (2004).

- 8) Babel S., Kurniawan T. A., *J. Hazard. Mater.*, **97**, 219–243 (2003).
- 9) Krishnan S. V., Gullett B. K., Jozewicz W., *Environ. Sci. Technol.*, **28**, 1506–1512 (1994).
- 10) Kadirvelu K., Goel J., Rajagopal C., *J. Hazard. Mater.*, **153**, 502–507 (2008).
- 11) Miretzky P., Cirelli A. F., *J. Hazard. Mater.*, **167**, 10–23 (2009), and references cited therein.
- 12) Kara A., Uzun L., Beşirli N., Denizli A., *J. Hazard. Mater.*, **106**, 93–99 (2004).
- 13) Liu A. M., Hidajat K., Kawi S., Zhao D. Y., *Chem. Commun.*, 1145–1146 (2000).
- 14) Liu X., Qi C., Bing T., Cheng X., Shangguan D., *Talanta*, **78**, 253–258 (2009).
- 15) Dave N., Chan M. Y., Huang P. J. J., Smith B. D., Liu J., *J. Am. Chem. Soc.*, **132**, 12668–12673 (2010).
- 16) Yu Y., Zhang B. W., Yu M., Deng B., Li L. F., Fan C. H., Li J. Y., *Sci. China Chem.*, **55**, 2202–2208 (2012).
- 17) Wang Y. S., Cheng C. C., Chen J. K., Ko F. H., Chang F. C., *J. Mater. Chem. A*, **1**, 7745–7750 (2013).
- 18) Huang P.-J. J., Liu J., *Chem.-Eur. J.*, **17**, 5004–5010 (2011).
- 19) He D., He X., Wang K., Zhao Y., Zou Z., *Langmuir*, **29**, 5896–5904 (2013).
- 20) Ono A., Togashi H., *Angew. Chem., Int. Ed.*, **43**, 4300–4302 (2004).
- 21) Katz S., *Biochim. Biophys. Acta*, **68**, 240–253 (1963).
- 22) Katz S., *J. Am. Chem. Soc.*, **74**, 2238–2245 (1952).
- 23) Thomas C., *J. Am. Chem. Soc.*, **76**, 6032–6034 (1954).
- 24) Yamane T., Davidson N., *J. Am. Chem. Soc.*, **83**, 2599–2607 (1961).
- 25) Yamane T., Davidson N., *Biochim. Biophys. Acta*, **55**, 780–782 (1962).
- 26) Miyake Y., Togashi H., Tashiro M., Yamaguchi H., Oda S., Kudo M., Tanaka Y., Kondo Y., Sawa R., Fujimoto T., Machinami T., Ono A., *J. Am. Chem. Soc.*, **128**, 2172–2173 (2006).
- 27) Tanaka Y., Oda S., Yamaguchi H., Kondo T., Kojima C., Ono A., *J. Am. Chem. Soc.*, **129**, 244–245 (2007).
- 28) Simpson R. B., *J. Am. Chem. Soc.*, **86**, 2059–2065 (1964).
- 29) Tanaka Y., Ono A., “Metal Complex-DNA Interactions,” ed. by Hadjiliadis N., Sletten E., John Wiley & Sons Ltd., Chichester, 2008, pp. 439–462 and references cited therein.
- 30) Kosturko L. D., Folzer C., Stewart R. F., *Biochemistry*, **13**, 3949–3952 (1974).
- 31) Mansy S., Wood T. E., Sprowles J. C., Tobias R. S., *J. Am. Chem. Soc.*, **96**, 1762–1770 (1974).
- 32) Mansy S., Tobias R. S., *Inorg. Chem.*, **14**, 287–291 (1975).
- 33) Gruenwedel D. W., Cruikshank M. K., *Biochemistry*, **1990**, 2110–2116 (1990).
- 34) Morzyk-Ociepa B., Michalska D., *J. Mol. Struct.*, **598**, 133–144 (2001).
- 35) Buncel E., Boone C., Joly H., Kumar R., Norris A. R., *J. Inorg. Biochem.*, **25**, 61–73 (1985).
- 36) Buncel E., Boone C., Joly H., *Inorg. Chim. Acta*, **125**, 167–172 (1986).
- 37) Kuklennyk Z., Marzilli L. G., *Inorg. Chem.*, **35**, 5654–5662 (1996).
- 38) Johannsen S., Paulus S., Düpre N., Müller J., Sigel R. K. O., *J. Inorg. Biochem.*, **102**, 1141–1151 (2008).
- 39) Benda L., Straka M., Tanaka Y., Sychrovský V., *Phys. Chem. Chem. Phys.*, **13**, 100–103 (2011).
- 40) Benda L., Straka M., Sychrovský V., Bouř P., Tanaka Y., *J. Phys. Chem. A*, **116**, 8313–8320 (2012).
- 41) Šebera J., Burda J., Straka M., Ono A., Kojima C., Tanaka Y., Sychrovský V., *Chem.-Eur. J.*, **19**, 9884–9894 (2013).
- 42) Uchiyama T., Miura T., Takeuchi H., Dairaku T., Komuro T., Kawamura T., Kondo Y., Benda L., Sychrovský V., Bour P., Okamoto I., Ono A., Tanaka Y., *Nucleic Acids Res.*, **40**, 5766–5774 (2012).
- 43) Torigoe H., Ono A., Kozasa T., *Chem.-Eur. J.*, **16**, 13218–13225 (2010).
- 44) Terenzi S., Biala E., Nguyen-Trung N. Q., Strazewski P., *Angew. Chem., Int. Ed.*, **42**, 2909–2912 (2003).
- 45) Kiy M. M., Zaki A., Menhaj A. B., Samadi A., Liu J., *Analyst*, **137**, 3535–3540 (2012).
- 46) Kiy M. M., Jacobi Z. E., Liu J., *Chem.-Eur. J.*, **18**, 1202–1208 (2012).

Regulated Incorporation of Two Different Metal Ions into Programmed Sites in a Duplex by DNA Polymerase Catalyzed Primer Extension**

Tatsuya Funai, Junko Nakamura, Yuki Miyazaki, Risa Kiri, Osamu Nakagawa, Shun-ichi Wada, Akira Ono, and Hidehito Urata*

Abstract: Metal-mediated base pairs formed by the coordination of metal ions to natural or artificial bases impart unique chemical and physical properties to nucleic acids and have attracted considerable interest in the field of nanodevices. Ag^{I} ions were found to mediate DNA polymerase catalyzed primer extension through the formation of a $\text{C}-\text{Ag}^{\text{I}}-\text{T}$ base pair, as well as the previously reported $\text{C}-\text{Ag}^{\text{I}}-\text{A}$ base pair. The comparative susceptibility of dNTPs to Ag^{I} -mediated enzymatic incorporation into the site opposite cytosine in the template was shown to be $\text{dATP} > \text{dTTP} \gg \text{dCTP}$. Furthermore, two kinds of metal ions, Ag^{I} and Hg^{II} , selectively mediate the incorporation of thymidine 5'-triphosphate into sites opposite cytosine and thymine in the template, respectively. In other words, the regulated incorporation of different metal ions into programmed sites in the duplex by DNA polymerase was successfully achieved.

Metal-mediated base pairs formed by the coordination of metal ions to natural or artificial bases impart unique chemical and physical properties to nucleic acids. For example, an increase in duplex and triplex stability^[1–3] and the assembly of programmable arrays of one or several kinds of metal ions into a duplex have been reported.^[4] Metal-mediated base pairs have thus attracted considerable interest in the field of nanodevices, for example, in the context of electronic wires,^[5] magnetic devices,^[6] and DNA-based logic gates.^[7]

Recently, it was reported that Hg^{II} and Ag^{I} ions coordinate to natural mismatched base pairs in oligodeoxynucleotide (ODN) duplexes and stabilize the base pairs through the formation of metal-mediated base pairs, such as $\text{T}-\text{Hg}^{\text{II}}-\text{T}$

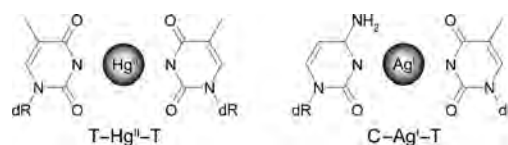


Figure 1. Structures of the $\text{T}-\text{Hg}^{\text{II}}-\text{T}$ and $\text{C}-\text{Ag}^{\text{I}}-\text{T}$ base pairs. dR = deoxyribose.

(Figure 1), $\text{U}-\text{Hg}^{\text{II}}-\text{U}$, and $\text{C}-\text{Ag}^{\text{I}}-\text{C}$.^[8–10] Hence, we focused on the biological relevance of metal-mediated base pairs and discovered that in the presence of Hg^{II} ions, DNA polymerases incorporate 2'-deoxythymidine 5'-triphosphate (dTTP) into the sites opposite thymine (T) in the template strand to synthesize the full-length product through the formation of a $\text{T}-\text{Hg}^{\text{II}}-\text{T}$ base pair.^[11] A metal-mediated base pair consisting of an artificial base was reported to be recognized by DNA polymerase as well.^[12] Furthermore, we found that Ag^{I} ions promoted the enzymatic incorporation of 2'-deoxyadenosine 5'-triphosphate (dATP) into the sites opposite cytosine (C) in the template strand through the formation of a $\text{C}-\text{Ag}^{\text{I}}-\text{A}$ base pair.^[13] This result was quite unexpected because an Ag^{I} ion was reported to selectively increase the thermodynamic stability of duplexes containing a C–C mismatched base pair.^[10] We found that Ag^{I} ions also increase the thermodynamic stability of duplexes containing a C–T mismatched base pair, probably through the formation of a $\text{C}-\text{Ag}^{\text{I}}-\text{T}$ base pair (Figure 1).^[14]

Herein, we report on a primer extension reaction in which DNA polymerase catalyzes the formation of a $\text{C}-\text{Ag}^{\text{I}}-\text{T}$ base pair within the DNA duplex to synthesize full-length product. The reaction involving the incorporation of dTTP into the sites opposite C in the template was highly specific for Ag^{I} ions. From the comparative study of the Ag^{I} -mediated incorporation of dNTPs into the site opposite C in the template, the strictly preferential incorporation of dATP and dTTP over dCTP was observed. In combination with the previously reported enzymatic formation of a $\text{T}-\text{Hg}^{\text{II}}-\text{T}$ base pair within the DNA duplex, the formation of a $\text{C}-\text{Ag}^{\text{I}}-\text{T}$ base pair enabled the accurately regulated enzymatic incorporation of dTTP into the sites opposite T and C in the template through the addition of Hg^{II} and Ag^{I} ions, respectively. The two different kinds of metal ions (Ag^{I} and Hg^{II} ions) were successfully incorporated into the programmed sites in the same duplex as metal-ion-mediated mismatched base pairs by DNA polymerase.

[*] T. Funai, J. Nakamura, Y. Miyazaki, R. Kiri, Dr. O. Nakagawa, Dr. S. Wada, Prof. H. Urata
Osaka University of Pharmaceutical Sciences
4-20-1 Nasahara, Takatsuki, Osaka 569-1094 (Japan)
E-mail: urata@gly.oups.ac.jp

Prof. A. Ono
Department of Material & Life Chemistry
Faculty of Engineering, Kanagawa University
3-27-1 Rokkakubashi, Kanagawa-ku, Yokohama 221-8686 (Japan)

[**] This work was supported in part by a Grant-in-Aid for Scientific Research (C) (24550199) (for H.U.) and Scientific Research (A) (24245037) (for A.O.) from the Ministry of Education, Science, Sports and Technology (Japan).

Supporting information for this article (including experimental details) is available on the WWW under <http://dx.doi.org/10.1002/anie.201311235>.

To elucidate the compatibility of the C–Ag^I–T base pair with DNA polymerases, a primer extension reaction was carried out with 3'→5'-exonuclease-deficient Klenow fragment (KF exo⁻). In the absence of Ag^I ions, KF exo⁻ stalled at the 19-mer site, however, the enzyme incorporated dTTP or dCTP into the site opposite C in the template to elongated the stalled product to yield the full-length product at increasing concentrations of Ag^I ions (Figure 2 a). The reversed reaction,

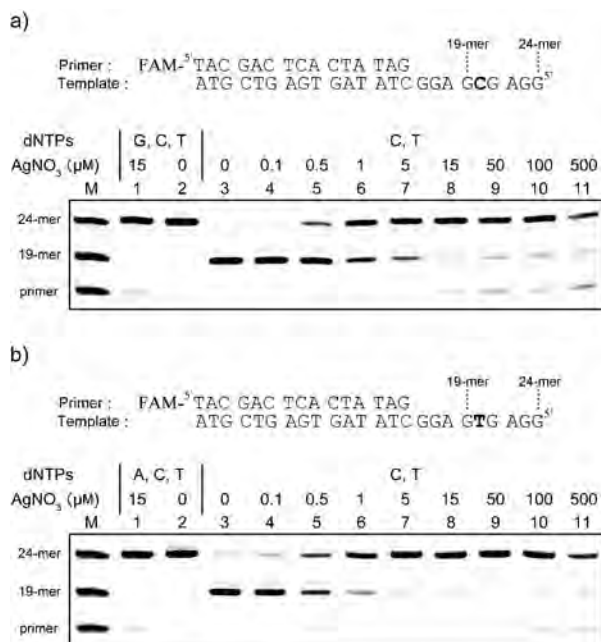


Figure 2. PAGE analysis showing the effect of Ag^I ion concentration on the primer extension reaction catalyzed by KF exo⁻. The reaction mixtures contained 20 μM dNTPs and 0.4 units of KF exo⁻ in the presence or absence of various concentrations of AgNO₃. M indicates markers for the primer, 19-mer, and 24-mer. FAM = 6-carboxyfluorescein.

Ag^I-mediated dTTP or dCTP incorporation into the site opposite T, also proceeded in the presence of Ag^I ions (Figure 2 b). To confirm the kind of dNTP incorporated by KF exo⁻, single-nucleotide insertions were carried out with the primed templates shown in Figure 3. For the Ag^I-independent incorporation of dNTP into the site opposite C in the template, dGTP was incorporated by the enzyme to yield the 20-mer ($n + 1$) product through the formation of a canonical Watson–Crick (G–C) base pair, regardless of the presence or absence of Ag^I ions (Figure 3 a, lanes 3 and 4). For Ag^I-dependent reactions, KF exo⁻ incorporated dATP into the site opposite C in the template through the formation of a C–Ag^I–A base pair in the presence of Ag^I ions (Figure 3 a, lane 1) as reported.^[12] Furthermore, the enzyme incorporated dTTP into the site opposite C in the template in the presence of Ag^I ions to yield the 20-mer ($n + 1$) product (Figure 3 a, lane 7). Unexpectedly, no incorporation of dCTP into the site opposite C was observed under these conditions (Figure 3 a, lane 5), although Ag^I ions show stronger stabilizing effects for duplexes containing a C–C mismatch than for those containing a C–T mismatch.^[10] The reverse reaction, the Ag^I-

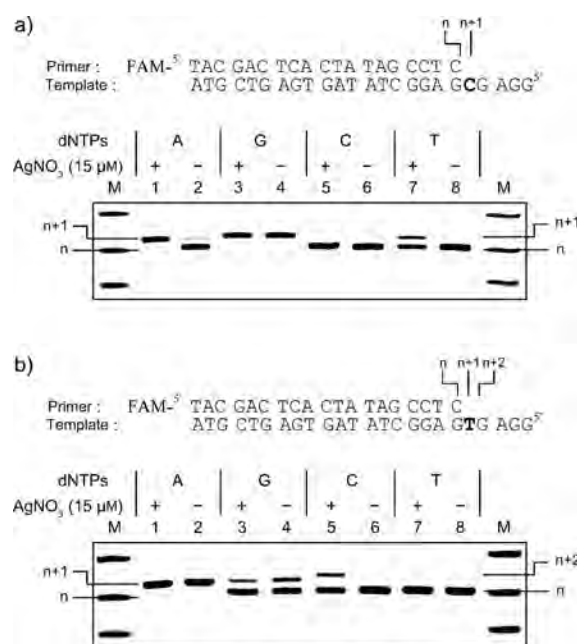
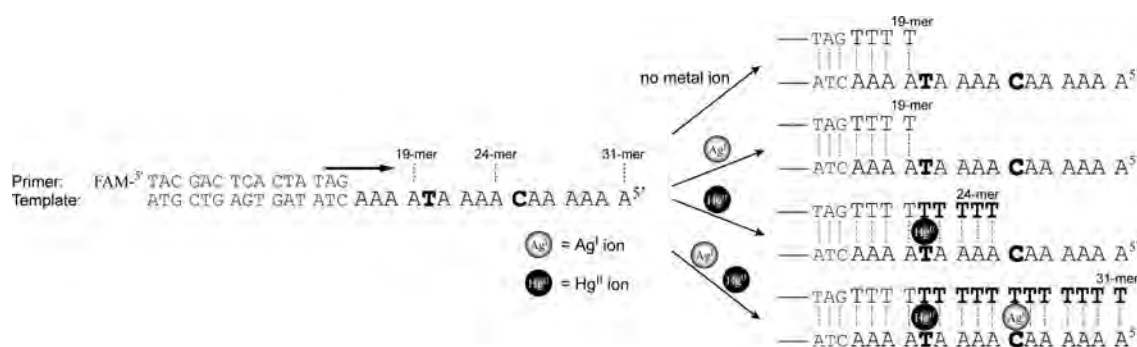


Figure 3. “PAGE analysis of single-nucleotide insertions into the sites opposite C (a) and T (b) in the template strands catalyzed by KF exo⁻. The reaction mixtures contained 10 μM dNTPs and 0.2 units of KF exo⁻ in the presence or absence of 15 μM AgNO₃. M indicates markers for the 15-mer, primer, and 24-mer.

mediated incorporation of dCTP into the site opposite T in the template also proceeded in the presence of Ag^I ions (Figure 3 b, lane 5). The compositions of the full-length products of the Ag^I-promoted reactions in Figure 2 were confirmed by MALDI-TOF mass spectrometry (see Figure S1 in the Supporting Information).

To investigate the effects of other metal ions, we performed the primer extension reactions in the presence of Mn^{II}, Fe^{II}, Fe^{III}, Co^{II}, Ni^{II}, Cu^{II}, Zn^{II}, Cd^{II}, Au^{III}, Hg^{II}, Tl^I, or Pb^{II} (Figure 4). The reactions proceeded to yield a full-length product only in the presence of Ag^I and Hg^{II} ions. Ag^I ions promoted both the extension reactions to yield the full-length products (24-mer; Figure 4 a and b). By contrast, only the incorporation of dTTP or dCTP into the site opposite T, and not the incorporation of dTTP or dCTP opposite C, proceeded in the presence of Hg^{II} ions (Figure 4 b). We then confirmed that dTTP was selectively incorporated into the site opposite T in the template by the Hg^{II}-mediated reaction (see Figure S2 in the Supporting Information) as reported.^[11] These results indicate that the incorporation of dTTP into the site opposite C in the template is highly specific to Ag^I ions.

In addition to the previously reported C–Ag^I–A base pair, we demonstrated the Ag^I-mediated formation of a C–Ag^I–T base pair within the DNA duplex by DNA polymerase. The formation of a C–Ag^I–C base pair was not observed in this work (Figure 3 a) or in previous work,^[12] despite the fact that Ag^I ions have been reported to selectively stabilize the C–C mismatched base pair among 16 kinds of matched and mismatched base pairs.^[10] Therefore, we compared the enzymatic incorporation of dATP, dTTP and dCTP into the site opposite C in the template by using various templates



Scheme 1. A schematic illustration of the regulated incorporation of Ag^{I} and Hg^{II} ions into programmed sites in the duplex.

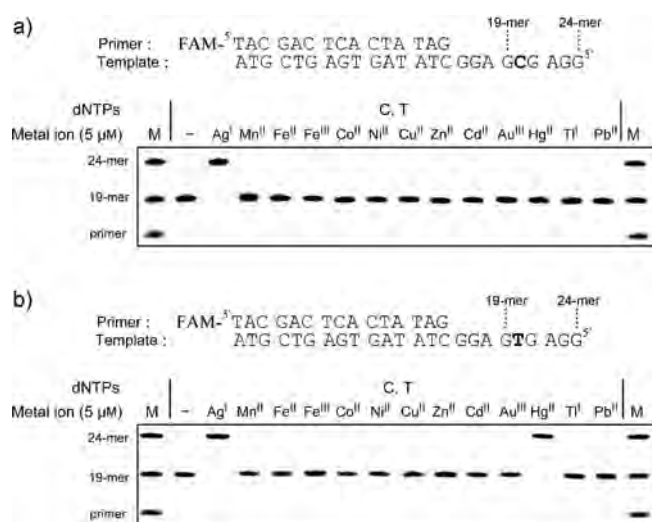


Figure 4. PAGE analysis showing the effect of various metal ions on the primer extension reaction. The reaction mixtures contained 20 μM dTTP and dCTP, 0.4 units of KF exo^- , and 15 μM various metal ions. M indicates markers for the primer, 19-mer, and 24-mer.

possessing different sequences in the upstream region of the incorporation site (see Figure S3 in the Supporting Information). In the presence of Ag^{I} ions, dATP was incorporated into almost all of the primed templates except for Duplexes 4 and 10, which may form a hairpin structure between the C-rich upstream and G-rich downstream regions of the incorporation site. The incorporation of dTTP was somewhat dependent on the upstream sequence of the incorporation site. However, dCTP was not incorporated into any of the primed templates under these assay conditions. Indeed, a lower efficiency for the incorporation of dCTP into the site opposite C in the template was recently reported.^[15] The use of larger amounts (0.8 units) of the enzyme and a higher concentration of dCTP (20 μM) allowed the incorporation of dCTP into some primed templates to form a C– Ag^{I} –C base pair (see Figure S4 in the Supporting Information). These results indicate that dTTP is a much better substrate for this reaction than dCTP. Hg^{II} ions deprotonate the imino protons of two thymine residues to form a neutral T– Hg^{II} –T base pair, whereas Ag^{I} ions should deprotonate one imino proton to form neutral base pairs such as C– Ag^{I} –T. The positively

charged C– Ag^{I} –C base pair may thus not easily be recognized as a “correct” substrate by DNA polymerases. This may suggest that the absence of a positive charge on a metal-mediated base pair is important for its polymerase-catalyzed integration into the duplex.

We have demonstrated that the incorporation of dTTP into the site opposite C in the template through the formation of a C– Ag^{I} –T base pair is strictly specific to Ag^{I} ions (Figure 3 a and Figure 4 a). In combination with the enzymatic formation of a T– Hg^{II} –T base pair within the DNA duplex, this reaction could make the regulated extension of primers and the regulated incorporation of different metal ions into the same duplex possible because an Ag^{I} ion mediates the incorporation of dTTP only opposite C and not opposite T in the template (Figure 3). We thus designed a novel metal-ion-triggered primer extension system, which enables the regulated incorporation of two different metal ions (Ag^{I} and Hg^{II} ions) into programmed sites in a duplex (Scheme 1). The results are shown in Figure 5. In the absence of Hg^{II} ions, KF exo^- did not catalyze the extension reaction at the site opposite T in the template to yield the 19-mer product, regardless of the presence or absence of Ag^{I} ions (lanes 2 and 3). However, by adding Hg^{II} ions, a T– Hg^{II} –T base pair was formed and the enzyme went through the site opposite T and subsequently stalled at the site opposite C to yield the 24-mer product (lane 4). The addition of both Ag^{I} and Hg^{II} ions promoted extension at the sites opposite T and C in the template to yield the full-length 31-mer product (Lane 5). The compositions of these stalled and full-length products were

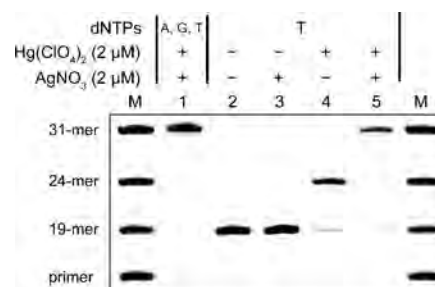


Figure 5. PAGE analysis of the regulated incorporation of Ag^{I} and Hg^{II} ions into the programmed sites by KF exo^- . The reaction mixtures contained 30 μM dNTPs and 0.4 units of KF exo^- in the presence of 2 μM AgNO_3 and/or $\text{Hg}(\text{ClO}_4)_2$. M indicates markers for the primer, 19-mer, 24-mer, and 31-mer.

confirmed by MALDI-TOF mass spectrometry (see Figure S5 in the Supporting Information). Furthermore, the metal-ion-triggered extension reaction with a primed template in which the C and T sites were exchanged with each other proceeded in a similar manner (Figure S6 in the Supporting Information). For both template configurations, the two different kinds of metal-mediated base pairs (T–Hg^{II}–T and C–Ag^I–T) were successfully formed at the programmed sites in the newly synthesized double-stranded DNA.

In conclusion, we demonstrated that Ag^I ions mediate DNA polymerase catalyzed primer extension through the formation of a C–Ag^I–T base pair, as well as the previously reported C–Ag^I–A base pair. The comparative susceptibility of dNTPs to Ag^I-mediated enzymatic incorporation into the site opposite C in the template was shown to be dATP > dTTP >> dCTP. In combination with T–Hg^{II}–T formation, C–Ag^I–T formation was used in a novel metal-ion-triggered primer extension system. The specific formation of two different kinds of metal-mediated base pairs was thus achieved at programmed sites in duplex DNA. To our knowledge, this is the first report of the successful regulated enzymatic incorporation of different metal ions into programmed sites in duplex DNA. Our findings open up the possibility of regulating a multistep replicating system with metal ions. Moreover, this enzymatic approach may overcome the difficulties in the preparation of large double-strand DNA molecules base-paired through selective interstrand coordination with different kinds of metal ions.^[16]

Received: December 27, 2013

Published online: ■ ■ ■ ■, ■ ■ ■ ■ ■

Keywords: DNA polymerase · DNA structures · mercury · metal-mediated base pairing · silver

- [1] a) G. H. Clever, C. Kaul, T. Carell, *Angew. Chem.* **2007**, *119*, 6340–6350; *Angew. Chem. Int. Ed.* **2007**, *46*, 6226–6236; b) G. H. Clever, M. Shionoya, *Coord. Chem. Rev.* **2010**, *254*, 2391–2402; c) Y. Takezawa, M. Shionoya, *Acc. Chem. Res.* **2012**, *45*, 2066–2076.
- [2] a) K. Tanaka, M. Shionoya, *J. Org. Chem.* **1999**, *64*, 5002–5003; b) E. Meggers, P. L. Holland, W. B. Tolman, F. E. Romesberg, P. G. Schultz, *J. Am. Chem. Soc.* **2000**, *122*, 10714–10715; c) S. Atwell, E. Meggers, G. Spraggon, P. G. Schultz, *J. Am. Chem. Soc.* **2001**, *123*, 12364–12367; d) K. Tanaka, A. Tengeiji, T. Kato, N. Toyama, M. Shiro, M. Shionoya, *J. Am. Chem. Soc.* **2002**, *124*, 12494–12498; e) C. Switzer, S. Shinha, P. H. Kim, B. D. Heu-berger, *Angew. Chem.* **2005**, *117*, 1553–1556; *Angew. Chem. Int. Ed.* **2005**, *44*, 1529–1532.
- [3] a) K. Tanaka, Y. Yamada, M. Shionoya, *J. Am. Chem. Soc.* **2002**, *124*, 8802–8803; b) Y. Takezawa, W. Maeda, K. Tanaka, M. Shionoya, *Angew. Chem.* **2009**, *121*, 1101–1104; *Angew. Chem. Int. Ed.* **2009**, *48*, 1081–1084.
- [4] a) K. Tanaka, G. H. Clever, Y. Takezawa, Y. Yamada, C. Kaul, M. Shionoya, T. Carell, *Nat. Nanotechnol.* **2006**, *1*, 190–194; b) G. H. Clever, T. Carell, *Angew. Chem.* **2007**, *119*, 254–257; *Angew. Chem. Int. Ed.* **2007**, *46*, 250–253; c) F.-A. Polonius, J. Müller, *Angew. Chem.* **2007**, *119*, 5698–5701; *Angew. Chem. Int. Ed.* **2007**, *46*, 5602–5604; d) S. Johannsen, N. Megger, D. Böhme, R. K. O. Sigel, J. Müller, *Nat. Chem.* **2010**, *2*, 229–234.
- [5] S. Liu, G. H. Clever, Y. Takezawa, M. Kaneko, K. Tanaka, X. Guo, M. Shionoya, *Angew. Chem.* **2011**, *123*, 9048–9052; *Angew. Chem. Int. Ed.* **2011**, *50*, 8886–8890.
- [6] a) K. Tanaka, A. Tengeiji, T. Kato, N. Toyama, M. Shionoya, *Science* **2003**, *299*, 1212–1213; b) G. H. Clever, S. J. Reitmeier, T. Carell, O. Schiemann, *Angew. Chem.* **2010**, *122*, 5047–5049; *Angew. Chem. Int. Ed.* **2010**, *49*, 4927–4929.
- [7] a) R. Freeman, T. Finder, I. Willner, *Angew. Chem.* **2009**, *121*, 7958–7961; *Angew. Chem. Int. Ed.* **2009**, *48*, 7818–7821; b) H. Pei, L. Liang, G. Yao, J. Li, Q. Huang, C. Fan, *Angew. Chem.* **2012**, *124*, 9154–9158; *Angew. Chem. Int. Ed.* **2012**, *51*, 9020–9024.
- [8] a) A. Ono, H. Torigoe, Y. Tanaka, I. Okamoto, *Chem. Soc. Rev.* **2011**, *40*, 5855–5866; b) Y. Miyake, H. Togashi, M. Tashiro, H. Yamaguchi, S. Oda, M. Kudo, Y. Tanaka, Y. Kondo, R. Sawa, T. Fujimoto, T. Machinami, A. Ono, *J. Am. Chem. Soc.* **2006**, *128*, 2172–2173; c) Y. Tanaka, S. Oda, H. Yamaguchi, Y. Kondo, C. Kojima, A. Ono, *J. Am. Chem. Soc.* **2007**, *129*, 244–245.
- [9] S. Johannsen, S. Paulus, N. Düpre, J. Müller, R. K. O. Sigel, *J. Inorg. Biochem.* **2008**, *102*, 1141–1151.
- [10] a) A. Ono, S. Cao, H. Togashi, M. Tashiro, T. Fujimoto, T. Machinami, S. Oda, Y. Miyake, I. Okamoto, Y. Tanaka, *Chem. Commun.* **2008**, 4825–4827; b) H. Torigoe, I. Okamoto, T. Dairaku, Y. Tanaka, A. Ono, T. Kozasa, *Biochimie* **2012**, *94*, 2431–2440.
- [11] H. Urata, E. Yamaguchi, T. Funai, Y. Matsumura, S. Wada, *Angew. Chem.* **2010**, *122*, 6666–6669; *Angew. Chem. Int. Ed.* **2010**, *49*, 6516–6519.
- [12] C. Kaul, M. Müller, M. Wagner, S. Schneider, T. Carell, *Nat. Chem.* **2011**, *3*, 794–800.
- [13] T. Funai, Y. Miyazaki, M. Aotani, E. Yamaguchi, O. Nakagawa, S. Wada, H. Torigoe, A. Ono, H. Urata, *Angew. Chem.* **2012**, *124*, 6570–6572; *Angew. Chem. Int. Ed.* **2012**, *51*, 6464–6466.
- [14] H. Urata, E. Yamaguchi, Y. Nakamura, S. Wada, *Chem. Commun.* **2011**, *47*, 941–943.
- [15] T. Tian, S. Peng, H. Xiao, Y. Long, B. Fu, X. Zhang, S. Guo, S. Wang, X. Zhou, S. Liuc, X. Zhouc, *Chem. Commun.* **2013**, *49*, 10085–10087.
- [16] J. Müller, *Nature* **2006**, *444*, 698.

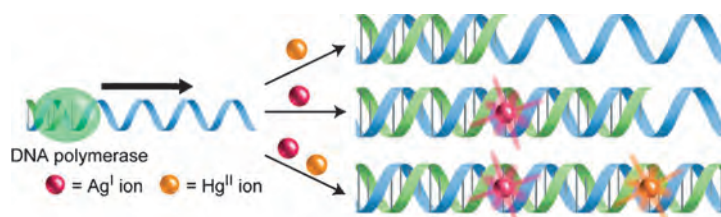
Communications



Bioinorganic Chemistry

T. Funai, J. Nakamura, Y. Miyazaki,
R. Kiri, O. Nakagawa, S. Wada, A. Ono,
H. Urata*     

Regulated Incorporation of Two Different
Metal Ions into Programmed Sites in
a Duplex by DNA Polymerase Catalyzed
Primer Extension



(Quick) silver DNA: Hg^{II} and Ag^I ions were found to specifically trigger DNA polymerase catalyzed primer extension in the absence of a Watson–Crick matched nucleotide through the formation of T–

Hg^{II}–T and newly discovered C–Ag^I–T base pairs. The strict base recognition by the metal ions enabled regulated incorporation of the two different metal ions into programmed sites in duplex DNA.



Photocatalytic activity of α -PbO₂-type TiO₂

Hidenobu Murata^{*,1}, Yusuke Kataoka², Tatsuya Kawamoto², Isao Tanaka^{3,4}, and Takashi Taniguchi¹

¹ Advanced Key Technologies Division, National Institute for Materials Science, 1-1 Namiki, Tsukuba, Ibaraki 305-0044, Japan

² Department of Chemistry, Kanagawa University, 2946 Tsuchiya, Hiratsuka, Kanagawa 259-1293, Japan

³ Department of Materials Science and Engineering, Kyoto University, Yoshida-Honmachi, Sakyo, Kyoto 606-8501, Japan

⁴ Nanostructures Research Laboratory, Japan Fine Ceramics Center, 2-4-1 Mutsuno, Atsuta, Nagoya 456-8587, Japan

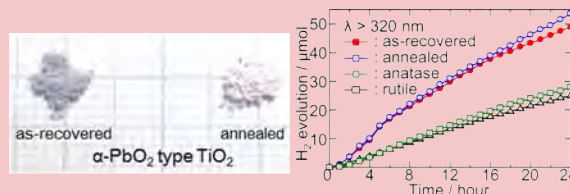
Received 7 June 2014, revised 22 August 2014, accepted 22 August 2014

Published online 28 August 2014

Keywords titanium dioxide, high-pressure synthesis, photocatalysts, first-principles calculations, hybrid functionals

* Corresponding author: e-mail MURATA.Hidenobu@nims.go.jp

The α -PbO₂-type TiO₂ is synthesized under high-pressure and high-temperature environment and it shows higher photocatalytic activity as compared to rutile and anatase under UV irradiation. The reduction in α -PbO₂-type TiO₂ induces visible-light photocatalytic activity. These results indicate that α -PbO₂-type TiO₂ is an important candidate material for use in a photocatalytic matrix.



© 2014 WILEY-VCH Verlag GmbH & Co. KGaA, Weinheim

1 Introduction Green engineering and materials have been studied for use in sustainable developments. Photocatalysts are promising technologies for use in the field of solar energy [1]. TiO₂ is one of the more typical photocatalytic materials [2–6] and it has a number of polymorphs. The natural occurrence phases are rutile, anatase, and brookite. The metastable phases, TiO₂(B), TiO₂(H), and TiO₂(R) have been synthesized [7–9]. In addition to these, there are several TiO₂ high-pressure phases, the α -PbO₂-type (TiO₂-II/columbite-type), baddeleyite-type, orthorhombic-I-type, fluorite-type, cotunnite-type, and Fe₂P-type phases [10–15]. In general, the high-pressure phases often transform into an ambient pressure phase or amorphous in the decompression process, and thus, there is a limited number of high-pressure phase applications.

Among the TiO₂ high-pressure phases, α -PbO₂-type TiO₂ can be recovered to ambient pressure [10]. The natural α -PbO₂-type TiO₂ is sometimes found in a meteorite impact crater [16]. It was also reported that α -PbO₂-type TiO₂ thin films and nanoparticles can be synthesized at ambient pressure [17–20]. While α -PbO₂-type TiO₂ was found in the 1960's [10], its photocatalytic properties were unrevealed. It was interesting that samples which partially

contain α -PbO₂-type TiO₂ have good photocatalytic activity [21, 22]. Therefore, it is essentially to investigate the photocatalytic property of α -PbO₂-type TiO₂. Theoretical approaches have been attempted on the high-pressure phases of TiO₂, but were limited to discussing only the basic properties, such as the band gaps [23].

We synthesized α -PbO₂-type TiO₂ samples under high-pressure and high-temperature (HPHT) conditions and found that they had much higher photocatalytic activity as compared to (reagent-grade) rutile and anatase under UV irradiation. We propose that α -PbO₂-type TiO₂ is a promising material for use as a photocatalytic matrix.

2 Procedures

2.1 Sample preparation Samples were prepared under high-pressure and high-temperature (HPHT) conditions using the belt-type HPHT apparatus, FB30H. The starting materials were rutile-type TiO₂ (4N, particle size of about 400 nm, Rare-metallic, Co. Ltd.), pre-calcined at 1000 °C for 12 h. These materials were sealed into a Pt capsule and it was put into a high-pressure cell. Details of the high-pressure experiments are presented in the Supporting Information. The HPHT treatments were performed at

7.7 GPa and 1100 °C for 1 h. The samples were quenched to room temperature and slowly depressurize to ambient pressure after these treatments. The recovered samples were ground with an alumina mortar and some of them were annealed at 300 °C for 12 h.

The reference samples for characterization and photocatalytic activity measurements were rutile-type TiO₂ (4N, grain size of about 400 nm, Rare-metallic, Co. Ltd.) preheated at 1000 °C for 12 h and anatase-type TiO₂ (99.6%, grain size of about 300 nm, Rare-metallic, Co. Ltd.).

2.2 Characterization The samples were characterized by using XRD, DTA, SEM, UV-VIS, and XPS. The XRD patterns of the samples were collected using a Rigaku RINT-2200V/PC with Cu K_α radiation and a graphite counter monochromator. The thermal analyses were carried out using a Rigaku Thermo-plus Evo TG-8120 in air. The rate of temperature increase was set to 10 °C/min. The SEM observations were carried out by using a JEOL JSM-5410 with a LaB₆ cathode. The accelerated voltage was set to 20 kV. The UV-VIS spectra were measured by using a JASCO V570 with an integrating sphere. The XPS was measured using a PHI Quantera SXM with monochromatic Al K_α. The binding energy was calibrated using an adventitious C-1s peak to 284.60 eV.

2.3 Photocatalytic activity The photocatalytic activity of TiO₂ polymorphs was evaluated with H₂ evolution

in the closed circulatory system using the same weight of TiO₂. The essence of the closed circulatory system was described in the Supporting Information. Preparation and measurements were performed in the same manner as described elsewhere [24]. For each measurement, it was used that 50 mg of the samples, 10 ml of water and 558 mg of EDTA-2Na, which acted as the sacrificial reagent. The light source was a 500 W Xe lamp with three types of cut-off filters ($\lambda > 320, 380, \text{ and } 420 \text{ nm}$). TCD detector and Ar-carrier gas were used in the gas-chromatography (Shimadzu GC-8A) to evaluate the output gas.

2.4 First-principles calculation The electronic and atomistic structures were calculated by using the projector augmented wave (PAW) method [25] implemented in the Vienna ab-initio simulation package (VASP) code [26, 27]. The HSE06 hybrid functional [28–30] was adapted as an exchange-correlational functional with the mixing of the Hartree–Fock term to be 20% [31]. The details concerning the computational conditions are presented in the Supporting Information.

3 Results and discussion HPHT syntheses of α -PbO₂-type TiO₂ were performed at 7.7 GPa and 1100 °C. The as-recovered samples exhibited a gray color, as shown in Fig. 1a, and they changed to white after annealing at 300 °C for 12 h in air. These are similar to that for reduced rutile, which exhibit a blue color [32, 33]. Indeed, the sam-

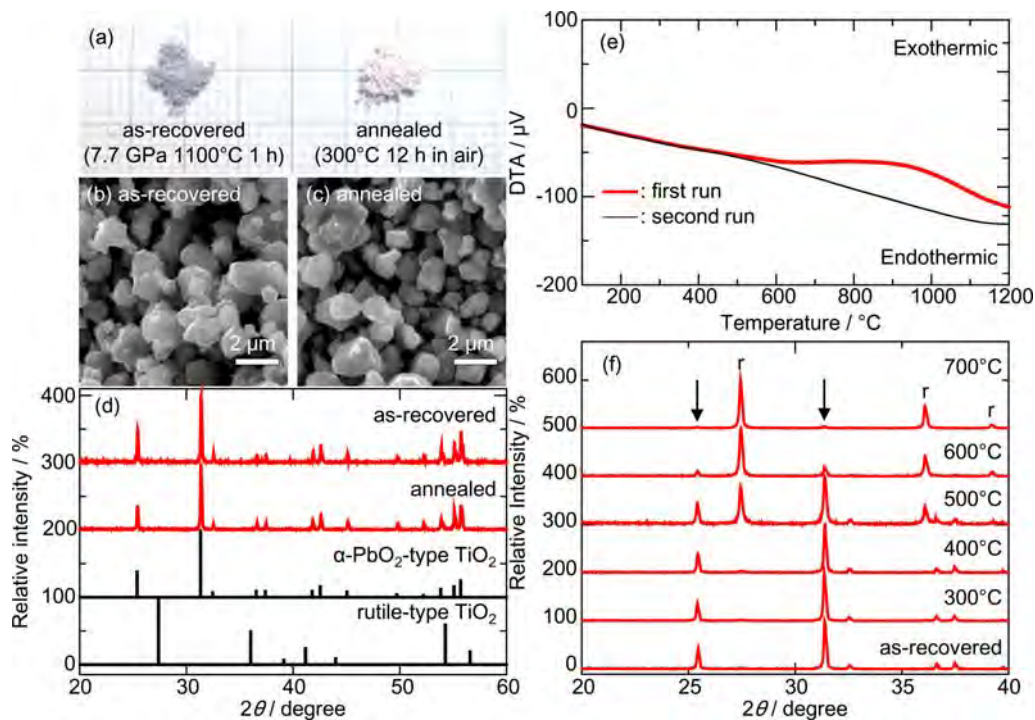


Figure 1 (a) Photograph and SEM images of (b) as-recovered and (c) annealed samples. (d) Typical XRD patterns of sample recovered from HPHT condition and reference data. (e) DTA of as-recovered sample in air. (f) XRD patterns of as-recovered sample calcined in air at different temperatures for 12 h. The “r” indicates the peaks assigned to the rutile phase. The other peaks are assigned to α -PbO₂-type TiO₂.

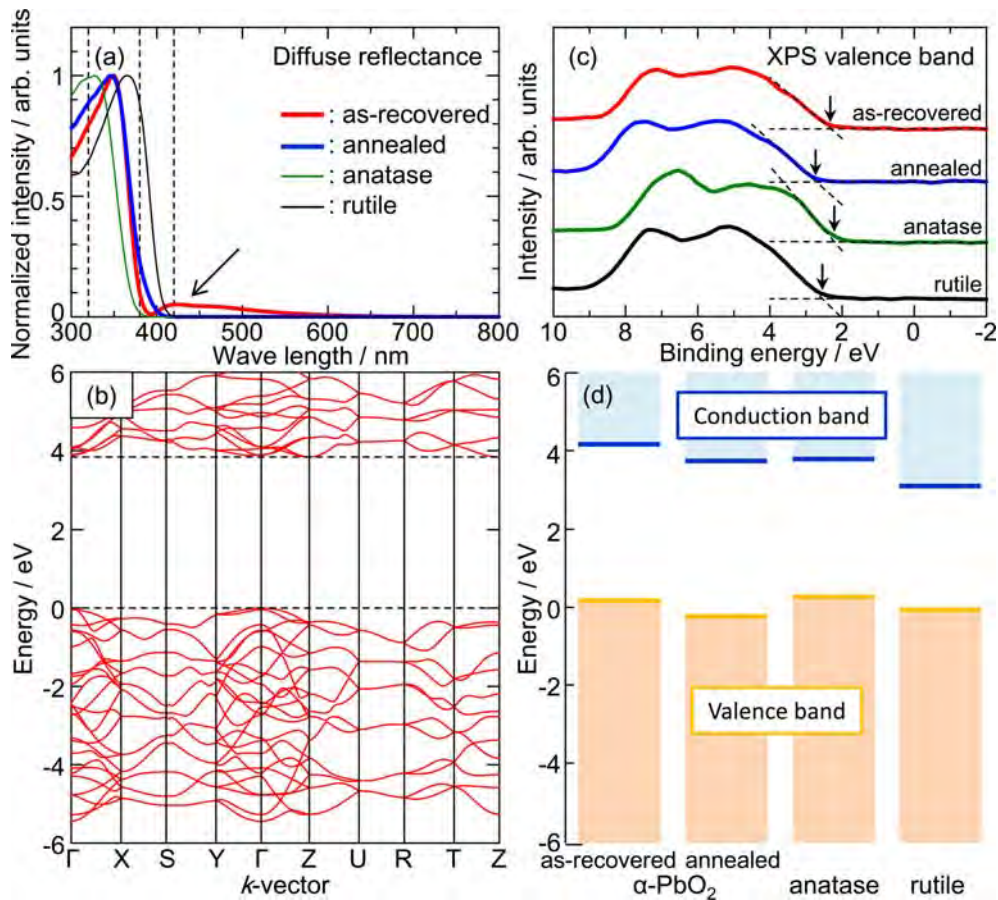


Figure 2 (a) Diffuse reflectance UV-VIS spectra. The vertical dashed lines were the cut-off wavelengths of the filters used in the photocatalytic activity measurements (Fig. 3). (b) Calculated band structure of α -PbO₂-type TiO₂ and (c) XPS valence band spectra. The arrows indicated the VBM. (d) Schematic band structure of TiO₂ polymorphs. The VBM of rutile is set to 0 eV.

ples recovered from 5.5 GPa and 1100 °C were blue-reduced rutile. This indicated that our HPHT experiments were somehow carried out in a reduction atmosphere. Therefore, our as-recovered samples were partially reduced and then exhibited a gray color.

Our SEM observations found that the grain sizes of our α -PbO₂-type TiO₂ samples were around 2 μ m (Fig. 1b and 1c). These are larger than the grain size of the starting material, which was 400 nm, and indicated that grain growth occurred under the HPHT condition. The annealing at 300 °C did not affect the grain size. Figure 1d shows the powder X-ray diffraction (XRD) patterns of the samples. The majority of peaks can be assigned to the α -PbO₂-type TiO₂ (ICDD-01-084-1750). It was confirmed that α -PbO₂-type TiO₂ was recovered to ambient pressure. A small amount of residual rutile, which was less than 5%, was also observed and determined by using the standard addition method. These behaviors were similar to that in previous reports [12, 14, 34].

We also evaluated the thermal stability of α -PbO₂-type TiO₂ by conducting a differential thermal analysis (DTA) on it, as shown in Fig. 1e. The DTA showed an exothermic reaction starting from 500 °C. This exothermic reaction

is similar to the anatase–rutile transition [35]. Annealing experiments were also carried out in air. Figure 1f shows the XRD patterns of a sample annealed in air for 12 h at different temperatures. The phase transition was barely observed below 400 °C. Above 500 °C, the α -PbO₂-type TiO₂ was transformed to the rutile phase, but a part of α -PbO₂ phases slightly remained after annealing at 700 °C for 12 h, which is indicated by the arrows. This means that the transition to the rutile phase was slow.

We next studied the optical nature of α -PbO₂-type TiO₂. Figure 2a shows the diffuse-reflectance ultraviolet-visible light (UV-VIS) spectra of α -PbO₂-type TiO₂, rutile and anatase. Both α -PbO₂-type TiO₂ samples had a large absorption rate around 390 nm. This was attributed to the band-edge absorption. The band gap of α -PbO₂-type TiO₂ is roughly estimated to be 3.2 eV, although the optical band gap might be underestimated because these measurements were carried out at room temperature [36, 37]. The as-recovered samples experienced additional absorption in the visible-light region, as shown by the arrow in Fig. 2a.

The first principles calculations were carried out using a hybrid-functional in order to discuss the band gap of TiO₂ polymorphs. The band structure of α -PbO₂-type TiO₂

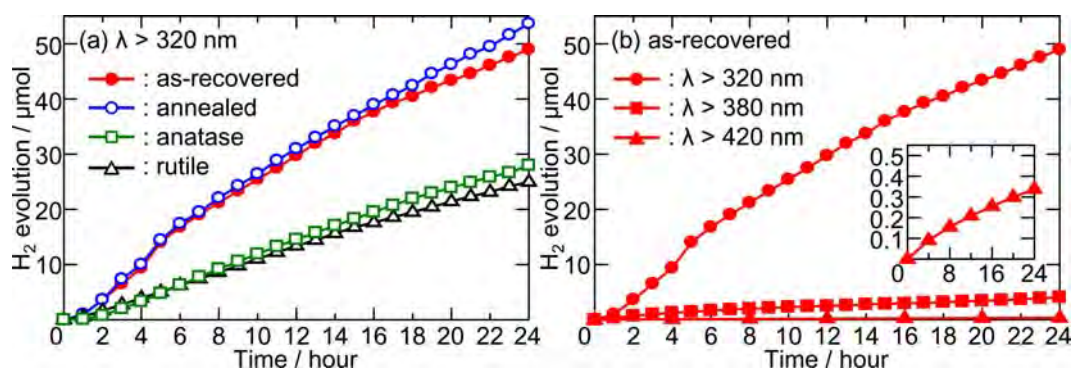


Figure 3 H₂ evolution of α -PbO₂-type TiO₂ under UV and visible light irradiations. (a) Comparison between TiO₂ polymorphs under UV irradiation ($\lambda > 320$ nm) and (b) wavelength dependence of as-recovered sample.

is shown in Fig. 2b. The calculated valence band maximum (VBM) was at the Γ -point. On the other hand, the conduction band minimum (CBM) was at the Z-point, whose energy was 0.05 eV smaller than at the Γ -point. Then α -PbO₂-type TiO₂ was found to have an indirect band gap of 3.84 eV. Except for the value of the band gap, the results matched the standard DFT results [23]. The experimental and calculated band gaps of TiO₂ polymorphs are summarized in Table 1.

The positions of the CBM and VBM were considered to be important for the photocatalytic activity. Figure 2c shows the X-ray photoelectron spectra (XPS) of the valence band of TiO₂ polymorphs and the values of the VBM are listed in Table 1. The band positions of rutile and anatase have been discussed on. Our results show the same tendency as the traditional description [38]. The VBM of the recovered samples had the largest binding energy while that of the annealed samples had the smallest one. Such a discrepancy was often observed in defective or doped TiO₂ [39, 40]. This was probably caused by intrinsic defects and dopants. A schematic band structure of TiO₂ polymorphs was summarized in Fig. 2d by using the calculated band gap and experimental VBM. This shows that the CBMs of α -PbO₂-type TiO₂ were similar or higher than that of anatase.

Then, the photocatalytic activity of the TiO₂ polymorphs with respect to the H₂ evolution were compared

Table 1 Band gaps and valence band maxima of TiO₂ polymorphs.

phase	band gap (eV)		binding energy of VBM (eV)
	expt.	calc.	
α -PbO ₂	as-recovered	(3.2)	3.84
	annealed		(indirect) 2.7
rutile		3.03 ^{a)}	3.06
			(direct) 2.6
anatase		3.2 ^{b)}	3.39
			(indirect) 2.2

^{a)} Ref. [36]; ^{b)} Ref. [38].

under UV light irradiation ($\lambda > 320$ nm). It should be noted that the XRD patterns of the samples did not change after the photocatalytic activity measurements. Since the activity may be dependent on the grain size, we used reagent-grade rutile and anatase for comparison, whose grain sizes are 400 and 300 nm. The grain size of our α -PbO₂-type TiO₂ samples was 2 μ m.

Luttrel et al. classified the factors that help to determine the photocatalytic activity into four types, i.e., the energy level of the light-induced carriers (positions of the VBM and CBM), the lifetime of the exciton, the charge mobility, and the surface properties [41]. As shown in Fig. 2, our α -PbO₂-type TiO₂ samples have similar VBM and CBM positions to anatase. It also has an indirect band gap, which should be related to a long exciton lifetime. These results suggest that α -PbO₂-type TiO₂ has a similar activity to that of anatase as a rule of thumb. In fact, our α -PbO₂-type TiO₂ samples exhibited much higher activity than that of the reagent-grade rutile and anatase, as can be seen in Fig. 3a. It may be fair to mention that the activity of our sample is still 50% that of a commercial TiO₂-photocatalyst, Aeroxide[®] TiO₂ P 25 (Evonik industries AG), which was examined under the same conditions. Yet, the α -PbO₂-type TiO₂ seems to be an important candidate material for use in a photocatalytic matrix.

Annealed samples had higher photocatalytic activity than as-recovered samples. The reduction of the TiO₂ forms defects, such as Ti³⁺ and oxygen vacancies, which behave as the recombination center of the light-induced carriers and decrease in the photocatalytic activity [40, 42]. This can be the reason why the photocatalytic activity of the as-recovered samples was slightly lower.

Generally, the visible light absorption does not always contribute to the photocatalytic activity [42, 43]. Since the as-recovered samples show there was visible light absorption as mentioned above, we also evaluated its photocatalytic activity under visible light irradiation. Figure 3b shows the H₂ evolution by using α -PbO₂-type TiO₂ under UV and visible light irradiation. The as-recovered samples clearly showed there was photocatalytic activity in both of UV and visible light regions. This means that the visible light absorption of the present samples contributes to the photoca-

talytic activity. This visible light absorption should be derived from the reduction in TiO₂.

In summary, α -PbO₂-type TiO₂ was synthesized under the HPHT conditions and its electronic structure and photocatalytic properties were evaluated. We prepared two types of α -PbO₂-type TiO₂ samples, as-recovered (gray) and annealed (white), whose difference was caused by the reduction. The α -PbO₂-type TiO₂ samples showed much higher photocatalytic activity as compared to the rutile and anatase under UV irradiation. The reduction in α -PbO₂-type TiO₂ had negative and positive effects on the photocatalytic activity. It forms a recombination center of light-induced carriers, and thus, the photocatalytic activity decreased. On the other hand, it induced visible light absorption and visible-light photocatalytic activity was observed. These results indicate that α -PbO₂-type TiO₂ is an important candidate material for use in a photocatalytic matrix.

Acknowledgements This work was supported by JSPS KAKENHI Grant No. 24-10639 (Grant-in-Aid for JSPS Fellows) and the Exploration of nanostructure-property relationships for materials innovation conducted by the Ministry of Education, Culture, Sports, Science and Technology (MEXT), Japan.

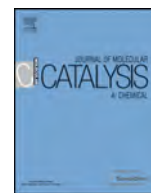
References

- [1] R. M. N. Yerga, M. C. Á. Galván, F. del Valle, J. A. V. de la Mano, and J. L. G. Fierro, *Chem. Sus. Chem.* **2**, 471–485 (2009).
- [2] A. L. Linsebigler, G. Lu, and J. T. Yates, Jr., *Chem. Rev.* **95**, 735–758 (1995).
- [3] X. Chen and S. S. Mao, *Chem. Rev.* **107**, 2891–2959 (2007).
- [4] M. K. Nowotny, L. R. Sheppard, T. Bak, and J. Nowotny, *J. Phys. Chem. C* **112**, 5275–5300 (2008).
- [5] S. G. Kumar and L. G. Devi, *J. Phys. Chem. A* **115**, 13211–13241 (2011).
- [6] R. Daghrir, P. Drogui, and D. Robert, *Ind. Eng. Chem. Res.* **52**, 3581–3599 (2013).
- [7] R. Marchand, L. Brohan, and M. Tournoux, *Mater. Res. Bull.* **15**, 1129–1133 (1980).
- [8] M. Lacroche, L. Brohan, R. Marchand, and M. Tournoux, *J. Solid. State. Chem.* **81**, 78–82 (1989).
- [9] J. Akimoto, Y. Gotoh, Y. Oosawa, N. Nonose, T. Kumagai, and K. Aoki, *J. Solid State Chem.* **113**, 27–36 (1994).
- [10] P. Y. Simons and F. Dacheille, *Acta Cryst.* **23**, 334–336 (1967).
- [11] H. Sato, S. Endo, M. Sugiyama, T. Kikegawa, O. Shimomura, and K. Kusaba, *Science* **251**, 786–788 (1991).
- [12] N. A. Dubrovinskaia, L. S. Dubrovinsky, R. Ahuja, V. B. Prokopenko, V. Dmitriev, H.-P. Weber, J. M. Osorio-Guillen, and B. Johansson, *Phys. Rev. Lett.* **87**, 275501 (2001).
- [13] L. S. Dubrovinsky, N. A. Dubrovinskaia, V. Swamy, J. Muscat, N. M. Harrison, R. Ahuja, B. Holm, and B. Johansson, *Nature* **410**, 653–654 (2001).
- [14] M. Mattesini, J. S. de Almeida, L. Dubrovinsky, N. Dubrovinskaia, B. Johansson, and R. Ahuja, *Phys. Rev. B* **70**, 212101 (2004).
- [15] H. Dekura, T. Tsuchiya, Y. Kuwayama, and J. Tsuchiya, *Phys. Rev. Lett.* **107**, 045701 (2011).
- [16] A. Goresy, M. Chen, P. Gillet, L. Dubrovinsky, G. Graup, and R. Ahuja, *Earth Planet. Sci. Lett.* **192**, 485–495 (2001).
- [17] J. Aarik, *Philos. Mag. Lett.* **73**, 115–119 (1996).
- [18] S. Y. Chen and P. Shen, *Phys. Rev. Lett.* **89**, 096106 (2002).
- [19] S. Sen, M. L. Ram, S. Roy, and B. K. Sarkar, *J. Mater. Res.* **14**, 841–848 (1999).
- [20] I. E. Grey, C. Li, I. C. Madsen, and G. Braunshausen, *Mat. Res. Bull.* **23**, 743–753 (1988).
- [21] J. Liu, Y. Yu, H. He, X. Jin, and K. Xu, *Mater. Res. Bull.* **35**, 377–382 (2000).
- [22] K. Saitow and T. Wakamiya, *Appl. Phys. Lett.* **103**, 031916 (2013).
- [23] M.-Y. Kuo, C.-L. Chen, C.-Y. Hua, H.-C. Yang, and P. Shen, *J. Phys. Chem. B* **109**, 8693–8700 (2005).
- [24] K. Sato, Y. Kataoka, and W. Mori, *J. Nanosci. Nanotechnol.* **12**, 585–590 (2012).
- [25] P. E. Blöchl, *Phys. Rev. B* **50**, 17953 (1994).
- [26] G. Kresse and J. Furthmüller, *Phys. Rev. B* **54**, 11169 (1996).
- [27] G. Kresse and D. Joubert, *Phys. Rev. B* **59**, 1758 (1999).
- [28] J. Heyd, G. E. Scuseria, and M. Ernzerhof, *J. Chem. Phys.* **118**, 8207 (2003).
- [29] J. Heyd, G. E. Scuseria, and M. Ernzerhof, *J. Chem. Phys.* **124**, 219906 (2006).
- [30] A. V. Krukau, O. A. Vydrov, A. F. Izmaylov, and G. E. Scuseria, *J. Chem. Phys.* **125**, 224106 (2006).
- [31] A. Janotti, J. B. Varley, P. Rinke, N. Umezawa, G. Kresse, and C. G. Van de Walle, *Phys. Rev. B* **81**, 085212 (2010).
- [32] W. A. Weyl and T. Förland, *Ind. Eng. Chem.* **42**, 257–263 (1950).
- [33] F. A. Grant, *Rev. Mod. Phys.* **31**, 646–674 (1959).
- [34] M. Akaogi, N. Horiuchi, T. Ishii, and H. Kojitani, *Phys. Chem. Minerals* **39**, 797–802 (2012).
- [35] J. Yang, Y. X. Huang, and J. M. F. Ferreira, *J. Mater. Sci. Lett.* **16**, 1933–1935 (1997).
- [36] J. Pascual, J. Camassel, and H. Mathieu, *Phys. Rev. B* **18**, 5606–5614 (1978).
- [37] H. Tang, F. Lévy, H. Berger, and P. E. Schmid, *Phys. Rev. B* **52**, 7771 (1995).
- [38] L. Kavan, M. Grätzel, S. E. Gilbert, C. Klemenz, and H. J. Scheel, *J. Am. Chem. Soc.* **118**, 6716–6723 (1996).
- [39] I. Takahashi, D. J. Payne, R. G. Palgrave, and R. G. Egdell, *Chem. Phys. Lett.* **454**, 314–317 (2008).
- [40] J. Wang, D. N. Tafen, J. P. Lewis, Z. Hong, A. Manivannan, M. Zhi, M. Li, and N. Wu, *J. Am. Chem. Soc.* **131**, 12290–12297 (2009).
- [41] T. Luttrell, S. Halpegamage, J. Tao, A. Kramer, E. Sutter, and M. Batzill, *Sci. Rep.* **4**, 4043 (2014).
- [42] H. Irie, Y. Watanabe, and K. Hashimoto, *J. Phys. Chem. B* **107**, 5483–5486 (2003).
- [43] Y. Nosaka, M. Matsushita, J. Nishino, and A. Y. Nosaka, *Sci. Tech. Adv. Mater.* **6**, 143–148 (2005).



Contents lists available at ScienceDirect

Journal of Molecular Catalysis A: Chemical

journal homepage: www.elsevier.com/locate/molcata

Editor's Choice paper

Zirconium(IV)- and hafnium(IV)-containing polyoxometalates as oxidation precatalysts: Homogeneous catalytic epoxidation of cyclooctene by hydrogen peroxide



Hiroki Aoto, Keisuke Matsui, Yoshitaka Sakai, Teppei Kuchizi, Hiromi Sekiya, Hironori Osada, Takuya Yoshida, Satoshi Matsunaga, Kenji Nomiya*

Department of Chemistry, Faculty of Science, Kanagawa University, Hiratsuka, Kanagawa 259-1293, Japan

ARTICLE INFO

Article history:

Received 8 May 2014

Received in revised form 8 July 2014

Accepted 12 July 2014

Available online 19 July 2014

Keywords:

Epoxidation

Hafnium(IV)

Zirconium(IV)

Hydrogen peroxide

Polyoxometalates

ABSTRACT

The homogeneous epoxidation of *cis*-cyclooctene with H₂O₂, catalyzed by various Zr/Hf-containing Keggin sandwich polyoxometalates (POMs), i.e., the 1:2 complexes [M(α-PW₁₁O₃₉)₂]¹⁰⁻ (M = Zr, **1** and M = Hf, **2**), the 4:2 complexes [M(H₂O)₂{M(H₂O)₂}₂(μ-OH)₃(μ-OH)₂](α-1,2-PW₁₀O₃₇)₂]⁷⁻ (M = Zr, **3** and M = Hf, **4**), the 2:2 complexes [M(μ-OH)(H₂O)₂(α-PW₁₁O₃₉)₂]⁸⁻ (M = Zr, **5** and M = Hf, **6**), and the 3:2 complex [Zr₃(μ₂-OH)₃(A-α-PW₉O₃₄)₂]⁹⁻ (**7**), was examined. At least two different reaction types exist: (1) one brought about by the highly catalytically active Venturello complex [PO₄{WO(O₂)₂}₄]³⁻, which was generated by reactions of the Zr/Hf-containing POMs with hydrogen peroxide, and (2) the reaction with active species formed on Zr/Hf clusters in the POMs. In the first type, the original sandwich structures are not maintained during the reactions (as shown in **1**, **2**, **3**, and **4**), but in the second type, the sandwich structures are maintained (as seen in **5** and **6**). **7** was inactive. The reaction, (**5** + *cis*-cyclooctene) + H₂O₂, was explicitly influenced by changing the reaction time of **5** and olefin, before addition of H₂O₂, indicating a significant interaction between **5** and olefin, such as coordination of olefin to the POM. Thus, for homogeneous olefin epoxidation by hydrogen peroxide catalyzed by di-Zr/Hf clusters, a new mechanism is proposed through olefin-coordinated species to di-Zr/Hf centers.

© 2014 Elsevier B.V. All rights reserved.

1. Introduction

In academic and industrial fields, the selective catalytic epoxidation of alkenes with an environmentally friendly oxidant, aqueous hydrogen peroxide, is an interesting objective [1–5]. Transition-metal-substituted polyoxometalates (POMs) have attracted considerable attention as oxidation catalysts because they are resistant to oxidative degradation. Furthermore, the “active sites” of their transition metals and countercations can undergo extensive synthetic modifications. The most commonly studied types of reaction are H₂O₂-based epoxidation and sulfoxidation catalyzed by metal-substituted POMs [6–18].

Several H₂O₂-based oxidation reactions catalyzed by titanium(IV)-substituted POMs have been extensively investigated [19], e.g., the monomeric Keggin monotitanium(IV)-substituted

POM [α-PW₁₁TiO₄₀]⁵⁻ [20–23] and its conjugated acid [α-P(TiOH)W₁₁O₃₉]⁴⁻ [21,23]; the dimeric Keggin monotitanium(IV)-substituted POM [(α-PTiW₁₁O₃₉)₂O]⁸⁻ [23], and the monomeric Keggin 1,5-dititanium(IV)-substituted POM [α-1,5-PW₁₀Ti₂O₄₀]⁷⁻ [22,24,25].

With regard to the catalytic activities of the dimeric mono-, di-, and tri-titanium(IV)-substituted α-Keggin polyoxotungstates [(α-PTiW₁₁O₃₉)₂O]⁸⁻ (**Ti1**), [(α-1,2-PW₁₀Ti₂O₃₈)₂O]¹⁰⁻ (**Ti2**), and [(α-1,2,3-PTi₃W₉O₃₇)₂O₃]¹²⁻ (**Ti3**) in alkene epoxidation with H₂O₂, it has been reported that the structure around the titanium centers has a strong influence on the catalytic activities [26]. The formation of catalytically active peroxo- and hydroperoxo-titanium(IV) species has been confirmed [26–29]. Previous studies of H₂O₂-based oxidation catalyzed by Ti-substituted POMs have also indicated that the protons in countercations and/or reaction solutions are crucial for the catalytic activities and the formation of active hydroperoxo-titanium and/or protonated peroxo species [23,26,30–35]. In alkene epoxidation with H₂O₂ catalyzed by Ti-substituted POMs, homolytic O–O cleavage of the Ti-hydroperoxo species, followed by oxygen transfer to the alkene [radical mechanism], has been proposed

* Corresponding author at: Department of Chemistry, Faculty of Science, Kanagawa University, Hiratsuka, Kanagawa 259-1293, Japan. Tel.: +81 463 59 4111; fax: +81 463 58 9684.

E-mail address: nomiya@kanagawa-u.ac.jp (K. Nomiya).

[33]. For example, it is generally accepted that in oxidation catalyzed by dititanium-containing 19-tungstodiarsonate(III), $[\text{Ti}_2(\text{OH})_2\text{As}_2\text{W}_{19}\text{O}_{67}(\text{H}_2\text{O})]^{8-}$, the Ti-hydroperoxy groups are the active oxygen-donating intermediates for alkene epoxidation [32].

In contrast, only a few examples of H_2O_2 -based oxidation catalyzed by Zr-containing POMs have been reported, by Kholdeeva's group, e.g., oxidation catalyzed by 2:2 complexes of Zr in dimeric Keggin POMs such as $(\text{Bu}_4\text{N})_7\text{H}[\{\text{PW}_{11}\text{O}_{39}\text{Zr}(\mu\text{-OH})\}_2]$, $(\text{Bu}_4\text{N})_8[\{\text{PW}_{11}\text{O}_{39}\text{Zr}(\mu\text{-OH})\}_2]$, and $(\text{Bu}_4\text{N})_9[\{\text{PW}_{11}\text{O}_{39}\text{Zr}(\mu\text{-OH})(\mu\text{-O})\}_2]$ [36]. Kholdeeva's group proposed that the active species for cyclohexene oxidation was an unstable Zr-peroxy species (^{31}P NMR at δ -12.3 ppm) generated by ligand exchange of the coordinating water ligands of the monomeric POM, $(\text{Bu}_4\text{N})_{3+n}[\text{PW}_{11}\text{O}_{39}\text{Zr}(\text{OH})_n(\text{H}_2\text{O})_{3(2)-n}]$ ($n=0$ and 1), with the peroxy (H_2O_2) ligand. They also suggested that the acid proton is crucial for catalysis by Zr-containing POMs. With respect to catalysis by Zr-containing POMs, Kortz's group reported the stoichiometric oxidation of L-methionine by the side-on peroxy species (i.e., $\mu\text{-}\eta^2\text{-peroxy}$ -containing Zr_2 species) of the dimeric Keggin POM $\text{K}_{12}[\text{Zr}_2(\text{O}_2)_2(\alpha\text{-SiW}_{11}\text{O}_{39})_2] \cdot 25\text{H}_2\text{O}$ [37].

In this work, we focused on epoxidation of *cis*-cyclooctene with aqueous hydrogen peroxide catalyzed by various structurally characterized Zr/Hf-containing Keggin sandwich POMs, i.e., $[\text{M}(\alpha\text{-PW}_{11}\text{O}_{39})_2]^{10-}$ ($\text{M}=\text{Zr}$, **1** and $\text{M}=\text{Hf}$, **2**), $[\{\text{M}(\text{H}_2\text{O})_2\}_2\{\text{M}(\text{H}_2\text{O})_2\}_2(\mu\text{-OH})_3(\mu\text{-OH})_2](\alpha\text{-1,2-PW}_{10}\text{O}_{37})_2]^{7-}$ ($\text{M}=\text{Zr}$, **3** and $\text{M}=\text{Hf}$, **4**), $[\{\text{M}(\mu\text{-OH})(\text{H}_2\text{O})\}_2(\alpha\text{-PW}_{11}\text{O}_{39})_2]^{8-}$ ($\text{M}=\text{Zr}$, **5** and $\text{M}=\text{Hf}$, **6**), and $[\text{Zr}_3(\mu_2\text{-OH})_3(\text{A-}\alpha\text{-PW}_9\text{O}_{34})_2]^{9-}$ (**7**). In the reactions with **5** and **6**, the original sandwich structures were kept after the reactions and the active species were formed on the Zr/Hf centers, whereas in the reactions with **1–4**, the reaction was brought about by the highly active Venturello complex [38–46], which was generated during the reaction. No catalytic activity was observed for **7** and the side-on peroxy species with heteroatom P $[\{\text{Zr}(\mu\text{-}\eta^2\text{-O}_2)\}_2(\alpha\text{-PW}_{11}\text{O}_{39})_2]^{10-}$ (**8**), the latter of which was synthesized from a reaction between **5** and aqueous H_2O_2 [see Supporting Information].

In this paper, we report full details of homogeneous *cis*-cyclooctene epoxidation with hydrogen peroxide catalyzed by Zr/Hf-containing Keggin sandwich POMs (**1–8**), and propose that a significant interaction between olefin and POMs (**5** and **6**), i.e., an olefin coordination process is present before attack of hydrogen peroxide.

2. Experimental

2.1. Materials

The following reactants were used as received: 30% aqueous H_2O_2 (Wako), Bu_4NCl (TCI), and CD_3CN and D_2O (Isotec). $\text{H}_3[\text{PW}_{12}\text{O}_{40}] \cdot 3\text{H}_2\text{O}$ was prepared by a traditional method and identified using FTIR spectroscopy, thermogravimetry (TG) and differential thermal analysis (DTA), and ^{31}P NMR spectroscopy.

Venturello complex $(\text{Bu}_4\text{N})_3[\text{PO}_4\{\text{WO}(\text{O}_2)_2\}_4]$ was synthesized using a modified version of the reported method [38] and characterized by elemental analysis, ^{31}P and ^{183}W NMR spectroscopy (see Supporting Information). $(\text{Et}_2\text{NH}_2)_8[\{\alpha\text{-PW}_{11}\text{O}_{39}\text{Zr}(\mu\text{-OH})(\text{H}_2\text{O})_2\}_2] \cdot 6\text{H}_2\text{O}$ (**EtN-5**) and the lithium salt (**Li-5**) were prepared using a modified version of the reported method [47], and identified by CHN analysis, FTIR spectroscopy, TG/DTA, and ^{31}P NMR spectroscopy. The side-on peroxy dinuclear Zr complex $(\text{Et}_2\text{NH}_2)_{10}[\{\text{Zr}(\mu\text{-}\eta^2\text{-O}_2)\}_2(\alpha\text{-PW}_{11}\text{O}_{39})_2] \cdot 11\text{H}_2\text{O}$ (**EtN-8**) was synthesized by a reaction of **EtN-5** with 30% aqueous H_2O_2 using a modified version of the reported method [37], and characterized by elemental analysis, TG/DTA, FTIR, ^{31}P NMR and x-ray crystallography (also see Supporting Information). Other precatalysts were prepared according to the reported methods or modified versions of these [47–52], and identified by elemental analysis, FTIR spectroscopy, TG/DTA, and ^{31}P NMR spectroscopy. The precatalysts and their abbreviations are shown in Table 1. The abbreviation consists of a combination of the counteranion and polyoxoanion (**EtN-** and **BuN-** represent Et_2NH_2 and Bu_4N counteranions, respectively). The polyoxoanion moieties are denoted as complexes, by a combination of the number of metal centers and the two lacunary POMs, i.e., 1:2 complexes of one metal center (Zr/Hf) and two monolacunary POMs (**EtN-1** and **EtN-2**) [49], 4:2 complexes of four metal centers (Zr/Hf) and two dilacunary POMs (**BuN-3** and **BuN-4**) [51,52], 3:2 complexes of three Zr centers and two trilacunary POMs (**BuN-7**) [50], and several types of 2:2 complexes such as (i) 2:2 complexes consisting of two hydrated metal centers (Zr/Hf) and two monolacunary POMs with a P heteroatom (**BuN-5**, **BuN-6**, and **Li-5**) [47], and (ii) 2:2 complexes consisting of a Zr_2 center with two side-on peroxy groups and two monolacunary POMs with a P heteroatom (**EtN-8**). Instrumentation/analytical procedures are described in Supporting Information.

2.2. Catalytic reactions

Homogeneous reactions of *cis*-cyclooctene, catalyzed by several POMs as Et_2NH_2 , Bu_4N , or Li salts (Table 1), were carried out in round-bottomed flasks. *cis*-Cyclooctene (1.0 mL, 7.70 mmol), 30% aqueous H_2O_2 (1.0 mL, 12.72 mmol), and a POM (0.01–0.02 mmol) in a mixed solvent (30 mL) consisting of CH_3CN and CH_2Cl_2 (15/15 v/v), a mixed solvent (31 mL) consisting of CH_3CN and water (30/1 v/v), or a mixed solvent (33 mL) consisting of CH_3CN and water (30/3 v/v) were mixed at 25 °C under air. The reaction solution was sampled after 0.0, 0.5, 0.75, 1.0, 1.5, 2.0, 2.25, 2.5, 3.0, 4.0, 5.0, 6.0, and 24 h and analyzed using Shimadzu GC-17AAT and Shimadzu GC-2010 Plus gas chromatographs (TCD) and a DB-FFAP capillary column (0.53 mm \times 15 m). The catalytic activities of POMs **1–8**, evaluated as turnover numbers (TON) and/or turnover frequencies per second (TOF), were compared with those of the Venturello complex and several previously reported Ti-containing Keggin POMs.

Table 1
Compositions, formulas, and abbreviations of precatalysts.

M: lacunary POM ratio	Formula	Abbreviation	Ref.
1:2 complex	$(\text{Et}_2\text{NH}_2)_{10}[\text{Zr}(\alpha\text{-PW}_{11}\text{O}_{39})_2] \cdot 7\text{H}_2\text{O}$	EtN-1	[49]
	$(\text{Et}_2\text{NH}_2)_{10}[\text{Hf}(\alpha\text{-PW}_{11}\text{O}_{39})_2] \cdot 8\text{H}_2\text{O}$	EtN-2	[49]
4:2 complex	$(\text{Bu}_4\text{N})_7[\{\{\text{Zr}(\text{H}_2\text{O})\}_2\{\text{Zr}(\text{H}_2\text{O})_2\}_2(\mu\text{-OH})_3(\mu_3\text{-OH})_2\}(\alpha\text{-1,2-PW}_{10}\text{O}_{37})_2] \cdot 3\text{H}_2\text{O}$	BuN-3	[51,52]
	$(\text{Bu}_4\text{N})_7[\{\{\text{Hf}(\text{H}_2\text{O})\}_2\{\text{Hf}(\text{H}_2\text{O})_2\}_2(\mu\text{-OH})_3(\mu_3\text{-OH})_2\}(\alpha\text{-1,2-PW}_{10}\text{O}_{37})_2] \cdot 2\text{H}_2\text{O}$	BuN-4	[51,52]
2:2 complex	$(\text{Bu}_4\text{N})_7\text{H}[\{\text{Zr}(\mu\text{-OH})(\text{H}_2\text{O})\}_2(\alpha\text{-PW}_{11}\text{O}_{39})_2] \cdot 3\text{H}_2\text{O}$	BuN-5	[47]
	$(\text{Bu}_4\text{N})_7\text{H}[\{\text{Hf}(\mu\text{-OH})(\text{H}_2\text{O})\}_2(\alpha\text{-PW}_{11}\text{O}_{39})_2] \cdot 3\text{H}_2\text{O}$	BuN-6	[47]
	$\text{Li}_8[\{\text{Zr}(\mu\text{-OH})(\text{H}_2\text{O})\}_2(\alpha\text{-PW}_{11}\text{O}_{39})_2] \cdot 20\text{H}_2\text{O}$	Li-5	[47]
	$(\text{Et}_2\text{NH}_2)_8[\{\text{Zr}(\mu\text{-OH})(\text{H}_2\text{O})\}_2(\alpha\text{-PW}_{11}\text{O}_{39})_2] \cdot 6\text{H}_2\text{O}$	EtN-5	[47]
	$(\text{Et}_2\text{NH}_2)_{10}[\{\text{Zr}(\mu\text{-}\eta^2\text{-O}_2)\}_2(\alpha\text{-PW}_{11}\text{O}_{39})_2] \cdot 11\text{H}_2\text{O}$	EtN-8	This work
3:2 complex	$(\text{Bu}_4\text{N})_{6.5}\text{H}_2.5[\text{Zr}_3(\mu\text{-OH})_3(\text{A-}\alpha\text{-PW}_9\text{O}_{34})_2]$	BuN-7	[50]

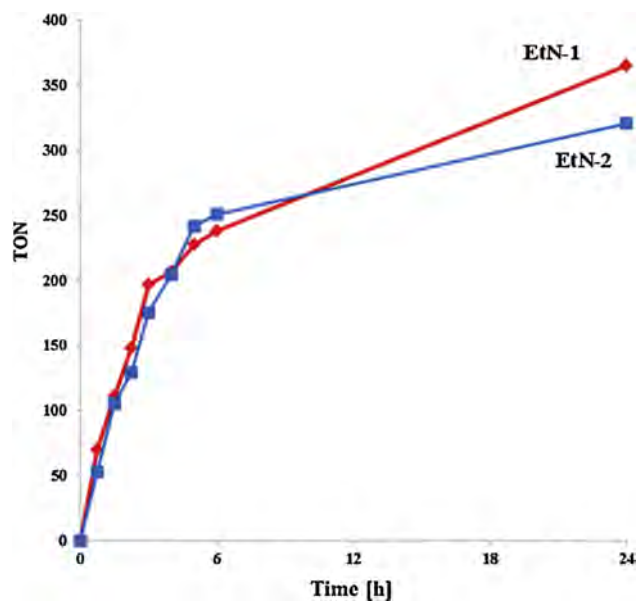


Fig. 1. TON-time curve of *cis*-cyclooctene epoxidation with 30% aqueous H_2O_2 catalyzed by POMs (**EtN-1** and **EtN-2**). Reaction conditions: catalysts 0.02 mmol, substrate 7.70 mmol, 30% H_2O_2 aq. 12.72 mmol, under air at 25 °C.

3. Results and discussion

3.1. Zr/Hf-containing POMs as precatalysts for *cis*-cyclooctene epoxidation by H_2O_2 : Catalysis by 1–4 and Venturello complex

Homogeneous epoxidation of *cis*-cyclooctene with hydrogen peroxide catalyzed by various Zr/Hf-containing POMs was examined under the conditions of POM (0.02 mmol), *cis*-cyclooctene (7.70 mmol) and 30% aqueous H_2O_2 (12.72 mmol) in a mixed solvent (30 mL) consisting of $\text{CH}_3\text{CN}:\text{CH}_2\text{Cl}_2$ (15/15 v/v), at 25 °C in air. The POMs used were 1:2 complexes (**EtN-1** and **EtN-2**), 4:2 complexes (**BuN-3** and **BuN-4**), and the freshly prepared Venturello complex, $(\text{Bu}_4\text{N})_3[\text{PO}_4\{\text{WO}(\text{O}_2)_2\}_4]$. The time course versus TON plots of epoxide formation are shown in Figs. 1 and 2.

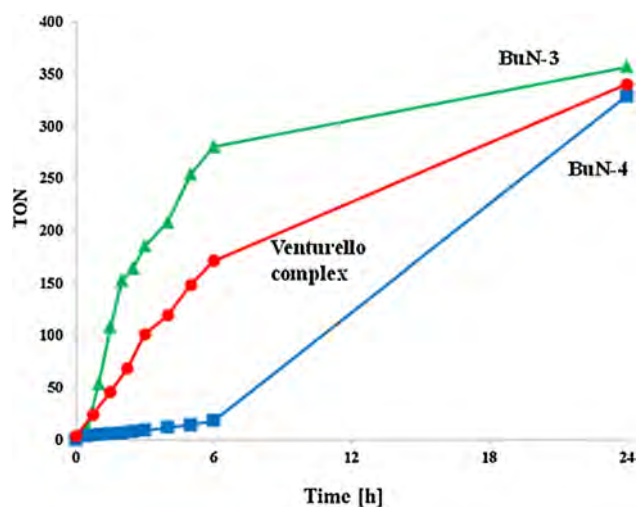


Fig. 2. TON-time curve of *cis*-cyclooctene epoxidation with 30% aqueous H_2O_2 catalyzed by POMs (freshly prepared Venturello complex, **BuN-3**, and **BuN-4**). Reaction conditions: catalysts 0.02 mmol, substrate 7.70 mmol, 30% H_2O_2 aq. 12.72 mmol, under air at 25 °C.

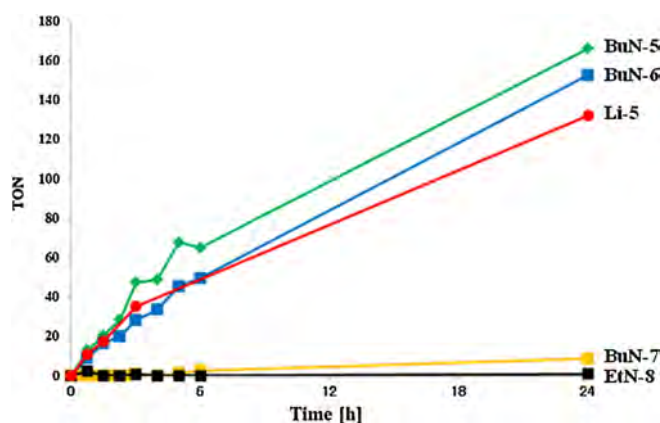


Fig. 3. TON-time curve of *cis*-cyclooctene epoxidation with 30% aqueous H_2O_2 catalyzed by POMs (**Li-5**, **BuN-5**, **BuN-6**, **BuN-7**, and **EtN-8**). Reaction conditions: catalysts 0.02 mmol, substrate 7.70 mmol, 30% H_2O_2 aq. 12.72 mmol, under air at 25 °C.

The conversions of *cis*-cyclooctene after 24 h-reactions were more than 83–95% for both **EtN-1** and **EtN-2**, and more than 77–95% for both **BuN-3** and **BuN-4**. **BuN-4** shows a rapid increase in activity after an induction period of more than 6 h and the final TON was almost the same as that of **BuN-3** after 24 h-reaction. The TONs after 24 h-reactions for **EtN-1** and **EtN-2** (Fig. 1) and those for **BuN-3** and **BuN-4** (Fig. 2) reached more than 300.

The reactions by **EtN-1**, **EtN-2**, **BuN-3** and **BuN-4** (Figs. 1 and 2) are quite different from those by **BuN-5** and **BuN-6** (Fig. 3). In the solutions of the 24 h-reactions of **EtN-1** and **EtN-2** (6.35 and 6.27 μmol , respectively) and H_2O_2 (0.636 mmol), formation of the Venturello complex was confirmed by ^{31}P NMR as signals at 3.57 ppm (from **EtN-1**) and 3.54 ppm (from **EtN-2**). In fact, the highly active reaction by the Venturello complex has been well known [38–46]. In Figs. 1 and 2, it should be noted that the TONs after 6 h-reactions for **EtN-1**, **EtN-2**, and **BuN-3** were about two times of the TON after 6 h-reaction for the separately prepared, fresh Venturello complex, indicating that the POMs (**EtN-1**, **EtN-2**, and **BuN-3**) generate 2 mol of the Venturello complex during the reactions.

Thus, the catalysis by **EtN-1**, **EtN-2**, **BuN-3**, and **BuN-4** was actually due to the Venturello complex, which was derived by direct reaction with hydrogen peroxide.

3.2. Homogeneous epoxidation of *cis*-cyclooctene with hydrogen peroxide catalyzed by POMs 5–8

The 2:2 complexes **BuN-5** and **BuN-6**, and the 3:2 complex **BuN-7** (POMs 0.02 mmol) were used in a mixed solvent (30 mL) consisting of $\text{CH}_3\text{CN}:\text{CH}_2\text{Cl}_2$ (15/15 v/v) as homogeneous catalysts for epoxidation of *cis*-cyclooctene. The 2:2 complex of Zr as a Li salt (**Li-5**, 0.01 mmol) and the separately prepared, side-on peroxo-Zr₂ species **EtN-8** (0.02 mmol), both of which were water soluble, but insoluble in organic solvents, were also used as homogeneous catalysts in a mixed solvent (31 mL) consisting of $\text{CH}_3\text{CN}/\text{water}$ (30/1 v/v). The TON-time course curves are shown in Fig. 3.

In the reactions by **5** and **6** in the presence of 30% aqueous H_2O_2 , a color change was not observed, i.e., the original colorless, clear, homogeneous solution was maintained during the course of the reaction. This is in contrast to the oxidation reactions with 30% aqueous H_2O_2 catalyzed by mono-, di-, and tri-titanium(IV)-substituted Keggin POMs (**Ti1**, **Ti2**, and **Ti3** as Bu_4N salts), in which the colors of all the POMs changed from colorless to yellow or orange as a result of formation of peroxotitanium(IV)

Table 2Epoxidation of olefins (*cis*-cyclooctene, cyclohexene, 1-octene, and styrene) with 30% aqueous H₂O₂ catalyzed by **BuN-5** and **Li-5**.

Precatalyst	Substrate	Epoxide	TON ^c	Selectivity (%) ^c	Other products
BuN-5^a	<i>cis</i> -cyclooctene	cyclooctene oxide	166	99	–
	cyclohexene	<i>trans</i> -cyclohexane-1,2-diol	101	37	2-hydroxycyclohexanone
	1-octene	1,2-epoxyoctane	23	–	heptanal
	styrene	styrene oxide	7	–	benzaldehyde
Li-5^b	<i>cis</i> -cyclooctene	cyclooctene oxide	132	99	–
	cyclohexene	<i>trans</i> -cyclohexane-1,2-diol	38	62	2-hydroxycyclohexanone
	1-octene	1,2-epoxyoctane	23	–	heptanal

^a Solvent 15:15 (v/v) CH₂Cl₂/CH₃CN, 30 mL.^b Solvent 30:1 (v/v) CH₃CN/H₂O, 31 mL.^c After 24 h.Reaction conditions: catalyst 0.02 mmol, substrate *cis*-cyclooctene 7.70 mmol, cyclohexene 9.86 mmol, 1-octene 6.37 mmol, or styrene 8.70 mmol, 30% H₂O₂ aq. 12.72 mmol, under air, at 25 °C.**Table 3**Epoxidation of mixed olefins (*cis*-cyclooctene and cyclohexene) with 30% aqueous H₂O₂ catalyzed by **BuN-5** and **Li-5**.

Precatalysts	Mixed substrate (mmol)	Total conversion (%) ^c	Products (mmol) ^c	TON ^c	Selectivity (%) ^c
BuN-5^a	<i>cis</i> -cyclooctene (1.54)	92	cyclooctene oxide (1.4)	71	99
	cyclohexene (4.62)	68	<i>trans</i> -cyclohexane-1,2-diol (1.2)	58	37
	<i>cis</i> -cyclooctene (4.62)	61	cyclooctene oxide (2.8)	138	97
	cyclohexene (1.54)	58	<i>trans</i> -cyclohexane-1,2-diol (0.2)	11	25
Li-5^b	<i>cis</i> -cyclooctene (1.54)	53	cyclooctene oxide (0.8)	41	99
	cyclohexene (4.62)	23	<i>trans</i> -cyclohexane-1,2-diol (0.5)	31	58
	<i>cis</i> -cyclooctene (4.62)	51	cyclooctene oxide (2.4)	118	99
	cyclohexene (1.54)	23	<i>trans</i> -cyclohexane-1,2-diol (0.2)	9	51

Reaction conditions: catalyst 0.02 mmol, mixed substrate *cis*-cyclooctene and cyclohexene, 30% H₂O₂ aq. 12.72 mmol, under air, at 25 °C.^a Solvent 15:15 (v/v) CH₂Cl₂/CH₃CN, 30 mL.^b Solvent 30:1 (v/v) CH₃CN/H₂O, 31 mL.^c After 24 h.

and/or hydroperoxotitanium(IV) intermediates [26,27]. The catalytic activities of **BuN-5** and **BuN-6** at 25 °C were monitored by GC during 24 h-reactions. Cyclooctene oxide was the major product (selectivity >99%), and no induction period was observed for these reactions. The ratio of the activity with **BuN-5** to that of the Venturello complex was about 38% after 6 h and 49% after 24 h. Also, the ratio of the activity with **BuN-6** to that of the Venturello complex was about 29% after 6 h and 45% after 24 h.

In comparing **Li-5** and **BuN-5** as precatalysts for cyclooctene epoxidation, it should be noted that the catalytic activity was **BuN-5** > **Li-5** (see Tables 2 and 3, Section 3.5. (4)), whereas the catalytic stability was **Li-5** > **BuN-5**. Powder samples of **BuN-5** and **BuN-6**, recovered after 24 h-reactions by evaporating the reaction solutions and reprecipitating with excess diethyl ether, were characterized using FTIR and ³¹P NMR spectroscopies. The original sandwich structures were maintained during and after the reactions. However, the recovered sample of the Bu₄N salt was contaminated with saturated Keggin POM species [PW₁₂O₄₀]³⁻ as minor species, which was confirmed by ³¹P NMR signal at -14.40 ppm in CD₃CN, whereas that of the Li salt was not. Repeated reuse of the Bu₄N salt resulted in increased amounts of the saturated Keggin [PW₁₂O₄₀]³⁻ species. Thus, with regard to catalyst stability, it appears that the Li salt is superior to the Bu₄N salt.

BuN-7 was inactive for epoxidation of *cis*-cyclooctene. The side-on coordinated peroxo-Zr₂ species (**EtN-8**) did not show any activity (Fig. 3); the TON after 24 h was 0.8 without addition of trifluoromethanesulfonic acid (TFSA) and 17.3/19.0 with addition of TFSA 1:2/1:4, respectively. Kortz et al. reported that the side-on peroxo species of a dimeric Zr complex with Si heteroatom was active in the stoichiometric oxidation of L-methionine, but the reaction was not catalytic [37]. In the POM with P heteroatom, the side-on peroxo species (**EtN-8**) is probably formed during the course of reaction from the active, end-on hydroperoxo species Zr-OOH, which will be formed at the early stage of the reaction of POM **5** with aqueous H₂O₂ (Fig. S3).

3.3. Homogeneous epoxidation of olefins with hydrogen peroxide catalyzed by **BuN-5** and **Li-5**: selection of *cis*-cyclooctene as a test substrate

The epoxidations of olefins (*cis*-cyclooctene, cyclohexene, 1-octene, and styrene) with 30% aqueous H₂O₂ catalyzed by **BuN-5** and **Li-5** were examined at 25 °C under air in a mixed solvent (30 mL) consisting of CH₃CN and CH₂Cl₂ (15/15 v/v) and a mixed solvent (31 mL) consisting of CH₃CN and water (30/1 v/v), respectively.

Cyclohexene has been known as a useful test substrate that allows one to distinguish between homolytic and heterolytic oxidation mechanism [35]. It has been said that formation of allylic oxidation products, 2-cyclohexene-1-ol, 2-cyclohexene-1-one, cyclohexene oxide is an indication of a homolytic oxidation by hydrogen peroxide (radical mechanism), whereas the selective formation of *trans*-cyclohexane-1,2-diol (major product) and cyclohexene oxide (minor product) suggests a heterolytic mechanism (ionic mechanism) [35]; distribution of products containing cyclohexene oxide depends on the reaction mechanism. Our results of cyclohexene oxidation suggest the ionic mechanism, i.e., heterolytic mechanism (Table 2), in which 2-hydroxycyclohexanone as other products is derived by further oxidation of *trans*-cyclohexane-1,2-diol.

In this work, we selected *cis*-cyclooctene as a test substrate for further studying the reaction in detail rather than cyclohexene, because *cis*-cyclooctene gave the best results in the viewpoints of the sole product of oxidation, i.e., highest selectivity for the epoxide, and the highest TON of the epoxide (Table 2).

3.4. Results from changing reaction times between **Li-5** and *cis*-cyclooctene before addition of H₂O₂ and between **Li-5** and H₂O₂ before addition of *cis*-cyclooctene (Control experiments #1)

Control experiments (Fig. 4) consisting of the reactions (I) (**Li-5** + *cis*-cyclooctene) + H₂O₂ (Entries 1–3) and (II)

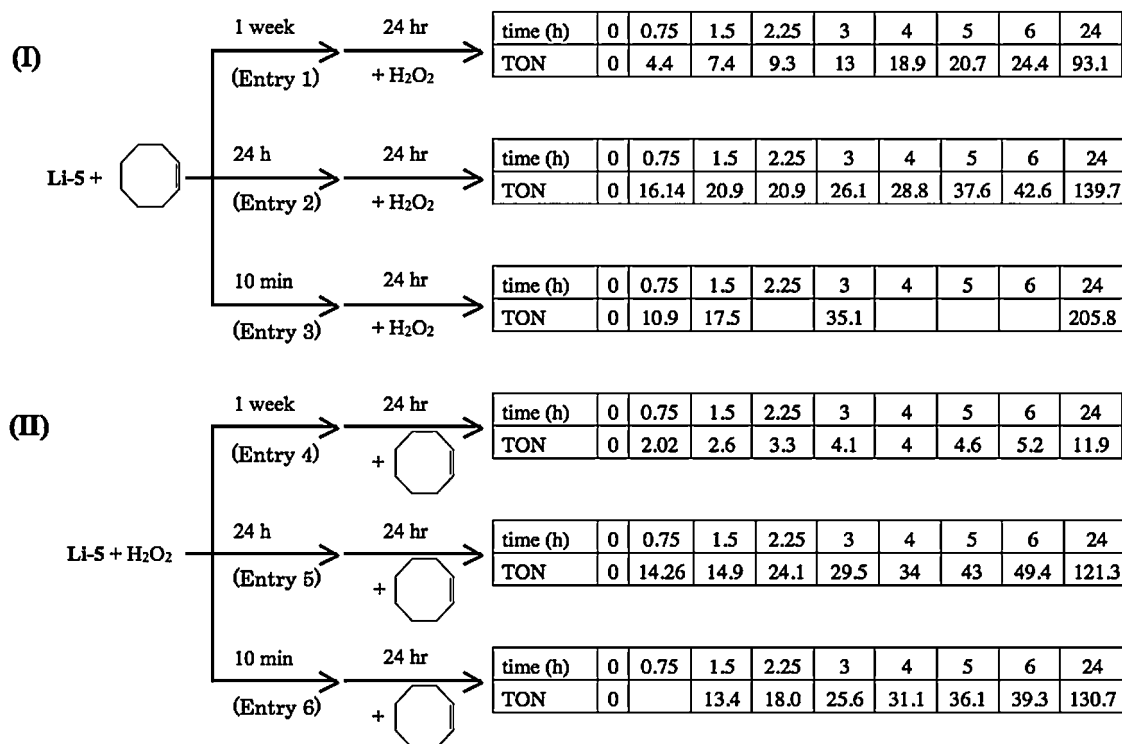


Fig. 4. Results of control experiments consisting of two types of reaction: (I) (Li-5 + olefin) + H₂O₂ and (II) (Li-5 + H₂O₂) + olefin, which were examined by changing the addition times of the second additive (olefin or H₂O₂) to Li-5. Reaction conditions for (I) and (II): catalysts 0.02 mmol, substrate 7.70 mmol, 30% H₂O₂ aq. 12.72 mmol, under air at 25 °C. Reaction product in (I) and (II): cyclooctene oxide.

(Li-5 + H₂O₂) + *cis*-cyclooctene (Entries 4–6) were carefully carried out by changing the reaction times of the second additive (*cis*-cyclooctene in (I) or H₂O₂ in (II)) to Li-5. GC analysis was performed during 24 h-reactions after addition of H₂O₂ in (I) or *cis*-cyclooctene in (II). In the reaction (I), the highest activity (TON 205.8) was observed for Entry 3, in which hydrogen peroxide was added on 10 min after Li-5 and *cis*-cyclooctene were mixed, and the final solution was analyzed after 24 h-reaction. As the reaction time of Li-5 and *cis*-cyclooctene increased, the activity decreased (Entries 1 and 2). This indicates that there is a significant interaction between the POM and *cis*-cyclooctene before addition of H₂O₂. An olefin coordination as such an interaction is proposed. Based on theoretical and experimental studies containing x-ray crystallography, several Zr^{IV} ion (d⁰)–olefin bonding complexes have been reported in the literature [53–57]. The longest reaction time (one week) between Li-5 and *cis*-cyclooctene resulted in the lowest activity (Entry 1). The reason may be attributable to polymerization such as ring-opening metathesis of *cis*-cyclooctene coordinated to Li-5 [58]. The coordinated olefin can undergo the nucleophilic attack of free and/or coordinated hydrogen peroxide. Thus, the reaction (I) is due to the ionic oxidation mechanism by hydrogen peroxide rather than the radical oxidation mechanism.

In contrast, the similar control experiments were also carried out using a dimeric trititanium(IV)-substituted Keggin POM (Ti3) that has been known as epoxidation catalysis via radical mechanism [26]. The reaction times between Ti3 and *cis*-cyclooctene were changed (1 h and one week), followed by adding H₂O₂, and analysing the products after 24 h-reactions. The TONs of epoxide produced during different reaction times (1 h and one week) were almost unchanged (~150). These results are quite different from the results using Li-5.

On the other hand, in (II), the reaction times between Li-5 and H₂O₂ were changed. TONs (130.7 and 121.3) of epoxide produced

on 24 h-reactions after addition of *cis*-cyclooctene (Entries 5 and 6, respectively) were much higher than that (TON 11.9) of Entry 4. TONs by changing reaction times of catalyst + H₂O₂, i.e., 24 h and 10 min indicate that decomposition of H₂O₂ does not occur. Entry 4 also shows that the lowest activity results from the formation of side-on peroxo species (POM 8) during the prolonged mixing time (see Fig. S3). Entries 5 and 6 are probably due to the active, end-on coordinated hydroperoxo species, which are alive at the early stage.

Since the activities in (I) are higher than those in (II), in the case of that Li-5, olefin and H₂O₂ are simultaneously co-existent, the process based on (I), i.e., olefin coordination and subsequent nucleophilic attack of free and/or coordinated hydrogen peroxide, will be proposed as plausible reaction scheme (Fig. 5).

3.5. Catalytic epoxidation of mixed substrates by Li-5 and BuN-5 (Control experiments #2)

Epoxidations of mixed substrates (*cis*-cyclooctene and cyclohexene in molar ratios of 1:3 and 3:1) with aqueous H₂O₂ catalyzed by BuN-5 and Li-5 were examined for 24 h. The results are shown in Table 3.

- (1) In cyclohexene oxidation, the products were cyclohexene epoxide as the minor product and *trans*-cyclohexane-1,2-diol as the major product. *trans*-Cyclohexane-1,2-diol was derived from cyclohexene epoxide in an acidic environment, based on dissociation of the coordinated water molecules in the Zr centers. The selectivity for cyclohexene epoxide is therefore actually the same as that for *trans*-cyclohexane-1,2-diol. The selectivity

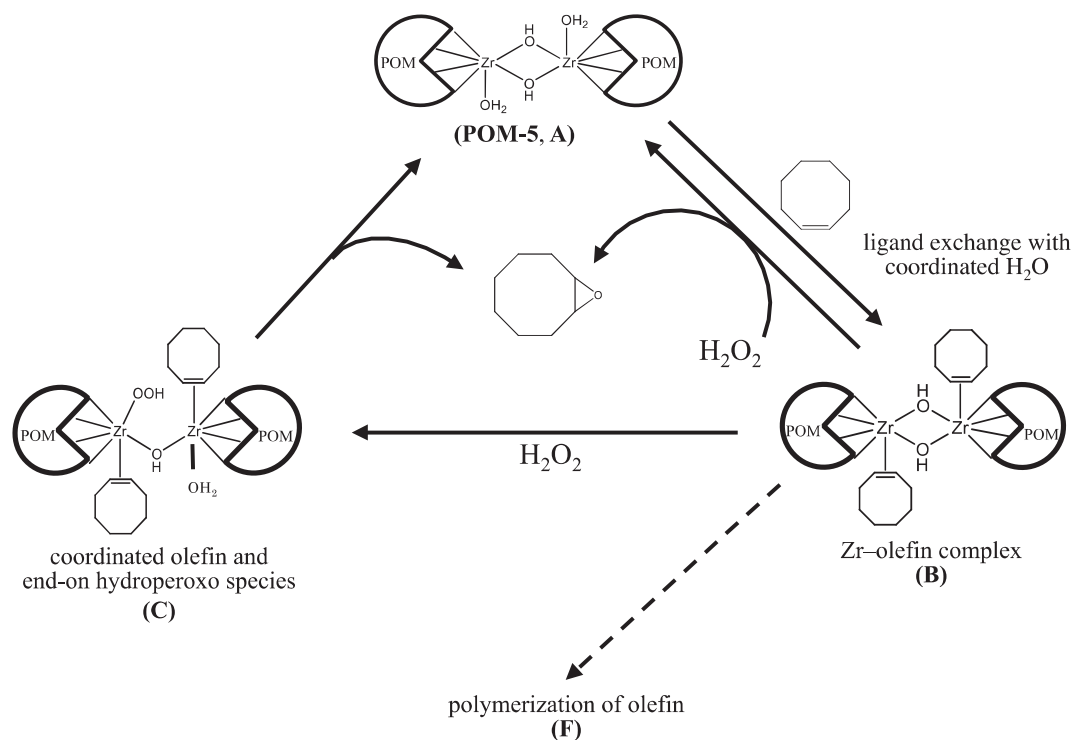


Fig. 5. Proposed reaction scheme.

after 24 h-reaction for *trans*-cyclohexane-1,2-diol was evaluated as

$$\frac{[\textit{trans} - \text{cyclohexane} - 1, 2 - \text{diol}]/([\text{cyclohexene}]_{t=0} - [\text{cyclohexene}]_{t=24})}{[\text{cyclohexene}]_{t=24}}$$

- Despite the different starting molar ratios of the mixed substrates, *cis*-cyclooctene was oxidized more than cyclohexene by either **BuN-5** or **Li-5**, showing strong substrate dependence of these precatalysts. This fact suggests that coordination ability of *cis*-cyclooctene to Zr centers is higher than that of cyclohexene. The coordination of cyclohexene and subsequent epoxidation will begin after the *cis*-cyclooctene has been almost consumed.
- The selectivity for *trans*-cyclohexane-1,2-diol in oxidation with **BuN-5** is lower than that with **Li-5**. The present reaction is significantly influenced by the solvent system. **BuN-5** in CH₃CN/CH₂Cl₂ (15/15 v/v, 30 mL) is much more active than **Li-5** in CH₃CN/H₂O (30/1 v/v, 31 mL). Thus, in catalysis by **BuN-5**, further oxidation products of *trans*-cyclohexane-1,2-diol such as 2-hydroxycyclohexanone can be also formed, resulting in lower selectivity.
- Difference between catalytic activities of **BuN-5** and **Li-5**: although the order of the catalyst stability is **Li-5** > **BuN-5**, that of the catalytic activity is **BuN-5** > **Li-5**. Both reactions proceed in homogeneous systems. The solubilities of **BuN-5** and **Li-5** are different in the constituent solvents: **Li-5** is soluble in H₂O, but insoluble in CH₃CN, whereas **BuN-5** is soluble in CH₃CN, but insoluble in CH₂Cl₂. The substrates are soluble in both CH₃CN and CH₂Cl₂. Since the present reaction is significantly influenced by the solvent systems, the different activities are attributable to the different reaction systems; the system consisting of **Li-5** in H₂O and CH₃CN becomes a

“homogeneous biphasic” system, whereas that consisting of **BuN-5** in CH₃CN and CH₂Cl₂ becomes a “homogeneous monophasic” system.

3.6. ³¹P NMR spectra of POM 5 in the presence of mixed or single substrate (*cis*-cyclooctene and/or cyclohexene) and aqueous H₂O₂

Solution ³¹P NMR spectra of **5** are strongly dependent on solvents and counteranions; **BuN-5** in CD₃CN shows a signal at −2.00 ppm, **EtN-5** in D₂O at −3.59 ppm, **Li-5** in D₂O at −3.53 ppm together with minor peaks at −4.47 and −4.58 ppm, and **Li-5** in CD₃CN at −2.07 ppm (Table S2). The ³¹P NMR spectrum of **Li-5** in CD₃CN in the presence of aqueous H₂O₂ showed a signal at −2.80 ppm as a broad peak after 1 h-mixing and at −2.57 ppm after 216 h-mixing. The latter signal was in good agreement with that of the separately prepared, side-on peroxy species **EtN-8** in CD₃CN (−2.55 ppm). Thus, the broad signal at −2.80 ppm is attributable to the end-on hydroperoxo species. The ³¹P NMR spectrum of **Li-5** in CD₃CN on 1 h after excess *cis*-cyclooctene or cyclohexene was added showed signals at −2.11 ppm or −2.14 ppm, respectively; the signals on 168 h after the addition were observed at −2.14 ppm for *cis*-cyclooctene and at −2.16 (main) and −2.60 ppm (minor) for cyclohexene. The signals at −2.11 ppm and −2.14 ppm are assignable to the olefin-coordinated species of *cis*-cyclooctene and cyclohexene, respectively. The ³¹P NMR signal at −2.08 ppm for **L-5** (2 mmol) in CD₃CN solution containing olefin mixtures of *cis*-cyclooctene (154 mmol) and cyclohexene (462 mmol) was the same as the signal for olefins mixed in a different ratio, i.e., *cis*-cyclooctene (462 mmol) and cyclohexene (154 mmol), even after 1 h and/or longer (Table S2). These facts are consistent with that the coordination ability of *cis*-cyclooctene is higher than that of cyclohexene. Thus, it is suggested that under the co-existence of *cis*-cyclooctene, neither cyclohexene coordinated species nor mixed coordinated species are formed. These results are also consistent

with those for epoxidation of mixed substrates with different molar ratios (see Section 3.5).

3.7. Comparison of present work with catalysis by Ti-containing POMs and Zr-containing POMs reported in the literature

- (1) The 2:2 complexes (**5** and **6**) and the 1:2 complexes $[M(PW_{11}O_{39})_2]^{10-}$ ($M = \text{Zr}$ **1** and Hf **2**) underwent mutual interconversion under appropriate pH conditions [47], suggesting that these complexes are not rigid, but flexible. However, they showed quite different catalytic behaviors in the epoxidation of *cis*-cyclooctene with H_2O_2 ; the 2:2 complexes formed active species on dinuclear Zr/Hf centers in sandwich structures, whereas the 1:2 complexes generated the highly active Venturello complex.
- (2) The active species formed by **5** and **6** are substantially different from those formed by Ti-substituted POMs. In the latter case, homolytic O–O cleavage of the Ti–hydroperoxy species, followed by oxygen transfer to the alkene, has been considered [33]. It is generally accepted that Ti–hydroperoxy groups are the active oxygen-donating intermediates for the epoxidation of alkenes, but the alkene-coordinating species have never been considered.
- (3) The active species formed by **5** and **6** are also different from that derived from the Zr₂-containing POMs reported by Kholdeeva's group [36], which has been proposed as an unstable Zr–peroxy species (³¹P NMR, $\delta -2.3$ ppm) formed by a ligand exchange of the monomeric species $(\text{Bu}_4\text{N})_{3+n}[\text{PW}_{11}\text{O}_{39}\text{Zr}(\text{OH})_n(\text{H}_2\text{O})_{3(2)-n}]$ ($n = 0$ and 1) with a peroxy (H_2O_2) ligand.

4. Conclusion

Two different types of *cis*-cyclooctene epoxidation with hydrogen peroxide were found in catalysis by Zr/Hf-based sandwich-structured POMs **1–8**. The reactions with **1–4**, which gave very high activities, were brought about by the Venturello complex $[\text{PO}_4\{\text{WO}(\text{O}_2)_2\}_4]^{3-}$ [38–46], which was generated by reactions with hydrogen peroxide, whereas the reactions with **5** and **6**, which gave moderate activities (about 45% those of **1–4**), proceeded via active species formed on dimeric Zr/Hf clusters in the sandwich structure. The 2:2 complex containing side-on peroxy species on the Zr₂ centers (**8**) and the 3:2 complex (**7**) showed almost no activities. Two control experiments (#1 and #2) suggest that the reactive species of **5** is formed as the dimeric species containing *cis*-cyclooctene coordinated to Zr atom. Thus, for homogeneous olefin epoxidation by hydrogen peroxide catalyzed by di-Zr/Hf clusters, a new mechanism is proposed through olefin-coordinated species to di-Zr/Hf centers. The epoxidation of olefin with H_2O_2 catalyzed by **5** probably proceeds via nucleophilic attack of free and/or coordinated hydrogen peroxide to the coordinated olefin (the ionic mechanism), which is contrasted to the catalysis by the Ti-substituted POMs via radical mechanism.

Acknowledgements

This work was supported by JSPS KAKENHI Grant number 22550065, and also by the Strategic Research Base Development Program for Private Universities of the Ministry of Education, Culture, Sports, Science, and Technology of Japan.

Appendix A. Supplementary data

Supplementary material related to this article can be found, in the online version, at <http://dx.doi.org/10.1016/j.molcata.2014.07.020>.

References

- [1] R.A. Sheldon, J.K. Kochi, *Metal-Catalyzed Oxidations of Organic Compounds*, Academic Press, New York, 1981 (Chapter 3).
- [2] G.W. Parshall, S.D. Ittel, *Homogeneous Catalysis: The Applications and Chemistry of Catalysis by Soluble Transition Metal Complexes*, 2nd ed, Wiley, New York, 1992, pp. 151.
- [3] K.S. Suslick, in: C.L. Hill (Ed.), *Activation and Functionalization of Alkenes*, Wiley, New York, 1989, p. 219.
- [4] K.A. Jorgensen, *Chem. Rev.* 89 (1989) 431–458.
- [5] B. Meanier, *Chem. Rev.* 92 (1992) 1411–1456.
- [6] N. Mizuno, K. Kamata, K. Yamaguchi, *Top. Catal.* 53 (2010) 876–893.
- [7] N. Mizuno, K. Yamaguchi, K. Kamata, *Coord. Chem. Rev.* 249 (2005) 1944–1956.
- [8] A.C. Estrada, I.C.M.S. Santos, M.M.Q. Simoes, M.G.P.M.S. Neves, J.A.S. Cavaleiro, A.M.V. Cavaleiro, *Appl. Catal. A* 392 (2011) 28–35.
- [9] N. Mizuno, K. Yamaguchi, K. Kamata, *Catal. Surv. Asia.* 15 (2011) 68–79.
- [10] N. Mizuno, K. Yamaguchi, *Chem. Rec.* 6 (1) (2006) 12–22.
- [11] N. Mizuno, S. Hikichi, K. Yamaguchi, S. Uchida, Y. Nakagawa, K. Uehara, K. Kamata, *Catal. Today* 117 (2006) 32–36.
- [12] C. Jahier, S.S. Mal, U. Kortz, S. Nlate, *Eur. J. Inorg. Chem.* (2010) 1559–1566.
- [13] M. Carraro, N. Nsouli, H. Oelrich, A. Sartorel, A. Soraru, S.S. Mal, G. Scorrano, L. Walder, U. Kortz, M. Bonchio, *Chem. Eur. J.* 17 (2011) 8371–8378.
- [14] M. Craven, R. Yahya, E. Kozhevnikova, R. Boomishankar, C.M. Robertson, A. Steiner, I. Kozhevnikov, *Chem. Commun.* 49 (2013) 349–351.
- [15] V. Mirkhani, M. Moghadam, S. Tangestaninejad, I. Mohammadpoor-Baltork, E. Shams, N. Rasouli, *Appl. Catal. A: Gen.* 334 (2008) 106–111.
- [16] R. Hajian, S. Tangestaninejad, M. Moghadam, V. Mirkhani, A. Reza Khosropour, *C. R. Chimie* 15 (2012) 975–979.
- [17] Z. Karimi, A.R. Mahjoub, S.M. Harati, *Inorg. Chim. Acta* 376 (2011) 1–9.
- [18] P.A. Shringarpure, A. Patel, *Ind. Eng. Chem. Res.* 50 (2011) 9069–9076.
- [19] K. Nomiya, Y. Sakai, S. Matsunaga, *Eur. J. Inorg. Chem.* (2011) 179–196.
- [20] O.A. Kholdeeva, G.M. Maksimov, R.I. Maksimovskaya, L.A. Kovaleva, M.A. Fedotov, *React. Kinet. Catal. Lett.* 66 (1999) 311–317.
- [21] O.A. Kholdeeva, R.I. Maksimovskaya, G.M. Maksimov, L.A. Kovaleva, *Kinet. Catal.* 42 (2001) 217–222.
- [22] T. Yamase, E. Ishikawa, Y. Asai, S. Kanai, *J. Mol. Catal. A: Chem.* 114 (1996) 237–245.
- [23] O.A. Kholdeeva, G.M. Maksimov, R.I. Maksimovskaya, L.A. Kovaleva, M.A. Feditiv, V.A. Grigoriev, C.L. Hill, *Inorg. Chem.* 39 (2000) 3828–3837.
- [24] E. Ishikawa, T. Yamase, *J. Mol. Catal. A: Chem.* 142 (1999) 61–76.
- [25] F. Gao, T. Yamase, H. Suzuki, *J. Mol. Catal. A: Chem.* 180 (2002) 97–108.
- [26] C.N. Kato, S. Negishi, K. Yoshida, K. Hayashi, K. Nomiya, *Appl. Catal. A: Gen.* 292 (2005) 97–104.
- [27] K. Hayashi, C.N. Kato, A. Shinohara, Y. Sakai, K. Nomiya, *J. Mol. Catal. A: Chem.* 262 (2007) 30–35.
- [28] K. Hayashi, M. Takahashi, K. Nomiya, *Dalton Trans.* (2005) 3751–3756.
- [29] C.N. Kato, K. Hayashi, S. Negishi, K. Nomiya, *J. Mol. Catal. A: Chem.* 262 (2007) 25–29.
- [30] O.A. Kholdeeva, T.A. Trubitsina, R.I. Maksimovskaya, A.V. Golovin, W.A. Nelwert, B.A. Kolesov, X. López, J.M. Poblet, *Inorg. Chem.* 43 (2004) 2284–2292.
- [31] O.A. Kholdeeva, T.A. Trubitsina, G.M. Maksimov, A.V. Golovin, R.I. Maksimovskaya, *Inorg. Chem.* 44 (2005) 1635–1642.
- [32] F. Hussain, B.S. Bassil, U. Kortz, O.A. Kholdeeva, M.N. Timofeeva, P. de Oliveira, B. Keita, L. Nadjo, *Chem. Eur. J.* 13 (2007) 4733–4742.
- [33] N.S. Antonova, J.J. Carboi, U. Kortz, O.A. Kholdeeva, J.M. Poblet, *J. Am. Chem. Soc.* 132 (2010) 7488–7497.
- [34] Y. Matsuki, Y. Mouri, Y. Sakai, S. Matsunaga, K. Nomiya, *Eur. J. Inorg. Chem.* (2013) 1754–1761.
- [35] O.A. Kholdeeva, *Eur. J. Inorg. Chem.* (2013) 1595–1605.
- [36] O.A. Kholdeeva, G.M. Maksimov, R.I. Maksimovskaya, M.P. Vanina, T.A. Trubitsina, D.Y. Naumov, B.A. Kolesov, N.S. Antonova, J.J. Carboi, J.M. Poblet, *Inorg. Chem.* 45 (2006) 7224–7234.
- [37] S.S. Mal, N.H. Nsouli, M. Carraro, A. Sartorel, G. Scorrano, H. Oelrich, L. Walder, M. Bonchio, U. Kortz, *Inorg. Chem.* 49 (2010) 7–9.
- [38] C. Aubry, G. Chottard, N. Platzer, J.-M. Bregeault, R. Thouvenot, F. Chauveau, C. Huet, H. Ledon, *Inorg. Chem.* 30 (1991) 4409–4415.
- [39] L.I. Kuznetsova, N.I. Kuznetsova, R.I. Maksimovskaya, G.I. Aleshina, O.S. Koscheeva, V.A. Utkin, *Catal. Lett.* 141 (2011) 1442–1450.
- [40] L. Liu, C. Chen, X. Hu, T. Mohamood, W. Ma, J. Lin, J. Zhao, *New J. Chem.* 32 (2008) 283–289.
- [41] D.C. Duncan, R.C. Chambers, E. Hecht, C.L. Hill, *J. Am. Chem. Soc.* 117 (1995) 681–691.
- [42] G. Roelfes, M. Lubben, R. Hage, L. Que Jr., B.L. Feringa, *Chem. Eur. J.* 6 (2000) 2152–2159.
- [43] I.W.C.E. Arends, R.A. Sheldon, *Appl. Catal. A* 212 (2001) 175–187.
- [44] C. Venturello, R. D'Aloisio, *J. Org. Chem.* 53 (1988) 1553–1557.
- [45] Z. Zhang, W. Zhao, B. Ma, Y. Ding, *Catal. Commun.* 12 (2010) 318–322.
- [46] R. Ishimoto, K. Kamata, N. Mizuno, *Eur. J. Inorg. Chem.* (2013) 1943–1950.
- [47] K. Nomiya, Y. Saku, S. Yamada, W. Takahashi, H. Sekiya, A. Shinohara, M. Ishimaru, Y. Sakai, *Dalton Trans.* (2009) 5504–5511.
- [48] H. Osada, A. Ishikawa, Y. Saku, Y. Sakai, Y. Matsunaga, K. Nomiya, *Polyhedron* 52 (2013) 389–397.
- [49] C.N. Kato, A. Shinohara, K. Hayashi, K. Nomiya, *Inorg. Chem.* 45 (2006) 8108–8119.

- [50] Y. Saku, Y. Sakai, A. Shinohara, K. Hayashi, S. Yoshida, C.N. Kato, K. Yoza, K. Nomiya, *Dalton Trans.* (2009) 805–813.
- [51] K. Nomiya, K. Ohta, Y. Sakai, T. Hosoya, A. Ohtake, A. Takakura, S. Matsunaga, *Bull. Chem. Soc. Jpn.* 86 (2013) 800–812.
- [52] K. Nomiya, N.C. Kasuga, S. Matsunaga, Y. Sakai, T. Hasegawa, T. Kimura, *Sci. J. Kanagawa Univ.* 21 (2010) 43–46.
- [53] H. Zhao, A. Ariafard, Z. Lin, *Inorg. Chim. Acta* 359 (2006) 3527–3534.
- [54] J.-F. Carpentier, Z. Wu, C.W. Lee, S. Strömberg, J.N. Christopher, R.F. Jordan, *J. Am. Chem. Soc.* 122 (2000) 7750–7767.
- [55] M. Dahlmann, G. Erker, K. Bergander, *J. Am. Chem. Soc.* 122 (2000) 7986–7998.
- [56] S. Kuroda, F. Dekura, Y. Sato, M. Mori, *J. Am. Chem. Soc.* 123 (2001) 4139–4146.
- [57] E. Negishi, F.E. Cederbaum, T. Takahashi, *Tetrahedron Lett.* 27 (1986) 2829–2832.
- [58] H. Martinez, N. Ren, M. Matta, M. Hillmyer, *Polym. Chem.* (2014), <http://dx.doi.org/10.1039/C3PY01787G>.

Article

Various Oxygen-Centered Phosphanegold(I) Cluster Cations Formed by Polyoxometalate (POM)-Mediated Clusterization: Effects of POMs and Phosphanes

Takuya Yoshida ^{1,2,3}, Yuta Yasuda ¹, Eri Nagashima ¹, Hidekazu Arai ¹, Satoshi Matsunaga ¹ and Kenji Nomiya ^{1,*}

¹ Department of Chemistry, Faculty of Science, Kanagawa University, Tsuchiya 2946, Hiratsuka, Kanagawa 259-1293, Japan; E-Mails: tyoshida@tmu.ac.jp (T.Y.);

yuy_inorg_chem@yahoo.co.jp (Y.Y.); r201470053hb@kanagawa-u.ac.jp (E.N.);

r201470040ur@kanagawa-u.ac.jp (H.A.); matsunaga@kanagawa-u.ac.jp (S.M.)

² Research Center for Gold Chemistry, Graduate School of Urban Environmental Sciences, Tokyo Metropolitan University, 1-1 Minami-osawa, Hachioji, Tokyo 192-0397, Japan

³ Department of Applied Chemistry, Graduate School of Urban Environmental Sciences, Tokyo Metropolitan University, 1-1 Minami-osawa, Hachioji, Tokyo 192-0397, Japan

* Author to whom correspondence should be addressed; E-Mail: nomiya@kanagawa-u.ac.jp; Tel.: +81-463-59-4111; Fax: +81-463-58-9684.

External Editor: Ahmed A. Mohamed

Received: 13 October 2014; in revised form: 13 November 2014 / Accepted: 14 November 2014 /

Published: 10 December 2014

Abstract: Novel phosphanegold(I) cluster cations combined with polyoxometalate (POM) anions, *i.e.*, intercluster compounds, [(Au{P(*m*-FPh)₃})₄(μ₄-O)]₂[(Au{P(*m*-FPh)₃})₂(μ-OH)]₂[α-PMo₁₂O₄₀]₂·EtOH (**1**), [(Au{P(*m*-FPh)₃})₄(μ₄-O)]₂[α-SiMo₁₂O₄₀]₂·4H₂O (**2**), [(Au{P(*m*-MePh)₃})₄(μ₄-O)]₂[α-SiM₁₂O₄₀] (*M* = W (**3**), Mo (**4**)) and [(Au{P(*p*-MePh)₃})₄(μ₄-O)]₂[(Au{P(*p*-MePh)₃})₃(μ₃-O)]₂[α-PW₁₂O₄₀] (**5**) were synthesized by POM-mediated clusterization, and unequivocally characterized by elemental analysis, TG/DTA, FT-IR, X-ray crystallography, solid-state CPMAS ³¹P NMR and solution (¹H, ³¹P{¹H}) NMR. Formation of the these gold(I) cluster cations was strongly dependent upon the charge density and acidity of the POMs, and the substituents and substituted positions on the aryl group of triarylphosphane ligands. These gold(I) cluster cations contained various bridged-oxygen atoms such as μ₄-O, μ₃-O and μ-OH groups.

Keywords: phosphanegold(I) cluster; polyoxometalate; oxygen-center; intercluster compound

1. Introduction

Polyoxometalates (POMs) are discrete metal oxide clusters that are of current interest as soluble metal oxides and for their applications in catalysis, medicine and materials science [1–6]. The preparation of POM-based materials is therefore an active field of research. One of the intriguing aspects of POMs is that their combination with cluster cations or macrocations has resulted in the formation of various intercluster compounds that are interesting from the viewpoints of conducting research on ionic crystals, crystal engineering, structure, sorption properties and so on. In many compounds, POMs have been combined with the independently prepared metal cluster cations [7,8].

Recently, we unexpectedly found the clusterization of monomeric phosphanegold(I) units $[\text{Au}(\text{PR}_3)]^+$ during the course of carboxylate elimination of a monomeric phosphanegold(I) carboxylate $[\text{Au}(\text{RS-pyrrld})(\text{PPh}_3)]$ ($\text{RS-Hpyrrld} = \text{RS-2-pyrrolidone-5-carboxylic acid}$). The previous representation of H_2pyrrld was changed to Hpyrrld ; thus, the formulation of $[\text{Au}(\text{RS-Hpyrrld})(\text{PPh}_3)]$ used so far was also changed to $[\text{Au}(\text{RS-pyrrld})(\text{PPh}_3)]$ [9] in the presence of the free-acid form of the Keggin POM $\text{H}_3[\alpha\text{-PW}_{12}\text{O}_{40}] \cdot 7\text{H}_2\text{O}$ [10]. This reaction resulted in the formation of a tetrakis{triphenylphosphanegold(I)} oxonium cation $[\{\text{Au}(\text{PPh}_3)\}_4(\mu_4\text{-O})]^{2+}$ as a counterion of the POM. In addition, we also found that the reaction of $[\text{Au}(\text{RS-pyrrld})(\text{PPh}_3)]$ with the sodium salt of the Keggin POM $\text{Na}_3[\alpha\text{-PW}_{12}\text{O}_{40}] \cdot 9\text{H}_2\text{O}$ gave a heptakis{triphenylphosphanegold(I)} dioxonium cation $[\{\{\text{Au}(\text{PPh}_3)\}_4(\mu_4\text{-O})\}\{\{\text{Au}(\text{PPh}_3)\}_3(\mu_3\text{-O})\}]^{3+}$ as a counterion of the POM [11]. Also, the novel intercluster compounds $[\{\{\text{Au}\{\text{P}(p\text{-RPh})_3\}\}_2(\mu\text{-OH})\}_2]_3[\alpha\text{-PM}_{12}\text{O}_{40}]_2 \cdot n\text{EtOH}$ ($R = \text{Me}, M = \text{W}; R = \text{Me}, M = \text{Mo}; R = \text{F}, M = \text{Mo}$) have been recently synthesized using the POM-mediated clusterization of monomeric para-substituted triarylphosphanegold(I) carboxylate $[\text{Au}(\text{RS-pyrrld})\{\text{P}(p\text{-RPh})_3\}]$ ($R = \text{Me}, \text{F}$) [12]. The formation of such phosphanegold(I) cluster cations was strongly dependent upon the bulkiness, acidity and charge density of the POMs, and substituents on the aryl group of phosphane ligands. The POMs appeared to act as a template in the clusterization of monomeric phosphanegold(I) units generated from the elimination of the carboxylate ligands [13,14].

The field of element-centered gold clusters $[\text{E}(\text{AuL})_n]^{m+}$ ($E =$ group 13–17 elements) has been extensively studied by the groups of Schmidbaur [15,16] and Laguna [17]. The trigold(I) oxonium cluster cations $[\{\text{Au}(\text{PR}_3)\}_3(\mu_3\text{-O})]^+$ have been reported to exhibit different forms of structural dimerization depending upon the bulkiness of phosphane ligands, *i.e.*, trigold(I) units are aggregated through crossed edges ($R = \text{Me}$) or parallel edges ($R = \text{Ph}$, *etc.*), resulting in the hexagold(I) dioxonium cluster cation as a dimer-of-trinuclear clusters $[\{\{\text{Au}(\text{PR}_3)\}_3(\mu_3\text{-O})\}_2]^{2+}$ [18–21]. Dimerization of the gold(I) cluster cations also indicates that the aurophilic interaction is the driving force for the oligomerization of many phosphanegold(I) cluster cations in the solid state. In our reported dimer-of-dinuclear gold(I) cluster cations $[\{\{\text{Au}\{\text{P}(p\text{-RPh})_3\}\}_2(\mu\text{-OH})\}_2]^{2+}$, the two digold(I) units $\{\{\text{Au}\{\text{P}(p\text{-RPh})_3\}\}_2(\mu\text{-OH})\}^+$ were dimerized by inter-cationic aurophilic interactions [12]. Also, the heptagold(I) dioxonium cluster cation $[\{\{\text{Au}(\text{PPh}_3)\}_4(\mu_4\text{-O})\}\{\{\text{Au}(\text{PPh}_3)\}_3(\mu_3\text{-O})\}]^{3+}$ was regarded as an assembly of the tetragold(I)

unit $\{\{\text{Au}(\text{PPh}_3)_4(\mu_4\text{-O})\}^{2+}$ and the trigold(I) unit $\{\{\text{Au}(\text{PPh}_3)_3(\mu_3\text{-O})\}^+$ induced by inter-cationic aurophilic interactions [11].

As continued work, we examined the POM-mediated clusterization of monomeric phosphanegold(I) units using the Keggin tungsto- and molybdo-POMs with heteroatoms P and Si, and the gold(I) carboxylate precursors with the *X*-substituted triarylphosphane ligands (*X* = *m*-F, *m*-Me and *p*-Me), $[\text{Au}(\text{RS-pyrrld})\{\text{P}(\text{XPh})_3\}]$.

In this paper, we report the syntheses and characterization of several novel intercluster compounds, $[(\text{Au}\{\text{P}(\text{m-FPh})_3\})_4(\mu_4\text{-O})]_2[\{\{\text{Au}\{\text{P}(\text{m-FPh})_3\}_2(\mu\text{-OH})\}_2][\alpha\text{-PMo}_{12}\text{O}_{40}]_2\cdot\text{EtOH}$ (**1**), $[(\text{Au}\{\text{P}(\text{m-FPh})_3\})_4(\mu_4\text{-O})]_2[\alpha\text{-SiMo}_{12}\text{O}_{40}]\cdot 4\text{H}_2\text{O}$ (**2**), $[(\text{Au}\{\text{P}(\text{m-MePh})_3\})_4(\mu_4\text{-O})]_2[\alpha\text{-SiW}_{12}\text{O}_{40}]$ (**3**), $[(\text{Au}\{\text{P}(\text{m-MePh})_3\})_4(\mu_4\text{-O})]_2[\alpha\text{-SiMo}_{12}\text{O}_{40}]$ (**4**) and $[\{\{\text{Au}\{\text{P}(\text{p-MePh})_3\}_4(\mu_4\text{-O})\}\}\{\{\text{Au}\{\text{P}(\text{p-MePh})_3\}_3(\mu_3\text{-O})\}\}][\alpha\text{-PW}_{12}\text{O}_{40}]$ (**5**). These compounds were formed by reactions of the Keggin POMs having varied charge densities and different acidities with the phosphanegold(I) complexes containing varied substituents on the aryl group.

2. Results and Discussion

2.1. Synthesis and Compositional Characterization

The intercluster compounds between the phosphanegold(I) cluster cations and the Keggin POM anions were obtained as **1** in 35.9% (0.089 g scale) yield, as **2** in 4.64% (0.014 g scale) yield, as **3** in 71.4% (0.247 g scale) yield, as **4** in 46.7% (0.137 g scale) yield and as **5** in 26.0% (0.026 g scale) yield. These compounds were prepared by reactions between $[\text{Au}(\text{RS-pyrrld})(\text{PR}_3)]$ (*R* = *m*-FPh (**1**, **2**), *m*-MePh (**3**, **4**) and *p*-MePh (**5**)) in CH_2Cl_2 and the Keggin POMs in mixed EtOH–H₂O solvents, *i.e.*, $\text{H}_3[\alpha\text{-PMo}_{12}\text{O}_{40}]\cdot 14\text{H}_2\text{O}$ (**1**), $\text{H}_4[\alpha\text{-SiMo}_{12}\text{O}_{40}]\cdot 12\text{H}_2\text{O}$ (**2**, **4**), $\text{H}_4[\alpha\text{-SiW}_{12}\text{O}_{40}]\cdot 10\text{H}_2\text{O}$ (**3**) and $\text{Na}_3[\alpha\text{-PW}_{12}\text{O}_{40}]\cdot 9\text{H}_2\text{O}$ (**5**). Their crystallizations were carried out by slow evaporation or liquid-liquid diffusion at room temperature. Characterization was performed by X-ray crystallography, CHN elemental analysis, thermogravimetric and differential thermal analysis (TG/DTA), Fourier transform infrared (FT-IR), solid-state cross-polarization magic-angle-spinning (CPMAS) ³¹P nuclear magnetic resonance (NMR) spectroscopy and solution (¹H, ³¹P{¹H}) NMR spectroscopy. The presence of any solvated molecules was confirmed by CHN elemental analysis, TG/DTA measurements under atmospheric conditions (Figures S1–S5), and ¹H NMR for solvated ethanol molecules.

All gold(I) cluster cations in these intercluster compounds **1–5** contained bridged-oxygen atoms such as $\mu_4\text{-O}$, $\mu_3\text{-O}$ and $\mu\text{-OH}$ groups, which were originated from water contained in the reaction system and/or the hydrated water molecules of the POMs.

The solid-state FT-IR spectra of **1–5** showed the characteristic vibrational bands on the basis of coordinating PR₃ ligands (Figures S6–S10). The FT-IR spectra also showed prominent vibrational bands owing to the α -Keggin molybdo- and tungsto-POMs [22]. In these spectra, the carbonyl vibrational bands of the anionic *RS*-pyrrld ligand in the $[\text{Au}(\text{RS-pyrrld})(\text{PR}_3)]$ precursors disappeared, showing that the carboxylate ligand was eliminated. Elimination of the carboxylate ligand was also confirmed by ¹H NMR in DMSO-*d*₆. The carboxylate plays a role of only the leaving group. In fact, not only pyrrolidone carboxylate, but also other carboxylates such as 5-oxotetrahydrofuran-2-carboxylate and acetylglycinate can serve as the leaving groups in the formation of the tetragold(I) clusters in the presence of POMs [10].

Table 1. Crystallographic data for 1–5.

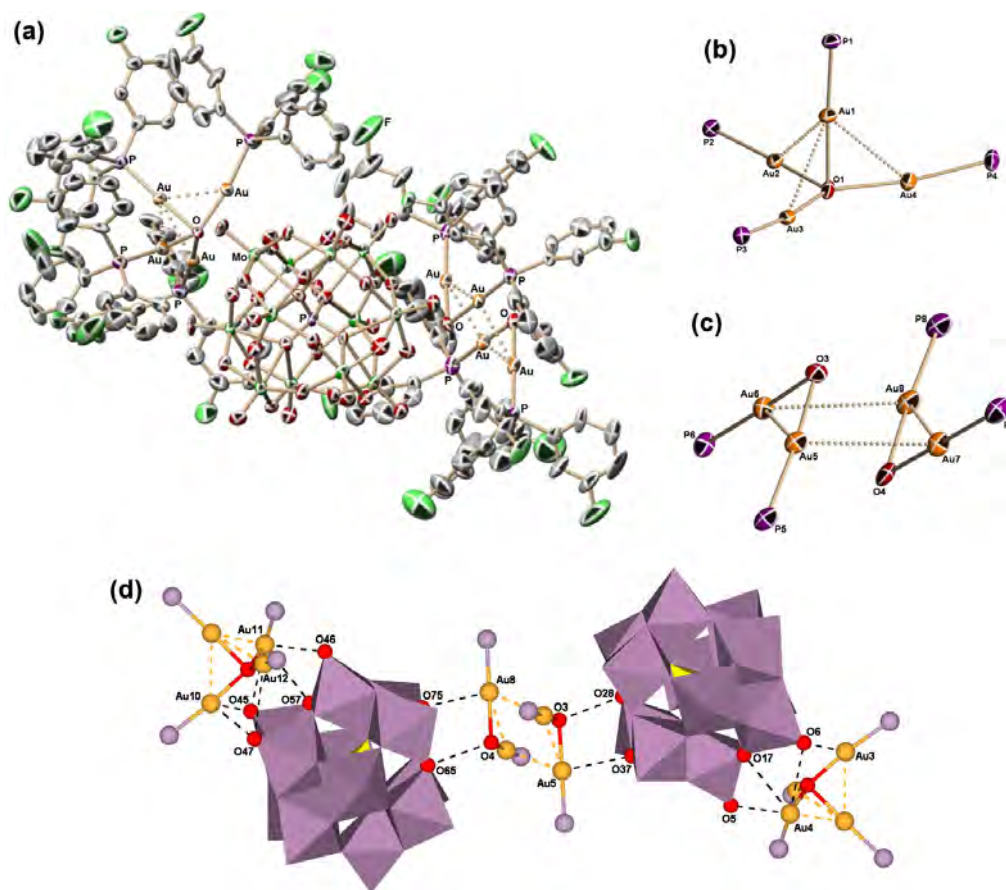
Parameters	1	2	3	4	5
Formula	C ₂₁₆ H ₁₄₆ Au ₁₂ F ₃₆ -Mo ₂₄ O ₈₄ P ₁₄	C ₁₄₄ H ₁₀₄ Au ₈ F ₂₄ -Mo ₁₂ O ₄₆ P ₈ Si	C ₁₆₈ H ₁₆₈ Au ₈ O ₄₆ -P ₈ SiW ₁₂	C ₁₆₈ H ₁₆₈ Au ₈ Mo ₁₂ -O ₄₆ P ₈ Si	C ₁₄₇ H ₁₄₇ Au ₇ O ₄₂ -P ₈ W ₁₂
Formula weight	9869.07	6029.13	6980.81	5925.89	6418.37
Color, shape	Orange-yellow, rod	Yellow, block	Pale-yellow, block	Yellow, block	Colorless, plate
Crystal system	Triclinic	Triclinic	Rhombohedral	Rhombohedral	Triclinic
Space group	<i>P</i> -1	<i>P</i> -1	<i>R</i> -3	<i>R</i> -3	<i>P</i> -1
<i>T</i> /K	100	120	120	100	100
<i>a</i> /Å	16.191(2)	16.296(3)	20.478(3)	20.3813(7)	17.7243(11)
<i>b</i> /Å	29.165(4)	16.357(3)			17.8341(10)
<i>c</i> /Å	35.365(4)	16.854(3)	36.726(7)	36.679(2)	31.7570(18)
α /°	99.801(2)	77.37(3)			104.8260(10)
β /°	99.153(2)	75.89(3)			92.640(2)
γ /°	104.963(2)	80.58(3)	120	120	109.6850(10)
<i>V</i> /Å ³	15533(3)	4222.3(15)	13337(4)	13195.2(11)	9040.0(9)
<i>Z</i>	2	1	3	3	2
<i>D</i> _{calc} /g cm ⁻³	2.110	2.371	2.607	2.237	2.358
<i>F</i> ₀₀₀	9208	2822	9594	8442	5852
GOF	1.027	1.066	1.311	1.074	1.373
<i>R</i> ₁ (<i>I</i> > 2.00 σ (<i>I</i>))	0.0723	0.0915	0.0547	0.0376	0.1466
<i>R</i> (all data)	0.1077	0.1042	0.0558	0.0390	0.2417
w <i>R</i> ₂ (all data)	0.1753	0.2502	0.1217	0.0862	0.4614

2.2. Molecular Structures of 1–5

Crystal data of **1–5** were given in Table 1. Bond lengths (Å) and angles (°) for **1–5** were shown in Supplementary Information (Tables S1–S5).

Single-crystal X-ray analysis revealed that **1** crystallizes in the Triclinic *P*-1 space group, and is composed of two tetragold(I) cluster cations $[(\text{Au}\{\text{P}(m\text{-FPh})_3\})_4(\mu_4\text{-O})]^{2+}$ and one dimer-of-dinuclear gold(I) cluster cation $[\{(\text{Au}\{\text{P}(m\text{-FPh})_3\})_2(\mu\text{-OH})\}_2]^{2+}$, and two Keggin POM anions $[\alpha\text{-PMo}_{12}\text{O}_{40}]^{3-}$ as counterions (Figure 1a).

Figure 1. (a) Molecular structure of **1**; (b) The partial structure of the tetragold(I) cluster cation moiety; (c) The partial structure of the dimer-of-dinuclear gold(I) cluster cation moiety; (d) The interactions among the tetragold(I) cluster cations, dimer-of-dinuclear gold(I) cluster cation and Keggin polyoxometalate (POM) anions.



The two tetragold(I) cluster cations $[(\text{Au}\{\text{P}(m\text{-FPh})_3\})_4(\mu_4\text{-O})]^{2+}$ adopt trigonal-pyramidal structures composed of three short edges associated with (Au1, Au2, Au3, Au4) atoms and (Au9, Au10, Au11, Au12) atoms, respectively (Au1–Au2: 2.9513 Å, Au1–Au3: 2.8978 Å, Au1–Au4: 2.8582 Å; Au9–Au10: 2.9293 Å, Au9–Au11: 2.8719 Å, Au9–Au12: 3.0815 Å), and a triangular plane of (Au2, Au3, Au4) atoms and (Au10, Au11, Au12) atoms, respectively, with longer edge lengths (Au2–Au3: 3.650 Å, Au2–Au4: 3.655 Å, Au3–Au4: 3.536 Å; Au10–Au11: 3.568 Å, Au10–Au12: 3.528 Å, Au11–Au12: 3.717 Å) (Figure 1b). The bridged-oxygen atoms ($\mu_4\text{-O}$) were placed within the basal plane composed of (Au2, Au3, Au4) atoms and (Au10, Au11, Au12) atoms, respectively (Au2–O1–Au3: 123.6°,

Au2–O1–Au4: 120.0°, Au3–O1–Au4: 116.1°; Au10–O2–Au11: 117.4°, Au10–O2–Au12: 116.2°, Au11–O2–Au12: 126.4°), resulting in a point group of C_{3v} for the tetragold(I) cluster cations. The distorted tetragold(I) cluster cations in **1** are similar to that of the previously reported tetragold(I) cluster cation $[(Au(PPh_3))_4(\mu_4-O)]^{2+}$ as the counterion of the POM [10,13].

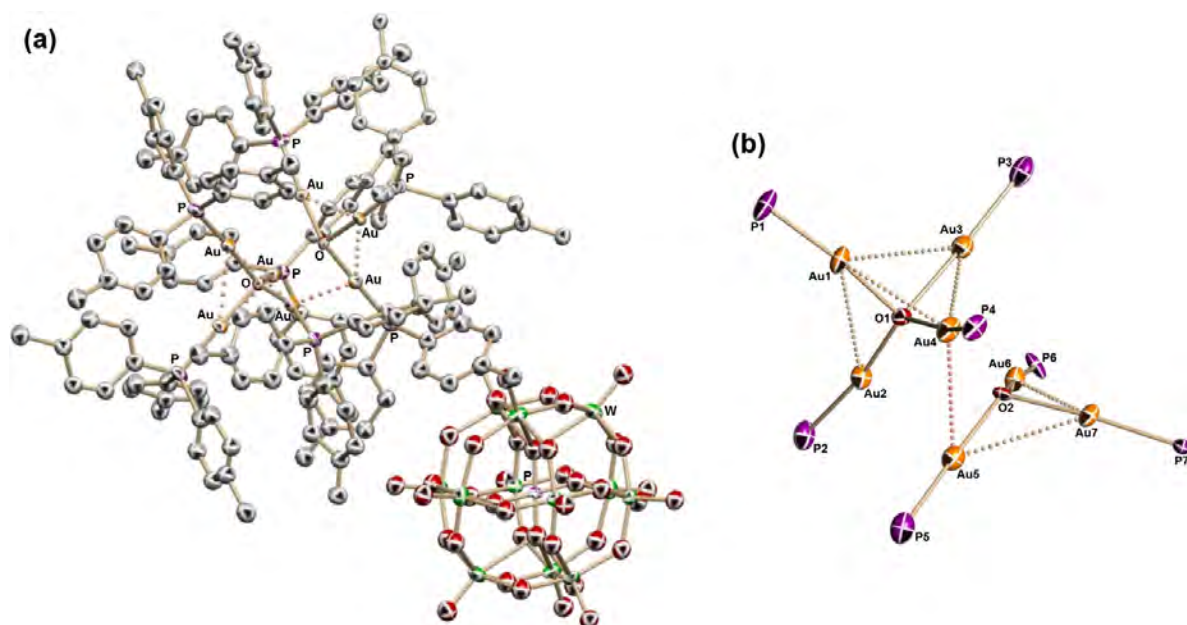
The dimer-of-dinuclear gold(I) cluster cation in **1** can be regarded as the dimerization of digold(I) units $\{(Au\{P(m-FPh)_3\})_2(\mu-OH)\}^+$. The digold(I) unit consists of two monomer subunits $(Au\{P(m-FPh)_3\})^+$ linked by a μ -OH group and is triangular in shape. Two digold(I) units dimerize to form the dimer-of-dinuclear gold(I) cluster cation $\{[(Au\{P(m-FPh)_3\})_2(\mu-OH)]_2\}^{2+}$ in a parallel-edge arrangement by inter-cationic aurophilic interactions (Au5–Au7: 3.2921 Å, Au6–Au8: 3.3454 Å) (Figure 1c). The dimer-of-dinuclear gold(I) cluster cation of a parallel-edge arrangement in **1** is similar to that of the previously reported dimer-of-dinuclear gold(I) cluster cation $\{[(Au\{P(p-FPh)_3\})_2(\mu-OH)]_2\}^{2+}$ with $[\alpha-PMo_{12}O_{40}]^{3-}$ [12].

The five gold(I) atoms Au3, Au4, Au10, Au11 and Au12 in the tetragold(I) cluster cation moiety interact with the terminal oxygen atoms and OMo₂ oxygen atoms of edge-shared MoO₆ octahedra of the Keggin POMs (Au3–O6: 2.943 Å, Au4–O5: 3.143 Å, Au4–O6: 3.136 Å, Au4–O17: 3.087 Å, Au10–O45: 3.179 Å, Au10–O47: 3.143 Å, Au11–O45: 3.112 Å, Au11–O46: 3.023 Å, Au11–O57: 3.047 Å, Au12–O47: 3.123 Å). The two gold(I) atoms Au5 and Au8 in the dimer-of-dinuclear gold(I) cluster cation moiety interact with the OMo₂ oxygen atoms of edge-shared MoO₆ octahedra of the Keggin POMs (Au5–O37: 2.945 Å, Au8–O75: 2.853 Å), and the short distances between dimer-of-dinuclear gold(I) cluster cation and Keggin POMs indicate the existence of a hydrogen bonding (O3–O28: 3.021 Å, O4–O65: 3.043 Å) (Figure 1d). The meta-substituted triarylphosphane ligand was few influence for the POM-mediated clusterization of monomeric phosphane-gold(I) units.

Single-crystal X-ray analysis revealed that **2** crystallizes in the Triclinic $P-1$ space group, and is composed of two tetragold(I) cluster cations $[(Au\{P(m-FPh)_3\})_4(\mu_4-O)]^{2+}$ and one Keggin POM anion $[\alpha-SiMo_{12}O_{40}]^{4-}$ as counterion (Figure S11a). Single-crystal X-ray analysis also revealed that **3** and **4** crystallize in the Rhombohedral $R-3$ space group, respectively, and are composed of two tetragold(I) cluster cations, $[(Au\{P(m-MePh)_3\})_4(\mu_4-O)]^{2+}$, and one Keggin POM anion $[\alpha-SiW_{12}O_{40}]^{4-}$ for **3** (Figure S12) and $[\alpha-SiMo_{12}O_{40}]^{4-}$ for **4** as counterions.

The tetragold(I) cluster cation $[(Au\{P(m-FPh)_3\})_4(\mu_4-O)]^{2+}$ of **2** was very similar to that of **1** (C_{3v} symmetry) (Figure S11b). The three gold(I) atoms Au2, Au3 and Au4 in the tetragold(I) cluster cation interact with the OMo₂ oxygen atoms of edge-shared MoO₆ octahedra and terminal oxygen atoms of the Keggin POM (Au2–O4: 3.094 Å, Au2–O9: 3.070 Å, Au3–O3: 3.139 Å, Au3–O8: 3.021 Å, Au4–O10: 2.916 Å). The tetragold(I) cluster cations $[(Au\{P(m-MePh)_3\})_4(\mu_4-O)]^{2+}$ of **3** and **4** adopt trigonal-pyramidal structures (C_{3v} symmetry) due to interactions with the Keggin POMs (Au2–O3: 3.178 Å, Au2–O7: 2.994 Å for **3**; Au2–O2: 3.144 Å, Au2–O4: 2.929 Å for **4**). The Keggin POM anion was disordered. Compound **4** is isostructural with **3**, with the different metal atom (W vs. Mo) in the Keggin POM anion.

Single-crystal X-ray analysis revealed that **5** crystallizes in the Triclinic $P-1$ space group, and is composed of a heptagold(I) cluster cation $\{[(Au\{P(p-MePh)_3\})_4(\mu_4-O)]\{[(Au\{P(p-MePh)_3\})_3(\mu_3-O)]\}^3\}^{3+}$ and one Keggin POM anion $[\alpha-PW_{12}O_{40}]^{3-}$ as counterion (Figure 2a). However, the crystals of **5** were not suitable for X-ray analysis. Although the existence of the heptagold(I) cluster cation was confirmed, the quality of the crystal data was poor (Table 1).

Figure 2. (a) Molecular structure of **5**; (b) The partial structure of the heptagold(I) cluster cation.

The heptagold(I) cluster cation was composed of the tetragold(I) cluster cation and trigold(I) cluster cation (Figure 2b). Two gold(I) cluster cations were linked by the one inter-cationic aurophilic interaction (Au4–Au5: 3.034 Å). The aurophilic interaction is longer than the Au–Au separation of metallic gold (2.88 Å) [23], but shorter than twice the van der Waals radius for gold (3.32 Å) [24]. In comparison with the previously reported heptagold(I) cluster cation $[\{\{\text{Au}(\text{PPh}_3)_4(\mu_4\text{-O})\}\{\{\text{Au}(\text{PPh}_3)_3(\mu_3\text{-O})\}\}]^{3+}$ [11], the heptagold(I) cluster cation in **5** has a similar structure, but the number of inter-cationic aurophilic interaction was decreased. This different coupled structure is produced by steric effects of the methyl groups in the para-substituted triarylphosphane ligands. On the other hand, the bridged-oxygen–oxygen distance (O1–O2: 2.830 Å) in the heptagold(I) cluster cation in **5** is shorter than that (3.096 Å) of the previously reported heptagold(I) cluster cation. This oxygen–oxygen distance is also shorter than twice the van der Waals radius for oxygen (3.04 Å) [24]. The tetragold(I) cluster moiety had a distorted tetrahedron structure due to four intra-cationic aurophilic interactions (Au1–Au2: 3.308 Å, Au1–Au3: 3.112 Å, Au1–Au4: 3.064 Å, Au3–Au4: 3.111 Å). The encapsulated oxygen atom ($\mu_4\text{-O}$) was placed within the distorted tetrahedron (Au2–O1–Au3: 126.9°, Au2–O1–Au4: 129.4°, Au3–O1–Au4: 92.4°; total 348.7°). The trigold(I) cluster moiety composed of two intra-cationic aurophilic interactions (Au5–Au7: 3.199 Å, Au6–Au7: 3.078 Å) and one long Au–Au edge (Au5–Au6: 3.606 Å) formed a triangular plane of the (Au5, Au6, Au7) atoms. The bridged-oxygen atom ($\mu_3\text{-O}$) was placed out-of-plane consisting a triangular plane of the three gold(I) atoms (Au5–O2–Au6: 127.9°, Au5–O2–Au7: 104.0°, Au6–O2–Au7: 98.2°; total 330.1°). Probably, the heptagold(I) cluster cation would be formed by the clusterization of monomeric triarylphosphane-gold(I) units $[\text{Au}(\text{PR}_3)]^+$ with smaller steric effects in the presence of the less-acidic POM, *i.e.*, $\text{Na}_3[\alpha\text{-PW}_{12}\text{O}_{40}] \cdot 9\text{H}_2\text{O}$ [11].

2.3. Solid-State CPMAS ^{31}P and Solution $^{31}\text{P}\{^1\text{H}\}$ NMR

The solid-state CPMAS ^{31}P and solution $^{31}\text{P}\{^1\text{H}\}$ NMR in DMSO- d_6 signals of **1–5** are listed in Table 2. The solid-state CPMAS ^{31}P NMR of **1** observed two broad signals at –3.4 and 24.4 ppm.

The signal at -3.4 ppm is assignable to the heteroatom phosphorus in the Keggin molybdo-POM anion, and the signal at 24.4 ppm is assignable to the overlapped signals of the tetragold(I) cluster cations and the dimer-of-dinuclear gold(I) cluster cation. The solid-state CPMAS ^{31}P NMR of **2**, **3** and **4** showed two broad signals at 19.6 and 24.4 ppm for **2**, 18.3 and 28.5 ppm for **3**, 17.4 and 27.7 ppm for **4** originating from the inequivalent phosphane groups. The three signals at 19.6 , 18.3 and 17.4 ppm are assignable to one apical phosphane group, respectively, and the other three signals at 24.4 , 28.5 and 27.7 ppm are assignable to the three basal phosphane groups in the trigonal-pyramidal structure, respectively [10,13]. The solid-state CPMAS ^{31}P NMR of **5** showed two broad signals at -14.6 and 23.1 ppm due to the Keggin tungsto-POM anion and phosphane groups of the heptagold(I) cluster cation, respectively. Although all phosphane groups of the heptagold(I) cluster cation are inequivalent as shown in X-ray analysis, their signals were observed as one broad peak at 23.1 ppm.

Table 2. Solid-state cross-polarization magic-angle-spinning (CPMAS) ^{31}P and solution $^{31}\text{P}\{^1\text{H}\}$ nuclear magnetic resonance (NMR) in DMSO- d_6 signals (ppm) of **1–5**.

Compound	Solid-State CPMAS ^{31}P	Solution $^{31}\text{P}\{^1\text{H}\}$
1	$-3.4, 24.4$	$-3.23, 26.31$ (main), $-0.40, 43.57$ (minor)
2	$19.6, 24.4$	25.67 (main), 43.38 (minor)
3	$18.3, 28.5$	insoluble
4	$17.4, 27.7$	insoluble
5	$-14.6, 23.1$	$-14.88, 22.39$

The solution $^{31}\text{P}\{^1\text{H}\}$ NMR signals of **1**, **2** and **5** in DMSO- d_6 were observed as major sharp signals at 26.31 , 25.67 and 22.39 ppm, respectively. These signals were shifted to a higher field from the monomeric phosphanegold(I) precursors (29.20 and 25.35 ppm), respectively. In general, the $^{31}\text{P}\{^1\text{H}\}$ NMR signals of oxygen-centered phosphanegold(I) clusters are observed in the higher field in comparison with those of the monomeric phosphanegold(I) precursors [10–12]. The peak at -3.23 ppm for **1** and -14.88 ppm for **5** are assignable to the heteroatom phosphorus in the Keggin POMs ($M = \text{Mo}, \text{W}$). Because Keggin molybdo-POMs are unstable in DMSO, the minor signals at -0.40 , 43.57 ppm of **1** and 43.38 ppm of **2** are assignable to the decomposition species. Because **3** and **4** are insoluble in any solvents, the solution $^{31}\text{P}\{^1\text{H}\}$ NMR data of **3** and **4** were not obtained.

3. Experimental Section

3.1. Materials

The following reactants were used as received: EtOH, CH_2Cl_2 , Et_2O (all from Wako, Osaka, Japan), and DMSO- d_6 (Isotec, Miamisburg, OH, USA). With respect to the α -Keggin POMs, $\text{H}_3[\alpha\text{-PMo}_{12}\text{O}_{40}] \cdot 14\text{H}_2\text{O}$, $\text{H}_4[\alpha\text{-SiMo}_{12}\text{O}_{40}] \cdot 12\text{H}_2\text{O}$, $\text{H}_4[\alpha\text{-SiW}_{12}\text{O}_{40}] \cdot 10\text{H}_2\text{O}$ and $\text{Na}_3[\alpha\text{-PW}_{12}\text{O}_{40}] \cdot 9\text{H}_2\text{O}$ were prepared according to the ether extraction method [25] and the literatures [26,27], and identified by FT-IR, TG/DTA and solution (^{29}Si , ^{31}P , ^{183}W) NMR spectroscopy. The $[\text{Au}(\text{RS-pyrrld})\{\text{P}(m\text{-XPh})_3\}]$ ($X = \text{F}, \text{Me}$) and $[\text{Au}(\text{RS-pyrrld})\{\text{P}(p\text{-MePh})_3\}]$ precursor complexes were synthesized according to the reported methods using $\text{P}(m\text{-XPh})_3$ ($X = \text{F}, \text{Me}$) or $\text{P}(p\text{-MePh})_3$ [9,12], and characterized by CHN elemental analysis, FT-IR, TG/DTA and solution (^1H , $^{13}\text{C}\{^1\text{H}\}$, $^{31}\text{P}\{^1\text{H}\}$) NMR spectroscopy.

3.2. Instrumentation and Analytical Procedures

CHN elemental analyses were carried out with a Perkin-Elmer (Waltham, MA, USA) 2400 CHNS Elemental Analyzer II (Kanagawa University, Kanagawa, Japan). IR spectra were recorded on a Jasco (Tokyo, Japan) 4100 FT-IR spectrometer in KBr disks at room temperature. TG/DTA were acquired using a Rigaku (Tokyo, Japan) Thermo Plus 2 series TG 8120 instrument. ^1H NMR (500.00 MHz) and $^{31}\text{P}\{^1\text{H}\}$ NMR (202.00 MHz) spectra in a DMSO- d_6 solution were recorded in 5-mm-outer-diameter tubes on a JEOL (Tokyo, Japan) JNM-ECP 500 FT-NMR spectrometer with a JEOL (Tokyo, Japan) ECP-500 NMR data processing system. The ^1H NMR spectra were referenced to an internal standard of tetramethylsilane (SiMe_4). The $^{31}\text{P}\{^1\text{H}\}$ NMR spectra were referenced to an external standard of 25% H_3PO_4 in H_2O in a sealed capillary. The $^{31}\text{P}\{^1\text{H}\}$ NMR data with the usual 85% H_3PO_4 reference are shifted to +0.544 ppm from our data. Solid-state CPMAS ^{31}P NMR (121.00 MHz) spectra were recorded in 6-mm-outer-diameter rotors on a JEOL JNM-ECP 300 FT-NMR spectrometer with a JEOL ECP-300 NMR data processing system. The spectra were referenced to an external standard of $(\text{NH}_4)_2\text{HPO}_4$ (δ 1.60).

3.3. Syntheses

$[(\text{Au}\{\text{P}(m\text{-FPh})_3\})_4(\mu_4\text{-O})]_2\{[(\text{Au}\{\text{P}(m\text{-FPh})_3\})_2(\mu\text{-OH})]_2\}[\alpha\text{-PMO}_{12}\text{O}_{40}]_2\cdot\text{EtOH}$ (**1**): A solution of $[\text{Au}(\text{RS-pyrrld})\{\text{P}(m\text{-FPh})_3\}]$ (0.192 g, 0.300 mmol) dissolved in 25 mL of CH_2Cl_2 was slowly added to a yellow clear solution of $\text{H}_3[\alpha\text{-PMO}_{12}\text{O}_{40}]\cdot 14\text{H}_2\text{O}$ (0.104 g, 0.050 mmol) dissolved in 15 mL of an EtOH– H_2O (5:1, v/v) mixed solvent. After stirring for 1 h at room temperature, the reaction solution was filtered through a folded filter paper (Whatman, Maidstone, UK, No. 5). The resulting yellow clear solution was slowly evaporated at room temperature in the dark. After 7 days, the orange yellow rod crystals were formed, and collected on a membrane filter (JG 0.2 μm), washed with EtOH (20 mL \times 2) and Et_2O (20 mL \times 2), and dried *in vacuo* for 2 h. Yield: 0.089 g (35.9%). The crystalline samples were soluble in DMSO, but insoluble in H_2O , EtOH and Et_2O . Calcd. for $\text{C}_{218}\text{H}_{152}\text{O}_{85}\text{F}_{36}\text{P}_{14}\text{Mo}_{24}\text{Au}_{12}$ or $[(\text{Au}\{\text{P}(m\text{-FPh})_3\})_4(\mu_4\text{-O})]_2\{[(\text{Au}\{\text{P}(m\text{-FPh})_3\})_2(\mu\text{-OH})]_2\}[\alpha\text{-PMO}_{12}\text{O}_{40}]_2\cdot\text{EtOH}$: C, 26.41; H, 1.55%. Found: C, 26.35; H, 1.15%. TG/DTA under atmospheric conditions: a weight loss of 1.22% because of desorption of EtOH was observed at temperature less than 200.5 $^\circ\text{C}$; calcd. 1.38% for three EtOH molecules. IR (KBr) (cm^{-1}): 1601 w, 1581 s, 1522 vw, 1476 m, 1422 m, 1305 vw, 1268 w, 1225 s, 1165 vw, 1096 w, 1062 m, 1000 vw, 957 s, 876 m, 812 vs, 782 vs, 682 m, 614 vw, 583 w, 522 w, 510 w, 481 w, 470 w, 409 w. $^{31}\text{P}\{^1\text{H}\}$ NMR (25.5 $^\circ\text{C}$, DMSO- d_6): δ -3.23, 26.31 (main), -0.40, 43.57 (minor) ppm. ^1H NMR (24.7 $^\circ\text{C}$, DMSO- d_6): δ 1.09 (t, J = 7.1 Hz, $\text{CH}_3\text{CH}_2\text{OH}$ solvate), 3.38 (q, J = 7.0 Hz, $\text{CH}_3\text{CH}_2\text{OH}$ solvate), 7.35–7.57 (m, Aryl) ppm. Solid-state CPMAS ^{31}P NMR (R.T.): δ -3.4, 24.4 ppm.

$[(\text{Au}\{\text{P}(m\text{-FPh})_3\})_4(\mu_4\text{-O})]_2[\alpha\text{-SiMO}_{12}\text{O}_{40}]\cdot 4\text{H}_2\text{O}$ (**2**): In the synthesis of **1**, $\text{H}_4[\alpha\text{-SiMO}_{12}\text{O}_{40}]\cdot 12\text{H}_2\text{O}$ (0.102 g, 0.050 mmol) was used instead of $\text{H}_3[\alpha\text{-PMO}_{12}\text{O}_{40}]\cdot 14\text{H}_2\text{O}$, and $[\text{Au}(\text{RS-pyrrld})\{\text{P}(m\text{-FPh})_3\}]$ (0.257 g, 0.400 mmol) was also used. After 10 days, the yellow block crystals were formed. Yield: 0.014 g (4.64%). The crystalline samples were soluble in DMSO, but insoluble in H_2O , EtOH and Et_2O . Calcd. for $\text{C}_{144}\text{H}_{104}\text{O}_{46}\text{F}_{24}\text{Si}_1\text{P}_8\text{Mo}_{12}\text{Au}_8$ or $[(\text{Au}\{\text{P}(m\text{-FPh})_3\})_4(\mu_4\text{-O})]_2[\alpha\text{-SiMO}_{12}\text{O}_{40}]\cdot 4\text{H}_2\text{O}$: C, 28.69; H, 1.74%. Found: C, 29.10; H, 1.49%. TG/DTA under atmospheric conditions: a weight loss of 1.07% because of desorption of H_2O was observed at temperature less than 240.4 $^\circ\text{C}$; calcd. 1.19% for four H_2O molecules.

IR (KBr) (cm^{-1}): 1601 m, 1579 s, 1475 m, 1420 m, 1305 vw, 1268 w, 1225 s, 1163 vw, 1095 w, 999 vw, 984 vw, 943 m, 900 vs, 870 m, 806 vs, 796 vs, 784 vs, 691 s, 683 s, 628 m, 583 s, 523 s, 511 s, 469 s. $^{31}\text{P}\{^1\text{H}\}$ NMR (26.4 °C, DMSO-*d*₆): δ 25.67 (main), 43.38 (minor) ppm. ^1H NMR (25.0 °C, DMSO-*d*₆): δ 7.37–7.72 (m, *Aryl*) ppm. Solid-state CPMAS ^{31}P NMR (R.T.): δ 19.6, 24.4 ppm.

$[(\text{Au}\{\text{P}(m\text{-MePh})_3\})_4(\mu_4\text{-O})]_2[\alpha\text{-SiW}_{12}\text{O}_{40}]$ (**3**): In the synthesis of **2**, $\text{H}_4[\alpha\text{-SiW}_{12}\text{O}_{40}] \cdot 10\text{H}_2\text{O}$ (0.153 g, 0.050 mmol) was used instead of $\text{H}_4[\alpha\text{-SiMo}_{12}\text{O}_{40}] \cdot 12\text{H}_2\text{O}$, and $[\text{Au}(\text{RS-pyrrld})\{\text{P}(m\text{-MePh})_3\}]$ (0.252 g, 0.400 mmol) was also used in place of $[\text{Au}(\text{RS-pyrrld})\{\text{P}(m\text{-FPh})_3\}]$. After 10 days, the pale-yellow block crystals were formed. Yield: 0.247 g (71.4%). The crystalline samples were insoluble in H_2O , EtOH, Et₂O and DMSO. Calcd. for $\text{C}_{168}\text{H}_{168}\text{O}_{42}\text{Si}_1\text{P}_8\text{W}_{12}\text{Au}_8$ or $[(\text{Au}\{\text{P}(m\text{-MePh})_3\})_4(\mu_4\text{-O})]_2[\alpha\text{-SiW}_{12}\text{O}_{40}]$: C, 29.17; H, 2.45%. Found: C, 28.68; H, 2.17%. TG/DTA under atmospheric conditions: no weight loss was observed at below 214.6 °C. IR (KBr) (cm^{-1}): 1592 w, 1576 w, 1476 m, 1448 m, 1403 m, 1379 w, 1311 w, 1277 vw, 1221 w, 1174 vw, 1108 m, 1039 vw, 1010 m, 996 w, 970 vs, 921 vs, 881 s, 805 vs, 691 vs, 569 m, 561 m, 531 s, 491 m, 465 m, 450 s. Solid-state CPMAS ^{31}P NMR (R.T.): δ 18.3, 28.5 ppm.

$[(\text{Au}\{\text{P}(m\text{-MePh})_3\})_4(\mu_4\text{-O})]_2[\alpha\text{-SiMo}_{12}\text{O}_{40}]$ (**4**): $[\text{Au}(\text{RS-pyrrld})\{\text{P}(m\text{-MePh})_3\}]$ (0.252 g, 0.400 mmol) was dissolved in 25 mL of CH_2Cl_2 . A yellow clear solution of $\text{H}_4[\alpha\text{-SiMo}_{12}\text{O}_{40}] \cdot 12\text{H}_2\text{O}$ (0.102 g, 0.050 mmol) dissolved in 15 mL of an EtOH– H_2O (5:1, *v/v*) mixed solvent was slowly added along an interior wall of a round-bottomed flask containing a colorless clear solution of the phosphanegold(I) complex. The round-bottomed flask containing two layers was sealed and left in the dark at room temperature. After 7 days, the yellow block crystals formed around the interface of the two layers, which were collected on a membrane filter (JG 0.2 μm), washed with EtOH (20 mL \times 2) and Et₂O (20 mL \times 2), and dried *in vacuo* for 2 h. Yield: 0.137 g (46.7%). The crystalline samples were insoluble in H_2O , EtOH, Et₂O and DMSO. Calcd. for $\text{C}_{168}\text{H}_{168}\text{O}_{42}\text{Si}_1\text{P}_8\text{Mo}_{12}\text{Au}_8$ or $[(\text{Au}\{\text{P}(m\text{-MePh})_3\})_4(\mu_4\text{-O})]_2[\alpha\text{-SiMo}_{12}\text{O}_{40}]$: C, 34.42; H, 2.89%. Found: C, 34.35; H, 2.70%. TG/DTA under atmospheric conditions: no weight loss was observed at below 222.4 °C. IR (KBr) (cm^{-1}): 1591 w, 1575 w, 1475 w, 1446 w, 1403 w, 1310 vw, 1221 vw, 1174 vw, 1107 w, 1040 vw, 995 vw, 983 w, 947 s, 902 vs, 861 m, 804 vs, 794 vs, 691 m, 681 m, 568 w, 532 w, 491 w, 465 w, 449 m. Solid-state CPMAS ^{31}P NMR (R.T.): δ 17.4, 27.7 ppm.

$\{[(\text{Au}\{\text{P}(p\text{-MePh})_3\})_4(\mu_4\text{-O})]\{(\text{Au}\{\text{P}(p\text{-MePh})_3\})_3(\mu_3\text{-O})\}][\alpha\text{-PW}_{12}\text{O}_{40}]\}$ (**5**): A solution of $[\text{Au}(\text{RS-pyrrld})\{\text{P}(p\text{-MePh})_3\}]$ (0.189 g, 0.300 mmol) dissolved in 25 mL of CH_2Cl_2 was slowly added to a colorless clear solution of $\text{Na}_3[\alpha\text{-PW}_{12}\text{O}_{40}] \cdot 9\text{H}_2\text{O}$ (0.155 g, 0.050 mmol) dissolved in 15 mL of an EtOH– H_2O (5:1, *v/v*) mixed solvent. After stirring for 1 h at room temperature, the reaction solution was concentrated to 15 mL with a rotary evaporator at 30 °C. A pale-yellow white powder was collected on a membrane filter (JV 0.1 μm), washed with H_2O (20 mL \times 2), EtOH (20 mL \times 2) and Et₂O (20 mL \times 2), and dried *in vacuo* for 2 h. At this stage, the pale-yellow white powder was obtained in a yield of 0.23 g.

Crystallization. The pale-yellow white powder (0.100 g) was dissolved in 20 mL of a CH_2Cl_2 –EtOH (3:1, *v/v*) mixed solvent and was filtered through a folded filter paper (Whatman No. 5). The pale-yellow clear filtrate was slowly evaporated at room temperature in the dark. After 3 days, colorless plate crystals were formed and collected on a membrane filter (JV 0.1 μm), washed with EtOH (10 mL \times 2) and Et₂O (10 mL \times 2), and dried *in vacuo* for 2 h. Yield: 0.026 g (26.0%). The crystalline samples were soluble in DMSO and sparingly soluble in CH_2Cl_2 , but insoluble in H_2O , EtOH and Et₂O. Calcd. for $\text{C}_{147}\text{H}_{147}\text{O}_{42}\text{P}_8\text{W}_{12}\text{Au}_7$ or $\{[(\text{Au}\{\text{P}(p\text{-MePh})_3\})_4(\mu_4\text{-O})]\{(\text{Au}\{\text{P}(p\text{-MePh})_3\})_3(\mu_3\text{-O})\}][\alpha\text{-PW}_{12}\text{O}_{40}]\}$:

C, 27.51; H, 2.31%. Found: C, 27.51; H, 2.63%. TG/DTA under atmospheric conditions: no weight loss was observed at below 203.6 °C. IR (KBr) (cm^{-1}): 1597 w, 1496 w, 1445 w, 1397 w, 1309 vw, 1189 w, 1103 m, 1079 s, 977 s, 896 m, 821 vs, 802 vs, 706 w, 647 w, 633 w, 619 w, 526 m, 510 m. $^{31}\text{P}\{^1\text{H}\}$ NMR (26.7 °C, DMSO- d_6): δ -14.88, 22.39 ppm. ^1H NMR (25.6 °C, DMSO- d_6): δ 2.25 (s, *Me*), 7.10–7.30 (m, *Aryl*) ppm. Solid-state CPMAS ^{31}P NMR (R.T.): δ -14.6, 23.1 ppm.

3.4. X-ray Crystallography

Single crystals with dimensions of $0.30 \times 0.08 \times 0.07 \text{ mm}^3$ for **1**, $0.06 \times 0.06 \times 0.04 \text{ mm}^3$ for **2**, $0.23 \times 0.13 \times 0.07 \text{ mm}^3$ for **3**, $0.31 \times 0.26 \times 0.15 \text{ mm}^3$ for **4** and $0.08 \times 0.07 \times 0.02 \text{ mm}^3$ for **5** were mounted on cryoloops using liquid paraffin and cooled by a stream of cooled N_2 gas. Data collection was performed on a Bruker (Madison, WI, USA) SMART APEX CCD diffractometer at 100 K for **1**, **4** and **5**, and Rigaku (Tokyo, Japan) VariMax with Saturn CCD diffractometer at 120 K for **2** and **3**. The intensity data were automatically collected for Lorentz and polarization effects during integration. The structure was solved by direct methods (program *SHELXS-97*) followed by subsequent difference Fourier calculation and refined by a full-matrix, least-squares procedure on F^2 (program *SHELXL-97*) [28]. Absorption correction was performed with *SADABS* (empirical absorption correction) [29]. The compositions and formulae of the POMs containing many solvated molecules were determined by CHN elemental analysis, TG/DTA and ^1H NMR. Any solvent molecules in the structure were highly disordered and impossible to refine by using conventional discrete-atom models. To resolve these issues, the contribution of the solvent electron density was removed by using the *SQUEEZE* routine in *PLATON* for **1** [30]. The details of the crystallographic data for **1–5** are listed in Table 1, and bond lengths (\AA) and angles ($^\circ$) for **1–5** are shown in Tables S1–S5. CCDC 1028278 (**1**), 1028279 (**2**), 1028280 (**3**), 1028281 (**4**) and 1028282 (**5**), respectively. Polyhedral representation in Figure 1 was drawn by using the VESTA 3 series [31].

4. Conclusions

In this paper, we prepared and characterized various novel intercluster compounds **1–5** by POM-mediated clusterization. Formation of these gold(I) cluster cations in **1–5** was strongly dependent upon the charge density and acidity of the POMs, and substituted position on the aryl group of triarylphosphane ligands as well. The structures of phosphanegold(I) cluster cations were stabilized by the intra-cluster and inter-cluster aurophilic interactions, and also interactions between the gold(I) cluster cations and POM anions. The two free-acid forms of Keggin POMs with heteroatom Si provided the trigonal-pyramidal structures of the tetraphosphanegold(I) cluster cations in the intercluster compounds, *i.e.*, $[(\text{Au}\{\text{P}(m\text{-FPh})_3\})_4(\mu_4\text{-O})]_2[\alpha\text{-SiMo}_{12}\text{O}_{40}] \cdot 4\text{H}_2\text{O}$ (**2**), $[(\text{Au}\{\text{P}(m\text{-MePh})_3\})_4(\mu_4\text{-O})]_2[\alpha\text{-SiW}_{12}\text{O}_{40}]$ (**3**) and $[(\text{Au}\{\text{P}(m\text{-MePh})_3\})_4(\mu_4\text{-O})]_2[\alpha\text{-SiMo}_{12}\text{O}_{40}]$ (**4**). The reaction of the less-acidic Keggin POM, *i.e.*, $\text{Na}_3[\alpha\text{-PW}_{12}\text{O}_{40}] \cdot 9\text{H}_2\text{O}$, with the monomeric gold(I) precursor complex containing para-methyl group substituted triarylphosphane ligands has formed the intercluster compound of heptaphosphanegold(I) cluster cation, *i.e.*, $\{[(\text{Au}\{\text{P}(p\text{-MePh})_3\})_4(\mu_4\text{-O})]\{(\text{Au}\{\text{P}(p\text{-MePh})_3\})_3(\mu_3\text{-O})\}][\alpha\text{-PW}_{12}\text{O}_{40}]$ (**5**). This work suggests the synthetic routes of a variety of oxygen-centered phosphanegold(I) clusters formed by a combination of the monomeric phosphanegold(I) carboxylate and the various POMs such as Dawson

and Anderson POMs, lacunary species of Keggin and Dawson POMs, and so on. Research in this direction is in progress.

Acknowledgments

This work was supported by JSPS KAKENHI grant number 22550065 and also by the Strategic Research Base Development Program for Private Universities of the Ministry of Education, Culture, Sports, Science and Technology of Japan.

Author Contributions

The synthesis and characterization of **1–4** were performed by Takuya Yoshida. The synthesis and characterization of **5** were performed by Yuta Yasuda. Characterization of these compounds were assisted by Eri Nagashima and Hidekazu Arai. Full research assistance and methodology were provided by Satoshi Matsunaga and Kenji Nomiya. The preparation of the manuscript was made by all the authors.

Conflicts of Interest

The authors declare no conflict of interest.

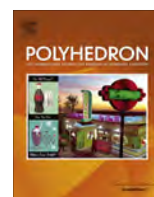
References

1. Pope, M.T.; Müller, A. Polyoxometalate Chemistry: An Old Field with New Dimensions in Several Disciplines. *Angew. Chem. Int. Ed. Engl.* **1991**, *30*, 34–48.
2. Hill, C.L.; Prosser-McCartha, C.M. Homogeneous catalysis by transition metal oxygen anion clusters. *Coord. Chem. Rev.* **1995**, *143*, 407–455.
3. Okuhara, T.; Mizuno, N.; Misono, M. Catalytic Chemistry of Heteropoly Compounds. *Adv. Catal.* **1996**, *41*, 113–252.
4. Proust, A.; Thouvenot, R.; Gouzerh, P. Functionalization of polyoxometalates: Towards advanced applications in catalysis and materials science. *Chem. Commun.* **2008**, 1837–1852.
5. Long, D.-L.; Tsunashima, R.; Cronin, L. Polyoxometalates: Building Blocks for Functional Nanoscale Systems. *Angew. Chem. Int. Ed.* **2010**, *49*, 1736–1758.
6. Nomiya, K.; Sakai, Y.; Matsunaga, S. Chemistry of Group IV Metal Ion-Containing Polyoxometalates. *Eur. J. Inorg. Chem.* **2011**, *2011*, 179–196.
7. Schulz-Dobrick, M.; Jansen, M. Supramolecular Intercluster Compounds Consisting of Gold Clusters and Keggin Anions. *Eur. J. Inorg. Chem.* **2006**, *2006*, 4498–4502.
8. Schulz-Dobrick, M.; Jansen, M. Synthesis and Characterization of Intercluster Compounds Consisting of Various Gold Clusters and Differently Charged Keggin Anions. *Z. Anorg. Allg. Chem.* **2008**, *634*, 2880–2884.
9. Noguchi, R.; Hara, A.; Sugie, A.; Nomiya, K. Synthesis of novel gold(I) complexes derived by AgCl-elimination between [AuCl(PPh₃)] and silver(I) heterocyclic carboxylates, and their antimicrobial activities. Molecular structure of [Au(*R,S*-Hpyrrld)(PPh₃)] (H₂pyrrld = 2-pyrrolidone-5-carboxylic acid. *Inorg. Chem. Commun.* **2006**, *9*, 355–359.

10. Nomiya, K.; Yoshida, T.; Sakai, Y.; Nanba, A.; Tsuruta, S. Intercluster Compound between a Tetrakis{triphenylphosphinegold(I)}oxonium Cation and a Keggin Polyoxometalate (POM): Formation during the Course of Carboxylate Elimination of a Monomeric Triphenylphosphinegold(I) Carboxylate in the Presence of POMs. *Inorg. Chem.* **2010**, *49*, 8247–8254.
11. Yoshida, T.; Nomiya, K.; Matsunaga, S. Novel intercluster compound between a heptakis{triphenylphosphinegold(I)}dioxonium cation and an α -Keggin polyoxometalate anion. *Dalton Trans.* **2012**, *41*, 10085–10090.
12. Yoshida, T.; Matsunaga, S.; Nomiya, K. Two types of tetranuclear phosphane-gold(I) cations as dimers of dinuclear units, $[(\text{Au}\{\text{P}(p\text{-RPh})_3\})_2(\mu\text{-OH})]_2^{2+}$ ($R = \text{Me}, \text{F}$), synthesized by polyoxometalate-mediated clusterization. *Dalton Trans.* **2013**, *42*, 11418–11425.
13. Yoshida, T.; Matsunaga, S.; Nomiya, K. Novel Intercluster Compounds Composed of a Tetra{phosphane-gold(I)}oxonium Cation and an α -Keggin Polyoxometalate Anion Linked by Three Monomeric Phosphane-gold(I) Units. *Chem. Lett.* **2013**, *42*, 1487–1489.
14. Yoshida, T.; Yasuda, Y.; Nagashima, E.; Arai, H.; Matsunaga, S.; Nomiya, K. Template Effects of Polyoxometalate (POM) in the Formation of Dimer-of-Dinuclear Phosphane-gold(I) Clusters by POM-Mediated Clusterization. Kanagawa university, Hiratsuka, Japan, Unpublished work, 2014.
15. Schmidbaur, H. Ludwig Mond Lecture. High-carat gold compounds. *Chem. Soc. Rev.* **1995**, *24*, 391–400.
16. Schmidbaur, H.; Schier, A. A briefing on aurophilicity. *Chem. Soc. Rev.* **2008**, *37*, 1931–1951.
17. Gimeno, M.C.; Laguna, A. Chalcogenide centred gold complexes. *Chem. Soc. Rev.* **2008**, *37*, 1951–1966.
18. Nesmeyanov, A.N.; Perevalova, E.G.; Struchkov, Y.T.; Antipin, M.Y.; Grandberg, K.I.; Dyadchenko, V.P. Tris{triphenylphosphinegold}oxonium salts. *J. Organomet. Chem.* **1980**, *201*, 343–349.
19. Yang, Y.; Ramamoorthy, V.; Sharp, P.R. Late transition metal oxo and imido complexes. 11. Gold(I) oxo complexes. *Inorg. Chem.* **1993**, *32*, 1946–1950.
20. Angermaier, K.; Schmidbaur, H. A New Structural Motif of Gold Clustering at Oxide Centers in the Dication $[\text{Au}_6\text{O}_2(\text{PMe}_3)_6]^{2+}$. *Inorg. Chem.* **1994**, *33*, 2069–2070.
21. Chung, S.-C.; Krüger, S.; Schmidbaur, H.; Rösch, N. A Density Functional Study of Trigold Oxonium Complexes and of Their Dimerization. *Inorg. Chem.* **1996**, *35*, 5387–5392.
22. Rocchiccioli-Deltcheff, C.; Fournier, M.; Franck, R.; Thouvenot, R. Vibrational Investigations of Polyoxometalates. 2. Evidence for Anion–Anion Interactions in Molybdenum(VI) and Tungsten(VI) Compounds Related to the Keggin Structure. *Inorg. Chem.* **1983**, *22*, 207–216.
23. Wells, A.F. *Structural Inorganic Chemistry*, 4th ed.; Clarendon Press: Oxford, UK, 1975; p. 1020.
24. Bondi, A. van der Waals Volumes and Radii. *J. Phys. Chem.* **1964**, *68*, 441–451.
25. North, E.O.; Haney, W. Silicomolybdic Acid. *Inorg. Synth.* **1939**, *1*, 127–129.
26. Tézé, A.; Hervé, G. α -, β -, and γ -Dodecatungstosilicic Acids: Isomers and Related Lacunary Compounds. *Inorg. Synth.* **1990**, *27*, 85–96.
27. Aoki, S.; Kurashina, T.; Kasahara, Y.; Nishijima, T.; Nomiya, K. Polyoxometalate (POM)-based, multi-functional, inorganic-organic, hybrid compounds: Syntheses and molecular structures of silanol- and/or siloxane bond-containing species grafted on mono- and tri-lacunary Keggin POMs. *Dalton Trans.* **2011**, *40*, 1243–1253.

28. Sheldrick, G.M. A short history of SHELX. *Acta Crystallogr.* **2008**, *64*, 112–122.
29. Sheldrick, G.M. *SADABS, Program for Area Detector Adsorption Correction*; University of Göttingen: Göttingen, Germany, 1997.
30. Spek, A.L. PLATON, an Integrated Tool for the Analysis of the Results of a Single Crystal Structure Determination. *Acta Crystallogr.* **1990**, *46*, c34.
31. Momma, K.; Izumi, F. VESTA 3 for three-dimensional visualization of crystal, volumetric and morphology data. *J. Appl. Crystallogr.* **2011**, *44*, 1272–1276.

© 2014 by the authors; licensee MDPI, Basel, Switzerland. This article is an open access article distributed under the terms and conditions of the Creative Commons Attribution license (<http://creativecommons.org/licenses/by/4.0/>).



Synthesis, characterization and antimicrobial activities of sodium salt of *L*-histidinatoargentate(I) derived from the pH 11 solution[☆]



Akihiko Takayama, Yoshitaka Takagi, Kousuke Yanagita, Chisato Inoue, Rie Yoshikawa, Noriko Chikaraishi Kasuga, Kenji Nomiya^{*}

Department of Chemistry, Faculty of Science, Kanagawa University, Tsuchiya, Hiratsuka, Kanagawa 259-1293, Japan

ARTICLE INFO

Article history:

Received 25 December 2013

Accepted 8 March 2014

Available online 20 March 2014

We dedicate this paper to Professor Vukadin Leovac on the occasion of his 70th birthday.

Keywords:

Anionic silver(I) complex

Histidine

Water-soluble

Antimicrobial activities

ESI-MS

ABSTRACT

As the silver(I) complex with solely coordinated by histidine (H_2his) ligand, three types of complexes have been reported as different states in the solid state and in aqueous solution; water-soluble, chiral neutral complexes $\infty\{[Ag(L-Hhis)]_2\}$ (*L-1*) and $\infty\{[Ag(D-Hhis)]_2\}$ (*D-1*), water-insoluble, chiral helical polymers $\infty[Ag(L-Hhis)]$ (*L-2*) and $\infty[Ag(D-Hhis)]$ (*D-2*), water-insoluble, achiral polymer $\infty[Ag_2(D-Hhis)(L-Hhis)]$ (*DL-3*). These complexes, obtained from neutral, aqueous solutions of Ag_2O and H_2his , have shown effective antimicrobial activities against selected bacteria, yeasts and molds. In addition, it should be noted that these complexes are not toxic to humans. In this work, we report the preparation, characterization via elemental analysis, TG/DTA, FT-IR, ESI-MS, powder X-ray diffraction (PXRD), solid state ^{13}C NMR, solution 1H NMR, X-ray absorption near edge structure (XANES), extended X-ray absorption fine structure (EXAFS) and antimicrobial activities of the fourth type of silver complex, i.e., sodium salt of anionic silver(I) complex with dianionic histidine, $\infty\{Na[Ag_3(L-his)_2] \cdot nH_2O\}$ (*L-4*) ($n = 1-5$), formed in the pH 11 solution.

© 2014 Elsevier Ltd. All rights reserved.

1. Introduction

Metallic silver, silver nanoparticles, silver salts, and silver complexes are known to exhibit antimicrobial activities [1–7]. To understand the interaction between the silver(I) ion and biomolecules a series of silver(I) complexes with amino acid ligands have been prepared [6–8].

Silver(I) complexes of amino acids with N and O donor atoms and without an S atom have been classified into four types (I–IV) based on the bonding modes of the silver(I) center [6,9]. Type I contains only Ag–O bonds, while type II contains alternating two-coordinate O–Ag–O and N–Ag–N bonding units. Type III contains repeating two-coordinate N–Ag–O bonding units and type IV contains only Ag–N bonds. Reactions of Ag_2O and histidine (*L*-, *D*-, *DL*- H_2his) in neutral aqueous solutions are known to produce three types (1–3) of Ag–N bonding complexes [10,11]. On the other hand, under acidic conditions the reaction of $AgNO_3$ with H_2his produces cationic histidine (H_3his^+) Ag–O complexes [12]. The first type of Ag–N bonding complex was found to be a water-soluble silver(I) complex with an *L*-histidine monoanion (*L*- $Hhis^-$) $\infty\{[Ag(L-Hhis)] \cdot 0.2EtOH\}_2\}$ (*L-1*).

In aqueous solution *L-1* existed as a dimer, whereas in the solid-state it existed as polymer formed through intermolecular hydrogen-bonding interactions between the CO_2^- group and the $N_{\delta 1}$ atoms of the dimeric $[Ag(L-Hhis)]_2$ cores [10]. Crystallization of *L-1* by slow evaporation and/or vapor diffusion gave water-insoluble crystals of the second type of Ag–N complex $\infty[Ag(L-Hhis)]$ (*L-2*). The *L-1* complex was a polymer formed by intermolecular hydrogen bonding interactions between dimeric $[Ag(Hhis)]_2$ cores in the solid-state, while *L-2* was a different polymer without a core complex. X-ray crystallography revealed that *L-2* was a left-handed helical polymer consisting of a bent, 2-coordinate silver(I) atom bonded to the N_{α} atom of one $Hhis^-$ ligand and the $N_{\delta 1}$ atom of a different $Hhis^-$ ligand. Notably, O_{carboxyl} atoms did not participate in the coordination. The FT-IR, and the solid-state ^{13}C NMR spectra showed that the dimeric core of *L-1* was formed through Ag–N bonds. The molecular ion of *L-1* was detected by positive-ion electrospray ionization mass spectrometry (ESI-MS). For *L-1*, characterization was performed by elemental analysis, TG/DTA, FT-IR, variable-temperature solid-state ^{13}C NMR and solution molecular weight measurements, and solution (^{109}Ag , 1H and ^{13}C) NMR spectroscopies. The third type of silver(I) histidinate complex was of the meso-form (*DL-3*) prepared from two neutral aqueous solutions of chiral silver(I) histidinates, *D-1* and *L-1*, indicating that the ligand exchange of *D*- $Hhis^-$ and *L*- $Hhis^-$ occurred around Ag^+ in water [11]. The crystal structure of *DL-3* showed that the coordination polymer of the

[☆] Note: The abbreviation for the neutral histidine molecule should be denoted as H_2his , but not $Hhis$ denoted in the references 10 and 11, because the histidine (2-) anion is coordinated to a silver(I) atom.

^{*} Corresponding author. Tel.: +81 463 59 4111; fax: +81 463 58 9684.

E-mail address: nomiya@kanagawa-u.ac.jp (K. Nomiya).

[Ag₂(D-Hhis)(L-Hhis)] cores was constructed by two kinds of Ag···Ag interaction. The core structure of DL-3 corresponded to the predicted structure of the dimeric [Ag(Hhis)]₂ core of L-1. The structure of DL-3 was different from those of the chiral helical polymers (D-2 and L-2).

The silver(I) complexes with Ag–N bonds, especially silver(I) histidines showed remarkable antimicrobial activities against selected bacteria, yeasts and a mold [10,11]. Not only did they show effective antimicrobial activities, but they were also relatively nontoxic to humans. In fact, the materials containing L-1 as a major component were recently commercialized by a Japanese company as a preservative agent [13]. The antibacterial and antifungal activities of L-1 were remarkable and comparable to those of silver(I)-N-heterocycle complexes. The water-insoluble Ag–N bonding complex DL-3 moderately inhibited the growth of bacteria and yeasts. Recently, “silver-resistant” bacteria were found, where the coordination of the histidine residue to Ag^I played an important role [12].

Histidine is a versatile amino acid with at least three tautomers that have been extensively studied using solid-state NMR [14]. During the course of our studies on silver amino-acid complexes, we found the fourth type of Ag–N bonding complex, i.e., the anionic, trinuclear silver(I) complex with dianionic histidine prepared under basic conditions. In this work, we report the preparation and antimicrobial activities of this complex as the sodium salt, ∞{Na[Ag₃(L-his)₂·nH₂O]} (L-4) (n = 1–5), formed under basic conditions (pH 11) (Chart 1).

2. Experimental

2.1. Materials

The following reagent-grade chemicals were used as received: Ag₂O, Et₂O, L-H₂his, dimethyl sulfoxide (DMSO), EtOH, CHCl₃, CH₂Cl₂, MeOH, EtOAc, CH₃CN, and acetone (Wako); 4, 4-dimethyl-4-silapentane-1-sulfonic acid (DSS) (Aldrich); and D₂O (99.9 D atom%, Isotec).

2.2. Measurements

CHN elemental analyses were performed using a Perkin-Elmer PE2400 series II CHNS/O analyzer. Thermogravimetric (TG) and differential thermal analyses (DTA) were performed under air with a temperature ramp of 4 °C min⁻¹ using a Rigaku Thermo Plus 2 TG 8120 instrument between 30 and 500 °C. Infrared spectra were recorded on a JASCO FT-IR 4100 spectrometer at room temperature using KBr disks. ESI-MS spectra in positive and negative-ion modes were recorded using JEOL JMS-T100LC in the range of *m/z* 100–4000. Sodium trifluoroacetate was used as an internal reference. PXD data were recorded on Rigaku Ultima IV at ambient temperature. Solid-state ¹³C NMR spectra were recorded in 6-mm outer diameter rotors on a JEOL JNM-ECP 300 FT-NMR spectrometer equipped with a cross-polarization/magic angle spinning accessory. Carbon chemical shifts were referenced to external hexamethylbenzene (17.13 ppm). ¹H NMR spectra in D₂O were recorded at ambient temperature on a JEOL ECP300 NMR or a JEOL ECP500 NMR spectrometer with DSS as the internal reference.

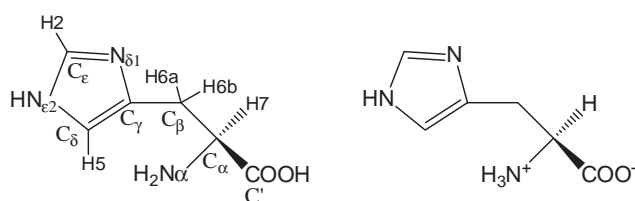


Chart 1. Structure and labelling of L-histidine (L-H₂his) and its zwitterion.

X-ray absorption near edge structure (XANES) and extended X-ray absorption fine structure (EXAFS) data were obtained by the Toray Research Center. The Ag K-edge (25516.5 eV) X-ray absorption spectra of L-4 were measured at the beamline NW10A at the Photon Factory of the High Energy Accelerator Research Organization in Tsukuba, Japan. Viscosity was measured using a TVC-5 viscometer of TOKI SANGYO Co. Ltd.

The antimicrobial activities of ∞{Na[Ag₃(L-his)₂·5H₂O]} (L-4, n = 5) were estimated by minimum inhibitory concentration (MIC: μg mL⁻¹) in water, as described elsewhere [15,16].

2.3. Synthesis and characterization of the sodium salt of the 3:2 complex, ∞{Na[Ag₃(L-his)₂·nH₂O]} (L-4) (n = 1–5), formed from the pH 11 solution

L-H₂his (0.310 g, 2.0 mmol) was added to Ag₂O (0.232 g, 1.0 mmol)-suspended in 30 mL water and the solution was stirred for 2 h. The pH of the pale yellow clear solution (ca. pH 7.0) was adjusted to ca. 11.0 using 1 M aqueous NaOH and the solution was stirred for 1 h. The pale yellow, clear gelatinous solution that formed was filtered through a folded filter paper (Whatman #5). The filtrate was added to 300 mL of EtOH. A white powder formed was collected on a membrane filter (JG 0.2 μm), washed with EtOH (50 mL × 2), and Et₂O (50 mL × 2), and was thoroughly dried in vacuo for 2 h. The yield was 0.39 g. The hygroscopic, white powder was soluble in water, but insoluble in other solvents. Anal. Calc. for C₁₂H₁₈O₆N₆Na₁Ag₃ or “Na[Ag₃(L-his)₂·2H₂O]” as a monomer unit: C, 20.92; H, 2.63; N, 12.20. Found: C, 20.93; H, 2.64; N, 12.00%. TG/DTA data: a weight loss of 7.38% was observed at before 205.4 °C due to the dehydration of 3 water molecules: calc. 7.65% for 3 H₂O molecules due to the hygroscopic nature of L-4. Decomposition began at around 205.4 °C with exothermic peaks at 210.2 and 509.7 °C. Prominent IR bands in 1800–400 cm⁻¹ region (KBr disk): 1570 vs 1559 vs 1507 m, 1465 s, 1410 s, 1350 m, 1290 w, 1227 w, 1154 vw, 1116 w, 1039 w, 971 vw, 929 vw, 834 w, 787 w, 655 m cm⁻¹.

PXD data showed that isolated powders of L-4 had low crystallinity. ¹H NMR (D₂O, 23.6 °C): δ 3.12–3.25 (2H, br, H6), 3.75 (1H, s, H7), 7.14 (1H, s, H5), 7.86 (1H, s, H2). When the powder was re-dissolved in water, highly viscous solution was reformed. Solution ¹³C and ¹⁰⁹Ag NMR spectra were not obtained because of the viscosity of the aqueous solution of L-4. Solid-state ¹³C NMR: 34.92 (Cβ), 58.42 (Cα), 126.16 (Cδ), 134.38 (Cγ), 144.17 (Cε), 179.41 (C').

ESI-MS in the negative-ion mode: [Ag(L-his)]¹⁻ (*m/z* found 259.95 and 261.96, calcd 259.96 and 261.99), [Ag(L-Hhis)₂]¹⁻ (*m/z* found 415.04 and 417.03, calcd 415.03 and 417.03), [Ag₂(L-Hhis)(L-his)]¹⁻ (*m/z* found 520.91, 522.93 and 524.93, calcd 520.93, 522.93 and 524.93), [Ag₃(L-his)₂]¹⁻ (*m/z* found 626.82, 628.80, 630.80 and 632.81, calcd 626.82, 628.82, 630.82 and 632.82), [Ag₃(L-Hhis)₂(L-his)]¹⁻ (*m/z* found 781.88, 783.88, 785.89 and 787.90, calcd 781.89, 783.89, 785.89 and 787.89); ESI-MS in the positive-ion mode: {[Ag(L-H₂his)]}¹⁺ (*m/z* found 261.99 and 263.99, calcd 261.97 and 263.97), {[Ag(L-H₂his)₂]}¹⁺ (*m/z* found 417.07 and 419.08, calcd 417.04 and 419.04), {Na[Ag(L-Hhis)]₂}¹⁺ (*m/z* found 544.98, 546.96 and 548.97, calcd 544.92, 546.92 and 548.92), {[Ag₃(L-Hhis)₂]}¹⁺ (*m/z* found 628.90, 630.89, 632.89 and 634.90, calcd 628.84, 630.84, 632.84 and 634.84). HR ESI-MS positive-ion mode: (*m/z*) 261.9794 and 263.9741, calcd for C₁₂H₁₈N₆O₄Ag or [Ag(L-H₂his)₂]¹⁺ 261.9745 and 263.9742.

3. Results and discussion

3.1. Characterization of L-4

Because histidine has several tautomers and several donor atoms, there are several coordination modes of histidine to silver(I).

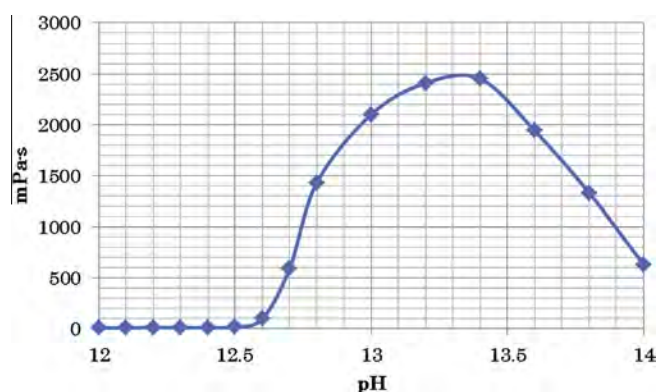


Fig. 1. Plot of pH vs. viscosity (mPa·s) of Ag_2O and $L\text{-H}_2\text{his}$ mixture (1:2 M ratio) in water.

Fromm and coworkers isolated $[\{\text{Ag}(L\text{-H}_2\text{his})_2\text{NO}_3\}_2]\cdot\text{H}_2\text{O}$, $[\{\text{Ag}(L\text{-H}_3\text{his})(\text{NO}_3)_2\}_2]\cdot\text{H}_2\text{O}$ and $[\{\text{Ag}_2(D\text{-H}_3\text{his})(L\text{-H}_3\text{his})(\text{NO}_3)_4\}]$ from L - or DL -histidine with AgNO_3 under neutral or acidic conditions [12]. Under neutral conditions, the N atom of the imidazole moiety coordinates to silver, while the oxygen atoms of carboxy group coordinate to the metal ions under acidic conditions.

We isolated water-soluble chiral complexes $[\text{Ag}(L\text{-Hhis})_2]$ ($L\text{-1}$), $[\text{Ag}(D\text{-Hhis})_2]$ ($D\text{-1}$), water-insoluble, chiral helical polymers

$[\text{Ag}(L\text{-Hhis})]$ ($L\text{-2}$) and $[\text{Ag}(D\text{-Hhis})]$ ($D\text{-2}$), water-insoluble, achiral polymer $[\text{Ag}_2(D\text{-Hhis})(L\text{-Hhis})]$ ($DL\text{-3}$) from Ag_2O and histidines without controlling the pH [10,11]. During our studies on the effect of pH by addition of alkali hydroxides, we found that the viscosity of the solution was dramatically increased at pH values greater than 12 due to the formation of a novel polymeric silver(I) histidine complex (Fig. 1). In addition to the sodium salt of silver(I) histidinate, potassium, rubidium and cesium salts were also prepared using the corresponding hydroxides. All formulas were denoted by $[\text{M}[\text{Ag}_3(\text{his})_2]\cdot n\text{H}_2\text{O}]$ ($\text{M} = \text{Na}, \text{K}, \text{Rb}$ and Cs) and the viscosities of the solutions were in the order of $\text{Na} < \text{K} < \text{Rb}$ and Cs . The purity of the sodium salt was the highest according to elemental analysis.

We isolated the complex ($L\text{-4}$) from the solution (pH 11, aqueous NaOH) by pouring the reaction mixture into ethanol before the mixture became highly viscous. The formula of the novel, hygroscopic silver(I) complex was determined by ESI-MS and elemental analysis as $[\text{Na}[\text{Ag}_3(L\text{-his})_2]\cdot n\text{H}_2\text{O}]$ ($n = 1\text{--}5$). The number of hydrated water molecules was evaluated by thermal analysis and elemental analysis. In the IR spectra of $L\text{-2}$ and $L\text{-4}$, the band at 1253 cm^{-1} based on the imidazole was shifted to 1226 cm^{-1} , suggesting the deprotonation of the imidazolium ion. The large difference between the $\nu_{\text{C=O}}$ of ($L\text{-1}$ and $L\text{-2}$ (1630 cm^{-1})) and $L\text{-4}$ (1570 cm^{-1}) may suggest the presence of a weak interaction between Na^+ and COO^- .

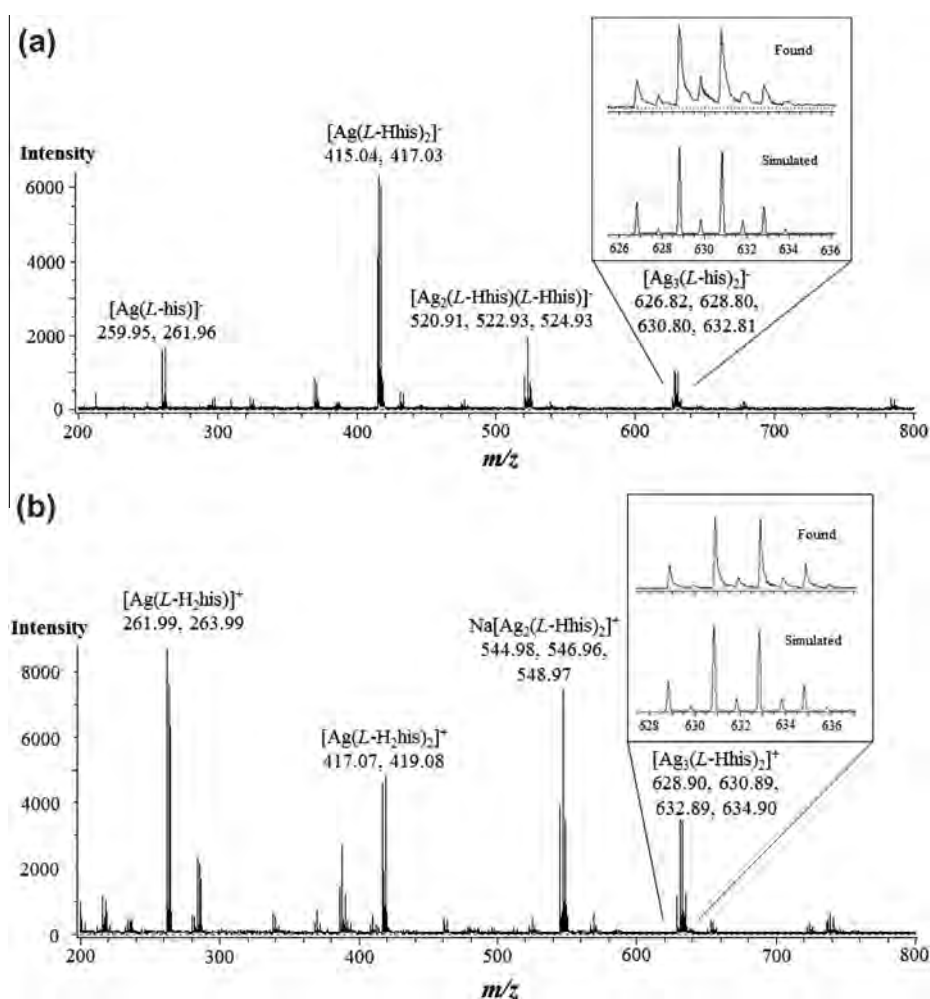


Fig. 2. (a) Negative-ion ESI-MS of an aqueous solution of $[\text{Na}[\text{Ag}_3(L\text{-his})_2]\cdot n\text{H}_2\text{O}]$ ($n = 1\text{--}5$) ($L\text{-4}$) in the range of m/z 230–800. The inset shows an enlargement around the peak m/z 630. (b) Positive-ion ESI-MS of an aqueous solution of $[\text{Na}[\text{Ag}_3(L\text{-his})_2]\cdot n\text{H}_2\text{O}]$ ($n = 1\text{--}5$) ($L\text{-4}$) in the range of m/z 230–800. The inset also shows an enlargement around the peak m/z 630.

ESI-MS in the negative-ion mode in aqueous solution was measured in the range of m/z 100–4000 (Fig. 2(a)). The natural abundance of ^{107}Ag and ^{109}Ag is 51.35% and 48.65%, respectively. The observed signals of silver(I) complexes were compared with simulated data. In Fig. 2 several peaks were observed due to the approximate 1:3:3:1 intensity ratio indicative of trinuclear ($[\text{Ag}_3(\text{L-Hhis})_2(\text{L-his})]^-$ and $[\text{Ag}_3(\text{L-his})_2]^-$) species, while the 1:2:1 intensity ratio is indicative of dinuclear ($[\text{Ag}_2(\text{L-Hhis})(\text{his})]^-$ and $[\text{Ag}_2(\text{L-Hhis})_2]^-$) species. The 1:1 intensity ratio is indicative of mononuclear ($[\text{Ag}(\text{L-his})]^-$ and $[\text{Ag}(\text{L-Hhis})_2]^-$) species. These data were consistent with the CHN elemental analysis data. ESI-MS in the positive-ion mode also showed that the molecular ion peak of the trinuclear 3:2 complex, i.e., $\{\text{H}_2[\text{Ag}_3(\text{his})_2]\}^{1+}$ or $\{\text{Ag}_3(\text{Hhis})_2\}^{1+}$ (m/z 628.90), consistent with ESI-MS in the negative mode (Fig. 2(b)). Several fragmentation peaks due to the dinuclear 2:2 complexes such as $\{\text{Na}[\text{Ag}(\text{Hhis})_2]\}^{1+}$ (m/z 544.98) and the mononuclear 1:2 and 1:1 complexes such as $\{\text{H}_2[\text{Ag}(\text{Hhis})_2]\}^{1+}$ (m/z 417.04) and $\{\text{H}[\text{Ag}(\text{Hhis})]\}^{1+}$ (m/z 261.99) were also observed.

Powder XRD shows that the trinuclear 3:2 complex had low crystallinity, suggesting that it was present as an amorphous polymer. Actually, crystallization of *L-4* was unsuccessful, because of the high viscosity of the aqueous solution of *L-4* even when the alkali metal cations were changed to K, Rb and Cs.

Changes in the solid-state ^{13}C NMR spectrum were observed in the histidine signals of *L-4* upon coordination (Fig. 3) compared to those of *L-1* and *L-2*. As the imidazole rings become anionic, C_γ , C_ϵ and C_δ shifted 7–10 ppm down field, compared to those of *L-1* and *L-2*. However, little variation in the signals was observed for C_α and C_β . The carbon chemical shifts of the carboxy groups (C') in *L-1*, *L-2* and *L-4* were almost unchanged, suggesting that the carboxy oxygen atoms were not coordinated to silver atoms. The carbon chemical shifts of the imidazole ring (C_γ , C_ϵ and C_δ) were notably shifted for *L-1* and *L-2* which contained the monoanion of histidine as compared to *L-4* with the dianion of histidine, suggesting that the N ($\text{N}\epsilon 2$ and $\text{N}\delta 1$) atoms coordinate to the metal ion in *L-4*. In the preparation of the silver(I) histidine complexes using AgNO_3 , under the acidic conditions the Ag–O bonding complex with H_3his^+ was formed ($[\text{Ag}(\text{L-H}_3\text{his})(\text{NO}_3)_2]_2$ and $[\text{Ag}_2(\text{D-H}_3\text{his})(\text{L-H}_3\text{his})(\text{NO}_3)_4]_n$

[12]. On the other hand under neutral conditions, the Ag–O, N bonding complex coordinated to two H_2his and NO_3^- ($[\text{Ag}(\text{L-H}_2\text{his})_2(\text{NO}_3)_2]$) was formed [12]. In the preparation of silver(I) histidine complexes using Ag_2O under neutral conditions, the Ag–N bonding complexes *L-1*, *L-2* and *DL-3* were formed [10,11], whereas under alkaline conditions, the trinuclear Ag–N bonding complex *L-4* was formed. On the other hand, the Ag–N bonding polymer consisting of silver(I) atom and a monoanion of imidazole, $[\text{Ag}(\text{imd})]_n$ (Himd = imidazole) as powder solids, has been prepared by a reaction of Himd and AgNO_3 under basic aqueous conditions by NaOH [16], whereas the cationic silver(I) complex $[\text{Ag}(\text{Himd})_2]\text{NO}_3$ has been synthesized by a reaction of Himd and AgNO_3 under neutral aqueous conditions [17]. In the former, two nitrogen atoms ($\text{N}\epsilon 2$ and $\text{N}\delta 1$) in the imidazole ring coordinate to silver(I) atom, while in the latter, only one nitrogen atom ($\text{N}\delta 1$) coordinates to silver(I) atom. These Ag–N bonding features and the synthetic conditions may be indicative to those of the silver(I)–histidine complexes. Broad signals of amorphous *L-1* and *L-4* in the solid-state ^{13}C NMR, compared to those of crystalline helical polymer *L-2*, may be attributed to multi-intermolecular interactions of *L-1* and *L-4*.

The radial distribution function of *L-4* (Fig. 4) calculated from K-edge EXAFS data showed peaks at 0.13, 0.17 and 0.27 nm, indicating the existence of Ag–Ag interactions in *L-4* aside from donor-atom coordination [18,19]. Although the molecular and crystal structures of *L-4* could not be determined from X-ray crystallography, the *L-4* complex is a novel anionic silver(I) complex with histidine and a polymeric structure with a repeating trinuclear $[\text{Ag}_3(\text{L-his})_2]^-$ core is proposed.

3.2. Antimicrobial activity of *L-4*

The antimicrobial activities of the silver(I) complexes are listed in Table 1. The antimicrobial activities of *L-4*, *L-1*, *L-2* and *DL-3* as well as *L-H}_2\text{his} against selected bacteria (*Escherichia coli*, *Bacillus subtilis*, *Staphylococcus aureus* and *Pseudomonas aeruginosa*), yeasts (*Candida albicans* and *Saccharomyces cerevisiae*) and molds (*Aspergillus brasiliensis* (*Aspergillus niger*) and *Penicillium citrinum*) were evaluated by minimum inhibitory concentration (MIC) with both*

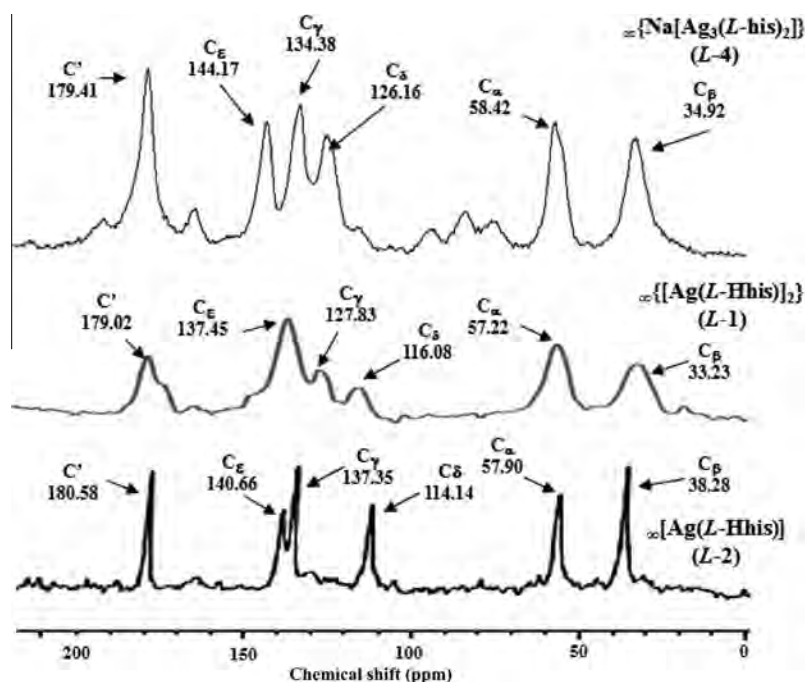


Fig. 3. Solid-state ^{13}C NMR spectra of $[\text{Na}[\text{Ag}_3(\text{L-his})_2]_n \cdot n\text{H}_2\text{O}]$ (*L-4*) ($n = 1-5$) and related complexes (*L-1*) and (*L-2*).

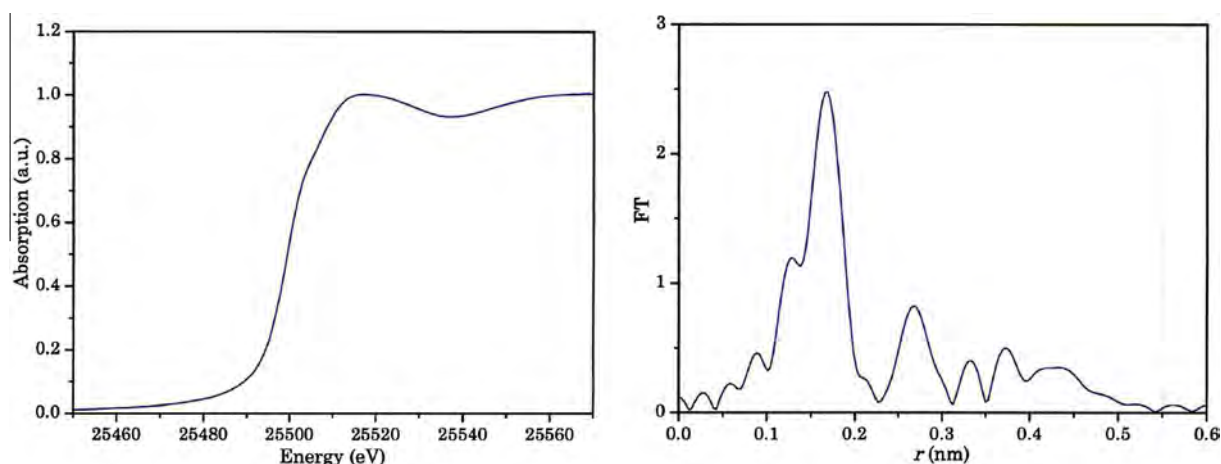


Fig. 4. The Ag K-edge X-ray absorption spectrum (left) and radial distribution function obtained from EXAFS data (right) of L-4.

Table 1

Antimicrobial activities of $\infty\{\text{Na}[\text{Ag}_3(\text{L-his})_2]\cdot n\text{H}_2\text{O}\}$ ($n = 1-5$) (L-4) and related complexes evaluated by minimum inhibitory concentration (MIC; $\mu\text{g mL}^{-1}$ and mM (mmol L^{-1}) representation).

	L-H ₂ his ^a		L-1 ^a $\infty\{[\text{Ag}(\text{L-Hhis})_2]\}$ Water-soluble		L-2 ^a $\infty\{[\text{Ag}(\text{L-Hhis})_2]\}$ Water-insoluble		DL-3 ^b $\infty\{[\text{Ag}_2(\text{D-Hhis})(\text{L-Hhis})]\}$ Water-insoluble		L-4 ^c $\infty\{\text{Na}[\text{Ag}_3(\text{L-his})_2]\cdot 5\text{H}_2\text{O}\}$ Water-soluble	
	$\mu\text{g mL}^{-1}$	(mM)	$\mu\text{g mL}^{-1}$	(mM)	$\mu\text{g mL}^{-1}$	(mM)	$\mu\text{g mL}^{-1}$	(mM)	$\mu\text{g mL}^{-1}$	(mM)
<i>Escherichia coli</i>	>1000	(>6.45)	15.7	(0.0300)	125	(0.239)	125	(0.239)	31.3	(0.0421)
<i>Bacillus subtilis</i>	>1000	(>6.45)	62.5	(0.119)	250	(0.477)	125	(0.239)	31.3	(0.0421)
<i>Staphylococcus aureus</i>	>1000	(>6.45)	62.5	(0.119)	250	(0.477)	31.3	(0.0597)	62.5	(0.0841)
<i>Pseudomonas aeruginosa</i>	>1000	(>6.45)	15.7	(0.0300)	250	(0.477)	125	(0.239)	15.7	(0.0211)
<i>Candida albicans</i>	>1000	(>6.45)	15.7	(0.0300)	125	(0.239)	125	(0.239)	500	(0.673)
<i>Saccharomyces cerevisiae</i>	>1000	(>6.45)	15.7	(0.0300)	125	(0.239)	31.3	(0.0597)	62.5	(0.0841)
<i>Aspergillus brasiliensis (niger)</i>	>1000	(>6.45)	125	(0.239)	250	(0.477)	250	(0.477)	250	(0.336)
<i>Penicillium citrinum</i>	>1000	(>6.45)	500	(0.954)	250	(0.477)	1000	(1.910)	1000	(1.346)

^a Data from Ref. [10].

^b Data from Ref. [11].

^c This work.

$\mu\text{g mL}^{-1}$ and mM (mmol L^{-1}) units, the latter being parenthesized in Table 1. Although the free ligand (L-H₂his) showed no activity, all of the Ag(I)-N bonding complexes showed a wide spectrum of effective activities. Water-soluble complexes (L-1 and L-4) showed higher activities than water-insoluble complexes (L-2 and DL-3). Anionic complex L-4 inhibited the growth of four bacteria (*E. coli*, *P. aeruginosa*, *B. subtilis*, and *S. aureus*), two yeasts (*C. albicans* and *S. cerevisiae*) and a mold (*P. citrinum*) with similar MIC values as L-1. Effective antibacterial activities of L-1 and L-4, rather than antifungal activities, should be noted.

Ligand-exchangeability of relatively weak Ag-N bonding complexes is higher than that of stronger Ag-S and Ag-P bonding complexes. Such Ag-N complexes can undergo ligand exchange with biomolecules of microorganisms such as proteins of lipid membranes [4,6,16]. Thus, we can explain a wide spectrum of the effective antimicrobial properties of Ag-N complexes. The solid-state polymer structures of water-soluble L-1 and L-4 will not be maintained in solution. We think that their solution structures will be based on the repeating core structures, i.e., the dimeric $[\text{Ag}(\text{L-Hhis})_2]$ core for L-1 and the trinuclear $[\text{Ag}_3(\text{L-his})_2]^-$ core for L-4. These structures will be different from the species in solution of water-insoluble L-2 and L-3. The relation between the antimicrobial activities and the solution structures of water-soluble L-1 and L-4 can be discussed based on ligand-exchangeability.

4. Conclusions

In summary, a coordination polymer based on trinuclear silver(I) core, $\infty\{\text{Na}[\text{Ag}_3(\text{L-his})_2]\cdot n\text{H}_2\text{O}\}$ (L-4) ($n = 1-5$), was prepared by mixing silver(I) oxide and histidine in aqueous solution (pH 11) and was characterized by CHN analysis, FT-IR, solid-state ¹³C NMR, XANES, EXAFS and ESI-MS in both negative and positive modes. The antimicrobial activities of L-4 against selected bacteria, yeasts and molds, as evaluated by MIC, revealed that complex L-4 inhibited the growth of four bacteria (*E. coli*, *P. aeruginosa*, *B. subtilis*, and *S. aureus*), two yeasts (*C. albicans* and *S. cerevisiae*) and a mold (*P. citrinum*) with similar MIC values as the water-soluble neutral silver(I) histidine complex, L-1.

Acknowledgements

Financial supports from the Research Institute for Integrated Science, Kanagawa University and Nippon Soda Co. Ltd., are acknowledged. We thank Professor Yuko Nishimoto for help with viscosity measurements and Dr. Hisako K. Ijuin for help with ESI-MS measurements.

References

- [1] C.N. Banti, S.K. Hadjikakou, *Metallomics* 5 (2013) 569.
- [2] J.A. Lemie, J.J. Harrison, R.J. Turner, *Nat. Rev. Microbiol.* 11 (2013) 371.

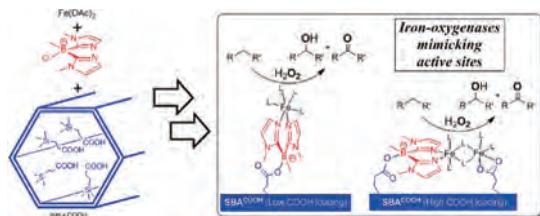
- [3] M.J. Hajipour, K.M. Fromm, A.A. Ashkarran, D.J. de Aberasturi, I.R. de Larramendi, T. Rojo, V. Serpooshan, W.J. Parak, M. Mohmoudi, *Trends Biotechnol.* 30 (2012) 499.
- [4] K. Nomiya, I. Azumaya, N.C. Kasuga, T. Kato, *Curr. Top. Biochem. Res.* 10 (2008) 1.
- [5] L. Antolini, L. Menabue, M. Saladini, *Inorg. Chim. Acta* 46 (1980) L77.
- [6] K. Nomiya, N.C. Kasuga, A. Takayama, in: A. Muñoz-Bonilla, M. Cerrada, M. Fernández-García (Eds.), *Polymeric Materials with Antimicrobial Activity*, RSC, 2014, p. 156. Chapter 7.
- [7] S. Eckhardt, P.S. Brunetto, J. Gagnon, M. Priebe, B. Giese, K.M. Fromm, *Chem. Rev.* 113 (2013) 4708.
- [8] B.O. Leung, F. Jalilehvand, V. Mah, M. Parvez, Q. Wu, *Inorg. Chem.* 52 (2013) 4593.
- [9] K. Nomiya, H. Yokoyama, *J. Chem. Soc., Dalton Trans.* (2002) 2483.
- [10] K. Nomiya, S. Takahashi, R. Noguchi, S. Nemoto, T. Takayama, M. Oda, *Inorg. Chem.* 39 (2000) 3301.
- [11] N.C. Kasuga, Y. Takagi, S. Tsuruta, W. Kuwana, R. Yoshikawa, K. Nomiya, *Inorg. Chim. Acta* 368 (2011) 44.
- [12] L. Mirolo, T. Schmidt, S. Eckhardt, M. Meuwly, K.M. Fromm, *Chem. Eur. J.* 19 (2013) 1754.
- [13] S. Arai, T. Kubota, M. Yabe, K. Nomiya, WO 2009098850, 2009.
- [14] S. Li, M. Hong, *J. Am. Chem. Soc.* 133 (2011) 1534.
- [15] K. Nomiya, Y. Kondoh, K. Onoue, N.C. Kasuga, H. Nagano, M. Oda, T. Sudoh, S. Sakuma, *J. Inorg. Biochem.* 58 (1995) 255.
- [16] K. Nomiya, K. Tsuda, T. Sudoh, M. Oda, *J. Inorg. Biochem.* 68 (1997) 39.
- [17] C.-J. Antti, B.K.S. Lundberg, *Acta Chem. Scand.* 25 (1971) 1758.
- [18] T.B. Coplen, J.K. Böhlke, P. De Bièvre, T. Ding, N.E. Holden, J.A. Hopple, H.R. Krouse, A. Lamberty, H.S. Peiser, K. Revesz, S.E. Rieder, K.J.R. Rosman, E. Roth, P.D.P. Taylor, R.D. Vocke Jr., Y.K. Xiao, *Pure Appl. Chem.* 74 (2002) 1987.
- [19] K.B. Nilsson, I. Persson, V.G. Kessler, *Inorg. Chem.* 45 (2006) 6912.

Mimicking the Active Sites of Non-heme Iron Oxygenases on the Solid Supports of Catalysts: Formation of Immobilized Iron Complexes with Imidazolyl and Carboxylate Ligands

Tomohiro Tsuruta, Tsubasa Yamazaki, Kazuki Watanabe, Yosuke Chiba, Akihiro Yoshida, Shuichi Naito, Jun Nakazawa, and Shiro Hikichi*

*Department of Material and Life Chemistry, Kanagawa University,
3-27-1 Rokkakubashi, Kanagawa-ku, Yokohama, Kanagawa 221-8686*

(E-mail: hikichi@kanagawa-u.ac.jp)



Iron oxygenases mimicking active sites have been constructed on the solid support by anchoring a bis(imidazolyl)borate ligand to carboxylate-functionalized mesoporous silica gels. Initial loading amounts of the organocarboxylic acid modifier on the silicates affect the hydrocarbon oxygenation catalyses with H₂O₂ due to changing the structures of the surface metallocomplex active sites.

REPRINTED FROM

Chemistry Letters

Vol.44 No.2 2015 p.144–146

CMLTAG
February 5, 2015

The Chemical Society of Japan

Mimicking the Active Sites of Non-heme Iron Oxygenases on the Solid Supports of Catalysts: Formation of Immobilized Iron Complexes with Imidazolyl and Carboxylate Ligands

Tomohiro Tsuruta, Tsubasa Yamazaki, Kazuki Watanabe, Yosuke Chiba, Akihiro Yoshida, Shuichi Naito, Jun Nakazawa, and Shiro Hikichi*

Department of Material and Life Chemistry, Kanagawa University,
3-27-1 Rokkakubashi, Kanagawa-ku, Yokohama, Kanagawa 221-8686

(E-mail: hikichi@kanagawa-u.ac.jp)

Iron oxygenases mimicking active sites have been constructed on the solid support by anchoring a bis(imidazolyl)-borate ligand to carboxylate-functionalized SBA-15 type mesoporous silica gels. Initial loading amounts of an organocarboxylic acid modifier on the silicates affect the hydrocarbon oxygenation catalyses with H_2O_2 due to changing of the structures of the surface metallocomplex active sites.

The active sites of non-heme iron oxygenases are mixed ligand-supporting iron complexes composed of imidazolyl [N-donor of histidine (= His) residue] and carboxylate [O-donor of aspartic acid (= Asp) or glutamic acid (= Glu) residues] groups.¹ Several O_2 -activating mononuclear iron(II) enzymes have a common mixed-ligand set, namely, the “2-His-1-carboxylate” facial triad motif.^{1,2} Dinuclear iron enzymes such as methane monooxygenase (= MMO) have active sites composed of His-involved “carboxylate-rich” ligands sets.^{1,3} To date, various synthetic non-heme iron complexes have been investigated as functional models or/and biomimetic catalysts. These complexes are utilized for homogeneous liquid-phase oxidation reactions.^{2,3b,4,5} However, accidental degradation of the complexes is caused by the leaching of the iron through the shifting of the coordination equilibrium state in solution. A more critical reason for the deactivation of the complex is intra- and intermolecular oxidative ligand transformation induced by an active oxygen complex.⁶ In order to avoid the intermolecular oxidative degradation, immobilization of the complex on solid supports with appropriate conditions is one of the considerable approaches.⁷

We have been developing organoborate ligands, namely, bis(*N*-methyl-2-imidazolyl)borates ($=[\text{B}(\text{Im}^{\text{N-Me}})_2(\text{X})\text{Me}]^-; \text{L}^{\text{X}}$).⁸ The ligands L^{X} are composed of a discrete monovalent borate anion and two imidazolyl groups which provide a coordination environment for the metal center similar to that found in non-heme metalloenzymes. The B–C_{imidazolyl} linkage in L^{X} is stable toward hydrolytic decomposition due to the higher covalency of the B–C bonds, which makes it possible to attach various functional groups X on the boron center. A carboxylate ligand, $[\text{B}(\text{Im}^{\text{N-Me}})_2(\text{OC}(=\text{O})\text{Me})\text{Me}]^- (\text{L}^{\text{OAc}})$, is formed by the nucleophilic substitution of X, from *O**i*-Pr or Cl to OAc. The boron–acetoxy linkage of L^{OAc} survives upon the treatment of the corresponding nickel complexes with OH^- .⁹ Therefore, a boron–carboxylate linkage would be employed as a junction to organic compounds anchored to inorganic supports. In this study, L^{X} is anchored on carboxylic acid-functionalized silica gels through the boron–carboxylate linkage (Figure 1). The carboxylic acid-functionalized silica gels are utilized as ligating agents of transition-metal species for the support of catalysts

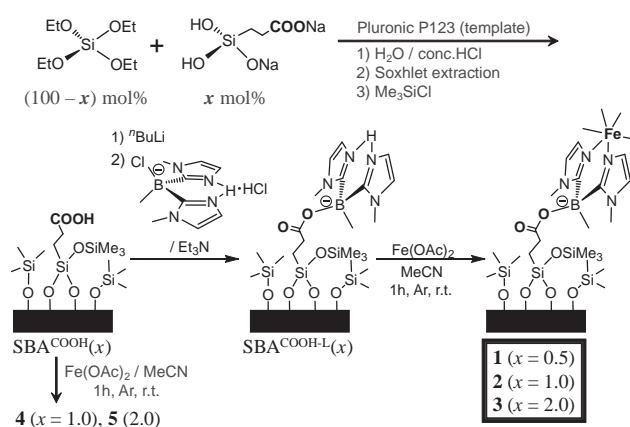


Figure 1. Preparation of the catalysts.

applied to heterogeneous reactions.^{10–12} An appropriate design of the surface structure of the support, i.e., controlling the loadings of carboxylic acid and the immobilization of L, is expected to architect the iron complexes similar to the carboxylate and imidazolyl-mixed active sites of non-heme enzymes on the solid support.

Our previously reported L-immobilized silica gels were prepared by the thiol-ene coupling of an allyl-functionalized ligand ($=[\text{B}(\text{Im}^{\text{N-Me}})_2(\text{allyl})\text{Me}]^-; \text{L}^{\text{allyl}}$) with a thiol group containing a silanol ester reagent or an organothiol-modified silica gel.¹³ In these L-immobilized silica gels, L was loaded up to ca. 0.2 mmol g⁻¹. The limitation of the loading amounts of L is probably due to the bulkiness of L. The loading amount of the organic-functionalized groups on the SBA-15 type silica gels can be controlled by changing the ratio of the precursors in the one-pot synthesis.¹⁴ The resulting anchored functionalized groups are randomly dispersed, which is efficient for the isolation of the catalytic active sites. Moreover, we have demonstrated that the surface morphology of the silica supports (relatively flat SBA-15 vs. rugged amorphous silica) influences the structure of the formed iron complexes with a Schiff base ligand and their catalytic performances. The activity of the SBA-15-based catalyst is higher than that of the amorphous silica catalyst with almost the same ligand loading density.^{7g} In this context, we designed a mesoporous silica support functionalized by an organocarboxylate linker with appropriate loading amounts. The carboxylate-functionalized SBA-15 ($= \text{SBA}^{\text{COOH}}(x)$; where x denotes the ratio of carboxy groups: see Table S-1 and Figure S-1) was prepared by the same procedure for the synthesis of an organoazide-immobilized SBA-15.¹¹ The condensation ratio of carboxyethylsilanetriol sodium salt (CES;

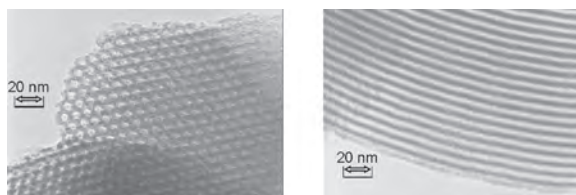


Figure 2. TEM images of **2**.

Table 1. Catalysts properties and activities on cyclohexene oxidation^a

Cat.	Loading on Cat./mmol g ⁻¹			L/Fe	TON per Fe ^b (E/(A + K))	
	COOH	L	Fe		As-prepared	Reuse
1	0.05	0.05	0.05	1.0	11.4 (0.25)	4.9 (0.24)
2	0.12	0.12	0.13	1.0	4.4 (0.17)	5.5 (0.26)
3	0.18	0.13	0.16	0.81	6.3 (0.23)	5.3 (0.24)
4	0.10	—	0.10	—	4.3 (0.25)	not tested
5	0.19	—	0.17	—	2.9 (0.15)	not tested

^aDetectable amounts of *cis*- and *trans*-1,2-cyclohexanediols were not formed. ^bTON = (cyclohexene oxide (E) + cyclohexen-1-ol (A) + cyclohexen-1-one (K) × 2)/iron.

x mol %) to tetraethoxysilane (TEOS; (100 - *x*) mol %) was selected to be *x* = 0.5, 1.0, and 2.0.

The reaction of a chlorine-containing bis(imidazolyl)borate L^{Cl} and a lithiated SBA^{COOH}(*x*), which were obtained by the treatment of SBA^{COOH} with *n*-BuLi, yielded the ligand-immobilized support (= SBA^{COOH-L}(*x*)). The immobilized amount of L on SBA^{COOH-L}(*x*) got up to ca. 0.13 mmol g⁻¹, and unmodified carboxy groups remained on the support with *x* = 2.0. Following reaction with a MeOH solution of Fe(OAc)₂ gave catalysts **1–3** (Figure 1). TEM observation revealed that the ordered mesoporous structure of the catalysts was maintained, and the particles of iron oxides and other cluster compounds were not formed after metalation (Figure 2). The immobilized amounts of L and iron were determined by elemental analyses and atomic absorption analyses, respectively. The loading amount of the carboxy group on the starting mesoporous silica, SBA^{COOH}(*x*), influenced the structures of the surface iron complexes of the resulting catalysts. In the low-carboxylate-loaded catalysts **1** (*x* = 0.5) and **2** (1.0), the ratio of the initial introduced COOH to the immobilized L to the loaded iron was almost 1:1:1. On the higher COOH-loaded catalyst **3**, the iron centers might be supported by not only the immobilized L but also the unmodified carboxylates (summarized in Table 1).

The activities of the prepared catalysts toward the oxidation of cyclohexene with H₂O₂ were examined (Tables 1 and S-2). The catalytic activity of an iron(II) complex with a phenyl group containing ligand, [Fe^{II}(L^{Ph})₂] (see Supporting Information), was also tested as a homogeneous control, but only trace amounts of

organic oxidized products were yielded. The color of the reaction mixture was gradually turned to pale yellow to pale brown, and unidentified precipitates appeared. We could not obtain a single ligand-supported complex (= [Fe^{II} or III(L')_{*n*}(L^{Ph})_{*n*}]) where L' denotes ligands other than L^{Ph} because no hindered metal-surrounding groups existed on L^{Ph}. In contrast to the inertness of [Fe^{II}(L^{Ph})₂] in the *homogeneous* system, the silica-immobilized iron complexes of the catalysts, namely, the *heterogeneous* system, exhibited oxidizing activities. Major products derived from all heterogeneous catalysts, **1–3**, and non-L-immobilized catalysts, **4** and **5**, were allylic oxidized ketone. The catalytic activity (= TON per Fe) of **3** was higher than that of the corresponding non-L-immobilized catalyst **5**. Although the activity of the as-prepared **2** was similar to that of **4**, the A/K ratio of the allylic oxidized products derived from **2** (0.74) was higher than that from **4** (0.55) as shown in Table S-2. The most active catalyst was the as-prepared **1**. Although the loading ratio of COOH to L to iron was the same (= 1:1:1), the activity of the as-prepared **2** was lower than that of **1**. An excess carboxylate-containing catalyst **3** exhibited better activity. The mean densities of COOH and L on the supports correlated with the activities of the catalysts.¹⁵ Therefore, the formed immobilized iron complexes might be varied depending on the loading of COOH and L on the support. The COOH groups were distributed randomly because SBA^{COOH}(*x*) was synthesized by the “one-pot method.”¹⁴ In such a situation, various iron complexes would form on the support. As shown in the control homogeneous reaction, [Fe(L)₂] might not contribute to the catalytic reaction. On the lower COOH loading catalysts **1** and **2**, almost COOH connect to L and the ratio of iron to the ligand is 1:1. Therefore, a mononuclear [Fe(L)] and a dinuclear [Fe₂(L)₂] species would be the active sites of these catalysts. In contrast, **3** contains the unmodified (i.e. non-L-connected) carboxy groups that are ligated to iron. Therefore, a dinuclear iron complex with L and carboxylates might be formed on **3** (Figure S-3). Although no leaching of iron from **1–3** was observed, the activities of the recovered catalysts **1** and **3** were lower than those of the as-prepared ones. In contrast, the recovered **2** showed somewhat higher activity compared to the as-prepared one.

By using **2**, we examined various reaction conditions on the cyclohexene oxidation (Figure 3). When the ratio of the substrate to H₂O₂ was 1:1, slow addition of H₂O₂ (by using a syringe pump) to the reaction mixture resulted in increasing the epoxide yield as well as the A/K values of allylic oxidized compounds at room temperature. At a higher temperature (333 K), the activities were improved in each case. In the presence of an excess amount of the substrate (cyclohexene: H₂O₂ = 5:1), hydroxylation of the allylic position of cyclohexene became a major reaction and concomitant epoxidation occurred. These observations suggest that some metal-based oxidants might exist, and the intrinsic activity of the species formed on the iron complex sites seems to be H abstraction rather than O-atom transfer.¹⁶

As predicted from the allylic oxidizing capability toward cyclohexene, all catalysts mediated alkane oxygenation at higher temperatures (Table S-3). Toward cyclohexane oxidation at 333 K, the order of the activities was **1** > **3** > **5** ≈ **2** > **4** and the A/K values derived from each catalyst were varied. Although all the catalysts yielded cyclohexanone as a major product, the yields of cyclohexanol were close to those of cyclohexanone in

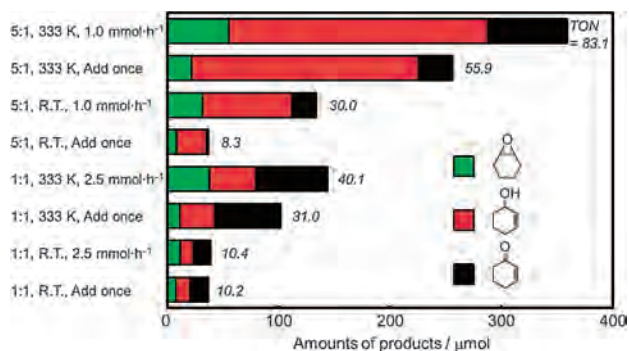


Figure 3. Dependence of the cyclohexene oxygenation catalyzed by **2** on the reaction conditions. Amount of applied catalyst = 5.0 μmol of iron. Amounts of cyclohexene and H₂O₂ were 2.5 mmol when cyclohexene:H₂O₂ = 1:1, or 5.0 mmol of cyclohexene and 1.0 mmol of cyclohexene when cyclohexene:H₂O₂ = 5:1. Reactions were carried under argon for 2 h.

the initial stage on each reaction system (Figure S-4). Therefore, the consecutive oxidation of cyclohexanol to cyclohexanone might occur. On adamantane oxidations, the values of 3°/2° [= ratio of (1-adamantanol + 1,3-diadamantanol):(2-adamantanol + 2-adamantanone) taking into account the correction for the number of C–H bonds in a group] were almost 2 given by each catalyst, which suggests the contribution of HO• under high temperature (353 K) conditions.¹⁷ The order of the activity of the catalysts (**3** > **2** > **1** > **4** > **5**; estimated by total TON after 3 h) suggested that **L** provided efficient active sites. However, the order of the initial TOF (values estimated by TON after 1 h) was **1** (54 h⁻¹) > **2** (45) > **3** (31) > **4** (27) > **5** (23). The difference in the orders suggests that the activities and stabilities of the iron complexes would be varied and that partial changing of the structures might occur during the reaction.

In summary, iron oxygenases mimicking complex-immobilized catalysts have been developed by anchoring bis(imidazolyl)borate to the carboxylate-functionalized mesoporous silica gels. The initial loading amounts of the organocarboxylic acid modifier on SBA-15 affect the oxidation catalyses due to changing the structures of the surface metallocomplex active sites. The immobilized bis(imidazolyl)borate scaffold provides efficient active sites, which might be similar to those of the mono- and dinuclear non-heme iron enzymes. The oxidants formed on the catalysts through the activation of H₂O₂ exhibit the radical character to induce the allylic oxidation of cyclohexene as well as the oxygenation of cycloalkanes.

This work was supported in part by Grant in-Aid for Scientific Research (No. 26420788) and a Strategic Development of Research Infrastructure for Private Universities from the Ministry of Education, Culture, Sports, Science and Technology (MEXT), Japan.

Supporting Information is available electronically on J-STAGE.

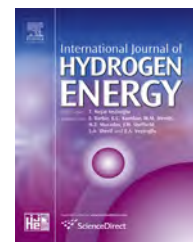
References and Notes

- a) E. I. Solomon, T. C. Brunold, M. I. Davis, J. N. Kemsley, S.-K. Lee, N. Lehnert, F. Neese, A. J. Skulan, Y.-S. Yang, J. Zhou, *Chem. Rev.* **2000**, *100*, 235. b) E. G. Kovaleva, M. B. Neibergall, S. Chakrabarty, J. D. Lipscomb, *Acc. Chem. Res.* **2007**, *40*, 475.
- M. Costas, M. P. Mehn, M. P. Jensen, L. Que, Jr., *Chem. Rev.* **2004**, *104*,

- 939.
- a) M. Merckx, D. A. Kopp, M. H. Sazinsky, J. L. Blazyk, J. Müller, S. J. Lippard, *Angew. Chem., Int. Ed.* **2001**, *40*, 2782. b) E. Y. Tshuva, S. J. Lippard, *Chem. Rev.* **2004**, *104*, 987. c) L. J. Murray, S. J. Lippard, *Acc. Chem. Res.* **2007**, *40*, 466.
- Review articles: a) K. Chen, M. Costas, L. Que, Jr., *J. Chem. Soc., Dalton Trans.* **2002**, 672. b) C. Bolm, J. Legros, J. Le Pailh, L. Zani, *Chem. Rev.* **2004**, *104*, 6217. c) B. S. Lane, K. Burgess, *Chem. Rev.* **2003**, *103*, 2457. d) E. B. Bauer, *Curr. Org. Chem.* **2008**, *12*, 1341. e) F. G. Gelalcha, *Adv. Synth. Catal.* **2014**, 356, 261.
- Selected examples of recent reports on homogeneous hydrocarbon oxygenation catalyses of non-heme iron complexes with H₂O₂: a) Y. Feng, J. England, L. Que, Jr., *ACS Catal.* **2011**, *1*, 1035. b) O. Y. Lyakin, R. V. Ottenbacher, K. P. Bryliakov, E. P. Talsi, *ACS Catal.* **2012**, *2*, 1196. c) O. Cussó, I. Garcia-Bosch, X. Ribas, J. Lloret-Fillol, M. Costas, *J. Am. Chem. Soc.* **2013**, *135*, 14871. d) I. Prat, A. Company, T. Corona, T. Parella, X. Ribas, M. Costas, *Inorg. Chem.* **2013**, *52*, 9229. e) P. E. Gormisky, M. C. White, *J. Am. Chem. Soc.* **2013**, *135*, 14052. f) Y. Hitomi, K. Arakawa, M. Kodera, *Chem.—Eur. J.* **2013**, *19*, 14697. g) M. Mitra, J. Lloret-Fillol, M. Haukka, M. Costas, E. Nordlander, *Chem. Commun.* **2014**, 50, 1408.
- See for example: a) D. Hong, S. Mandal, Y. Yamada, Y.-M. Lee, W. Nam, A. Llobet, S. Fukuzumi, *Inorg. Chem.* **2013**, *52*, 9522. b) D. Pijper, P. Saisaha, J. W. de Boer, R. Hoen, C. Smit, A. Meetsma, R. Hage, R. P. van Summeren, P. L. Alsters, B. L. Feringa, W. R. Browne, *Dalton Trans.* **2010**, 39, 10375.
- Examples on iron complex-immobilized catalysts (except our previous bis(imidazolyl)borate work): a) T. J. Terry, G. Dubois, A. Murphy, T. D. P. Stack, *Angew. Chem., Int. Ed.* **2007**, *46*, 945. b) G. D. Pirngruber, L. Frunz, M. Luchinger, *Phys. Chem. Chem. Phys.* **2009**, *11*, 2928. c) B. Malvi, C. Panda, B. B. Dhar, S. S. Gupta, *Chem. Commun.* **2012**, 48, 5289. d) S. Yamaguchi, T. Fukura, C. Fujita, H. Yahiro, *J. Chem. Lett.* **2012**, 41, 713. e) V. Jollet, B. Albela, K. Sénéchal-David, P. Jégou, E. Kolodziej, J. Sainton, L. Bonneviot, F. Banse, *Dalton Trans.* **2013**, 42, 11607. f) D. Sheet, P. Halder, T. K. Paine, *Angew. Chem., Int. Ed.* **2013**, *52*, 13314. g) T. Akashi, J. Nakazawa, S. Hikichi, *J. Mol. Catal. A: Chem.* **2013**, 371, 42.
- a) K. Fujita, S. Hikichi, M. Akita, Y. Moro-oka, *J. Chem. Soc., Dalton Trans.* **2000**, 117. b) K. Fujita, S. Hikichi, M. Akita, Y. Moro-oka, *J. Chem. Soc., Dalton Trans.* **2000**, 1255. c) S. Hikichi, K. Fujita, Y. Manabe, M. Akita, J. Nakazawa, H. Komatsuzaki, *Eur. J. Inorg. Chem.* **2010**, 5529.
- K. Fujita, M. Akita, S. Hikichi, *Inorg. Chim. Acta* **2009**, 362, 4472.
- a) L. Han, Y. Sakamoto, O. Terasaki, Y. Li, S. Che, *J. Mater. Chem.* **2007**, *17*, 1216. b) Q. Chen, L. Han, S. Che, *Chem. Lett.* **2009**, 38, 774.
- a) C.-T. Tsai, Y.-C. Pan, C.-C. Ting, S. Vetrivel, A. S. T. Chiang, G. T. K. Fey, H.-M. Kao, *Chem. Commun.* **2009**, 5018. b) C.-S. Chen, C.-C. Chen, C.-T. Chen, H.-M. Kao, *Chem. Commun.* **2011**, 47, 2288. c) C. S. Chen, Y. T. Lai, T. W. Lai, J. H. Wu, C. H. Chen, J. F. Lee, H. M. Kao, *ACS Catal.* **2013**, 3, 667.
- a) A. J. Butterworth, J. H. Clark, P. H. Walton, S. J. Barlow, *Chem. Commun.* **1996**, 1859. b) M. Nowotny, L. N. Pedersen, U. Hanefeld, T. Maschmeyer, *Chem.—Eur. J.* **2002**, *8*, 3724. c) N. J. Schoenfeldt, Z. Ni, A. W. Korinda, R. J. Meyer, J. M. Notestein, *J. Am. Chem. Soc.* **2011**, *133*, 18684.
- S. Hikichi, M. Kaneko, Y. Miyoshi, N. Mizuno, K. Fujita, M. Akita, *Top. Catal.* **2009**, 52, 845.
- a) J. Nakazawa, T. D. P. Stack, *J. Am. Chem. Soc.* **2008**, *130*, 14360. b) J. Nakazawa, B. J. Smith, T. D. P. Stack, *J. Am. Chem. Soc.* **2012**, *134*, 2750.
- Correlation between mean density of immobilized ligand and catalytic performance has been demonstrated: a) J. Nakazawa, T. Hori, T. D. P. Stack, S. Hikichi, *Chem.—Asian J.* **2013**, *8*, 1191. b) J. Nakazawa, A. Yata, T. Hori, T. D. P. Stack, Y. Naruta, S. Hikichi, *Chem. Lett.* **2013**, 42, 1197.
- An Fe^{IV}=O species exhibits allylic oxidation rather epoxidation and cis-dihydroxylation activity toward cyclohexene: W. N. Oloo, Y. Feng, S. Iyer, S. Parmelee, G. Xue, L. Que, Jr., *New J. Chem.* **2013**, 37, 3411.
- M. Costas, K. Chen, L. Que, Jr., *Coord. Chem. Rev.* **2000**, 200–202, 517.

Available online at www.sciencedirect.com

ScienceDirect

journal homepage: www.elsevier.com/locate/he

Effects of Re addition upon aqueous phase reforming of ethanol over TiO₂ supported Rh and Ir catalysts

Toshiaki Nozawa, Akihiro Yoshida, Shiro Hikichi, Shuichi Naito*

Department of Material and Life Chemistry, Kanagawa University, 3-27-1 Rokkakubashi, Kanagawa-ku, Yokohama, 221-8686, Japan

ARTICLE INFO

Article history:

Received 4 December 2014

Received in revised form

21 January 2015

Accepted 26 January 2015

Available online 20 February 2015

Keywords:

Aqueous phase reforming of ethanol

Rhodium

Iridium

Rhenium

Titanium dioxide

ABSTRACT

Effect of addition of rhenium was investigated during catalysis of TiO₂-supported Rh and Ir metals for aqueous phase reforming of ethanol. By adding Re to Rh/TiO₂ and Ir/TiO₂ catalysts, the initial rates of H₂, CH₄, and CO₂ formation increased 3–4 times, together with the extraordinary increase of acetic acid formation. Detailed mechanisms of the reforming reaction were investigated using various physicochemical techniques. The role of added Re was the acceleration of the hydration of acetaldehyde to form acetic acid rather than the decomposition of acetaldehyde to form CH₄ and CO on both Rh/TiO₂ and Ir/TiO₂ catalysts. Well dispersed bimetallic nano-composites would work as the active sites for ethanol dehydrogenation and acetaldehyde decomposition, whereas partially oxidized ReO_x sites may work for the hydration of acetaldehyde to form acetic acid.

Copyright © 2015, Hydrogen Energy Publications, LLC. Published by Elsevier Ltd. All rights reserved.

Introduction

The production of hydrogen as a clean energy carrier from bio-renewable sources is regarded as an extremely promising means to minimize the global environmental problems that are associated with fossil fuel combustion [1,2]. Among bio-renewable liquid feedstock for producing hydrogen, ethanol is an extremely promising candidate because of its high hydrogen content, non-toxicity, and facile storage and handling. Catalytic reforming of ethanol can be categorized into two methods: steam reforming (SR) and aqueous phase reforming (APR). During the SR of ethanol many competing reactions take place and produce undesirable light

hydrocarbons and CO, which requires a lower temperature water-gas shift process. In addition, most catalysts for ethanol SR have problems of severe deactivation by material degradation and carbon deposition at higher temperatures. As compared with a usual SR reaction, the advantages of APR are the possibility to make more compact and simple reaction equipment and the obviation of evaporation energy for aqueous solutions.

Recently, Dumesic et al. reported the APR of methanol, ethylene glycol and other oxygenates with water over supported Pt and Ni catalysts [3–5]. The mechanism of H₂ production from ethylene glycol was described by Shabaker et al. [6,7]. It involved the cleavage of C–C bonds as well as C–H bonds to form adsorbed CO followed by the water-gas shift to

* Corresponding author. Tel.: +81 45 481 5661x3641; fax: +81 45 413 9770.

E-mail address: naitos01@kanagawa-u.ac.jp (S. Naito).
<http://dx.doi.org/10.1016/j.ijhydene.2015.01.152>

0360-3199/Copyright © 2015, Hydrogen Energy Publications, LLC. Published by Elsevier Ltd. All rights reserved.

H₂ and CO₂ formation. Consequently, a good catalyst for APR process of oxygenated compounds must be active in the cleavage of C–C bonds and water-gas shift reaction, but must inhibit the cleavage of C–O bond and methanation reactions. Actually, Ni shows a good activity for C–C bond scission followed by water-gas shift reaction, but it also exhibits high reaction rates for methanation. The Dumesic research group reported that addition of Sn to Ni increases selectivity for hydrogen production by decreasing the selectivity for alkane formation [5,6,8]. King et al. reported the APR of glycerol for H₂ production over carbon supported Pt–Re catalysts [9].

Several years ago, we investigated the catalytic activity of various silica-supported precious metal catalysts for the methanol APR, which revealed that Pt/SiO₂ was the most active, whereas Ir/SiO₂ was the most selective catalyst for CO₂ formation against CO [10,11]. To improve the catalytic properties of these metals, we investigated the effect of various additives such as Mo, W, and Re over Pt/Al₂O₃ and Pt/TiO₂ catalysts [12,13]. We inferred two means of enhancement depending on the kind of supports and additives as well as the addition methods (co-impregnation and successive impregnation). In the cases of Mo and W, the formation of low valence thin oxide layers over Al₂O₃ and TiO₂ were revealed by XRD, XPS, and XAFS measurements, which realized highly dispersed stable cationic Pt particles and enhanced methanol APR. However, for Re addition, the formation of alloy with Pt was observed, which caused rather poor activity for the improvement of catalytic activity. On the other hand, in the case of methanol APR over Ir/SiO₂ catalysts the addition of Re enhanced the activity more than one order of magnitude, and reached a value comparable to that of Pt–Ru/SiO₂ [14]. The catalytic activity also depended greatly on the kind of support, and TiO₂, ZrO₂, and CeO₂ supports significantly enhanced the catalytic activity of Ir–Re catalysts, which might be attributed to the interaction between support oxides and Ir species in addition to the formation of the bimetallic nano-composites of Ir–Re.

For Rh/SiO₂ catalysts, Tomishige and co-workers reported that addition of Re, Mo, and W enhanced the catalytic activity of the glycerol hydrogenolysis using water as a solvent [15,16]. Modification with Re gave the highest conversion and yield of 1,3-propanediol. The optimized Rh–ReO_x/SiO₂ (Re/Rh = 0.5) catalyst maintained high selectivity to propane diols and suppressed C–C bond breaking. Tomishige et al. proposed the synergetic effect between ReO_x and Rh. The reaction might proceed on the interface between Rh metal surface and attached ReO_x species. In the case of Ir–Re/SiO₂ catalysts, similar results of direct hydrogenolysis of glycerol into 1,3-propanediol were reported by the same research group, through the attack of active hydrogen species on Ir metal to 1-glyceride species formed on the oxidized Re cluster [17].

However, for ethanol APR, it is difficult to obtain H₂ and CO₂ selectively as complete reforming products because of its non-activated methyl group, which is easily transformed into methane [18–20]. Accordingly, in ordinary cases we will obtain a 1:1 ratio of CH₄ and CO₂ together with acetic acid. In addition, the formed CO₂ is transformed into CH₄ through a methanation reaction, which results in excess CH₄ compared to CO₂. Some possibility exists of acetic acid presence in SR as well APR at lower temperatures [21–26]. Recently, we

investigated the dependence of Ru particle size upon the activity and selectivity for APR of ethanol and acetic acid over Ru/TiO₂ at 473 K. In both cases of ethanol and acetic acid over larger Ru metal catalysts, 1:1 ratio of CH₄ and CO₂ was formed at the initial stage, followed by the hydrogenation of CO₂ forming excess CH₄. However, in the case of acetic acid APR over positively charged smaller Ru catalyst, a 2:1 ratio of H₂ and CO₂ was formed constantly, indicating the operation of a complete reforming reaction with water [27].

For the present study, we have investigated the effects of Re addition on the APR of ethanol over Rh/TiO₂ and Ir/TiO₂ catalysts. Results show that the activity and selectivity were enhanced dramatically by adding Re. The intrinsic role of Re was clarified by application of various surface analysis techniques such as XPS, XRD, and TEM as well as kinetic investigation.

Experimental method

Preparation of catalysts

TiO₂-supported Rh and Ir catalysts (5 wt%) were prepared using a conventional impregnation method employing RhCl₃·3H₂O and H₂IrCl₆·6H₂O as precursors and TiO₂ (P-25, surface area = 50 m²/g) as a support. Re addition was conducted using a successive impregnation method as follows; NH₄ReO₄ precursor (Re/Rh or Re/Ir = 0.1–2.0) was initially impregnated to TiO₂, followed by calcination at 773 K. Then RhCl₃·3H₂O or H₂IrCl₆·6H₂O precursors were impregnated.

Aqueous phase reforming of ethanol with water

The reaction was conducted in a stainless steel autoclave in a batch mode (volume: 400 ml) connected to an online TCD gas chromatograph to analyze the gas phase products during the reaction (molecular sieve 13X column and Porapak Q column). After reduction of the catalyst (0.5 g) with H₂ at 623 K, 80 ml of degassed ethanol solution (EtOH: H₂O = 1:10) was introduced into the reactor under nitrogen atmosphere and reaction experiments were conducted at 473 K under 2 MPa. During the reaction, the liquid phase content of the autoclave was stirred using a magnetic stirrer. A small part of the liquid-phase products was sampled by online sampling tube (1 ml) and analyzed by FID gas chromatograph (CP PoraBOND Q).

Characterization of catalysts

An X-ray photoelectron spectrometer (JPS-9010, JEOL) with Mg K α X-ray source (10 kV, 10 mA) was applied for chemical states of supported catalysts. After reduction with H₂, the catalyst was pressed into a 20 mm diameter disk and pretreated by H₂ at 623 K. Then the disk was mounted on the sample holder of XPS preparation chamber and reduced again by H₂ at 623 K and transferred to the analysis chamber without exposure to air. A transmission electron microscope (JEM2010, JEOL) with an acceleration voltage of 200 kV and LaB₆ cathode was applied for the observation of the images of supported catalysts. Samples were prepared by suspending the catalyst powder ultrasonically in 2-propanol and depositing a drop of

the suspension on a standard copper grid covered with carbon monolayer film.

The adsorption amount of CO after 623 K reduction was measured using a static volumetric adsorption apparatus (Omnisorp 100CX, Beckmann Coulter) at 298 K. Before measurement, the samples were reduced at 623 K for 1.5 h in a flow of hydrogen atmospheric pressure. The dispersion ($D(\%)$; percentage of metal atoms exposed to the surface) of supported metal was evaluated from the amount of chemisorbed CO and adsorption stoichiometry (CO/metal atom = 1).

Fourier transform infrared spectroscopy (FT-IR) measurements were conducted using a self-support catalyst disk mounted in a transmission cell and a FT-IR spectrometer (FT-IR/6100; Jasco) equipped with a closed gas circulation system.

Results and discussion

Aqueous phase reforming of ethanol over various precious metal catalysts supported on TiO₂

Prior to investigate the effects of Re addition for the improvement of EtOH APR activity, we estimate catalytic performance of a series of M/TiO₂ where M = Ru, Rh, Ir, and Pt. Table 1 (entries 1–4) presents the amount of various products formed after 10 h of the aqueous phase reforming of ethanol (EtOH) over various 5 wt% TiO₂ supported precious metal catalysts at 473 K. The obtained major products were H₂, CH₄ and CO₂ in the gas phase and acetaldehyde (AcH) and acetic acid (AcOH) in the liquid phase. The activity order of the metals for the amounts of H₂ formation were as Rh > Ir > Ru > Pt, whereas, the EtOH conversion was Ru > Rh > Ir > Pt. No CO was detected during the reaction on all the catalysts. Therefore, the water–gas shift reaction to form CO₂ is expected to occur rapidly under aqueous phase reaction conditions.

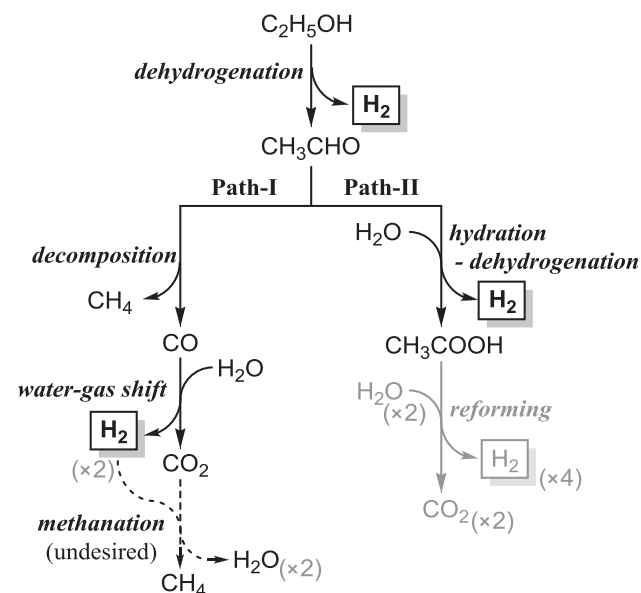
A plausible reaction scheme occurred in the present aqueous ethanol reforming system is shown in Scheme 1. The first step would be the dehydrogenation of EtOH giving AcH. Then two different reaction pathways proceed as follows: (1) decomposition of AcH to form CH₄ and CO, and subsequent water-gas shift reaction giving CO₂ and H₂ (Path-I: CH₃CHO + H₂O → CH₄ + CO, then CO + H₂O → CO₂ + H₂) and (2) hydration of AcH and following dehydrogenation to form AcOH (Path-II: CH₃CHO + H₂O → CH₃COOH + H₂). If reforming of AcOH occurred, ideal reforming of EtOH giving CO₂ and H₂ is completed through the reaction Path-II (i.e., C₂H₅OH + 3H₂O → 2CO₂ + 6H₂). Over Pt/TiO₂ catalyst, the latter reaction path-II took place more than the former reaction Path-I because the amounts of AcH and AcOH formed in the liquid phase were 2–4 times more than CH₄ and CO₂ in the gas phase. Although the yield of AcH derived over Ir/TiO₂ catalyst was not so high, higher yield of AcOH compared to CH₄ and CO₂ might indicate the AcH hydration activity of Ir/TiO₂ was higher than that of Pt/TiO₂. In contrast, the amounts of CH₄ and CO₂ were much more than AcOH over Rh/TiO₂ and Ru/TiO₂, indicating the predominant occurrence of the reaction Path-I over these catalysts. Excess amounts of CH₄ formation compared to CO₂ (CH₄/CO₂ ratios: 1.4 for Rh and 4.0 for

Ru) might be explained by the successive methanation reaction of CO₂.

Time course of the reaction profiles on M/TiO₂ shown in Fig. 1 (a–d) were consistent with the above described natures of each catalysts. Ir and Pt catalysts exhibited very similar reaction profiles. The yields of the liquid phase products on Rh and Ru catalysts were quite low. However, the time-dependent gas-phase products distributions might suggest the difference of the nature of the catalysis between Rh and Ru catalysts. On Rh catalyst, the formation rates of H₂, CH₄ and CO₂ were almost constant from the initial stage till 10 h. In contrast, the CH₄ formation rate on Ru catalyst increased over reaction period, concomitant with decreasing the formation rates of H₂ and CO₂. These observations clearly indicate that the activity of Ru catalyst toward the successive methanation reaction of CO₂ with the generated H₂ is higher than that of Rh catalyst.

Re addition effect upon the aqueous phase reforming of ethanol

Then we explored the Re addition effect onto the above mentioned catalysts. Entries 6–9 shown in Table 1 indicate the yields of the products and conversion of EtOH over M-Re/TiO₂ catalysts. The conversion of EtOH and yield of H₂ were increased over all Re added catalysts compared to those derived from the corresponding prototype M/TiO₂ catalysts.

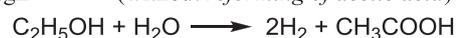


Conversion of ethanol in our system

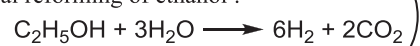
through **Path-I** (without methanation) :



through **Path-II** (without reforming of acetic acid) :



(ideal reforming of ethanol :



Scheme 1 – Plausible reactions occurred in the aqueous ethanol reforming system.

Table 1 – Product distributions and EtOH conversion after 10 h of EtOH + H₂O reaction at 473 K over various TiO₂ supported precious metal catalysts.

Entry	Catalysts	Gas-phase/mmole g _{cat} ⁻¹			Liquid-phase/mmole g _{cat} ⁻¹			EtOH conv./% (10 h)
		H ₂	CH ₄	CO ₂	AcH	AcOH	AcOEt	
1	Ru/TiO ₂ ^a	34.5	124.0	30.6	1.2	3.8	0.1	30.1
2	Rh/TiO ₂ ^a	61.2	45.3	32.1	0.3	0	0	14.2
3	Ir/TiO ₂ ^a	40.9	6.2	4.9	1.4	8.0	0.6	5.9
4	Pt/TiO ₂ ^a	29.2	1.6	1.5	4.5	5.2	0.3	4.3
5	Re/TiO ₂ ^b	28.9	0.3	0.3	0.8	6.7	0.6	3.3
6	Ru–Re/TiO ₂ ^c	85.2	109.3	33.8	0.3	24.5	–	36.4
7	Rh–Re/TiO ₂ ^c	131.3	89.0	54.6	0.3	23.9	1.5	36.1
8	Ir–Re/TiO ₂ ^c	86.6	5.6	4.1	0.7	30.2	2.4	14.7
9	Pt–Re/TiO ₂ ^c	52.5	0.6	0	0.9	11.9	–	5.5

Catalyst; 0.5 g. Reactant; 10 vol% EtOH aq 80 mL (274.0 mmole g_{cat}⁻¹).
Pretreatment; H₂ reduction at 623 K, Reaction temp.; 473 K.

^a Loading amount of principal metal (Ru, Rh, Ir, and Pt) = 5 wt%.

^b Loading amount of Re = 9.5 wt%.

^c Additive Re/principal metal molar ratio = 1.

The order of the EtOH conversion on M-Re/TiO₂ was where M = Ru ≈ Rh > Ir > Pt, and the extents of the increasing the conversion (in comparison with the yields over the corresponding M/TiO₂ catalysts) were 2.5 times for the Rh and Ir catalysts whereas only 1.2–1.3 times for the Ru and Ir catalysts, respectively. The order of the H₂ producing activities is M = Rh > Ir ≈ Ru > Pt of M-Re/TiO₂ catalysts, and the yields increased about twice (1.8 (Pt), 2.1 (Ir), 2.3 (Rh), and 2.5 (Ru) times) for all catalysts.

Also, changing the yields of other products by adding Re were different depending on the kind of precious metal (=M). For the gas phase products CH₄ and CO₂, these yields increased by adding of Re on the Rh catalyst (twice for CH₄ and 1.7 times for CO₂), while the yields of them were almost identical or decreasing in the case of other metal catalysts. The liquid phase product AcOH increased on all the Re-added catalysts where the order of the extension of the AcOH yields was Rh >> Ru > Ir > Pt. However, the yields of AcH over M-Re/TiO₂ were identical or decreasing. Therefore, the addition of Re seems to lead to acceleration of the reaction Path-II in all catalysts. The acceleration of the reaction Path-II by Re is consistent with the catalytic behavior of Re/TiO₂ (Entry 5 in Table 1). Although H₂ production activity as well as EtOH conversion of Re/TiO₂ catalyst was the lowest in the compared catalysts, its trend of products distribution (high yield of AcOH whereas low yields of AcH, CH₄ and CO₂) might imply that the intrinsic catalysis of Re/TiO₂ is acceleration of reaction Path-II. The yields of products on the Re-added catalysts were certainly higher than the sum of those on the independent catalysts. That is, M-Re/TiO₂ catalysts exhibited higher activity due to synergy effect.

The results showing in Fig. 1 also support the difference of the catalyses of M and the synergy effect of the added Re as described above. The reaction profiles of the Re-added Ir and Pt catalysts ((h) and (i) of Fig. 1) were close as well as these observed for the corresponding M/TiO₂ ((c) and (d)). The effects of Re addition to the Ru and Rh catalysts were more drastic as indicated by the comparison of the set of graphs (a) and (f) for Ru and (b) and (g) for Rh, respectively. On the both M-Re/TiO₂ where M = Ru and Rh, initial H₂ production rates were

accelerated with increasing the AcOH production rates. In case of Ru–Re/TiO₂, however, a yield of H₂ reached plateau within 5 h and the yield of CH₄ exceeded that of H₂ due to the high methanation activity of Ru. In contrast, the initial rates of all gas phase products were accelerated 2.5–3.5 times by the addition of Re to the Rh catalyst. Accordingly, the role of added Re on Rh/TiO₂ is apparently the acceleration of both Path-I and II.

As indicated above, the most active catalyst for H₂ production was Rh–Re/TiO₂ and the second one was Ir–Re/TiO₂. However, the catalytic behavior of Rh–Re/TiO₂ was rather different from that of Ir–Re/TiO₂. Therefore, we focused on clarifying the role of added Re in the case of Rh- and Ir-based catalysts. The dependencies of the initial production rates of various compounds upon the ratios of Re/Rh and Re/Ir were investigated as depicted in Fig. 2. In the case of the Ir-based catalysts, the initial formation rates of H₂ and AcOH increased with the increase of Re/Ir ratios to 1.0, while slight decrease of the rates at Re/Ir = 2.0. In the reaction on the Rh-based catalysts, the trend of the formation rates of H₂ and AcOH with respect to the Re/Rh ratio is similar to that observed on the Ir-based catalysts. However, the formation rates of CH₄ and CO₂ reached to the maximum on Re/Rh = 0.5, and that would be a strong support for the acceleration of both Path-I and II on Rh–Re/TiO₂. Two possible active site structures may be suggested from these results. The first one is the formation of some nano-composites between Re and Rh or Ir, which work as the active species for this reaction, although the structures of the bimetallic nano-composites might be different from each other. The other one is the operation of the two kind metals together, but separately, to change the reaction pathways.

Reaction of acetaldehyde with H₂O over Rh and Ir catalysts

The principle role of the added Re would be acceleration of the reaction Path-II. However, the catalytic behaviors of the Ir-based catalysts (Ir/TiO₂ and Ir–Re/TiO₂) were quite different from those of the Rh-based catalysts (Rh/TiO₂ and Rh–Re/TiO₂). Especially, addition of Re on the Rh catalyst seems to

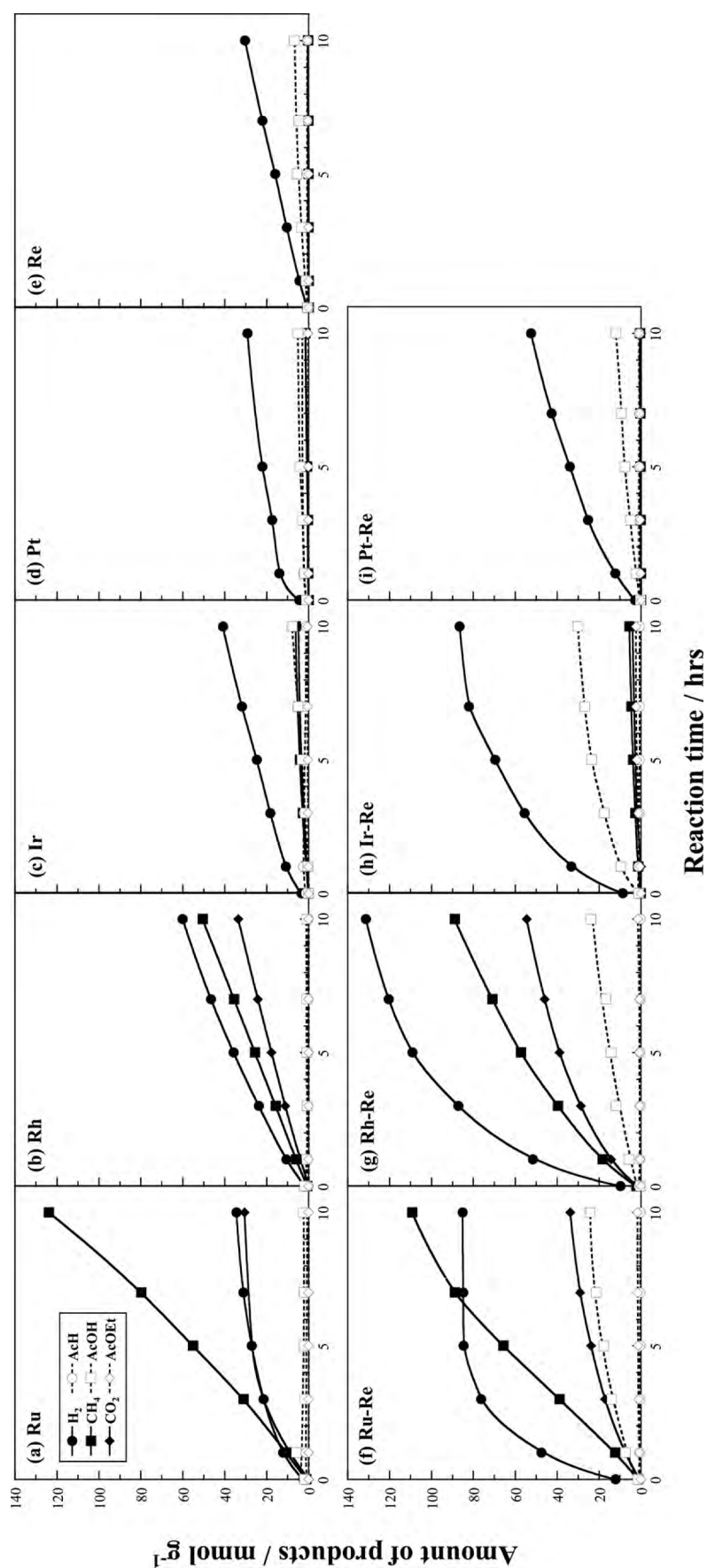


Fig. 1 – Time courses of aqueous phase reforming of ethanol with water over various 5 wt% (except Re/TiO₂, Re loading amount = 9.5 wt%) TiO₂ supported metal catalysts at 473 K. (a) Ru/TiO₂, (b) Rh/TiO₂, (c) Ir/TiO₂, (d) Pt/TiO₂, (e) Re/TiO₂, (f) Ru-Re(1:1)/TiO₂, (g) Rh-Re(1:1)/TiO₂, (h) Ir-Re(1:1)/TiO₂, (i) Pt-Re(1:1)/TiO₂.

accelerate the reaction Path-I as well as Path-II. Therefore, we examined the activity of the Rh- and Ir-based catalysts toward aqueous phase reaction of acetaldehyde at 473 K as shown in Fig. 3 for time-course of reaction profiles.

Conversions of AcH were almost completed in any conditions, however, distributions and formation rates of products were diverse depending on the catalysts and substrate contents (1 vol% or 5 vol%). In the case of 1 vol% aqueous AcH reaction over Re/TiO₂, H₂ and AcOH were major gas-phase and liquid-phase products, and the yields of CH₄ and CO₂ were quite low. On the other hand, considerable amount of EtOH was formed due to the equilibrium between EtOH and AcH through dehydrogenation-hydrogenation (Fig. 3(e)). These observations suggest that the intrinsic activity of the Re site immobilized on TiO₂ was the acceleration of Path-II in Scheme 1.

When 1 vol% aqueous AcH was applied to the Rh catalysts, the selectivity of H₂ in the gas-phase products and yield of the liquid-phase AcOH were increased over the Re-added catalyst (see (a) and (b) of Fig. 3). Formation rates of H₂ and AcOH as well as consumption rate of AcH increased on Rh–Re/TiO₂ compared to those on Rh/TiO₂. The presented Rh-based catalysts did not catalyze the aqueous phase reforming of acetic acid (data not shown), and therefore, formation of CO₂ and CH₄ indicated the decomposition of AcH. Although the acceleration of reaction Path-I over Rh–Re/TiO₂ could not be confirmed when 1 vol% aqueous AcH reactant was applied, higher AcH content reactions (=5 vol% aqueous AcH reactant) suggested that not only Path-II but also Path-I were accelerated over the Re-added Rh catalyst as found for increasing the formation rates of AcOH, CH₄, and CO₂ ((f) and (g) of Fig. 3).

In the cases of the Ir-based catalysts Ir/TiO₂ and Ir–Re/TiO₂, their reaction profiles were clearly different from those observed on the corresponding Rh-based catalysts as shown in Fig. 3. The yields of AcOH over the Ir catalysts were higher than those on the Rh systems, and that is consistent with the difference of the nature of the catalysis of Rh and Ir observed on the EtOH reforming activities (i.e., predominant occurrence of the reaction Path-I over Rh and Path-II over Ir). Both H₂ and AcOH formation rates on Ir–Re/TiO₂ became higher than that

on Ir/TiO₂. In contrast, the formation rates of the other gas-phase products (=CH₄ and CO₂) were almost identical or decreasing by addition of Re on the Ir catalyst. Therefore, we conclude that the added Re effect on the Ir catalyst is the acceleration of the reaction Path-II.

Characterization of catalysts by TEM and XPS analyses as well as CO adsorption by FT-IR and volumetric methods

In order to get insights into the structural natures of the active species, TEM observation, XPS analyses as well as CO adsorption by FT-IR and volumetric methods were conducted as presented in Table 2 and Figs. 4–6. Fig. 4 shows TEM images of Rh/TiO₂, Rh–Re(1:1)/TiO₂, Ir/TiO₂, Ir–Re(1:1)/TiO₂, and Re/TiO₂ catalysts after reduction at 623 K. The dark particles observed in all the photographs could be assigned to Rh, Ir, and Re metals by energy dispersive X-ray spectroscopy (EDS) analysis. In the case of Re/TiO₂, we were able to observe well-dispersed small Re metal particles with average sizes of 1.2 nm. For Rh/TiO₂ catalysts, the average particle sizes (d_{TEM}) decreased from 2.5 to 1.9 nm by adding Re, however, in the case of Ir/TiO₂ catalysts, the average particle sizes (d_{TEM}) increased from 1.6 to 1.9 by adding Re.

Fig. 5 portrays results of XPS analyses of the reduced Rh/TiO₂, Ir/TiO₂ and their Re added catalysts followed by in situ introduction of H₂O vapor. The binding energy of Rh3d_{5/2} transition was almost zero valence (306.9 eV), which did not change by adding Re. By deconvolution of the Rh peak we may detect the existence of a few % Rh³⁺ species in Rh⁰ peak. The situation closely resembled that in the case of reduced Ir/TiO₂ catalysts except that the amount of oxidized Ir⁴⁺ species was estimated around 1/3 of Ir⁰ peak, which was one order of magnitude larger than the case of Rh/TiO₂ catalyst. For both catalysts, the binding energy of the added Re indicated the presence of zero valence Re species in their reduced state, again suggesting the formation of bimetallic nanocomposites. By introduction of H₂O vapor at 473 K, in-situ XPS observation revealed partially oxidized Re species, which are expected to be similar to the actual aqueous EtOH reaction condition.

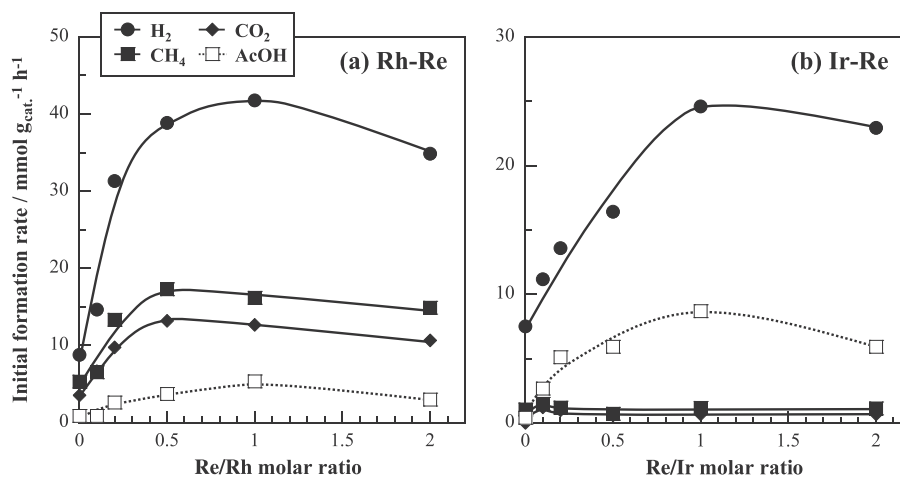


Fig. 2 – Dependences of the initial rates of various products formation upon the amounts of added Re/Rh and Re/Ir ratios over (a) Rh–Re/TiO₂ and (b) Ir–Re/TiO₂ catalysts.

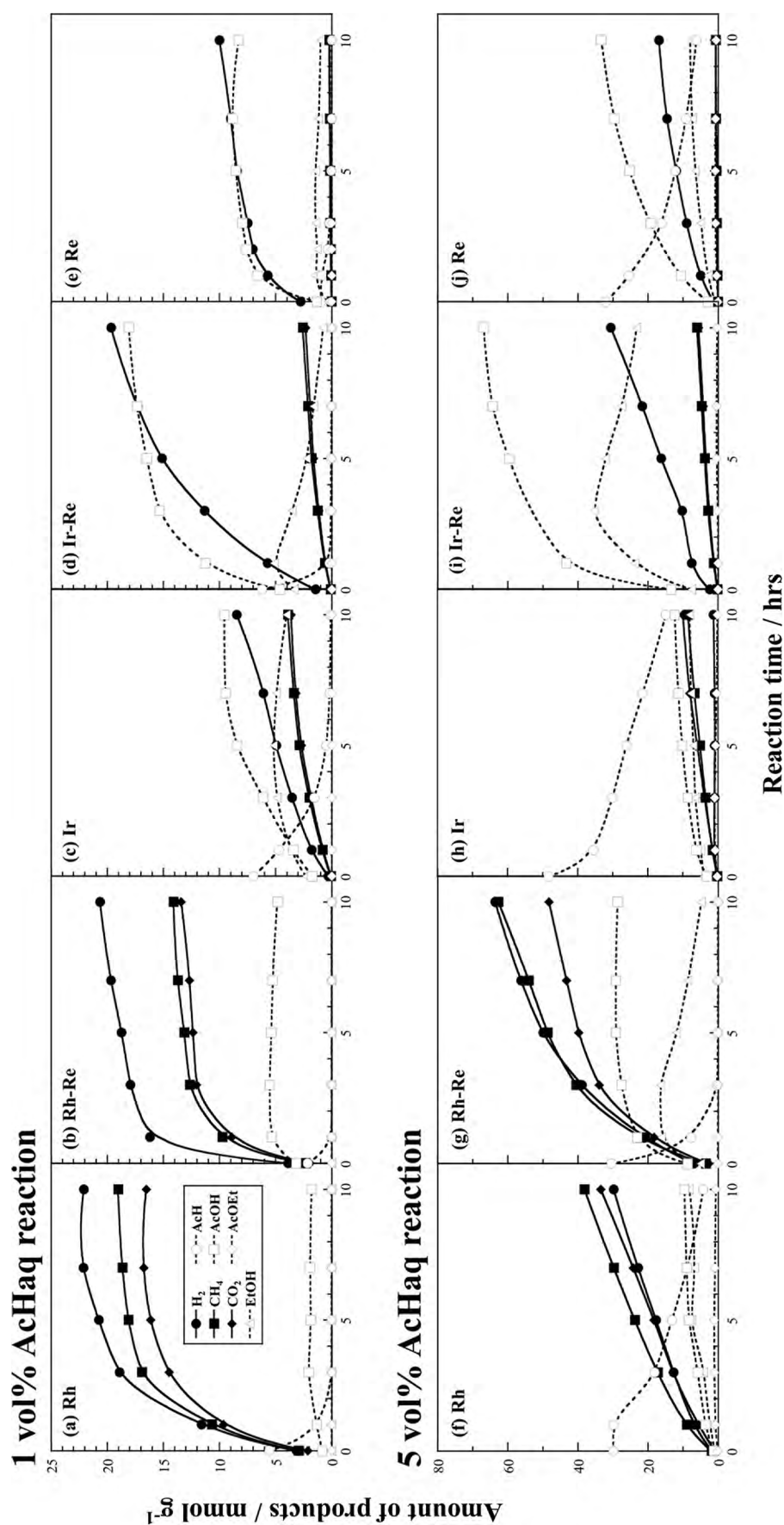


Fig. 3 – Time courses of aqueous phase reforming of (a–e) 1 vol% and (f–j) 5 vol% acetaldehyde with water over (a, f) Rh–TiO₂, (b, g) Rh–Re(1:1)/TiO₂, (c, h) Ir–TiO₂, (d, i) Ir–Re(1:1)/TiO₂, and (e, j) Re/TiO₂ at 473 K.

Table 2 presents the amount of adsorbed CO, percent dispersion (D %), and the estimated particle sizes (d_{CO}) over various TiO_2 -supported Rh and Ir catalysts after 623 K reduction. It is noteworthy that over Rh/ TiO_2 and Ir/ TiO_2 catalysts, the estimated d_{CO} values were 3.7 and 2.9 nm, which were much larger than the d_{TEM} values (2.5 and 1.6 nm) described above. These phenomena might be explained by the strong metal support interaction (SMSI) effect between TiO_2 support and Rh or Ir metal particles. The amounts of adsorbed CO decreased gradually by the addition of Re in both metals, and 1:1 ratio catalysts exhibited the increase of the estimated d_{CO} values of 7.2 nm (Rh–Re) and 3.5 nm (Ir–Re), respectively. It is noteworthy to emphasize that all the values of metal particle sizes estimated from CO adsorption (d_{CO}) are rather different from the particle sizes observed by TEM photographs (d_{TEM}). This discrepancy may be explained reasonably if we assume that excess rhenium oxide left by the formation of a thin oxide overlayer may cover the Rh and Ir metal surfaces and inhibit the adsorption of CO.

To study the active site structures in more detail, gas-phase adsorption of CO followed by its temperature-programmed desorption was investigated by FT–IR spectroscopy. As depicted in Fig. 6(a), when 10 Torr of CO was introduced onto the freshly reduced Rh/ TiO_2 at room temperature, a strong absorption band was observed at 2061 cm^{-1} together with the pair peaks at 2108 and 2048 cm^{-1} (shoulder), respectively assignable to the linear CO(a) species on top of Rh^0 species and geminal CO(a) peaks on $\text{Rh}^{\delta+}$ species. Buchanan et al. reported the disruption of metallic Rh clusters on reduced Rh/ TiO_2 by adsorbed CO at temperatures as low as 160 K and the development of two bands around 2100 and 2030 cm^{-1} at room temperature, assignable to the asymmetric and symmetric stretching mode of $\text{Rh}^+(\text{CO})_2$ [12], which are very similar to the results obtained in the present study. By raising the evacuation temperature, the intensities of these peaks decreased gradually and almost disappeared at 473 K. The situation was similar in the case of adsorbed CO over Rh–Re(1:1)/ TiO_2 catalyst, as depicted in Fig. 6(b). The main peak was observed at 2049 cm^{-1} with the shoulder at 2105 and 2061 cm^{-1} assignable to the geminal CO(a) and linear species, of which the intensity were nearly half that of the non-Re-added Rh/ TiO_2 catalyst corresponding rather well to the case of CO adsorption (Table 2). By evacuation at elevated

temperatures, the intensities of these peaks decreased considerably and almost disappeared at 473 K.

In the case of CO adsorption over freshly reduced Ir/ TiO_2 , two overlapping peaks were observed at 2076 and 2065 cm^{-1} assignable to the linear CO(a) species, together with a shoulder peak at 1986 cm^{-1} assignable to the bridged CO(a), as depicted in Fig. 6(c). By evacuation at elevated temperatures the linear CO(a) peaks shifted to the lower wavenumber side (2065 – 2049 cm^{-1}) with a slight decrease of their intensities. However, the bridged CO(a) peak stayed at the same position with intensity increased at 573 K evacuation. The situation was rather different in the case of adsorbed CO over Ir–Re(1:1)/ TiO_2 catalyst, as depicted in Fig. 6(d). The main peak was observed at 2066 cm^{-1} assignable to the linear CO(a), of which the intensity was almost identical to that of the Ir/ TiO_2 catalyst. Additionally, characteristic shoulder peaks were observed at 2009 and $1980, 1951\text{ cm}^{-1}$, which were rather similar to those of CO(a) over Re/ TiO_2 , as depicted in Fig. 6(e). By evacuation at elevated temperatures, the peak position shifted to the lower wavenumber side, although almost no decrease in intensity was apparent even at 473 K evacuation.

Efficient active site structures for ethanol APR reaction

In the present study Re addition procedure was carried out by successive impregnation method as follows; Re precursor NH_4ReO_4 was initially impregnated onto TiO_2 support followed by calcination at 773 K. It is reported that highly dispersed $\text{Re}_2\text{O}_7/\text{TiO}_2$ sample shows the Raman bands at 1005 and 795 cm^{-1} , which are attributed to the symmetric and asymmetric stretching mode of terminal $\text{Re}=\text{O}$ of the dehydrated surface rhenium oxide species on TiO_2 . We could obtain the similar Raman bands in the present study (not shown) [13,28,29]. After that, Rh and Ir precursors were impregnated to Re/ TiO_2 , followed by the reduction with H_2 at 623 K for 2 h. In the case of Rh/ TiO_2 catalyst, the average particle size determined by TEM decreased to 4/5 by adding Re, probably because of some stronger interaction of Rh precursors with ReO_x overlayers on top of TiO_2 support and the prevention of Rh metal sintering. On the other hand, in the case of Ir/ TiO_2 catalysts, the average particle size determined by TEM increased to 4/3 by adding Re, suggesting the stronger

Table 2 – Characterization of various TiO_2 supported catalysts.

Entry	Catalysts	Surf. Area/ $\text{m}^2\text{ g}^{-1}$	Amt. of CO(a)/ $\text{cm}^3\text{ g}^{-1}$	Disp./%	Particle size/nm	
					CO ^(a)	TEM
1	Ru/ TiO_2^{a}	49.8	2.1	19.3	6.8	2.3
2	Rh/ TiO_2^{a}	51.1	3.0	27.7	3.7	2.5
3	Ir/ TiO_2^{a}	48.6	2.5	43.6	2.9	1.6
4	Pt/ TiO_2^{a}	44.7	0.3	5.8	19.2	–
5	Re/ TiO_2^{b}	–	2.1	–	–	1.2
6	Rh–Re/ TiO_2^{c}	36.8	2.3	20.8	5.2	1.9
7	Ir–Re/ TiO_2^{c}	37.9	2.1	35.4	3.6	1.9

^a Loading amount of principal metal(Ru, Rh, Ir, and Pt) = 5 wt%.

^b Loading amount of Re = 9.5 wt%.

^c Additive Re/principal metal molar ratio = 1.

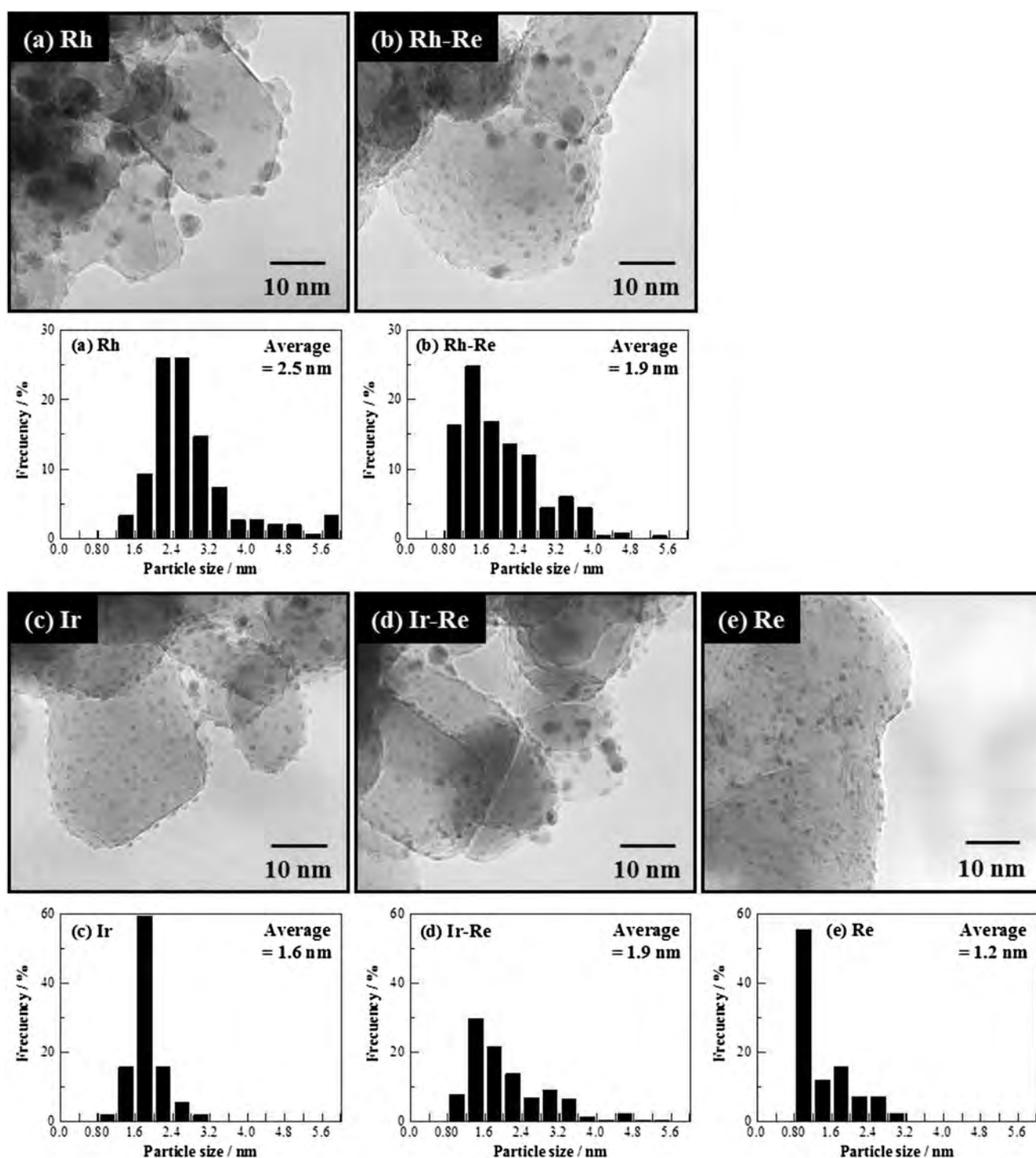


Fig. 4 – TEM images and particle size distributions of various TiO₂ supported Rh and Ir catalysts. (a) Rh/TiO₂, (b) Rh–Re(1:1)/TiO₂, (c) Ir/TiO₂, (d) Ir–Re(1:1)/TiO₂, (e) Re/TiO₂.

interaction between Ir and Re during the reduction process after successive impregnation of Ir precursors.

As mentioned already in Introduction section, we investigated the effect of Re addition upon APR of methanol over SiO₂, ZrO₂ and TiO₂ supported Ir catalysts [14]. Two different enhancement manners were realized depending on the complicated combination between the kind of additives and

supports. In the cases of Ir–Re/SiO₂ and Ir–Re/ZrO₂, hydrogen formation rate was accelerated remarkably by the formation of some nano-composites between Ir and Re, where the reaction proceeds through partially dehydrogenated alcohol intermediate and the rate determining step is dehydrogenation of methanol [10]. On the other hand, in the case of Ir–Re/TiO₂, the formation of thin monolayer-like structure of ReO_x

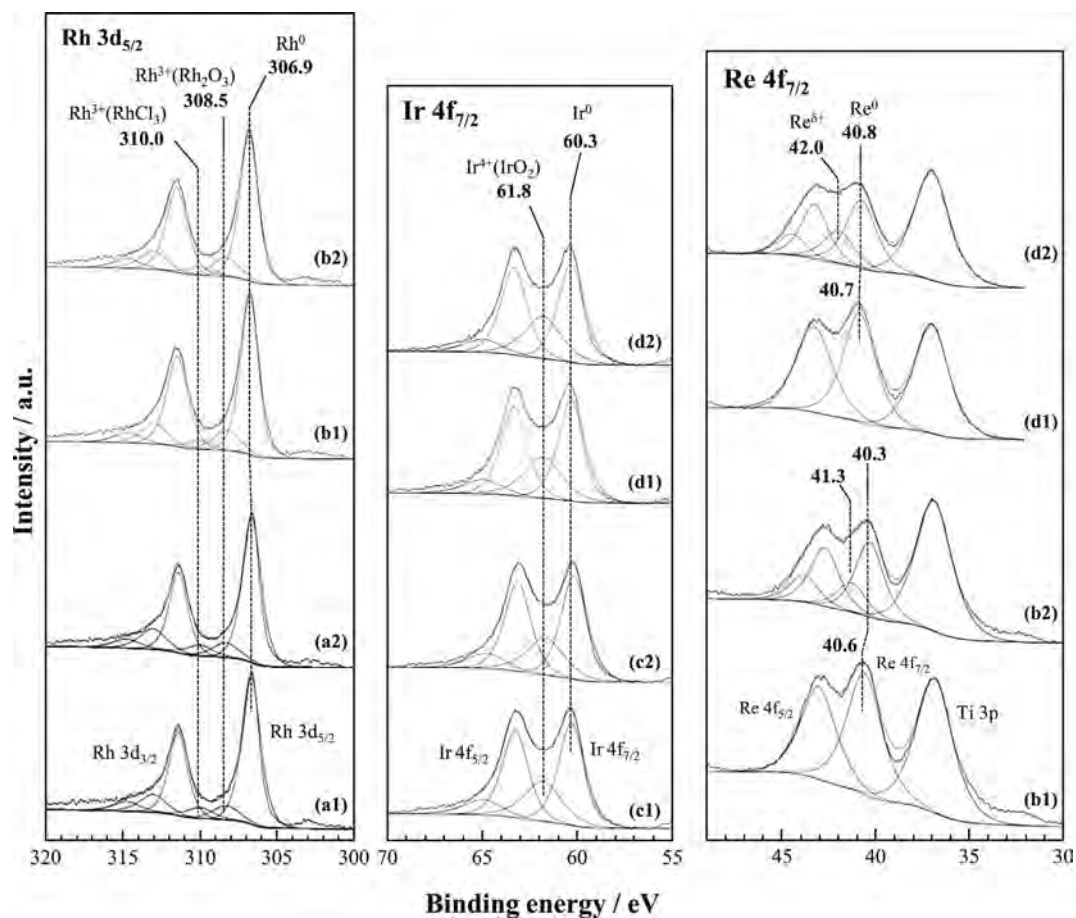


Fig. 5 – XPS analyses of Rh/TiO₂, Ir/TiO₂ and Re added catalysts. (a) Rh/TiO₂, (b) Rh–Re(1:1)/TiO₂, (c) Ir/TiO₂, (d) Ir–Re(1:1)/TiO₂; (1) after in-situ reduction at 623 K, and (2) after in-situ exposure to H₂O vapor at 473 K.

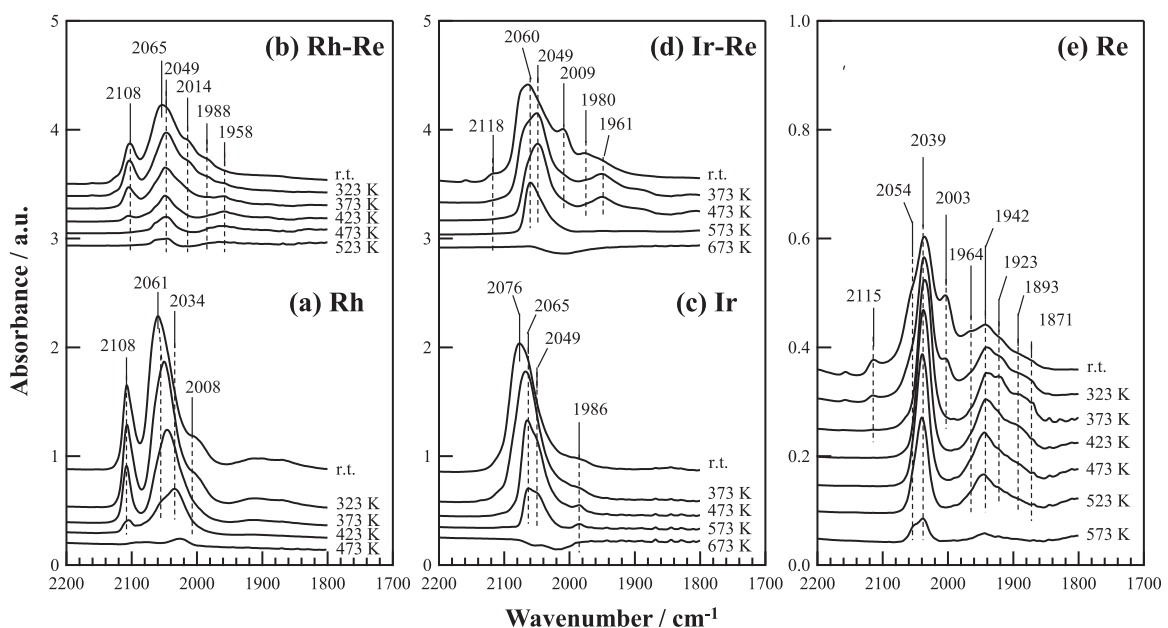


Fig. 6 – FT-IR spectra of CO adsorption at room temperature and following TPD over (a) Rh/TiO₂, (b) Rh–Re(1:1)/TiO₂, (c) Ir/TiO₂, (d) Ir–Re(1:1)/TiO₂, (e) Re/TiO₂.

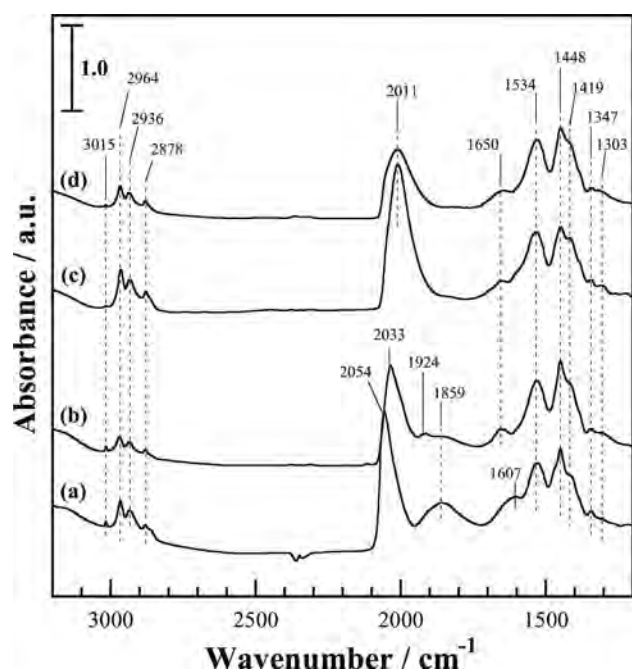


Fig. 7 – FT-IR spectra of adsorbed species during EtOH + H₂O reaction at 473 K over (a) Rh/TiO₂, (b) Rh–Re(1:1)/TiO₂, (c) Ir/TiO₂ (d) Ir–Re(1:1)/TiO₂.

on TiO₂ surface was important for the acceleration of hydration process. As described in the previous section, we may have both kinds of active site structures on Ir–Re/TiO₂ catalysts, which may play important roles in the acceleration of EtOH reaction.

In order to obtain the information about the active site structures during APR reaction, model reaction of gas-phase EtOH + H₂O was carried out at 473 K inside the IR cell. Fig. 7(a) presents the FT-IR spectra of adsorbed species when gaseous ethanol and water vapor was introduced onto freshly reduced Rh/TiO₂ disk at 473 K for 1 h. A linearly adsorbed CO(a) peak was observed at 2053 cm⁻¹. However, no germinal peak was observed, indicating the absence of Rh^{δ+} species during gaseous EtOH + H₂O reaction at 473 K. Instead, a rather strong peak was observed at 1859 cm⁻¹, which can be assigned to bridged CO(a) species. In the case of Rh–Re/TiO₂ (Fig. 7(b)), the linear CO(a) peak shifted to 2033 cm⁻¹ with the disappearance of bridge CO(a). In the case of EtOH + H₂O reaction over Ir/TiO₂, a linearly adsorbed CO peak was observed at 2011 cm⁻¹, of which the position was 50 cm⁻¹ lower in wavenumber than that of the CO(a) peak observed in gaseous CO adsorption (Fig. 7(c)). These results show that rather drastic steric as well as electronic modification might proceed during reforming reaction at 473 K.

Conclusions

The catalytic properties of a series of M/TiO₂ to the aqueous phase reforming of ethanol were compared, and the order of the H₂ production activity was Rh > Ir > Ru > Pt. The intrinsic

catalysis of the precious metals supported on TiO₂ was diverse; Rh and Ru drove the decomposition of the initial formed acetaldehyde and following water-gas shift reaction, whereas Ir and Pt mediated the acetic acid formation through the hydration of acetaldehyde. Addition of Re onto M/TiO₂ led improvements in the EtOH conversion as well as the yields of H₂ and acetic acid in all catalysts, and drastic additive effect was observed on the Rh and Ir catalysts. The following points are key findings on the effects of Re addition on the APR of ethanol over Rh/TiO₂ and Ir/TiO₂ catalysts:

- (1) In the case of Rh/TiO₂, Re addition effect for ethanol APR was as follows; the amounts of both H₂ and CH₄ increased two times more with 1.5 times for CO₂, while the amount of AcOH was greatly enhanced. Average particle sizes (d_{TEM}) decreased to four fifth by adding Re, because of certain anchoring effect of ReO_x overlayers on top of TiO₂ surface during the successive impregnation process of Rh precursors. Rh–Re bimetallic nano-composites were formed by the following reduction process.
- (2) In the case of Ir/TiO₂, the amounts of H₂ and AcOH increased twice and four times more respectively by the addition of Re, although the amounts of CH₄ and CO₂ were almost the same. Average particle sizes (d_{TEM}) increased to four third by adding Re, suggesting the stronger interaction between Ir and Re during the reduction process of Ir precursors, and forming Ir–Re bimetallic nano-composites.
- (3) The role of added Re was the acceleration of the hydration of AcH to form AcOH rather than the decomposition of AcH to form CH₄ and CO on both Rh/TiO₂ and Ir/TiO₂ catalysts. Well dispersed bimetallic nano-composites would work as the active sites for EtOH dehydrogenation and AcH decomposition, whereas partially oxidized Re sites may work for the hydration of AcH to form AcOH.

Acknowledgments

The authors are grateful for financial support through “a Strategic Development of Research Infrastructure for Private Universities from the Ministry of Education, Culture, Sports, Science, and Technology (MEXT), Japan”.

REFERENCES

- [1] Haryanto A, Fernando S, Murali N, Adhikari S. Current status of hydrogen produced by steam reforming of ethanol. *Energy Fuels* 2005;19:2098–106.
- [2] Ni M, Leung DY, Leung MK. A review of reforming bio-ethanol for hydrogen production. *Int J Hydrogen Energy* 2007;32:3238–47.
- [3] Cortright RD, Davda RR, Dumesic JA. Hydrogen from catalytic reforming of biomass-derived hydrocarbons in liquid water. *Nature* 2002;18:964–7.

- [4] Shabaker JW, Davda RR, Huber GW, Cortright RD, Dumesic JA. Aqueous-phase reforming of methanol and ethylene glycol over alumina-supported platinum catalysts. *J Catal* 2003;215:344–52.
- [5] Shabaker JW, Huber GW, Dumesic JA. Aqueous-phase reforming of oxygenated hydrocarbons over Sn-modified Ni catalysts. *J Catal* 2004;222:180–91.
- [6] Shabaker JW, Dumesic JA. Kinetics of aqueous-phase reforming of oxygenated hydrocarbons: Pt/Al₂O₃ and Sn-modified Ni catalysts. *Ind Eng Chem Res* 2004;43:3105–12.
- [7] Chu X, Liu J, Sun B, Dai R, Pei Y, Qiao M, et al. Aqueous-phase reforming of ethylene glycol on Co/ZnO catalysts prepared by the coprecipitation method. *J Mol Catal A Chem* 2011;335:129–35.
- [8] Huber GW, Shabaker JW, Dumesic JA. Raney Ni-Sn catalyst for H₂ production from biomass-derived hydrocarbon. *Science* 2003;300:2075–7.
- [9] King DL, Zhang L, Xia G, Karim GX, Heldebrant DJ, Wang X, et al. Aqueous phase reforming of glycerol for hydrogen production over Pt-Re supported on carbon. *Appl Catal B Env* 2010;99:206–13.
- [10] Miyao T, Yamauchi M, Naito S. Liquid phase methanol reforming with water over silica supported Pt–Ru catalysts. *Catal Today* 2003;87:227–35.
- [11] Miyao T, Watanabe Y, Teramoto M, Naito S. Catalytic activity of various supported Ir-Re catalysts for liquid phase methanol reforming with water. *Catal Commun* 2005;6:113–7.
- [12] Sakamoto T, Morishima H, Yoshida A, Naito S. Marked effect of Mo and Fe addition upon liquid phase methanol reforming with water over Al₂O₃ supported Pt catalysts. *Catal Lett* 2009;131:419–24.
- [13] Sakamoto T, Kikuchi H, Miyao T, Yoshida A, Naito S. Remarkable effect of transition metal element addition upon liquid phase reforming of methanol with water over TiO₂ supported Pt catalysts. *Appl Catal A Gen* 2010;375:156–62.
- [14] Sakamoto T, Miyao T, Yoshida A, Naito S. Effect of Re and Mo addition upon liquid phase methanol reforming with water over SiO₂, ZrO₂ and TiO₂ supported Ir catalysts. *Int J Hydrogen Energy* 2010;35:6203–9.
- [15] Shinmi Y, Koso S, Kubota T, Nakagawa Y, Tomishige K. Modification of Rh/SiO₂ catalyst for the hydrogenolysis of glycerol in water. *Appl Catal B Env* 2010;94:318–26.
- [16] Nakagawa Y, Tomishige K. Heterogeneous catalysis of the glycerol hydrogenolysis. *Catal Sci Tech* 2011;1:179–90.
- [17] Nakagawa Y, Shinmi Y, Koso S, Tomishige K. Direct hydrogenolysis of glycerol into 1,3-propanediol over rhenium-modified iridium catalyst. *J Catal* 2010;272:191–4.
- [18] Sheng P-Y, Yee A, Bowmaker A, Idriss H. H₂ production from ethanol over Rh-Pt/CeO₂ catalysts: the role of Rh for the efficient dissociation of the carbon-carbon bond. *J Catal* 2002;208:393–403.
- [19] Tang Z, Monroe J, Dong J, Nenoff T, Weinkauff D. Platinum-loaded NaY zeolite for aqueous phase reforming of methanol and ethanol to hydrogen. *Int Eng Chem Res* 2009;48:2728–33.
- [20] Roy B, Artyushkova K, Pham HN, Li L, Datye AK, Leclerc CA. Effect of preparation method on the performance of the Ni/Al₂O₃ catalysts for aqueous-phase reforming of ethanol: part II-characterization. *Int J Hydrogen Energy* 2012;37:18815–26.
- [21] Takanabe T, Aika K, Seshen K, Lefferts L. Sustainable hydrogen from bio-oil-steam reforming of acetic acid as a model oxygenate. *J Catal* 2004;227:101–8.
- [22] Basagiannis AC, Verykios XE. Catalytic steam reforming of acetic acid for hydrogen production. *Int J Hydrogen Energy* 2007;32:3343–55.
- [23] Basagiannis AC, Verykios XE. Influence of the carrier on steam reforming of acetic acid over Ru-based catalysts. *Appl Catal B Env* 2008;82:77–88.
- [24] Thaicharoensutcharittham S, Meeyoo V, Kitiyanan B, Rangsunvigit P, Rirksomboon T. Hydrogen production by steam reforming of acetic acid over Ni-based catalysts. *Catal Today* 2011;164:257–61.
- [25] Iwasa N, Yamane T, Arai M. Influence of alkali metal modification and reaction conditions on the catalytic activity and stability of Ni containing smectite-type material for steam reforming of acetic acid. *Int J Hydrogen Energy* 2011;36:5904–11.
- [26] Wan H, Chaudhari RV, Subramaniam B. Aqueous phase hydrogenation of acetic acid and its promotional effect on p-cresol hydrodeoxygenation. *Energy Fuels* 2013;27:487–93.
- [27] Nozawa T, Mizukoshi Y, Yoshida A, Naito S. Aqueous phase reforming of ethanol and acetic acid over TiO₂. *Appl Catal B Env* 2014;146:221–6.
- [28] Wachs IE. Raman and IR studies of surface metal oxide species on oxide supports: supported metal oxide catalysts. *Catal Today* 1996;27:437–55.
- [29] Mitra B, Gao X, Wachs IE, Hirt AM, Deo G. Characterization of supported rhenium oxide catalysts: effect of loading, support and additives. *Phys Chem Chem Phys* 2001;3:1144–52.

Efficient-Oxygen Induced Mineralization of Melt-Processable Fluoropolymers in Subcritical and Supercritical Water

Hisao Hori,^{†,*} Takehiko Sakamoto,[†] Kenta Ohmura,[†] Haruka Yoshikawa,[†] Tomohisa Seita,[†] Tomoyuki Fujita,[‡] and Yoshitomi Morizawa[‡]

[†]Department of Chemistry, Faculty of Science, Kanagawa University, 2946 Tsuchiya, Hiratsuka, Kanagawa 259-1293, Japan

[‡]Research Center, Asahi Glass Co., 1150 Hazawa-cho, Kanagawa-ku, Yokohama, Kanagawa 221-8755, Japan

ABSTRACT: The decomposition of poly(vinylidene fluoride) (PVDF) and ethylene–tetrafluoroethylene copolymer (ETFE) in subcritical and supercritical water was investigated. Heating PVDF in supercritical water at 380 °C for 6 h with an approximately 5.8-fold molar excess of O₂ relative to the fluorine or carbon content in the polymer afforded F[−] and CO₂ in 96.9% and 99.3% yields, respectively. ETFE was also efficiently mineralized to F[−] (97.6%) and CO₂ (98.2%) with an 11-fold molar excess of O₂ relative to the fluorine or carbon content of the polymer under the same reaction conditions. The PVDF and ETFE reactivities differed markedly under argon: PVDF formed mainly F[−], CO₂ formation was suppressed, and a carbon-rich residue formed; in contrast, ETFE was unreactive. This difference suggests that PVDF decomposed via dehydrofluorination in the absence of O₂, whereas ETFE did not. Adding stoichiometric Ca(OH)₂ to the reaction in the presence of O₂ afforded X-ray spectrometrically pure CaF₂.

INTRODUCTION

Owing to their high chemical and thermal stability, fluoropolymers (olefinic polymers in which some or all of the hydrogen atoms are replaced by fluorine atoms) are used in industrial equipment to impact corrosion resistance. Poly-(tetrafluoroethylene) (PTFE, $-(CF_2CF_2)_n-$) is the most frequently used fluoropolymer.¹ However, PTFE cannot be processed by melt molding, a conventional technique for fabricating thermoplastic polymers, because the viscosity of the PTFE melt (10^9 – 10^{11} Pa s) is about 6 orders of magnitude higher than that of common thermoplastic polymers.¹ To overcome this weakness, melt-processable fluoropolymers, such as poly(vinylidene fluoride) (PVDF, $-(CF_2CH_2)_n-$) and ethylene–tetrafluoroethylene copolymer (ETFE, $-(CH_2CH_2)_m(CF_2CF_2)_n-$), which can be fabricated by melt processes including extrusion, injection, compression, and blow molding, have been developed and introduced in industry.^{1–5} Melt-processable fluoropolymers show high resistance to temperature, chemicals, ignition, mechanical stresses, UV irradiation, and weather and have been used for various applications, including piping, tubing, valves, sinks, cables, films, and lithium ion battery electrode binders. It is estimated that the proportion of PTFE to the total global fluoropolymer demand will decrease gradually to 52% in 2016 (from 61% in 1996), during which time total fluoropolymer demand is expected to increase from 115 000 to 305 000 tons.¹ Wider use of melt-processable polymers will require the establishment of waste treatment. Some of these polymers are recycled, and they can also be incinerated. However, incineration requires high temperatures to break the strong C–F bonds, and the hydrogen fluoride gas that forms can damage the firebrick of an incinerator. Thus, in many cases, the wastes of these polymers are disposed of in landfills. If the polymers could be decomposed to F[−] ions (that is, mineralized) by means of environmentally benign techniques, the well-established proto-

col for treatment of F[−] ions could be used, whereby Ca²⁺ is added to the system to form CaF₂, which is a raw material for hydrofluoric acid. Thus, the development of such a method would allow the recycling of fluorine, the global demand for which is increasing.

Several studies have focused on the degradation of PVDF and ETFE.^{6–13} However, most of the previous studies examined the thermal stability or aging characteristics of the polymers; none focused on their decomposition to obtain F[−] ions for waste treatment. Only one report, a patent¹³ describing monomer production for numerous polymers in supercritical water, noted PVDF as an applicable species, but no specific results were shown.

Reactions in subcritical or supercritical water are recognized as an innovative and environmentally benign waste-treatment technique, owing to the high diffusivity and low viscosity of these media, as well as their ability to hydrolyze many organic compounds.¹⁴ Subcritical water is defined as hot water with sufficient pressure to maintain the liquid state, and supercritical water is defined as water at temperatures and pressures higher than the critical point, 374 °C and 22.1 MPa. Recently, supercritical water was used for pilot- and practical-plant-scale decomposition of trinitrotoluene¹⁵ and polychlorinated biphenyls.¹⁶ Depolymerization of common polymers such as poly-(ethylene terephthalate) in subcritical water was also investigated.^{17–19} We previously demonstrated that a perfluoroalkyl sulfonic acid membrane polymer for fuel cells can be efficiently decomposed in subcritical water in the presence of metals.²⁰ Herein, we report on the decomposition of PVDF and ETFE in subcritical and supercritical water, and we present an effective

Received: January 30, 2014

Revised: March 30, 2014

Accepted: April 3, 2014

Published: April 3, 2014

method for complete mineralization of the fluorine and carbon in these polymers to F^- and CO_2 , respectively. Furthermore, we report that CaF_2 forms upon addition of a stoichiometric amount of $Ca(OH)_2$ to the reaction system.

EXPERIMENTAL SECTION

Materials. Powered PVDF was purchased from SynQuest Laboratories (Alachua, FL). Size-exclusion chromatography indicated that the weight-average molecular weight of this polymer was 6.47×10^5 with a polydispersity of 2.52. ETFE powder with an estimated weight-average molecular weight of 10^5 – 10^6 and a 50/50 ethylene/tetrafluoroethylene ratio (i.e., the m/n ratio in $-(CH_2CH_2)_m(CF_2CF_2)_n-$) was obtained from Asahi Glass (Tokyo, Japan).²¹ Combustion ion chromatography²² revealed that the fluorine contents in PVDF and ETFE were 60.7 and 60.6 wt %, respectively; these values are slightly higher than the corresponding ideal values (both 59.3 wt %). These analytical values were used to calculate the F^- yields of the reactions. Argon (99.99%), O_2 (99.999%), and CO_2 (0.995%)/ N_2 gases were purchased from Taiyo Nippon Sanso (Tokyo, Japan). C_2H_4 (99.5%) and C_2H_6 (99.5%) were obtained from GL Sciences (Tokyo, Japan). $HOOCCH_2COOH$ (>98%), $HOOC-COOH$ (>98%), 1,3,5-trifluorobenzene, and other reagents were obtained from Wako Pure Chemical Industries (Osaka, Japan).

Reaction Procedures. Reactions were carried out in a stainless steel high-pressure reactor fitted with a gold vessel to prevent contamination from the reactor material. The internal volume of the reactor was 96 mL. In a typical run in the presence of O_2 , oxygen-saturated Milli-Q water (30 mL) and 90 mg of the polymer (PVDF or ETFE) were introduced into the reactor, which was then pressurized to 0.60 MPa with O_2 , sealed, and heated to the desired temperature (150–380 °C). During the reactions, the mixture was stirred with a gold-plated impeller. After a specified time passed, the reactor was quickly cooled to room temperature, and the reaction solution was subjected to ion chromatography and attenuated total reflection infrared (ATR-IR) spectrometry. The gas phase was collected with a sampling bag and subjected to gas chromatography (GC) and gas chromatography–mass spectrometry (GC/MS). Control experiments were conducted with argon instead of O_2 . The reactions involving stoichiometric amount of $Ca(OH)_2$ (the molar amount was half the molar amount of fluorine atoms in the polymer) were also performed: the white precipitate that formed during these reactions was collected by centrifugation, washed with pure water, and subjected to X-ray diffractometry (XRD).

Analysis. The molecular weight of PVDF was determined by means of size-exclusion chromatography with a refractive index detector (RID-10A, Shimadzu, Kyoto, Japan) and an analytical column (PLgel 10 μ m Mixed-B \times 2, Agilent Technologies, Santa Clara, CA). The mobile phase was *N,N*-dimethylformamide containing LiBr (10 mM), and the flow rate was 1.0 mL min^{-1} . Molecular weight and molecular weight distribution are reported relative to polystyrene as a standard. The fluorine content in the polymers was quantified by combustion ion chromatography at Nissan Arc (Yokosuka, Japan) on an instrument consisting of a combustion unit (AQF-100, Dia Instruments, Chigasaki, Japan; matrix combustion temperature, 1100 °C) and an ion chromatograph unit (Dionex ICS-3000, Thermo Fisher Scientific, Waltham, MA). The fluorine content of the sample was converted to HF by combustion and absorbed into a solution containing Na_2CO_3

(2.7 mM), $NaHCO_3$ (0.3 mM), and H_2O_2 (26.5 mM) and was then transferred to the ion-chromatography unit.

The F^- concentrations were measured with an ion-chromatography system (IC-2001, Tosoh, Tokyo, Japan) consisting of an automatic sample injector (30 μ L injection volume), a degasser, a pump, a guard column (TSKguard column Super IC-A, 4.6 mm i.d., 1.0 cm length, Tosoh), a separation column (TSKgel Super IC-Anion, 4.6 mm i.d., 15 cm length, Tosoh), a column oven (40 °C), and a conductivity detector with a suppressor device. The mobile phase was an aqueous solution containing $Na_2B_4O_7$ (6 mM), H_3BO_3 (15 mM), and $NaHCO_3$ (0.2 mM); the flow rate was 0.8 mL min^{-1} . An ion-chromatography system (IC-2001) with a separation column (TSKgel Super IC-AP, 4.6 mm id, 7.5 cm length, Tosoh) was also used to quantify the organic acids ($HOOCCH_2COOH$ and $HOOC-COOH$). The mobile phase was an aqueous solution containing $NaHCO_3$ (1.7 mM), Na_2CO_3 (1.8 mM), and acetonitrile (23 vol %). ATR-IR spectra were recorded with a FTIR spectrophotometer (Spectrum 100, PerkinElmer, Waltham, MA) with a diamond ATR cell. The reaction solution was dropped into the ATR cell, concentrated to dryness with a gentle N_2 stream, and then subjected to measurement.

A GC system (GC 323, GL Sciences) consisting of an injector (150 °C), a column oven (110 °C), and a thermal conductivity detector (130 °C) was used to quantify CO_2 . The column was an active carbon column (60/80 mesh, 2.17 mm i.d., 2 m length), and the carrier gas was argon. The products in the gas phase were also analyzed with a GC/MS (QP2010 SE, Shimadzu) system with a fused-silica capillary column (Rt-Q-BOND, Restek, Bellefonte, PA). The carrier gas was helium, and the injection temperature was held constant at 120 °C. The sample gas was introduced into the GC/MS system in split mode (ratio, 20/1) and analyses were conducted in full-scan mode (m/z 2.0–200). The oven temperature was held constant at 30 °C for 30 min or kept at 30 °C for 5 min, raised to 200 °C at a rate of 20 °C min^{-1} , and held at that temperature for 20 min. XRD patterns were measured with $Cu K\alpha$ radiation (Multiflex, Rigaku, Tokyo, Japan).

RESULTS AND DISCUSSION

Reactions of PVDF. Initially, we carried out the reactions of PVDF in the presence of argon (i.e., in the absence of O_2) to investigate the reactivity of the polymer in pure subcritical and supercritical water. The temperature dependences of the amount of F^- in the reaction solution and CO_2 in the gas phase at a constant reaction time of 6 h are shown in Figure 1a. A solid residue was present after all these reactions. At 250 °C, almost no mineralization of the polymer occurred: the amount of F^- in the aqueous phase after 6 h was 0.028 mmol, which corresponds to a F^- yield [(moles of F^- formed)/(moles of fluorine in the polymer)] of 0.97%. Similarly, the amount of CO_2 was 0.014 mmol, which corresponds to a yield [(moles of CO_2 formed)/(moles of carbon in the polymer)] of 0.50%. In contrast, F^- clearly formed during the reaction at around 300 °C, and the amount of F^- increased with increasing reaction temperature. At 380 °C, the temperature at which the water reached the supercritical state, the amount of F^- reached 2.56 mmol (88.9%; Table 1, entry 1). Note that in this study, the temperature at which efficient decomposition of PVDF was observed in subcritical water (≥ 300 °C) was considerably lower than that (~ 440 °C) reported for a pyrolysis experiment.⁶

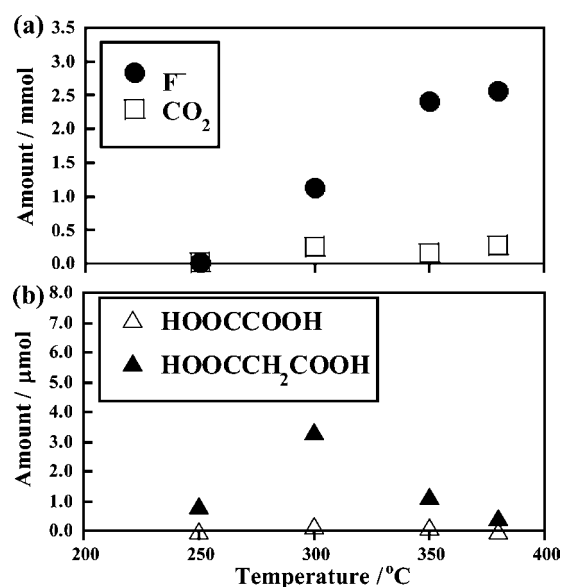


Figure 1. Temperature dependence of PVDF decomposition in the presence of argon: detected amounts of (a) F⁻ and CO₂ and (b) organic acids. PVDF (90 mg; fluorine content, 2.88 mmol; carbon content, 2.81 mmol) and pure water (30 mL) were introduced into the reactor, which was pressurized with argon (0.60 MPa) and heated at 250–380 °C for 6 h.

Although a large amount of F⁻ was detected, the amount of CO₂ that formed remained low and was almost constant from 300 to 380 °C (Figure 1a); even when the reaction was carried out at 380 °C, only 0.27 mmol of CO₂ formed (9.6%; Table 1, entry 1). This yield was considerably lower than F⁻ yield (88.9%). GC/MS measurement revealed that the gas phase contained trace amounts of C₂H₆ (0.09 μmol) and 1,3,5-trifluorobenzene (0.35 μmol). We used ion chromatography to quantify the organic acids that formed in the reaction solution: some of the solutions contained small amounts (on the order of micromoles) of HOOCCH₂COOH and HOOC-COOH. The amounts of the organic acids reached maxima at around 300 °C and then decreased as the temperature was increased further (Figure 1b), suggesting that these species were reaction intermediates.

Although organic acids were detected in the reaction solutions, the amounts were 3 orders of magnitude lower than the amount of F⁻. This result and the low yield of CO₂ suggest that most of carbon was in the solid residue. Consistent with this suggestion, elemental analysis of the solid after the

reaction at 380 °C for 6 h indicated that most of the solid was carbon (C, 79.6 wt %; F, 4.3 wt %).

The reported data for thermolysis of PVDF^{6–8} suggest two plausible mechanisms for PVDF decomposition: dehydrofluorination (Scheme 1a) and depolymerization (Scheme 1b). The former mechanism results in the formation of carbon-rich residue, whereas depolymerization produces CH₂CF₂ monomer, as has been reported for the thermolysis of PTFE.^{23–25} The fact that in our reaction, in the presence of argon, no CH₂CF₂ was detected (as indicated by GC/MS) and a carbon-rich solid and a large amount of F⁻ formed suggests that under these conditions, the decomposition of PVDF proceeded via the dehydrofluorination mechanism. Dehydrofluorination was followed by scission of the polymer chain, as reflected by the formation of 1,3,5-trifluorobenzene.

Effect of O₂. Mineralization of the fluorine in PVDF to F⁻ was not complete (88.9% yield) in pure supercritical water in the presence of argon. Furthermore, the formation of the solid residue is not ideal for waste treatment, because the solid requires additional treatment. Therefore, to achieve complete mineralization, we performed reactions in the presence of O₂. The addition of O₂ (initial pressure 0.6 MPa, i.e., 16.5 mmol) to the reaction system dramatically changed the product distribution (Figure 2). Compared to the reactions in the presence of argon, the reaction in the presence of O₂ resulted in a greater degree of mineralization to F⁻ and efficient formation of CO₂.

When the reaction was carried out at 380 °C with O₂, the amounts of both F⁻ and CO₂ reached 2.79 mmol (96.9% and 99.3% yields, respectively; Table 1, entry 2). In contrast to the reactions in the presence of argon, the reactions in the presence of O₂ resulted in no quantifiable amounts of gaseous products other than CO₂. The reaction atmosphere also affected the temperature dependence of the formation of organic acids. When the reaction was carried out in the presence of O₂, the amount of HOOCCH₂COOH increased with increasing temperature (Figure 2b), which indicates that scission of the polymer chain efficiently occurred.

Increasing the initial amount of O₂ to 30.5 mmol resulted in F⁻ and CO₂ yields that were almost the same as those when 16.5 mmol of O₂ was used (compare entries 2 and 3 in Table 1). Thus, virtually complete mineralization of the polymer was achieved in the presence of at least 16.5 mmol of O₂, which is approximately 5.8 times the molar amount of fluorine or carbon in the polymer. PVDF decomposition at 380 °C in the presence of 16.5 mmol of O₂ with shorter reaction time was also investigated (Table 2). The mineralization of the polymer was not complete after 0.5 h, as indicated by the fact that F⁻ and

Table 1. Decomposition of PVDF and ETFE in Supercritical Water^a

entry	polymer	initial O ₂ (mmol)	reaction pressure (MPa)	F ⁻ (mmol) [yield (%)] ^b	CO ₂ (mmol) [yield (%)] ^c	HOOC-COOH (μmol)	HOOCCH ₂ COOH (μmol)
1	PVDF	none ^d	24.2	2.56 [88.9]	0.27 [9.6]	n.d. ^e	0.44
2	PVDF	16.5	23.8	2.79 [96.9]	2.79 [99.3]	n.d.	4.31
3	PVDF	30.5	24.9	2.83 [98.3]	2.70 [96.1]	n.d.	0.45
4	ETFE	none	23.7	0.24 ± 0.04 [8.4 ± 1.4]	0.05 ± 0.01 [1.8 ± 0.3]	n.d.	trace
5	ETFE	9.95	23.3	1.55 [54.0]	1.79 [63.7]	n.d.	0.21
6	ETFE	16.5	23.3	2.49 [86.8]	2.37 [84.3]	0.12	0.88
7	ETFE	30.2	23.6	2.80 [97.6]	2.76 [98.2]	n.d.	0.49

^aThe polymer (90 mg) and pure water (30 mL) were introduced into the reactor, which was pressurized with O₂ and then heated at 380 °C for 6 h.

^bF⁻ yield (%) = [(moles of F⁻ formed)/(moles of fluorine in polymer)] × 100. ^cCO₂ yield (%) = [(moles of CO₂ formed)/(moles of carbon in polymer)] × 100. ^dReaction in the presence of argon. ^eNot detected.

Scheme 1. Possible Mechanisms for the Decomposition of PVDF in the Presence of Argon, as Suggested by Thermolysis Data

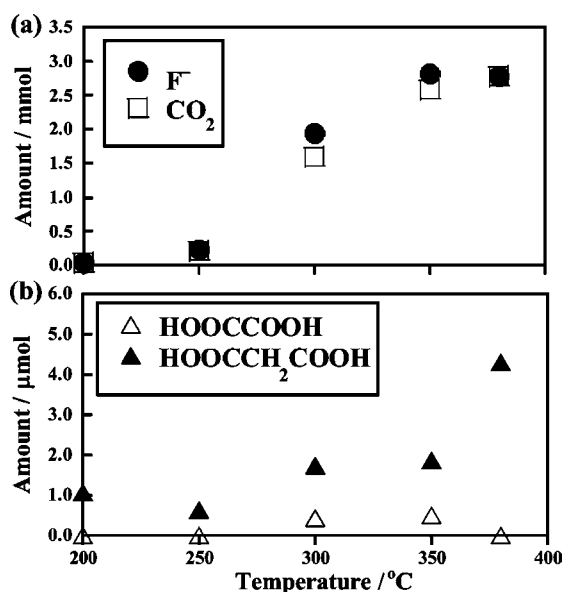
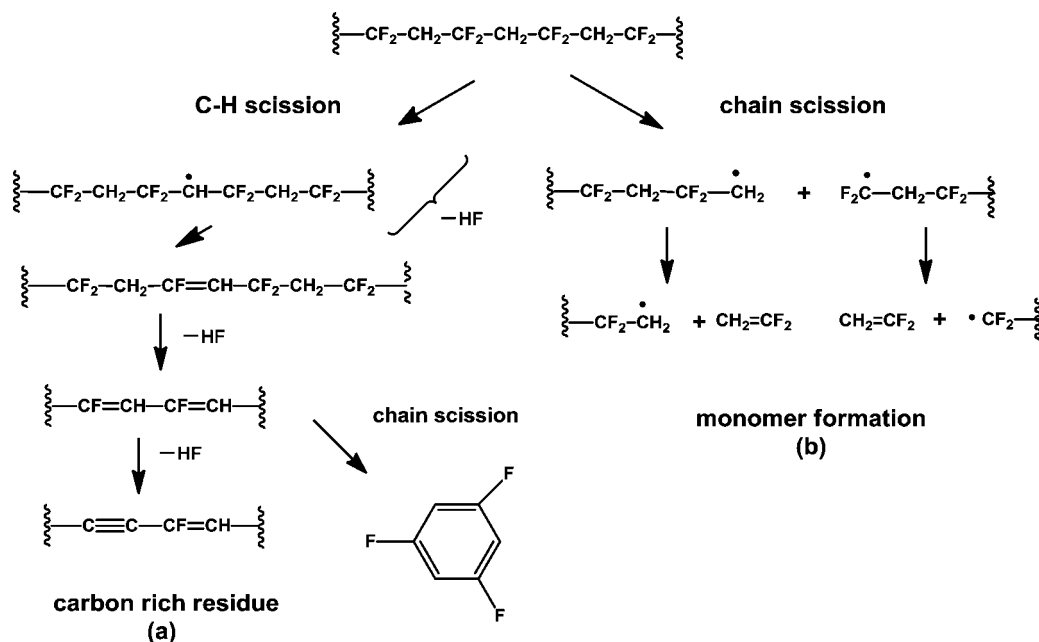
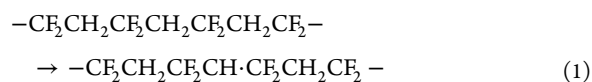


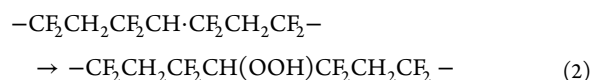
Figure 2. Temperature dependence of PVDF decomposition in the presence of O₂: (a) detected amounts of F⁻ and CO₂ and (b) organic acids. PVDF (90 mg; fluorine content, 2.88 mmol; carbon content, 2.81 mmol) and pure water (30 mL) were introduced into the reactor, which was pressurized with O₂ (0.60 MPa; 16.5 mmol) and heated at 200–380 °C for 6 h.

CO₂ yields were 89.9% and 89.3%, respectively (entry 1). After 1 h, the F⁻ and CO₂ yields reached 98.3% and 102%, respectively (entry 2). These values were similar to those after 6 h (entry 3), indicating that reaction time of 1–6 h was enough for complete mineralization.

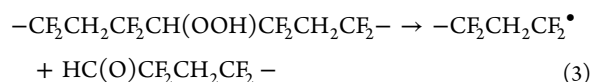
On the basis of our analysis of the products, we propose the reaction mechanism outlined in Scheme 2 for the decomposition of PVDF in the presence of O₂. First, a hydrogen atom is abstracted from a –CH₂– group:



The resulting radical reacts with O₂ in the presence of water to produce a hydroperoxide:



This product is unstable and can cause scission of the main chain, which results in a terminal –CF₂[•] radical and an aldehyde:

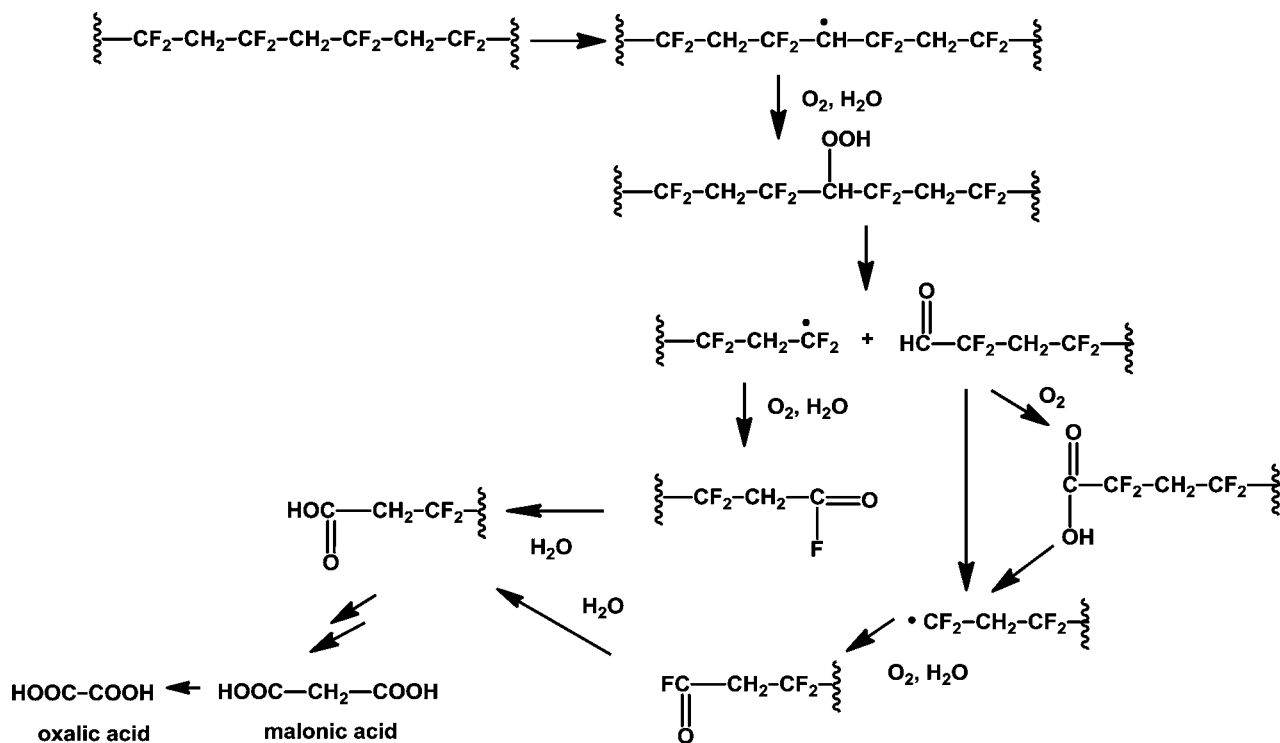


The –CF₂[•] radical can be transformed to an acid fluoride (–COF) in the presence of O₂, and the aldehyde can either

Table 2. Time Dependence of PVDF Decomposition in the Presence of O₂ in Supercritical Water^a

entry	reaction time (h)	reaction pressure (MPa)	F ⁻ (mmol) [yield (%)]	CO ₂ (mmol) [yield (%)]	HOOCOOH (μmol)	HOOCCH ₂ COOH (μmol)
1	0.5	22.9	2.59 [89.9]	2.51 [89.3]	n.d.	0.69
2	1	24.3	2.83 [98.3]	2.87 [102]	n.d.	1.83
3	6	23.8	2.79 [96.9]	2.79 [99.3]	n.d.	4.31

^aThe polymer (90 mg) and pure water (30 mL) were introduced into the reactor, which was pressurized with O₂ (16.5 mmol) and then heated at 380 °C.

Scheme 2. Proposed Mechanism for the Decomposition of PVDF in the Presence of O₂

undergo direct cleavage of the C–C bond to form a terminal $-\text{CF}_2^\bullet$ radical or can be oxidized to a carboxylic acid, which is subsequently cleaved as shown in Scheme 2. The acid fluoride is hydrolyzed to the corresponding carboxylic acid. This sequence of steps leads to complete mineralization of PVDF.

Reactions of ETFE. Because PVDF was efficiently mineralized in the presence of O₂, reactions of ETFE in subcritical and supercritical water were also carried out by means of the same approach (Figure 3). When the reaction of ETFE in the presence of O₂ (16.5 mmol) was carried out at 150 °C for 6 h, almost no F[−] and CO₂ formed (Figure 3a), and a solid residue formed. The formation of F[−] and CO₂ was clearly observed at 200 °C, and the ATR-IR spectrum of the reaction mixture showed broad peaks around 1600–1700 cm^{−1}, which can be assigned to carboxyl groups, indicating that the polymer had been oxidized. The solid residue did not form when the reaction temperature exceeded above 250 °C, and the amounts F[−] and CO₂ increased monotonously with increasing temperature. When the reaction was carried out at 380 °C, the amounts of F[−] and CO₂ reached 2.49 and 2.37 mmol (86.8% and 84.3% yields, respectively; Table 1, entry 6). These values are somewhat lower than those observed for PVDF under the same reaction conditions (96.9% and 99.3%; Table 1, entry 2). In the reaction solutions, small amounts of HOOCCH₂COOH and HOOC-COOH were also detected (Figure 3b). In an attempt to achieve complete mineralization, we extended the reaction time of ETFE in supercritical water at 380 °C in the presence of O₂ (16.5 mmol) (Figure 4). Although the amounts of F[−] and CO₂ increased rapidly at the beginning of the reaction (<1 h), the amounts tended to saturate after 4.5 h (Figure 4a). When the reaction time was prolonged to 18 h, the amounts of F[−] and CO₂ reached 2.44 and 2.40 mmol (85.0% and 85.4% yields, respectively), values that were almost the same as those observed for the 6 h reaction. Next, reactions

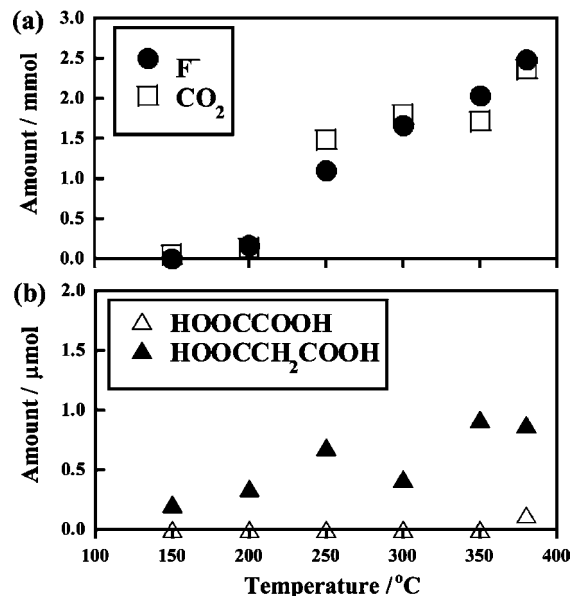


Figure 3. Temperature dependence of ETFE decomposition in the presence of O₂: detected amounts of (a) F[−] and CO₂ and (b) organic acids. ETFE (90 mg; fluorine content, 2.87 mmol; carbon content, 2.81 mmol) and pure water (30 mL) were introduced into the reactor, which was pressurized with O₂ (0.60 MPa; 16.5 mmol) and heated at 150–380 °C for 6 h.

with a higher amount of O₂ were carried out. Increasing the amount of O₂ to 30.2 mmol increased the amounts of F[−] and CO₂ to 2.80 and 2.76 mmol, respectively, after reaction for 6 h (97.6% and 98.2% yields, respectively; Table 1, entry 7). That is, virtually complete mineralization of ETFE was achieved with

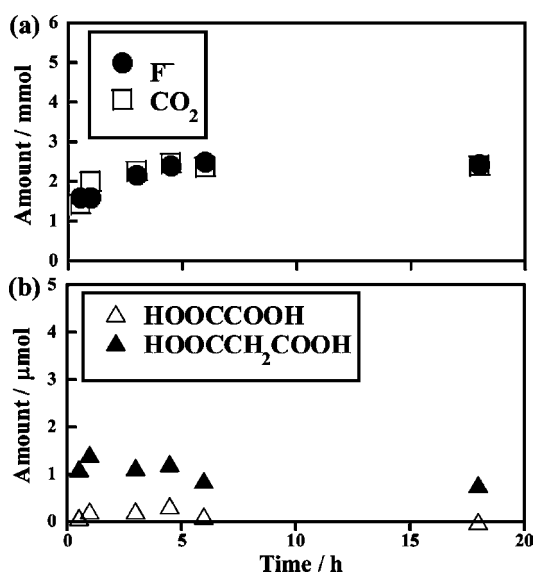


Figure 4. Time dependence of ETFE decomposition in the presence of O₂: detected amounts of (a) F⁻ and CO₂ and (b) organic acids. ETFE (90 mg; fluorine content, 2.87 mmol; carbon content, 2.81 mmol) and pure water (30 mL) were introduced into the reactor, which was pressurized with O₂ (0.60 MPa; 16.5 mmol) and heated at 380 °C for 0.5–18 h.

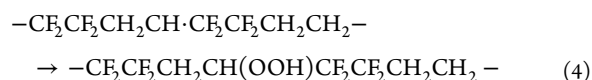
30.2 mmol of O₂, which is 11 times the molar amount of fluorine or carbon in the polymer.

Whereas CO₂ formation from PVDF depended on the amount of O₂, F⁻ formed efficiently even if O₂ was absent (Figure 1a), although the amount of F⁻ was somewhat lower than that in the presence of O₂. In the case of ETFE, the formation of both F⁻ and CO₂ depended on the amount of O₂. When the reaction was carried out with relatively low amount of O₂ (9.95 mmol) for 6 h, the amounts of F⁻ and CO₂ dramatically decreased, to 1.55 and 1.79 mmol (54.0% and 63.7% yields, respectively; Table 1, entry 5). Furthermore, in the absence of O₂, that is, in the presence of argon, the amounts of F⁻ and CO₂ further decreased, to 0.24 ± 0.04 and 0.05 ± 0.01 mmol (8.4 ± 1.4% and 1.8 ± 0.3% yields, respectively; Table 1, entry 4), and a solid residue formed. Elemental analysis indicated that the solid consisted of both carbon and fluorine with a high ratio (C 53.5 wt %, F 40.0 wt %). This result indicates that unreacted ETFE remained under these reaction conditions. These observations suggest that dehydro-fluorination made only a minor contribution to the decomposition of ETFE, in contrast to the decomposition of PVDF.

Monomer formation during the reactions of ETFE was investigated. When the reaction was carried out at 380 °C with O₂ (16.5 mmol) for 6 h, no monomer species (C₂F₄, C₂H₄, and CH₂CF₂) were detected. In contrast, in the absence of O₂, a trace amount (0.02–0.03 μmol) of C₂H₄ was detected, whereas no C₂F₄ or CH₂CF₂ was detected. That is, the reactions in supercritical water did not produce meaningful amounts of monomer species.

As described above, when the reaction was carried out in the presence of argon (in the absence of O₂), PVDF produced a large amount of F⁻ and a carbon-rich residue, whereas very little of either F⁻ or CO₂ formed from ETFE. The poor reactivity of ETFE in the absence of O₂ may be ascribed to the

difficulty of the abstracting a methylene hydrogen atom. In PVDF, each -CH₂- group is connected to two -CF₂- groups, which are strongly electron withdrawing. The alternation of -CH₂- and -CF₂- groups may facilitate the abstraction of a hydrogen atom and subsequent dehydrofluorination along the chain. In contrast, ETFE used here consists of alternation of -CH₂CH₂- and -CF₂CF₂- groups, that is, the -CH₂- group is connected to one -CF₂- group and one -CH₂- group. This arrangement may suppress abstraction of the hydrogen atom when O₂ is absent. In other words, the difference in the environment around the -CH₂- group gives rise to different mineralization behavior of the two polymers. When O₂ is present, abstraction of a hydrogen atom from ETFE can occur to a significant extent to produce a hydroperoxide group in the main chain:



After formation of the hydroperoxide group, the decomposition of ETFE may proceed via scission of the main chain, in a similar manner to that proposed for PVDF (Scheme 2).

CaF₂ Formation. To determine whether CaF₂ formed in our reaction system, we performed polymer decomposition reactions in the presence of Ca(OH)₂. When PVDF (90 mg) and a stoichiometric amount of Ca(OH)₂ (1.44 mmol) in pure water (30 mL) were heated at 380 °C for 6 h with O₂ (30.2 mmol), a white precipitate formed. The XRD pattern of the precipitate measured after it was collected and washed with pure water indicated that it was pure CaF₂ (Figure 5). The

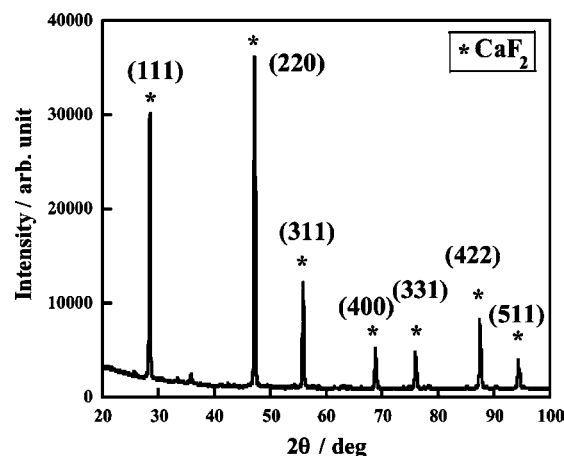


Figure 5. XRD pattern of the precipitate obtained from reaction in the presence of Ca(OH)₂. PVDF (90 mg), Ca(OH)₂ (1.44 mmol) and pure water (30 mL) were introduced into the reactor, which was pressurized with O₂ (1.1 MPa, 30.2 mmol) and heated at 380 °C for 6 h, after which the precipitate was collected.

molar amount of CaF₂ was 1.02 mmol, which corresponds to 2.04 mmol of fluorine atoms (or 70.8% of the 2.88 mmol of fluorine atoms in PVDF). In a similar manner, when ETFE (90 mg) was reacted in the presence of a stoichiometric amount of Ca(OH)₂ (1.44 mmol) and O₂ (30.2 mmol) at 380 °C for 6 h, X-ray spectrometrically pure CaF₂ (0.943 mmol, 65.7% yield) was obtained.

CONCLUSION

Decomposition of PVDF and ETFE in subcritical and supercritical water was investigated. Addition of O₂ to the reaction system led to efficient mineralization of both polymers to F⁻ and CO₂. When PVDF was heated in supercritical water at 380 °C for 6 h with an approximately 5.8-fold molar excess of O₂ relative to the fluorine or carbon content in the polymer, the F⁻ and CO₂ yields reached 96.9% and 99.3%, respectively; that is, virtually complete mineralization of the polymer was achieved. ETFE was also efficiently mineralized, although more O₂ was required (an 11-fold molar excess relative to the fluorine or carbon content in the polymer), leading F⁻ and CO₂ yields of 97.6% and 98.2%, respectively, after reaction at 380 °C for 6 h. The reactivities of PVDF and ETFE differed markedly in the presence of argon, that is, in the absence of O₂: the reaction of PVDF produced a large amount of F⁻ but little CO₂, and a carbon-rich residue formed; whereas ETFE was unreactive under these conditions, showing very little formation of either F⁻ or CO₂. These results suggest that PVDF can decompose via dehydrofluorination, whereas ETFE cannot. Addition of stoichiometric Ca(OH)₂ to the reaction system resulted in the formation of X-ray spectrometrically pure CaF₂ (70.8% and 65.7% yields for PVDF and ETFE, respectively).

Further application of this method to other fluoropolymers is being investigated in our laboratory.

AUTHOR INFORMATION

Corresponding Author

*Tel: (+81)-463-59-4111. Fax: (+81)-463-58-9688. E-mail: h-hori@kanagawa-u.ac.jp.

Notes

The authors declare no competing financial interest.

ACKNOWLEDGMENTS

This work was supported by the Asahi Glass Research Collaboration Program.

REFERENCES

- (1) Drobny, J. G. *Technology of Fluoropolymers*, 2nd ed; CRC Press: Boca Raton, FL, 2009.
- (2) Ameduri, B.; Boutevin, B. *Well-Architected Fluoropolymers: Synthesis, Properties and Applications*; Elsevier: Oxford, U.K., 2004.
- (3) Banks, R. E.; Smart, B. E.; Tatlow, J. C., Eds. *Organofluorine Chemistry: Principles and Applications*; Plenum Press: New York, 1994.
- (4) Ameduri, B. From vinylidene fluoride (VDF) to the applications of VDF-containing polymers and copolymers: recent developments and future trends. *Chem. Rev.* **2009**, *109*, 8832.
- (5) Boschet, F.; Ameduri, B. (Co)polymers of chlorotrifluoroethylene: synthesis, properties, and applications. *Chem. Rev.* **2014**, *114*, 927.
- (6) Hirschler, M. M. Effect of oxygen on the thermal decomposition of poly(vinylidene fluoride). *Eur. Polym. J.* **1982**, *18*, 463.
- (7) Loginova, N. N.; Madorskaya, L. Y.; Podlesskaya, N. K. Relations between the thermal stability of partially fluorinated polymers and their structure. *Polym. Sci. USSR* **1983**, *25*, 2995.
- (8) Zulfıqar, S.; Zulfıqar, M.; Rizvi, M.; Munir, A.; McNeill, I. C. Study of the thermal degradation of polychlorotrifluoroethylene, poly(vinylidene fluoride), and copolymers of chlorotrifluoroethylene and vinylidene fluoride. *Polym. Degrad. Stab.* **1994**, *43*, 423.
- (9) Morelli, J. J.; Sandreczki, T. C. The vacuum pyrolysis and thermal degradation in air of irradiated poly(ethylene-co-tetrafluoroethylene) films. *J. Anal. Appl. Pyrolysis* **1995**, *35*, 121.
- (10) Atanassov, A.; Genieva, S.; Vlaev, L. Study on the thermooxidative degradation kinetics of tetrafluoroethylene-ethylene copolymer filled with rice husks ash. *Polym.—Plast. Technol. Eng.* **2010**, *49*, 541.
- (11) Chen, X.-Y.; Yuan, W. Z.; Zhao, J.; Yang, L.; Li, H.; Li, L.; Zhang, Y. Thermal-mechanical stability of ethylene tetrafluoroethylene alternating copolymer, and modification thereof. *J. Polym. Res.* **2012**, *19*, 9820.
- (12) Ito, M.; Umeda, K.; Murakami, K. Application of chemical stress relaxation to the degradation of elastomers by heat and radiation. *Angew. Makromol. Chem.* **1998**, *261/262*, 101.
- (13) Lee, S.; Gencer, M. A.; Fullerton, K. L.; Azzam, F. O. *Depolymerization Process*, United States Patent No. 5386055, 1995.
- (14) *Chemical Synthesis Using Supercritical Fluids*; Jessop, P. G., Leitner, W., Eds.; Wiley-VCH: Weinheim, Germany, 1999.
- (15) Hawthorne, S. B.; Lagadec, A. J. M.; Kalders, D.; Lilke, A. V.; Miller, D. J. Pilot-scale destruction of TNT, RDX, and HMX on contaminated soils using supercritical water. *Environ. Sci. Technol.* **2000**, *34*, 3224.
- (16) Kawasaki, S.-I.; Oe, T.; Anjoh, N.; Nakamori, T.; Suzuki, A.; Arai, K. Practical supercritical water reactor for destruction of high concentration polychlorinated biphenyls (PCB) and dioxin waste streams. *Process Saf. Environ. Prot.* **2006**, *84*, 317.
- (17) Liu, Y.; Wang, M.; Pan, Z. Catalytic depolymerization of polyethylene terephthalate in hot compressed water. *J. Supercrit. Fluids* **2012**, *62*, 226.
- (18) Gao, J.; Jin, Z.; Pan, Z. Depolymerization of poly(trimethylene terephthalate) in hot compressed water at 240–320 °C. *Polym. Degrad. Stab.* **2012**, *97*, 1838.
- (19) Huang, F.; Huang, Y.; Pan, Z. Depolymerization of ODPA/ODA polyimide in a fused silica capillary reactor and batch autoclave reactor from 320 to 350 °C in hot compressed water. *Ind. Eng. Chem. Res.* **2012**, *51*, 7001.
- (20) Hori, H.; Murayama, M.; Sano, T.; Kutsuna, S. Decomposition of perfluorinated ion-exchange membrane to fluoride ions by using zerovalent metals in subcritical water. *Ind. Eng. Chem. Res.* **2010**, *49*, 464.
- (21) Arai, K.; Funaki, A.; Phongtamrug, S.; Tashiro, K. Influence of alternating sequential fraction on the melting and glass transition temperatures of ethylene-tetrafluoroethylene copolymer. *Polymer* **2010**, *51*, 4831.
- (22) Miyake, Y.; Yamashita, N.; Rostkowski, P.; So, M. K.; Taniyasu, S.; Lam, P. K. S.; Kannan, K. Determination of trace levels of total fluorine in water using combustion ion chromatography for fluorine: A mass balance approach to determine individual perfluorinated chemicals in water. *J. Chromatogr. A* **2007**, *1143*, 98.
- (23) Simon, C. M.; Kaminsky, W. Chemical recycling of polytetrafluoroethylene by pyrolysis. *Polym. Degrad. Stab.* **1998**, *62*, 1.
- (24) Ellis, D. A.; Mabury, S. A.; Martin, J. W.; Muir, D. D. G. Thermolysis of fluoropolymers as a potential source of halogenated organic acids in the environment. *Nature* **2001**, *412*, 321.
- (25) Garcia, A. N.; Viciano, N.; Font, R. Products obtained in the fuel rich combustion of PTFE at high temperature. *J. Anal. Appl. Pyrolysis* **2007**, *80*, 85.

IRON-INDUCED EFFICIENT DECOMPOSITION OF PERCHLORATE USING PRESSURIZED HOT WATER

Hori H^{1*}, Sakamoto T¹, Tanabe T¹, Kasuya M¹, Chino A¹, Wu Q², Kannan K²

¹Department of Chemistry, Faculty of Science, Kanagawa University, 2946 Tsuchiya, Hiratsuka 259-1293, Japan; ²Wadsworth Center, New York State Department of Health, and Department of Environmental Health Sciences, School of Public Health, State University of New York at Albany, Empire State Plaza, P. O. Box 509, Albany, New York 12201-0509, USA

Introduction

Perchlorate has been reported to occur in aquatic environments, drinking water and foodstuffs, and in humans¹⁻⁸. The ammonium and potassium salts of ClO_4^- are used as oxidizers in jet and rocket fuels, pyrotechnic devices, explosives, fireworks, vehicle air bag inflators and so forth. Improper treatment of wastes associated with manufacture and use of these products can act as significant stationary sources of ClO_4^- in the environment⁶. Furthermore, sources attributable to industrial effluents⁷, fireworks manufacturing operations⁵, and fireworks displays³ were recently indicated. Therefore, development of decomposition technologies for ClO_4^- to harmless Cl^- under mild condition is desired as a measure against stationary sources of emission.

Recently, reactions with pressurized hot water (PHW) have been recognized as an innovative and environmentally benign technique in water treatment. PHW is defined as hot water at sufficient pressure to maintain the liquid state, below the critical point of water (374 °C, 22.1 MPa). PHW has many characteristics that are favorable for chemical reactions: high diffusivity, low viscosity, and the ability to accelerate acid- and base-catalyzed reactions⁹.

In this study, we examined decomposition of ClO_4^- in PHW up to 300 °C, and examined the effect of several zerovalent metals in the reaction system¹⁰. Among metals we tested, iron led to the most efficient decomposition of ClO_4^- to Cl^- ion, with no formation of other chlorinated species such as chlorate (ClO_3^-) and chlorite (ClO_2^-). We also applied this method to the decomposition of a ClO_4^- contaminated water sample from a man-made reflecting pond, following fireworks display in Albany, New York³.

Materials and methods

A stainless steel high-pressure tube reactor (11 mL volume) equipped with two stainless steel screw caps was used. In a typical run, an argon-saturated aqueous (Milli-Q water) solution (3.5 mL) of ClO_4^- (101–204 μM) and metal powder (0.91 mmol) were introduced into the reactor under an argon atmosphere by use of a globe bag, and the reactor was sealed. Then the reactor was placed into an oven, and the reactor temperature was raised at a rate of ca 10 °C min^{-1} to the desired reaction temperature (80–300 °C), and the temperature was held constant for a specified time (e.g., 6 h). After the specified time, the reactor was quickly cooled to room temperature. The reactor was opened, and the reaction mixture was centrifuged to separate the reaction solution and the solid phase (metal powder). The reaction solution was analyzed by ion chromatography for the quantification of residual ClO_4^- and the product, Cl^- , and other ionic species, if present.

The decomposition of ClO_4^- in water from a man-made reflecting pond following fireworks display was also examined. To decompose ClO_4^- in this sample, iron powder (1.82 mmol) was added to the sample (3.5 mL) and

the mixture was introduced into the reactor, and then reacted in the same manner as described above. Quantification of ClO_4^- in the samples before and after the reactions was carried out by liquid chromatography-tandem mass spectrometry (LC-MS/MS) at Wadsworth Center, New York State Department of Health, where the samples were analyzed immediately before and after the reaction experiments. Other major ions present in the sample prior to the reaction (Cl^- and SO_4^{2-}) were measured by ion chromatography.

The ion-chromatograph system (Tosoh IC-2001) consisted of an automatic sample injector (injection volume: 30 μL), a degasser, a pump, a guard column, a separation column (Tosoh TSKgel Super IC-AP), a column oven, and a conductivity detector with a suppressor device. The mobile phase was an aqueous solution containing NaHCO_3 (1.7 mM), Na_2CO_3 (1.8 mM), and acetonitrile (23 vol%). The detection limit of ClO_4^- was 0.58 μM (58 $\mu\text{g L}^{-1}$), calculated from a signal-to-noise ratio of 3. An LC-MS/MS system consisting of an HPLC system (Agilent 1100), an anion-exchange column (IonPac AS-21, Dionex), and a mass spectrometer (Micromass Quatro, Waters) was used to quantify ClO_4^- in the water sample from the man-made reflecting pond following fireworks display and its reaction solution. The detection limit of ClO_4^- was 0.20 nM (0.02 $\mu\text{g L}^{-1}$)³.

Results and discussion

Initially, we studied the decomposition of ClO_4^- in PHW in the absence of a metal additive. The densities of the liquid and gas phases of pure water at 300 °C, at which the two phases coexist, are reported to be 0.71214 and 0.046168 g mL^{-1} , respectively¹¹. These density values and the water amount (3.5 g) and the internal reactor volume (11 mL) in the present study indicate that the volumes of the liquid and gas phases at 300 °C, the highest temperature tested, were 4.5 and 6.5 mL, respectively. This fact demonstrated that the reactions proceeded in PHW. The effect of temperature on ClO_4^- decomposition, in the absence of a metal, is shown in Fig. 1; the reaction time was 6 h and the initial concentration of ClO_4^- was 103 μM . The residues of ClO_4^- gradually decreased with increasing the temperature and Cl^- was detected in the reaction solution. However, the reactivity of ClO_4^- in PHW was considerably low: when the reaction was carried out at 300 °C, the highest temperature tested, 84% of the initial ClO_4^- remained, accompanied by the formation of a very small concentration of Cl^- , with a yield [(molar concentration of Cl^- formed) / (molar concentration of the initial ClO_4^-)] of 10%. The low yield reflects the high thermal and chemical stability of ClO_4^- . Total recovery of chlorine, i.e., the molar ratio of total chlorine in Cl^- formed and remaining ClO_4^- to total chlorine atoms in the initial ClO_4^- was 94%, indicating that ClO_4^- and Cl^- were virtually the only chlorinated species present in the reaction solution. Consistently, other chlorinated species such as ClO_3^- and ClO_2^- were not detected in the reaction solution, indicating that these two species are unstable in PHW.

To enhance the decomposition of ClO_4^- in PHW, we carried out reactions in the presence of a metal powder. The results are summarized in Table 1; the reaction was carried out at 150 °C for 6 h. In the absence of a metal (entry 1), most (99%) of the initial ClO_4^- (103 μM) remained, accompanied by a very small yield (3%) of Cl^- . Addition of aluminum did not enhance the formation of Cl^- (entry 2). Alternatively, addition of other metals clearly enhanced the decomposition of ClO_4^- to Cl^- , with an increasing order of, $\text{Cu} < \text{Zn} < \text{Ni} \ll \text{Fe}$ (entries 3–6). The highest enhancement of decomposition of ClO_4^- to Cl^- was achieved by the addition of iron. After the reaction in PHW with iron for 6 h, no ClO_4^- was detected in the reaction solution, while Cl^- was formed, with a high yield (85%) (entry 6). The enhancement of the decomposition of ClO_4^- to Cl^- was not reflected by the reducing power of the metals, because the order of ClO_4^- reduction (or Cl^- increase) was different from the order of the redox potentials (E_0 , V vs. NHE) of metals in the more negative direction of Cu/Cu^{2+} (0.34) $<$ Ni/Ni^{2+} (-0.26) $<$ Fe/Fe^{2+} (-0.44) $<$

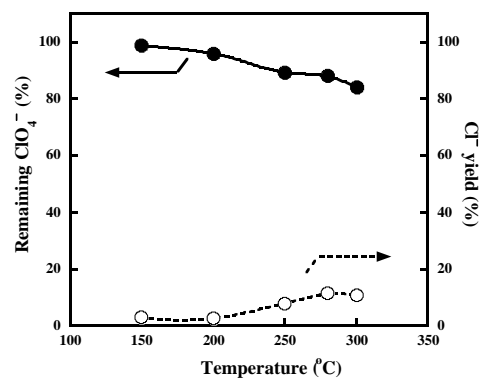


Fig. 1. Effect of temperature on the decomposition of perchlorate (ClO_4^-) in pressurized hot water (PHW) in the absence of metal at a constant reaction time of 6 h¹⁰. An argon saturated aqueous solution (3.5 mL) of ClO_4^- (103 μM) was introduced in a sealed reactor, then the reactor temperature was raised between 150 and 300 °C.

Zn/Zn^{2+} (-0.76) < Al/Al^{3+} (-1.68). This finding suggests that the reduction of ClO_4^- on metal surface is not a simple redox reaction. It appears that specific interaction between ClO_4^- and metal surface (such as adsorption) plays an important role in the decomposition of ClO_4^- . In each case, ClO_3^- and ClO_2^- were not detected in the reaction solution.

Table 1
Decomposition of perchlorate (ClO_4^-) in pressurized hot water (PHW) with and without metal additives ^{a 10)}

entry	Metal additive	Weight of metal additive (mg)	Particle size of metal additive (μm)	Initial ClO_4^- concentration (μM)	Remaining ClO_4^- (%)	Cl^- yield (%)
1	none	–	–	103	99	3
2	Al	24.5	< 75	103	93	1
3	Cu	57.7	< 75	101	86	13
4	Zn	59.3	< 75	102	51	22
5	Ni	53.4	< 53	100	46	43
6	Fe	50.8	< 53	104	< 1 ^b	85 \pm 1

^a An argon saturated aqueous solution (3.5 mL) of ClO_4^- and metal powder (0.91 mmol) were introduced into the reactor under argon, and the reactor was heated to 150 °C for 6 h.

^b Below the detection limit of ion chromatography.

Because the addition of iron powder led to the most efficient Cl^- formation among the metals tested, we further investigated the decomposition of ClO_4^- to Cl^- with iron by changing the reaction conditions. The reaction-time dependence of the residual ClO_4^- ratio and Cl^- yield in the reaction solution is shown in Fig. 2; the initial concentration of ClO_4^- was 104 μM and the reaction temperature was 150 °C. The amount of ClO_4^- remaining in the solution decreased from 100 to 94% after addition of iron at 23 °C: 6% of the initial ClO_4^- was removed from the solution even before heating, with no Cl^- formed. This may be due to the adsorption of ClO_4^- on the iron surface. After heating, the concentration of ClO_4^- rapidly decreased with increasing reaction time, following pseudo-first-order-kinetics with a rate constant of 4.3 h^{-1} , while Cl^- increased. After 1 h, ClO_4^- was not detected in the reaction solution. The formation of Cl^- showed saturation in 2 h, which indicates that the reaction was almost complete during this period, and the yield of Cl^- reached 85% after 6 h.

The effect of temperature on ClO_4^- decomposition in the presence of iron is shown in Fig. 3; the reaction time was 6 h and the initial concentration of ClO_4^- was 104 μM . Raising the reaction temperature from 23 °C dramatically decreased the residual ClO_4^- and increased Cl^- yield. After the reaction at 80 °C for 6 h, 45% of the initial ClO_4^- remained, followed by a Cl^- yield of 46%.

The concentration of ClO_4^- decreased below the detection limit at 150 °C, and the Cl^- yield increased to a maximum (85%). Therefore, it was clear that the best reaction temperature for the decomposition of ClO_4^- to Cl^- induced by iron in the present study was 150 °C, at which temperature the reaction was almost complete in 2 h (Fig. 2).

We used perchlorate-contaminated water from a man-made reflecting pond following a fireworks display, to

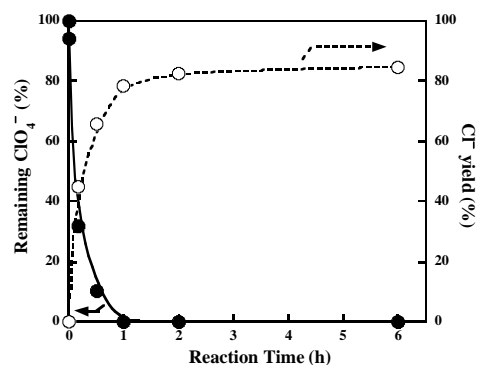


Fig. 2. Reaction-time dependence of the residual ClO_4^- ratio and the Cl^- yield¹⁰⁾. Iron powder (0.91 mmol) was added to an argon saturated aqueous solution (3.5 mL) of ClO_4^- (104 μM) under argon atmosphere, and the mixture in the sealed reactor was heated at 150 °C for 1–6 h. Two dots for ClO_4^- at time 0 correspond to the values obtained before (higher value) and after (lower value) addition of iron.

evaluate the efficiency of the developed method for the remediation of contaminated waters. This sample contained 5.22 μM of ClO_4^- and much higher concentrations of Cl^- (472 μM) and SO_4^{2-} (130 μM), which might interfere with the decomposition of ClO_4^- . Therefore, we prolonged the reaction time to 18 h and increased the amount of iron to 1.82 mmol. Consequently, the concentration of ClO_4^- was dramatically reduced to $0.03 \pm 0.01 \mu\text{M}$ after the reaction at 150 $^\circ\text{C}$: 99% of the initial ClO_4^- was effectively removed from the water.

References:

1. Parker DR, Seyffert AL, Reese BK. (2008); *Environ. Sci. Technol.* 42: 1465-1471.
2. Kannan K, Praamsma ML, Oldi JF, Kunisue T, Sinha RK. (2009); *Chemosphere* 76: 22-26.
3. Wu Q, Oldi JF, Kannan K. (2011); *Environ. Toxicol. Chem.* 30: 2449-2455.
4. Wu Q, Zhang T, Sun HW, Kannan K. (2010); *Arch. Environ. Con. Tox.* 58: 543-550.
5. Zhang T, Wu Q, Sun HW, Rao J, Kannan, K. (2010); *Environ. Sci. Technol.* 44: 6947-6953.
6. Dasgupta PK, Dyke JV, Kirk, A, Jackson WA. (2006); *Environ. Sci. Technol.* 40: 6608-6614.
7. Kosaka K, Asami M, Matsuoka Y, Kamohisa M. (2007); *Water Res.* 41: 3474-3482.
8. Guruge KS, Wu Q, Kannan K. (2011); *J. Environ. Monitor.* 13: 2312-2320.
9. Jessop PG, Leitner W (Eds.). (1999); *Chemical Synthesis Using Supercritical Fluids*. Wiley-VCH, Weinheim.
10. Hori H, Sakamoto T, Tanabe T, Kasuya M, Chino A, Wu Q, Kannan K (2012); *Chemosphere* 89: 737-742.
11. Lemmon EW, McLinden MO, Friend DG. (2012); Thermophysical Properties of Fluid Systems in NIST Chemistry Webbook, in: Linstrom, P.J., Mallard, W.G. (Eds.), NIST Standard Reference Database Number 69, National Institute of Standards and Technology, Gaithersburg MD.

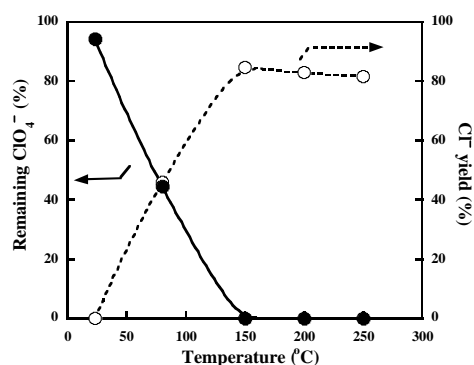
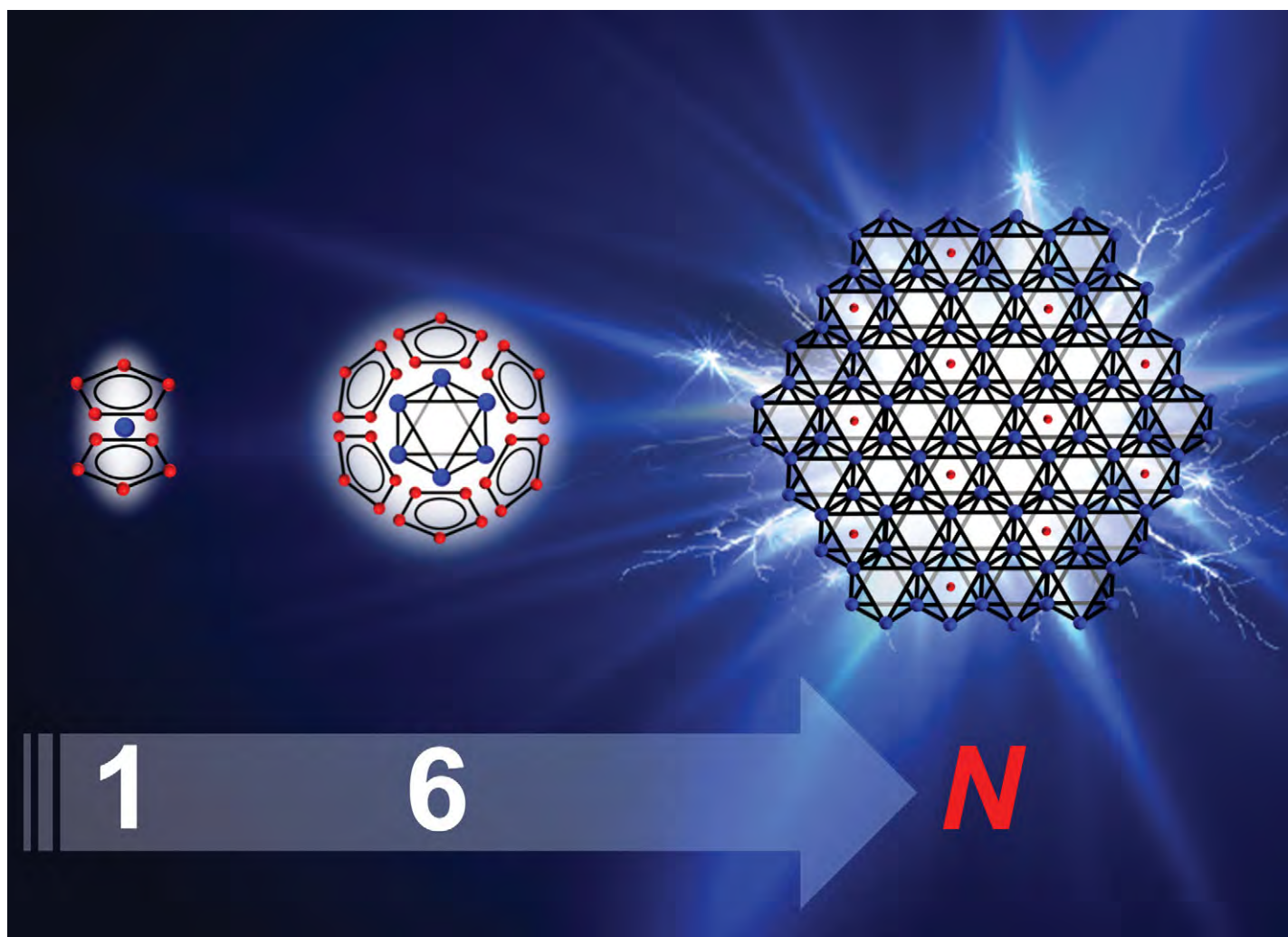


Fig. 3. Effect of temperature on the decomposition of ClO_4^- in PHW in the presence of iron at a constant reaction time of 6 h¹⁰. An argon saturated aqueous solution (3.5 mL) of ClO_4^- (104 μM) and iron powder (0.91 mmol; 50.8 mg, < 53 μm) were introduced in the sealed reactor under argon atmosphere, then the reactor temperature was raised between 80 and 250 $^\circ\text{C}$.

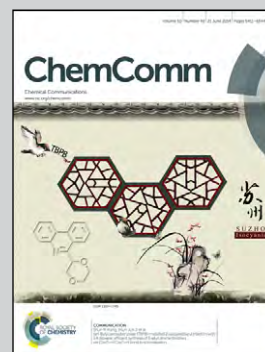


Showcasing research from Abe group in Environmental Remediation Materials Unit, National Institute for Materials Science, Japan

Synthesis and electrocatalytic performance of atomically ordered nickel carbide (Ni_3C) nanoparticles

Nickel evolves: mono-atomic nickel cyclopentadienyl (Ni_1Cp_2) was chemically reduced to form six-membered Ni-Cp clusters (Ni_6Cp_6). The Ni_6Cp_6 clusters were finally converted to N -membered Ni-carbide nanoparticles (Ni_3C Nps), exhibiting better catalytic performance than Au Nps in an environmentally-benign energy-generation reaction, electro-oxidation of sodium borohydride.

As featured in:



See Gubbala V. Ramesh,
Hideki Abe *et al.*,
Chem. Commun., 2014, **50**, 6451.



www.rsc.org/chemcomm

Registered charity number: 207890

Synthesis and electrocatalytic performance of atomically ordered nickel carbide (Ni₃C) nanoparticles†

Cite this: *Chem. Commun.*, 2014, 50, 6451

Received 20th February 2014,
Accepted 7th April 2014

DOI: 10.1039/c4cc01336k

www.rsc.org/chemcomm

Nor A. Fadil,^{ab} Govindachetty Saravanan,^{ac} Gubbala V. Ramesh,^{*a} Futoshi Matsumoto,^d Hideki Yoshikawa,^f Shigenori Ueda,^e Toyokazu Tanabe,^{ad} Toru Hara,^a Shinsuke Ishihara,^g Hideyuki Murakami,^f Katsuhiko Ariga^{gh} and Hideki Abe^{*ai}

Atomically ordered nickel carbide, Ni₃C, was synthesized by reduction of nickel cyclopentadienyl (NiCp₂) with sodium naphthalide to form Ni clusters coordinated by Cp (Ni–Cp clusters). Ni–Cp clusters were thermally decomposed to Ni₃C nanoparticles smaller than 10 nm. The Ni₃C nanoparticles showed better performance than Ni nanoparticles and Au nanoparticles in the electrooxidation of sodium borohydride.

Energy generation by polymer electrolyte membrane fuel cells (PEMFCs) has become increasingly critical as an alternative to combustion engines.^{1–3} In particular, PEMFCs using more transportable and energetically dense fuels than hydrogen, direct-methanol fuel cells (DMFCs) and direct-borohydride fuel cells (DBFCs), are a focal point of interest.^{4–6} DBFCs have advantages over DMFCs in terms of the output voltage because the oxidation potential of borohydrides is much lower than that of methanol or hydrogen.^{7–9} DBFCs require metal catalysts on anodes to complete the electro-oxidation of borohydrides. Precious metals, including Pt, Pd and/or Au, are excellent catalysts, but they are expensive.^{10–13} Ni might be an alternative to precious metals because of its low cost and corrosion resistance in the alkaline electrolytes used in DBFCs, but it has a poor

catalytic activity. In particular, the high onset potential of Ni toward the electrooxidation of borohydrides, which is higher than those of the precious metals by +0.4 V or more, diminishes the applicability of Ni to DBFCs.^{14,15} We and our collaborators have recently demonstrated that ordered alloys of Pt and electronegative elements, such as PtPb and PtBi, are superior anode catalysts to pure Pt, especially in terms of the lower onset potentials for the electrooxidation of methanol.^{16–21} The discovery of PtPb and PtBi has prompted research for efficient anode catalysts in DBFCs among the ordered alloys of Ni and electronegative elements including carbon.

Here, we report that an atomically ordered nickel carbide, Ni₃C, can be synthesized in the form of nanoparticles (Nps) smaller than 10 nm and is expected to be an excellent anode catalyst for DBFCs. Nickel carbides have been previously synthesized as bulk materials, films or particles through mechanical alloying or the pyrolysis of organometallic compounds but have not been applied to catalysis, likely due to their large particle size (>40 nm), resulting in low surface areas.^{22–24} As illustrated in Fig. 1, we first reduce nickel cyclopentadienyl (NiCp₂) using sodium naphthalide (NaNaph) in dry tetrahydrofuran (THF) at room temperature to obtain Cp-coordinated Ni clusters (Ni–Cp clusters).^{25,26} Ni–Cp clusters are then heated at 200 °C in vacuum to yield nanoparticles of Ni₃C with an average size of 6 nm. The Ni₃C Nps exhibit a better catalytic activity than synthesized Ni Nps toward the electrooxidation of NaBH₄ because of their low onset potential close to that of Au Nps.

^a National Institute for Materials Science (NIMS), 1-1 Namiki, Tsukuba, Ibaraki 305-0044, Japan. E-mail: GUBBALA.Venkataramesh@nims.go.jp

^b Universiti Teknologi Malaysia, 81310 Skudai, Johor Bahru, Johor, Malaysia

^c CSIR-National Environmental Engineering Research Institute (CSIR-NEERI), Environmental Materials Division, Nehru Marg, Nagpur 440020, India

^d Kanagawa University, 3-27 Rokkakubashi, Yokohama, Kanagawa 221-8686, Japan

^e Synchrotron X-ray Station at SPring-8, National Institute for Materials Science, 1-1-1 Kouto, Sayo, Hyogo, 679-5148, Japan

^f National Institute for Materials Science (NIMS), 1-2-1 Sengen, Tsukuba, Ibaraki 305-0047, Japan

^g MANA, National Institute for Materials Science (NIMS), 1-1 Namiki, Tsukuba, Ibaraki 305-0044, Japan

^h CREST, Japan Science and Technology Agency (JST), 1-1 Namiki, Tsukuba, Ibaraki 305-0044, Japan

ⁱ PRESTO, Japan Science and Technology Agency (JST), 4-1-8 Honcho, Kawaguchi, Saitama 332-0012, Japan. E-mail: Abe.Hideki@nims.go.jp

† Electronic supplementary information (ESI) available: Experimental details, compound syntheses and characterization, and additional data. See DOI: 10.1039/c4cc01336k

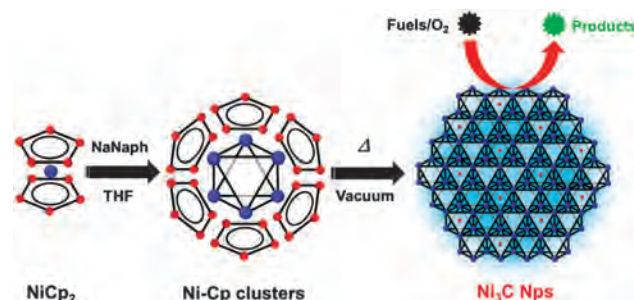


Fig. 1 Synthetic scheme for Ni₃C Nps through chemical reduction of NiCp₂.

Ultrahigh-vacuum transmission electron microscopy (UHV-TEM) images showed that the synthesized Ni₃C Nps were spherical and ranged in size from 3 to 9 nm (Fig. 2a and b). Ordered lattice fringes were observed on the Ni₃C Nps, showing that the Nps were atomically ordered (Fig. 2c). The interval of the lattice fringe, calculated to be 0.201 nm from the Fourier-transformation image (inset of Fig. 2c), was consistent with the *d*-value of the Ni₃C (113) plane (*d*₁₁₃ = 0.201 nm).^{22,23,27} The synthesized Ni₃C Nps were much smaller in size than the previously prepared Ni₃C materials, most likely because Ni-Cp clusters acted as effective precursors, promoting the formation reaction at low temperatures.

Ni-Cp clusters were obtained by reduction of NiCp₂ with NaNaph as a black, air-sensitive powder.^{25,26} Fourier-transform infrared spectroscopy (FTIR) demonstrated that both the C=C- and in-plane C-H stretching modes of Cp molecules in the Ni-Cp clusters were dispersed in wavenumber and blue-shifted relative to those in NiCp₂ (Fig. S1, ESI†).²⁸ The powder X-ray diffraction (pXRD) profile for the Ni-Cp clusters had a single peak at 45.0°, which was slightly larger than the reported 111 reflection angle for FCC-type Ni (*Fm* $\bar{3}$ *m*, *a* = 0.352 nm), 44.5° (Fig. 2d).²⁹ The reflection peak shifted toward lower angles when the material was annealed in vacuum at 100 °C. Small reflection peaks became visible upon annealing at 200 °C at

39.3°, 41.8°, 58.7° and 71.4° (red curve), corresponding to the 006, 110, 116 and 300 reflections of the Ni₃C Nps (*R* $\bar{3}$ *c*; *a* = 0.455 nm, *c* = 1.29 nm), respectively.^{22,23,27} A broad peak was observed at 51.5° corresponding to the 200 reflection of an impurity phase, FCC-type Ni. The Ni₃C Nps were decomposed to FCC-type Ni and carbon when the annealing temperature exceeded 500 °C, consistent with reports in the literature.^{30,31}

Hard X-ray photoemission measurements (HX-PES; photon energy = 5.95 keV) were performed on the Ni₃C Nps (Fig. 2e and f).³² The C 1s photoemission peak was observed for the Ni₃C Nps at 283.7 ± 0.2 eV, in addition to the C 1s- (285.7 ± 0.2 eV) and Sr 3p_{1/2} (280.0 ± 0.2 eV) photoemission peaks for the substrates. The binding energy of the Ni 2p_{3/2} photoemission peak for the Ni₃C Nps was 0.2 eV larger than those for bulk Ni and Ni Nps (Fig. 2f). Both of the binding energies of the C 1s- and Ni 2p_{3/2} peaks for the Ni₃C Nps were consistent with those reported in the literature.^{23,33} The chemical composition of the Ni₃C Nps was calculated to be Ni:C = 1.0:0.31 ± 0.03 from a wide-range HX-PES data (S7, ESI†), indicating that the desired stoichiometric Ni₃C Nps were successfully materialized.

The electrocatalytic activity of the Ni₃C Nps was tested for different reactions in PEMFCs. Fig. 3a shows line-scan voltammograms (LV) for the electrooxidation of NaBH₄ over the Ni₃C Nps and the Ni Nps (average size = 3 nm, see Fig. S9–S11, ESI†). The mass activity of the Ni Nps started to increase at an onset potential of -0.43 V. The Ni₃C Nps showed an increase in the LV curve at an onset potential of -0.85 V, which was 0.42 V lower than the onset potential of the Ni Nps and close to that of Au Nps, -0.86 V (Fig. 3b, see Fig. S12, ESI† for details). In addition, the mass activity of the Ni₃C Nps was, at -0.4 V, 6.5 times larger than that of the Ni Nps. The Ni₃C Nps were more catalytically active than the Ni Nps toward the electrooxidation of NaBH₄, in terms of the lower onset potential and the larger mass activity.

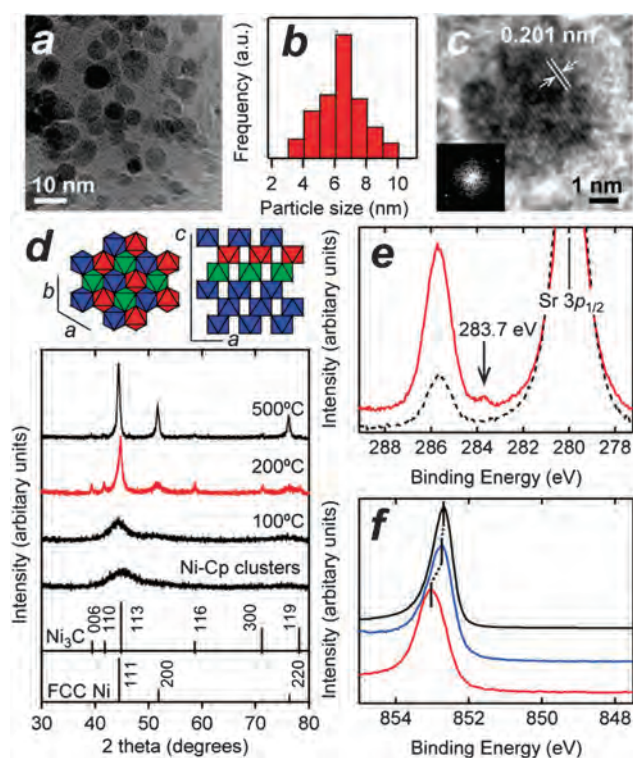


Fig. 2 (a) Bright-field TEM image, (b) particle-size distribution and (c) high-resolution TEM image of Ni₃C Nps. The inset shows a Fourier-transformation image of this TEM image. (d) pXRD profiles for Ni-Cp clusters and the products obtained by annealing Ni-Cp clusters at different temperatures. Structural models for Ni₃C are presented at the top. The polyhedra correspond to Ni₆C-octahedra. Simulated pXRD peaks for Ni₃C and FCC-type Ni are shown by solid markers at the bottom. (e) HX-PES profiles in the C 1s region for Ni₃C Nps (red) and a SrTiO₃ substrate (black broken curve). (f) HX-PES profiles in the Ni 2p_{3/2} region for bulk Ni (black), Ni Nps (blue) and Ni₃C Nps (red). The inset shows HX-PES profiles in the valence region.

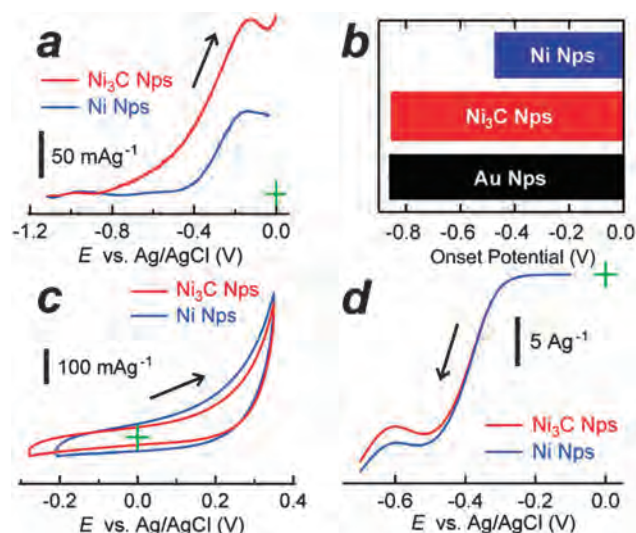


Fig. 3 (a) Line-scan voltammograms for the electro-oxidation of NaBH₄ over the Ni₃C- and the Ni Nps. (b) Onset potentials of the Ni- (blue), Ni₃C- (red) and Au (black) Nps toward the electrooxidation of NaBH₄. (c) Cyclic voltammograms for the electrooxidation of methanol and (d) line-scan voltammograms for the oxygen reduction reaction (ORR) over the Ni₃C- and Ni Nps.

Unlike the case of the electrooxidation of NaBH_4 , the Ni_3C Nps were as catalytically active as the Ni Nps toward both the electrooxidation of methanol and the oxygen-reduction reaction (ORR). Fig. 3c shows cyclic voltammograms (CV) for the electrooxidation of methanol over the Ni_3C - and Ni Nps in a range from -0.3 to $+0.35$ V. The CV curve for the Ni_3C Nps was similar to that for the Ni Nps over the entire potential range (Fig. S11, ESI[†]). Fig. 3d shows LV curves for the ORR over the Ni_3C - and Ni Nps. The Ni_3C - and Ni Nps had the same onset potential, -0.3 V, and their mass activities at the half-wave potential were virtually the same. Moreover, it was demonstrated that the Ni_3C Nps can retain their chemical composition and crystal structure even when subjected to repeated CV cycles in the NaBH_4 solution (S8, ESI[†] see the corresponding caption for details). Although Ni_3C is a thermally meta-stable phase,^{30,31} the synthesized Ni_3C Nps can function as durable catalysts for the repeated operation of DBFCs.

The Ni_3C - and Ni Nps exhibited the same mass activities toward methanol electrooxidation and ORR, which indicates that the enhanced NaBH_4 -electrooxidation activity of the Ni_3C Nps may be attributed to the inherent electronic properties of the Ni_3C Nps, not to the size or dispersity of the Nps. As shown in Fig. S6 (ESI[†]), the Ni_3C Nps had a depleted density-of-state (DOS) near the Fermi level (EF) due to strong hybridization between the Ni 3d- and C 2p orbitals.³⁴ It is known that the ever developed Ni-based alloys are good catalysts for the hydrolysis of BH_4^- but not for the electrooxidation of fuels because of the predominant adsorption of OH^- to the Ni surface.³⁵ The depleted DOS at the EF of the Ni_3C Nps can weaken the adsorption of OH^- to inhibit the formation of insulating $\text{Ni}(\text{OH})_2$ surface layers, resulting in the enhanced electrooxidation activity of BH_4^- over the Ni_3C Nps.

In conclusion, we have successfully synthesized the smallest Ni_3C Nps ever produced through thermal decomposition of Ni-Cp clusters. The Ni_3C Nps exhibited a catalytic activity superior to that of Ni Nps in the electrooxidation of NaBH_4 , demonstrating their applicability to DBFCs. The successful development of an electrode catalyst comprising Ni_3C Nps will promote the use of catalytic carbides in precious-metal-free PEFCs, which will help address the energy challenges that we face.^{36,37}

This work was preliminarily supported by the JST PRESTO program, the Ministry of Education, Culture, Sports, Science and Technology (MEXT) and the Japan Society for the Promotion of Science (JSPS) through Grant-in-Aid 23560855. The HX-PES measurements were performed under the approval of the NIMS Synchrotron X-ray Station (Proposal No.2010B4609). The authors are grateful to HiSOR, Hiroshima University, and JAEA/SPring-8 for the development of HX-PES at BL15XU of SPring-8.

Notes and references

- H. A. Gasteiger and N. M. Marković, *Science*, 2009, **324**, 48.
- R. Borup, J. Meyers, B. Pivovar, Y. S. Kim, R. Mukundan, N. Garland, D. Myers, M. Wilson, F. Garzon, D. Wood, P. Zelenay, K. More, K. Stroh, T. Zawodzinski, J. Boncella, J. E. McGrath, M. Inaba, K. Miyatake, M. Hori, K. Ota, Z. Ogumi, S. Miyata, A. Nishikata, Z. Siroma, Y. Uchimoto, K. Yasuda, K. I. Kimijima and N. Iwashita, *Chem. Rev.*, 2007, **107**, 3904.
- H. A. Gasteiger, S. S. Kocha, B. Sompalli and F. T. Wagner, *Appl. Catal., B*, 2005, **56**, 9.
- E. Reddington, A. Sapienza, B. Gurau, R. Viswanathan, S. Sarangapani, E. S. Somtkin and T. E. Mallouk, *Science*, 1998, **280**, 1735.
- B. H. Liu and Z. P. Li, *J. Power Sources*, 2009, **187**, 527.
- J. H. Wee, *J. Power Sources*, 2006, **155**, 329.
- K. Wang, J. Lu and L. Zuang, *Catal. Today*, 2011, **170**, 99.
- Z. P. Li, B. H. Liu, K. Arai and S. Suda, *J. Alloys Compd.*, 2005, **404**, 648.
- B. H. Liu, Z. P. Li, K. Arai and S. Suda, *Electrochim. Acta*, 2005, **50**, 3719.
- P. He, Y. Wang, F. Pei, H. Wang, L. Liu and L. Yi, *J. Power Sources*, 2011, **196**, 1042.
- G. Guella, B. Patton and A. Miotello, *J. Phys. Chem. C*, 2007, **111**, 18744.
- M. Chatenet, F. Micoud, I. Roche and E. Chainet, *Electrochim. Acta*, 2006, **51**, 5459.
- J. H. Kim, H. S. Kim, Y. M. Kang, M. S. Song, S. Rajendran, S. C. Han, D. H. Jung and J. Y. Lee, *J. Electrochem. Soc.*, 2004, **151**, A1039.
- H. Çelikkan, M. Şahin, M. L. Aksu and T. N. Veziroğlu, *Int. J. Hydrogen Energy*, 2007, **32**, 588.
- B. H. Liu, Z. P. Li and S. Suda, *J. Electrochem. Soc.*, 2003, **150**, A398.
- Y. Liu, M. A. Lowe, F. J. DiSalvo and H. D. Abruña, *J. Am. Chem. Soc.*, 2010, **114**, 14929.
- Y. Liu, H. Abe, H. M. Edverson, F. J. DiSalvo and H. D. Abruña, *Phys. Chem. Chem. Phys.*, 2010, **12**, 12978.
- L. R. Alden, C. Roychowdhury, F. Matsumoto, D. K. Han, V. B. Zeldovich, H. D. Abruña and F. J. DiSalvo, *Langmuir*, 2006, **22**, 10465.
- C. Roychowdhury, F. Matsumoto, V. B. Zeldovich, S. C. Warren, P. F. Mutolo, M. Ballesteros, U. Wiesner, H. D. Abruña and F. J. DiSalvo, *Chem. Mater.*, 2006, **18**, 3365.
- L. R. Alden, D. K. Han, F. Matsumoto, H. D. Abruña and F. J. DiSalvo, *Chem. Mater.*, 2006, **18**, 5591.
- E. Casado-Rivera, D. J. Volpe, L. R. Alden, C. Lind, C. Downie, T. Vázquez-Alvarez, A. C. D. Angelo, F. J. DiSalvo and H. D. Abruña, *J. Am. Chem. Soc.*, 2004, **126**, 4043.
- Z. L. Schaefer, K. M. Weeber, R. Misra, P. Schiffer and R. E. Schaak, *Chem. Mater.*, 2011, **23**, 2475.
- Y. Goto, K. Taniguchi, T. Omata, S. Otsuka-Yao-Matsuo, N. Ohashi, S. Ueda, H. Yoshikawa, Y. Yamashita, H. Ohashi and K. Kobayashi, *Chem. Mater.*, 2008, **20**, 4156.
- Y. G. Leng, Y. Liu, X. B. Song and X. G. Li, *J. Nanosci. Nanotechnol.*, 2008, **8**, 4477.
- M. S. Paquette and L. F. Dahl, *J. Am. Chem. Soc.*, 1980, **102**, 6621.
- H. W. Chiu and S. M. Kauzlarich, *Chem. Mater.*, 2006, **18**, 1023.
- L. He, *J. Magn. Magn. Mater.*, 2010, **322**, 1991.
- É. Bencze, B. V. Lokshin, J. Mink, W. A. Herrmann and F. E. Kühn, *J. Organomet. Chem.*, 2001, **627**, 55.
- Pearson's Handbook of Crystallographic Data for Intermetallic Phases*, ed. P. L. Villars and L. D. Calvert, American Society of Metals: Metals Park, OH, USA, 1985.
- S. Nagakura, *J. Phys. Soc. Jpn.*, 1958, **13**, 1005.
- S. Nagakura, *J. Phys. Soc. Jpn.*, 1957, **12**, 482.
- T. Ohsawa, Y. Adachi, I. Sakaguchi, K. Matsumoto, H. Haneda, S. Ueda, H. Yoshikawa, K. Kobayashi and N. Ohashi, *Chem. Mater.*, 2009, **21**, 144.
- G. J. Kovács, I. Bertóti and G. Radnóczy, *Thin Solid Films*, 2008, **516**, 7942.
- L. Yue, R. Sabiryanov, E. M. Kirkpatrick and D. L. Leslie-Pelecky, *Phys. Rev. B*, 2000, **62**, 8969.
- F. Gobal, Y. Valadbeigi and L. M. Kasmae, *J. Electroanal. Chem.*, 2011, **650**, 219.
- C. D. A. Brady, E. J. Rees and G. T. Burstein, *J. Power Sources*, 2008, **179**, 17.
- M. Nagai, M. Yoshida and H. Tominaga, *Electrochim. Acta*, 2007, **52**, 5430.



Short Communication

Visible light induced decomposition of organic compounds on WO₃ loaded PtPb co-catalysts

Takao Gunji^a, Takashi Tsuda^a, Arockiam John Jeevagan^a, Masanari Hashimoto^a, Toyokazu Tanabe^a, Shingo Kaneko^a, Masahiro Miyauchi^{b,c}, Govindachetty Saravanan^d, Hideki Abe^{c,e}, Futoshi Matsumoto^{a,*}

^a Department of Material and Life Chemistry, Kanagawa University, 3-27-1, Rokkakubashi, Kanagawa-ku, Yokohama, Kanagawa 221-8686, Japan

^b Department of Metallurgy and Ceramic Science, Graduate School of Science and Engineering, Tokyo Institute of Technology, 2-12-1 Ookayama, Meguro-ku, Tokyo 152-8552, Japan

^c PRESTO, Japan Science and Technology Agency (JST), 4-1-8 Honcho, Kawaguchi, Saitama 332-0012, Japan

^d CSIR-National Environmental Engineering Research Institute (CSIR-NEERI), Nehru Marg, Nagpur 440020, India

^e National Institute for Materials Science (NIMS), Sengen 1-2-1 Sengen, Tsukuba, Ibaraki 305-0047, Japan

ARTICLE INFO

Article history:

Received 30 May 2014

Received in revised form 4 July 2014

Accepted 5 July 2014

Available online 12 July 2014

Keywords:

Photocatalysis

Co-catalyst

Ordered intermetallic compound

Photo-decomposition

ABSTRACT

Tungsten oxide (WO₃)-supported ordered intermetallic PtPb nanoparticles (PtPb NPs/WO₃) were prepared through a co-reduction of Pt and Pb precursors with sodium borohydride in anhydrous methanol containing WO₃. The PtPb NPs/WO₃ were characterized based on the crystal structure obtained through powder X-ray diffraction (pXRD) as well as X-ray photoemission spectroscopy (XPS) and transmission electron microscopy (TEM). The formation of an ordered PtPb intermetallic phase on the WO₃ surface was confirmed. The PtPb NPs/WO₃ were more efficient when decomposing acetic acid (AcOH) and acetaldehyde (AcH) with visible light irradiation compared to the same process over WO₃ loaded with Pt nanoparticles (Pt NPs/WO₃).

© 2014 Published by Elsevier B.V.

1. Introduction

Semiconductor photocatalysts, such as titanium oxide (TiO₂) and tungsten oxide (WO₃), have received significant attention for several decades because they are a potential solution for the current energy and environmental problems. Semiconductor photocatalysts are versatile candidates for environment remediation [1], water splitting [2], CO₂ reduction [3] and solar energy conversion [4]. Recently, numerous visible light-driven semiconductor photocatalysts have been developed [5]. Metal oxides, particularly WO₃, have attracted attention because they act as ideal visible light photocatalysts; this behavior is attributed due to their small band gap energies (2.4–2.8 eV) and the high oxidation power of their valence band holes [6]. However, WO₃ exhibits a low photocatalytic activity due to the rapid recombination of its photoexcited electrons and holes. To suppress this process and significantly increase the photocatalytic efficiency, the consumption of photoexcited electrons and holes should be enhanced using co-catalysts. Abe and co-workers have demonstrated that Pt-loaded WO₃ samples were highly efficient during the decomposition of organic compounds under visible light irradiation with an oxygen reduction, which consumed the photoexcited electrons [7]. Consequently, Pt nanoparticles (NPs) were

used as co-catalysts with WO₃ to facilitate a multi-electron reduction of O₂, allowing O₂ to accept electrons despite the insufficient reduction potential of the conduction band electrons (in WO₃) during its single-electron reduction; furthermore, photocatalytic activity can be improved by selecting appropriate co-catalysts. Recently, a new approach that prevents the inherent problems of disordered alloy catalysts has been proposed by Abruña et al. toward highly active electrocatalysts for fuel cell applications [8]. In contrast with disordered alloys, intermetallic compounds with definite compositions and structures, such as PtPb and PtBi, exhibit excellent electrocatalytic performances toward formic acid (FA) oxidations in acidic solutions in terms of their onset potentials and current densities [9,10]. After the report by Abruña, many papers describing intermetallic NPs, such as PtBi, PtPb, Pt₃Ti and carbon black (CB)-supported intermetallic NPs, have been published for FA, methanol (MeOH) and ethanol (EtOH) oxidations and oxygen reduction reactions (ORR) [11–13]. In our previous study, the electrocatalytic activity of the ordered intermetallic PtPb compounds exhibited higher electrocatalytic activity toward FA, MeOH and EtOH oxidation [14] compared to conventional Pt-based alloys and Pt. In addition, we have recently reported that ordered PtPb intermetallic NPs accelerated ORR in acidic solutions [15]. Therefore, the ordered PtPb ordered intermetallic NPs should be competent co-catalysts at the oxidation and reduction sites on WO₃. We report a simple one-pot approach toward WO₃-

* Corresponding author.

supported ordered intermetallic PtPb NP catalysts. Furthermore, we investigated the effects of using ordered intermetallic PtPb compounds as co-catalysts with photocatalytic activity during the oxidative decomposition of acetic acid (AcOH) and acetaldehyde (ACh).

2. Experimental

The WO_3 particles were purchased from Kojundo Chemical Laboratory Co. Ltd. (Type: WW004PB). Fine particulate WO_3 particles (50–200 nm) were separated from the commercial WO_3 powder, as reported in Ref. [7]. The photodeposited Pt NPs/ WO_3 sample was synthesized as reported by Abe et al. [7]. The procedure used to prepare Pt NPs/ WO_3 via chemical deposition with a Pt precursor and a reducing agent is described in the ESI†. The synthesis of PtPb NPs/ WO_3 (PtPb loading: 1.0 wt.%) proceeded as follows. WO_3 powder (0.5 g) was suspended in 15 mL of anhydrous methanol for 15 min in a two neck round bottomed flask. Afterwards, 0.013 mmol of chloroplatinic acid ($\text{H}_2\text{PtCl}_6 \cdot 6\text{H}_2\text{O}$, Wako, Japan) and 0.026 mmol of lead(II) acetate ($\text{Pb}(\text{CH}_3\text{COO})_2$, Sigma-Aldrich) were dissolved in 15 mL of anhydrous methanol in a shielded vial under Ar before being transferred to the WO_3 suspensions. The solution was stirred for 30 min to yield a homogeneous yellow solution. Afterwards, 3 mmol of sodium borohydride (NaBH_4 , Sigma-Aldrich) in methanol was injected into the suspension to reduce the precursors. The product was centrifuged and washed with anhydrous methanol three times before being dried under vacuum. The as-prepared PtPb NPs/ WO_3 were yellowish green. The other experimental conditions are described in the Supplementary information.

3. Results and discussion

Fig. 1A shows the powder X-ray diffraction (pXRD) profiles of the WO_3 , Pt NPs/ WO_3 and PtPb NPs/ WO_3 (Supplementary information for the pXRD procedure). To confirm the formation of the ordered intermetallic NPs on the WO_3 through pXRD, the Pt loading on WO_3 was adjusted to 5 wt.% on both the Pt NPs/ WO_3 and PtPb NPs/ WO_3 , while 0.1 or 1.0 wt.% Pt and ordered intermetallic PtPb were used when testing the photocatalytic activity. The simulated pXRD patterns for the Pt

phase (face-centered cubic (fcc), $Fm\bar{3}m$, $a = 0.3925$ nm, JCPDS 04-0802) and the ordered intermetallic PtPb phase (NiAs structure, $P6_3/mmc$, $a = b = 0.426$ nm, $c = 0.548$ nm) are denoted by the solid bars below the graph. The pXRD profile (Fig. 1A-(a)) for WO_3 shows several major peaks, which are attributed to monoclinic WO_3 (JCPDS 43-1035). In addition, the pXRD profiles (Fig. 1A-(b, c)) for the Pt NPs/ WO_3 and the as-prepared PtPb NPs/ WO_3 exhibit small characteristic peaks at 39.8° for Pt and at 41.0° and 42.4° for the ordered intermetallic PtPb phases. The retention of the pXRD peaks at 41.0° and 42.4° , even after heat-treating the as-prepared PtPb NPs/ WO_3 (the reason for the heat-treatment will be explained in Fig. 3), could be ascribed to the formation of stable, ordered PtPb intermetallic NPs on the WO_3 (Fig. S1).

Fig. 1(B) and (C) shows low-magnification and high-resolution (HR)-TEM images of the annealed 1.0 wt.% PtPb NPs/ WO_3 . Several low-magnification images were obtained from a PtPb NPs/ WO_3 sample, as shown in Fig. S2, to show the particle size and the degree of dispersion of the PtPb NPs on the WO_3 . The size distributions of the PtPb NPs were evaluated based on the sizes of approximately 100 particles in the TEM images. The average diameter of the PtPb NPs was 9.5 nm, and they exhibited a large particle-size distribution. In particular, the PtPb NPs are different sizes within the observation area even when the images were obtained from a single sample, as shown in Fig. S2. However, the Pt NPs (average diameter: 5.4 nm) were well dispersed on the WO_3 surface (the TEM images of the Pt NPs/ WO_3 prepared through chemical and photodeposition are shown in Figs. S3 and S4). The HR-TEM image (C) of the interface between the PtPb and WO_3 phases shows clear lattice fringes, indicating that the PtPb NPs have atomically ordered structures on the WO_3 surface. Furthermore, the d -value is clearly different from that of WO_3 . The interval of the lattice fringe (0.223 nm) on the PtPb phase is consistent with the d -value for the {110} planes of the ordered PtPb intermetallic phase ($d = 0.213$ nm, ICDD PDF File # 06-0374) but is not consistent with any d -values for Pt phases (fcc structure). The fast Fourier-transformation (FFT) pattern (Fig. S5) demonstrates that the atoms in the PtPb NPs are, as expected based on the pXRD data, arranged in a NiAs-type structure. The compositional maps (Fig. 2) based on the STEM images reveal that the Pt and Pb are uniformly distributed in the PtPb NPs. STEM-energy dispersive spectroscopy (EDS) maps in Fig. 2

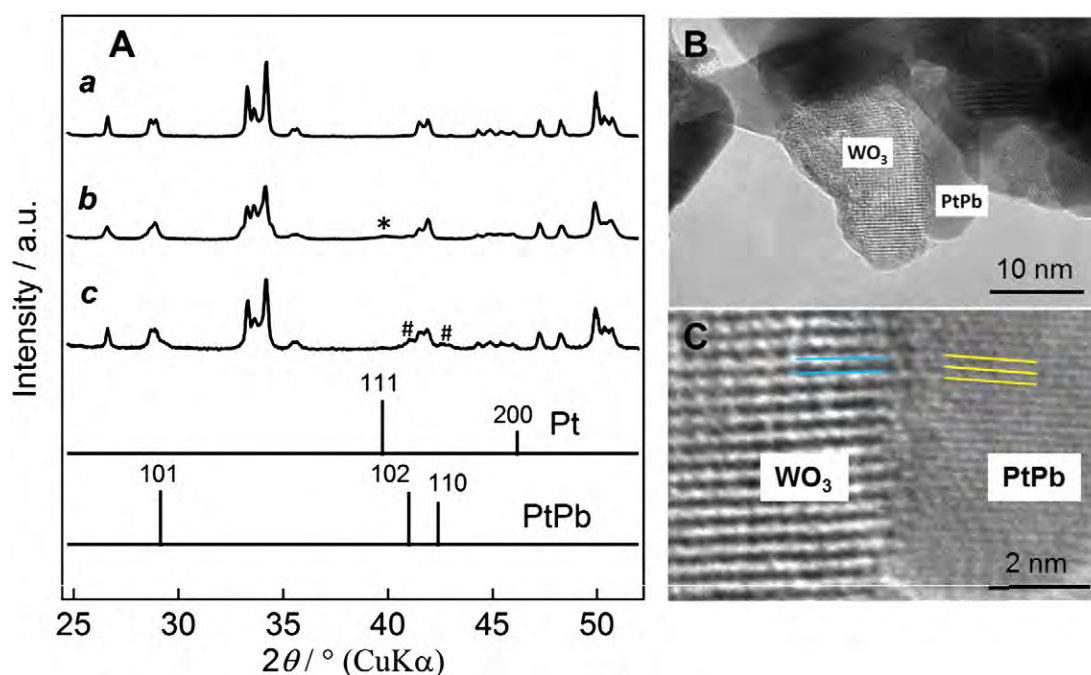


Fig. 1. (A) pXRD diffractograms of the WO_3 (a), Pt NPs/ WO_3 (b) and PtPb NPs/ WO_3 (c) (for b and c, 5 wt.% Pt on WO_3). (B) TEM image of the annealed PtPb NPs/ WO_3 photocatalyst (1.0 wt.% PtPb on WO_3) and (C) a high-resolution (HR)-TEM image of the interface between the PtPb and WO_3 phases. The marks (* and #) in (A) correspond to the peaks for Pt and PtPb, respectively.

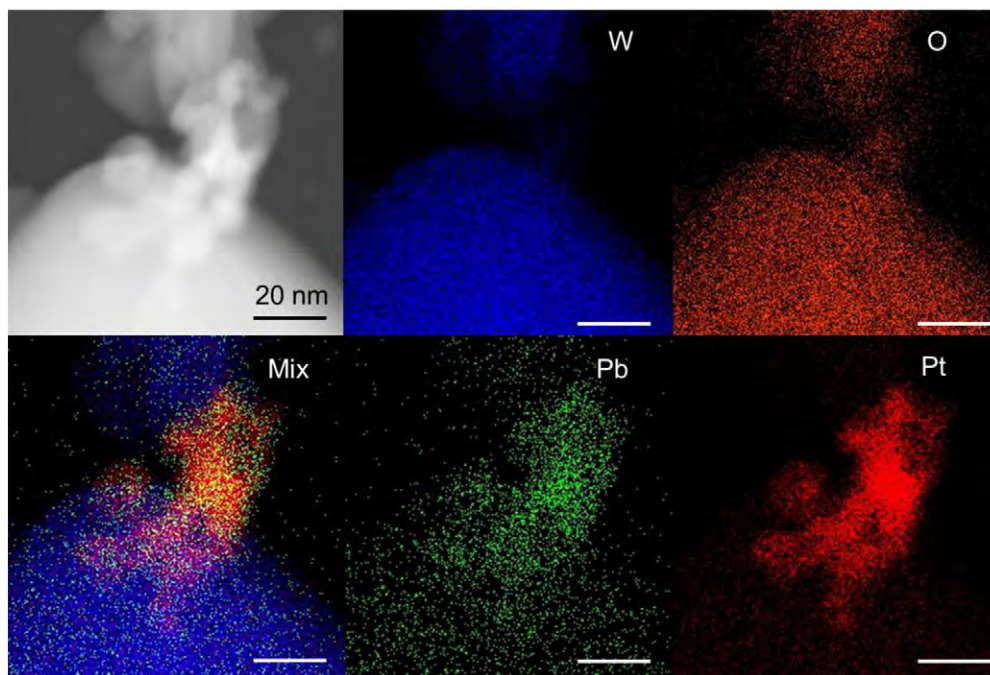


Fig. 2. Scanning transmission electron microscopy (STEM) image of the annealed PtPb NPs/WO₃ (PtPb loading weight on WO₃: 1.0 wt.%) and the corresponding compositional mapping images.

demonstrate that the average molar ratios of Pt to Pb for the PtPb NPs (Pt: Pb = 56.2:43.8) were consistent with the desired values for PtPb (Pt:Pb = 1:1). Inductively coupled plasma-mass spectroscopy (ICP-MS) showed that the average molar ratio of Pt to Pb for the PtPb NPs on WO₃ was Pt:Pb = 49.8:50.2 for the as-prepared and annealed samples. The *p*XRD and TEM/STEM data clearly indicate that an ordered intermetallic PtPb phase can be formed on a WO₃ surface through a one-pot process.

Fig. 3 shows the diffuse reflectance UV–Vis absorption spectra for the Pt NPs/WO₃ prepared from the Pt precursor on a WO₃ support when using NaBH₄ as the reducing agent. To evaluate the influence of the reducing agent on the support after the Pt ions were reduced in anhydrous methanol containing dispersed WO₃, UV–Vis spectra (Supplementary information for the UV–Vis absorption spectroscopy procedure) were collected, as shown in **Fig. 3A**. Non-treated, pure WO₃ (a) exhibits an apparent absorption edge at 465 nm, as reported previously [16]. The as-prepared Pt NPs/WO₃ catalysts exhibit a visible absorption above 450 nm due to the reduction of the W⁶⁺ to W⁵⁺ or W⁴⁺; the reducing agent reduced the Pt precursor in anhydrous methanol containing dispersed WO₃. A significant change in the visible

absorption of the Pt NPs/WO₃ is induced through a heat treatment in air at 100 °C over 1 h. Afterwards, the absorption band exhibited no obvious change compared to the pure WO₃, indicating that the oxidation state on the Pt NPs/WO₃ photocatalyst sample was restored to its original state. The XPS results obtained with the as-prepared and annealed Pt NPs/WO₃ also support our hypothesis regarding the change in the oxidation state of the W ions (Supplementary information for the XPS procedure). The XPS spectra showing the W 4*f* region of (a) non-treated WO₃, (b) as-prepared Pt NPs/WO₃ and (c) annealed (100 °C) Pt NPs/WO₃ are shown in **Fig. 3B**. All of the binding energies in **Fig. 3B** are assigned based on the literature values for WO₃ [17–19]. The XPS spectra were curve-fitted, and each curve was assigned to the corresponding oxidation state in the W 4*f* level. A doublet was used to fit the W 4*f* level, as observed in **Fig. 3B**-(a). The peak for W 4*f*_{7/2} can be observed at 35.4 eV and is generated by the photoelectrons emitted from W⁺⁶ species (WO₃). The spectrum (b) recorded with the as-prepared Pt NPs/WO₃ can be assigned two doublets; the peak (W 4*f*_{7/2}) of the first doublet is located at 35.4 eV and is generated by photoelectrons emitted from W⁺⁶ species; the peak (W 4*f*_{7/2}) for the second doublet is located

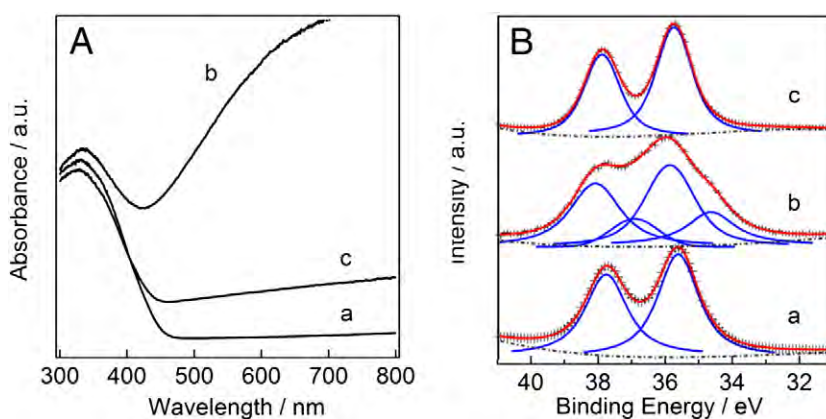


Fig. 3. (A) Diffuse reflectance UV–Vis absorption spectra for the (a) non-treated WO₃, (b) as-prepared Pt NPs/WO₃ and (c) annealed (100 °C) Pt NPs/WO₃ (for b and c, 1.0 wt.% Pt on WO₃). (B) XPS spectra (red lines) and fitted curves (blue lines) in the W 4*f* region for the (a) non-treated WO₃, (b) as-prepared Pt NPs/WO₃ and (c) annealed (100 °C) Pt NPs/WO₃.

at 34.4 eV and can be attributed to the photoelectrons emitted from tungsten atoms near the oxygen vacancies formed by the reduction reactions when the oxidation state of W is below +6. As observed in (c), the second doublet was removed after treating the Pt NPs/WO₃ at 100 °C, reforming the W⁶⁺. For the PtPb NPs/WO₃, a clear absorbance change could be observed between non-treated WO₃ and as-prepared PtPb NPs/WO₃ (Fig. S6-A), but no drastic changes were observed in the oxidation state of WO₃ based on the XPS spectra (Fig. S6-B). The annealing process (in air at 100 °C for 1 h) was applied to the as-prepared PtPb NPs/WO₃ samples to return the optical properties of the WO₃ in PtPb NPs/WO₃ to that of the untreated WO₃ supports. The UV–Vis absorption spectra of the annealed Pt NPs/WO₃ and annealed PtPb NPs/WO₃ are overlaid in Fig. S7 to compare their optical absorption properties. The Pt NPs/WO₃ exhibit a higher visible absorption than the PtPb NPs/WO₃.

The photocatalytic activities of the photodeposited Pt NPs/WO₃, chemically deposited Pt NPs/WO₃ and annealed PtPb NPs/WO₃ photocatalysts were examined during a photocatalytic decomposition of AcOH in aerated aqueous suspensions (Supplementary information contains the procedure used to evaluate the decomposition rate of the AcOH). Fig. 4(A) plots the CO₂ generated during the liquid-phase decomposition of AcOH over the Pt NPs- and PtPb NPs-loaded WO₃. The rates of CO₂ generation over the Pt NPs/WO₃ and PtPb NPs/WO₃ photocatalysts were estimated using the slope of the CO₂ formation vs. time plot from 0 to 100 min. The CO₂ generation rate over the PtPb NPs/WO₃ (115.3 μmol·mg⁻¹·h⁻¹) was higher than that of the photodeposited- (56.33 μmol·mg⁻¹·h⁻¹) and chemically deposited (50.24 μmol·mg⁻¹·h⁻¹) Pt NPs/WO₃. The low activity of the annealed-chemically deposited Pt NPs/WO₃ versus the photodeposited Pt NPs/WO₃ might be attributed to the reduced tungsten ions in the WO₃ in the annealed-chemically deposited Pt NPs/WO₃. However, the XPS data in Fig. 3B-(c) do not show any XPS peaks attributed to reduced tungsten ions (W⁵⁺ or W⁴⁺) after annealing. Therefore, the contradictory data from the activity test and XPS measurements should be examined. Although the low activity of the annealed-chemically deposited Pt NPs/WO₃ is attributed to a small change in the oxidation state of the tungsten ions that cannot be detected through XPS, we propose that the differences in the deposition sites of the Pt NPs on the WO₃ of the annealed-chemically deposited Pt NPs/WO₃ and photodeposited Pt NPs/WO₃ samples

should also be examined. In the annealed-chemically deposited Pt NPs/WO₃ the Pt NPs were randomly deposited on the WO₃ surfaces. On the surfaces of the photodeposited Pt NPs/WO₃ sample, however, the Pt NPs were site-selectively deposited on the WO₃. Because the Pt NPs were formed by reductive deposition with photoexcited electrons, the Pt NPs were deposited on the site (reduction site) where the photoexcited electrons appear on the surfaces of the WO₃. The co-catalysts deposited on the reduction site actively catalyze the reduction reaction under visible light. Fig. 4(B) shows the AcH decomposition and CO₂ generation profiles over WO₃ that was annealed after exposure to a reducing agent, photodeposited- and chemically deposited Pt NPs/WO₃, and annealed PtPb NPs/WO₃ photocatalysts under visible light irradiation (λ > 420 nm) (Supplementary information details the procedure used to evaluate the decomposition rate of AcH). With visible light irradiation, the amounts of AcH in the gas phase over the Pt NPs/WO₃ and PtPb NPs/WO₃ decreased rapidly when the CO₂ generation increased versus WO₃. The complete decomposition of AcH is proven by the molar yield of CO₂ (ca. 530 ppm), which is twice that of the molar amount of AcH injected (ca. 280 ppm). The Pt NPs/WO₃ and PtPb NPs/WO₃ photocatalysts completely decomposed AcH to form CO₂ over different reaction times. In contrast, WO₃ could not decompose AcH completely because the catalyst was deactivated by the products that accumulated on its surface [20]. Of the examined samples, PtPb NPs/WO₃ perform the best by completely decomposing AcH to CO₂ within 120 min.

4. Conclusion

Samples of WO₃ loaded with Pt and PtPb NPs were used to photocatalyze the decomposition of organic compounds in the liquid and gas phases with visible light irradiation (λ > 420 nm). PtPb NPs/WO₃ exhibit a higher photocatalytic activity than the conventional Pt NPs/WO₃ and the pure WO₃. This enhanced photocatalytic activity might be attributed to the efficient multi-electron ORR and the oxidative decomposition of organic compounds, which induces charge separations in the PtPb. The particles of the ordered PtPb intermetallic NPs on WO₃ are much larger than the Pt NPs on WO₃; the Pt NPs on WO₃ have much larger surface areas exposed to the AcOH solution and to the gas phase containing AcH than the PtPb NPs fixed on WO₃. Although

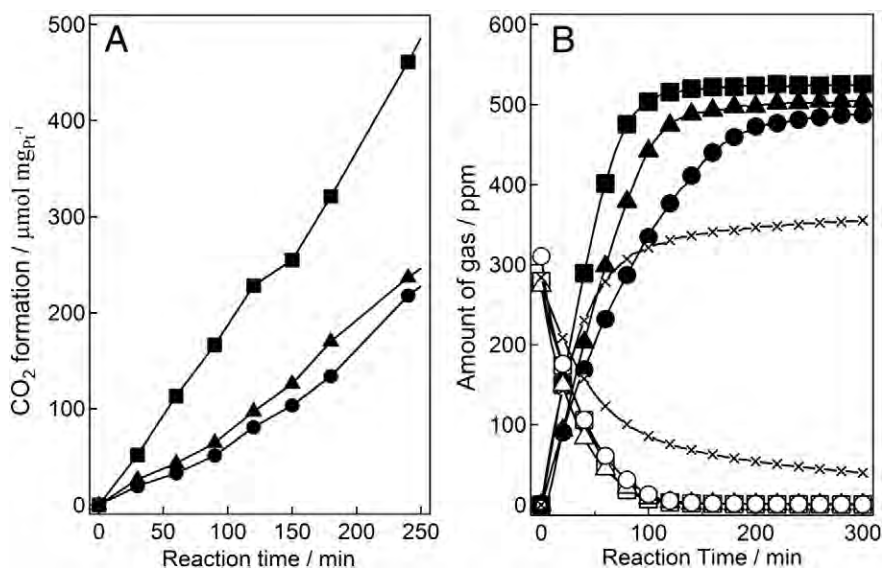


Fig. 4. (A) The time courses of the CO₂ evolution during the decomposition of AcOH over the chemically deposited Pt NPs/WO₃ (solid circle, 1 wt.% Pt), photodeposited Pt NPs/WO₃ (solid triangle, 1 wt.% Pt) and annealed PtPb NPs/WO₃ (1 wt.% PtPb, solid square) photocatalysts suspended in aqueous AcOH in the presence of O₂ with visible light irradiation (λ > 420 nm). (B) The time trials for the decomposition of AcH (open symbol) and the evolution of CO₂ (solid symbol) in the presence of O₂ over WO₃ (cross), Pt/WO₃ (triangle, Pt was deposited by photo deposition, 0.1 wt.% Pt), Pt NPs/WO₃ (circle, Pt was deposited by chemical deposition, 0.1 wt.% Pt) and annealed PtPb NPs/WO₃ (square, 0.1 wt.% PtPb) photocatalysts with visible light irradiation (λ > 420 nm).

the surface area of the PtPb NPs is smaller than that of the reported catalysts utilized in this work, the Pt NPs/WO₃ exhibit a higher visible absorption than the PtPb NPs/WO₃; PtPb showed enhanced photocatalytic activity relative to the Pt NPs/WO₃. Therefore, the surfaces of the ordered intermetallic PtPb NPs are more efficient as co-catalysts on WO₃. Our strategy for preparing PtPb NPs on WO₃ was successful, and the results demonstrate highly efficient visible light-induced photocatalytic systems using ordered intermetallic NP co-catalysts.

Acknowledgments

We thank Dr. Akihiro Yoshida and Prof. Shuichi Naito of Kanagawa University for help measuring photocatalytic activity. This work was financially supported by the Strategic Research Base Development Program for Private Universities of the Ministry of Education, Culture, Sports, Science and Technology of Japan.

Appendix A. Supplementary data

Supplementary data to this article can be found online at <http://dx.doi.org/10.1016/j.catcom.2014.07.013>.

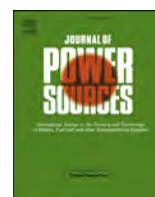
References

- [1] A. Fujishima, T.N. Rao, D.A. Tryk, *J. Photochem. Photobiol. C* 1 (2000) 1–21.
- [2] K. Maeda, K. Domen, *J. Phys. Chem. Lett.* 1 (2010) 2655–2661.
- [3] K. Mori, H. Yamashita, M. Anpo, *RSC Adv.* 2 (2012) 3165–3172.
- [4] M.G. Walter, E.L. Warren, J.R. McKone, S.W. Boettcher, Q. Mi, E.A. Santori, N.S. Lewis, *Chem. Rev.* 110 (2010) 6446–6473.
- [5] K. Maeda, M. Higashi, D. Lu, R. Abe, K. Domen, *J. Am. Chem. Soc.* 132 (2010) 5858–5868.
- [6] G.R. Bamwenda, H. Arakawa, *Appl. Catal., A* 210 (2001) 181–191.
- [7] R. Abe, H. Takami, N. Murakami, B. Ohtani, *J. Am. Chem. Soc.* 130 (2008) 7780–7781.
- [8] E. Casado-Rivera, Z. Gál, A.C.D. Angelo, C. Lind, F.J. DiSalvo, H.D. Abruña, *ChemPhysChem* 4 (2003) 193–199.
- [9] E.D. Casado-Rivera, J. Volpe, L. Alden, C. Lind, C. Downie, T. Vázquez-Alvarez, A.C.D. Angelo, F.J. DiSalvo, H.D. Abruña, *J. Am. Chem. Soc.* 126 (2004) 4043–4049.
- [10] Y. Kang, L. Qi, M. Li, R.E. Diaz, D. Su, R.R. Adzic, E. Stach, J. Li, C.B. Murray, *ACS Nano* 6 (2012) 2818–2825.
- [11] L.D. Shao, W. Zhang, M. Ambruster, D. Teschner, F. Girgsdies, B.S. Zhang, O. Timpe, M. Friedrich, R. Schlögl, D.S. Su, *Angew. Chem. Int. Ed.* 50 (2011) 10231–10235.
- [12] A.C. Chen, P.H. Hindle, *Chem. Rev.* 110 (2010) 3767–3804.
- [13] H. Abe, F. Matsumoto, L.R. Alden, S.C. Warren, H.D. Abruña, F.J. DiSalvo, *J. Am. Chem. Soc.* 130 (2008) 5452–5458.
- [14] F. Matsumoto, C. Roychowdhury, F.J. DiSalvo, H.D. Abruña, *J. Electrochem. Soc.* 155 (2008) B148–B154.
- [15] T. Gunji, G. Saravanan, T. Tanabe, T. Tsuda, M. Miyauchi, G. Kobayashi, H. Abe, F. Matsumoto, *Catal. Sci. Technol.* 4 (2014) 1436–1445.
- [16] D. Tsukamoto, M. Ikeda, Y. Shiraishi, T. Hara, N. Ichikuni, S. Tanaka, T. Hirai, *Chem. Eur. J.* 17 (2011) 9816–9824.
- [17] W. Li, J. Li, X. Wang, Q. Chen, *Appl. Surf. Sci.* 263 (2001) 157–162.
- [18] A. Mozalev, V. Khatko, C. Bittencourt, A.W. Hassel, G. Gorokh, E. Llobet, X. Correig, *Chem. Mater.* 20 (2008) 6482–6493.
- [19] W. Li, Z. Fu, *Appl. Surf. Sci.* 256 (2010) 2447–2452.
- [20] T. Arai, M. Yanagida, Y. Konishi, Y. Iwasaki, H. Sugihara, K. Sayama, *J. Phys. Chem. C* 111 (2007) 7574–7577.



Contents lists available at ScienceDirect

Journal of Power Sources

journal homepage: www.elsevier.com/locate/jpowsour

Facile route for the preparation of ordered intermetallic Pt₃Pb–PtPb core–shell nanoparticles and its enhanced activity for alkaline methanol and ethanol oxidation



Takao Gunji^a, Toyokazu Tanabe^a, Arockiam John Jeevagan^a, Sho Usui^a, Takashi Tsuda^a, Shingo Kaneko^b, Govindachetty Saravanan^c, Hideki Abe^{d,e}, Futoshi Matsumoto^{a,*}

^a Department of Material and Life Chemistry, Kanagawa University, 3-27-1, Rokkakubashi, Kanagawa-ku, Yokohama, Kanagawa 221-8686, Japan

^b Research Institute for Engineering, Kanagawa University, 3-27-1, Rokkakubashi, Kanagawa-ku, Yokohama, Kanagawa 221-8686, Japan

^c CSIR-National Environmental Engineering Research Institute (CSIR-NEERI), Nehru Marg, Nagpur 440020, India

^d National Institute for Materials Science (NIMS), 1-2-1 Sengen, Tsukuba, Ibaraki 305-0047, Japan

^e PRESTO, Japan Science and Technology Agency (JST), 4-1-8 Honcho, Kawaguchi, Saitama 332-0012, Japan

HIGHLIGHTS

- Pt₃Pb–PtPb core–shell NPs were prepared on carbon black at room temperature.
- The core–shell structure was characterized with XRD, XPS and TEM.
- The core–shell NPs showed higher activity for EtOH oxidation compared to PtPb.
- The relationship between the surface structure and the catalytic activity was evaluated.

ARTICLE INFO

Article history:

Received 10 July 2014

Received in revised form

14 September 2014

Accepted 30 September 2014

Available online 6 October 2014

Keywords:

Electrocatalysis

Ordered intermetallic compound

Core–shell structure

Ethanol oxidation

Fuel cell

ABSTRACT

Pt₃Pb(core)–PtPb(shell) intermetallic compound nanoparticles (NPs) were synthesized on carbon black (CB) by converting nanocrystalline Pt to an ordered intermetallic compound with the reduction of Pb ions. The Pt₃Pb–PtPb core–shell NPs were characterized by analyzing their crystal structures with powder X-ray diffraction (pXRD), hard X-ray photoemission spectroscopy (HX-PES), and transmission electron microscopy (TEM). The synthesized NPs exhibited enhanced catalytic activity and relatively stable cycle performance towards methanol (MeOH) and ethanol (EtOH) oxidation in an alkaline aqueous solution. The improved catalytic performance of the Pt₃Pb–PtPb core–shell NPs might be attributed to both the enhancement of EtOH dehydrogenation and the higher concentration of surface OH_{ads} at lower potential on the modified PtPb surface in the Pt₃Pb–PtPb core–shell NPs.

© 2014 Published by Elsevier B.V.

1. Introduction

In recent years, within the polymer electrolyte membrane fuel cell research field, enormous attention has been directed towards the development of direct fuel cells (DFCs) in which small organic molecule (SOM) liquid fuels, such as methanol (MeOH), ethanol (EtOH), and formic acid (FA), are used as fuels [1,2]. Among the main fuel molecules, EtOH is a promising alternative fuel because of its relatively low toxicity and high energy density and because it does not release carbon that was previously sequestered

underground as coal, petroleum, or natural gas into the atmosphere [3]. However, the full potential of DFCs has not been fulfilled due to the slow kinetics in the anode reactions [4]. It has been reported that the oxidation kinetics of organic fuels in acidic media exhibits slower kinetics than in alkaline environments due to catalyst poisoning by reaction intermediates [5]. One of the research and development challenges facing alkaline-type polymer electrolyte fuel cells using SOMs is the design of better alternatives to the Pt, Pd, and Pt–Ru alloys currently used as the anode catalysts [6,7]. To improve the electrocatalytic activity, Pt- and Pd-based alloy electrocatalysts have been investigated in alkaline media [8]. Although the aforementioned alloys are promising materials, there are problems associated with the use of disordered alloys (and alloys in general) as catalysts for fuel cell applications, including the surface

* Corresponding author. Fax: +81 45 413 9770.

E-mail address: fmatsumoto@kanagawa-u.ac.jp (F. Matsumoto).

segregation of metal atoms and the partial poisoning by CO due to insufficient quantities of the bimetallic elements on the surface.

Recently, a new approach that avoids the problems inherent in disordered alloy catalysts has been proposed for highly active electrocatalysts for fuel cell applications [9]. In contrast with disordered alloys, intermetallic compounds with definite compositions and structures, such as PtPb and PtBi, exhibit excellent electrocatalytic performance towards FA oxidation in acidic solutions in terms of onset potential and current density [10,11]. Abruña et al. have examined the FA, MeOH, and EtOH oxidation activities with a wide range of intermetallic compounds (PtPb, PtBi, and Pt₃Ti) in acidic media and found that the intermetallic compounds exhibit enhanced catalytic activity when compared with pure Pt [10,11]. In our previous study, we reported that PtPb and PtBi ordered intermetallic compounds exhibited higher electrocatalytic activity towards MeOH and EtOH oxidation in alkaline aqueous solutions than Pt, Pt–Ru alloy, and other Pt-based ordered intermetallic compounds [12]. In this paper, we report on the enhancement of the electrocatalytic activity of PtPb ordered intermetallic compounds towards MeOH and EtOH oxidation in alkaline aqueous solutions. To achieve this, carbon black (CB)-supported Pt₃Pb(core)–PtPb(shell) intermetallic NPs (Pt₃Pb–PtPb NPs/CB) were synthesized via a method (hereafter referred to as the “converting reaction method”) in which the CB-supported Pt NPs react with a Pb precursor in the presence of a reducing agent under microwave irradiation. In the converting reaction method, the Pb atoms were only observed in the PtPb NPs and not on the CB surfaces. In other words, Pb NPs were not formed on CB in the reaction with microwaves, indicating the selective reaction of Pb atoms with Pt NPs on the CB surfaces, as previously reported by Bauer and our group [13,14]. By controlling the amount of Pb atoms, the core–shell structure with Pt₃Pb and PtPb intermetallic phases can be formed in a NP. The activities of Pt₃Pb–PtPb NPs/CB were compared with those of the reference samples consisting of pure PtPb NPs/CB and Pt₃Pb NPs/CB, which were prepared on the CB through the co-reduction reaction of the Pt and Pb precursors in the presence of a reducing agent and CB (hereafter referred to as the “co-reduction reaction method”). As mentioned above, previously, we have reported that PtPb and PtBi ordered intermetallic phases are the most promising electrocatalysts for MeOH and EtOH oxidations via the exhaustive screening of the ordered intermetallic phases for alkaline MeOH and EtOH oxidations [12]. Yang also reported promising electrocatalytic activity of PtBi towards alkaline MeOH oxidation, which is comparable to our results for the MeOH oxidation observed on pure PtBi and PtPb NPs [15]. In addition, several Pd-based alloys have also been examined towards the EtOH oxidation in an alkaline environment [16–18]. Among Pd-based alloys, Pd alloyed with Ni (PdNi) [16] demonstrated the highest alkaline EtOH oxidation activity and the activity is comparable with that of the pure PtPb NPs. In this research, our current results obtained with Pt₃Pb–PtPb NPs/CB were compared with that of works mentioned above.

2. Experimental section

2.1. Materials

The following chemicals were used to synthesize the NPs: dichloro(1,5-cyclooctadiene)platinum(II) (Pt(COD)Cl₂) (99.9%, Aldrich), (CH₃COO)₂Pb·3H₂O (99%, Wako), ethylene glycol (99.5%, Kanto Chemical) and Vulcan carbon black (CB, XC-72R, E-TEK).

For the electrochemical experiments, sulphuric acid (H₂SO₄, 99.999%, Aldrich), potassium hydroxide (KOH, 85%, Wako), formic acid (FA, 88% analytical reagent, Mallinckrodt), isopropyl alcohol (99.7%, Wako), methanol (MeOH, 99%, Wako), ethanol (EtOH, 99%,

Wako) and Nafion solution (Aldrich, wt. 5 % in water/aliphatic alcohols, 1100 EW) were used as received.

2.2. Synthesis of pure PtPb NPs using the co-reduction reaction method

Pt(COD)Cl₂ (0.0151 mmol), (CH₃COO)₂Pb·3H₂O (0.0227 mmol) and Vulcan CB (0.020 g) were dissolved in 50 mL of ethylene glycol. Then, 0.04 mmol potassium hydroxide was added to the mixture. The mixture was sonicated in a bath-type ultrasonicator and treated in a flask with a reflux apparatus for 6 min under 300 W microwave radiation. The mixture in the flask was then cooled to room temperature with water and treated again under microwave (focused microwave instrument, CEM) radiation of 300 W for 6 min. After the mixture cooled, the PtPb NPs/CB were collected via centrifugation, washed sequentially with EtOH and water, and finally dried under vacuum.

2.3. Synthesis of Pt₃Pb(core)–PtPb(shell) NPs using the converting reaction method

Pt(COD)Cl₂ (0.0151 mmol), (CH₃COO)₂Pb·3H₂O (0.0076 mmol) and Vulcan CB (0.020 g) were dissolved in 50 mL of ethylene glycol. Then, 0.04 mmol potassium hydroxide was added to the mixture. The mixture was sonicated in a bath-type ultrasonicator and treated in a flask with a reflux apparatus for 6 min under 300 W microwave radiation. The mixture in the flask was then cooled to room temperature with water and treated again under microwave (focused microwave instrument, CEM) radiation of 300 W for 6 min. After the mixture cooled, the PtPb NPs/CB was collected via centrifugation, washed sequentially with EtOH and water, and finally dried under vacuum.

2.4. Synthesis of bulk ordered intermetallic PtPb

Polycrystalline bulk samples of intermetallic PtPb were synthesized using an arc furnace in a pure Ar atmosphere (99.9999%) as a reference for the hard X-ray photoemission spectroscopy (HX-PES) measurements. All of the starting materials were purchased from Furuya Kinzoku Co. Stoichiometric quantities of Pt (99.9%) and Pb (99.999%) were melted together in a pure Ar (99.9999%) atmosphere at 2000 °C or higher for 24 h and subsequently cooled to room temperature. *p*XRD analysis confirmed that the bulk PtPb exists as a pure hexagonal phase of space group *P6₃/mmc*.

2.5. Preparation of pure Pt₃Pb NPs/CB

Carbon supported Pt₃Pb was prepared by wet-chemical approach using NaBH₄ as a reducing agent. In the synthesis, H₂PtCl₆·6H₂O (0.062 mmol), Pb(NO₃)₂ (0.027 mmol) and CB (60 mg) were dissolved in anhydrous methanol and transferred to a double neck round bottom flask without exposing into air. 6 mmol of NaBH₄ was dissolved in anhydrous methanol and then injected to the precursor solutions under Ar-atmosphere. The solutions were stirred for 15 h to complete the reaction under Ar-atmosphere. The black colour suspensions were centrifuged for 10 min at 2000 rpm to yield a black colour precipitate and then subsequently washed with 20 mL of anhydrous methanol for three times and dried under vacuum. The sample obtained was heat treated for 2 h at 600 °C in Ar.

2.6. Characterization of the synthesized NPs

Powder X-ray diffraction (*p*XRD) was performed using CuK α radiation (Panalytical X'Pert PRO; λ = 0.1548 nm) with an

increment of 0.02° in a range of diffraction angles from 20 to 80° . An obliquely cut Si crystal (non-reflection Si plate) was used as a sample holder to minimize the background. HX-PES was performed using X-rays with a photon energy of 5.95 keV at BL15XU of SPring-8, Japan. Sample powders were first dispersed in EtOH and dropped onto carbon substrates. The sample was thoroughly dried in air and transferred into an ultra-high-vacuum (UHV) chamber equipped with an electron spectrometer (Vacuum Generator, Scienta R4000). The binding energy of the photoelectrons was referenced to the Fermi energy of a Au film that was electrically contacted to the sample. Transmission electron microscopy (TEM/STEM) images were obtained with a JEOL 2100-F microscope with an operating voltage of 200 kV. The composition of the PtPb NPs/CB was analyzed by an energy-dispersion spectroscopic (EDS, Oxford link system) analyzer, which was coupled to the TEM. The sample for TEM was prepared by dropping a MeOH suspension of the sample powder onto a copper microgrid. The sample was thoroughly dried in vacuum prior to the observation. The chemical composition of the CB-supported NPs was determined using inductively coupled plasma-mass spectrometry (ICP-MS, PE-3300 DV, Perkin Elmer).

2.7. Preparation of PtPb NPs/CB- and Pt NPs/CB-coated GC electrodes and their electrochemistry

A suspension of the PtPb or Pt NP/CB ink was prepared by mixing 4 mg of the dried NP/CB sample, 3.98 mL of water, 1 mL of isopropyl alcohol, and 20 μ L of 5% w/w Nafion solution. The mixture was then sonicated in a bath-type ultrasonicator for 15 min. 6 μ L of each NP suspension was loaded onto a glassy carbon (GC) electrode with a diameter of 5 mm. The loading weight (0.96 μ g cm^{-2} of Pt NPs) on the GC electrode surface was maintained throughout the experiments. A conventional electrochemical setup was used to evaluate the efficiency of the NPs towards the oxidations of FA, MeOH, and EtOH under an Ar atmosphere. The NP-coated GC electrode, a platinum wire, and an Ag/AgCl (NaCl 3 M) electrode (0.209 V vs. NHE) were used as the working, auxiliary, and reference electrodes, respectively. The NP-coated GC electrodes were rotated to remove bubbles from the electrode surface that likely formed during the oxidation reactions. Pt–Ru alloy NPs and Pd NPs (on a Vulcan XC-72R, E-TEK) were used as reference samples for MeOH and EtOH oxidations.

CO stripping voltammograms were obtained in 0.1 M KOH or H_2SO_4 solutions. In these experiments, NP-coated GC electrodes were prepared under identical conditions. In the first experiment, 0.1 M KOH or H_2SO_4 solutions were purged with Ar gas for 30 min, after which high-purity CO (99.9%) was injected (note that CO should only be used in a well-ventilated hood) into the solutions for 30 min while maintaining the electrode potential at the initial open-circuit potential. The dissolved CO was subsequently removed from the solution by bubbling through nitrogen gas for 30 min while maintaining the applied electrode potential. Finally, the CO stripping voltammograms were obtained via positive scanning from the applied electrode potential at scan rate of 10 mV s^{-1} in N_2 -saturated 0.1 M KOH or H_2SO_4 solutions.

3. Results and discussion

Fig. 1 shows the *p*XRD profiles for the (a) CB, (b) Pt NPs/CB, (c) converting reaction-synthesized PtPb NPs/CB and (d) co-reduction reaction-synthesized PtPb NPs/CB. Simulated *p*XRD patterns for the Pt phase (face-centred cubic (fcc), $Fm\text{-}3m$, $a = 0.3925$ nm), PtPb (hexagonal, $P63/mmc$, $a = b = 0.426$ nm, $c = 0.548$ nm), and Pt_3Pb ordered intermetallic phases (Cu_3Au , $Pm\text{-}3m$, $a = b = c = 0.393$ nm) are indicated by the solid bars in the bottom portion of the figure. All of the *p*XRD profiles in Fig. 1 exhibit two peaks at 25.0° and 43.5°

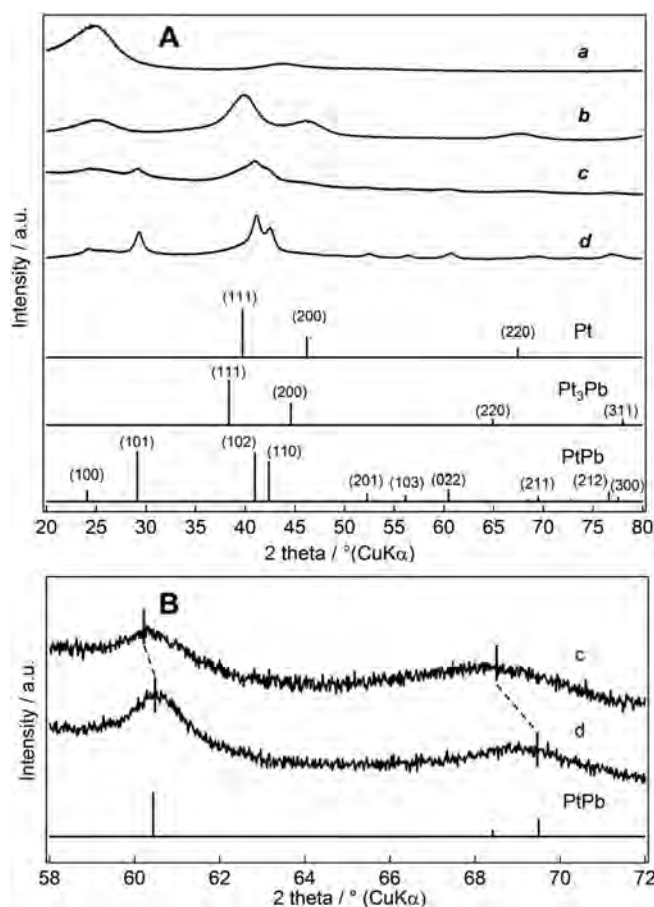


Fig. 1. (A) *p*XRD patterns of CB (a), Pt NPs/CB used as a starting material (b), converting reaction- (c) and conventional reaction-synthesized PtPb NPs/CB (d). The solid bars in the bottom half of the figure are the simulated *p*XRD peaks for the Pt and the ordered intermetallic PtPb and Pt_3Pb phases. (B) *p*XRD patterns of samples (c) and (d) from 58° to 72° .

that correspond to the $(0\ 0\ 2)$ and $(1\ 0\ 1)$ reflections of carbon (trace a), respectively. The *p*XRD profile of Pt NPs/CB (trace b) reveals peaks at 39.8° , 45.3° and 67.5° , corresponding to the $(1\ 1\ 1)$, $(2\ 0\ 0)$, and $(2\ 2\ 0)$ reflections, respectively, of an fcc-type structure ($Fm\text{-}3m$, $a = 0.393$ nm) similar to that of pure Pt ($Fm\text{-}3m$, $a = 0.3925$ nm), as indicated in the simulated *p*XRD peaks. The profiles of the samples obtained through the converting reaction and co-reduction reaction (traces c and d) show peak patterns that can be indexed to the hexagonal-type structure of PtPb ordered intermetallic structure. This includes the characteristic peaks for the PtPb ordered intermetallic phase, which distinguish the PtPb ordered intermetallic phase from the Pt fcc structure. These peaks can be observed from 50 to 80° in both traces (c) and (d). The NPs prepared via the converting reaction also exhibit small peaks for the Pt_3Pb $(1\ 1\ 1)$ and $(2\ 0\ 0)$ phases at 38.4° and 44.6° , respectively, indicating the coexistence of PtPb and Pt_3Pb phases in the NPs. It is evident from the data that the Pt_3Pb phase was also formed in the NPs by a wet-chemical approach. Peak shifts for the PtPb $(0\ 2\ 2)$ and $(2\ 1\ 1)$ phases to smaller angles were observed in the region from 58 to 72° for the NPs prepared via the converting reaction (Fig. 1B), resulting in an increase in the lattice parameter of the $(0\ 2\ 2)$ and $(2\ 1\ 1)$ phases. The shift of the $(2\ 1\ 1)$ peak is 1.2° . The PtPb NPs (trace d) prepared by the co-reduction reaction do not exhibit peaks apart from those assigned to the PtPb ordered intermetallic phase, respectively, nor do they exhibit any peak shifts. These results confirmed the formation of pure PtPb ordered intermetallic NPs

produced by the co-reduction reaction to be used as reference samples for the electrocatalytic activity tests.

Fig. 2 displays the HX-PES profiles in the Pt 4f region for PtPb NPs prepared with (a) the converting reaction and (b) the co-reduction reaction as well as the bulk references (c) PtPb and (d) Pt. The Pt 4f peak for the bulk PtPb was shifted 0.3 eV towards higher binding energies relative to the corresponding peak for the bulk Pt. The Pt 4f peaks for the NPs/CB prepared via the converting reaction and co-reduction reaction were consistent with those of the bulk PtPb, indicating that the chemical composition and atomic environment of the NP surfaces prepared via either of the two methods were identical to those of the bulk PtPb. Therefore, we conclude that the surfaces of the NPs prepared via the converting and co-reduction reactions consist of a PtPb ordered intermetallic phase.

Figs. 3 and 4(A) and (B) show the TEM images obtained with commercially available Pt NPs/CB and (A) co-reduction- and (B) converting reaction-synthesized NPs/CB. Pt and PtPb NPs appeared as dark spots that were uniformly dispersed on the CB. The distributions of the size of the Pt and PtPb NPs were evaluated using approximately 100 particles in the TEM images. The average diameters of the Pt NPs and the co-reduction- and converting reaction-synthesized PtPb NPs were calculated as 2.5, 3.0, and 4.6 nm, respectively, and they exhibited a narrow particle-size distribution. We also calculated the theoretical diameter of hemispherical PtPb ordered intermetallic compound NPs to be 3.0 nm on the basis of the density (15.51 g cm^{-3}) [19] of the PtPb ordered intermetallic compound. The hemispherical Pt NPs with a diameter of 2.5 nm were reacted with Pb^{2+} to prepare the PtPb ordered intermetallic compound. The particle size increased to the theoretical value when the PtPb ordered intermetallic compounds were formed on CB, as shown in Fig. 4B. In addition, from a comparison of the TEM image of the converting reaction-synthesized PtPb NPs/CB with that of Pt NPs/CB used as a starting material for the converting reaction, it can be observed that the degree of spatial dispersivity of the Pt NPs on the CB is retained on the NPs/CB prepared via the

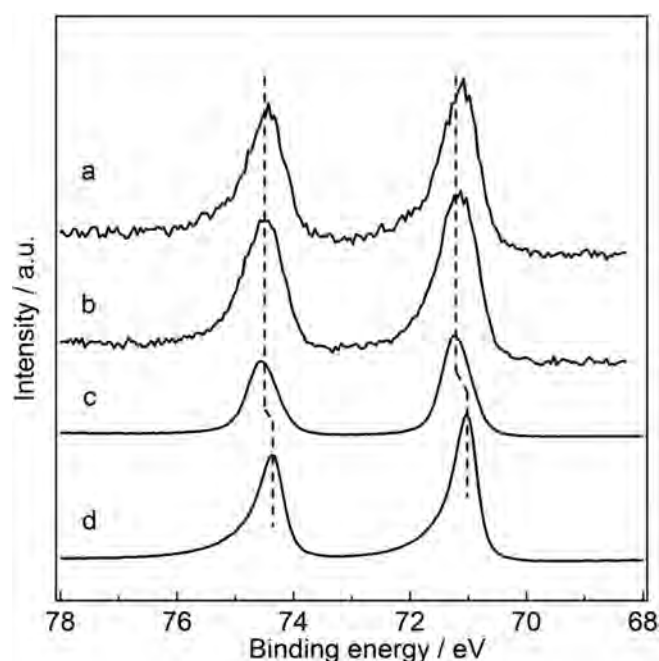


Fig. 2. HX-PES profiles in the Pt 4f region for PtPb NPs/CB prepared via (a) the converting reaction method and (b) conventional synthesis. The HX-PES spectra obtained with (c) ordered intermetallic bulk phase PtPb and (d) bulk Pt are shown as references.

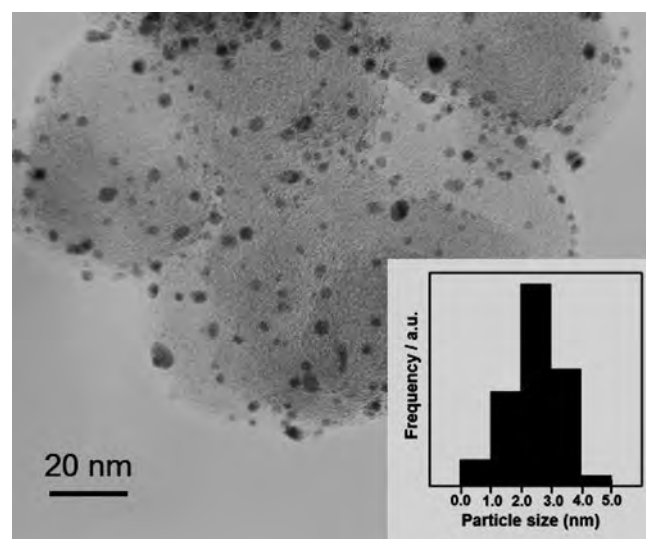


Fig. 3. Low-resolution TEM image of commercially available 20 wt% Pt NPs/CB and its particle size distribution histograms.

converting reaction due to the conversion of nanocrystalline Pt metals to the PtPb intermetallic compound.

Fig. 5 shows low-resolution (LR) and high-resolution (HR) TEM images of Pt_3Pb NPs prepared with the co-reduction reaction, and compositional mapping of Pt and Pb atoms. The average diameters of the Pt_3Pb NPs prepared with the co-reduction reaction were calculated as 4.2 nm. The particle-size distribution is similar to those observed with PtPb and Pt NPs/CB. The HR-TEM image (Fig. 5B) and FFT patterns (inset of Fig. 5C) of the Pt_3Pb NPs prepared using the co-reduction reaction indicate that the NPs are single crystalline. The d lattice spacings of the NPs presented in the HR-TEM image are 0.233 and 0.190 nm, which closely match those of the (1 1 1) and (2 0 0) planes, respectively, for Pt_3Pb ordered intermetallic compounds (0.233 nm for the (1 1 1) plane and 0.190 nm for the (2 0 0) plane). STEM–energy dispersive spectroscopy (EDS) mappings also demonstrated that the average mole ratios of Pt to Pb for Pt_3Pb NPs prepared with the co-reduction reaction were consistent with the desired value for Pt_3Pb , namely, $\text{Pt}:\text{Pb} = 80.3:19.7$.

Fig. 6A and B displays HR-TEM images of the NPs prepared via the co-reduction and converting reactions, respectively, and the corresponding fast Fourier-transform (FFT) patterns obtained from the selected areas are denoted by the dotted squares. The HR-TEM image and FFT patterns of the NPs prepared using the co-reduction reaction indicate that the NPs are single crystalline. The d lattice spacings of the NPs presented in the HR-TEM image are 0.215 and 0.218 nm, which closely match those of the (2 2 0) and (2 0 0) planes, respectively, for PtPb ordered intermetallic compounds (0.216 nm for the (2 2 0) plane, 0.218 nm for the (2 0 0) plane). On the other hand, the HR-TEM image of the NPs prepared via the converting reaction exhibits two crystalline phases in the parts of core and shell of the NPs. The d lattice spacings (0.336 and 0.227 nm) in the core and shell differ from that of the (1 0 0) planes of the Pt_3Pb ordered intermetallic phase (0.406 nm) and the (2 0 0) planes of the PtPb ordered intermetallic phase (0.218 nm), indicating an expansion and contraction of the d lattice spacings in the PtPb shell and Pt_3Pb core. The two FFT images shown in Fig. 6B collected from the core and shell demonstrate that the Pt and Pb atoms were arranged in crystal structures corresponding to structurally modified Pt_3Pb and PtPb ordered intermetallic phases. Fig. 6C and D displays the profiles of the EDS line scans along with

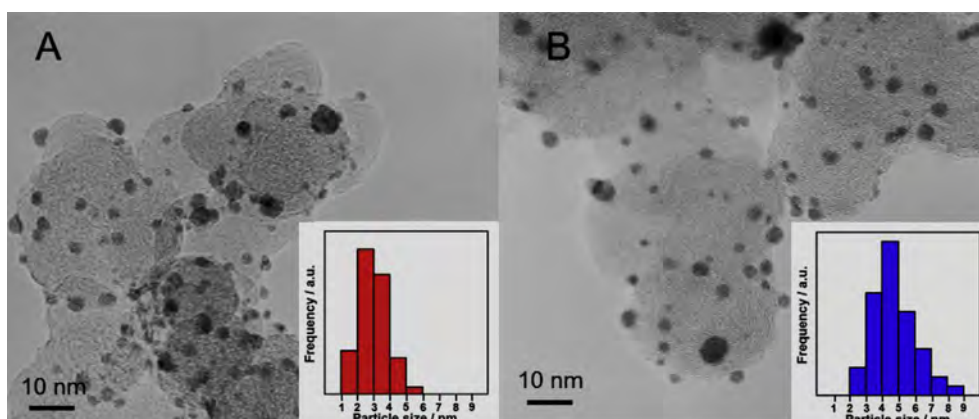


Fig. 4. TEM images of NPs prepared via (A) the co-reduction and (B) the converting reaction synthesis and their particle size distribution histograms.

the lines presented in the insets of figure depicting the two NPs prepared using the co-reduction and converting reaction. When compared with the two line profiles, a Pt-rich core for Pt₃Pb can be clearly observed in the shadowed regions of Fig. 6D. The average mole ratios of Pt to Pb, which were evaluated with STEM–EDS mappings, were consistent with the desired value for PtPb, Pt:Pb = 53.0 ± 3:47.0 ± 3 on any point on the PtPb NPs prepared with the co-reduction reaction. The average mole ratios of Pt to Pb in the PtPb NPs prepared with the converting reaction were Pt:Pb = 70.5:29.5 in the centre of the NPs, as shown in Fig. 6B, and Pt:Pb = 54.2:45.8 on the surface of the NPs. These *p*XRD, HX-PES, TEM/STEM results suggest the formation of Pt₃Pb–PtPb intermetallic compound core–shell NPs, pure PtPb and Pt₃Pb NPs synthesized from the converting reaction and co-reduction reaction methods, respectively. The formation of the Pt₃Pb phase as a core in NPs during the converting reaction can be easily understood by

considering the crystal structure of Pt and Pt₃Pb ordered intermetallic phases. When Pb atoms are formed by the reduction of Pb ions with reducing agents because a small amount of Pb atoms react with an absolutely large amount of Pt atoms in the early stage of the reaction, Pb atoms enter into the fcc type structure of Pt NPs. The stable crystal structure that will be formed in the NPs as a result of Pb atoms entering into Pt NPs might be an ordered intermetallic Pt₃Pb phase having the structure type of Cu₃Au. As the reaction proceeds, the ratio of Pb atoms in the NPs surface gradually increases and the surface structure becomes the hexagonal *P63/mmc* structure of the PtPb ordered intermetallic phase. The core–shell structure composed of Pt₃Pb and PtPt ordered intermetallic phases can be formed by optimizing the composition of the reaction solution containing a Pb precursor, Pt NPs/CB powder, and a reducing agent as well as the reaction temperature and time and the power of the microwave. Naturally, when the rate of Pb reduction is higher

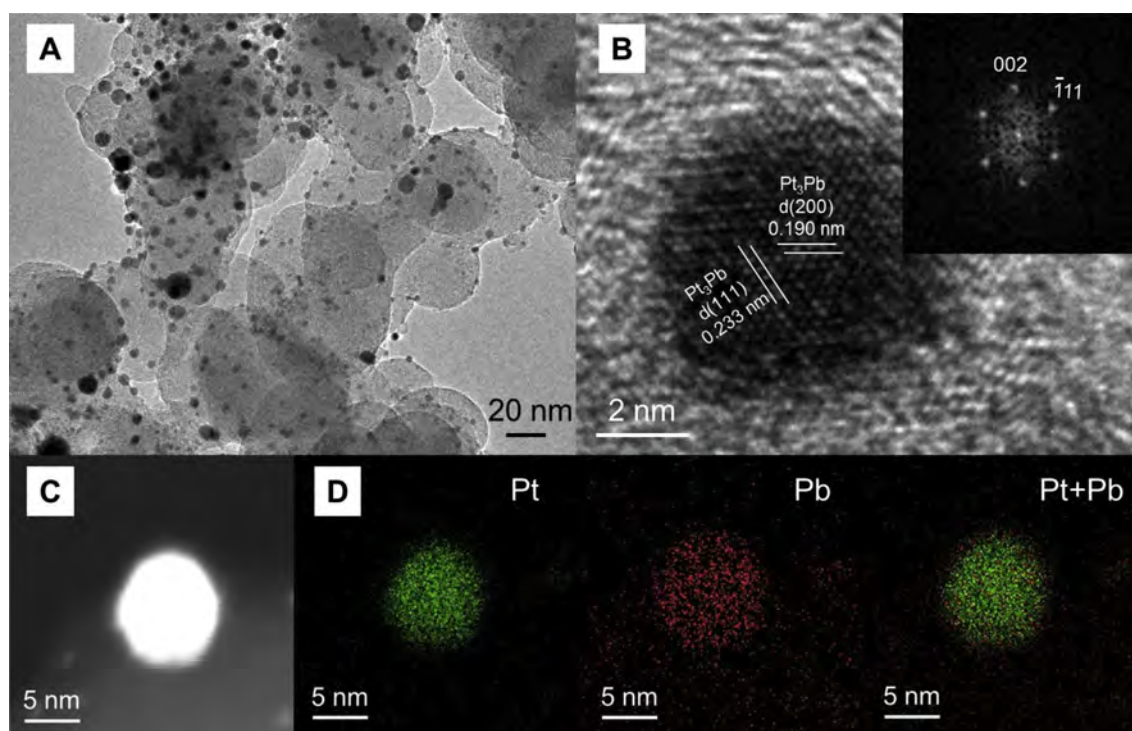


Fig. 5. (A) Low-resolution and (B) high-resolution TEM and (C) STEM and (D) STEM-EDS mapping profile images of CB-supported Pt₃Pb NPs. Inset: FFT pattern obtained from image B.

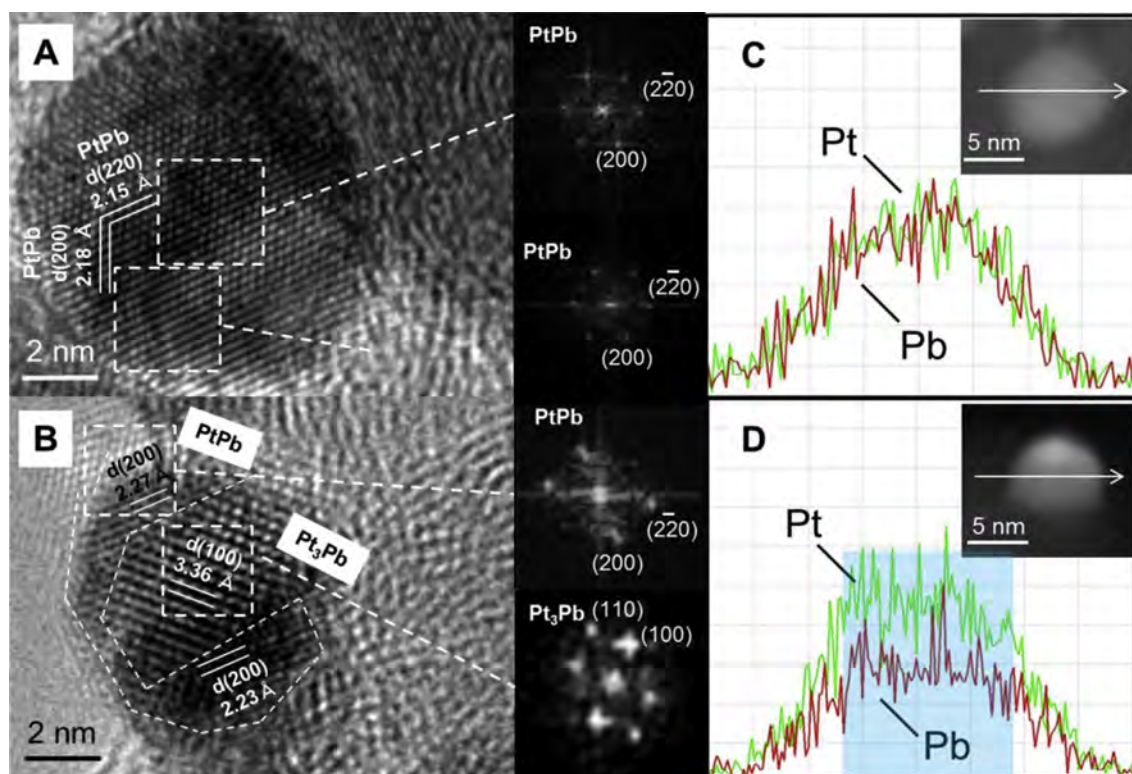


Fig. 6. (A, B) HR-TEM images and (C, D) EDS Pt (green line) and Pb (red line) line profiles of the NPs prepared via (A, C) the co-reduction reaction and (B, D) the converting reaction. The FFT images in (A, B) were collected from the selected areas denoted by the dotted square (For interpretation of the references to color in this figure legend, the reader is referred to the web version of this article.).

than the diffusion rate of Pb atoms into the Pt NPs, the Pb layer is formed on the surface of Pt NPs. It is important to consider the balance of the reduction rate of Pb ions on the NP surfaces and the diffusion rate of Pb atoms into the NPs. The core–shell structure of Pt₃Pb and PtPb ordered intermetallic phases, which were prepared with care and over several trials to find the appropriate conditions, was examined to enhance the electrocatalytic activities of MeOH and EtOH oxidations. ICP-MS measurements revealed that the weight percentages of Pt in PtPb NPs/CB, Pt₃Pb NPs/CB, and Pt₃Pb–PtPb NPs/CB were 12.8, 18.3, and 20.0 wt%, respectively.

Fig. 7A represents the linear sweep voltammograms (LSVs) for the FA oxidation on Pt NPs/CB-, pure PtPb NPs/CB-, intermetallic Pt₃Pb–PtPb core–shell NPs/CB-, and pure Pt₃Pb NPs/CB-immobilized glassy carbon (GC) electrodes in a 0.5 M FA aqueous solution containing 0.1 M H₂SO₄. The oxidation currents were normalized to the weight of the Pt atoms immobilized on the GC electrodes and are presented as the mass activity (MA) in mA μg⁻¹. The Pt₃Pb NPs/CB exhibited the highest mass activity towards FA oxidation in acidic media among the four examined NPs/CB samples. The FA oxidation activities can be ranked as: Pt NPs/CB < Pt₃Pb–PtPb NPs/CB < pure PtPb NPs/CB < Pt₃Pb NPs/CB. Murray et al. have reported the electrocatalytic activity for FA oxidation on Pt₃Pb NPs (average particle size: 3.7 nm)/CB in 0.5 M FA and 0.1 M H₂SO₄ at a potential scan rate of 20 mV s⁻¹ and found that the mass activity at 0.3 V (vs. NHE) was 0.375 mA μg_{-Pt}. Our pure Pt₃Pb NPs exhibited a higher mass activity (0.52 mA μg_{-Pt} at 0.3 V (vs. NHE)) than one reported by Murray et al. in the FA oxidation [20]. Therefore, our higher activity Pt₃Pb NPs were used to compare the electrocatalytic activities for MeOH and EtOH oxidation in alkaline media. In addition, Guo et al. synthesized Pt(core)–PtPb(shell) NPs on CB with a two-step microwave-assisted polyol process, such as the process that we used to prepare

Pt₃Pb–PtPb NPs, and reported that the Pt–PtPb NPs exhibited enhanced catalytic activity (0.78 mA μg_{-Pt} at 0.3 V vs. NHE) and durability for FA oxidation. Our Pt₃Pb–PtPb NPs (0.20 mA μg_{-Pt} at 0.3 V vs. NHE) are far lower than their Pt–PtPb NPs in terms of their activity for FA oxidation [21]. However, the alkaline MeOH (Fig. 7B) and EtOH (Fig. 7C) oxidations on pure PtPb, pure Pt₃Pb, and intermetallic Pt₃Pb–PtPb core–shell NPs exhibited different properties: the surfaces of the intermetallic Pt₃Pb–PtPb core–shell NPs largely enhance the MeOH and EtOH oxidations. In particular, the EtOH oxidation current substantially exceeded the MeOH oxidation current. Commercially available CB-supported Pt–Ru alloy and Pd catalysts that have been recognized as anode catalysts [22–24] were also tested in the MeOH and EtOH oxidations in alkaline solutions for comparison. The oxidation activities of the Pt–Ru alloy and Pd NPs/CB are clearly lower than those of the Pt₃Pb–PtPb NPs/CB. As shown in Fig. 4, the average particle sizes of the NPs are significantly different from those produced by co-reduction and those produced by the converting reaction, with the former being smaller. The difference in the surface areas of the NPs exposed to the test solutions should also be taken into account for the comparison of their catalytic activity. The comparison of catalytic activities should be evaluated with NPs that have the same surface areas or should be compared using specific activities calculated with surface areas. However, as observed in the results of Fig. 4, the converting reaction-synthesized Pt₃Pb–PtPb NPs that have a smaller surface area (and larger particle size) exhibit higher catalytic activity. This difference in activity between NPs prepared with the co-reduction and converting reactions clearly indicates that if the specific catalytic activities were calculated with the surface areas of the NPs, a much larger difference in the catalytic activity will be evaluated between pure PtPb and Pt₃Pb–PtPb NPs. The Pt₃Pb–PtPb NPs will exhibit higher activities than that of pure PtPb

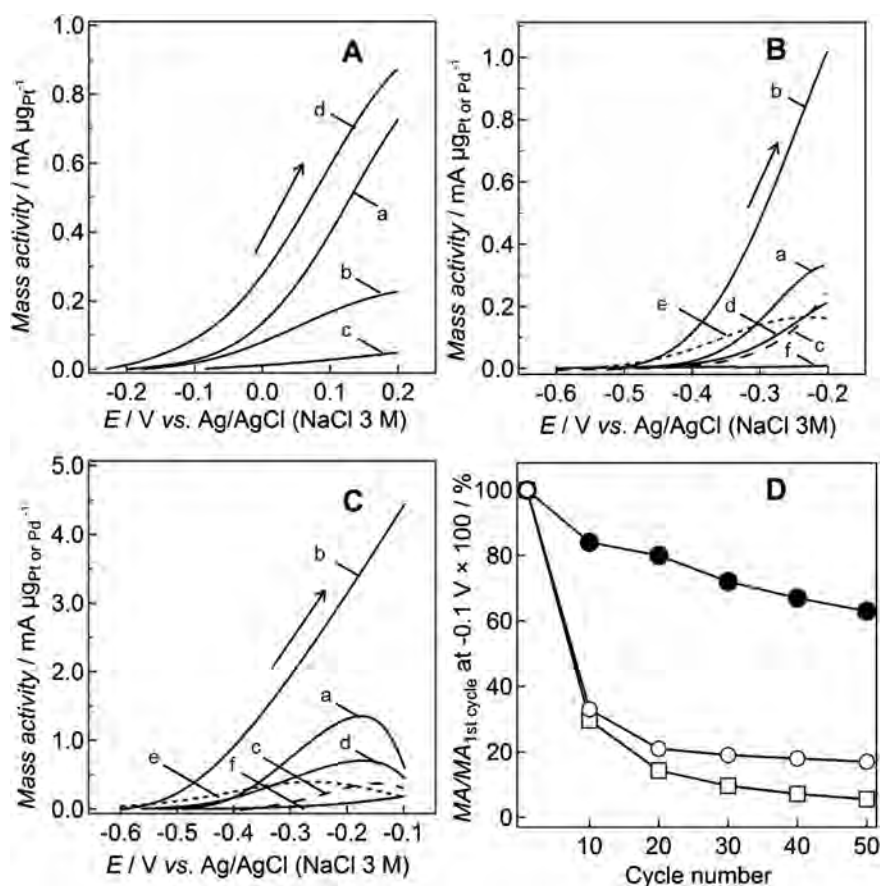


Fig. 7. LSVs obtained in (A) 0.5 M FA + 0.1 M H_2SO_4 , (B) 0.5 M MeOH + 0.1 M KOH, and (C) 0.5 M EtOH + 0.1 M KOH aqueous solutions with (a) co-reduction reaction-synthesized PtPb NPs/CB, (b) converting reaction-synthesized PtPb NPs/CB, (c) Pt NPs/CB, (d) Pt_3Pb NPs/CB, (e) Pt–Ru alloy NPs/CB and (f) Pd NPs/CB-fixed GC electrodes at a scan rate of 10 mV s^{-1} and an electrode rotation speed of 2000 rpm. Panel D represents the dependences of the oxidative mass activity (MA) at -0.1 V (vs. Ag/AgCl (3 M NaCl)) on the cycle number with Pt NPs/CB (\circ), Pt_3Pb –PtPb NPs/CB (\bullet) and pure PtPb NPs/CB (\square).

NPs. As a result of the comparison of our current results with work mentioned above, it can be concluded that Pt_3Pb –PtPb intermetallic core–shell NPs show much higher electrocatalytic activity towards MeOH and EtOH, especially in EtOH oxidation than that of the previously reported results [12,15,16]. Long-term durability of the electrocatalytic activity is critical for real fuel cell applications. The long-term activity and stability of Pt, pure PtPb and Pt_3Pb –PtPb NPs/CB were examined using cyclic voltammetry (CV) with regard

to the EtOH oxidation reaction. The CVs for pure PtPb and Pt_3Pb –PtPb NPs recorded during 10 cycles are shown in Fig. 8. The changes in oxidation current at the Pt NPs, pure PtPb, and Pt_3Pb –PtPb fixed GC electrodes, monitored at -0.1 V for 50 cycles with a rotation rate of 2000 rpm, are summarized in Fig. 7D. For the Pt NPs- (open circles) and pure PtPb NPs-fixed (open squares) electrodes, the oxidation currents dropped during the first several cycles for the EtOH oxidation. The Pt_3Pb –PtPb NPs prepared via the

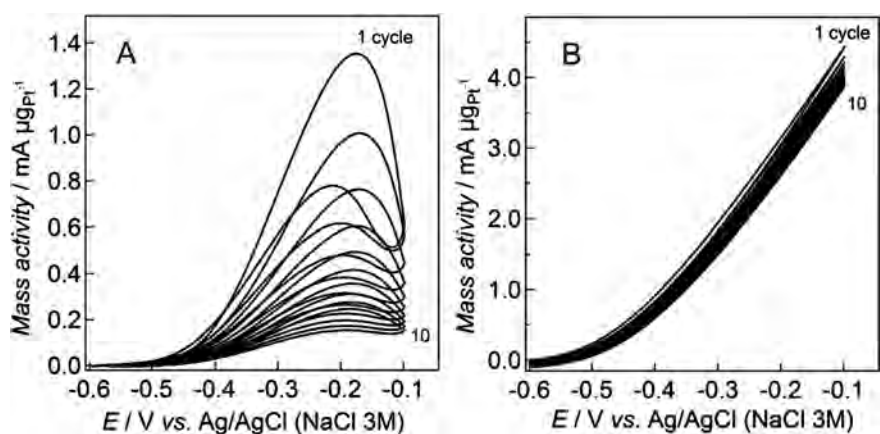


Fig. 8. Cyclic voltammograms for EtOH oxidation with NPs/CB prepared using (A) the co-reduction and (B) the converting reactions in a N_2 -saturated 0.5 M EtOH + 0.1 M KOH aqueous solution at 2000 rpm and 10 mV s^{-1} .

converting reaction method maintained relatively stable oxidation currents of approximately 60% for 50 cycles (solid circles). Accumulation of the intermediate species adsorbed on the Pt sites during the EtOH oxidation results in the currents drop quickly with potential cycling. The surface of Pt₃Pb–PtPb intermetallic core–shell NPs has the catalytic activity to release the Pt active sites for further adsorption of reaction species. In contrast, in the pure PtPb surface, the intermediate species are accumulated on the Pt atoms because its surface does not have ability to remove the intermediate species from the Pt atoms. The origin of the ability to remove the intermediate species will be discussed with the reaction mechanism for EtOH oxidation.

To make clear the difference in the surface structure between pure PtPb and Pt₃Pb–PtPb NPs, CO poisoning tests were performed with Pt₃Pb–PtPb and pure PtPb NPs. Fig. 9 presents the CO stripping voltammograms with Pt NPs/CB, pure PtPb NPs/CB, and Pt₃Pb–PtPb intermetallic core–shell NPs/CB in acidic media. The voltammogram obtained with Pt NPs (Fig. 9A) shows a sharp oxidation stripping peak caused by the oxidation of CO molecules adsorbed on the Pt surfaces at -0.59 V (vs. Ag/AgCl 3 M). The CO stripping CV peak from the Pt₃Pb–PtPb NPs is shifted towards higher potential compared with that of the Pt NPs but to lower potentials when compared to that observed for pure PtPb NPs. The decrease in the charge for the oxidation of adsorbed CO molecules can also be observed with the shift of the stripping peak. Because the charge for the oxidative CO stripping is a measure of the CO tolerance on the NP surface, the decrease in the charge for the oxidative CO stripping on the PtPb and Pt₃Pb–PtPb NPs indicates that the PtPb and Pt₃Pb–PtPb NPs still have a higher CO tolerance than the Pt NPs. Therefore, the order of the FA oxidation activity shown in Fig. 7A is consistent with the degree of the shift of the CO stripping peak. Additionally, in alkaline aqueous solutions, pure PtPb and Pt₃Pb–PtPb NPs exhibited a smaller charge for the CO stripping when compared with Pt NPs. The charge for the oxidation of adsorbed CO on the NP surfaces is the smallest in the Pt₃Pb–PtPb NP surface (Fig. 10). From these CO stripping data, it can be confirmed that the surface structure of Pt, pure PtPb and Pt₃Pb–PtPb NPs is significantly different from each other. The dramatic drop in the quantity of CO adsorbed onto the Pt₃Pb–PtPb intermetallic compound core–shell NP surface is considered to be caused at least in part by a direct consequence of its structure, specifically, the difference between the Pt–Pt distance in pure PtPb and modified PtPb on the Pt₃Pb–PtPb intermetallic core–shell NPs. The increase in the lattice parameters for the (2 0 0) planes of the

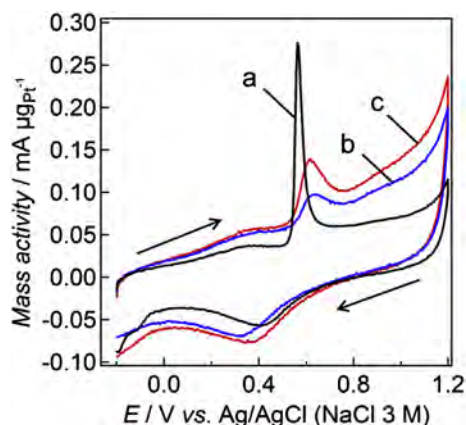


Fig. 9. CO-stripping voltammograms obtained using (a) commercial Pt NPs/CB, (b) pure PtPb NPs/CB, and (c) Pt₃Pb–PtPb NPs/CB in Ar-saturated 0.1 M H₂SO₄ aqueous solution at 2000 rpm and 10 mV s⁻¹.

PtPb shell may prevent the CO from binding to the bridge or three-fold hollow site configurations on the modified PtPb phase in Pt₃Pb–PtPb intermetallic compound core–shell NPs.

As is well known, Pt is the most widely used anode catalyst. However, pure Pt is not efficient catalyst for alcohol oxidation and Pt-based bimetallic alloys with Ru, Rh, Ir, Sn and Sb have been investigated extensively [25–30]. For example, Jin et al. have discussed potential-dependent phase diagrams for surface oxidants of OH_{ads} formation on Pt(1 1 1), Pt(2 1 1) and Sn adatom-modified Pt(1 1 1) and Pt(2 1 1) surfaces for the EtOH oxidation, which have been determined using density functional theory (DFT) calculations and considered that in the presence of Sn, both the OH_{ad} formation and C–C dissociation are more difficult on the Pt(2 1 1) surface, whereas the acetic acid formation is more facile over both Pt(2 1 1) and Pt(1 1 1) surfaces, shifting the production selectivity towards acetic acid. It was concluded that the large increase in the rate observed in their experiment is associated with both the decrease in the activation barriers of C–C dissolution as well as the increased concentration of surface OH_{ads} at low potential on the Pt(1 1 1) surfaces due to the presence of Sn [25]. They calculated the onset potentials of OH_{ad} formation on Pt(1 1 1) and Sn modified Pt(1 1 1) surfaces. Sn modified Pt(1 1 1) surface shifted the onset potential of OH_{ad} formation from 0.59 V (on Pt sites) to 0.23 V (on PtSn sites), indicating that the modification of Pt by Sn can provide OH⁻ adsorption sites at low potentials. Sheng et al. have also found using DFT calculations in the models of transition metals (Ru, Rh, Pd, Os and Ir) alloyed on the top layer of Pt(1 1 1) that the active metals increase the activity of β-dehydrogenation of EtOH but lower the OH_{ad}

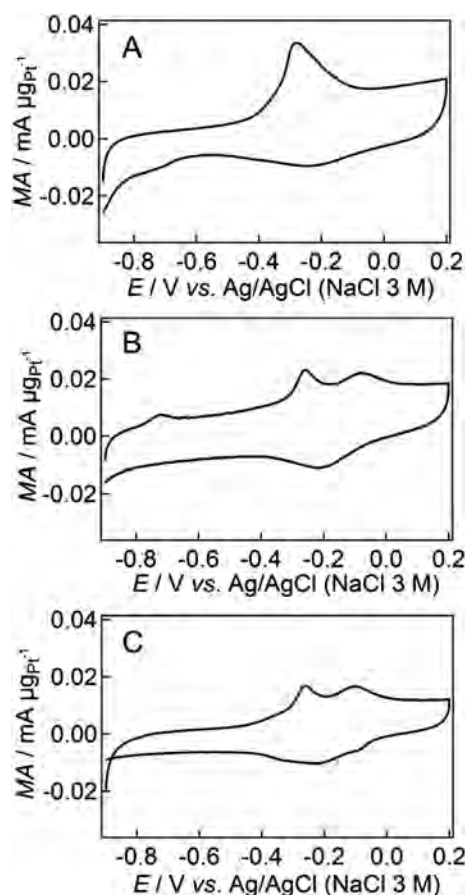
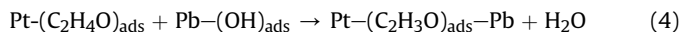
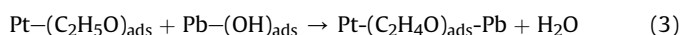


Fig. 10. CO-stripping voltammograms obtained using commercial (a) Pt NPs/CB, (b) pure PtPb NPs/CB, and (c) Pt₃Pb–PtPb NPs/CB in Ar-saturated 0.1 M KOH aqueous solution at 2000 rpm and 10 mV s⁻¹.

formation potential resulting in the active site being deposited with transition metals. By considering both β -dehydrogenation and OH_{ad} formation, the transition metals Ru, Os and Ir are identified to be unsuitable for the promotion of CO_2 selectivity and only Rh is able to increase the selectivity of CO_2 in the EtOH oxidation [31].

The possible EtOH oxidation reaction mechanism in alkaline media might be explained by the following process (Eqs. (1)–(4)) [32,33]. Because the onset potential for CO oxidation on the Pt_3Pb – PtPb intermetallic core–shell NPs is much higher than that for alcohol oxidation, Pt_3Pb – PtPb intermetallic core–shell NP surfaces work more efficiently in the dehydrogenation of the EtOH oxidation. The EtOH dehydrogenation actively continues on the catalyst surface around the onset potential of EtOH oxidation to increase the oxidation current. The OH_{ads} supplied by the solution of OH^- ions are key species that catalyze the EtOH oxidation reaction. OH_{ads} species can be generated on Pb atoms by the discharge of OH^- in alkaline solution. The formation of Pb – OH_{ads} would be accelerated on the surface of the Pt_3Pb – PtPb intermetallic compound core–shell NPs in alkaline media and would contribute to the increase in the oxidation currents of EtOH at lower electrode potential, although some Pt – OH_{ads} species also work in the EtOH oxidation reactions at higher electrode potential. The OH_{ads} species on Pb atoms can react with the intermediate species adsorbed on the Pt sites to release the Pt active sites for further adsorption of reaction species.



It can be considered that Pb atoms in the surface of the Pt_3Pb – PtPb intermetallic compound core–shell NPs associate with both the decrease in the activation barriers of dehydrogenation as well as the increased concentration of surface OH_{ads} at low potential and that the Pb atoms in the Pt_3Pb – PtPb intermetallic compound core–shell NPs work more efficiently in the EtOH dehydrogenation and OH_{ad} formation than other metals.

4. Conclusions

We have successfully synthesized intermetallic Pt_3Pb – PtPb core–shell NPs through a converting reaction in ethylene glycol under microwave irradiation by reacting Pt precursors with Pt NPs to form ordered intermetallic phases of Pt_3Pb and PtPb . The pXRD, HX-PES and TEM/STEM characterizations demonstrated that pure PtPb NPs, pure Pt_3Pb NPs and Pt_3Pb – PtPb intermetallic core–shell NPs could be prepared by conventional co-reduction and converting reaction synthesis methods, respectively, without annealing. The intermetallic Pt_3Pb – PtPb core–shell NPs exhibited higher catalytic activity towards MeOH and EtOH oxidation reactions in an alkaline aqueous solution. The enhanced electrocatalytic activities

and tolerance for CO-poisoning as well as the improved stability of Pt_3Pb – PtPb NPs was validated by comparison with commercial Pt NPs, pure PtPb and Pt_3Pb NPs. The structural modification of the PtPb surface influenced by the Pt_3Pb core on the Pt_3Pb – PtPb NPs produces a considerable improvement of the catalytic performance, such as high and stable oxidation activities of EtOH, which might be due to the enhancement of dehydrogenation of EtOH on Pt atoms and the increase of the concentration of OH_{ad} on Pb atoms.

References

- [1] N.W. Deluca, Y.A. Elabd, J. Polym. Sci., Part B: Polym. Phys. 44 (2006) 2201–2225.
- [2] W. Qian, D.P. Wilkinson, J. Shen, H. Wang, J. Zhang, J. Power Sources 154 (2006) 202–213.
- [3] E. Antolini, J. Power Sources 170 (2007) 1–12.
- [4] A.V. Tripković, K.D. Popović, B.N. Grgur, B. Bliznac, P.N. Ross, N.M. Marković, Electrochim. Acta 47 (2002) 3707–3714.
- [5] J.S. Spendlow, A. Ieckowski, Phys. Chem. Chem. Phys. 9 (2007) 2654–2675.
- [6] A. Verma, S. Basu, J. Power Sources 145 (2005) 282–285.
- [7] F.P. Hu, P.K. Shen, J. Power Sources 173 (2004) 877–881.
- [8] M. Nie, H. Tang, Z. Wei, S.P. Jiang, P.K. Shen, Electrochem. Commun. 9 (2007) 2375–2379.
- [9] E.D. Casado-Rivera, J. Volpe, L. Alden, C. Lind, C. Downie, T. Vázquez-Alvarez, A.C.D. Angelo, F.J. DiSalvo, H.D. Abruña, J. Am. Chem. Soc. 126 (2004) 4043–4049.
- [10] D. Volpe, E.D. Casado-Rivera, L. Alden, C. Lind, K. Hagerdon, C. Downie, C. Korzeniewski, F.J. DiSalvo, H.D. Abruña, J. Electrochem. Soc. 151 (2004) A971–A977.
- [11] F. Matsumoto, C. Roychowdhury, F.J. DiSalvo, H.D. Abruña, J. Electrochem. Soc. 155 (2008) B148–B154.
- [12] F. Matsumoto, Electrochemistry 80 (2012) 132–138.
- [13] J.C. Bauer, X. Chen, Q. Liu, T.-H. Phan, R.E. Schaak, J. Mater. Chem. 18 (2008) 275–282.
- [14] A.J. Jeevagan, T. Gunji, N. Sawano, G. Saravanan, T. Kojima, S. Kaneko, G. Kobayashi, F. Matsumoto, ECS Trans. 58 (2014) 25–31.
- [15] M. Yang, J. Power Sources 229 (2013) 42–47.
- [16] Z. Zhang, L. Xin, K. Sun, W. Li, Int. J. Hydrogen Energy 36 (2011) 12686–12697.
- [17] Z.X. Liang, T.S. Zhao, J.B. Xu, L.D. Zhu, Electrochim. Acta 54 (2009) 2203–2208.
- [18] E. Antolini, Energy Environ. Sci. 2 (2009) 915–931.
- [19] second ed., in: T.B. Massalski (Ed.), Binary Phase Diagrams, Vol. 1, ASM International, Materials Park, OH, 1990.
- [20] Y. Kang, L. Qi, M. Li, R.E. Diaz, D. Su, R.R. Adzic, E. Stach, J. Li, C.B. Murray, ACS Nano 6 (2012) 2818–2825.
- [21] Y. Huang, S. Zheng, X. Lin, L. Su, Y. Guo, Electrochim. Acta 63 (2012) 346–353.
- [22] C. Bianchini, P.K. Shen, Chem. Rev. 109 (2009) 4183–4206.
- [23] V. Bambagioni, C. Bianchini, A. Marchionni, J. Filippi, F. Vizza, J. Teddy, P. Serp, M. Ziani, J. Power Sources 190 (2009) 241–251.
- [24] R.N. Singh, A. Singh, Anindita, Int. J. Hydrogen Energy 34 (2009) 2052–2057.
- [25] J.-M. Jin, T. Sheng, X. Lin, R. Kavanagh, P. Hamer, P. Hu, C. Hardacre, A.M. -Bonastre, J. Sharman, D. Thompsett, W.-F. Lin, Phys. Chem. Chem. Phys. 16 (2014) 9432–9440.
- [26] N. Erini, R. Loukrakpam, V. Petkov, E.A. Baranova, R. Yang, D. Teschner, Y. Huang, S.R. Brankovic, P. Strasser, ACS Catal. 4 (2014) 1859–1867.
- [27] A. Kowal, M. Li, M. Shao, K. Sasaki, M.B. Vukmirovic, J. Zhang, N.S. Marinkovic, P. Liu, A.I. Frenkel, R.R. Adzic, Nat. Mater. 8 (2009) 325–330.
- [28] A.O. Neto, R.R. Dias, M.M. Tusi, M. Linardi, E.V. Spinacé, J. Power Sources 166 (2007) 87–91.
- [29] J. Ribeiro, D.M. dos Anjos, K.B. Kokoh, C. Coutanceau, J.-M. Leger, P. Olivi, A.R. de Andrade, G. Tremiliosi-Filho, Electrochim. Acta 52 (2007) 6997–7006.
- [30] J.M.S. Ayoub, A.N. Geraldes, M.M. Tusi, E.V. Spinace, A.O. Neto, Ionics 17 (2011) 559–564.
- [31] T. Sheng, W.-F. Lin, C. Hardacre, P. Hu, Phys. Chem. Chem. Phys. 16 (2014) 13248–13254.
- [32] R. Manoharan, J. Prabhuram, J. Power Sources 96 (2001) 220–225.
- [33] W. Du, K.E. Mackenzie, D.F. Milano, N.A. Deskins, D. Su, X. Teng, ACS Catal. 2 (2012) 287–297.



Short Communication

Enhanced oxygen reduction reaction on PtPb ordered intermetallic nanoparticle/TiO₂/carbon black in acidic aqueous solutionsTakao Gunji^a, Keisuke Sakai^a, Yukiko Suzuki^a, Shingo Kaneko^b, Toyokazu Tanabe^a, Futoshi Matsumoto^{a,*}^a Department of Material and Life Chemistry, Kanagawa University, 3-27-1, Rokkakubashi, Kanagawa-ku, Yokohama 221-8686, Japan^b Research Institute for Engineering, Kanagawa University, 3-27-1, Rokkakubashi, Yokohama, Kanagawa 221-8686, Japan

ARTICLE INFO

Article history:

Received 30 June 2014

Received in revised form 26 August 2014

Accepted 23 October 2014

Available online 28 October 2014

Keywords:

Oxygen reduction reaction

Electrocatalyst

Ordered intermetallic compound

Catalyst support

ABSTRACT

The electrochemical oxygen reduction reaction (ORR) was accelerated on PtPb ordered intermetallic nanoparticles (NPs) deposited on titanium oxide (TiO₂)/carbon black (CB) and compared with the benchmarked rate on Pt NPs/CB. Immobilization of the PtPb NPs on TiO₂ was a key factor to enhance ORR activity on the PtPb NP surface. The electric interaction between the PtPb NPs and TiO₂ improved the electrocatalytic activity for ORR in a 0.1 M HClO₄ acidic solution.

© 2014 Elsevier B.V. All rights reserved.

1. Introduction

In the research and development of polymer electrolyte fuel cells (PEFCs), one of the challenges is to design better alternatives to the state-of-art Pt catalyst as anode and cathode catalysts in PEFCs, for which high power density has been obtained at room temperature [1]. In particular, the oxygen reduction reaction (ORR) kinetics in the cathode are very slow, even at the surface of the Pt catalyst. Therefore, a large overpotential is required for the ORR to proceed at any practical speed under the operating conditions of PEFCs [2]. To accelerate the ORR kinetics to reach a practical usable level in fuel cells, there has been a strong demand for the development of cathode ORR catalysts that can solve significant cost and durability issues as well as sluggish ORR kinetics. The partial [3,4] or complete [5,6] replacement of Pt metal with other metals has attracted considerable interest due to its potential to reduce the high costs of market batteries and to enhance electrocatalytic activity. Recently, we reported that PtPb/TiO₂ showed substantial electrocatalytic activity for ORR [7]. The nature of the support, the composition of catalytic sites as well as their interaction with the support, and the electronic structure of catalytic sites all most likely influenced the observed electrochemical behavior. Such enhancement of PtPb NPs in the ORR activity was mainly explained as follows: (i) change in the orbital structure of Pt atoms caused by coexisting with Pb atoms, and (ii) change in Pt–Pt interatomic distance by insertion of Pb atoms into the Pt crystal structure. In addition, the enhancement of the catalytic activity, due to the presence of metal

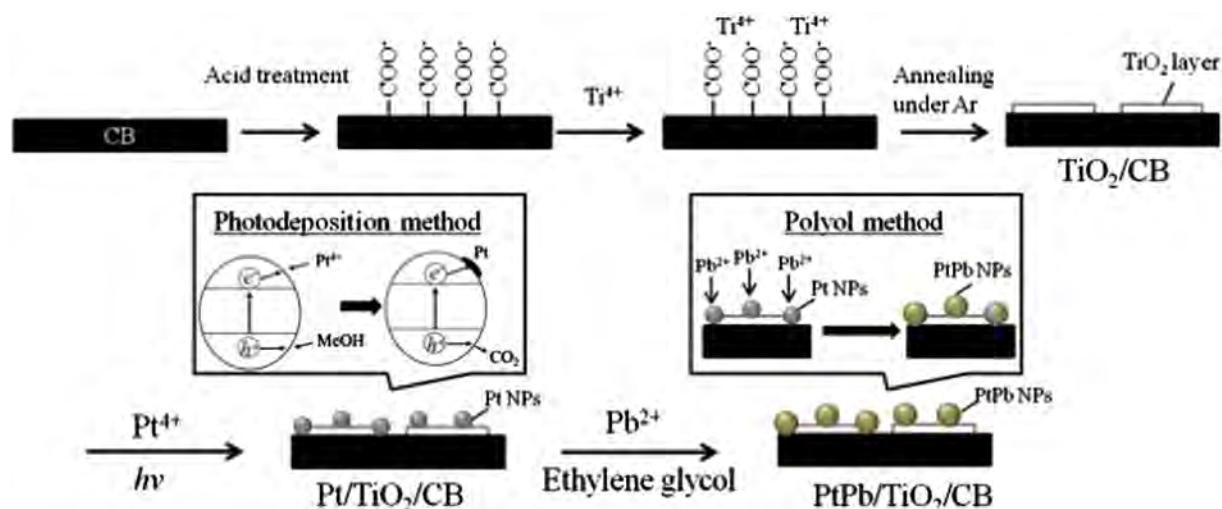
oxide support, is often called strong metal support interactions (SMSI) and significant effort has been devoted to understand this phenomenon [8–10]. SMSI has been reported also in the papers on the enhancement of ORR [11–13]. SMSI is usually explained in terms of partial charge transfer [14] or substrate-induced change in the lattice parameter of the metal deposited [15]. Particularly the change of the electronic properties of the NPs was attributed to overlapping of *d* orbitals (occupied) from deposited metal and the unoccupied *d* orbitals of the support. This PtPb NPs/TiO₂ system can be expected to exhibit the synergistic effect of the inherent electrocatalytic activity of PtPb ordered intermetallic surfaces and the electronic interaction between PtPb NPs and TiO₂ in the enhancement of ORR. However, in our previous study, the voltammograms obtained using a PtPb NPs/TiO₂-fixed glassy carbon (GC) electrode for ORR exhibited a broad shape caused by high electron resistance (IR resistance) because the PtPb nanoparticles (NPs, particle size 3.0 nm) were deposited on high resistivity TiO₂ particles (particle size <25 nm) and because the Pt NPs/TiO₂ was fixed on a GC electrode with carbon black (CB) and Nafion. In this study, PtPb NPs were chemically deposited on small, thin TiO₂ particles that were prepared on CB, to obtain ORR voltammograms that did not show IR resistance. The step-by-step deposition of Pt and Pb intentionally designed for this study achieved the restrictive fixation of PtPb NPs on the small, thin TiO₂ particles.

2. Experimental

Scheme 1 shows a schematic depiction of the step-by-step preparation method of PtPb NPs/TiO₂/CB by annealing under inert gas atmosphere with Ti-alkoxide for TiO₂, photodeposition for Pt NPs and

* Corresponding author. Tel.: +81 45 481 5661; fax: +81 45 413 9770.

E-mail address: fmatsumoto@kanagawa-u.ac.jp (F. Matsumoto).



Scheme 1. Schematic representation of the step-by-step method to prepare ordered intermetallic PtPb NPs/TiO₂/CB.

microwave synthesis to prepare ordered intermetallic PtPb NPs on TiO₂ via the reaction of Pb²⁺ with Pt NPs on TiO₂/CB. A commercial CB (Vulcan-XC72R E-TEK) was treated with an acidic mixture solution of H₂SO₄ (6 M, 95.0%, Wako) and HNO₃ (6 M, 69.0%, Wako) at 90 °C for 12 h to introduce carboxylic acid functional groups on the surface and then washed with water, followed by drying overnight at 110 °C. A Ti precursor solution was prepared by dissolving titanium(IV) isopropoxide (TTIP, 0.1 g, Sigma-Aldrich) in iso-propanol (200 mL, 99.7%, Wako). Functionalized carbon was added to the solution under vigorous stirring. De-ionized water (0.3 mL) was used to accelerate the reaction of TTIP. After further stirring for 60 min, the resulting mixture was collected and dried overnight at 110 °C, followed by heat-treatment at 600 °C for 1 h under Ar atmosphere to yield CB-supported TiO₂ (TiO₂/CB) [16]. Pt NPs were photochemically deposited on TiO₂/CB, as reported by Abe *et al.*, to prepare Pt NPs/TiO₂/CB [17]. The Pb(CH₃COO)₂·3H₂O (0.03 mmol, Sigma-Aldrich) was dissolved in 50 mL of ethylene glycol (99.5%, Kanto Chemical) and then Pt NPs/TiO₂/CB (0.020 g) was added in the solution. The mixture was then sonicated in a bath-type ultrasonicator and treated in the flask with a reflux set for 1 min under 300-W microwave radiation (focused microwave instrument, CEM) to react Pb²⁺ ions with Pt NPs on the TiO₂/CB. The mixture in the flask was cooled to room temperature with water. The mixture was again treated under microwave radiation of 300 W for 5 min. After the mixture cooled, the PtPb NPs/TiO₂/CB was collected via centrifugation, washed sequentially with methanol and dried under vacuum [18]. Powder X-ray diffractometry (pXRD) was performed using CuK_α radiation (Rigaku RINT-UltimaIII; λ = 0.1548 nm) with an increment of 0.02° in a range of diffraction angles from 20 to 80°. X-ray photoelectron spectroscopy (XPS) measurements (JEOL, JP-9010 MC) were performed to examine the chemical states (Pt 4f) of the catalyst. MgK_α was used as the X-ray source for XPS measurements with anodic voltage (10 kV) and current (10 mA). All XPS spectra of the samples were obtained with a take-off angle of 45° with respect to the specimens by using the pass energies of 100 eV and 200 eV for narrow and survey scans, respectively. A 200 kV transmission electron microscope (TEM and/or STEM, JEM-2100F, JEOL) equipped with two aberration correctors (CEOS GmbH) for the image- and probe-forming lens systems and an X-ray energy-dispersive spectrometer (JED-2300T, JEOL) for compositional analysis was used.

An aliquot of 1 mg PtPb NPs/TiO₂/CB was suspended in a solution of 995 μL of distilled water and 250 μL of isopropyl alcohol. Additionally, 5 μL of a 5% w/w Nafion® solution (EW: 1100, Aldrich) in alcohol was added to this suspension. The resulting suspension was sonicated for 1 h. The suspension was coated onto a 5-mm-diameter GC electrode. The ORR activities of PtPb NPs/TiO₂/CB, Pt NPs/TiO₂/CB, PtPb NPs/CB

and Pt NPs/CB were subsequently examined in O₂-saturated 0.1 M HClO₄ using a three-electrode cell with an Ag/AgCl (3 M NaCl) reference electrode and a salt bridge of NaClO₄. The electrochemical tests were performed at room temperature (23 ± 1 °C), at a sweep rate of 10 mV s⁻¹ and a rotation speed of 2000 rpm. The geometric area of the GC electrode was used to calculate the current density of ORR. The electrode potential measured with the Ag/AgCl reference electrode was converted to the value referred to reversible hydrogen electrode (RHE) in voltammograms.

3. Results and discussion

Fig. 1 shows pXRD patterns of TiO₂ (a), TiO₂/CB (b), CB (c), commercially available 10 wt.% Pt NPs/CB (d), synthesized Pt NPs/TiO₂/CB (e), PtPb NPs/CB (f) and PtPb NPs/TiO₂/CB (g). The pXRD pattern (a) was obtained using TiO₂ powder (*anatase*, particle size <25 nm, 99.7 %) purchased from Sigma Aldrich. The sample (b) prepared by annealing Ti precursor adsorbed on CB shows broad peaks that match well to the pattern observed in the TiO₂ powder (a), indicating the formation of TiO₂ on CB. Simulated pXRD patterns for the FCC-type Pt phase (*Fm-3m*, *a* = 0.3925 nm, JCPDS 04-0802) and PtPb phase (*hexagonal*,

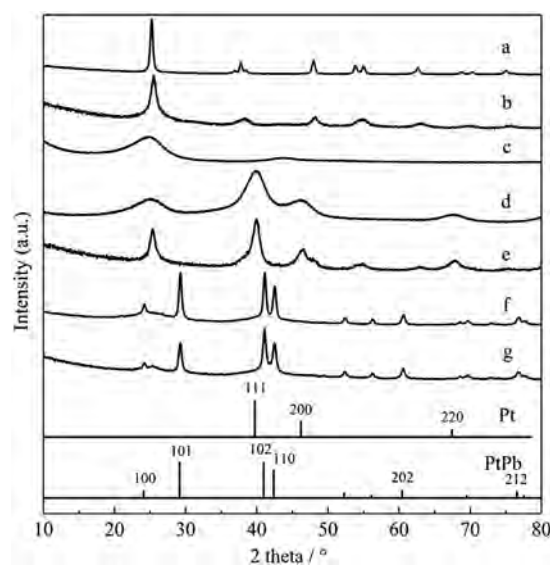


Fig. 1. The pXRD profiles of (a) TiO₂, (b) TiO₂/CB, (c) carbon black, (d) commercially available 10 wt.% Pt NPs/CB, (e) Pt NPs/TiO₂/CB, (f) PtPb NPs/CB and (g) PtPb NPs/TiO₂/CB.

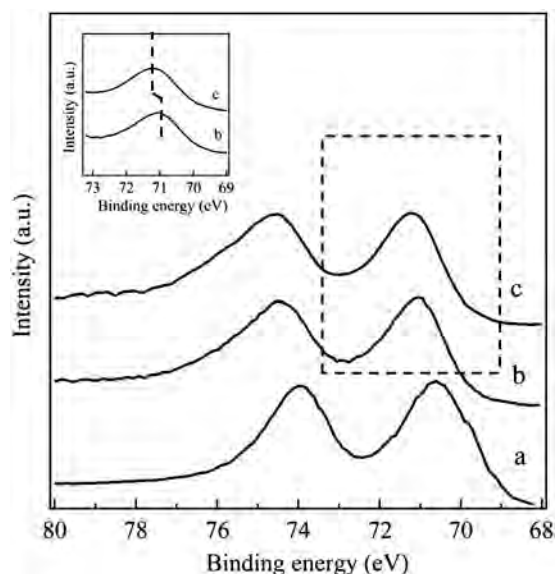


Fig. 2. XPS analysis (4f) of (a) Pt NPs/CB, (b) PtPb NPs/CB, and (c) PtPb NPs/TiO₂/CB.

space group $P6_3/mmc$, $a = b = 0.426$ nm, $c = 0.548$ nm, ICDD PDF File # 06-0374) are indicated by solid bars in Fig. 1 [19]. The *p*XRD patterns (c) for CB show two intense peaks at 25.0° and 43.5° in 2θ , corresponding to the 002- and 101 reflections of carbon. In the *p*XRD patterns (d–g) of all samples prepared with CB, the two intense peaks overlap with the peaks assigned to the reflections of PtPb ordered intermetallic or Pt phases. Commercially available Pt NPs on CB show two broad peaks (d) corresponding to the 111- and 200 reflections of Pt phase. An average Pt crystal domain size of 4.6 nm can be calculated from the Scherer equation. As observed from the comparison of full width at half maximum of the *p*XRD peaks (e), the Pt NPs formed on TiO₂/CB have a larger domain size than the commercially available Pt NPs on CB. The patterns (f) and (g) of the samples prepared by reacting Pb²⁺ ions to Pt NPs on CB or TiO₂ show peak patterns that can be indexed to the hexagonal

type of PtPb ordered intermetallic structure, including the characteristic peaks for the PtPb ordered intermetallic phase, which distinguish the PtPb ordered intermetallic phase from the Pt fcc structure, which can be observed from 50 to 80° in both profiles (f) and (g). Based on the comparison of the particle sizes among the samples with full width at half maximum of the *p*XRD peaks, the PtPb NPs formed with photodeposited Pt/TiO₂/CB and Pb²⁺ ions have larger crystal domain sizes than Pt NPs on TiO₂/CB and CB. The particle size of Pt and PtPb deposited CB and TiO₂ can be ranked as: PtPb/TiO₂/CB > Pt/TiO₂/CB > commercially available Pt/CB.

Fig. 2 shows the XPS results in the Pt 4f region for reference Pt NPs/CB (a), PtPb NPs/CB (b) and PtPb NPs/TiO₂/CB (c). The Pt 4f_{7,2} peak for the PtPb NPs on CB was +0.35 eV higher in binding energy compared with the corresponding peak for Pt NPs on CB, indicating that the average atomic environment around Pt atoms in the sample prepared on CB was changed by reacting the Pt atoms with Pb atoms. That is, the change can be understood with the electron donation from Pt to Pb due to the difference in electron negativity. The difference in the binding energy for the Pt 4f_{7,2} peak between the PtPb NPs prepared on TiO₂/CB and CB is much smaller +0.15 eV than the value of observed between PtPb NPs/CB and Pt NPs. This difference is due to the interaction between PtPb NPs and TiO₂, that is, Pt atoms in PtPb were also influenced by the TiO₂ support as well as the Pb atoms surrounding a Pt atom in the ordered intermetallic phase of PtPb. The electronic interaction between Pt and metal oxide support, which shifts to the higher binding energies with respect to those for the Pt NPs, has been already reported by Horsley [20], Chen [21,22] and Ohsaka [23] although Pt 4f down-shift due to the interaction between Pt and metal oxide has been also reported [24–26]. They have proposed the electronic interaction between Pt and metal oxide via the bridging by O atoms which forms metal–O–Pt bonds. Therefore, on the basis of their results, we can also propose the electronic interaction between Pt and TiO₂ via the Ti–O–Pt bridging.

To confirm NP distribution and that Pt NPs were certainly formed on TiO₂, a STEM image and its compositional mappings (Fig. 3) were obtained using Pt/TiO₂/CB. White spots in the STEM image correspond to Pt NPs. The NPs were heterogeneously dispersed on the surfaces. Green and red, indicating the existence of Pt and Ti atoms, respectively,

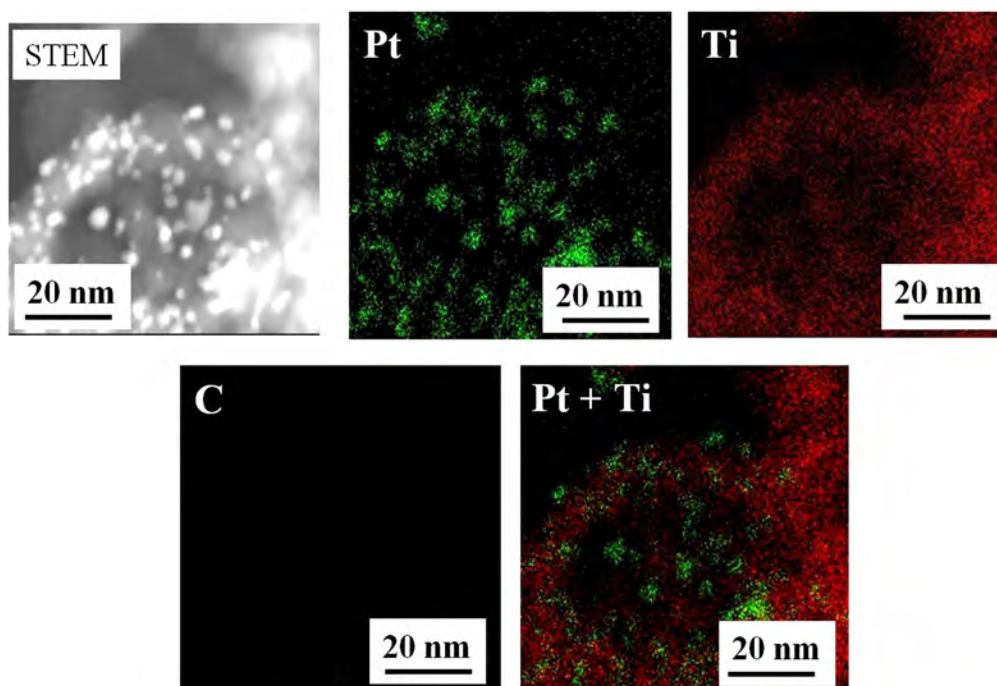


Fig. 3. Scanning transmission electron microscope (STEM) images of Pt NPs/TiO₂/CB and the corresponding compositional mapping images. (For interpretation of the references to color in this figure legend, the reader is referred to the web version of this article.)

always overlap in the compositional mappings obtained from the deposition of Pt NPs on the TiO_2 . Fig. 4 shows a high-resolution STEM image and its compositional mapping of PtPb/ TiO_2 /CB, which was obtained to confirm the composition of Pt and Pb atoms on an ordered intermetallic NP. The atomic ratio of Pt:Pb was fairly consistent with the desired value of a PtPb ordered intermetallic phase, $61 \pm 2:39 \pm 2.0$. In the mapping image, the Pb atoms could be observed only in PtPb NPs, not on CB surfaces; that is, Pb NPs were not formed on CB in the reaction with microwaves, indicating the selective reaction of Pb^{2+} ions with Pt NPs on the TiO_2 /CB surfaces, as reported by Bauer and us [18,27]. The pXRD and TEM/STEM characterization results clearly indicate that the formation of an ordered intermetallic PtPb phase can be achieved on the TiO_2 fixed on CB.

Fig. 5 shows linear-sweep ORR voltammograms for (a) commercially available 10 wt.% Pt NPs/CB, (b) Pt NPs/ TiO_2 /CB, (c) PtPb NPs/CB and (d) PtPb NPs/ TiO_2 /CB in an oxygen-saturated 0.1 M HClO_4 solution. The element mapping in Fig. 3 indicates Pt particles deposited on both CB and TiO_2 surfaces. However, it is doubtful that the activity of this catalyst originates from only PtPb/ TiO_2 /CB. Therefore, in order to extract the origin of the ORR enhancement, the results obtained with Pt/CB, Pt/ TiO_2 /CB, PtPb/CB and PtPb/ TiO_2 /CB were carefully compared. Here, CB-supported Pt NPs (a) were used as a control. The ORR curve (b) obtained with Pt/ TiO_2 /CB shifts to the positive direction, owing to the interaction between Pt NPs and TiO_2 when compared with Pt/CB. The PtPb NPs also accelerate the ORR even on the CB (c). The samples of PtPb/ TiO_2 /CB were superior in their ORR activity to all of the other samples. The particle size of PtPb ordered intermetallic NPs on TiO_2 is larger than one of Pt NPs on TiO_2 and CB; the Pt NPs fixed on TiO_2 and CB have much larger surface areas exposed to the test solution than one of the PtPb NPs fixed on TiO_2 . Although the surface area of PtPb NPs is smaller than that of the reference Pt catalysts utilized in this work, the surfaces of the ordered intermetallic PtPb NPs work more efficiently for ORR. The synergistic effect of the inherent electrocatalytic activity of PtPb ordered intermetallic surfaces and the electronic interaction [28,29] between PtPb NPs and TiO_2 , which was taken from the XPS results, might produce superior ORR activity. It can be considered that the electronic interaction between Pt and TiO_2 via the Ti–O–Pt bridging as mentioned in the XPS results contributes to the enhancement of ORR with the following two factors. (i) OH adsorbed on the Pt surface in the PtPb NPs is spilled over to the TiO_2 (reduction of the

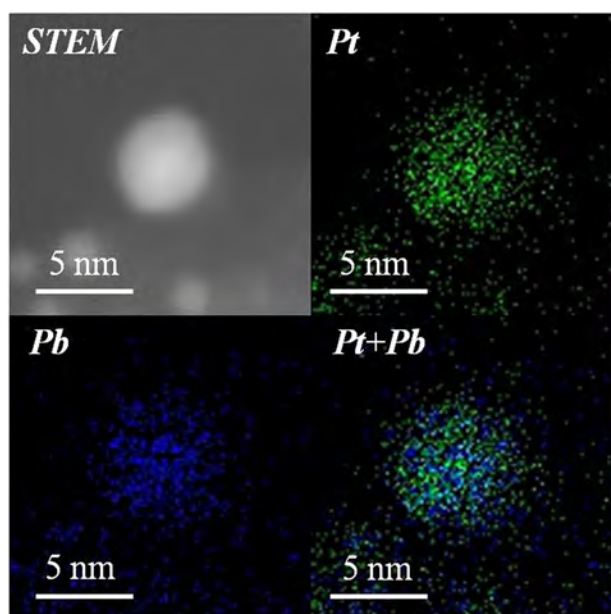


Fig. 4. Scanning transmission electron microscope (STEM) images of PtPb NPs/ TiO_2 /CB and the corresponding compositional mapping images.

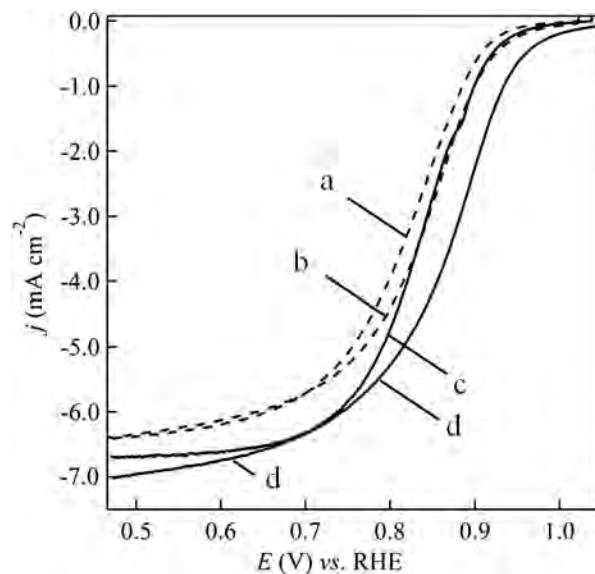


Fig. 5. Linear sweep voltammograms obtained for (a) commercially available 10 wt.% Pt NPs/CB, (b) Pt NPs/ TiO_2 /CB, (c) PtPb NPs/CB and (d) PtPb NPs/ TiO_2 /CB for ORR in O_2 -saturated 0.1 M HClO_4 aqueous solution.

formation of OH on the Pt surface) [23,30] and (ii) the d orbital electron in the Pt atoms is donated to Ti atoms through the bridging Ti–O–Pt bond (d orbital vacancy, resulting in enhanced 2π electron donation from O_2 to the surface of PtPb and back donation of the electrons) [23, 31], both of which facilitate the O_2 adsorption on the Pt surface, that is, the first step of the ORR to produce fast and desirable two H_2O molecules.

4. Conclusions

In this study, the deliberate formation of PtPb on TiO_2 to make the most of electric interaction between PtPb NPs and TiO_2 was successfully achieved. The formation of PtPb NPs on TiO_2 was confirmed with XRD, XPS, TEM and STEM, from the viewpoint of crystallinity, size, the degree of dispersion, and the electronic states of the NPs. The XPS results in the Pt $4f$ region for PtPb NPs/ TiO_2 /CB and PtPb NPs/CB showed the difference in binding energy between Pt atoms in PtPb NPs/ TiO_2 /CB and PtPb NPs/CB. Among the Pt NPs/CB, PtPb NPs/CB, Pt NPs/ TiO_2 /CB and PtPb NPs/ TiO_2 /CB samples, The PtPb NPs/ TiO_2 /CB showed the highest ORR activity. The difference in the electronic state of Pt atoms in the PtPb NPs immobilized on the TiO_2 , which was evaluated from the XPS results, might lead to the acceleration of ORR on the surface of PtPb NPs on TiO_2 /CB in an acidic solution.

Acknowledgment

This work was financially supported by the Strategic Research Base Development Program for Private Universities of the Ministry of Education, Culture, Sports, Science and Technology of Japan.

References

- [1] H.A. Gasteiger, S.S. Kocha, B. Sompalli, F.T. Wagner, *Appl. Catal. B Environ.* 56 (2005) 9–35.
- [2] K. Kinoshita, *Electrochemical Oxygen Technology*, Wiley, New York, 1992.
- [3] J. Kim, Y. Lee, S. Sun, *J. Am. Chem. Soc.* 132 (2010) 4996–4997.
- [4] Y. Kang, C.B. Murray, *J. Am. Chem. Soc.* (2010) 7568–7569.
- [5] Z. Yang, Z. Yao, G. Li, G. Fang, H. Nie, Z. Liu, X. Zhou, X. Chen, S. Huang, *ACS Nano* 6 (2012) 205–211.
- [6] J.L. Fernandez, D.A. Waish, A.J. Bard, *J. Am. Chem. Soc.* 127 (2005) 357–365.
- [7] T. Gunji, G. Saravanan, T. Tanabe, T. Tsuda, M. Miyauchi, G. Kobayashi, H. Abe, F. Matsumoto, *Catal. Sci. Technol.* 4 (2014) 1436–1445.
- [8] N.V. Krstajic, L.M. Vracar, V.R. Radmilovic, S.G. Neophytides, M. Labou, J.M. Jaksic, R. Tunold, P. Falaras, M.M. Jaksic, *Surf. Sci.* 601 (2007) 1949–1966.

- [9] E. Antolini, E.R. Gonzalez, *Solid State Ionics* 180 (2009) 746–763.
- [10] C.-P. Lo, V. Ramani, *ACS Appl. Mater. Interfaces* 4 (2012) 6109–6116.
- [11] V.T.T. Ho, C.-J. Pan, J. Rick, W.-N. Su, B.-J. Hwang, *J. Am. Chem. Soc.* 133 (2011) 11716–11724.
- [12] M. Yang, Z. Cui, F.J. DiSalvo, *Phys. Chem. Chem. Phys.* 15 (2013) 7041–7044.
- [13] N.G. Akalework, C.-J. Pan, W.-N. Su, J. Rick, M.-C. Tsai, J.-F. Lee, J.-M. Lin, L.-D. Tsai, B.-J. Hwang, *J. Mater. Chem.* 22 (2012) 20977–20985.
- [14] X. Liu, M.-H. Liu, Y.-C. Luo, C.-Y. Mou, S.D. Lin, H. Cheng, J.-M. Chen, J.-F. Lee, T.-S. Lin, *J. Am. Chem. Soc.* 134 (2012) 10251–10258.
- [15] L. Timperman, A. Lewera, W. Vogel, N.A. Vante, *Electrochem. Commun.* 12 (2010) 1772–1775.
- [16] S. Beak, D. Jung, K.S. Nahm, P. Kim, *Catal. Lett.* 134 (2010) 288–294.
- [17] R. Abe, H. Takami, N. Murakami, B. Ohtani, *J. Am. Chem. Soc.* 130 (2008) 7780–7781.
- [18] J.C. Bauer, X. Chen, Q. Liu, T.-H. Phan, R.E. Schaak, *J. Mater. Chem.* 18 (2008) 275–282.
- [19] P.L. Villars, L.D. Calvert (Eds.), *Pearson's Handbook of Crystallographic Data for Intermetallic Phases*, vol. 3, American Society for Metals, Metals Park, OH, USA, 1985, p. 3044 (3058, 3059).
- [20] J.A. Horsley, *J. Am. Chem. Soc.* 101 (1979) 2870–2874.
- [21] Y. Chen, J.L.G. Fierro, T. Tanaka, I.E. Wachs, *J. Phys. Chem. B* 107 (2003) 5243–5250.
- [22] Y. Chen, I.E. Wachs, *J. Catal.* 217 (2003) 468–477.
- [23] Z. Awaludin, M. Suzuki, J. Masud, T. Okajima, T. Ohsaka, *J. Phys. Chem. C* 115 (2011) 25557–25567.
- [24] A. Lewear, L. Timperman, A. Roguska, N.A. Vante, *J. Phys. Chem. C* 115 (2011) 20153–20159.
- [25] N. Zhang, S. Zhang, C. Du, Z. Wang, Y. Shao, F. Kong, Y. Lin, G. Yin, *Electrochim. Acta* 117 (2014) 413–419.
- [26] A. Kumar, V. Ramani, *ACS Catal.* 4 (2014) 1516–1525.
- [27] A.J. Jeevagan, T. Gunji, N. Sawano, G. Saravanan, T. Kojima, S. Kaneko, G. Kobayashi, F. Matsumoto, *ECS Trans.* 58 (2014) 25–31.
- [28] A. Bruix, *J. Am. Chem. Soc.* 134 (2012) 8968–8974.
- [29] C.T. Campbell, *Nat. Chem.* 4 (2012) 597–598.
- [30] J.M. Jaksic, D. Labou, G.D. Papakonstantinou, A. Siokou, M.M. Jaksic, *J. Phys. Chem. C* 114 (2010) 18298–18312.
- [31] K. Hyun, J.H. Lee, C.W. Yoon, Y. Kwon, *Int. J. Electrochem. Sci.* 8 (2013) 11752–11767.

Photocatalytic Activity of Pt₃Ti/WO₃ Photocatalyst under Visible-Light Irradiation

Masanari Hashimoto¹, Takao Gunji¹, Arockiam John Jeevagan¹, Toyokazu Tanabe¹,
Takashi Tsuda¹, Shingo Kaneko², Masahiro Miyauchi³ and Futoshi Matsumoto^{*1}

¹*Department of Material and Life Chemistry, Kanagawa University, 3-27-1,
Rokkakubashi, Kanagawa, Yokohama 221-8686, Japan*

²*Research Institute for Engineering, Kanagawa University, 3-27-1, Rokkakubashi,
Kanagawa, Yokohama 221-8686, Japan*

³*Department of Metallurgy and Ceramic Science, Graduate School of Science
and Engineering, Tokyo Institute of Technology, 2-12-1 Ookayama, Meguro,
Tokyo, 152-8552, Japan*

Abstract

We have prepared Pt-Ti nanoparticles (NPs) loaded tungsten oxide (WO₃) composites by hand grinding of WO₃ powder with chemically prepared Pt-Ti NPs. The Pt-Ti/WO₃ composites exhibited higher efficiency for the decomposition of acetic acid (AcOH) and acetaldehyde (AcH) under visible light irradiation ($\lambda > 420$ nm) than that of the composite prepared using WO₃ and the conventional cocatalyst of Pt NPs. The higher photocatalytic activity of the composites could be attributed to the efficient oxidative decomposition of organic compounds and/or reduction of O₂ on the Pt-Ti NPs surface.

Introduction

In recent years, considerable attention has been focused on semiconductor photocatalysis for environmental remediation because it can utilize solar energy to decompose various organic compounds in air^{1,2} and in aqueous systems.^{3,4} Many researchers have focused on the efficient decomposition of environmental organic contaminants under visible light irradiation or under indoor fluorescent light. Tungsten trioxide (WO₃) is a visible-light-responsive photocatalyst with narrow band gap energy and its valence band potential is similar to that of TiO₂. However, the reaction efficiency of the WO₃ is the major bottleneck for practical applications in a photocatalyst research field. When WO₃ is modified with Pt^{3,5,6} nanoparticles (NPs) as cocatalysts, it exhibits a higher photocatalytic activity for the decomposition of organic compounds under visible light irradiation. The cocatalysts serve as an effective candidate to enhance the oxygen reduction reaction (ORR) that occurs on the surface of WO₃. In order to attain such higher reaction efficiency of the photocatalysts, cocatalysts that exhibit a lower overpotential for the redox reaction in an aqueous system have to be immobilized on the photocatalyst surface. Recently, we have found that Pt₃Ti alloy NPs accelerate the electrochemical oxidation of small organic compounds compared with conventional Pt and Pt-Ru.⁷ In addition, other research groups have also been reported that Pt₃Ti alloy exhibits higher ORR activity than that of Pt catalyst.⁸⁻¹⁰ In consideration of these results, Pt₃Ti NPs immobilized on WO₃ can be expected to enhance the photocatalytic activities than that of conventional Pt NPs/WO₃. However, a strong reducing agent should be used in a WO₃ powder-suspended solution containing the Pt and Ti precursors to chemically form Pt₃Ti NPs on the WO₃ surfaces by reducing Ti⁴⁺ ions, which have a considerably

lower standard redox potential. The strong reducing agent is capable of reducing the WO_3 surface. Because the reduced tungsten ions facilitate the recombination of photogenerated carriers, exposing the WO_3 matrices to the reducing agent would decrease the photocatalytic activity. In the present study, at first we have prepared Pt-Ti NPs by chemical reduction method, later the chemically prepared Pt-Ti NPs were thoroughly mixed with WO_3 powder by facile hand grinding for the preparation of Pt-Ti NPs/ WO_3 composite. The photocatalytic activity of the composites formed from Pt-Ti NPs and WO_3 powder and Pt NPs and WO_3 (reference catalyst) photocatalysts were evaluated through the decomposition reaction of acetic acid (AcOH) and acetaldehyde (AcH) under visible light irradiation.

Experimental

Commercially available WO_3 powder was purchased from the Kojundo Chemical Laboratory Co., Ltd. (Type: WWO04PB). Fine particulate WO_3 with a particle size of 50–200 nm was separated from the commercial WO_3 powder, as reported in Ref. 2. The Pt NPs and Pt-Ti NPs were prepared via chemical reduction with metal precursors and a reducing agent. For the Pt-Ti NPs, a precursor solution was prepared by dissolving 0.095 mol of platinum (1,5-cyclooctadiene)dichloride (Strem Chemicals) and 0.36 mmol of titanium(IV) chloride tetrahydrofuran complex (Sigma Aldrich) in 15 mL of tetrahydrofuran (Kanto Chemicals) under a dry Ar atmosphere. Then, the precursor solution was stirred for 30 min under a dry Ar atmosphere. Afterward, 2 mL of a lithium triethylborohydride tetrahydrofuran solution (1.0 mol/L) was transferred into the precursor solution under a completely dry atmosphere. The dark brown solution was stirred overnight to complete the reaction. The solvent was removed by distilling under reduced pressure to afford a dark brown precipitate. The precipitate was then washed with methanol. The obtained powder was stable in air and was black in color. The Pt-Ti NPs were annealed under vacuum at 900°C for 10 h to confirm the compositions of Pt and Ti atoms in the prepared Pt-Ti NPs. Pt NPs were prepared for control experiments using 0.032 mmol of hexachloroplatinate (Wako) and 0.632 mmol of sodium borohydride (Sigma-Aldrich) in methanol (Kanto Chemical) under a dry Ar atmosphere. The preparation of Pt-Ti/ WO_3 photocatalysts is as follows. The cocatalyst powders of the as-prepared Pt-Ti NPs (2 mg) were thoroughly mixed with WO_3 powder (198 mg) by hand grinding to prepared 1.0 wt% composite. The composites were used in the photocatalytic activity tests. The prepared photocatalysts were characterized by powder X-ray diffraction (*p*XRD) and transmission electron microscope (TEM) methods. *p*XRD was performed using CuK_α radiation (Rigaku RINT- Ultima III; $\lambda = 0.1548$ nm). TEM (JEM-2010, JEOL, operated at 200 kV) was used to characterize the morphology of the photocatalysts.

Photocatalytic activity measurements

The photocatalytic decomposition of AcOH in the liquid phase was conducted in a circulation system, in which a suspension of the photocatalyst powder (30 mg) in an aerated aqueous AcOH solution (5 vol%, 50 mL) was continuously stirred using a magnetic stirrer. The components were analyzed by gas chromatography (GC-8A, Shimadzu). The sample was illuminated with a 300 W Xe lamp (PE-300BF, BA-X300ES, Eagle Co. Ltd, Japan) equipped with an optical fiber coupler, a UV cut-off filter (L-42, HOYA Co. Ltd., Japan), with a cold mirror unit (MR5090/CM, Eagle Co., Ltd). The experiments for the photocatalytic activity in the gas phase were performed in a

cylindrical glass air-filled static reactor (500 mL total volume) with a quartz window. An O₂ (20 %)-N₂ gas mixture was adjusted to a relative humidity of 30 % and was used to fill the reaction vessel. The sample was illuminated with a blue LED lamp (LP-3024RA, TKG-3029-6000, Hayashi Tokei-works Co. Ltd.). The catalyst (80 mg) was placed in a circular glass dish and mounted in the reactor. The AcH and CO₂ concentrations were measured using an INNOVA 1412 multi gas monitor.

Results and discussion

Figure 1 shows the *p*XRD profiles of the as-prepared Pt-Ti NPs (a), as-prepared Pt NPs (b), annealed Pt-Ti NPs (c), the composite of the as-prepared Pt-Ti/WO₃ (d) and pure WO₃ powder (e). The as-prepared Pt-Ti and Pt NPs show three broad peaks at approximately 40.5°, 47.5° and 69.3°. The *p*XRD patterns of both photocatalysts were consistent with the *p*XRD peaks simulated for Pt (average Pt and Pt-Ti crystal domain sizes of 7.51 and 4.43 nm, respectively, can be calculated using the Scherer equation). However, from annealing of the as-prepared Pt-Ti NPs, the formation of the Pt₃Ti alloy phase in the as-prepared Pt-Ti NPs was confirmed because the annealed Pt-Ti NPs exhibited characteristic small peaks in the range of 20-34° and 50-60°, which are assigned to the (100), (110), (210) and (211) reflection planes of the ordered Pt₃Ti intermetallic phase with the Cu₃Au-type structure (*Pm-3m*; *a* = 0.3898 nm). The complex peaks in the pattern of the Pt-Ti/WO₃ composite, attributed to monoclinic WO₃ (JCPDS 43-1035), do not change even after hand grinding of the WO₃ powder and as-prepared Pt-Ti NPs. This feature in the XRD data means that the hand grinding does not destroy the crystal structure of monoclinic WO₃.

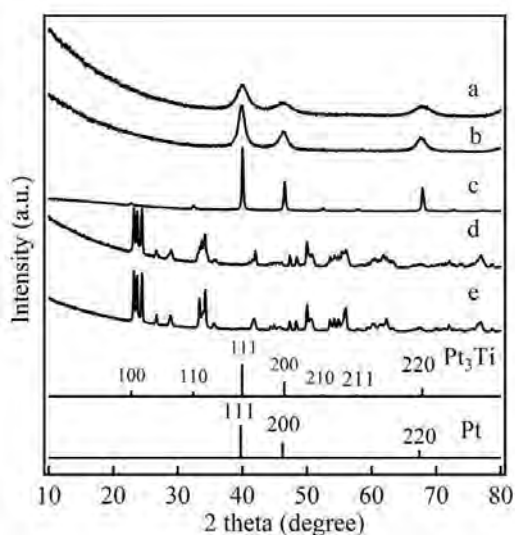


Figure 1. *p*XRD patterns of as-prepared Pt-Ti NPs (a), Pt NPs (b), annealed Pt-Ti NPs (c), and composite of the as-prepared Pt-Ti NPs/WO₃ (d) and pure WO₃ powder (e). The solid bars at the bottom are the simulated *p*XRD peaks for the ordered intermetallic phase of Pt₃Ti and Pt.

Figures 2 (A) and (B) shows the TEM images of Pt-Ti and Pt NPs on WO₃. The TEM images indicate that the average particle diameters of the Pt-Ti NPs and Pt NPs on the WO₃ surface are 8.3 and 11.3 nm, respectively. The particle size of Pt-Ti and Pt NPs

are approximately consistent with the domain size of 3.5 nm that was determined from the *p*XRD data. These results suggest that the Pt-Ti and Pt NPs are heterogeneously dispersed with the same degree on WO₃ even by hand grinding.

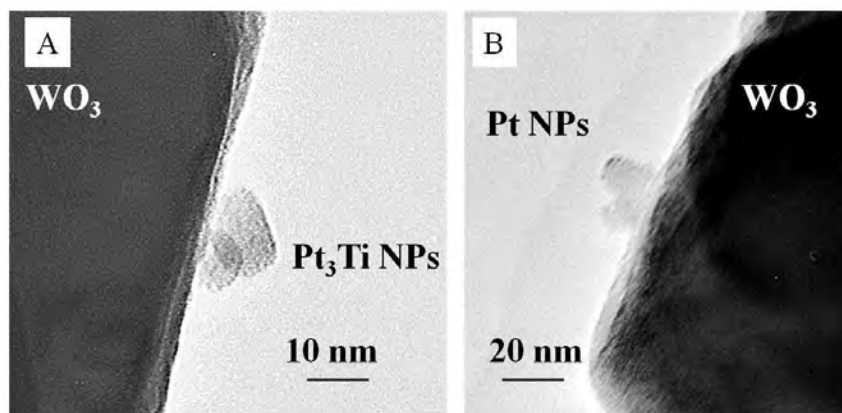


Figure 2. TEM images of Pt-Ti NPs (A) and Pt NPs (B) NPs on WO₃ photocatalysts (NP loading: 1.0 wt%).

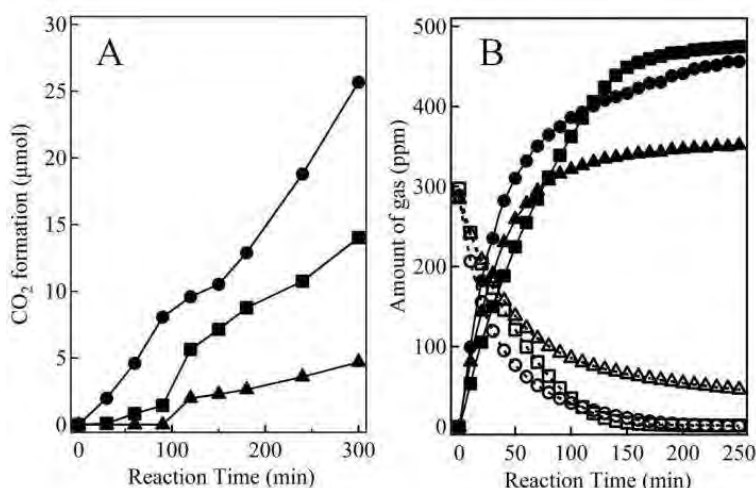


Figure 3. (A) The time courses of CO₂ evolution during the decomposition of AcOH over WO₃ powder (triangles), composite of Pt NPs/WO₃ (squares) and Pt-Ti NPs/WO₃ (circles) in an aqueous AcOH solution in the presence of O₂ under visible light irradiation (20 mWcm⁻²). NP loading: 1.0 wt%. (B) The time courses of the decomposition of AcH (open symbols) and the evolution of CO₂ (solid symbols) in the presence of O₂ under visible light irradiation over WO₃ (triangles), Pt/WO₃ composite (squares), and Pt-Ti NPs/WO₃ composite (circles). NP loading: 0.1 wt%.

The photocatalytic activities of the Pt-Ti NPs/WO₃ and Pt NPs/WO₃ composites were examined through the photocatalytic decomposition of AcOH in aerated aqueous suspensions. Figure 3(A) represents the plot of CO₂ generation during the liquid-phase decomposition of AcOH over the Pt-Ti NPs- and Pt NPs-loaded WO₃. The CO₂ generation rate over the Pt-Ti NPs/WO₃ and Pt NPs/WO₃ photocatalysts were estimated from the slope of the CO₂ formation *vs.* time curve in the time range of 0-300 min. The

CO₂ generation rate over the Pt-Ti NPs/WO₃ (5.132 μmol·h⁻¹) was higher than that over the Pt NPs/WO₃ (2.802 μmol·h⁻¹).

Figure 3(B) represents the AcH decomposition in a gas-phase reaction and the CO₂ generation profiles over the as-prepared Pt-Ti NPs and Pt NPs on WO₃ under visible light irradiation ($\lambda > 420$ nm). With the onset of visible light irradiation, the amounts of AcH in the gas phase over the Pt-Ti NPs/WO₃ and Pt NPs/WO₃ were decreased rapidly together with an increase in CO₂ generation when compared to pure WO₃. The time profiles of the Pt-Ti NPs/WO₃ and Pt NPs/WO₃ photocatalysts show the steady state CO₂ concentration at approximately 250 min, indicating that the successful decomposition of AcH. When the concentration of AcH is high under the initial irradiation time, photocatalytic reaction follows light limited condition and depends on the electron-hole charge separation efficiency.¹¹ In contrast, photocatalysis follows diffusion and adsorption of AcH under the light rich condition. Therefore, we compared the photocatalytic activities in the time range of 0-50 min after the start of light irradiation, and the rate of CO₂ generation over the Pt-Ti NPs/WO₃ (372 ppm·h⁻¹) was observed as the higher value among the other photocatalysts such as Pt NPs/WO₃ composite (310 ppm·h⁻¹) and pure WO₃ (270 ppm·h⁻¹) catalysts.

Conclusion

In the cases of both AcOH decomposition (liquid-phase reaction) and AcH decomposition (gas-phase reaction), the Pt-Ti NPs enhanced the decomposition of organic compounds over WO₃ photocatalysts, as expected based on the previous results of electrocatalytic activities. Although the photocatalytic activity of Pt-Ti NPs/WO₃ is considerably less than that of photodeposited Pt/WO₃,² our photocatalysts can be prepared by a facile mixing process. The comparison of the photocatalytic activities between Pt-Ti NPs/WO₃ and Pt NPs/WO₃ composites suggests the effectiveness of Pt-Ti NPs as a cocatalyst for suppressing the recombination of photoexcited carriers by consuming photoexcited carriers and, as a result, for significantly increasing the photocatalytic efficiency.

Acknowledgement

We thank Dr. Akihiro Yoshida and Prof. Shuichi Naito of Kanagawa University for photocatalytic activity measurements. This work was financially supported by the Strategic Research Base Development Program for Private Universities of the Ministry of Education, Culture, Sports, Science and Technology of Japan. This work was also financially supported by the ACT-C project, JST.

References

1. Z.-G. Zhao and M. Miyauchi, *Angew. Chem.*, **120**, 7159 (2008).
2. X. Chen, Y. Zhou, Q. Liu, Z. Li, J. Liu and Z. Zou, *ACS Appl. Mater. Interfaces*, **4**, 3372 (2012).
3. M. Sadakane, K. Sasaki, H. Kunioku, B. Ohtani, W. Ueda and R. Abe, *Chem. Commun.*, 6552 (2008).
4. D. Tsukamoto, M. Ikeda, Y. Shiraishi, T. Hara, N. Ichikuni, S. Tanaka and T. Hirai, *Chem. Eur. J.*, **17**, 9816(2011).
5. R. Abe, H. Takami, N. Murakami and B. Ohtani, *J. Am. Chem. Soc.*, **130**, 7780 (2008).

6. M. Sadakane, K. Sasaki, H. Kunioku, B. Ohtani, W. Ueda and R. Abe, *Chem. Commun.*, 6552 (2008).
7. R. Abe, K. Shinmei, N. Koumura, K. Hara and B. Ohtani, *J. Am. Chem. Soc.*, **135**, 16872 (2013).
8. H. Abe, F. Matsumoto, L.R. Alden, S. C. Warren, H. D. Abruna and F.J. DiSalvo, *J. Am. Chem. Soc.*, **130**, 5452(2008).
9. M.K. Jeon and P.J. McGinn, *J. Power Sources*, **195**, 2664 (2010).
10. E. Ding, K.L. More and T. He, *J. Power Sources*, 175, 794 (2010).
11. G. Saravanan, T. Hara, H. Yoshikawa, Y. Yamashita, S. Ueda, K. Kobayashi and H. Abe, *Chem. Commun.*, **48**, 7441 (2012).
12. Y. Ohko, D. A. Tryk, K. Hashimoto and A. Fujishima, *J. Phys. Chem. B*, **102**, 2699(1998).

Site-Selective Deposition of Ordered Intermetallic PtPb Nanoparticle Co-catalysts on WO₃ Surfaces to Enhance Photocatalytic Activity

Takao Gunji¹, Takashi Tsuda¹, Arockiam John Jeevagan¹, Masanari Hashimoto¹,
Shingo Kaneko², Toyokazu Tanabe¹, Futoshi Matsumoto¹

¹Department of Material and Life Chemistry, Kanagawa University, 3-27-1,
Rokkakubashi, Kanagawa, Yokohama, Kanagawa 221-8686, Japan

²Research Institute for Engineering, Kanagawa University,
3-27-1, Rokkakubashi, Kanagawa-ku, Yokohama, Kanagawa 221-8686, Japan

Abstract

The site-selective deposition of PtPb nanoparticles (PtPb NPs) on oxidation sites and of Pt NPs on reduction sites as co-catalysts was attempted on tungsten oxide (WO₃) using a photodeposition reaction and the chemical reduction of Pt and Pb precursors for photoexcited electrons and holes to be efficiently consumed without the recombination of photogenerated carriers during the photochemical decomposition of acetic acid (AcOH). The synthesized PtPb/Pt/WO₃ exhibited higher photocatalytic performance for the decomposition of AcOH under visible light irradiation ($\lambda > 420$ nm) than that observed using the conventional photodeposited Pt/WO₃ or chemically deposited PtPb/WO₃. The results of this study highlight the importance of controlling the deposition site for co-catalysts on photocatalyst surfaces.

Introduction

For four decades following the report of the Honda-Fujishima effect,¹ numerous studies on energy conversion and on the oxidative degradation of environmental pollutants using photocatalysts have been reported. One of the primary aims of these studies is determining how to separate photoexcited electrons and holes such that the photogenerated carriers can be efficiently consumed without recombining. The recombination of photoexcited electrons and holes considerably influences the efficiencies of photocatalysts. Immobilization of co-catalysts, such as Pt² and Pd,³ on the surfaces of photocatalysts has been demonstrated to be an effective approach to promote charge separation and transfer, to suppress charge recombination and to consequently enhance the photocatalytic activity. Therefore, the photocatalytic activity can be significantly influenced by the selection of the type of co-catalyst, by the sizes and amounts of co-catalysts and by the loading sites. In this study, in an attempt to improve the catalyst efficiency, we have investigated the loading sites for co-catalysts based on our hypothesis that co-catalysts should be immobilized on the catalyst surfaces where many photoexcited electrons or holes can arrive. Deposits formed through the photodeposition reaction tell us about the site at which photoexcited electrons or holes appear on the photocatalyst surfaces because, during the photodeposition reaction, for example, the photoexcited electrons or holes that appear on the surfaces are used to

deposit Pt and PbO₂ on the sites; Pt is formed by reducing Pt ions with photoexcited electrons, and PbO₂ is formed by oxidizing Pb ions with photoexcited holes.⁴ We have developed a method to site-selectively form functional nanoparticles (NPs) as co-catalysts on the visible-light photocatalyst tungsten oxide (WO₃) using WO₃-photodeposited Pt NPs as starting materials for the site-selective deposition of co-catalysts. PtPb NPs were selected as a co-catalyst to be deposited on the oxidation site in which photoexcited holes are consumed during the photoinduced decomposition of acetic acid (AcOH). PtPb has been reported to exhibit excellent electrocatalytic activities for the oxidation of formic acid, methanol and ethanol in acidic and alkaline solutions.⁵⁻⁹ The PtPb NPs deposited on the oxidation sites are expected to enhance the photocatalytic activity for the decomposition of AcOH by activating the oxidation of AcOH on the co-catalyst surface.

Experimental

1. Preparation of PtPb NPs on the oxidation sites of WO₃

Figure 1 shows a schematic diagram for the preparation of PtPb (oxidation site)/Pb (reduction site)/WO₃. During the first step, the photodeposition of NPs from H₂PtCl₆•6H₂O (0.01 mmol) was performed under visible light ($\lambda > 420$ nm) in a 10 vol% aqueous methanol solution containing WO₃ (500 mg, Kojundo Chemical Laboratory Co. Ltd. (Type: WWO04PB)) for 120 min. After the deposition of Pt NPs on the reduction sites, PbO₂ was photochemically deposited from a 100 ml aqueous solution of lead(II) nitrate (Pb(NO₃)₂) (1.0 mM) under visible light at room temperature using the reduction of protons to hydrogen gas on the reduction sites of the Pt NPs. Finally, the PbO₂/Pt/WO₃ samples (0.20 g) and H₂PtCl₆•6H₂O (5.1 μ mol) were dissolved in 50 ml of ethylene glycol. The mixture was then sonicated in a bath-type ultrasonicator and treated in a flask by refluxing for 2 min under 300-W microwave radiation (focused microwave instrument, CEM). The mixture in the flask was cooled to room temperature with water. The mixture was again treated under 100-W microwave radiation for 5 min. After the mixture was cooled, the PtPb/Pt/WO₃ was collected via centrifugation; washed sequentially with ethanol, acetone and water; and then dried under vacuum. During the microwave reaction, reduction reactions of both PbO₂ to Pb and of Pt⁴⁺ to Pt occur to form PtPb NPs on the WO₃ surfaces. The loading weights of Pt and Pb on the synthesized samples were estimated using inductively coupled plasma-mass spectrometry (ICP-MS, Agilent, 7700x). A transmission electron microscope (TEM, JEM-2010, JEOL) operating at 200 kV was used.

2. Evaluation of the decomposition rate of acetic acid (AcOH) with synthesized samples

The photocatalytic decomposition of AcOH was conducted in a circulation system composed of Pyrex, in which a suspension of the photocatalyst powder (30 mg) in an aerated aqueous AcOH solution (5 vol%, 50 ml) was continuously stirred using a magnetic stirrer. A 300 W Xe lamp was used as the light source. The components were analyzed in the gas phase using a gas chromatograph (GC-8A, Shimadzu) equipped with a 2 m Porapak-Q column, a 2 m molecular sieve 3X column, and a flame ionization detector with Ar as the carrier gas. The sample was illuminated with a 300 W Xe lamp (PE-300BF, BA-X300ES, Hayashi Tokei Works Co., Ltd, Japan) in conjunction with an optical fiber coupler, a UV cut-off filter (L-42, HOYA Co. Ltd., Japan), and a cold mirror

unit (MR5090/CM, Eagle Co., Ltd). A spectro-radiometer (USR-45D, Ushio Co.) was used to measure the visible light intensity, which was adjusted to 20 mWcm^{-2} .

Results and discussion

The photocatalytic activities of the prepared samples of Pt(1)(reduction sites)/WO₃(A), PbO₂(oxidation sites)/Pt(reduction sites)/WO₃(B), PtPb(oxidation sites)/Pt(reduction sites)/WO₃(C), and Pt(2)(reduction sites, Pt loading is equal to one of PtPb/Pt/WO₃)/WO₃(D) were examined in the photocatalytic decomposition of AcOH in aerated aqueous suspensions under visible light irradiation ($\lambda > 420 \text{ nm}$). ICP-MS analysis of the prepared samples demonstrated that the atomic ratio of Pt:Pb was fairly consistent with the desired value, $53 \pm 2.47 \pm 2.0$. In addition, ICP-MS indicated that the weight percentages (wt%) of Pt in Pt(1)/WO₃ and PbO₂/Pt/WO₃ was 0.3 wt% and that the wt% of Pt on PtPb/Pt/WO₃ increased due to the addition of Pt atoms to the oxidation sites to form PtPb NPs; the Pt wt% was 0.6 %. To compare the photocatalytic activity under the same Pt loading on the WO₃, a Pt(2)/WO₃ sample with the same Pt loading on the WO₃ as that on PtPb/Pt/WO₃ was prepared through a photodeposition reaction.

Figure 2 presents the TEM images of (A) Pt(1)/WO₃, (B) Pt(2)/WO₃, (C) PbO₂/Pt/WO₃ and (D) PtPb/Pt/WO₃. In all of the TEM images, the NPs were heterogeneously dispersed on the WO₃ surfaces. The number of Pt NPs increased on the Pt(2)/WO₃ when compared with Pt(1)/WO₃, and the particle size was maintained. The particle size of the PtPb NPs on the PtPb/Pt/WO₃ is larger than that of PbO₂ because of the addition of Pt atoms to the Pb NPs.

Figure 3 presents the plot of CO₂ generation during the liquid-phase decomposition of AcOH over (A) Pt(1)/WO₃, (B) PbO₂/Pt/WO₃, (C) PtPb/Pt/WO₃ and (D) Pt(2)/WO₃. The rates of CO₂ generation over Pt(1)/WO₃, PbO₂/Pt/WO₃, PtPb/Pt/WO₃ and Pt(2)/WO₃ were estimated from the slope of CO₂ formation *vs.* time in the time range of 0-300 min. The CO₂ generation rates were 19.6, 17.6, 13.7, and 10.38 mol·h⁻¹ over Pt(1)/WO₃, PbO₂/Pt/WO₃, PtPb/Pt/WO₃ and Pt(2)/WO₃, respectively. The PtPb/Pt/WO₃ sample exhibited the highest photoinduced decomposition activity for AcOH among the tested samples. This result indicates that the surfaces of the PtPb NPs work more efficiently as a co-catalyst on oxidation sites of WO₃ for the decomposition of AcOH. Consequently, the PtPb/Pt/WO₃ sample exhibited higher activity than did conventional Pt/WO₃. Clear evidence for the dissolution of Pb atoms could not be obtained during analysis of the test solution with ICP-MS after the photocatalytic activity test.

Conclusions

A WO₃ sample in which reduction and oxidation sites were used as areas to deposit functional co-catalysts was prepared as a photocatalyst through a combination of photodeposition and chemical reduction reactions. The synthesized PtPb/Pt/WO₃ exhibited higher photocatalytic activity, as estimated from the rate of CO₂ formation, than the conventional photodeposited Pt NP/WO₃. The results demonstrated that the site-selective deposition of co-catalysts on photocatalyst surfaces is a solution for increasing the reaction efficiency in photocatalytic reactions.

Acknowledgement

We thank Dr. Akihiro Yoshida and Prof. Shuichi Naito of Kanagawa University for photocatalytic activity measurements. This work was financially supported by the

Strategic Research Base Development Program for Private Universities of the Ministry of Education, Culture, Sports, Science and Technology of Japan.

References

1. A. Fujishima, K. Honda, *Nature*, 238, 37 (1972).
2. R. Abe, H. Takami, N. Murakami, B. Ohtani, *J. Am. Chem. Soc.*, 130, 7780 (2008).
3. T. Arai, M. Horiguchi, M. Yanagida, T. Gunji, H. Sugihara, K. Sayama, *Chem. Commun.*, 5567(2008).
4. S. Anandan, M. Miyauchi, *Chem. Commun.*, 48, 4323(2012).
5. H. Abe, F. Matsumoto, L.R. Alden, S. C. Warren, H. D. Abruna, F.J. DiSalvo, *J. Am. Chem. Soc.*, 130, 5452(2008).
6. F. Matsumoto, C. Roychowdhury, F.J. DiSalvo, H.D. Abruña, *J. Electrochem. Soc.*, 155(2), B148 (2008).
7. M.C. Orilall, F. Matsumoto, C. Zhou, H. Sai, H.D. Abruña, F.J. DiSalvo, U. Wiesner, *J. Am. Chem. Soc.*, 131(26), 9389 (2009)
8. L.R. Alden, C. Roychowdhury, F. Matsumoto, D. K. Han, V. B. Zeldovich , H.D. Abruña, F.J. DiSalvo, *Langmuir*, 22, 10465 (2006).
9. F. Matsumoto, *Electrochemistry*, 80(3), 132 (2012).

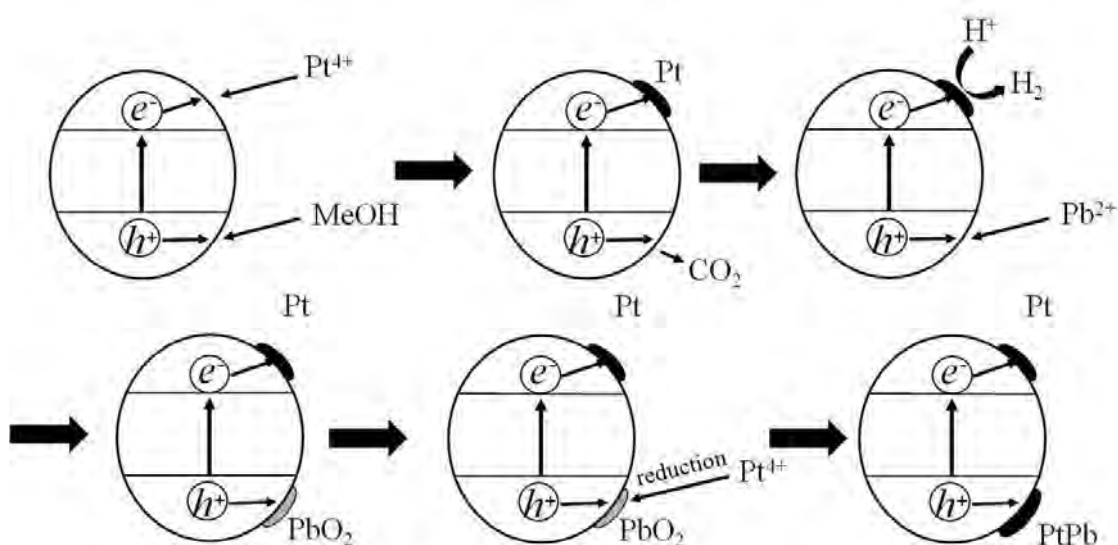


Figure 1. Schematic diagram for the preparation of a PtPb/Pt/WO₃ sample through photodeposition and chemical reduction.

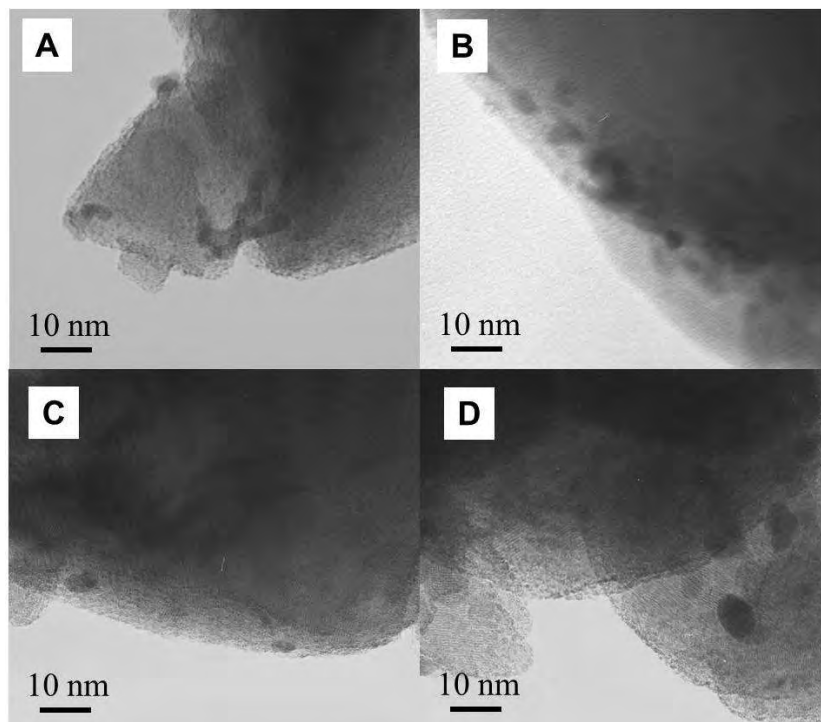


Figure 2. TEM images of (A) Pt(1)/WO₃, (B) Pt(2)/WO₃, (C) PbO₂/Pt/WO₃ and (D) PtPb/Pt/WO₃.

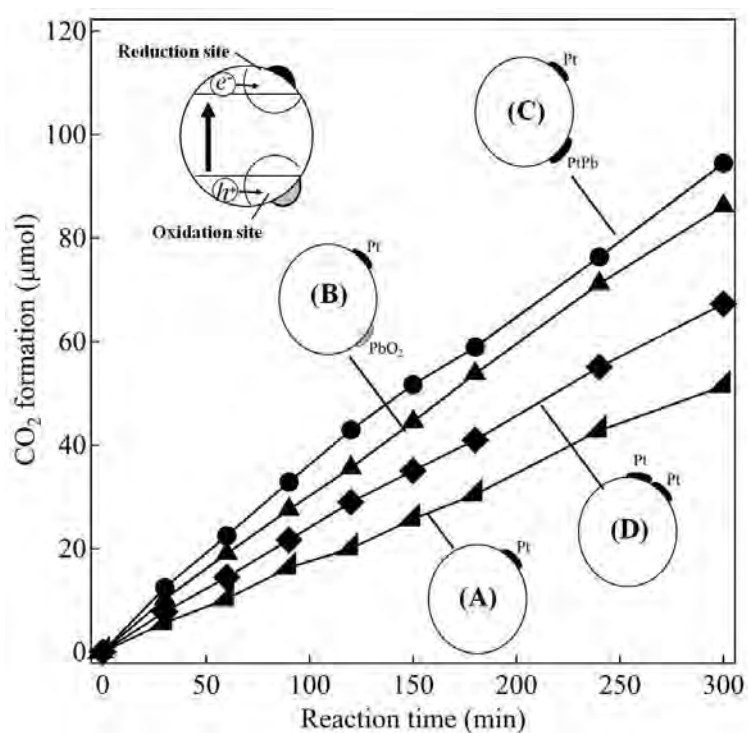


Figure 3. The time courses of the CO₂ evolution during the decomposition of AcOH in an aqueous AcOH solution in the presence of O₂ under visible light irradiation over (A) Pt(1)/WO₃, (B) PbO₂/Pt/WO₃, (C) PtPb/Pt/WO₃ and (D) Pt(2)/WO₃.

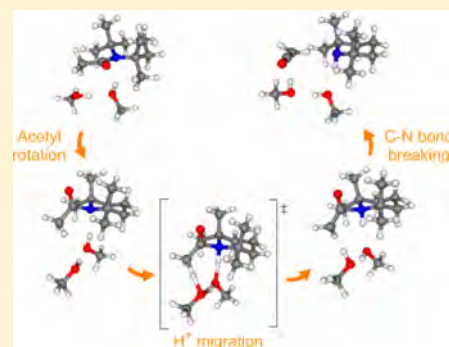
Computational Study of the Effects of Steric Hindrance on Amide Bond Cleavage

Toshiaki Matsubara* and Chikako Ueta

Department of Chemistry, Faculty of Science, Kanagawa University, 2946, Tsuchiya, Hiratsuka, Kanagawa 259-1293, Japan

Supporting Information

ABSTRACT: The reaction mechanism of amide bond cleavages of the 2,2,6,6-tetramethylpiperidine derivatives, which proceeds in methanol solvent under mild conditions, is examined by the density functional method (B3LYP) using a model substrate. We performed the calculations to clarify the reason why the amide bond is readily broken in the present system, on the basis of an experimentally proposed “proton switching pathway” that is different from the generally known mechanisms. As a result, it was found that the stepwise decomposition of the amide bond by the “proton switching pathway” significantly lowers the energy barrier. The delocalization of the π electron in the $-\text{C}(=\text{O})-\text{N}<$ part is hindered by the steric effect of the four Me groups of the piperidine so that the acetyl group can easily rotate around the C—N axis and then the α -H migrates to the amide N. The subsequent amide bond dissociation, which is thought to be a rate-determining step in the experiment, was very facile. The reaction is completed by the addition of methanol to the formed ketene. Both the energy barriers of the α -H migration to the amide N and the methanol addition to ketene are largely decreased by the mediation of methanol solvent molecules. The rate-determining step of the entire reaction was found to be the α -H migration.



INTRODUCTION

Because the delocalization of the π electron of the amide N to the carbonyl group reinforces the amide bond, the amide bond is very strong and cannot be broken easily.^{1–3} For example, a protein with peptide bonds exists stably inside a body and a polyamide, which is a polymer connected by amide bonds, is tough and has a high thermal resistance. Therefore, the breaking of the amide bond is usually performed by an enzyme or under intense conditions with a strong acid or base.^{1,2} However, in recent years, cleavages of the amide bonds of the 2,2,6,6-tetramethylpiperidine derivatives have been achieved in methanol solvent at a low temperature of 18° by Lloyd-Jones, Booker-Milburn, and co-workers.⁴ This methanolysis reaction under mild conditions without an enzyme such as protease in the organism is of great interest in the mechanistic aspects.

The antibiotic penicillin is a representative compound that is decomposed by hydrolysis,^{5–9} although it has an amide bond. Its hydrolysis reaction of the amide bond readily proceeds due to the deformation of the β -lactam ring including the amide bond. Usually, the amide bond has a kind of double bond character due to the delocalization of the π electron in the $-\text{C}(=\text{O})-\text{N}<$ part so that the $-\text{C}(=\text{O})-\text{N}<$ has a planar structure and the rotation around the C—N axis needs a large energy. This is why the amide bond is much stronger than the ester bond that has a similar structure. However, the planarity of the amide in the β -lactam ring of penicillin is largely strained by the next ring. As a result, the sp^2 hybridization of the amide N is transformed to the sp^3 hybridization and the lactam has essentially a “ketonic $\text{C}=\text{O}$ ”. The amide bond, which no

longer has a π bond character, is easily hydrolyzed. Tani et al. have successfully synthesized 2-quinuclidone, which has a unique ring structure of the amide.¹⁰ In this compound, the two planes of $-\text{C}(=\text{O})-$ and $-\text{N}<$, which should be on the same plane, are twisted and almost perpendicular to each other. Distorted amides have also been reported for other compounds.^{11–13} Such a ring structure of an amide is easily opened by the nucleophile- or electrophile-induced cleavage of the amide bond,^{14–20} because the delocalization of the π electron in the $-\text{C}(=\text{O})-\text{N}<$ part is hindered by the distorted structure of amides. The stability of the amide bond is thus significantly affected by the tilt and twist angles, θ and ϕ ,^{14–17} which control the delocalization of the π electron in the $-\text{C}(=\text{O})-\text{N}<$ part, as shown by Scheme 1.

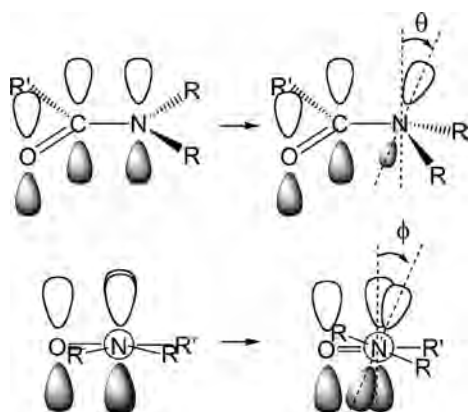
The reaction rate of the methanolysis of the amide reported by Lloyd-Jones, Booker-Milburn, and co-workers also remarkably depends on the structure of the amide.⁴ As presented in Scheme 2, the reaction when the NR_2 group is 2,2,6,6-tetramethylpiperidine (TMP) is, for example, more than 10 000 times faster compared to the reaction in the case of another NR_2 group, $\text{N}(i\text{Pr})_2$. A small deviation of the $-\text{C}(=\text{O})-\text{N}<$ part from planarity is observed in experiment only in the case of TMP. In the cases of other groups, $\text{N}(i\text{Pr})_2$, $\text{N}(\text{Et})t\text{Bu}$, and $\text{N}(i\text{Pr})t\text{Bu}$, the $-\text{C}(=\text{O})-\text{N}<$ part has a typical planar structure. This structural deformation in the case of TMP

Received: May 5, 2014

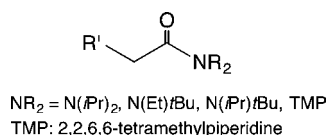
Revised: August 29, 2014

Published: September 11, 2014

Scheme 1



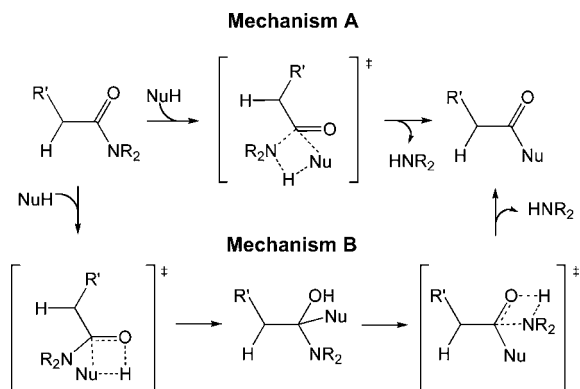
Scheme 2



would cause a steric hindrance to the delocalization of the π electron in the $-\text{C}(=\text{O})-\text{N}<$ part and increase the reactivity of the amide bond.

For the amide bond cleavage of the distorted amide, reaction mechanisms A and B presented in Scheme 3 have been

Scheme 3

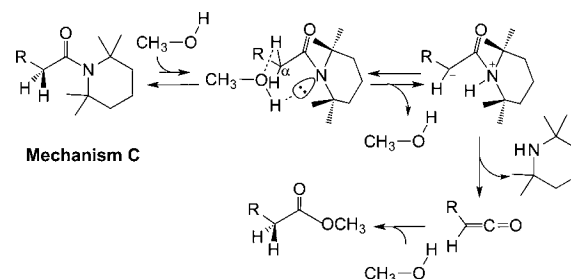


generally proposed on the basis of the computational results.^{21–34} In mechanism A, the O—H bond of the nucleophile methanol adds to the amide bond and the reaction completes by one step via the four-centered transition state. For mechanism A, a large energy barrier is expected, because both the retardation of the delocalization of the π electron in the $-\text{C}(=\text{O})-\text{N}<$ part and the activation of the C—N σ bond have to be accomplished at the same time.²¹ On the other hand, mechanism B is a stepwise reaction consisting of two steps, i.e., the first step of the addition of the methanol O—H to the carbonyl C=O bond and the second step of the migration of the formed —OH hydrogen to the amide N. The energy barrier of the first step would not be low,²¹ because the retardation of the delocalization of the π electron in the $-\text{C}(=\text{O})-\text{N}<$ part in addition to the breaking of the methanol O—H and the carbonyl C=O bonds is required. However, the second step of

the C—N σ bond cleavage, which is accompanied by the proton migration, after the retardation of the π electron delocalization would be relatively facile.

On the other hand, Lloyd-Jones, Booker-Milburn, and co-workers have proposed a new mechanism C (Scheme 4), which

Scheme 4



is completely different from the generally considered mechanisms A and B, for the breaking of the amide bond of 2,2,6,6-tetramethylpiperidine derivatives. In mechanism C, the α -H is thought to migrate to the amide N as a proton at first. After the α -H migration, ketene is formed by the C—N bond cleavage. Finally, the methanol solvent molecule adds to ketene to form the product. A deuterium-labeling experiment using methanol CD_3OD suggests that the methanol solvent molecule mediates the α -H migration. It is therefore predicted that the methanol solvent molecule can come into the space between the α -H and the amide N that is adjusted by the rotation of the acyl group around the C—N axis. The rotation of the acyl group would be facilitated by the steric hindrance of the four Me groups attached to the piperidine ring to the delocalization of the π electron in the $-\text{C}(=\text{O})-\text{N}<$ part, as mentioned above. On the basis of the experimental data, they concluded that the C—N bond cleavage is a rate-determining step whereas the subsequent methanol addition to the highly reactive ketene is facile.

In the present study, we calculated the amide bond cleavage by the methanolysis reported by Lloyd-Jones, Booker-Milburn, and co-workers using 1-acetyl-2,2,6,6-tetramethylpiperidine as a model substrate by the density functional method (B3LYP) to examine whether the new mechanism C is really more favorable than the generally known mechanisms A and B. The surrounding methanol solvent was approximated by the polarized continuum model (PCM). Following the explanation of the computational details, we will first discuss the steric and electronic effects of the four Me groups of the piperidine on the structure of the $-\text{C}(=\text{O})-\text{N}<$ part and the rotation of the acetyl group around the C—N axis, which would significantly affect the amide bond cleavage. In the subsequent sections, mechanisms A, B, and C are discussed in turn. Conclusions are summarized in the final section.

■ COMPUTATIONAL DETAILS

We used two kinds of model molecules, 1-acetyl-2,2,6,6-tetramethylpiperidine and 1-acetylpiperidine, to examine the steric effect of the four Me groups of the piperidine ring by comparing two molecules. The surrounding solvent molecules were approximated by the polarized continuum model (PCM).

All the calculations other than the PCM calculations were performed using the GAUSSIAN03 program package.³⁵ The geometry optimizations were performed by the density

functional theory (DFT) at the B3LYP level, which consists of a hybrid Becke + Hartree–Fock exchange and Lee–Yang–Parr correlation functional with nonlocal corrections.^{36–38} For the basis set, we adopted 6-311++G(d,p) for all the atoms. All equilibrium structures and transition states were identified by the number of imaginary frequencies calculated from the analytical Hessian matrix. The reaction coordinates were followed from the transition state to the reactant and the product by the intrinsic reaction coordinate (IRC) technique.³⁹ The energies of the optimized structures were improved using a higher level basis set aug-cc-pVTZ. The thermal correction, which was calculated at the B3LYP/6-311++G(d,p) level with a scale factor of 0.9614⁴⁰ for calculated vibrational frequencies at the temperature of 298.15 K, was used to calculate the Gibbs free energy at the B3LYP/aug-cc-pVTZ level. The NBO analysis⁴¹ was performed to obtain the atomic charge. The methanol solvent was taken into account by the PCM approximation^{42,43} with the dielectric constant of 32.613 for the methanol medium using the GAUSSIAN 09 program.⁴⁴

We added A, B, and C as suffixes to the labels of the equilibrium and the transition state structures to distinguish three mechanisms, A, B, and C, and M and H to distinguish the substituents of the piperidine ring of the substrate, Me and H, and also added 0, 1, and 2 to distinguish the number of methanol molecules mediating the reaction. The energies relative to the optimized structure of the starting compound 1-acetyl-2,2,6,6-tetramethylpiperidine or 1-acetyl-piperidine are presented throughout.

RESULTS AND DISCUSSION

Substituent Effects in 1-Acetyl-2,2,6,6-tetramethylpiperidine. The optimized structure of 1-acetyl-2,2,6,6-tetramethylpiperidine **1-M0** is displayed in Figure 1. The six-membered

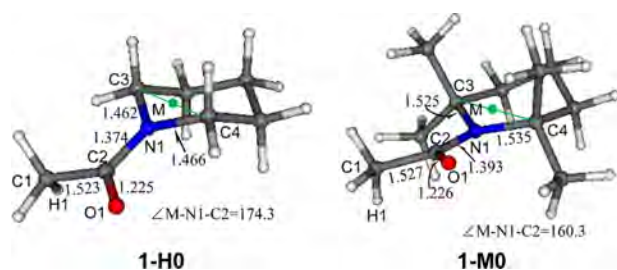


Figure 1. Optimized structures of 1-acetyl-piperidine **1-H0** and 1-acetyl-2,2,6,6-tetramethylpiperidine **1-M0** (Å and degree). M is the middle point of the distance C3—C4.

ring of piperidine takes the energetically stable chair conformation. Here, it should be noted that the angle $\angle C2-N1-M$ is 160.3° , which is about 20° smaller than 180° . This means that the $-C(=O)-N<$ part deviates from the plane and the orbital of the amide N takes the sp^3 hybridization rather than the sp^2 hybridization. The acetyl group also rotates by about 15° around the C2—N1 axis. These features in the structure are attributed to the steric repulsion between the four Me groups of the piperidine and the acetyl group. In fact, when the four Me groups of the piperidine are replaced by the H atoms, the angle $\angle C2-N1-M$ increases to 174.3° , and the hybridization of the amide N returns to the sp^2 (see **1-H0** in Figure 1). Also, the acetyl group rotates a little around the C2—N1 axis.

When we rotate the acetyl group around the C2—N1 axis varying the dihedral angle $\angle O1-C2-N1-C4$, the energy of **1-M0** changed as presented in Figure 2. With the increase in

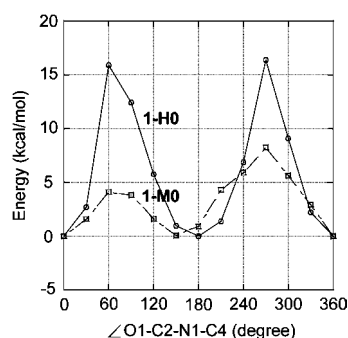


Figure 2. Plots of the energies of **1-M0** (dotted line) and **1-H0** (normal line) versus the dihedral angle $\angle O1-C2-N1-C4$.

the dihedral angle $\angle O1-C2-N1-C4$, the energy of **1-M0** increases and reaches maximum at 60° . By the further increase in the dihedral angle $\angle O1-C2-N1-C4$, the energy of **1-M0** oppositely decreases and takes a minimum at 150° . The energy then again reaches a maximum at 270° and finally takes a minimum at 360° . The rotation energy of the acetyl group was calculated to be 4–8 kcal/mol from this energy change, which is in great agreement with the rotation energy of about 7 kcal/mol⁴⁵ experimentally estimated. Although the energy similarly changed with the dihedral angle $\angle O1-C2-N1-C4$, the rotation energy of the acetyl group was about 16 kcal/mol in the case of **1-H0** without the Me groups of the piperidine, which is 2–4 times larger compared to the case of **1-M0**. This calculated rotation energy for **1-H0** is in good agreement with those calculated previously for the amide with the planar structure.^{46–50} The two maxima at 60° and 270° are due to the loss of the delocalization energy of the π electron, because the two planes of $O1-C2-N1$ and $C2-N1-C4$ are almost perpendicular to each other. Because the delocalization of the π electron is already prevented to some extent at 0° by the sp^3 hybridization of N1 in the case of **1-M0**, the destabilization energy at 60° and 270° is much smaller for **1-M0** than for **1-H0**.

The molecular orbitals concerning the $-C(=O)-N<$ part of **1-H0** with the dihedral angle $\angle O1-C2-N1-C4$ of 0° are displayed as ψ_{29} and ψ_{35} in Figure 3. The π electron delocalizes over the $-C(=O)-N<$ part in ψ_{29} , whereas it localizes at both ends, O1 and N1, in ψ_{35} . These molecular orbitals ψ_{29} and ψ_{35} in **1-H0** correspond to ψ_{50} and ψ_{51} in **1-M0**, respectively. ψ_{51} of **1-M0** is similar to ψ_{35} of **1-H0**, but ψ_{50} of **1-M0**, which is a nonbonding orbital of N1, is different from ψ_{29} of **1-H0**. The orbital of N1 has an sp^3 hybridized character so that we cannot find any delocalization of the π electron over the $-C(=O)-N<$ part in ψ_{50} . The lobe of the orbital of N1 expanding downward will readily join with a proton. On the other hand, when the dihedral angle $\angle O1-C2-N1-C4$ is 90° , the π orbital delocalized over the $-C(=O)-N<$ part is split into the nonbonding orbital on N1 and the localized $C=O$ π orbital in both **1-M0** and **1-H0**, because its delocalization becomes geometrically impossible. However, a hyperconjugation between the $C2-O1$ σ and the $C2-C1$ σ orbitals and the vacant p orbital of N1 exists in **1-M0** as shown by ψ_{30} , which results in the stabilization of the structure with the $\angle O1-C2-N1-C4$

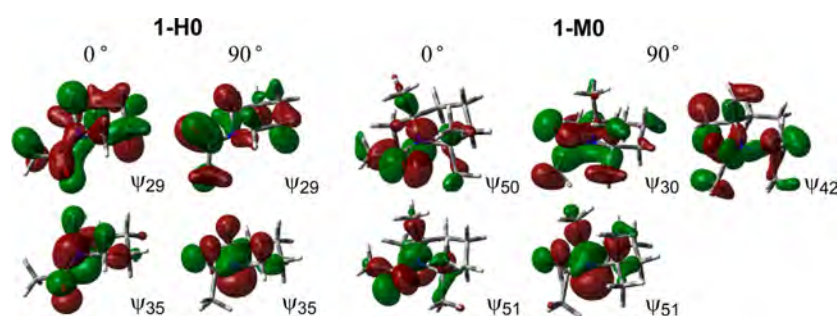


Figure 3. Selected molecular orbitals of **1-H0** and **1-M0** with the dihedral angle $\angle\text{O1-C2-N1-C4}$ of 0° and 90° .

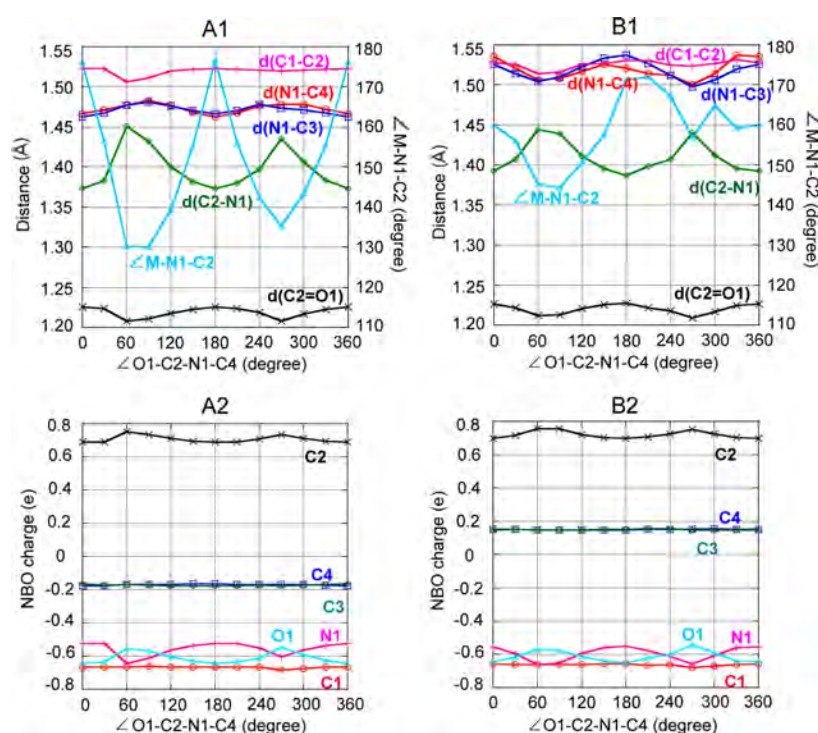


Figure 4. Plots of the geometric parameters (1) and the NBO charges (2) of **1-H0** (A) and **1-M0** (B) versus the dihedral angle $\angle\text{O1-C2-N1-C4}$.

of 90° . Thus, the energy barrier of the rotation of the acetyl group is smaller for **1-M0** than for **1-H0**, because in **1-M0** the sp^3 hybridized orbital of N1 makes the rotation of the acetyl group easy and the hyperconjugation stabilizes the structure with the rotated acetyl group.

The plots of the geometric parameters versus the dihedral angle $\angle\text{O1-C2-N1-C4}$ are presented in Figure 4. It is obvious that the geometric parameters are affected by the retardation of the delocalization of the π electron in the $-\text{C}(=\text{O})-\text{N}<$ part at 60° and 270° . In the case of **1-H0**, the bond distance $d(\text{C2-N1})$ is stretched with the increase in the dihedral angle $\angle\text{O1-C2-N1-C4}$ and takes a maximum at 60° and 270° . In contrast, the distance $d(\text{C2-O1})$ takes a minimum at 60° and 270° . These changes in two distances $d(\text{C2-N1})$ and $d(\text{C2-O1})$ are consistent with the retardation of the π electron delocalization. Here, the magnitude of the change is larger for the $d(\text{C2-N1})$ than for the $d(\text{C2-O1})$, which shows that the $d(\text{C2-N1})$ is more largely affected. The angle $\angle\text{M-N1-C2}$ is also largely affected by the dihedral angle $\angle\text{O1-C2-N1-C4}$. When the

dihedral angle $\angle\text{O1-C2-N1-C4}$ is 60° or 270° , the angle $\angle\text{M-N1-C2}$ decreases to about 130° , because the π electron in the $-\text{C}(=\text{O})-\text{N}<$ part is localized and the orbital hybridization of the N1 atom changes from sp^2 to sp^3 . Both bond distances $d(\text{N1-C3})$ and $d(\text{N1-C4})$ also change with the dihedral angle $\angle\text{O1-C2-N1-C4}$. The fluctuation in the electron density on N1 by the change in the π electron delocalization would affect both σ bonds N1-C3 and N1-C4. On the other hand, the bond distance $d(\text{C1-C2})$ is little affected by the dihedral angle $\angle\text{O1-C2-N1-C4}$.

In the case of **1-M0**, the distance $d(\text{C2-N1})$ is already stretched to about 1.40 \AA even when the dihedral angle $\angle\text{O1-C2-N1-C4}$ is 0° , because the orbital of N1 becomes sp^3 hybridized and the delocalization of the π electron in the $-\text{C}(=\text{O})-\text{N}<$ part is prevented to some degree by the steric repulsion between the four Me groups of the piperidine and the acetyl group, as mentioned above. When the dihedral angle $\angle\text{O1-C2-N1-C4}$ becomes 60° or 270° by the rotation of the acetyl group and then the delocalization of the π electron in the $-\text{C}(=\text{O})-\text{N}<$ part is completely prevented, the distance

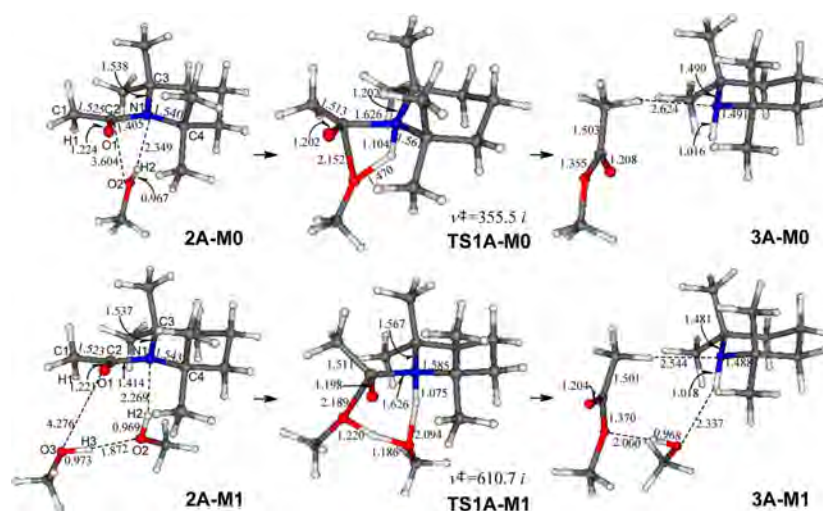


Figure 5. Optimized equilibrium and transition state structures (Å) involved in mechanism A with and without the mediation of a methanol solvent molecule at the B3LYP/6-311++G(d,p) level. The imaginary frequencies (cm^{-1}) are also presented together for the transition states.

$d(\text{C}2-\text{N}1)$ is elongated to about 1.45 Å as in the case of **1-HO**. The distance $d(\text{C}2-\text{O}1)$ also changes with the dihedral angle $\angle\text{O}1-\text{C}2-\text{N}1-\text{C}4$, the increase and the decrease being opposite to the case of the distance $d(\text{C}2-\text{N}1)$. These changes in the two distances $d(\text{C}2-\text{N}1)$ and $d(\text{C}2-\text{O}1)$ with the dihedral angle $\angle\text{O}1-\text{C}2-\text{N}1-\text{C}4$ are reasonable and similar to the case of **1-HO**. On the other hand, both distances $d(\text{N}1-\text{C}3)$ and $d(\text{N}1-\text{C}4)$ are longer by about 0.05 Å and the tendency in the change against the dihedral angle $\angle\text{O}1-\text{C}2-\text{N}1-\text{C}4$ is reversed compared to the case of **1-HO** due to the electronic effects of the Me groups of the piperidine. Although the angle $\angle\text{M}-\text{N}1-\text{C}2$ is sensitively affected by the dihedral angle $\angle\text{O}1-\text{C}2-\text{N}1-\text{C}4$, which is similar to the case of **1-HO**, its fluctuation is small, because N1 already takes sp^3 hybridization at 0° in **1-MO** as mentioned above.

The change in the NBO charge on each atom by the dihedral angle $\angle\text{O}1-\text{C}2-\text{N}1-\text{C}4$ is also presented in Figure 4. In both cases of **1-HO** and **1-MO**, C2 is largely positively charged, whereas O1 and N1 on both sides of C2 are largely negatively charged. It should be noted here that C1 is also largely negatively charged like O1 and N1. Accordingly, the three α -H attached to C1 have positive charges of 0.21–0.23 e, which would make facile the migration of the α -H to the N1 atom as a proton, as mentioned below. The signs of charges of C3 and C4 are different between **1-HO** and **1-MO**; i.e., both are negative in **1-HO** and positive in **1-MO**, due to the electronic effect of the Me substituents of the piperidine ring. The charges of the atoms, N1, C2, and O1, sharing the π electron change with the dihedral angle $\angle\text{O}1-\text{C}2-\text{N}1-\text{C}4$ in both **1-HO** and **1-MO**. When the dihedral angle $\angle\text{O}1-\text{C}2-\text{N}1-\text{C}4$ is 60° and 270° , the values of the negative charge of O1 and the positive charge of C2 become maximum whereas that of the negative charge of N1 becomes minimum, because the electron migration from N1 to $\text{C}2=\text{O}1$ is retarded.

Mechanism A. The methanol O—H bond adds to the amide bond in mechanism A. This reaction proceeds by one step. The optimized structures of the reactant, transition state, and the product of this reaction are presented in Figure 5. In the reactant **2A-MO**, the hydrogen rather than the oxygen of the methanol O—H first attacks the amide N, as shown by the relatively short distance $d(\text{H}2-\text{N}1)$ of 2.349 Å and the long

distance $d(\text{O}2-\text{C}2)$ of 3.604 Å. The distance $d(\text{H}2-\text{N}1)$ shortened to 1.104 Å in the transition state **TS1A-MO**, which is only 0.088 Å longer than that of the product **3A-MO**, shows that the H2—N1 bond is almost formed in the transition state. The distance $d(\text{O}2-\text{H}2)$ is consequently stretched to 1.470 Å, which is very long compared to that of the free methanol (0.961 Å). On the other hand, the distance $d(\text{O}2-\text{C}2)$ of 2.152 Å is still long. These features in the transition state of the methanol O—H addition to the amide bond are different from those in the transition state of the methanol O—H addition to the $\text{C}=\text{C}$ double bond of ketene in mechanism C (see below). Because O2 and N1 on both sides of C2 have large negative charges, the O2—C2 bond formation and the C2—N1 bond breaking would proceed concertedly. The precedent binding of H2 with N1 weakens the C2—N1 bond. The energy profile of this reaction by one step, **2A-MO** \rightarrow **TS1A-MO** \rightarrow **3A-MO**, is displayed in Figure 6. The large energy barrier of 40.0 kcal/mol is thought to be required to prevent the delocalization of the π electron in the $-\text{C}(=\text{O})-\text{N}<$ part that strengthens the amide bond.

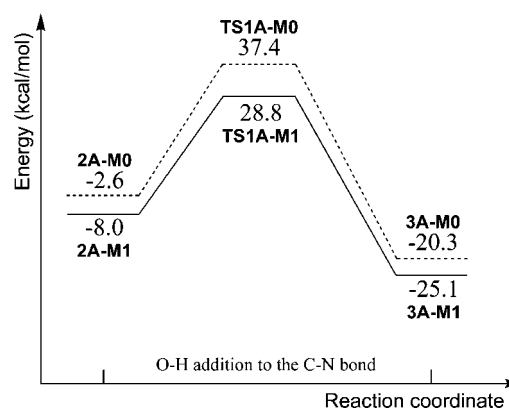


Figure 6. Energy profiles of the amide bond cleavages by mechanism A at the B3LYP/6-311++G(d,p) level. Dotted line: without the mediation of a methanol solvent molecule. Normal line: with the mediation of one methanol solvent molecule.

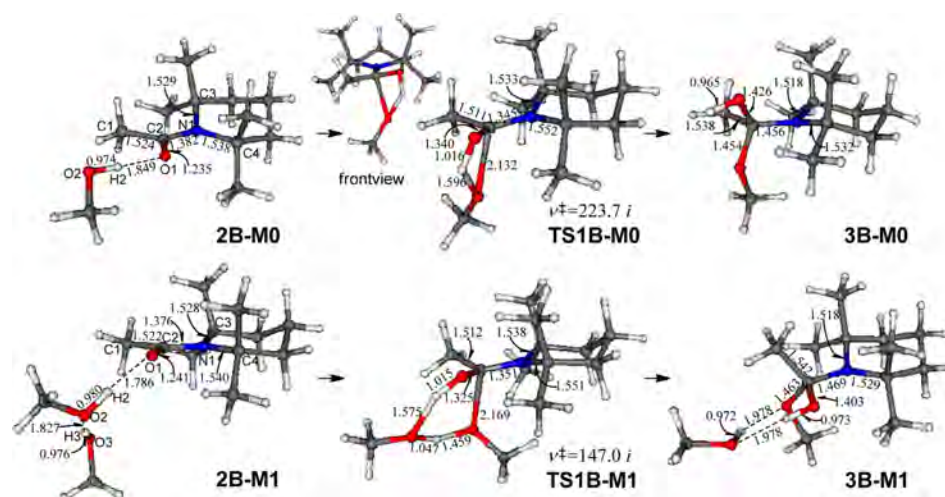


Figure 7. Optimized equilibrium and transition state structures (Å) involved in the first step of mechanism B with and without the mediation of a methanol solvent molecule at the B3LYP/6-311++G(d,p) level. The imaginary frequencies (cm^{-1}) are also presented together for the transition states.

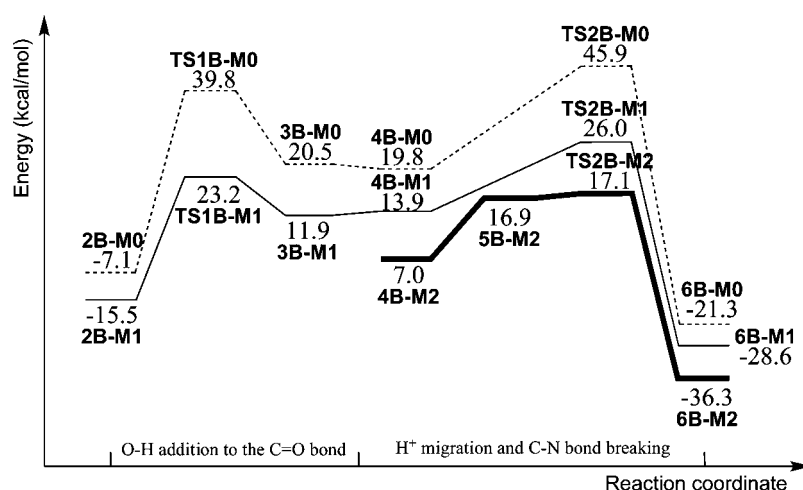


Figure 8. Energy profiles of the amide bond cleavages by mechanism B at the B3LYP/6-311++G(d,p) level. Dotted line: without the mediation of a methanol solvent molecule. Normal line: with the mediation of one methanol solvent molecule. Bold line: with the mediation of two methanol solvent molecules.

We also examined the participation of one methanol solvent molecule in the reaction, which would relax the stress in the geometry in the transition state **TS1A-M1**. H2 is almost transferred from O2 to N1 in **TS1A-M1**, as shown by the short distance $d(\text{N1}-\text{H2})$ of 1.075 Å and the long distance $d(\text{O2}-\text{H2})$ of 2.094 Å. O2 receives H3 from O3 and O3 attacks C2. Here, it is thought on the basis of the geometry that H3 is under migration and O3 is still far from C2. Thus, the migration of H2 and H3 occurs in turn. The two hydrogens H2 and H3 migrate as a proton, and the C2—N1 bond is broken heterolytically when the generated MeO_3^- forms the bond with C2. The energy barrier of 36.8 kcal/mol is still large even when the additional methanol solvent molecule participates in the reaction, as displayed in Figure 6, although the energy barrier becomes smaller by 3 kcal/mol compared to the case without the additional methanol solvent molecule.

We also calculated for 1-acetylpiperidine instead of 1-acetyl-2,2,6,6-tetramethylpiperidine in both cases with and without the additional methanol molecule to examine the effects of the

Me group of the piperidine ring (Figures S1 and S2, Supporting Information). The energy barrier in the case of 1-acetylpiperidine was nearly the same as that in the case of 1-acetyl-2,2,6,6-tetramethylpiperidine. The heat of reaction, however, is 19 kcal/mol more exothermic in the case of 1-acetyl-2,2,6,6-tetramethylpiperidine. The steric repulsion between the four Me groups of the piperidine and the incoming substrate disappears after the C2—N1 bond breaking so that the exothermicity becomes large. The advantage in the reaction by the hindrance of π electron delocalization for 1-acetyl-2,2,6,6-tetramethylpiperidine would be countervailed by the steric repulsion between the four Me groups of the piperidine and the substrate.

Mechanism B. Mechanism B consists of two steps. The methanol O—H adds to the C2=O1 double bond in the first step, and the formed —OH hydrogen moves to the amide N and the C2—N1 amide bond is broken in the second step. The optimized structures for the first step are displayed in Figure 7. We calculated only the case where the methanol O—H

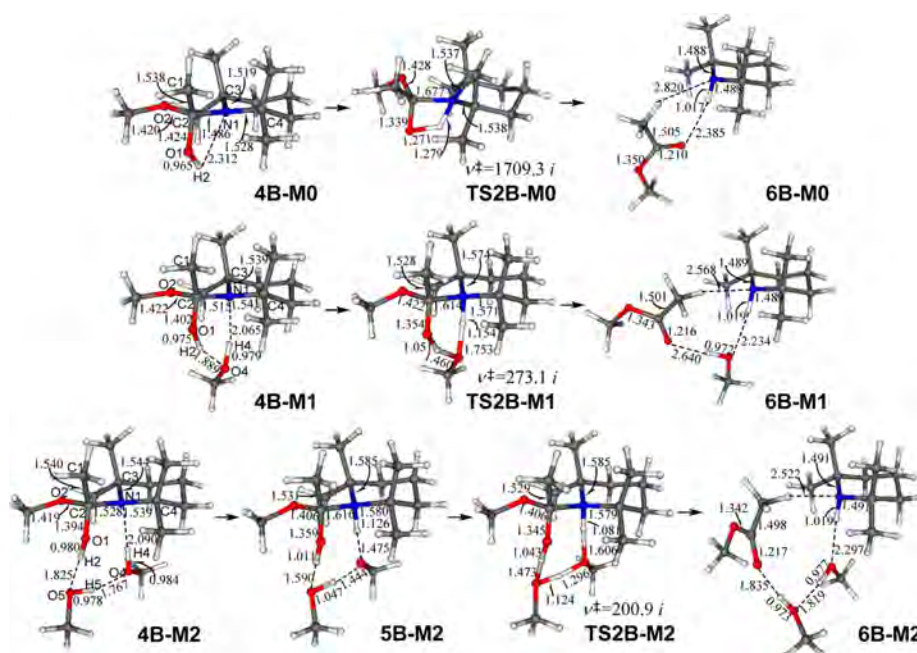


Figure 9. Optimized equilibrium and transition state structures (Å) involved in the second step of mechanism B with and without the mediation of methanol solvent molecules at the B3LYP/6-311++G(d,p) level. The imaginary frequencies (cm^{-1}) are also presented together for the transition states.

approaches C2=O1 from the underside, because a large space is provided on the underside. In the reactant **2B-M0**, the methanol O—H hydrogen interacts with the C2=O1 oxygen by the H-bond with a $d(\text{H2—O1})$ distance of 1.849 Å. The reaction proceeds by the electrophilic attack of the O—H hydrogen on the C2=O1 oxygen rather than the nucleophilic attack of the methanol O—H oxygen on the C2=O1 carbon, as shown by the relatively long distance $d(\text{O2—C2})$ of 2.132 Å and the short distance $d(\text{H2—O1})$ of 1.016 Å in the transition state **TS1B-M0**. As a result, the distance $d(\text{O2—H2})$ is stretched to 1.596 Å. As shown in Figure 8, this first step is 28 kcal/mol endothermic, and the energy barrier was calculated to be 46.9 kcal/mol. Although the delocalization of the π electron in the $-\text{C}(=\text{O})-\text{N}<$ part is retarded to some extent in 1-acetyl-2,2,6,6-tetramethylpiperidine, as mentioned above, the methanol O—H addition to the carbonyl double bond as well as the methanol O—H addition to the amide bond in mechanism A has a large energy barrier.

We further performed the calculations considering the participation of an additional methanol solvent molecule in the reaction. However, there is no drastic change in the geometry of the transition state **TS1B-M1** (Figure 7). Here, the migration of both H2 and H3 as a proton through the H-bond is nearly completed, which is followed by the attack of O3 of the formed methoxide anion on C2. The energy barrier of this step is reduced by 8 kcal/mol compared to the case without an additional methanol solvent molecule (Figure 8) but is still very large.

In the second step, the hydrogen of the formed $-\text{O1H2}$ group is transferred to N1. The positively charged H2 has an electrostatic interaction with the negatively charged N1 in the reactant **4B-M0** as presented in Figure 9. The O1—H2 bond is elongated by about 30% in the transition state **TS2B-M0**, which shows that the H2 migration is a driving force of the second step. On the other hand, the C2—N1 bond is elongated by

about only 10% even in the transition state **TS2B-M0**. The H2 shifts as a proton and the two electrons left on O1 are used to generate the π bond C2=O1. Accordingly, the C2—N1 σ bond is broken heterolytically, where N1 receives the shared electrons. The energy barrier of 26.1 kcal/mol in the second step is more than 20 kcal/mol smaller than that of 46.9 kcal/mol in the first step (Figure 8), because the extra energy to prevent the delocalization of the π electron in the $-\text{C}(=\text{O})-\text{N}<$ part is not required in the second step.

The deformation in the structure of the reaction part in the transition state was much improved, when an additional methanol solvent molecule mediates the reaction. As displayed in Figure 9, the stress especially on O1 and N1 in **TS2B-M0** is relaxed in **TS2B-M1**. The $-\text{OH}$ hydrogen migrates as a proton to the amide N through the H-bond, as shown by **TS2B-M1**, where the H4 shifts at first and later the H2 shifts. The C2=O1 π bond formation by this proton migration would cause the C2—N1 bond breaking. The energy barrier is largely reduced from 26.1 to 12.1 kcal/mol by the mediation of a methanol molecule (Figure 8). Even if we add one more methanol molecule, the structure of the reaction part of the transition state is not basically changed, as shown by **TS2B-M2**, so that the energy barrier is reduced by only 2 kcal/mol. **5B-M2**, which we found as the equilibrium structure before reaching the transition state **TS2B-M2** (Figure 9), would be an artificial intermediate, because the energy and the structure of the transition state between **4B-M2** and **5B-M2** were extremely close to those of **5B-M2**. As shown by the entire energy profile displayed in Figure 8, the rate-determining step of mechanism B is thought to be the first step.

The optimized structures and the energy profiles in the case of 1-acetyl-2,2,6,6-tetramethylpiperidine are presented in Figures S3 and S4 (Supporting Information). The energy barrier of the first step was similar to the case of 1-acetyl-2,2,6,6-tetramethylpiperidine, because the first step loses the advantage that the delocalization

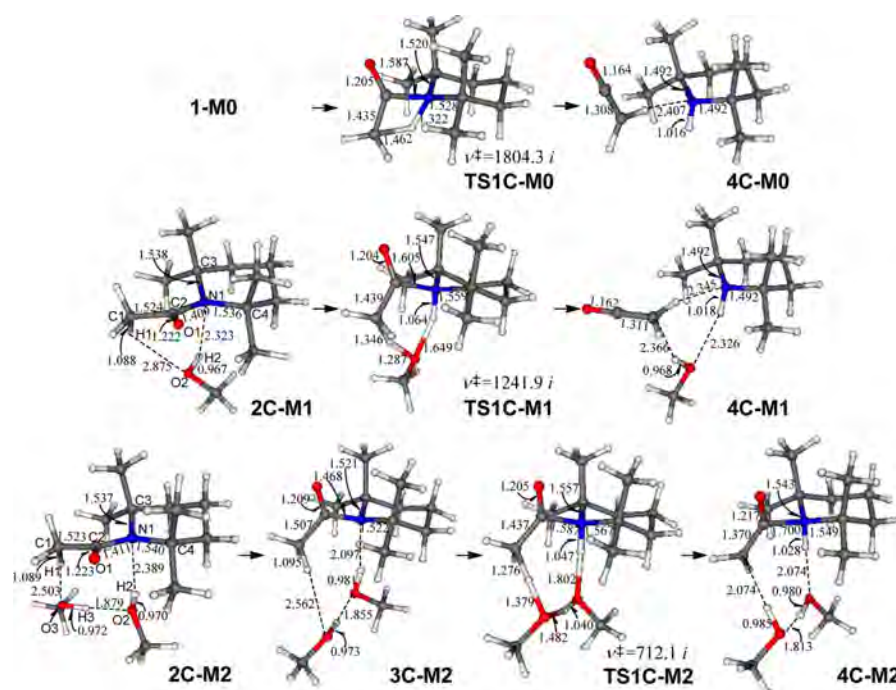


Figure 10. Optimized equilibrium and transition state structures (Å) involved in the first step of mechanism C with and without the mediation of methanol solvent molecules at the B3LYP/6-311++G(d,p) level. The imaginary frequencies (cm^{-1}) are also presented together for the transition states.

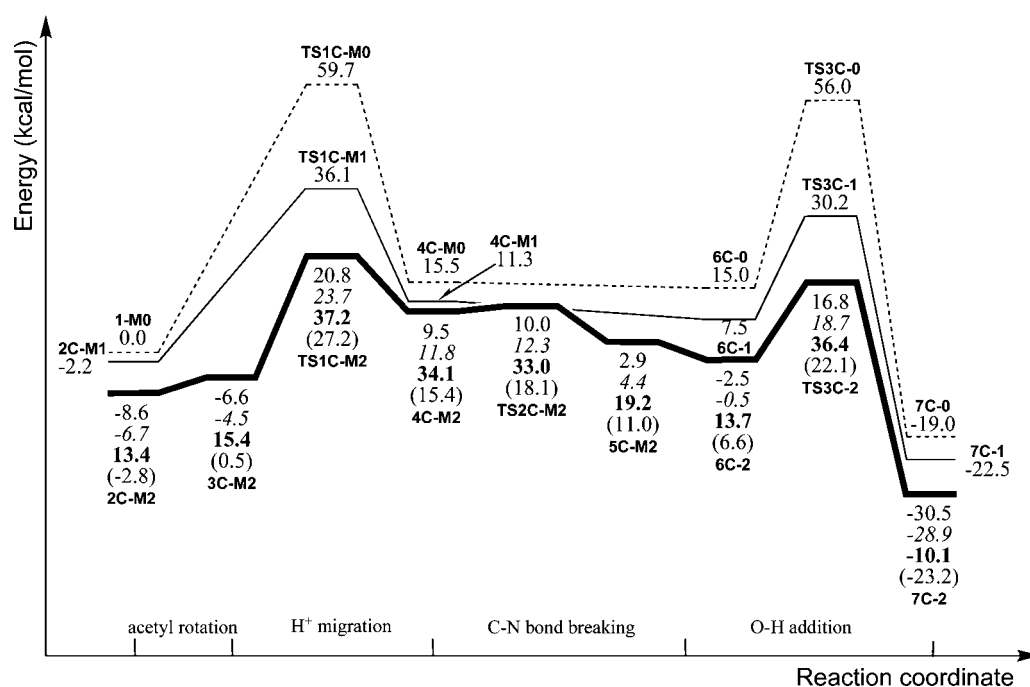


Figure 11. Energy profiles of the amide bond cleavages by mechanism C at the B3LYP/6-311++G(d,p) level. Dotted line: without the mediation of a methanol solvent molecule. Normal line: with the mediation of one methanol solvent molecule. Bold line: with the mediation of two methanol solvent molecules. Plain type: B3LYP/6-311++G(d,p) level. Italic type: B3LYP/6-311++G(d,p) level. Bold type: Gibbs free energy at the B3LYP/6-311++G(d,p) level. Plain type in parentheses: B3LYP/6-311++G(d,p) level in a dielectric medium.

of the π electron in the $-\text{C}(=\text{O})-\text{N}<$ is prevented but gains the advantage that there is no steric repulsion between the incoming substrate and the piperidine. This is the same as the case of mechanism A. On the other hand, the energy barrier of

the second step becomes a little larger, because the exothermicity of this step is reduced.

Mechanism C. Mechanism C is composed of three steps: first step, the proton migration; second step, the C—N bond

breaking; third step, the methanol addition. The optimized equilibrium and transition state structures involved in the first step without the mediation of a methanol solvent molecule are presented in Figure 10. The migration of the α -H to the amide N, **1-M0** \rightarrow **TS1C-M0** \rightarrow **4C-M0**, is accompanied by the rotation of the acetyl group around the amide bond. In the starting 1-acetyl-2,2,6,6-tetramethylpiperidine **1-M0**, N1 takes an sp^3 hybridization due to the steric effect of the four Me groups, which makes facile the rotation of the acetyl group around the C2—N1 axis, as mentioned above. The acetyl group, therefore, rotates by about 90° in the transition state **TS1C-M0**, by which the α -H is directed to N1. The α -H would be transferred to N1 as a proton. In fact, in **TS1C-M0**, the positive charge of the migrating H1 increased to 0.412 and the negative charges of C1 and N1 also increased to -0.824 and -0.675 e, respectively. On the other hand, the positive charges of the α -H other than H1 did not change and kept the values of 0.22 – 0.23 e. The electrostatic interaction $C1(\delta^-)\cdots H1(\delta^+)\cdots N1(\delta^-)$ would stabilize the transition state **TS1C-M0**. The two electrons left on C1 by the proton transfer form the C1=C2 π bond, and the subsequent shift of the shared electrons between C2 and N1 to N1 causes the C2—N1 σ bond breaking. As displayed in Figure 11, this migration of the α -H, which is accompanied by the amide bond breaking, is 15.5 kcal/mol endothermic and the energy barrier is 59.7 kcal/mol. The large energy barrier would be attributed to the significant deviation from the tetrahedron structure of the sp^3 hybridization for C1 and N1 in **TS1C-M0**.

We therefore considered the mediation of a methanol solvent molecule in the reaction, as Lloyd-Jones, Booker-Milburn, and co-workers have experimentally suggested, to relax the deformation of the reaction part of the transition state **TS1C-M0**. The additional methanol molecule bridges H1 and N1 in the reactant **2C-M1**, as shown by the distances $d(H2-N1)$ of 2.323 Å and $d(H1-O2)$ of 2.875 Å. Here, H1 interacts with O2 like a H-bond, because C1 as well as N1 has a large negative charge. The reaction is also thought to proceed by the proton transfer similarly, where H2 and H1 migrate in turn as reflected in the short $d(H2-N1)$ of 1.064 Å and the long $d(H1-O2)$ of 1.287 Å in the transition state **TS1C-M1**. This proton migration is accompanied by the C1=C2 π bond formation and the C2—N1 σ bond breaking. The energy barrier of 38.3 kcal/mol for this reaction is reduced by more than 20 kcal/mol compared to the case without an additional methanol solvent molecule (Figure 11), because the stress on the sp^3 hybridization of C1 and N1 is largely relaxed in **TS1C-M1**. The electrostatic interactions in the alternately arranged negative and positive charges $C1(\delta^-)\cdots H1(\delta^+)\cdots O2(\delta^-)\cdots H2(\delta^+)\cdots N1(\delta^-)$ in **TS1C-M1** would also contribute to the decrease in the energy barrier.

We added one more methanol solvent molecule in the starting **2C-M2**. The two additional methanol molecules successfully fit the space between H1 and N1, as shown by the distance $d(H1-O3)$ of 2.503 Å, which is shorter by 0.372 Å than the distance $d(H1-O2)$ of 2.875 Å in **2C-M1**. Because the H-bond between H2 and N1 acts to prevent the π electron delocalization in the $-C(=O)-N<$ part and makes the rotation of the acetyl group more facile, the rotation angle of the acetyl group is easily adjusted to provide a suitable space for the incoming methanol molecules. In this case with two methanol solvent molecules, **3C-M2**, where the molecular plane of the acetyl group is completely rotated up (the dihedral angle $\angle O1-C2-N1-C4$ is 62.5°), exists as an equilibrium

structure and is only 2 kcal/mol less stable than **2C-M2**. By this rotation of the acetyl group, the proton migration to N1 would become easier, because the lone electron pair is completely localized on N1. The proton migration of H2, H3, and H1 is not concerted, as we have seen in mechanisms A and B. H2, H3, and H1 shift in turn, as shown by the plots of the geometric parameters versus the reaction coordinate (Figure S5, Supporting Information). The values of the negative and the positive charges alternately arranged as $C1(\delta^-)\cdots H1(\delta^+)\cdots O3(\delta^-)\cdots H3(\delta^+)\cdots O2(\delta^-)\cdots H2(\delta^+)\cdots N1(\delta^-)$ in **3C-M2** increase in the transition state **TS1C-M2**, which would stabilize in energy the transition state **TS1C-M2**. This increase in the charge of each atom also suggests that the hydrogen migrates as a proton. It should be noted here that the C2—N1 bond remains without breaking in **4C-M2**. This would be due to the interactions of two methanol molecules with C1 and H2 after the mediation. The electrons to be used for the formation of the C1=C2 π bond are detained on C1 by the C1 \cdots H1 electrostatic interaction. On the other hand, the lone electron pair on N1 is attracted to H2 by the O2 \cdots H2 H-bond. However, the short $d(C1-C2)$ distance of 1.370 Å, which is similar to that of the free ketene, and the long $d(C2-N1)$ distance of 1.700 Å show that the C1—N1 bond is already very weak.

The energy barrier is the smallest in the case with two additional methanol solvent molecules (Figure 11). The energy barrier of 27.4 kcal/mol in the case with two additional methanol molecules is about 11 kcal/mol smaller than that in the case with one additional methanol molecule. As mentioned above, two methanol molecules just fit to the space between H1 and N1 and relax the geometric deformation of the reaction part in the transition state. Furthermore, the two mediating methanol molecules successfully avoid the steric repulsion with the four Me groups of the piperidine ring, which is different from the cases of mechanisms A and B, because their bridges are a little far from the piperidine ring. When we use 1-acetyl-2,2,6,6-tetramethylpiperidine instead of 1-acetyl-2,2,6,6-tetramethylpiperidine, the energy barriers of both cases with and without methanol solvent molecules become large by 7 – 13 kcal/mol (Figure S7, Supporting Information) due to the loss of the advantage on the hindrance of the π electron delocalization. The equilibrium structure corresponding to **3C-M2** also does not exist (Figure S6, Supporting Information), because the rotation of the acetyl group around the C2—N1 axis is not easy in the case of 1-acetyl-2,2,6,6-tetramethylpiperidine as mentioned above.

The C—N bond breaking independently exists as the second step only in the case with two additional methanol molecules, as this step is involved in the first step in other cases. The optimized equilibrium and transition state structures in this step are presented in Figure 12. In the transition state **TS2C-M2**, the C2—N1 bond stretches from 1.700 to 2.025 Å and the angle $\angle C1-C2-O1$ of the ketene moiety increases from 136.1° to 146.1° to break the C2—N1 bond. The C2—N1 bond breaking actually has a small energy barrier of only 0.5 kcal/mol (Figure 11), because the C2—N1 bond is already largely weakened, as mentioned earlier.

The third step is the methanol O—H addition to the C=C double bond of the ketene formed in the second step. The features of the transition state of this addition reaction are different from those of the addition reactions in mechanisms A and B. In **TS3C-0**, the distance $d(O4-C2)$ of 1.827 Å is relatively short whereas the distance $d(H4-C1)$ of 1.417 Å is relatively long, as presented in Figure 13, which shows that the

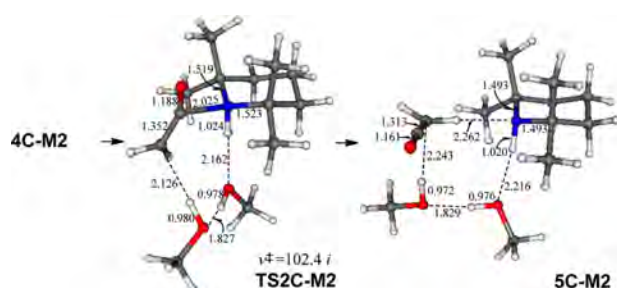


Figure 12. Optimized equilibrium and transition state structures (Å) involved in the second step of mechanism C with the methanol solvent molecules at the B3LYP/6-311++G(d,p) level. The imaginary frequency (cm^{-1}) is also presented together for the transition state.

methanol O—H oxygen rather than hydrogen at first attack the ketene carbon. As shown by the front view, the lone electron pair of the methanol O4 attacks the positively charged ketene C2 from the side. The C1—C2—O1 axis of the ketene moiety is bent by 27.3° . The electron on O4 accumulates on the originally negatively charged C1 by the O4—C2 bond formation. In fact, the negative charge of C1 increases from -0.773 to -0.863 e when 6C-0 passes TS3C-0. The highly negatively charged C1 would receive H4 as a proton changing its orbital from sp^2 to sp^3 . This reaction is 34 kcal/mol exothermic (Figure 11), and this large exothermicity is in accordance with the general consensus that ketene is highly reactive. Although the energy barrier is 41.0 kcal/mol, this value becomes smaller by considering the mediation of the methanol solvent molecules.

When we add one methanol molecule, the energy barrier decreased to 22.7 kcal/mol. Here, the heat of the reaction does not change so much. The geometric stress especially on C1 and C2 in the transition state TS3C-1 is improved by the addition of a methanol molecule. As a result, the angle $\angle\text{C1—C2—O1}$ decreases to 140.2° and the distance $d(\text{C2—O4})$ shortens to 1.634 Å. On the other hand, the distance $d(\text{C1—H5})$ lengthens to 1.631 Å. By the addition of one more methanol molecule, the structure of the transition state TS3C-2 was further improved so that the energy barrier became less than 20 kcal/mol.

The entire energy profiles of mechanism C are presented in Figure 11. It is obvious that mechanism C is more favorable in energy than mechanisms A and B when two additional methanol molecules mediate the reaction. The entire energy profile shows that the rate-determining step is not the second step of the C—N bond breaking, $4\text{C-M2} \rightarrow \text{TS2C-M2} \rightarrow 5\text{C-M2}$, as experimentally thought, but the first step of the proton migration, $3\text{C-M2} \rightarrow \text{TS1C-M2} \rightarrow 4\text{C-M2}$. The tendency in the entire energy profile did not change so much even if we use the highly improved basis set aug-cc-pVTZ and the polarized continuum model to consider the solvent. However, the entire energy profile was destabilized by 2–7 kcal/mol. The entire energy profile by the Gibbs free energy was also destabilized by 13–22 kcal/mol due to the entropy effect.

CONCLUDING REMARKS

In recent years, the amide bond cleavages of the 2,2,6,6-tetramethylpiperidine derivatives in methanol solvent have been accomplished under mild conditions, although it is well-known that the amide linkage is very strong due to the delocalization of the π electron on the amide N to the carbonyl

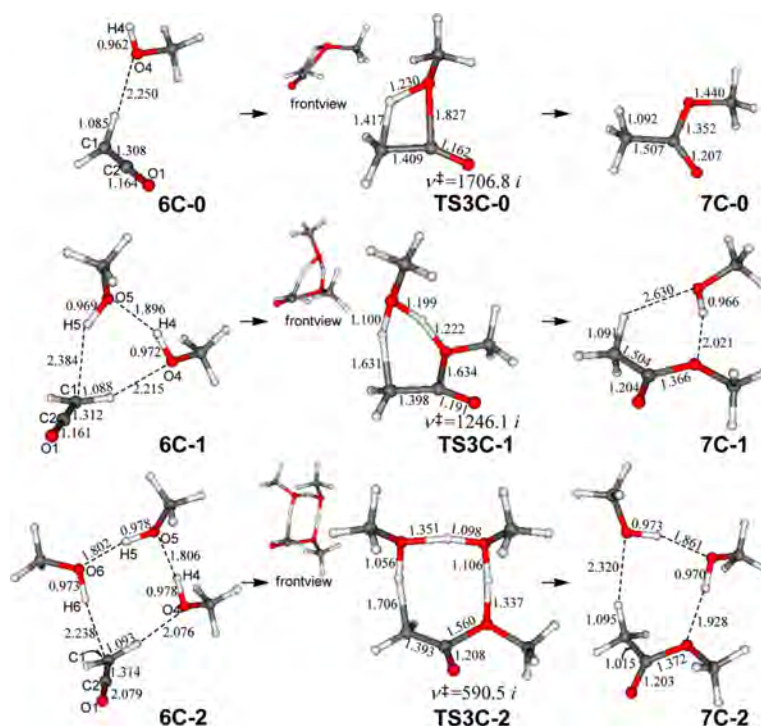


Figure 13. Optimized equilibrium and transition state structures (Å) involved in the third step of mechanism C with and without the mediation of methanol solvent molecules at the B3LYP/6-311++G(d,p) level. The imaginary frequencies (cm^{-1}) are also presented together for the transition states.

group. In this study, we examined the mechanism of this reaction using 1-acetyl-2,2,6,6-tetramethylpiperidine as a model by means of the density functional method (B3LYP). The calculations were performed for both the generally known mechanisms A and B and the recently proposed new mechanism C for the 2,2,6,6-tetramethylpiperidine derivatives. The amide bond is broken by the addition of the nucleophile methanol to the amide bond in mechanism A and by the addition of the nucleophile methanol to the carbonyl double bond and the subsequent migration of the hydrogen of the formed $-OH$ to the amide N in mechanism B. On the other hand, the amide bond is broken by the “proton switching pathway” in mechanism C. The orbital of the amide N is transformed from the sp^2 to the sp^3 hybridization in the starting substrate 1-acetyl-2,2,6,6-tetramethylpiperidine by the steric repulsion between the four Me groups of the piperidine ring and the acetyl group. Therefore, the delocalization of the π electron of the amide N is hindered to some extent. This advantage in the C—N bond cleavage is, however, counter-vailed by the steric repulsion between the four Me group of the piperidine and the incoming nucleophile methanol in the generally known mechanisms A and B. As a result, the energy barriers of both mechanisms A and B are very large. In contrast, this advantage is effectively utilized in the C—N bond cleavage in the new mechanism C. The first step of the migration of the α -H to the amide N is accompanied by the rotation of the acetyl group around the C—N axis, because this rotation becomes easy due to the steric effect of the Me groups of the piperidine. By this rotation, the delocalized π electron is completely localized on the amide N, which promotes the α -H migration. The energy barrier of the α -H migration was significantly reduced by the mediation of methanol solvent molecules, because the geometric stress in the transition state is largely relaxed. The amide bond highly activated by the localization of the π electron on the amide N is readily broken in the second step. The reaction is completed in the third step of the addition of methanol to ketene formed in the second step. The energy barrier of the third step is also decreased by the participation of the methanol solvent molecules to the reaction. On the basis of the entire energy profile, it was found that the first step is the rate-determining step. The small energy barrier of the rate-determining first step in mechanism C compared to the energy barriers of mechanisms A and B shows that mechanism C is the most favorable in energy.

■ ASSOCIATED CONTENT

Supporting Information

Figure S1: Optimized equilibrium and transition state structures involved in mechanism A in the case of 1-acetylpiperidine. Figure S2: Energy profiles of the amide bond cleavages by mechanism A in the case of 1-acetylpiperidine. Figure S3: Optimized equilibrium and transition state structures involved in mechanism B in the case of 1-acetylpiperidine. Figure S4: Energy profiles of the amide bond cleavages by mechanism B in the case of 1-acetylpiperidine. Figure S5: Plots of the selected geometric parameters versus the reaction coordinate of the α -H migration in mechanism C with the mediation of two methanol solvent molecules. Figure S6: Optimized equilibrium and transition state structures involved in the first step of mechanism C in the case of 1-acetylpiperidine. Figure S7: Energy profiles of the first step of mechanism C in the case of 1-acetylpiperidine. Tables of the NBO charges of the selected atoms of the equilibrium

structures and the transition states involved in mechanisms A, B, and C. Listings giving the optimized Cartesian coordinates of all equilibrium structures and transition states presented in this paper. This material is available free of charge via the Internet at <http://pubs.acs.org>.

■ AUTHOR INFORMATION

Notes

The authors declare no competing financial interest.

■ ACKNOWLEDGMENTS

Part of the computations was performed at the Research Center for Computational Science, Okazaki, Japan.

■ REFERENCES

- (1) Vollhardt, K. P. C.; Schore, N. E. *Organic Chemistry -Structure and Function*, 6th ed.; W. H. Freeman: New York, 2011.
- (2) Bruice, P. Y. *Organic Chemistry*, 5th ed.; Prentice Hall: Upper Saddle River, NJ, 2007.
- (3) McMurry, J. *Organic Chemistry*, 8th ed.; Cengage Learning: Belmont, PA, 2012.
- (4) Hutchby, M.; Houlden, C. E.; Haddow, M. F.; Tyler, S. N. G.; Lloyd-Jones, G. C.; Booker-Milburn, K. I. Switching Pathways: Room-Temperature Neutral Solvolysis and Substitution of Amides. *Angew. Chem., Int. Ed.* **2012**, *51*, 548–551.
- (5) Mustafi, D.; Knock, M. M.; Shaw, R. W.; Mäkinen, M. W. Conformational Changes in Spin-Labeled Cephalosporin and Penicillin upon Hydrolysis Revealed by Electron Nuclear Double Resonance Spectroscopy. *J. Am. Chem. Soc.* **1997**, *119*, 12619–12628.
- (6) Mustafi, D.; Mäkinen, M. W. Structure, Conformation, and Probable Mechanism of Hydrolysis of a Spin-Labeled Penicillin Revealed by Electron Nuclear Double Resonance Spectroscopy. *J. Am. Chem. Soc.* **1995**, *117*, 6739–6746.
- (7) McCarrick, T. A.; McLafferty, F. W. Penicillin Hydrolysis, a Kinetic Study of a Multistep, Multiproduct Reaction. *J. Chem. Educ.* **1984**, *61*, 463–464.
- (8) Grant, N. H.; Clark, D. E.; Alburn, H. E. Imidazole- and Base-Catalyzed Hydrolysis of Penicillin in Frozen Systems. *J. Am. Chem. Soc.* **1961**, *83*, 4476–4477.
- (9) Wang, Z.; Xu, J.; Wang, L.; Bao, D.; Qi, H. Thermodynamic Equilibrium Control of the Enzymatic Hydrolysis of Penicillin G in a Cloud Point System without pH Control. *Ind. Eng. Chem. Res.* **2006**, *45*, 8049–8055.
- (10) Tani, K.; Stoltz, B. M. Synthesis and Structural Analysis of 2-Quinuclidonium Tetrafluoroborate. *Nature* **2006**, *441*, 731–734.
- (11) Clayden, J.; Moran, W. J. The Twisted Amide 2-Quinuclidone: 60 Years in the Making. *Angew. Chem., Int. Ed.* **2006**, *45*, 7118–7120.
- (12) Szostak, M.; Aubé, J. Medium-Bridged Lactams: a New Class of Non-Planar Amides. *Org. Biomol. Chem.* **2011**, *9*, 27–35.
- (13) Golden, J. E.; Aubé, J. A Combined Intramolecular Diels–Alder/Intramolecular Schmidt Reaction: Formal Synthesis of (\pm)-Stenine. *Angew. Chem., Int. Ed.* **2002**, *41*, 4316–4318.
- (14) Somayaji, V.; Brown, R. S. Distorted Amides as Models for Activated Peptide N-C=O Units Produced during Enzyme-Catalyzed Acyl Transfer Reactions. 1. The Mechanism of Hydrolysis of 3,4-Dihydro-2-oxo-1,4-ethanoquinoline and 2,3,4,5-Tetrahydro-2-oxo-1,5-ethanobenzazepine. *J. Org. Chem.* **1986**, *51*, 2676–2686.
- (15) Šlebocka-Tilk, H.; Brown, R. S. Effect of Distortion on the Hydrolytic Reactivity of Amides. 2. N-Pyramidalization: Decomposition of N-Benzoylaziridines in Aqueous Media. *J. Org. Chem.* **1987**, *52*, 805–808.
- (16) Brown, R. S.; Santarsiero, B. D. Distorted Amides as Models for Activated Peptide N-C(O) Units. 3. Synthesis, Hydrolytic Profile, and Molecular Structure of 2,3,4,5-Tetrahydro-2-oxo-1,5-propanobenzazepine. *J. Am. Chem. Soc.* **1991**, *113*, 5757–5765.
- (17) Bennet, A. J.; Wang, Q. P.; Šlebocka-Tilk, H.; Brown, R. S.; Somayaji, V.; Santarsiero, B. D. Relationship between Amidic

Distortion and Ease of Hydrolysis in Base. If Amidic Resonance Does Not Exist, Then What Accounts for the Accelerated Hydrolysis of Distorted Amides? *J. Am. Chem. Soc.* **1990**, *112*, 6383–6385.

(18) Kirby, A. J.; Komarov, I. V.; Wothers, P. D.; Feeder, N. The Most Twisted Amide: Structure and Reactions. *Angew. Chem., Int. Ed.* **1998**, *37*, 785–786.

(19) Kirby, A. J.; Komarov, I. V.; Feeder, N. Spontaneous, Millisecond Formation of a Twisted Amide from the Amino Acid, and the Crystal Structure of a Tetrahedral Intermediate. *J. Am. Chem. Soc.* **1998**, *120*, 7101–7102.

(20) Kirby, A. J.; Komarov, I. V.; Feeder, N. Synthesis, Structure and Reactions of the Most Twisted Amide. *J. Chem. Soc., Perkin Trans. 2* **2001**, 522–529.

(21) Mujika, J. I.; Mercero, J. M.; Lopez, X. Water-Promoted Hydrolysis of a Highly Twisted Amide: Rate Acceleration Caused by the Twist of the Amide Bond. *J. Am. Chem. Soc.* **2005**, *127*, 4445–4453.

(22) Oie, T.; Loew, G. H.; Burt, S. K.; Binkley, J. S.; MacElroy, R. D. Quantum Chemical Studies of a Model for Peptide Bond Formation: Formation of Formamide and Water from Ammonia and Formic Acid. *J. Am. Chem. Soc.* **1982**, *104*, 6169–6174.

(23) Weiner, S. J.; Singh, U. C.; Kollman, P. Simulation of Formamide Hydrolysis by Hydroxide Ion in the Gas Phase and in Aqueous Solution. *J. Am. Chem. Soc.* **1985**, *107*, 2219–2229.

(24) Krug, J. P.; Popelier, P. L. A.; Bader, R. F. W. Theoretical Study of Neutral and of Acid and Base-Promoted Hydrolysis of Formamide. *J. Phys. Chem.* **1992**, *96*, 7604–7616.

(25) Jensen, J. H.; Baldrige, K. K.; Gordon, M. S. Uncatalyzed Peptide Bond Formation in the Gas Phase. *J. Phys. Chem.* **1992**, *96*, 8340–8351.

(26) Antonczak, S.; Ruiz-López, M. F.; Rivail, J. L. Ab Initio Analysis of Water-Assisted Reaction Mechanisms in Amide Hydrolysis. *J. Am. Chem. Soc.* **1994**, *116*, 3912–3921.

(27) Antonczak, S.; Ruiz-López, M. F.; Rivail, J. L. The Hydrolysis Mechanism of Formamide Revisited: Comparison between Ab Initio, Semiempirical and DFT Results. *J. Mol. Mod.* **1997**, *3*, 434–442.

(28) Hori, K.; Kamimura, A.; Ando, K.; Mizumura, M.; Ihara, Y. Ab Initio Molecular Orbital Study on the Mechanism of Amide Hydrolysis Dependent on Leaving Groups. *Tetrahedron* **1997**, *53*, 4317–4330.

(29) Kallies, B.; Mitzner, R. Models of Water-Assisted Hydrolyses of Methyl Formate, Formamide, and Urea from Combined DFT-SCRF Calculations. *J. Mol. Mod.* **1998**, *4*, 183–196.

(30) Zheng, Y. J.; Ornstein, R. L. Theoretical Study of a Nucleophilic Addition Reaction in the Gas Phase and in Aqueous Solution: Peptide Bond Hydrolysis. *J. Mol. Struct.* **1998**, *429*, 41–48.

(31) Bakowies, D.; Kollman, P. A. Theoretical Study of Base-Catalyzed Amide Hydrolysis: Gas- and Aqueous-Phase Hydrolysis of Formamide. *J. Am. Chem. Soc.* **1999**, *121*, 5712–5726.

(32) Strajbl, M.; Florián, J.; Warshel, A. Ab Initio Evaluation of the Potential Surface for General Base-Catalyzed Methanolysis of Formamide: a Reference Solution Reaction for Studies of Serine Proteases. *J. Am. Chem. Soc.* **2000**, *122*, 5354–5366.

(33) Chalmet, S.; Harb, W.; Ruiz-López, M. F. Computer Simulation of Amide Bond Formation in Aqueous Solution. *J. Phys. Chem. A* **2001**, *105*, 11574–11581.

(34) Lopez, X.; Mujika, J. I.; Blackburn, G. M.; Karplus, M. Alkaline Hydrolysis of Amide Bonds: Effect of Bond Twist and Nitrogen Pyramidalization. *J. Phys. Chem. A* **2003**, *107*, 2304–2315.

(35) Frisch, M. J.; Trucks, G. W.; Schlegel, H. B.; Scuseria, G. E.; Robb, M. A.; Cheeseman, J. R.; Montgomery, Jr., J. A.; Vreven, T.; Kudin, K. N.; Burant, J. C.; et al. *Gaussian 03*, revision E.01; Gaussian, Inc.: Wallingford, CT, 2004.

(36) Becke, A. D. Density-Functional Exchange-Energy Approximation with Correct Asymptotic Behavior. *Phys. Rev. A* **1988**, *38*, 3098–3100.

(37) Lee, C.; Yang, W.; Parr, R. G. Development of the Colle-Salvetti Correlation-Energy Formula into a Functional of the Electron Density. *Phys. Rev. B* **1988**, *37*, 785–789.

(38) Becke, D. Density-Functional Thermochemistry. III. The Role of Exact Exchange. *J. Chem. Phys.* **1993**, *98*, 5648–5652.

(39) Fukui, K.; Kato, S.; Fujimoto, H. Constituent Analysis of the Potential Gradient along a Reaction Coordinate. Method and an Application to Methane + Tritium Reaction. *J. Am. Chem. Soc.* **1975**, *97*, 1–7.

(40) Scott, A. P.; Radom, L. Harmonic Vibrational Frequencies: An Evaluation of Hartree-Fock, Mller-Plesset, Quadratic Configuration Interaction, Density Functional Theory, and Semiempirical Scale Factors. *J. Phys. Chem.* **1996**, *100*, 16502–16513.

(41) Glendening, E. D.; Reed, A. E.; Carpenter, J. E.; Weinhold F. NBO Version 3.1.

(42) Miertus, S.; Scrocco, E.; Tomasi, J. Electrostatic Interaction of a Solute with a Continuum. A Direct Utilizaion of Ab Initio Molecular Potentials for the Prevision of Solvent Effects. *Chem. Phys.* **1981**, *55*, 117–129.

(43) Miertus, S.; Tomasi, J. Approximate Evaluations of the Electrostatic Free Energy and Internal Energy Changes in Solution Processes. *Chem. Phys.* **1982**, *65*, 239–245.

(44) Frisch, M. J.; Trucks, G. W.; Schlegel, H. B.; Scuseria, G. E.; Robb, M. A.; Cheeseman, J. R.; Scalmani, G.; Barone, V.; Mennucci, B.; Petersson, G. A.; et al. *Gaussian 09*, revision A.01; Gaussian, Inc.: Wallingford, CT, 2009.

(45) Lunazzi, L.; Macciantelli, D.; Tassi, D.; Dondoni, A. Conformational Studies by Dynamic Nuclear Magnetic Resonance. Part 17. Stereodynamic Processes in Hindered Piperidyl-amides and -amidines. *J. Chem. Soc., Perkin Trans. 2* **1980**, 717–723.

(46) Wiberg, K. B.; Laidig, K. E. Barriers to Rotation Adjacent to Double Bonds. 3. The Carbon-Oxygen Barrier in Formic Acid, Methyl Formate, Acetic Acid, and Methyl Acetate. The Origin of Ester and Amide Resonance. *J. Am. Chem. Soc.* **1987**, *109*, 5935–5943.

(47) Wiberg, K. B.; Breneman, C. M. Resonance Interactions in Acyclic Systems. 3. Formamide Internal Rotation Revisited. Charge and Energy Redistribution along the C-N Bond Rotational Pathway. *J. Am. Chem. Soc.* **1992**, *114*, 831–840.

(48) Wiberg, K. B.; Hadad, C. M.; Rablen, P. R.; Cioslowski, J. Substituent Effects. 4. Nature of Substituent Effects at Carbonyl Groups. *J. Am. Chem. Soc.* **1992**, *114*, 8644–8654.

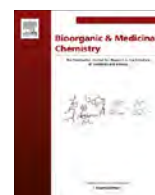
(49) Wiberg, K. B.; Rablen, P. R. Why Does Thioformamide Have a Larger Rotational Barrier Than Formamide? *J. Am. Chem. Soc.* **1995**, *117*, 2201–2209.

(50) Jean, Y.; Demachy, I.; Lledos, A.; Maseras, F. Electronic against Steric Effects in Distorted Amides. *J. Mol. Struct. (THEOCHEM)* **2003**, *632*, 131–144.



Contents lists available at ScienceDirect

Bioorganic & Medicinal Chemistry

journal homepage: www.elsevier.com/locate/bmc

Direct evidence for the function of crustacean insulin-like androgenic gland factor (IAG): Total chemical synthesis of IAG



Hidekazu Katayama^{a,*}, Nozomi Kubota^a, Hironobu Hojo^b, Ayumi Okada^c, Sayaka Kotaka^c, Naoaki Tsutsui^d, Tsuyoshi Ohira^c

^a Department of Applied Biochemistry, School of Engineering, Tokai University, 4-1-1 Kitakaname, Hiratsuka, Kanagawa 259-1292, Japan

^b Institute for Protein Research, Osaka University, 3-2 Yamadaoka, Suita, Osaka 565-0871, Japan

^c Department of Biological Sciences, Faculty of Science, Kanagawa University, Hiratsuka, Kanagawa 259-1293, Japan

^d Ushimado Marine Institute, Faculty of Science, Okayama University, 130-17 Kashino, Ushimado, Setouchi, Okayama 701-4303, Japan

ARTICLE INFO

Article history:

Received 22 August 2014

Revised 11 September 2014

Accepted 12 September 2014

Available online 20 September 2014

Keywords:

Crustacean

Glycopeptide

Insulin-like androgenic gland factor

Marsupenaeus japonicus

Solid-phase peptide synthesis

ABSTRACT

Insulin-like androgenic gland factor (IAG) is presumed to be a sex differentiation factor so-called androgenic gland hormone (AGH) in decapod crustacean, although the function of IAG peptide has not yet been reported. In this study, we synthesized IAG from the prawn, *Marsupenaeus japonicus*, and its function was assessed by an in vitro bioassay. As a result, IAG with the insulin-type disulfide bond arrangement showed biological activity, whereas its disulfide isomer did not. These results strongly suggest that the native IAG peptide has an insulin-type disulfide, and it is the decapod AGH.

© 2014 Elsevier Ltd. All rights reserved.

1. Introduction

Sex differentiation in crustacean has been shown to be under hormonal regulation by Charniaux-Cotton in 1954.¹ This intrinsic factor, so-called androgenic gland hormone (AGH), is secreted from the male specific organ, androgenic gland (AG). AGH was firstly purified from a terrestrial isopod, *Armadillidium vulgare*,² and its chemical structure was determined to be a heterodimeric glycopeptide with an insulin-like amino acid sequence.³ At the almost the same time, a cDNA encoding the AGH precursor was cloned.⁴ Up to now, full-length cDNAs encoding AGH precursors have been cloned from 12 isopod species.^{5,6} On the other hand, no AGH molecule has been purified from decapod species.

In 2007, an insulin-like gene expressed specifically in AG was cloned using a cDNA library prepared from the male AGs of Australian red-claw crayfish, *Cherax quadricarinatus*.⁷ This was the first report that insulin-like gene was expressed in the AG of decapod species. After that, insulin-like genes expressed in AGs, termed insulin-like androgenic gland factor (IAG), have been cloned from several decapod species.^{8–12} IAGs show amino acid sequence similarity to *A. vulgare* AGH, and especially, six Cys residues completely conserved in insulin-family are also found in

all IAG sequences. Therefore, IAG is presumed to be the decapod AGH. Actually, it has been reported that the gene silencing of IAG by RNAi affected phenotypical gender differentiation.^{8,13,14} On the other hand, no direct evidence for the function of IAG peptide molecule has been reported. To analyze the function of IAG peptide, the peptide molecule should be prepared. Although the preparation of insulin-like heterodimeric peptide by recombinant protein expression systems is generally difficult, the chemical synthetic strategy may give a good solution to this problem.

In our previous study, we synthesized *A. vulgare* AGH and analyzed its function.¹⁵ In the case of *A. vulgare* AGH, the disulfide bond arrangement is different from that in the vertebrate insulin,¹⁶ and the correct disulfide bond pairing is required for AGH function.¹⁵ In addition, the carbohydrate moiety attached to Asn residue in the A chain is crucial for conferring the biological activity in *A. vulgare* AGH.¹⁵ In the sequences of most decapod IAGs, putative N-glycosylation motifs are found, whereas the sites are not conserved not only between isopod AGH and decapod IAGs but also among IAGs. In the IAG from the kuruma prawn, *Marsupenaeus japonicus*, an N-glycosylation motif is found in the B chain,⁹ although it is quite difficult to presume whether an N-linked glycan is actually attached or not. In addition, it is also unclear whether the disulfide bond arrangement in *M. japonicus* IAG is the same as that of *A. vulgare* AGH (AGH-type) or as that of vertebrate insulin (insulin-type). In this paper, we show the direct

* Corresponding author. Tel./fax: +81 463 50 2075.

E-mail address: katay@tokai-u.jp (H. Katayama).

evidence for the *M. japonicus* IAG structure and its function through the chemical synthetic strategy.

2. Results and discussion

2.1. Synthetic strategy of IAG

The amino acid sequence of *M. japonicus* IAG is shown in Figure 1. In the synthesis of IAG peptide, the Pro residue at the A chain C-terminus is problematic. In the ordinary 9-fluorenylmethoxycarbonyl (Fmoc)-based solid-phase peptide synthesis (SPPS) method, when the C-terminal amino acid is linked via a nonbulky ester group, diketopiperadine structure is sometimes formed during the Fmoc removal of second residue by piperidine treatment, generating the incomplete peptide chain which lacks the C-terminal two amino acid residues.¹⁷ This problem is serious particularly in the case of peptides having C-terminal Pro residue. To suppress this unfavorable side reaction, it has been reported that triisopropylsilyloxy carbonyl (Tsoc)-amino acid/amino acid fluoride strategy is effective.¹⁸ In this strategy, Tsoc-protected amino acid is introduced to the amino group of C-terminal Pro on the resin. Then, Fmoc-amino acid fluoride of 3rd residue and a catalytic amount of tetra-*n*-butylammonium fluoride (TBAF) are added to the resin. The fluoride ion removes the Tsoc group generating a free amino group, which is immediately acylated by the amino acid fluoride with simultaneous regeneration of a fluoride ion. For use of this strategy, Tsoc-Val pentafluorophenyl ester (Tsoc-Val-OPfp) was prepared at first by Ohfuné's conditions.¹⁹

Since the disulfide bond arrangement in IAG has not yet been determined, we decided to synthesize two possible disulfide isomers, the insulin-type and the AGH-type. In *M. japonicus* IAG, there are one intrachain disulfide in the A chain and two interchain disulfides between A and B chains. To form disulfide bonds regioselectively, three orthogonal Cys protecting groups, trityl (Trt), *p*-methoxybenzyl (MeOBn) and acetamidomethyl (Acm) groups, were used. For synthesizing A chain of the insulin-type disulfide isomer, Fmoc-Cys(MeOBn)-OH and Fmoc-Cys(Acm)-OH were used at Cys^{A26} and Cys^{A9}, respectively, and the other Cys sites at the positions 8 and 17, Fmoc-Cys(Trt)-OH was used for forming the intrachain disulfide at first. On the other hand, to form the disulfide bonds as AGH-type, Fmoc-Cys(Acm)-OH and Fmoc-Cys(Trt)-OH were used at the positions 8 and 9, respectively, in which these Cys derivatives were used oppositely for synthesizing the insulin-type isomer.

As mentioned in Introduction section, the carbohydrate structure at Asn^{B2} is still remained unclear. To investigate the influence of carbohydrate moiety on the peptide conformation and the biological activity, we decided to synthesize both nonglycosylated and GlcNAc-attached IAGs. For introduction of GlcNAc moiety into the peptide, Fmoc-Asn(GlcNAcBn₃)-OH was used in Fmoc-SPPS.

2.2. Chemical synthesis of IAG

The B chain of *M. japonicus* IAG was synthesized by the ordinary Fmoc-SPPS strategy at first. After the chain assembly using a

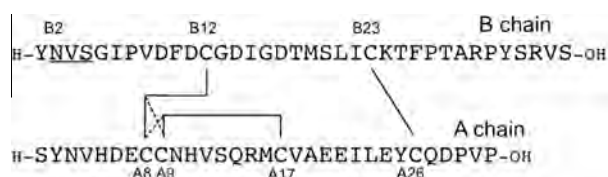


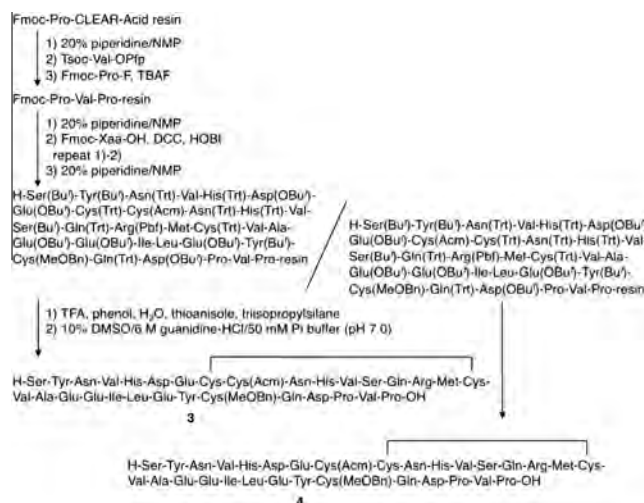
Figure 1. Amino acid sequence of *Marsupinaeus japonicus* IAG. Solid lines and dotted lines indicate the disulfide bonds of insulin-type and AGH-type isomers, respectively. Underline represents the putative N-glycosylation motif.

nonglycosylated Asn derivative at Asn^{B2}, the crude peptide was cleaved from solid support by a trifluoroacetic acid (TFA) cocktail treatment, and purified by reversed-phase (RP)-HPLC, giving nonglycosylated B chain **1** in 13% yield. To obtain GlcNAc-attached B chain **2**, the B chain was synthesized again using the GlcNAc-Asn derivative at Asn^{B2} site. After the cleavage of peptide from the resin by the TFA cocktail treatment, benzyl groups used for the protection of carbohydrate moiety were removed by the low-acidity trifluoromethanesulfonic acid (TfOH) treatment.²⁰ The desired glycopeptide **2** was obtained by the RP-HPLC purification in 11% yield.

Next, we synthesized two types of A chains, Cys⁹(Acm), Cys²⁶(MeOBn)-A chain (A chain for the insulin-type isomer) **3** and Cys⁸(Acm), Cys²⁶(MeOBn)-A chain (A chain for the AGH-type isomer) **4**, by Fmoc-SPPS strategy as shown in Scheme 1. Starting from Fmoc-Pro-CLEAR-Acid resin, Fmoc group was removed by piperidine treatment, and then Tsoc-Val-OPfp was introduced to the resin. The third amino acid was introduced using Fmoc-Pro-F in the presence of a catalytic amount of TBAF, giving Fmoc-Pro-Val-Pro-resin. Then, the peptide chain was elongated by the Fmoc-SPPS strategy, and two types of protected peptide resins were obtained. After cleaving peptides from the resins, the crude peptides were separately dissolved in a phosphate buffer containing 6 M guanidine-HCl, and the intramolecular disulfide bond was formed by oxidation using dimethyl sulfoxide (DMSO). The insulin-type and the AGH-type A chains, **3** and **4**, were obtained by RP-HPLC purification in 5.2% and 5.0% yields, respectively.

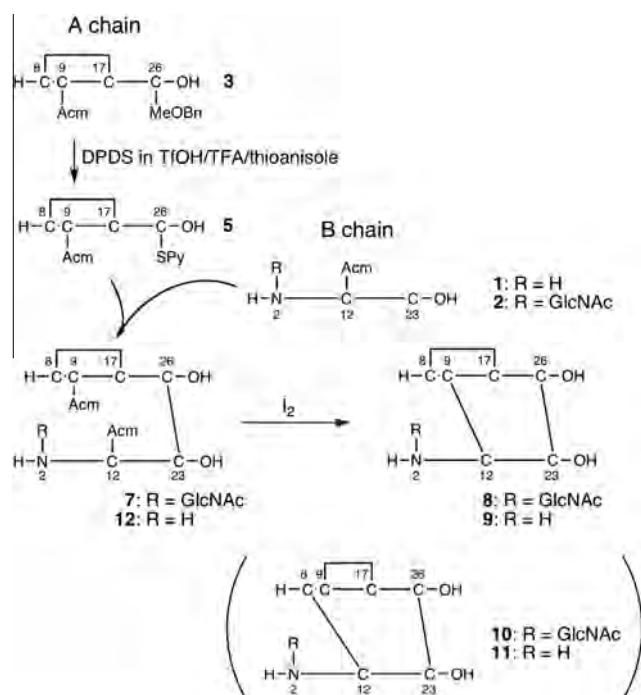
The interchain disulfide bonds were formed regioselectively by the strategy shown in Scheme 2. To synthesize the insulin-type isomer, MeOBn group attached at Cys^{A26} of peptide **3** was removed by TfOH/TFA treatment. By the addition of 2,2'-dipyridyl disulfide (DPDS) in the deprotection reagent, the deprotected Cys side chain was simultaneously pyridylsulfenylated, giving Cys⁹(Acm), Cys²⁶(SPy)-A chain **5** in 93% yield. Cys⁸(Acm), Cys²⁶(SPy)-A chain **6** was also derived from peptide **4** by the same manner as for peptide **5** in 93% yield.

The first interchain disulfide bond was formed by mixing equimolar pyridylsulfenylated A chain (**5** or **6**) and nonglycosylated or GlcNAc-attached B chain (**1** or **2**) in a sodium bicarbonate aqueous solution. To obtain the GlcNAc-attached insulin-type isomer intermediate **7**, peptides **2** and **5** were mixed in the aqueous solution. In the RP-HPLC analysis, both A and B chains were almost completely consumed within an hour, and a new peak corresponding to the desired heterodimeric peptide **7** appeared (Fig. 2). After quenching



Scheme 1. Synthetic procedure of the A chain.

the reaction with adding acetic acid, peptide **7** was obtained by RP-HPLC purification in 67% yield. The second interchain disulfide bond was then formed by the iodine oxidation reaction under



Scheme 2. Synthetic route for IAGs with the insulin-type disulfide bonds **8** and **9**, and the schematic structures of AGH-type isomers **10** and **11**.

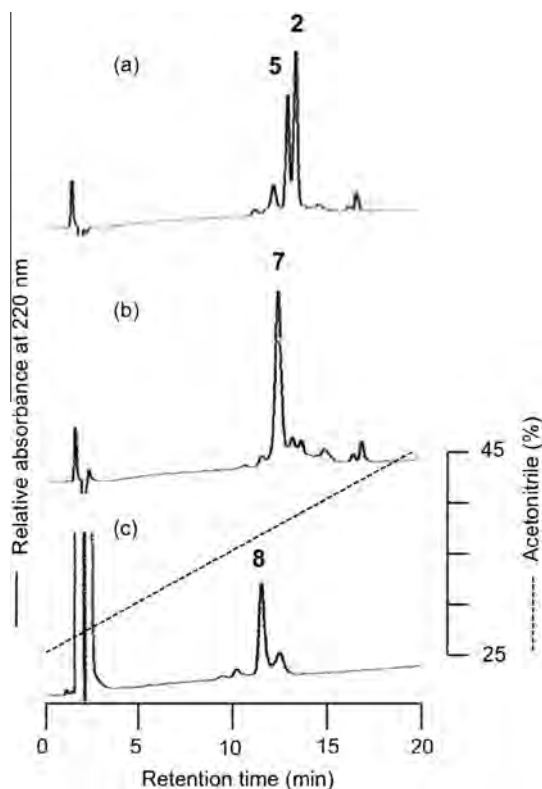


Figure 2. Reversed-phase HPLC elution profiles in regioselective disulfide formation reactions of insulin-type isomer carrying GlcNAc moiety **8**. (a) Reaction mixture of peptides **2** and **5** (0 h). (b) 1 h. **7**, Asn^{B2}(GlcNAc), Cys^{A9,B12}(AcM)-IAG. (c) After the iodine oxidation. Elution condition: column, Inertsil ODS-3 (4.6φ × 150 mm, GL Science, Japan) at a flow rate of 1 mL/min.

acidic conditions, giving the glycosylated insulin-type isomer **8** in 51% yield. The nonglycosylated insulin-type isomer **9** was also obtained from peptides **1** and **5** by the same manner as for peptide **8**. The GlcNAc-attached and nonglycosylated AGH-type isomers **10** and **11** were also synthesized from peptides **2** and **6** and from peptides **1** and **6**, respectively, by essentially the same manner as for peptide **8**. (The isolated yields of peptides **9–11** and those intermediates **12–14** are described in Section 4.)

2.3. Circular dichroism spectral analysis

In order to confirm the conformation of synthetic IAG peptides **8–11**, their circular dichroism (CD) spectra in a neutral aqueous solution were recorded. As shown in Figure 3, the spectral patterns of insulin-type isomers **8** and **9** (Fig. 3a) were clearly different from those of AGH-type isomers **10** and **11** (Fig. 3b). Especially, the insulin-type isomers showed the spectra with negatively swelled shape nearby 220 nm, which is the typical pattern for the α -helical structure, indicating that the disulfide bond arrangement affected the conformation of IAG. The GlcNAc moiety attached at Asn^{B2} also gave some effects on the CD spectral pattern at the region of 200–220 nm, and the spectra of **8** and **10** (gray lines in Fig. 3) were slightly different from those of **9** and **11** (black lines in Fig. 3), respectively.

The spectral patterns of the synthetic IAGs are similar to those of the other insulin-family peptides.^{21–23} The CD spectra of *A. vulgare* AGH and its disulfide isomer have been reported.¹⁵ Interestingly, IAG with insulin-type disulfide bonds showed the spectral pattern similar to that of *A. vulgare* AGH with AGH-type disulfide bonds rather than that of AGH with the insulin-type disulfide bonds.

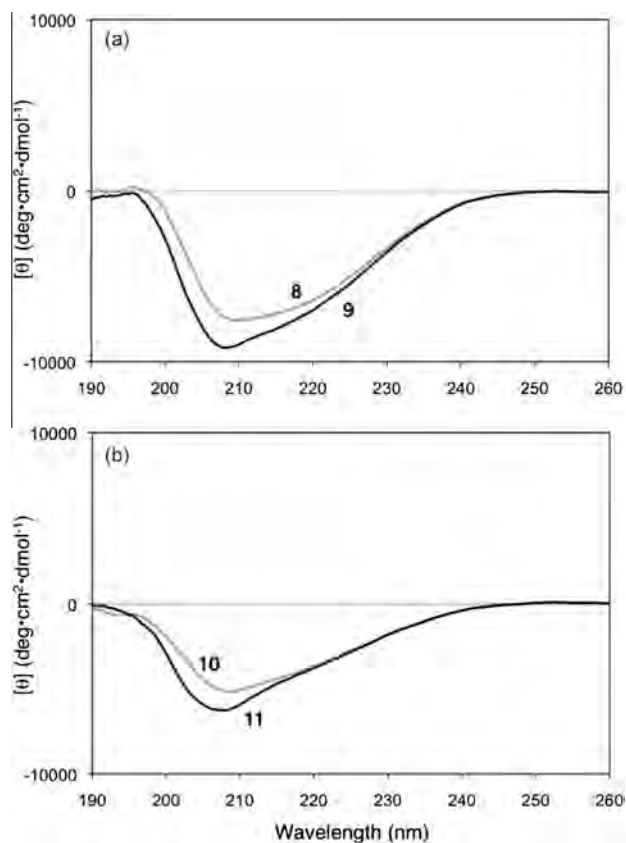


Figure 3. CD spectra of the synthetic IAGs **8–11**. (a) IAG with an insulin-type disulfide bond arrangement. (b) IAG with an AGH-type disulfide bond arrangement. Black and gray lines represent nonglycosylated and glycosylated IAGs, respectively.

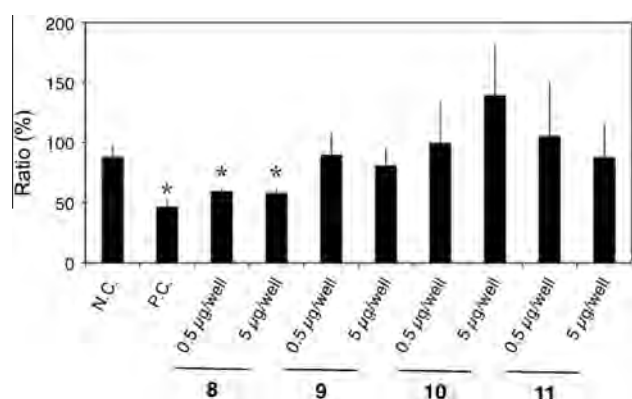


Figure 4. Biological activity of the synthetic IAGs. N.C., negative control; P.C., Pej-SGP-VII (1 sinus gland equivalent) as a positive control. Values are expressed as means \pm SE ($n = 5$). Asterisks indicate the significant differences from the value of negative control ($P < 0.05$).

2.4. Biological activity of the synthetic peptides

In the red-claw crayfish *C. quadricarinatus*, intersex animals are found in both wild and cultured populations. The removal of the androgenic glands from the intersex crayfish induced vitellogenin gene expression, indicating that the gene is negatively regulated by AGH.²⁴ Therefore, in this study, the biological activities of the synthetic IAGs were assessed by an in vitro assay system using vitellogenin gene expression level in the female ovaries as an index, which was previously developed for measuring vitellogenesis-inhibiting hormone activity.²⁵

The biological activity of each sample was assessed at the two dosage levels, 5 and 0.5 $\mu\text{g}/\text{well}$. The insulin-type isomer carrying GlcNAc at the B chain **8** suppressed the vitellogenin gene expression at both doses, and the values were significantly different from that of negative control ($P < 0.05$). However, the nonglycosylated insulin-type isomer **9** showed no activity at any doses. On the other hand, the AGH-type disulfide isomers **10** and **11** did not suppress the vitellogenin gene expression at any dosage levels tested regardless of its N-linked carbohydrate structure. These results strongly suggest that the native IAG peptide has the disulfide bond arrangement same as that of the vertebrate insulin, and its B chain is glycosylated (see Fig. 4).

In *A. vulgare* AGH, only AGH-type disulfide isomer showed AGH activity in vivo, and the insulin-type isomer did not. These results are opposite to our results obtained in this study using *M. japonicus* IAG. Interestingly, the carbohydrate moiety was essential for the biological activity in both peptides, although the glycosylation site is different from each other; the A chain was glycosylated in AGH whereas the glycosylation site existed in the IAG B chain. In the most decapod IAG sequences, putative N-glycosylation sites are found in A and/or B chains with some exceptions; IAGs from the shrimp, *Palaemon pacificus*, and from the blue crab, *Callinectes sapidus*, have no putative N-glycosylation site in their sequence. Therefore, it is difficult to consider that significance of carbohydrate moiety in IAG for its biological function is strictly conserved during the molecular evolution pathway of the crustacean insulin-family peptides. AGH and IAG receptors may get the binding affinity with the glycosylated ligand in independent manner.

3. Conclusion

We have synthesized two disulfide isomers of nonglycosylated or GlcNAc-attached *M. japonicus* IAGs. The CD spectra of these peptides indicated that the disulfide bond arrangement affected the conformation of IAG. IAG carrying GlcNAc with the insulin-type

disulfide bonds showed the obvious activity in vitro, strongly suggesting that the native IAG undergoes the glycosylation and has the insulin-type disulfide bond arrangement. This is the first report for the functional analysis of crustacean IAG peptide.

4. Experimental procedure

4.1. General

MALDI-TOF mass spectra were recorded using a Voyager-DE PRO spectrometer (Applied Biosystems, CA). Amino acid composition was determined using a LaChrom amino acid analyzer (Hitachi, Tokyo, Japan) after hydrolysis with a 6 M HCl solution at 150 $^{\circ}\text{C}$ for 2 h in a vacuum-sealed tube. Circular dichroism (CD) spectra were measured with a Jasco J-820 spectropolarimeter (JASCO, Tokyo, Japan) at room temperature with a 2-mm path length cell using a phosphate buffer (50 mM, pH 7.0) as a solvent.

4.2. Cys¹²(Acm)-B chain 1

Fmoc-Ser(Bu^t)-Wang resin (0.70 mmol/g, 140 mg, 0.10 mmol) was subjected to microwave-assisted peptide synthesis using a Liberty peptide synthesizer (CEM, NC), and H-Tyr(Bu^t)-Asn(Trt)-Val-Ser(Bu^t)-Gly-Ile-Pro-Val-Asp(OBu^t)-Phe-Asp(OBu^t)-Cys(Acm)-Gly-Asp(OBu^t)-Ile-Gly-Asp(OBu^t)-Thr(Bu^t)-Met-Ser(Bu^t)-Leu-Ile-Cys(Trt)-Lys(Boc)-Thr(Bu^t)-Phe-Pro-Thr(Bu^t)-Ala-Arg(Pbf)-Pro-Tyr(Bu^t)-Ser(Bu^t)-Arg(Pbf)-Val-Ser(Bu^t)-resin (540 mg) was obtained. A part of the resin (200 mg) was treated with a TFA cocktail (TFA/thioanisole/phenol/H₂O/triisopropylsilane, 82.5/5/5/5/2.5, 3 mL) at room temperature for 2 h. TFA was removed under Ar stream and the peptide was precipitated with diethyl ether. After washing twice with ether, the precipitate was dried in vacuo. The crude peptide was purified by RP-HPLC on an Inertsil ODS-3 column (GL science, Tokyo, Japan) with a linear gradient of acetonitrile containing 0.1% TFA to give peptide **1** (4.9 μmol , 13% yield). MALDI-TOF mass, found: m/z 3995.5, calcd: 3995.9 for (M+H)⁺. Amino acid analysis: Asp_{5.27}Thr_{2.88}Ser_{3.25}Pro_{2.95}Gly₃Ala_{0.85}Val_{3.12}Met_{0.97}Ile_{2.97}Leu_{1.12}Tyr_{2.09}Phe_{2.12}Lys_{1.09}Arg_{1.66}.

4.3. Asn²(GlcNAc), Cys¹²(Acm)-B chain 2

Fmoc-Ser(Bu^t)-Wang resin (0.31 mmol/g, 810 mg, 0.25 mmol) was swelled in 1-methyl-2-pyrrolidinone (NMP) for 30 min, and was treated with 20% piperidine/NMP for 5 and 15 min. After washing with NMP, Fmoc-Val-OH, which was prepared by mixing Fmoc-Val-OH (1.0 mmol), 1 M *N,N*-dicyclohexylcarbodiimide (DCC)/NMP (1.5 mL) and 1 M 1-hydroxybenzotriazole (HOBt)/NMP (1.5 mL) at room temperature for 30 min, was added and the reaction mixture was mixed with vortex at 50 $^{\circ}\text{C}$ for 1 h. The resin was washed with NMP and 50% dichloromethane (DCM)/methanol, treated with 10% acetic anhydride (Ac₂O)/5% *N,N*-diisopropylethylamine (DIEA)/NMP for 5 min, and washed with NMP. The peptide chain was elongated in essentially the same manner as described above, and H-Tyr(Bu^t)-Asn(GlcNAcBn₃)-Val-Ser(Bu^t)-Gly-Ile-Pro-Val-Asp(OBu^t)-Phe-Asp(OBu^t)-Cys(Acm)-Gly-Asp(OBu^t)-Ile-Gly-Asp(OBu^t)-Thr(Bu^t)-Met-Ser(Bu^t)-Leu-Ile-Cys(Trt)-Lys(Boc)-Thr(Bu^t)-Phe-Pro-Thr(Bu^t)-Ala-Arg(Pbf)-Pro-Tyr(Bu^t)-Ser(Bu^t)-Arg(Pbf)-Val-Ser(Bu^t)-resin (2.03 g) was obtained. A part of the resin (100 mg) was treated with the TFA cocktail (2 mL) at room temperature for 2 h. TFA was removed under Ar stream and the peptide was precipitated with diethyl ether. After washing twice with ether, the precipitate was dried in vacuo. The precipitant was then dissolved in TFA/dimethyl sulfide/*m*-cresol (5/3/1, 900 μL), and cooled to -15 $^{\circ}\text{C}$. Trifluoromethanesulfonic acid (TfOH, 100 μL) was added to the solution, and kept at -15 $^{\circ}\text{C}$ for 2 h. The

peptide was precipitated with cold diethyl ether, and washed twice with ether. After drying in vacuo, the crude peptide was purified by RP-HPLC on an Inertsil ODS-3 column with a linear gradient of acetonitrile containing 0.1% TFA to give peptide **2** (1.4 μ mol, 11% yield). MALDI-TOF mass, found: m/z 4198.5, calcd: 4199.0 for (M+H)⁺. Amino acid analysis: Asp_{5.24}Thr_{2.87}Ser_{3.43}Pro_{3.24}Gly₃Ala_{1.22}Val_{3.14}Met_{0.86}Ile_{2.62}Leu_{1.02}Tyr_{1.99}Phe_{1.99}Lys_{1.02}Arg_{2.09}.

4.4. Cys⁹(Acm), Cys²⁶(MeOBn)-A chain 3

Fmoc-Pro-CLEAR acid resin (0.29 mmol/g, 1030 mg, 0.30 mmol) was swelled in NMP for 30 min, and was treated with 20% piperidine/NMP for 5 and 15 min. After washing with tetrahydrofuran (THF), Tsoc-Val-OPfp (290 mg, 0.60 mmol)/THF (4 mL) solution was added and the reaction mixture was mixed with vortex at 50 °C for 30 min. Another Tsoc-Val-OPfp (290 mg, 0.60 mmol)/THF (4 mL) solution was added to the resin, and the reaction mixture was mixed with vortex at 50 °C for 30 min. After the resin was washed with DCM, 0.2 M Fmoc-Pro-F/DCM solution (6 mL) and 1 M TBAF/THF solution (30 μ L) were added. After mixing with vortex for 30 min at room temperature, the resin was washed with NMP and 50% DCM/methanol, treated with 10% Ac₂O/5% DIEA/NMP for 5 min, and washed with NMP. Then, the resin was treated with 20% piperidine/NMP for 5 and 15 min. After washing with NMP, Fmoc-Asp(OBu^t)-OBt, which was prepared by mixing Fmoc-Asp(OBu^t)-OH (1.2 mmol), 1 M DCC/NMP (1.8 mL) and 1 M HOBt/NMP (1.8 mL) at room temperature for 30 min, was added and the reaction mixture was mixed with vortex at 50 °C for 1 h. The resin was washed with NMP and 50% DCM/methanol, treated with 10% Ac₂O/5% DIEA/NMP for 5 min, and washed with NMP. The peptide chain was elongated in essentially the same manner as described above, and Fmoc-His(Trt)-Val-Ser(Bu^t)-Gln(Trt)-Arg(Pbf)-Met-Cys(Trt)-Val-Ala-Glu(OBu^t)-Glu(OBu^t)-Ile-Leu-Glu(OBu^t)-Tyr-(Bu^t)-Cys(MeOBn)-Gln(Trt)-Asp(OBu^t)-Pro-Val-Pro-resin was obtained. Using a half of the resin, the peptide chain was further elongated in essentially the same manner as described above, and H-Ser(Bu^t)-Tyr(Bu^t)-Asn(Trt)-Val-His(Trt)-Asp(OBu^t)-Glu(OBu^t)-Cys(Trt)-Cys(Acm)-Asn(Trt)-His(Trt)-Val-Ser(Bu^t)-Gln(Trt)-Arg(Pbf)-Met-Cys(Trt)-Val-Ala-Glu(OBu^t)-Glu(OBu^t)-Ile-Leu-Glu(OBu^t)-Tyr-(Bu^t)-Cys(MeOBn)-Gln(Trt)-Asp(OBu^t)-Pro-Val-Pro-resin (1.28 g) was obtained. A part of the resin (100 mg) was treated with the TFA cocktail (2 mL) at room temperature for 2 h. TFA was removed under Ar stream and the peptide was precipitated with diethyl ether. After washing twice with ether, the precipitate was dried in vacuo. The crude peptide was dissolved in 6 M guanidine-HCl/50 mM phosphate buffer (pH 7.0, 9 mL), and dimethyl sulfoxide (DMSO, 1 mL) was added to the solution. The mixture was gently stirred for 2 d, and the insoluble material was removed by filtration. The crude peptide was purified by RP-HPLC on an Inertsil ODS-3 column with a linear gradient of acetonitrile containing 0.1% TFA to give peptide **3** (610 nmol, 5.2% yield). MALDI-TOF mass, found: m/z 3798.9, calcd: 3799.6 for (M+H)⁺. Amino acid analysis: Asp_{3.70}Ser_{1.48}Glu_{5.27}Pro_{2.06}Ala₁Val_{3.51}Met_{0.68}Ile_{0.87}Leu_{0.93}Tyr_{1.78}His_{1.75}Arg_{0.77}.

4.5. Cys⁹(Acm), Cys²⁶(MeOBn)-A chain 5

Peptide **3** (610 nmol) was dissolved in TFA (400 μ L) and thioanisol (40 μ L) containing 2,2'-dipyridyl disulfide (DPDS, 4.5 mg), and cooled to -10 °C. TFOH (20 μ L) was added to the solution, and the mixture was kept at -10 °C for 5 min. The crude peptide was precipitated with diethyl ether, washed twice with ether, and dried in vacuo. The residue was applied to the gel filtration HPLC using a TSKgel G3000PW_{XL} column (7.8 ϕ × 300 mm, Tosoh) with 0.1% TFA/50% acetonitrile aqueous solution as a solvent at a flow rate of 0.5 mL/min, to give peptide **5** (560 nmol, 93%). MALDI-TOF mass,

found: m/z 3788.0, calcd: 3788.5 for (M+H)⁺. Amino acid analysis: Asp_{3.59}Ser_{1.47}Glu_{5.16}Pro_{2.93}Ala₁Val_{3.38}Met_{0.69}Ile_{0.86}Leu_{0.90}Tyr_{1.80}His_{1.76}Arg_{0.87}.

4.6. Asn^{B2}(GlcNAc), Cys^{A9,B12}(Acm)-IAG 7

Peptides **2** (160 nmol) and **5** (160 nmol) were dissolved in 40% acetonitrile/50 mM sodium bicarbonate aqueous solution (2 mL) and the solution was gently stirred at room temperature for 1 h. The reaction was quenched by adding acetic acid (100 μ L), and the mixture was purified by RP-HPLC on an Inertsil ODS-3 column with a linear gradient of acetonitrile containing 0.1% TFA to give peptide **7** (88 nmol, 56% yield). MALDI-TOF mass, found: m/z 7883.7, calcd: 7880.7 for (M+H)⁺ (average). Amino acid analysis: Asp_{9.31}Thr_{2.91}Ser_{5.11}Glu_{5.90}Pro_{5.36}Gly₃Ala_{2.09}Val_{6.96}Met_{1.59}Ile_{3.64}Leu_{1.96}Tyr_{3.89}Phe_{1.90}Lys_{0.99}His_{1.90}Arg_{3.02}.

4.7. Asn^{B2}(GlcNAc)-IAG with insulin-type disulfides 8

Peptide **7** (88 nmol) was dissolved in distilled water (750 μ L), and the solution was added dropwise to methanol (3 mL) containing 20 mM I₂/methanol (90 μ L) and 6 M HCl (30 μ L). The reaction was quenched by adding an ascorbic acid aqueous solution until the brownish color was abolished. The mixture was purified by RP-HPLC on an Inertsil ODS-3 column with a linear gradient of acetonitrile containing 0.1% TFA to give peptide **8** (53 nmol, 60% yield). MALDI-TOF mass, found: m/z 7734.3, calcd: 7736.6 for (M+H)⁺ (average). Amino acid analysis: Asp_{9.76}Thr_{3.00}Ser_{5.49}Glu_{6.18}Pro_{5.34}Gly₃Ala_{2.04}Val_{7.36}Met_{1.91}Ile_{3.80}Leu_{2.02}Tyr_{4.09}Phe_{2.07}Lys_{1.05}His_{1.74}Arg_{3.05}.

4.8. Cys^{A9,B12}(Acm)-IAG 12

Peptides **1** (440 nmol) and **5** (440 nmol) were dissolved in 40% acetonitrile/50 mM sodium bicarbonate aqueous solution (5 mL) and the solution was gently stirred at room temperature for 1 h. The reaction was quenched by adding acetic acid (250 μ L), and the mixture was purified by RP-HPLC on an Inertsil ODS-3 column with a linear gradient of acetonitrile containing 0.1% TFA to give peptide **12** (290 nmol, 67% yield). MALDI-TOF mass, found: m/z 7678.8, calcd: 7677.5 for (M+H)⁺ (average). Amino acid analysis: Asp_{9.48}Thr_{2.97}Ser_{5.25}Glu_{5.95}Pro_{5.49}Gly₃Ala_{2.09}Val_{6.88}Met_{1.57}Ile_{3.87}Leu_{2.10}Tyr_{3.99}Phe_{2.04}Lys_{1.02}His_{1.90}Arg_{2.85}.

4.9. IAG with insulin-type disulfides 9

Peptide **12** (290 nmol) was dissolved in distilled water (2 mL), and the solution was added dropwise to methanol (8 mL) containing 20 mM I₂/methanol (240 μ L) and 6 M HCl (80 μ L). The reaction was quenched by adding an ascorbic acid aqueous solution until the brownish color was abolished. The mixture was purified by RP-HPLC on an Inertsil ODS-3 column with a linear gradient of acetonitrile containing 0.1% TFA to give peptide **9** (150 nmol, 51% yield). MALDI-TOF mass, found: m/z 7533.0, calcd: 7533.4 for (M+H)⁺ (average). Amino acid analysis: Asp_{9.34}Thr_{2.86}Ser_{5.15}Glu_{5.60}Pro_{5.12}Gly₃Ala_{1.98}Val_{6.88}Met_{1.71}Ile_{3.79}Leu_{2.11}Tyr_{4.10}Phe_{2.14}Lys_{1.03}His_{1.88}Arg_{2.83}.

4.10. Cys⁸(Acm), Cys²⁶(MeOBn)-A chain 4

Using the remained half of Fmoc-His(Trt)-Val-Ser(Bu^t)-Gln(Trt)-Arg(Pbf)-Met-Cys(Trt)-Val-Ala-Glu(OBu^t)-Glu(OBu^t)-Ile-Leu-Glu(OBu^t)-Tyr(Bu^t)-Cys(MeOBn)-Gln(Trt)-Asp(OBu^t)-Pro-Val-Pro-resin prepared as described above, peptide chain was elongated manually essentially according to the same manner as described above, and H-Ser(Bu^t)-Tyr(Bu^t)-Asn(Trt)-Val-His(Trt)-Asp(OBu^t)-Glu(OBu^t)-

Cys(Acm)-Cys(Trt)-Asn(Trt)-His(Trt)-Val-Ser(Bu^t)-Gln(Trt)-Arg(Pbf)-Met-Cys(Trt)-Val-Ala-Glu(OBu^t)-Glu(OBu^t)-Ile-Leu-Glu(OBu^t)-Tyr-(Bu^t)-Cys(MeOBn)-Gln(Trt)-Asp(OBu^t)-Pro-Val-Pro-resin (1.27 g) was obtained. A part of the resin (100 mg) was treated with the TFA cocktail (2 mL) at room temperature for 2 h. TFA was removed under Ar stream and the peptide was precipitated with diethyl ether. After washing twice with ether, the precipitate was dried in vacuo. The intrachain disulfide was formed according to the same manner as for peptide **3**. The crude peptide was purified by RP-HPLC on an Inertsil ODS-3 column with a linear gradient of acetonitrile containing 0.1% TFA to give peptide **4** (590 nmol, 5.0% yield). MALDI-TOF mass, found: m/z 3799.3, calcd: 3799.6 for (M+H)⁺. Amino acid analysis: Asp_{4.19}Ser_{1.64}Glu_{5.92}Pro_{2.37}Ala₁Val_{3.99}Met_{0.78}Ile_{1.01}Leu_{1.07}Tyr_{2.02}His_{1.96}Arg_{1.01}.

4.11. Cys⁸(Acm), Cys²⁶(SPy)-A chain **6**

Peptide **4** (590 nmol) was dissolved in TFA (400 μL) and thioanisole (40 μL) containing DPDS (4.5 mg), and cooled to -10 °C. TfOH (20 μL) was added to the solution, and the mixture was kept at -10 °C for 5 min. The crude peptide was precipitated with diethyl ether, washed twice with ether, and dried in vacuo. The residue was applied to the gel filtration HPLC using a TSKgel G3000PW_{XL} column (7.8φ × 300 mm, Tosoh) with 0.1% TFA/50% acetonitrile aqueous solution as a solvent at a flow rate of 0.5 mL/min, to give peptide **6** (550 nmol, 93%). MALDI-TOF mass, found: m/z 3788.1, calcd: 3788.5 for (M+H)⁺. Amino acid analysis: Asp_{3.94}Ser_{1.60}Glu_{5.68}Pro_{2.55}Ala₁Val_{3.72}Met_{0.89}Ile_{0.92}Leu_{0.96}Tyr_{1.91}His_{1.89}Arg_{1.05}.

4.12. Asn^{B2}(GlcNAc), Cys^{A8,B12}(Acm)-IAG **13**

Peptides **2** (160 nmol) and **6** (160 nmol) were dissolved in 40% acetonitrile/50 mM sodium bicarbonate aqueous solution (5 mL) and the solution was gently stirred at room temperature for 1 h. The reaction was quenched by adding acetic acid (250 μL), and the mixture was purified by RP-HPLC on an Inertsil ODS-3 column with a linear gradient of acetonitrile containing 0.1% TFA to give peptide **13** (96 nmol, 58% yield). MALDI-TOF mass, found: m/z 7877.7, calcd: 7880.7 for (M+H)⁺ (average). Amino acid analysis: Asp_{9.28}Thr_{2.88}Ser_{5.16}Glu_{5.62}Pro_{5.34}Gly₃Ala_{2.06}Val_{7.00}Met_{1.65}Ile_{3.72}Leu_{2.01}Tyr_{4.01}Phe_{2.05}Lys_{1.02}His_{1.84}Arg_{2.68}.

4.13. Asn^{B2}(GlcNAc)-IAG with AGH-type disulfides **10**

Peptide **13** (96 nmol) was dissolved in distilled water (750 μL), and the solution was added dropwise to methanol (3 mL) containing 20 mM I₂/methanol (90 μL) and 6 M HCl (30 μL). The reaction was quenched by adding an ascorbic acid aqueous solution until the brownish color was abolished. The mixture was purified by RP-HPLC on an Inertsil ODS-3 column with a linear gradient of acetonitrile containing 0.1% TFA to give peptide **10** (59 nmol, 61% yield). MALDI-TOF mass, found: m/z 7736.2, calcd: 7736.6 for (M+H)⁺ (average). Amino acid analysis: Asp_{9.31}Thr_{3.00}Ser_{5.24}Glu_{6.08}Pro_{4.97}Gly₃Ala_{1.87}Val_{6.97}Met_{1.73}Ile_{3.73}Leu_{1.98}Tyr_{3.95}Phe_{1.95}Lys_{1.02}His_{1.87}Arg_{2.65}.

4.14. Cys^{A8,B12}(Acm)-IAG **14**

Peptides **1** (440 nmol) and **6** (440 nmol) were dissolved in 40% acetonitrile/50 mM sodium bicarbonate aqueous solution (5 mL) and the solution was gently stirred at room temperature for 1 h. The reaction was quenched by adding acetic acid (250 μL), and the mixture was purified by RP-HPLC on an Inertsil ODS-3 column with a linear gradient of acetonitrile containing 0.1% TFA to give peptide **14** (290 nmol, 67% yield). MALDI-TOF mass, found: m/z 7678.6 calcd: 7677.5 for (M+H)⁺ (average). Amino acid analysis:

Asp_{9.29}Thr_{2.98}Ser_{5.15}Glu_{6.12}Pro_{5.00}Gly₃Ala_{2.05}Val_{6.92}Met_{1.12}Ile_{3.93}Leu_{2.11}Tyr_{3.96}Phe_{1.98}Lys_{1.05}His_{1.92}Arg_{2.72}.

4.15. IAG with AGH-type disulfides **11**

Peptide **14** (290 nmol) was dissolved in distilled water (2 mL), and the solution was added dropwise to methanol (8 mL) containing 20 mM I₂/methanol (240 μL) and 6 M HCl (90 μL). The reaction was quenched by adding an ascorbic acid aqueous solution until the brownish color was abolished. The mixture was purified by RP-HPLC on an Inertsil ODS-3 column with a linear gradient of acetonitrile containing 0.1% TFA to give peptide **11** (150 nmol, 60% yield). MALDI-TOF mass, found: m/z 7535.1, calcd: 7533.4 for (M+H)⁺ (average). Amino acid analysis: Asp_{9.34}Thr_{2.86}Ser_{5.15}Glu_{5.60}Pro_{5.12}Gly₃Ala_{1.98}Val_{6.88}Met_{1.71}Ile_{3.79}Leu_{2.11}Tyr_{4.10}Phe_{2.14}Lys_{1.03}His_{1.88}Arg_{2.83}.

4.16. Bioassay

Immature *M. japonicus* females serving as ovarian fragment donors were purchased from an aquaculture company in Kagoshima Prefecture, Japan. Prawns ranged from 16.3 to 19.8 g (average 18.0 g) in body weight and from 0.31% to 0.88% (average 0.73%) in gonadosomatic index. Pej-SGP-VII, which is one of six VIHs in *M. japonicus*, was purified from the sinus gland extract using the Sep-Pak C18 cartridge and reversed-phase HPLC as described previously,^{26,27} and one sinus gland equivalent of this peptide was used as a positive control in this assay. For the negative control, the ovarian fragments were cultured in the medium alone. The biological activity of the synthetic peptides was assessed at the dosage levels of 0.5 and 5 μg/200 μL culture medium. Culture of ovarian fragments, total RNA extraction, and quantitative real-time PCR were performed according to the methods described previously.²⁵ Student's *t*-test was used to analyze statistical differences between the values for the zero control and those for the experimental groups.

Acknowledgments

This work was supported in part by grant-in-aid from Kato Memorial Bioscience Foundation, by Research and Study Program of Tokai University Educational System General Research Organization, by Grants-in-Aid for Scientific Research (No. 25850143) from the Ministry of Education, Culture, Sport, Science and Technology of Japan, and by the SUNBOR GRANT from the Suntory Institute for Bioorganic Research.

References and notes

- Charniaux-Cotton, H. C. R. *Acad. Sci. Paris* **1954**, 239, 780–782.
- Okuno, A.; Hasegawa, Y.; Nagasawa, H. *Zool. Sci.* **1997**, 14, 837–842.
- Martin, G.; Sorokine, O.; Moniatte, M.; Bulet, P.; Hetru, C.; Dorsselaer, A. V. *Eur. J. Biochem.* **1999**, 262, 727.
- Okuno, A.; Hasegawa, Y.; Ohira, T.; Katakura, Y.; Nagasawa, H. *Biochem. Biophys. Res. Commun.* **1999**, 264, 419.
- Ohira, T.; Hasegawa, Y.; Tominaga, S.; Okuno, A.; Nagasawa, H. *Zool. Sci.* **2003**, 20, 75.
- Cerveau, N.; Bouchon, D.; Bergès, T.; Grève, P. *Gene* **2014**, 540, 71.
- Manor, R.; Weil, S.; Oren, S.; Glazer, L.; Afalo, E. D.; Ventura, T.; Chalifa-Caspi, V.; Lapidot, M.; Sagi, A. *Gen. Comp. Endocrinol.* **2007**, 150, 326.
- Ventura, T.; Manor, R.; Afalo, E. D.; Weil, S.; Raviv, S.; Glazer, L.; Sagi, A. *Endocrinology* **2009**, 150, 1278.
- Banzai, K.; Ishizaka, N.; Asahina, K.; Suito, K.; Izumi, S.; Ohira, T. *Fish. Sci.* **2011**, 77, 329.
- Chung, J. S.; Manor, R.; Sagi, A. *Gen. Comp. Endocrinol.* **2011**, 173, 4.
- Banzai, K.; Izumi, S.; Ohira, T. *JARQ-Jpn. Agr. Res. Q.* **2012**, 46, 105.
- Ma, K. Y.; Lin, J. Y.; Guo, S. Z.; Chen, Y.; Li, J. L.; Qiu, G. F. *Gen. Comp. Endocrinol.* **2013**, 185, 90.
- Rosen, O.; Manor, R.; Weil, S.; Gafni, O.; Afalo, E. D.; Ventura, T.; Sagi, A. *PLoS One* **2010**, 5, e15281.

14. Ventura, T.; Manor, R.; Afalo, E. D.; Weil, A.; Rosen, O.; Sagi, A. *Biol. Reprod.* **2012**, *86*, 90.
15. Katayama, H.; Hojo, H.; Ohira, T.; Ishii, A.; Nozaki, T.; Goto, K.; Nakahara, Y.; Takahashi, T.; Hasegawa, Y.; Nagasawa, H.; Nakahara, Y. *Biochemistry* **2010**, *49*, 1798.
16. Okuno, A.; Hasegawa, Y.; Nishiyama, M.; Ohira, T.; Ko, R.; Kurihara, M.; Matsumoto, S.; Nagasawa, H. *Peptides* **2002**, *23*, 567.
17. Fields, G. B.; Noble, R. L. *Int. J. Pept. Prot. Res.* **1990**, *35*, 161.
18. Sakamoto, K.; Nakahara, Y.; Ito, Y. *Tetrahedron Lett.* **2002**, *43*, 1515.
19. Sakaitani, M.; Ohfuné, Y. *J. Org. Chem.* **1990**, *55*, 870.
20. Tam, J. P.; Heath, W. F.; Merrifield, R. B. *J. Am. Chem. Soc.* **1986**, *108*, 5242.
21. Maruyama, K.; Nagata, K.; Tanaka, M.; Nagasawa, H.; Isogai, A.; Ishizaki, H.; Suzuki, A. *J. Protein Chem.* **1992**, *11*, 1.
22. Hua, Q.-X.; Jia, W.; Frank, B. H.; Phillips, N. F. B.; Weiss, M. A. *Biochemistry* **2002**, *41*, 14700.
23. Hua, Q.-X.; Mayer, J. P.; Jia, W.; Zhang, J.; Weiss, M. A. *J. Biol. Chem.* **2006**, *281*, 28131.
24. Abdu, U.; Davis, C.; Khalaila, I.; Sagi, A. *Gen. Comp. Endocrinol.* **2002**, *127*, 263.
25. Tsutsui, N.; Katayama, H.; Ohira, T.; Nagasawa, H.; Wilder, M. N.; Aida, K. *Gen. Comp. Endocrinol.* **2005**, *144*, 232.
26. Yang, W. J.; Aida, K.; Nagasawa, H. *Peptides* **1997**, *18*, 479.
27. Nagasawa, H.; Yang, W. J.; Aida, K.; Sonobe, H. In *Peptide Science—Present and Future*; Shimonishi, Y., Ed.; Kluwer Academic Publishers: London, 1999; pp 453–454.

*Isolation of crustacean hyperglycemic hormone-family peptides with vitellogenesis-inhibiting activity from the shiba shrimp *Metapenaeus joyneri**

**Midori Fukushima, Sayaka Kotaka,
Naoaki Tsutsui, Kiyoshi Asahina,
Susumu Izumi & Tsuyoshi Ohira**

Fisheries Science

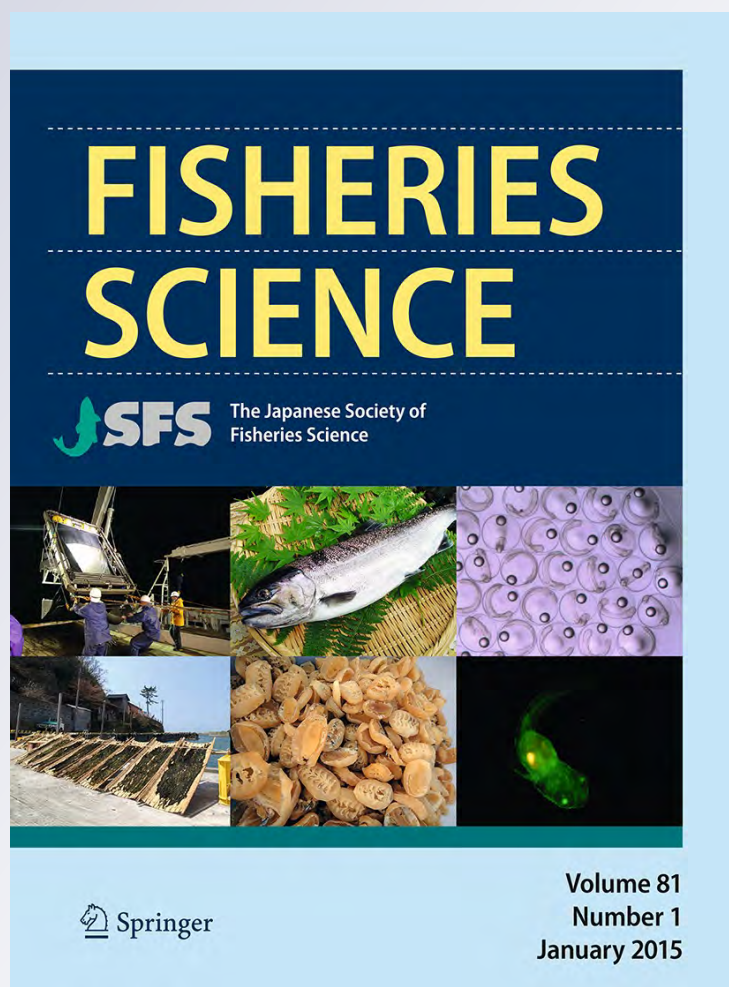
ISSN 0919-9268

Volume 81

Number 1

Fish Sci (2015) 81:65-72

DOI 10.1007/s12562-014-0834-7



 Springer

Your article is protected by copyright and all rights are held exclusively by Japanese Society of Fisheries Science. This e-offprint is for personal use only and shall not be self-archived in electronic repositories. If you wish to self-archive your article, please use the accepted manuscript version for posting on your own website. You may further deposit the accepted manuscript version in any repository, provided it is only made publicly available 12 months after official publication or later and provided acknowledgement is given to the original source of publication and a link is inserted to the published article on Springer's website. The link must be accompanied by the following text: "The final publication is available at link.springer.com".

Isolation of crustacean hyperglycemic hormone-family peptides with vitellogenesis-inhibiting activity from the shiba shrimp *Metapenaeus joyneri*

Midori Fukushima · Sayaka Kotaka · Naoaki Tsutsui · Kiyoshi Asahina · Susumu Izumi · Tsuyoshi Ohira

Received: 24 July 2014 / Accepted: 21 November 2014 / Published online: 5 December 2014
© Japanese Society of Fisheries Science 2014

Abstract Vitellogenesis-inhibiting hormone (VIH) in Crustacea belongs to the crustacean hyperglycemic hormone (CHH)-family. In order to characterize multiple VIH molecules in the shiba shrimp *Metapenaeus joyneri*, four CHH-family peptides designated as Mej-SGP-I, -II, -III, and -IV were purified by reversed-phase HPLC and identified by N-terminal amino acid sequencing. The vitellogenesis-inhibiting activities of these peptides were examined using *ex vivo* incubation of ovarian fragments of the kuruma prawn *Marsupenaeus japonicus*. All of the four peptides significantly reduced vitellogenin mRNA levels in the ovarian fragments. Among them, the inhibitory activity of Mej-SGP-III which was the most abundant CHH-family peptide in the sinus gland was apparent. Therefore, a cDNA encoding the Mej-SGP-III precursor was cloned by RT-PCR coupled with 5'- and 3'-RACE. The mature Mej-SGP-III was found to consist of 72 amino acid residues containing six conserved cysteine residues and possess an amidated C-terminus. The mature Mej-SGP-III showed the highest sequence identity to Pej-SGP-V (one of six CHH/VIHs in *M. japonicus*) and Liv-SGP-G (one of six VIHs in *Litopenaeus vannamei*). These results indicate that Mej-SGP-III is one of the hormones regulating vitellogenesis in *M. joyneri*.

Keywords Crustacea · Crustacean hyperglycemic hormone-family · Vitellogenesis-inhibiting activity · Shiba shrimp · *Metapenaeus joyneri* · Sinus gland

Introduction

Vitellogenesis is an essential physiological event in the reproduction of oviparous animals. Various nutritive materials including carbohydrates, proteins, lipids, minerals, and vitamins destined for utilization in embryonic development are accumulated in the oocytes during this process. In crustaceans, vitellogenesis is negatively regulated by a neuropeptide, vitellogenesis-inhibiting hormone (VIH), which is synthesized in and secreted from the X-organ/sinus gland complex in the eyestalks. Until now, limited numbers of VIH peptides have been characterized by means of *in vivo* administration experiment; in the American lobster *Homarus americanus* [1] and terrestrial isopod *Armadillidium vulgare* [2].

It has been shown that various types of neuropeptides are produced in the X-organ and stored in the sinus gland [3]. Among these neuropeptides, the amino acid sequences of four hormones, VIH, crustacean hyperglycemic hormone (CHH), molt-inhibiting hormone (MIH), and mandibular organ-inhibiting hormone (MOIH), are similar, forming a peptide family referred to as the CHH-family [3]. CHH-family peptides consist of 72–83 amino acid residues including six conserved cysteine residues that form three intramolecular disulfide bonds. It is supposed that CHH-family peptides have evolved from a common ancestral molecule because they have been isolated not only from decapod to isopod crustaceans, but also from insects [4] and a spider [5]. Furthermore, genes for putative CHH-family peptide were found in some nematode species [6].

M. Fukushima · K. Asahina
College of Bioresource Science, Nihon University,
1866 Kameino, Fujisawa, Kanagawa 252-8510, Japan

S. Kotaka · S. Izumi · T. Ohira (✉)
Faculty of Science, Kanagawa University, 2946 Tsuchiya,
Hiratsuka, Kanagawa 259-1293, Japan
e-mail: ohirat-bio@kanagawa-u.ac.jp

N. Tsutsui
Ushimado Marine Institute, Faculty of Science, Okayama
University, Ushimado, Setouchi, Okayama 701-4303, Japan

CHH-family peptides are divided into two subtypes, types I and II. Type II peptide has a glycine residue at position 12 in the mature peptide, whereas type I peptide lacks it at the corresponding position [7, 8]. CHH is classified into type I, and MIH, MOIH and VIH are classified into type II. There are, however, some exceptions, including a type I peptide from *H. americanus* having both hyperglycemic and molt-inhibiting activities [9], a type I peptide with molt-inhibiting activity in the crayfish *Procambarus bouvieri* [10], and a type I peptide from the crab *Libinia emarginata*, showing both hyperglycemic and mandibular organ-inhibiting activities [11]. These exceptions demonstrate that classification into the different subtypes does not necessarily reflect peptide activity.

Intensive research has been conducted to search for VIH in the commercially important penaeid shrimp species. In the kuruma prawn *Marsupenaeus japonicus*, eight CHH-family peptides, which were designated as Pej-SGP (sinus gland peptide)-I to -VII and Pej-MIH-B, have been purified from the sinus glands [7, 8, 12–14]. Two type II peptides, Pej-SGP-IV and Pej-MIH-B, exhibited molt-inhibiting activity but no significant effect on *vitellogenin* (*vg*) gene expression [7, 14–16], while the other six type I peptides (Pej-SGP-I, II, III, V, VI, and VII) displayed vitellogenesis-inhibiting activity (in terms of the inhibition of *vg* expression) on the ovary as well as hyperglycemic activity [8, 13, 15, 16]. In the whiteleg shrimp *Litopenaeus vannamei*, six type I peptides (Liv-SGP-A, -B, -C, -E, -F, and -G) represented similar vitellogenesis-inhibiting activity, but a type II peptide Liv-SGP-D did not [17]. These results suggest that type I peptides probably regulate *vg* expression in the ovary in addition to hemolymph glucose level in penaeid shrimp species. On the other hand, a type II peptide, Pem-GIH, has been reported to regulate ovarian *vg* expression in *Penaeus monodon* [18]. Regarding the regulation in the extraovarian site, it has recently been reported that another type II peptide, lvVIH, derived from the eyestalk and brain possesses vitellogenesis-inhibiting activity on the hepatopancreas of *L. vannamei* [19]. Thus, it has been shown that various CHH-family peptides are involved in the regulation of vitellogenesis using *vg* expression as a molecular index in commercially important penaeid species.

The shiba shrimp *Metapenaeus joyneri* is distributed throughout the East Asian coastal areas. The shiba shrimp is an economically important shrimp species and is fished in East Asian countries such as Japan, South Korea, and China. The annual catch of this shrimp species in 2012 became only about 20 % compared with those of the peak periods from 1991 to 1992 (Food and Agriculture Organization (FAO); <http://www.fao.org/fishery/statistics/global-capture-production/query/en>). The reason for the decrease of this species is still unclear. To solve this

problem, artificial maturation and spawning techniques, which are able to be applied to shrimp aquaculture and sea farming, are required. Therefore, it is desirable to gain a better understanding of the regulatory mechanisms of vitellogenesis in this species. In this study, we purified and structurally determined four CHH-family peptides from the sinus glands of *M. joyneri* and studied the possibility that these peptides regulate vitellogenesis in this species.

Materials and methods

Animals

Fresh adult shiba shrimps *M. joyneri* recently captured in Nagasaki Prefecture were purchased. Five hundred sinus glands were dissected from 250 shrimps under a stereoscopic microscope using a technique described previously [12].

Purification of CHH-family peptides from *M. joyneri*

Peptides were extracted from the sinus glands by the same methods as described previously [12]. The extract was subjected to a Sep-Pak C₁₈ Cartridge (Waters, Milford, MA, USA), which was eluted with 60 % acetonitrile in 0.05 % trifluoroacetic acid (TFA). After concentration, the resultant solution was applied to reversed-phase HPLC (RP-HPLC) on a Shodex Asahipak ODP-50 column (4.6 × 250 mm, Showa Denko, Tokyo, Japan). Elution was performed with a 40-min linear gradient of 20–40 % acetonitrile in 0.05 % TFA at a flow rate of 1 ml/min. Elution was monitored at 225 nm, and each peak fraction was collected manually. As the results of mass spectral and amino acid sequence analyses described below show, four CHH-family peptides purified by RP-HPLC were designated as Mej-SGP-I, -II, -III and -IV, respectively.

Mass spectral analysis

Mass spectra of the four CHH-family peptides were measured on a MALDI-TOF mass spectrometer (AXIMA[®]-CFR, Shimadzu, Kyoto, Japan) with α -cyano-4-hydroxycinnamic acid as a matrix in the positive ion mode.

Amino acid sequence analysis

N-terminal amino acid sequences of the four CHH-family peptides were analyzed on Applied Biosystems model 491cLC and model 491HT protein sequencers (Applied Biosystems, Foster City, CA, USA) in the pulsed-liquid mode.

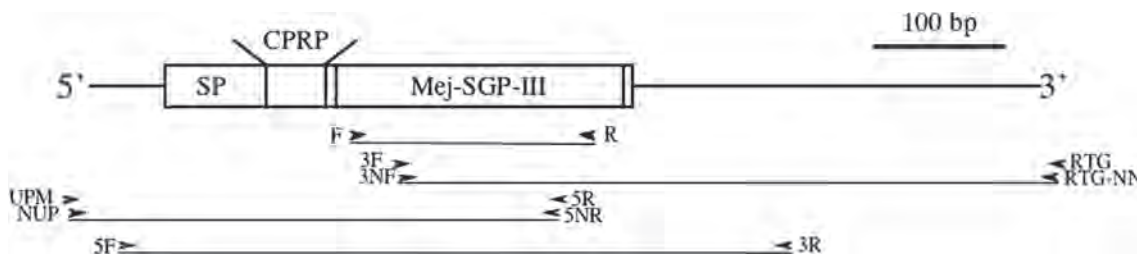


Fig. 1 Schematic representation of structures of the cDNA for Mej-SGP-III, and locations of the oligonucleotide primers. Arrowheads represent the primers, and lines under the arrowheads indicate the

cDNA fragments that were amplified. Boxes represent the open reading frame. The 5'- and 3'-untranslated regions are shown by thin lines. SP signal peptide, CPRP CHH precursor-related peptide

Ex vivo bioassay for vitellogenesis-inhibiting activity

Immature *M. japonicus* females serving as ovarian fragment donors were purchased from an aquaculture company in Kagoshima Prefecture. Prawns ranged from 16.0 to 22.2 g in body weight and from 0.32–1.01 % in gonadosomatic index. Almost all prawns with these GSI values have only previtellogenic oocytes in the ovary [20]. In order to use a positive control molecule, Pej-SGP-III, which is one of six CHH/VIHs in *M. japonicus*, was purified by the same methods as described previously [12]. Culture of ovarian fragments, total RNA extraction, and quantitative real-time PCR for measuring of *vg* mRNA levels were performed according to the methods described previously [15].

Statistical analysis

Differences between groups were analyzed with GraphPad Prism 4.0 (GraphPad Software, San Diego, CA) using two-way analysis of variance (ANOVA) followed by Bonferroni post hoc test.

Reverse transcription (RT)-PCR for amplifying of Mej-SGP-III cDNA fragment

The content of Mej-SGP-III in the sinus gland was the highest among the four CHH-family peptides. In addition, Mej-SGP-III exhibited significant vitellogenesis-inhibiting activity. In this study, therefore, we focused on Mej-SGP-III and then conducted cDNA cloning of Mej-SGP-III in order to elucidate its complete primary structure. A schematic showing the cDNA cloning procedure is shown in Fig. 1.

Total RNA from the eyestalk of *M. joyneri* was extracted using ISOGEN (Nippongene, Tokyo, Japan). First strand cDNA was synthesized with 300 ng of the total RNA using a SuperScript II™ Reverse Transcriptase (Invitrogen, Carlsbad, CA, USA). In this reaction, *Not I* dT primer (Table 1) was used as a reverse transcription primer. For RT-PCR, two degenerate oligonucleotide primers (F and R

Table 1 Nucleotide sequences of primers used for RT-PCR, 5'-RACE and 3'-RACE

Primer name	Nucleotide sequence (5'→3')
<i>Not I</i> -dT	AAGTGAAGAATTCGCGGCCGCAGGAA(T ₁₈)
RTG	AAGTGAAGAATTCGCGGCCG
RTG-NN	AAGAATTCGCGGCCGCAGGAA
F	TCATGYACTGGNGTNTAYAA
R	AGRCAC TGDATRAANGCCAT
3F	TACAACAGGGAGGTCATACT
3NF	CATACTGAGGCTTAACCGCCT
5R	GCAGTTCCTCTGCATTCTGTGGAGACA
5NR	AATCGTCACACAGGCGGTTAAGCCTCAG
5F	GAATTCCCAACTACGGTGAA
3R	TGGGGATCGGGTTTGAAGAT

in Table 1) were designed based on the determined N-terminal amino acid sequence of Mej-SGP-III. The first strand cDNA was used as a template, and amplification was carried out with primers F and R using GoTaq® Green Master Mix (Promega, Madison, WI, USA) with 20 µl reaction volume (Fig. 1). The following program was used for PCR amplification: 40 cycles of 30 s at 94 °C (3 min and 30 s for the first cycle only), 30 s at 53 °C, and 30 s at 72 °C (3 min for the last cycle only).

3'-Rapid amplification of cDNA ends (3'-RACE) for amplifying 3'-region of Mej-SGP-III cDNA

Two specific oligonucleotide primers (3F and 3NF in Table 1) were designed based on the nucleotide sequence of the Mej-SGP-III cDNA fragment amplified by RT-PCR. A 3'-region of Mej-SGP-III cDNA was amplified by two rounds of PCR. In the first PCR, the eyestalk first strand cDNA described in RT-PCR was used as a template, and amplification was carried out with primers 3F and RTG (Fig. 1) using TaKaRa LA PCR Kit Ver. 2.1 (Takara, Shiga, Japan) with 20 µl reaction volume. In the second PCR, the first PCR product was used as a template, and amplification

was carried out with primers 3NF and RTG-NN (Fig. 1) using the same reaction as the first PCR. The following program was used for each PCR amplification: 35 cycles of 30 s at 94 °C (3 min and 30 s for the first cycle only), 30 s at 52 °C, and 1 min at 72 °C (4 min for the last cycle only).

5'-RACE for amplifying of 5'-region of Mej-SGP-III cDNA

First-strand cDNA was newly synthesized with 150 ng of the eyestalk total RNA by using a SMART RACE cDNA Amplification Kit (Clontech, Mountain View, CA, USA) according to the instructions of the manufacturer with the exception that MMLV Reverse Transcriptase (Clontech) was substituted by SuperScript™ II Reverse Transcriptase (Invitrogen). In this reaction, a 5'-cDNA synthesis (CDS) primer (Clontech) was used as a reverse transcription primer. Two specific oligonucleotide primers (5R and 5NR in Table 1) were designed based on the nucleotide sequence of the Mej-SGP-III cDNA fragment amplified by RT-PCR and 3'-RACE. A 5'-region of the Mej-SGP-III cDNA was amplified by two rounds of PCR. In the first PCR, the newly synthesized eyestalk first strand cDNA was used as a template, and amplification was carried out with 5R and Universal Primer Mix (UPM, Clontech) as shown in Fig. 1 using TaKaRa LA PCR Kit Ver. 2.1 (Takara) with a 20 µl reaction volume. In the second PCR, the first PCR product was used as a template, and amplification was carried out with 5NR/Nested Universal Primer (NUP, Clontech) as shown in Fig. 1, using the same reaction as the first PCR. The following program was used for each PCR amplification: 25 cycles of 30 s at 94 °C (3 min and 30 s for the first cycle only), 30 s at 68 °C, and 2 min at 72 °C (5 min for the last cycle only).

Confirmation of the nucleotide sequence of Mej-SGP-III cDNA

The nucleotide sequence of the cDNA fragment including the full-length open reading frame (ORF) was confirmed by PCR amplification using specific primers (5F and 3R in Table 1).

Nucleotide sequence analysis

All PCR products were subcloned into a pMD-20T vector (Takara) using a Mighty TA-cloning kit (Takara). Both strands of the plasmid DNAs were sequenced on an ABI PRISM 3130 genetic analyzer (Applied Biosystems) using a Big Dye Terminator v3.1 Cycle Sequencing Kit (Applied Biosystems).

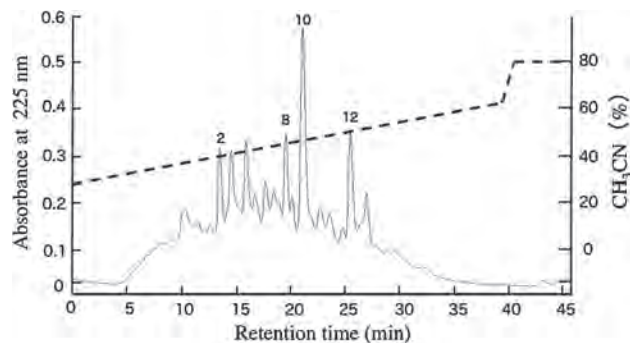


Fig. 2 Reversed-phase HPLC elution profile of extracts from 500 sinus glands of *Metapenaeus joyneri*. Chromatographic conditions are described in detail in “Materials and methods”. Concentration of acetonitrile is indicated by the dotted line

Results

Purification of CHH-family peptides from *M. joyneri*

Peptides were extracted from a total of 500 sinus glands and separated by RP-HPLC. The elution profile of RP-HPLC is shown in Fig. 2. In the TOF mass spectra of eluted peak fractions 2, 8, 10 and 12, protonated molecular ion peaks were observed at m/z 8,530, 8,976, 8,507 and 8,393, respectively. These results suggest that peaks 2, 8, 10 and 12 contained CHH-family peptides in *M. joyneri*, because their molecular weights were within the expected ranges of those of CHH-family (8,000–9,500).

N-terminal amino acid sequences of *M. joyneri* CHH-family peptides

N-terminal amino acid sequences of the four peak materials were analyzed, resulting more than 55 amino acid residues, although these sequences were not complete (Fig. 3). All four peptides showed considerable sequence similarity to CHH-family peptides of other crustacean species. In this study, these four CHH-family peptides contained in peaks 2, 8, 10 and 12 were named Mej-SGP-I, -II, -III and -IV, respectively. Unidentified residues at positions 7, 23, 26, 39, 43, and 52 of the four peptides were likely cysteine residues conserved in CHH-family peptides.

Ex vivo bioassay for vitellogenesis-inhibiting activities of *M. joyneri* CHH-family peptides

The vitellogenesis-inhibiting activities of the four CHH-family peptides were examined by an ex vivo bioassay (Fig. 4). Mej-SGP-III exhibited significant inhibitory activities at both concentrations of 0.05 and 5 nM, whereas inhibitory activities of Mej-SGP-I, -II and -IV were

10 20 30 40 50 60

P2 PLFDAS? TGVY DRQLLMRLSRV? DD? YNVFREPTVSTE? RSN? YNNLVFRQ? MEYIVSDHLHLEH

P8 SYIENT? RGVMGNRDIYKKVQRV? ED? TNI? RLPGLDGM? RDR? FNNEWELV? LKAANRN

P10 SLFDLS? TGVY NREVILRLNRL? DD? YNVYREP NVSTE? RRN? FVNMAFIQ? LEY

P12 ALFDPS? TGVF DRELLGRLN RV? DD? YNVFRDPKVATM? RSN? FLNPAFIQ? LEY

Fig. 3 N-terminal amino acid sequences of CHH-family peptides from *Metapenaeus joyneri*. Residues indicated as question marks were unidentifiable, and those at positions 7, 23, 26, 39, 43, and 52 are likely Cys residues (see text)

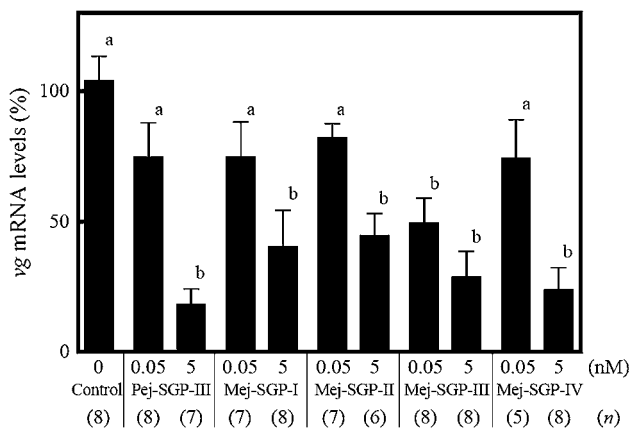


Fig. 4 The effects of Pej-SGP-III (positive control), which is one of the six CHH/VIHs in *Marsupenaeus japonicus*, and four CHH-family peptides from *Metapenaeus joyneri* on vg mRNA levels in incubated ovarian fragments. Relative vg mRNA levels are expressed as the percentage change relative to that of incubated counterpart ovarian fragments with medium only. In the control group, both sides of ovarian fragments from the single prawn were incubated with medium only, and the relative vg mRNA was calculated by left/right \times 100. Data are presented as mean \pm SEM. Differing letters indicate a significant difference ($P < 0.001$; two-way ANOVA followed by Bonferroni test). Numbers in parentheses indicate numbers of individuals used for respective groups

significant at only 5 nM. As a positive control, Pej-SGP-III, which is one of six CHH/VIHs in *M. japonicus*, was also assayed. Pej-SGP-III significantly reduced vg mRNA levels at a concentration of 5 nM.

Molecular cloning of a cDNA encoding Mej-SGP-III

The full-length sequence of Mej-SGP-III cDNA was compiled from the results of RT-PCR, 5'- and 3'-RACE (Fig. 5). The determined nucleotide sequence of the cDNA encoding the Mej-SGP-III has been deposited in the DNA Data Bank of Japan (DDBJ) database (Accession no. AB622205). The Mej-SGP-III cDNA consisted of 617 bp including a 5'-untranslated region (UTR) (71 bp), an open reading frame (ORF) (345 bp), and a 3'-UTR (201 bp). The 3'-UTR contains a polyadenylation signal (AATAAA). The ORF was conceptually translated into a putative pre-peptide comprising 114 amino acid residues. The

N-terminal part, Met⁻²⁴-Ala⁻¹, was predicted as a signal peptide by SignalP 3.0 program (<http://www.cbs.dtu.dk/services/SignalP/>). The segment of Arg¹-Ala¹⁴ was thought to be a CHH precursor-related peptide (CPRP). This CPRP was immediately followed by Lys¹⁵-Arg¹⁶, a putative dibasic cleavage site. The amino acid sequence of Ser¹⁷-Tyr⁷¹ was identical to the analyzed N-terminal sequence of the purified Mej-SGP-III as described above (Fig. 3). The sequences of Ser¹⁷-Val⁸⁸ and of Gly⁸⁹-Lys⁹⁰ are thought to be a mature Mej-SGP-III and an amidation signal, respectively. The theoretical mass value, 8507.3 (M + H)⁺, calculated from the mature Mej-SGP-III sequence with amidated C-terminus agreed closely with the analyzed value (m/z 8507.3) of the purified peptide by MALDI-TOF mass analysis.

Mej-SGP-III showed the highest sequence similarity with two CHH-family peptides having vitellogenesis-inhibiting activity in penaeid shrimp species, *M. japonicus* CHH/VIH (Maj-SGP-V) and *L. vannamei* VIH (Liv-SGP-G), by tBLASTn analysis. Then, the amino acid sequence of Mej-SGP-III was aligned with those of Maj-SGP-V and Liv-SGP-G in addition to the two known VIHs, *H. americanus* VIH (Hoa-VIH) and *A. vulgare* VIH (Arv-VIH) (Fig. 6). Mej-SGP-III shared amino acid identities 66.7 % with Maj-SGP-V and 66.7 % with Liv-SGP-G. On the other hand, Mej-SGP-III exhibited low amino acid identities of 28.4 % with Arv-VIH and 25.3 % with Hoa-VIH.

Discussion

In this study, four CHH-family peptides, which were considered to be VIH candidates, were purified from the sinus glands of *M. joyneri*. One of the four peptides (Mej-SGP-II) was categorized as a type II peptide, because a glycine residue was observed at position 12 (Fig. 3). The other three peptides (Mej-SGP-I, -III and -IV) were considered to be type I peptides, because of the lack of the glycine residue at 12th position (Fig. 3). A multiplicity of CHH-family peptides have been observed frequently in penaeid shrimp species. In *M. japonicus*, eight different CHH-family peptides, six type I and two type II, were purified from the sinus glands [8, 13, 14]. Seven CHH-family peptides, six type I

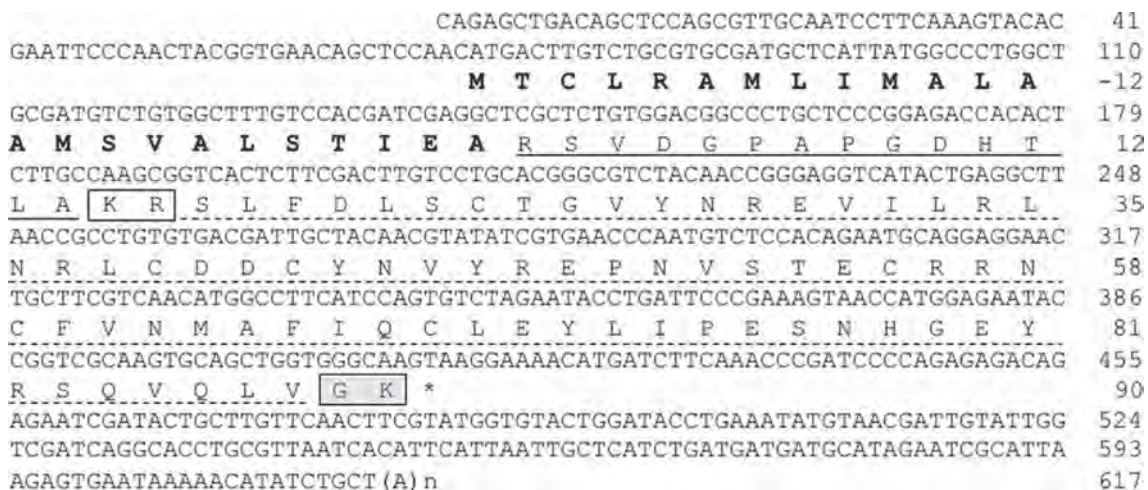


Fig. 5 Nucleotide and deduced amino acid sequences of a cDNA encoding the Mej-SGP-III precursor. Amino acid numbering starts at the N-terminal residue of the propeptide of Mej-SGP-III, and the putative signal peptide is indicated by *negative numbers*. The amino acid sequence of the putative signal peptide is marked in *bold*, that of the putative CHH precursor-related peptide (CPRP) is *underlined*,

and that of the mature Mej-SGP-III is *underlined with a dotted line*. The *open box* indicates the putative dibasic cleavage site. The *gray box* represents the putative amidation signal. The nucleotide sequence of the Mej-SGP-III cDNA has been deposited in the DNA Data Bank of Japan (accession no. AB622205)



Fig. 6 Amino acid sequence alignment of the mature Mej-SGP-III with another four VIHs. The Mej-SGP-III sequence was aligned using the CLUSTAL W program (<http://clustalw.ddbj.nig.ac.jp/top-e.html>) with four VIHs: *Marsupenaeus japonicus* CHH/VIH (Pej-SGP-V) [8], *Litopenaeus vannamei* VIH (Liv-SGP-G) [17], *Homarus*

americanus VIH (Hoa-VIH) [1], and *Armadillidium vulgare* VIH (Arv-VIH) [2]. *Open boxes* indicate the positions of conserved Cys residues. *Gray box* represents characteristic of type II peptides, which is an insertion of a Gly residue at position 12

and a type II, were also identified from *L. vannamei* [17]. In *Penaeus monodon*, six CHH-family peptides, four type I and two type II, were observed [21]. The elucidation of the total number of CHH-family peptides would be helpful in establishing the artificial maturation and spawning techniques. Using an RNA interference, the gene knockdown of Pem-GIH, which is thought to be a VIH in *P. monodon*, increased *vg* mRNA levels [18]. Applying a similar technique to *M. joinery*, if we targeted all CHH-family peptides having vitellogenesis-inhibiting activity, the efficiency could be improved. Therefore, the number and biological activity of CHH-family peptides in *M. joinery* revealed in this study is important information in order to propagate this species, whose catch has been declining recently (see “Introduction” section).

The three type I peptides (Mej-SGP-I, -III and -IV) exhibited significant vitellogenesis-inhibiting activity using the *M. japonicus* ovarian incubation system. This result is consistent with previous studies in which all

type I peptides of *M. japonicus* and *L. vannamei* showed a similar inhibitory activity using the same bioassay system [15–17]. However, meaningful inhibitory activity was observed also in a type II peptide (Mej-SGP-II) in the present study. In the previous studies, Pej-SGP-IV from *M. japonicus* and Liv-SGP-D from *L. vannamei* belonging to type II reduced *vg* mRNA levels in the cultured ovary to 65–70 % of control at 5–100 nM although those changes were not statistically significant [15, 17]. Therefore, it was assumed that type-II peptides in penaeid shrimp species may have no vitellogenesis-inhibiting activity on the ovary, but Mej-SGP-II showed significant activity in the present study. One possibility which might explain this observation is that Mej-SGP-II might have a C-terminal amide. Our previous study showed that a C-terminal amide of a CHH-family peptide was important for conferring vitellogenesis-inhibiting activity, using a similar bioassay system [22]. Moreover, the C-terminal amide of Pej-SGP-I, which is an *M. japonicus* CHH-family peptide

having vitellogenesis-inhibiting and hyperglycemic activities [8, 16], was important for the folding of the molecule to its natural conformation and significant for conferring hyperglycemic activity [23]. These results suggest that Mej-SGP-II might have a C-terminal amide. On the other hand, a cDNA encoding a new CHH-family peptide (IvVIH) was cloned from *L. vannamei* recently and its recombinant peptide inhibited hepatopancreas *vg* expression in vitro primary cell culture [19]. Both IvVIH and the aforementioned Pem-GIH are classified as type II and possess a free C-terminus. Mej-SGP-II may have vitellogenesis-inhibiting activity regardless of absence or presence of an amidated C-terminus. Except for penaeid species, type-II CHH-family peptides have only been characterized as VIH molecules in *H. americanus* and *A. vulgare* [1, 2]. The nature of the authentic and biologically relevant VIH is still unclear. In order to clarify this point, further accumulation of information on VIH, i.e., biological activities confirmed by various bioassays and molecular structure, from extensive crustacean species will be needed.

The vitellogenesis-inhibiting activities of the four CHH-family peptides were examined by ex vivo bioassay using *M. japonicus* ovary. The shiba shrimp *M. joyneri* is not cultivated in Japan. Its supply depends on wild populations, and they are mostly distributed as fresh or frozen shrimp, therefore live *M. joyneri* is not able to be obtained. On the other hand, live *M. japonicus* is easy to obtain from a local fish market all year round in Japan and is closely related to *M. joyneri*. That is why the heterologous bioassay was employed in this study. Although the four CHH-family peptides showed significant vitellogenesis-inhibiting activity by ex vivo bioassay using *M. japonicus* ovary, it is necessary to establish a bioassay system using *M. joyneri* in order to examine their original functions.

A cDNA encoding a Mej-SGP-III precursor was cloned for further characterization of its primary structure and precursor organization. Mej-SGP-III precursor deduced from the nucleotide sequence of its cDNA has a typical structure for a type I peptide; a CPRP was located between the signal peptide and a hormonal moiety (Figs. 1, 5), and an amidation signal (Gly-Lys) was located following the hormonal moiety. This result is in good agreement with the result that natural Mej-SGP-III lacks a Gly residue at position 12 which is a structural characteristic of type II peptides. The cDNA encoding the Mej-SGP-III precursor has enough length to be used as a template DNA for in vitro synthesis of double-stranded RNA. Mej-SGP-III was the most abundant CHH-family peptide in the sinus gland (Fig. 3) and showed significant vitellogenesis-inhibiting activity (Fig. 5). It shows the possibility that Mej-SGP-III is the most important molecule regulating vitellogenesis in *M. joyneri*. Therefore, we might be able to induce ovarian maturation in *M. joyneri* artificially by the injection of the

double-stranded RNA for gene knockdown of Mej-SGP-III. On the other hand, there is a possibility that the knockdown of only Mej-SGP-III is insufficient to induce vitellogenesis. In that case, all peptides having vitellogenesis-inhibiting activity will be targeted for knockdown as mentioned above, and cDNA cloning for Mej-SGP-I, -II, and -IV will be a prerequisite.

In conclusion, four CHH-family peptides were purified from the sinus glands of *M. joyneri* and their N-terminal sequences were determined. All of the four CHH-family peptides exhibited significant vitellogenesis-inhibiting activity, which indicates that the four molecules possibly regulate vitellogenesis negatively in *M. joyneri*. The full length of a cDNA encoding the most abundant molecule in the sinus gland among the four CHH-family peptides was cloned. With this information, it should be possible to develop an effective method for artificial maturation in this species using gene knockdown as reported in *P. monodon* [18].

Acknowledgments This work was supported partly by Grants-in-Aid for Scientific Research (No. 23780204 for T. O.; No. 25850143 for N. T.) from the Ministry of Education, Culture, Sport, Science and Technology of Japan, and by the SUNBOR GRANT from the Suntory Institute for Bioorganic Research (N. T.).

References

1. Soyez D, Le Caer JP, Noel PY, Rossier J (1991) Primary structure of two isoforms of the vitellogenesis inhibiting hormone from the lobster *Homarus americanus*. *Neuropeptides* 20:25–32
2. Gréve P, Sorokine O, Berges T, Lacombe C, Dorsseleer A, Martin G (1999) Isolation and amino acid sequence of a peptide with vitellogenesis inhibiting activity from the terrestrial isopod *Armadillidium vulgare* (Crustacea). *Gen Comp Endocrinol* 115:406–414
3. Keller R (1992) Crustacean neuropeptides: structures, functions and comparative aspects. *Experientia* 48:439–448
4. Audsley N, McIntosh C, Phillips JE (1992) Isolation of a neuropeptide from locust corpus cardiacum which influences ileal transport. *J Exp Biol* 173:261–274
5. Gasparini S, Kiyatkin N, Drevet P, Boulain JC, Tacnet F, Ripoché P, Forest E, Grishin E, Ménez A (1994) The low molecular weight protein which co-purifies with α -latrotoxin is structurally related to crustacean hyperglycemic hormones. *J Biol Chem* 269:19803–19809
6. Montagné N, Desdevises Y, Soyez D, Toullec JY (2010) Molecular evolution of the crustacean hyperglycemic hormone family in ecdysozoans. *BMC Evol Biol* 10:62
7. Yang WJ, Aida K, Terauchi A, Sonobe H, Nagasawa H (1996) Amino acid sequence of a peptide with molt-inhibiting activity from the kuruma prawn *Penaeus japonicus*. *Peptides* 17:197–202
8. Yang WJ, Aida K, Nagasawa H (1997) Amino acid sequences and activities of multiple hyperglycemic hormones from the kuruma prawn, *Penaeus japonicus*. *Peptides* 18:479–485
9. Chang ES, Prestwich GD, Bruce MJ (1990) Amino acid sequence of a peptide with both molting-inhibiting and hyperglycemic activities in the lobster *Homarus americanus*. *Biochem Biophys Res Commun* 171:818–826
10. Aguilar MB, Falchetto R, Shabanowitz J, Hunt DF, Huberman A (1996) Complete primary structure of the molt-inhibiting

- hormone (MIH) of the Mexican crayfish *Procambarus bowieri* (Ortmann). *Peptides* 17:367–374
11. Liu L, Laufer H (1996) Isolation and characterization of sinus gland neuropeptides with both mandibular organ inhibiting and hyperglycemic effects from the spider crab *Libinia emarginata*. *Arch Insect Biochem Physiol* 32:375–385
 12. Yang WJ, Aida K, Nagasawa H (1995) Amino acid sequences of a hyperglycaemic hormone and its related peptides from the kuruma prawn, *Penaeus japonicus*. *Aquaculture* 135:205–212
 13. Nagasawa H, Yang WJ, Aida K, Sonobe H (1999) Chemical and biological characterization of neuropeptides in the sinus glands of the kuruma prawn, *Penaeus japonicus*. In: Shimonishi Y (ed) *Peptide science—present and future*. Kluwer Academic Publishers, London, pp 453–454
 14. Ohira T, Katayama H, Tominaga S, Takasuka T, Nakatsuji T, Sonobe H, Aida K, Nagasawa H (2005) Cloning and characterization of a molt-inhibiting hormone-like peptide from the prawn *Marsupenaeus japonicus*. *Peptides* 26:259–268
 15. Tsutsui N, Katayama H, Ohira T, Nagasawa H, Wilder MN, Aida K (2005) The effects of crustacean hyperglycemic hormone-family peptides on vitellogenin gene expression in the kuruma prawn, *Marsupenaeus japonicus*. *Gen Comp Endocrinol* 144:232–239
 16. Tsutsui N, Nagakura-Nakamura A, Nagai C, Ohira T, Nagasawa H (2013) The ex vivo effects of eyestalk peptides on ovarian vitellogenin gene expression in the kuruma prawn *Marsupenaeus japonicus*. *Fish Sci* 79:33–38
 17. Tsutsui N, Ohira T, Kawazoe I, Takahashi A, Wilder MN (2007) Purification of sinus gland peptides having vitellogenesis-inhibiting activity from the whiteleg shrimp *Litopenaeus vannamei*. *Mar Biotechnol* 9:360–369
 18. Treeratrakool S, Panyim S, Chan SM, Withyachumnarnkul B, Udomkit A (2008) Molecular characterization of gonad-inhibiting hormone of *Penaeus monodon* and elucidation of its inhibitory role in vitellogenin expression by RNA interference. *FEBS J* 275:970–980
 19. Chen T, Zhang LP, Wong NK, Zhong M, Ren CH, Hu CQ (2014) Pacific white shrimp (*Litopenaeus vannamei*) vitellogenesis-inhibiting hormone (VIH) is predominantly expressed in the brain and negatively regulates hepatopancreatic vitellogenin (VTG) gene expression. *Biol Reprod*. doi:10.1095/biolreprod.113.115030
 20. Jasmani S (2000) Physiological studies on vitellogenesis in the kuruma prawn, *Penaeus japonicus*. PhD dissertation, The University of Tokyo, Tokyo
 21. Krungkasem C, Ohira T, Yang WJ, Abdullah R, Nagasawa H, Aida K (2002) Identification of two distinct molt-inhibiting hormone-related peptides from the giant tiger prawn *Penaeus monodon*. *Mar Biotechnol* 4:132–140
 22. Ohira T, Okumura T, Suzuki M, Yajima Y, Tsutsui N, Wilder MN, Nagasawa H (2006) Production and characterization of recombinant vitellogenesis-inhibiting hormone from the American lobster *Homarus americanus*. *Peptides* 27:1251–1258
 23. Katayama H, Ohira T, Aida K, Nagasawa H (2002) Significance of a carboxyl-terminal amide moiety in the folding and biological activity of crustacean hyperglycemic hormone. *Peptides* 23:1537–1546

HETEROCYCLES, Vol. 90, No. 1, 2015, pp. 462 - 481. © 2015 The Japan Institute of Heterocyclic Chemistry
Received, 26th June, 2014, Accepted, 29th July, 2014, Published online, 19th August, 2014
DOI: 10.3987/COM-14-S(K)43

SYNTHESIS OF BICYCLIC DIOXETANES BEARING A HYDROXYPHENANTHRENE OR HYDROXY[4]HELICENE MOIETY AND THEIR BASE-INDUCED CHEMILUMINESCENT DECOMPOSITION

Yohei Koyama, Nobuko Watanabe, Hisako K. Ijuin, and Masakatsu
Matsumoto*

Department of Chemistry, Kanagawa University, Tsuchiya, Hiratsuka, Kanagawa
259-1293, Japan *E-mail address:* matsumo-chem@kanagawa-u.ac.jp

Abstract – Six bicyclic dioxetanes bearing a 1-hydroxyphenanthren-3-yl **2-iv**, 3-hydroxyphenanthren-1-yl **2-ov**, 4-hydroxyphenanthren-2-yl **2-oh**, 2-hydroxyphenanthren-4-yl **2-ih**, 4-hydroxy[4]helicen-2-yl **3-iv** and 2-hydroxy[4]helicen-4-yl group **3-ov** were synthesized and their base-induced chemiluminescent decomposition was investigated in a TBAF (tetrabutylammonium fluoride) / MeCN system. For dioxetanes in the *iv*-series **2-iv** and **3-iv** including α -naphthol-analog **17a** and those in the *ov*-series **2-ov** and **3-ov** including β -naphthol-analog **17b**, we investigated how the chemiluminescence properties changed with an increase in the number of fused benzene rings of a hydroxyarene moiety attached to a dioxetane ring. The results showed that a) maximum wavelength of chemiluminescence $\lambda_{\max}^{\text{CL}}$ tended to shift to a longer wavelength region as the number of fused benzene rings increased, b) the k^{CTID} values for the *iv*-series were >1000 times larger than those for the *ov*-series regardless of the number of fused benzene rings, and c) a dioxetane in the *iv*-series tended to have a higher singlet-chemiexcitation efficiency Φ_{S} than the corresponding dioxetane in the *ov*-series. This tendency could be explained by the “*syn/anti*” rotational isomerism of an aromatic electron donor, where an *anti*-rotamer gives Φ_{S} far more effectively than a *syn*-rotamer.

INTRODUCTION

A dioxetane bearing an aromatic electron donor such as oxidoaryl anion undergoes intramolecular charge-transfer-induced decomposition (CTID) with an accompanying emission of bright light.¹⁻⁶ This phenomenon has received considerable attention from the viewpoints of mechanistic interest related to bioluminescence and its potential for application to clinical and biological analysis.^{7,8} Thus, intensive studies have been conducted, and have shown that an aromatic electron donor significantly affects the

chemiluminescence properties such as the chemiluminescence spectrum, chemiluminescence efficiency and the rate of decomposition for CTID-active dioxetanes. Such effects are mainly due to the structure of the π -electron system and the bulkiness of the aromatic electron donor.

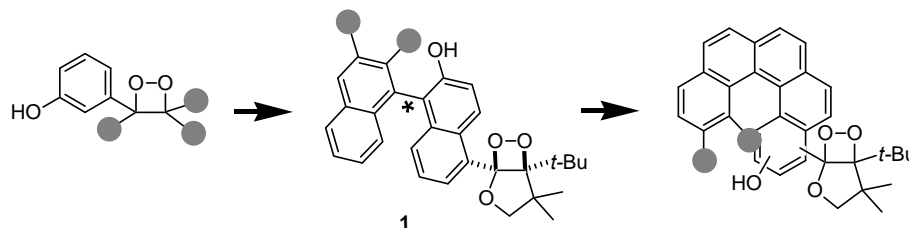


Figure 1. CTID-active dioxetanes bearing a chiral aromatic electron donor

On the other hand, the chirality of an aromatic electron donor such as a biaryl due to atropisomerism leads to unique chemiluminescence for a CTID-active dioxetane. For instance, optically active bicyclic dioxetanes **1** bearing a chiral binaphthyl moiety have very recently been found to show chiral-induced chemiluminescence in an optically anisotropic microenvironment (Figure 1).^{9,10} In addition to this phenomenon, it would be interesting to determine whether or not CTID of optically active dioxetanes shows the emission of polarized light. For observing such an unprecedented phenomenon, an important preliminary subject may be to design and synthesize dioxetanes bearing a helicene-type electron donor that could be expected to exhibit a large specific rotation due to its large helicity (Figure 1).

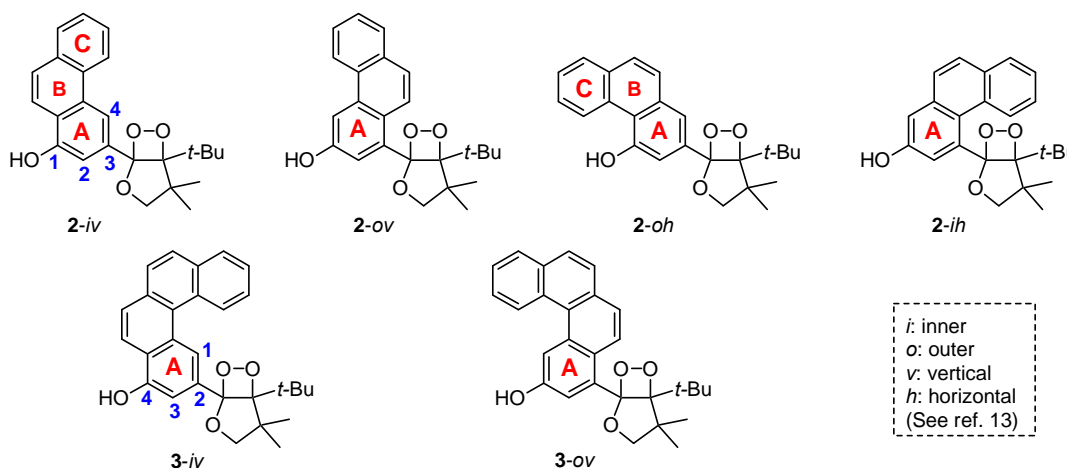


Figure 2. Bicyclic dioxetanes bearing a hydroxyphenanthrene or hydroxyl[4]helicene moiety

A promising candidate for such a CTID-active dioxetane would be one bearing a hydroxyhelicene moiety. However, there are too many substitution patterns when both a hydroxy group as a trigger and a dioxetane ring are introduced to an *ortho*-fused polyacene ring: there are 66 patterns for a [4]helicene (benzo[*c*]phenanthrene) and 91 for [5]helicene! Furthermore, little is currently known about the synthetic feasibility and chemiluminescence properties of a dioxetane bearing a helicene moiety. In light of the chemiluminescence properties for the CTID of dioxetanes bearing a hydroxynaphthyl group,¹¹ we decided to fundamentally investigate the CTID of racemic bicyclic dioxetanes bearing a phenanthrene

moiety in which both a hydroxy group and a dioxetane ring lie in an “*odd*” relationship on the A-ring.^{11,12} The thus-realized dioxetanes were **2-iv**, **2-ov**, **2-oh** and **2-ih**, as shown in Figure 2.¹³ Based on an evaluation with respect to the chemiluminescence properties, thermal stability, and synthetic feasibility of **2**, two selected dioxetanes bearing a hydroxyl[4]helicene moiety **3-iv** and **3-ov** were further synthesized and their CTID was investigated.

RESULTS AND DISCUSSION

Synthesis of bicyclic dioxetanes bearing a hydroxyphenanthrene or hydroxy[4]helicene moiety

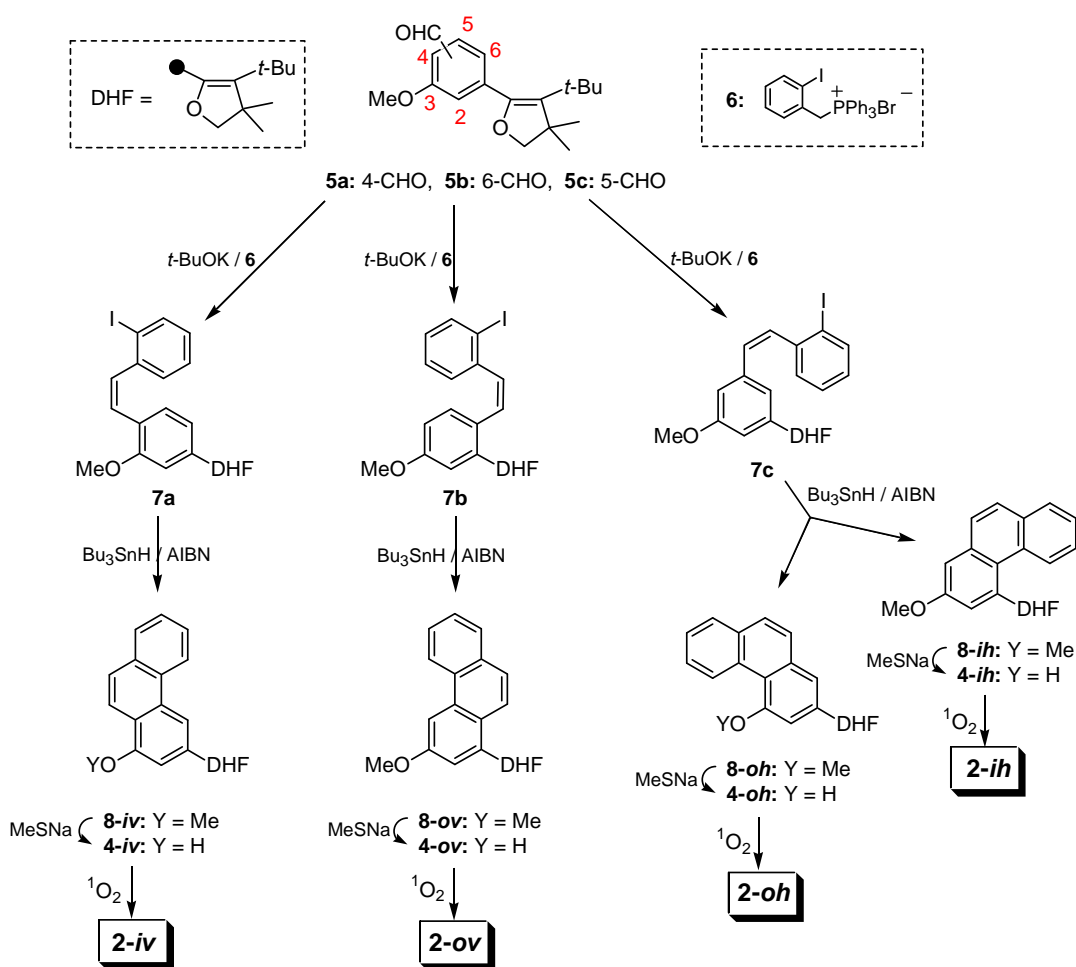
Bicyclic dioxetanes **2** bearing a hydroxyphenanthrene moiety were synthesized by singlet oxygenation of the corresponding dihydrofurans **4**. The key step in the synthesis of precursors **4** was the construction of di-substituted phenanthrene rings. Thus, we applied the cyclization of an *o*-halogeno-*Z*-stilbene using Bu₃SnH.¹⁴ The synthetic sequence leading to precursor **4-iv** for dioxetane **2-iv** is described here as a representative example (Scheme 1). First, we conducted a Wittig reaction of dihydrofuran **5a** bearing a 4-formyl-3-methoxyphenyl group with 2-iodobenzyltriphenylphosphorane prepared from phosphonium bromide **6** to give dihydrofuran **7a** bearing a 3-methoxyphenyl moiety substituted with a *Z*-(2-iodophenyl)ethenyl group at the 4-position in 96% yield along with a small amount of its *E*-isomer. When **7a** and Bu₃SnH were heated in the presence of AIBN (azobisisobutyronitrile) in toluene, the desired 1-methoxyphenanthren-3-yl-substituted dihydrofuran **8-iv** was produced in 85% isolated yield. Demethylation of a methoxy group in **8-iv** was attained by heating with sodium thiomethylate in DMF to give precursor **4-iv** in 99% yield.

As shown in Scheme 1, *Z*-stilbene-type compounds **7b** and **7c** were also prepared by the Wittig reaction of the corresponding aldehydes **5b** and **5c**. Cyclization of **7b** as for **7a** gave 3-methoxyphenanthrene **8-ov** in 86% yield, while the similar cyclization of **7c** gave 4-methoxyphenanthrene **8-oh** and its 2-methoxy-isomer **8-ih** in respective yields of 58% and 31%. These methoxyphenanthryl-substituted dihydrofurans **8-ov**, **8-oh** and **8-ih** were demethylated as in the case of **8-iv** to give the corresponding hydroxyphenanthryl-substituted dihydrofurans **4-ov**, **4-oh** and **4-ih** in yields of 87-98%.

When dihydrofuran **4-iv** was irradiated with a Na-lamp in the presence of a catalytic amount of tetraphenylporphyrin (TPP) in CH₂Cl₂ under an O₂ atmosphere at 0 °C, 1,2-addition of singlet oxygen to **4-iv** effectively proceeded to give thermally stable dioxetane **2-iv** in 78% isolated yield. Similar singlet oxygenation of precursors **4-ov** and **4-oh** smoothly took place to give thermally stable dioxetanes **2-ov** and **2-oh** in respective yields of 96% and 68%. On the other hand, singlet oxygenation of **4-ih** proceeded to mainly give keto ester **9-ih**, which was produced from thermally unstable dioxetane **2-ih**: all efforts to isolate pure **2-ih** were unsuccessful, so that we could obtain only a mixture of **2-ih** and **9-ih**. The structures of dioxetanes **2-iv**, **2-ov** and **2-oh** were determined by ¹H NMR, ¹³C NMR, IR, Mass and HRMass spectral analyses: the structure of **2-ih** was determined by ¹H NMR. All dioxetanes **2-iv**, **2-ov** and **2-oh** selectively gave the corresponding keto esters **9-iv**, **9-ov** and **9-oh** when heated in *p*-xylene (Figure 3).

Synthetic feasibility for dioxetanes **2-iv**, **2-ov**, **2-oh**, and **2-ih** suggested that the design of dioxetanes

bearing a hydroxyhelicene moiety appeared to be promising for the development of dioxetanes such as **2-iv** and **2-ov**. Thus, two selected dioxetanes bearing a hydroxy[4]helicene moiety **3-iv** and **3-ov** were synthesized according to a strategy similar to that for dioxetanes **2**. The precursor dihydrofurans **10-iv** and **10-ov** bearing a hydroxy[4]helicene moiety were synthesized starting from dihydrofurans **5a** and **5b**, respectively (Scheme 2). First, dihydrofurans **5a** and **5b** were reacted with a phosphorane prepared from phosphonium bromide **11** to give the corresponding *Z*-diarylethenes **12a** and **12b** in good yields. Cyclization of **12a** and **12b** was carried out as in the case of **7** to give the corresponding methoxy[4]helicene-substituted dihydrofurans **13-iv** and **13-ov** in respective yields of 45 and 62%. These



Scheme 1. Synthesis of bicyclic dioxetanes bearing a hydroxyphenanthrene moiety

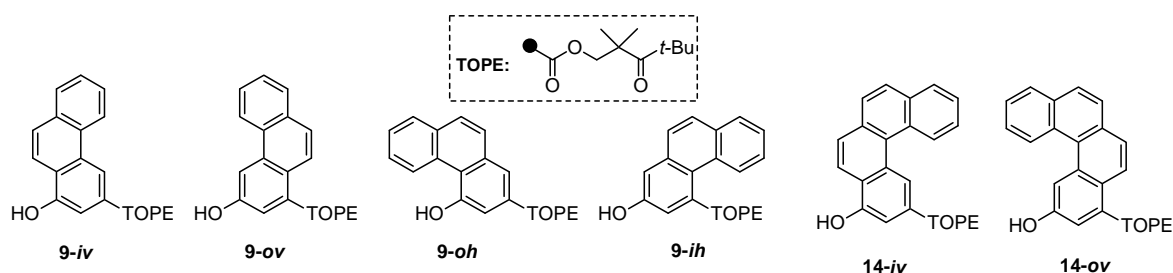
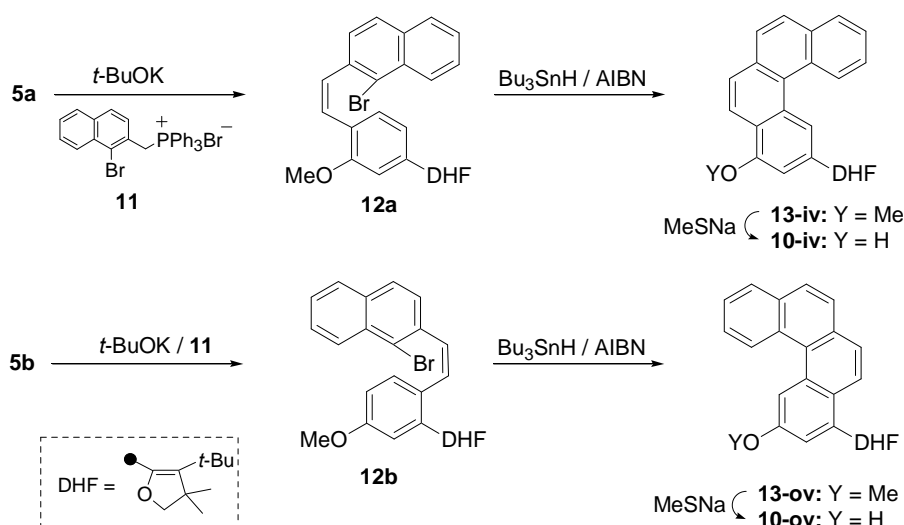


Figure 3. Hydroxyarene carboxylic acid esters of 2,2,4,4-tetramethyl 3-oxopentanol

methoxyaryl-substituted dihydrofurans **13-iv** and **13-ov** were demethylated as in the case of **8-iv** to effectively give the precursor dihydrofurans **10-iv** and **10-ov**, respectively. Finally, singlet oxygenation of **10-iv** and **10-ov** was carried out at 0 °C to give dioxetanes **3-iv** and **3-ov** in respective yields of 60 and 86%. These dioxetanes were thermally stable, but selectively decomposed to the corresponding keto esters **14-iv** and **14-ov** under heating in *p*-xylene. Dioxetanes **3-iv** and **3-ov** gave satisfactory ¹H NMR, ¹³C NMR, Mass, and HRMass spectral data. Furthermore, X-ray single-crystallographic analysis was successfully performed for both dioxetanes **3-iv** and **3-ov**. Figure 4 shows their ORTEP views, from which we can infer that the [4]helicene ring is skewed by about 37°.



Scheme 2. Synthesis of bicyclic dioxetanes bearing a hydroxy[4]helicene moiety

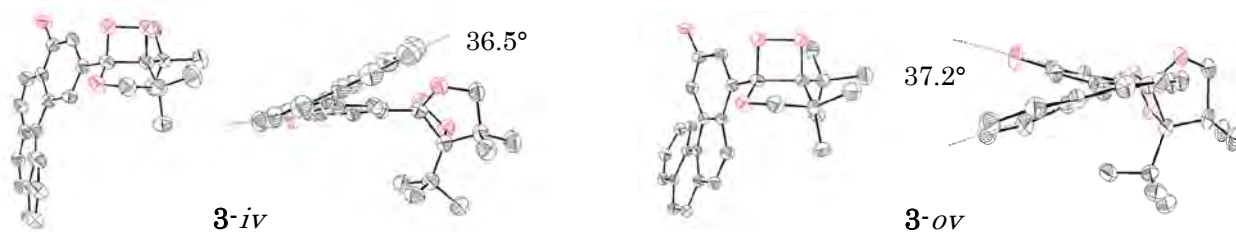
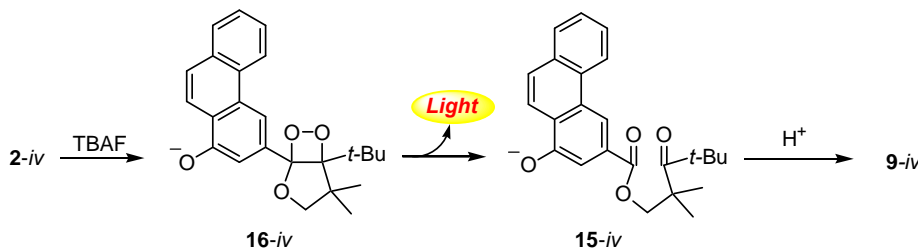


Figure 4. ORTEP views of bicyclic dioxetanes bearing a hydroxy[4]helicene moiety

Base-induced chemiluminescent decomposition of bicyclic dioxetanes bearing a hydroxyphenanthrene or hydroxy[4]helicene moiety

When a solution of **2-iv** in acetonitrile was added to a solution of tetrabutylammonium fluoride (TBAF, large excess) in acetonitrile at 25 °C, **2-iv** decomposed according to pseudo-first order kinetics independent of the TBAF concentration with an accompanying emission of yellow light, the spectrum of which is shown in Figure 6. The chemiluminescence properties of **2-iv** were as follows: maximum wavelength $\lambda_{\max}^{\text{CL}} = 506 \text{ nm}$, chemiluminescence efficiency $\Phi^{\text{CL}} = 5.2 \times 10^{-2}$,^{15,16} rate of CTID $k^{\text{CTID}} = 2.5 \text{ s}^{-1}$, and half-life $t_{1/2}^{\text{CTID}} = 0.28 \text{ s}$ (Table 1). The spent reaction mixture exclusively gave keto ester

9-iv after careful neutralization. Authentic oxido anion **15-iv** generated from **9-iv** in TBAF/acetonitrile gave fluorescence, the spectrum of which coincided with the chemiluminescence spectrum of **2-iv**. These results indicate that CTID of **2-iv** proceeded through an intermediary dioxetane **16-iv** to give anionic keto ester **15-iv** accompanied by the emission of light (Scheme 3). Thus, based on the fluorescence efficiency (Φ^{fl}) of **15-iv**, the chemiexcitation efficiency ($\Phi_{\text{S}} = \Phi^{\text{CL}}/\Phi^{\text{fl}}$) was estimated to be 0.10 (Table 1).



Scheme 3. TBAF-induced chemiluminescent decomposition of bicyclic dioxetane **2-iv**

Under similar treatment with TBAF in acetonitrile, **2-ov**, **2-oh**, and **2-ih** showed chemiluminescence, the spectra and properties of which are shown in Figure 6 and Table 1: **2-ih** was used as a mixture that included a large amount (ca. 30%) of **9-ih**. The chemiluminescence properties for dioxetanes **2** were compared to those for dioxetanes bearing a rather simple hydroxyaryl group, i.e., a 1-hydroxynaphthalen-3-yl **17a** or 3-hydroxynaphthalen-1-yl group **17b**, together with those for dioxetane **18** bearing a 3-hydroxyphenyl group (Figures 5 and 6 and Table 1): **17a** was synthesized according to the procedure for **17b**.^{9b} The data of Table 1 show that a) the Φ^{CL} values for all three of the hydroxyphenanthryl-substituted dioxetanes **2-iv**, **2-ov**, and **2-oh** were higher than or comparable to that for hydroxynaphthyl-substituted dioxetane **17b** though lower than that for **17a**, and b) the k^{CTID} values for dioxetanes bearing a β -naphthol-type arene moiety, i.e., **17b** and **2-ov**, were far lower than those for dioxetanes bearing an α -naphthol-type arene moiety, i.e., **17a**, **2-iv** and **2-oh**.

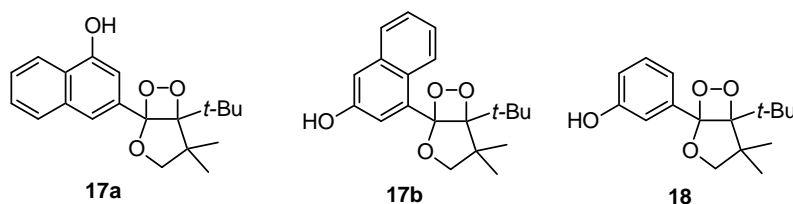


Figure 5. Bicyclic dioxetanes bearing a naphthol or phenol moiety

When dioxetane **3-iv** was treated with TBAF in acetonitrile as with **2**, **3-iv** decomposed to give a flash of yellow light with $\lambda_{\text{max}}^{\text{CL}} = 559 \text{ nm}$, the spectrum of which is shown in Figure 6 [A] together with those of **2-iv**, **2-ih**, **17a** and **18**. On the other hand, the TBAF-induced decomposition of **3-ov** showed a glowing light with $\lambda_{\text{max}}^{\text{CL}} = 530 \text{ nm}$, the spectrum of which is shown in Figure 6 [B] together with those of **2-oh**, **2-ov**, **17b** and **18**. The chemiluminescence properties for **3-iv** and **3-ov** are summarized in Table 1, which shows that their Φ^{CL} values were somewhat lower than that for **2-ov**. Thus, we attempted to

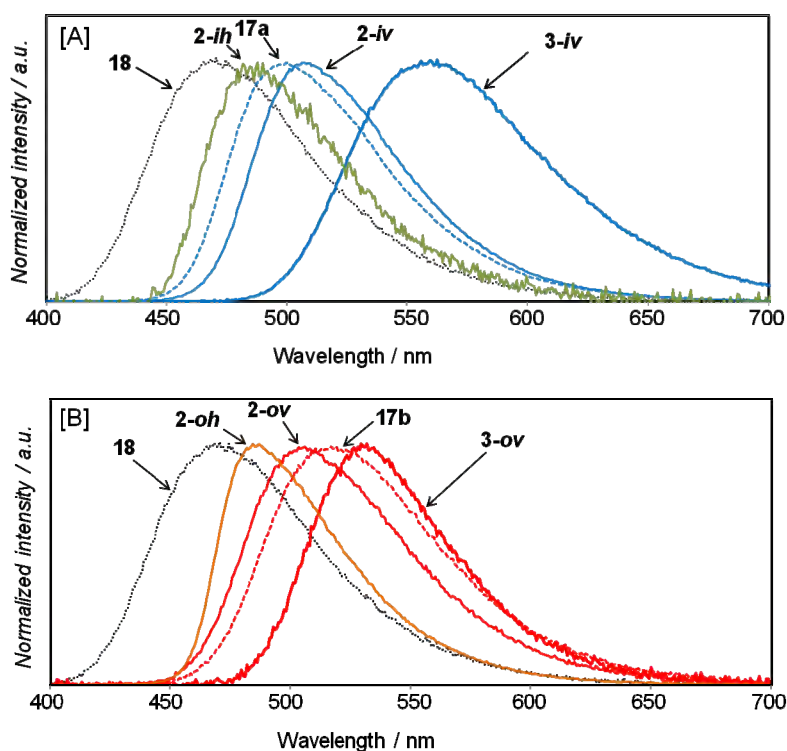


Figure 6. Chemiluminescence spectra for TBAF-induced decomposition of bicyclic dioxetanes bearing a hydroxyarene moiety

Table 1. Chemiluminescence properties of bicyclic dioxetanes bearing a hydroxyaryl moiety in a TBAF/acetonitrile system^{a)}

Dioxetane	λ_{\max} / nm	$\Phi^{\text{CL b)}$	Φ^{fl}	Φ_{S}	$k^{\text{CTID}} / \text{s}^{-1}$	$t_{1/2}^{\text{CTID}} / \text{s}$
17a	500	0.13	0.49	0.28	13	5.2×10^{-2}
2-iv	506	5.2×10^{-2}	0.52	0.10	2.5	0.28
2-oh	485	4.8×10^{-2}	0.23	0.21	0.46	1.5
3-iv	559	1.4×10^{-2}	0.22	0.07	3.6	0.19
17b^{c)}	515	2.6×10^{-2}	0.49	0.05	8.2×10^{-4}	850
2-ov	504	2.4×10^{-2}	0.29	0.08	6.3×10^{-4}	1100
2-ih	485	---- ^{d)}	---- ^{d)}	---- ^{d)}	---- ^{d)}	---- ^{d)}
3-ov	530	1.9×10^{-2}	0.36	0.05	1.8×10^{-3}	380
18^{e)}	471	0.11	0.24	0.46	2.8×10^{-2}	25

a) Unless stated otherwise, a solution of a dioxetane in MeCN (1.0×10^{-4} – 1.0×10^{-5} M, 1 mL) was added to a solution of TBAF in MeCN (1.0×10^{-2} M, 2 mL) at 25 °C. b) All of the Φ^{CL} values presented here were estimated based on the value reported for the chemiluminescent decomposition of 3-adamantylidene-4-(3-siloxyphenyl)-4-methoxy-1,2-dioxetane ($\Phi^{\text{CL}} = 0.29$) in TBAF/DMSO [Ref. 16]. c) [Ref. 9b] d) Not estimated. e) [Ref. 17]

understand how $\lambda_{\max}^{\text{CL}}$, k^{CTID} and Φ^{CL} changed with a change in the number of fused benzene rings from phenol to hydroxy[4]helicene for two series, i.e., the *iv*-series and *ov*-series, of hydroxyaryl-substituted dioxetanes, **18** → **17** → **2** → **3**.

Table 1 shows that $\lambda_{\max}^{\text{CL}}$ tended to shift to a longer wavelength region for both the *iv*-series and the *ov*-series as the number of fused benzene rings increased, with the exception of **2-ov**. This tendency may be due to the expansion of the π -conjugation system from oxidophenyl anion → oxidonaphthyl anion → oxidophenanthryl anion and finally to oxido[4]helicenyl anion. On the other hand, the k^{CTID} values for the *iv*-series were >1000 times larger than those for the *ov*-series regardless of the number of fused benzene rings. The significant difference in k^{CTID} values between the *iv*-series and *ov*-series is presumably attributed to the difference in the ease of oxidation of oxidoarene anions, which act as an electron donor for CTID. In fact, the anion of α -naphthol, corresponding to **17a**, has been reported to possess a formal oxidation potential ($E = -498$ mV vs Ag/Ag⁺ in DMSO) that is considerably lower than that of an anion of β -naphthol, corresponding to **17b** ($E = -369$ mV).¹⁸ This may also be the case for **2** and **3**: all of the dioxetanes in the *iv*-series have an α -naphthol-type arene moiety, while those in the *ov*-series have a β -naphthol-type arene moiety.

Table 1 further shows that the Φ_{S} value for a dioxetane bearing an α -naphthol-type arene (Table 1) tended to be higher than that for the corresponding dioxetane bearing a β -naphthol-type arene: **17a** >> **17b**, **2-oh** >> **2-iv** > **2-ov**, and **3-iv** > **3-ov**. This tendency can be explained by the “*syn/anti*” rotational isomerism of an aromatic electron donor, in which an *anti*-rotamer gives Φ_{S} far more effectively than a *syn*-rotamer (Scheme 4).^{19,20}

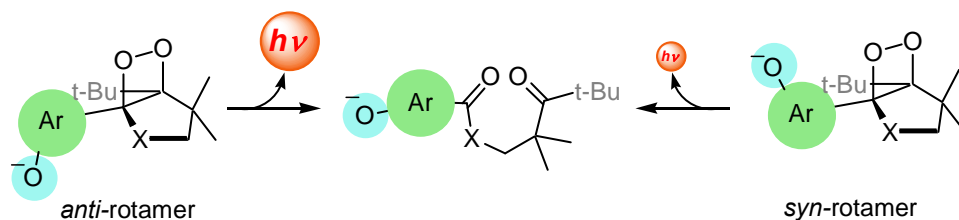
Table 2. Relationship between Φ_{S} and *syn/anti* rotational isomerism of an aromatic electron donor for the base-induced chemiluminescent decomposition of hydroxyaryl-substituted dioxetanes^{a)}

Dioxetane	Φ_{S}	$\Delta E_{\text{syn-anti}}$ /kcal mol ⁻¹	$\Delta E_{\text{rotation}}$ ^{b)} /kcal mol ⁻¹
18	0.46	-1.1	11.3, 13.5
17a	0.28	-1.7	9.9, 13.8
17b	0.05	1.1	13.3, 28.1
2-oh	0.21	-1.3	11.1, 13.3
2-iv	0.10	-1.2	11.5, 13.7
2-ov	0.08	0.6	13.8, 28.8
3-iv	0.07	-0.3	9.4, 15.0
3-ov	0.05	1.3	13.2, 28.3

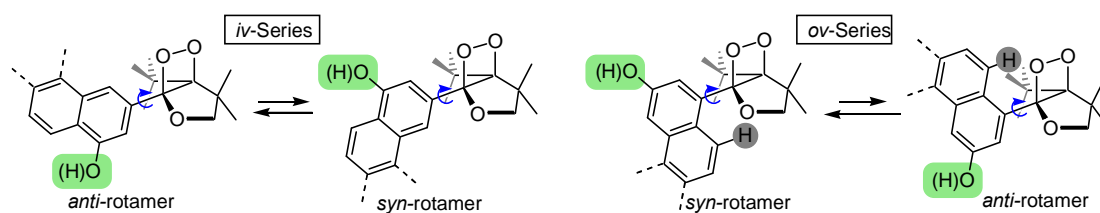
a) An oxido-anion form of dioxetane was calculated. b) Two energy barriers exist due to steric interaction of an aromatic ring to an oxygen of tetrahydrofuran ring as well as to *tert*-butyl group.

A *syn*-rotamer, typically shown in Figure 4, is likely to be more stable than an *anti*-rotamer for dioxetanes in the *ov*-series because of steric hindrance by a *peri*-hydrogen of an aromatic electron donor (Scheme 5). Thus, we carried out an MO calculation (Gaussian 03, HF/6-31G) to estimate the energy difference $\Delta E_{\text{anti-syn}}$ between the *syn*- and *anti*-rotamers and the barriers to rotation $\Delta E_{\text{rotation}}$ from the most stable rotamer

(*syn* or *anti*) to the other stable rotamer (*anti* or *syn*) (Table 2). The results show that a) the *syn*-rotamer is more stable than the *anti*-rotamer for the *ov*-series, while the *anti*-rotamer is more stable for the *iv*-series, and b) $\Delta E_{\text{rotation}}$ values for the *ov*-series tend to be higher than those for the *iv*-series. Thus, we can see that, for a dioxetane in the *iv*-series, the *anti*-rotamer is presumably predominant compared to the *syn*-rotamer, while a dioxetane in the *ov*-series shows the opposite tendency. Hence, a dioxetane in the *iv*-series would give a singlet-excited emitter more effectively than the corresponding dioxetane in the *ov*-series under these reaction conditions.



Scheme 4. Marked dependence of chemiluminescence efficiency on *syn/anti* rotational isomerism



Scheme 5. *syn/anti* Rotational isomerism of dioxetanes in *iv*-series and *ov*-series

CONCLUSION

Four bicyclic dioxetanes bearing a phenanthrene moiety possessing a hydroxy group in the A-ring **2-iv**, **2-ov**, **2-oh**, and **2-ih** were synthesized. Except for **2-ih**, these dioxetanes were thermally stable and underwent TBAF-induced decomposition with the accompanying emission of bright light. As an extension, we synthesized two dioxetanes **3-iv** and **3-ov** bearing a 4-hydroxy[4]helicen-2-yl or 2-hydroxy[4]helicen-4-yl group and found that their CTID effectively gave light. Thus, we investigated how the chemiluminescence properties of the *iv*-series and *ov*-series of dioxetanes changed with an increase in the number of fused benzene rings of a hydroxyarene moiety attached to a dioxetane ring. The results showed that a) $\lambda_{\text{max}}^{\text{CL}}$ tended to shift to a longer wave-length region for both the *iv*-series and the *ov*-series as the number of fused benzene rings increased, b) the k^{CTID} values for the *iv*-series were >1000 times larger than those for the *ov*-series regardless of the number of fused benzene rings, and c) the Φ_{S} value for a dioxetane bearing an α -naphthol-type arene (*iv*-series) tended to be higher than that for the

corresponding dioxetane bearing a β -naphthol-type arene (*ov*-series): **17a** >> **17b**, **2-oh** >> **2-iv** > **2-ov**, and **3-iv** > **3-ov**. This tendency could be explained by the “*syn/anti*” rotational isomerism of an aromatic electron donor, in which an *anti*-rotamer gives Φ_S far more effectively than a *syn*-rotamer.

EXPERIMENTAL

General

Melting points were uncorrected. IR spectra were taken on a FT/IR infrared spectrometer. ^1H and ^{13}C NMR spectra were recorded on a 300 MHz, 400 MHz and 500 MHz spectrometers. Mass spectra were obtained using double-focusing mass spectrometers and an ESI-TOF mass spectrometer. Column chromatography was carried out using silica gel.

Synthesis of 4-*tert*-butyl-5-{4-[*Z*-2-(2-iodophenyl)ethenyl]-3-methoxyphenyl}-3,3-dimethyl-2,3-dihydrofuran (**7a**): typical procedure.

Potassium *tert*-butoxide (1.82 g, 16.3 mmol) was added to a solution of 2-iodobenzyltriphenylphosphonium bromide (**6**) (7.43 g, 13.3 mmol) in dry THF (100 mL) under a nitrogen atmosphere at 0 °C and stirred for 30 min. To the solution was added dropwise 4-*tert*-butyl-5-(4-formyl-3-methoxyphenyl)-3,3-dimethyl-2,3-dihydrofuran (**5a**) (3.56 g, 12.4 mmol) in dry THF (90 mL) over 10 min at room temperature, and the mixture was stirred for 3 h. The reaction mixture was poured into H₂O and extracted with Et₂O. The organic layer was washed with sat. aq. NaCl, dried over anhydrous MgSO₄ and concentrated *in vacuo*. The residue was chromatographed on silica gel with AcOEt–hexane (1:4) to give **7a** (5.80 g, 11.9 mmol, 96%).

7a: colorless oil. ^1H NMR (400 MHz, CDCl₃): δ_{H} 1.03 (s, 9H), 1.31 (s, 6H), 3.81 (s, 3H), 3.86 (s, 2H), 6.56 (d, $J = 12.2$ Hz, 1H), 6.62 (dd, $J = 7.7$ and 1.4 Hz, 1H), 6.76 (s with fine coupling, 1H), 6.78 (d, $J = 12.2$ Hz, 1H), 6.82–6.88 (m, 1H), 6.87 (d, $J = 7.7$ Hz, 1H), 6.99–7.08 (m, 2H), 7.84 (dd, $J = 7.7$ and 1.0 Hz, 1H) ppm. ^{13}C NMR (125 MHz, CDCl₃): δ_{C} 27.4, 32.4, 32.4, 47.2, 55.5, 83.1, 99.8, 112.1, 122.0, 125.1, 125.8, 126.3, 127.7, 128.4, 129.6, 130.3, 134.1, 136.5, 138.8, 141.6, 149.7, 156.7 ppm. IR (liquid film): $\tilde{\nu}$ 3050, 2956, 2865, 1650, 1601, 1582, 1559 cm⁻¹. Mass (m/z , %): 488 (M⁺, 31), 474 (24), 473 (100), 363 (19), 345 (30), 215 (16), 165 (35). HRMS (ESI): 489.1303, calcd for C₂₅H₃₀IO₂ [M+H⁺] 489.1291; 511.1106, calcd for C₂₅H₂₉IO₂Na [M+Na⁺] 511.1110; 527.0849, calcd for C₂₅H₂₉IO₂K [M+K⁺] 527.0849.

7b: 57% yield. colorless columns, mp 76.5–77.0 °C (from AcOEt–hexane). ^1H NMR (500 MHz, CDCl₃): δ_{H} 1.10 (s, 9H), 1.37 (s, 6H), 3.76 (s, 3H), 3.91 (s, 2H), 6.44 (d, $J = 12.1$ Hz, 1H), 6.54 (dd, $J = 8.6$ and 2.8 Hz, 1H), 6.65 (d, $J = 12.1$ Hz, 1H), 6.77 (d, $J = 2.8$ Hz, 1H), 6.86–6.90 (m, 1H), 6.89 (d, $J = 8.6$ Hz, 1H), 7.10 (ddd, $J = 7.6$, 7.3 and 0.9 Hz, 1H), 7.16 (dd, $J = 7.6$ and 1.6 Hz, 1H), 7.87 (dd, $J = 8.0$ and 0.9 Hz, 1H) ppm. ^{13}C NMR (125 MHz, CDCl₃): δ_{C} 27.2, 32.1, 32.6, 47.2, 55.2, 83.2, 100.1, 113.7, 115.6, 126.6, 127.8, 128.1, 128.4, 128.9, 130.2, 130.3, 132.4, 137.2, 138.9, 141.8, 148.0, 158.3 ppm. IR (liquid film): $\tilde{\nu}$ 2963, 2860, 1604, 1564, 1461, 1307 cm⁻¹. Mass (m/z , %): 488 (M⁺, 38), 473 (28), 431 (17) 256 (7). HRMS (ESI): 511.1110, calcd for C₂₅H₂₉IO₂Na [M+Na⁺] 511.1110; 527.0861, calcd for C₂₅H₂₉IO₂K [M+K⁺] 527.0861.

[M+K⁺] 527.0849.

7c: 58% yield. colorless oil. ¹H NMR (400 MHz, CDCl₃): δ_H 0.98 (s, 9H), 1.28 (s, 6H), 3.59 (s, 3H), 3.82 (s, 2H), 6.52 (d, *J* = 12.0 Hz, 1H), 6.57 (dd, *J* = 2.4 and 1.3 Hz, 1H), 6.61 (d, *J* = 12.0 Hz, 1H), 6.64 (dd, *J* = 2.4 and 1.3 Hz, 1H), 6.67 (s with fine coupling, 1H), 6.87–6.92 (m, 1H), 7.11–7.18 (m, 2H), 7.85–7.88 (m, 1H) ppm. ¹³C NMR (125 MHz, CDCl₃): δ_C 27.3, 32.3, 32.5, 47.1, 55.0, 83.0, 99.5, 113.7, 114.8, 123.4, 125.5, 128.0, 128.6, 130.4, 130.8, 134.0, 137.1, 137.3, 139.0, 141.6, 149.4, 158.8 ppm. IR (liquid film): $\tilde{\nu}$ 2955, 2866, 1653, 1585, 1464 cm⁻¹. Mass (*m/z*, %): 488 (M⁺, 28), 474 (25), 473 (100). HRMS (ESI): 489.1292, calcd for C₂₅H₃₀IO₂ [M+H⁺] 489.1291; 511.1104, calcd for C₂₅H₂₉IO₂Na [M+Na⁺] 511.1110.

12a: 84% yield. colorless columns, mp 101.0–102.0 °C (from AcOEt–hexane). ¹H NMR (400 MHz, CDCl₃): δ_H 1.03 (s, 9H), 1.31 (s, 6H), 3.84 (s, 3H), 3.86 (s, 2H), 6.57 (dd, *J* = 7.8 and 1.4 Hz, 1H), 6.79 (d, *J* = 1.4 Hz, 1H), 6.90 (d, *J* = 7.8 Hz, 1H), 6.93 (s, 2H), 7.16 (d, *J* = 8.5 Hz, 1H), 7.45 (d, *J* = 8.5 Hz, 1H), 7.48 (dd with fine coupling, *J* = 8.0 and 6.9 Hz, 1H), 7.57 (dd with fine coupling, *J* = 8.5 and 6.9 Hz, 1H), 7.72 (d with fine coupling, *J* = 8.0 Hz, 1H), 8.34 (d with fine coupling, *J* = 8.5 Hz, 1H) ppm. ¹³C NMR (125 MHz, CDCl₃): δ_C 27.4, 32.4, 32.4, 47.1, 55.5, 83.1, 112.0, 121.9, 123.7, 125.2, 125.8, 126.3, 126.7, 126.8, 127.1, 127.1, 128.0, 128.2, 129.9, 130.7, 132.4, 133.5, 136.2, 136.7, 149.6, 156.7 ppm. IR (KBr): $\tilde{\nu}$ 2954, 2925, 2855, 1650, 1604, 1463 cm⁻¹. Mass (*m/z*, %): 492 (M⁺+2, 36), 490 (M⁺, 37), 478 (28), 477 (100), 475 (98), 395 (32), 367 (35), 365 (35), 340 (48), 215 (49). HRMS (ESI): 513.1399, calcd for C₂₉H₃₁⁷⁹BrO₂Na [M+Na⁺] 513.1405; 515.1387, calcd for C₂₉H₃₁⁸¹BrO₂Na [M+Na⁺] 515.1385.

12b: 72% yield. colorless columns, mp 129.0–130.0 °C (from Et₂O–hexane). ¹H NMR (500 MHz, CDCl₃): δ_H 1.12 (s, 9H), 1.39 (s, 6H), 3.75 (s, 3H), 3.93 (s, 2H), 6.49 (dd, *J* = 8.6 and 2.8 Hz, 1H), 6.78 (d, *J* = 12.1 Hz, 1H), 6.79 (d, *J* = 2.8 Hz, 1H), 6.81 (d, *J* = 12.1 Hz, 1H), 6.92 (d, *J* = 8.6 Hz, 1H), 7.25 (d, *J* = 8.6 Hz, 1H), 7.49 (dd with fine coupling, *J* = 7.9 and 6.9 Hz, 1H), 7.53 (d, *J* = 8.6 Hz, 1H), 7.57 (dd with fine coupling, *J* = 8.6 and 6.9 Hz, 1H), 7.74 (d, *J* = 7.9 Hz, 1H), 8.34 (d, *J* = 8.6 Hz, 1H) ppm. ¹³C NMR (125 MHz, CDCl₃): δ_C 27.3, 32.2, 32.6, 47.2, 55.2, 83.3, 113.7, 115.7, 123.8, 128.3, 126.3, 126.6, 127.0, 127.1, 127.2, 128.0, 128.3, 129.2, 129.4, 130.7, 132.5, 133.5, 136.6, 137.3, 148.0, 158.4 ppm. IR (KBr): $\tilde{\nu}$ 2956, 2863, 1602, 1487, 1049 cm⁻¹. Mass (*m/z*, %): 492 (M⁺+2, 1), 490 (M⁺, 1), 252 (1), 221 (4), 215 (5), 57 (100). HRMS (ESI): not observed.

Synthesis of 4-*tert*-butyl-5-(1-methoxyphenanthren-3-yl)-3,3-dimethyl-2,3-dihydrofuran (**8-iv**):

typical procedure. AIBN (177 mg, 1.08 mmol) and tributyltin hydride (3.40 mL, 12.6 mmol) were added to a solution of **7a** (2.57 g, 5.26 mmol) in dry toluene (180 mL) under a nitrogen atmosphere at room temperature, and the solution was stirred at 90 °C for 10 h. The reaction mixture was concentrated *in vacuo*. The residue was crystallized from AcOEt–hexane to give 4-*tert*-butyl-5-(1-methoxyphenanthren-3-yl)-3,3-dimethyl-2,3-dihydrofuran (**8-iv**) (1.61 g, 4.47 mmol, 85%).

8-iv: colorless columns, mp 141.0–142.0 °C (from Et₂O–hexane). ¹H NMR (400 MHz, CDCl₃): δ_H 1.11 (s, 9H), 1.42 (s, 6H), 3.98 (s, 2H), 4.05 (s, 3H), 6.93 (d, *J* = 1.0 Hz, 1H), 7.59 (dd with fine coupling, *J* = 7.7 and 6.9 Hz, 1H), 7.63 (dd with fine coupling, *J* = 8.2 and 6.9 Hz, 1H), 7.75 (d, *J* = 9.1 Hz, 1H), 7.89 (dd, *J* = 7.7 and 1.5 Hz, 1H), 8.21 (d, *J* = 9.1 Hz, 1H), 8.22 (s, 1H), 8.66 (d, *J* = 8.2 Hz, 1H) ppm. ¹³C

NMR (125 MHz, CDCl₃): δ_C 27.5, 32.5, 32.6, 47.3, 55.7, 83.1, 107.5, 116.7, 120.2, 122.8, 123.2, 126.0, 126.3, 126.4, 126.6, 128.5, 130.0, 130.9, 132.3, 134.4, 150.5, 155.5 ppm. IR (KBr): $\tilde{\nu}$ 2959, 2866, 1654, 1611, 1599 cm⁻¹. MASS (*m/z*, %): 360 (M⁺, 30), 346 (26), 345 (100), 289 (17), 235 (17), 57 (13). HRMS (ESI): 361.2168, calcd for C₂₅H₂₉O₂ [M+H⁺] 361.2168; 383.1991, calcd for C₂₅H₂₈O₂ Na [M+Na⁺] 383.1987; 415.2255, calcd for C₂₆H₃₂O₃Na [M+MeOH+Na⁺]415.2249.

8-ov: 86% yield. colorless columns, mp 136.0–137.0 °C (from AcOEt–hexane). ¹H NMR (500 MHz, CDCl₃): δ_H 1.01 (s, 9H), 1.43 (s, 3H), 1.49 (s, 3H), 4.02 (q_{AB}, *J* = 8.0 Hz, 2H), 4.02 (s, 3H), 7.21 (d, *J* = 2.4 Hz, 1H), 7.55–7.65 (m, 2H), 7.63 (d, *J* = 9.2 Hz, 1H), 7.81 (d, *J* = 9.2 Hz, 1H), 7.87 (dd, *J* = 7.6 and 1.1 Hz, 1H), 8.07 (d, *J* = 2.4 Hz, 1H), 8.60 (d, *J* = 8.0 Hz, 1H) ppm. ¹³C NMR (125 MHz, CDCl₃): δ_C 27.3, 27.6, 32.0, 32.6, 47.3, 55.5, 83.4, 104.6, 118.8, 122.8, 124.3, 124.9, 125.8, 126.1, 126.6, 127.9, 128.5, 129.8, 131.8, 132.3, 135.8, 147.6, 157.5 ppm. IR (liquid film): $\tilde{\nu}$ 2987, 2960, 2867, 1650, 1604, 1046 cm⁻¹. Mass (*m/z*, %): 360 (M⁺, 9), 345 (8), 288 (12), 245 (12), 235 (11), 215 (16), 202 (17), 57(100). HRMS (ESI): 361.2170, calcd for C₂₅H₂₉O₂ [M+H⁺] 361.2168; 383.1994, calcd for C₂₅H₂₈O₂Na [M+Na⁺] 383.1987.

8-oh: 58% yield. colorless columns, mp 113.5–114.0 °C (from AcOEt–hexane). ¹H NMR (300 MHz, CDCl₃): δ_H 1.10 (s, 9H), 1.40 (s, 6H), 3.96 (s, 2H), 4.15 (s, 3H), 7.08 (d, *J* = 1.5 Hz, 1H), 7.48 (d, *J* = 1.5 Hz, 1H), 7.54–7.67 (m, 2H), 7.68 (d, *J* = 8.7 Hz, 1H), 7.74 (d, *J* = 8.7 Hz, 1H) 7.87 (dd, *J* = 7.6 and 1.8 Hz, 1H), 9.64 (d with fine coupling, *J* = 8.1 Hz, 1H) ppm. ¹³C NMR (125 MHz, CDCl₃): δ_C 27.5, 32.5, 32.6, 47.3, 55.8, 83.3, 109.9, 120.4, 122.9, 126.0, 126.2, 126.4, 127.2, 128.1, 128.2, 128.6, 130.1, 132.9, 134.1, 134.3, 149.7, 158.4 ppm. IR (KBr): $\tilde{\nu}$ 3064, 2984, 2951, 1655, 1601, 1567 cm⁻¹. Mass (*m/z*, %): 360 (M⁺, 30), 346 (26), 345 (100), 289 (15), 235 (13). HRMS (ESI): 361.2179, calcd for C₂₅H₂₉O₂ [M+H⁺] 361.2168; 383.1985, calcd for C₂₅H₂₈O₂Na [M+Na⁺] 383.1987; 399.1771, calcd for C₂₅H₂₈O₂K [M+K⁺] 399.1726.

8-ih: 31% yield. colorless columns, mp 162.5–163.0 °C (from AcOEt–hexane). ¹H NMR (500 MHz, CDCl₃): δ_H 0.97 (s, 9H), 1.44 (s, 3H), 1.52 (s, 3H), 3.92 (s, 3H), 4.10(q_{AB}, *J* = 8.2 Hz, 2H) 7.18 (d, *J* = 2.9 Hz, 1H) 7.25 (d, *J* = 2.9 Hz, 1H), 7.50 (dd with fine coupling, *J* = 7.7 and 6.9 Hz, 1H), 7.54 (dd with fine coupling, *J* = 8.4 and 6.9 Hz, 1H) 7.62 (d, *J* = 8.8 Hz, 1H), 7.68 (d, *J* = 8.8 Hz, 1H), 7.82 (d with fine coupling, *J* = 7.7 Hz, 1H), 9.16 (d, *J* = 8.4 Hz, 1H) ppm. ¹³C NMR (125 MHz, CDCl₃): δ_C 26.2, 27.9, 31.7, 32.7, 47.1, 55.4, 83.7, 110.0, 122.1, 123.4, 124.0, 125.4, 125.7, 126.4, 127.1, 127.9, 128.4, 130.5, 132.0, 134.3, 134.9, 151.1, 156.6 ppm. IR (KBr): $\tilde{\nu}$ 3051, 2956, 2867, 1641, 1600, 1575, 1263, 1231, 1202 cm⁻¹. Mass (*m/z*, %): 360 (M⁺, 28), 346 (25), 345 (100), 303 (13), 289 (14), 235 (12). HRMS (ESI): 361.2187, calcd for C₂₅H₂₉O₂ [M+H⁺] 361.2168; 383.1989, calcd for C₂₅H₂₈O₂Na [M+Na⁺] 383.1987; 399.1758, calcd for C₂₅H₂₈O₂K [M+K⁺] 399.1726.

13-iv: 45% yield. colorless columns, mp 170.0–171.0 °C. (from CH₂Cl₂–hexane). ¹H NMR (300 MHz, CDCl₃): δ_H 1.15 (s, 9H), 1.41 (s, 6H), 3.96 (s, 2H), 4.10 (s, 3H), 6.94 (d, *J* = 1.0 Hz, 1H), 7.57–7.69 (m, 2H), 7.82 (d, *J* = 8.5 Hz, 1H), 7.83 (d, *J* = 8.8 Hz, 1H), 7.89 (d, *J* = 8.5 Hz, 1H), 8.00 (dd, *J* = 7.5 and 1.8 Hz, 1H), 8.39 (d, *J* = 8.8 Hz, 1H), 8.64 (s with fine coupling, 1H), 9.87 (d with fine coupling, *J* = 8.1 Hz, 1H) ppm. ¹³C NMR (125 MHz, CDCl₃): δ_C 27.5, 32.6, 32.6, 47.3, 55.8, 83.2, 106.5, 120.8, 121.9, 124.7,

125.7, 125.9, 126.0, 126.4, 126.8, 127.2, 127.6, 128.1, 128.4, 130.4, 130.8, 131.4, 133.5, 134.1, 150.7, 155.4 ppm. IR (KBr): $\tilde{\nu}$ 2958, 2866, 1652, 1601 cm^{-1} . Mass (m/z , %): 410 (M^+ , 38), 396 (28), 395 (100), 339 (15), 285 (11), 242 (11), 214 (10). HRMS (ESI): 411.2331, calcd for $\text{C}_{29}\text{H}_{31}\text{O}_2$ [$\text{M}+\text{H}^+$] 411.2324; 433.2149, calcd for $\text{C}_{29}\text{H}_{30}\text{O}_2\text{Na}$ [$\text{M}+\text{Na}^+$] 433.2144.

13-ov: 62% yield. colorless needles, mp 136.0–136.5 °C. (from CH_2Cl_2 –hexane). ^1H NMR (500 MHz, CDCl_3): δ_{H} 1.05 (s, 9H), 1.45 (s, 3H), 1.51 (s, 3H), 4.01 (s, 3H), 4.04 (q_{AB}, $J = 8.1$ Hz, 2H), 7.26 (d, $J = 2.5$ Hz, 1H), 7.60 (dd with fine coupling, $J = 7.9$ and 6.8 Hz, 1H), 7.66 (dd with fine coupling, $J = 8.5$ and 6.8 Hz, 1H) 7.72 (d, $J = 8.6$ Hz, 1H), 7.79 (d, $J = 8.5$ Hz, 1H), 7.87 (d, $J = 8.5$ Hz, 1H), 7.98 (d, $J = 8.6$ Hz, 1H), 8.01 (d with fine coupling, $J = 7.9$ Hz, 1H), 8.57 (d, $J = 2.5$ Hz, 1H), 9.16 (d, $J = 8.5$ Hz, 1H) ppm. ^{13}C NMR (125 MHz, CDCl_3): δ_{C} 27.3, 27.6, 32.0, 32.7, 47.4, 55.6, 83.4, 109.8, 118.6, 125.0 (x 2), 125.6, 125.9, 126.8, 126.9, 127.2, 127.5, 127.5, 128.0, 128.6, 130.5, 131.4, 131.7, 133.4, 135.5, 147.8, 157.2 ppm. IR (KBr): $\tilde{\nu}$ 3052, 2956, 2862, 1648, 1601 cm^{-1} . Mass (m/z , %): 410 (M^+ , 100), 396 (18), 395 (60), 380 (15), 365 (16), 339 (15). HRMS (ESI): 411.2324, calcd for $\text{C}_{29}\text{H}_{31}\text{O}_2$ [$\text{M}+\text{H}^+$] 411.2324; 433.2147, calcd for $\text{C}_{29}\text{H}_{30}\text{O}_2\text{Na}$ [$\text{M}+\text{Na}^+$] 433.2144.

Synthesis of 4-tert-butyl-5-(1-hydroxyphenanthren-3-yl)-3,3-dimethyl-2,3-dihydrofuran (4-iv) : typical procedure. Sodium thiomethoxide (119 mg, 1.70 mmol) was added to a solution of **8-iv** (301 mg, 0.835 mmol) in dry DMF (10 mL) and stirred under a nitrogen atmosphere at 150 °C for 30 min. The reaction mixture was poured into sat. aq. NH_4Cl and extracted with AcOEt. The organic layer was washed with sat. aq. NaCl, dried over anhydrous MgSO_4 and concentrated *in vacuo*. The residue was chromatographed on silica gel with AcOEt–hexane (5:1) to give **4-iv** (286 mg, 0.854 mmol, 99%).

4-iv: colorless columns, mp 218.0–218.5 °C (from Et_2O –hexane). ^1H NMR (400 MHz, CDCl_3): δ_{H} 1.10 (s, 9H), 1.41 (s, 6H), 3.97 (s, 2H), 5.40 (s, 1H), 6.92 (d, $J = 1.2$ Hz, 1H), 7.56–7.66 (m, 2H), 7.72 (d, $J = 9.0$ Hz, 1H), 7.88 (d with fine coupling, $J = 7.6$ Hz, 1H), 8.09 (dd, $J = 9.0$ and 0.6 Hz, 1H), 8.22 (s, 1H), 8.64 (d, $J = 8.1$ Hz, 1H) ppm. ^{13}C NMR (125 MHz, CDCl_3): δ_{C} 27.4, 32.6, 32.6, 47.3, 83.2, 112.6, 117.1, 119.9, 121.8, 123.2, 126.3, 126.4, 126.5, 126.6, 128.5, 130.0, 131.2, 132.2, 133.9, 149.8, 151.6 ppm. IR (KBr): $\tilde{\nu}$ 3333, 2955, 2869, 1654, 1614, 1601 cm^{-1} . MASS (m/z , %): 346 (M^+ , 29), 332 (24), 331 (100), 275 (17), 221 (20), 165 (14). HRMS (ESI): 369.1831, calcd for $\text{C}_{24}\text{H}_{26}\text{O}_2\text{Na}$ [$\text{M}+\text{Na}^+$] 369.1831; 385.1574, calcd for $\text{C}_{24}\text{H}_{26}\text{O}_2\text{K}$ [$\text{M}+\text{K}^+$] 385.1570.

4-ov: 97% yield. colorless columns, mp 139.0–139.5 °C (from CH_2Cl_2 –hexane). ^1H NMR (300 MHz, CDCl_3): δ_{H} 1.01 (s, 9H), 1.43 (s, 3H), 1.50 (s, 3H), 4.02 (q_{AB}, $J = 8.1$ Hz, 2H), 5.11 (s, 1H), 7.13 (d, $J = 2.4$ Hz, 1H), 7.54–7.61 (m, 2H), 7.62 (d, $J = 8.9$ Hz, 1H), 7.79 (d, $J = 8.9$ Hz, 1H), 7.82–7.87 (m, 1H), 8.00 (d, $J = 2.4$ Hz, 1H), 8.47–8.52 (m, 1H) ppm. ^{13}C NMR (125 MHz, CDCl_3): δ_{C} 27.3, 27.4, 31.9, 32.6, 47.3, 83.3, 107.8, 119.3, 122.8, 124.1, 124.9, 125.6, 126.1, 126.6, 128.3, 128.4, 129.5, 132.0, 132.2, 135.4, 147.2, 153.4 ppm. IR (KBr): $\tilde{\nu}$ 3311, 2983, 2967, 2870, 1653, 1614, 1602 cm^{-1} . Mass (m/z , %): 346 (M^+ , 3), 221 (10), 165 (49), 164 (13), 163 (15), 95 (25), 57 (100). HRMS (ESI): 369.1835, calcd for $\text{C}_{24}\text{H}_{26}\text{O}_2\text{Na}$ [$\text{M}+\text{Na}^+$] 369.1831; 385.1579, calcd for $\text{C}_{24}\text{H}_{26}\text{O}_2\text{K}$ [$\text{M}+\text{K}^+$] 385.1570.

4-oh: 98% yield. colorless columns, mp 179.5–180.0 °C (from AcOEt–hexane). ^1H NMR (300 MHz, CDCl_3): δ_{H} 1.10 (s, 9H), 1.39 (s, 6H), 3.94 (s, 2H), 5.77 (s, 1H), 6.95 (d, $J = 1.5$ Hz, 1H), 7.46 (d, $J = 1.5$

Hz, 1H), 7.54–7.68 (m, 2H), 7.66 (d, $J = 8.9$ Hz, 1H), 7.72 (d, $J = 8.9$ Hz, 1H), 7.87 (d with fine coupling, $J = 7.6$ Hz, 1H), 9.61 (d with fine coupling, $J = 8.3$ Hz, 1H) ppm. ^{13}C NMR (125 MHz, CDCl_3): δ_{C} 27.4, 32.5, 32.6, 47.3, 83.1, 114.9, 119.3, 122.9, 126.0, 126.4, 126.9 (broad), 127.0, 128.0, 128.1, 128.6, 130.1, 132.6, 133.7 (broad), 134.4, 149.1, 154.2 ppm. IR (KBr): $\tilde{\nu}$ 3212, 3061, 2956, 2866, 1661, 1610, 1599, 1570 cm^{-1} . Mass (m/z , %): 346 (M^+ , 31), 332 (24), 331 (100), 275 (16), 221 (16), 165 (11). HRMS (ESI): 347.2016, calcd for $\text{C}_{24}\text{H}_{27}\text{O}_2$ [$\text{M}+\text{H}^+$] 347.2011; 369.1829, calcd for $\text{C}_{24}\text{H}_{26}\text{O}_2\text{Na}$ [$\text{M}+\text{Na}^+$] 369.1831. 385.1584, calcd for $\text{C}_{24}\text{H}_{26}\text{O}_2\text{K}$ [$\text{M}+\text{K}^+$] 385.1570.

4-ih: 87% yield. colorless columns, mp 155.5–156.0 °C (from CH_2Cl_2 –hexane). ^1H NMR (500 MHz, CDCl_3): δ_{H} 0.95 (s, 9H), 1.44 (s, 3H), 1.52 (s, 3H), 4.13 (q_{AB}, $J = 8.3$ Hz, 2H) 5.87 (broad s, 1H), 6.91 (dd, $J = 4.7$ and 2.7 Hz, 1H), 7.07 (d, $J = 2.8$ Hz, 1H), 7.31 (dd, $J = 8.8$ and 4.7 Hz, 1H), 7.50 (dd with fine coupling, $J = 7.7$ and 6.9 Hz, 1H), 7.54 (dd with fine coupling, $J = 8.4$ and 6.9 Hz, 1H), 7.60 (d, $J = 8.8$ Hz, 1H), 7.80 (dd, $J = 7.7$ and 1.4 Hz, 1H), 9.13 (d, $J = 8.4$ Hz, 1H) ppm. ^{13}C NMR (125 MHz, CDCl_3): δ_{C} 26.1, 27.9, 31.6, 32.7, 47.1, 83.6, 113.4, 122.0, 123.3, 124.4, 125.5, 125.7, 126.3, 126.9, 127.9, 128.5, 130.4, 132.0, 133.9, 134.9, 150.6, 152.6 ppm. IR (KBr): $\tilde{\nu}$ 3347, 3049, 2977, 2953, 2869, 1640, 1617, 1571 cm^{-1} . Mass (m/z , %): 346 (M^+ , 27), 332 (24), 331 (100), 289 (13), 275 (11), 221 (12), 165 (11). HRMS (ESI): 369.1829, calcd for $\text{C}_{24}\text{H}_{26}\text{O}_2\text{Na}$ [$\text{M}+\text{Na}^+$] 369.1831.

10-iv: 91% yield. colorless columns, mp 155.5–156.0 °C (from CH_2Cl_2 –hexane). ^1H NMR (300 MHz, CDCl_3): δ_{H} 1.16 (s, 9H), 1.40 (s, 6H), 3.95 (s, 2H) 5.41 (broad s, 1H), 6.94 (d, $J = 1.2$ Hz, 1H), 7.58–7.70 (m, 2H), 7.81 (d, $J = 8.4$ Hz, 1H), 7.81 (d, $J = 8.8$ Hz, 1H), 7.90 (d, $J = 8.4$ Hz, 1H), 8.01 (d with fine coupling, $J = 7.4$ Hz, 1H), 8.28 (d with fine coupling, $J = 8.8$ Hz, 1H), 8.65 (d, $J = 1.2$ Hz, 1H), 9.08 (d with fine coupling, $J = 8.0$ Hz, 1H) ppm. ^{13}C NMR (125 MHz, CDCl_3): δ_{C} 27.4, 32.5, 32.6, 47.2, 83.0, 111.7, 120.6, 122.2, 123.8, 125.7, 125.9, 126.2, 126.6, 126.8, 127.2, 127.5, 128.1, 128.4, 130.4, 131.0, 131.3, 133.4, 133.4, 150.0, 151.6 ppm. IR (KBr): $\tilde{\nu}$ 3396, 2957, 2921, 2868, 1651. 1606 cm^{-1} . Mass (m/z , %): 396 (M^+ , 34), 382 (28), 381 (100), 325 (15), 271 (14), 215 (10). HRMS (ESI): 397.2178, calcd for $\text{C}_{28}\text{H}_{29}\text{O}_2$ [$\text{M}+\text{H}^+$] 397.2168; 419.1989, calcd for [$\text{M}+\text{Na}^+$] 419.1987.

10-ov: 86% yield. colorless columns, mp 169.0–170.0 °C (from AcOEt –hexane). ^1H NMR (500 MHz, CDCl_3): δ_{H} 1.04 (s, 9H), 1.44 (s, 3H), 1.51 (s, 3H), 4.05 (q_{AB}, $J = 8.0$ Hz, 2H), 5.39 (s, 1H), 7.17 (d, $J = 2.5$ Hz, 1H), 7.57 (dd with fine coupling, $J = 7.8$ and 6.9 Hz, 1H), 7.61 (dd with fine coupling, $J = 8.3$ and 6.9 Hz, 1H), 7.68 (d, $J = 8.8$ Hz, 1H), 7.76 (d, $J = 8.5$ Hz, 1H), 7.84 (d, $J = 8.5$ Hz, 1H), 7.95 (d, $J = 8.8$ Hz, 1H), 7.97 (d with fine coupling, $J = 7.8$ Hz, 1H), 8.46 (d, $J = 2.5$ Hz, 1H), 9.03 (d, $J = 8.3$ Hz, 1H) ppm. ^{13}C NMR (125 MHz, CDCl_3): δ_{C} 27.3, 27.4, 31.9, 32.7, 47.3, 83.3, 112.6, 118.8, 124.7, 124.9, 125.5, 125.9, 126.3, 126.7, 127.3, 127.3, 127.5, 128.4, 128.4, 130.4, 131.3, 131.8, 133.2, 135.2, 147.4, 153.2 ppm. IR (KBr): $\tilde{\nu}$ 3348, 3051, 2958, 2869, 1650, 1603 cm^{-1} . Mass (m/z , %): 396 (M^+ , 2), 324 (10), 295 (4), 271 (12), 226 (11), 215 (33), 213 (37), 57 (100). HRMS (ESI): 419.1992, calcd for $\text{C}_{28}\text{H}_{28}\text{O}_2\text{Na}$ [$\text{M}+\text{Na}^+$] 419.1987; 435.1741, calcd for $\text{C}_{28}\text{H}_{28}\text{O}_2\text{K}$ [$\text{M}+\text{K}^+$] 435.1726.

Synthesis of 5-tert-butyl-1-(1-hydroxyphenanthren-3-yl)-4,4-dimethyl-2,6,7-trioxabicyclo[3.2.0]heptane (2-iv) : typical procedure. A solution of **4-iv** (201 mg, 0.580 mmol) and tetraphenylporphyrin (TPP) (2.0 mg) in CH_2Cl_2 (20 mL) was irradiated externally with a 940 W Na lamp

under an O₂ atmosphere at 0 °C for 35 min. The residue was chromatographed on silica gel with Et₂O–hexane (1:9) to give **2-iv** (171 mg, 0.452 mmol, 78%) to give colorless solid.

2-iv: colorless columns, mp 99.5–100.5 °C (from Et₂O–hexane). ¹H NMR (400 MHz, CDCl₃): δ_H 1.02 (s, 9H), 1.21 (s, 3H), 1.47 (s, 3H), 3.91 (d, *J* = 8.2 Hz, 1H), 4.68 (d, *J* = 8.2 Hz, 1H), 5.53 (s, 1H), 7.21 (s, 1H), 7.62 (dd with fine coupling, *J* = 7.8 and 7.0 Hz, 1H), 7.67 (dd with fine coupling, *J* = 8.2 and 7.0 Hz, 1H), 7.80 (d, *J* = 9.1 Hz, 1H), 7.91 (dd, *J* = 7.8 and 1.1 Hz, 1H), 8.13 (d, *J* = 9.1 Hz, 1H), 8.61 (s, 1H), 8.71 (d, *J* = 8.2 Hz, 1H) ppm. ¹³C NMR (125 MHz, CDCl₃): δ_C 18.5, 25.2, 26.9, 36.9, 45.7, 80.3, 105.2, 110.1, 116.1, 116.9, 119.7, 122.5, 123.3, 126.9, 127.0, 127.4, 128.7, 130.2, 131.1, 132.3, 134.1, 151.7 ppm. IR (KBr): $\tilde{\nu}$ 3419, 3238, 2979, 2895, 1620, 1603, 1576 cm⁻¹. Mass (*m/z*, %): 378 (M⁺, 20), 322 (18), 238 (36), 221 (100) 193 (16), 165 (26), 57 (41). HRMS (ESI): 401.1734, calcd for C₂₄H₂₆O₄Na [M+Na⁺] 401.1729.

2-ov: 96% yield. colorless columns, mp 163.0–163.5 °C (from CH₂Cl₂–hexane). ¹H NMR (500 MHz, CDCl₃): δ_H 0.92 (s, 9H), 1.32 (s, 3H), 1.67 (s, 3H), 4.12 (d, *J* = 8.7 Hz, 1H), 4.72 (d, *J* = 8.7 Hz, 1H), 5.17 (broad s 1H), 7.57–7.65 (m, 2H), 7.63 (d, *J* = 9.4 Hz, 1H), 7.83–7.87 (m, 1H), 7.97 (broad, 1H), 8.21 (d, *J* = 2.8 Hz, 1H), 8.38–8.48 (m, 1H), 8.57 (d, *J* = 7.8 Hz, 1H) ppm. ¹³C NMR (125 MHz, CDCl₃): δ_C 20.2, 26.2, 26.8, 36.9, 45.7, 80.8, 106.5, 109.3, 117.3, 120.2, 123.1, 124.3, 124.4, 124.9, 126.4, 127.0, 128.2, 129.8, 131.6, 133.2, 133.9, 153.1 ppm. IR(KBr): $\tilde{\nu}$ 3452, 2975, 2891, 1614, 1405, 1217 cm⁻¹. Mass (*m/z*, %): 378 (M⁺, 39), 322 (20), 238 (50), 222 (16), 221 (100). HRMS (ESI): 401.1726, calcd for C₂₄H₂₆O₄Na [M+Na⁺] 401.1729; 417.1504, calcd for C₂₄H₂₆O₄K [M+K⁺] 417.1468.

2-oh: 68% yield. pale yellow columns, mp 140.5–141.5 °C (from CH₂Cl₂–hexane). ¹H NMR (400 MHz, CDCl₃): δ_H 1.02 (s, 9H), 1.20 (s, 3H), 1.46 (s, 3H), 3.90 (d, *J* = 8.3 Hz, 1H), 4.66 (d, *J* = 8.3 Hz, 1H), 5.83 (s, 1H), 7.25 (d, *J* = 1.6 Hz, 1H), 7.59–7.70 (m, 2H), 7.73 (d, *J* = 8.9 Hz, 1H), 7.77 (d, *J* = 8.9 Hz, 1H), 7.80 (d, *J* = 1.6 Hz, 1H), 7.90 (d with fine coupling, *J* = 7.8 Hz, 1H), 9.64 (d with fine coupling, *J* = 8.4 Hz, 1H) ppm. ¹³C NMR (125 MHz, CDCl₃): δ_C 18.5, 25.1, 26.9, 36.8, 45.7, 80.3, 105.3, 112.5, 116.6, 120.1, 121.8, 126.4, 126.7, 127.3, 128.2, 128.5, 128.7, 129.9, 133.0, 133.8, 134.3, 154.3 ppm. IR (KBr): $\tilde{\nu}$ 3245, 3051, 2968, 1627, 1574, 1402 cm⁻¹. Mass (*m/z*, %): 378 (M⁺, 24), 322 (19), 238 (39), 222 (17), 221 (100), 193 (19), 165 (51). HRMS (ESI): 401.1719, calcd for C₂₄H₂₆O₄Na [M+Na⁺] 401.1729.

3-iv: 60% yield. pale yellow columns mp 190.0–91.0 °C (from CH₂Cl₂–hexane). ¹H NMR (300 MHz, CDCl₃): δ_H 1.07 (s, 9H), 1.21 (s, 3H), 1.50 (s, 3H), 3.89 (d, *J* = 8.2 Hz, 1H), 4.67 (d with fine coupling, *J* = 8.2 Hz, 1H), 5.49 (s 1H), 7.25 (broad d, *J* = 1.1 Hz, 1H), 7.59–7.70 (m, 2H), 7.83 (d, *J* = 8.5 Hz, 1H), 7.89 (d, *J* = 8.8 Hz, 1H), 7.92 (d, *J* = 8.5 Hz, 1H), 7.99–8.05 (m, 1H), 8.33 (d with fine coupling, *J* = 8.8 Hz, 1H), 9.01–9.07 (m, 2H) ppm. ¹³C NMR (125 MHz, CDCl₃): δ_C 18.5, 25.0, 27.0, 36.9, 45.7, 80.3, 105.5, 109.1, 117.2, 120.5, 121.0, 124.3, 126.0, 126.2, 126.7, 127.2, 127.5, 127.9 (x 2), 128.5, 130.3, 130.8, 131.5, 133.5, 133.6, 151.8 ppm. IR (KBr): $\tilde{\nu}$ 3439, 3052, 3005, 2964, 2898, 1613, 1603, 1413 cm⁻¹. Mass (*m/z*, %): 428 (M⁺, 62), 372 (31), 288 (39), 272 (22), 271 (100), 57 (43). HRMS (ESI): 451.1895, calcd for C₂₈H₂₈O₄Na [M+Na⁺] 451.1885.

3-ov: 86% yield. pale yellow columns, mp 192.0–193.0 °C (from AcOEt–hexane). ¹H NMR (400 MHz, CDCl₃): δ_H 0.95 (s, 9H), 1.33 (s, 3H), 1.69 (s, 3H), 4.14 (d, *J* = 8.5 Hz, 1H), 4.74 (d, *J* = 8.5 Hz, 1H), 5.21

(s 1H), 7.58–7.70 (m, 2H), 7.70 (d, $J = 9.0$ Hz, 1H), 7.77 (d, $J = 8.5$ Hz, 1H), 7.89 (d, $J = 8.5$ Hz, 1H), 7.96–8.03 (m, 1H), 8.00 (dd, $J = 7.9$ and 1.3 Hz, 1H), 8.56–8.64 (m, 1H), 8.62 (d, $J = 2.2$ Hz, 1H), 9.04 (d, $J = 8.3$ Hz, 1H) ppm. ^{13}C NMR (125 MHz, CDCl_3): δ_{C} 20.2, 26.2, 26.9, 37.0, 45.7, 80.8, 106.4, 114.3, 119.9, 124.4, 124.8, 125.8, 126.2, 126.4, 126.6, 126.8, 127.7, 128.0, 128.6, 127.7, 128.0, 128.6, 130.4, 130.7, 132.9, 133.4, 133.6, 152.6 ppm. IR (KBr): $\tilde{\nu}$ 3460, 3050, 2998, 2977, 2896, 1616 cm^{-1} . Mass (m/z , %): 428 (M^+ , 63), 372 (24), 288 (58) 272 (22), 271 (100), 215 (30), 57 (30). HRMS (ESI): 429.2110, calcd for $\text{C}_{28}\text{H}_{29}\text{O}_4$ [$\text{M}+\text{H}^+$] 429.2066; 451.1876, calcd for $\text{C}_{28}\text{H}_{28}\text{O}_4\text{Na}$ [$\text{M}+\text{Na}^+$] 451.1885.

Synthesis of 2,2,4,4-tetramethyl-3-oxopentyl 1-hydroxyphenanthrene-3-carboxylate (9-iv): typical procedure. TBAF (1M in THF, 0.75 mL, 0.75 mmol) in MeCN (1.5 mL) was added to a solution of **2-iv** (57.0 mg, 0.151 mmol) in MeCN (1.5 mL) and stirred for 5 min. The reaction mixture was poured into sat. aq. NH_4Cl and extracted with AcOEt. The organic layer was washed with sat. aq. NaCl, dried over anhydrous MgSO_4 and concentrated *in vacuo*. The residue was chromatographed on silica gel and recrystallization with Et_2O –hexane (1:3) gave **9-iv** (53.0 mg, 0.140 mmol, 93%).

9-iv: pale yellow needles, mp 164.5–165.0 °C (from CH_2Cl_2 –hexane). ^1H NMR (400 MHz, CDCl_3): δ_{H} 1.35 (s, 9H), 1.47 (s, 6H), 4.53 (s, 2H), 6.13 (s, 1H), 7.58 (s with fine coupling, 1H), 7.64 (dd with fine coupling, $J = 7.3$ and 7.1 Hz, 1H), 7.69 (dd with fine coupling, $J = 8.2$ and 7.1 Hz, 1H), 7.86 (d, $J = 9.1$ Hz, 1H), 7.92 (d, $J = 7.3$ Hz, 1H), 8.18 (d, $J = 9.1$ Hz, 1H), 8.67 (d, $J = 8.2$ Hz, 1H), 8.96 (s, 1H) ppm. ^{13}C NMR (125 MHz, CDCl_3): δ_{C} 23.8, 28.2, 46.0, 49.5, 72.4, 110.0, 117.0, 120.1, 123.0, 125.3, 127.0, 127.1, 127.4, 128.5, 128.7, 130.3, 131.1, 132.2, 152.8, 167.0, 217.1 ppm. IR (KBr): $\tilde{\nu}$ 3433, 2971, 1695, 1604, 1274 cm^{-1} . Mass (m/z , %): 378 (M^+ , 31), 322 (24), 238 (36), 222 (16), 221 (100), 193 (13), 165 (20), 57 (31). HRMS (ESI): 401.1741, calcd for $\text{C}_{24}\text{H}_{26}\text{O}_4\text{Na}$ [$\text{M}+\text{Na}^+$] 401.1729.

9-ov: colorless columns, mp 163.0–163.5 °C (from CH_2Cl_2 –hexane). ^1H NMR (400 MHz, CDCl_3): δ_{H} 1.29 (s, 9H), 1.44 (s, 6H), 4.51 (s, 2H), 5.90 (s, 1H), 7.58–7.66 (m, 2H), 7.69 (d, $J = 2.6$ Hz, 1H), 7.69 (d, $J = 9.4$ Hz, 1H), 7.84–7.90 (m, 1H), 8.28 (d, $J = 2.6$ Hz, 1H), 8.52–8.57 (m, 1H), 8.63 (d, $J = 9.4$ Hz, 1H) ppm. ^{13}C NMR (125 MHz, CDCl_3): δ_{C} 23.7, 28.2, 46.0, 49.3, 72.5, 111.7, 119.5, 122.8, 123.5, 125.3, 126.3, 126.4, 127.1, 128.4, 129.2, 129.5, 131.9, 132.8, 153.1, 167.2, 216.9 ppm. IR (KBr): $\tilde{\nu}$ 3420, 2965, 2928, 1714, 1674, 1620, 1229 cm^{-1} . Mass (m/z , %): 378 (M^+ , 40), 322 (21), 238 (50), 222 (16), 221 (100), 165 (33), 57 (22). HRMS (ESI): 401.1728, calcd for $\text{C}_{24}\text{H}_{26}\text{O}_4\text{Na}$ [$\text{M}+\text{Na}^+$] 401.1729.

9-oh: yellow columns, mp 163.0–163.5 °C (from CH_2Cl_2 –hexane). ^1H NMR (400 MHz, CDCl_3): δ_{H} 1.33 (s, 9H), 1.45 (s, 6H), 4.51 (s, 2H), 6.35 (broad s, 1H), 7.60 (d, $J = 1.6$ Hz, 1H), 7.62 (dd with fine coupling, $J = 7.8$ and 7.0 Hz, 1H), 7.67 (dd with fine coupling, $J = 8.3$ and 7.0 Hz, 1H), 7.73 (d, $J = 8.9$ Hz, 1H), 7.78 (d, $J = 8.9$ Hz, 1H), 7.91 (dd, $J = 7.4$ and 1.6 Hz, 1H), 8.13 (d, $J = 1.6$ Hz, 1H), 9.70 (d, $J = 8.4$ Hz, 1H) ppm. ^{13}C NMR (125 MHz, CDCl_3): δ_{C} 23.7, 28.2, 46.0, 49.4, 72.4, 112.7, 122.9, 123.0, 126.7, 126.9, 127.1, 127.4, 128.2, 128.6, 129.1, 130.0, 133.4, 134.2, 155.5, 166.9, 217.2 ppm. IR (KBr): $\tilde{\nu}$ 3356, 2976, 1720, 1690, 1669, 1227 cm^{-1} . Mass (m/z , %): 378 (M^+ , 1), 238 (2), 221 (4), 165 (18), 163 (11), 57 (100). HRMS (ESI): 401.1728, calcd for $\text{C}_{24}\text{H}_{26}\text{O}_4\text{Na}$ [$\text{M}+\text{Na}^+$] 401.1729.

9-ih: colorless columns, mp 148.5–149.0 °C (from CH_2Cl_2 –hexane). ^1H NMR (400 MHz, CDCl_3): δ_{H} 1.07 (s, 9H), 1.29 (s, 6H), 4.99 (s, 2H), 5.48 (broad s, 1H), 7.25 (d, $J = 2.7$ Hz, 1H), 7.30 (d, $J = 8.8$ Hz,

1H), 7.81–7.85 (m, 1H), 8.07–8.11 (m, 1H) ppm. ^{13}C NMR (125 MHz, CDCl_3): δ_{C} 23.6, 27.7, 45.8, 48.9, 73.7, 114.6, 117.8, 121.6, 125.5, 125.9, 126.0, 126.4, 128.4, 128.5, 128.9, 131.9, 134.8, 153.3, 171.9, 216.7 ppm. IR (KBr) : $\tilde{\nu}$ 3371, 2981, 2875, 1720, 1667, 1621 cm^{-1} . Mass (m/z , %): 378 (M^+ , 1), 221 (4) 193 (6), 165 (19), 57 (100). HRMS (ESI): 401.1733, calcd for $\text{C}_{24}\text{H}_{26}\text{O}_4\text{Na}$ [$\text{M}+\text{Na}^+$] 401.1729.

14-iv: yellow needles, mp 197.0–198.0 °C (from AcOEt–hexane). ^1H NMR (400 MHz, CDCl_3): δ_{H} 1.27 (s, 9H), 1.46 (s, 6H), 4.53 (s, 2H), 5.95 (broad s, 1H), 7.60 (d, $J = 1.3$ Hz, 1H), 7.66 (dd with fine coupling, $J = 7.9$ and 7.0 Hz, 1H), 7.76 (dd with fine coupling, $J = 8.5$ and 7.0 Hz, 1H), 7.84 (d, $J = 8.5$ Hz, 1H), 7.94 (d, $J = 8.5$ Hz, 1H) 7.95 (d, $J = 8.8$ Hz, 1H), 8.03 (dd, $J = 7.9$ and 1.4 Hz, 1H), 8.37 (d with fine coupling, $J = 8.8$ Hz, 1H), 9.05 (d, $J = 8.5$ Hz, 1H), 9.44 (s with fine coupling, 1H) ppm. ^{13}C NMR (125 MHz, CDCl_3): δ_{C} 23.6, 28.3, 45.9, 49.4, 72.1, 108.8, 120.8, 122.9, 126.1, 126.6, 126.6, 126.8, 127.0, 127.8, 128.0, 128.1, 128.5, 128.5, 130.1, 130.8, 131.4, 133.6, 152.7, 167.3, 216.8 ppm. IR (KBr): $\tilde{\nu}$ 3416, 3048, 2976, 2964, 1698, 1603, 1418, 1278 cm^{-1} . Mass (m/z , %): 428 (M^+ , 58), 372 (30), 288 (43), 272 (20), 271 (100), 243 (16), 242 (11), 215 (18), 213 (15), 57 (28). HRMS (ESI): 451.1888, calcd for $\text{C}_{28}\text{H}_{28}\text{O}_4\text{Na}$ [$\text{M}+\text{Na}^+$] 451.1885.

14-ov: colorless columns, mp 133.0–133.5 °C (from CH_2Cl_2 –hexane). ^1H NMR (500 MHz, CDCl_3): δ_{H} 1.30 (s, 9H), 1.45 (s, 6H), 4.53 (s, 2H), 5.84 (s, 1H), 7.60 (ddd, $J = 7.8$, 6.9 and 1.1 Hz, 1H), 7.65 (ddd, $J = 8.2$, 6.9 and 1.6 Hz, 1H), 7.75 (d, $J = 8.9$ Hz, 1H), 7.77 (d, $J = 2.5$ Hz, 1H), 7.78 (d, $J = 8.5$ Hz, 1H), 7.90 (d, $J = 8.5$ Hz, 1H), 8.00 (dd, $J = 7.8$ and 1.6 Hz, 1H), 8.70 (d, $J = 2.5$ Hz, 1H), 8.75 (d, $J = 8.9$ Hz, 1H), 8.96 (d, $J = 8.2$ Hz, 1H) ppm. ^{13}C NMR (125 MHz, CDCl_3): δ_{C} 23.7, 28.2, 46.0, 49.3, 72.5, 116.6, 119.3, 124.3, 125.8, 126.2, 126.3, 126.3, 126.5, 126.9, 127.4, 128.1, 128.6, 129.2, 130.2, 131.1, 132.5, 133.4, 152.7, 167.2, 216.6 ppm. IR (KBr): $\tilde{\nu}$ 3341, 2979, 2959, 1687, 1603, 1210 cm^{-1} . Mass (m/z , %): 428 (M^+ , 61), 372 (23), 289 (12), 288 (57), 272 (22), 271 (100), 243 (11), 242 (11), 215 (30), 213 (17), 57 (25). HRMS (ESI): 451.1878, calcd for $\text{C}_{28}\text{H}_{28}\text{O}_4\text{Na}$ [$\text{M}+\text{Na}^+$] 451.1885.

Chemiluminescence measurement and time-course for the charge-transfer-induced decomposition of dioxetane. general procedure: Chemiluminescence was measured using a spectrophotometer and/or a multi-channel detector.

A freshly prepared solution (2.0 mL) of TBAF (1.0×10^{-2} mol dm^{-3}) in MeCN was transferred to a quartz cell (10 x 10 x 50 mm) and the latter was placed in a spectrometer, which was thermostated with stirring at 25 °C. After ca. 1 min, a solution of dioxetane **2** or **3** in MeCN (1.0×10^{-4} or 1.0×10^{-5} mol dm^{-3} , 1.0 mL) was added by a syringe, and measurement was started immediately. The time-course of the intensity of light emission was recorded and processed according to first-order kinetics. The total light emission was estimated by comparing it to that of an adamantylidene-dioxetane, the chemiluminescence efficiency Φ^{CL} of which has been reported to be 0.29 and which was used here as a standard.^{15,16}

Fluorescence Measurement of Authentic Emitters 9 and 14: A freshly prepared solution of 2.0×10^{-5} ~ 3.0×10^{-4} mol dm^{-3} of **9** or **14** and 1.0×10^{-3} mol dm^{-3} of TBAF in MeCN was transferred to a quartz cell (10 x 10 x 50 mm), and the latter was placed in the spectrometer, which was thermostated with stirring at 25 °C. Thus, the fluorescence spectra of **9** and **14** were measured and their fluorescence efficiencies (Φ^{fl}) were estimated using quinine hydrosulfate as a standard.

X-Ray single crystallographic analysis of **3-iv** and **3-ov**

X-Ray diffraction data were collected on a Rigaku Mercury CCD diffractometer with graphite monochromated Mo K α ($\lambda=0.71070$ Å) radiation. Data were processed using CrystalClear.[†] The structures were solved by direct method (SIR2008)[‡] and expanded using Fourier techniques. The non-hydrogen atoms were refined anisotropically. Hydrogen atoms were refined using the riding model. The final cycle of full-matrix least-squares refinement on F^2 was based on 5094 observed reflections and 318 variable parameters (for **3-iv**) and on 5009 observed reflections and 318 variable parameters (for **3-ov**). All calculations were performed using the CrystalStructure crystallographic software package.^{§,¶}

† Rigaku Corporation, 1999.

‡ SIR2008: M.C. Burla, R. Caliendo, M. Camalli, B. Carrozzini, G.L. Cascarano, L. De Caro, C. Giacovazzo, G. Polidori, D. Siliqi, R. Spagna (2007).

§ CrystalStructure 4.0: Crystal Structure Analysis Package, Rigaku Corporation (2000-2010). Tokyo 196-8666, Japan.

¶ CRYSTALS Issue 11: Carruthers, J.R., Rollett, J.S., Betteridge, P.W., Kinna, D., Pearce, L., Larsen, A., and Gabe, E. Chemical Crystallography Laboratory, Oxford, UK. (1999).

Crystal data for **3-iv**: C₂₈H₂₈O₄ ($M_r = 428.53$), pale yellow block, 0.12 x 0.10 x 0.05 mm, monoclinic, space group $P2_{1/c}$ (#14), $a = 16.45(5)$ Å, $b = 12.31(2)$ Å, $c = 11.029(17)$ Å, $\beta = 90.101(19)^\circ$, $V = 2233(9)$ Å³, $Z = 4$, $\rho_{\text{calcd}} = 1.274$ g cm⁻³, $T = 120$ K, $F(000) = 912.00$, reflections collected/unique 23562 / 5094 ($R_{\text{int}} = 0.0587$), $\mu(\text{MoK}\alpha) = 0.84$ cm⁻¹. An empirical absorption correction was applied which resulted in transmission factors ranging from 0.898 – 1.0000. The data were corrected for Lorentz and polarization effects. $R1 = 0.062$ [$I > 2\sigma(I)$], $wR2 = 0.186$ (all data) GOF on $F^2 = 1.004$, and residual electron density 0.43 / -0.43 e⁻Å⁻³.

Crystal data for **3-ov**: C₂₈H₂₈O₄ ($M_r = 428.53$), pale yellow prism, 0.15 x 0.10 x 0.07 mm, monoclinic, space group $P2_{1/c}$ (#14), $a = 16.75(3)$ Å, $b = 12.336(11)$ Å, $c = 11.202(12)$ Å, $\beta = 108.40(13)^\circ$, $V = 2196(5)$ Å³, $Z = 4$, $\rho_{\text{calcd}} = 1.296$ g cm⁻³, $T = 120$ K, $F(000) = 912.00$, reflections collected/unique 22506 / 5009 ($R_{\text{int}} = 0.051$), $\mu(\text{MoK}\alpha) = 0.854$ cm⁻¹. An empirical absorption correction was applied which resulted in transmission factors ranging from 0.923 – 1.0000. The data were corrected for Lorentz and polarization effects. $R1 = 0.0454$ [$I > 2\sigma(I)$], $wR2 = 0.0984$ (all data) GOF on $F^2 = 1.002$, and residual electron density 0.34 / -0.33 e⁻Å⁻³.

Crystallographic data for the structural analysis of compound **3-iv** and **3-ov** have been deposited at the Cambridge Crystallographic Data Center, CCDC-989777 and CCDC-989778. Copies of the data can be obtained, free of charge, on application to CCDC, 12 Union Road, Cambridge CB2 1EZ, UK, (fax: +44-(0)1223-336033 or e-mail: deposit@ccdc.cam.ac.uk).

ACKNOWLEDGEMENTS

We gratefully acknowledge financial assistance provided by Grants-in-aid (No. 25350269 No. 25410056

and No. 25410057) for Scientific Research from the Ministry of Education, Culture, Sports, Science, and Technology, Japan.

REFERENCES AND NOTES

1. A. P. Schaap and S. D. Gagnon, *J. Am. Chem. Soc.*, 1982, **104**, 3504.
2. (a) A. P. Schaap, R. S. Handley, and B. P. Giri, *Tetrahedron Lett.*, 1987, **28**, 935; (b) A. P. Schaap, T. S. Chen, R. S. Handley, R. DeSilva, and B. P. Giri, *Tetrahedron Lett.*, 1987, **28**, 1155.
3. (a) S. Beck and H. Köster, *Anal. Chem.*, 1990, **62**, 2258; (b) W. Adam, D. Reihardt, and C. R. Saha-Möller, *Analyst.*, 1996, **121**, 1527; (c) M. Matsumoto, *J. Photochemphotobiol. C: Photochem. Rev.*, 2004, **5**, 27; (d) M. Matsumoto and N. Watanabe, *Bull. Chem. Soc. Jpn.*, 2005, **78**, 1899.
4. (a) W. Adam and A. V. Trofimov, In *The Chemistry of Peroxides*; ed. by Z. Rappoport; Wiley: New York, 2006; Vol. 2, pp. 1171–1209; (b) W. J. Baader, C. V. Stevani, and E. L. Bastos, In *The Chemistry of Peroxides*; ed. by Z. Rappoport; Wiley: New York, 2006; Vol. 2, pp. 1211–1278.
5. (a) A. V. Trofimov, R. F. Vasil'ev, K. Mielke, and W. Adam, *Photochem Photobiol.*, 1995, **62**, 35; (b) W. Adam, I. Bronstein, B. Edwards, T. Engel, D. Reinhardt, F. W. Schneider, A. V. Trofimov, and R. F. Vasil'ev, *J. Am. Chem. Soc.*, 1996, **118**, 10400; (c) W. Adam, I. Bronstein, A. V. Trofimov, and R. F. Vasil'ev, *J. Am. Chem. Soc.*, 1999, **121**, 958.
6. (a) M. Matsumoto, N. Watanabe, N. C. Kasuga, F. Hamada, and K. Tadokoro, *Tetrahedron Lett.*, 1997, **38**, 2863; (b) W. Adam, M. Matsumoto, and A. V. Trofimov, *J. Am. Chem. Soc.*, 2000, **122**, 8631.
7. (a) I. Bronstein, B. Edwards, and J. C. Voyta, *J. Biolumin. Chemilumin.*, 1989, **4**, 99; (b) A. P. Schaap, H. Akhavan, and R. J. Romano, *Clin. Chem.*, 1989, **35**, 1863.
8. M. Yamada, K. Kitaoka, M. Matsumoto, and N. Watanabe, In *Bioluminescence and Chemiluminescence*, ed. by A. Tsuji, M. Matsumoto, M. Maeda, L. J. Kricka, and P. E. Stanley; World Scientific: Singapore, 2004; pp. 487–490.
9. (a) M. Matsumoto, K. Hamaoka, Y. Takashima, M. Yokokawa, K. Yamada, N. Watanabe, and H. K. Ijuin, *Chem. Commun.*, 2005, 808; (b) N. Hoshiya, N. Watanabe, H. K. Ijuin, and M. Matsumoto, *Tetrahedron*, 2006, **62**, 12424.
10. M. Matsumoto, N. Watanabe, N. Hoshiya, and H. K. Ijuin, *Chem. Rec.*, 2008, **8**, 213.
11. (a) B. Edward, A. Sparks, J. C. Voyta, and I. Bronstein, *J. Biolumin. Chemilumin.*, 1990, **5**, 1; (b) B. Edward, A. Sparks, J. C. Voyta, Strong, O. Murphy, and I. Bronstein, *J. Org. Chem.*, 1990, **55**, 6225; (c) N. Watanabe, H. Kobayashi, M. Azami, and M. Matsumoto, *Tetrahedron*, 1999, **55**, 6831; (d) N. Hoshiya, N. Hukuda, H. Maeda, N. Watanabe, and M. Matsumoto, *Tetrahedron*, 2006, **62**, 5808.
12. An “odd/even” relationship between the chemiluminescence properties and substitution pattern of a trigger group for CTID of oxyaryl-substituted dioxetanes was initially observed for dioxetanes bearing a 6- or 7-oxynaphthyl group. An “odd” pattern is one which the donor’s ($-O^-$) point of attachment to the acceptor (dioxetane ring) is such that the total number of ring carbon atoms

separating these points, including the atoms at the point of attachment, is an odd whole number [Refs. 11(a) and 11(b)].

13. For convenience, we refer to the four hydroxyphenanthryl-substituted dioxetanes investigated here as follows. For the structural formula shown in Figure 2, there are two types of isomers, i.e., one **2-*v*** possesses a phenanthrene C ring that lies *vertically* and the other **2-*h*** has a ring that lies *horizontally* with respect to the dioxetane ring. Second, these two isomers can each be separated into two isomers in which the helix of the phenanthrene ring is oriented *inner* or *outer* with respect to the dioxetane ring. Thus, there are four possible types, i.e., **2-*iv***, **2-*ov***, **2-*oh***, and **2-*ih***, for dioxetane **2**. A similar discussion can be applied to dioxetanes **3-*iv***, and **3-*ov***.
14. C. D. Harrowven, L. L. Guy, and L. Nanson, *Angew. Chem. Int. Ed.*, 2006, **45**, 2242.
15. All of the Φ^{CL} values presented here were estimated based on the value reported for the chemiluminescent decomposition of 3-adamantylidene-4-(3-siloxyphenyl)-4-methoxy-1,2-dioxetane ($\Phi^{\text{CL}} = 0.29$) in TBAF/DMSO.¹⁶
16. A. V. Trofimov, K. Mielke, R. F. Vasil'ev, and W. Adam, *Photochem. Photobiol.*, 1996, **63**, 463.
17. M. Matsumoto, Y. Mizoguchi, T. Motoyama, and N. Watanabe, *Tetrahedron Lett.*, 2001, **42**, 88692.
18. A. Nishinaga, M. Yano, T. Kuwashige, K. Maruyama, and T. Mashino, *Chem. Lett.*, 1994, 817.
19. For convenience sake, we call a rotamer an *anti*-form when the dioxetane O-O and a hydroxy group on an aromatic ring are on opposite sides of the furan ring, while in the *syn*-form the dioxetane O-O and a hydroxy group on an aromatic ring are on the same side of the furan ring.
20. (a) M. Matsumoto, H. Suzuki, N. Watanabe, H. K. Ijuin, J. Tanaka, and C. Tanaka, *J. Org. Chem.*, 2011, **76**, 5006; (b) N. Watanabe, K. Matsumoto, T. Tanaka, H. Suzuki, H. K. Ijuin, and M. Matsumoto, *Tetrahedron Lett.*, 2012, **53**, 5309.

■原 著■ 2013 年度神奈川大学総合理学研究所共同研究助成論文

チタン (IV) 三置換 Dawson 型ポリ酸塩単量体とそれを用いた NH₄⁺ イオン内包テトラポッド型四量体の合成

松木悠介¹ 星野貴弘¹ 増田佳奈¹ 松井敬祐¹ 力石紀子¹
松永 諭^{1,2} 野宮健司¹

Syntheses of Monomeric Tri-Titanium(IV)-Substituted Dawson Polyoxo-
metalate (POM) and Non-Bridging Tetrameric POM
Encapsulating Ammonium Cation

Yusuke Matsuki¹, Takahiro Hoshino¹, Kana Masuda¹, Keisuke Matsui¹
Noriko Chikaraishi Kasuga¹, Satoshi Matsunaga^{1,2} and Kenji Nomiya¹

¹ Department of Chemistry, Faculty of Science, Kanagawa University, Hiratsuka City, Kanagawa 259-1293, Japan

² To whom correspondence should be addressed. E-mail: matsunaga@kanagawa-u.ac.jp

Abstract: The monomeric tri-Ti(IV)-substituted Dawson polyoxometalate (POM), Na₁₂[P₂W₁₅Ti₃O₆₂]·NaCl·6H₂O, was synthesized by basic hydrolysis of the bridging Dawson tetramer with an encapsulated chloride ion, Na₁₉H₂[{P₂W₁₅Ti₃O₅₉(OH)₃}₄{μ₃-Ti(H₂O)₃}₄Cl]·124H₂O, at pH 9.0 and unequivocally characterized by complete elemental analysis, thermogravimetric and differential thermal analysis (TG/DTA), FTIR spectroscopy and solution ³¹P NMR spectroscopy. The monomeric tri-Ti(IV)-substituted Dawson POM could not be derived from either a direct reaction of the trilacunary Dawson species, [P₂W₁₅O₅₆]¹²⁻, with Ti source or the non-bridging Dawson tetramer, [{P₂W₁₅Ti₃O_{57.5}(OH)₃}₄Cl]²⁵⁻. It could be prepared for the first time by hydrolysis of the bridging Dawson tetramer with an encapsulated Cl⁻ ion. In this work, the non-bridging Dawson tetramer with an encapsulated ammonium cation was synthesized by using the monomeric tri-Ti(IV)-substituted Dawson POM. This fact indicates that the monomeric tri-Ti(IV)-substituted Dawson POM can be used as a precursor for the synthesis of novel oligomeric POMs and organometallic-supported POMs.

Keywords: polyoxometalate, titanium, monomer, NH₄⁺-encapsulating tetramer

序論

分子性の酸化物クラスターであるポリ酸塩 (polyoxometalate: POM) は、強酸性、耐酸性、豊富な酸化還元特性などの極めて多彩な性質を有しているため、触媒、表面化学、材料科学、医薬など様々な観点から広く研究がなされている¹⁾。POM 骨格を構成する金属は、主にタングステン (VI) やモリブデン (VI) が用いられているが、これらの金属を位置選択的に欠損させた欠損型 POM を合成することが可能である。欠損型 POM は、飽和型 POM に比べて欠損部位が高い表面塩基性度を有しているため、異種金属イオンを欠損部位に取り込んだ金属置換型 POM の合成に利用することができる。通常のタン

グステン (VI) やモリブデン (VI) などの構成金属を異種金属で置換することで表面電荷密度を制御することができ、さらなる機能拡張部位として期待できる。これまでにタングステン (VI) 三原子を、バナジウム (V) やニオブ (V) で置換した三置換 Dawson 型 POM 単量体 (図 1 上) が合成され、その表面に有機金属種を担持できることが報告されている²⁾。これは VI 価のタングステン酸を V 価の異種金属イオンで置換しているため POM 上の表面負電荷密度が大きくなり、カチオン性有機金属種との相互作用が向上したためと考えることができる。一方で、チタン (IV) のイオン半径 (0.75 Å) はタングステン

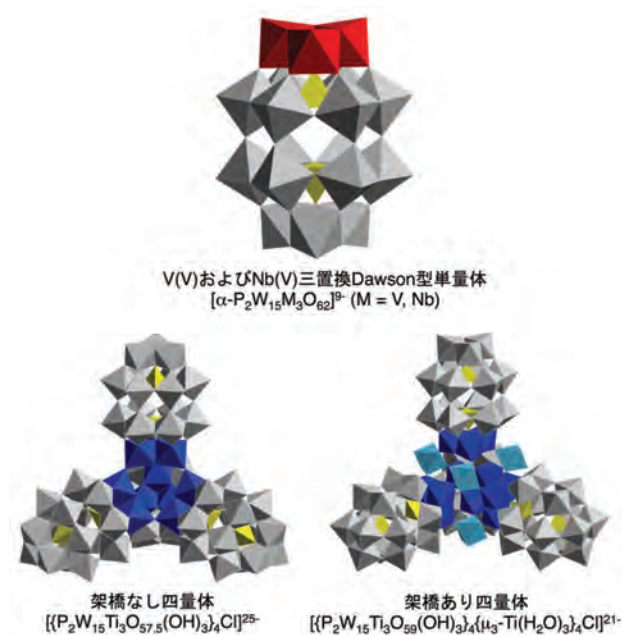


図1. バナジウム(V)およびニオブ(V)三置換 Dawson 型 POM 単量体(上)と二種類のチタン(IV)三置換 Dawson 型 POM 四量体(下). 中心空間にカプセル化されている Cl⁻ イオンは省略している. 赤はバナジウムもしくはニオブ, 青と水色はチタンを表している.

(VI) のイオン半径 (0.74 Å) とほぼ等しく、欠損部位にチタン(IV)が導入されたチタン置換 POM の合成が可能である³⁾. チタンはIV価であるため、上記のバナジウム(V)やニオブ(V)に比べてさらなる表面負電荷密度の増大が予想される。これまでに当研究室では、Dawson 型 POM 三欠損種から導かれるチタン(IV)三置換体の合成を行ってきたが、チタン(IV)置換 POM は分子間の Ti-O-Ti 結合を形成しやすく、単量体ではなく Ti-O-Ti 結合により縮合したテトラポッド型四量体として単離された(図1下)^{4,5)}. また、チタン(IV)三置換 Dawson 型四量体は、反応条件に応じて二種類の四量体、つまり [P₂W₁₅Ti₃O_{57.5}(OH)₃]₄Cl]²⁵⁻ (架橋なし四量体)⁴⁾ と [P₂W₁₅Ti₃O₅₉(OH)₃]₄{ μ_3 -Ti(H₂O)₃Cl}²¹⁻ (架橋あり四量体)⁵⁾ を形成することを明らかにした。これら二種類のチタン(IV)三置換 Dawson 型四量体は、中心空間に様々なイオン(Cl⁻, Br⁻, I⁻, NO₃⁻等)をカプセル化することができる^{6,7)}.

我々は、これまで四量体としてのみ合成されたチタン(IV)三置換 Dawson 型 POM の単量体 Na₁₂[P₂W₁₅Ti₃O₆₂]・NaCl・6H₂O の合成に成功した。さらにチタン(IV)三置換 Dawson 型 POM 単量体を前駆体に用いて、中心空間に NH₄⁺ カチオンをカプセル化した架橋なし四量体を合成したので報告する。

材料と方法

材料

エタノール、ジエチルエーテル(和光純薬工業(株))は、購入したものをそのまま用いた。Cl⁻カプセル化架橋あり四量体 Na₁₉H₂{[P₂W₁₅Ti₃O₅₉(OH)₃]₄{ μ_3 -Ti(H₂O)₃Cl}²¹⁻・124H₂O は既報⁵⁾に従い合成した。

合成法

チタン(IV)三置換 Dawson 型 POM 単量体 Na₁₂[P₂W₁₅Ti₃O₆₂]・28H₂O Cl⁻カプセル化架橋あり四量体 Na₁₉H₂{[P₂W₁₅Ti₃O₅₉(OH)₃]₄{ μ_3 -Ti(H₂O)₃Cl}²¹⁻・124H₂O (4.8 g, 0.253 mmol) を純水 20 mL に溶解し、1 M NaOH 水溶液を用いて pH 9.0 に調整した。この溶液に NaCl (8.0 g, 0.137 mmol) を加え一時間攪拌した。析出した白色粉末をメンブランフィルター(JG 0.2 μ m)を使って濾取し、エタノール 30 mL で3回、ジエチルエーテル 50 mL で3回洗浄し、減圧乾燥を2時間行い、白色粉末としてチタン(IV)三置換 Dawson 型 POM 単量体を収率 41.7% (2.0 g スケール)で得た。

NH₄⁺ カチオンをカプセル化した架橋なし四量体

Na₁₂[P₂W₁₅Ti₃O₆₂]・NaCl・6H₂O (0.50 g, 0.11 mmol) を純水 12 mL に溶解し、そこへ NH₄Cl (0.06 g, 1.12 mmol) を加えた。0.1 M 塩酸を用いて pH 8.4 に調整した後、80°C で30分間攪拌した。この溶液をロータリーエバポレーターを用いて白色粉末が析出するまで濃縮を行った。純水 1 mL を加え、35°C で析出した粉末を溶かし、室温までゆっくりと冷却した。析出した無色針状結晶をメンブランフィルター(JG 0.2 μ m)で濾取し、エタノール 10 mL で3回、ジエチルエーテル 50 mL で3回洗浄し、減圧乾燥を3時間行うことで、NH₄⁺ カチオンをカプセル化した架橋なし四量体を白色粉末として収率 14.3% (0.067 g スケール)で得た。

結果と討論

合成と同定

チタン(IV)三置換 Dawson 型 POM 単量体は、Dawson 型三欠損種とチタン(IV)から直接合成することはできず、速やかな自己縮合で Ti-O-Ti 結合を形成し四量体になってしまう^{4,5)}. しかし、既に我々が報告している架橋あり四量体 [P₂W₁₅Ti₃O₅₉(OH)₃]₄{ μ_3 -Ti(H₂O)₃Cl}²¹⁻ を NaOH 水溶液で加水分解することにより、単量体 [P₂W₁₅Ti₃O₆₂]¹²⁻ を合成することができた(図2)。架橋あり四量体を溶解した溶液を NaOH 水溶液で pH 9.0 まで塩基性になると、塩基加水分解により単量体が生成した。これ

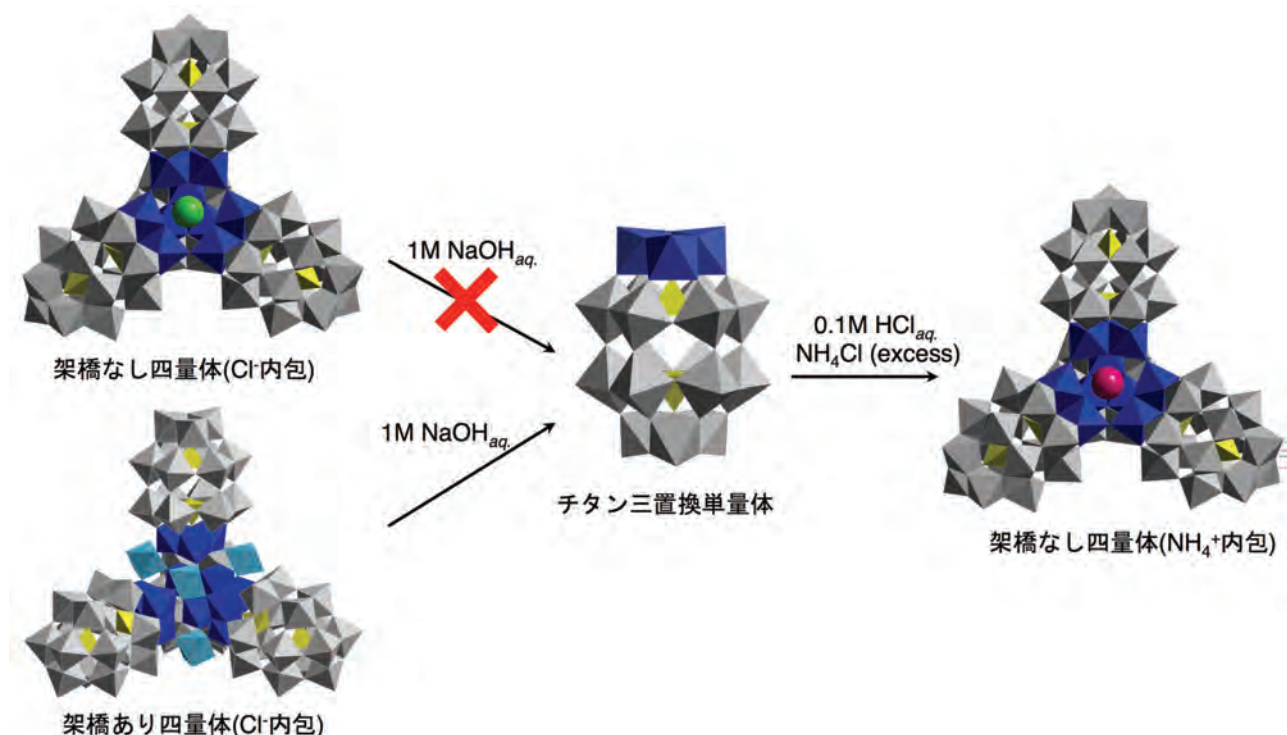


図 2. チタン (IV) 三置換 Dawson 型 POM 単量体の合成ルートと、それを用いた NH_4^+ カプセル化架橋なし四量体の合成.

表 1. チタン (IV) 三置換 Dawson 型 POM 単量体の元素分析結果

	H	Cl	Na	O	P	Ti	W	Total (%)
calcd.	0.28	0.81	6.80	24.74	1.41	3.27	62.71	100
found	0.27	0.84	5.85	23.9	1.40	4.09	61.90	98.24

calcd. for $\text{Na}_{12}[\text{P}_2\text{W}_{15}\text{Ti}_3\text{O}_{62}] \cdot \text{NaCl} \cdot 6\text{H}_2\text{O}$ (MW: 4397.56)
Mikroanalytisches Labor Pascher (Remagen, Germany).

は Dawson 型 POM の cap 部分 1 カ所をチタン (IV) で置換した POM やチタン (IV) 一置換および二置換 Keggin POM に一般的に見られる現象であり、溶液を酸性にすると多量体構造が、塩基性にすると単量体構造が生成する³⁾。しかし、架橋なし四量体からは pH を高くしても単量体への加水分解は起こらず、架橋あり四量体からのみ単量体構造を単離することができた。FTIR の結果から、架橋あり及び架橋なし四量体に特徴的な分子間 Ti-O-Ti に基づく振動バンド ($690\text{-}650\text{ cm}^{-1}$) が観測されなかったことから、単量体構造であることが確認できた。全元素分析の結果 (表 1) から、組成を塩化ナトリウム 1 分子を含む $\text{Na}_{12}[\text{P}_2\text{W}_{15}\text{Ti}_3\text{O}_{62}] \cdot \text{NaCl} \cdot 6\text{H}_2\text{O}$ と決定し、found の合計値も 98.24 % と純度良く合成することができた。D₂O 中での ³¹P NMR 測定では、 $\delta = -4.94, -14.61\text{ ppm}$ に一対の二本線ピークが観測された (図 3a)。低磁場側のピークはチタン (IV) で置換されたサイトに近い P 原子に由来し、高磁場側のピークはタングステン (VI) で cap されたサイトに近い P 原子に由来すると考えられ、単量体が選択的に得

られたことが明らかとなった。前駆体である架橋あり四量体の化学シフトは $-7.04, -13.77\text{ ppm}$ であることから (図 3d)⁵⁾、単量体構造への変換に伴うピークのシフトが明確に観測されている。

チタン (IV) 三置換 Dawson 型 POM 単量体は、前述の通りバナジウム (V) 三置換体やニオブ (V) 三置換体に比べ高い負電荷密度を有していることから、これを利用したカチオン性有機金属種の担持や自己縮合による多量化などのさらなる分子修飾が期待される。そこで、過剰の NH_4^+ カチオン存在下、チタン (IV) 三置換 Dawson 型 POM 単量体を 0.1 M 塩酸添加により縮合させることで、 NH_4^+ をカプセル化した架橋なし四量体の合成に成功した (図 2)。架橋なし四量体は、分子内 Ti-O-Ti 結合を形成する稜共有酸素原子への H^+ 付加の有無により、中心空間の電荷を制御できることが明らかとなっている。例えば、酸性下では分子内 Ti-O-Ti 結合の酸素原子に H^+ が計 12 個付加しているため、 TiO_6 八面体 12 個で形成される中心空間はカチオン性の高い状態になっており、 Cl^- アニオンを内包する。一方、 H^+ が分子内

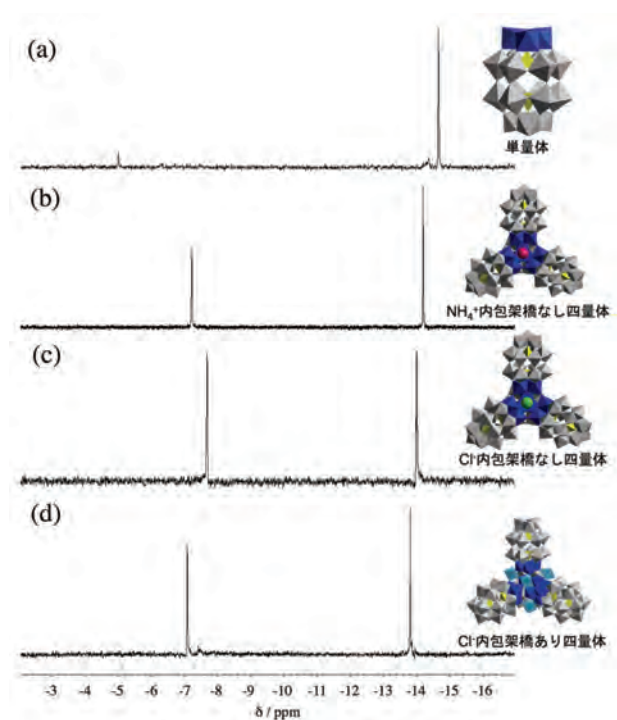


図 3. D_2O 中での ^{31}P NMR スペクトル. (a) 今回合成したチタン (IV) 三置換 Dawson POM 単量体, (b) NH_4^+ を内包した架橋なし四量体, (c) Cl^- を内包した架橋なし四量体, (d) 前駆体として用いた Cl^- を内包した架橋あり四量体.

Ti-O-Ti 結合の酸素原子に付加していない場合、中心空間はアニオン性の高い状態になり、 NH_4^+ カチオンが中心空間に取り込まれる。本合成法では、pH を 8.4 に調整するため、稜共有酸素は H^+ 付加が起こらずカチオンである NH_4^+ イオンを内包していた。 ^{31}P NMR からは、 Cl^- カプセル化架橋なし四量体の化学シフト ($\delta = -7.6, -14.0$ ppm, 図 3c)⁴⁾ とは異なるピーク ($\delta = -7.21, -14.2$ ppm, 図 3b) を示し、これは従来の方法で合成した NH_4^+ カプセル化架橋なし四量体のピーク ($\delta = -7.15, -14.23$ ppm)⁷⁾ と良く一致した。 NH_4^+ カプセル化架橋なし四量体は、これまでに (1) チタン (IV) 三置換ペルオキソ種 $Na_9[P_2W_{15}(TiO_2)_3O_{56}(OH)_3] \cdot 14H_2O$ を固体状態で $200^\circ C$ にて加熱し、これに NH_4Cl を加える方法と、(2) Cl^- カプセル化架橋なし四量体の 12 個の H^+ をアンモニア水で中和する方法の 2 種類で合成が可能であったが⁷⁾、本方法は単量体を原料として NH_4^+ 存在下で四量体へと縮合する新しい方法である。

まとめ

チタン (IV) 置換 POM は分子間の Ti-O-Ti 結合を形成しやすく、これまでは単量体ではなく Ti-O-Ti 結合により縮合したテトラポッド型四量体として単離されてきた。本研究では、チタン (IV) 三置換 Dawson

型 POM 架橋あり四量体 $\{[P_2W_{15}Ti_3O_{59}(OH)_3]_4 \{\mu_3-Ti(H_2O)_3Cl\}^{21-}$ を塩基加水分解することにより、単量体 $Na_{12}[P_2W_{15}Ti_3O_{62}] \cdot NaCl \cdot 6H_2O$ の合成に初めて成功した。さらにチタン (IV) 三置換 Dawson 型 POM 単量体を前駆体を用いて、中心空間に NH_4^+ カチオンをカプセル化した架橋なし四量体を合成する新たな方法を見出すことができた。今回合成に成功したチタン (IV) 三置換 Dawson 型 POM 単量体は、これまで報告されてきたバナジウム (V) およびニオブ (V) 三置換体 Dawson 型 POM 単量体に比べて高い負電荷密度を有しているため、今後はカチオン性有機金属種を担持した新たな機能性 POM の合成を行う予定である。

謝辞

本研究は、2013 年度総合理学研究所共同研究の研究助成を受けて行いました。厚く御礼申し上げます。

文献

- Hill CL, Ed. (1998) Polyoxometalates. *Chem. Rev.* **98**: 1-390.
- Pohl M, Lyon DK, Mizuno N, Nomiya K and Finke RG (1995) Polyoxoanion-supported catalyst precursors. Synthesis and characterization of the iridium(I) and rhodium(I) precatalysts $[(n-C_4H_9)_4N]_5Na_3[(1,5-COD)M \cdot P_2W_{15}Nb_3O_{62}]$ ($M = Ir, Rh$). *Inorg. Chem.* **34**: 1413-1429.
- Nomiya K, Sakai Y and Matsunaga S (2011) Chemistry of group IV metal ion-containing polyoxometalates. *Eur. J. Inorg. Chem.*: 179-196.
- Sakai Y, Yoza K, Kato CN and Nomiya K (2003) A first example of polyoxotungstate-based giant molecule. Synthesis and molecular structure of a tetrapod-shaped Ti-O-Ti bridged anhydride form of Dawson tri-titanium(IV)-substituted polyoxotungstate. *Dalton Trans.* **32**: 3581-3586.
- Sakai Y, Yoza K, Kato CN and Nomiya K (2003) Tetrameric, trititanium(IV)-substituted polyoxotungstates with an α -Dawson substructure as soluble metal-oxide analogues: molecular structure of the giant ‘tetrapod’ $[(\alpha-1,2,3-P_2W_{15}Ti_3O_{62})_4\{\mu_3-Ti(OH)_3Cl\}]^{45-}$. *Chem. Eur. J.* **9**: 4077-4083.
- Sakai Y, Yoshida S, Hasegawa T, Murakami H and Nomiya K (2007) Tetrameric, tri-titanium(IV)-substituted polyoxometalates with an α -Dawson substructure as soluble metal oxide analogues. Synthesis and molecular structure of three giant ‘tetrapods’ encapsulating different anions (Br^- , I^- , and NO_3^-). *Bull. Chem. Soc. Jpn.* **80**: 1965-1974.
- Sakai Y, Ohta S, Shintoyo Y, Yoshida S, Taguchi Y, Matsuki Y, Matsunaga S and Nomiya K (2011) Encapsulation of anion/cation in the central cavity of tetrameric polyoxometalate, composed of four trititanium(IV)-substituted α -Dawson subunits, initiated by protonation/deprotonation of the bridging oxygen atoms on the intramolecular surface. *Inorg. Chem.* **50**: 6575-6583.



環境調和型物質変換及び新エネルギープロセス創出の 基盤となるナノ構造触媒の開発

引地 史郎* 内藤 周弑** 吉田 曉弘*** 中澤 順***

Development of Nano-scale Fine Structure Catalysts for Green Chemistry and Novel Energy Processes

Shiro HIKICHI* Shuichi NAITO** Akihiro YOSHIDA*** Jun NAKAZAWA***

1. 緒言

近年のシェール革命と称される動向にみられるように、非在来型天然ガスの開発・利用が促進されつつある今日においても、石油や石炭、在来型天然ガスも含めた化石燃料資源は、依然として我々の生活を支える主要なエネルギー源であると同時に様々な物質の原材料でもある。従って、石油・石炭・天然ガスといった炭化水素類の利用効率を向上させ、かつエネルギーの過剰消費や環境負荷物質排出を抑制した環境調和型物質変換プロセスを構築することは喫緊の課題である。

化学反応による物質変換(物質生産や環境汚染物質の無害化等)の効率向上に資する触媒は、環境調和型物質変換プロセス創出を達成するために欠くべからざるものであり、その高性能化は今なお社会からの要請が多い検討課題である。また触媒にはこれまで貴金属が多用されてきたが、希少な金属資源を用い続けることは次第に困難になりつつあり、いわゆる“元素戦略”の観点からも触媒に画期的な高性能化をもたらす技術革新が求められている。そこで本研究では、持続可能な社会構築の基盤となる高性能触媒の開発を研究目標に掲げ、サブナノ～ナノスケールで構造が制御された触媒、すなわち“ナノ構造触媒”の開発を検討している。サブナノ～ナノといったサイズは原子・分子から分子集合体程度の大きさであり、このような触媒構造の手本となるものは天然の高性能触媒である酵素である¹⁾。

2012年度より開始した本共同研究では、高い耐熱性と機械的強度を有し、ナノスケールで構造制御された無機酸化物多孔体を担体とし、これに分子構造や原子配列が制御された触媒活性点を構築した、新奇なナノ構造触媒を開発してきた²⁾。以下本稿では2013年度の成果を中心に開発の現状を述べる。

2. 人工酸化酵素の開発

生体内における分子状酵素の活性化を経た炭化水素への酸素添加反応は主に鉄・銅などの遷移金属を活性中心とする酵素により触媒されている³⁾。酵素の特異な反応特性は、アミノ酸やホルフィリンなどの補欠分子族によって精密に立体および電子的特性が制御された金属配位空間と、その周囲を取り巻く、基質認識や疎水性(疎水性や親水性)制御に関わる二次元反応場空間によりもたらされる。これら酵素の特徴を取り入れて設計された高機能触媒、すなわち“人工酵素”は本研究で開発を目指しているナノ構造触媒の一つである⁴⁾。そしてこのコンセプトに基づいて開発した固定化錯体触媒が、酵素反応と同様な温和な条件の下でアルカンやアルケン⁵⁾の酸化反応を選択的に進行させることを明らかにしてきた⁶⁾。そこですでに開発に成功している配位子固定化担体に様々な金属を導入することや、配位子の分子構造を一部変化させることにより触媒システムの拡張を図った。またいくつかの酸化酵素の触媒活性点では複数のイミダゾリル基が金属支持配位子となっているが、これに類似した金属配位空間が構築できるアニオン性キレート配位子を用いて、酸化触媒として機能する金属錯体の創成及びその反応機構の解明といった、触媒設計に欠かせない基礎的検討を行うとともに、これらを用いた固定化錯体触媒の開

*教授 物質生命化学科

Professor, Dept. of Material and Life Chemistry

**名誉教授 工学研究科客員教授

Professor Emeritus

***特別助教 物質生命化学科

Assistant Professor, Dept. of Material and Life Chemistry

発を行った。

2. 1. ピリジルアミン配位子を用いた固定化錯体触媒システムの拡張

筆者らは既に有機アジド基修飾メソ多孔性シリカゲル (SBA-N₃) に対し、窒素上にプロハルギル基 (-CH₂-C≡CH) を導入したビス(ピリジルメチル)アミンを作用させることにより、アジド基と末端アルキン部位の Huisgen[3+2]環化付加反応(クリック反応)によるトリアゾリル基形成反応を利用して配位子を固定することに成功している。そして形成された配位子固定化担体 SBA-tz-N(Py)₂ に Ni(II) を導入することで、メタクロロ過安息香酸 (*m*CPBA) を酸化剤とするアルカン水酸化触媒系を構築した⁶⁾。この触媒系では反応中間体は観測されないため直接的な反応機構解析には至っていないが、後述するように Ni(II) 活性点での *m*CPBA の活性化が進行していると類推され、配位子の分子設計に応じた触媒特性の制御が可能であると考えられる。ところでここで用いている配位子 X-tz-N(Py)₂ (図 1(b)) は、錯体化学研究で多用されているトリス(ピリジルメチル)アミン (TPA; 図 1(a)) のピリジル基の一つをトリアゾリルで置換したものに相当する⁶⁾。そして残るピリジルメチル基を他の金属配位基に置換した構造へと誘導することも可能である。そこで本研究では一つのピリジル基をカルボキシ基 (-CH₂-COOH) に置換した配位子 X-tz-N(Py)(COOH) (図 1(c)) を設計し、これを SBA-N₃ に作用させることによりカルボキシ基・ピリジル基・トリアゾリル基を金属配位基として含む多座アミン配位子固定化担体 SBA-tz-N(Py)(COOH) を構築した。そして既報の SBA-tz-N(Py)₂ も併せ、Ni(II)、Co(II)、Fe(III) および Mn(II) を導入した固定化錯体触媒を調製してそれらの *m*CPBA を酸化剤とするアルカン酸化触媒特性を比較した。さらに鉄触媒について過酸化水素 (H₂O₂) の酸化剤としての適用性を検討した⁷⁾。

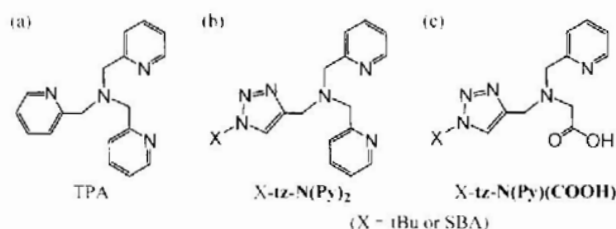
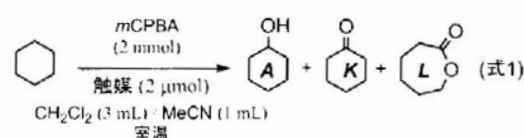


図 1. (ピリジルメチル)アミン配位子の構造

2. 1. 1. *m*CPBA を酸化剤とするアルカン酸化触媒特性の比較

固定化錯体触媒における活性点のモデルとみなせる錯

体 M/tBu-tz-N(Py)₂ および M/tBu-tz-N(Py)(COOH) も含め、一連の触媒の活性を比較した(式 1)。



液相均一系で機能する錯体触媒 M/tBu-tz-N(Py)₂ および M/tBu-tz-N(Py)(COOH) について中心金属と活性の相関を検討したところ、伊東らにより報告されている TPA 錯体と同様、活性の序列は Ni ≥ Co > Fe > Mn であった⁶⁾。しかしアルコール (A) 選択性は配位子により異なり、TPA 錯体が Co > Ni > Fe > Mn であるのに対して M/tBu-tz-N(Py)₂ では Ni > Co ≥ Fe > Mn、M/tBu-tz-N(Py)(COOH) では Ni > Fe > Co > Mn であった。また同一金属の触媒間で比較したところ、いずれの金属についても M/tBu-tz-N(Py)₂ のほうが M/tBu-tz-N(Py)(COOH) よりも高活性であった。

固定化錯体触媒についても同様に比較した。まず金属種に応じた反応性の差異を比較するため、配位子の固定密度が低く孤立した錯体触媒活性点が形成される、N₃ 基の固定量が 0.5 % の担体を用いて調製した触媒の活性を比較した。M/SBA-tz-N(Py)₂ 0.5 における活性の序列は Co ≥ Ni > Fe > Mn であり、上述の錯体触媒による均一系反応の結果と一致していた。一方、M/SBA-tz-N(Py)(COOH)-0.5 では Co > Fe > Ni > Mn であり、対応する錯体触媒の均一系反応の結果とは異なっていた。これらの結果は、担体表面で形成される錯体種の構造と対応するモデル錯体の溶存状態の構造が類似しているか否かは、配位子の特性に応じて異なるためと解釈できる。M/SBA-tz-N(Py)(COOH) では、配位子のカルボキシ基がプロトン化されて解離するといった、構造変化が起こることが考えられる。そのため錯体の固定化によって、溶存状態とは異なる錯体種が形成して、反応性も変化することが考えられる。

昨年度報告した Ni or Co/SBA-tz-N(Py)_{2-x} の検討で明らかにしてきたように、配位子固定密度は活性点構造や触媒安定性、反応性に影響を及ぼす^{4,5)}。そこで種々の金属を導入した触媒のうち、x=0.5 と 4 のものについて活性を比較した。Ni/SBA-tz-N(Py)_{2-x} では、配位子固定密度の増大に伴い [Ni(L)₂] のような配位飽和な錯体種が担体上に形成されやすくなり、これが置換活性を示さないため活性が低下するのに対し⁴⁾、M=Co の触媒では配位子と金属が 1:1 の組成からなる錯体種が多く形成され、余剰の配位子が Co の流出抑制効果を示すために触媒活性が維持される¹⁾。そこで新たに調製した M=Fe および

な錯体種 $[\text{Fe}(\text{L})_2]$ が一部形成しており、それが置換不活性で触媒活性を示さないことが考えられる。これに対し、 $\text{Fe/SBA-tz-N(Py)}(\text{COOH})_x$ では $x = 1.0$ の触媒が最も活性が高く、また $x = 2.0$ の触媒が最も高いエホキシド選択性を示した。これは担体表面上で配位子同士が近接している場合、空気中の酸素や水に由来するオキシ基や配位子に含まれるカルボキシ基が架橋した二核錯体が形成されることで活性点構造が変化し、反応性にまで影響が及ぶことが考えられる。

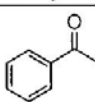
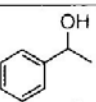
最も活性の高かった $\text{Fe/SBA-tz-N(Py)}_2-0.5$ について、様々な基質に対する酸化触媒能を検討した(表 1)。エチルベンゼン(EB)の酸化では、二級炭素の酸化のみが進行していたことから、鉄錯体上に発生した活性種はラジカル的性質を強く帯びた種であると推測される。しかしスチレン(S)を基質とした場合には、主生成物はラジカル的な反応を経て生じるベンズアルデヒドであったものの、 $\text{C}=\text{C}$ への酸素原子の付加物であるスチレンオキシドの生成も確認され、さらにチオアニソール(TA)の硫黄原子への酸素添加によるスルホキシド生成も進行したことから、親電子的な性質を帯びた活性種による反応も併発しているものと推測される。ところで TPA を支持配位子とした単核鉄錯体と H_2O_2 や過酢酸との反応により形成される高原子価鉄オキシ(Fe(IV or V)=O)種は、酸化剤の種類や添加物の有無に応じてその反応性が変化することが報告されている。すなわちアルケンの酸化に際しては、酸化剤の種類や反応条件に応じて発生する活性種における鉄の酸化状態・分子構造が異なり、過酢酸を酸化剤とした場合には Fe(IV)=O 種が発生してラジカル的な反応によるアリル酸化が進行するのに対し、過酸化水素を酸化剤とした場合、反応系に大過剰の酢酸が添加されることで酢酸イオンが配位した Fe(V)=O 種が発生して親電子的反応によるエホキシ化が優先的に進行し、酢酸が存在し

ないときには水に由来する水酸基が配位した Fe(V)=O 種が活性種となって酸素と水酸基の協奏的な移行反応による *cis*-1,2-ジオール化が進行する⁹⁾。本研究で開発した Fe 触媒による過酸化水素を酸化剤とするシクロヘキセンの酸化反応ではアリル酸化が優先的に進行したことより、ラジカル的な反応性を示す Fe(IV)=O 種が活性種となっていると推測される。開発した触媒は TPA に類似した配位子からなるものの、ヒリジル基よりも電子供与能・配位力が低いトリアゾリル基を含むために鉄中心の立体および電子の特性が異なり、 Fe(III)-(OOH) 中間体の O-O 結合のイオニック開裂を経た Fe(V)=O 種生成は起こりにくいものと考えられる。

2. 2. トリス(ピラゾリル)ボレート配位子を用いた触媒反応機構の解明と固定化錯体触媒の開発

酸化酵素や酸素分子の運搬・貯蔵を行うタンパク質では、酸素分子や過酸化物を結合・活性化する非ヘム金属中心が複数のイミダゾリル基由来の窒素原子に保持された構造が多くみられる(図 2(a))¹⁰⁾。そしてこのような金属中心に類似した配位環境を構築できる金属支持配位子の1つにトリス(ピラゾリル)ボレート、通称 Tp^R (図 2(b))がある。この配位子はイミダゾールの構造異性体であるピラゾールの脱プロトン体3個がホウ素に結合したもので、ホウ素にはさらにもう1つ官能基(水素化物イオンやアルキル基等)が結合している。これによりホウ素中心は4配位のボレートアニオン(陰イオン)種となっており、 Tp^R 全体で-1個イオンとなる。ところで1分子中に複数の金属配位基を含む多座配位子では、キレート(1つの金属中心に複数の配位基が同時に結合した状態)を形成することで系全体のエントロピーが増大するために平衡は錯体を形成した状態に偏ることが知られており、このような熱力学的安定化効果は“キレート効果”と称される。3座配位子として機能する Tp^R の場合、このキレート効果により高い錯体形成能を示すことに加え、前述のように Tp^R 自体が-1個アニオンであるために金属との間に静

表 1. $\text{Fe/SBA-tz-N(Py)}_2-0.5$ の酸化触媒活性

substrate	oxidized products	
	major	minor
		
		
		

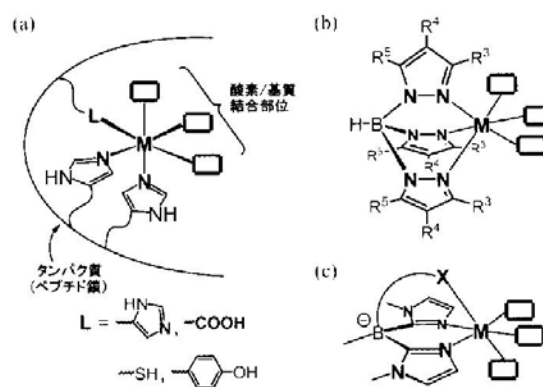


図 2. 酵素の活性点とアニオン性キレート配位子

電引力(クーロン相互作用)が働き解離しにくいという特徴を持つ。また Tp^R のピラゾリル基として様々な置換基を持つものが適用可能であり、このことに基づく分子設計に応じた金属錯体の特性制御が比較的容易に行える。そのため錯体化学全般で広く用いられ、これまでに多くの不安定錯体種の単離・構造決定等にも貢献すると共に、錯体触媒における配位子としての応用も検討されてきた⁽¹¹⁾。そこで本研究では、 Tp^R を用いて Ni 錯体触媒によるアルカン酸化機構の解明を目指した基礎研究を行った⁽¹²⁾。さらに Tp^R を無機酸化物担体上に固定した固定化錯体触媒の開発を行った⁽¹⁴⁾。

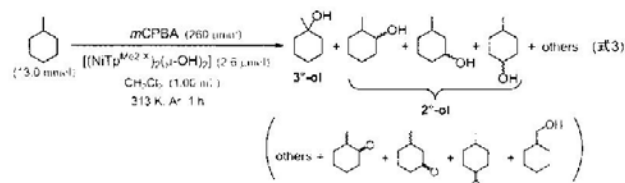
2. 2. 1. ニッケル錯体触媒によるアルカン選択水酸化の反応機構の解明

触媒中の金属活性点における酸化剤の活性化過程で生じる金属-酸化剤付加体は、熱的に不安定な化学種であることが多いが、この不安定種の化学的特性についての知見は、触媒反応機構の直接的な理解につながるのみならず、これを更なる分子設計にフィードバックすることで、より高性能な触媒開発につながることを期待される。そこで本研究では Ni 錯体触媒による *m*CPBA を酸化剤とするアルカン水酸化機構の解明を目指して、モデル錯体による検討を行うこととした。ところで *m*CPBA は有機合成化学における汎用的な酸化剤であり、高温であれば触媒不在でもアルカンの酸化が進行するが、これは O-O 結合の開裂によって生じたフリーラジカル種が活性種であるために反応選択性はきわめて低い。しかし適切な触媒と組み合わせることで、温和な条件でも酸化反応が進行するようになり、かつ触媒の構造や電子的特性に応じた反応選択性が発現する。従って Ni 錯体触媒による *m*CPBA を酸化剤とした反応過程において、Ni 中心にアシルペルオキシドイオンが遷位した中間体の形成を経て反応が進行するものと推定されている。しかし我々が開発した固定化錯体触媒も含め、既報の Ni 錯体触媒において反応中間体は一切検出されておらず、反応機構に関する提案は推測の域を出ない⁽¹⁵⁾。そこで我々は、置換基の導入により錯体金属中心の立体および電子的特性を自在に制御することが可能な Tp^R を支持配位子とする Ni(II)錯体を用いて、錯体の分子構造と触媒特性の相関の解明、および反応中間体を検出・同定に基づく反応機構の考察を行なった。

まず他の Ni 錯体触媒と同様に、シクロヘキサンに対する酸化触媒活性を検討したところ、 Tp^R の立体および電子的特性が触媒活性発現の鍵となっていることが明らかとなった。錯体形成時に金属中心をかき高いイソプロピ

ル(iPr)基が覆う Tp^{Pr2} を配位子とする錯体では、iPr 基の酸化(分子内反応)は進行したものの、外部より添加したシクロヘキサンの酸化は進行しなかった。一方立体障害が小さいメチル(Me)基が金属近傍に位置する Tp^{Me2} を配位子とする錯体は、シクロヘキサンを高選択的に対応するアルコール(シクロヘキサノール)へと変換し、アルカン水酸化反応に対する触媒活性を有することが明らかになった。さらに立体的な環境を維持したまま電子状態のみ摂動を加えるために Tp^{Me2} のピラゾリル基の4位(4x2(b))における R^4 に電子吸引基である臭素(Br)を導入した $\text{Tp}^{\text{Me2,Br}}$ を配位子とする錯体では、反応速度は低下するものの生成物に占めるアルコールの選択性が向上した⁽¹²⁾。

さらに基質をメチルシクロヘキサンとしたところ、 Tp^{Me2} および $\text{Tp}^{\text{Me2,Br}}$ 錯体を触媒とすることで、C-H 結合開裂エネルギーが高いものの立体障害が小さい2級炭素部位の酸化が優先した(式3; 生成量 2°-ol > 3°-ol)。触媒が存在しないときには C-H 結合開裂エネルギーが低い3級炭素部位が選択的に酸化される⁽¹²⁾。以上の結果は、錯体分子中の立体的に込み合った Ni 中心上に発生した活性種により酸化反応が進行していることを意味しており、金属支持配位子の精密分子設計によって、より高度な反応選択性(位置あるいは立体選択性)の発現が期待できることを示唆するものである。



触媒活性を示した Tp^{Me2} および $\text{Tp}^{\text{Me2,Br}}$ 錯体、および分子内でのアルキル置換基の酸化のみが進行した Tp^{Pr2} および $\text{Tp}^{\text{Pr2,Br}}$ 錯体について、低温での Ni(II)-OH 錯体 $[\text{Ni}(\text{Tp}^R)_2(\mu\text{-OH})_2]$ と *m*CPBA の反応を UV-vis や *in situ* IR スペクトルにより追跡したところ、Ni(II)-アシルペルオキシド付加体 $[\text{Ni}^{\text{II}}(\text{OOC}(\text{-O})\text{C}_6\text{H}_4\text{Cl})\text{Tp}^R]$ が生成していることが確認できた。このアシルペルオキシド付加体の安定性は、触媒特性と同様に Tp^R に導入した置換基の立体的なかさ高さおよび電子的特性に支配されており、外部から基質が接近できない程にかき高い iPr 基が Ni 中心を覆い、かつ電子吸引基である臭素が導入されている $\text{Tp}^{\text{Pr2,Br}}$ を配位子とする錯体が最も安定であった。しかしいずれの付加体も溶液状態で -40°C 以上では分解してしまい、単離には至らなかった⁽¹²⁾。Ni(II)-アシルペルオキシ錯体の本質的な反応特性を理解するためには、アシルペルオキシ錯体そのもの単離する必要がある。そこで Tp^R の分子設計によって、外部基質に対する反応性を維持したまま

安定化を図った。置換基の特性について精査し、適度な立体的なかさ高さと電子吸引性に基づく安定化効果が期待され、さらには酸化耐性にも優れるトリフルオロメチル(CF₃)基がNi中心を覆うTp^{CF₃M_e}を選択した。これにより得られたNi(II)-*m*CPBA錯体[Ni^{II}(OOC(=O)C₆H₄Cl)Tp^{CF₃M_e}]¹³は、基質不在であれば期待通り室温においても安定であり、単離およびX線単結晶構造解析による分子構造の決定に成功した⁽¹³⁾。

単離したNi(II)-*m*CPBA錯体の様々な基質に対する酸化特性を速度論的解析および反応生成物分析により検討した。この錯体は*m*CPBAの持つ本質的な反応性を維持しており、スルフィドの硫黄原子やアルケンのC=Cへの親電子的酸素移行に活性を示した。さらに興味深いことに、この錯体は1,4-シクロヘキサジエンや9,10-ジヒドロアントラセン、キサンテン、フルオレン等の活性メチレン化合物(C-H結合解離エネルギーが低いメチレン部位を有する化合物)から水素原子を引き抜くことが明らかとなった(図3)。この水素引き抜き反応は、Ni(II)-*m*CPBA錯体の消失速度が錯体濃度と基質濃度の両方に依存している2次反応であったが、その反応速度と各基質のC-H結合解離エネルギーの間には相関はなく、立体障害が小さくニッケルに配位したアシルペルオキシドに接近しやすいと考えられる1,4-シクロヘキサジエンとの反応が最も速かった。したがってNi(II)-*m*CPBA錯体は、O-O結合を開裂することなく直接脂肪族炭化水素を酸化することが明らかとなった。その一方、シクロヘキサンを基質とした場合、対応する酸化生成物は得られるものの、Ni(II)-*m*CPBA錯体の消失過程はその速度は錯体濃度のみに依存している1次反応であってシクロヘキサンの濃度には依存していなかった。これは基質のC-H結合解離エネルギーが高い場合には、Ni(II)-*m*CPBA錯体が直接の活性種ではないことを意味しており、ニッケルに配位した*m*CPBAのO-O結合開裂により生じた高原子価Ni-オキソ(Ni(III)=O)種あるいはNi(II)-酸素ラジカル付加体が活性種となっているものと考えられる⁽¹³⁾。以上より、

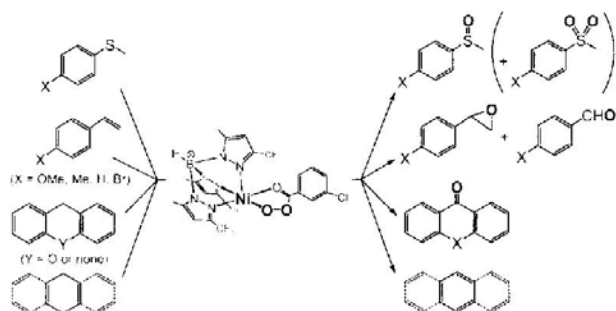
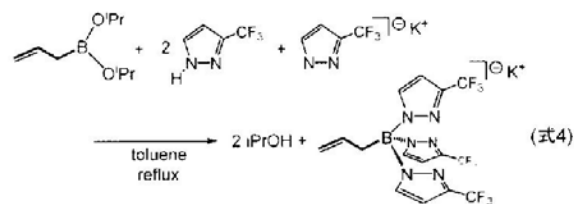


図3. [Ni^{II}(OOC(O)C₆H₄Cl)Tp^{CF₃M_e}]¹³の基質酸化活性

Ni(II)-*m*CPBA錯体は基質に応じて活性種、あるいは活性種の前駆体として機能することが明らかとなった。

2. 2. 2. 固定化錯体触媒への展開

Tp^Rを配位子とする錯体を固体担体に担持することにより不均一系触媒反応に適用した例がこれまでにいくつか報告されているが、これらの固定化錯体触媒において、Tp^R配位子錯体はシリカゲル表面のシラノール(Si-OH)基との相互作用(=吸着)を介して固定されている⁽¹⁶⁾。しかし吸着による担持では反応中に錯体分子が溶出してしまうため、固定化錯体触媒としてはTp^R自体が担体上に共有結合により固定化されていることが望ましい。ところで我々は、Tp^Rの類縁体と見なせるイミダゾリルポレート配位子L(図2(c))のホウ素にアリル基(-CH₂-CH=CH₂)を導入することで、有機チオール基で修飾したシリカゲル担体に共有結合を介して固定化することに成功し、これを用いた固定化錯体触媒を開発している。そこで本研究ではTp^Rのヒドリド基をアリル基に置換したallyl-Tp^Rを合成し(式4)、これをチオール基修飾メソ多孔性シリカゲル担体への固定化することで固定化錯体触媒を開発した⁽¹⁴⁾。



合成したallyl-Tp^{CF₃}の錯形成能を確認するため、配位構造に応じた特徴的なUV-visスペクトルを与えるCo(II)錯体の合成を検討した。合成した錯体のうち単結晶X線構造解析によりCo(II)-Br錯体[Co^{II}(allyl-Tp^{CF₃})(Br)]の分子構造を決定した。Co(II)中心は歪んだ四面体型の配位構造を採っていたが、溶液および固体状態でのUV-visスペクトルにおいて600~700 nmの領域に四面体型Co(II)種のd-d遷移に帰属される特徴的な吸収帯を与えることと一致する。またCo(II)-Br錯体の合成時に副生した錯体についても単結晶X線構造解析に成功し、これが6配位八面体型Co(II)錯体[Co^{II}(allyl-Tp^{CF₃})]であることを明らかにした。さらに5配位Co(II)錯体種として、allyl-Tp^{CF₃}のカリウム塩と酢酸コバルト(II)(=Co(OAc)₂·4H₂O)の反応によりCo(II)-OAc錯体[Co^{II}(allyl-Tp^{CF₃})(OAc)]も合成した。これらの錯体の溶液および固体状態でのUV-visスペクトルを比較したところ、いずれの錯体も溶液状態と固体状態でスペクトルの形状は一致しておりCo(II)中心の配位構造は保たれていること、そしてCo(II)中心の配位数が

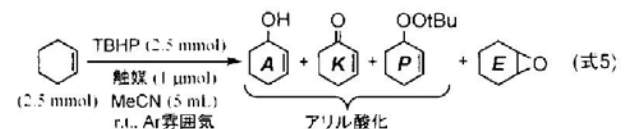
増加するにつれて吸収極大波長が高エネルギー(短波長)にシフトしていた。

配位子を固定するためのチオール基修飾メソ多孔性シリカゲル担体は、前述のアミノピリジル配位子固定化担体の前駆体である SBA-N₃ と同様の手法により調製した。シリカ源である TEOS (= Si(OEt)₄) と有機チオール含有シラノールエステル MPTMS (= HS(CH₂)₃Si(OMe)₃) の仕込み比 (= TEOS : MPTMS = (100 - x) : x) を調節することで、細孔壁表面のチオール基修飾量を制御した。ここで Tp^{CF3} の立体的なかさ高さを考慮すると配位子固定量の増加は見込めないことから、チオール基の密度をあまり高くする必要はないと判断し x = 0.5 または 1.0 とした。その後担体表面の残留シラノール基をトリメチルシリル基によりエンドキャップを施すことで SBA-SH-x を得た。これと allyl-Tp^{CF3} に対して AIBN を開始剤とするチオール-ene カップリング反応を適用することで配位子固定化担体 SBA-SH-Tp^{CF3}-x を調製した。ここで x = 0.5 の担体では、チオール基と Tp^{CF3} の固定量はほぼ等しかった (SH : 0.052 mmol·g⁻¹, Tp^{CF3} : 0.051 mmol·g⁻¹) のに対し、x = 1.0 の担体では導入されたチオール基の約 3 割には Tp^{CF3} が連結しなかった (SH : 0.097 mmol·g⁻¹, Tp^{CF3} : 0.05 mmol·g⁻¹)。そこで Tp^{CF3} が連結しなかった残留チオール基に対して塩化アシル (= CH₃C(=O)Cl) を作用させることによりチオ酢酸エステルに変換したアシル化処理配位子固定化担体 SBA-SAc-Tp^{CF3}-x も調製した(図4)。

調製した配位子固定化担体に臭化コバルト(II) (= CoBr₂·6H₂O) のアセトニトリル溶液を作用させることで、対応する固定化コバルト錯体触媒 Co/SBA-SH or SAc-Tp^{CF3}-x を得た(図4)。担体表面に形成されている Co(II)錯体活性点の構造を明らかにするため、固体拡散反射 UV-vis スペクトルを測定し、上述の 4、5 および 6 配

位 Co(II)錯体 ([Co^{II}(allyl-Tp^{CF3})(Br)], [Co^{II}(allyl-Tp^{CF3})(OAc)], [Co^{II}(allyl-Tp^{CF3})₂]) のスペクトルと比較した。x = 0.5 の触媒のスペクトルは、残留チオール基のアシル化処理の有無に関わらず、[Co^{II}(allyl-Tp^{CF3})(Br)] のスペクトルに類似のハターンを与えた。担体上のチオール基および Tp^{CF3} の固定量と Co(II)導入量がほぼ等しいことを考え合わせると、チオール基固定密度が低い触媒では、担体に連結された Tp^{CF3} に保持された 4 配位 Co(II)活性点が高選択的に生成しているものと推測される。なお残留チオール基のアシル化処理を施していない Co/SBA-SH-Tp^{CF3}-0.5 のスペクトルには、420 nm 付近に [Co^{II}(allyl-Tp^{CF3})] において観測されるものと類似した吸収帯も観測されたことから、6 配位 Co(II)種も同時に生成しているものと推測される。一方チオール基固定密度が高い x = 1.0 の触媒では、残留チオール基のアシル化処理の有無に応じて錯体活性点の構造が大きく異なっていることが判明した。すなわち Co/SBA-SAc-Tp^{CF3}-1.0 のスペクトルは [Co^{II}(allyl-Tp^{CF3})(OAc)] のそれに類似していたことから、残留チオール基をアセチル化処理した触媒では 5 配位の Co(II)錯体が多く形成されているのに対し、Co/SBA-SH-Tp^{CF3}-1.0 のスペクトルは [Co^{II}(allyl-Tp^{CF3})(OAc)] と [Co^{II}(allyl-Tp^{CF3})₂] のスペクトルを重ね合わせたようなパターンであり、5 配位種と 6 配位 Co(II)錯体が共存しているものと推定される。

調製した触媒について、アルキルヒドロペルオキシド (*tert*-BuOOH ; TBHP) を酸化剤とするアルケン(シクロヘキセン)の酸化活性試験を行った(式5)。いずれの触媒を



用いてもアリル位酸化が優先的に進行したが、特にシクロヘキセニル基と *tert*-ブチルアルキルペルオキシラジカルのカップリング生成物 (P) が多く生成していたことより、Co 錯体活性点は TBHP の分解に寄与してラジカル的な反応が進行したものと解釈できる。Co 原子 1 個当たりの活性(触媒回転数 ; TON) が最も高かった触媒は Co/SBA-SAc-Tp^{CF3}-0.5 であり、次いで活性が高かった触媒は Co/SBA-SAc-Tp^{CF3}-1.0 であった。よって残留チオール基は触媒活性を阻害してしまうこと、Tp^{CF3} に保持された 4 または 5 配位 Co(II)種が高い活性を示す一方、6 配位 Co(II)種は低活性であるものと推測される。また特筆すべきは、担体に固定していない [Co^{II}(allyl-Tp^{CF3})(Br)] を液相均一系反応に適用した場合よりも、固定化錯体触媒の方が高活性であったことである。これは液相均一系

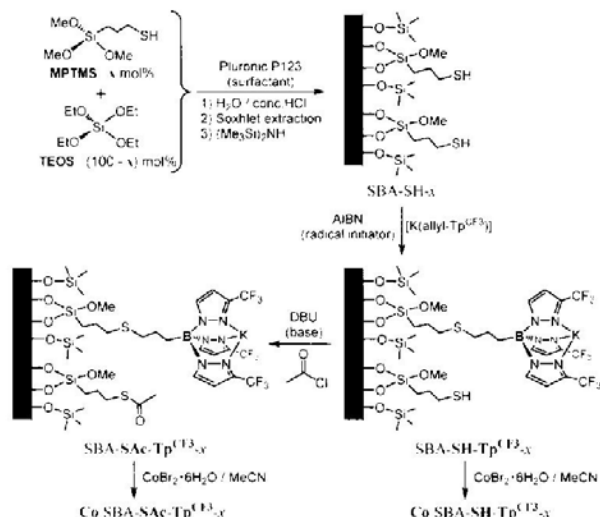


図4. Tp 配位子固定化錯体触媒の調製経路

反応では触媒自体の酸化的分解が起こりやすいのに対し、固定化錯体触媒では錯体触媒活性点が孤立しているために分解反応が起こりにくいと考えられる。

2. 3. イミダゾリル基含有キレート配位子を用いた固定化錯体触媒の開発

前節で解説した Tp^{R} は、一見複雑な構造体であるものの合成は容易であり、また目的・用途に合わせた分子設計も行いやすいという利点を有するが、ヒラゾリル基とホウ素との間の B-N 結合は比較的イオン結合性が高く、酸性条件下では加水分解を受けやすいという欠点があることから、触媒に適用するにあたっては反応条件が制約されることが懸念される。またピラゾールはイミダゾールの構造異性体であるが、イミダゾールの方が塩基性が高く、配位子として機能する際には金属中心への電子供与能が高いことが知られている。また酸化酵素の金属錯体触媒活性点における配位基はイミダゾリル基である。そこで我々は、共有結合性が高く加水分解耐性に優れた B-C 結合を基本骨格とし、かつイミダゾリル基を金属配位基とするアニオン性キレート配位子 L^{X} (= $[\text{B}(\text{Im}^{\text{NMe}_2})_2\text{MeX}]$) を開発してきた⁽¹⁾。 L^{X} はアニオン電荷を担っているホウ素中心上に様々な官能基 X の導入が可能であり、この特性を活かしてチオール基をリンカーとした固定化鉄錯体触媒の開発にも既に成功している⁽¹²⁾。そこで本研究では、 L^{X} における X としてアセトキシ基の導入が可能であることを踏まえ⁽¹⁸⁾、非ヘム鉄酸化酵素と同様なイミダゾリル基とカルボキシ基が共存する触媒活性金属配位場の構築や、水素結合形成に基づく触媒特性の向上を期待し、カルボキシ基修飾担体に L を固定することによって酵素模倣型固定化錯体触媒を開発した⁽¹⁹⁾。

担体となるカルボキシ基修飾メソ多孔性シリカゲルは、本研究で活用してきた SBA-N_3 や SBA-SH と同様の手法によりカルボキシ基固定量を制御したものを調製した。シリカ源である TEOS とカルボキシ基含有シランカップリング剤 CES (= $\text{Na}_2\text{O}_2\text{CC}_6\text{H}_4\text{SiO}(\text{OH})_2$) の仕込み比を調節することで、カルボキシ基修飾量を変化させたメソポーラスシリカ担体 (= $\text{SBA-COOH-}x$; x は CES の仕込み比, $x = 0.5, 1.0, 2.0 \text{ mol\% of Si}$) を調製した。調製した $\text{SBA-COOH-}x$ をアルカリ分解し、その分解物の $^1\text{H NMR}$ による分析の結果、担体のカルボキシ基修飾量は、 SBA-N_3 や SBA-SH の場合と同様に、導入する官能基前駆体 (= CES) の仕込み比に対応していることを確認した。 $\text{SBA-COOH-}x$ に $n\text{BuLi}$ を作用させてカルボキシ基をリチウム塩化した後に L^{Q} を作用させることで、配位子固定化担体 $\text{SBA-COOH-L-}x$ に誘導した(図 5)。担体上の

カルボキシ基と L の固定量の相関を検討したところ、 $x = 0.5$ および 1.0 の配位子固定化担体ではほぼ全てのカルボキシ基に L が連結していたのに対し、担体調製時のカルボキシ基導入量が多い $\text{SBA-COOH-L-}2.0$ では L が連結していないカルボキシ基が残留していた。そしてこれらの配位子固定化担体に酢酸鉄(II) (= $\text{Fe}(\text{OAc})_2$) を反応させることで、固定化鉄錯体触媒 $\text{Fe/SBA-COOH-L-}x$ を得た。 $x = 0.5$ および 1.0 の触媒では L と鉄の導入量がほぼ等しかったのに対し、 $x = 2.0$ の触媒では L の固定量を上回る鉄が導入されており、残留カルボキシ基も金属配位サイトとなっているものと推定した(表 2)。

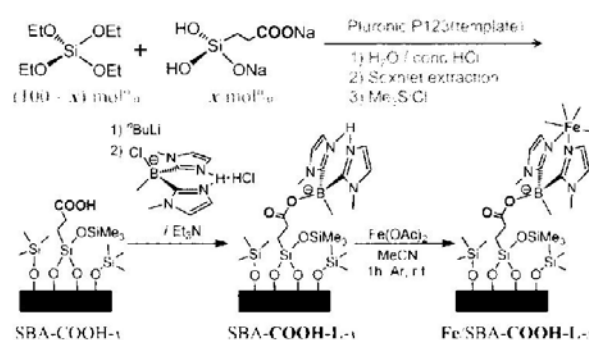


図 5. $\text{SBA-COOH-L-}x$ の調製

表 2. $\text{Fe/SBA-COOH-L-}x$ の酸化触媒活性

Cat.		x	L / Fe on Cat.	TON per Fe (E/(A+K))	TON on reuse
Fe/SBA-COOH-L-x		0.5	1.0	15.4 (0.22)	6.7 (0.17)
		1.0	1.0	6.4 (0.19)	9.5 (0.20)
		2.0	0.81	9.3 (0.12)	5.8 (0.20)
Fe/SBA-COOH-x		1.0	—	6.2 (0.22)	not tested
		2.0	—	3.6 (0.10)	not tested

調製した固定化鉄錯体触媒について、過酸化水素を酸化剤とするシクロヘキセンの酸化活性試験を実施した(表 2)。L を固定していない $\text{SBA-COOH-}x$ に Fe(II) を導入した、カルボキシ基のみが鉄を保持している触媒 ($\text{Fe/SBA-COOH-}x$; $x = 1.0, 2.0$) に比べ、L を固定した担体に鉄を導入した触媒のほうが鉄原子 1 個当たりの触媒回転数が高かった。ところで担体に固定していない L^{Ph} (= $[\text{B}(\text{Im}^{\text{NMe}_2})_2\text{MePh}]$) を配位子とする Fe(II) 錯体 $[\text{Fe}(\text{L}^{\text{Ph}})]$ による液相均一系での過酸化水素によるシクロヘキセンの酸化はほとんど進行しなかった。よって L を担体に固定することで配位不飽和な Fe 錯体 $[\text{Fe}(\text{L})]$ が形成されるようになり、これが本質的に触媒活性であると推測される。一連の Fe 触媒 $\text{Fe/SBA-COOH-L-}x$ の過酸化水素を酸化剤としたシクロヘキセンおよびシクロヘキサンに対

する酸化活性は $x=0.5 > 2.0 > 1.0$ の序列であった。特に $x=0.5$ と 1.0 の触媒では、固定されているLと鉄原子の量がともにほぼ等しい(L/Fe=1)ことから、この触媒活性の差異は担体上のカルボキシ基およびLの固定密度に応じた[Fe(L)]サイトの疎密(サイト間の距離の違い)によるものと推測される。すなわち $x=0.5$ の触媒では多くの[Fe(L)]サイトが孤立した単核錯体種として存在するのに対し、これよりも[Fe(L)]サイトが密に存在する $x=1.0$ の触媒では何らかの配位子が鉄中心間を架橋して複核錯体化が進んでいるものと考えられる。なお $x=2.0$ の触媒では残留カルボキシ基が配位子となった特異な活性点が形成されていることが考えられる(図6)。なおいずれの触媒による反応でも、シクロヘキセンを基質とした際にはアリル位酸化が優先的に進行し、またシクロヘキサンを基質とした場合にもケトンが主生成物であったことから、これらの触媒と過酸化水素の反応により生じる酸化活性種は、酸素原子添加活性よりもC-H結合からの水素引き抜きに活性な種であり、前述のFe/SBA-tz-N(Py)₂およびFe/SBA-tz-N(Py)(COOH)と同様に、Fe(III)-OOH種のO-O結合のラジカル的開裂によりFe(IV)=O種を生じているものと推測される。

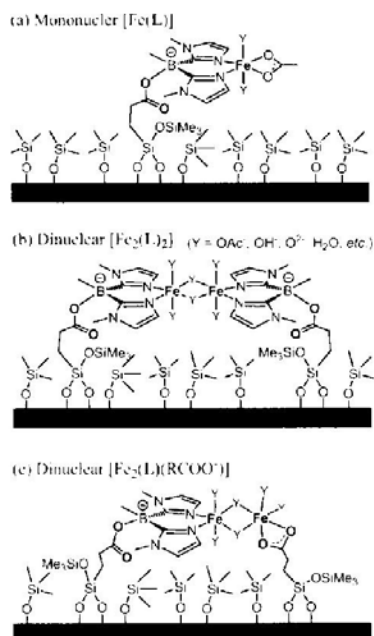


図6. Fe/SBA-COOH-L-xにおける推定活性点構造

3. ペプチド修飾メソ多孔性シリカによる不斉ナノ空間反応場の構築と触媒特性の解明

アミノ酸のキラリティー(対映性)に基づく不斉空間認識能をナノ構造触媒に導入することを目的として、本共同研究では様々な鎖長(2~30量体程度)のペプチドで修飾したメソ多孔性シリカゲルを開発してきた⁽²⁾。その過

程でジペプチド修飾 SBA-15 は酸-塩基触媒機能を示し、ケトンとアルデヒドのカップリングによるβ-ヒドロキシカルボニル化合物の生成(直接的アルドール反応)を触媒することを見出したが、活性・生成物の立体選択性ともに低く、またメソ多孔性シリカゲルの担体効果等、不明な点が多く残っていた。そこで本研究ではカルボン酸残基を有し酸触媒として機能することが期待されるアスパラギン酸(Asp)と、イミノ基に起因する塩基触媒能をホスプロリン(Pro)を含むオリゴペプチド(ジペプチド Asp-Pro 及びトリペプチド Asp-Pro-Pro)で修飾したメソ多孔性シリカゲル、すなわち固定化オリゴペプチド触媒 SBA-Asp-(Pro)_n ($n=1$ or 2 ; 図7)を調製し、それらのアルドール反応に対する不斉触媒能を検討した(式6)⁽²⁰⁾。

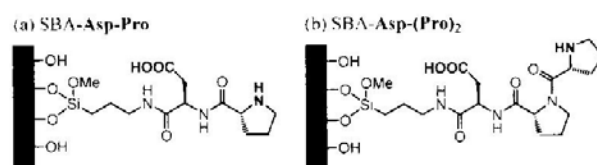
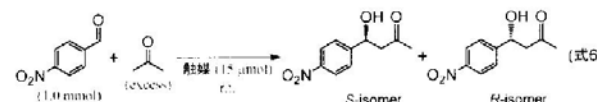


図7. 固定化オリゴペプチド触媒の構造



固定化オリゴペプチド触媒 SBA-Asp-(Pro)_nは、ペプチドを固定化していないアミノ基修飾メソ多孔性シリカゲル SBA-NH₂よりも反応初速度が高く、高収率でアルドール体を与えた。またトリペプチド触媒($n=2$)の方がジペプチド触媒($n=1$)よりも高活性であったが、これは担体に固定していないオリゴペプチドを液相均一系反応の触媒に適用した場合と同様の傾向である。

担体の効果を検証するために、Pro-Pro-Aspをアミノメチルポリスチレンレジンに固定化した触媒(Resin-Asp-(Pro)₂; Resin触媒)を調製し SBA-Asp-(Pro)₂(SBA触媒)と活性を比較したところ、SBA触媒の方がResin触媒よりも20倍以上の反応初速度を示し、高活性であった。また興味深いことにこれらの触媒では立体選択性が異なっていた。Resin触媒では65%の鏡像体過剰率(ee)でS体が優先的に生成したのに対し、SBA触媒では16%という低いeeであるもののR体が優先的に生成した。液相均一系において同じ配列からなるトリペプチド(=NH₂-Asp-Pro-Pro-COOH)はS体を優先的に生成することから、SBA触媒では反応に寄与する活性点が変わったことが示唆された。

アルドール反応は酸点と塩基点の協働作用により促進されることが知られているため、触媒上の官能基を選択的に不活性化することで、反応に寄与する酸塩基点の特定を試みた。Asp側鎖のカルボキシ基をメチルエステル

化した Asp(OMe)-Pro-Pro を SBA-15 に固定した SBA-Asp(OMe)-(Pro)₂ は、エステル化していない SBA 触媒よりも高活性であった。このとき立体選択性はほぼほとんど変化がみられなかった。すなわちメソ多孔性シリカゲル担体に固定化したトリヘプチドでは、Asp のカルボキシ基は活性や立体選択性の発現に寄与せず、むしろ活性を低下させることが判明した。SBA-Asp-(Pro)₂ において立体選択性が主に Pro によって決定されることは、Pro のみを D 体とした SBA-(L)Asp-(D)Pro₂ において立体選択性が反転したことから確認された。一方 Resin 触媒上のカルボキシル基のメチルエステル化を施した Resin-Asp(OMe)-(Pro)₂ では、エステル化していない Resin 触媒とは生成物の立体選択性が反転した。したがってイミノ基とカルボキシ基による多点的な相互作用が存在すれば S 体が優先的に生成するのに対し、イミノ基単独では R 体を優先的に生成することが明らかとなった。SBA 触媒における Asp のカルボキシ基が立体選択性の発現に寄与しない理由としては、SBA 担体表面上に存在するシラノール(Si-OH)基とカルボキシ基が水素結合していることが考えられる。また SBA 触媒のシラノール基をトリメチルシリル基でキャップしたところ、反応初速度は 1/7 程度になり、著しい活性低下が認められた。Jones らは、SBA-NH₂ における直接的アルドール反応に対して有効な酸塩基点の検討を行っている⁽²¹⁾。これによれば、カルボキシ基とアミノ基の酸塩基対よりも、酸強度がカルボキシ基よりも弱くアミノ基のプロトン化を引き起こさないシラノール基とアミノ基の酸塩基対の方が高活性である。よってシラノール基がキャップされていない SBA 触媒では Jones らの報告と同様に、カルボキシル基とプロリン末端ではなく、シラノール基とプロリン末端が酸塩基対となり協働的に作用することで高い反応活性が発現したものと推測される。

4. 結言

2012 年度の研究で確立した、メソ多孔性シリカ担体のナノスケール細孔内部の有機官能基による化学修飾法を活用して、種々の固定化錯体触媒を開発した。担体上の配位子固定密度が適切に制御された固定化錯体触媒では、錯体触媒活性点どうしは適切な距離を隔てて配置されていることから、金属中心に発生した活性種が他の錯体触媒分子と反応することはなく、錯体自体の本質的な反応性を反映した触媒反応が進行したものと推測される。さらに錯体化学的なアプローチにより触媒反応機構の解明や担体表面に形成された錯体触媒活性点の分子構造解析を行い、固定化錯体触媒が固体触媒における活性点構造

の精密制御の手法の 1 つとして有効であることを示せた。

また固定化オリゴヘプチド触媒において、シリカゲル担体が触媒活性に重要な役割を担っていることが明らかになった。このことは、担体と分子触媒(金属錯体触媒および有機分子触媒)の協働効果を巧みに取り入れることで、新たな高機能性触媒が創出できることを示している。

今後は本稿で紹介した、精密有機合成の環境調和型プロセスの構築に貢献しえる触媒の更なる高性能化を推し進めるとともに、エネルギーや環境問題の解決に貢献しえる触媒の開発も推進していく計画である。

参考文献

- (1) 引地 史郎, 中澤 順, *触媒* **52** (2010) 243.
- (2) 引地 史郎, 内藤 周次, 吉田 曉弘, 中澤 順, *神奈川大学工学研究新報* **36** (2013) 77.
- (3) 引地 史郎, 中澤 順, *化学工業* **64** (2013) 756.
- (4) T. Akashi, J. Nakazawa, S. Hikichi, *J. Mol. Catal. A: Chem.*, **371** (2013) 42.
- (5) J. Nakazawa, T. Hori, T. D. P. Stack, S. Hikichi, *Chem. Asian J.*, **8** (2013) 1191.
- (6) T. Nagataki, Y. Tachi and S. Itoh, *Chem. Commun.*, (2006) 4016
- (7) Y. Doi, J. Nakazawa, S. Hikichi, to be submitted.
- (8) J. Nakazawa, A. Yata, T. Hori, T. D. P. Stack, Y. Naruta, S. Hikichi, *Chem. Lett.*, **42** (2013) 1197.
- (9) W. N. Oloo, Y. Feng, S. Iyer, S. Parmelee, G. Xue, L. Que, Jr., *New J. Chem.*, **37** (2013), 3411.
- (10) 引地 史郎, *触媒* **46** (2004) 262.
- (11) 引地 史郎, *神奈川大学工学研究新報* **29** (2006) 10.
- (12) S. Hikichi, K. Hanaue, T. Fujimura, H. Okuda, J. Nakazawa, Y. Ohzu, C. Kobayashi, M. Akita, *Dalton Trans.*, **42** (2013) 3346.
- (13) J. Nakazawa, S. Terada, M. Yamada, S. Hikichi, *J. Am. Chem. Soc.*, **135** (2013) 6010.
- (14) A. Nakamizu, T. Kasai, J. Nakazawa, S. Hikichi, to be submitted.
- (15) T. Nagataki, K. Ishii, Y. Tachi, S. Itoh, *Dalton Trans.*, (2007) 1120.
- (16) M. M. Diaz-Requejo, T. R. Belderrain, M. C. Nicasio, P. J. Pérez, *Organometallics*, **19** (2000) 285.
- (17) S. Hikichi, M. Kaneko, Y. Miyoshi, N. Mizuno, K. Fujita, M. Akita, *Top. Catal.*, **52** (2009) 845.
- (18) K. Fujita, M. Akita, S. Hikichi, *Inorg. Chim. Acta*, **362** (2009) 4472.
- (19) 鶴田 智弘, 中澤 順, 引地 史郎, 第 112 触媒討論会, 2J05 (2013 年 9 月).
- (20) 吉田 曉弘, 海老 良典, 佐藤 隆介, 内藤 周次, 第 114 触媒討論会, 2D01 (2014 年 9 月).
- (21) N. A. Brunelli, K. Venkatasubbaiah, C. W. Jones, *Chem. Mater.*, **24** (2012) 2433.